NUCLEAR SCIENCE

Annual Report
1975

Lawrence Berkeley Laboratory
University of California/Berkeley

Prepared for the U.S. Energy Research and Development Administration under Contract W-7405-ENG-48

LBL-5075
c.1

Printed in the United States of America
Available from
National Technical Information Service
U.S. Department of Commerce
5285 Port Royal Road
Springfield, Virginia 22161
Price: Printed Copy $11.00 Microfiche $3.00

LBL-5075
UC-34c
Physics-Nuclear
TID 4500-R65

NUCLEAR SCIENCE

Annual Report
1975

B.G. HARVEY
Director

H.E. CONZETT
H.H. HECKMAN
W.D. MYERS
Editors

Lawrence Berkeley Laboratory
University of California/Berkeley

ERRATUM for LBL Nuclear Science Report LBL-5075, pg. 8 (1975).

Gamma and Alpha Decay from the 2.1-msec Isomer ^{213m}Ra

D. G. Raich, H. R. Bowman, R. E. Eppley, and J. O. Rasmussen,
Lawrence Berkeley Laboratory, University of California,
Berkeley, California 94720
and
I. Rezanka
Heavy Ion Accelerator Laboratory, Yale University,
New Haven, Connecticut 06520

An error was made in calculating the alpha-decay hindrance factors show in italics in Fig. 3 (p. 10) of the original article. Corrected values are given in the following table:

Final State in ^{209}Rn (keV)	Alpha Decay Hindrance Factors from Initial State	
	^{213m}Ra	^{213}Ra
214.7	1.0×10^4	6.1
110.1	2100	2.0
0.	1700	5.7

GENERAL INTRODUCTION

B. G. Harvey, Division Head

This is the first Annual Report of the Nuclear Science Division of Lawrence Berkeley Laboratory. The Nuclear Science Division was formed on November 1, 1975 as part of an extensive reorganization of the Laboratory's scientific structure. Most of its components came from the Nuclear Chemistry Division which had existed since 1946, initially under the leadership of Glenn T. Seaborg. Isadore Perlman became Director of the Division in 1958 and served in this capacity until Glenn Seaborg's return in 1972 from his service as Chancellor of the University of California and then as Chairman of the Atomic Energy Commission. Earl K. Hyde served as Deputy Director of the Division with Glenn Seaborg until Hyde became Deputy Director of the Laboratory in 1973.

During those 39 years, the Nuclear Chemistry Division had grown into a multidisciplinary organization whose research ranged over an increasingly large number of widely separated fields. The nuclear science components of the Nuclear Chemistry Division form the bulk of the Nuclear Science Division; these were joined by the Heckman Group from the Physics Division (now the Heckman/Greiner Group).

The new Division was charged with the responsibility of organizing all the Laboratory's research in nuclear science with the exception of heavy element chemistry and the medium energy nuclear science work in the Physics Division. It therefore has supervisory and financial responsibility for the high energy heavy ion nuclear science (Bevalac) research of several groups who elected to remain in the Physics Division because the major portion of their work is in high energy physics or medium energy nuclear sicence. In addition, the Nuclear Science Division is responsible for the operation of the 88-inch Cyclotron and its increasingly large Outside User program. (Operation of the SuperHILAC and Bevalac National Accelerators remains the responsibility of LBL's Accelerator Division).

The nuclear science research is done by twelve groups in the Nuclear Science Division plus three Physics Division groups. Of this total of fifteen, six groups work exclusively on high-energy heavy ion physics at the Bevalac, three work only at the 88-inch Cyclotron, while four use beams from both the Cyclotron and the SuperHILAC. The Nuclear Theory Group is involved in a wide range of activities with increasing emphasis upon high energy heavy ion physics. The Table of Isotopes Group is nearing completion of the Seventh Edition of the Table: the computer-prepared "manuscript" will go to the publisher early in 1977.

The Nuclear Science Division includes 44 professional permanent staff members, 47 post-doctoral fellows and U.S. visitors and 21 foreign visitors (these visitors come from Great Britain, Australia, Egypt, Mexico, France, Japan, Germany and India). The Division also includes 27 graduate students, and in the period covered by this report, it awarded 3 Ph.D. degrees.

During 1976, the work of the Division received two major reviews. The Division's Visiting Committee came to Berkeley in February and reported very favorably on our activities to the Laboratory Director. As part of an ERDA review of nuclear physics accelerators, the research at the 88-inch Cyclotron received a penetrating study and again the conclusions were high favorable.

The research that is described in this first Annual Report of the Nuclear Science Division continues the high tradition of excellence that was established by the Nuclear Chemistry Division. Our closer association with our colleagues in the Physics Division is rapidly bringing about a broadening of perspectives and a greater appreciation of the essential unity of low and high energy research. Even though financial limits may be placed upon the physical growth of the Nuclear Science Division, there are no restraints upon the intellectual development of its members. With the stimulus of our new colleagues and pushed by the new ideas that are continually exposed in our corridors and seminar rooms, the climate is indeed most favorable for the new Division.

CONTENTS

B. Nuclear Reactions and Scattering

1. Microscopic

a. Light Ions

2. Macroscopic

D. Mesonic Atoms and Atomic Physics

II. THEORY

A. Nuclear Reactions

1. Microscopic

I.

EXPERIMENTAL RESEARCH

A. NUCLEAR STRUCTURE

LONG-LIVED STATES AT HIGH EXCITATION ENERGIES IN ^{8}Be AND ^{10}B*

F. Ajzenberg-Selove,† C. F. Maguire,‡ D. L. Hendrie,
D. K. Scott, and J. Mahoney

This experiment was undertaken to study possibly narrow states at high excitation energies in ^{8}Be and ^{10}B. Above E_x = 19.2 MeV in ^{8}Be all known[1] states have intrinsic widths $\gtrsim$ 0.7 MeV with the exception of the T = 2 state at 27.492 MeV,[2] which has a $\Gamma \sim 10$ keV. One knows from the level structure of ^{8}Li that a sharp state [Γ < 40 keV] exists at E_x = 6.53±0.02 MeV.[3] Attempts in a study of ^{6}Li (t,p)^{8}Li to determine its J^{π} have been unsuccessful,[4] but Barker has predicted[5] a 4^+ state whose parameters [including $\gamma_n^2 \sim 0$] are consistent with the experimental observations. Thus, an isobaric analog T = 1 state would be expected in ^{8}Be at $E_x \sim 23$ MeV. Such a T = 1 state would be expected to be quite pure, since the nearest T = 0 4^+ states, observed in the phase shift analysis[6] of ^{4}He (α,α), are located at E_x = 19.9 and 25.5 MeV. The only other reported sharp state in ^{8}Li is at an E_x = 7.1±0.1 MeV [$\Gamma \sim 350$ keV].[7] Thus, we wished to study excited states with $E_x > 22$ MeV in order to try to observe the expected two T = 1 states.

The situation in the A = 10 triad is similar: the level structure of ^{10}B is quite well known[1] below E_x = 9 MeV. At higher energies only the states[8] at E_x = 11.53±0.04 and 12.57±0.03 MeV are definitely known to be quite sharp (Γ = 270±50 and 90±30 keV, respectively), although there is indication[9] of a number of relatively sharp resonances in ^{9}Be(p,γ_0) and (p,γ_1) [$\Gamma \approx 0.15$ to 0.5 MeV], corresponding to $10.8 < E_x < 19.7$ MeV. The results from ^{9}Be(p,p$_0$),[10] ^{10}B(e,e$'$),[11] and ^{11}B(p,d)[12] with respect to ^{10}B states with $E_x > 11$ MeV are not conclusive. In the analog region in ^{10}Be, Anderson et al.[13] have recently reported states from a study of the ^{9}Be(d,p)^{10}Be reaction at E_x = 9.27, 9.4, 10.57±0.03, and 11.76±0.02 MeV. The levels ^{10}Be* (9.3,11.8) are also reported in a study[14] of ^{9}Be(p,π^+)^{10}Be. The analog of these four states would be expected to lie at $E_x \approx$ 11.0, 11.1, 12.3, and 13.5 MeV in ^{10}B.

The ^{9}Be(^{3}He,α)^{8}Be and ^{11}B(^{3}He,α)^{10}B reactions have been studied at E(^{3}He) = 49.3 MeV using the 88-inch cyclotron and the Berkeley QSD magnetic spectrometer.[15] The identification depended on a measurement of Bρ using a resistive-wire position-sensitive proportional counter and a double (dE/dx) measurement in the transmission proportional counters, combined with a measurement of the time of flight (α M/Q) between a scintillator foil at the entrance of the spectrometer and a plastic scintillator behind the focal plane detectors. The E_α vs channel calibration was obtained by using a carbon target and moving the groups from very well known bound states of ^{11}C [from ^{12}C(^{3}He,α) runs] were made at θ_{lab} = 14.5°, 30°, and 48° and at magnetic fields which would match those of the ^{9}Be and ^{11}B runs, so that contaminant subtraction would be possible.

All three targets were oriented at an angle of 30° with the incident ^{3}He beam. The ^{9}Be and ^{11}B (98% enriched) targets had a thickness of 400 and 500 μg cm^2, respectively, as measured by an α gauge (±15%). The thickness of the carbon target was not measured directly but from the shifting of channel positions of identical groups when the carbon target and the ^{9}Be target were used it appears that its thickness was approximately 800 μg/cm^2. The effective thickness of the ^{9}Be and ^{11}B targets was 60 and 80 keV, respectively. The carbon contamination of the ^{9}Be target was ~0.5%, while that of the ^{11}B target was small. Groups from ^{16}O(^{3}He,α)^{15}O were observed in the ^{11}B(^{3}He,α) spectra.

Spectra were obtained at θ_{lab} = 14.5° and 30° covering $16 < E_x < 29$ MeV in ^{8}Be. Figure 1 shows a composite display of the two runs taken at 30°. The well-known states ^{8}Be (16.91, 17.64, 18.15, and 19.22) are clearly seen: their [J^{π}; T] are [2^+;0 +1], [1^+;1], [1^+; 0], and [3^+; (1)], respectively. The other 2^+, mixed isospin state ^{8}Be* (16.63) is very

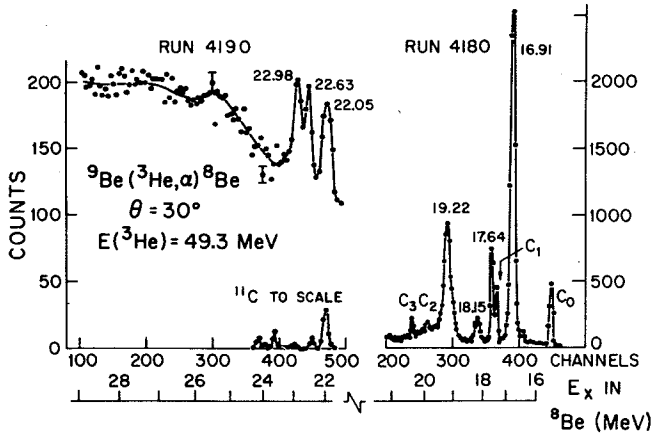

Fig. 1. Spectrum of the α particles from the ^{9}Be (^{3}He,α)^{8}Be reaction at θ_{lab} = 30°, E(^{3}He) = 49.3 MeV. Run 4180 was made with a spectrograph frequency of 22.606 MHz and a charge of 2.12 mC: the right-hand ordinate shows the average number of counts in a four-channel bin; the abscissa covers $16 < E_x < 21$ MeV in ^{8}Be. The groups labeled $C_0 \rightarrow C_3$ corresponds to ^{11}C* (0, 2.00, 4.32, and 4.80). Run 4190 was carried out at a frequency of 21.000 MHz and a charge of 1.71 mC: the left-hand ordinate also represents the average number of counts in a four-channel bin; the abscissa covers $21.8 < E_x < 29$ MeV. The curve labeled "^{11}C" is plotted to scale from a run made under analogous conditions with a carbon target, corrected for the 0.5% carbon contamination of the ^{9}Be target: see text for details. The curve covers the region $6.2 < E_x < 8.8$ MeV in ^{11}C. (XBL 766-8322)

weakly populated both at this angle and at 14.5°, as is $^{8}Be^{*}$ (18.91). The measured excitation energy of the 3+ state is 19.22±0.03 MeV, suggesting little contribution from the known 3+ state $^{8}Be^{*}$ (19.06).

The spectra clearly show the carbon contamination and the groups leading to $^{11}C^{*}$ (0, 2.00, 4.32, and 4.80): they provide both an energy reference and a calibration for the intensity of contaminant groups in the region of the higher excited states of ^{8}Be. The intrinsic width $\Gamma_{c.m.}$ of $^{8}Be^{*}$ (17.64) is known to be 10.7±0.5 keV: its measured full width at half maximum (FWHM) was used first to determine the instrumental width [≈ 50 keV]; to check the widths of $^{8}Be^{*}$ (16.91, 18.15, and 19.22); and then to determine the widths of the higher excited states of ^{8}Be.

The three new states in ^{8}Be are shown in Fig.1 and their parameters are displayed in Table 1. The errors in the E_x and $\Gamma_{c.m.}$ are arbitrarily increased and reflect uncertainties in the energy calibration and in the subtraction of the many particle background. It should be noted that the carbon contaminant peaks shown in this E_x region on Fig. 1 of course shift kinematically more slowly than do the ^{8}Be peaks: the 14.5° results make unambiguous the assignment of the three peaks to ^{8}Be. There is some indication of a broad state at $E_x \sim 25$ MeV: such a state has been seen[1] earlier. Within statistics we do not observe any influence on the two spectra of the T=2 state at 27.5 MeV. We feel that the present paper presents the first evidence for sharp states of ^{8}Be at these high E_x.

One and possibly two of the states $^{8}Be^{*}$ (22.05, 22.63, and 22.98) should be the analogs of $^{8}Li^{*}$ (6.53, 7.1). It is tempting, on the basis of the smaller width, to assign $^{8}Be^{*}$ (22.63) to be the analog of $^{8}Li^{*}$ (6.53), and on the basis of the resultant energy difference to assume that $^{8}Be^{*}$ (23.0) and $^{8}Li^{*}$ (7.1) are analogs. The analog of $^{8}Be^{*}$ (22.05) is not reported in ^{8}Li. This is clearly a guess since the J^{π} of none of these states is established, and calculations of energy shifts are precluded. However, the evidence for such long-lived states at very high excitation energies in ^{8}Be suggests the need for additional experimental and theoretical work.

Spectra involving states of ^{10}B were obtained at $\theta_{lab} = 14.5°$ and 30° for $6 < E_x < 30$ MeV, at 20°, 25°, and 36° for $6 < E_x < 15$ MeV, and at θ = 48° and 55° for $7 < E_x < 14$ MeV. Figure 2 shows a composite display of two of the runs taken at 30°. The third run at 30°, which covered $24 < E_x < 30$ MeV, and the run at 14.5° which covered $20 < E_x <$ MeV, did not show any sharp structure ($\Gamma < 0.5$ MeV) above the multiparticle breakup background.

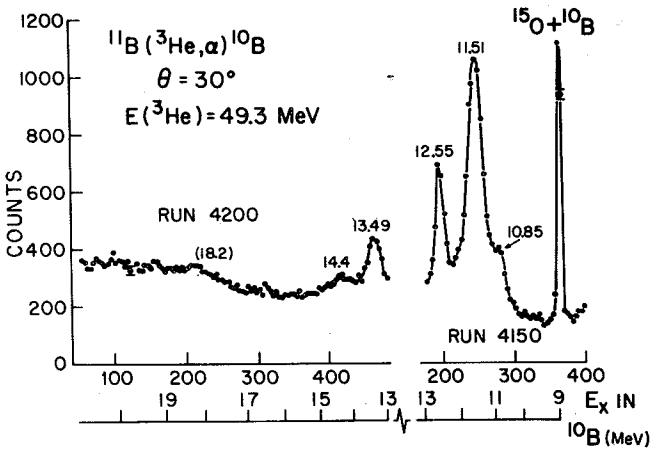

Fig. 2. Spectrum of the α particles from the $^{11}B(^{3}He,\alpha)^{10}B$ reaction at $\theta_{lab} = 30°$, E(^{3}He) = 49.3 MeV. The ordinate shows the average number of counts in a four-channel bin: statistical errors are shown for two representative points. Run 4150 was made with a spectrograph frequency of 22.606 MHz and a charge of 1.42 mC: the abscissa covers $9 < E_x < 13$ MeV in ^{10}B. Run 4200 was carried out at a frequency of 21.000 MHz and a charge of 1.44 mC: the abscissa covers $13 < E_x < 20.8$ MeV. The peak labeled $^{15}O + ^{10}B$ $^{15}O + ^{10}B$ is a composite of $^{15}O^{*}$ (6.18) [from $^{16}O(^{3}He,\alpha)^{15}O$] and of one or more of the ^{10}B states at $E_x = 8.89$ MeV. $^{15}O^{*}$ (6.18) is resolved at other angles. (XBL 766-8323)

The widths calculated for the ^{10}B states were determined in the manner discussed previously using the experimental width of $^{10}B^{*}$ (6.56) whose intrinsic width is known to be 25.1 keV.

The summary of our results is shown in Table 1. (1) We confirm the existence of $^{10}B^{*}$ (10.85, 11.51, and 12.55), although our width for $^{10}B^{*}$ (11.51) is puzzlingly larger than previously reported. (2) We report a new state $^{10}B^{*}$ (13.49) and possibly two other wider states. Our work suggests that the $^{9}Be(p,\gamma)$ work[9] should be analyzed further. Comparison with the analog region in ^{10}Be shows four relatively sharp states in both nuclei: $^{10}Be^{*}$ (9.27, 9.4, 10.57, and 11.76)[13] and $^{10}B^{*}$ (10.85, 11.51, 12.55, and 13.49) (as summarized in Table 1). Since information on the J^{π} of these states is not known with certainty at this time [(4^{-}) and (2^{+}) have been suggested[1] for $^{10}Be^{*}$ (9.27, 9.4) and $(0^{+}, 1^{+}, 2^{+})$ would be assigned to $^{10}B^{*}$ (12.55, 13.49) if these are the states seen in the $^{9}Be(p,\gamma)$ work], definite analog assignments cannot be made.

Table 1. Summary of the results.

State in	E_x (MeV)	$\Gamma_{c.m.}$ (keV)	$d\sigma/d\Omega_{c.m.}$[a] (μb/sr)	at	$\theta_{c.m.}$
^{8}Be	22.05 ±0.10	270± 70	1.2± 0.4		42.5°
^{8}Be	22.63 ±0.10	100± 50	1.2± 0.3		42.5°
^{8}Be	22.98 ±0.10	230± 50	2.5± 0.5		42.5°
^{10}B	10.85 ±0.10	300±100	~11		40°
^{10}B	11.505±0.05	500±100	74 ±20		40°
^{10}B	12.549±0.05	150± 50	23 ± 8		40°
^{10}B	13.494±0.05	300± 50	~15		40°
^{10}B	14.4 ±0.1	800±200			
^{10}B	18.2 ±0.2	1500±300			

[a] The errors shown reflect corrections for background and contaminant subtraction.

Footnotes and References

*Condensed from Phys. Rev. C 13, 46 (1976).

†Permanent address: University of Pennsylvania, Philadelphia, Penn.

‡Present address: Department of Physics, Vanderbilt University, Nashville, Tennessee.

1. F. Ajzenberg-Selove and T. Lauritsen, Nucl. Phys. A227, 1 (1974).

2. R. G. H. Robertson, W. S. Chien, and D. R. Goosman, Phys. Rev. Lett. 34, 33 (1975).

3. J. W. Watson, F. Ajzenberg-Selove, and R. Middleton, Phys. Lett. 18, 302 (1965).

4. F. Ajzenberg-Selove, E. R. Flynn, J. D. Garrett, and O. Hansen, Bull. Amer. Soc. 20, 596 (1975).

5. F. C. Barker, Nucl. Phys. 83, 418 (1966).

6. A. D. Bacher, F. G. Resmini, H. E. Conzett, R. de Swiniarski, H. Meiner, and J. Ernst, Phys. Rev. Lett. 29, 1331 (1972).

7. D. G. Foster (private communication).

8. J. D. Purvis, F. Ajzenberg-Selove, and L. M. Polsky, Phys. Rev. 162, 1005 (1967).

9. A. Fisher, Ph.D. thesis, Stanford University, 1970 (unpublished) (see Table 10.11 of Ref. 1 for a summary of the results).

10. H. J. Votava, T. B. Clegg, E. J. Ludwig, and W. J. Thompson, Nucl. Phys. A204, 529 (1973); L. W. J. Wild and G. B. Crinean, Aust. J. Phys. 27, 663 (1974).

11. P. Kossanyl-Demay and G. J. Van Praet, Nucl. Phys. 81, 529 (1966).

12. D. Bachelier, M. Bermas, I. Brissaud, C. Detraz, and P. Radvanyi, Nucl. Phys. A126, 60 (1969).

13. R. E. Anderson, J. J. Kraushaar, M. E. Rickey, and W. R. Zimmerman, Nucl. Phys. A236, 77 (1974).

14. S. Dahlgren, P. Grafström, B. Höistad, and A. Asberg, Nucl. Phys. A204, 53 (1973).

15. B. G. Harvey, J. Mahoney, F. G. Puhlhofer, F. S. Goulding, D. A. Landis, J.-C. Faivre, D. G. Kovar, M. S. Zisman, J. R. Meriwether, S. W. Cooper, and D. L. Hendrie, Nucl. Instrum. Methods 104, 21 (1972).

ENERGY LEVELS OF ^{12}N*

C. F. Maguire,† D. L. Hendrie, D. K. Scott,
J. Mahoney, and F. Ajzenberg-Selove‡

Comparison of the known[1,2] states in ^{12}B with those in the mirror nucleus, ^{12}N, immediately reveals the incomplete nature of our understanding of the structure of ^{12}N (see Table 1). The reasons for this are easy to understand. While a wide variety of reactions with convenient characteristics (i.e., high + Q-values, outgoing charged particles) populate ^{12}B, the situation is quite different in ^{12}N. States in ^{12}N can, for all practical purposes, be populated only by the reactions ^{10}B(^{3}He,n) [1.569], ^{12}C(p,n) [-18.126], ^{12}C(^{3}He,t) [-17.362], and ^{14}N(p,t) [-22.141] [Q_m in brackets],[3] and by comparable reactions involving heavy ions. The difficulties of accurate measurements of neutron energies and of obtaining the highly energetic, monoenergetic beams of particles needed to overcome the negative Q-values have only recently begun to be solved. With the exception of the ^{12}C(^{3}He,t) study of Ball and Cern[4] at E(^{3}He) = 49.8 MeV who reported on states with E_x < 5.3 MeV, most of the evidence on the levels of ^{12}N derives from studies of ^{10}B(^{3}He,n), particularly those by Fuchs et al.[5] at E(^{3}He) = 12.5-13 MeV and by Zafiratos et al.[6] at E(^{3}He) = 4.0 and 5.8 MeV. (See Ref. 1 for a more complete listing of the experiments relating to ^{12}N.)

The ^{12}C(^{3}He,t)^{12}N has been studied at E(^{3}He) = 49.3 MeV using the 88-inch cyclotron and the Berkeley QSD magnetic spectrometer.[7] The detail of the procedures followed have been described earlier,[8] except that the E_t vs channel calibration was made by using a carbon target and moving the groups from ^{12}N*(0.964) across the length of the detector by varying the magnetic field.

The target used was an isotopic carbon target (98.9% ^{12}C) whose thickness was ~ 800 μg/cm^2. It was oriented at 30° and its thickness corresponded to an energy loss of ~ 100 keV for 49 MeV ^{3}He ions. Contamination from ^{13}C(^{3}He,t) and ^{16}O(^{3}He,t) was not observed: Q_m for these two reactions are -2.239 and -15.448 MeV to the ground states of ^{13}N and ^{16}F.[3] This experiment was concerned with determining the level structure of ^{12}N with 0<E_x<10 MeV and, to some extent, the region with E_x < 15 MeV. Since Q_m for the ^{12}C(^{3}He,t)^{12}N reaction is -17.362 MeV, we would be concerned with contaminant groups in ^{13}N with 14 ≤ E_x ≤ 24 MeV and with ^{16}F states with 2 ≤ E_x ≤ 12 MeV. The level structure of ^{16}F is very poorly known but we have searched for all known energetically permissible states due to ^{13}C and ^{16}O contamination, and we find evidence for none.

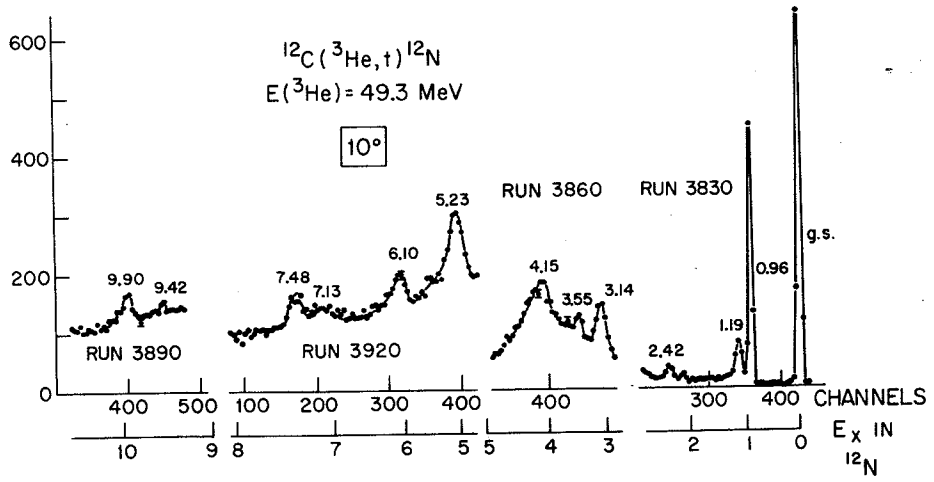

Fig. 1. Spectrum of the tritons from the $^{12}C(^3He,t)^{12}N$ reaction at $\theta_{lab} = 10°$, $E(^3He) = 49.3$ MeV. This composite figure shows the results from four runs: 3830[32.152 MHz, 0.235 mC1], run 3860[30.010 MHz, 0.407 mC], run 3920[29.302 MHz, 1.14 mC] and run 3890 [26.000 MHz, 1.30 mC] [frequency of spectrograph, incident charge]. A complete plot of run 3890, and a plot of run 3900[23.499 MHz, 1.0 mC] show no other groups in ^{12}N with $E_x < 15$ MeV; see the discussion in the text. The ordinate shows the average number of counts in a four-channel bin; statistical errors are shown for four points. The abscissa shows E_x in ^{12}N (in MeV).
(XBL 766-8320)

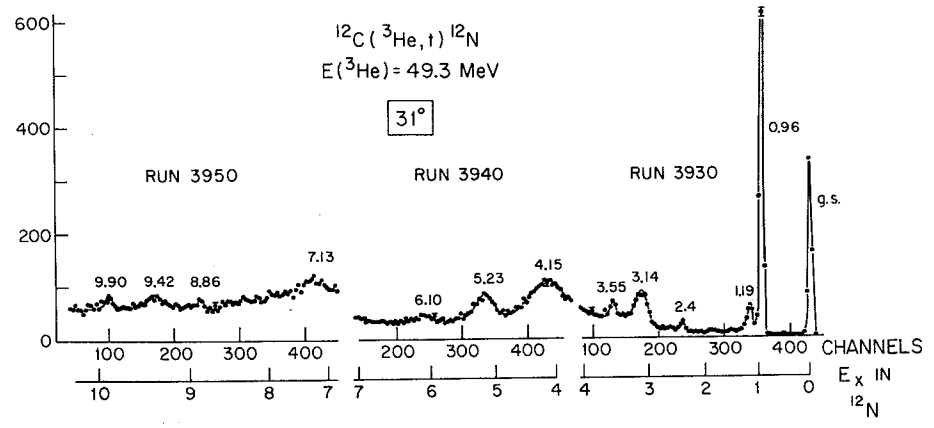

Fig. 2. Spectrum of the tritons at $\theta_{lab} = 31°$. This composite figure shows the results from run 3930 [30.753 MHz, 1.09 mC], 3940 [28.296 MHz, 1.37 mC] and 3950 [26.301 MHz, 3.63 mC]. Plots of runs 3960 and 3970 which cover $10 < E_x < 13$ MeV in ^{12}N show no other groups. See also caption of Fig. 1. (XBL 766-8321)

The results we have obtained at $\theta_{lab} = 10°$ and 31° are shown in Figs. 1 and 2 and displayed in Table 1 where they are compared with previous results.

In conclusion, this investigation of the states of ^{12}N has confirmed the existence of one doubtful state, [$^{12}N^*(2.4)$], casts doubt on another [$^{12}N^*(1.7)$], reports the existence of four new states, raises questions concerning selective population by the (^3He,n) and (^3He,t) reactions, and by comparison with the analog region in ^{12}B, clearly shows that the level structure of ^{12}N is still very poorly known.

Table 1. States in ^{12}N.

Previous results[a]			Present results	
E_x (MeV ± keV)	J^π	$\Gamma_{c.m.}$ (keV)	E_x (MeV ± keV)	$\Gamma_{c.m.}$ (keV)
g.s.	1^+	Bound	g.s.	Bound
0.964±8	2^+	<35	≡0.964	<20
1.192±9	$(2)^-$	140±35	1.190±20	80±30
(1.72 ±0.08)			-[b]	
2.43 ±40			2.415±20	45±15
3.114±15	π=+	210±50	3.136±30	240±40
3.533±15	$(2)^+$	170±50	3.550±50	150±100
4.25 ±30		290±70	4.150±80[c]	650±100
5.320±12		180±20	5.230±80[c]	400±80
			6.100±80	300±100
(6.4)[d]				
(6.9)[d]			7.130±100	500±100
7.629±20		200±40	7.480±100	180±80
8.446±17		90±30		
			(8.860±100)	~100
9.035±12		16±20		
(9.2)[d]			9.420±100	~200
			9.900±100	100±50

[a] The states with $E_x < 3.6$ MeV have been reported in several experiments: see Ref. 1 (Tables 12.25,12,26, and 12.27). The higher states come primarily from the $^{10}B(^3He,n)^{12}N$ study of Ref. 5. Correspondence with analog states in ^{12}B and ^{12}C is established only for the first three states and probably for $^{12}N^*$ (3.53). The other states are shown listed in line with that state in ^{12}B which has most closely the same E_x.

[b] We see no evidence for this state.

[c] The ΔE_x of the 5.23 and 4.15 MeV state is the same as the two states 5.32, 4.25 observed by Fuchs et al.[5] but the absolute values appear to be really 100 keV lower (our errors are conservative). Our E_x, when comparable, for the higher states always tend to be lower: for instance 7.48 - 7.63. In the case of the 4.15 - 4.25 and 5.23 - 5.32 states the widths we observe are substantially larger: the (^{3}He,t) reaction may be exciting additional (unresolved) states.

[d] See Ref. 7.

Footnotes and References

*Condensed from Phys. Rev. C 13, 993 (1976).

†Present address: Department of Physics, Vanderbilt University, Nashville, Tennessee.

‡Permanent address: University of Pennsylvania, Philadelphia, Pennsylvania.

1. F. Ajzenberg-Selove, Nucl. Phys. A 248, 1 (1975).

2. F. Ajzenberg-Selove, R. Middleton and J. D. Garrett, Phys. Rev. C 12, (1975).

3. N. B. Gove and A. H. Wapstra, Nuclear Data Tables 11, 127 (1972).

4. G. C. Ball and J. Cerny, Phys. Rev. 177, 1466 (1969).

5. H. Fuchs, K. Grabisch, D. Hilscher, U. Jahnke, H. Kluge, T. Masterson and H. Morgenstern, Nucl. Phys. A 234, 61 (1974).

6. C. D. Zafiratos, F. Ajzenberg-Selove and F. S. Dietrich, Nucl. Phys. 77, 81 (1966); ibid. 89, 706 (1966).

7. B. G. Harvey, J. Mahoney, F. G. Pühlhofer, F.S. Goulding, D. A. Landis, J.-C. Faivre, D. G. Kovar, M. S. Zisman, J. R. Meriwether, S. W. Cooper, and D. L. Hendrie, Nucl. Instr. and Meth. 104, 21 (1972).

8. F. Ajzenberg-Selove, C. F. Maguire, D. L. Hendrie, D. K. Scott, and J. Mahoney, Phys. Rev. C 13, 46 (1976).

GAMMA AND ALPHA DECAY FROM THE 2.1 msec ISOMER ^{213}Ra

D. E. Raich,* H. R. Bowman, R. E. Eppley,†
J. O. Rasmussen, and I. Rezanka‡

The isomer ^{213m}Ra was produced by the reaction ^{209}Bi(^{10}B, 6n), as well as by bombardments of ^{12}C on Pb isotopes, ^{14}N on Bi, and ^{16}O on natural Hg, with projectile energies in the range 60-100 MeV. The isomer decays with a half-life of 2.1 ms both via gamma internal transitions and via alpha branching to levels in ^{209}Rn. A level scheme is proposed in which the isomeric state is assigned as either $17/2^-$ or $13/2^+$ with shell-model configurations either of the $h_{9/2}$ protons coupled to a $p_{1/2}$ neutron hole, or of an uncoupled $i_{13/2}$ neutron hole. On the basis of alpha decay rate predictions from the new Fliessbach theory, the $17/2^-$ isomeric assignment is to be preferred.

In most of the early experimental runs a heavy-metal target foil was placed at about a 45° angle in the Yale HILAC beam. Counting was carried out simultaneously with irradiation, using a detector positioned 90° from the beam line, obliquely facing the front of the target.

For the coincidence experiments a second Ge(Li) detector was placed 180° from the first, obliquely facing the back of the thin target. Three- and four-parameter coincidence events (E_1,E_2, nanosecond time between the two γ-rays, and sometimes millisecond time since beam burst) were recorded serially on magnetic tape by the PDP-8/I for later computer sorting and analysis.

The alpha spectroscopy experiments were performed at Berkeley SuperHILAC using the helium-jet technique to catch recoiling reaction products and transfer them to a low-background counting chamber.

When we used the ^{206}Pb-enriched target, we encountered strong interference from the twin doublets of the ^{214}Fr and ^{214m}Fr α-groups. The francium energies are shown at the bottom of Table 1; they are ideally positioned to mask our expected ^{213m}Ra energies, especially since they also have millisecond half-lives, 5.5 and 3.6 ms, respectively, for ^{214}Fr and its isomer. The ^{214}Fr is presumably produced both by reaction with the small ^{207}Pb fraction in the target--via the direct p4n-out reaction which should go at nearly the same energy as ^{206}Pb(^{12}C,5n)^{213}Ra--and via the direct p3n-out reaction with ^{206}Pb.

We were able to reduce the ^{214}Fr interference considerably by turning to a ^{204}Pb-enriched target. The reaction ^{204}Pb(^{12}C,3n)^{215}Ra was expected to peak at about 61 MeV, very near the Coulomb barrier. The low energy largely eliminate the competing ^{214}Fr production since the pn-out reaction cross section is greatly reduced.

The results are summarized in Table 1.

Table 1. Results of alpha spectroscopy. (Probable error in last digit is given in parentheses.)

	Present work		Reported in literature		
Isotope [Q_α (MeV)[a]]	E_α (MeV)	Decay %	E_α (MeV)	Decay %	Ref.
^{213}Ra	6.731(5)	46(3)	6.730(5)	45(2)	2
[6.893(5)]	6.624(5)	47(3)	6.623(5)	49(2)	
	6.522(5)	6(1)	6.520(5)	6(1)	
	6.411(5)	0.5(1)	6.408	0.4	
^{213m}Ra	8.467(5)	69(7)			
[8.663(5)]	8.358(10)	28(6)			
	8.266(10)	3(2)			
^{214}Fr			8.426(5)	93.0	3
			8.358(5)	4.7	
^{214m}Fr			8.549(8)	51(2)	4
			8.477(8)	49(2)	

Note: Ratio measured of $\frac{^{213m}\text{Ra}}{^{213}\text{Ra}}$ α-decays = $8.8(9)\times10^{-4}$ (not corrected for cell's fast delivery fraction).

[a]Corrected for recoil and screening.

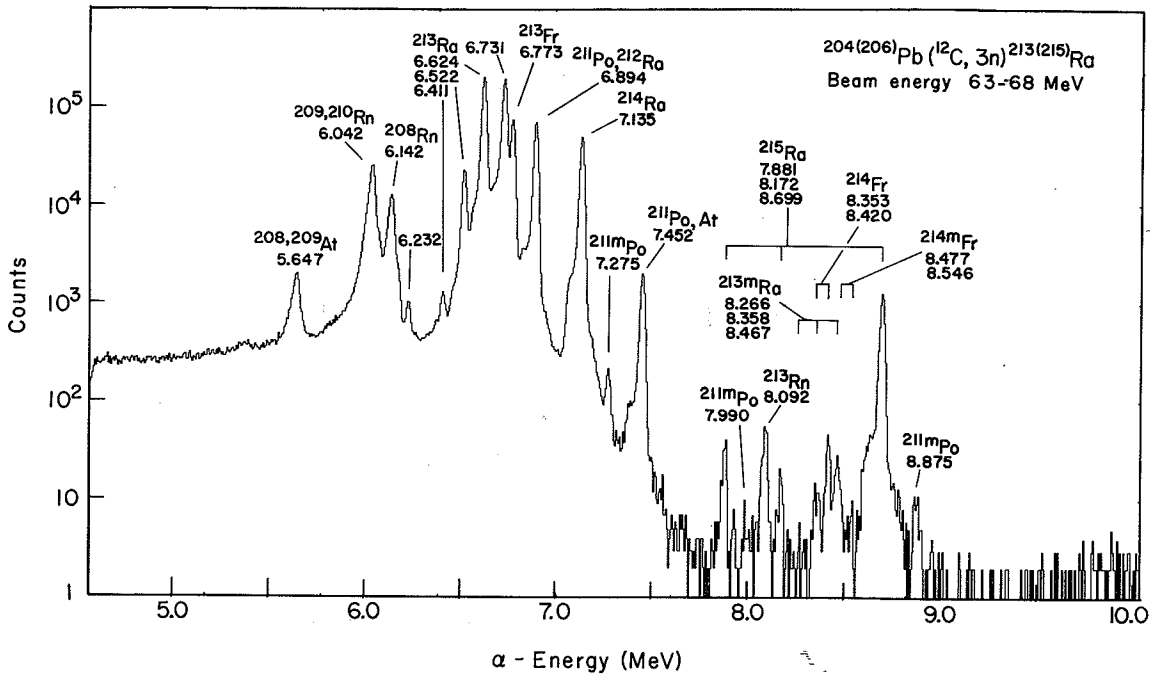

Fig. 1. Alpha-particle spectrum showing ^{213m}Ra. (XBL 761-41)

The unsorted alpha spectrum from our runs at 63-68 MeV is shown in Fig. 1, and a detail at the energies of interest in two time intervals appears in Fig. 2.

We propose the level scheme illustrated in Fig. 3 of states populated in the 2.1-ms ^{213m}Ra decay. The ^{213}Ra nucleus is sufficiently close to doubly-magic ^{208}Pb that the spherical single-particle model should predict lower energy levels fairly well. We expect the single hole in the 126-neutron shell to dominate the configurations of the first few states, resulting in a ground state with $J = 1/2^-$, and first two excited states $5/2^-$ and $3/2^-$ (with the neutron hole successively occupying $p_{1/2}$, $f_{5/2}$, $p_{3/2}$ shell-model orbitals). Higher-seniority configurations involving the $h_{9/2}$ protons are expected to become significant somewhat above 1 MeV and excitations of the ^{208}Pb core should not appear below ~ 2.5 MeV.

Low-lying high-spin states are a common cause of isomerism and are readily populated in heavy-ion reactions. Two candidates for such a state suggest themselves. First, on the basis of level trends we expect an $i_{13/2}^{-1}$ $(13/2^+)$ neutron-hole state near 1800 keV. Second in ^{214}Ra the 8^+ $\pi(h_{9/2}^6)8^+$ state at 1864 keV is isomeric, with an E2-transition half-life much longer than that seen for other E2's in similar cascades, probably reflecting cancellation in the pairing factor $(U_iU_f - V_iV_f)^2$ near the half-filled $h_{9/2}$ proton shell. This $\pi(h_{9/2}^6)_8$ state might couple in ^{213}Ra with the $p_{1/2}^{-1}$ neutron hole to produce a long-lived $17/2^-$ state of about the correct energy. In a separate report we test these two possibilities with Fliessbach's new normalized α-decay theory[1] by comparing predictions of branching ratios to the daughter states from each of the hypothetical parent states. The pattern of intensities fits our α-spectroscopic data much better

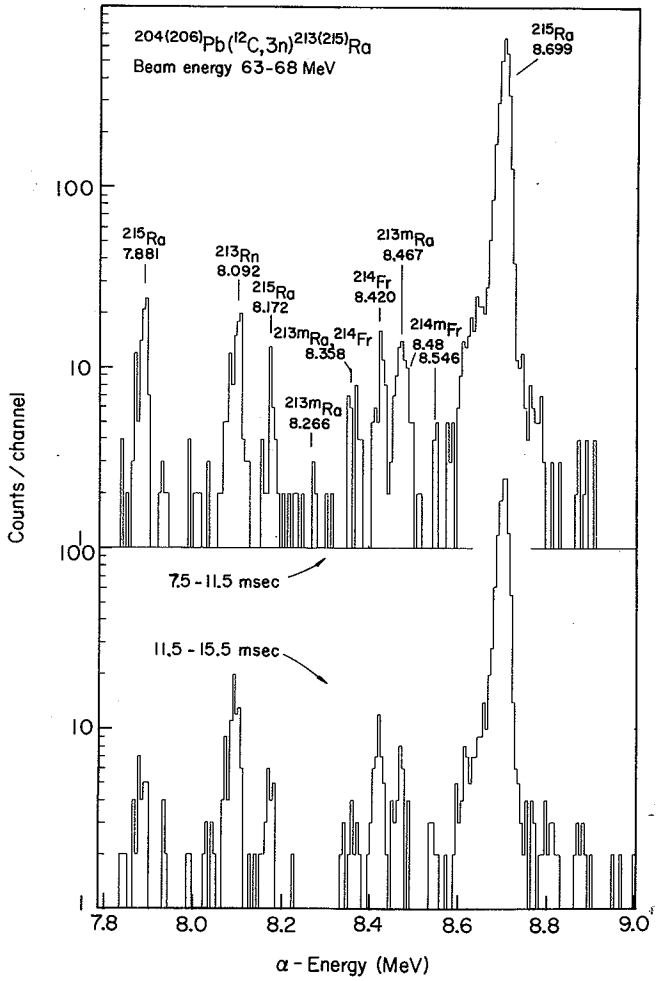

Fig. 2. Detail of two time intervals contributing to the α-spectrum of Fig. 1. (XBL 761-40)

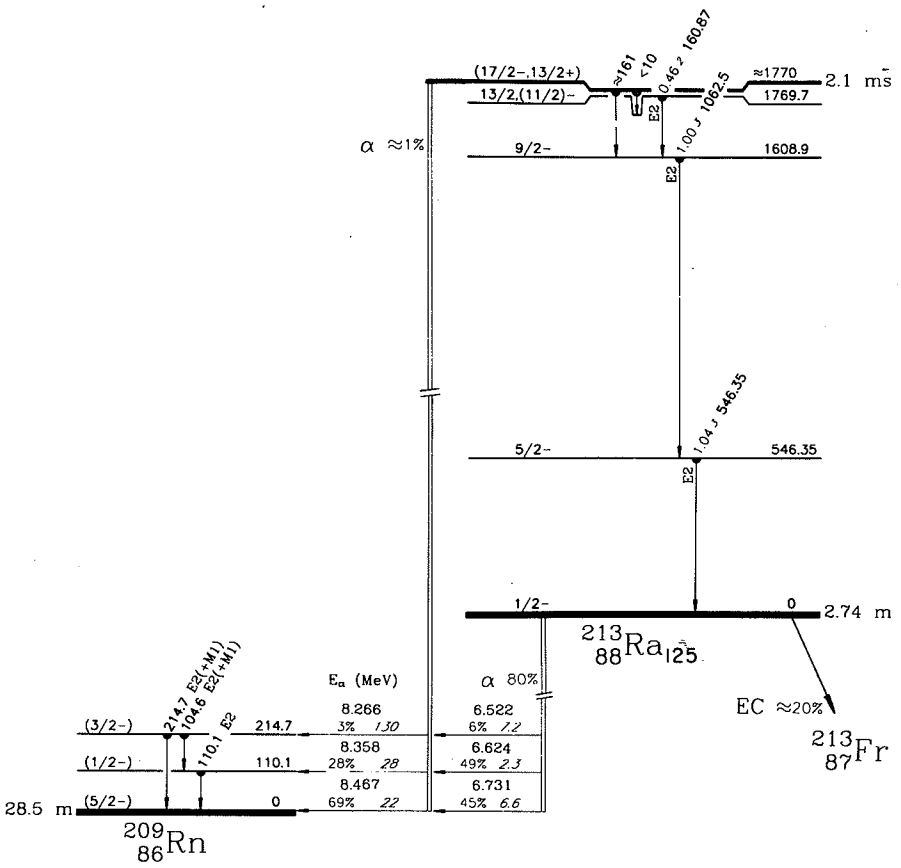

Fig. 3. Proposed ^{213m}Ra decay scheme. Relative photon intensities (and uncertainties) are shown in front of transition energies. Approximate hindrance factors follow α-feeding percentages. (XBL-761-145)

assuming a $17/2^-$ isomeric state, so we report this as our preferred interpretation.

Footnotes and References

*Present address: Chemistry Division, Argonne National Laboratory, Argonne, IL 60439.

†Present address: Monsanto Research Corp., Mound Laboratory, Miamisburg, OH 45342.

‡Present address: Research Laboratory, Xerox Corp., Rochester, NY 14600

1. T. Fliessbach, Z. Phys. A272, 39 (1975).

2. K. Valli, W. Treytl, E. K. Hyde, Phys. Rev. 161, 1284 (1967).

3. D. F. Torgerson and R. D. Macfarlane, Phys. Rev. C2, 2309 (1970).

4. K. Valli and E. K. Hyde, Phys. Rev. 176, 1377 (1968).

EXTENSION OF THE Tz = -3/2 BETA-DELAYED PROTON PRECURSOR SERIES TO ^{57}Zn*

D. J. Vieira, D. F. Sherman, M. S. Zisman,
R. A. Gough, and Joseph Cerny

The well-known series of A = 4n+1, T_z=-3/2 β-delayed proton precursors has been completed from ^{9}C through ^{49}Fe[1] with the recent addition of ^{45}Cr.[2] Such studies both establish the decay properties of proton rich nuclei far from stability and, with the use of the isobaric multiplet mass equation, permit an excellent prediction of the precursor's mass. Although the β-delayed proton activity from the heavier nuclides in this series, through ^{41}Ti, has been produced in reasonable yield (~ 30-250 μb) by the (^{3}He,2n) reaction on T_z = 0 targets, extension of these studies further into the fp shell by employing the ^{32}S(^{16}O,3n)^{45}Cr,[2] and ^{40}Ca(^{12}C,3n)^{49}Fe,[3] reactions has been hampered by much lower cross sections (~ 300-500 nb). We wish herein to report the observation of ^{53}Ni via the ^{40}Ca(^{16}O,3n) reaction and of ^{57}Zn via the ^{40}Ca(^{20}Ne,3n) reaction in which even lower yields were observed (~ 25 and ~ 60 nb, respectively).

Beta-delayed protons emitted from precursors retained in the target were detected in a semiconductor counter telescope subtending an effective solid angle of 0.24 sr. These precursors were produced by employing pulsed beams of ^{16}O^{+3} (60 and 65 MeV, ~ 100 particle-nA) or ^{20}Ne^{+4} (62 and 70 MeV, ~ 60 particle-nA) from the 88-inch cyclotron in irradiations of natural calcium targets rotated to a target angle of 70°. A slotted rotating wheel system, similar to that described in Ref. 4, controlled the pulsing of the beam and protected the detectors while the target was being irradiated. Several detector telescope combinations were used.

For completeness the ^{53}Ni results (shown in Fig. 1a), discussed in the previous Annual Report (LBL-4000), have been included. The large group at 1.59 MeV(c.m.) is known to arise from direct proton radioactivity of ^{53m}Co [4] produced via the competing ^{40}Ca(^{16}O,p2n) reaction, while the 1.94±0.05 MeV (c.m.), $T_{1/2}$ = 45±15 ms activity is attributed to β-delayed proton decay of ^{53}Ni produced via the ^{40}Ca (^{16}O,3n) reaction (see decay scheme in Fig. 2b).

The proton spectrum resulting from the 70 MeV ^{20}Ne bombardment of a 1.8 mg/cm^2 calcium target for 20,000 μC (as 10$^+$) is shown in Fig. 1b. Again, ^{53m}Co arising from the competing ^{40}Ca(^{20}Ne,αp2n) reaction was observed. Three proton groups at energies of 1.95±.05, 2.58±.05, and 4.65±.05 MeV (c.m.) were observed, corresponding to a total delayed-proton yield of ~60 nb. The half-life of each group is consistent with the 40±10 ms value determined from the sum of all three groups. These activities are very compatible with the β-delayed proton emission expected from ^{57}Zn whose predicted threshold via the ^{40}Ca(^{20}Ne,3n) reaction is ~ 50.0 MeV (assuming a mass excess of -32.77 MeV, calculated using the Kelson-Garvey charge symmetry relations[5] and two predicted T_z = -1/2 masses from Ref. 6). The proposed ^{57}Zn decay scheme is given in Fig. 2b.

The groups observed at 4.65 MeV and 1.95 MeV can be assigned to the isospin-forbidden proton decay of the lowest T = 3/2 state of ^{57}Cu to the ground state and first excited state of ^{56}Ni, respectively. This energy difference of 2.70±.07 MeV agrees very well with the known separation between these ^{56}Ni states of 2.702±.003 MeV.[7] Based on these two groups, the excitation energy of the lowest T = 3/2 state of ^{57}Cu, 5.35±.04 MeV (assuming the ground state mass excess of ^{57}Cu is -47.31$_4$ MeV),[6] compares well with its known analog state in ^{57}Ni at 5.23±.01 MeV.[8] The group at 2.58 MeV could be attributed to isospin-allowed proton decay of a T = 1/2 state at 3.28±.05 MeV in ^{57}Cu, which could be the mirror of one of the two known 7/2$^-$ states in ^{57}Ni at 3.23±.02 and 3.36±.02 MeV.[8]

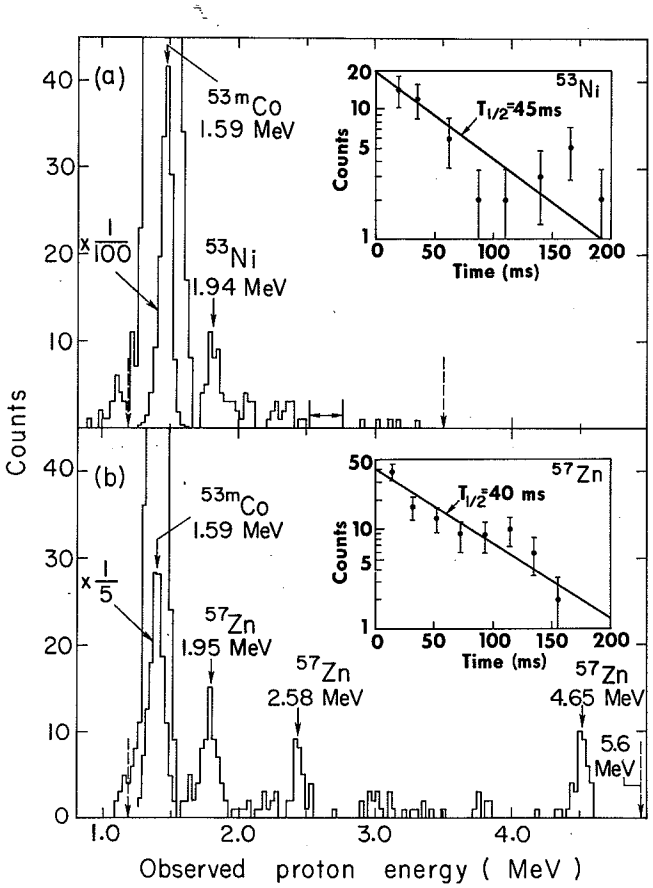

Fig. 1. Proton spectra observed following the bombardment of calcium with (a) 65 MeV ^{16}O and (b) 70 MeV ^{20}Ne. Dashed vertical arrows indicate the energy region in both spectra over which protons could be reliably observed. The precursor and the center-of-mass energy are labeled above each proton group. The horizontal arrows in (a) designate the energy region where proton decay to the ground state of ^{52}Fe would be expected (see text). Decay curves for the ^{53}Ni group and the sum of the three ^{57}Zn groups are shown in the insets. (XBL 759-4141)

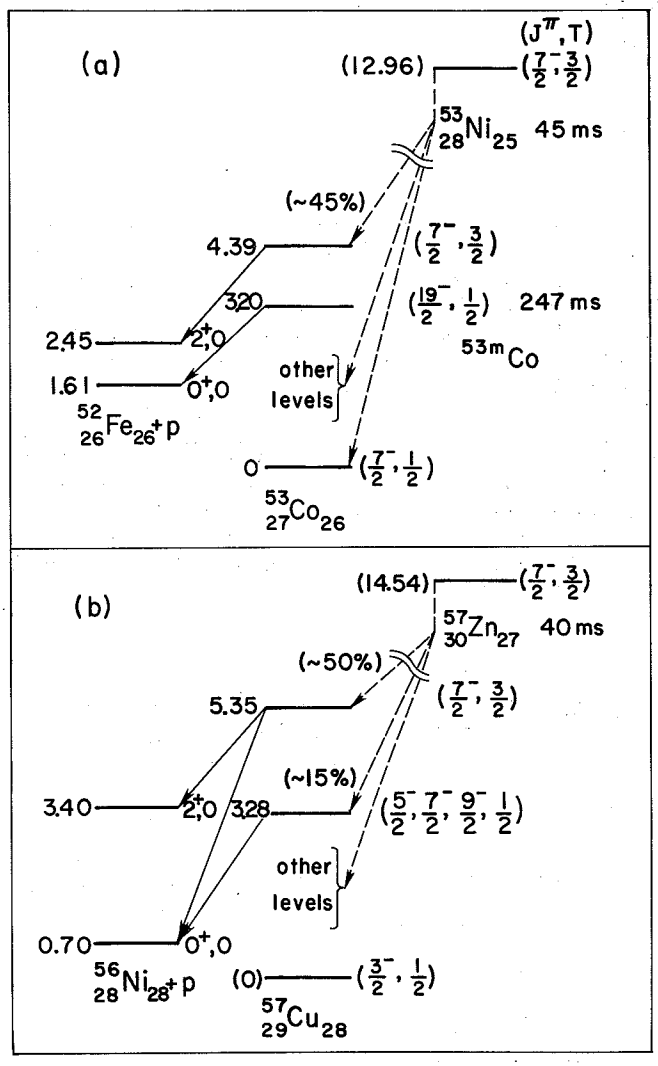

Fig. 2. The proposed decay schemes for (a) ^{53}Ni and (b) ^{57}Zn. Decays which have not been directly observed are indicated with dashed lines. All energies are given in MeV relative to the ground state mass of the appropriate $T_z = -1/2$ nuclide. Predicted energies, assumed spin, parity and isospin values, and estimated branching ratios are shown in parentheses.
(XBL 759-4142)

If the mass excesses of the lowest $T = 3/2$ states in the $T_z = -1/2$ nuclei ^{53}Co(-38.26±.06 MeV) and ^{57}Cu(-41.97±.04 MeV), together with those of the corresponding $T = 3/2$ states in the $T_z = +3/2$ and $+1/2$ members of each multiplet, are used in the isobaric multiplet mass equation (IMME), the predicted mass excesses for ^{53}Ni and ^{57}Zn are -29±.18 MeV and -32.63±.13 MeV, respectively. For ^{53}Ni, good agreement between this prediction and the Kelson-Garvey type mass prediction[9] of -29.69 MeV or the Coulomb energy calculation of -29.65 MeV[10] is found. Similar agreement is obtained between the IMME result for the mass excess of ^{57}Zn and the Kelson-Garvey prediction (described earlier) of -32.77 MeV.

Surveying the β-delayed proton decay of the $J^\pi = 7/2^-$, $T_z = -3/2$ nuclei from ^{45}Cr to ^{57}Zn, we see that only in the case of ^{57}Zn has isospin-forbidden proton decay from the analog state (in the emitter) to the ground state of the $T_z = 0$ residual nucleus been observed, a result which may largely be due to the enhanced stability of the doubly magic ^{56}Ni. On the basis of penetrability calculations alone, an intensity ratio for proton decay from the ^{57}Cu ($T = 3/2$) state to the ground state (0^+) relative to the first excited state (2^+) in ^{56}Ni of ~28/1 would be expected. The observed ratio of ~0.6/1 indicates that the reduced width for (isospin-forbidden) proton decay to the ground state is ~1/45 of that for decay to the first excited state. Such a reduced width ratio is consistent with the limits observed[2,3] in the proton decays of the analog states in ^{45}V, ^{49}Mn, and ^{53}Co, which indicate $\gamma_p^2(0^+)/\gamma_p^2(2^+) < 1/8$.

Footnotes and References

*Condensed from Physics Letters 60B, 261 (1976).

1. J. C. Hardy, in Nuclear Spectroscopy and Reactions - Part C, , ed. J. Cerny, (Academic Press, New York, 1974) p. 417.

2. K. P. Jackson, J. C. Hardy, H. Schmeing, R. L. Graham, J. S. Geiger, and K. W. Allen, Phys. Lett. 49B, 341 (1974).

3. J. Cerny, C. U. Cardinal, H. C. Evans, K. P. Jackson, and N. A. Jelley, Phys. Rev. Lett. 24, 1128 (1970).

4. J. Cerny, R. A. Gough, R. G. Sextro, and J. E. Esterl, Nucl. Phys. A188, 666 (1972).

5. I. Kelson and G. T. Garvey, Phys. Lett. 23, 689 (1966).

6. M. Harchol, A. A. Jaffe, J. Miron, I. Unna, and J. Zioni, Nucl. Phys. A90, 459 (1967).

7. H. Nann and W. Benenson, Phys. Rev. C 10, 1880 (1974).

8. F. M. Edwards, J. J. Kraushaar, and B. W. Ridley, Nucl. Phys. A199, 463 (1973).

9. D. Mueller, E. Kashy, W. Benenson, and H. Nann, Phys. Rev. C 12, 51 (1975).

10. F. D. Becchetti, D. Dehnhard, and T. G. Dzubay, Nucl. Phys. A168, 151 (1971).

^{61}Ge: A NEW BETA-DELAYED PROTON PRECURSOR

D. J. Vieira, D. M. Moltz,
M. S. Zisman, and Joseph Cerny

Further efforts to extend the series of A = 4n +1, T_z = -3/2 β-delayed proton precursors have succeeded by observing β-delayed protons from ^{61}Ge produced via the ^{40}Ca(^{24}Mg,3n) reaction.

As in the ^{53}Ni and ^{57}Zn experiments[1] discussed in the previous report, β-delayed protons emitted from precursors retained in the target were detected by a counter telescope protected by a slotted rotating wheel as illustated in Fig. 1. These precursors were produced by employing a recently developed pulsed beam of 85 MeV ^{24}Mg^{+4} (~50 particle-nA) from the 88-inch cyclotron in irradiations of a 1.5 mg/cm^2 natural calcium target rotated to a target angle of 70°.

Figure 2 shows the identified proton spectrum observed in 25,000 μC of integrated beam using a 15-μm ΔE and 250-μm E detector telescope. A proton group at an energy of 3.15±.07 MeV (c.m.) was observed at a yield of ~30 nb with a half-life of 40±15 ms. A much weaker group at 1.81±.07 MeV was also observed, but this activity exhibited a half-life much longer than the counting period of 120 ms. This latter proton group is consistent with a large fluctuation occurring at 1.7 to 1.8 MeV observed in the continuum β-delayed proton spectrum of ^{65}Ge (E_p (c.m.) = 1.0 - 2.3 MeV, $T_{1/2}$ = 30.8 sec[2]), which could be produced by (^{24}Mg,Xn) reactions with heavier isotopes present in the natural calcium target. Repeating the experiment at a bombarding energy of 78 MeV produced similar results with the 1.81 MeV activity increasing slightly in yield (supporting ^{65}Ge as its probable source), while the 3.15 MeV activity decreased in yield.

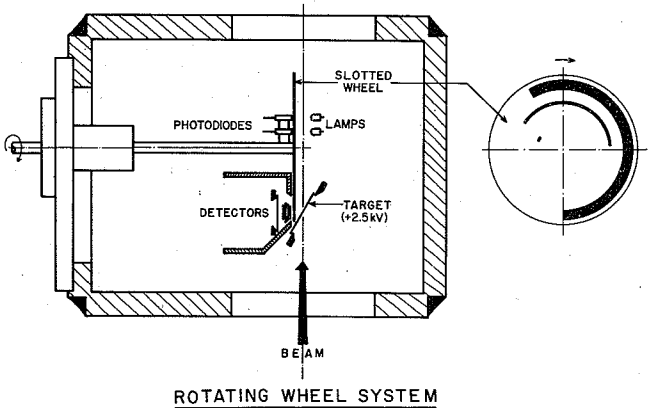

Fig. 1. Diagram of the slotted, rotating wheel. Photodiodes control pulsing of the cyclotron beam and provide timing signals for the counting period. A detector telescope backed by a reject detector is protected by the 1.5 mm thick Ta wheel when the beam is on and allowed to view the target through a large slot in the wheel when the beam is off. (XBL 743-606)

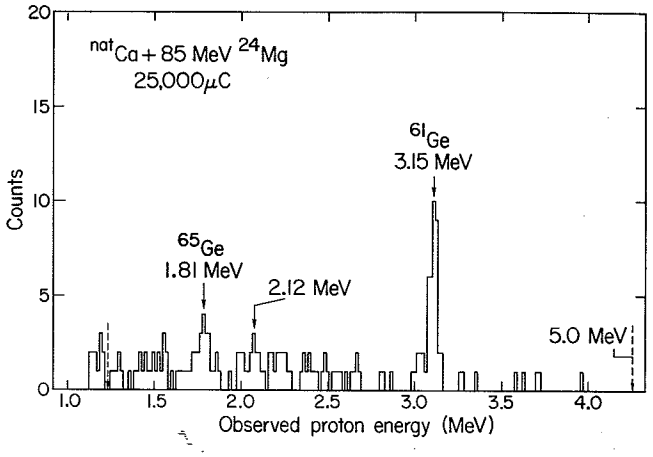

Fig. 2. The proton spectrum observed following the bombardment of calcium with 85 MeV ^{24}Mg. Dashed vertical arrows indicate the energy region over which protons could be reliably identified. The precursor and the center-of-mass energy are labeled above each proton group. For the possible source of the 2.12 MeV group, see text. (XBL 764-2739)

The 3.15 MeV activity is most reasonably explained as arising from the β-delayed proton decay of ^{61}Ge produced via the ^{40}Ca(^{24}Mg,3n) reaction (threshold ~61.3 MeV assuming a mass excess of -34.7 MeV for ^{61}Ge estimated from Coulomb energy systematics discussed below). Since ^{61}Ge is sufficiently far from stability that the only previously known member of this isospin quartet was the ^{61}Cu ground state, it is necessary to estimate the expected excitation energy of the analog state in ^{61}Ge from Coulomb displacement energy data[3,4] adjusted for the mass 61 system. These calculations predict that the analog state should be near 3.53 MeV, which agrees well with an excitation energy of 3.47 MeV obtained when the 3.15 MeV activity is attributed to proton decay to the ground state of ^{60}Zn (see Fig. 3). Decay of this analog state to the first excited state of ^{60}Zn would be expected at an energy of 2.15 MeV. Weak evidence for such a proton group is observed at 2.12 MeV, but due to poor statistics and possible interference from ^{65}Ge, the source of this group is uncertain. If attributed to ^{61}Ge, this branch would correspond to an upper limit of ~20%. Additional experiments on separated isotope ^{40}Ca targets will be necessary to confirm the origin of this 2.12 MeV group.

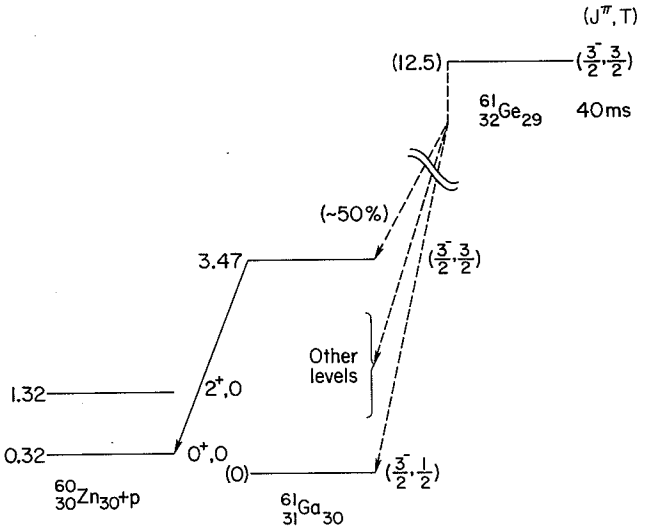

Fig. 3. The preliminary decay scheme of ^{61}Ge. Decays which have not been directly observed are indicated with dashed lines. All energies are given in MeV relative to the predicted mass excess of -47.22 MeV for the ground state of ^{61}Ga.[4] Predicted energies, assume spin, parity isospin values, and estimated branching ratios are shown in parentheses. (XBL 764-2740)

References

1. D. J. Vieira, D. F. Sherman, M. S. Zisman, R. A. Gough, and J. Cerny, Phys. Lett. 60B, 261 (1976).

2. J. A. Macdonald, H. Schmeing, J. C. Hardy, H. R. Andrews, J. S. Geiger, R. L. Graham, and K. P. Jackson, Chalk River Nuclear Laboratories Report (1975) AECL 5226 and J. C. Hardy, private communication.

3. W. J. Courtney and J. D. Fox, Atomic Data and Nuclear Data Tables 15, 141 (1975).

4. M. Harchol, A. A. Jaffe, J. Miron, I. Unna, and J. Zioni, Nucl. Phys. A90, 459 (1967).

REVISED SINGLE-PARTICLE ENERGIES IN N = 83 NUCLEI*

P. Kleinheinz,† M. R. Maier,‡ R. M. Diamond,
F. S. Stephens, and R. K. Sheline

The single-neutron states in N = 83 nuclei have been extensively investigated,[1] mainly by deuteron stripping on targets of the stable isotones with N = 82. The data suggest the systematic occurrence of three states in each nucleus populated by high-angular momentum transfers; these levels vary smoothly with proton number and lie below 2 MeV excitation. The (d,p) angular distributions for these states were assigned as $l = 5$ transfers, and the levels therefore were interpreted as $h_{9/2}$ fragments. More recently, radioactivity[2] and $(\alpha,n\gamma)$ experiments[3] extended the systematics of these high-j states to ^{147}Gd which is not accessible in single-neutron transfer. Except for ^{139}Ba, where a recent (d,p) study[4] conflicts with the earlier investigations,[1] none of these studies located the $i_{13/2}$ single particle excitation which, from systematics, is expected to lie within the range of excitation covered by these experiments.

We have used the following compound nuclear reactions followed by particle emission to populate levels in the N = 83 isotones of Ce, Nd, Sm, and Gd: ^{139}La(^{7}Li,αn)^{141}Ce and ^{139}La(^{7}Li,3n)^{143}Nd at E_{Li} = 30 MeV, ^{144}Nd(α,3n)^{145}Sm at E_{α} = 40 MeV, and ^{147}Sm(α,4n)^{147}Gd at E_{α} = 57 MeV. The experiments were carried out at the Berkeley 88-inch cyclotron, using standard in-beam γ-ray spectroscopy techniques[5] with various combinations of 8 cm^3 planar Ge, 30 cm^3 and 50 cm^3 coaxial Ge(Li) detectors. Measurements of γ-ray excitation functions and two-point angular distributions as well as two-detector four-parameter coincidences were used to establish the level schemes of Fig. 1. In each of these nuclei essentially the entire decay intensity proceeds through the previously known lowest-lying high-j level, but our measurements show these levels to be isomeric with nanosecond half-lives. They decay via single γ-transitions to the well established[6] $f_{7/2}$ ground state of each nucleus. This fact is clearly inconsistent with a $9/2^-$ assignment for these states.

The half-lives were extracted from the $\gamma\gamma$-time spectra. They are listed in the table.[§] Comparison with the single-particle estimate[7] classified the

Table 1. Half-lives of $i_{13/2}$ states in N = 83 isotones.

Nucleus	energy (keV)	$T_{1/2}$ (ns)	Enhancement $T^{SP}_{1/2}/T^{exp}_{1/2}$
^{141}Ce	1370.8	4±2	9±4
^{143}Nd	1230.0	6±2	12±4
^{145}Sm	1105.8	12±2	12±2
^{147}Gd	997.4	20±3	15±3

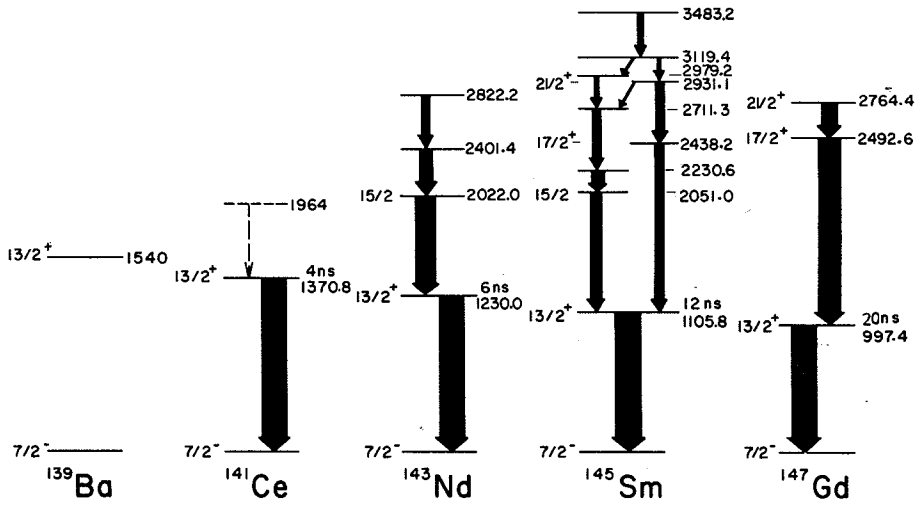

Fig. 1. Partial level schemes for N = 83 isotones as deduced from the present work and from Ref. 4. The excitation energies are accurate to 1 keV. (XBL 766-8231)

deexcitation transitions as E3, whereas M1 transitions, as required by the previous assignments, would have to be 10^6 times retarded in all cases. The life-times, together with the observed strong transfer intensities, argue for the identification in all these nuclei of the first high-j state as an $i_{13/2}$ single-neutron state. We have also included in Fig. 1 the $i_{13/2}$ state in ^{139}Ba. The angular momentum transfer to this level has been measured as $l = 6$ in a (d,p) experiment with 20 MeV deuterons,[4] a result which has been ignored[‖] in more recent work.[2,8]

The proposed $i_{13/2}$ assignments in the N = 83 nuclei remove a number of discrepancies connected with the earlier $9/2^-$ assignments. The stripping data into the N = 83 isotones of Ba, Ce, Nd, and Sm quoted in Ref. 1 consistently gave spectroscopic strengths for $l = 5$ transfer in excess of the sum-rule limit for $h_{9/2}$, in Nd and Sm by as much as 70%. With the $i_{13/2}$ assignment for the lowest state, the remaining observed $l = 5$ strengths become compatible with the sum-rule limit, and the reported cross sections to the high-j state of lowest energy are consistent with a predominant $i_{13/2}$ configuration. Moreover, in the β^+ decay of the $h_{11/2}$ isomer of ^{147}Tb (Ref. 2), two high-lying states in ^{147}Gd were found to be populated with log ft values ≤ 4.4 and assigned $9/2^-$. The third high-j level (the one presently being considered), which from (α,n) data was also assigned as $9/2^-$, is only populated with very small intensity in the β^+ decay and this feature is explained by our $13/2^+$ assignment of this level.

Footnotes and References

*Condensed from Phys. Lett. 53B, 442 (1975).

†Now at Institut für Kernphysik, KFA Julich, D-5170 Julich, W. Germany.

‡Visitor from Physik Department, Technische Universitat Munchen, D-8046 Garching, W. Germany.

§The data also revealed a previously unreported half-life of 28±2 ns for the 2101 keV 4^+ level in ^{142}Nd which was populated by the (^{7}Li,4n) reaction.

‖In contrast to the authors of Ref. 4 an $11/2^+$ assignment has been adopted for this level in a recent compilation.[8]

1. E. Newman, K. S. Toth, and I. R. Williams, Phys. Rev. C7 290 (1973) and references given therein.

2. E. Newman, K. S. Toth, D. C. Hensley, and W. D. Schmidt-Ott, Phys. Rev. C9 674 (1974).

3. J. Kownacki, H. Ryde, V. O. Sergejev, and Z. Sujkowski, Physica Scripta 5 66 (1972).

4. S. S. Ipson, W. Booth, and J. G. B. Haigh, Nucl. Phys. A206, 114 (1973).

5. J. Gizon et al., Nucl. Phys. A222, 557 (1974).

6. C. Ekstrom, S. Ingelman, M. Olsmats and B. Wannberg, Physica Scipta 6, 181 (1972).

7. C. M. Lederer, J. M. Hollander, and I. Perlman, Table of Isotopes, Sixth Ed. (John Wiley & Sons Inc., New York, London, Sidney 1968) p. 578.

8. L. R. Greenwood, Nucl. Data Sheets 12, 139 (1974).

TRIAXIAL SHAPES IN LIGHT La NUCLEI*

P. A. Butler,† J. Meyer-ter-Vehn,‡ D. Ward,§ H. Bertschat,‖
P. Colombani,¶ R. M. Diamond, and F. S. Stephens

The yrast levels of the light odd lanthanum isotopes have been identified[1] as a decoupled band in which an $h_{11/2}$ proton has its spin maximally aligned with the rotation axis of a prolate core. A number of such examples have since been observed, but in some cases it has been shown[2] that the data available on additional states indicate deviations from axial symmetry. As a test of the triaxial description we have measured lifetimes for the $15/2^-$ and $19/2^-$ levels in ^{129,131}La.

We have used the recoil-distance method to measure lifetimes using the reactions ^{119}Sn(^{14}N,4n)^{129}La at 67 MeV, ^{118}Sn(^{16}O,4n)^{130}Ce at 82 MeV and ^{116}Cd(^{19}F,4n)^{131}La at 72 MeV. The heavy-ion beams were provided by the LBL 88-inch cyclotron. The Sn targets were stretched self-supporting foils of 0.75 mg cm^{-2} thickness. The Cd target was 0.6 mg cm^{-2} of enriched Cd evaporated on 0.2 mg cm^{-2} nickel. Gamma rays were detected in a planar Ge detector placed at 0° with respect to the beam direction. For the lowest transitions in the yrast sequence, recoil-distance decay curves were derived by integrating the stopped (I_s) and moving (I_m) γ-ray peaks and plotting the ratio $I_s/(I_s+I_m)$ versus plunger setting (Fig. 1). The average recoil velocity was derived from the centroid shifts of stopped and moving γ-ray components, and after correction for the finite solid angle of the Ge detector was found to be 0.87% of c for ^{129}La, 1.03% for ^{130}Ce and 1.05% for ^{131}La. For each nucleus, lifetimes for the $19/2^-$ (4^+) and $15/2^-$ (2^+) levels were obtained by fitting simultaneously the two decay curves using a least-squares fitting procedure. The behavior of the feeding ahead of the $19/2^-$ state, approximated by two or more levels whose lifetimes were free parameters, could be determined partly by the shape of the $23/2^- \rightarrow 19/2^-$ decay curve and partly by the constraint that all the curves pass through a common origin. Where the experimental relative intensities of the cascade transitions markedly decreased with increasing spin, feeding into the band from other levels was also taken into account. The results are shown in Table 1, where it can be seen that for ^{130}Ce, the only case where other measurements are available for comparison, the present value for the $2 \rightarrow 0$ transition is in excellent agreement with that measured by Dehnhardt et al.[3]

Calculated B(E2) values for transitions between the lowest yrast states of an $h_{11/2}$ quasiparticle coupled to an asymmetric core are shown in Fig. 2. For the $11/2^-$, $15/2^-$, and $19/2^-$ states the total angular momentum tends to localize about the intrinsic $\hat{2}$-axis (oblate symmetry axis at $\gamma = 60°$). If the total angular momentum points along the $\hat{2}$ axis the E2-transition probability can be approximated by

$$B(E2)_{class} \cong \frac{5}{16\pi} (Q_{22}^{(\hat{2})})^2$$

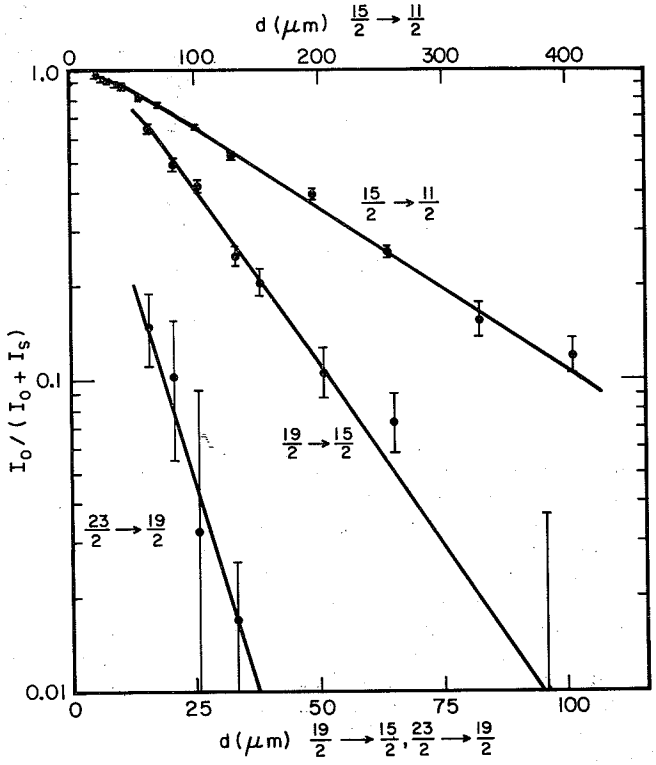

Fig. 1. Recoil-distance decay curve for ^{131}La. (XBL 753-2430)

where $Q_{22}^{(\hat{2})} = Q_0 \cdot \sin(\gamma - 60°)/\sqrt{2}$ is the $\mu = 2$ component of the intrinsic quadrupole tensor related to the $\hat{2}$-axis (lower dashed line in Fig. 2). The exactly calculated B(E2)'s for the $15/2^- \rightarrow 11/2^-$ and the $19/2^- \rightarrow 15/2^-$ transitions closely follow this classical limit over the range $10° < \gamma < 35°$ (Fig. 2). For states with $I > 19/2$ the total angular momentum of the system tends to align with the $\hat{1}$-axis prolate symmetry axis at $\gamma = 0°$, since this axis has the largest moment of inertia in the triaxial region, and thereby minimizes the core rotational energy. This tendency now dominates over the preference of the particle for the $\hat{2}$-axis. The B(E2)'s of higher transitions (e.g., $27/2^- \rightarrow 23/2^-$) therefore peak near $\gamma = 30°$ where $Q_{22}^{(\hat{1})} = Q_0 \cdot \sin(\gamma + 60°)/\sqrt{2}$ has its maximum (upper dashed line in Fig. 2).

The B(E2) values calculated from the asymmetric rotor model with $\gamma = 22°$ (^{129}La) and $\gamma = 23°$ (^{131}La) are also shown in Table 1 together with predictions of the symmetric rotor model and the weak coupling model. The experimental results for the $15/2^- \rightarrow 11/2^-$ and $19/2^- \rightarrow 15/2^-$ transitions in ^{129}La and ^{131}La, plotted also in Fig. 2, are seen to follow closely the predictions of the asymmetric model. The prediction of weak coupling for the B(E2; $15/2^-$

Table 1. Lifetimes and B(E2) values in ^{129,131}La and their respective core nuclei. The experimental results are compared with predictions from various theoretical models. References are given in parentheses.

Nucleus	E_γ (keV)	τ (psec)	$B(E2)\downarrow_{exp.}$ (e^2b^2)	Strong coupling		Weak coupling	Rotation aligned (triaxial core)	
				K = 1/2	K = 11/2		$\gamma = 0$	γ_{exp}[b]
^{128}Ba								
2 →0	279	140±30(4)	0.33±0.07					
^{130}Ce	254	225±19(3)	0.33±0.02					
2 →0		211±9[a]						
^{129}La								$\gamma = 22^o$
15/2→11/2	269	130±6[a]	0.42±0.02	0.53	0.07	0.33	0.50	0.37[c]
19/2→15/2	475	8.7±1.3[a]	0.38±0.06	0.55	0.22		0.52	0.42[c]
^{130}Ba								
2 →0	357		0.24±0.08(5)					
^{132}Ce	325	67.9±9.5(3)	0.32±0.05					
±#±La								$\gamma = 23^o$
15/2→11/2	336	55±2[a]	0.34±0.02	0.49	0.06	0.30	0.45	0.32[d]
19/2→15/2	533	5.8±0.6[a]	0.33±0.03	0.50	0.20		0.47	0.37[d]

[a] Present results.

[b] Estimated from the systematics of the 2^+, $2^{+'}$, and 4^+ levels in the core nuclei.

[c] Model parameters: $\beta \cdot A^{2/3} = 6.8$ derived from B(E2; $2^+ \rightarrow 0^+$) of core nuclei, Fermi energy $\lambda_F = (\varepsilon_1 + \varepsilon_2)/2$ estimated from Nilsson level scheme (ε_ν s.p. energies of $h_{11/2}$ shell), $\Delta = 1.0$ MeV from odd-even mass differences.

[d] Model parameters: $\beta \cdot A^{2/3} = 6.4$, $\lambda_F = (\varepsilon_1 + \varepsilon_2)/2$, $\Delta = 1.0$ MeV derived in the same way as for ^{129}La.

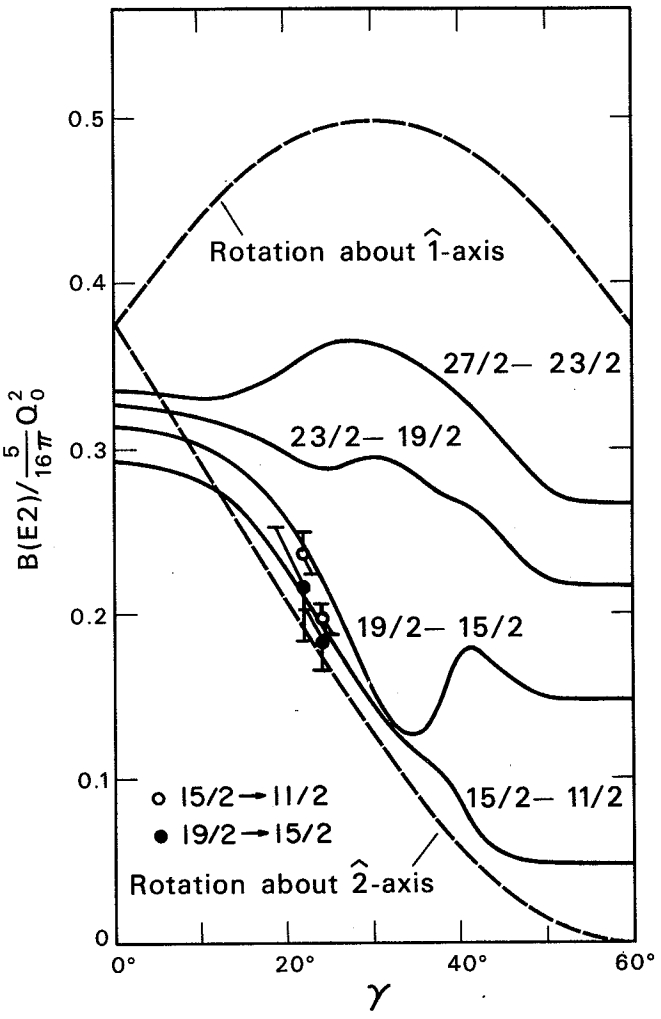

Fig. 2. Calculated transition probabilities as functions of the core asymmetry γ. The calculations are accurate to within about 5% for a range of $\beta \cdot A^{2/3}$ given by $4 \leq \beta \cdot A^{2/3} \leq 7$ and a range of λ_F given by $\varepsilon_1 \leq \lambda_F \leq \varepsilon_2$. The broken lines give classical limits for B(E2). Shown also are the experimental data for ^{129}La ($\gamma = 23^0$). The transition probabilities are given in terms of $\frac{5}{16\pi} Q_0^2$ is given by

$$Q_0 = \frac{3}{\sqrt{5\pi}} (1.2)^2 \, Z\beta \, A^{2/3} \, (\text{fm})^2.$$

(XBL 751-4646)

$\rightarrow 11/2^-$) values are next best, but they differ significantly from the experimental results, being systematically smaller in magnitude. The lack of precise experimental data on the core $4^+ \rightarrow 2^+$ transition makes further quantitative comparison with the weak coupling model difficult, but with the additional assumption of a simple rotational or vibrational core one would obtain a value of respectively 1.4 and 2.0 for the ratio B(E2; $19/2^- \rightarrow 15/2^-$): B(E2; $15/2^- \rightarrow 11/2^-$) in contradiction to the experimental evidence.

Footnotes and References

*Condensed from Phys. Lett. 56B, 453 (1975).

†U.K. S.R.C./N.A.T.O. Fellow.

‡Permanent address: TU München, 8046 Garching, West Germany.

§Permanent address: Chalk River Nuclear Laboratories, Ontario, Canada.

‖D.A.A.D. Fellow; permanent address: Hahn-Meitner-Institut, Berlin, West Germany.

¶Permanent address: Institut de Physique Nucléaire, 91406 Orsay, France.

1. J. R. Leigh, K. Nakai, K. H. Maier, F. Pühlhofer, F. S. Stephens, and R. M. Diamond, Nucl. Phys. A213, 1 (1973); F. S. Stephens, R. M. Diamond, J. R. Leigh, T. Kammuri, and K. Nakai, Phys. Rev. Lett. 29, 438 (1972).

2. J. Meyer-ter-Vehn, F. S. Stephens, and R. M. Diamond, Phys. Rev. Lett. 32, 1383 (1974).

3. W. Dehnhardt, S. J. Mills, M. Müller-Veggian, U. Neumann, D. Pelte, G. Poggi, B. Povh, and P. Taras, Nucl. Phys. A225, 1 (1974).

HIGH-SPIN STATES IN ^{127,129}La; A TEST OF BACKBENDING IN THE EVEN Ba AND Ce NUCLEI*

D. Ward,† H. Bertschat,‡ P. A. Butler, P. Colombani,§
R. M. Diamond, and F. S. Stephens

The rotation-aligned coupling scheme[1] has had considerable success in describing the collective bands in a number of weakly deformed odd-mass nuclei. It has also been pointed out that the presence of backbending in an odd-mass rare-earth nucleus is an important clue as to the cause of backbending in the adjacent doubly-even nuclei. If a particular rotation-aligned particle delays or prevents the occurrence of backbending in the odd-mass case, it is likely that this particle is involved in the structure of the band whose intersection with the ground band causes the backbending in the doubly-even nucleus.[2] Conversely, if the odd-particle band does backbend, this particle must not be such an important component.[3] Application of this idea has shown the importance of $i_{13/2}$ neutrons in the backbending behavior observed in the lighter deformed nuclei Dy,[4] Er,[2] and Yb.[5] Very recently the importance of rotation-aligned $h_{9/2}$ protons in the backbending of the heavier deformed Hf, W, and Os nuclei has been demonstrated by studying ^{167}Lu[6] and ^{181}Re,^{181,183}Os.[7]

In this paper we report a study of the high-spin decoupled states of ^{127,129}La from which we can draw conclusions concerning the causes of the backbending observed in the neighboring Ba and Ce nuclei. Previous studies of high-spin states in ^{126,128}Ba[8] and ^{130}Ce[9] have shown that the ground bands backbend around spin 10^+. This corresponds to a spin of $31/2^-$ in the $11/2^-$ band in La, but the earlier work on ^{127,129}La[10] only assigned levels as high as $27/2^-$. In the present work we have identified levels to spin $35/2^-$, just beyond the critical region. To obtain as complete a comparison as possible, we have also studied the ground band in ^{128}Ce, since it was previously known[11] only to spin 8^+.

The experiments were performed at the LBL 88-inch cyclotron, using the reactions ^{117}Sn(^{14}N,4nγ)^{127}La with 75 MeV ^{14}N, ^{119}Sn(^{14}N,4nγ)^{129}La with 67 and 75 MeV ^{14}N, and ^{116}Sn(^{16}O,4nγ)^{128}Ce with 88 MeV ^{16}O. The targets were made by evaporating the tin isotope to ~ 50 mg/cm^2 of lead. Gamma rays were detected both in singles and in coincidence mode using two 45 cc coaxial Ge(Li) detectors. The 0° to 90° anisotropy of the γ-rays was measured to test the main cascade sequences were indeed stretched E2 transitions.

Typical coincidence spectra for ^{129}La are shown in Fig. 1, and the cascade sequences deduced from individual gates set on the known ground-band

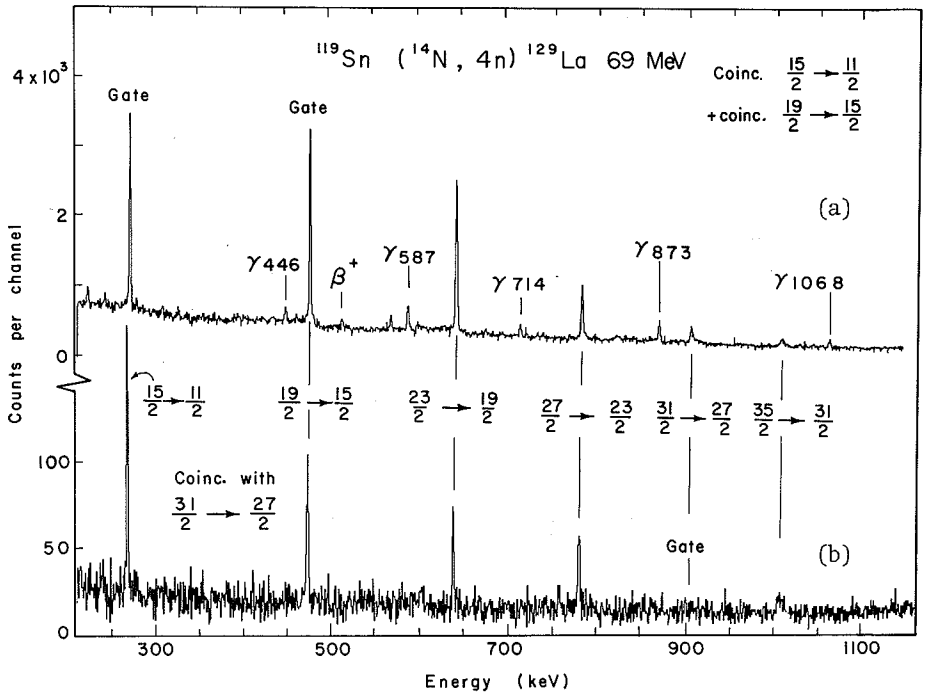

Fig. 1. Coincidence spectra for ^{129}La, spectrum (a) is for the sum of gates set on the lowest two rotational transitions, (b) is for the $31/2 \rightarrow 27/2$ transition. Spectra corresponding to background events have been subtracted in an appropriate way. (XBL 7412-8448)

transitions are summarized in Table 1. The A_2 values derived from the anisotropy measurements assuming $A_4 = -0.05 \pm 0.05$ are consistent with stretched E2 assignments (Table 1). The level schemes are in Fig. 2.

To compare the systematics of the core states in ^{127,129}La with those of the corresponding Ba and Ce nuclei we have calculated the moments of inertia, $\mathcal{J}$ and the rotational frequencies, ω, according to the formulae given in [3]. Plots of $\mathcal{J}$ vs. ω^2 are shown in Fig. 3. It can be seen that the $11/2^-$ decoupled band in La does not backbend, even for rotational frequencies appreciably higher than those for which the Ba and Ce nuclei do backbend. This fact suggests that a rotation alignment of two such $h_{11/2}$ protons is involved in the backbending in the even barium and cerium nuclei. In fact it seems likely that the backbending is caused by an intersection of the ground band with a band composed of two $h_{11/2}$ protons maximally aligned with the rotation axis. It is of interest not only that the backbending is caused by protons rather than neutrons in this region, but also that it is most likely due to a rotation-alignment effect like that observed in the rare-earth region, rather than to a shape change as is the case for the neutron-deficient Hg nuclei. It appears that the technique of studying an even-even case by observing its behavior with various particle orbits blocked, is applicable to this Ba-Ce region, as well as to the deformed rare-earth region, and can probably be applied rather generally.

Table 1. Summary of the rotational cascades in ^{127,129}La and ^{128}Ce observed in this experiment. Assignments in La nuclei to spin $27/2^-$ (8^+) have been made previously.[10] Values for ^{126,128}Ba and ^{130}Ce are from previous work; ^{128}Ce assignments[8,9] to spin 8^+ have been made previously.[11] Uncertainties in the relative intensities and A_2 coefficients are shown in parentheses.

Spin	^{128}Ba[a]	^{129}La (75 MeV)			^{130}Ce[b]
I (or I - 11/2	E_γ (keV)	E_γ	Int	A_2	E_γ
2	284	269.3	100	0.35(3)	254.1
4	479	474.8	81(8)	0.32(3)	456.7
6	644	641.9	55[c](16)	0.35(3)	614.2
8	782	785.6	29(3)	0.31(4)	729.6
10	894	910.5	11[c](2)	0.26(15)	757.0
12	906	1013.5	8[c](2)	0.02(30)	503.3
14					549.0
16					693.5

Spin	^{126}Ba[8]	^{127}La (76 MeV)			^{128}Ce (88 MeV)		
I (or I - 11/2	E_γ (keV)	E_γ	Int	A_2	E_γ	Int	A_2
2	256	252.4	100	0.19(3)	207.3	100	0.26(3)
4	455	458.6	73(7)	0.28(3)	399.6	88(9)	0.23(3)
6	621	630.8	48(5)	0.23(3)	550.6	88(9)	0.32(3)
8	757	780.3	31(4)	0.13(4)	662.6	50(5)	0.26(4)
10	852	908	8(2)	0.10(15)	711.1	33(3)	0.31(6)
12	805	1003	5(1)	0.16(30)	576.5	28(3)	0.25(6)
14	672				560.6	22[c](2)	0.24(6)
16	825				689.9	14[c](2)	0.38(10)

a. Ref. 8.
b. Ref. 9.
c. Not single lines in the direct spectra. Relative intensities taken from spectra in coincidence with the $2^+ \rightarrow 0^+$ ($15/2^- \rightarrow 11/2^-$) transitions.

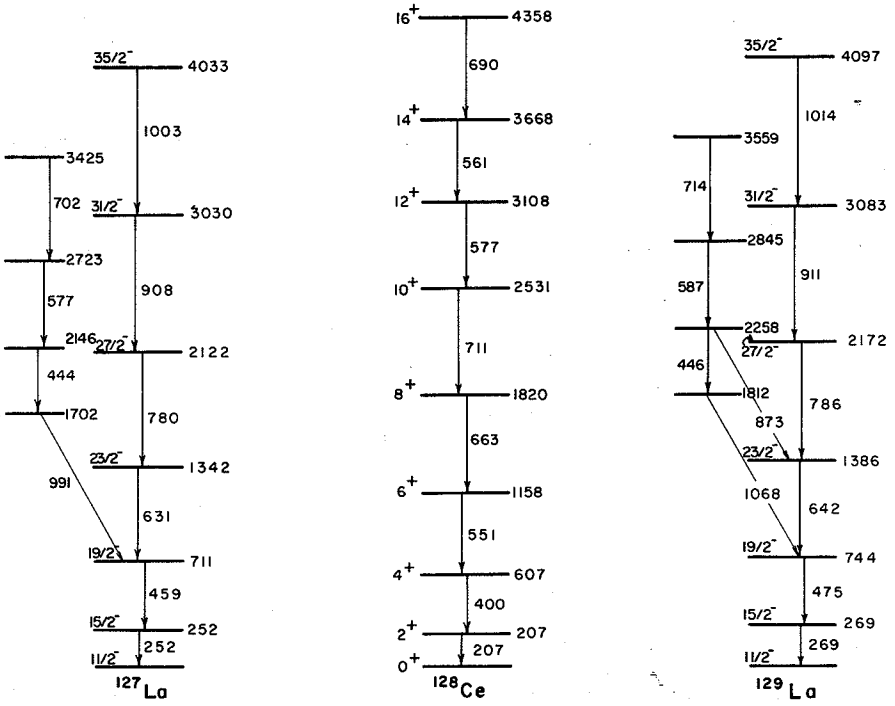

Fig. 2. Level scheme for ^{127,129}La and ^{128}Ce. (XBL 7412-8447)

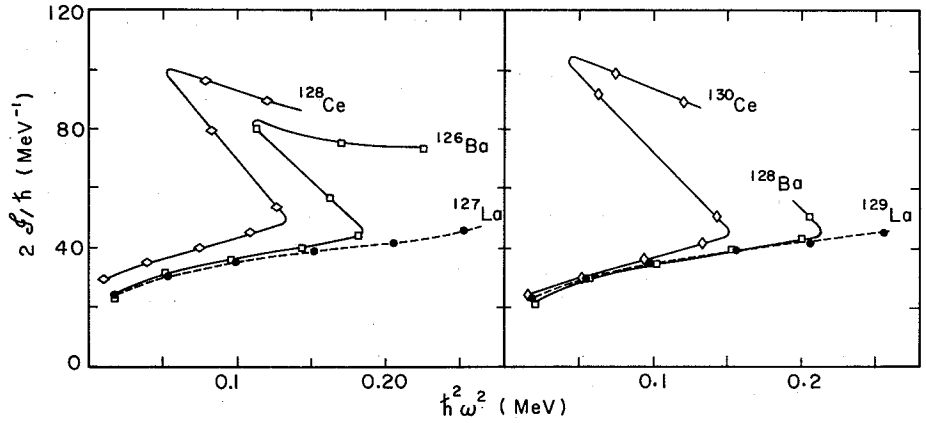

Fig. 3. Comparison of backbending plots for *core states* in ^{127,129}La with adjacent even nuclei. (XBL 7412-8446)

Footnotes and References

*Condensed from Phys. Letters 56B, 139 (1975).

†Permanent address: Chalk River Nuclear Laboratories, Ontario, Canada.

‡DAAD-Fellow; permanent address: Hahn-Institut, Berlin, Germany.

§Permanent address: Institut de Physique Nucléaire, 91406 Orsay, France.

1. F. S. Stephens, R. M. Diamond, and S. G. Nilsson, Phys. Lett. 44B, 429 (1973).

2. E. Grosse, F. S. Stephens, and R. M. Diamond, Phys. Rev. Lett. 31, 840 (1973).

3. E. Grosse, F. S. Stephens, and R. M. Diamond, Phys. Rev. Lett. 32, 74 (1974).

4. W. F. Davidson, R. M. Lieder, H. Beuscher, A. Neskakis, and C. Mayer-Böricke, Proceedings of the International Conference on Reactions between Complex Nuclei, eds. R. L. Robinson, F. K. McGowan, J. B. Ball, and H. J. Hamilton (North-Holland, Amsterdam, 1974) Vol. 1, p. 190.

5. L. L. Riedinger, G. J. Smith, P. H. Stelson, E. Eichler, G. B. Hagemann, D. C. Hensley, N. R. Johnson, R. L. Robinson, and R. O. Sayer, Phys. Rev. Lett. 33, 1346 (1974).

6. C. Foin and D. Barnéoud, Phys. Rev. Lett. 33, 1049 (1974).

7. W. F. Davidson, R. M. Lieder, H. Beuscher, A. Neskakis, and C. Mayer-Böricke, preprint. International Conference on Nuclear Structure and Spectroscopy, Amsterdam, 1974.

8. C. Flaum, D. Cline, A. W. Sunyar, and O. C. Kistner, Phys. Rev. Lett. 33, 973 (1974).

9. D. Ward, H. R. Andrews, G. J. Costa, J. S. Geiger, R. L. Graham, and P. Taras, American Phys. Soc. Bull. 19, 502 (1974).

10. J. R. Leigh, K. Nakai, K. H. Maier, F. Pühlhofer, F. S. Stephens, and R. M. Diamond, Nucl. Phys. A213, 1 (1973).

11. D. Ward, R. M. Diamond, and F. S. Stephens, Nucl. Phys. A117, 309 (1968).

REDUCED TRANSITION PROBABILITIES FOR HIGH SPIN STATES IN ^{232}Th*

M. W. Guidry, P. A. Butler,† P. Colombani,‡ I. Y. Lee, D. Ward,‡
R. M. Diamond, F. S. Stephens, E. Eichler,§ N. R. Johnson,§ and R. Sturm‖

The measurement of lifetimes, or equivalently, reduced transition probabilities, for high-spin states is of considerable interest because these measurements provide a stringent test of nuclear models. These lifetimes normally lie outside the range of conventional electronic methods, but are often amenable to determinations by three complementary techniques: 1) the Doppler-shift recoil-distance method (RD), 2) the Doppler-broadened lineshape method (DBLS), and 3) multiple Coulomb excitation methods (COULEX). We have applied a variety of these methods to measurement of the lifetimes and reduced transition probabilities for spins 6^+ - 18^+ of the ground state rotational band in ^{232}Th.

In Fig. 1 the reduced transition probability $B(E2)_{Exp}/B(E2)_{Rot}$ determined by all techniques discussed in this report are displayed. For completeness we have also plotted ratios from previously published recoil-distance measurements with ^{40}Ar projectiles.[1] The mutual consistency of the results and their agreement with the rotational model is striking. In Fig. 2 we plot the weighted average of all B(E2) ratios determined by lifetime measurements in the present work. For all states that have been studied, the average B(E2) values are those of a good rotor, within the limits of experimental uncertainty.

Insofar as was practical, the various analyses

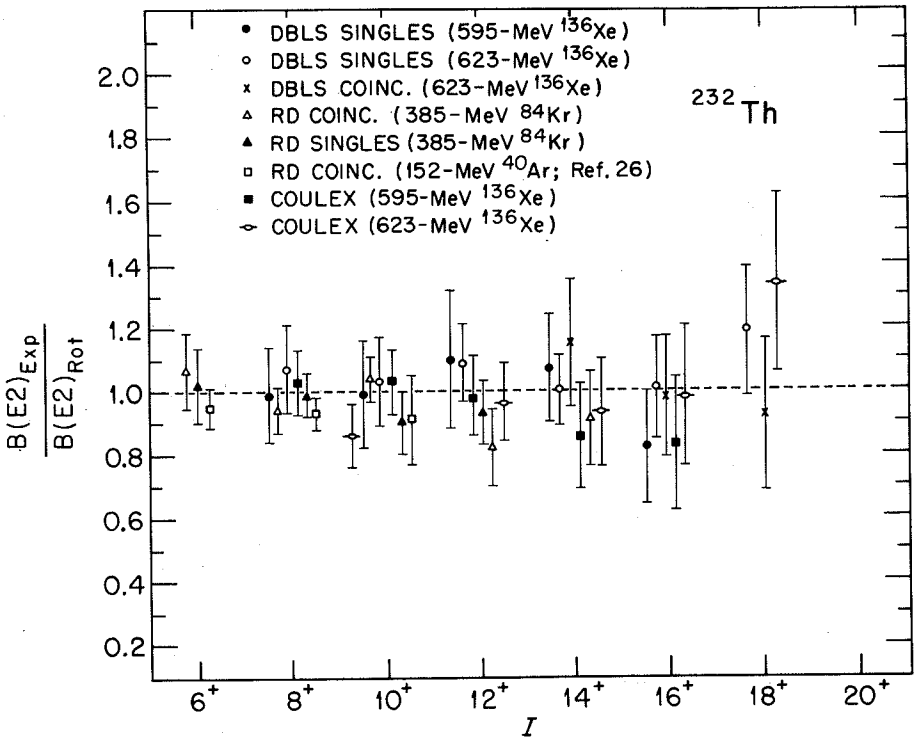

Fig. 1. Values of the ratio $B(E2)_{exp}/B(E2)_{rot}$ for states in ^{232}Th determined in this experiment and in previous work. (XBL 765-1804)

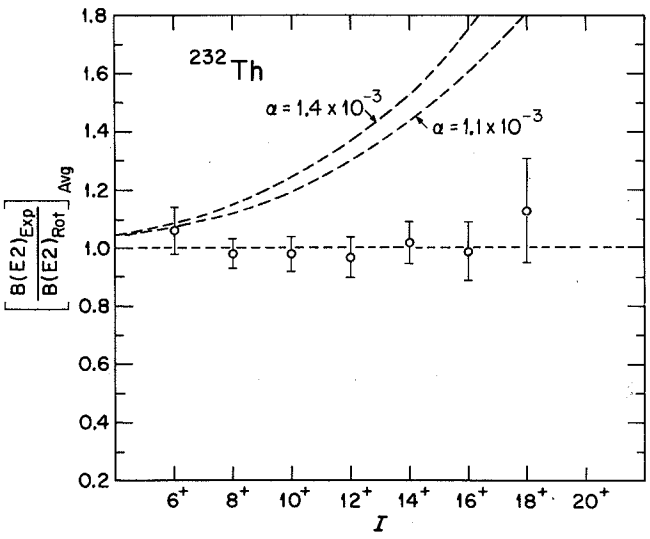

Fig. 2. Weighted average of the ratio $B(E2)_{exp}/B(E2)_{rot}$ determined from RD methods (^{84}Kr projectiles in backscatter coincidence and in singles), and from the DBLS experiment (^{136}Xe projectiles in singles and backscatter coincidence modes). The dashed lines represent the B(E2) ratios expected from simple centrifugal stretching and β-band mixing models, as discussed in the text. (XBL 765-1803)

described here were carried out independently. Therefore the results displayed in Figs.1 and 2 provide criteria for judging the mutual consistency of the methods employed, which is seen to be quite good.

Phenomenologically, the moment-of-inertia for deformed nuclei is known to be spin dependent.[2] The variation of the moment-of-inertia with angular momentum manifests itself in the rotational energy-level spacings. Thus the energy of the 16^+ state in ^{232}Th is ~ 15% below that of the rigid-rotor prediction using the energy of the 2^+ state. The smooth deviations of the energy levels from those of a pure rotor have generally been described with a formalism employing some combination of 4th-order cranking, Coriolis anti-pairing, centrifugal stretching, or band-mixing calculations. These suggest that the moment-of-inertia depends both on the pairing and the deformation, while we expect the transition probabilities, to first order, to be sensitive to the deformation only. Therefore non-rotational energy spacings need not be attended by non-rotational transition probabilities.

If one considers a 1st-order band-mixing model, the B(ES) values for the ground band can be written as[3]

$$B(E2, I \to I-2) = B(E2, I \to I-2)_{Rot} \left\{ \frac{1 + 1/2\alpha\, I+1) + (I-2)(I-1)}{1 + 3\alpha} \right\}^2 . \quad (1)$$

The parameter α may be specified if explicit assumptions are made about the nature of the bands being mixed into the ground band.[3] Thus, if we assume the mixing of a pure β-vibration into the ground band, the parameter α is fixed by two E2 matrix elements connecting the ground and β-bands. Using B(E2, $0_g \to 2_\beta$) and B(E2, $2_g \to 0_\beta$) of McGowan, et al.,[4] we deduce $\alpha \approx 1.1 \times 10^{-3}$.

Similarly, if one attributes deviations of the ground band moment-of-inertia to centrifugal stretching, α may be approximated from the energy spacings in the ground band,[3] and has a value in this case of $\alpha \approx 1.4 \times 10^{-3}$. In Fig. 2 we plot the B(E2) ratios expected from 1st-order mixing of the ground and β-bands using values of α determined from the ground-to-β matrix elements and from the energy spacings. Clearly neither curve is consistent with the experimental data.

The failure of the curve determined from the centrifugal-stretching model to fit the lifetime data is not difficult to understand, since the moment-of-inertia is sensitive to other than centrifugal-stretching effects. For instance, alterations in the pairing interaction brought about by Coriolis anti-pairing effects will have significant effect on the moment-of-inertia, but should have little influence on the nuclear deformation and on the transition probabilities, which are determined primarily by the deformation. In addition one must consider the possible admixture of bands other than the β-band, such as higher-lying K = 0 bands and the K = 2 γ-band, into the ground band.

The α parameter derived from the matrix elements is less model-dependent than that derived from the energy spacings since it is related directly to transition probabilities between the ground and higher-lying band. In Ref. 4 it is concluded that the lowest excited 0^+ level is of β-vibrational character. The matrix elements used to derive α only connect the lowest two members of the ground and β-bands. Therefore, our results are consistent with admixture of a pure β-band at low spins since the small deviations of the B(E2) from rotational values at low spins lie within experimental uncertainty. At higher spins our results are incompatible with continued admixture of a single band with the same characteristics as that determined by the matrix elements of Ref. 4.

We may use Eq. (1) and the experimental B(E2) values phenomenologically to set upper limit of $|\alpha| \leq 2 \times 10^{-4}$ for the higher-spin region. Assuming the collective B(E2) values to depend only on the nuclear shape we have[3]

$$\frac{\Delta\beta_2(I)}{\beta_2(0)} \approx \alpha\, I(1+1) \quad (2)$$

and on the basis of the present data we conclude $\Delta\beta_2(16^+)/\beta_2(0) \leq 0.06$. This lack of softness against further quadrupole deformation for well-deformed nuclei is consistent with the behavior of many rare-earth nuclei in recent deformed shell-model calculations.[5]

Footnotes and References

*Condensed from LBL 4038, Nucl. Phys. A (to be published).

†U.K. S.R.C./N.A.T.O. Fellow.

‡Permanent address: Institut de Physique Nucléaire, 91406 Orsay, France.

‡Present address: Chalk River Nuclear Laboratories, Ontario, Canada.

§Oak Ridge National Laboratory, Oak Ridge, Tennessee.

‖Max Kade Foundation Fellow. Present address: University of Marburg, Marburg, Germany.

1. N. R. Johnson, R. J. Sturm, E. Eichler, M. W. Guidry, G. D. O;Kelley, R. O. Sayer, D. C. Hensley, N. C. Singhal, and J. H. Hamilton, Phys. Rev. C 12, 1927 (1975).

2. M. A. Mariscotti, G. Scharf-Goldhaber, and B. Buck, Phys. Rev. 178, 1864 (1969).

3. R. M. Diamond, G. D. Symons, J. L. Quebert, K. H. Maier, J. R. Leigh, and F. S. Stephens, Nucl. Phys. A184, 481 (1972).

4. F. K. McGowan, C. E. Bemis, Jr., W. T. Milner, J. L. C. Ford, Jr., R. L. Robinson, and P. H. Stelson, Phys. Rev. C 19, 1146 (1974).

5. R. Bengtsson, S. E. Larsson, G. Leander, P. Möller, S. D. Nilsson, S. Aberg, Z. Szymanski, Preprint, June 1975.

COULOMB EXCITATION OF HIGH-SPIN STATES IN ^{238}U*

E. Grosse,† J. de Boer,‡ R. M. Diamond,
F. S. Stephens, and P. Tjom§

The strong electromagnetic interaction produced in the encounter of a deformed target nucleus by a heavy projectile excites high-spin states in the ground-state rotational band and in rotational bands built on collective states coupled to the ground-state band. Such multiple Coulomb excitation is a powerful tool for investigating collective nuclear properties at high rotational frequencies. Of special interest are the rotational bands of the strongly deformed actinide nuclei, which cannot be studied by (HI,xnγ) reactions due to the strong fission competition. We have studied levels in the ground-state and octupole-vibrational bands of ^{238}U excited by Kr and Xe ions up to I ~ 20ħ.

Thick metallic targets, enriched in ^{238}U, were bombarded at the LBL SuperHILAC with beams of ^{84}Kr (385±5 MeV), ^{86}Kr (394±6 MeV), ^{132}Xe (605±20 MeV), and ^{136}Xe (640±40 MeV). The decay γ-rays were observed by two (~ 40 cc) coaxial Ge(Li) detectors, at $\theta_\gamma = 0°$ and $\theta_\gamma = 90°$ with respect to the beam direction and 4-5 cm from the target. Singles, γ-backscattered projectile and γ-γ coincidences were simultaneously stored. The low-energy portion of the singles γ-ray spectrum and the γ-γ coincidence spectrum is shown in Fig. 1 for the ^{136}Xe bombardment. Almost all the lines shown here belong to the

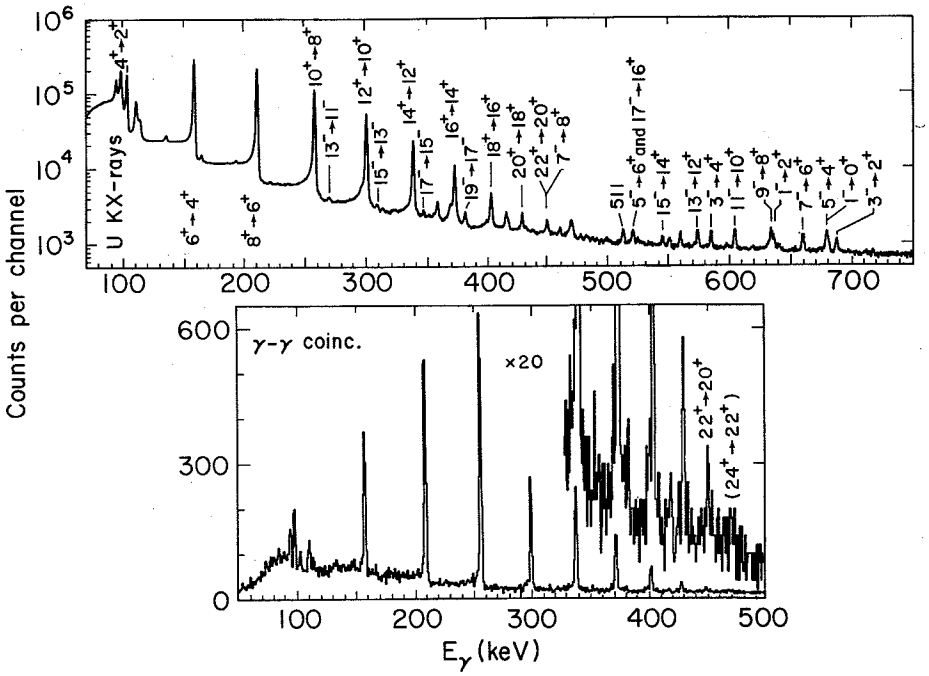

Fig. 1. Portions of the γ-ray singles spectrum (top) and γ-γ coincidence spectrum (bottom) from a thick ^{238}U target Coulomb excited with 640 MeV ^{136}Xe ions. The γ-γ coincidence spectrum is the sum of spectra gated by the 6-4, 8-6, 10-8, 12-10, and 14-12 transitions. (XBL 755-3037)

ground-state and lowest-energy octupole bands of ^{238}U. The resulting decay scheme is shown in Fig. 2.

The moments-of-inertia of the ground and octupole bands are shown as a function of the square of the rotational frequency in Fig. 3a. This type of plot corresponds to that generally made to display backbending behavior of nuclei in the rare-earth region. The ground band of ^{238}U does not backbend up to spin 22 (tentatively 24) even though the moment-of-inertia increases by ~ 50%. It is obvious that the octupole band has a larger apparent moment-of-inertia than the ground band, and behaves in a somewhat unusual manner with increasing rotational frequency. The nature of this band has been of interest for some time. The very general occurrence of collective octupole vibrational states, having a frequency $\omega \sim 15/A^{1/3}$ MeV, is well known and the sharp drop in energy of components of this state at the beginning of the rare-earth and expecially the actinide deformed regions is understood and has been qualitatively reproduced in recent calculations.[1,2] Four low-lying octupole bands are expected in ^{238}U having K values 0,1,2, and 3, and three collective negative-parity bands are known[3] below 1200 keV which may correspond to the K = 0,1, and 2 bands. The lowest observed band is the one shown in Fig. 2, which has (initially) a predominant K value of zero. There are at least three plausible types of behavior for these octupole bands at higher rotational frequencies. If the other rotation-vibration interactions are weak, then the Coriolis force will align the vibrational angular momentum along the rotation axis, producing a lowest band with energy spacings identical to those of the ground band, but having spins 3ħ higher. Or, the octupole deformation might be stabilized by the rotation, resulting in the even and odd spin states merging into one band having the usual I(I+1) energy spacings. A third possibility is that the collective octupole character of the band might be destroyed, for example by independent alignment of its particle (and/or hole) components, leading to irregular level spacings.

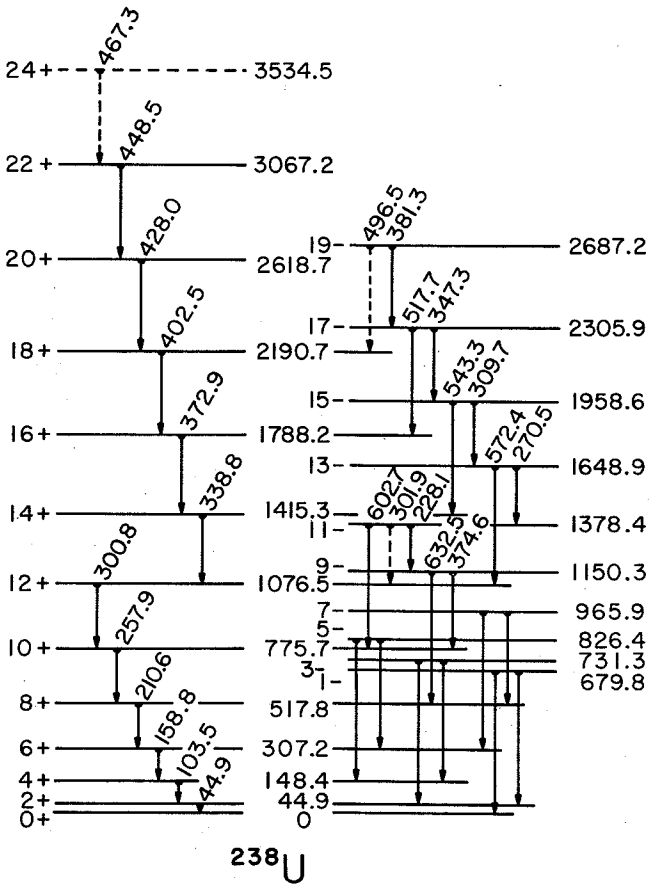

Fig. 2. Level scheme for the ground and lowest-energy octupole bands of ^{238}U.

(XBL 755-3038)

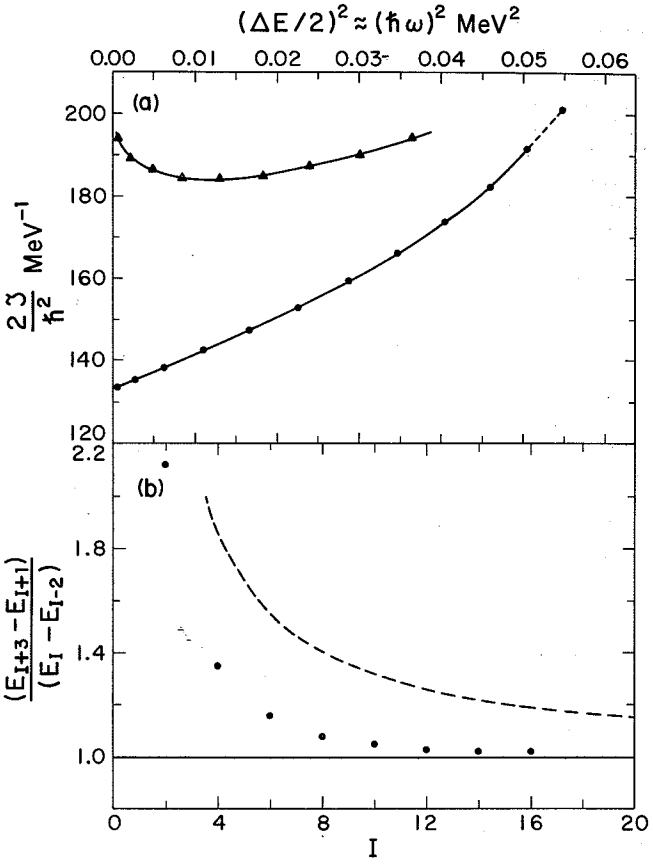

Fig. 3. (a) Backbending plots for the ground and octupole bands of ^{238}U. The ordinate is $2\mathcal{I}/\hbar^2 = (41\text{-}2)/(E_I\text{-}E_{I-2})$ and the abscissa is $(\hbar\omega)^2 = (E_I\text{-}E_{I-2})^2/4$. (b) Comparison of the data for the octupole band (dots) with the aligned-vibrator prediction (solid line) and the single-band prediction (dashed line).

(XBL 755-3039)

The experimental level energies of the lowest odd-parity band in ^{238}U are compared with these possibilities in Fig. 3b. The plot is constructed such that the rotation-aligned vibrator prediction is unity; whereas, the dashed line is the stable octupole-shaped rotor (one-band) prediction. The data are very regular and converge rather convincingly to the rotation-aligned limit. This result is in excellent accord with explanations that have been given for the compression (large moments-of-inertia) of the lowest few states of this octupole band, explanations involving Coriolis mixing of the K = 0,1,

2, and 3 octupole component.[1] It is also interesting to consider the effect on the E3 transitions. At sufficiently high spin values each rotation-aligned state has a nearly unique value of core angular momentum, R. The E3 transitions cannot change R, so that the $I_{gnd} \rightarrow (I+3)_{oct}$ transitions to the aligned (lowest) band pick up all the E3 strength, and the other transitions between these two bands become small. The previous Coriolis calculations[1,2] have shown this tendency in the $0^+ \rightarrow 3^-$ transitions, in agreement with the experimental data.

The present Coulomb excitation experiments provide much the highest spin values known in actinide-region nuclei. The data show that ^{238}U does not backbend up to spin 22ħ (probably not to 24ħ); though it is not yet clear that it will not backbend at still higher spin values. The evidence suggests that at the higher spin values observed, the octupole band aligns its angular momentum (3ħ) with that of the rotating core. This concept of the Coriolis force aligning an angular momentum vector along the rotation axis has previously been applied to one-particle states in weakly deformed nuclei,[4] and to two-particle states in strongly deformed even-even nuclei.[5] One sees from the ^{238}U case that this idea may apply to any angular momentum vector in a rotating system, including, in some circumstances, collective angular momenta.

Footnotes and References

*Condensed from Phys. Rev. Lett. 35, 565 (1975).

†On leave from Max-Planck-Institut für Kernphysik, 69 Heidelberg, Germany; supported by the Deutscher Akademischer Austauschdienst.

‡On leave from Ludwig-Maximilians Universität, München, Germany; supported by the Bundesministerium für Forschung und Technologie.

§On leave from the University of Oslo, Norway.

1. K. Neergård and P. Vogel, Nucl. Phys. A145, 33 (1970).

2. K. Neergård and P. Vogel, Nucl. Phys. A149, 217 (1970).

3. F. K. McGowan, C. E. Bemis, Jr., W. T. Milner, J. L. C. Ford, R. L. Robinson, and P. H. Stelson, Phys. Rev. C 10, 1146 (1974).

4. F. S. Stephens, R. M. Diamond, J. R. Leigh, T. Kammuri, and K. Nakai, Phys. Rev. Lett. 29, 438 (1972).

5. F. S. Stephens and R. Simon, Nucl. Phys. A183, 257 (1972).

HIGH-SPIN STATES OF $^{174,176}Yb$ STUDIED IN COULOMB EXCITATION WITH Kr AND Xe BEAMS*

D. Ward,† P. Colombani,‡ I. Y. Lee, P. A. Butler,§
R. S. Simon,‖ R. M. Diamond, and F. S. Stephens

The availability of beams of Kr and Xe at energies up to 8.5 MeV/nucleon has opened up the possibility of Coulomb exciting high-spin states in stable and near-stable deformed nuclei. In the actinide region, states up to spin 18^+ for ^{232}Th and 22^+ for ^{238}U have been observed by Coulomb excitation with Kr and Xe beams.[1-3] In recent studies of the rare-earth region, Kearns et al.[4] have identified some 12^+ and 14^+ states using ^{84}Kr ions at about 350 MeV. Coulomb excitation of rare earth nuclei with projectiles sufficiently heavy so that states of angular momentum larger than 16 are populated is quite interesting since: (i) the method of populating states is different than from a (HI, xn) reaction, so that additional states may be seen (of particular interest in this region is the study of backbending nuclei) and (ii) some nuclei that cannot be reached by (HI, xn) reactions can be Coulomb excited. Examples of this latter type would be the actinides and the neutron rich rare earth nuclei, including ^{174}Yb and ^{176}Yb. Also the high recoil momentum of the target nuclei following Coulomb excitation with heavy ions makes them ideal for lifetime studies using analyses of the doppler-broadened line shapes.

In addition to studying the γ-spectrum in singles with a Ge(Li) detector, we have used a new type of annular particle detector and have detected γ-rays in coincidence with specified ranges of the particle scattering angle. A description of this apparatus has been given in the more complete report of this work.[5] The sensitivity of the method was improved further by demanding an additional γ-ray event to be detected in either of two 7.5×7.5 cm NaI(Tl) detectors placed at ± 90°. All events in the range $100 \leq E_\gamma \leq 900$ keV were accepted from the NaI(Tl) detectors. This additional γ-ray condition had the effect of suppressing low-multiplicity events, whilst γ-rays in paths of high multiplicity (e.g., $20^+ \rightarrow 18^+$) were not affected. The spectra for ^{176}Yb and ^{174}Yb are shown in Figs. 1 and 2.

Details for the extraction of lifetimes can be obtained from the full report of this work.[5] A summary of the experimental lifetimes is shown in Fig. 3 where they are compared to the rotational values. For the ^{174}Yb $8^+ \rightarrow 6^+$, $10^+ \rightarrow 8^+$ and $12^+ \rightarrow 10^+$ transitions, the present measurements agree with the second set of Manchester values[6] within their combined errors; however, the present adopted values tend to be systematically about 8% higher. The Manchester data were obtained using a ^{84}Kr beam with γ-rays detected in singles, and if we make the comparison with the present ^{86}Kr singles data only, the systematic discrepancy is reduced to +5%, of which about +3% can be attributed to the different choice

of stopping powers. To within an accuracy of ~13% the average of the measured transitions in both ^{174}Yb and ^{176}Yb are consistent with the rotational model. However, there might be a systematic trend for the measured ratios to decrease with increasing spin.

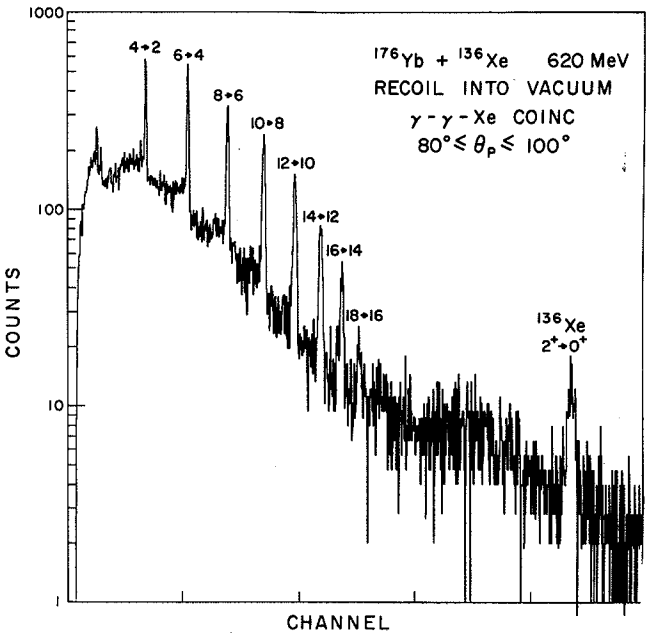

Fig. 1. Gamma rays in coincidence with ^{136}Xe ions scattered in the annulus $80° \leq \theta \leq 100°$. The target of ^{176}Yb was about 1 mg cm^{-2} and inclined at 45° to the beam direction. There is an additional γ-ray coincidence (NaI) requirement on this spectrum.
(XBL 765-1800)

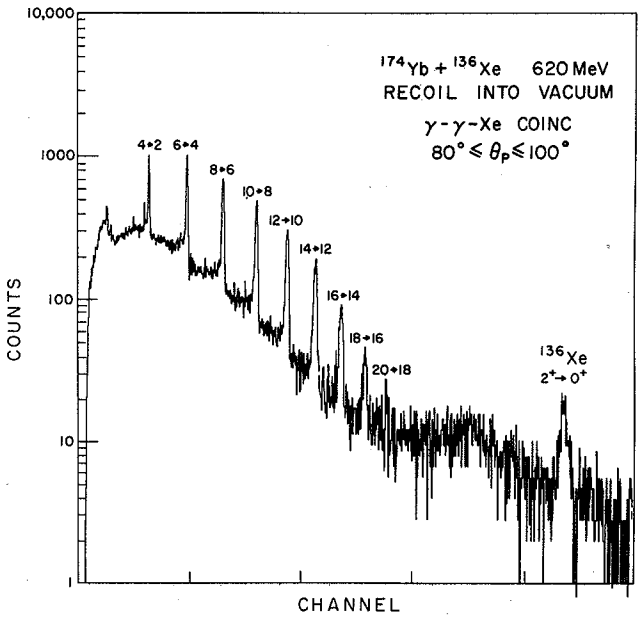

Fig. 2. Gamma-rays in coincidence with ^{136}Xe ions for ^{174}Yb. The arrangement was the same as that described for Fig. 1. (XBL 766-8328)

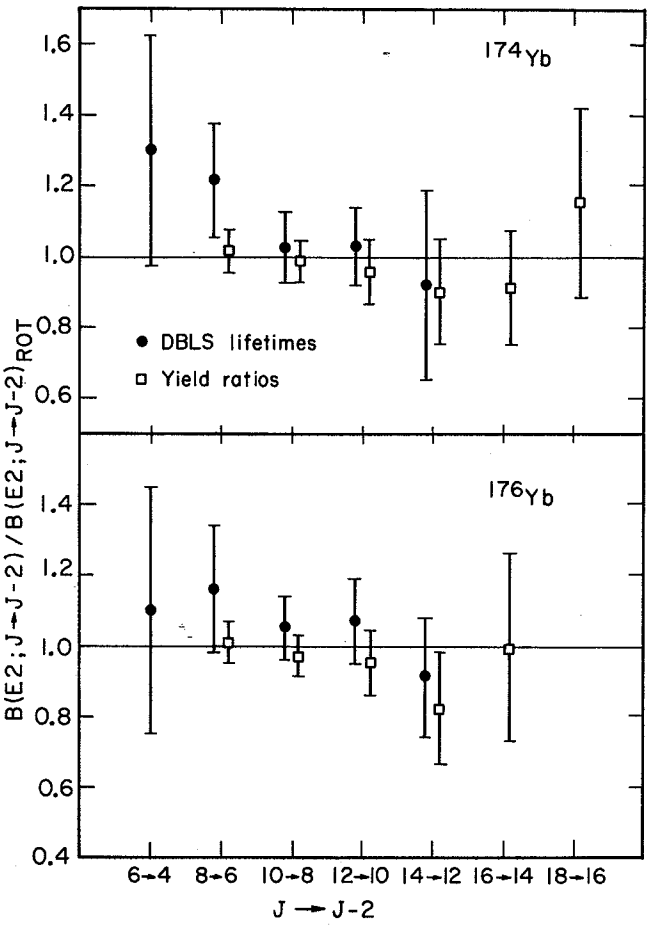

Fig. 3. Comparison of the lifetimes obtained by Doppler-broadened line analysis with the rotational model. The yield ratio R (see the full report) is also approximately equal to $B(E2)_{exp}/B(E2)_{rotational}$.
(XBL 763-5228)

There is now considerable interest in high-spin states, due to the pronounced anomalies (backbendings) that have been observed around I = 16 in the ground state rotational bands of some rare earth nuclei. At least three explanations have been considered for these effects: 1) a collapse of the pairing correlations;[7] 2) a change in shape of the nuclei;[8] and 3) an alignment of the angular momenta of two particular high-j nucleons ($i_{13/2}$ neutrons in the light rare earth region) with the rotational angular momentum of the core.[9] Most of the information on these high-spin states has come from studies of the gamma-ray de-excitation of (HI,xn) products. The present work has, however, provided the first data on neutron-rich rare earth nuclei. The information on the high-spin states of the Yb nuclei from mass 164 to 176 is shown on the usual backbending type of plot in Fig. 4. Two interesting features are apparent in these plots. The first is that ^{168}Yb shows less backbending than its neighbors, ^{166}Yb and ^{170}Yb. This has been previously noted by Faessler[10] and ascribed by him as a pairing effect due to the lower level density at just this neutron number (98). This kind of pairing effect was previously suggested[11] to be responsible for the somewhat larger moments of inertia (compared with the

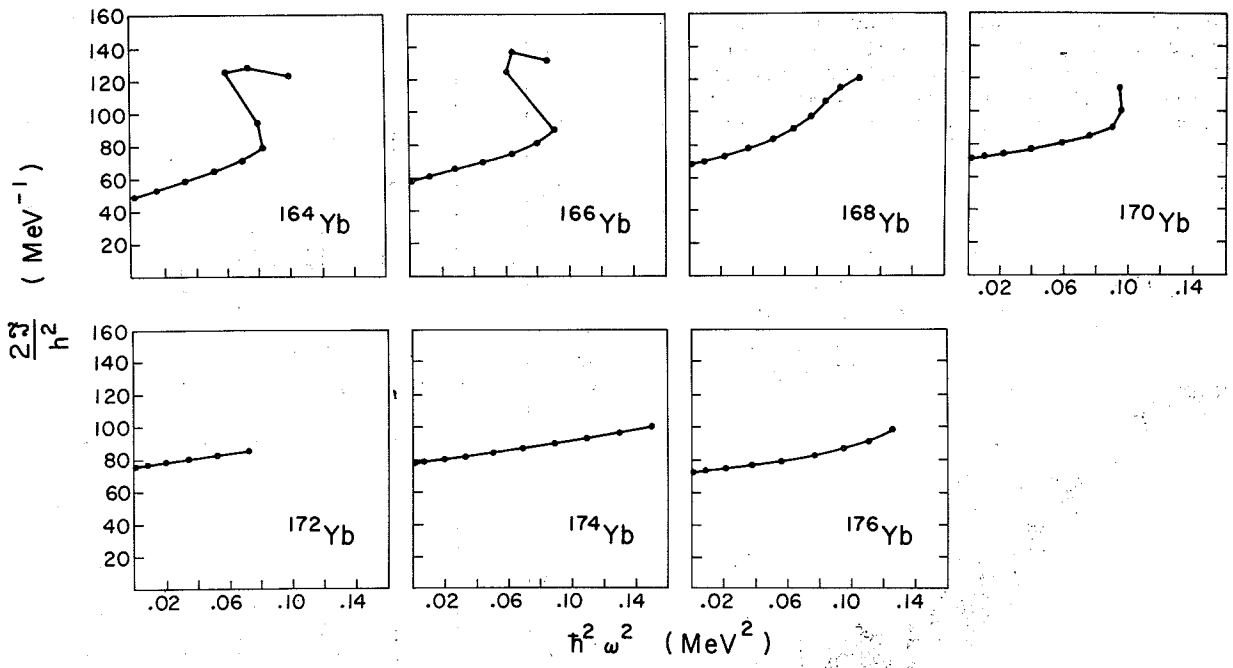

Fig. 4. Plots of the moment-of-inertia versus rotational frequency (squared) for the Yb isotopes. (XBL 765-1802)

neighboring nuclei) of the 98-neutron HF and W isotopes. This explanation of the reduced backbending in ^{168}Yb is still consistent with the generally accepted idea that the backbending in this mass region is caused mainly by the alignment of two $i_{13/2}$ neutrons; since, in the alignment mechanism, the moment of inertia plays a strong role, and a larger ground band moment of inertia would certainly go in the direction of weakening the backbending. Thus a pairing explanation for the weak backbending of ^{168}Yb seems likely to be correct, although it is not clear whether the weaker pairing in ^{168}Yb prevents the alignment of the $i_{13/2}$ neutrons in the yrast states or just modifies it somewhat.

The other interesting feature in Fig. 4 is the very regular behavior of the high-spin states in ^{174,176}Yb compared with that of the lighter Yb isotopes. This behavior is easy to understand in the alignment model, and was predicted to occur.[9] It happens because the alignment requires the low-Ω components from a j-shell, and (for a prolate shape) these essential components lie higher in energy as the shell fills. For example, the Fermi level is near the $\Omega = 5/2$ component of the $i_{13/2}$ shell in ^{167}Yb; whereas, it is up to $\Omega = 9/2$ in ^{177}Yb. Thus one can easily understand why the alignment of two $i_{13/2}$ neutrons would be difficult in ^{174}Yb or ^{176}Yb. However, backbending does recur in the W and Os nuclei having neutron numbers similar to ^{174,176}Yb. In these cases, it has been shown that the alignment of two $h_{9/2}$ protons play a major role in the backbending, and this process is less likely to occur in ^{174,176}Yb because: 1) Yb has fewer protons; 2) the moment-of-inertia is larger in the Yb region; and 3) ε_4 is less positive (β_4 less negative) for the Yb isotopes.[12] Thus the lack of backbending in ^{174,176}Yb seems quite consistent with our present understanding of this process.

Footnotes and References

*Condensed from LBL-4375, Nucl. Phys. B (to be published).

†Permanent address: Chalk River Nuclear Laboratories, Ontario, Canada.

‡Permanent address: Institut de Physique Nucléaire, 91406 Orsay, France.

§U.K. S.R.C./N.A.T.O. fellow.

‖On leave from Sektion Physik der Ludwig-Maximilians-Universität München, 8046 Garching, Germany; sponsored by the Bundesministerium für Forschung und Technologie.

1. E. Grosse, J. DeBoer, R. M. Diamond, F. S. Stephens, and P. Tjom, Phys. Rev. Lett. 35, 565 (1975).

2. P. Colombani, J. C. Jacmart, N. Poffé, M. Riou, P. P. Singh, C. Stephen, and A. Weidinger, Phys. Lett. B 48B, 315 (1974).

3. M. W. Guidry, P. A. Butler, P. Colombani, I. Y. Lee, R. M. Diamond, D. Ward, F. S. Stephens, E. Eichler, N. R. Johnson, and R. Sturm, to be published (1976).

4. F. Kerns, G. Dracoulis, T. Inamura, J. C. Lisle, and J. C. Willmott, J. Phys. A7, 111 (1976).

5. A Winther and J. DeBoer, Coulomb Excitation (Academic Press, New York, 1966), p. 303.

6. T. Inamura, F. Kearns, J. C. Lisle, G. Varley, and J. C. Willmott, Annual Report 1974, Schuster Lab., University of Manchester, p. 75.

7. B. R. Mottelson and J.-G. Valatin, Phys. Lett. 5, 511 (1960).

8. P. Thieburger, Phys. Lett. 45B, 417 (1973).

9. F. S. Stephens and R. S. Simon, Nucl. Phys. A138, 257 (1972).

10. A. Faessler, F. Grümmen, L. Lin, and J. Urbano, Phys. Lett. A138, 87 (1974).

11. F. S. Stephens, N. Lark, and R. M. Diamond, Phys. Rev. Lett. 12, 225 (1964).

12. F. S. Stephens, P. Kleinheinz, R. K. Sheline, and R. S. Simon, Nucl. Phys. A222, 235 (1974).

TRANSITIONS BETWEEN HIGH-SPIN NUCLEAR STATES*

M. V. Banaschik,† R. S. Simon,‡ P. Colombani,§
F. S. Stephens, and R. M. Diamond

Studies of transitions between high-spin nuclear states can give information about moments of inertia, shapes, and other structural features of such nuclei. High spin values (up to 80ħ) can be brought into compound nuclei following heavy-ion reactions; however, γ-ray studies following such reactions have thus far produced information mainly on states having spins below ~20ħ. The reason is that all the transitions between higher-spin states are too weak individually to be resolved, and thus comprise an apparent continuum. There were some early attempts to study this continuum,[1,2] but these studies have only recently been resumed.[3-6] In the present work, the energies, angular correlations, and number of continuum γ rays have been measured, and the information obtained from these quantities has been related directly to nuclear moments of inertia at angular momenta up to 60ħ.

We have studied mainly the reactions ^{82}Se(^{40}Ar, xn)$^{122-x}$Te and ^{126}Te(^{40}Ar,xn)$^{166-x}$Yb by using 183-MeV Ar beams from the Lawrence Berkeley Laboratory SuperHILAC. In addition, a limited survey over target (Al, Cu, As, Ag, Sn, and Sm) and projectile (^{16}O and ^{40}Ar) at several bombarding energies was made. The targets were ~1mg/cm^2 thick, and were evaporated onto 25-μm Pb backings, which stopped the beam and recoiling nuclei with very little background. To measure the continuum γ rays, we used three 7.5-cm × 7.5-cm NaI(Tl) detectors at angles of 0, 45, and 90° to the beam direction. Each detector had an absorber of 0.32-cm Pb and 0.32-cm Cu, and was placed 60 cm from the target. This long flight path to the NaI detector permitted an almost complete separation between neutrons and γ rays in the time spectrum. The three NaI spectra were recorded event by event in coincidence with pulses from a Ge detector which was 5 cm from the target at an angle of 225° to the beam direction. The Ge singles spectrum was stored simultaneously. To obtain the true NaI γ-ray spectrum, $N(E_\gamma)$, the pulse-height distribution must be corrected for the detector response (unfolded). The raw and unfolded 0° NaI-detector spectra in coincidence with the full Ge-detector spectrum are shown for three targets in Fig. 1.

For the heavier product nuclei ($Z \gtrsim 50$ or $A \gtrsim 110$), two features of the continuum spectra are clear. Above ~3 MeV the intensity falls of approximately exponentially with increasing energy, where-

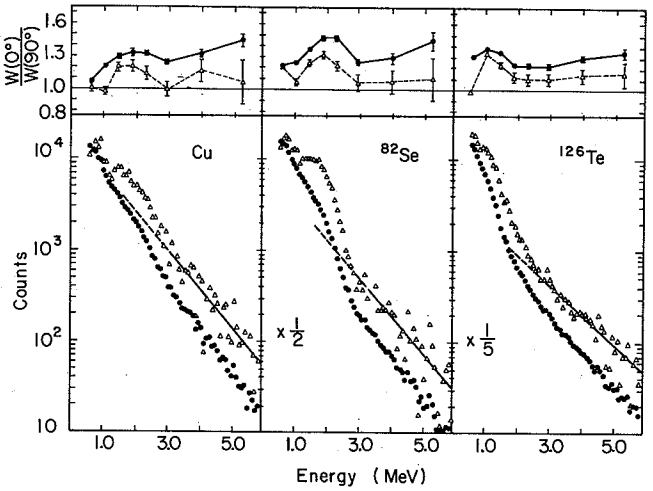

Fig. 1. The raw (dots) and unfolded (triangles) continuum spectra in coincidence with the full Ge-detector spectrum for 183-MeV ^{40}Ar projectiles on natural Cu, ^{82}Se, and ^{126}Te targets. The straight lines are fitted to the unfolded spectrum between 3.2 and 6.2 MeV (solid portion) and extrapolated to lower energies (dashed protion). The upper plots show the 0°-90° ratios for the raw data (dots) and for the unfolded data corrected for recoil motion (triangles). The error bars indicated statistical errors only. (XBL 751-2146)

as somewhere below this energy a prominent bump occurs. These features seem very likely to result from the statistical and yrast cascades as has been predicted,[7] and recently observed in Yb nuclei with ^{16}O projectiles.[6] The slope of the exponential part of the spectrum is rather similar for all the targets we have studied and corresponds to "temperatures" ranging from 1 to 1.5 MeV ($T = -dE/d\ \ln N$) in good agreement with the expectations for a purely statistical cascade.[8] The bump is shown by the angular correlations to be composed almost completely of stretched E2 transitions whose energies are rather low and decrease with increasing product mass in a very systematic way, suggestive of a moment-of-inertia effect. Also, the energy and the intensity of the stretched-E2 component of the bump generally

increase with angular-momentum input. These properties strongly suggest identification of this bump with the yrast cascade, though there is not yet any direct experimental evidence that this cascade occurs close to the yrast line. The yrast bump is generally less prominent for products below $Z \sim 50$ as is illustrated by the curve for a Cu target in Fig. 1.

More detailed information about yrast energies comes from studies of the individual reaction channels. This is illustrated in Fig. 2, which shows raw and unfolded spectra from the reaction ^{82}Se(^{40}Ar, xnγ)$^{122-x}$Te, where coincidence requirements in the Ge detector allowed selection of the 4n (^{118}Te; 606, 601, 615, and 753 keV) and 6n(^{116}Te; 679, 681, 643, and 771 keV) reaction channels.[8] These spectra each have a rather sharp drop, but at quite different energies: 2.4 MeV for the 4n reaction and 1.7 MeV for the 6n reaction. An estimate of the angular momentum in each channel can be made from the $\bar{N}_\gamma$ values, which are 29, 20, and 13, for the 4n, 5n, and 6n reactions. Assuming that the few missed transitions below 0.6 MeV compensate for the dipoles present, we can estimate the average angular momentum in these channels to be $\sim 2\,\bar{N}_\gamma$, or 58, 40, and 26ħ. This procedure has been shown in other cases[5] to be consistent with estimates of the channel angular momentum based on cross-section measurements. Since the highest value of the angular momentum having appreciable intensity, rather than with the average value, we must estimate this "highest" value. For the 6n reaction, a point midway between the 6n and 5n average values (33ħ) seems unlikely to be in error by more than ~15%. The 4n value should be rather near the measured average, and 64ħ (the Bass-model[9] dynamic limit for this reaction) seems likely to be correct within ~15%. These estimates give $2\mathcal{I}/\hbar^2$ values of 75 MeV^{-1} for $I \sim 33$ and 110 MeV^{-1} for $I \sim 64$. For

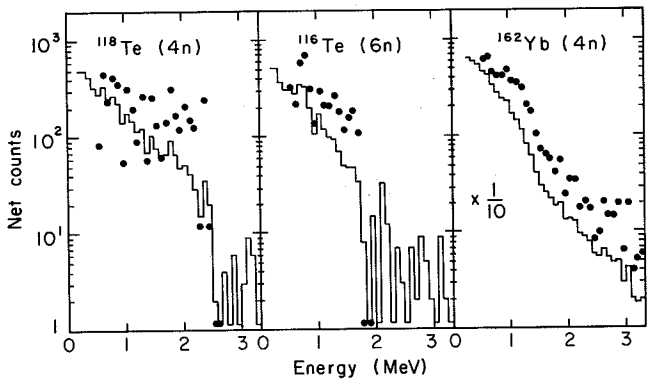

Fig. 2. The histograms show the raw continuum spectra in coincidence with the (background-corrected) γ-ray lines from specific reaction products (labeled). Negative or zero counts are plotted at the bottom of the figure. The dots show the unfolded spectra in regions where the statistical variations are not too large. (XBL 752-2239)

comparison, the value of $2\mathcal{I}/\hbar^2$ is 39 MeV^{-1} for the 8→6 transition[8] in ^{118}Te, and 85 MeV^{-1} for a rigid sphere of mass 118. The liquid-drop estimates[10] for I = 33 and 64 in ^{118}Te are 91 and 104 MeV^{-1}. The spectrum for ^{162}Yb from the ^{40}Ar+^{126}Te reaction is also shown in Fig. 2, and an estimate similar to those above gives $2\mathcal{I}/\hbar^2 \sim 140$ MeV^{-1} at $I \sim 48$. The rigid-sphere value for this case is 141 MeV^{-1} and the liquid-drop estimate is 154 MeV^{-1}. There is, no doubt, much yet to be learned about extracting moments of inertia from these spectra; however, it seems likely that these transition energies and associated spins are roughly correct.

Footnotes and References

*Condensed from Phys. Rev. Lett. 34, 892 (1975).

†NATO Fellow, Institut für Strahlen- und Kernphysik, Bonn, West Germany.

‡Sektion Physik Universität München, Garching, West Germany.

§Permanent address: Institut de Physique Nucléaire, 91406 Orsay, France.

1. J. F. Mollenauer, Phys. Rev. 127, 867 (1962).

2. Yu. Ts. Oganesyan, Yu. V. Lobanov, B. N. Markov, and G. N. Flerov, Zh. Eksp. Teor. Fiz. 44, 1171 (1963) [Sov. Phys. JETP 17, 791 (1963).

3. E. der Mateosian, O. C. Kistner, and A. W. Sunyar, Phys. Rev. Lett. 33, 596 (1974).

4. G. B. Hagemann, R. Broda, B. Herskind, M. Ishihara, and H. Ryde, in Proccedings of the International Conference on Reactions between Complex Nuclei, Nashville, Tennessee, 1974, edited by R. L. Robinson, F. K. McGowan, J. B. Vall, and J. H. Hamilton (North-Holland, Amsterdam, 1974), Vol. 1, p. 110.

5. P. O. Tjøm, F. S. Stephens, R. M. Diamond, J. De Boer, and W. E. Meyerhof, Phys. Rev. Lett. 33, 593 (1974).

6. J. O. Newton, J. C. Lisle, G. D. Dracoulis, J. R. Leigh, and D. C. Weisser, Phys. Rev. Lett. 34, 99 (1975).

7. J. R. Grover and J. Gilat, Phys. Rev. 157, 802, 814 (1967).

8. A. Luukko, A. Kerek, I. Rezanka, and C. J. Herrlander, Nucl. Phys. A135, 49 (1969).

9. R. Bass, Phys. Lett. 47B, 139 (1973), and Nucl. Phys. A231, 45 (1974).

10. D. P. Soroka and W. J. Swiatecki, private communication.

MOMENTS OF INERTIA IN ^{162}Yb AT VERY HIGH SPINS*

R. S. Simon,† M. V. Banaschik,‡ P. Colombani,§
D. P. Soroka, F. S. Stephens, and R. M. Diamond

The purpose of this work was to obtain nuclear moments of inertia at very high spins by studying the γ-ray spectrum following (HI,xnγ) reactions leading to the final nucleus ^{162}Yb. Two reactions were investigated: ^{150}Sm(^{16}O,4n)^{162}Yb and ^{126}Te(^{40}Ar,4n)^{162}Yb. We measured the continuum spectrum in three 7.5×7.5-cm NaI(Tℓ) detectors at 0°, 45° and 90° with respect to the beam direction and 60 cm from the target. These detectors were gated by coincident pulses from a Ge detector at 225° to the beam and 5 cm from the target. The energy distribution of the continuum gamma rays was obtained from the observed NaI pulse-height spectra by an unfolding procedure[1] using a carefully adjusted response function and the measured total efficiency curve of the NaI detecotors, with a small correction for the motion of the recoiling product nucleus. By normalizing to the number of singles events in the gating lines of the Ge detector, the isotropic unfolded spectrum can be given in absolute events per decay and may be integrated to yield the average gamma-ray multiplicity, $\overline{N}_\gamma$, of the reaction. For the ^{40}Ar reaction at 181 MeV, raw and unfolded spectra are shown in Fig. 1, as well as the ratio of events at 0° to those at 90°.

The anisotropy (Fig. 1) suggests that most of the bump transitions are of stretched E2 character, so that an estimate of the average angular momentum, $\overline{\ell}$, in the channel can be obtained. Assuming no angular momentum is carried off by neutrons or the statistical cascade, we subtract the statistical transitions (all those in the exponential tail plus an estimated background underneath the bump—a total of ~4 transitions in all cases) and multiply the rest by 2ħ. Both this estimated $\overline{\ell}$ and the total $\overline{N}_\gamma$ are given in Table 1. For the ^{16}O and low-energy ^{40}Ar cases, these $\overline{\ell}$ estimates are in excellent agreement with average values obtained from measured reaction channel cross sections, $\overline{\ell}(\sigma)$, using the sharp-cut-off model. Therefore, in these cases the upper boundary angular momentum, ℓ_u, given by the cross-section measurements seems very likely to be the

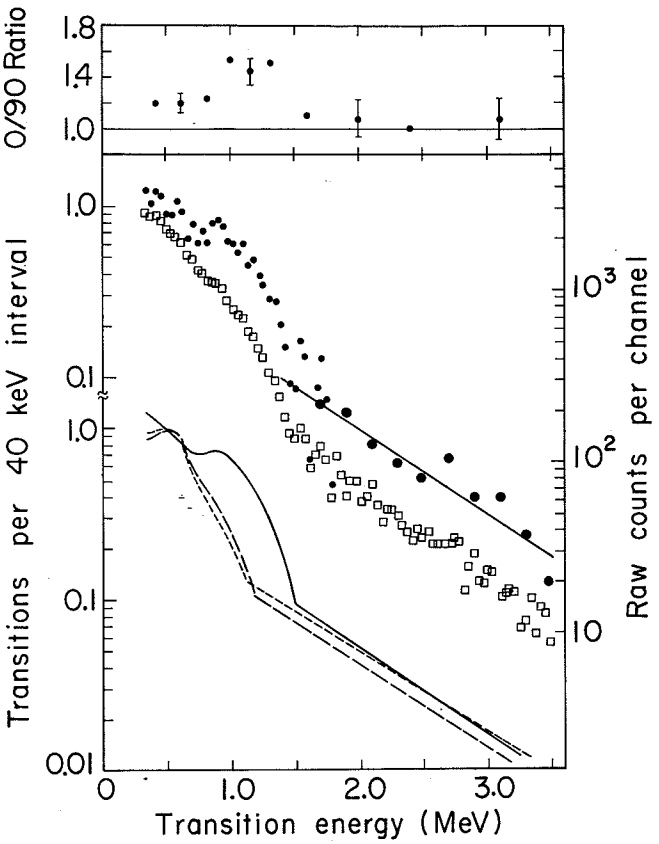

Fig. 1. Raw (□) and unfolded (●) continuum gamma spectra from the ^{126}Te(^{40}Ar,4n) ^{162}Yb reaction at 181 MeV. The larger solid dots represent 5 channel averages. Also shown is the 0/90 ratio for the unfolded spectrum. At the bottom are schematic spectra for this case (solid line), the ^{126}Te(^{40}Ar,4n) ^{162}Yb reaction at 157 MeV (longer-dashed line) and the ^{150}Sm(^{16}O,4n)^{162}Yb reaction at 87 MeV (shorter-dashed line). (XBL 7511-9561)

Table 1. Data used to obtain moments of inertia.

Reaction	E_{proj} MeV	N_γ	$\overline{\ell}$ ħ	E_{edge} MeV	σ(4n) mbarn	$\sum_{x=4}^{6}\sigma(xn)$[a] mbarn	$\ell_u(4n)$ ħ	$\overline{\ell}(\sigma)$[b] ħ
^{150}Sm + ^{16}O	87	17	26	1.2	540	760	36	27
^{126}Te + ^{40}Ar	157	17	27	1.16	220	280	39	28
^{126}Te + ^{40}Ar	181	23	39	1.40	220	620	63	56

[a] Includes 15% for charged-particle channels. In the 5n reaction the measured $i_{13/2}$ band population was increased by 35% to allow for other bands.

[b] $\overline{\ell}(\sigma) = 0.67[\ \ell_u^3(4n) - \ell_u^3(5n)]\ /\ [\ \ell_u^2(4n) - \ell_u^2(5n)]$.

maximum angular momentum in the yrast (collective) cascade. For the 181 MeV ^{40}Ar case the two $\bar{\ell}$ values do not agree, possibly indicating a net angular momentum carried by the neutrons and/or the statistical cascade. For our purposes the $\bar{\ell}$ based on the unfolded spectrum is more relevant, and the maximum angular momentum in the yrast cascade is estimated (based on the other two cases) to be about 11$\hbar$ larger than this $\bar{\ell}$, giving a value of ~ 50$\hbar$. This number, however, is less certain than that for the other two cases.

There are two methods for obtaining effective moments of inertia, $\mathcal{I}$, from these data. One depends on relating a transition energy, E_t, to the corresponding spin, I, according to the approximate relation: $E_t = (\hbar^2/2\mathcal{I})(4I-2)$. Both the raw and unfolded spectrum of Fig. 1 show a rather sharp upper edge of the bump. This edge is found to be lower for the ^{16}O and low-energy ^{40}Ar cases (shown schematically in the bottom part of Fig. 1) where less angular momentum is brought into the system. This suggests that the energies of the edge can be associated with gamma transitions between the highest spin states in the yrast cascade (estimated above). Three values for $2\mathcal{I}/\hbar^2$ can be obtained in this way and are plotted on Fig. 2 against $(\hbar\omega)^2$ in the usual backbending type of plot, where $\hbar\omega$ is taken to be $E_t/2$. Also shown are the moments of inertia of the known low-spin states in ^{162}Yb and, for comparison, the low-spin data for the isotone ^{160}Er.

The same method can be applied for transitions in a region of the spectrum corresponding to ℓ values below which there is no appreciable direct population into the channel of interest. This region is likely to be below 30-35$\hbar$ for the 4n channel in the 181 MeV ^{40}Ar case (Fig. 1) since most of the population with lower spins goes into the 5n or 6n channels, but it would be less than 20$\hbar$ for the ^{16}O and low-energy ^{40}Ar cases. Provided there is a monotonic increase of transition energy with spin (no backbending), a spin value for each transition energy can be obtained by summing all the transitions (less the estimated statistical cascade background) up to that transition energy and multiplying by two. This method is applicable between ~ 0.7 and 1.0 MeV in Fig. 1, leading to moments of inertia given by the dots connected by a solid line in Fig. 2.

The preceding method is an "integral" one, and thus is not very sensitive to local variations in the moment of inertia. The second method is a "differential" one, and can show such local variations. Each point on the unfolded spectrum of Fig. 1 gives the number of transitions per 40 keV energy interval. The reciprocal of this is the difference, ΔE_t, between transition energies and is related to the moment-of-inertia by

$$\Delta E_t \approx \frac{8\hbar^2}{2\mathcal{I}} - 2E_t \frac{d\ell n\mathcal{I}}{dI} \qquad (1)$$

where E_t is the transition energy for which ΔE_t is evaluated. This method also requires the full population in the channel, and thus can only be applied below 30-35$\hbar$ for the 181 MeV ^{40}Ar case. For the region 0.7-1.0 MeV in Fig. 1, $\mathcal{I}$ is nearly constant, so that the last term of Eq. (1) can be neglected, giving $2\mathcal{I}/\hbar^2 \approx 8/\Delta E_t$. This procedure leads to the

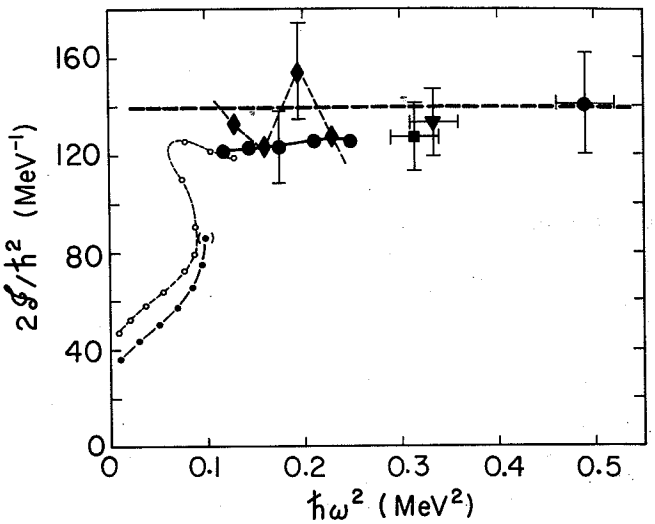

Fig. 2. Backbending plot for ^{162}Yb. The small solid dots correspond to the known low-spin states of ^{162}Yb, whereas the open circles are for the isotone ^{160}Er. The large dots correspond to values derived by the integral method from the 181 MeV ^{40}Ar data. The triangle and square come from the 157 MeV ^{40}Ar and 87 MeV ^{16}O spectra using the same method. The diamonds are values from the differential method applied to the 181 MeV ^{40}Ar case. The horizontal dashed line is the moment-of-inertia of a rigid sphere with A = 162. (XBL 7511-9562)

diamonds and dashed line in Fig. 2. The results are in good agreement with those of the integral method and suggest that there might be a local increase in the moment of inertia around $(\hbar\omega)^2 \sim 0.2$ MeV^2 or $E_t \sim 0.9$ MeV. This possible rise can be seen directly in both the unfolded and raw spectra of Fig. 1, but it is not clearly outside the present uncertainty limits.

The effective moment-of-inertia values measured by the techniques described above are compared in Fig. 2 with that of a rigid diffuse sphere of mass 162, having an equivalent rms radius of 6.71 fm.[2] The deformed rigid-body value for the moment-of-inertia would be roughly 10% larger than this rigid-sphere value. It will obviously be of interest to improve these methods in order to see more details of these moments of inertia and to extend the measurements to other nuclei.

Footnotes and References

*Condensed from Phys. Rev. Letters 36, 359 (1976).

†On leave from Sektion Physik der Ludwig-Maximilians-Universität München, 8046 Garching, Germany, sponsored by the Bundesministerium für Forschung und Technologie.

‡Present address: Technische Hochschule, Darmstadt, Germany.

§Permanent address: Institut de Physique Nucléaire, 94106 Orsay, France.

1. J. F. Mollenauer, Lawrence Radiation Laboratory Report UCRL-9748 (1961).

2. W. D. Meyers, Nucl. Phys. A204, 465 (1973).

EXPERIMENTAL STATUS OF HIGH-SPIN STATES*

F. S. Stephens

High-spin nuclear states are interesting at the present time, both because they are experimentally accessisble, and because there have recently been several rather dramatic changes observed at high spins, and others even more dramatic are predicted. I want to describe very briefly just what these are, what we now know about them, and what we are trying to find out about them.

One of the changes occurring in high-spin states is the reduction and eventual quenching[1] of the pairing correlations. There is now stron evidence[2] that the pairing is, indeed, decreasing with increasing spin even at the lowest spin values. However, it is also reasonably clear that it has not disappeared by spin 20$\hbar$ in many rare-earth nuclei. It is certainly an interesting experimental problem to determine just where and how the pairing is quenched, and we have recently obtained some evidence that suggests there may still be some pairing left at ~35$\hbar$ in at least one case.

Changes in the nuclear shape are a second type of effect expected to occur with increasing spin. Small increases in deformation are known[3] to occur at low ($\lesssim$12$\hbar$) spin values in a number of nuclei with moderate or small deformation, and a rather sudden change from slightly oblate to rather strongly prolate shapes has been observed[4,5,6] in several light Hg nuclei. The liquid drop model (with rigid-body moments of inertia) predicts[7] oblate shapes to be most stable up to high spin values (50 to 70 $\hbar$ for $A \approx 160$) and then triaxial shapes with increasing deformation leading to fission (at 70-80$\hbar$). According to recent calculations[8,9] the shell corrections do not change the basic liquid-drop tendencies. The prolate-deformed rare earth nuclei, for example, are predicted to become (or tend to become) oblate via triaxial shapes at moderate spin values (30-50$\hbar$) and then follow the liquid drop estimates. Two interesting conclusions from both the liquid-drop and the rotating-deformed-oscillator calculations are that there should be very high-spin isomeric states in the oblate region and also rapidly increasing moments of inertia in the triaxial region preceding fission. These effects are being searched for at the present time.

A third phenomenon that is expected to occur at high-spin values is the alignment of individual particle angular momenta. This is the dominant structure of the low-energy high-spin states in spherical and near-spherical nuclei, as is well known, and this process should compete with collective motion at higher spin values in the more deformed nuclei. Recently a model[10] involving the alignment of the angular momentum of an odd nucleon with that due to the core rotation has had considerable success for many weakly deformed nuclei. However, it is not yet entirely clear to what extent the core motion must be purely rotational in such a model. Also, it now seems rather likely that the "backbending" which has been observed[11] in some of the light rare earth nuclei is due to the alignment[12] of two particular nucleons ($i_{13/2}$ neutrons in this mass region) with the core rotation. If the oblate shapes predicted by the liquid drop model are reached, all the angular momentum would be carried by aligned particles. This would be signaled rather unambiquously by the occurrence of the high-spin isomeric states mentioned above. Thus, at least three effects--loss of pairing, shape changes, and alignment--are known to be occurring in nuclei as the spins increase, and the interplay and competition of these (and perhaps still other) processes makes the study of high-spin states rather exciting at the present time.

Footnotes and References

*Summary of invited paper, Proceedings of the Conference on Highly Excited States in Nuclei, Vol. 2, Jülich, Germany, Sept. 1975, to be published.

1. B. R. Mottelson and J. G. Valatin, Phys. Rev. Lett. 5, 511 (1960).

2. R. A. Sorenson, Rev. Mod. Phys. 45, 353 (1973), and references therein.

3. R. M. Diamond, F. S. Stephens, K. Nakai, and R. Nordhdgen, Phys. Rev. C 3, 344 (1971).

4. D. Proetel, R. M. Diamond, P. Kienle, J. R. Leigh, M. R. Maier, and F. S. Stephens, Phys. Rev. Lett. 31, 896 (1973).

5. N. Rud, D. Ward, H. R. Andrews, R. L. Graham, and J. S. Geiger, Phys. Rev. Lett. 31, 1421 (1973).

6. D. Proetel, R. M. Diamond, and F. S. Stephens, Phys. Letters 48B, 102 (1974).

7. S. Cohen, F. Plasil, and W. J. Swiatecki, Annals of Physics 82, 557 (1974).

8. R. Bengtsson, S. E. Larsson, G. Leander, P. Möller, S. G. Nilsson, S. Agerg, and Z. Szymanski, preprint, June 1975.

9. A. Faessler, private communication, July 1975.

10. F. S. Stephens, Rev. Mod. Phys. 47, 43 (1975), and references therein.

11. A. Johnson, H. Ryde, and J. Sztarkier, Phys. Lett. 34B, 605 (1971).

12. F. S. Stephens and R. S. Simon, Nucl. Phys. A183, 257 (1972).

CONTINUUM GAMMA RAYS FOLLOWING (HIxnγ) REACTIONS*

R. M. Diamond

From simple considerations one can estimate the angular momentum brought to a reaction by a heavy ion,

$$\ell_{max}\hbar = [2\mu(E-V)]^{1/2}\ (R_p + R_t)$$

where μ is the reduced mass, E and V are the energy and Coulomb barrier in the center-of-mass system, and R_p and R_t are the projectile and target radii, respectively. To estimate the angular momentum actually retained in the compound system and to what extent it is formed requires a model-dependent approach. But whether limited by entrance-channel restrictions[1] or by fission,[2] nuclei with upto 70ħ are expected in the mass region 100-180 with Ar or Kr projectiles of the appropriate energy. Such a value is far more than can be accounted for by the discrete γ-ray transitions. A very large amount of angular momentum must be carried off by the continuum γ-rays that precede the discrete transitions.

By the use of a coincidence system,[3-8] usually NaI-Ge, the reaction product can be specified by gates in the Ge detector spectrum, and the average number of gamma rays in the cascades passing through the gates, the average γ-ray multiplicity for that reaction channel, can be determined. Results of our early measurement on the ^{166}Yb compound-nuclear system are given in Table 1. Listed are the values of the average γ-ray multiplicities of transitions above 0.6 MeV; for the total average γ-ray multiplicity, one must add the number of coincident γ-rays below 0.6 MeV, meaning essentially the average number of discrete ground-band transitions observed.

The striking feature of Table 1 is the great variation in the value of $\bar{N}_{>0.6}$ for different reactions. We believe this is a natural result of angular momentum considerations. Nuclei with a large amount of angular momentum tend to emit fewer neutrons and have a longer yrast cascade, while those with little angular momentum emit more neutrons but fewer cascade γ rays. The average multiplicity, $\bar{N}_{>0.6}$, should then be proportional to the average angular momentum of the nuclei leading to that product. Figure 1 shows that there is such a rough proportionality with the value of $\bar{\ell}$ determined from the cross section for that reaction, and that the angular momentum is far more decisive in determining the value of $\bar{N}_{>0.6}$ than is the nature of the projectile or the number of neutrons emitted. We believe that this is the most important conclusion to come out of our first study; a secondary conclusion is that there

Table 1. Average number of continuum γ-rays above 0.6 MeV.

		347 MeV ^{84}Kr+^{82}Se	88 MeV ^{16}O+^{150}Sm			26 MeV ^{1}H+^{165}Ho
E(keV)	$I_i \to I_f$	$\bar{N}_{>0.6}$	$\bar{N}_{>0.6}$	E(keV)	$I_i \to I_f$	$\bar{N}_{>0.6}$
		^{162}Yb(4n)			^{163}Er(3n)	
166	$2 \to 0$	11	8	127	$13/2^+ \to 9/2^+$	1.2
320	$4 \to 2$	14	10	165	$15/2^+ \to 13/2^+$	2.2
437	$6 \to 4$	12	9	171	$13/2^- \to 11/2^-$	2.3
521	$8 \to 6$	12	9	190	$9/2^- \to 7/2^-$	1.3
579	$10 \to 8$		9	213	$15/2^+ \to 11/2^+$	1.3
				218	$17/2^+ \to 13/2^+$	1.7
		^{163}Yb(3n)		236	$11/2^- \to 7/2^-$	1.6
202	$17/2^+ \to 13/2^+$	20	14			
345	$21/2^+ \to 17/2^+$	19	9		^{164}Er(2n)	
				208	$4 \to 2$	3.7
		^{161}Yb(5n)		314	$6 \to 4$	3.3
232	$17/2^+ \to 13/2^+$	10	5	410	$8 \to 6$	3.2

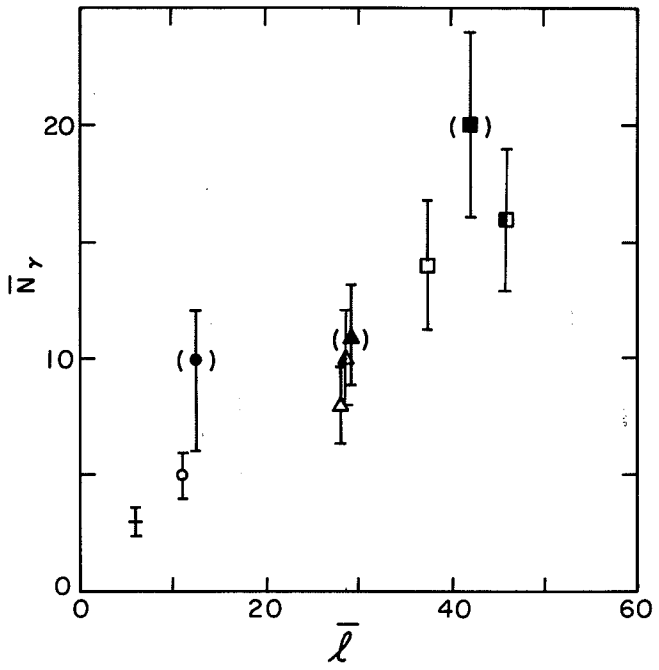

Fig. 1. Average number of continuum γ-rays with $E_\gamma > 0.6$ MeV coincident with the lowest observed discrete transition ($2^+ \rightarrow 0^+$ or $17/2^+ \rightarrow 13/2^+$) vs. the initial average angular momentum of the compound nucleus leading to that reaction. The cross is for the reactions $^{165}Ho(^1H,xn\gamma)^{163,164}Er$, and the circles, triangles and squares are for the 5n, 4n, and 3n reactions from $^{16}O+^{150}Sm$ (open), $^{84}Kr+^{82}Se$ (closed), $^{40}Ar+^{126}Te$ (half-closed). The parentheses on the ^{84}Kr data indicate that considerable uncertainty in the values of $\bar{\ell}$ is introduced by the target thickness in this case. (XBL 746-3366)

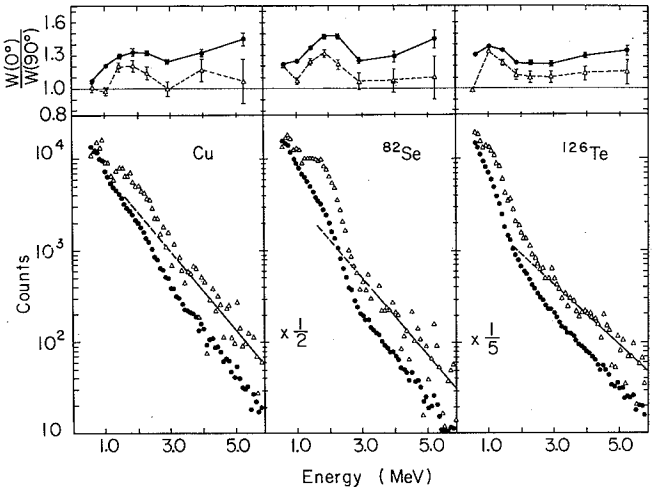

Fig. 2. The raw (dots) and unfolded (triangles) continuum spectra in coincidence with the full Ge-detector spectrum for 183 MeV ^{40}Ar projectiles on Cu, ^{82}Se, and ^{126}Te targets. The straight lines are fitted to the unfolded spectrum between 3.2 and 6.2 MeV (solid portion) and extrapolated to lower energies (dashed portion). The upper plots show the 0°/90° intensity ratios for the raw data (dots) and for the unfolded data corrected for recoil motion (triangles). The error bars indicate statistical errors only. (XBL 751-2146)

does appear to be some fractionation by spin into the different xn reactions.

The points in Fig. 1 determine a curve with a slope of ~ 1/2. Such a value with the known cascade feeding times of < 10 picosecond is consistent only if the majority of the continuum γ-rays are stretched E2 transitions. To check this, we have measured the angular correlation of the γ-rays absorbed in the NaI counters in coincidence with the entire spectrum in the Ge counter. The results for three nuclei made by irradiating the listed targets with 183 MeV ^{40}Ar are shown in the top of Fig. 2. The ratio W(0°)/W(90°) for the raw pulse height spectra is given as solid lines, but after unfolding and correcting for Doppler shift at 0°, these points are replotted as dashed lines. At the lower γ-ray energies, where most of the transitions are concentrated (note logarithmic scale for bottom part of figure giving the spectra) the anisotropy does indicate mostly stretched E2 transitions.

The spectra in Fig. 2 also illustrate that there is a gross structure in the continuum spectra, namely a division into a high-energy, nearly exponential tail, and a low-energy bump containing most of the intensity and consisting predominantly of stretched E2 transitions. It seems most natural to associate the exponential tail with the first 3-4 transitions that follow neutron emission and constitute a statistical gamma-ray cascade. But after a few such γ-rays, of a few MeV each, the yrast region is reached and now the nucleus is hard-pressed to lose angular momentum with a minimum loss in excitation energy. So the nature of the transitions changes to stretched E2 γ-rays of moderate (~1 MeV) energy; this is the yrast cascade. If only a single sequence of γ-rays were involved, they would have enough intensity to be seen as discrete lines so there must be a number of such sequences. And because of the short de-excitation times for the whole cascade, the E2 transitions must be enhanced and form members of (several collective bands. We have made preliminary studies of the dependence of the yrast bump on the projectile size, projectile energy, and compound-nuclear mass number.

Although much is yet to be learned about the dependencies just mentioned, information of another type can be extracted from the data to give some clues as to the nature of the high-spin states that are at the top of the yrast cascade. In particular, values of effective moments of inertia can be determined from the expression, $E_t = \frac{\hbar^2}{2\mathcal{I}}(4I-2)$, if corresponding values of I and the transition energy, E_t can be determined. With the assumption that the transition energies increase monotonically with spin (no backbending) the break in the curve indicating the end of the yrast cascade for a particular reaction channel is the highest energy transition, and corresponds to the highest spin state. An estimate of a spin can be obtained from the multiplicity, and

so yields a value for $\frac{2\mathcal{J}}{\hbar^2}$. Three values so obtained in ^{162}Yb made by an ^{16}O and two ^{40}Ar bombardment are shown in Fig. 3 plotted against $(\hbar\omega)^2$ as in the usual backbending figure, along with the values determined from the ground band and from the ground band in the isotone ^{160}Er. Such measurements seem capable of giving very useful information on the nature and properties of these high-spin states, that cannot be reached by any other method at present.

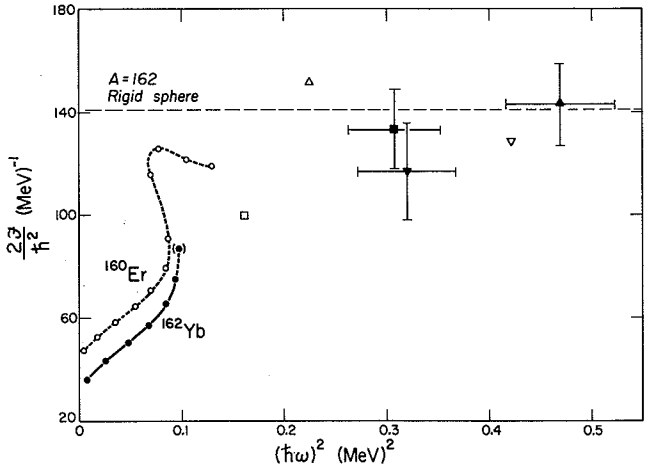

Fig. 3. Plot of $\frac{2\mathcal{J}}{\hbar^2}$ vs. $(\hbar\omega)^2$ for ^{162}Yb. The filled square and triangles are determined as described in the text; the circles are the discrete transitions in the ground band. The open circles are the discrete ground-band transitions in the isotone ^{160}Er, which backbends; it seems likely that ^{162}Yb will also backbend at higher spin. The dashed line is the rigid-sphere value. (XBL 756-3235)

Footnotes and References

* Shortened version of LBL-4081, lectures given at the Eighth Masurian School in Nuclear Physics, Mikolajki, Poland, Nukleonika 21, 29 (1976).

1. J. Wilczynski, Nucl. Phys. A216, 386 (1973).

2. S. Cohen, F. Plasil, W. S. Swiatecki, in Proceedings of the Third Conference on Reactions between Complex Nuclei, ed. by A. Ghiorso, R. M. Diamond, and H. E. Conzett, (Univ. of Calif. Press, Berkeley, Calif., 1963) p. 325.

3. E. der Mateosian, O. C. Kistner, and A. W. Sunyar, Phys. Rev. Lett. 33, 596 (1974).

4. G. B. Hagemann, R. Broda, B. Herskind, M. Ishihara, S, Ogaza, and H. Ryde, Nucl. Phys. A245, 166 (1975).

5. M. Fenzl and O. W. B. Schult, Z. Physik 272, 207 (1975).

6. P. O. Tjøm, F. S. Stephens, R. M. Diamond, J. de Boer, and W. E. Meyerhof, Phys. Rev. Lett. 33, 593 (1974).

7. M. V. Banaschik, R. S. Simon, P. Colombani, D. P. Soroka, F. S. Stephens, and R. M. Diamond, Phys. Rev. Lett. 34, 892 (1975).

8. J. O. Newton, J. C. Lisle, G. D. Dracoulis, J. R. Leigh, and D. C. Weisser, Phys. Rev. Lett. 34, 99 (1975).

^{40}Ar BOMBARDMENTS OF TARGETS AROUND THE N = 126 Z = 82 CLOSED SHELLS

A. Ghiorso, J. M. Nitschke, and R. E. Leber

To assess the impact of shell closure and shape excursions on compound-nucleus excitation and, more specifically, (H.I., xn) reactions, a series of ^{40}Ar + ^{208}Pb and ^{40}Ar + ^{209}Bi experiments have been performed. Oganessian et al.,[1] reported recently that the magicity of lead isotopes coupled with the dissipative shape transitions to deformed compound nuclei provide reaction Q values of sufficiently greater magnitude to substantially lower the excitation energy of the compound intermediate.

Through detection of spontaneous-fission events, the Dubna group concluded that two- or three-neutron evaporative decay is the most likely (H.I., xn) process in this regime, with charged-particle emission being negligibly small. Their work includes the production of ^{246}Fm with a 7 nanobarn cross section and ^{244}Fm with 1.5 nanobarns via ^{208}Pb(^{40}Ar,xn) reactions, where xn = 2n and 4n, respectively. (The product of the xn = 3n reaction, ^{245}Fm, was not observed since it lacks a fission branch.) Also reported is the formation of ^{256}104, 2n-evaporation residue from the bombardment of ^{208}Pb with magic ^{50}Ti.

Clearly, obtaining nuclei comparably "cool" to these systems has important implications for the heavy/superheavy element search; however, the Dubna observations differ appreciably from calculations. The model presented by Alonso,[2] for example, predicts (for R_o = 1.208 fm) that the cross section for the xn = 3n reaction will be roughly two orders of magnitude larger than that for xn = 2n. To attempt resolution of this discrepancy, it was decided to bombard ^{208}Pb with ^{40}Ar.

The procedure for this investigation was, as

detailed elsewhere,[3] to do alpha spectroscopy on recoil products transferred to a low-background counting area through a helium-jet capillary. The activity is deposited on a vertical wheel which is stepped at a determined rate to position the activity spots in front of gold surface-barrier silicon detectors. Data are passed through a CAMAC interface to a PDP-9 computer for on-line sorting and magnetic tape storage for subsequent off-line sorting on LBL's CDC 7600 computer.

In these experiments ^{246}Fm (xn = 2n) could not be seen above a detection limit of about 1 nb. However, ^{245}Fm was observed and characterized by half life and excitation function; moreover, the agreement between empirical and predicted excitation functions is relatively good (Fig. 1). (Some difficulties were encountered in specifying projectile energies due to straggling and possible local helium density variations from beam heating.)

Therefore, we tentatively conclude that, insofar as the two-neutron evaporation cross section is not at approximate parity with the 3n-out process, the extent of "cooling" imparted to the compound nucleus through shape changes may not be of the degree claimed elsewhere.[1]

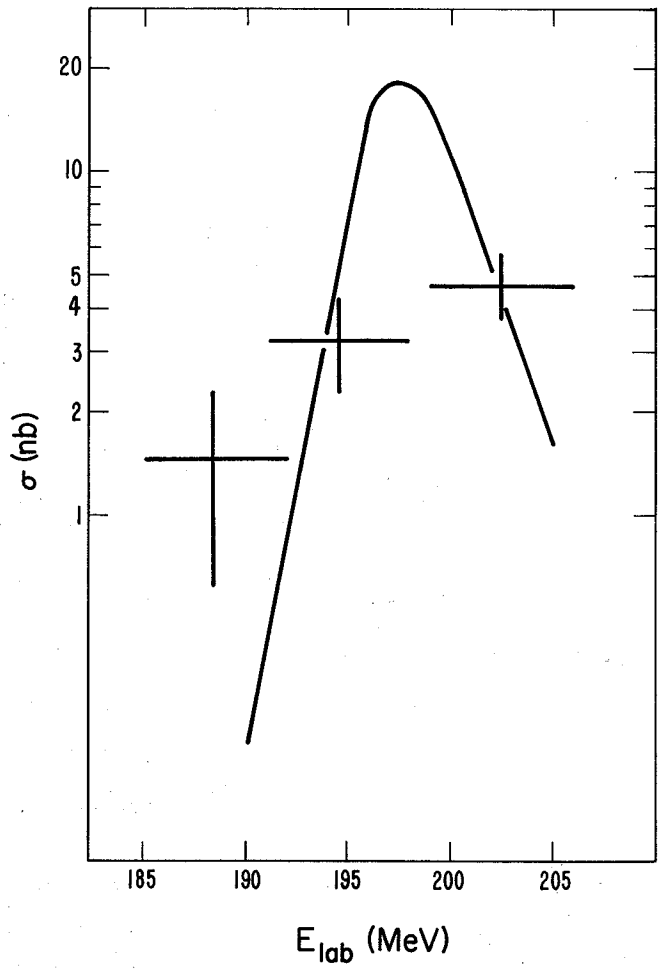

Fig. 1. Excitation function for the $^{208}Pb(^{40}Ar,3n)^{245}Fm$ reaction [solid line is theoretical (R_o = 1.208 fm) function]. (XBL 766-8247)

Of particular interest in the $^{209}Bi + ^{40}Ar$ experiments is an alpha line at 7.90±0.05 MeV with a half life of 21±4 secs, good evidence for ^{243}Es (E_α = 7.90 MeV, $T_{1/2}$ = 20 secs). Produced in a $^{209}Bi(^{40}Ar,\alpha 2n)$ reaction, this activity--while not a direct contradiction of the above mentioned statement in Ref. 1, since the mass defect of ^{208}Pb exceeds that of ^{209}Bi by some 3.5 MeV--indicates that charged-particle emission cannot be easily assumed negligible or disregarded in this transuranium region.

Transfer products near the lead and bismuth targets were produced in abundance in these experiments. Nuclides observed were: ^{211}Bi, $^{211,211m}Po$, ^{212m}Po, ^{211}At, and $^{212,212m}At$. In smaller yields ^{221}Ra and ^{222}Ac were produced--evidently through ^{13}C transfer--from ^{208}Pb and ^{209}Bi, respectively.

Restricting the helium flow through the target chamber so as to limit recoil collection to an acceptance angle of about 10° with respect to the beam axis gave an interesting result: for ^{211}Po, population of the ground state tended to be more forward peaked than the distribution of the isomer, ^{211m}Po. This may be evidence for different entrance-channel mechanisms (quasi-elastic vs. a deep-inelastic process for ^{211}Po and ^{211m}Po, respectively).

Noteworthy, too, is the propensity for ^{13}C transfer, responsible for ^{221}Ra with the ^{208}Pb target and $^{222,222m}Ac$ with ^{209}Bi. These activities, identified by time correlation with their respective daughters and granddaughters, were reproducible and mutually exclusive. Further, there was no apparent evidence for ^{14}C transfer.

Because the melting point of lead metal (328°C) is too low to use the elementally pure material as a target, a lead compound from which to make a suitable, chemically and mechanically stable target had to be found. Initial trials were with natural and separated Pbs. Prepared by precipitation with hydrogen from the nitrate solution, PbS could be obtained in good yield as a finely divided black powder. As a target, however, the sulfide proved inadequate when beam heating caused the target temperature to exceed 490°C. At temperatures in excess of about 450°C, the sulfur atoms tend to leave their lattice sites and diffuse out of the crystal.[4] Such a variable stoichiometry is untenable for our application since the target composition continuously changes and the lead metal residue is relatively volatile.

Lead monoxide proved a more suitable alternative. Precipitation of the hydroxide from a nitric acid solution followed by dehydration of the $Pb(OH)_2$ in a vacuum furnace gave either one or both of the allotropic forms of PBO. The thermodynamics of this material, however, were such that it was subject to reduction by the molybdenum backing foil at elevated temperatures. Effective solutions to this problem include convective cooling of the target by helium flow through a double window and vapor depositing onto the Mo a thin (~ 250 μg/cm^2) Pd film onto which the PbO is evaporated.

References

1. Yu. Ts. Oganessian, Yu. P. Tretyakov, A. S. Iljinov, A. G. Demin, A. A. Pleve, S. P. Tretyakova, V. M. Plotko, M. P. Ivanov, N. A. Danilov, Yu. S. Korotkin, and G. N. Flerov, JINR, D7-8099 (1974).

2. J. R. Alonso, Gmelin, Handbuch der Anorganischen Chemie, Band 7b, Teil A1, p. 28.

3. A Ghiorso, J. M. Nitschke, J. R. Alonso, C. T. Alonso, M. Nurmia, and G. T. Seaborg, Phys. Rev. Lett. 33, 1490 (1974).

4. W. W. Scanlon, Phys. Rev. 92, 1573 (1953).

SEARCH FOR SPONTANEOUS FISSION IN NEUTRON DEFICIENT ISOTOPES OF Pu, Cm, AND Cf

Kimberly Williams and Matti Nurmia

The systematics of the spontaneous fission half-lives for even-even isotopes of elements from plutonium to nobelium are shown in Fig. 1. Not only does the 152-neutron subshell produce a well-known effect on the spontaneous fission half-lives, but it also shows up as a characteristic kink in the alpha energy systematics with an alpha energy minimum around 152 neutrons (Fig. 2). There is a similar kink at 145 neutrons (which suggests there may be another neutron subshell at 144 neutrons, 8 neutrons below the 152-neutron subshell.

Since a subshell manifests itself as a gap in the Nilsson diagram at a particular value of nuclear deformation, it is "valid" over only a limited area in the nuclide chart. Thus, the assumed 144-neutron subshell should no longer necessarily affect the Fm isotopes, just as no effect is seen of the 152-neutron subshell in the spontaneous fission systematics of the heavy Pu isotopes. The spontaneous fission half-lives of the light Pu, Cm, and Cf isotopes, therefore, may not decrease as drastically as those of Fm.

Figure 1 shows purely systematic predictions fitting a parabola of the form $\text{Log } T_{1/2SF} = A+B(N-N_0)^2$

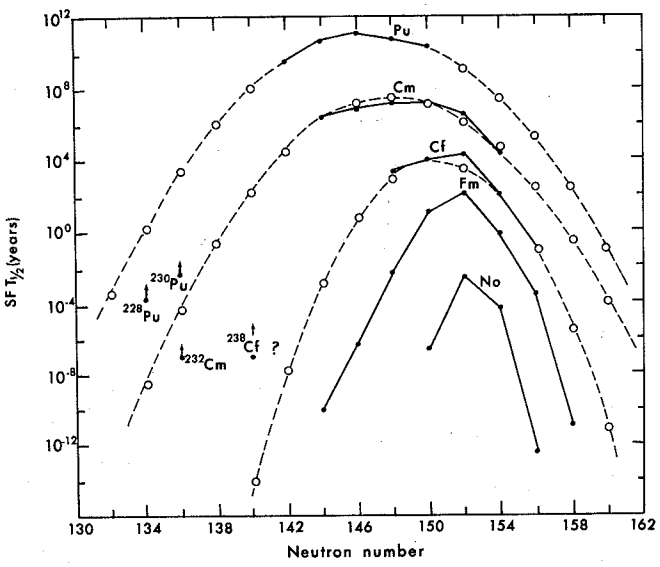

Fig. 1. Spontaneous fission half-lives vs. neutron number for the indicated elements. (XBL 766-8233)

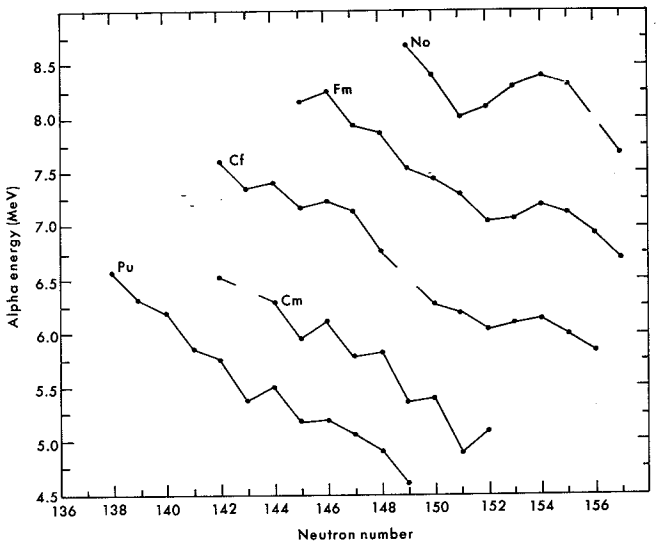

Fig. 2. Alpha-particle energies vs. neutron number for the indicated elements. (XBL 766-8234)

to known points for Pu, Cm, and Cf. These predictions do not take into account the fact that the light isotopes, Pu in particular, are expected to approach spherical shape and, therefore, probably do not have spontaneous fission half-lives as short as these. In fact, it is not unreasonable to expect to observe a minimum spontaneous fission half-life somewhere between 130 and 135 neutrons, the spontaneous fission half-lives beginning to increase again as the 126-neutron subshell is approached.

In an effort to observe the spontaneous fission decay of some of these light isotopes, the experiments listed in Table 1 were performed at the 88-inch cyclotron using a rotating drum system equipped with mica detectors.[1] Experimental upper limits for the percentage of spontaneous fission branching for the listed isotopes are obtained by assuming a production cross-section. Lower limits for the spontaneous fission half-life are based on the experimental spontaneous fission branching ratio and an estimated total half-life obtained by extrapolation of the known alpha and electron capture half-lives for the even-even isotopes. With the possible exception of the ^{40}Ar+Hg bombardment, no fissions other than a normal background were detected. Future work will include repeating the

Table 1. Spontaneous fission (SF) of light isotopes of Pu, Cm, and Cf.

Reaction	Isotope	σ_{Calc}[a]	$\%SF_{Expt}$[b]	$T_{1/2SF\text{-}Expt}$[b]	$T_{1/2SF\text{-}Pred}$[c]
$^{3}He+^{233}U$	^{228}Pu	1.24 nb	<49%	>1.93 m	1.5 y
$^{24}Mg+Pb$	^{228}Pu	11 μb	<0.88%	>1.8 h	
$^{3}He+^{233}U$	^{230}Pu	140 nb	<0.34%	>1.8 d	2.1×10^{3} y
$^{28}Si+Pb$	^{232}Cm	220 nb	<15%	>3.3 s	28 m
$^{40}Ar+Hg$	^{238}Cf	20 nb	<80%	> ~ s	260 ns

[a]These calculations are based on the model used by J. R. Alonso, Gmelin, Handbuch der Anorganischen Chemie, Band Fb, Teil A1. p. 28.

[b]These limits are based on the assumed cross section and assumed total half-life.

[c]These values are obtained from the parabolic fits shown in Fig. 1.

$^{40}Ar+Hg$ experiment and using other target/projectile combinations to produce the light Cm and Cf isotopes.

Reference

1. For a description of the equipment, see E. K. Hulet et al., Phys. Rev. Lett. 26, 253 (1971).

A 51-SECOND SPONTANEOUS FISSION ACTIVITY IN THE REACTION $^{22}Ne + ^{209}Bi$

L. P. Somerville, M. J. Nurmia, and A. Ghiorso

The one-minute spontaneous fission activity produced from the reaction $^{22}Ne + ^{209}Bi$ by Dubna experimenters Kuznetsov et al.,[1] has been verified at the Berkeley 88-inch cyclotron, where 115 MeV ^{22}Ne ions struck a rotating Bi target mounted over the entire circumference of a brass wheel (see Fig. 1). The ^{22}Ne ions struck the wheel at 72° from normal incidence, instead of at normal incidence, to deposit the recoils in a thin layer of the target so that a calculated spontaneous fission detection efficiency of 90% could be obtained. Spontaneous fission events were recorded by fixed 3.1-cm-wide mica detectors about a millimeter from the spinning Bi target wheel, rotating at 1.14 cm/sec. A total of 138 spontaneous fission tracks were recorded by the mica detectors for an exposure of 8.3 μA-hrs $^{22}Ne^{+5}$ with an inherent detection efficiency of ~ 100%. The tracks were enlarged to a few microns in size by chemical etching in 48% hydrofluoric acid for about one hour at 60° C. The mica sheets were scanned for fission tracks using a X100 power microscope with ~ 70% measured efficiency. The beam intensity was measured by using the ^{209}Bi target wheel as a Faraday cup. Using the width of the excitation function (corrected for energy loss in the target) obtained by the Dubna group of about 3.5 mg/cm^2 of ^{209}Bi, a cross section of 0.66±0.33 nb at the peak of the excitation function was obtained. This value

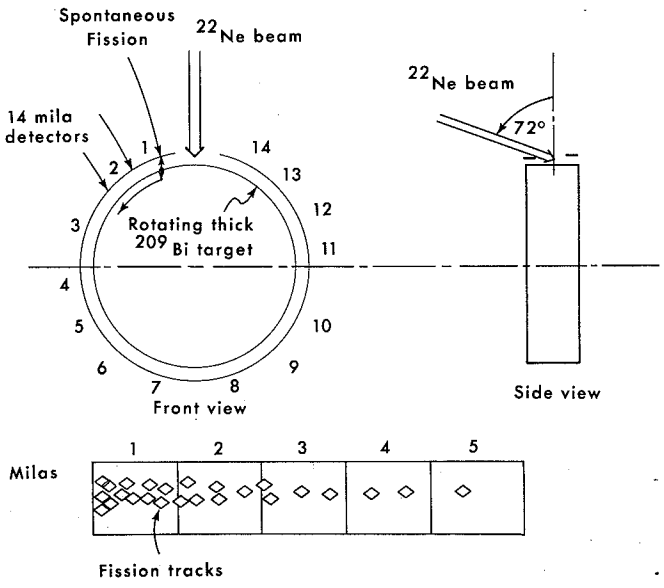

Fig. 1. Rotating drum assembly for detecting spontaneous fission. The beam intensity was measured by using the target as a Faraday cup.
(XBL 7611-4380)

compares with the Dubna measurement of 0.45±0.08 nb. The half-life of this spontaneous fission activity was obtained by least squares fit of the decay points in Fig. 2 to be 51±15 seconds with no background subtracted. The Dubna value of 60±5 seconds is in agreement within experimental error with this result.

The Dubna group concluded on the basis of theoretical arguments that the observed fission activity was due to ^{228}Np or ^{227}Np which decays by electron capture to a fission isomer of ^{228}U or ^{227}U.[1-3] This hypothetical decay mode was called "delayed fission." They excluded the possibility of a primary production reaction in which a proton is emitted by showing that the spontaneous fission activity is not produced in the reaction ^{22}Ne + Pb. A reaction in which an alpha particle is emitted was also excluded based on the absence of spontaneous fission activity from the reaction ^{18}O + ^{209}Bi.

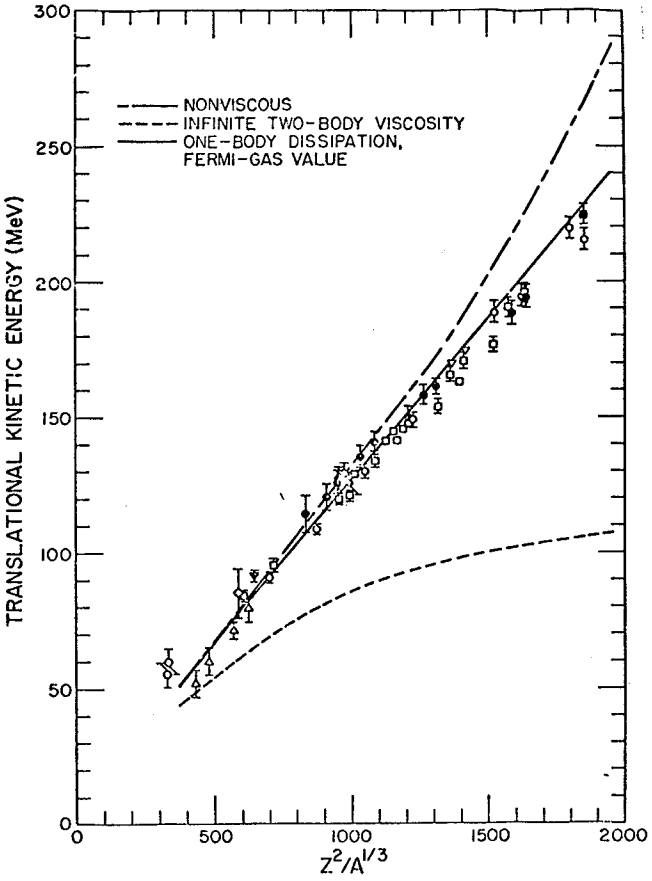

Figure 2. Decay curve for the spontaneous fission activity. (XBL 766-8224)

Future experiments may be attempted in Berkeley to look for rare uranium x-rays from the electron capture decay of ^{228}Np or ^{227}Np followed by coincidence counting of spontaneous fission events. Such a direct verification of "delayed fission" has not yet been accomplished. Upper limits on the spontaneous fission branching ratio have been set by the non-observation of spontaneous fission from the reactions ^{233}U(p,6n)^{228}Np $\xrightarrow{S.F.}$ ($< 4 \times 10^{-3}$) and ^{232}U(p,5n)^{228}Np $\xrightarrow{S.F.}$ ($< 2 \times 10^{-3}$).[4]

Population of a fission isomer state of a nuclide elsewhere in the region of atomic numbers near the target produced by a noncompound nucleus reaction is also a possibility. However, no such fission isomers have been found in reactions ^{20}Ne + ^{209}Bi ($< .1$ nb), ^{16}O + nat.Pb, ^{20}Ne + ^{207}Pb, ^{20}Ne + nat.Pb, and ^{24}Mg + nat.Pb. The possibility of a 51-second fission isomer of ^{228}Np has not been ruled out, but the longest-lived known fission isomer, ^{242m}Am, has a half-life of only 13.7 milliseconds.

References

1. V. I. Kuznetsov, N. K. Skobelev, and G. N. Flerov. J. Nucl. Phys. (USSR) 4, 279 (1966).

2. N. K. Skobelev, Sov. J. Nucl. Phys. 15, 249 (1972).

3. E. E. Berlovich and Yu. P. Novikov, Sov. Physics-Dok. 14, 349 (1969).

4. R. L. Hahn, Oak Ridge National Laboratory, private communication.

NEW ATTEMPT TO FIND THE DUBNA "0.1-s ^{260}104" ACTIVITY

A. Ghiorso, P. A. Baisden, I. Binder, R. E. Leber, D. Lee, D. Morrissey, J. M. Nitschke, M. J. Nurmia, R. J. Otto, L. P. Somerville, K. Thomas, K. E. Williams, E. K. Hulet,* R. W. Loughheed,* J. F. Wild,* J. H. Landrum,* R. J. Silva,† C. E. Bemis,† and M. Fowler‡

The followng paper details recent experiments designed to settle with finality whether or not the isotope ^{260}104 is a spontaneous-fission emitter with half-life of about 0.1 sec as claimed by the Dubna heavy elements group.[1] These experiments were conducted at the 88-inch cyclotron by a team of scientists from Lawrence Livermore, Oak Ridge National Laboratory, Los Alamos Scientific Laboratory, and Lawrence Berkeley Laboratory. More details are available in LBL reports.

The principal reaction used in our recent attempts to produce the Dubna ~0.1-sec SF activity was ^{249}Bk(^{15}N,4n)^{260}104. As in the earlier experiments[2] which were also unsuccessful, the reaction recoils were caught in vacuum on the periphery of a rotating drum. These products were quickly carried next to thin mica sheets so that spontaneous fission events could be spatially detected. A completely new apparatus was built for these experiments with an important difference being the use of a longer

drum to spread out the long-lived SF background activity from ^{256}Fm produced in the bombardments from its e.c.-mother, ^{256}Md. The ^{249}Bk target used consisted of about 85 μgm/cm^2) vacuum evaporated as BkF_3 onto 2.08 mg/cm^2 Be in a circle 4.8 mm in diameter. The target was placed 21 mm from the surface of a 254-mm diameter water-cooled drum, which was rotated typically at 60 revolutions per minute. The nuclear-reaction recoils passed in vacuum through an opening 20-mm square to strike the drum surface. The 360 mm long drum was scanned axially, usually at a speed of 7.7 mm/sec. The mica fission-track detectors, 31 mm wide and 50 mm long, were held in a curved holder about 0.8 mm away from the drum surface and completely surrounded the drum in a 31-mm slice.

The ^{15}N ion energies used were obtained by three settings of the 88-inch cyclotron and the use of Be-foil degraders. The nominal values of the energies out of the cyclotron, calculated from the cyclotron frequencies and fields, were 91.6, 93,6 and 105 MeV, thought to be accurate to better than 0.5 MeV. In the 93.6-MeV case, a special analysis was made by D. Hendrie using the large beam analyzer magnet and the energy was found to be 93.74±0.01 MeV. The Be degraders used to obtain lower energies were weighed and the final energies at the 0.5 mg/cm^2 ^{249}Bk target were obtained by calculation. The drop in energy of the ^{15}N ions through the Bk itself was about 0.5 MeV. The early experiments showed that the beam profile attained a needle-sharp focus when tuned for maximum beam current, and indeed we melted small holes through two old targets with currents in the vicinity of 3-5 charge microamperes. A three-phase 60-Hz wobbler was installed about 5 m upstream following the last beam quadrupole magnet. The wobbler was simply the stator of an induction motor and succeeded in moving the beam in a small circle at a 60-Hz rate with the loss of about 15% of the beam intensity. With this arrangement, we were able to use beam currents as high as 4 μA, but normally we limited the beam to about 3 μA to have a margin of safety. An infrared detection system was installed to guard against any unusual excursions of the beam and was similar to the one used in the Berkeley element 106 experiments.[3]

We found it advantageous to put a very thin (26 μg/cm^2) aluminum foil between the target and the drum to prevent any of the target material from being knocked out by the beam onto the drum surface and thus increasing the spontaneous fission background. This also served as a rough monitor of the beam current, since as much as 5% of the ^{256}Md that was produced stopped in these foils.

In addition to the regular drum experiments we made measurements of the long-lived recoil products directly. This was accomplished with a special holder mounted next to the target. In these experiments, an external Faraday cup was used to give accurate beam readings. An excitation function for ^{256}Md, which is made with a large cross section, is shown in Fig. 1 and was obtained by stopping its recoils in 1.0 mg/cm^2 Al and counting the foils directly in a fission counter. The growth and decay in one of these runs, a 1.65 μA-hr bombardment at 88 MeV for 2.0 hrs shown in Fig. 2, shows quite clearly that very little ^{256}Fm is produced directly since the data can be fitted by a curve, assuming that only ^{256}Md is produced. The berkelium target was prepared at the Lawrence Livermore Laboratory after being chemically separated from its californium daughter just a few days before the first bombardment. This timing of the separation is important because the half life of ^{249}Bk is only 314 days and it very soon

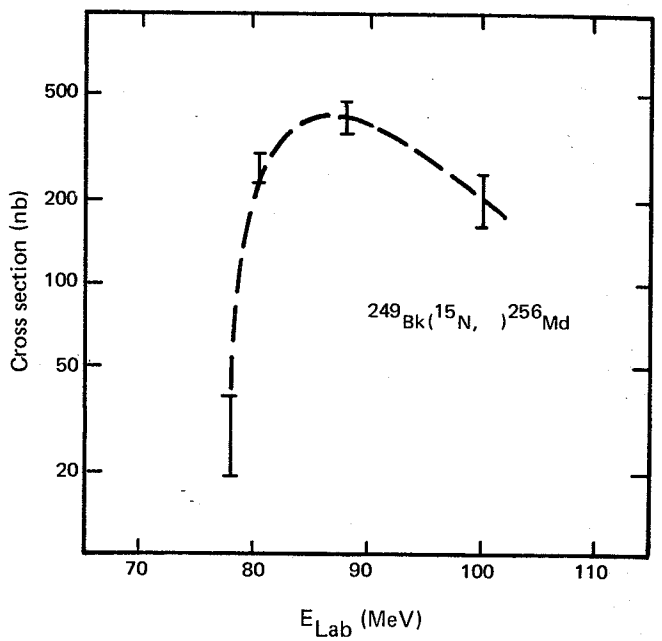

Fig. 1. Excitation function for ^{256}Md. Cross section in nanobarns. (XBL 766-8241)

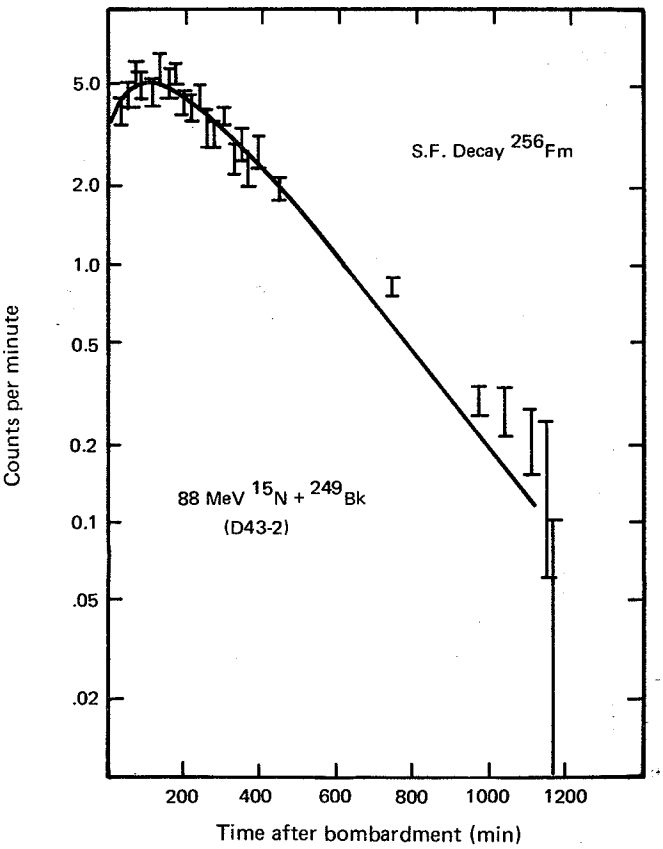

Fig. 2. Growth and decay curve of ^{256}Fm (from ^{256}Md). (XBL 766-8243)

becomes contaminated by its 360-yr daughter. The series of bombardments were then carried out with the chief objective being the attempt to see whether an ~ 0.1-sec SF activity was produced. It was not and we decided to make as many cross checks as we could so that there would be no question of the validity of our attempts.

Bombardments were made with 78, 82, 86, 88 and 100 MeV ^{15}N ions entering the target. There is general agreement that the cross section for the ^{249}Bk $(^{15}N,4n)^{260}104$ reaction should peak at about 82 MeV so this series adequately covers this range. Approximately 40 μA-hrs of beam were devoted at each of these energies in the search for the 80-msec activity. The results of the bombardment at 82 MeV are shown in the decay curve in Fig. 3. A calculated computer fit is also plotted. As can be seen, the maximum amount of a hypothetical 80-msec[4] activity that can be extracted from these data is very small. It corresponds to a cross section of less than 0.5 nanobarns if an excursion 2 σ higher than observed is allowed.

These decay curves were extracted from the raw scanning data by the following method. An early test run with a thick ^{241}Am target to produce the 2.3-sec ^{252}No via the ^{15}N,4n reaction at 82 MeV gave us an actual situation of recoiling nuclei made by complete fusion. The angular distribution of these recoils is very narrow, being broadened mostly by neutron boil-off and multiple scattering within the target. When the tracks were summed in slices along the direction of rotation of the drum, the distribution shown in Fig. 4 was obtained; such a distribution indicates that most of the fusion-produced nuclei can be measured by selecting a relatively narrow "window" in the transverse direction. Because in the case of the berkelium bombardments the background activity is the long-lived $^{256}Md \rightarrow ^{256}Fm$, which is spread out on the entire drum surface, we gained about a factor of 2 in signal-to-background ratio.

To make sure that our track counting efficiency was normal, a few test exposures of our mica were made from a ^{252}Cf source with and without an aluminum foil 250 μg/cm^2 in thickness, which is equal to the calculated CN-recoil range. Our average efficiency was 90%.

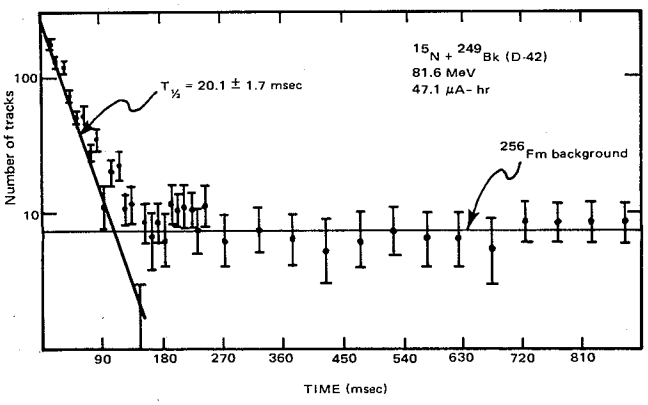

Fig. 3. Decay curve for spontaneous-fission events detected at 81.6 MeV. Solid lines represent computer fit to the data. (XBL 766-8243)

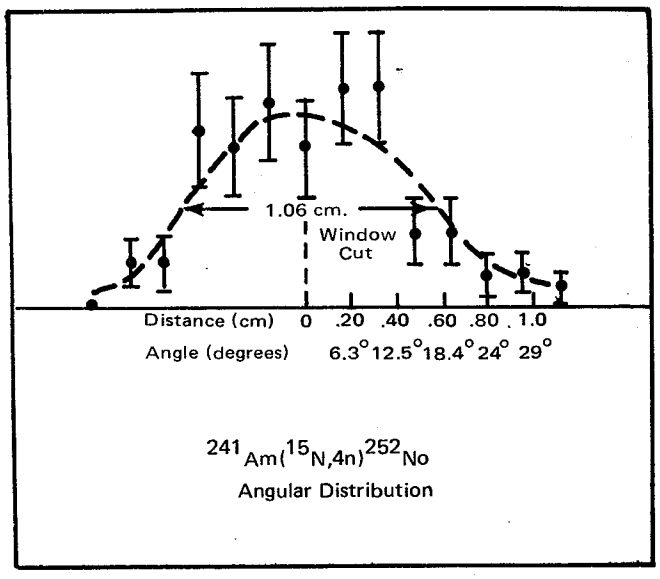

Fig. 4. Transverse distribution of ^{252}No fission tracks from $^{241}Am(^{15}N,4n)$ reaction at 81 MeV. (XBL 766-8244)

Though our decay curves show no hint of the so-called 80-msec SF activity, they very clearly show one with a half life of ~ 20 msec. This same activity was first reported by Ghiorso at the Welch Conference in 1969 (Ref. 2, p. 148).

The maximum cross section for producing the "~ 20 msec" activity is about 10 nb when made by ^{15}N ion bombardment of ^{249}Bk and has the excitation function shown in Fig. 5. However, on the basis of this data alone we cannot exclude the possibility that the yields include some fission from the 13.7-msec SF isomer, ^{242m}Am, produced by some sort of transfer

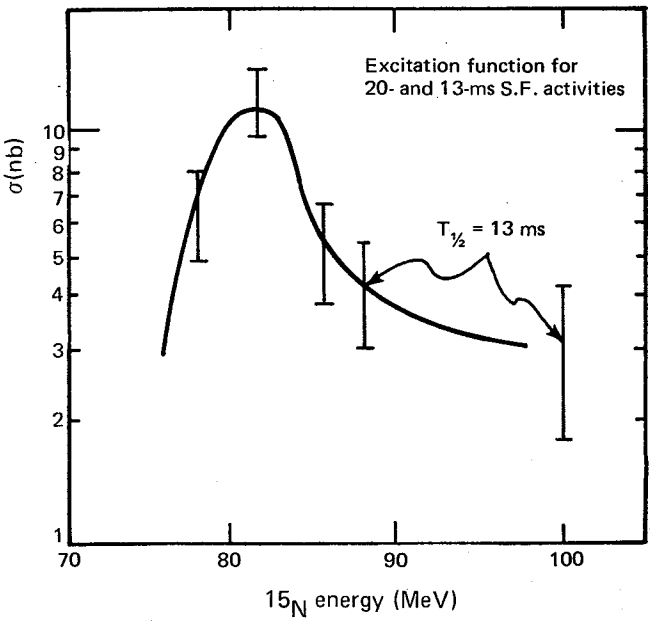

Fig. 5. Excitation function of the "~ 20-msec" spontaneous-fission activity. (XBL 766-8245)

or other reaction. The transverse track distribution for the "~20-msec" activity is remarkably narrow at 83 MeV (see Fig. 6). These data would seem to point to a complete fusion reaction except that its production σ is somewhat lower than expected (see below). Just prior to undertaking the berkelium bombardments, we bombarded ^{248}Cm with ^{16}O ions and ^{246}Cm with ^{18}O ions at about 93 MeV and once again observed the "~20-msec" SF activity without observing the hypothetical 80-msec Dubna activity. No excitation function was measured because of lack of time. It is possible that the "~20-msec" activity includes ^{260}104 since it passes some of the tests required. It may take some time before we can state with certainty whether or not we have observed this nuclide since there is the distinct possibility that this activity is due to ^{261}Lr or similar nuclide. This situation points up again the great difficulties that are encountered when working with spontaneous fission activities when the only parameter that is measured is half-life.

Although we set a maximum cross section for the ^{15}N, 4n reaction on ^{249}Bk to produce the 80-msec activity which was more than an order of magnitude less than the 5 nb claimed by Dubna,[5] it should be remembered that the actual cross section to produce ^{260}104 by this mechanism is expected to be as much as 25 nb. The reasoning is as follows: the cross section for the identical reaction to make ^{260}105 in bombardments of ^{249}Cf has been found experimentally to be ~ 12 nb. This new value was obtained by a re-evaluation of the old Berkeley data by Pirkko Eskola and appears in her recent thesis at the University of Helskinki. The cross section to make ^{260}104 by the same reaction should be larger since the values of $\Gamma_n/(\Gamma_n+\Gamma_f)$ and R_0 are more favorable. Indeed a calculation adjusted to the ^{260}105 production cross section shows that the production of ^{260}104 will be about twice as large. Our limit on the amount of the 80-msec activity that is made in the ^{249}Bk plus ^{15}N reaction is thus almost two orders of magnitude below that expected if it is due to ^{260}104.

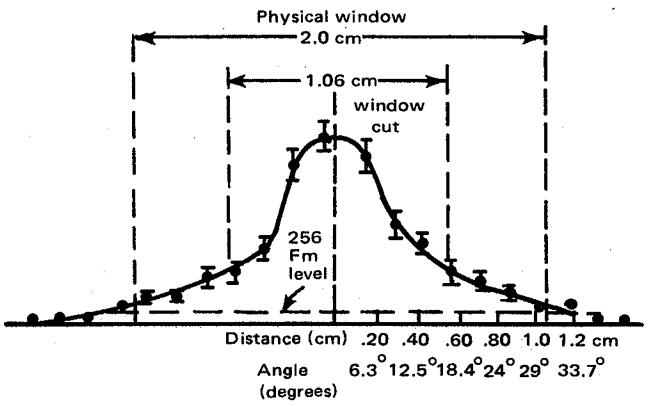

Fig. 6. Transverse track distribution of the "~20-msec" spontaneous-fission activity at 81.6 MeV. (XBL 766-8246)

There is no escape from the conclusion that can be drawn on the basis of our data. The mass 260 isotope of element 104, rutherfordium, does not decay by spontaneous fission with a half-life of "0.3 sec," or "0.1 sec," or "80 msec."

We extend our thanks to the staff and operations crew of the 88-inch cyclotron. Their help was invaluable to the success of these experiments.

We would like to acknowledge with gratitude the concentrated effort by many colleagues that went into the task of making these latest experiments so definitive. In particular, we would like to thank Glenn T. Seaborg for following developments very closely and providing inspiration and scientific guidance.

Footnotes and References

*Lawrence Livermore Laboratory.

†Oak Ridge National Laboratory.

‡Los Alamos Scientific Laboratory.

1. G. N. Flerov et al., Atomnaya Energiya 17, 310 (1964); Sov. J. Atomic Energy 17, 1046 (1964); Phys. Lett. 13, 73 (1964).

2. A. Ghiorso, Proc. of the Robt. A. Welch Foundation Conf. on Transuranium Elements, Houston, Nov. 1969 (p. 107).

3. A. Ghiorso et al., Phys. Rev. Lett. 33, 1490 (1974).

4. The "~0.1-sec" SF activity has recently been designated by Dubna as having an 80-msec $T_{1/2}$.

5. I. Zvara, private communication.

B. NUCLEAR REACTIONS AND SCATTERING

1. Microscopic

a. Light Ions

POLARIZARION EFFECTS IN THE FINAL-STATE INTERACTION REGION OF THE p-d BREAKUP REACTION*

F. N. Rad,† H. E. Conzett, R. Roy,‡ and F. Seiler§

Among the experimental observables in the three-nucleon system, the elastic cross section, inelastic cross section, and elastic analyzing power have been intensively investigated.[1] Inelastic analyzing powers comprise one class of observables which has received very little attention. That is, only a few experiments have been done which even show the presence of polarization effects, and theoretical interpretation and predictions via exact three-body calculations have not, as yet, been made. The three-nucleon calculations based on the Faddeev equations with separable potentials for the $^1S_0$, $^3S_1$-$^3D_1$, and P-wave components of the nucleon-nucleon interaction,[2,3] have provided predictions of the vector and tensor polarizations which are in good agreement with the experimental data in the elastic channel,[4-6] whereas the S-wave forces alone had been sufficient to give agreement with the differential cross-section data. Similarly, calculations which have been successful in fitting inelastic cross-section data, have been restricted to two-nucleon S-wave interactions[7] and, thus, cannot predict analyzing powers for incident polarized protons or deuterons. It seems that experimental evidence of substantial polarization effects, such as reported here, are required in order to encourage or even compel the addition of the tensor force and P-wave contributions to three-body calculations.

The polarized proton or deuteron beam from the Berkeley 88-inch cyclotron was passed through a gas target in a 36-in. diameter scattering chamber. A description of the experimental arrangement and of the data acquisition procedure has been given elsewhere.[5]

Our experimental results for the proton analyzing power $A_y(\theta)$ in the $^2H(\vec{p},p)d^*$ reaction at $E_p = 22.7$ MeV are shown in Fig. 1, where the errors indicated are purely statistical. Here, d* denotes final-state np pairs with relative energy $E_{np} \leq 1$ MeV, in both singlet and triplet states. For comparison the smooth curve represents the elastic scattering analyzing powers measured in the same experiment. As can be seen, $A_y(\theta)$ in the breakup reaction reaches substantial values at angles greater than $\theta_{c.m.} = 70°$, and its angular distribution is quite similar to that of the elastic analyzing power. Figure 2 shows our experimental results for the deuteron vector analyzing power in the $^1H(\vec{d},p)d^*$ reaction at $E_d = 45.4$ MeV, corresponding to the same center-of-mass energy as in the $^2H(\vec{p},p)d^*$ reaction. Again the errors indicated are purely statistical and the solid line is a smooth curve drawn through the elastic scattering

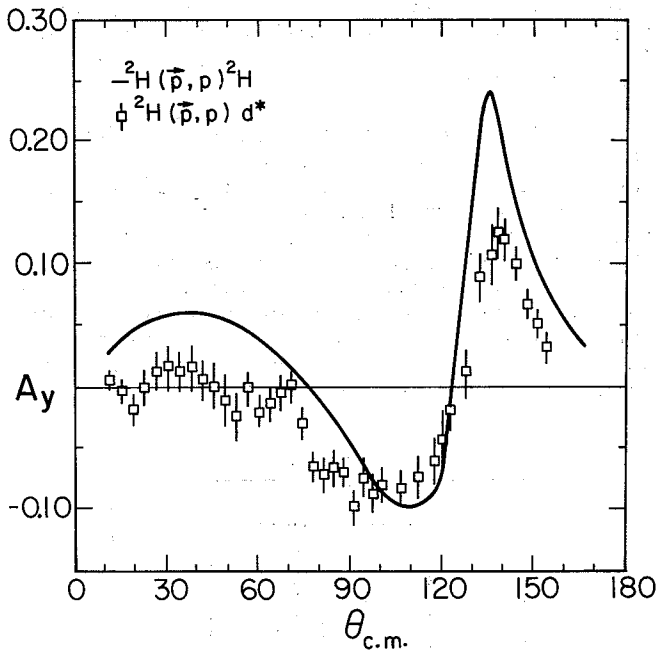

Fig. 1. The proton analyzing power $A_y(\theta)$ in the $^2H(\vec{p},p)d^*$ reaction at $E_p = 22.7$ MeV for the transition to the FSI region with relative energy $E_{np} \leq 1$ MeV. The smooth curve represents the elastic scattering analyzing powers measured in the same experiment. (XBL 753-2612)

results.[5] Here also, the similarly between the inelastic and elastic analyzing powers is quite definite.

This similarity between the angular distribution of the analyzing powers for the elastic and inelastic scattering is rather unexpected in view of the results reported by Brückman et al.,[8] in the analysis of their $^1H(d,pp)n$ cross-section data at the slightly higher energy of $E_d = 52.3$ MeV. In their analysis they used the Watson FSI factorization assumption[9] to determine the separate contributions to the $^1H(d,d^*)p$ cross section from the production of singlet and triplet np pairs.

$$(d\sigma/d\Omega)_{d^*} = (d\sigma/d\Omega)^s_{d^*} + (d\sigma/d\Omega)^t_{d^*}. \quad (1)$$

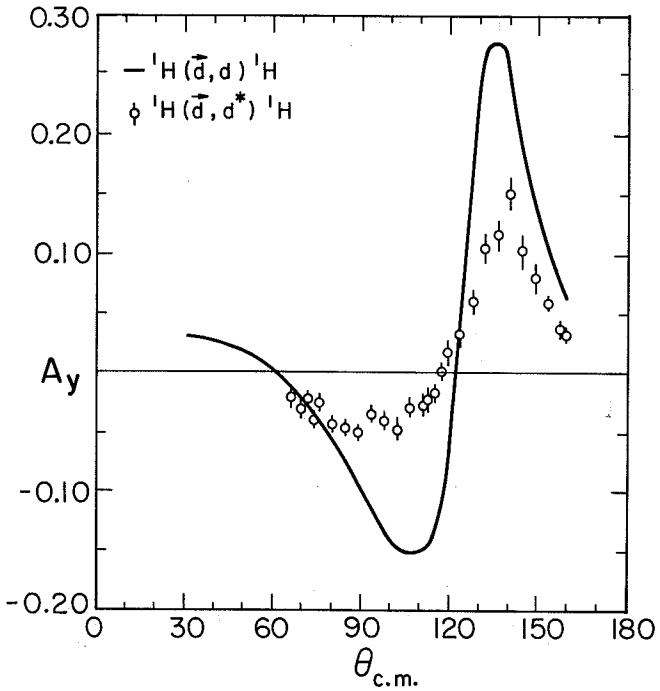

Fig. 2. The deuteron analyzing power $A_y(\theta)$ in the $^1H(\vec{d},d^*)^1H$ reaction at $E_d = 45.4$ MeV for the transition to the FSI region with relative energy $E_{np} \leq 1$ MeV. The smooth curve represents the deuteron elastic scattering analyzing powers of Ref. 5.
(XBL 753-2613)

They found that between $\theta_{c.m.} = 85°$ and 150° the production of singlet pairs exceeded that of triplet pairs for $E_{np} \leq 1$ MeV, with the ratio $R = (d\sigma/d\Omega)^s_{d*}/(d\sigma/d\Omega)^t_{d*}$ reaching a value of about 10 near $\theta_{c.m.} = 120°$. The angular dependence of $(d\sigma/d\Omega)^t_{d*}$ was similar in shape to that of the elastic cross section, and their Born approximation calculation, in which the final-state np wave function used was effectively that of a deuteron with binding energy $E_B = 0$, was in excellent agreement with $(d\sigma/d\Omega)^t_{d*}$. However, $(d\sigma/d\Omega)^s_{d*}$ was quite different, with the result that the combined singlet plus triplet cross-section showed little resemblance to the elastic angular distribution. The more recent exact three-body calculations of Kluge et al.,[10] using spin-dependent separable potentials for the relative S-state of the two nucleons, substantiate the earlier findings of Brückman et al. in the determination of the separate singlet and triplet d* production cross sections. Furthermore their calculated ratio $|T^s|^2/|T^t|^2 = (d\sigma/d\Omega)^t_{d*} / (d\sigma/d\Omega)^t_{d*}$ for $E_{np} = 0$ is in good agreement with the ratio R deduced by Brückman et al., from the analysis of their data. This ratio was shown to be as high as 20 in the backward angular region.

We can, in the same way, express our analyzing power results as the incoherent sum of the singlet and triplet d* production contributions,

$$A_y^{d*} = \frac{A_y^s\,(d\sigma/d\Omega)^s_{d*} + A_y^t\,(d\sigma/d\Omega)^t_{d*}}{(d\sigma/d\Omega)^s_{d*} + (d\sigma/d\Omega)^t_{d*}} \qquad (2)$$

where A_y^s and A_y^t are the analyzing powers for production of np pairs in the $^1S_0$ and $^3S_1$ states, respectively. If triplet d* production were the major contribution to the cross section, one could expect the similarity between the elastic and inelastic vector analyzing powers seen in Figs. 1 and 2. However, it is the singlet d* production which is the major contribution to the cross section in just the backward angular region of maximum analysing power. In view of the fact that the ratio, R, is found to be quite large over a considerable region of backward angles, Eq. (2) there reduces to $A_y^{d*} \simeq A_y^s$, implying that the angular distribution of the vector analyzing power in the elastic channel is similar to that in the breakup channel with the np pair in the singlet state. This condition is quite unexpected, especially in view of the marked dissimilarity between $(d\sigma/d\Omega)^s_{d*}$ and $(d\sigma/d\Omega)^t_{d*}$ for d* production. Although the exact three-body calculations very nicely reproduce the singlet and triplet d* production cross sections, there is an obvious need to include the more realistic nucleon-nucleon tensor and P-wave interactions in an effect to explain the measurements of the analyzing power results presented here.

Footnotes and References

*Condensed from Phys. Rev. Lett. 35, 1134 (1975).

†Nuclear Science Lab., M.I.T., Cambridge, Mass.

‡Physics Dept., Laval Univ., Quebec, Canada.

§Physics Dept., University of Basel, Switzerland

1. H. E. Conzett, in Proc. Int'l Conf. on Few Body Problems in Nuclear and Particle Physics (Les Presses De L'Université Laval, Québec, 1975).

2. P. Doleschall, Nucl. Phys. A220, 491 (1974); Nucl. Phys. A201, 264 (1973).

3. S. C. Pieper, Nucl. Phys. A193, 529 (1973).

4. J. S. C. McKee, H. E. Conzett, R. M. Larimer, and Ch. Leemann, Phys. Rev. Lett. 29, 1613 (1972); A. Fiore, J. Arvieux, N. Van Sen, G. Perrin, F. Merchez, J. C. Gondrand, C. Perrin, J. L. Durand, and R. Darves Blanc, Phys. Rev. C 8, 2019 (1973)

5. F. N. Rad, J. Birchall, H. E. Conzett, S. Chintalapudi, and R. Roy. Phys. Rev. Lett. 33, 1227 (1974).

6. F. N. Rad, J. Birchall, H. E. Conzett, and R. Roy. Phys. Rev. Lett. 33, 1579 (1974).

7. R. T. Cahill and J. H. Sloan, Nucl. Phys. A165, 161 (1971); W. Ebenhöh, Nucl. Phys. A191, 97 (1972)

8. H. Brückmann, W. Kluge, H. Mathäy, L. Schänzler, and K. Wick, Nucl. Phys. A157, 209 (1970).

9. M. C. Goldberger and K. M. Watson, Collision Theory (Wiley, New York, 1964) p. 540.

10. W. Kluge, R. Schlüfter, and W. Ebenhöh, Nucl. Phys. A228, 29 (1974).

VECTOR ANALYZING POWER IN THE $^3He(\vec{d},^3He)np$ REACTION*

R. Roy,† F. N. Rad,‡ H. E. Conzett, and F. Seiler§

During the past decade, substantial investigations of polarization effects have been made in the three-nucleon system.[1] The polarization in nucleon-deuteron elastic scattering has received the principal attention of both the experimental and the theoretical effort, while the study of such effects in the breakup reaction has received very little attention. The exact three-body calculations using the Faddeev equations have shown a remarkably good agreement with the proton and deuteron analyzing powers in p-d elastic scattering.[1] However, in the breakup channel the theoretical calculations[2] have been restricted to the use of nucleon-nucleon S-wave forces and, therefore, cannot predict any polarizations. Until recently, experimental measurements of polarization effects in the breakup reaction had yielded values which were very small or consistent with zero.[3] The first evidence of significant polarizations was seen by Rad et al.,[4,5] in their measurements of the vector analyzing power A_y for the transition to the np final state interaction (FSI) region. The $^1H(\vec{d},p)np$ and $^2H(\vec{p},p)np$ reactions, studied at the same center-of-mass energy, showed not only significant values of the vector analyzing powers, but also a definite similarity of its angular distribution with that of the elastic channel.

Since the spin structure of the deuteron breakup on ^3He and ^1H is the same, the nondynamical properties of the two reactions are identical. Thus, it is of interest to look for similar polarization effects in the $^3He(\vec{d},^3He)d^*$ reaction, where d^* denotes final-state np pairs with low relative energy E_{np}, in both singlet and triplet states. We report here measurements of the vector analyzing power A_y in this reaction at E_d = 30, 35, and 40 MeV for $E_{np} < 2.0$ MeV. Our results are shown in Fig. 1. The statistical errors are smaller than the symbols. For comparison, the analyzing powers in $\vec{d}$-^3He elastic scattering at the same energies are shown as the smooth curves. It is seen that A_y in the $^3He(d,^3He)d^*$ reaction reaches substantial values and follows that of the elastic channel at d^* production angles beyond 90° c.m. The peak values near $\theta_{c.m.}$ = 135° and 155° are quite constant in magnitude and position over the 10-MeV energy interval studied. In a comparison of our results with the previous measurements,[4] near $\theta_{c.m.}$ = 135° the ratio A_y (elastic)/A_y (d^*) is ≈ 3 in both the $^3He(\vec{d},d^*)^3He$ and $^1H(\vec{d},d^*)^1H$ reactions, and the ratio is ≈ 1.4 and ≈ 1.9, respectively, near $\theta_{c.m.}$ = 155°. We are presently involved in a comparison of these data with DWBA calculations of $A_y(\theta)$ in transitions which produce both the $^1S_0$ and $^3S_1$ final state d^*.

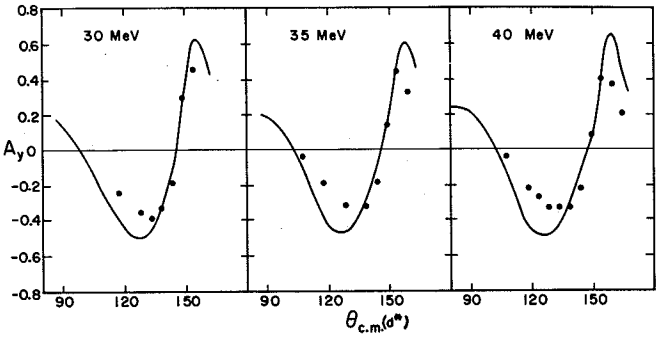

Fig. 1. The vector analyzing power, $A_y(\theta)$, in the reaction $^3He(\vec{d},^3He)d^*$. The smooth curves represent the analyzing powers in $\vec{d}$-^3He elastic scattering at the same energies. (XBL 756-3182)

Footnotes and References

*Proc. Fourth Int'l Symposium on Polarization Phenomena in Nuclear Reactions (Birkhäuser Verlag, Basel, 1976).

†Physics Dept., Laval University, Quebec, Canada.

‡Nuclear Science Lab., MIT, Cambridge, Mass.

§Physics Dept., University of Basel, Switzerland.

1. H. E. Conzett, in Proc. Int'l Conf. on Few Body Problems in Nuclear and Particle Physics (Les Presses de l'Université Laval, Québec, 1975).

2. R. T. Cahill and I. H. Sloan, Nucl. Phys. A165 (1971) 161; W. Ebenhöh, Nucl. Phys. A191 (1972) 97.

3. F. N. Rad, L. C. Northcliffe, J. G. Rogers, and D. P. Saylor, Phys. Rev. Lett. 31 (1973) 57; Phys. Rev. C8 (1973) 1248; J. Arvieux, et al., Nucl. Phys. A150 (1970) 75; C. O. Blyth, et al., Proc. Int'l Conf. on Few Body Problems in Nuclear and Particle Physics (Les Presses de l'Université Laval, Québec, 1975).

4. F. N. Rad, R. Roy, H. E. Conzett, J. Birchall, F. Seiler, and R. M. Larimer, Bull. Am. Phys. Soc. 20 (1975) 578.

5. F. N. Rad, H. E. Conzett, R. Roy, and F. Seiler, Fourth Polarization Symposium.

POLARIZATION PHENOMENA IN FEW-BODY SYSTEMS*

H. E. Conzett

My intention is to survey the recent developments in the study of polarization effects in the two, three-, and several-nucleon systems.[1,2] Because these measurements or calculations essentially have to do with cross sections for particular selected spin states, it is clear that these studies provide more detailed information and test more detailed calculations than is possible with the usual spin-averaged cross sections.

One of the nucleon-nucleon discussion sessions at the Quebec conference considered experiments for the next decade, with a stress on polarization experiments.[3] Included among the several suggestions for future experiments were: (1) a need for more accurate p-p cross-section and polarization data below 20 MeV because of significant discrepancies among the existing data; (2) measurements of the neutron to proton polarization transfer (D_t) or the spin-correlation coefficient, C_{nn}, in n-p scattering at 50 MeV, in order to make a substantial improvement in the determination of ε_1, the $^3S_1$-$^3D_1$ mixing parameter, since the available data left ε_1 undetermined between -10° to +3° at 50 MeV;[4] and (3) a general request for measurements above the inelastic threshold of total cross sections for various spin orientations of both beam and target, and for measurements of the analyzing powers and spin correlation coefficients, at the higher energies above the inelastic threshold. I am happy to report the significant progress that has already been made in these three areas at just the beginning of that decade.

Hutton et al.,[5] have recently reported on measurements of the analyzing power in p-p scattering at 10 MeV. Their results are shown in Fig. 1. Note that the maximum (negative) value is 2×10^{-3} and the typical error is 10% of that, or 2×10^{-4}, so these are accurate data, with more than an order of magnitude better precision than had been attained previously. Traditionally, the low energy p-wave phase shifts have been obtained with phenomenological extrapolations from higher energies. The dot-dash curve in Fig. 1 is the analyzing power calculated from the phase shifts resulting from the 1 - 27.6 MeV analysis of Arndt et al.,[6] in which the overall normalizations of the cross-section data were kept fixed. That is clearly inconsistent with these data, whereas an analysis with the normalizations taken as adjustable parameters resulted in calculated analyzing powers that are in reasonable agreement with the data. The solid curve is the calculated analyzing power from a phase-shift analysis of these and nearby 9.9 MeV cross-section results. The s- and p-wave phase shifts determined in this analysis[5] are the first model independent determinations made below 25 MeV.

With respect to the n-p mixing parameter ε_1, Johnson et al.,[7] reported at Zürich on their measurements at 50 MeV of the n-p spin correlation parameter A_{yy} (equal to C_{nn} for parity conserving or time-reversal invariant interactions). Their results are shown in Fig. 2, along with curves calculated from phase-shift solutions with the indicated values of ε_1. The -8° value seems to be ruled out, but an additional overall normalization uncertainty of ≃ 25% leaves the error on ε_1 considerably larger than the ± 1° envisioned by Binstock and Bryan. Their calculations,[4] in fact, whith $\varepsilon_1 = 2.8°$ gives A_{yy} (i.e. C_{nn}) = 0.38 at θ_{cm} = 120°, which is a value 35% larger than that shown as the calculated result in Fig. 2. This discrepancy between the two calculations must certainly be resolved, but these measurements, requiring both a polarized neutron beam and polarized proton target, clearly demonstrate an impressive experimental achievement.

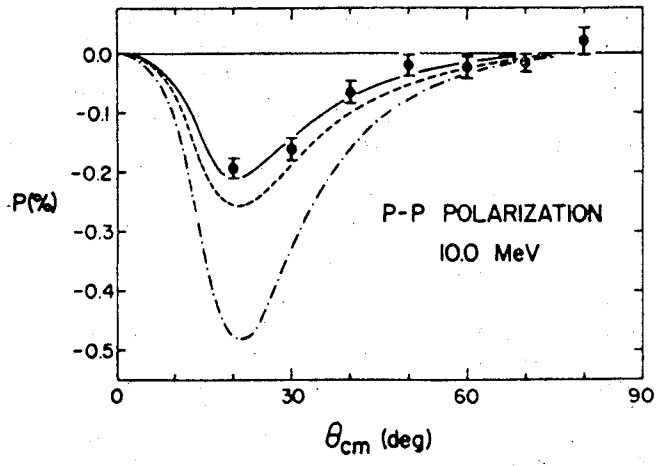

Fig. 1. Analyzing power in $\vec{p}$-p scattering at 10 MeV (Ref. 5). (XBL 7512-10054)

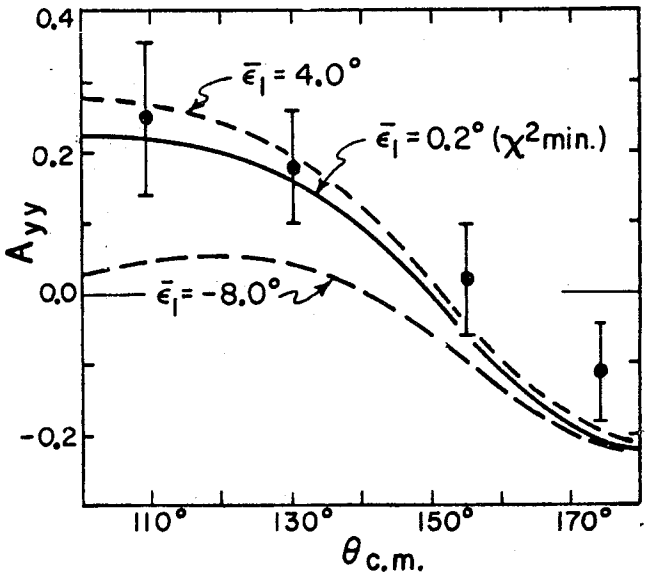

Fig. 2. The n-p spin correlation parameter A_{yy} at 50 MeV (Ref. 7). (XBL 7512-10055)

Hopefully, this experiment will be further pursued in order to reduce the experimental errors and thus reduce the uncertainty in ε_1.

Concerning polarization effects in the N-d breakup reaction, there have been recent noteworthy reports of both theoretical and experimental results. Rad et al.,[8] have reported on measurements, at E_p = 22.7 MeV, of both the proton and deuteron (vector) analyzing powers in the p-d breakup transition to the np final-state interaction (FSI) region of the three-body spectrum. These data are shown in Fig. 3, where the smooth curves represent the elastic p-d proton and deuteron analyzing powers. The substantial values of these inelastic analyzing powers demonstrated a clear need for the exact N-d breakup calculations to include more than the simple s-wave N-N interactions that had been sufficient to fit the cross-section data. Such calculations are now underway. The first of these at E_n = 22.7 MeV, is reported in a contribution to this conference by Bruinsma and van Wageningen.[9] Their work shows that the tensor force affects the cross section in the region of the FSI peak but has little influence in the quasi-free scattering region. Their calculated deuteron tensor analyzing powers show very substantial values, an example is shown in Fig. 4. In particular, T_{20} exceeds 0.35 in the FSI region for the particular θ_1,θ_2 angle combination chosen here. These predictions of substantial tensor analyzing powers will certainly encourage experimentalists to measure them. The calculated deuteron vector analyzing powers are less than 0.05 for this angle combination, so the situation seems to be comparable to that of the elastic N-d case, where the $^3S_1 - {}^3D_1$ tensor force was chiefly responsible for the observed tensor polarizations while the N-N p-wave interactions were the source of the vector polarizations. It is

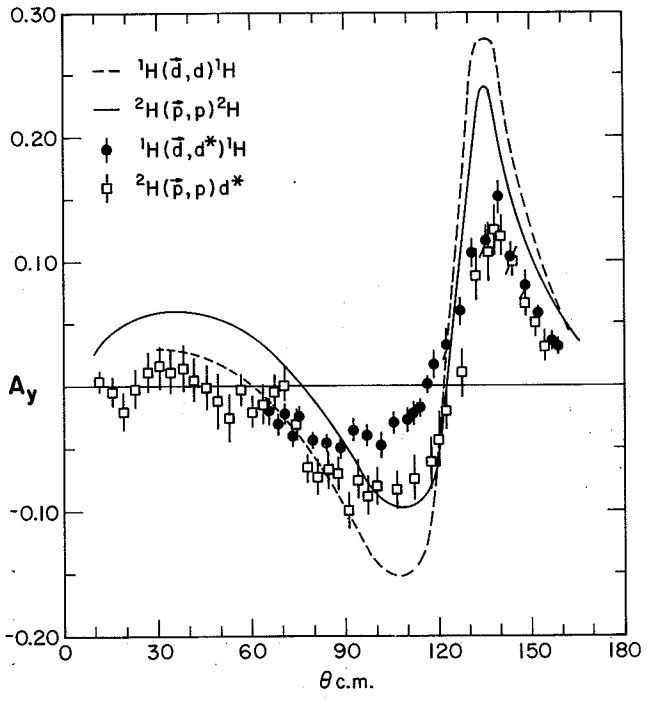

Fig. 3. The proton and deuteron analyzing powers A_y in the p-d breakup reaction at 22.7 MeV (Ref. 8). (XBL 753-2664)

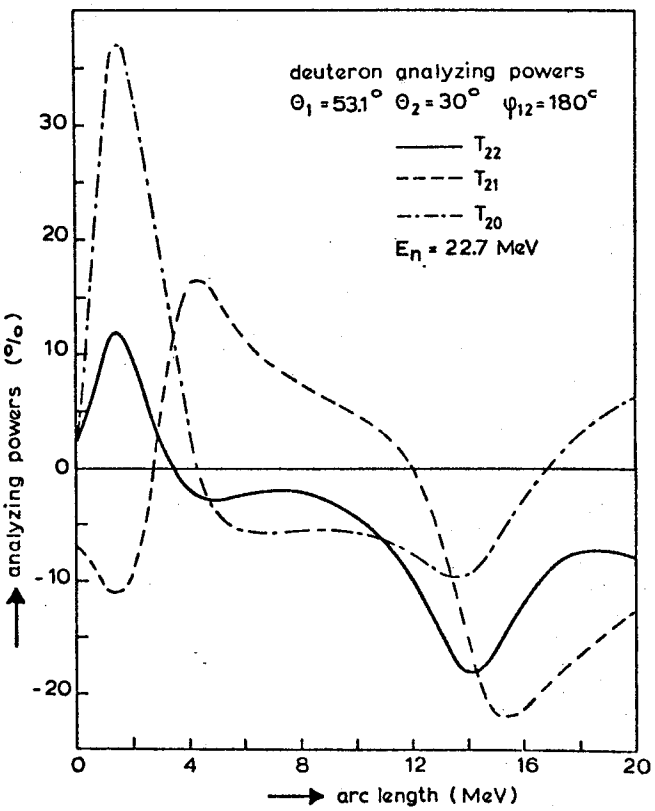

Fig. 4. Calculated deuteron tensor analyzing powers T_{2q} in the n-d breakup reaction at 22.7 MeV (Ref. 9). (XBL 7512-10060)

planned to next add the p-wave N-N interactions in these breakup calculations. There is now a real promise that the very fruitful interchange which occurred between theory and experiment with respect to polarization observables in elastic N-d scattering can now be repeated for the breakup reaction.

There have been two rather recent developments that show the consequent effects on polarizations that follow from particular symmetries of the nuclear interaction. The first of these involves charge-symmetry or isospin conservation. Experiments on the $^3H(p,n)^3He$ and $^7Li(p,n)^7Be$ reactions[10] had shown that the neutron polarizations p_y and the proton analyzing powers A_y were essentially equal, with limited exceptions. This equality was seen to result from charge-symmetry,[11] and it is an approximate equality because of the presence of the Coulomb interaction. However, it is in just those regions of significant difference between p_y and A_y that useful information can be derived on the structure of the nuclei studied.[12] Recent studies of $p_y = A_y$ in (p,n) reactions on other nuclei were reported at Zürich. Figure 5 shows the data of Lisowski et al.,[13] on ^9Be. At 8.1 MeV the older P_y values (crosses) are quite different from those reported here (dots), and the latter are close to the measured A_y values (triangles). Final corrections to the A_y values from background subtractions are expected to improve the agreement. As is suggested by the comparison at 9.1 MeV, new measurements will be made there of p_y as a check on the old values (crosses).

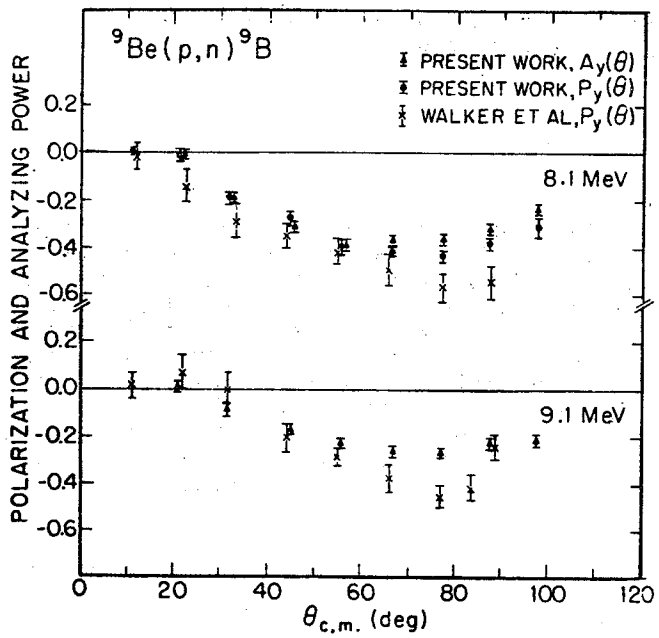

Fig. 5. Polarizations p_y and analyzing powers A_y in the ^{9}Be(p,n)^{9}B reaction at 8.1 and 9.1 MeV (Ref. 13). (XBL 7512-10061)

The second development shows that for reactions with identical or charge-symmetric particles in the initial state, the angular-distribution symmetry of the analyzing powers can provide a clear signature of the reaction mechanism.[14]

In summary, recent polarization studies in N-N scattering at and below 50 MeV have provided specific and significant improvements in the phase-shift parameters. High energy investigations with both polarized proton beams and targets have shown unexpectedly large spin effects, and this provides a challenge for theoretical effort to explain these results. Experimental and theoretical work on the three-nucleon problem continues to yield new and interesting results, with the emphasis now shifting to polarization studies in the breakup reaction. Ongoing work on several-nucleon systems continues to provide polarization data for general analyses, nuclear structure information, or specific resonance effects. Finally, the basic interaction symmetries continue to have unique and important consequences for polarization observables.

Footnotes and References

*Excerpted from Proc. Seventh Int'l. Conference on Few-Body Problems in Nuclear and Particle Physics, Delhi, India, Dec. 1975, to be published.

1. Few Body Problems in Nuclear and Particle Physics, eds. R. J. Slobodrian, B. Cujec, and K. Ramavataram (Les Presses de L'Université Laval, Quebec, 1975).

2. Proc. Fourth Int'l. Symposium on Polarization Phenomena in Nuclear Reactions, Zurich, August 1975 (Birkhauser Verlag, Basel), to be published.

3. J. Jovanovitch and J. Edgington, Ref. 1, p. 170.

4. J. Binstock and R. Bryan, Phys. Rev. D9 (1974) 1528.

5. J. D. Hutton, W. Haeberli, L. D. Knutson, and P. Signell, Phys. Rev. Lett. 35 (1975) 429, and Ref. 2.

6. R. A. Arndt, R. H. Hackman, and L. D. Roper, Phys. Rev. C9 (1974) 555.

7. S. W. Johnson, F. P. Brady, N. S. P. King, M. W. McNaughton, and P. Signell, Ref. 2.

8. F. N. Rad, H. E. Conzett, R. Roy, and F. Seiler, Phys. Rev. Lett. 35 (1975) 1134.

9. J. Bruinsma and R. van Wageningen, 1975, Proc. Seventh Int'l. Conference on Few-Body Problems in Nuclear and Particle Physics, Delhi, India (to be published).

10. R. C. Haight, J. J. Jarmer, J. E. Simmons, J. C. Martin, and T. R. Donoghue, Phys. Rev. Lett. 28 (1972) 1587; Phys. Rev. C 9 (1974) 1292; U. Rohrer and L. Brown, Nucl. Phys. A221 (1974) 325.

11. H. E. Conzett, Phys. Lett. 51B (1974) 445; L. G. Arnold, Ref. 2.

12. L. G. Arnold, R. G. Seyler, T. R. Donoghue, L. Brown, and U. Rohrer, Phys. Rev. Lett. 32 (1974) 310.

13. P. W. Lisowski, G. Mack, R. C. Byrd, W. Tornow, S. S. Skubic, R. L. Walter, and T. B. Clegg, Ref. 2.

14. H. E. Conzett, Ref. 2.

VECTOR ANALYZING POWER IN ELASTIC DEUTERON-DEUTERON SCATTERING BETWEEN 20 AND 40 MeV

H. E. Conzett, W. Dahme,† R. M. Larimer,
Ch. Leemann, and J. S. C. McKee‡

The subject of d-d elastic scattering has not received very much attention in the past. The cross sections are quite smooth functions of energy in the region up to 20 MeV where there are the most data available. However, the complexity of the spin structure and the low threshold for inelastic processes has made any meaningful phase-shift analysis impossible because of the large number of parameters involved even with the restrictive assumption of channel-spin conservation.[1] A resonating-group calculation[2] has obtained good agreement with the cross-section data between 5 and 20 MeV, but the use of a purely central nucleon-nucleon potential precludes the prediction of any spin-polarization observables.

From an experimental point of view, the polarization experiments in elastic d-d scattering have raised a qualitative question. Previous measurements of the vector analyzing power iT_{11} in $\vec{d}$-d scattering have been made at several energies below 12 MeV,[1,3] and at 21.4 MeV.[4] Nonzero but very small values of iT_{11} were obtained, reaching a maximum value of about 0.04 at 21.4 MeV. These values are almost an order of magnitude smaller than the nucleon and deuteron vector analyzing powers found in other elastic processes involving few nucleon systems, e.g., $\vec{p}$ + ^{2}H, ^{3}He, ^{4}He and $\vec{d}$ + ^{3}He, ^{4}He. Since sizable contributions of S, P, and D-waves were required to fit the d-d data,[1,2] the rather insignificant polarization effects could not be explained as a consequence of a predominance of S-wave scattering. Thus, its reason remained unexplained.

We have extended the measurements of vector analyzing powers in $\vec{d}$-d scattering to 40 MeV to examine whether or not its anomalously small value persists at these higher energies. Also, another determination near 20 MeV was desired, since the older measurement at 21.4 MeV was rather uncertain because of lack of knowledge of the beam polarization. We used the axially injected vector-polarized deuteron beam from the Berkeley 88-inch cyclotron. Left-right asymmetry data were taken simultaneously at two angles separated by 20°, using pairs of ΔE-E silicon detector telescopes. A polarimeter, consisting of a gas target and a pair of ΔE-E counter telescopes, was placed downstream of the main scattering chamber and provided continuous monitoring of the beam polarization. The analyzer used was ^{4}He, whose vector analyzing power in $\vec{d}$-^{4}He elastic scattering has been measured in detail.[5] The differential cross section for vector-polarized deuterons is given by

$$\sigma(\theta) = \sigma_0(\theta)\,[1 + 2\,(it_{11})(iT_{11})], \qquad (1)$$

where $\sigma_0(\theta)$ is the differential cross section for unpolarized deuterons and it_{11} is the beam polarization. A left-right asymmetry measurement gives

$$\varepsilon(\theta) = 2\,(it_{11})(iT_{11}), \qquad (2)$$

and the simultaneous determination of the beam polarization yields the vector analyzing powers iT_{11}. Figure 1 shows our data at $E_{\vec{d}}$ = 20, 30, and 40 MeV; the particle symmetry requires that $iT_{11}(\theta) = -iT_{11}(\pi-\theta)$. Our 20-MeV values are a factor of 2 larger than the previous results at 21.4 MeV, and clearly the vector analyzing powers increase rapidly with increasing energy. These values, when compared with the analyzing powers in $\vec{d}$-p elastic-scattering measured at comparable center-of-mass energies,[6] can no longer be considered anomalously small.

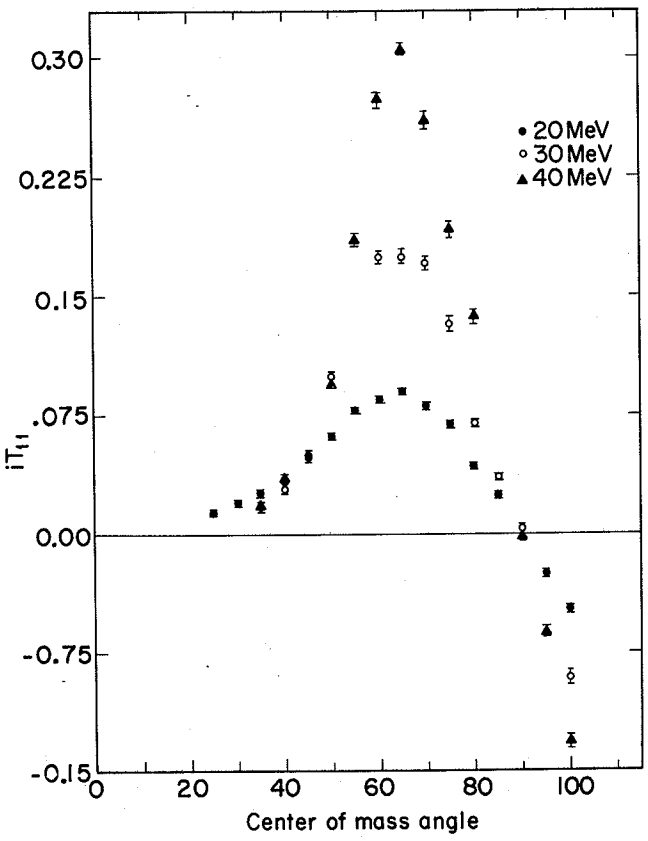

Fig. 1. Vector analyzing power, iT_{11}, in $\vec{d}$-d scattering between 20 and 40 MeV.
(XBL 728-3846)

Footnotes and References

*Proc. Fourth Int'l. Symposium on Polarization Phenomena in Nuclear Reactions (Birkhäuser Verlag, Basel, 1976).

†Sektion Physik der Universität München, 8046 Garching, Germany.

‡University of Manitoba, Winnipeg, Manitoba, Canada.

1. G. R. Plattner and L. G. Keller, Phys. Letters 30B, (1969) 327; P. D. Lien, Nucl. Phys. A178 (1972) 375; H. O. Meyer and P. Schiemenz, Nucl. Phys. A197 (1972) 259.

2. F. S. Chwieroth, Y. C. Tang, and D. R. Thompson, Nucl. Phys. A189 (1972) 1.

3. W. Grüebler, V. König, R. Risler, P. A. Schmelzbach, R. E. White, and P. Marmier, Nucl. Phys. A193 (1972) 149.

4. J. Arvieux, J. Goudergues, B. Mayer, and A. Papineau, Phys. Letters 22 (1966) 610.

5. H. E. Conzett, W. Dahme, Ch. Leemann, J. A. Macdonald, and J. P. Meulders, Fourth Polarization Symp.

6. J. S. C. McKee, H. E. Conzett, R. M. Larimer, and Ch. Leemann, Phys. Rev. Lett. 29 (1972) 1613.

THE VECTOR ANALYZING POWER IN THE $^2H(\vec{d},p)^3H$ REACTION AT 30 MeV*

H. E. Conzett, J. S. C. McKee,†
R. M. Larimer, and Ch. Leemann

The $^2H(d,p)^3H$ reaction has been studied at energies up to 12 MeV by a number of groups.[1] Grüebler et al., in particular have measured the differential cross sections and the deuteron analyzing powers at 9 energies between 3.0 and 11.5 MeV, and have analyzed their data in terms of possible resonances in ^4He. Their analysis of the coefficients in a Legendre expansion fit to the data showed that no simple isolated state of this system exists between 24 and 30 MeV excitation of ^4He since relatively strong interference effects were observed.

The present experiment was undertaken at E_d=30 MeV in order to study the $^2H(d,p)^3H$ reaction in a region of considerably higher excitation of ^4He. Also, it is to be expected that the direct nucleon transfer mode should be enhanced with respect to the compound-nucleus reaction mechanism at this higher energy. Measurements were made of the differential cross-section and the vector analyzing power iT_{11}. The iT_{11} results are shown in Fig. 1, and the surprising feature is the approximate antisymmetry of the data with respect to $\theta_{cm} = 90°$. The degree of symmetry observed is quite remarkable because the iT_{11} data at $E_d = 11.5$ MeV show little symmetry of any kind and are almost uniformly positive in sign.

The entrance channel particle identity requires that $\sigma(\theta) = \sigma(\pi-\theta)$, and in the inverse $^3H(\vec{p},d)^2H$ reaction the exit-channel particle identity requires that $A_y(\theta) = -A_y(\pi-\theta)$ for the proton analyzing power.[2] There is, *a priori*, no such symmetry condition imposed on the analyzing powers in the $^2H(\vec{d},p)^3H$ reaction. However, it can be shown that if the reaction mechanism is entirely that of direct nucleon transfer, the indistinguishability of the neutron transfers between the two deuterons results in exact symmetries in the deuteron analyzing powers.[3] In particular for our purposes

$$iT_{11}(\theta) = - iT_{11}(\pi-\theta), \qquad (1)$$

so the near antisymmetry of our data is clear evidence of a predominantly direct nucleon-transfer reaction mode at this higher energy. Of course, the *certain* conclusion is that deviations from Eq. (1) show that other than the direct nucleon-transfer process is contributing to the reaction. It is possible, in principle, for the compound-nucleus reaction mechanism to give the result (1) if the reaction should proceed entirely through a single state or through states of the same parity so that only the even-L terms would contribute in the Legendre expansion

$$\sigma(\theta) iT_{11}(\theta) = \sum a_L \, p_L^1 \, (\cos\theta).$$

In view of the data and analysis of Grüebler at al., this circumstance is most unlikely in this reaction.

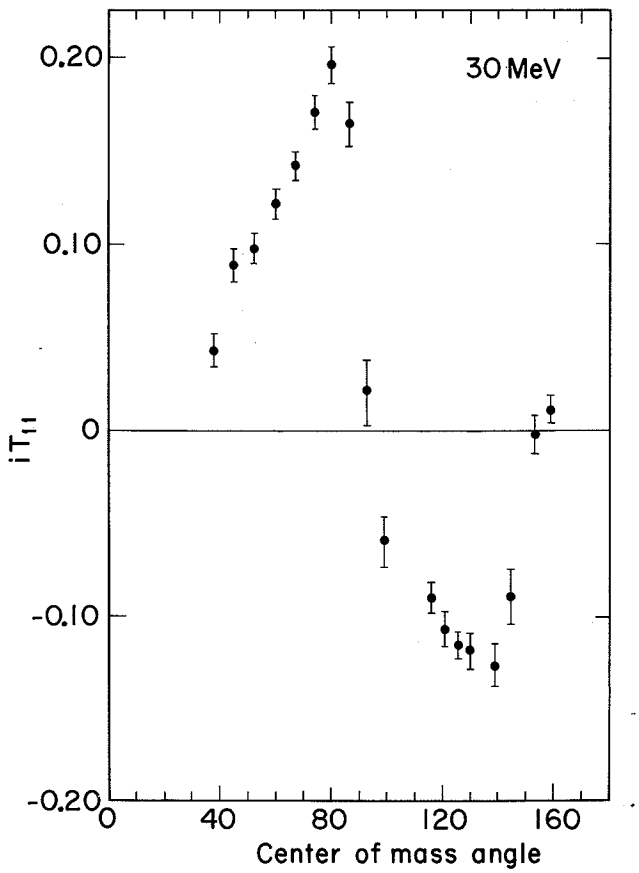

Fig. 1. Vector analyzing power, iT_{11}, in the $^2H(d,p)^3H$ reaction at 30 MeV. (XBL 728-3848)

In summary, we have found in the $^2H(\vec{d},p)^3H$ reaction that the entrance-channel particle identity imposes definite symmetries on the polarization observables that are clear signatures of the direct-reaction process. We know of no other example of a condition by which this process can be identified so clearly.

Footnotes and References

*Proc. Fourth Int'l. Symposium on Polarization Phenomena in Nuclear Reactions (Birkhäuser Verlag, Basel, 1976).

†University of Manitoba, Winnipeg, Manitoba, Canada.

1. W. Grüebler et al., Nucl. Phys. A193 (1972) 129, and references therein.

2. We follow the Madison convention, Polarization Phenomena in Nuclear Reactions, eds. H. H. Barschall and W. Haeberli (Univ. of Wisc. Press, Madison, 1971) p. xxv.

3. H. E. Conzett, J. S. C. McKee, R. M. Larimer, and Ch. Leemann, to be published.

VECTOR ANALYZING POWER IN THE $^2H(d,p)^3H$ REACTION BETWEEN 15 AND 25 MeV*

H. E. Conzett, R. M. Larimer, F. N. Rad,†
R. Roy,‡ and F. Seiler§

The charge-symmetric reactions $^2H(d,p)^3H$ and $^2H(d,n)^3He$ have been studied in considerable detail at energies up to 15 MeV.[1,2] Differential cross sections, nucleon polarizations, and deuteron vector and tensor analyzing powers have been measured, and differences in these observables for the two reactions have been examined for evidence of a possible deviation from the charge symmetry of the nuclear interactions. The more recent comparisons and calculations[3] have been able to explain the observed differences between the two reactions in terms of the Coulomb effect, including the Q-value difference.

The reactions, in addition to being charge symmetric, each possess the additional symmetry of entrance-channel particle identity. This requires that $\sigma(\theta) = \sigma(\pi-\theta)$ and $p(\theta) = -p(\pi-\theta)$ for the differential cross sections and the nucleon polarizations, respectively. In general, no comparable symmetry is imposed on the angular distributions of the deuteron analyzing-power components, and, indeed, no suggestion of symmetry is seen in the data at deuteron energies up to 11.5 MeV.[2] However, recent measurements of the vector analyzing power in the $^2H(\vec{d},p)^3H$ readtion at 30 MeV have disclosed the surprisng result that, there, the symmetry

$$A_y(\theta) = -A_y(\pi-\theta) \qquad (1)$$

is approximately fulfilled.[4] Also, it has been shown that the condition (1) holds exactly if the reaction should proceed entirely by way of the direct nucleon-transfer process.[5] Thus, in this particular case deviations from the symmetry (1) constitute clear qualitative evidence that the reaction proceeds (also) via the intermediate (compound) ^4He. Thus, at the lower energies analyses of the data in terms of states in ^4He are certainly appropriate.

We report here on measurments of $A_y(\theta)$ in the $^2H(\vec{d},p)^3H$ reaction at 15,20, and 25 MeV which were made in order to examine the transition from the complete lack of symmetry at 11.5 MeV toward that of (1) at 30 MeV. Our results, which are displayed in Fig. 1, show that the transition is a gradual one. Thus, the change from the compound-nucleus reaction mechanism to the predominantly direct nucleon-transfer reaction mode is correspondingly gradual, and at 30 MeV and above analysis in terms of the direct-reaction process is clearly appropriate.

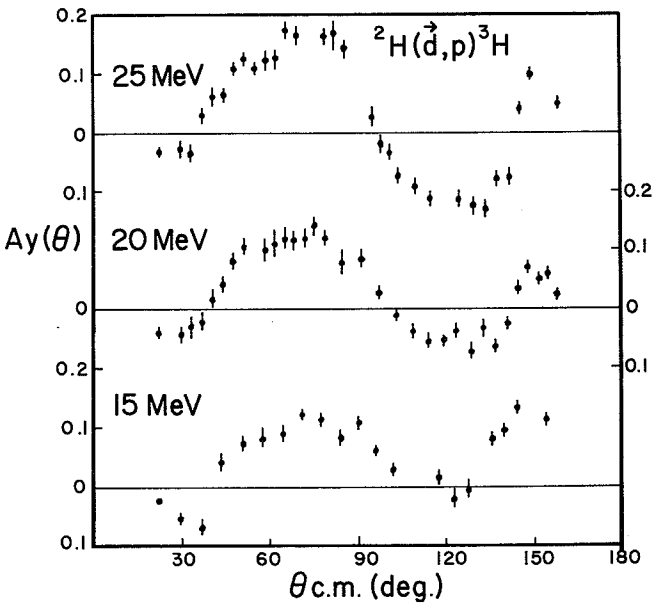

Fig. 1. Vector analyzing power, $A_y(= 2/\sqrt{3}\ iT_{11})$, in the $^2H(\vec{d},p)^3H$ reaction between 15 and 25 MeV. (XBL 756-1551)

Footnotes and References

*Proc. Fourth Int'l. Symposium on Polarization Phenomena in Nuclear Reactions (Birkhäuser Verlag, Basel, 1976).

†Present address: Nuclear Science Lab., M.I.T., Cambridge, Mass.

‡Present address: Physics Dept., Laval University, Quebec, Canada.

§Present address: Physics Dept., University of Basel, Switzerland.

1. R. A. Hardepopf, R. L. Walter, and T. B. Clegg, Phys. Rev. Lett. 28 (1972) 760 and references therein.

2. W. Grüebler et al., Nucl. Phys. A193 (1972) 129.

3. Reference 41 (unpublished) of Ref. 2.

4. H. E. Conzett, J. S. C. McKee, R. M. Larimer, and Ch. Leemann, Fourth Polarization Symp.

5. H. E. Conzett, J. S. C. McKee, R. M. Larimer, and Ch. Leemann, to be published.

CROSS-SECTIONS AND VECTOR ANALYZING POWERS IN THE $^3He(\vec{d},d)^3He$ AND $^3He(\vec{d},p)^4He$ REACTIONS BETWEEN 15 AND ^{40}MeV*

R. Roy,† F. Seiler,‡ H. E. Conzett,
F. N. Rad,§ and R. M. Larimer

Differential cross-sections and angular distributions of the vector analyzing power iT_{11} were obtained for the $^3He(\vec{d},d)^3He$ and $^3He(\vec{d},p)^4He$ reactions at intervals of 5 MeV between 15 and 40 MeV. At each energy data were taken at 25-35 angles. Figure 1 shows the $^3He(\vec{d},p)^4He$ results. The statistical errors are shown wherever they are larger than the symbols. The scale of the cross-sections is subject to a systematic error, estimated to be less than 6%. The data at 15 MeV join smoothly to measurements of lower energies.[1] Fits were made to these data in terms of Legendre polynominals,[2]

$$\frac{d\sigma}{d\Omega} = \frac{\sigma_{TOT}}{4\pi} \lambda^2 \sum_L d_{00}(L)\ P_L\ (\cos\theta)$$

$$\left(iT_{11}\right)\times\left(\frac{d\sigma}{d\Omega}\right) = \frac{\sigma_{TOT}}{4\pi} \lambda^2 \sum_L d_{11}(1)\ P_{L,1}(\cos\theta).$$

Plots of the energy dependence of the coefficients $d_{00}(L)$ and $d_{11}(L)$ are shown in Fig. 2.

The coefficients of the cross-section for unpolarized particles $d_{00}(L)$ for even degree L show some evidence of a broad structure near 20 and 40 MeV, while the odd-degree coefficients repeat only the 20 MeV structure. This coincides with a shift away from a predominance of the coefficients $d_{11}(2)$ to $d_{11}(1)$. The latter indicates large interference terms between reaction matrix elements of opposite parity. This is also visible in the angular distributions of iT_{11}, which shift from antisymmetry with respect to 90°, to a more symmetric distribution. This observation adds support to the result of two recent analyses[2,3] which postulate mostly interference between d-wave levels below 11.5 MeV and a strong $d_{7/2^+}$ - $f_{7/2^-}$ interference at higher energies.

The Legendre coefficients from an analysis of the $^3He(\vec{d},d)^3He$ elastic scattering data lend support to these tentative conclusions because similar variations are found near 20 and 40 MeV.

In view of the quite smooth energy dependence of these data, we are making optical model analyses of the elastic scattering results and DWBA analyses of the $(\vec{d},p)$ data.

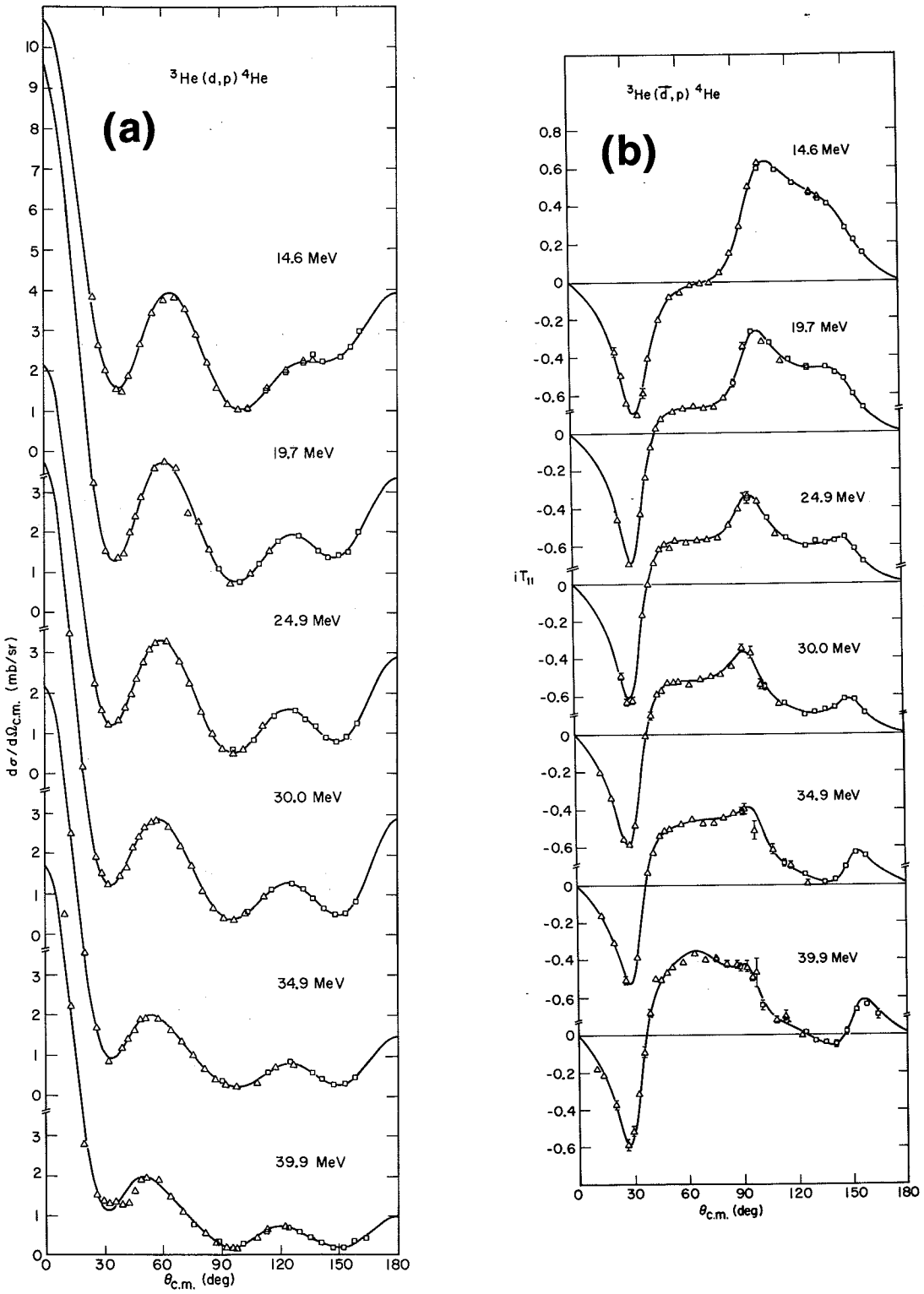

Fig. 1. Angular distributions of (a) the cross sections and (b) the vector analyzing power iT_{11} for the $^3He(\vec{d},p)^4He$ reaction between 15 and 40 MeV. The solid curves are Legendre polynomial fits to the data. (1a: XBL 7512-9207) (1b: XBL 7512-9209)

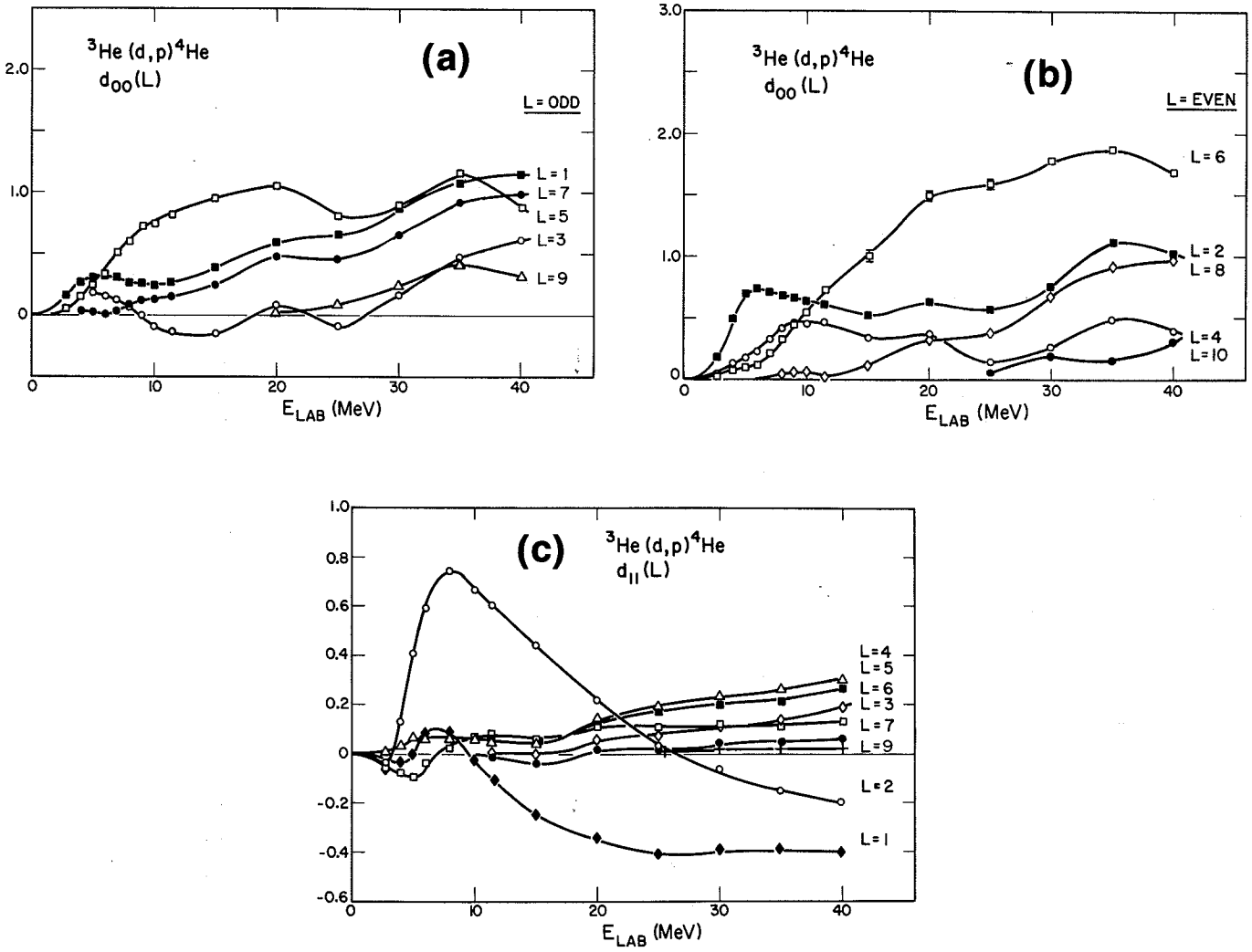

Fig. 2. The coefficients $d_{00}(L)$ and $d_{11}(L)$ of the Legendre polynomial expansion fits of Fig. 1. (2a: XBL 756-3193) (2b: XBL 756-3189) (2c: XBL 756-3194)

Footnotes and References

*Proc. Fourth Int'l. Symposium on Polarization Phenomena in Nuclear Reactions (Birkhäuser Verlag, Basel, 1976).

†Present address: Physics Dept., Laval University, Quebec, Canada.

‡Present address: Physics Dept., University of Basel, Switzerland.

§Present address: Nuclear Science Lab., M.I.T., Cambridge, Mass.

1. W. Grüebler, V. König, A. Ruh, P. A. Schmelzbach, R. E. White, and P. Marmier, Nucl. Phys. A176 (1971) 631.

2. F. Seiler, Nucl. Phys. A244 (1975) 236.

3. D. D. Dodder and G. M. Hale, Fourth Polarization Symp.

MAXIMUM TENSOR ANALYZING POWER $A_{yy} = 1$ IN THE $^3He(\vec{d},p)^4He$ REACTION*

F. Seiler†

Maximum possible values of the analyzing power have been found in the elastic scattering of both spin-1/2 and spin-1 particles from spin-0 nuclei, and have rapidly become the basis for the calibration of particle polarizations. Plattner and Bacher[1] showed analytically that values $A_y = \pm 1$ must occur at several energies in nucleon-^4He and ^3He-^4He elastic scattering. In the elastic scattering of deuterons from ^4He, a similar procedure was used by Grüebler et al., to identify three points $(E_0; \theta)$ below 12 MeV where the tensor analyzing power A_{yy} is unity.[2] It has thus been demonstrated that extreme values of polarization efficiencies do occur in elastic scattering with the spin configurations $1/2 + 0 \rightarrow 1/2 + 0$ and $1 + 0 \rightarrow 1 + 0$. It is the purpose of this letter to furnish considerable evidence for the first $A_{yy} = 1$ point observed in a nuclear reaction (as opposed to elastic scattering) and to point out that such points are quite generally of importance in the analysis of the process.

An inspection of the $^3He(\vec{d},p)^4He$ data obtained by Grüebler et al.[3] between 2.8 and 11.5 MeV shows sizeable values for the spherical tensor moments $T_{kq}(\theta)$ but none approach the physical limits closely. The Cartesian efficiency

$$A_{yy}(\theta) = -\frac{1}{2}\sqrt{2}\{T_{20}(\theta)+\sqrt{6}\,T_{22}(\theta)\}, \qquad (1)$$

as computed from the data of Grüebler et al., shows large positive values near 10 MeV for both forward and backward angles (Fig. 1). Thus the data available show only that the largest values of $A_{yy}(E,0)$ should be found near $E_d = 9$ MeV and $\theta_{CM} = 27°$ and should lie very close to unity.

For the spin space $1/2 + 1 \rightarrow 1/2 + 0$ of the $^3He(d,p)^4He$ reaction, the conditions for $A_{yy} = 1$ are

$$M_{1,1/2;1/2} = -M_{-1,1/2;1/2},$$
$$M_{1,-1/2;1/2} = -M_{-1,-1/2;1/2}, \qquad (2)$$

where the indices denote the spin projections of the deuteron, ^3He and proton respectively. It should be noted that the proof, usually given for the existence of an extreme value of the analyzing power, does not hold here. While only one complex amplitude must be zero for the elastic scattering processes discussed up to now,[1,2] Eqs. (2) require that two amplitudes must vanish simultaneously. Thus all that can possibly be shown is that A_{yy} is equal to unity within certain limits. For practical purposes, however, it should be quite sufficient if a close approximation to the extreme value can be demonstrated.

Finally, it should be emphasized that the conditions imposed on the transition matrix at an extreme point of the analyzing power are linear in the amplitudes. This holds independent of the spin space of the process and the rank of the polarization observable. These linear constraints are similar to those obtained by the requirement of parity conservation or time reversal invariance, except that they only hold for a particular energy and angle. Of course, any value of the analyzing power imposes constraints on the reaction amplitudes, but these are usually highly nonlinear. At an extreme point (E_0,θ_0), however, simple linear condition result. These can be very useful in an analysis of the process, since they are additional to the usual set of the bilinear equations. By analyzing data taken at and near such a point, these constraints can be imposed directly on the analysis, considerably restricting the solution space. Even in the simple cases, where the existence of the extreme can be proven directly,[1,2] this may be of some importance since the quality of the analysis needed for that kind of proof is not very high. In view of the difficulties encountered quite generally in the analysis of nuclear processes between particles with spin, this use of extreme points of the analyzing power may well be more important than the more obvious application as absolute calibration points for particle polarizations.

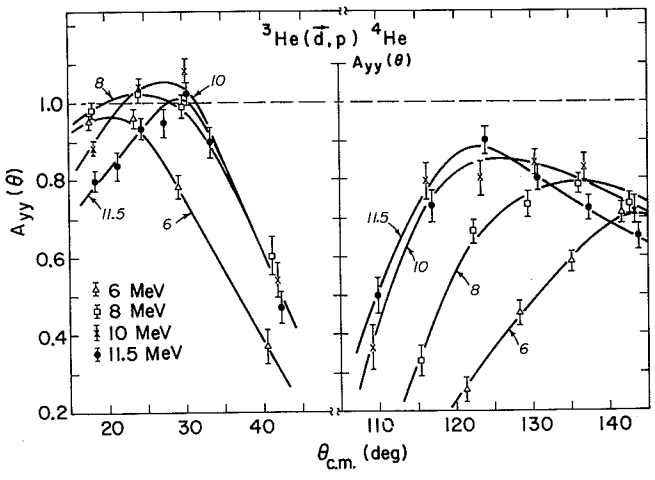

Fig. 1. Tensor analyzing power A_{yy} for the $^3He(\vec{d},p)^4He$ reaction between 6 and 11.5 MeV, calculated from the data of Reference 3. (XBL 753-2495)

Footnotes and References

*Condensed from Phys. Lett. 61B, 144 (1976).

†Present address: Physics Dept., University of Basel, Switzerland.

1. G. R. Plattner and A. D. Bacher, Phys. Lett. 36B (1971) 211.

2. W. Grüebler et al., Nucl. Phys. A242 (1975) 285.

3. W. Grüebler, V. König, and P. A. Schmelzbach, Results of measurements and analyses of nuclear reactions induced by polarized and unpolarized deuterons, Eidg. Techn. Hochschule Zürich, internal report, May 1973.

POINTS OF MAXIMUM ANALYZING POWER IN THE $^3He(\vec{d},p)^4He$ REACTION*

F. Seiler,† R. Roy,‡ H. E. Conzett, and F. N. Rad§

The $^3He(\vec{d},p)^4He$ reaction has been the first process, other than elastic scattering, in which a point (E_0,θ_0) of maximum possible tensor analyzing power $A_{yy}=1$ has been proposed.[1] An inspection of the complete deuteron polarization data of Grüebler et al.,[2] at 11.5 MeV and of the i T_{11} measurements of Roy et al.,[3] at 15 MeV indicates the possibility of large positive values of both A_y and A_{yy} near $\theta_{cm}=120°$ and thus of a point $A_y=A_{yy}=1$ between these energies. The necessary but not sufficient conditions $A_{xx}=A_{zz}=-1/2$ and $A_{xz}=0$ are nearly fulfilled at 11.5 MeV.[1,4] Unfortunately these tensor observables are not available at higher energies. For the investigation and possible identification of such a point, the relevant conditions on the M-matrix have to be verified. Using the representation[5,6,7]

$$M=\frac{1}{\sqrt{2}}\begin{pmatrix} -iA-D & \sqrt{2}F & -iA+D & -B-C & \sqrt{2}E & -B+C \\ B-C & \sqrt{2}E & B+C & -iA+D & \sqrt{2}F & -iA-D \end{pmatrix}$$

they are $A=B=0$ for an extreme value $A_{yy}=1$; for $A_y=\pm 1$ they are $A=B=0$, $C=\mp iF$. Imposing these conditions on the formulae for the observables[6,7] gives the following

$$A_y = \pm 1 \tag{1}$$

$$A_{yy} = K^{y'}_{o,y} = 1, \tag{2}$$

$$A_{xx} = A_{zz} = -1/2 \tag{3}$$

$$A_{xz} = K^{y'}_{xz} = C_{xz,y} = 0 \tag{4}$$

$$K^{x'}_x = K^{x'}_z = K^{x'}_{xy} = K^{x'}_{yz} = 0 \tag{5}$$

$$K^{z'}_x = K^{z'}_z = K^{z'}_{xy} = K^{z'}_{yz} = 0 \tag{6}$$

$$C_{x,x} = C_{z,x} = C_{xy,x} = C_{y,zx} = 0, \tag{7}$$

$$C_{x'z} = C_{z,z} = C_{xy,z} = C_{yz,z} = 0, \tag{8}$$

$$p^{y'} = A_{o,y} = K^{y'}_{yy} = -C_{yy,y} = t, \tag{9}$$

$$K^{y'}_y = -C_{y,y} = \pm t, \tag{10}$$

$$C_{xx,y} = -K^{y'}_{xx} = C_{zz,y} = -K^{y'}_{zz} = 1/2\ t, \tag{11}$$

$$K^{x'}_{o,x} = -K^{z'}_{o,z} = u, \tag{12}$$

$$K^{x'}_{o,z} = K^{z'}_{o,x} = v. \tag{13}$$

Here σ_o, A, P, K, and C denote the unpolarized cross-section, analyzing power, particle polarizations, polarization transfer coefficients and efficiency correlation coefficients, respectively. The first subscripted index stands for the beam, the second for the target polarization. Thus 24 polarization observables involving two or less particle polarizations are numerically determined, while the other 14 are given by the three parameters t, u, and v. With the cross-section for unpolarized particles there are thus four parameters that can be determined experimentally. By a careful selection of the experiments, through an inspection of the general formulae,[5,6] a verification of an extreme point of the components A_y and A_{yy} should be feasible. The establishment of such a point would be very important in an analysis of the process, due to the restrictions imposed on some elements of the M-matrix.

Footnotes and References

*Proc. Fourth Int'l. Symposium on Polarization Phenomena in Nuclear Reactions (Birkhäuser Verlag, Basel, 1976).

†Present address: Physics Dept., University of Basel, Switzerland.

‡Present address: Physics Dept., Laval University, Quebec, Canada.

§Present address: Nuclear Science Lab., M.I.T., Cambridge, Mass.

1. F. Seiler, Phys. Lett. 61B, 144 (1976).

2. W. Grüebler, V. König, A. Ruh, P. A. Schmelzbach, R. E. White, and P. Marmier, Nucl. Phys. A176 (1971) 631.

3. R. Roy, F. Seiler, H. E. Conzett, F. N. Rad, and R. M. Larimer, Fourth Polarization Symp.

4. F. Seiler, F. N. Rad, and H. E. Conzett, LBL-report, LBL-3496.

5. P. L. Csonka, M. J. Moravcsik, and M.D. Scadron, Phys. Rev. 143 (1966) 775.

6. G. G. Ohlsen, Rep. Prog. Phys. 35 (1972) 717.

7. J. L. Gammel, P. W. Keaton, and G. G. Ohlsen, Los Alamos Scientific Laboratory, Report No. LA-4492-MS, July 1970.

VECTOR ANALYZING POWER IN $\vec{d}$ - ^{4}He ELASTIC SCATTERING BETWEEN 15 AND 45 MeV*

H. E. Conzett, W. Dahme,† Ch. Leemann,
J. A. Macdonald,‡ and J. P. Meulders§

Phase shift analyses of d - ^{4}He elastic scattering data below 17 MeV have led progressively to improved agreement with the data and to the determination of level parameters for those states of ^{6}Li that appear as resonances in the d + ^{4}He channel.[1,2] These data have shown substantial values of the vector and tensor analyzing powers, so we selected ^{4}He as a potentially good analyzer for the higher energy polarized deuteron beams. Also, two independent determinations[2,3,4] of the absolute vector analyzing power $A_y(E_d,\theta_{cm})$ have been made which are in very good agreement. In the scattering of a purely vector-polarized deuteron beam the measured left-right asymmetry is given by

$$\varepsilon(\theta) = (3/2)\, p_y\, A_y(\theta), \qquad (1)$$

where p_y is the beam polarization. Asymmetry data were taken at 5 MeV intervals from 15 to 45 MeV at center-of-mass angles from 30° to 165°. At all angles the elastically scattered deuterons were detected with ΔE-E counter telescopes placed at equal angles to the left and right of the beam axis. Particle identification served to separate deuterons from protons which came from the deuteron breakup reaction. A gas target of ^{4}He at ≈ 1 atm pressure was used with beams typically of 50 nA. A polarimeter, consisting similarly of a gas target and a left-right pair of counter telescopes, was placed downstream of the main scattering chamber, and it provided continuous monitoring of the beam polarization during the course of the experiment.

Absolute normalization of our data to the calibration point A_y(11.5 MeV, 118°) = -0.410±0.010 (Refs. 2,3) was achieved in the following manner. The beam of energy E_1 (e.g., 15 or 20 MeV) incident at the first target was degraded in aluminum to an energy E_2 = 11.5 at the polarimeter where the asymmetry ε_2(11.5, 118°) was measured. At the same time, $\varepsilon_1(E_1,\theta)$ was measured in the main scattering chamber, so from (2)

$$A_y(E_1,\theta) = A_y(11.5,\ 118°)\ \varepsilon_1/\varepsilon_2, \qquad (2)$$

which gives $A_y(E_1,\theta)$ in terms of the measured asymmetries and the A_y calibration value. At higher energies for E_1 a previously determined value for $A_y(E_2,\theta_2)$ served as a reference polarimeter analyzing power. We also used the complete angular distribution of Ref. 5 at 15 MeV for an independent absolute normalization of our 15 MeV data. We found this to correspond to a value of A_y(11.5 MeV, 118°) = -0.415±010, in very good agreement with the other calibration value.

Our 20-45 MeV results are shown in Fig. 1, and our 15-MeV data are in excellent agreement with those of Ref. 5. It is seen that $\vec{d}$ - ^{4}He elastic scattering serves as a very good vector-polarization

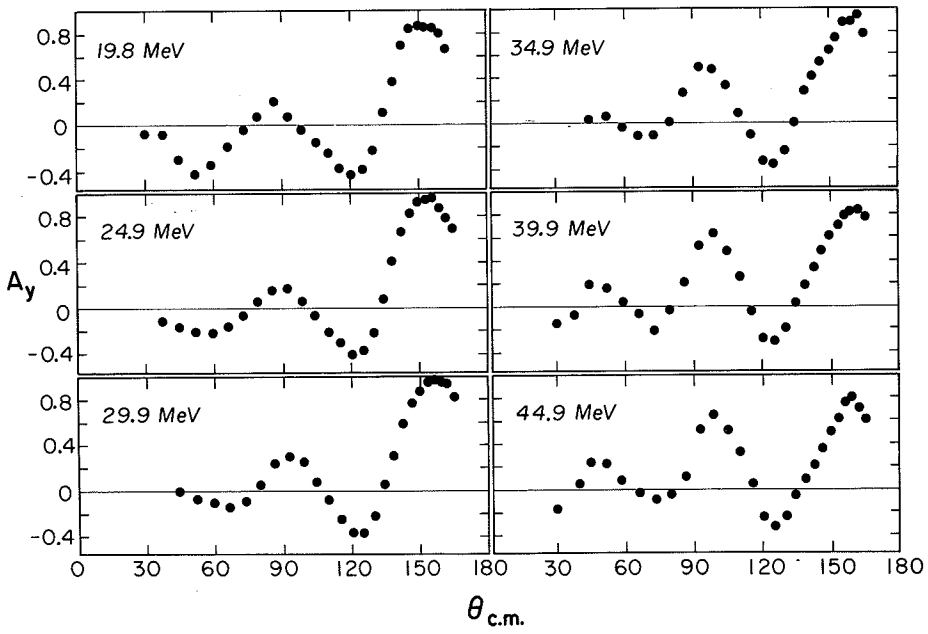

Fig. 1. Vector analyzing powers, $A_y(\theta)$, in $\vec{d}$ - ^{4}He elastic scattering between 20 and 45 MeV. (XBL 756-3155)

analyzer over a wide range of deuteron energies.

Of particular interest is the fact that A_y (155°) reaches values near 1.0 at 24.9 and 29.9 MeV. It has been shown recently that at an energy and angle for which $A_y(E,\theta) = \pm 1.0$ in $\vec{d}$ - ^{4}He scattering, all the analyzing-power components are fixed and determined.[6] This result has been extended to apply to all two-body reactions with incident polarized deuterons, and it is independent of the spins of the target and reaction products.[7] In view of our results, a point near $\theta_{cm} = 155°$ between 25 and 30 MeV in $\vec{d}$ - ^{4}He scattering is the best candidate for reaching the extreme value $A_y = 1$ (Ref. 8). The possibility of an $A_y = -1$ value at $\theta_{cm} = 55°$ at 11.88 MeV[6] is not supported by the $A_y(E,\theta)$ data in that region.[4]

Footnotes and References

*Proc. Fourth Int'l. Symposium on Polarization Phenomena in Nuclear Reactions (Birkhäuser Verlag, Basel, 1976).

†Sektion Physik der Universität München, 8046 Garching, Germany.

‡Chalk River Nuclear Laboratories, Chalk, River, Ontario, Canada

§Centre de Physique Nucleaire, Université de Louvain, Belgium.

1. P. A. Schmelzbach et al., Nucl. Phys. A184 (1972) 193, and Refs. therein.

2. W. Grüebler et al., Nucl. Phys. A242 (1975) 265.

3. W. Grüebler et al., Nucl. Phys. A134 (1969) 686; V. Konig et al., Nucl. Phys. A166 (1971) 393.

4. G. G. Ohlsen et al., Phys. Rev. C8 (1973) 1262.

5. R. A. Hardekopf et al., Los Alamos Report LA-5051 (1972).

6. W. Grüebler et al., Nucl. Phys. A242 (1975) 285.

7. F. Seiler, F. N. Rad and H. E. Conzett, Fourth Polarization Symp.

8. H. E. Conzett, F. Seiler, F, N. Rad, R. Roy, and R. M. Larimer, Fourth Polarization Symp.

TENSOR ANALYZING POWER Ayy IN $\vec{d}$ - ^{4}He ELASTIC SCATTERING FROM 20 TO 45 MeV

E. J. Stephenson, H. E. Conzett, R. M. Larimer,
B. T. Leeman, and R. Roy*

Even though tensor-polarized deuteron beams at energies above 20 MeV have been available for some time, there are no measurements of tensor analyzing powers in this energy region suitable for use as a secondary polarization standard. This paper reports measurements of angular distributions of the tensor analyzing power A_{yy} in d - ^{4}H elastic scattering from 20 to 45 MeV deuteron bombarding energy. The target, ^{4}He, was chosen because it is a simple system with analyzing powers that vary slowly with energy and angle, and because ^{4}He has proved in the past to have large analyzing powers for a variety of polarized projectiles.

The analyzing powers discussed in this paper are defined in accordance with the Madison Convention.[1] The tensor-polarized deuteron beam was produced by an atomic beam polarized-ion source that injected the beam axially into the 88-inch cyclotron. The tensor analyzing power was determined by comparing the count rates measured with the polarizing intermediate-field r.f. transition alternately on and off. Because of a vector-polarized component in the beam, it was necessary to observe the count rate simultaneously on either side of the beam to cancel the effect of the vector analyzing power. From these four count rates, Y, the tensor analyzing power is given by

$$A_{yy} = \frac{1}{p_{yy}} \left\{ \frac{Y_{LP}}{Y_{LU}} + \frac{Y_{RP}}{Y_{RU}} - 2 \right\}$$

where L and R denote the two sides of the beam, P and U denote polarized and unpolarized, and p_{yy} is the tensor beam polarization.

In the experiment, the beam passed first through the main scattering chamber where the angular distributions were measured and then through a smaller chamber used as a polarimeter. Each chamber contained a ^{4}He gas target. During the experiment the beam energy was raised from 20 to 45 MeV in 5 MeV steps. At each new energy, the polarimeter detectors were set at the angle and energy of an analyzing power point measured previously at a lower energy. The beam energy was reduced after the main scattering chamber by placing an aluminum absorber in the beam. Polarimeter calibration points were chosen at 17, 25, and 35 MeV and at laboratory angles between 80° and 90°.

The initial value of the tensor analyzing power A_{yy} at 17 MeV was taken from Ohlsen's measurements,[2] which are accurate to within 0.02. (The

accumulation of statistical errors in our method increases this uncertainty to 0.03 at 35 MeV.) Figure 1 shows angular distributions of A_y, A_{yy}, and A_{xx} measured at 17 MeV from this experiment and the earlier measurements of Ohlsen. Using the angular distribution of A_{yy} as a calibration standard, good agreement was obtained with the magnitude of all the analyzing powers. The origin of the discrepancy in A_{xx} at forward angles is not understood. A comparison with the tensor calibration point[3] at E_d = 11.9 MeV where A_{yy} = 1 was accurate to within 5%.

The measured angular distributions from 20 to 45 MeV (see Fig. 2) show large values of A_{yy} at all energies. The last negative and positive excursions

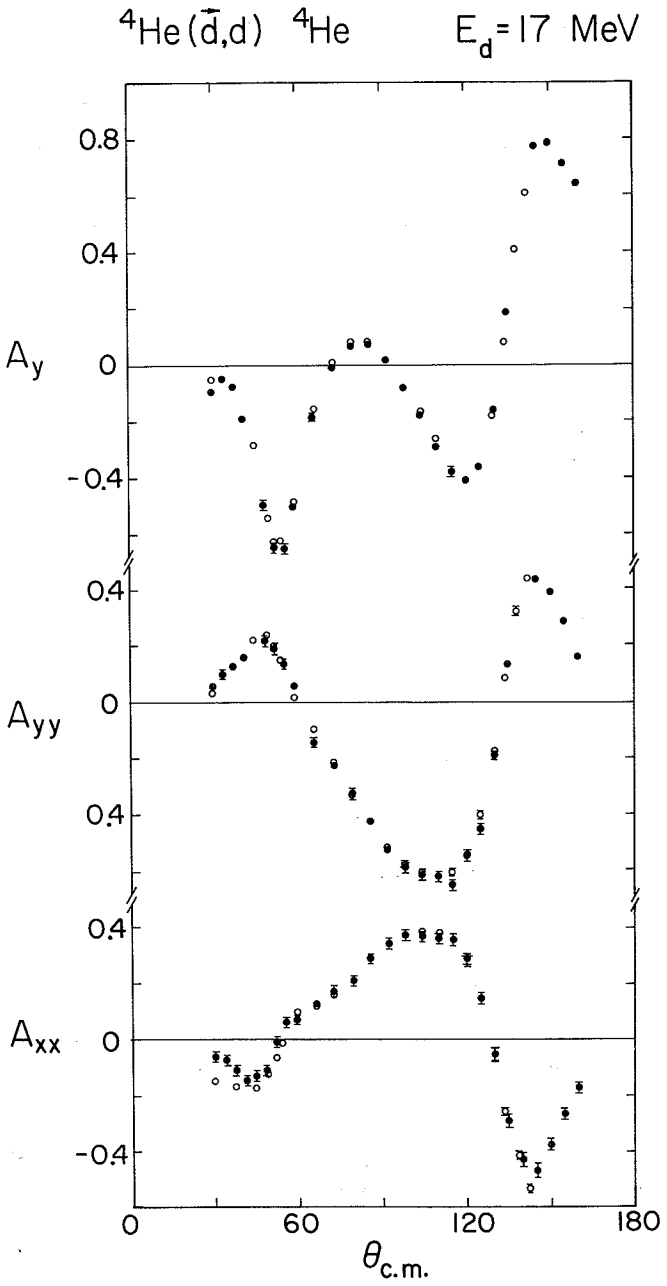

Fig. 1. Measurements of three analyzing powers in d - ^{4}He elastic scattering at E_d = 17 MeV. The solid circles are measurements from this experiment and the open circles are from Ref. 2. (XBL 764-2662)

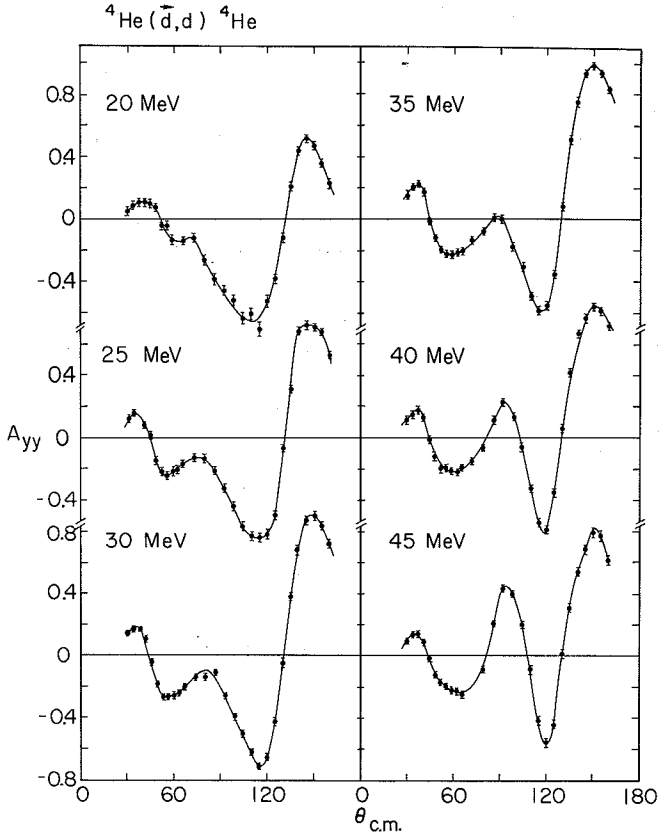

Fig. 2. Measurements of A_{yy} in d - ^{4}He elastic scattering. The deuteron bombarding energy is noted. The curves are a guide to the eye. (XBL 764-2664)

in each angular distribution are good candidates for use in a polarimeter. The analyzing power varies slowly in energy and angle, making the geometric corrections small.

The efficiency of a polarimeter, given approximately by $A_{yy}^2\sigma$, is shown in Fig. 3 for the last two excursions as a function of energy. A polarimeter observing particles at the angle of the positive peak is more efficient over most of the energy range, even though the cross section there is smaller by a factor of about 3. If instead one observes the recoil α-particles from this positive peak, the efficiency increases for the same detection geometry by a factor between 5 and 10. However, in this case the energy resolution must be good in order to cleanly separate α-particles which originate from elastic scattering and the deuteron breakup reaction.

From this experiment it is clear that the observation of deuterons elastically scattered from ^{4}He is suitable as a polarization standard in the energy region from 20 to 45 MeV. Measurements of angular distributions of the tensor analyzing power A_{xx} are planned. With these measurements and the measurements of the vector analyzing power A_y, enough data should be available to perform a phase-shift analysis of ^{4}He(d,d)^{4}He elastic scattering in this energy region. Such an analysis would indicate

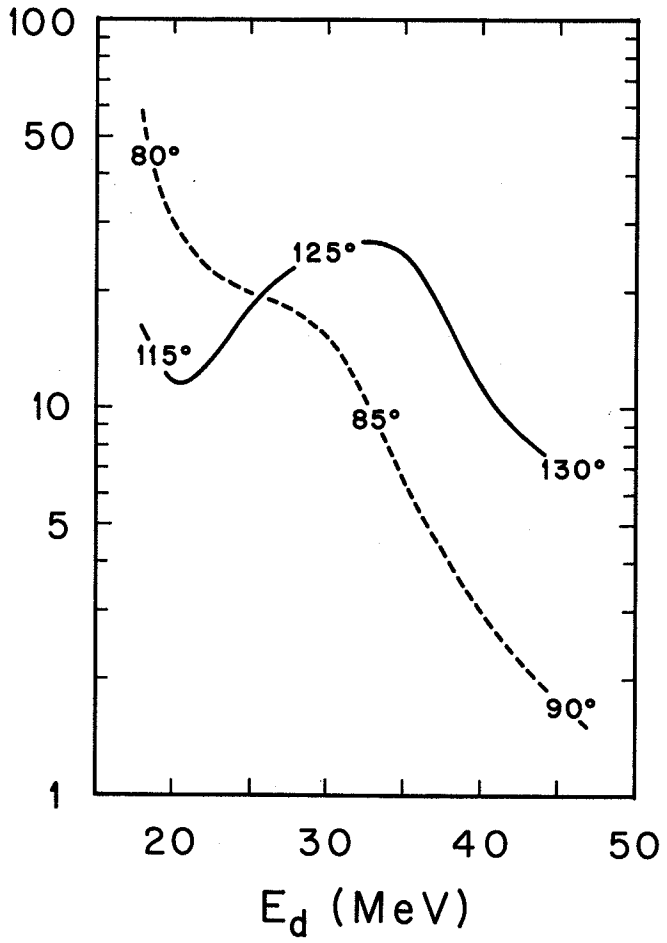

Fig. 3. Polarimeter efficiency, $A_{yy}^2\sigma$, for the center-of-mass scattering angles noted on each curve. These angles correspond to extreme values of A_{yy}. Measurements at different energies are connected by a smooth curve. The y-axis scale is arbitrary. (XBL 764-1385)

whether the tensor analyzing power A_{yy} reaches its maximal value of 1 in the vicinity of $E_d = 35$ MeV and $\theta_{c.m.} = 150°$. If it does, this point would become a primary standard for the measurement of the tensor beam polarization.

Footnote and References

*Present address: Physics Dept., Laval University, Quebec, Canada.

1. Polarization Phenomena in Nuclear Reactions, ed. by H. H. Barschall and W. Haeverli (Univ. of Wisconsin Press, Madison, 1971) p. xxv.

2. G. G. Ohlsen, P. A. Lovoi, G. C. Salzman, U. Meyer-Berkhout, C. K. Mitchell, and W. Grüebler, Phys. Rev. C8, 1262 (1973).

3. W. Grüebler, P. A. Schmelzbach, V. König, R. Risler, B. Jenney, and D. Boerma, Nucl. Phys. A242, 285 (1975).

EXTREME VALUES Ay = ± 1 OF THE ANALYZING POWER FOR SPIN-1 POLARIZATION*

F. Seiler,† F. N. Rad,‡ and H. E. Conzett

Maximum possible values of the analyzing power have been identified at several energies and angles in the elastic scattering of spin-1/2 and spin-1 particles from spin-0 nuclei,[1,2] and evidence for at least one extreme value of the tensor component $A_{yy} = 1$ has been found in the $^3He(d,p)^4He$ reaction.[3] The recent analysis by Grüebler et al.[2] of d-^{4}He elastic scattering data between 3 and 17 MeV has proved the existence of points at which the component A_{yy} of the spin-1 analyzing power reaches its maximum possible value of unity. Also, for points of maximum vector analyzing power, $A_y = \pm 1$, they examined the resulting conditions among elements of the transition matrix M which connects initial and final spin states, $\chi_f = M\chi_i$. At such a point three equations must be satisfied among the M-matrix amplitudes, with the consequence, then, that all the remaining analyzing powers are determined:

$$A_{yy} = +1, \quad A_{xx} = A_{zz} = -\frac{1}{2}, \quad A_{xz} = 0. \qquad (1)$$

In addition to its usefulness in an absolute calibration of deuteron vector polarization, the occurrence of such a unique and restrictive point would clearly be of great interest and value, since there the relative values of all the M-matrix elements are determind.

We show in this paper that the necessary, but not sufficient, conditions (1) for the existence of a point $A_y = \pm 1$ are valid for reactions with the general spin structure $1 + a \to b + c$, where a, b, and c are arbitrary spins. This follows from a property of the spin-1 density matrix, and examination of the $3(2a+1)$ by $(2b+1)(2c+1)$ M-matrix is not required.

Methods of specifying a "degree of polarization" for an ensemble of polarized spin-1 particles produced in a nuclear reaction have been given by Lakin,[5] Fano,[6] and Minnaert.[7] They are based on the fact that the density matrix of the ensemble is positive semidefinite. Its expansion in terms of an

irreducible set of tensor operators τ_{kq} imposes conditions on the tensor moments $t_{kq} = \langle \tau_{kq} \rangle$.[5,7] Identical limitations apply for the polarization efficiencies T_{kq} due to time reversal invariance. They are particularly simple in a transverse coordinate system S' with the z'=axis perpendicular to the reaction plane.

$$(T'_{20} + \sqrt{2})^2 \geq 3(T'_{10})^2 + 6|T'_{22}|^2. \qquad (2)$$

In the space $(T'_{10}, \sqrt{2}|T'_{22}|, T'_{20})$, Eq. (2) defines the interior of a cone (Fig. 1). Points on the surface or the base $(T'_{20} = \frac{1}{2}\sqrt{2})$ of the Lakin cone correspond to restricted combinations of the maximum possible values of the T'_{kq}. In terms of the observables T_{kq} or A_{ij} defined by the Madison convention,[8] the T'_{kq} are:

$$\begin{aligned} T'_{10} &= \sqrt{2}\, i\, T_{11} = \tfrac{1}{2}\sqrt{6}\, A_y, \\ T'_{20} &= -\tfrac{1}{2}(T_{20} + \sqrt{6}\, T_{22}) = \tfrac{1}{2}\sqrt{2}\, A_{yy}, \\ T'_{22} &= \tfrac{1}{4}(\sqrt{6}\, T_{20} - 2\, T_{22}) - i\, T_{21} \\ &= \tfrac{1}{6}\sqrt{3}\,[(A_{zz} - A_{xx}) + i2A_{xz}]. \end{aligned} \qquad (3)$$

Thus points with $A_{yy} = 1$ lie on the base of the Lakin cone. Only there, values of $A_y = \pm 1$ can be attained (Fig. 1), points A and B), and then only if $|T'_{22}| = 0$. This results in the conditions of Eqs. (1). As noted, this was shown for d-^{4}He elastic scattering by direct calculation with the appropriate 3 by 3 M-matrix.[2] From the derivation given here, it is clear that Eqs. (1) are valid in general and are independent of the spin space of the process. For all reactions involving polarized spin-1 particles they therefore provide a clear signature of points where $A_y = \pm 1$ is possible.

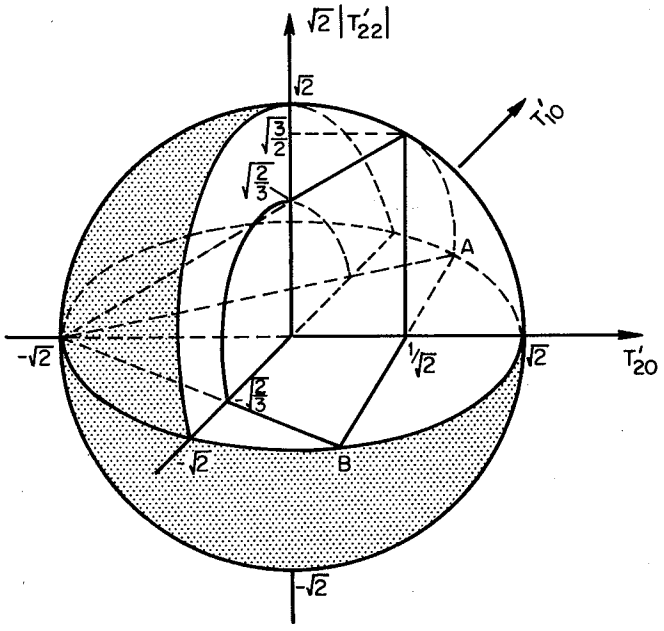

Fig. 1. Cutaway drawing of the cone defined by Eq. (2). The points A and B correspond to the extreme values $A_y = \pm 1$. (XBL 754-2652)

It should be noted that the agreement of the experimental data with Eqs. (1) are necessary but not sufficient conditions for the existence of an extreme value of the efficiency A_y. Any point along the line AB in Fig. 1 satisfies Eqs. (1). Using a beam with calibrated tensor polarization,[2] it is possible to determine that a point on the line AB is reached. However, the calibration of spin-1 vector polarizations is still so uncertain that it cannot be shown experimentally that point A or B is indeed attained. Although such a unique and restrictive point is a priori quite unlikely, an experimental value of $A_y \geq 0.98$ has been measured in d-^{4}He elastic scattering at $E_d = 26.8$ MeV near $\theta_L = 135°$ (Ref. 4). Hence, these criteria are of practical interest.

^{6}Li(d,α)^{4}He. Measurements by Grüebler et al.[10] show values of A_{yy} compatible with unity near 6 MeV and $\theta_{cm} = 30°$ and near 8 MeV and $\theta_{cm} = 90°$ (Fig. 2). Near 8 MeV only A_{yy} can reach unity, since the particle symmetry in the exit channel requires that $A_y(90°) = 0$. Near 6 MeV there are drastic changes in the angular distributions of all efficiencies, which makes a comparison with Eqs. (1) difficult. The component A_y near 30° varies rapidly from negative values at 4 MeV to large positive values at 6 MeV, decreasing again above 7 MeV.[10] It is thus possible that the value $A_y = 1$ is attained. The component A_{xz} changes sign at forward angles between 6 and 7 MeV, while the values of A_{xx} and A_{zz} are close to - 1/2. In this region the conditions necessary for $A_y = 1$ may therefore be fulfilled.

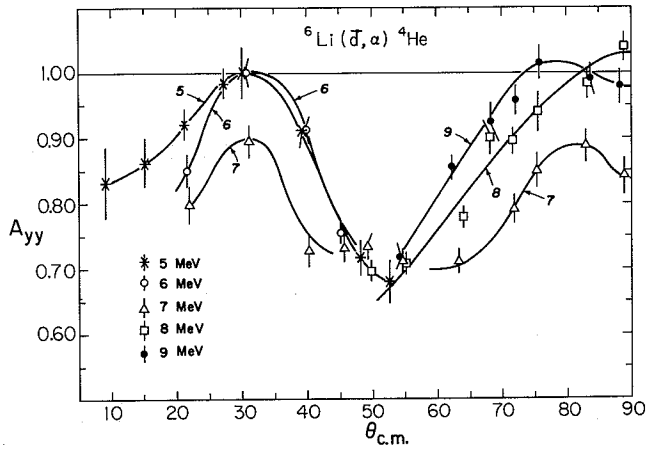

Fig. 2. Values of the efficiency A_{yy} in the ^{6}Li(d,α)^{4}He reaction at 5, 6, 7, 8, and 9 MeV, showing two points with $A_{yy} \simeq 1$. (XBL 753-2614)

^{3}He(d,p)^{4}He. One point with $A_{yy} = 1$ has been tentatively identified near 9 MeV and $\theta_{c.m.} = 27°$.[3] Since $A_{zz} \simeq -1$, $A_{xx} \simeq 0$ and $A_{xz} \simeq -1.1$,[10] it is clear that A_y cannot reach the value -1. The situation is different for the possible A_{yy} maximum above 11.5 MeV, where no measurements are available. At 11.5 MeV a value of $A_{yy} \simeq 0.9$ is found near $\theta_{cm} = 120°$ (see Fig. 1 of Ref. 3). The vector analyzing power A_y is large and positive both at 11.5 MeV and 15 MeV.[10,11] The values for A_{xx} and A_{xz} below 11.5

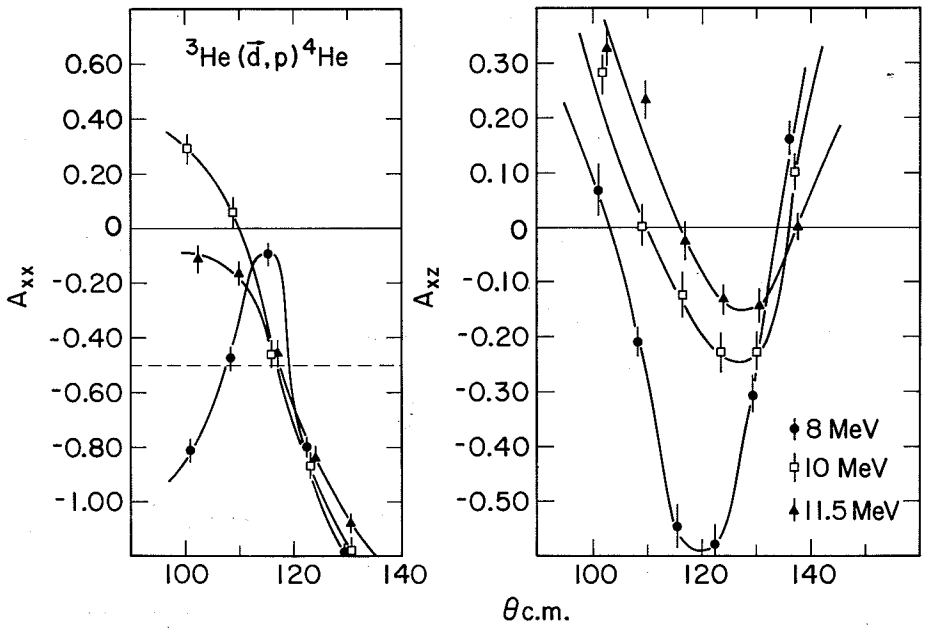

Fig. 3. Components A_{xx} and A_{xz} of the analyzing power in the ^{3}He(d,p)^{4}He reaction below 11.5 MeV. (XBL 754-2663)

MeV are plotted in Fig. 3. Clearly A_{xx} and, due to the condition $A_{xx} + A_{yy} + A_{zz} = 0$, also A_{zz} lie near - 1/2 at 120°, while $A_{xz} = 0$ obtains at angles moving toward 120° as the energy increases. Thus the necessary conditions for $A_y = 1$ may be met near this angle at some energy between 12 and 15 MeV.

Footnotes and References

*Condensed from LBL-3496, submitted to Phys. Rev. for publication.

†Present address: Physics Dept., University of Basel, Switzerland.

‡Present address: Nuclear Science Lab., M.I.T., Cambridge, Mass.

1. G. R. Plattner and A. D. Bacher, Phys. Lett. 36B, 211 (1971).

2. W. Grüebler, P. A. Schmelzbach, V. König, R. Risler, B. Jenny, and D. Boerma, Nucl. Phys. A242, 285 (1975).

3. F. Seiler, Phys. Letters 61B, 144 (1976).

4. H. E. Conzett, F. Seiler, F. N. Rad, R. Roy, and R. M. Larimer, Proc. Fourth Int'l. Symp. on Polarization Phenomena in Nuclear Reactions (Birkhäuser Verlag, Basel, 1976).

5. W. Lakin, Phys. Rev. 98, 139 (1955).

6. U. Fano, Rev. Mod. Phys. 29, 74 (1957).

7. P. Minnaert, Phys. Rev. Lett. 16, 672 (1966).

8. Polarization phenomena in nuclear reactions, H. H. Barschall and W. Haeberli eds. (University of Wisconsin press, 1971), p. xxv.

9. F. Seiler, R. Roy, H. E. Conzett, and F. N. Rad, to be published.

10. W. Grüebler, V. König, and P. A. Schmelzbach, Results of measurements and analyses of nuclear reactions induced by polarized and unpolarized deuterons, Eidgenössische Technische Hochschule Zürich, internal report, May 1973.

11. R. Roy, F. Seiler, H. E. Conzett, F. N. Rad, and R. M. Larimer, Proc. Fourth Int'l. Symp. on Polarization Phenomena in Nuclear Reactions (Birkhäuser Verlag, Basel, 1976).

MEASUREMENT OF THE VECTOR ANALYZING POWER NEAR THE VALUE $A_y = 1.0$ $\vec{d}$-^{4}He ELASTIC SCATTERING*

H. E. Conzett, F. Seiler,†F. N. Rad,‡
R. Roy,§and R. M. Larimer

Points in energy and angle (E,θ) at which a component of the analyzing power for spin-polarization reaches its theoretical maximum are of particular interest and importance. Experimentally, they provide valuable absolute calibrations. Theoretically, there exist at such points important conditions on, or relations among, the M-matrix amplitudes. As a consequence, other polarization observables are determined, and in reactions with particularly simple spin structure it is possible that all such observables are determined.

The simplest case is that with the spin structures $1/2 + 0 \rightarrow 1/2 + 0$, for which it has been shown that points for which $A_y(E,\theta) = \pm 1$ do exist in N-^{4}He and ^{3}He-^{4}He elastic scattering.[1] The resulting condition on the two M-matrix amplitudes f and g is that $g = \pm i f$, and the other polarization observable, the spin rotation angle, is determined. Similar investigations in d-^{4}He elastic scattering $(1+0 \rightarrow 1+0)$ have led to identification of points for which, the tensor analyzing-power component $A_{yy} = 1$ (Ref. 2). The corresponding linear relations among the M-matrix elements at points $A_{yy} = 1$ and $A_y = \pm 1$ have been given,[2,3] and it was shown[2]) that $A_{yy} = 1$ is a necessary condition for the existence of a point of $A_y = \pm 1$. This latter result has now been proved to be valid more generally, that is, it is valid for all reactions with the spin structure $1 + a \rightarrow b + c$, where a, b, and c are arbitrary spins.[4] Relations among, and determinations of, the other polarization observables have also been given for several reactions.[5]

Since a point of $A_y = \pm 1$ for spin 1 is so unique and restrictive, and *a priori* perhaps so unlikely, the location and identification of such a point would be of considerable value. The best candidate for such a point was suggested in the measurements of $A_y(\theta)$ in $\vec{d}$-^{4}He elastic scattering between 15 and 45 MeV.[6] There, values of $A_y(\theta_L = 135^\circ) \geq 0.97$ were found near 25 and 30 MeV. Therefore, we have examined this energy region to determine the maximum value of $A_y(E,\theta)$. The experimental details and the calibration procedures are described elsewhere.[6] We find that A_y reaches its maximum value near 28.6 MeV, and we show in Fig. 1 our preliminary results for A_y(28.6 MeV, θ_L). Although finite geometry corrections and polynomial fits to all our data in this energy and angular region must be made before the maximum value of A_y is determined, it is clear from Fig. 1 that A_y does indeed reach a value very close to unity near $\theta_L = 135^\circ$ at 28.6 MeV.

We have also measured $A_{yy}(E,\theta)$ over the same regions, using the ^{4}He$(\vec{d},d)^4$He A_{yy} data of Ref. 3 at 17 MeV for the determination of the tensor polarization of our beam. Again, our preliminary result is that A_{yy} reaches a maximum value approaching unity near 28.6 MeV and $\theta_L = 135^\circ$, as would be required to fulfill the necessary condition that $A_{yy} = 1$ at a point for which $A_y = 1$.

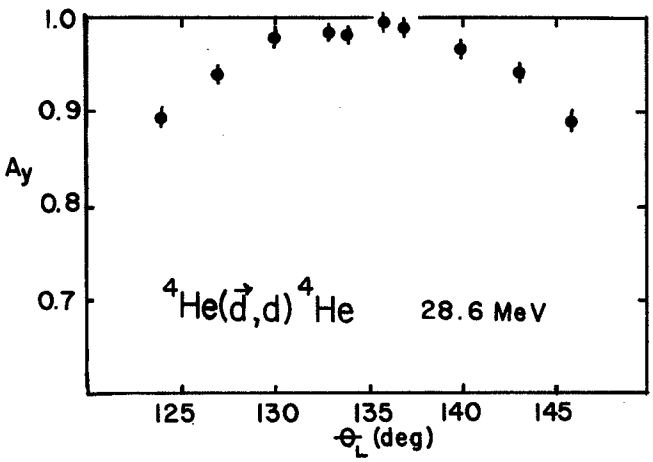

Fig. 1. The vector analyzing power, $A_y(\theta)$, in d-^{4}He elastic scattering at 28.6 MeV.
(XBL 756-1531)

Footnotes and References

*Proc. Fourth Int'l. Symposium on Polarization Phenomena in Nuclear Reactions (Birkhäuser Verlag, Basel, 1976).

†Present address: Physics Dept., University of Basel, Switzerland.

‡Present address: Nuclear Science Lab., M.I.T., Cambridge, Mass.

§Present address: Physics Dept., Laval University, Quebec, Canada.

1. G. R. Plattner and A. D. Bacher, Phys. Lett. 36B (1971) 211.

2. W. Grüebler et al., Nucl. Phys. A242 (1975) 285.

3. G. G. Ohlsen et al., Phys. Rev. C 8 (1973) 1262.

4. F. Seiler, F. N. Rad, and H. E. Conzett, Fourth Polarization Symp.

5. F. Seiler, Fourth Polarization Symp., F. Seiler, H. E. Conzett, F. N. Rad and R. Roy, ibid.; F. Seiler, H. E. Conzett, and F. N. Rad, ibid.; F. Seiler, F. N. Rad, H. E. Conzett and R. Roy, ibid.

6. H. E. Conzett et al., Fourth Polarization Symp.

EXTREME VALUES OF THE ANALYZING POWER IN THE $^6Li(d,\alpha)^4He$ REACTION*

F. Seiler,† F. N. Rad,‡ H. E. Conzett, and R. Roy §

Extreme values of the analyzing power have been identified in $\vec{p}$-^{4}He and $\vec{d}$-^{4}He elastic scattering.[1,2] Recently it has been proposed that similar points exist also in reactions.[3] A calculation of the cartesian tensor A_{yy} from the $^6Li(d,\alpha)^4He$ data of Grüebler et al.,[4] shows experimental values with $A_{yy} \simeq 1$ at two points (Fig. 1). Although more data are clearly needed, extreme values $A_{yy} = 1$ are possible. A definite identification requires the elements of the M-matrix to fulfill certain conditions. For $A_{yy} = 1$ the M-matrix[5]

$$M = -\frac{1}{2}\,(a\text{-}e, \sqrt{2}\,f,\ a+e;\ \sqrt{2}\,h,\ -2k,\ -\sqrt{2}\,h;\ a+e,\ \sqrt{2}\,f,\ a-e) \qquad (1)$$

must satisfy $a = 0$. If an analysis is not available, the influence of this condition on certain observables can be tested. Beside the efficiencies A^1_{ij} for deuteron polarization and A^2_{kl} for ^{6}Li polarization, only the efficiency correlation coefficients $C_{ij,kl}$ are available. The 25 linearly independent observables[5] yield

$$A^1_{yy} = A^2_{yy} = 1 \qquad (2)$$

$$C_{x,z} = C_{z,x} = C_{x,x} = C_{z,z} = 0 \qquad (3)$$

$$C_{xy,x} = C_{xy,z} = C_{yz,x} = C_{yz,z} = 0. \qquad (4)$$

Near 6 MeV all efficiencies undergo rapid changes and near 30° A_y is large and positive. The possibility $A_y = 1$ (Ref. 6) should therefore be investigated with closely spaced efficiency measurements. If $A_y = 1$ is found, the conditions

$$a = 0, \quad h = \pm ie, \quad k = \pm if \qquad (5)$$

should be tested. Experimentally this yields

$$A^1_y = \pm 1$$
$$A^1_{yy} = A^2_{yy} = 1$$
$$A^1_{xx} = A^1_{zz} = -1/2$$
$$A^1_{xz} = C_{xz,y} = C_{xz,xz} = C_{xz,zz} = 0$$
$$2C_{zz,y} = \pm C_{y,y}$$
$$2C_{zz,xz} = \pm C_{y,xz}$$
$$2C_{zz,zz} = \pm C_{y,zz},$$

in addition to Eqs. (3) and (4). Since efficiency correlation experiments are difficult, it is likely that a verification of the conditions will be done using the results of an analysis. The conditions above may help in the selection of the data base necessary, since measurements near a suspected extreme point are a powerful tool in an analysis.[3] It is also very likely that similarly large values of A_{yy} and A_y will be found for polarized ^{6}Li-beams, since these maxima seem correlated with certain excited states in the intermediate system.

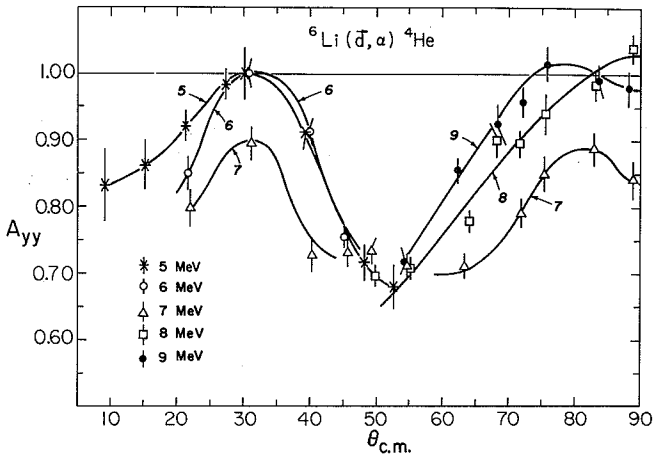

Fig. 1. Regions of $A_{yy} \simeq 1$ in the $^6Li(\vec{d},\alpha)^4He$ reaction (Ref. 4). (XBL 753-2614)

Footnotes and References

*Proc. Fourth Int'l. Symposium on Polarization Phenomena in Nuclear Reactions (Birkhäuser Verlag, Basel, 1976).

†Present address: Physics Dept., University of Basel, Switzerland.

‡Present address: Nuclear Science Lab., M.I.T., Cambridge, Mass.

§Present address: Physics Dept., Laval University, Quebec, Canada.

1. G. R. Plattner and A. D. Bacher, Phys. Lett. 36B (1971) 211.

2. W. Grüebler et al., Nucl. Phys. A242 (1975) 285.

3. F. Seiler, Phys. Lett. 61B (1976) 144.

4. W. Grüebler et al., Results of Measurements and Analyses, Eidgenössische Technische Hochschule, Zürich, May 1973.

5. W. E. Kohler and D. Fick, Z. für Phys. 215 (1968) 408.

6. F. Seiler, F. N. Rad and H. E. Conzett, LBL-report, LBL-3496, and to be published.

POINTS OF MAXIMUM POLARIZATION EFFICIENCY IN ^{4}He(d,d)^{4}He*

F. Seiler,† H. E. Conzett, F. N. Rad,‡ and R. Roy§

Several points (E_i,θ_i) of maximum possible analyzing power have recently been identified in d-^{4}He elastic scattering. From an analysis of data between 3 and 17 MeV, three points with $A_{yy}=1$ were found below 12 MeV and another with $A_y=-1$ may exist above that energy.[1] An experimental indication that extreme values of the analyzing power A_y may occur comes from measurements near $E_d=28$ MeV and $\theta_{c.m.}\simeq 154°$, where $A_y\simeq A_{yy}\simeq 1$.[2]

Reaching an extreme value of some component of the analyzing power imposes certain conditions on the elements of the transition matrix M. In the parametrization of Ohlsen et al.,[3]

$$M=\frac{1}{2}\begin{pmatrix} A-B & \sqrt{2}\,D & -A-B \\ -\sqrt{2}\,D & 2\,C & \sqrt{2}\,D \\ -A-B & -\sqrt{2}\,D & A-B \end{pmatrix},$$

an extreme value of $A_{yy}=1$ requires $B=0$. For an extreme value $A_y=\pm 1$, however, $A=C=\pm iD$ and $B=0$ is necessary. Thus $A_{yy}=1$ is a prerequisite for $A_y=\pm 1$,[1,4] and both components must peak at the same critical point (E_i,θ_i). A definite identification of points with extreme values of the analyzing power can be carried out by using a phase-shift analysis to compute the amplitudes A through D and to verify the validity of the relevant conditions.[1] In an alternate approach[5] these conditions are introduced into the formulae for the observables[3] and can then be checked experimentally. The requirement $B=0$ for $A_{yy}=1$ yields

$$A_{yy} = p^{y'y'} = K_{yy}^{y'y'} = 1 \qquad (1)$$

$$A_{xx} = p^{x'x'} = K_{yy}^{x'x'} = K_{xx}^{y'y'} \qquad (2)$$

$$A_{zz} = p^{z'z'} = K_{zz}^{y'y'} = K_{yy}^{z'z'} \qquad (3)$$

$$K_x^{x'} = K_z^{x'} = K_{xy}^{x'} = K_{yz}^{x'} = 0 \qquad (4)$$

$$K_x^{z'} = K_z^{z'} = K_{xy}^{z'} = K_{yz}^{z'} = 0 \qquad (5)$$

$$K_x^{x'y'} = K^{x'y'} = K_{xy}^{x'y'} = K_{yz}^{x'y'} = 0 \qquad (6)$$

$$K_x^{y'z'} = K_z^{y'z'} = K_{xy}^{y'z'} = K_{yz}^{y'z'} = 0. \qquad (7)$$

Equations (4) to (7) are particularly important, since a value of zero at (E_i,θ_i) does not depend on the calibration of any polarizations. For an extreme value $A=\pm 1$, the relative values of all M-matrix elements are determined and the common constant is given by the cross section σ_o at (E_i,θ_i). Thus all 51 polarization observables are numerically determined, and in addition to Eqs. (4) to (7) the following conditions hold

$$A_y = p^{y'} = K_y^{y'y'} = K_{yy}^{y'} = \pm 1 \qquad (8)$$

$$A_{yy} = p^{y'y'} = K_y^{y'} = K_{yy}^{y'y'} = 1 \qquad (9)$$

$$A_{xz} = p^{x'z'} = K_{xz}^{x'z'} = 0 \qquad (10)$$

$$K_{xz}^{y'} = K_{xz}^{x'x'} = K_{xz}^{y'y'} = K_{xz}^{z'z'} = 0 \qquad (11)$$

$$K_y^{x'z'} = K_{xx}^{x'z'} = K_{yy}^{x'z'} = K_{zz}^{x'z'} = 0 \qquad (12)$$

$$K_y^{z'z'} = K_{zz}^{y'} = K_y^{x'x'} = K_{xx}^{y'} = \mp 1/2 \qquad (13)$$

$$K_{zz}^{z'z'} = K_{xx}^{z'z'} = K_{zz}^{x'x'} = K_{xx}^{x'x'} = 1/4 \qquad (14)$$

$$A_{xx} = A_{zz} = K_{xx}^{y'y'} = K_{zz}^{y'y'} = -1/2 \qquad (15)$$

$$p^{x'x'} \quad p^{z'z'} = K_{yy}^{x'x'} = K_{yy}^{z'z'} = -1/2. \qquad (16)$$

The quantities p, A and K denote the polarization of the scattered deuterons, the analyzing power and the polarization transfer coefficients respectively. With these conditions a straightforward experimental identification of a point $A_y=\pm 1$ or $A_{yy}=1$ is possible. Care should be taken to verify each condition in several ways, choosing the observables by an inspection of the general formulae and taking into account the relations between observables required by other symmetries.[3]

Footnotes and References

*Proc. Fourth Int'l. Symposium on Polarization Phenomena in Nuclear Reactions (Birkhäuser Verlag, Basel, 1976).

†Present address: Physics Dept., University of Basel, Switzerland.

‡Present address: Nuclear Science Lab., M.I.T., Cambridge, Mass.

§Present address: Physics Dept., Laval University, Quebec, Canada.

1. W. Grüebler, P. A. Schmelzbach, V. König, R. Risler, B. Jenny, and D. Boerma, Nucl. Phys. A242 (1975) 285.

2. H. E. Conzett, F. Seiler, F. N. Rad, R. Roy, and R. M. Larimer, Fourth Polarization Symp.

3. G. G. Ohlsen, J. L. Gammel, and P. W. Keaton, Phys. Rev. C5 (1972) 1205.

4. F. Seiler, F. N. Rad, and H. E. Conzett, Fourth Polarization Symp.

5. F. Seiler, Phys. Lett. 61B (1976) 144.

DEVIATIONS FROM CHARGE-SYMMETRY IN THE REACTION $^4He(\vec{d},t)^3He$*

W. Dahme,† P. J. A. Buttle,‡ H. E. Conzett, J. Arvieux,°
J. Birchall and R. M. Larimer

For nuclear reactions in which the final nuclei belong to the same isospin multiplet, Simonius[1] showed that the concept of charge symmetry of the nuclear forces requires the angular distributions of the cross section to be symmetric and the vector analyzing power to be antisymmetric with respect to 90° in the c.m. system. Experimental evidence of deviations from this theorem was reported by Gross et al.[2] for the cross section of the reaction $^2H(\alpha, t)^3He$. In order to provide additional information for a more detailed study of the symmetry-violating mechanism we measured the vector analyzing powers iT_{11} of the mirror reactions $^4He(\vec{d},t)^3He$ and $^4He(\vec{d}, ^3He)^3H$ at $E_{d\ lab} = 32.0$ and 41.0 MeV.[3] The angular distributions of iT_{11} for the ^3He and triton channel differ by as much as 0.08 (Fig. 1).

The simplest method of taking into account Coulomb effects is a coherent superposition of slightly different proton and neutron transfer amplitudes in a DWBA calculation, as also considered by Gross et al.: $T(\vec{k}_f) = T_p(\vec{k}_f) + T_n(-\vec{k}_f)$. Choosing the coordinate system according to the Madison Convention we get, using Satchler's[4] notation:

$$T^{M_A m_a}_{M_B}(\theta,0) = T^{M_A m_a}_{pM_B m_b}(\theta,0) + (-1)^m\, T^{M_A m_a}_{nm_b M_B}(\pi-\theta,0).$$

The reaction in question also is of a spin type not usually treated in DWBA formalisms: $1 + 0 \rightarrow 1/2 + 1/2$. Because of the similarity of ^3He and ^3H we assume their LS interactions to be identical and use channel spin $\vec{S}$ in the final channel. The zero-range DWBA code DWUCK was modified to sum over S = 0,1 and to add the two transfer amplitudes coherently.

The optical model parameters used in these DWBA calculations were obtained by fitting to the 15 to 45 MeV elastic $\vec{d}+^4He$ vector analyzing power data of Leemann et al.[5] along with the cross sections of Willmes[6] and the 6 to 32 MeV elastic $^3He+^3H$ cross section data of Bacher et al.[7] and Batten et al.[8] No $^3He+^3H$ analyzing power data are available at present. The derived parameters are listed in Table 1 for the two energies of interest here. Good fits are achieved over the entire energy region of the $\vec{d}+^4He$ data. Fits of less quality were obtained for the $^3He+^3H$ data. The bound state form factors were calculated as by Gross et al.

Figure 1 shows a comparison of our preliminary calculations with the experimental data. The structure is reproduced but the quantitative agreement is not satisfactory. The fit to the cross section is of similar quality. At present, the discrepancies seem to be due to the uncertainties of the $^3He+^3H$ optical potential.

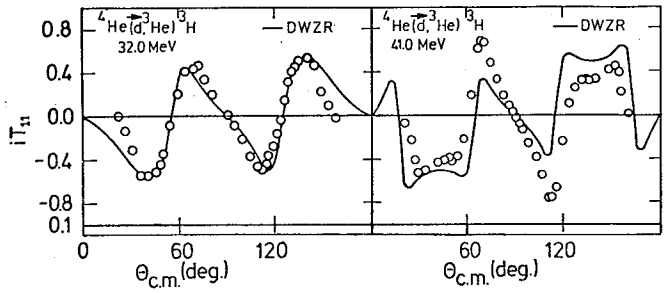

Fig. 1. Vector analyzing powers, iT_{11}, in the $^4He(\vec{d},^3He)^3H$ reaction at 32 and 41 MeV. The curves are from DWBA calculations. (XBL 766-8273)

Table 1. Optical model parameters (r_C = 1.3 fm).

	E_d	V_o	r_o	a_o	W_V	W_S	r_I	a_I	V_{LS}	r_{LS}	a_{LS}
$d+^4He$	32.0	68.7	1.18	0.56	0.0	2.55	2.56	0.5	4.6	1.18	0.5
	41.0	62.2	1.18	0.56	0.0	3.27	2.56	0.5	4.6	1.18	0.5
$^3H+^3He$	32.0	192.5	1.30	0.60	0.74	0.0	1.60	0.5	8.0	1.30	0.5
	41.0	205.0	1.30	0.60	17.5	0.0	1.60	0.5	8.0	1.30	0.5

Footnotes and References

*Proc. Fourth Int'l. Symposium on Polarization Phenomena in Nuclear Reactions (Birkhäuser Verlag, Basel, 1976).

†Present address: Sektion Physik der Universitat Munchen, Garching, Germany.

‡Permanent address: University of Manchester, England.

§Present address: I.S.N., University of Grenoble, France.

‖Present address: University of Basel, Switzerland.

1. M. Simonius, Phys. Letters 37B (1971) 446.

2. E. E. Gross et al., Phys. Rev. C5 (1972) 602.

3. W. Dahme et al., Proc. Int. Conf. on Nucl. Phys., Munich 1973 (North Holland, Amsterdam 1973) p. 444.

4. G. R. Satchler, Nucl. Phys. 55 (1964) 1.

5. Ch. Leemann et al., Bull. Am. Phys. Soc. 17 (1972) 562.

6. H. Willmes, private communication.

7. A. D. Bacher et al., Nucl. Phys. A119 (1968) 481.

8. R. J. Batten et al., Nucl. Phys. A151 (1970) 56.

POLARIZATION SYMMETRIES IN DIRECT REACTIONS: $^3He(\vec{t},d)^4He$ AND $^2H(\vec{d},p)^3H$*

H. E. Conzett

The observable consequences of particle symmetry or charge symmetry in reactions of the type b(a,c)c' are well known. Here, the final-state particles c and c' are the charge-symmetric members of an isospin doublet or are identical particles, c = c'. The symmetries imposed on the angular distributions of the cross section and the analyzing powers have been given by Barshay and Temmer[1] and Simonius:[2]

$$\sigma(\theta) = \sigma(\pi-\theta) \quad \text{for a state of definite isospin.} \tag{1A}$$

$$T_{kq}(\theta) = (-1)^q T_{kq}(\pi-\theta) \tag{1B}$$

These symmetries are exact for c = c', but significant deviations from (1) have been observed in the $^4He(d,t)^3He$ reaction (or its inverse) at deuteron energies ranging from threshold (21.5 MeV) to 41 MeV. Nocken et al.,[3] have concluded that the lower energy cross-section data from the inverse reaction[4] are explained in terms of the compound-nucleus reaction mechanism, and they suggest that the deviations from symmetry about $\theta = \pi/2$ result from isospin mixing in the ^6Li intermediate nucleus. At the higher energies E_d = 32 and 41 MeV, deviations from the symmetries (1) in both the cross-section[5] and in the deuteron vector analyzing power[6] have, in large measure, been explained via DWBA calculations as resulting from the slightly different proton and neutron transfer amplitudes.[5,7,8] This explanation in terms of expected Coulomb effects thus retains the concept of basic charge-symmetry at these higher energies.

There is no symmetry condition such as (1B) imposed on the polarizations, $t_{kq}(\theta)$, of the outgoing particle in the $b(a,\vec{c})c'$ reaction; so, it follows that in a reaction $a'(\vec{a},c)d$, where the identical particles (a' = a) or isospin partners are in the initial state, the condition (1B) on the analyzing powers does, in general, not apply. However, in this paper it is shown that if the reaction mechanism is a purely direct transfer process, condition (1B) is imposed on the analyzing powers in the $a'(\vec{a},d)d$ reaction. This symmetry then becomes, in this class of reactions, a clear signature of the direct transfer mechanism as contrasted with the compound-nucleus, or intermediate state, process.

Figure 1 shows the two direct transfer amplitudes which are added coherently; N_1 and N_2 are the transferred nucleons or nucleon clusters. As examples, in the $^2H(\vec{d},p)^3H$ reaction $N_1 = N_2 = n$, and in the $^3He(\vec{t},d)^4He$ reaction $N_1 = n$ and $N_2 = p$. As is noted in Fig. 1, the M-matrix amplitude $M^{(2)}_{m_d m_c m_a m_{a'}}(\pi-\theta)$ for the transfer of N_2, producing particle d at the angle $\pi-\theta$, is described in the coordinate system with the y-axis along $\vec{k}_i \times (-\vec{k}_f)$. Rotation of the coordinate system through an angle π around the z-axis, so that the y-axis is along $\vec{k}_i \times \vec{k}_f$, gives[9] $(-1)^m M^{(2)}_{m_d m_c m_a m_{a'}}(\pi-\theta)$ for the N_2-transfer amplitude. Here $m = m_a + m_{a'} - m_c - m_d$ and m_a, $m_{a'}$, m_c, m_d are the spin magnetic substates of particles a,a',c, and d. The complete M-matrix amplitude is then

$$M_{m_c m_d m_a m_{a'}}(\theta) = M^{(1)}_{m_c m_d m_a m_{a'}}(\theta) + (-1)^m M^{(2)}_{m_d m_c m_a m_{a'}}(\pi-\theta). \tag{1}$$

The particle identity or charge symmetry provides that

$$M^{(1)}_{m_c m_d m_a m_{a'}}(\theta) = M^{(2)}_{m_d m_c m_a m_{a'}}(\theta). \tag{2}$$

In terms of the transition matrix M, the analyzing powers are given by the expression

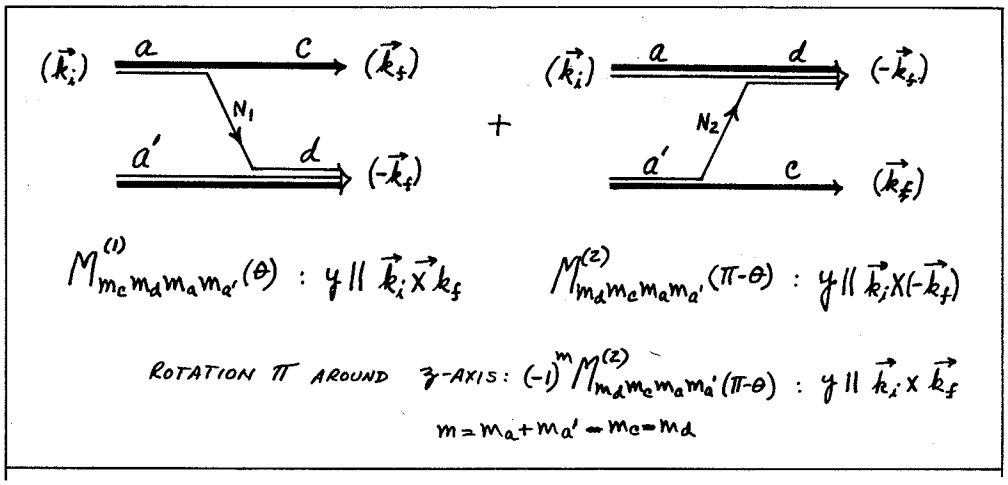

Fig. 1. The two direct-transfer amplitudes which add coherently in the a'(a,c)d reaction. (XBL 758-1867)

$$\sigma(\theta)\, T_{kq}(\theta) = \mathrm{Tr} M(\theta)\, \tau_{kq} M^{+}(\theta), \qquad (3)$$

where the τ_{kq} are spherical tensor operators.[9,10] Using (1) and (2) in Eq. (3) it has been shown[11] that

$$T_{kq}(\theta) = (-1)^q\, T_{kq}(\pi\ \theta) \quad \text{for } a' = a. \qquad (4)$$

The symmetry (10) thus provides clear indication of a purely direct transfer process. Of course, if the reaction should proceed through a single J^π state or states of the same parity in the compound nucleus, this symmetry condition could also result. However, an examination of the energy dependence of $T_{kq}(\theta)$ should resolve any ambiguity. Also, the excitation energies of the intermediate nuclei which are accessible in this class of reactions with polarized beams would, almost certainly, be in regions of overlapping levels.

As a clear example of these considerations, Fig. 2 shows angular distributions of the vector analyzing power $A_y(\theta) = (2/\sqrt{3})\, iT_{11}(\theta)$ in the $^2H(\vec{d},p)^3H$ reaction at energies from 11.5 to 30 MeV. The 11.5 MeV data are from Zürich,[12] and the other data are from Berkeley.[13] The corresponding range of excitation energies in ^4He is 29.6 to 38.8 MeV, and one sees the obvious transition from a complete lack of symmetry in the angular distribution to one of near antisymmetry with respect to $\theta = \pi/2$, as given by Eq. (10). The Zürich data range down to ^4He excitation energies of 24.2 MeV, and all the analyzing power components $T_{kq}(\theta)$ are consistent in that no such symmetry exists. Hence, analysis of these data in terms of ^4He intermediate states is required at the lower deuteron energies, whereas analysis in terms of the direct nucleon-transfer process is appropriate above 30 MeV. It should be noted from the data of Fig. 2, that evidence persists for some contribution from the compound-nucleus process at energies above that of the highest suggested excited state of ^4He, $^4He^*$ (32 MeV) corresponding to $E_d = 16.5$ MeV.[14]

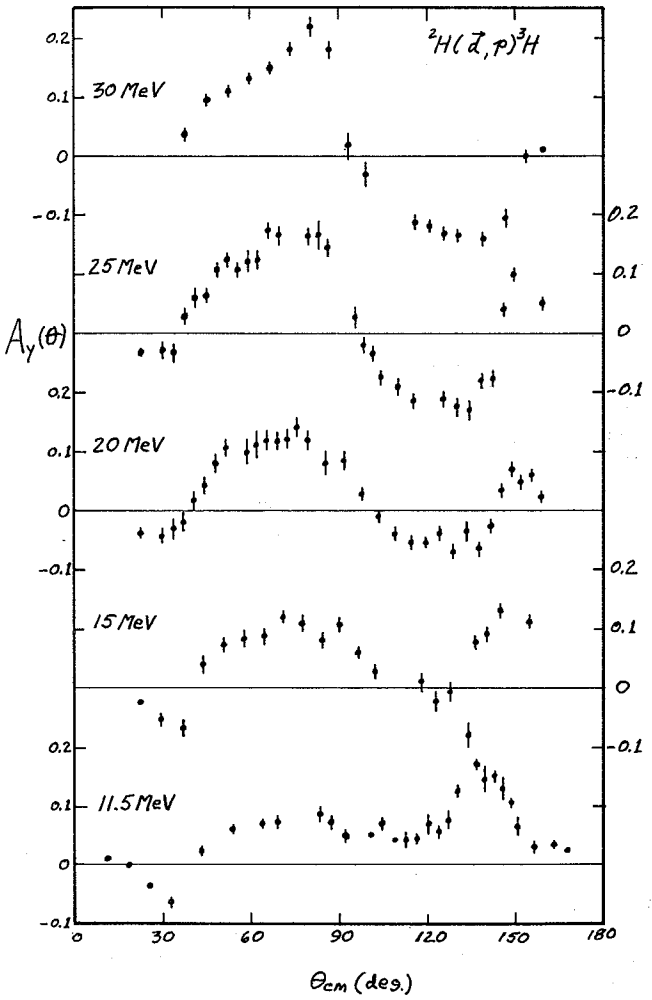

Fig. 2. The vector analyzing power $A_y(\theta)$ in the $^2H(\vec{d},p)^3H$ reaction between 11.5 and 30 MeV. The 11.5-MeV data are from Ref. 12. (XBL 758-1865)

Another case of interest is the $^3He(\vec{t},d)^4He$ (or $^3H(\vec{^3He},d)^4He$) reaction. As was noted before, it has been reported[3] that the lower energy cross section data suggest isospin mixing in the compound nucleus ^6Li. Support for this conclusion could be provided by measurements at those energies of the analyzing power $iT_{11}(\theta)$ in the $^3He(\vec{t},d)^4He$ reaction. The lack of symmetry of the form (4) would be confirming evidence for the compound-nucleus reaction mechanism. With respect to the higher energies, a DWBA calculation has been made of the analyzing power in the $^3He(\vec{t},d)^4He$ reaction at an energy equivalent to $E_d = 32$ MeV in the inverse reaction. The parameter values were those used by Dahme, Buttle et al.,[8] in their fits to $\sigma(\theta)$ and $iT_{11}(\theta)$ in that inverse reaction $^4He(\vec{d},t)^3He$. The near antisymmetry of $A_y(\theta)$ about $\theta = \pi/2$ is distinct.

Considering the presently available polarized beams, we list in Table 1 examples of reactions in which measurements of $T_{kq}(\theta)$ may provide unambiguous information on the reaction mechanism.

Table 1.

$^2H(\vec{d},p)^3H$	$^6Li(\vec{^6Li},p)^{11}B$
$^3He(\vec{t},d)^4He$	$^6Li(\vec{^6Li},d)^{10}B$
$^3He(\vec{t},p)^5He$	$^6Li(\vec{^6Li},{}^3He)^9Be$
$^3He(\vec{^3He},p)^5Li$	$^6Li(\vec{^6Li},\alpha)^8Be$
	$^6Li(\vec{^6Li},{}^7Li)^5Li$
	$^6Li(\vec{^6Li},{}^7Be)^5He$

The $^6\vec{L}i + {}^6Li$ reactions, for example, could be particularly interesting, since deviations from the symmetry (4) would provide qualitative information about states in ^{12}C which have some overlap with the appropriate cluster configurations.

In summary, we find that the analyzing powers, in reactions with identical or charge-symmetric particles in the initial state, can provide definite identification of the reaction mechanism, whereas no such information is available from cross-section data alone.

Footnote and References

*Condensed from invited paper, Proc. Fourth Int'l. Symposium on Polarization Phenomena in Nuclear Reactions (Birkhäuser Verlag, Basel, 1976).

1. S. Barshay and G. M. Temmer, Phys. Rev. Letters 12 (1964) 728.

2. M. Simonius, Phys. Letters 37B (1971) 446.

3. U. Nocken et al., Nucl. Phys. A213 (1973) 97,

4. G. J. Wagner et al., Few Particle Problems in the Nuclear Interaction, eds. I. Slaus et al. (North Holland, Amsterdam, 1972) p. 747.

5. E. E. Gross et al., Phys. Rev. C5 (1972) 602.

6. W. Dahme et al., Proc. Int. Conf. on Nucl. Phys. (Munich 1973) Vol 1, 444.

7. S. Edwards et al., Phys. Rev. C8 (1973) 456.

8. W. Dahme et al., Fourth Polarization Symp.

9. See, e.g., M. Simonius, Lect. Notes in Physics 30 (Springer-Verlag, Heidelberg 1974) p. 38.

10. W. Lakin, Phys. Rev. 98 (1955) 139.

11. H. E. Conzett, Fourth Polarization Symp.

12. W. Grüebler et al., Nucl. Phys. A193 (1972) 129

13. H. E. Conzett, J. S. C. McKee et al., Fourth Polarization Symp., H. E. Conzett, R. M. Larimer et al., Fourth Polarization Symp.

14. E. K. Lin et al., Nucl. Phys. A179 (1972) 65; E. L. Haase et al., Nucl. Phys. A188 (1972) 89.

DEPOLARIZATION PARAMETER IN $\vec{p}$ - ^{10}B ELASTIC SCATTERING AND THE SPIN-SPIN INTERACTION*

J. Birchall,† H. E. Conzett, F. N. Rad,‡
S. Chintalapudi,§ and R. M. Larimer

Sherif and Hussein[1] have pointed out that the depolarization parameter D is a sensitive probe of the spin-spin interaction in nucleon-nucleus elastic scattering. Other parameters, such as the cross-section and asymmetry, polarization and spin rotation parameters, are relatively insensitive.

Two types of spin-spin force have been considered. A spherical term:

$$U_{ss}(r) = V_{ss}F_0(r)\,\underline{\sigma}\cdot\underline{I},$$

and a tensor term:

$$U_{st}(r) = -1/2\,V_{st}F_t(r)\{3(\underline{\sigma}\cdot\hat{r})(\underline{I}\cdot\hat{r}) - \underline{\sigma}\cdot\underline{I}\},$$

where $\underline{\sigma}$ and $\underline{I}$ are the spins of the incident proton and the target nucleus, respectively, and $\hat{r}$ is a unit vector in the direction of a line connecting the centers of the projectile and target. The depth V_{ss} and the form factor $F_0(r)$ of the spherical term can be estimated from the nucleon-nucleon

spin-spin interaction and the single nucleon wave function in the target nucleus.[2] The form and strength of the tensor interaction have not yet been estimated, so a phenomenological Woods-Saxon form was taken for $F_t(r)$ and the strength V_{st} of the interaction was treated as a free parameter in the calculated fits to the available sparse depolarization data.[3] It is clear that more measurements of $D(\theta)$ to good accuracy over wider angular ranges are needed in a continuing study of the effects of the target spin in nucleon-nucleus elastic scattering.

We have measured $D(\theta)$ at several angles in the elastic scattering of 26-MeV polarized protons from ^{10}B. The polarization of the scattered protons is given by

$$p(\theta) = \{A(\theta) + D(\theta)p_o\} / \{1 + p_o A(\theta)\},$$

where p_o is the beam polarization and $A(\theta)$ is the target analyzing power. The polarization of the beam was continuously monitored by scattering from a ^4He gas target downstream from the ^{10}B. The polarization of the elastically scattered protons was measured by a polarimeter with high figure of merit and good energy resolution.[4] The polarimeter used a 1-mm thick silicon solid state detector as polarization analyzer and two side detectors at ±27° to the polarimeter axis. Protons which passed unscattered through the analyzer detector were stopped in a "zero degree" detector. The zero degree collimation had the same angular width as the analyzer, with respect to the target center, but much reduced angular height. The analyzing power of the target was deduced from the spin up--spin down count ratio in the zero-degree detector.

Geometrical errors in the determination of D were minimized by careful monitoring and adjustment of beam alignment during the runs, by deducing D from spin-up/spin-down ratios in each side detector and by obtaining results with the silicon polarimeter placed on each side of the beam. As a check on these procedures the D-parameter of ^{12}C was measured at a number of angles (D for elastic scattering from a spin zero nucleus should be identically 1.0). Values of D consistent with 1.0 were found in each case.

Results of our D-parameter measurements are shown in Fig. 1. The curves are not fits to our data. They are calculations from Ref. 1, where the values of V_{st} were chosen to reproduce a data point from Saclay[5] at 65° c.m. and 19.8 MeV. It was pointed out by Sherif and Hussein that the tensor strengths V_{st} extracted in their fits to the data were rather large. As a result, very recent theoretical effort has disclosed another contribution to deviations from unity of $D(\theta)$, which has been termed the quadrupole spin-flip effect.[6] This effect can be present for nuclei that have ground-state quadrupole deformations, and, as such, $I \geq 1$. Hence, further investigations are required to determine the separate effects from the explicit spin-spin interaction and from the quadrupole deformations.

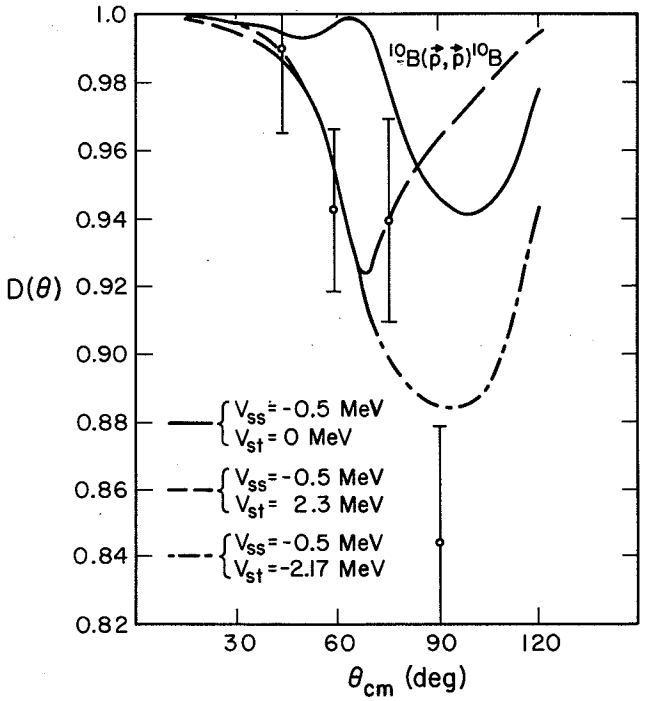

Fig. 1. Depolarization parameter, $D(\theta)$, in $\vec{p}$-^{10}B elastic scattering at 26 MeV. The calculated curves are from Reference 1. (XBL 743-2523)

Footnotes and References

*Proc. Fourth Int'l. Symposium on Polarization Phenomena in Nuclear Reactions (Birkhäuser Verlag, Basel, 1976).

†University of Basel, Switzerland.

‡Nuclear Science Lab., M.I.T., Cambridge, Mass.

§Bhabha Atomic Research Centre, Trombay, India.

1. H. S. Sherif and A. H. Hussein, Phys. Lett. 41B (1972) 465; Phys. Rev. C8 (1973) 518.

2. G. R. Satchler, Particles and Nuclei 1 (1971) 397.

3. J. Birchall et al., Phys. Lett. 53B (1974) 165, and references therein.

4. J. Birchall et al., Nucl. Instr. and Meth. 123 (1975) 105.

5. R. Beurtey, P. Cattillon and P. Schnabel, J. de Phys. 31, Supp. C2 (1970) 96; P. Schnabel, thesis, University of Paris, 1971 (unpublished).

6. J. S. Blair and H. S. Sherif, Bull. Amer. Phys. Soc. 19 (1974) 1010; J. S. Blair, M. P. Baker, and H. S. Sherif, Phys. Lett. 60B (1975) 25.

CROSS SECTIONS AND REACTION MECHANISMS OF (p,pxn) REACTIONS ON ^{208}Pb IN THE 24-52 MeV RANGE*

J. O. Rasmussen, R. Donangelo, H. Kawakami,† M. Koike,†
K. Komura,† M. Sakai,† and N. Yoshikawa†

The cross section for the reactions ^{208}Pb(p,pn)^{207m}Pb, ^{208}Pb(p,p2n)^{206m}Pb have been measured for 24, 28, 36, 44, 52 MeV incident protons. The experimental results are shown to be consistent with the clean knockout mechanism for the (p,pn) reaction and with knockout of one neutron followed by evaporation of another for the (p,p2n) reaction. We deduce a theoretical formula for the cross section for these reactions.

The target used was metallic foil of an enriched isotope (99.9%) of ^{208}Pb. A target foil of 8.3 mg/cm^2 thickness was prepared by electrodeposition. The FM cyclotron pulse width of 0.078 ms was used, with delayed gamma rays counted in the 1.06 ms interval between beam pulses.

The delayed 802.9 keV ($2_1^+ \rightarrow 0_g^+$) γ-rays were counted from 0.053 to 0.352 ms (0.299 ms) in the decay curve after the beam pulse. The prompt γ-rays completely decayed out earlier than 0.053 ms. The cross section for formation of the 0.12 ms 7- isomer at 2.2 MeV in ^{206}Pb was calculated from the intensity of the 802.9-keV gamma ray.

The excitation function for the reaction ^{208}Pb(p,pn)^{207m}Pb(13/2$^+$ isomer of 0.80-sec half-life at 1.623 MeV) was measured with the 1063.7 and 569.8-keV γ-rays.

Singles γ-ray spectra were also observed with the debunched proton beam. The cross section associated with the 2$^+$ state in ^{206}Pb was estimated from the 802.9 keV ($2_1^+ \rightarrow 0_g^+$) γ ray, and similarly the 569.8 keV (5/2$^-$ - 1/2$^-$)$_g$ transition in ^{207}Pb was used to calculate the 5/2$^-$ state cross section. The numerical values for these cross sections are given in Table 1.

We will classify the possible reaction processes in two broad categories: (a) those in which the incident proton interacts strongly with only one or two nuclear neutrons which leave the nucleus with little or no excitation, and (b) those where the incident proton leaves the nucleus in an excited state above the neutron binding energy (after maybe knocking out a neutron in the process). The excited nucleus usually decays subsequently by the evaporation of one neutron.

Table 1. Excitation functions for the reactions ^{208}Pb(p,pn)^{207m}Pb and ^{208}Pb(p,p2n)^{206m}Pb.

	^{207m}Pb		^{206m}Pb	
E_p (MeV)	13/2$^+$ σ(mb)	5/2$^-$ σ(mb)	7$^-$ σ(mb)	2$^+$ σ(mb)
24	21±4		2±1	
28	45±9		8±3	
36	58±12		34±11	
44	58±12	120±25	57±18	95±20
52	65±13		57±18	

Using the notation of Grover and Caretto[1] we will designate as Clean Knockout (CKO) the process described in (a) and as Inelastic Scattering followed by Evaporation of a neutron (ISE) the one described in (b).

We conclude then that the isomer ratios for isotopes one and two neutrons less than the target are consistent with a reaction mechanism consisting of one direct neutron ejection by the incoming proton with (CKO) knockout from orbitals in the first shell below the Fermi energy leading to the (p,pn) reaction and (KOE) knockout followed by evaporation from the second shell below the Fermi energy leading to the (p,p2n) reaction.

The fact that the isomer yield ratios suggest certain processes does not imply that the others do not occur at all, but only that their contribution is small. For this same reason we have not considered other processes, such as compound nucleus formation, which give a small contribution to the total cross section.

The conclusions we reached here are in agreement with the analysis made by Rao and Yaffe[2] on the proton induced reaction in ^{181}Ta.

From our discussion on the isomer ratio evidence in part 2 we reached the conclusion that these reactions are peripheral. We now attempt to formulate a quantitative expression for their cross sections.

According to Wong[3] the total charged particle nuclear reaction cross section can be expressed approximately as

$$\sigma_W(E) = (R_o^2 \hbar\omega_o/2E)\ln\left\{1 + \exp[2\pi(E-E_o)/\hbar\omega_o]\right\}$$

where E is the charged particle energy

E_o is the height of the Coulomb barrier

$\hbar\omega_o = \hbar\,[d^2V(r)/dr^2|_{R_o}/\mu]^{1/2}$

μ is the reduced mass

$V(r)$ the effective (nuclear + Coulomb) potential for the reaction

R_o is the nuclear radius, calculated from $dV(r)/dr|_{R_o} = 0$.

Using the facts that the reactions are peripheral and that the cross section is dominated by the exit proton penetrability we derive the expression for the cross section:

$$\sigma(E_{in}) = (\Delta R/E_{in}) \left\{ R_o \hbar\omega_o \ln[1 + \exp(2\pi(E-E_o)/\hbar\omega_o)] + \pi R_o E_o [1 + \exp(-2\pi(E-E_o)/\hbar\omega_o)]^{-1} \right\} .$$

The energies E_{in} and E_{out}, proton energies before and after reaction, are related through the ejected neutrons separation energies

$$(p,pn) \rightarrow E_{in} = E_{out} + \alpha S_{n_1}$$
$$(p,p2n) \rightarrow E_{in} = E_{out} + \alpha' S_{n_1} + S_{n_2}$$

α and α' ($1 \leq \alpha,\alpha' \leq 2$) are parameters included to take into account that more energy than the threshold binding energies is required on the average to remove a neutron. R_o and $\hbar\omega_o$ were determined by taking a potential

$$V(r) = (Ze^2/r) - V_o \left\{ 1 + \exp[(r-R)/b] \right\}^{-1} .$$

The values taken for the parameters in this potential are[4]

$$R = 1.25\ A^{1/3}\ \text{Fm}$$

$$b = 0.65\ \text{Fm}$$

$$V_o = 30\ \text{MeV}.$$

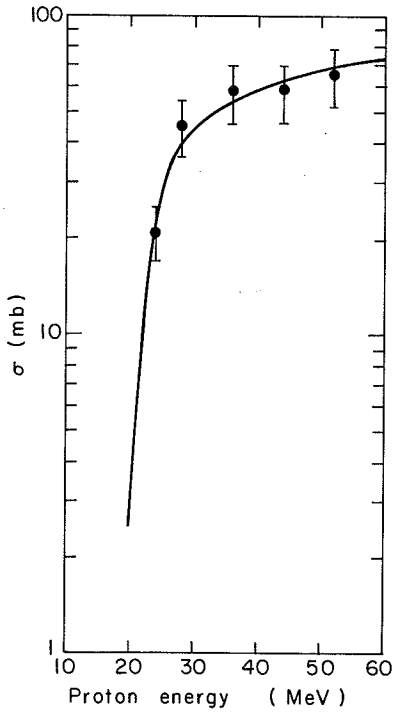

Fig. 1. Theoretical excitation curve for the ^{208}Pb(p,pn)^{207m}Pb reaction ($13/2^+$ isomer). The data are from this work. (XBL 759-4075)

The parameters α, α' and ΔR were fitted to the experimental results. Besides our ^{208}Pb data we fitted the Rao and Yaffe[2] data for the ^{181}Ta(p,pn)^{180m}Ta reaction. The cross sections are plotted in Figs. 1-3.

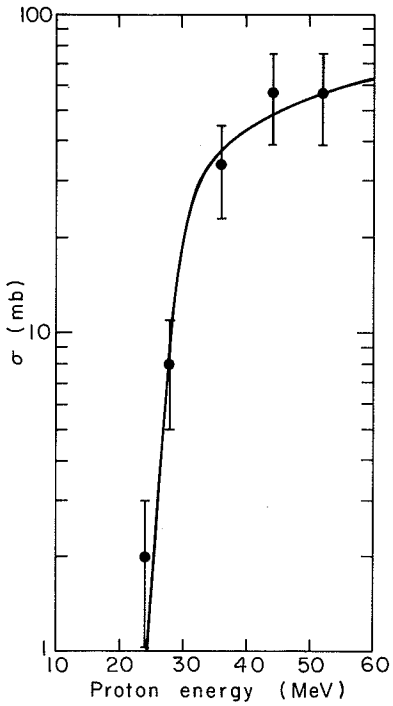

Fig. 2. Theoretical excitation curve for the ^{208}(p,p2n)^{206m}Pb reaction (7^- isomer). The data are from this work. (XBL 759-4076)

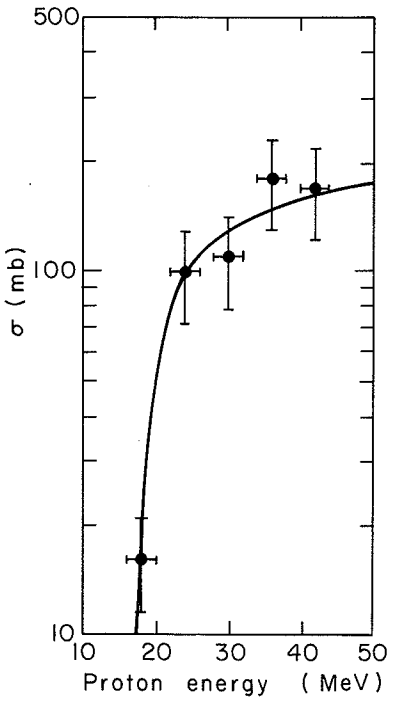

Fig. 3. Theoretical excitation curve for the ^{181}Ta(p,pn)^{180m}Ta reaction. Data from Rao and Yaffe.[2] (XBL 759-4077)

That this simple expression fits the energy dependence of the cross sections is mainly a consequence of the dominant importance of barrier transmission by the outgoing proton, which must be at least lower in energy than the incoming proton by the neutron binding energy, regardless of the exact mechanism. The excess of α or α' over unity represents the finite kinetic energy carried off by the neutrons(s) on the average. The fact that α is as large as 1.5 for the (p,pn) reaction points to several MeV average kinetic energy of the neutrons and favors the CKO mechanism as dominant over ISE.

Footnotes and References

*Condensed from Nucl. Phys. A262, 52 (1976).

†Institute for Nuclear Studies, Univ. of Tokyo, Tanashi, Tokyo, Japan.

1. J. R. Grover and A. A. Caretto, Jr., Ann. Rev. Nucl. Sci. 14 (1964), 51.

2. C. L. Rao and L. Yaffe, Can. Journ. Chem. 41 (1963), 2516.

3. C. Y. Wong, Phys. Rev. Lett. 31 (1973), 766.

4. M. A. Preston, Nuclear Physics (Addison-Wesley, 1962), p. 547.

THE (α,^{2}He) REACTION AS A SPECTROSCOPIC TOOL FOR INVESTIGATING HIGH SPIN STATES*

R. Jahn,† G. J. Wozniak,
D. P. Stahel, and Joseph Cerny

Experimental systems capable of detecting nuclear reaction products in resonant final states with good efficiency and energy resolution can open up a wide range of unexplored nuclear reactions. Although at present such studies are largely confined to the detection of ^{8}Be nuclei, Robson[1] has pointed out many other interesting resonant systems which can be detected as reaction products. Additionally, the well known final state interaction in the two-nucleon T = 1 system can be utilized; in particular, this interaction in the ^{2}He system localizes the two breakup protons into a narrow cone. Thus ^{2}He can readily be detected with two proton detectors arranged in an appropriate geometry.

A very interesting reaction which can be studied at reasonably high bombarding energies with such a detection system is that of (α,^{2}He), potentially a direct 2n-transfer reaction very similar to the direct np-transfer reaction (α,d). The demonstrated selectivity of the (α,d) reaction[2,3] makes it a valuable spectroscopic tool with which to investigate high spin states in nuclei with $T_z = T_z$ (target), and therefore one can anticipate that the (α,^{2}He) reaction might selectivity populate high spin states in nuclei with $T_z = T_z$ (target) +1. This reaction is particularly appealing due to the unavailability of high energy triton beams, so that the analogous (t,p) reaction has not been investigated under conditions of large angular momentum transfer. We report here the results of this initial observation of the (α,^{2}He) reaction on ^{12}C,^{13}C and ^{16}O (as SiO_2) targets induced by 65 MeV α-particles from the 88-inch cyclotron. These data establish the expected high selectivity of this reaction and its usefulness as an important spectroscopic tool.

Figure 1(a) shows the ^{2}He detection system, consisting of two ΔE-E counter telescopes. The ΔE detectors were phosphorus-diffused Si, 380 μm thick and the E detectors were Si(Li), 5mm thick, all having the same area of 1 × 1.4 cm^2. Two collimator slits separated by a post were employed, so that the system subtended a 15° vertical and a 4° horizontal acceptance angle. ^{2}He events were identified by using standard particle identification techniques as well as subnanosecond fast timing between the two ΔE counters, which drastically reduced random events. In addition, fast pileup rejection was utilized so that high singles counting rates (30 kHz) could be tolerated in the ΔE counters.

Figure 1(b) shows the relative time distribution of observed proton coincidences from the reaction ^{13}C(α,^{2}He)^{15}C at 13° lab angle. The observed maximum difference in the time-of-flight of the two protons of 1.1 ns (FWHM) agrees with prediction based on the assumption of 400 keV breakup energy. The coincidence counting rate was measured at different geometries obtained by varying the distance between the target and the collimator. Figure 1(c) depicts the relative experimental efficiency versus the calculated efficiency for three different ^{2}He energies at three distances. The experimental data, normalized at 10 cm, are well reproduced by the calculations. The agreement between the calculated and experimental relative efficiencies and the narrow ΔTOF peak (random coincidences from a single beam burst would have spanned up to 12 ns FWHM) require that the detected pp coincidences are from the breakup of the unbound ^{2}He system.

Figure 2 presents representative spectra from the (α, ^{2}He) reaction on ^{12}C, ^{13}C, and ^{16}O at forward angles. The experimental energy resolution of 350 keV was principally determined by kinematic broadening due to the 4° acceptance angle. As can be seen in the spectra, the (α,^{2}He) reaction is extremely selective, only very few states in the residual nuclei are populated. In ^{14}C strong transitions were observed to a 3$^-$ level at 6.73 MeV and

to 4^+ level at 10.55 MeV with weaker transitions to the ground state and to a level at 14.67 MeV. The ^{15}C spectrum shows only strong transitions to the $5/2^+$ level at 0.74 MeV and to two states at 6.85 MeV and 7.35 MeV excitation energy, while in ^{18}O only selective population of the 4^+ level at 3.55 MeV was observed (weak transitions would be obscured due to the reactions on the Si in the target).

Preferential population of high spin states has been observed in the (α,d) reaction induced by 40-53 MeV α-particles on many light nuclei;[2,3] the selectively populated levels [e.g., of $(d_{5/2})^2_{5+}$ or $(f_{7/2})^2_{7+}$ character] correspond to particular kinematically-favored transitions in which the np pair can be simply captured in a relative triplet state about an undisturbed target core. Since similar kinematic behavior and Q-values occur in the $(\alpha,{}^2He)$ reaction, one also expects to observe predominantly high spin states, but now those in which the nn pair is captured in a relative singlet state. At 65 MeV bombarding energy, the transferred angular momentum in a surface interaction on these targets is about 4-5 ħ and thus transitions to levels formed by capturing the two stripped neutrons into d-orbitals with configurations of $(d_{5/2})^2_{4+}$ should be enhanced.

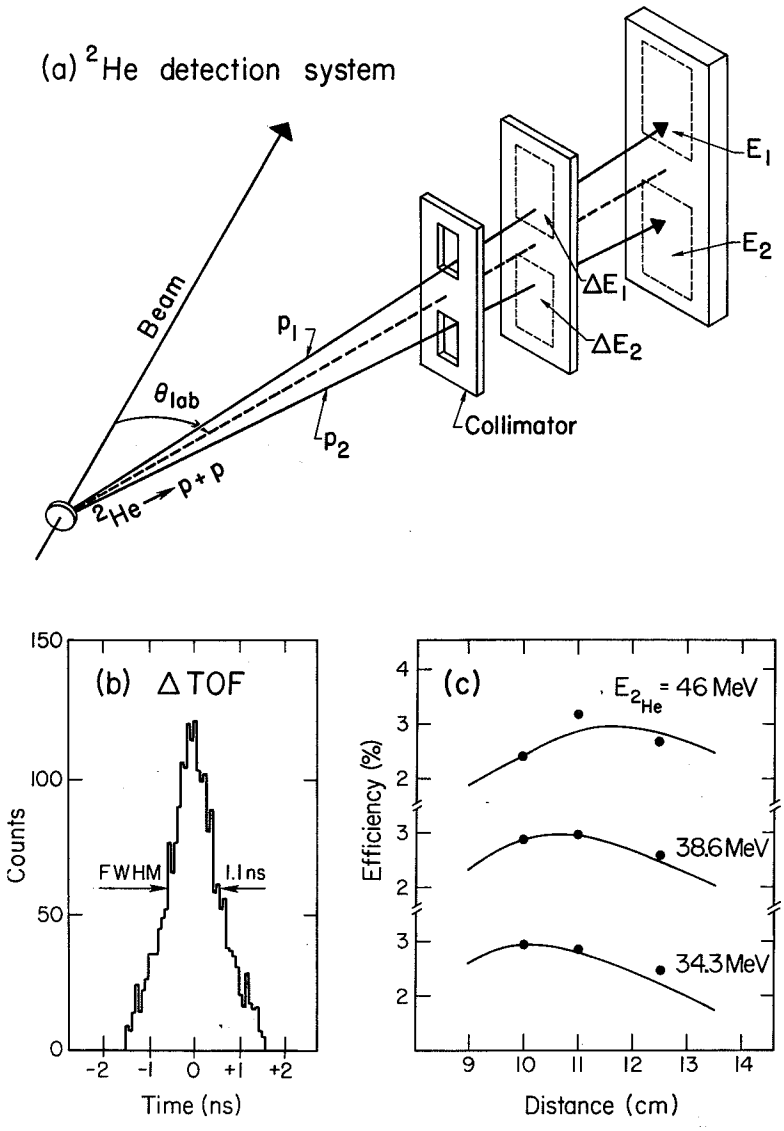

Fig. 1. (a) Schematic diagram of the ^{2}He detection system. (b) Spectrum of the time of flight difference ΔTOF between the two breakup protons. (c) Comparison of experimental (dots) and theoretical (solid lines) ^{2}He detection efficiencies as a function of the distance between target and collimator. The experimental efficiencies have been normalized to the calculations at a distance of 10 cm.

(XBL 766-2941)

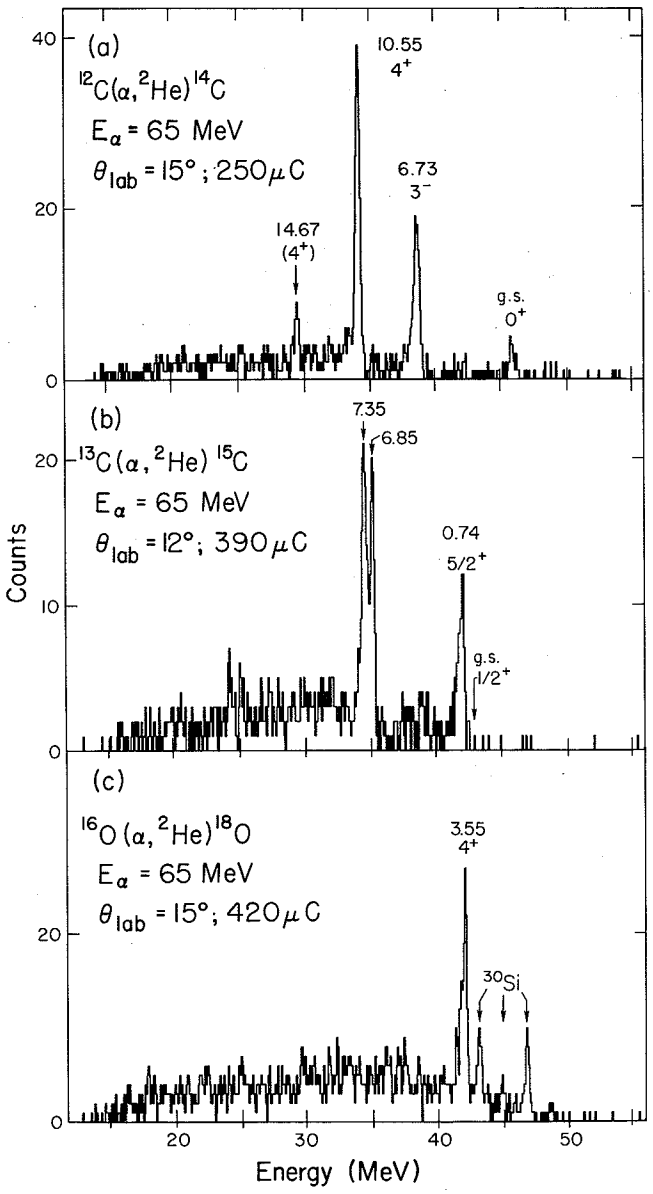

Fig. 2. ^{2}He energy spectra obtained from the reactions (a) $^{12}C(\alpha,^2He)^{14}C$; (b) $^{13}C(\alpha,^2He)^{15}C$; and (c) $^{16}O(\alpha,^2He)^{18}O$ at an α-particle energy of 65 MeV. (XBL 766-2940)

The observed strong population of the 4^+ states in ^{14}C and ^{18}O, which have substantial $(d_{5/2})^2_{4+}$ character,[4,5,6] is in agreement with this simple picture.

Noting Fig. 2(a), except for the weak population of the ^{14}C ground state, transitions to the other observed states in ^{14}C can be explained as kinematically favored transitions to S = 0 components in the known 6.73 MeV $(d_{5/2}\ p_{1/2})_{3^-}$ state[4] and in the 14.67 MeV state [possibly 4^+ ? of $(d_{5/2}\ d_{3/2})_{4+}$ character[4] though without additional calculations $(d_{5/2}\ f_{7/2})_{5^-}$ cannot be excluded.]

Since the ^{12}C and ^{13}C targets only differ by a $p_{1/2}$ neutron, one expects the $(\alpha,^2He)$ reaction on ^{13}C to populate preferentially the same two-neutron configurations originally observed in reactions on ^{12}C, but now coupled to the $1/2^-$ core. Thus the states observed in the ^{14}C spectrum should be split into two components in the ^{15}C spectrum, as has observed in the analogous (α,d) reactions on ^{12}C and ^{13}C. Noting Fig. 2(b), then the doublet observed at 6.85 MeV - 7.35 MeV in ^{15}C can be interpreted as configuration $[\{^{12}C(0^+)p_{1/2}\}_{1/2^-} \otimes (d_{5/2})^2_{4+}]_{7/2^-,9/2^-}$. Although this model does not predict the assignment of spins to the two components of the split state, relative enhancement via the (2J+1) statistical factor implies that the 7.35 MeV level might have the higher spin $(9/2^-)$ because of its larger cross section. Since the $5/2^+$ state at 0.74 MeV has a configuration $[\{^{12}C(0^+)p_{1/2}\}_{1/2^-} \otimes p_{1/2}d_{5/2}]_{5/2^+}$, the $p_{1/2}$ neutron of ^{13}C and the transferred $p_{1/2}$ neutron must couple to spin 0 and no splitting can arise. These three $^{13}C(\alpha,^2He)^{15}C$ transitions and the $^{16}O(\alpha,^2He)^{18}O$ transition to the 3.55 MeV $(d_{5/2})^2_{4+}$ state all show the expected forward peaked, structureless angular distributions. In addition, the observed cross sections of the transitions to the known 4^+ state in ^{14}C (10.55 MeV), the sum of the split states in ^{15}C, and the 4^+ state in ^{18}O are all equal within errors, which is further evidence for the assumption of a common $(d_{5/2})^2_{4+}$ configuration for these states.

These results clearly demonstrate the utility of the $(\alpha,^2He)$ reaction as a new spectroscopic tool capable of locating many unobserved two-neutron states of high spin in the 2s-1d and higher shells. Furthermore, extension of this approach towards studying resonant final systems as reaction products to other cases seems particularly practical and fruitful.

Footnotes and References

*Condensed from LBL-5038, Phys. Rev. Lett. 37, 812 (1976).

†DAAD Fellow, on leave from Institut für Strahlen- und Kernphysik der Universität Bonn, Germany.

1. D. Robson, Nucl. Phys., A204, 523 (1973).

2. E. Rivet, R. H. Pehl, J. Cerny, and B. G. Harvey, Phys. Rev. 141, 1021 (1966).

3. C. C. Lu, M. S. Zisman, and B. G. Harvey, Phys. Rev. 186, 1086 (1969).

4. W. W. True, Phys. Rev. 130, 1530 (1963).

5. S. Lie, Nucl. Phys. A181, 517 (1972).

6. T. T. S. Kuo and G. E. Brown, Nucl. Phys. 85, 40 (1966).

7. N. Anyas-Weiss, et.al., Phys. Lett. 12C, 201 (1974).

THE (α,^{8}Be) REACTION IN THE 1p SHELL*

G. J. Wozniak, D. P. Stahel,
N. A. Jelley,† and Joseph Cerny

The existence and the importance of multinucleon correlations in nuclei, and in particular of α-like four nucleon correlations, has intrigued physicists for decades. Recently, detailed theoretical calculations have been made of the extent of α-clustering in light nuclei[1,2] and the (d,^{6}Li), (^{3}He,^{7}Be) and (α,2α) reactions have been employed to verify experimentally these predictions.[3,4]

To complement the information acquired with the above three reactions, a very detailed study on 1p shell targets has been made with the (α,^{8}Be) reaction. This reaction has an a priori simplicity because the ^{8}Be ground state looks very much like two α particles weakly bound in a relative s-state; further, since the projectile, the transferred α particle and the ^{8}Be ground state all have zero spin, simple selection rules result. Although ^{8}Be is particle-unstable ($t_{1/2} \sim 10^{-16}$s), its ground state is long-lived compared with nuclear transit times, and one should be able to treat it as a single nucleus in a direct reaction.

The present investigation was carried out at moderately high bombarding energies (65-72.5 MeV) where it was hoped that direct processes would dominate and thus make possible the extraction of experimental spectroscopic factors. All stable 1p shell targets were investigated and the data were analyzed in the framework of the exact finite-range distorted-wave Born-approximation (EFR-DWBA).

In the distorted-wave Born approximation, the differential cross section for the reaction B(α,^{8}Be)A is given by:

$$\frac{d\sigma}{d\Omega}(\theta) = \sum_L S^L(B\to A+\alpha)\; S(Be\to\alpha+\alpha)\,\sigma^L_{DWBA}(\theta) \quad (1)$$

where L runs over all the allowed angular momentum transfers. The kinematic part of the cross section, σ^L_{DWBA}, was calculated using DeVries' EFR-DWBA code LOLA.[5] The optical model potentials needed to generate the distorted waves in the entrance and exit channels were determined by fitting tabulated α-particle elastic scattering data on ^{12}C, ^{13}C, ^{14}N, and ^{15}N at 40.5 MeV[6] and on ^{16}O at 65 MeV[7] with the search code GENOA.[8] The scattering data for each target were fitted individually with Woods-Saxon potentials having both real and imaginary volume terms. For the ^{9}Be, ^{10}B and ^{11}B targets no tabulated scattering data were available in the appropriate region. Thus a potential from the literature[9] similar to ^{13}C (see Table 1), which reproduced 46 MeV α-scattering on ^{11}B, was used.

In order to approximate a potential for the particle-unstable ^{8}Be, GENOA was used to determine an optical potential which reproduced 50 MeV ^{9}Be elastic scattering data[10] on ^{12}C (potential AA in Table 1). Since the ^{16}O(α,^{8}Be)^{12}C reaction calculations were found to be relatively insensitive to the exit channel potential and no ^{9}Be elastic scattering data existed for the other exit channels, potential AA was used to generate the distorted waves in the ^{8}Be channel for all of the 1p shell targets.

The bound state wave functions, which describe the motion of an α cluster in the target nucleus B and in ^{8}Be, were calculated in the usual way using a real Woods-Saxon potential whose well-depth was adjusted to give the observed α binding energy. The radius of the Woods-Saxon well describing the target nuclei was chosen to be $R = r_o A^{1/3}$. An r_o of 2.0 was used for all targets; this give a radius which was larger than the physical size of the core A. This larger radius could correspond to the transferred α-particle existing at the surface of the core.

Table 1. Optical model potentials used in the DWBA calculations.

Target	Projectile	$E_{proj.}$ MeV	V MeV	r^a_R fm	a_R fm	W MeV	r^a_I fm	a_I fm	r^a_C fm	Potential
^{16}O	α	65	89.3	1.56	.57	27.7	1.39	.72	1.2	A[b]
^{15}N	α	40.5	279	1.22	.65	17.6	1.55	.65	1.2	B[c]
^{14}N	α	40.5	279	1.22	.65	17.6	1.55	.65	1.2	B[c]
^{13}C	α	40.5	170	1.47	.55	20.8	1.56	.35	1.2	C[c]
^{12}C	α	40.5	36.7	1.80	.41	7.6	1.96	.66	1.2	D[c]
^{11}B, ^{10}B, ^{9}Be	α	46	194	1.38	.60	24	1.60	.60	1.2	E[d]
^{12}C	^{9}Be	50	35.2	1.72	.92	12	2.65	.50	1.2	AA[e]

Decreasing r_o from 2.0 to 1.2 had only a small effect on the shape of the fits but caused a strong decrease in the magnitude of the cross section.

Although ^{8}Be is unbound by 92 keV, it is effectively bound by its Coulomb barrier during the reaction time. To generate a bound state wave function for the calculations, it was assumed that the ^{8}Be internal wave function varied smoothly and slowly when its binding energy was changed from -92 keV to +10 keV. The ^{8}Be internal wave function was calculated for an α particle bound to a second one by 10 keV in a Woods-Saxon well with a radius of 3.2 fm. (Changing the binding energy from 100 keV to 10 keV produced no change in the shape of the calculated cross sections and only a 7% decrease in their magnitudes.)

In deriving experimental spectroscopic factors, we have tried to maintain consistent criteria for choosing the center-of-mass angle at which to relate experiment and theory, since the shapes of the calculated and experimental cross sections are not identical. If an experimental maximum existed in the angular distribution, the theoretical and experimental yields were compared at this angle. For the flatter angular distributions, the spectroscopic factor was calculated at a data point between $\theta_{c.m.}$ = 25 and 35°. The values of the theoretical α-particle spectroscopic factors $S^L(B\to A+\alpha)$ in Eq. 1 were taken from Rotter[1] and from Kurath.[2] For $S(^8Be\to\alpha+\alpha)$ the theoretical value of 1.5 was taken from Kurath.[2] The calculated cross sections and the experimental data for all targets are given in Ref. 11 while only the ^{16}O target data and fits are discussed below.

A comparison of the (α,^{8}Be) experimental (symbols) and absolute calculated (solid curves) cross sections for transitions populating the ^{12}C ground state and several excited states is shown in Fig. 1. The similar magnitudes of the experimental and calculated cross sections demonstrate good agreement between the theoretical α-particle spectroscopic factors and experiment. The shapes of the theoretical cross sections reproduce some of the features of the experimental data - most notably the relative spacing and magnitude of the two forward maxima in the ground state angular distribution. Furthermore, the damping of the oscillatory character observed experimentally in the L = 2 and L = 4 angular distributions, compared to that of the L = 0 ground state, is also reproduced by the calculations.

In Fig. 2 are shown ratios R^{abs} of experimental to theoretical S_α where R^{abs} is defined by:

$$R^{abs} = \frac{S(exp)}{S(theory)} = \frac{d\sigma/d\Omega\ (\theta)_{exp}}{d\sigma/d\Omega\ (\theta)_{th}} .$$

For consistency, Kurath's theoretical α-particle spectroscopic factors[2] are used for all targets. In general these ratios lie below the dashed line at R^{abs} = 1.0, but deviate from it by less than 50%. (Of course this comparison is very sensitive to systematic errors either in the experimental data or in the reaction calculations; an example of the latter is that the magnitude of the calculated cross section is affected by the value of r_o used in calculating the bound state wave functions). The ^{6}Li

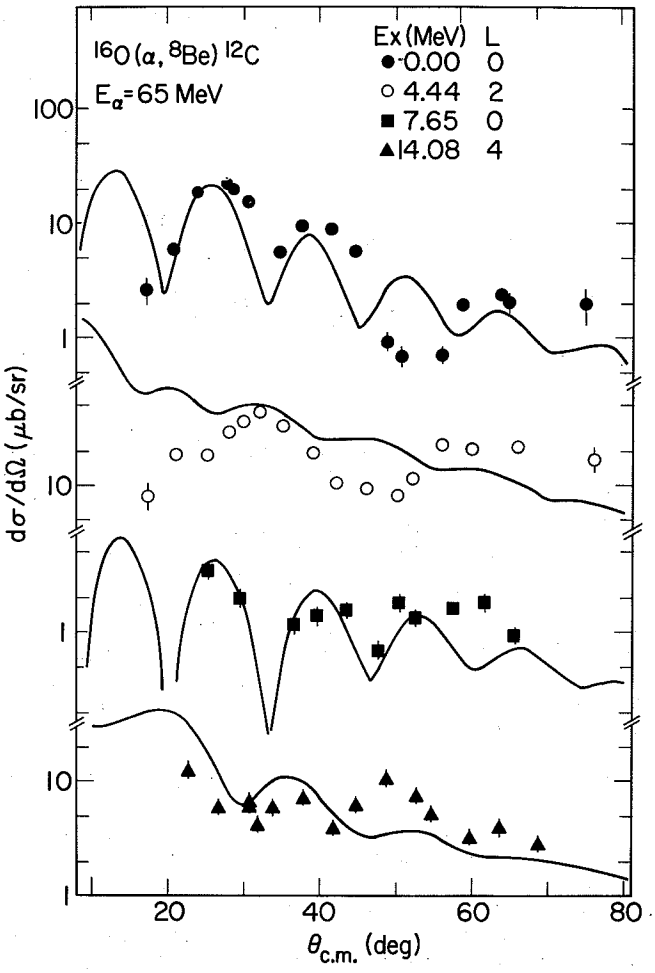

Fig. 1. Absolute experimental (symbols) and calculated (solid curves) (α,^{8}Be) cross sections at E_α = 65 MeV for transitions populating the ^{12}C(g.s.) and several excited states. A statistical error is given if it exceeds the height of the data point. In addition, the width of each data point corresponds to the angular acceptance of the ^{8}Be identifier used in measuring that point.

(XBL 7512-9930)

(g.s.) point is off-scale because of its very small theoretical S_α.

In order to minimize systematic errors, the above ratio of spectroscopic factors, R^{abs}, was divided by the ratio for the ground state transition. The ratio R^{rel} is defined by:

$$R^{rel} = \frac{R^{abs}\ (B\to A+\alpha)}{R^{abs}\ (B\to A(g.s.)+\alpha)} .$$

Part b of Fig. 2 presents this relative ratio of S_α; R^{rel} is again plotted against the final state populated. Better agreement between experiment and theory is seen in Fig. 2b in that the values of R^{rel} cluster closer to 1 than those for R^{abs} in Fig. 2a with only four values of R^{rel} farther than ±50% from unity; the ^{6}Li(g.s) point is again off scale.

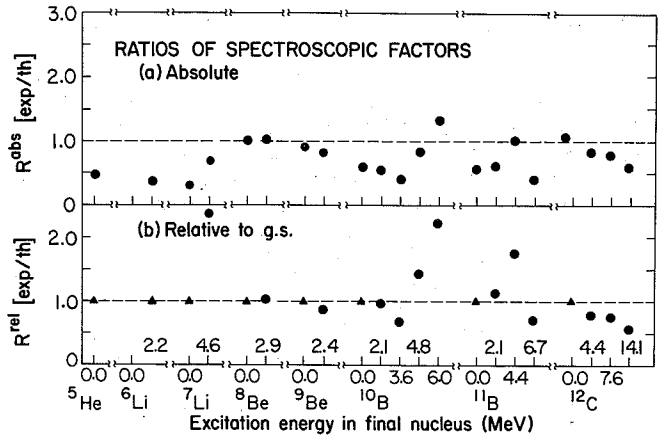

Fig. 2. (a) A comparison of the ratios of experimental to Kurath's[2] theoretical spectroscopic factors [$R^{abs} \equiv S(exp)/S(theory)$]. (b) A comparison of these ratios relative to the ground state ratio for each target (see discussion in text). Note that the ratio (R^{rel}) of S_α relative to the 2.2 MeV state in ^{6}Li is given for $^{10}B \rightarrow {}^{6}Li + \alpha$. In both parts (a) and (b), the ^{6}Li(g.s.) point is off-scale because of its very small theoretical S_α.
(XBL 7512-9926)

The selectivity and good quantitative agreement with theoretical predictions illustrate that the (α,^{8}Be) reaction is a useful spectroscopic probe with which to measure the extent of α-clustering in nuclei.

Footnotes and References

*Condensed from LBL-4368, Phys. Rev. C 14, 815 (1976).

†Present address: Nuclear Physics Laboratory, University of Oxford, England.

1. I. Rotter, Fortschr. Phys. 16, 195 (1968).

2. D. Kurath, Phys. Rev. C7, 1390 (1973).

3. K. Bethge, Ann. Rev. of Nucl. Sci. 20, 255 (1970).

4. J. D. Garrett in the Proceedings of the Symposium on Two-Nucleon Transfer and Pairing Excitations, Argonne Physics Division Informal Report PHY-1972H 232 (1972).

5. R. M. DeVries, Phys. Rev. C8, 951 (1973).

6. B. G. Harvey, J. R. Meriwether, J. Mahoney, A. Bussiere De Nercy and D. J. Horen, Phys. Rev. 146, 712 (1966). See University of California Radiation Laboratory Report-16573 for tabulated data.

7. B. G. Harvey, E. J-M. Rivet, A. Springer, J. R. Meriwether, W. B. Jones, J. H. Elliott, and P. Darriulat, Nucl. Phys. A52, 465 (1964). D. L. Hendrie, private communication.

8. F. G. Perey, optical-model search code (unpublished).

9. B. Zeidman, H. T. Fortune, and A. Richter, Phys. Rev. C2, 1612 (1970).

10. D. P. Stahel, G. J. Wozniak, B. D. Jeltema, M. S. Zisman, R. Jahn, and J. Cerny, The (^{9}Be,^{8}Be) Reaction at 50 MeV, in this Annual Report.

11. G. J. Wozniak, D. P. Stahel, Joseph Cerny, and N. A. Jelley, Phys. Rev. C14, 815 (1976).

THE (α,^{8}Be) REACTION IN THE 2s-1d SHELL

D. P. Stahel, G. J. Wozniak,
M. S. Zisman, and Joseph Cerny

In recent years, there have been several calculations [1-5] of α-spectroscopic factors S_α of 2s-1d shell nuclei with SU(3) shell model wave functions.[6] A comparison of these theoretical values with experimental ones should be a sensitive test of these predictions and thus the validity of the SU(3) shell model. Since the (α,^{8}Be) reaction has been successfully utilized to determine experimental S_α values for 1p shell nuclei,[7] our study of this reaction has been extended to 2s-1d shell targets.

Targets of ^{24}Mg, ^{28}Si, and ^{40}Ca were bombarded with 60 MeV α-particles from the 88-inch cyclotron. The ^{8}Be detection system employed has been described elsewhere.[7] Typical ^{8}Be energy spectra are shown in Fig. 1. Spectra from the ^{24}Mg and ^{28}Si targets exhibit preferential population of the ground state rotational band and some menbers of higher-lying bands in the residual nuclei. This is consistent with the results of SU(3) shell model calculations[2] which show that in a good SU(3) nucleus the α strength can be highly concentrated in a few rotational bands.

In the ^{20}Ne spectrum, there is evidence for population of members of the ground state rotational band up to spin 8^+. No population of the 2^- state of the K = 2 band is observed at this angle. At other angles, however, there is some evidence for weak population of this unnatural parity state, indicating that multi-step reaction processes could be present.[8] In the ^{36}Ar spectrum only the ground state and the first 2^+ and 4^+ states are excited. There is no significant population of higher members of this "ground state rotational band" that were predicted in the SU(3) scheme,[3] although the kinematics would favor transitions to these high spin states. However, in the upper half of the 2s-1d shell, SU(3) may not be a

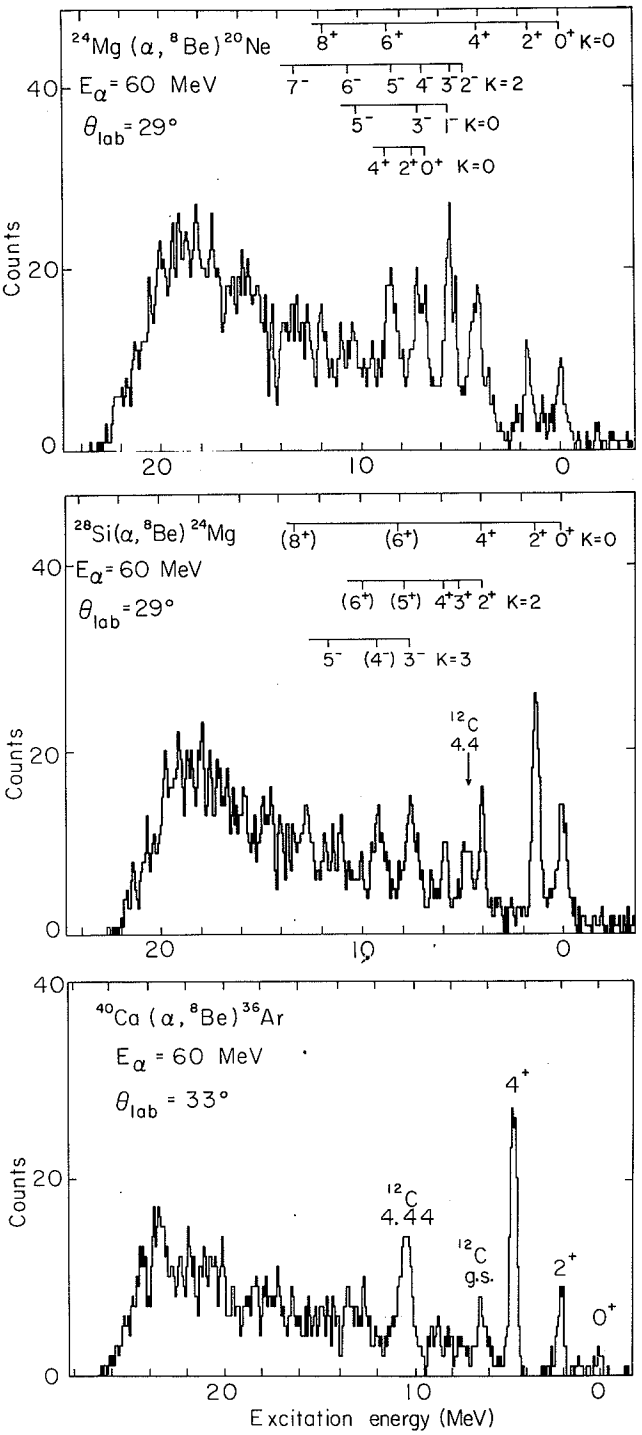

Fig. 1. Energy spectra of ^{8}Be from the (α, ^{8}Be) reactions on ^{24}Mg, ^{28}Si and ^{40}Ca. (XBL 767-8316)

good symmetry.

Angular distributions were measured for the transitions to the ground and several excited states and are shown in Fig. 2. They show forward peaking and diffraction structure that tends to be washed out for the larger ℓ-transfers. Typical peak cross sections of 1-5 μb/sr are observed. For the ground state ℓ = 0 transitions, there is a rather large angular momentum mismatch of about 4ħ for the ^{24}Mg and about 7ħ for the ^{28}Si and ^{40}Ca targets, which causes the cross sections to be much smaller than for the (α, ^{8}Be) reaction on even-even 1p shell targets.[7] The distributions were analyzed using the exact finite-range DWBA code LOLA,[9] assuming a simple ground state α-cluster transfer mechanism. The optical model parameters for the entrance channels were taken from published elastic α-scattering data. For the exit channels, the parameters were determined from elastic ^{9}Be scattering data.[10] The results of some preliminary calculations are shown in Fig. 2. Although the shapes of the distributions are reproduced fairly well, they are out of phase with respect to the data, and the extracted relative

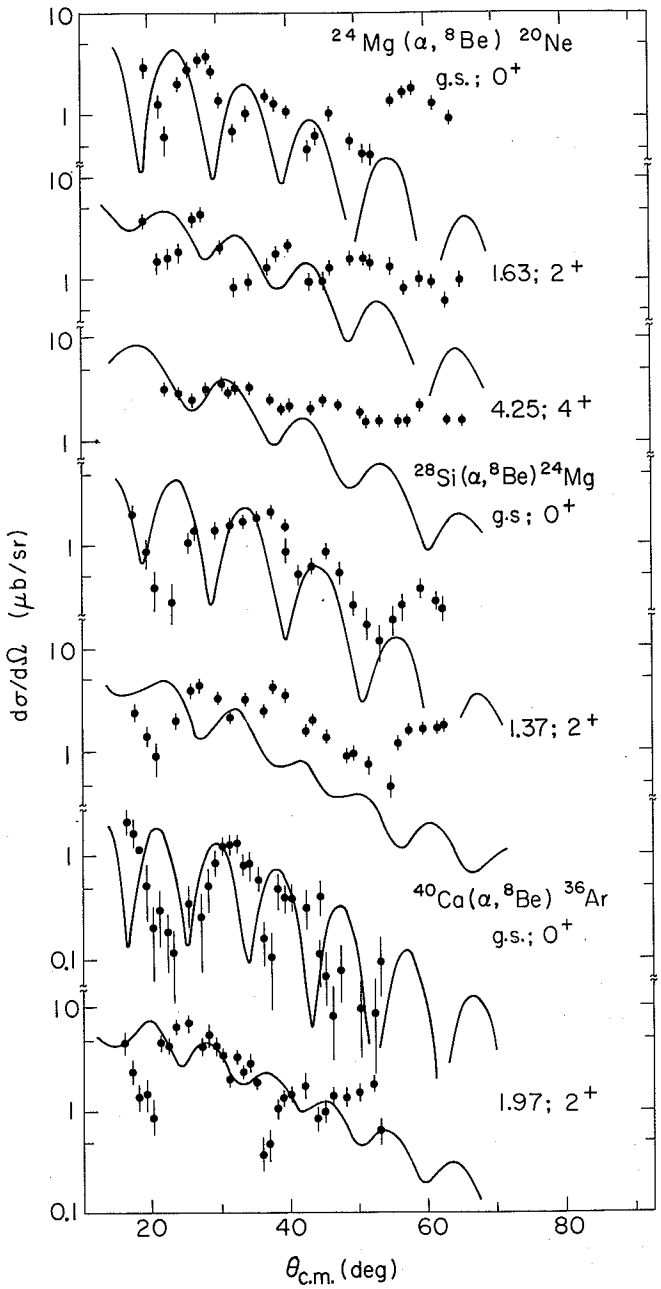

Fig. 2. Angular distributions of ^{8}Be from the (α, ^{8}Be) reaction on ^{24}Mg, ^{28}Si and ^{40}Ca. The solid curves are exact finite-range DWBA calculations. (XBL 766-8317)

S_α values are only in moderate agreement with the SU(3) predictions, as shown in Table 1. This could be due to the momentum mismatch which makes the calculations rather sensitive to variations of parameters. Furthermore, in reactions involving deformed, collective nuclei, multi-step processes, which cannot be handled by first-order DWBA, may play an important role. Thus, a more elaborate (and expensive) coupled-channels analysis may be required before quantitative structure information can be extracted from data such as these.

Table 1. α-spectroscopic factors.

Target nucleus	Final nucleus	Level (MeV)	J^π	Relative S_α	
				$(\alpha, {}^8Be)$	SU(3)[a]
^{24}Mg	^{20}Ne	g.s.	0^+	1.00	1.00
		1.63	2^+	1.29	.13
		4.25	4^+	1.62	.80
^{28}Si	^{24}Mg	g.s.	0^+	1.00	1.00
		1.37	2^+	1.27	1.20
^{40}Ca	^{36}Ar	g.s.	0^+	1.00	1.00
		1.97	2^+	3.95	1.17

[a]Ref. 4 for ^{24}Mg and ^{28}Si; Ref. 3 for ^{40}Ca.

References

1. A. Arima et al., in Adv. in Nucl. Phys., Vol. 5, M. Baranger and E. Vogt, eds. (Plenum Press, New York, 1972).

2. M. Ichimura et al., Nucl. Phys. A204, 225 (1973).

3. J. B. McGrory, Phys. Lett. 47B, 481 (1973).

4. J. P. Draayer, Nucl. Phys. A237, 157 (1975).

5. K. T. Hecht and D. Braunschweig, Nucl. Phys. A244, 365 (1975).

6. M. Harvey, in Adv. in Nucl. Phys., Vol. 1, M. Baranger and E. Vogt, eds. (Plenum Press, New York, 1968).

7. G. J. Wozniak, D. P. Stahel, N. A. Jelley, and J. Cerny, preceding report.

8. J. R. Comfort et al., Phys. Lett. 40B, 456 (1972).

9. R. M. DeVries, Phys. Rev. C 8, 951 (1973).

10. D. P. Stahel, G. J. Wozniak, B. D. Jeltema, M. S. Zisman, R. Jahn, and J. Cerny, The $(^9Be, ^8Be)$ Reaction at 50 MeV, in this Annual Report.

EXOTIC MASS MEASUREMENTS USING THE (^{4}He,^{8}He) REACTION

G. KeKelis, M. Zisman, D. Scott,
R. Jahn, and Joseph Cerny

The four neutron pick-up reaction (^{4}He,^{8}He) is a valuable tool for reaching nuclei far from stability.[1] The 88-inch cyclotron is ideally suited to the measurement of these reactions for two reasons. First, the cyclotron produces sufficientenergy alpha beams to perform reactions with Q-values of -50 to -60 MeV. Second, the magnetic spectrometer provides the large solid angle and sophisticated detection system required to measure cross sections in the 1-nb/sr region.

Most of the emphasis of the present experimental program has been directed to reducing extraneous background in the magnetic spectrometer to the sub-nanobarn level. This background is produced by three processes. First, γ-rays and neutrons produced at the Faraday cup cause misidentification in time-of-flight measurements by producing between-beam-burst counts in the plastic scintillator "start" signal of the focal plane and the NE111-photomultiplier "stop" signal. The problem has been greatly alleviated by using a gas proportional counter[2] as the "stop" signal since it is relatively insensitive to γ rays and neutrons. The second contribution to the background is the intense elastic scattering. At small angles the elastics produce count rate problems as well as scattering from the walls of the spectrometer, thereby entering the focal plane detector with peculiar trajectories. The last identification problem is due to high energy protons, deuterons, and tritons which are lightly ionizing and easily misidentified. These last two problems have been eliminated by introducing a new focal plane detector designed by B. Harvey[3] which allows double ΔE and double position (trajectory) measurements.

The ^{58}Ni(^{4}He,^{8}He)^{54}Ni reaction was investigated with the above system before the new focal plane detector and proportional counter time-zero

system were introduced. The resulting ^{8}He spectrum is shown in Fig. 1. Background in this spectrum is on the order of the cross section of interest, that is 5-10 nb/sr. However, it does appear that a peak with a cross section of about 8 nb/sr is located at the expected position, as well as a possible excited state at 2 MeV excitation. The peak location is based on the mass of ^{54}Ni as predicted by Harchol et al.,[4] This experiment is being repeated using the new focal plane detector and time zero systems in order to produce a clean spectrum.

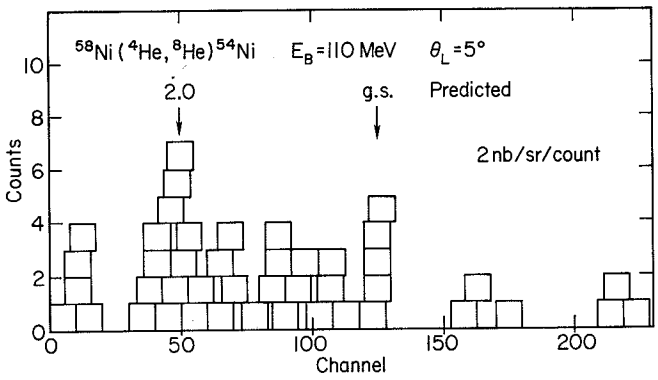

Fig. 1. Energy spectrum of the ^{58}Ni(^{4}He,^{8}He)^{54}Ni reaction at E_L = 110 MeV. The predicted ground state location was taken from Ref. 4.
(XBL 764-2744)

References

1. J. Cerny, in Proceeding of the International Conference on Reactions Between Complex Nuclei, edited by R. L. Robinson et al., (North-Holland, Amsterdam, 1974), Vol. 2, p. 483.

2. G. Kekelis, G. Gabor, D. Scott, and C. K. Gelbke, A Proportional Counter Time Zero System, in this Annual Report.

3. B. G. Harvey, J. Mahoney, and R. F. Burton, Spectrometer Focal Plane Detector System, in this Annual Report.

b. Heavy Ions

STUDIES OF ^{4}H AND ^{5}H BY THE TWO-PRONTON PICKUP REACTION (^{6}Li,^{8}B)

R. B. Weisemiller, K. H. Wilcox,* D. Ashery,†
G. J. Wozniak, and Joseph Cerny

Although the heavy hydrogen isotope ^{4}H has been the focus of numerous theoretical and experimental investigations, considerably less information is available on the level structure of ^{5}H.[1,2] In an attempt to obtain further information on ^{5}H, we have studied and compared results from the ^{6}Li(^{6}Li,^{8}B)^{4}H and ^{7}Li(^{6}Li,^{8}B)^{5}H reactions. This two-proton transfer reaction, which has been extensively investigated in the 1p-shell region,[3] offers a particularly simple way of probing these isotopes.

Lithium ions (produced in an internal PIG ion source) were accelerated in the 88-inch cyclotron. A 93.3-MeV beam energy was chosen for this experiment because of the extreme kinematic conditions and the highly negative Q-values (which for the simplest particle breakup thresholds correspond to -17.77 MeV for the ^{4}H system and -25.02 MeV for the ^{5}H system). ^{8}B reaction products were detected in a standard three-counter-telescope; adequate identification of the ^{8}B isotopes was accomplished off-line by cross-gating the ratio of the two independent particle identification signals generated by each of the two thin transmission detectors. At each set of angles data were collected sequentially from a ^{7}Li, ^{6}Li, ^{12}C, and ^{16}O target. Since carbon and oxygen are major target contaminants, this procedure assured an accurate calibration of the spectra from reactions induced on lithium.

An energy spectrum of the ^{6}Li(^{6}Li,^{8}B)^{4}H reaction is shown in Fig. 1a. The smooth curve corresponds to the phase-space distribution for the three-body breakup ^{6}Li + ^{6}Li → ^{8}B + t + n; the thresholds for other multi-body breakup modes are indicated. The observed enhancement above this phase-space distribution can be attributed to the known[1] t + n final state interaction corresponding to transitions to the 2^- ground state of ^{4}H with possible contributions from transitions to probable 1^- and 0^- levels in ^{4}H (these states are all broad). This enhancement was seen with appropriate kinematics at all of the four angles studied, and assuming that all of the counts above phase space correspond to this transition, then the observed yield is ~4 μb/sr (c.m.).

In contrast to these results, the spectrum of the ^{7}Li(^{6}Li,^{8}B)^{5}H reaction, displayed in Fig. 1b, shows no obvious evidence for a strong final-state interaction in the ^{5}H system; this spectrum was accumulated for a total of 6200 μC (^{6}Li^{3+}), a factor of 6.5 more than for the ^{4}H spectrum. The counts seen above the smooth curve drawn in Fig. 1b, which corresponds to the phase-space distribution for the four-body breakup ^{6}Li + ^{7}Li → ^{8}B + t + n + n, can arise from contributions from other multi-body breakup channels, such as the three-body breakup ^{8}B + t + (2n) or ^{8}B + ^{4}H + n, or from the (^{6}Li,^{8}B) reaction on carbon and oxygen contaminants in the ^{7}Li target. This yield above the phase-space curve corresponds to ~100 nb/sr-MeV (c.m.) in contrast to the ^{4}H transition yield of ~1 μb/sr-MeV (c.m.). As such there is no indication in these data, or in the

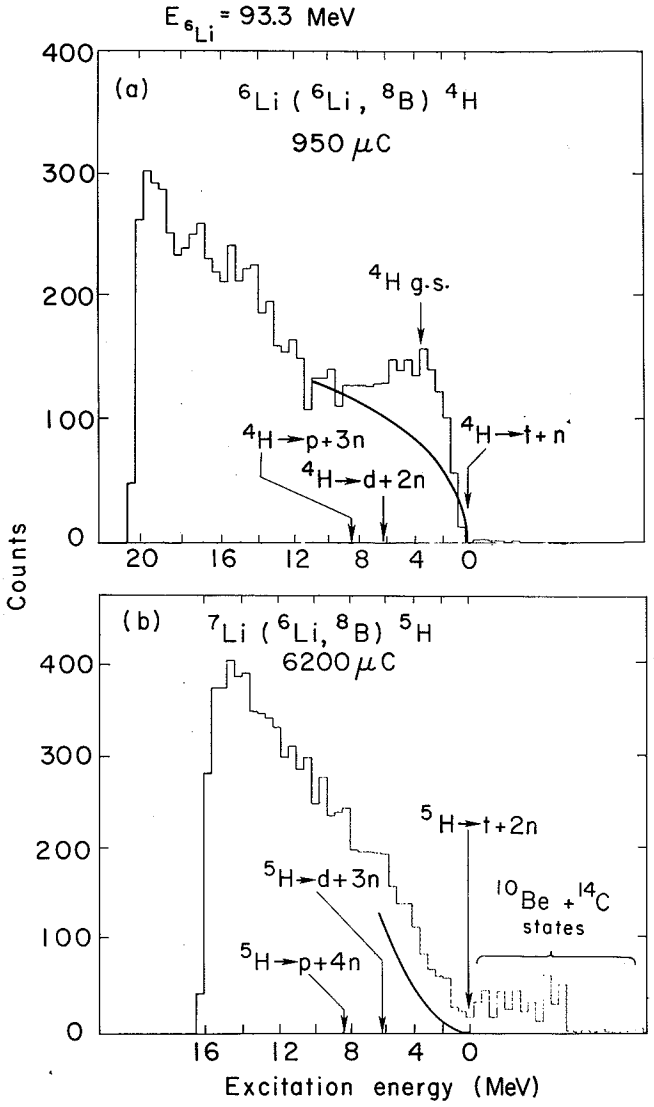

Fig. 1. (a) An energy spectrum of the $^{6}Li(^{6}Li, ^{8}B)$ ^{4}H reaction ($E(^{6}Li) = 93.3$ MeV) collected at $\theta_{lab} = 14.7°$ for 950 μC. These data are four channel sums and the curve corresponds to three-body phase-space (see text). (b) An energy spectrum of the $^{7}Li(^{6}Li,^{8}B)^{5}H$ reaction ($E(^{6}Li) = 93.3$ MeV) collected at $\theta_{lab} = 14.7°$ for 6200 μC. These data are four channel sums and the curve corresponds to four-body phase-space. The ^{10}Be and ^{14}C levels arise from ^{12}C and ^{16}O contaminants in the target (see text).
(XBL 768-3907)

investigation at three other angles, for any narrow ^{5}H state, which agrees with the results from studies of the ^{9}Be $(\alpha,^{8}B)^{5}H$ reaction[4] and the ^{3}H (t,p) ^{5}H reaction.[5]

Footnotes and References

*Present address: Energy and Resources Group, University of California, Berkeley, CA 94705.

†Present address: University of Tel-Aviv, Israel.

1. For mass 4 see S. Fiarman and W. E. Meyerhof, Nucl. Phys. A206, 1 (1973).

2. For mass 5 see F. Ajzenberg-Selove and T. Lauritsen, Nucl. Phys. A227, 1 (1974) and references therein.

3. R. B. Weisenmiller, N. A. Jelley, K. H. Wilcox, G. J. Wozniak, and J. Cerny, Phys. Rev. C13, 1330 (1976).

4. R. L. McGrath, J. Cerny, and S. W. Cosper, Phys. Rev. 165, 1126 (1968).

5. P. G. Young, R. H. Stokes, and G. G. Ohlsen, Phys. Rev. 173, 949 (1968).

THE (^{9}Be, ^{8}B) REACTION AND THE UNBOUND NUCLIDE ^{10}Li*

K. H. Wilcox, R. B. Weisenmiller, G. J. Wozniak,
N. A. Jelly,† D. Ashery,‡ and Joseph Cerny

Mass measurements of new highly neutron-excess nuclei provide important tests of the theoretical relations used to predict the limits of nuclear stability and the onset of new nuclear decay modes.[1] Experimental masses in the very light nuclei have proved particularly interesting since large discrepancies have been found between predicted and observed mass-excesses. If one excludes many-neutron systems and hydrogen isotopes, all $T_z = 2$ nuclei in the light elements are nucleon stable and have known masses with the exception of ^{10}Li, which has been established to be particle unbound[2,3] but for which a mass-excess has not been determined. By employing the $|\Delta T_z| = 3/2$ rearrangement reaction, (^{9}Be,^{8}B), we have produced ^{10}Li via the $^{9}Be(^{9}Be,^{8}B)$ ^{10}Li reaction.

A 121 MeV $^{9}Be^{+3}$ beam from the Lawrence Berkeley Laboratory 88-inch cyclotron was used to bombard a 0.68 mg/cm^2 ^{9}Be foil. Beryllium vapor was supplied to the arc by support-gas-induced sputtering of a piece of Be metal located just outside of the arc. ^{8}B exit particles were identified by a detector telescope, subtending a solid angle of 0.3 msr, consisting of two transmission (ΔE) detectors, 53 and 45 μm thick, a 210- μm E detector, and a 500-μm reject detector. The method of data handling has been described previously[4] and involves in part a comparison of two particle identification signals to reduce background; this comparison eliminated ~25% of the ^{9}Be-induced events.

Due to the low yield of the (^{9}Be, ^{8}Be) re-

action, it was necessary to reduce the background from target contaminants and random pulse pileup by additionally requiring the ^{8}B particles to be in coincidence with an event in a recoil telescope. The recoil telescope subtended a solid angle of 15 msr and consisted of ΔE and E detectors of thickness 11 and 48 μm, respectively, backed by a 500-μm reject detector. Figure 1 shows schematically the location of the detectors in the scattering chamber. A large recoil solid angle is required because the recoiling ^{10}Li nucleus decays in flight to ^{9}Li + n, resulting in a ^{9}Li maximum breakup cone angle of about 10 degrees in the laboratory. The thickness of the ΔE detector was chosen to eliminate background from the $^{12}C(^{9}Be, ^{8}B)^{13}B$ and $^{16}O(^{9}Be, ^{8}B)^{17}N$ reactions, induced on target contaminants, by stopping the ^{13}B and ^{17}N recoil nuclei while permitting the ^{9}Li recoil daughters to pass through into the E detector. Fast timing techniques were used in establishing the coincidence between the ^{8}B and its associated recoil and to eliminate inter-beam-burst pileup. (A more detailed discussion of the experimental technique is given in Ref. 5.).

An energy calibration for the $(^{9}Be, ^{8}B)$ reaction was obtained by observing at small angles the $^{40}Ca(^{6}Li, ^{8}B)\ ^{38}Ar$ reaction to the ground and first excited (2.17 MeV) states of ^{38}Ar, initiated by an 80.6 MeV $^{6}Li^{+2}$ beam. In addition the $^{28}Si(^{6}Li, ^{8}B)^{26}Mg$ and $^{16}O(^{6}Li, ^{8}B)^{14}C$ ground state reactions were used. These reactions[6] have reasonable cross sections (5-10 μb/sr) and populate discrete states yielding ^{8}B with energies between 62 and 71 MeV, close to the energy of ~ 75 MeV expected from the $^{9}Be(^{9}Be, ^{8}B)^{10}Li$ ground state reaction at 14°.

The $^{12}C(^{9}Be, ^{8}B)^{13}B$ reaction was also studied separately, both to obtain a calibration point at higher energies and to study the yield of the $(^{9}Be, ^{8}B)$ reaction on a major target contaminant. A ^{8}B energy spectrum from this reaction at 14° is shown in Fig. 2(a). The ground state population is too low (~ 200 nb/sr) to be useful for calibration purposes. However, the sharp peak at $E_{lab} = 81$ MeV provided a useful point. This, together with the $(^{6}Li, ^{8}B)$ data, established an accurate energy calibration.

A spectrum of all the ^{8}B data from reactions on the ^{9}Be target, representing 6950 μC of ^{9}Be beam (fully stripped), is shown in Fig. 2(b). The same data, with the additional requirement that each count be in coincidence with an event in the recoil detector (located at 33° in the laboratory), are seen in Fig. 2(c). With this requirement, elimination of ^{8}B nuclei arising from reactions on major target contaminants was essentially complete. Further, although isotope resolution in the recoil particle identification spectra was poor, it was adequate to show that all the associated recoils from the events in Fig. 2(c) appear in the region expected for ^{9}Li nuclei.

We have assumed of necessity that the observed peak arises predominantly from the population of ^{10}Li in its ground state. (Based on simple particle-particle, hole-hole theorems, the two lowest states of ^{10}Li could be very similar to those of ^{12}B, in which they are separated by 0.95 MeV.) The width of this peak, approximately 1.2 ± 0.3 MeV FWHM, (c.m.), is of the correct order of magnitude for a single unbound state on the

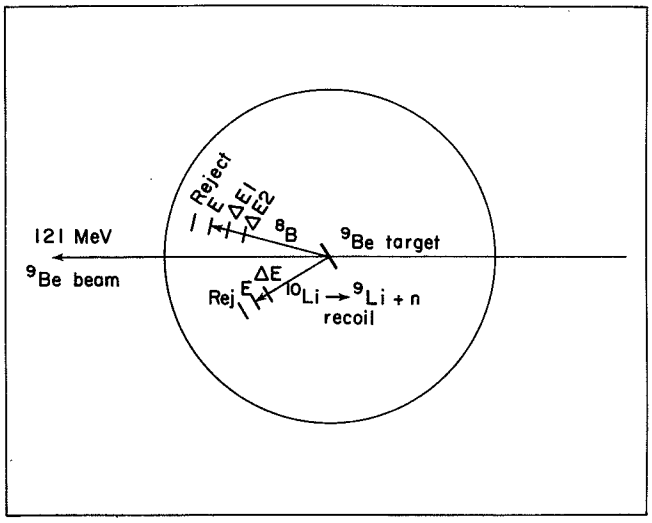

Fig. 1. Schematic drawing of the scattering chamber setup showing orientation of the detectors and target; the solid angles of the ^{8}B and recoil telescopes were 0.3 and 15 msr, respectively.
(XBL 758-3663) [Part (a) only]

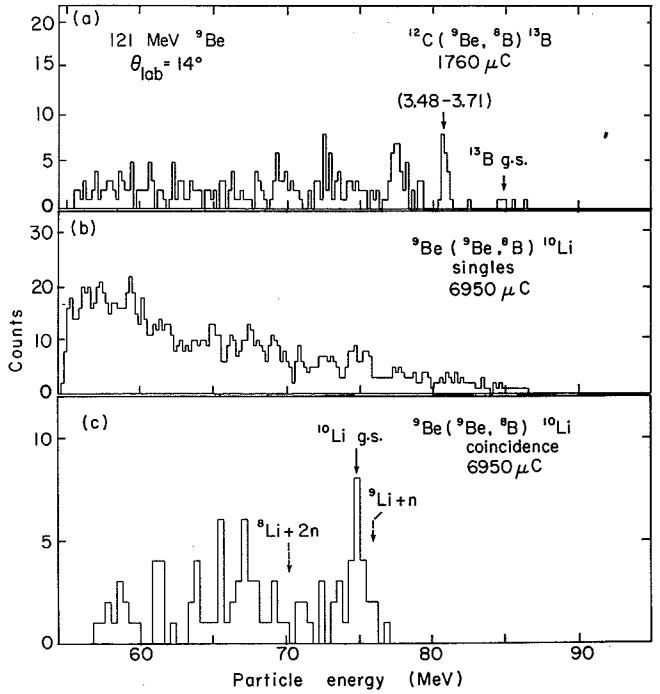

Fig. 2. Several energy spectra resulting from the bombardment of ^{12}C and ^{9}Be targets by a 121 MeV ^{9}Be beam and observed at 14° in the laboratory; (a) The $^{12}C(^{9}Be, ^{8}B)\ ^{13}B$ reaction; (b) the $^{9}Be(^{9}Be, ^{8}B)\ ^{10}Li$ reaction singles events, and (c) a two-channel sum of the $^{9}Be(^{9}Be, ^{8}B)\ ^{10}Li$ reaction coincidence events. (XBL 758-3664)

basis of neutron-tunneling calculations. At this angle of 14° the cross section for population of the ground state of ^{10}Li was 30 nb/sr (c.m.). The observed Q value for the ^{9}Be(^{9}Be,^{8}B)^{10}Li ground state reaction was -34.06 ± 0.25 MeV, corresponding to a mass-excess for ^{10}Li of 33.83 ± 0.25 MeV. The nucleus ^{10}Li is thus unbound to ^{9}Li plus a neutron by 0.80 ± 0.25 MeV (using the recent remeasurement[7] of the ^{9}Li mass), somewhat more unbound than the current prediction[8] of 0.21 MeV based on the Garvey-Kelson method.

An attempt was also made with the (^{9}Be,^{8}B) reaction to determine the mass-excess of the T_z = 5/2 nuclide ^{15}B by reactions on a ^{14}C target. A 121 MeV ^{9}Be beam was again used, bombarding a 100 μg/cm^2 carbon target enriched to ~ 80% in ^{14}C. The experimental technique was similar to that described for the ^{9}Be(^{9}Be,^{8}B)^{10}Li reaction, except that a single recoil counter of about 20 μm thickness, backed by a reject detector, was used. ^{8}B particles from the relatively high-yield ^{12}C(^{9}Be, ^{8}B)^{13}B reaction were not sufficiently eliminated by the recoil angle requirement to permit positive identification of any peaks due to the formation of ^{15}B. An upper limit of 50 nb/sr (c.m.) can be set for the ^{14}C(^{9}Be,^{8}B)^{15}B ground state reaction at 14° in the laboratory. (Also see Ref. 5.)

These results on ^{10}Li add another $|\Delta T_z|$ = 3/2 nuclear rearrangement reaction as demonstrated tools to employ (albeit not always successfully) in studying the spectroscopy of new highly neutron-excess light nuclei.

Footnotes and References

*Condensed from Phys. Letters 59B, 142 (1975).

†Present Address: Nuclear Physics Laboratory, University of Oxford, England.

‡Permanent Address: Tel-Aviv University, Israel.

1. J. Cerny, Proc. Int. Conf. Reactions between complex Nuclei, Nashville, 1974, ed. R. L. Robinson, F. K. McGowan, J. B. Ball, and J. H. Hamilton, (North-Holland, Amsterdam/American Elsevier, N. Y., 1974) Vol. 2, p. 483.

2. A. M. Poskanzer, S. W. Cosper, E. K. Hyde, and J. Cerny, Phys. Rev. Letters 17, 1271 (1966).

3. J. D. Bowman, A. M. Poskanzer, R. G. Korteling, and G. W. Butler, Phys. Rev. C9, 836 (1974).

4. K.H. Wilcox, N.A.Jelley, G. J. Wozniak, R. B. Weisenmiller, H. L. Harney, and J. Cerny, Phys. Rev. Letters 30, 866 (1973).

5. K. H. Wilcox, Lawrence Berkeley Laboratory Report No. LBL-4029 (Ph. D. Thesis), 1975 (unpublished.

6. R. B. Weisenmiller, K. H. Wilcox, N. A. Jelley, G. J. Wozniak, and J. Cerny, to be published.

7. E. Kashy, W. Benenson, D. Mueller, R. G. H. Robertson, and D. R. Goosman, Phys. Rev. C11, 1959 (1975).

8. N. A. Jelley, J. Cerny, D. P. Stahel, and K. H. Wilcox, Phys. Rev. C11, 2049 (1975).

THE (^{9}Be, ^{8}Be) REACTION AT 50 MeV

D. P. Stahel, G. J. Wozniak, B. D. Jeltema,
M. S. Zisman, R. Jahn, and Joseph Cerny

In recent years, single nucleon transfer reactions induced by light heavy ions, such as ^{7}Li, ^{12}C, ^{13}C, ^{14}N, and ^{16}O, have gained increased attention for nuclear reaction and structure investigations. The (^{9}Be, ^{8}Be) reaction has not been studied, mainly because of a lack of a suitable ^{8}Be detection system. This reaction, however, has several experimental advantages over other heavy ion one-neutron stripping reactions. Because the ^{8}Be identifier[1] eliminates ^{8}Be* events, the ^{8}Be energy spectra lack the shadow peaks observed in other reactions that produce exit particles with bound excited states. Furthermore, the ^{8}Be events can be clearly distinguished from the more copious elastically and inelastically scattered ^{9}Be particles. With these advantages in mind, we have surveyed the (^{9}Be,^{8}Be) reaction on several 1p and 2s-1d shell targets.

The ^{9}Be(2+) ions, obtained from a PIG source, were accelerated by the 88-inch cyclotron to 50 MeV. Beam currents of 100-200 nA (as 4+) were readily delivered on target. The ^{8}Be particles ($\tau \sim 10^{-16}$s) were detected by means of their breakup α particles. A position sensitive detector (PSD) was used to measure the direction and energy of the original ^{8}Be and split ΔE detectors were employed to reduce random α-α background. An energy resolution of ~ 400 keV (FWHM) was achieved with an angular acceptance of ~ 1°.

Simultaneously with the ^{8}Be particles, ^{9}Be elastic scattering was measured utilizing a single 5×1 cm^2 PSD. The collimator consisted of a tantalum plate with 8 vertical slits, each with a horizontal acceptance angle of ~ 0.5°. The energy signal was routed by the position signal thus allowing us to simultaneously measure elastic scattering at 8 angles each separated by 1°.

^{8}Be energy spectra of the (^{9}Be, ^{8}Be) reaction on ^{12}C, ^{16}O, ^{28}Si and ^{40}Ca are shown in Fig. 1. They exhibit clearly the high selectivity of the reaction. Only states with an appreciable single-particle strength as known from (d,p) reactions are populated. In order to test whether current direct reaction models, such as the DWBA, can account for

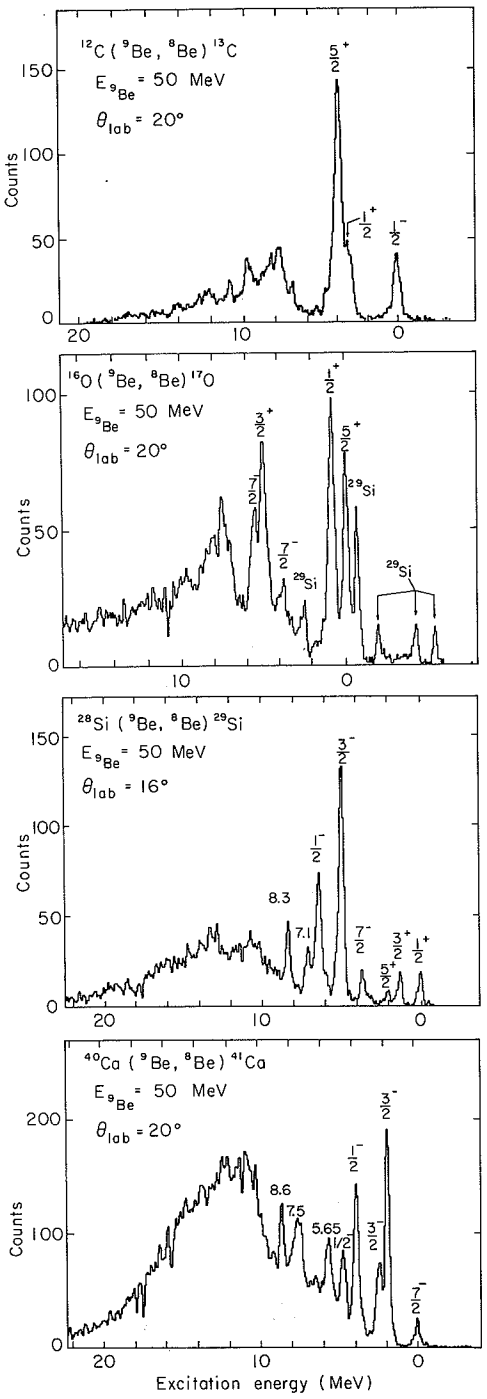

Fig. 1. Energy spectra of the (^{9}Be, ^{8}Be) reaction on ^{12}C, ^{16}O, ^{28}Si and ^{40}Ca. (XBL 767-8313)

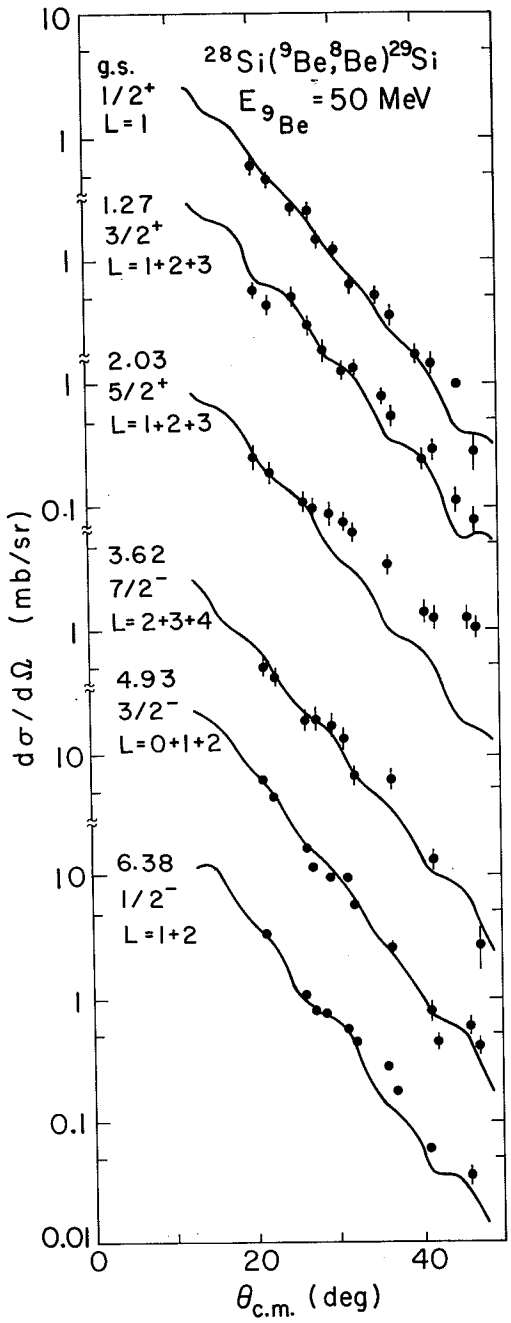

Fig. 2. Angular distributions of ^{8}Be from the ^{28}Si(^{9}Be, ^{8}Be)^{29}Si reaction. The solid lines represent exact finite-range DWBA calculations using optical model potential set V. (XBL 755-8314)

the kinematics of the reaction, angular distributions for the ^{28}Si(^{9}Be, ^{8}Be) ^{29}Si and the ^{40}Ca(^{9}Be, ^{8}Be) ^{41}Ca reactions were measured and are shown in Figs. 2 and 3. Whereas for the ^{28}Si target the distributions display some diffraction structure, those for ^{40}Ca are almost featureless, as is typical of low-energy heavy-ion reactions. The distributions were analyzed in terms of the exact finite-range distored-wave Born-approximation using the computer code LOLA.[2] The optical model parameters were determined by fitting our measured elastic scattering data with the search code GENOA.[3] A list of the extracted potentials is given in Table 1. In the DWBA calculations, the same parameter set was used for the initial and final channels. The results are shown in Figs. 2 and 3, and the extracted spectroscopic factors are listed in Table 2. For the spectroscopic factor of ^{9}Be, the theoretical value[4] of 0.58 was used. For the ^{28}Si target, the shapes of the distributions are well reproduced, and the absolute and relative

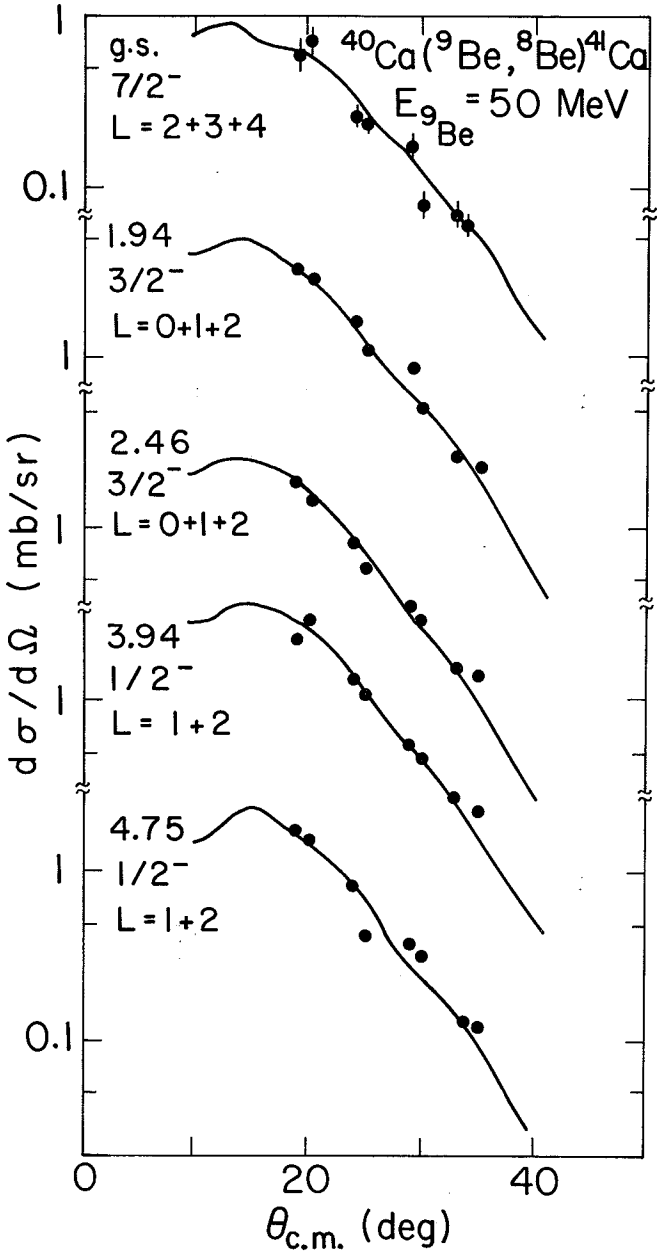

Fig. 3. Angular distributions of ^{8}Be from the ^{40}Ca(^{9}Be, ^{8}Be) ^{41}Ca reaction. The solid lines represent exact finite-range DWBA calculations using optical model potential set VII.

(XBL 766-8315)

spectroscopic factors are in good agreement with the values determined from (d,p) data.[5] Although for the ^{40}Ca target the calculated shapes of the distributions fit the data well and the relative spectroscopic factors agree with the (d,p) values, the magnitude of the predicted cross sections is too large, which is reflected in absolute spectroscopic factors about 3.5 times smaller than the corresponding (d,p) values.[6] A possible explanation for this discrepancy is the fact that the normalization could not be done at the grazing angle of ~12° (c.m.), where the cross section peaks, because of mechanical restrictions. It is known from other heavy ion reactions that DWBA calculations frequently overestimate the cross section at angles greater than the grazing angle. In spite of this problem, the DWBA reproduces correctly the observed Q-value and ℓ-transfer dependence of the cross sections. There is a clear enhancement for transitions with Q-values around $Q_{opt} = 0$. Since the typical ground state Q values for the (^{9}Be, ^{8}Be) reaction are positive, a preferential population of excited states can be observed. In ^{29}Si and ^{41}Ca states up to ~ 8 MeV were strongly populated. The angular momentum matching is such that transitions involving small ℓ-transfers are favored, and the mismatch for large ℓ-transfers results in a significant reduction of the yield, as seen in the reaction to the ground state of ^{41}Ca for which ℓ = 2,3, and 4.

Thus, the (^{9}Be, ^{8}Be) reaction promises to be a useful spectroscopic tool for studying low-spin single-particle states at high excitation, even at tandem energies where the majority of heavy ion neutron transfer reactions do not give large yields.

Table 1. Optical model parameters for 50-MeV elastic ^{9}Be scattering.

Target	V (MeV)	r_{0R} [a] (fm)	a_R (fm)	W (MeV)	r_{0I} (fm)	a_I (fm)	r_{0C} [a] (fm)	Set
^{12}C	30.9	1.84	0.88	8.50	2.78	0.46	1.2	I
	85.5	1.93	0.64	23.7	1.81	0.86	1.2	II
	114.1	1.21	0.88	12.0	2.64	0.52	1.2	III
^{28}Si	35.2	1.83	0.70	6.5	2.66	0.70	1.2	IV
	85.8	1.68	0.64	15.8	2.07	0.85	1.2	V
	209.8	1.28	0.71	38.2	1.74	0.93	1.2	VI
^{40}Ca	70.8	1.42	0.73	9.7	2.06	0.82	1.2	VII
	322.7	1.03	0.77	22.0	1.83	0.89	1.2	VIII

[a] $R = r_0 A_{tgt}^{1/3}$

Table 2. Spectroscopic factors.

Nucleus	Level (MeV)	J^π	(^{9}Be, ^{8}Be) S_{abs}	(^{9}Be, ^{8}Be) S_{rel}	(d,p) [a] S_{abs}	(d,p) [a] S_{rel}
^{29}Si	g.s.	$1/2^+$	0.42	1.00	0.53	1.00
	1.27	$3/2^+$	0.70	1.67	0.74	1.40
	2.03	$5/2^+$	0.11	0.26	0.12	0.23
	3.62	$7/2^-$	0.30	0.71	0.38	0.72
	4.93	$3/2^-$	0.48	1.14	0.56	1.06
	6.38	$1/2^-$	0.51	1.21	0.53	1.00
^{41}Ca	g.s	$7/2^-$	0.27	1.00	0.95	1.00
	1.95	$3/2^-$	0.23	0.85	0.70	0.74
	2.46	$3/2^-$	0.10	0.37	0.25	0.26
	3.94	$1/2^-$	0.20	0.74	0.67	0.71
	4.75	$1/2^-$	0.10	0.37	0.19	0.20

[a] Ref. 5 for ^{29}Si; Ref. 6 for ^{41}Ca.

References

1. G. J. Wozniak, N. A. Jelley, D. P. Stahel, and J. Cerny, A Large Solid Angle Be Identifier, this Annual Report.

2. R. M. DeVries, Phys. Rev. C 8, 951 (1973).

3. F. G. Perey, Optical-Model Search Code Genoa (unpublished).

4. S. Cohen and D. Kurath, Nucl. Phys. A101, 1 (1967).

5. M. C. Mermaz et al., Phys. Rev. C 4, 1778 (1971).

6. D. C. Kocher and W. Haeberli, Nucl. Phys. A196, 225 (1972).

"DOUBLE CHARGE EXCHANGE" REACTIONS $^{26}Mg(^{18}O, ^{18}Ne)$ ^{26}Ne AND $^{24}Mg(^{11}B, ^{11}Li)$ ^{24}Si

G. KeKelis, M. Zisman, Joseph Cerny, D. Scott, R. Jahn,
F. Ajzenberg-Selove, D. Hendrie, M. Buenerd, and C. Olmer

When measuring nuclear masses far from stability, a potentially important technique for reaching unknown masses is the "double charge exchange" reaction. Two such reactions are (^{11}B, ^{11}Li) and (^{18}O, ^{18}Ne). Q-values for these reactions are -40 to -60 MeV for the former and -20 to -30 MeV for the latter.

These reactions have been attempted using the magnetic spectrometer at the 88-inch cyclotron: the first to measure the mass of ^{26}Ne and the second to measure the mass of ^{24}Si. Prior to attempting the $^{26}Mg(^{18}O, ^{18}Ne)$ ^{26}Ne reaction, the $^{24}Mg(^{18}O, ^{18}Ne)$ ^{24}Ne reaction was observed in order to evaluate the reaction cross section for double charge exchange. As shown in Fig. 1, the cross section for the $^{24}Mg(^{18}O, ^{18}Ne)$ ^{24}Ne reaction to the ground state of ^{24}Ne was found to be about 800 nb/sr. In Fig. 2 the spectrum obtained from the $^{26}Mg(^{18}O, ^{18}Ne)$ ^{26}Ne reaction is shown. The ground state cross section has dropped to about 100 nb/sr. The predicted ground state location is between two possible peaks, making a positive identification of the ground state difficult, especially since either peak would correspond to a substantial error in the mass predictions of Jelley et al.[1] or those of Garvey and Kelson.[2] Due largely to the high background, the experiment will be repeated.

The $^{24}Mg(^{11}B, ^{11}Li)$ ^{24}Si was also performed at 114 MeV to attempt to measure the mass of ^{24}Si. Although 15,000 μC of charge were collected at θ_L = 5° and 6°, no discernible peak could be identified. An upper limit for the cross section of the (^{11}B, ^{11}Li) double charge exchange reaction to the ground state of ^{24}Si can therefore be set at 3 nb/sr.

Reactions of this type still appear to us to be very promising for measuring masses such as ^{12}O, ^{30}Mg and ^{34}Si. The major difficulty thus far has been in maintaining sufficient beam on target for the long periods of time required to measure nanobarn cross sections. Efforts are currently being devoted to increasing the amount of "steady-state" beam and to improving our ability to take data at more forward lab angles,[3] where the cross sections are expected to be larger.

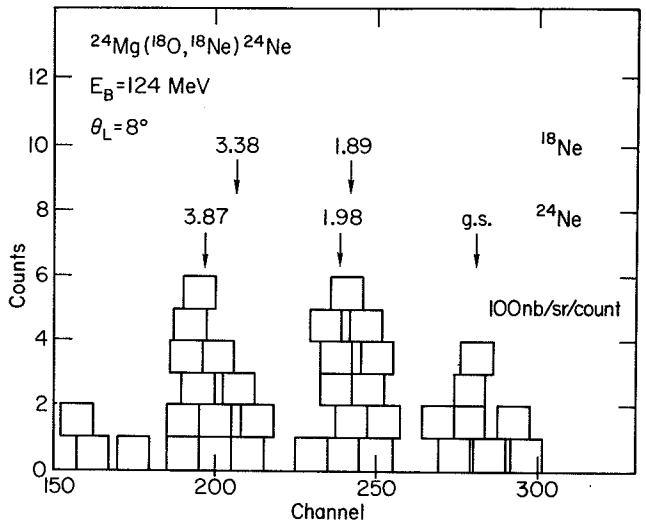

Fig. 1. Energy spectrum of the $^{24}Mg(^{18}O,^{18}Ne)^{24}Ne$ reaction at E_B = 124 MeV. (XBL 764-2746)

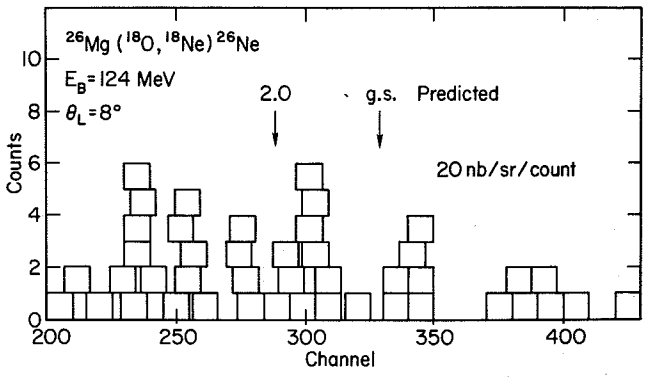

Fig. 2. Energy spectrum of the $^{26}Mg(^{18}O,^{18}Ne)^{26}Ne$ reaction at E_B = 124 MeV. The predicted location was calculated using the ^{26}Ne mass prediction of Jelley et al.[1] (XBL 764-2745)

References

1. N. Jelley, J. Cerny, D. Stahel, and K. Wilcox, Phys. Rev. C4, 2049 (1975).

2. G. Garvey, W. Gerace, R. Jaffe, I. Talmi, and I. Kelson, Rev. Mod. Phys. 41, S1 (1969); I. Kelson and G. Garvey, Phys. Letts. 23, 689 (1966).

3. G. Kekelis, G. Gabor, D. Scott, and C. K. Gelbke, A Proportional Counter Time Zero System, in this Annual Report.

PRODUCTION OF ^{11}Li IN THE (^{11}B,^{11}Li) REACTION ON ^{232}Th

D. K. Scott, M. Buenerd,* D. L. Hendrie, G. KeKelis, J. Mahoney, A. Menchaca-Rocha,† and C. Olmer

Since the theoretical predictions of the masses of exotic light nuclei are based on extrapolations from the valley of stability, it is clear that the most stringent test of these theories will come from the study of nuclei close to the limit of stability. Although spectacular advances in determining this limit for neutron-excess light nuclei have been achieved by means of reactions on heavy nuclei induced by high energy protons[1] and medium energy heavy ions,[2] the measurement of nuclear masses even three or four neutrons removed from stability has progressed very slowly.[3] In a recent experiment[4] to measure the mass-excess of ^{29}Mg by the 3n transfer reaction (^{11}B, ^{8}B) on ^{26}Mg the ground state cross section was only 15 nb/sr. Because of the systematic decrease of cross sections with the transfer of a greater number of uncorrelated nucleons onto light targets, an extension to heavier isotopes is not promising.

The larger cross sections observed with heavy targets have recently been exploited to measure the mass of ^{21}O — also three neutrons removed from stability — by observing the ground state transition in the reactions ^{232}Th(^{22}Ne, ^{21}O) ^{233}U (Ref. 5) and ^{208}Pb(^{18}O, ^{21}O) ^{205}Pb (Ref. 6), in which the cross sections were of order 1μb/sr. An interesting question now is whether these methods can be extended to make mass measurements at the limit of stability, with currently available experimental techniques. In order to explore this possibility we have studied the production of ^{11}Li, the last stable isotope of lithium, by the (-2p+2n) transfer reaction ^{232}Th(^{11}B, ^{11}Li) ^{232}U for which the ground-state Q-value is accurately known from the measured[7] mass-excess of ^{11}Li. The g.s. cross section is compared to that for producing ^{22}O by essentially the same (-2p+2n) transfer process ^{232}Th(^{22}Ne, ^{22}O) ^{232}U which was used recently[5] to measure the mass-excess of ^{22}O.

The QSD spectrometer with a solid angle of 1.3 msr, was used to detect reaction products arising from the bombardment of a ^{232}Th target, 4.7 mg/cm^2 thick, with a ^{11}B beam of 114 MeV produced at the 88-inch cyclotron. In order to identify ^{11}Li particles, produced with cross sections of order nb/sr, it was necessary to make several independent particle identifications. The magnetic rigidity (Bρ) was measured with a position-sensitive Borkowski-Kopp counter, and the specific energy loss (dE/dx) in a second proportional counter. In addition, the time-of-flight (TOF) was determined by a "time-zero" detector consisting of an 870 μg/cm^2 foil of NE 111 at the entrance of the spectrometer and a large plastic scintillator mounted behind the focal plane proportional counters. An identification spectrum is shown in Fig. 1(a). Although the ^{11}Li events appear to be clearly separated, they are contaminated by a TOF tail from the adjacent, more abundant ^{7}Li^{2+} group. These tails are clearly seen

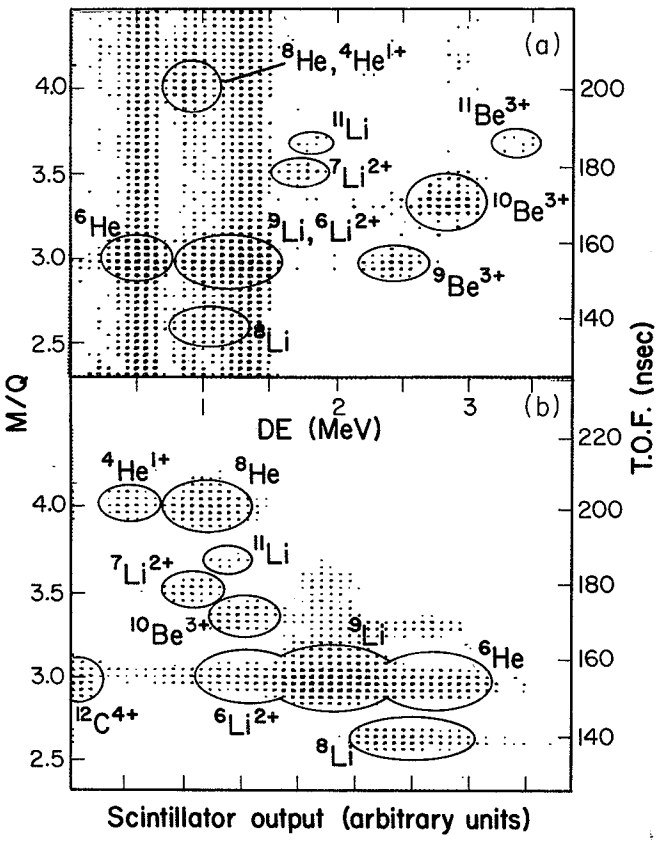

Fig. 1. Identification of particles in the reaction ^{11}B + ^{232}Th at 114 MeV and 20°: (a) on the vertical axis is plotted TOF ∝ M/Q and on the horizontal is DE ∝ M^{2}Z^2/Q^2; (b) plot of TOF versus E as measured by a scintillator in the focal plane. The tail due to pile-up in the TOF, evident in (a), is removed by fast pile-up rejection.

(XBL 762-2322)

for the high-yield reaction products ^{9}Li, ^{6}He and ^{8}He (with an intensity of order 1% of the peak) and originate from "pile-up" in the time-zero detector. The contamination was eliminated by fast pile-up rejection as illustrated in Fig. 2(b), which also shows how the reliability of identification was further improved by measuring the residual energy in the focal plane scintillator. The energy spectra for different particle groups were obtained by multiparameter gating of these 2D-spectra.

Energy spectra for the (^{11}B, ^{9}Li) and (^{11}B, ^{11}Li) reactions on ^{232}Th are shown in Fig.2 at 20°. In spite of the poor resolution of the experiment (≈ 0.5 MeV), it is clear that the two proton transfer selectively populates the g.s. of ^{234}U (in which there are ≈ 10 levels in the first MeV of excitation). The differential cross section for this group was 5.8 μb/sr. The spectrum for (^{11}B, ^{11}Li) is shown in Fig. 2(b) with the predicted ground state for a Q-value of ≈ -31 MeV corresponding to the measured mass-excess[5] of -40.94 for ^{11}Li. The spectrum extends to the ground state region, with a cross section of 2.7 nb/sr. In view of the production cross section in the g.s of 1.2 μb/sr for the (^{22}Ne, ^{22}O) reaction it is interesting to see if this variation of three orders of magnitude in the "double-exchange" cross section can be accounted for theoretically, in order to test the feasibility of extending the technique to the measurement of other nuclei at the limit of stability.

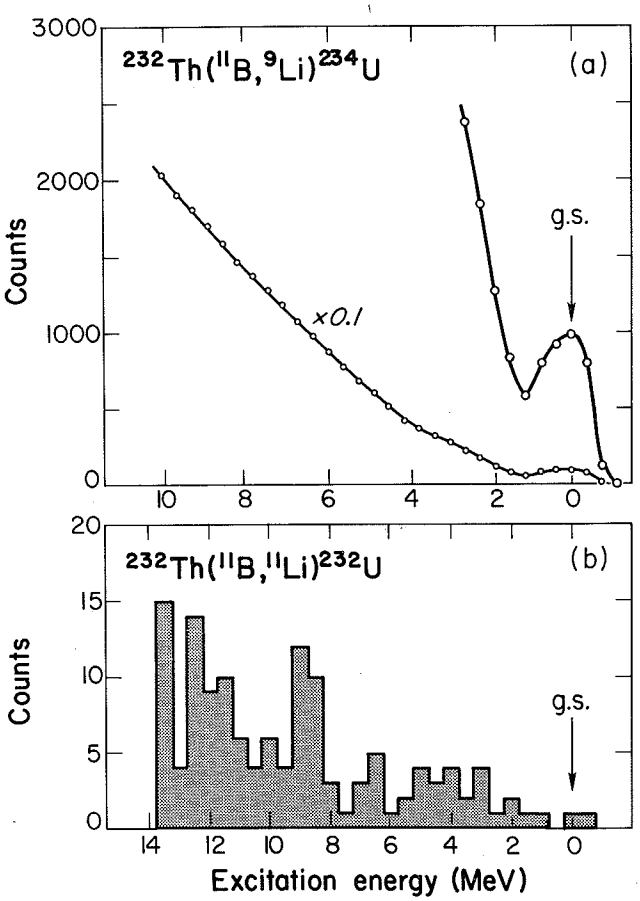

Fig. 2. Energy spectra for the reactions
(a) ^{232}Th(^{11}B, ^{9}Li) ^{234}U and
(b) ^{232}Th(^{11}B, ^{11}Li) ^{232}U at 114 MeV and 20°. The arrows locate the production of the final nuclei in their ground states. (XBL 762-2304)

The reaction mechanism for multinucleon transfer reactions of the type discussed here contains both direct and statistical features. Although the differential cross sections peak at the grazing angle for direct transfer, the observation that the total production cross section at this angle for a series of isotopes depends exponentially on the ground state Q-value has a natural explanation in the statistical model;[8] then for the reaction $x+A \rightarrow y+B$,

$$\sigma = \sigma_0 \exp\left[\left(\frac{a_x + a_A}{E_i - V_{xA}}\right)^{1/2}(Q_{yB} + \Delta E_c)\right] \quad (1)$$

where "a" is 0.05 times the mass number of x or A, E_i is the incident energy, V_{xA} the Coulomb barrier, Q_{yB} the ground state Q-value for the channel y + B, and ΔE_c is the change in Coulomb energy between the initial and final channels. In the production of a series of isotopes, only Q changes, accounting for the exponential dependence. We use Eq. (1) as a rough guide for the systematics of g.s. cross sections; obviously in transitions to individual states, variations due to shell and pairing energy effects will be encountered.

For reactions induced by ^{22}Ne at 174 MeV, and ^{11}B at 114 MeV on ^{232}Th, the coefficient $[(a_x + a_A/E_i - V_{xA})]^{1/2}$ has approximately the same value of 0.42. This value is also in reasonable agreement with the empirical value of 0.58 determined by Eq.(1) from the ratio of approximately 50 for the total and ground state[5] cross sections observed for the production of ^{20}O and ^{22}O. We therefore also use the value of 0.58 to predict a ratio for the reactions (^{11}B, ^{9}Li) and (^{11}B, ^{11}Li), with Q-values of ≈ -18 and -31 MeV respectively, of 1800 in good agreement with our experimental result of 5.8 b/2.7 nb. ≈ 2150.

Accepting $d\sigma/d\Omega \approx |nb|sr$ as an experimental limit, it seems that multinucleon transfer reactions induced by neutron excess heavy-ion beams on heavy targets present a feasible method of measuring the mass excess of exotic light nuclei at the limit of stability.

Footnotes and References

*Permanent Address: Instituto de Fisica, U.N.A.M., Mexico.

†Permanent Address: Institute des Sciences Nucléaires, Grenoble, France.

1. J. D. Bowman, A. M. Poskanzer, R. G. Korleting and G. W. Butler, Phys. Rev. C9, 836 (1974) and refs. therein.

2. A. G. Artukh, V. V. Avdeichikov, G. F. Gridnev, V. L. Mikheev, V. V. Volkov, and J. Wilcynski, Nucl. Phys. A176, 284 (1971) and refs. therein.

3. For a recent review, see J. Cerny, Reactions. Between Complex Nuclei, ed. R. C. Robinson, F. K. McGowan and J. B. Ball (North Holland, Amsterdam, (1974) Vol. 2, p. 483.

4. D. K. Scott, B. G. Harvey, D. L. Hendrie, L. Kraus, C. F. Maguire, J. Mahoney, Y. Terrien and K. Yagi, Phys. Rev. Lett. 33, 1343 (1974).

5. A. G. Artukh, G. F. Gridnev, V. L. Mikheev, V. V. Volkov and J. Wilzynski, Nucl. Phys. A192 (1970) 170.

6. G. C. Ball, W. G. Davies, J. S. Forster and H. R. Andrews, Phys. Lett. 60B, 265 (1976).

7. C. Thibault, R. Klapisch, C. Rigaud, A. M. Poskanzer, R. Preils, L. Hessand and W. Reisdorf, Phys. Rev. C 12, 644 (1975).

8. A. Y. Abul-Magd, K. El-Abed and M. El-Nadi, Phys. Lett. 39B (1972) 166.

STATES AT HIGH EXCITATION IN ^{16}O OBSERVED IN THE REACTION $^{12}C(^{20}Ne, ^{16}O)\,^{16}O$

A. Menchaca-Rocha,* M. Buenerd,† D. L. Hendrie, C. Olmer, and D. K. Scott

Heavy-ion induced multinucleon-transfer reactions have been widely used to locate high spin states. Although the angular distributions of such reactions are, in general, structureless and lead mainly to a determination of the reaction mechanism, the strong selectivity of the reactions for populating simple states at high excitation has led to interesting comparisons with the predictions of shell and cluster structure models.[1] In studying the $^{12}C(^{20}Ne,^{16}O)^{16}O$ reaction at incident energies between 150 and 294 MeV, we find a strong variation with incident energy of the cross section of a given state that is characteristic of the spin of the state. The incident energy dependence of states with known J-values is found to be in agreement with predictions of a semiclassical model. This technique is used to investigate the J-values of three new states which we observe in ^{16}O in the 21 to 24 MeV excitation region.

The $^{20}Ne^{5+,6+}$ beams from the 88-Inch Cyclotron were used to bombard 100 $\mu g/cm^2$ targets of ^{12}C. The reaction products were detected and identified using the QSD magnetic spectrometer.

The energy spectra (Fig. 1) show groups at positions corresponding to well-known ^{16}O states at 6.1 ($J^\pi = 0^+,3^-$), 6.9 ($2^+,1^-$), 10.4 (4^+), 14.6 (5^-), 16.2 (6^+), 20.8 (7^-) MeV. States are also observed at 21.7, 22.2 and 23.5 MeV. The angular distributions do not have any prominent diffraction structure and fall off exponentially with angle. Figure 2 shows the differential cross sections for the various groups, integrated over the observed angular range and plotted as a function of the incident energy. In the following section we briefly describe a semiclassical model whose predictions correspond closely to the smooth energy dependence of the experimental cross-sections for states of known J^π.

In a semiclassical description of heavy ion reactions a cluster transferred from a state with orbital and magnetic quantum numbers ℓ_1, λ_1 in the projectile to a state labelled by ℓ_2, λ_2 in the residual nucleus has a transition probability of the form:[1]

$$P(\ell_1\lambda_1, \ell_2\lambda_2) = P_0(R)\; S_1^2 S_2^2 \left| Y_{\ell_1}^{\lambda_1}\left(\tfrac{\pi}{2},0\right)\right| \left| Y_{\ell_2}^{\lambda_2}\left(\tfrac{\pi}{2},0\right)\right|^2 \cdot \exp\left[-\left(\frac{R\Delta k}{\pi}\right)^2 - \left(\frac{(\Delta L)}{\sqrt{\gamma R}}\right)^2\right] \qquad (1)$$

where $R = R_1 + R_2$; γ is related to an average of the binding energies[2] ε of the initial and final states, according to $\gamma^2 = 2m\varepsilon/\hbar^2$, where m is the transferred mass. The quantities ΔL and ΔK are defined by:

$$\Delta L = \lambda_2 - \lambda_1 + \tfrac{1}{2} k_0 (R_1 - R_2) + Q_{eff}/\hbar v \qquad (2)$$

$$\Delta k = k_0 - \lambda_1/R_1 - \lambda_2/R_2 \qquad (3)$$

Here v is the relative velocity of the cores in the region of transfer, $k_0 = mv/\hbar$ and $Q_{eff} = Q - (Z_1^f Z_2^f - Z_1^i Z_2^i)e^2/R$, S_1 and S_2 are spectroscopic factors of the cluster in the initial and final nuclei and $P_0(R)$ depends on the radial wavefunctions of the inital and final channels at the point R; for the purpose of obtaining relative cross sections we use the value $|\psi_2(R)|^2$ where $\psi_2(R)$ is the wavefunction of the transferred cluster at the surface of the residual nucleus.

The curves in Fig. 2 show the predicted values of P as a function of energy for various states; the absolute values were normalized to fit the corresponding experimental data. As seen in the figure, the states at 21.7 and 22.2 are consistent with the trend for $J \geqslant 6$. From angular correlation studies of the α-decay of this state excited in the (^6Li,d) reaction, a spin of 6 has been assigned.[2] However our observed energy dependence agrees better with J = 8,9. The 23.5 MeV groups follows a similar trend, but due to the large error bars, a spin as low as J = 5 is not inconsistent with the data.

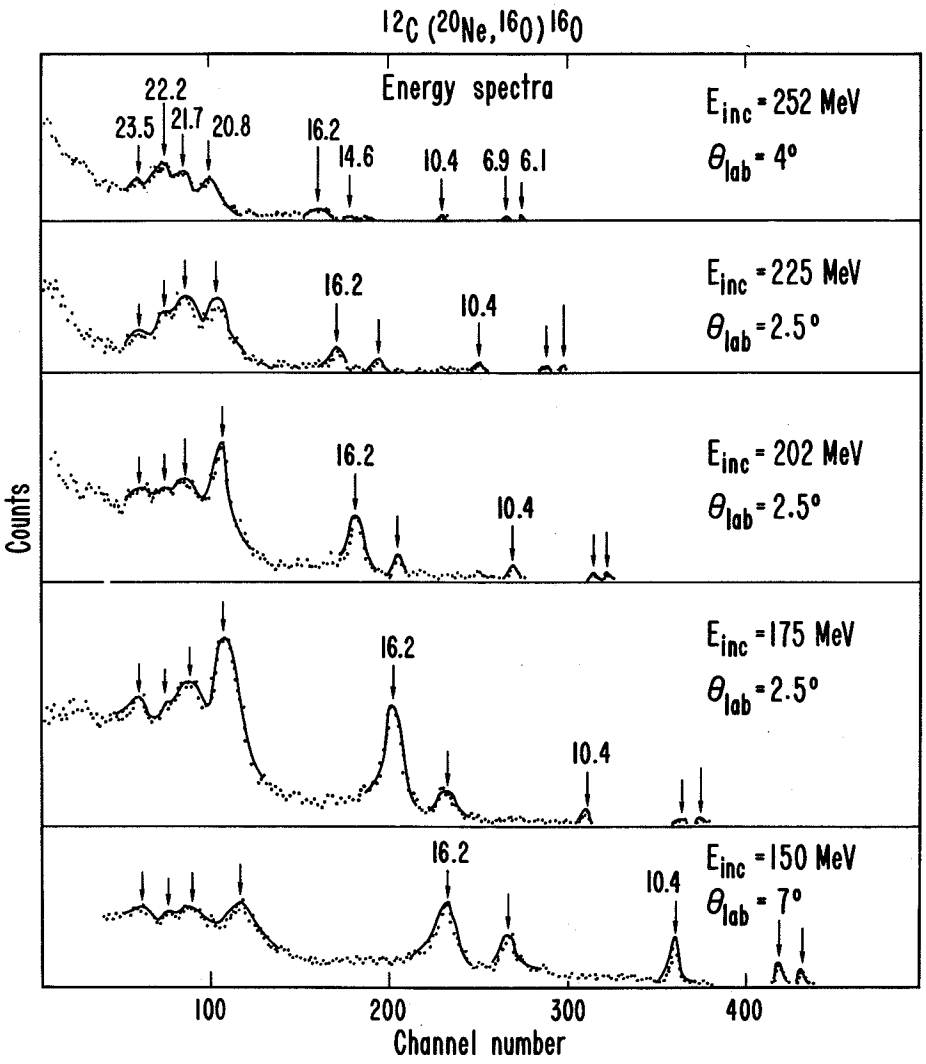

Fig. 1. Energy spectra for the $^{12}C(^{20}Ne, ^{16}O)$ ^{16}O reaction at incident energies between 150 and 252 MeV. (XBL 763-7537)

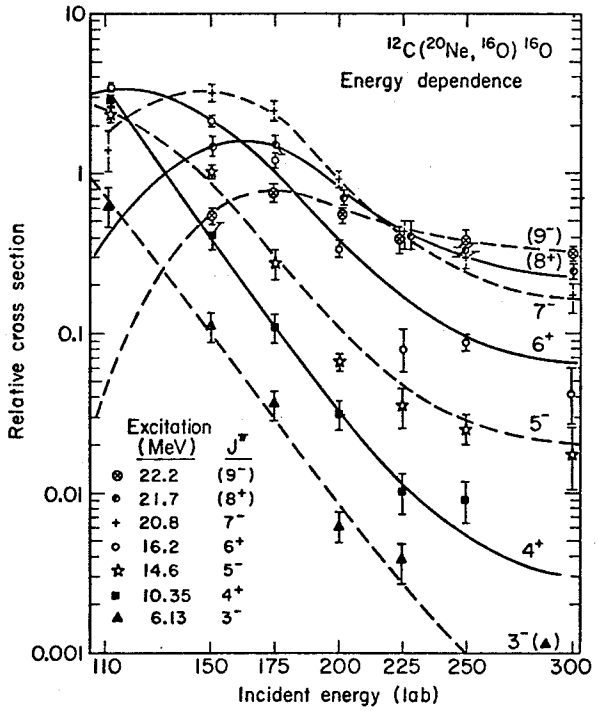

Fig. 2. Observed energy dependence for the excitation of states in the $^{12}C(^{20}Ne, ^{16}O)$ ^{16}O reaction as a function of incident energy. (XBL 763-2531)

An interesting feature of the present data is that the $(^{20}Ne, ^{16}O)$ reaction does not populate the 4^+_2 (11.1 MeV) state - which is populated in other α-transfer reactions - whose structure is predicted to be of a complicated nature involving a $^{12}C^*_{4.43}(2^+)$ core. We interpret this result as evidence for a pure α-transfer mechanism. Both the calibration and the energy dependence for the state observed at 14.6 MeV is consistent with the 5^- assignment[3] while the states at 14.39 (4^+) and 14.82 (6^+), of dominant 2p - 2h configurations, are not favored, as expected in a direct α-transfer model. Since we observe groups corresponding to all known members of the $K = 0^+$ (80) band, the state at 21.7 MeV, which appears to follow the trend of a $J = 8$ state, is a good candidate to be the 8^+ member of this band. Theoretical predictions place it at an excitation energy between 20 and 30 MeV. Various attempts to locate this state at an excitation energy up to 21 MeV have been unsuccessful. The systematics indicate that the state at 22.2 MeV

is of higher spin. The possibility of 9^- necessitates a configuration involving an odd number of nucleons in the fp shell, i.e. $(sd)^3(fp)^1$ or $(sd)^1(fp)^3$, although such configurations have not been needed so far to explain the experimental data at lower energies where there is a good matching with sd shell orbitals ($\approx$ 10 MeV/nucl $\approx 2\hbar\omega$ on k shell targets); at the present energies of up to 300 MeV ($\approx$ 15 MeV/A $\approx 3\hbar\omega$ on p shell targets), fp shell orbits are better matched and states having configurations that include nucleons in the fp shell might be enhanced.

We have shown that the energy dependence of multinucleon transfer reactions might be a useful method for locating cluster states. Using this method and the semiclassical formalism we have made tentative spin assignments to three new states in ^{16}O, one of which (22.2 MeV, J = 8) is a good candidate for the $K = 0^+$ (80) rotational band of ^{16}O.

Footnotes and References

*Permanent Address: Institutõ de Fisica, U.N.A.M., Mexico.

†Permanent Address: Institut des Sciences Nucléaires, Grenoble, France.

1. N. Anyas-Weiss, J. C. Cornell, P. S. Fisher, P. N. Hudson, A. Menchaca-Rocha, D. J. Millener, A. D. Panagiotou, D. K. Scott, D. Strottman, D. M. Brink, B. Buck, P. J. Ellis, and T. Engeland, Phys. Reports 12C, 201 (1974).

2. M. Avril, M. Lepareux, N. Saunier, A. Foti, G. Pappalardo and A. Strazzeri, J. de Phys., (Letters) 36, L-229 (1975).

3. K. P. Artemov, V. Z. Goldberg, I. P. Petrov, V. P. Rudakov, I. N. Serikov and V. A. Timofeev, Phys. Lett. 37B, 61 (1971).

THE CONTRIBUTION OF ALPHA CLUSTER EXCHANGE TO ELASTIC AND INELASTIC ^{16}O-^{20}Ne SCATTERING

R. Stock,† W. F. W. Schneider,† U. Jahnke,§ D. L. Hendrie, J. Mahoney, C. F. Maguire, D. K. Scott, and G. Wolschin

Several recent studies of the ^{20}Ne ground state rotational band in microscopic α-cluster plus core models have led to the conclusion that it may be characterized as an alpha-particle-like configuration of s-d-shell nucleons rotating around a spherical ^{16}O core.[1] Furthermore, the core may be, to a good approximation, identified with the ground state of ^{16}O. In the scattering of ^{20}Ne from ^{16}O, the exchange of the α-cluster between two identical ^{16}O cores should then contribute to the observed cross sections. Viewed in a simple one-step direct-reaction mechanism, the cluster can remain with the ^{16}O core of the incident ^{20}Ne projectile leading to elastic or inelastic scattering; in the latter case, the angular momentum transfer, ℓ, of the reaction arises from the excitation of cluster rotation with angular momentum $L = \ell$ leading to a final ^{20}Ne state with J = L. This part of the reaction may be described by optical model and DWBA amplitudes, respectively. In a coupled channel treatment, the corresponding amplitudes include the effect of virtual transitions between the rotational states of ^{20}Ne in the reaction. On the other hand, the cluster may be exchanged to the ^{16}O target nucleus forming one of the ^{20}Ne rotational states. Then the cross section at backward angles where the interference with the non-exchange contribution may be neglected is proportional to S_α^2, the square of the spectroscopic amplitude. Furthermore, the interference structure at intermediate angles is very sensitive to S_α. This quantity can thus be determined from measured absolute cross sections more sensitively than in a transfer reaction like $^{16}O(^6Li,d)^{20}Ne$.

In order to test the prediction of microscopic models that the members of the ^{20}Ne ground state rotational band are alpha cluster configurations with more or less constant alpha particle spectroscopic factors, we have measured angular distributions of the reactions $^{20}Ne+^{16}O \rightarrow {}^{16}O\,(g.s.) + {}^{20}Ne(0^+(g.s.)\ 2^+,4^+)$ at an incident ^{20}Ne energy of 50 MeV which is slightly above the Coulomb barrier. Self supporting targets of aluminum - and nickel - oxide, with thicknesses of 250 and 100 $\mu g/cm^2$ respectively, were mounted in a scattering chamber equipped with a liquid nitrogen cooling finger close to the target as a trap for pump oil vapors, in order to reduce the carbon buildup on the target during the experiment. Two ΔE-E-counter telescopes with 5μ ORTEC ΔE transmission detectors and a solid angle of $2\cdot10^{-4}$ sr were used along with a monitor detector. The telescope events were sent to a computer, stored in ΔE-(E+ΔE) arrays and analyzed off-line with a program for energy calibration, peak integration, peak unfolding and background subtraction. Energy calibration of the spectra was obtained from the peak positions of the elastic ^{20}Ne scattering from Ni, ^{27}Al and ^{16}O. For each scattering angle and telescope, both the spectra of outgoing ^{20}Ne and ^{16}O (g.s.) products were obtained. Figure 1 shows these spectra for $\Theta_{Lab} = 29°$. Since the ^{16}O (g.s) angular distributions at forward angles correspond to the angular distributions of the elastic and inelastic ^{20}Ne backward scattering it was sufficient to cover the forward angles.

The resulting angular distributions for the ground state, 2^+ and 4^+ states of ^{20}Ne are shown in Fig. 2. The error bars include errors due to statistics, background correction, and uncertainties in the unfolding of impurity peaks. For

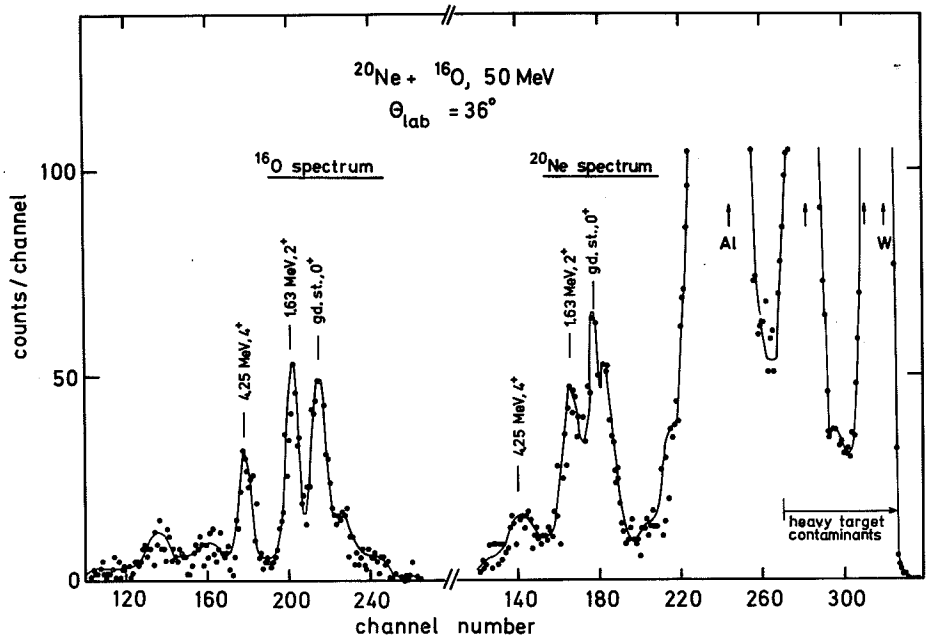

Fig. 1. Spectra of outgoing ^{20}Ne and ^{16}O at Θ_{Lab} = 36°.
(XBL 766-8503)

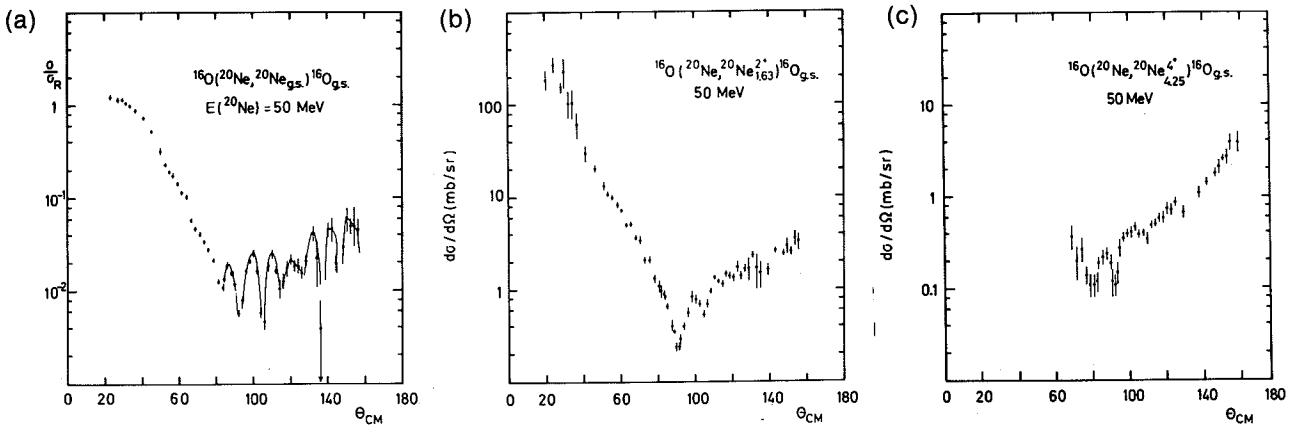

Fig. 2. Angular distributions for elastic and inelastic ^{20}Ne + ^{16}O scattering to the ground state, 2^+ (1.63 MeV) and 4^+ (4.25 MeV) states of ^{20}Ne. The smooth curve in the ground state transition is drawn to guide the eye. (XBL 766-8527)

the 4^+ transition, the peaks could only be identified in the ^{16}O spectra with sufficient reliability, thus limiting the angular distribution to $\Theta_{c.m.} \gtrsim 70°$.

A backward rise is observed in all three angular distributions, suggesting that a mechanism different from direct elastic or inelastic scattering takes over at angles beyond about 90°. The pronounced oscillations at intermediate angles, observed for the ground state transition, appear damped in the inelastic reactions.

The ^{16}O+^{20}Ne ground state transition was calculated as a coherent superposition of elastic scattering and cluster transfer using the code BRUNHILD of Braun-Munzinger et al.[2] In the reaction amplitude

$$T(\Theta) = T(\Theta)_{OM} + S_\alpha T_{DWBA}(\pi-\Theta)$$

the relative phase is fixed by the symmetry of the system.[3] The set of optical model parameters used in both amplitudes, was V_0 = 100 MeV, W = 35 MeV, $r_V = r_W = 1.2$ fm, $a_V = 0.49$ fm, $a_W = 0.32$ fm, representing a strongly absorbing potential. No ℓ-dependence of the absorption was taken into account because enough direct exit channels are available to carry the grazing angular momentum $\ell_0 \approx 10$; among these the low-lying collective states are

particularly strongly excited in inelastic scattering.

Cluster formfactors are shown in Fig. 3, according to Tomoda et al.[4] and Hiura et al.[5] together with Woods-Saxon formfactors obtained with $r_0 = 1.4$ fm that are normalized so as to fit the asymptotic parts ($R \geq 5$ fm). In the nuclear interior the microscopic formfactors are drastically reduced due to the antisymmetrization, and the major part of the alpha particle probability amplitude is pushed into the surface region. The formfactor of Hiura et al. with $S^{c.m.} = 0.45$ exhibits the same surface amplitude as the Woods-Saxon formfactor with $r_0 = 1.4$ and a normalization $S^{W.S.} = 0.8$. The latter will be used in the DWBA analysis.

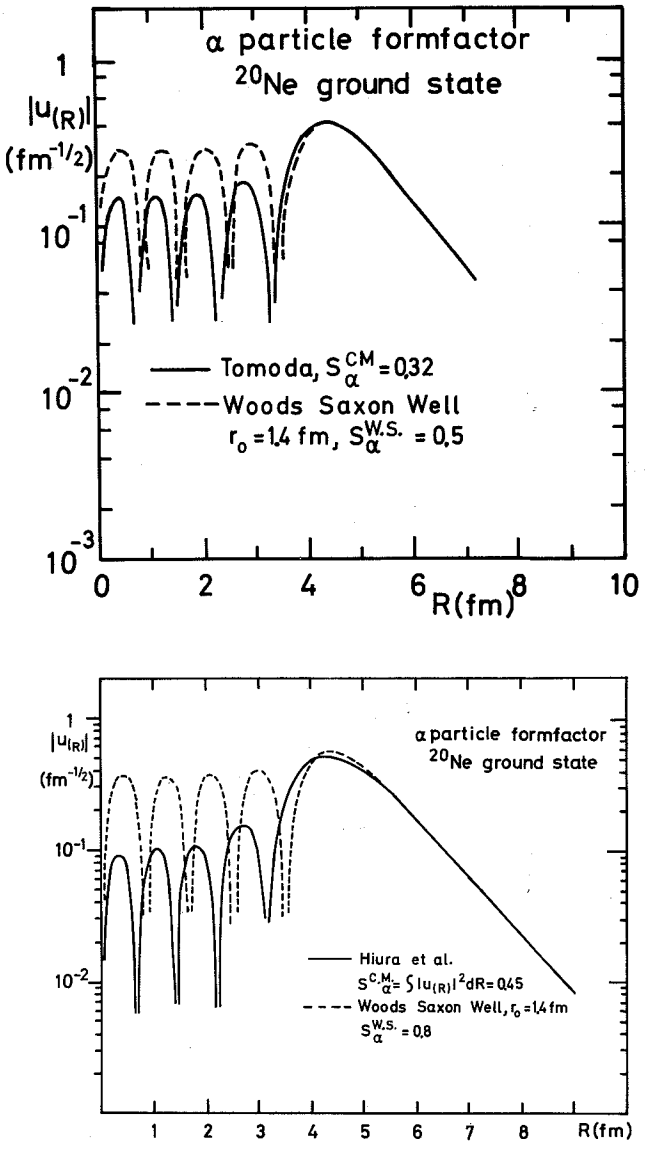

Fig. 3. Alpha particle relative motion formfactors for the ^{20}Ne ground state. Microscopic calculations of Tomoda and Arima (Ref. 5; upper part) and Hiura et al. (Ref. 4; lower part) are matched by Woods-Saxon solutions in the external region ($R > 5$ fm). (XBL 766-8526)

The results of the optical model and elastic transfer calculations are compared with the ground state transition data in Fig. 4. Both fits are identical for $\Theta_{c.m.} \lesssim 80°$; in this domain, the data are well reproduced. The OM cross section continues to fall off towards larger angles, in a manner typical for strongly absorbing potentials, whereas interference oscillations and a backward rise develop in the elastic transfer angular distribution for $\Theta_{c.m.} > 80°$. However, the experimental cross sections are largely underestimated at intermediate angles, where also the phase of the oscillations is not well reproduced.

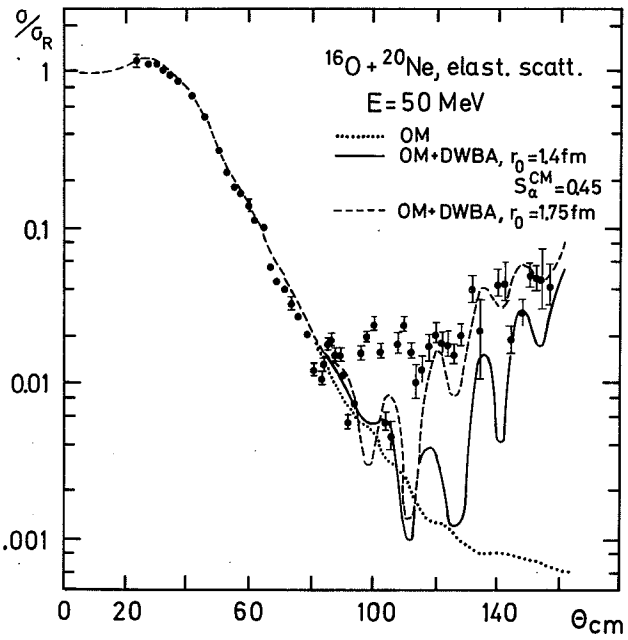

Fig. 4. Results of optical model (OM) and elastic transfer (OM+DWBA) calculations for the ^{20}Ne + ^{16}O ground state transition. (XBL 766-8504)

A variation of the optical model parameters did not yield significant improvements insofar as a better agreement with the backward oscillatory pattern could only be achieved at the expense of fit quality at forward angles. Apparently, the DWBA amplitude falls off too rapidly from backward angles towards 90°, or the OM amplitude is inadequate for $\Theta_{c.m.} > 80°$. Attempts to improve the fit by scaling the DWBA amplitude with a larger bound state form factor normalization were unsuccessful. For example, an arbitrary normalization to $S^{W.S.} = 2$ shifted the angular distribution upward by a uniform factor of about four for $\Theta \geq 100°$, improving the agreement at intermediate angles but far overestimating the cross sections at the very backward angles. A somewhat better overall fit was obtained by increasing the Woods-Saxon well radius from $r_0 = 1.4$ fm, as prescribed by the microscopic models, to $r_0 = 1.75$ fm, at the same time reducing the overall normalization to $S^{W.S.} = 0.5$. The corresponding fit is also shown in Fig. 4. However, this procedure implies an alpha particle surface reduced width twice as high as given by the microscopic wave functions appropriate to the ^{20}Ne ground state. This corresponds to

an alpha cluster localization far beyond the limits indicated for low-lying ^{20}Ne states by microscopic models.[1]

It was therefore concluded that the first-order elastic scattering and exchange mechanism, underlying the OM plus DWBA approximation to elastic transfer, is not appropriate in the $^{16}O + ^{20}Ne$ case. A second-order calculation would have to include virtual transitions to the excited, collective states of ^{20}Ne both in the entrance and exit channels, as well as the transfer of the alpha cluster among excited states. No computer code was available to the authors that would take all these transitions into account, along with an appropriate treatment of recoil effects.

In order to demonstrate the second order effects on the optical model amplitude alone, a coupled channel calculation was done for elastic and inelastic $^{16}O + ^{20}Ne$ scattering using the code of Ascuitto and Glendenning.[6] No exchange contributions were taken into account. The relevant deformation constants, associated with a radius R (projectile) = 1.2 $(20)^{1/3}$ were deduced from the deformation length in Ref. 7. The Coulomb deformation β_2^C was reduced slightly from the value 0.87 reported by Stelson and Grodzins,[7] because second order coupling was included. The results of this calculation are shown in Fig. 5, which also gives the optical model fit (without channel coupling) for elastic scattering. The effect of channel coupling for the ground state transition is clearly exhibited. At intermediate scattering angles where the elastic transfer calculation (Fig. 4) was systematically underestimating the observed cross section, the CC cross sections are much larger than the OM cross sections. The 2^+ transition cross section is underestimated at the very forward angles. It should be noted, however, that we did not attempt any parameter optimization, and that the experimental error bars are large in this region (c.f. Fig. 2) due to normalization and background correction uncertainties. The coupled channel calculation for the ground state transition indicates that the OM amplitude is too small at backward angles. This may in part explain the low cross sections and wrong phases obtained in the intermediate angle elastic transfer calculations. One might, therefore, try to improve the model replacing the OM amplitude in by a coupled channeled amplitude. This was not done for the following reasons: (a) the second order effects should be similarly important for the DWBA amplitude at intermediate angles, and (b) the model would be still unsatisfactory as long as ^{20}Ne is treated macroscopically in the CC amplitude and microscopically in the DWBA amplitude.

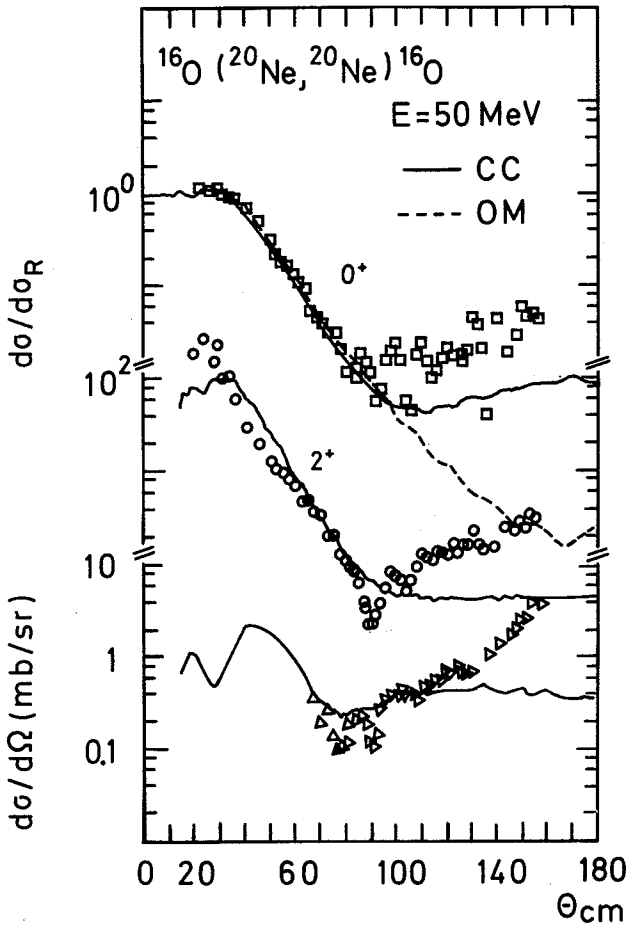

Fig. 5. Results of optical model (OM) and coupled channel (CC, no exchange) calculations for $^{20}Ne+^{16}O$ scattering to the first three states in ^{20}Ne. Potential parameters are the same as in the elastic transfer calculation except W = 15 MeV. Deformation parameters are $\beta_2^N = 0.43$, $\beta_4^n = 0.26$, $\beta_2^C = 0.8$ and $\beta_4^C = 0.4$. (XBL 766-8505)

Footnotes and References

*Condensed from LBL-5051.

†Permanent Address: Fachbereich Physik, Universität Marburg, W. Germany.

‡Permanent Address: Gesellschaft für Schwerionenforschung, Darmstadt, W. Germany.

§Permanent Address: Hahn-Meitner Institut für Kernforschung, Berlin, W. Germany.

1. See for example, A. Arima, Proc. Int. Conf. Nucl. Phys., Munich 1973, ed. by J. deBoer and H. J. Mang, North Holland (1973), Vol. 2, p.183.

2. P. Braun-Munzinger, H. L. Harney and S. Wenneis, Nucl. Phys. A235, 190 (1974).

3. P. Braun-Munzinger et al., Z. Phys. A276, 107 (1976).

4. T. Tomoda and A. Arima, Proc. INS-IPCR Symposium on Cluster Structure, ed. H. Kamitsubo et al., Tokyo, 1975, p. 90 and private communication.

5. J. Hiura, F. Nemoto and H. Bando, Prog. Th. Phys. Suppl. 52, 173 (1973) and private communication by F. Nemoto.

6. R. J. Ascuitto and N. K. Glendenning, Phys. Rev. 181, 1396 (1969).

7. R. H. Stelson and L. Grodzins, Nucl. Data Sec. A1, 21 (1965).

EXCITATION OF GIANT RESONANCES IN ^{197}Au AND ^{208}Pb BY INELASTIC SCATTERING OF HEAVY IONS

D. Ashery, M. S. Zisman, R. B. Weisenmiller,
A. Guterman, D. K. Scott, and C. Maguire

The region of excitation energy in nuclei where the giant monopole and giant quadrupole resonances are expected to be, has been extensively investigated in recent years. Enhancements in the cross sections were observed in experiments in which photons, electrons, protons and ^{4}He ions were used. While the existence of the resonances was established and various properties were studied, a definite conclusion about the multipolarity of the resonances observed has not been reached; the tendency is to believe that they are of E2 character. The population of these resonances by inelastic scattering of heavy ions through the Coulomb excitation process should help in identification of their multipolarity since only the 2^+ component will be excited.

Self-supporting ^{197}Au and ^{208}Pb targets were bombarded with 104-MeV ^{16}O and 130-MeV ^{20}Ne beams at the 88-inch cyclotron. The inelastically scattered ions were detected at the focal plane of the magnetic spectrometer, placed at 55° and 60°. These angles are well below the grazing angle and the Coulomb excitation requirement should still be reasonably satisfied. The expected cross sections for population of the giant quadrupole resonance, assuming a B(E2) value equal to 100% of the energy weighted sum-rule, is of the order of 1 - 2 μb/sr. Due to the large background observed in the experiment, only upper limits could be set and are listed in Table 1. Since calculations of the Coulomb excitation process indicate that it tends to shift the position of the peak to a somewhat lower excitation energy and also to make it a little narrower, the upper limits are quoted per MeV of the width in the expected position. The upper limits are taken as two standard deviations of the background.

Measurements were also taken with a 140-MeV ^{16}O beam bombarding ^{197}Au and the inelastically scattered ions detected at 43° and 54°. Under these conditions, we are well above the Coulomb barrier. A broad peak was clearly observed at both angles at the expected excitation energy for the 2^+ (or 0^+) giant resonance. The spectrum obtained at 43° is shown in Fig. 1, and is the first observation of this resonance by inelastic scattering of heavy ions. The observed width is about 3.5 MeV but the enhancement could include some contribution from the adjacent giant E1 resonance. The cross sections, integrated over the observed peak, are listed in Table 1.

Table 1.

Target	Projectile	Energy (MeV)	θ_{lab}	Cross section or upper limit (μb/sr)
^{197}Au	^{16}O	103.15	55°	< 3.3/MeV
^{197}Au	^{16}O	103.15	60°	< 7.5/MeV
^{208}Pb	^{16}O	103.15	55°	< 2.2/MeV
^{197}Au	^{20}Ne	128.96	55°	< 3.0/MeV
^{208}Pb	^{20}Ne	128.96	55°	< 7.0/MeV
^{197}Au	^{16}O	139.21	43°	670
^{197}Au	^{16}O	139.21	54°	85

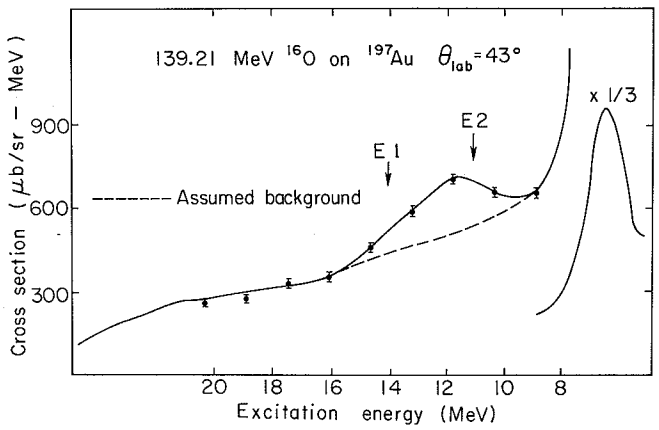

Fig. 1. ^{16}O + ^{197}Au inelastic scattering at θ_{LAB} = 43°. (XBL 766-8271)

ARGON ION REACTION STUDIES ON TANTALUM AND GOLD NEAR COULOMB BARRIER ENERGIES*

R. C. Eggers,† W. S. Ribbe,‡ and J. O. Rasmussen

Gold and tantalum targets were bombarded with a ^{40}Ar beam at 183 and 209 MeV, close to the Coulomb barrier height. Angular distributions of recoiling reaction products were measured by collecting an Al catcher foils. The radioactivity was counted after the irradiation by Ge(Li) detectors. One-neutron and one- and two-proton transfer products were prominent. Simple semiclassical transfer theory adequately fits the backward peaking angular distributions at or below the Coulomb barrier but fails at bombarding energies above the barrier. Yields of some products more than two mass numbers removed from reactants were observed in thicker targets at 235 MeV, and their significance is discussed.

To see what differences there might be between spherical and spheroidal targets we chose to run catcher foil experiments at the Berkeley Super Heavy Ion Accelerator. As targets we chose as spherical nuclei, gold, and as deformed, tantalum. These nuclei are as close in mass and charge as feasible, since the boundary between strongly deformed and spherical nuclei is not sharp in this region. We ran our experiment at energies close to the Coulomb barrier to make it possible to compare theories involving nucleon tunneling with the projectile not deviating much from a Rutherford trajectory. We made our measurements at 183, 209, and 235 MeV lab energy. For the two lower energies we used a 400 $\mu g/cm^2$ gold target and a 99 $\mu g/cm^2$ tantalum target on 100 $\mu g/cm^2$ carbon backing. At the 235 MeV energy we used a 5 mg/cm^2 gold target and a 10 mg/cm^2 tantalum target. Table 1 gives a list of the differential reaction cross-sections by product

One-Neutron Transfer Results and Discussion

Let us look at the evidence for differences (angle and energy integrated) between spherical and deformed nuclei. We have compared our ^{41}Ar angular distributions to theoretical calculations using the Semi-Classical Transfer Theory (SCTT), expressions of Alder, Morf, Pauli, and Trautmann.[1]

Their formulation goes beyond that of Breit and Ebel[2] notably in the inclusion of dependence on the angular momenta of the particular shell-model orbitals involved. For energies above the barrier Alder et al.[1] suggest that one may still be able to apply the theory by replacing the Rutherford cross section factor by an experimental or optical model elastic cross section.

Figure 1 shows excellent agreement at the lowest energy point, 183 MeV, for gold. There is only a slight dip in cross section at the most backward angle, indicating a slight absorption into other channels for the nearly head-on collisions.

Table 1. Transfer reaction cross sections for argon-40 beam (mb/sr c.m.)

Target	Product	Lab Energy	6° - 15° 8° - 18°	15° - 45° 18° - 54°	45° - 75° 54° - 88°	75° - 105° 88° - 118°	105° - 135° 118° - 144°	135° - 165° 144° - 168°	165° - 174° 168° - 175°	Total (mb)
Ta	^{41}Ar	183 MeV	28 ± 2	0.42±0.19	0.50±0.17	1.50±0.15	3.4±0.4	1.50±0.40	0 ± 3.96	18.6±1.40
		209 MeV	26 ± 4	1.37±0.30	10.3±1.0	0.90±0.20	0.53±0.22	0 ± 1.01	0 ± 5.1	44.1±3.78
	^{39}Cl	183 MeV	12.4±4.2	0 ± 0.38	0±0.64	0.60±0.30	3.08±1.42	2.74±0.54	0 ± 8.24	12.7±4.18
		209 MeV	0 ± 5.30	0 ± 0.356	5.48±1.18	.596±.274	0 ± 0.466	2.92±1.16	0 ± 14.9	24.4±4.77
	^{38}S	183 MeV	0 ± 3.06	0 ± 0.314	0 ± 0.283	.258±.120	1.46±.386	1.30±.559	0 ± 7.6	5.68±1.86
		209 MeV	0 ± 2.99	.181±.248	0 ±.757	0 ±.145	0 ±.292	0 ±.929	0 ± 7.63	0.89±3.05
Au	^{41}Ar	183 MeV	0 ± 0.77	0 ± 0.70	.077±.052	0.40±0.04	2.65±0.32	2.77±0.21	2.59±1.25	11.3±1.75
		209 MeV	1.64±0.57	0.60±0.20	4.0±0.2	2.85±0.20	1.3±0.1	0.67±0.15	0 ± 2.1	37.9±1.1
	^{39}Cl	183 MeV	5.54±4.06	0 ± 0.106	0 ±0.192	0 ±0.082	1.26±0.28	2.84±0.26	9.12±5.98	7.08±1.23
		209 MeV	3.16±1.28	0 ± .122	1.46±0.20	1.90±0.30	1.22±0.32	.432±.154	0 ± 4.32	17.8±1.53
	^{38}S	183 MeV	1.88±2.95	0 ± .097	0 ±.089	0 ±.043	0 ±.385	0.95±0.19	0 ± 2.25	1.08±1.02
		209 MeV	0 ± 1.06	0 ± .107	.718±.120	.472±.069	.282±.146	0 ± .194	1.47±1.68	6.12±0.70

All differential cross sections are in millibarns per steradian, center-of-mass system. Upper angular range in heading is laboratory system angles and lower range is for center-of-mass.

All total cross sections are missing any unmeasured cross section recoiling into the angular range 0-15° and 175-180° lab.

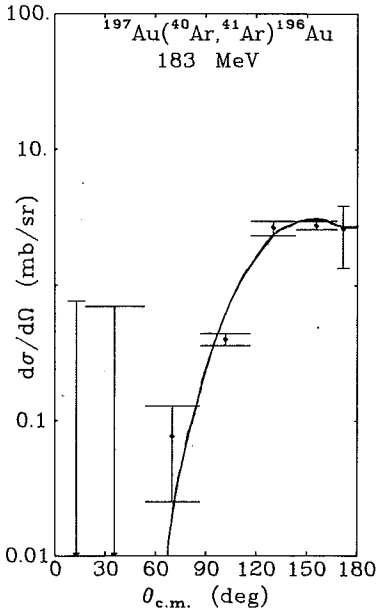

Fig. 1. Angular distribution of ^{41}Ar produced from the reaction of ^{40}Ar on ^{197}Au at 183 MeV (lab). The solid line is the SCTT theory[4] with an elastic cross section taken from an optical model program with real and imaginary Woods-Saxon potential of radius constant 1.28 fm and diffuseness 0.4 fm. The potential depth is taken as 70 MeV for the real part and 15 MeV for the imaginary. Note that the theory fits the angular distribution rather well. The theoretical curve here is for the $f_{7/2}$ neutron orbital in argon and $p_{3/2}$ in gold, but the angular distribution is essentially the same for gold orbitals of other j values. The absolute theoretical cross section has been normalized upward by a factor of 8.0, but absolute cross sections depend sensitively on the radius constant used in the SCTT theory, here taken as 1.25 fm.
(XBL 743-2714)

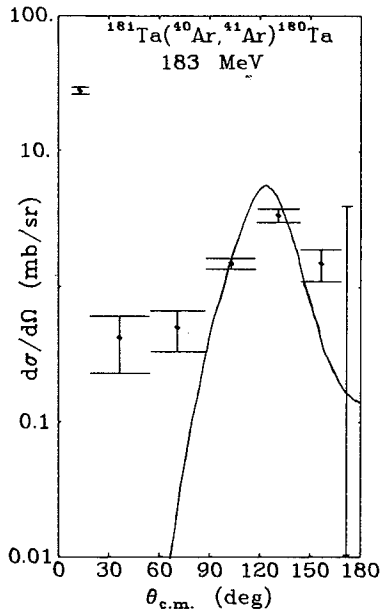

Fig. 2. Angular distribution of ^{41}Ar produced from the reaction of ^{40}Ar on ^{181}Ta at 183 MeV. The solid line is the SCTT theory[4] with an elastic cross section calculated in the same manner as for Fig. 1, but with renormalization factor of 2.0 and $i_{13/2}$ neutron orbital. The most forward angle point is unreliable, since ^{40}Ar scattered into the catcher foil might transfer there. (XBL 743-2711)

In Fig. 2 for Ta at 183 MeV, the agreement of SCTT theory and our data is not as good, in that the experimental angular distribution away from the peak does not drop as far as the theoretical. The same flattening trend is even more pronounced for the higher energy points, Figs. 3 and 4.

Clearly the semi-classical transfer theory patched by the above-barrier elastic scattering cross section is not adequate for the angular distributions we measured. It is likely that much of the excess cross section away from the classical grazing angle arises from inelastic transfer, where the ^{41}Ar and its complement ^{196}Au, are left in higher excited states.

There are no systematic differences between the Au and Ta results that we can attribute simply to deformation. Evidently only a localized zone on the spheroidal surface is active for transfer, and the angular distribution is no less sharp than for spherical nuclei.

The angular distributions for ^{39}Cl and ^{38}S can be seen from Table 1 to be rather similar to those for ^{41}Ar.

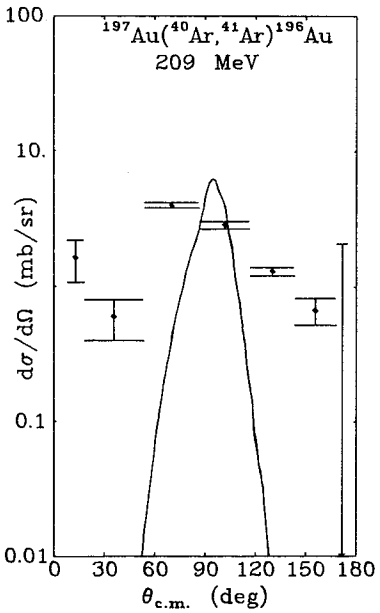

Fig. 3. Angular distribution similar to Fig. 1, except for 209 MeV. Note that there is a marked disagreement between the theory and the experiment as to the width of the peak at the classical grazing angle. The theoretical curve has been renormalized upward by a factor of 8.4. (XBL 743-2715)

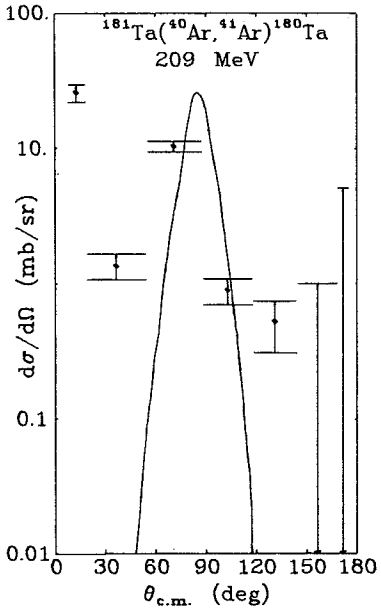

Fig. 4. This is a similar angular distribution to Fig. 2, except that the energy here is 209 MeV. The theoretical curve is normalized upward by a factor of 10. Note that there is again a marked disagreement between the theory and the experiment as to the width of the peaking at the classical grazing angle. (XBL 743-2712)

Footnotes and References

*Condensed from Nucl. Phys A263, (1976) 500.

†Present Address: Cyclotron Institute, Texas A&M University, College Station, Texas.

‡Present Address: Stadt Rudolf-Virchow-Krankenhaus, Strahlungsabteilung, West Germany.

1. K. Alder, R. Morf, M. Pauli and D. Trautmann, Nucl. Phys. A191 (1972) 399.

2. G. Breit and M. E. Ebel, Phys. Rev. 103 (1956) 679.

SEMICLASSICAL AND QUANTUM MECHANICAL ASPECTS OF ONE- AND TWO-NUCLEON TRANSFER*

D. K. Scott, D. L. Hendrie, L. Kraus,† C. F. Maguire, J. Mahoney, Y. Terrien,‡ and K. Yagi§

The criterion for the validity of the semiclassical approach to heavy-ion reactions is often expressed by the fact that the wavelength of relative motion of the cooliding ions is short compared to the interaction radius, and consequently the particles are localized on classical trajectories. Although this condition is usually well fulfilled for heavy-ion reactions at incident energies above the Coulomb barrier, the observed onset of quantum mechanical effects in going from one- to two-nucleon transfer in this energy region shows that other criteria are necessary. Here we give an analytical description of the transition between quantum mechanical and classical behavior in terms of the number of partial waves contributing significantly to the reactions, and we illustrate the results by comparing one- and two-nucleon transfer reactions induced by 78-MeV ^{12}C ions on ^{144}Nd.

We begin by making the partial-wave expansion of the scattering amplitude:

$$f(\theta) = (2ik)^{-1} \Sigma_\ell (2\ell+1)\eta_\ell \exp(2i\delta_\ell) P_\ell(\cos\theta). \quad (1)$$

On account of the peripheral nature of heavy-ion collisions at high energy, it has been shown[1] that the magnitude of η_ℓ can be well described by

$$\eta_\ell = \eta_{\ell_0} \exp -(\ell-\ell_0)^2/(\Delta\ell)^2 \quad (2)$$

which has a maximum for partial wave $\ell_0 = kR$, where R is the interaction radius. The spread of contributing ℓ values, $\Delta\ell$, is determined by strong absorption ($\ell < \ell_0$) and by the decay of the form factor ($\ell > \ell_0$).

For δ_ℓ, we make a Taylor expansion:

$$\delta_\ell = \delta_{\ell_0} + (d\delta/d\ell)_{\ell_0}(\ell-\ell_0) + \tfrac{1}{2}(d^2\delta/d\ell^2)_{\ell_0}(\ell-\ell_0)^2 + \ldots . \quad (3)$$

Using the WKB formalism, the phase shift δ_ℓ and the scattering angle θ_ℓ, associated with partial wave ℓ, are related by $\theta_\ell = 2(d\delta_\ell/d\ell)$. Substituting into Eq. (3), we obtain

$$\delta_\ell = \delta_{\ell_0} + \tfrac{1}{2}\theta_0(\ell-\ell_0) + \tfrac{1}{4}(d\theta_\ell/d\ell)_{\ell_0}(\ell-\ell_0)^2 \cdots , \quad (4)$$

where θ_0 is the angle of deflection of the trajectory corresponding to the grazing partial wave ℓ_0. The scattering amplitude $f(\theta)$ in Eq. (1) can be evaluated with the above expressions for δ_ℓ and η_ℓ, together with the asymptotic form of P_ℓ valid for large ℓ, and by replacing the sum over ℓ by an integral. These additional simplifications depend on the conditions $\ell_0 \gg \Delta\ell \gg 1$, valid for a peripheral reaction at high incident energy. For the differential cross section we obtained[2,3]

$$\frac{d\sigma}{d\Omega} = |f(\theta)|^2 \propto \exp\frac{-(\theta-\theta_0)^2}{(\Delta\theta)^2} + \exp\frac{-(\theta+\theta_0)^2}{(\Delta\theta)^2} + (\text{interference terms}). \quad (5)$$

This equation can be interpreted as the superposition of two "classical" distributions centered around the grazing trajectories at $\pm \theta_0$, with an interference term in the region of overlap. For the purposes of this work, we ignore the effects of the interference which are discussed in Ref. 2 and consider only the first term in Eq. (5). This term corresponds to a distribution centered at the angle θ_0, of width $\Delta\theta$:

$$(\Delta\theta)^2 = 2/(\Delta\ell)^2 + \frac{1}{2}\left(d\theta_\ell/d\ell\right)^2_{\ell_0} (\Delta\ell)^2 . \quad (6)$$

We now use the *strictly classical result* of a Rutherford orbit, that $\ell = \eta\cot(\theta/2)$, where η is the Sommerfeld parameter, and therefore

$$\left(d\theta_\ell/d\ell\right)_{\ell_0} = -2\eta^{-1} \sin^2(\theta_0/2) . \quad (7)$$

The curve of $\Delta\theta$ versus $\Delta\ell$ derived from Eqs. (6) and (7) is shown in Fig. 1 for a typical reaction of 78-MeV ^{12}C ions on ^{144}Nd, in which $(d\theta/d\ell)_{\ell_0} = 0.013$. This curve has a minimum value at

$$\Delta\ell = \left[2(d\ell/d\theta_\ell)_{\ell_0}\right]^{1/2} = \sqrt{\eta}\ \csc(\theta_0/2) \quad (8)$$

defining the transition at $\Delta\ell \approx 12$ between a region of quantal dispersion, $\Delta\ell << \sqrt{\eta}\csc(\theta_0/2)$, where $\Delta\theta$ decreases with increasing $\Delta\ell$, and a classically dispersive region, $\Delta\ell >> \sqrt{\eta}\csc(\theta_0/2)$, where $\Delta\theta$ increases with increasing $\Delta\ell$. Also, shown in Fig. 1 are separate curves corresponding to the two dispersive terms in Eq. (6).

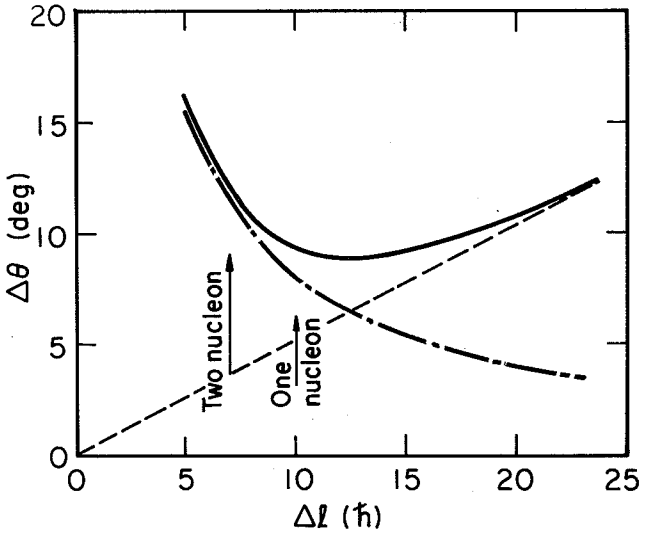

Fig. 1. The variation of $\Delta\theta$ with $\Delta\ell$ predicted from Eq. (6). The dashed and dot-dashed curves represent the limits of Eq. (6), obtained by setting the first and second dispersive terms to zero, respectively. The $\Delta\ell$ values derived from fitting Eq. (2) to the DWBA reaction amplitudes for the one- and two-neutron transfer data of Fig. 2 are marked in the figure. (XBL 752-2266)

The values of $\Delta\ell$ pertaining to the one- and two-neutron transfer reactions $^{144}Nd(^{12}C,^{13}C)^{143}Nd$ (g.s.) and $^{144}Nd(^{12}C,^{14}C)^{142}Nd$ (0^+, 2.98 MeV) at an incident energy of 78 MeV are shown in Fig. 2. The $\Delta\ell$ values were obtained from DWBA calculations using a typical set of optical-model parameters (potential A of Table 1). For a single-nucleon transfer $\Delta\ell = 10$, and the corresponding value of $\Delta\theta = 9.2°$ is almost exactly equal to the observed half-width of the differential cross section at $1/e$ of the maximum. Our theoretical curve for $\Delta\ell$ versus $\Delta\theta$ is therefore in good agreement with the data for one-nucleon transfer. Furthermore, since $\Delta\ell$ lies close to the minimum of the curve, our model predicts that the width of the differential cross section for one-nucleon transfer should be relatively stable against variations of $\Delta\ell$ brought about, for example, by changes in the optical-model potential. This prediction is illustrated in Fig. 2(a), by comparing DWBA calculations with potential A and potential B, which is another typical potential from the literature. Both potentials lead to differential cross sections which are almost indistinguishable in the region of the bell-shaped maximum. Our model therefore gives a physical interpretation of the persistence in single-nucleon

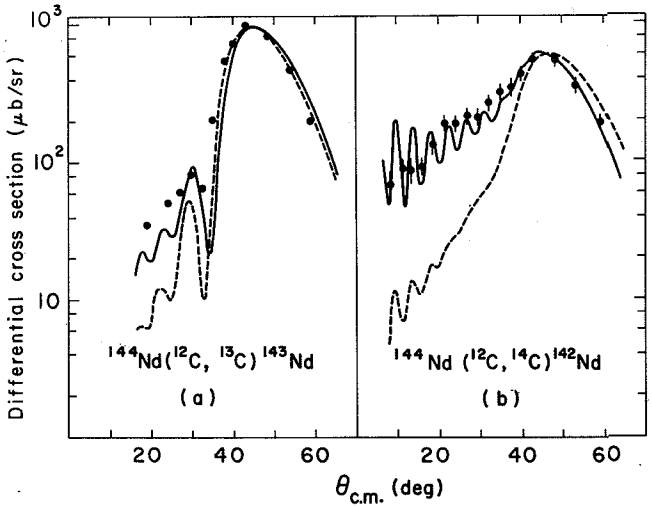

Fig. 2. Differential cross sections for (a) the reaction $^{144}Nd(^{12}C, ^{13}C)^{143}Nd$ and (b) the reaction $^{144}Nd(^{12}C, ^{14}C)^{142}Nd$ at an incident energy of 78 MeV. The theoretical curves in (a) are DWBA predictions normalized to the data using the optical potentials of Table I: potential A (solid line) and potential B (dashed line). In (b) both predictions use a potential of type A, with r_W = 1.26 fm (solid line) and 1.36 fm (dashed line). (XBL 752-2268)

Table 1. Optical parameters used in analysis of ^{12}C + ^{144}Nd at 78 MeV.

Potential	V	W	r_V	r_W	a_V	a_W
A	-40	-15	1.31	1.31	0.45	0.45
B	-100	-40	1.22	1.22	0.49	0.60

transfer of the ambiguity in optical-model parameters which is well known for elastic scattering.[4,5]

The ambiguity is less for the two-neutron transfer data as illustrated in Fig. 2(b) which compares two calculations with potentials of type A, and values of r_w = 1.36 and 1.26 fm [the result obtained with potential B gave an almost identical distribution to potential A with r_w = 1.36 fm, so the comparison is essentially the same as in Fig. 2(a)]. We wish to emphasize the sensitivity to the parameter r_w in which a reduction of a few percent increases the forward-angle cross section by a factor of 10. From an intuitive viewpoint, the greater sensitivity of two-nucleon transfer to details of the optical potential has been ascribed[6] to the sharper fall-off of the form factor which renders the forward cross section more sensitive to close trajectories deflected forward by the attractive nuclear potential.

In our model the greater sensitivity of the two-nucleon transfer cross section is due to the fact that the associated $\Delta\ell$ values of approximately $6\hbar$ lie on the steeply rising portion of the curve in Fig. 1. For these reactions then, whereas the one-nucleon transfer lies in the transition region between semiclassical and quantum mechanics, the two-nucleon transfer lies well in the quantum-mechanical region. To define a classical trajectory, a certain spread of contributing ℓ values is necessary, and the model gives an analytical determination of this limit. It fails, however, to reproduce exactly the observed width of the distribution for two-nucleon transfer, since $\Delta\ell = 6\hbar$ corresponds to $\Delta\theta = 12°$, compared to the experimental value of 16°. For this case the form of η_ℓ and δ_ℓ deduced from the DWBA phase shifts showed that, although the Gaussian parametrization of η_ℓ in Eq. (2) was still adequate, the expansion of δ_ℓ in Eq. (3) had to be carried to the next order. The inclusion of a third-order term has indeed been shown[2] theoretically to lead to a broader angular distribution and to the asymmetric rise at forward angles observed in our data for two-neutron transfer.

The analytical model we have described for peripheral heavy-ion reactions at incident energies well above the Coulomb barrier establishes the regions of semiclassical and quantum mechanical behavior. It was used to give physical insight into the form of differential cross sections for one- and two-nucleon transfer.

Footnotes and References

*Condensed from Phys. Rev. Lett. 36, 226 (1976).

†On leave from Centre de Recherches Nucléaires et Université Pasteur, Strasbourg, France.

†On leave from Centre d'Etudes Nucléaires de Saclay, Saclay, France.

§On leave from Osaka University, Osaka, Japan. Present address: Tsukuba University, Ibaraki, Japan.

1. V. M. Strutinskii, Phys. Lett. 44B, 245 (1973).

2. W. A. Friedman, W. K. McVoy, and G. W. T. Shuy, Phys. Rev. Lett. 33, 308 (1974).

3. S. Kahana, in *Reactions Between Complex Nuclei*, edited by R. L. Robinson, F. K. McGowan, J. B. Ball, and J. H. Hamilton (North-Holland, Amsterdam, 1974), Vol. 2, p.189.

4. N. K. Glendenning, in *Reactions Between Complex Nuclei*, edited by R. L. Robinson, F. K. McGowan, J. B. Ball, and J. H. Hamilton (North-Holland, Amsterdam, 1974), Vol. 2, p.137.

5. G. R. Satchler, in *Reactions Between Complex Nuclei*, edited by R. L. Robinson et al. (North-Holland, Amsterdam, 1974), Vol. 2, p.171.

6. R. J. Ascuitto and N. K. Glendenning, Phys. Lett. 48B, 6 (1974).

NEW ASPECTS OF HIGH ENERGY, HEAVY-ION INDUCED TRANSFER REACTIONS ON HEAVY TARGETS

C. Olmer, M. Buenerd,* C. K. Gelbke, D. L. Hendrie,
J. Mahoney, A. Menchaca-Rocha,† and D. K. Scott

Single and multi-nucleon transfer reactions induced by high-energy heavy ions on heavy targets are currently being investigated using 20 MeV/amu beams developed at the 88-Inch Cyclotron. Experiments have been performed using 312-MeV ^{16}O and 250-MeV ^{14}N projectiles incident on targets of ^{208}Pb, ^{197}Au and ^{232}Th. The reaction products were detected with the QSD magnetic spectrometer and focal plane detection system, permitting the separation and identification of individual isotopes.

Our motivation for commencing this work was provided by earlier studies[1] at the 88-Inch Cyclotron of heavy-ion induced single-proton stripping reactions at lower incident energies. Typical spectra obtained near the grazing angles for the $^{208}Pb(^{16}O, ^{15}N)^{209}Bi$ reaction at 104, 140 and 217 MeV are shown in Fig. 1(a-c). Prominent in these spectra are transitions to well-known proton single particle states in ^{209}Bi, and these are labelled by their shell model orbitals. These spectra, and others measured for similar transfer reactions, exhibit a j-dependence of the transfer cross section, such that the proton removed from a $j = \ell - 1/2 = j_<$ orbital (as in ^{16}O) would then be preferentially transferred to a $j = \ell + 1/2 = j_>$ orbital in the residual nucleus. An explanation of this observation, and its apparent disapperance

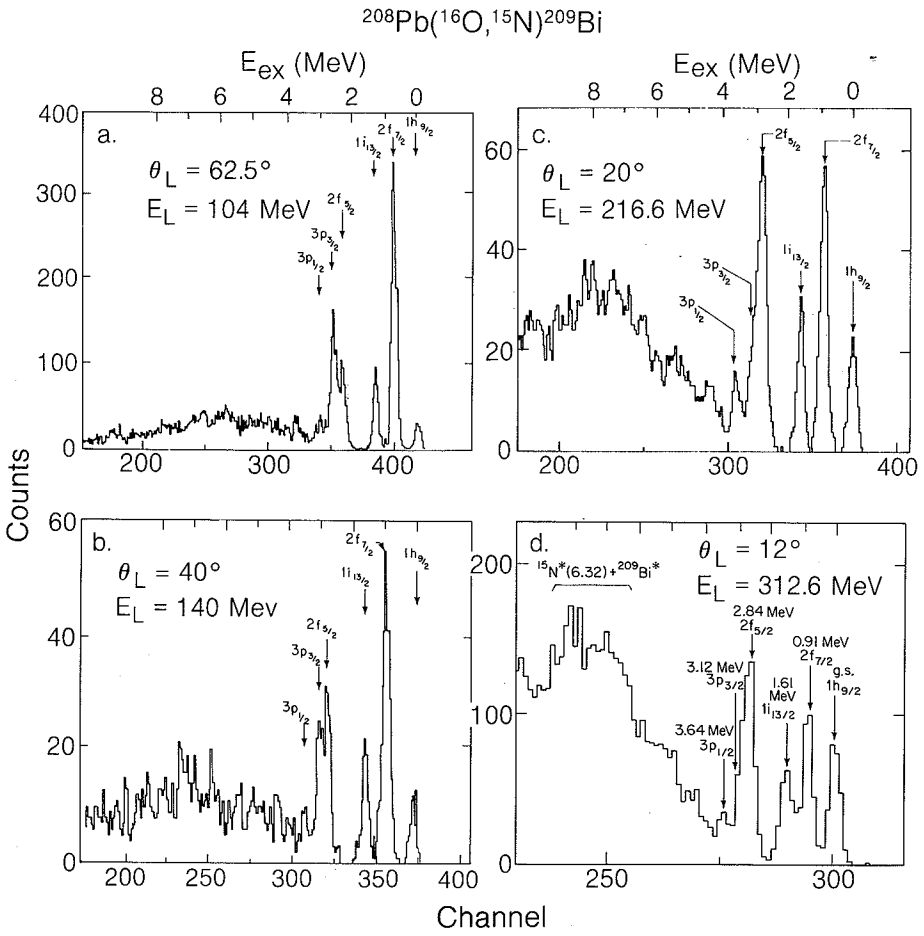

Fig. 1. Energy spectra obtained for the $^{208}Pb(^{16}O, ^{15}N)^{209}Bi$ reaction for incident energies of 104, 140, 217 and 312 MeV. Transitions to known proton single particle states are labelled according to thier shell model orbitals. (XBL 7612-4518)

at higher incident energies (as evidenced by the equal population of the $2f_{7/2}$ and $2f_{5/2}$ levels), was found by invoking recoil effects in the DWBA analysis, thereby providing experimental evidence for the major importance of a previously neglected theoretical consideration.

Interest in the current work was sparked by the observation, within these measured data, of a broad structure centered at ~ 8 MeV in excitation, the strength of which appears to increase relative to the single particle strength as the incident energy was increased. The fact that this peak appeared to be constant in excitation energy over a wide range of bombarding energy indicated that this phenomenon was not the result of kinematic factors favoring the population of different final states, but may reflect the increasingly stronger population of the same individual state(s) in the residual nucleus. To investigate the nature of this structure, we have examined this same reaction, and other complementary transfer reactions, at higher incident energies where a more favorable population of the structure appears to be indicated.

A contracted spectrum of the $^{208}Pb(^{16}O,^{15}N)$ ^{209}Bi reaction obtained near the grazing angle for an incident energy of 312 MeV is shown in Fig. 1d for comparison with the data at lower incident energies. Several features in the current spectrum are of interest. First, the population of known high-spin proton single particle states is again indicated, and the experimental cross sections for these transitions are similar in magnitude to those obtained at the lower energies. Thus the population of the wide structure, observed again at ~ 8 MeV in excitation, appears to be strongly energy dependent (unlike the discrete states) and to increase rapidly with increasing incident energy.

An additional feature in these spectra is the apparent reversal of the j-dependence seen at the lower bombarding energies. Whereas the population of $j_>$ states appears to be more favorable at 104 and 140 MeV, and to equal the population of $j_<$ states at 217 MeV, the present high-energy work indicates a favoring of $j_<$ over $j_>$ final states. Semiclassical arguments, in the framework of the Brink model,[2] can explain this effect by invoking momentum conservation, as viewed

schematically in Fig. 2. A maximum transfer probability will occur if the component of momentum of the transferred nucleon (of mass m) along the beam direction is almost conserved, i.e.

$$\hbar\Delta k = P_i - P_f = mv - \hbar\left(\frac{\lambda_i}{R_i} + \frac{\lambda_f}{R_f}\right) \approx 0 \ .$$

Thus for small incident energies, λ_i and λ_f are of opposite sign (for the equality to hold) so that the previously observed j-dependence will be seen, namely that $j_> \rightarrow j_<$ and $j_< \rightarrow j_>$. For higher incident energies, however, λ_i and λ_f are of the same sign so that a reversal of the j-dependence will be observed, namely that $j_> \rightarrow j_>$ and $j_< \rightarrow j_<$. Finite range, full recoil DWBA calculations are already in progress to investigate whether a more complete analysis can similarly account for this energy dependence.

A larger portion of the spectrum displayed in Fig. 1d is shown in Fig. 3, together with other (^{16}O, ^{15}N) spectra obtained with ^{197}Au and ^{232}Th targets. The excitation of several wide structures in the residual nuclei is indicated, and relatively intense yields are observed. In particular, several such peaks appear in the $^{197}Au \rightarrow {}^{198}Hg$ spectrum, in addition to the expected ground state peak. The ^{208}Pb and ^{197}Au targets were 0.7 and 2.7 mg/cm^2 thick, respectively, and the ^{232}Th target was 5 mg/cm^2 thick so that comparable structure in the $^{232}Th \rightarrow {}^{233}Pa$ spectrum may be unresolved.

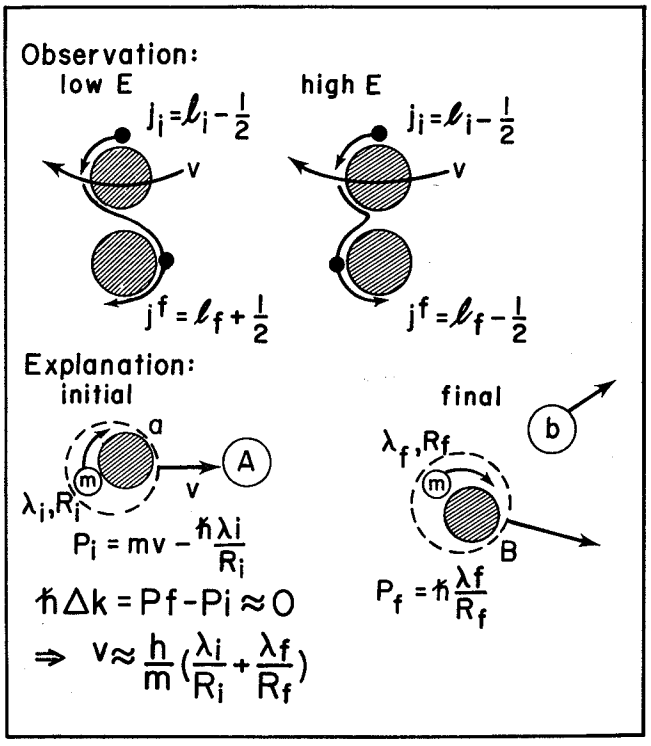

Fig. 2. Schematic diagram of the A(a,b)B transfer reaction, explaining the changing j-dependence of the cross section in terms of different orbit matching at low and high incident energies. (XBL 766-8324)

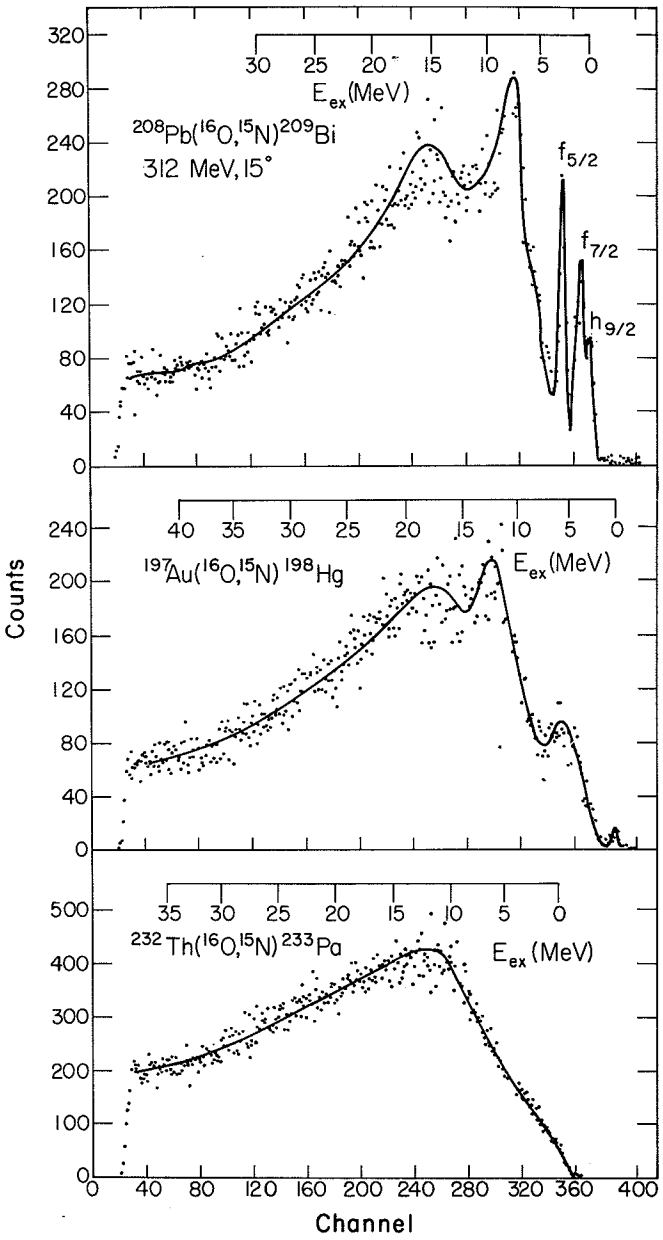

Fig. 3. Energy spectra at 15° for the (^{16}O, ^{15}N) reaction induced by 312 MeV ^{16}O on targets of ^{208}Pb, ^{197}Au and ^{232}Th. (XBL 763-2562)

Spectra for the corresponding (^{16}O,^{15}O) neutron transfer reaction are shown in Fig. 4. Again, the strong population of several broad structures is evident, some of which occur at nearly the same excitation energy as observed in the proton transfer spectra. As in the (^{16}O,^{15}N) results, the intensities of these broad structures has increased strongly both absolutely and relative to the single particle transitions for incident energies between 104 and 312 MeV. The intense population of high spin single particle states is seen here also, especially for the $^{208}Pb \rightarrow {}^{209}Pb$ spectrum. Also evident in the spectrum is a candidate for the $j_{15/2}$ fragment state, which was observed at the same excitation energy, but only weakly populated in the neutron transfer studies

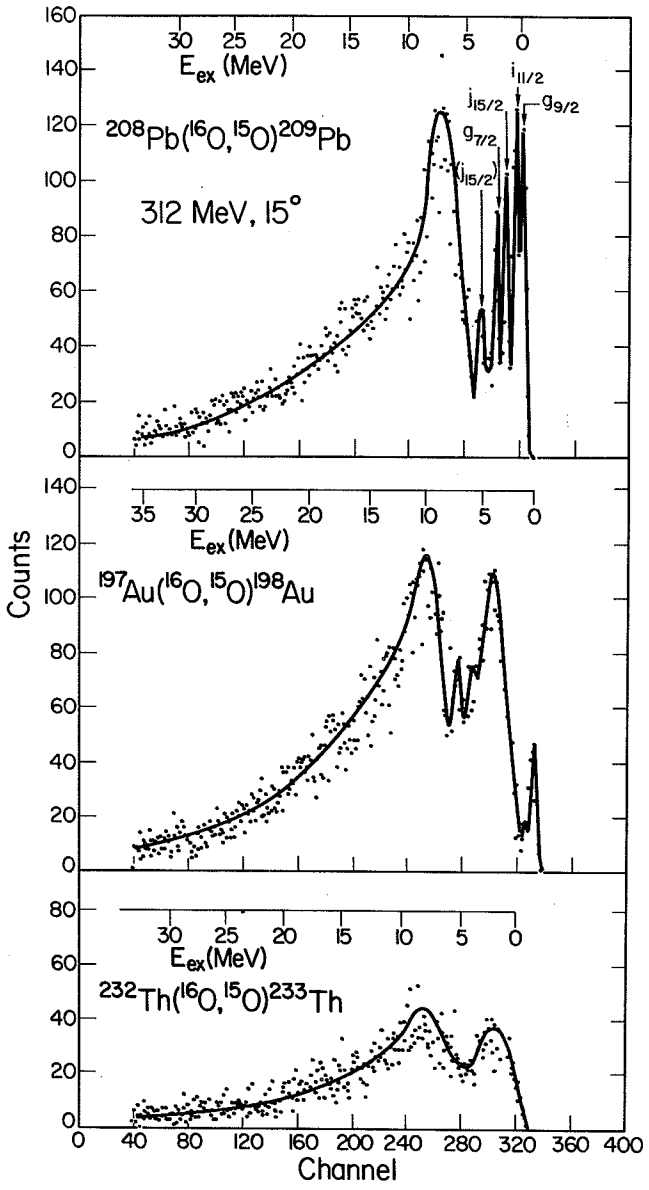

Fig. 4. Energy spectra at 15° for the (^{16}O, ^{15}O) reaction induced by 312 MeV ^{16}O on targets of ^{208}Pb, ^{197}Au and ^{232}Th. (XBL 763-2474)

at lower energies.[3] The more intense population of the $g_{9/2}$ state relative to the $g_{7/2}$ state is observed, contrary to the new expectations, deduced from the proton transfer data measured at these higher incident energies. However, the $^{208}Pb(^{16}O, ^{15}O)^{209}Pb$ spectra obtained by Becchetti et al.[3] at 140 MeV incident energy indicates that the intensity of the $g_{7/2}$ peak. This result is to be compared with the present data in which this ratio is observed to be less than a factor of two. From this observation, and the larger angular momentum involved in the neutron transfer case (4ħ rather than 3ħ), it seems reasonable to conclude that for the neutron transfer data, higher incident energies than are considered here will be necessary in order to observe the reversal of the j-dependence.

One possible source of the broad structures observed in all these data could be the simultaneous excitation of the residual nucleus and the ^{15}N or ^{15}O reaction products, most probably the $p_{3/2}$ hole state at 6.32 and 6.18 MeV, respectively. The subsequent in-flight gamma ray decay of the reaction product would then give rise to a Doppler-broadened peak in the spectrum. In order to investigate this possibility, proton and neutron transfer reactions were performed on ^{208}Pb, ^{197}Au and ^{232}Th targets using a 250 MeV incident ^{14}N beam. Since ^{13}N has no particle-stable excited states, significant differences between the (^{16}O, ^{15}N) and (^{14}N, ^{13}N) spectra may indicate that the ^{16}O-induced transfer data contain peaks originating from the excitation of ^{15}N and ^{15}O, together with a lower excitation of the residual nuclei.

Spectra for the neutron and proton transfer reactions induced by ^{14}N are shown in Figs. 5 and

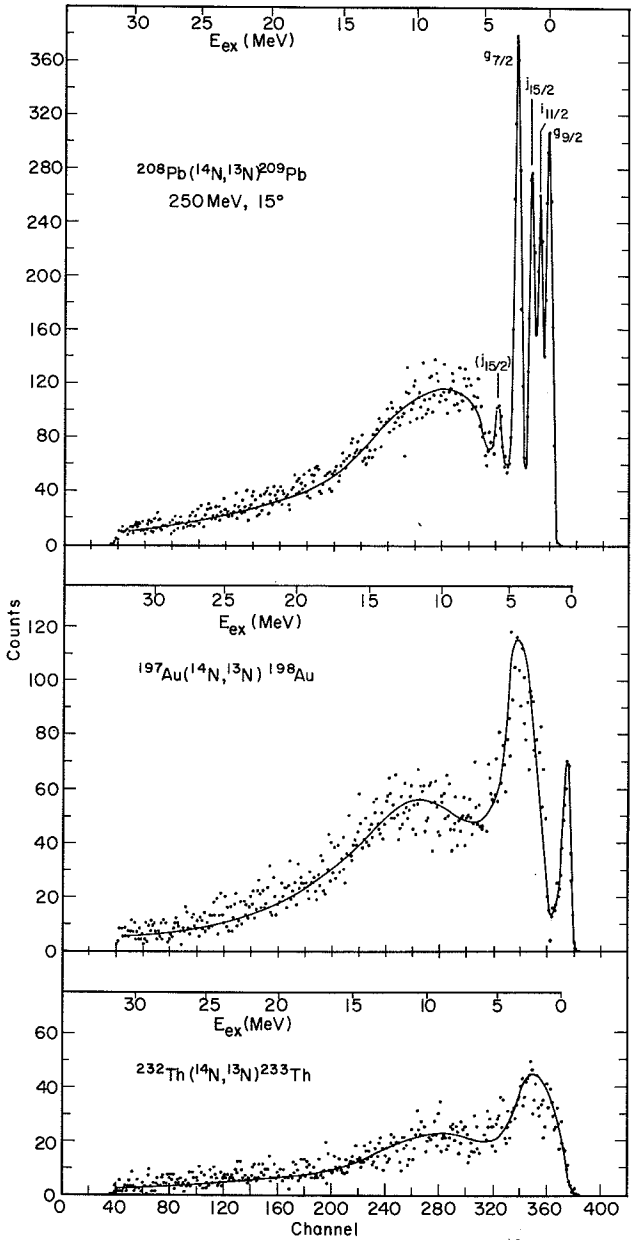

Fig. 5. Energy spectra at 15° for the (^{14}N, ^{13}N) reaction induced by 250 MeV ^{14}N on targets of ^{208}Pb, ^{197}Au and ^{232}Th. (XBL 763-5322)

6. A comparison of the (^{16}O, ^{15}O) and (^{14}N, ^{13}N) spectra shows remarkable similarities, and suggests that ejectile excitation is not a major problem in the present work, although unambiguous evidence for this conclusion is not yet available. A further similarity between ^{16}O-and ^{14}N-induced transfer reactions is observed in the population of discrete states from single nucleon transfer on ^{208}Pb. As in the (^{16}O,^{15}N) reaction data, the enhanced population of the $f_{5/2}$ state relative to the $f_{7/2}$ state is observed. In addition, for the (^{14}N,^{13}N) reaction, a comparable population of the $g_{9/2}$ and $g_{7/2}$ levels is seen, and the suspected $j_{15/2}$ fragment state also appears.

Differences among these spectra also exist, and several mysteries in these data still remain.

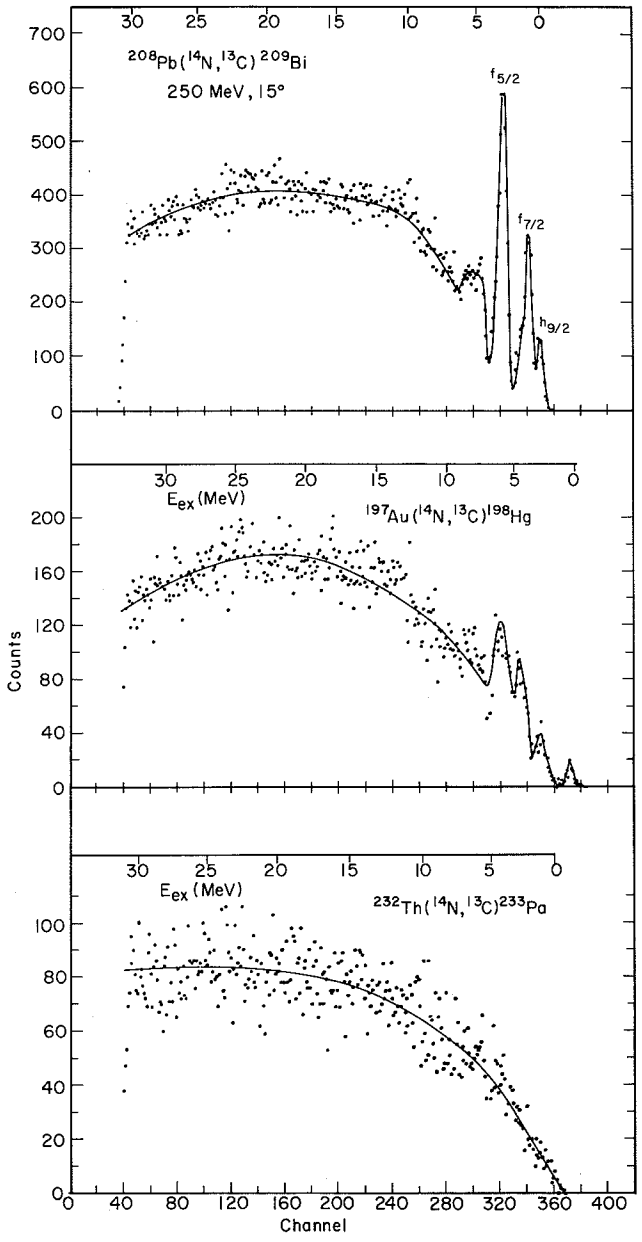

Fig. 6. Energy spectra at 15° for the (^{14}N, ^{13}C) reaction induced by 250 MeV ^{14}N on targets of ^{208}Pb, ^{197}Au and ^{232}Th. (XBL 763-5321)

First, a marked difference is observed between neutron and proton transfer spectra. For the (^{14}N, ^{13}C) spectra especially and, to a lesser degree, for the (^{16}O, ^{15}N) spectra, a significant, underlying continuum-type background exists which does not appear for neutron transfer spectra. Although the shape of this structure is reminiscent of that expected from projectile fragmentation, it is not at all clear why only proton and not neutron decay of the projectile would be observed in the present work.

An additional feature in these data, which is not understood at present, is the microscopic nature of the broad structures which appear in all the spectra. It is tantalizing to note that the observed centroids of many of these structures correspond almost exactly to known giant resonance states, seen, for example, in inelastic electron, proton, ^{3}He and alpha particle scattering. The recent (p,p') work of Bertrand and Kocher[4] indicates a resonance at ~ 4 MeV excitation (FWHM ~ 2 MeV) and a wider resonance at ~12 MeV excitation (FWHM ~ 4 MeV) in ^{197}Au. These energies match almost exactly those observed in the present single nucleon transfer data on ^{197}Au, and similar correspondences of the observed ^{209}Pb and ^{209}Bi peaks to known giant resonances in ^{208}Pb can also be made. It is premature at this stage to attribute the observed broad transitions to giant resonances states although, if recently obtained ^{16}O inelastic scattering data should exhibit these same excitations, then such a conclusion would not seem unreasonable.

The single nucleon transfer data reported here represent only a portion of the total data accumulated during the experiments. In particular, data for several angles over a wide excitation energy range for many different isotopes (from ^{6}Li to ^{19}F) are presently being processed. It is hoped that all these data, together with the inelastic scattering data, will be able to resolve the question as to whether giant resonances are being populated in the present work. This information will be especially useful in the recent investigations by many experimental and theoretical groups concerning the microscopic nature of deep inelastic processes. In particular, the theory of Broglia et al.[5] invokes just these giant resonances to explain the large energy, mass and charge losses which are experimentally observed and, in a macroscopic framework, attributed to frictional forces.

Footnotes and References

*Permanent address: Institut des Sciences Nucléaires, Grenoble, France.

†Permanent address: Instituto de Fisica, U.N.A.M., Mexico.

1. D. G. Kovar, F. D. Becchetti, B. G. Harvey, F. Pühlhofer, J. Mahoney, D. W. Miller and M. S. Zisman, Phys. Rev. Lett. 29, 1023 (1972); D. G. Kovar, B. G. Harvey, F. D. Becchetti, J. Mahoney and M. S. Nagarajan, Nuclear Chemistry Annual Report (1972) LBL-1666, P. 90.

2. D. M. Brink, Phys. Lett. 40B, 37 (1972).

3. F. D. Becchetti, B. G. Harvey, D. Kovar, J. Mahoney, C. Maguire and D. K. Scott, Phys. Rev. C 12, 894 (1975).

4. F. E. Bertrand and D. C. Kocher, submitted to Phys. Rev. C.

5. R. A. Broglia, C. H. Dasso and A. Winther, Phys. Lett. 61B, 113 (1976).

EVIDENCE FOR SHALLOW STRONGLY ABSORBING HEAVY-ION OPTICAL POTENTIALS

J. G. Cramer,* R. M. DeVries,† D. A. Goldberg,‡
M. S. Zisman, and C. Maguire

Over the past several years we have conducted a detailed investigation of the elastic scattering of ^{16}O from ^{28}Si and similar targets over a range of energies. We have concluded from this study that there are three principal regions of the nuclear potential which are probed by this type of elastic scattering analysis: (a) the extreme tail region of the potential, which is probed by elastic scattering performed very near the Coulomb barrier; (b) the strong absorption radius (or more quantitatively, the semi-classical turning radius of the grazing partial wave), which is probed by scattering at essentially all bombarding energies between the Coulomb barrier and about 100 MeV; and (c) the surface region and "outer interior," which are probed by scattering at bombarding energies above about 100 MeV, where enough energy is avilable to observe nuclear "rainbow" scattering.

Thus if the nuclear potential is assumed to be independent of energy, it can be mapped by simultaneously fitting data of types (a), (b), and (c), as described above. In an effort to enlarge the information from the interior region, we have in a collaborative experiment studied the scattering of ^{16}O from ^{28}Si at a laboratory bombarding energy of 215.2 MeV, using the ^{16}O beam from the LBL 88-inch cyclotron. These data, together with data collected at lower energies[1] were fitted with a global analysis, requiring the same energy-independent six-parameter Woods-Saxon potential to fit both high and low energy data. The results are shown in Fig. 1. The potentials used in generating the curves in Fig. 1 are given in Table 1.

There is a clear preference for the shallow potentials in this analysis. While it is possible to find deeper potentials that can fit either the low energy data or the high energy data, we have found no deep potential capable of fitting both low and high energy data at the same time. This fit is "unique" only in the context of energy-independent Woods-Saxon potentials.

It should perhaps be mentioned that Satchler has recently analyzed the data set shown in Fig. 1 from the point of view of the folding model.[2] He has started with a realistic nucleon-nucleon potential and obtained an effective real potential with a double-folding procedure while using an empirical Woods-Saxon imaginary potential. It was found to be necessary to renormalize the real potential and to use an energy-dependent geometry for the imaginary potential, but with these modifications, it was possible to obtain quite a good fit to these data. Thus it is clear that deeper non-Woods-Saxon energy-dependent potentials are quite capable of fitting the data set.

The results presented here pose an interesting question: Does the preference which has been found for a 10 MeV real well depth really mean that overlapping ^{16}O and ^{28}Si nuclei have such a weak interaction? Even at our highest incident energies, "notch-perturbation" tests of potential

Table 1. Derived optical model potentials.

Label	V_0	r_0	a_0	W_0 (volume)	r_I	a_I	χ^2/N (215.2 MeV)	χ^2/N (38.0 MeV)
E18	10	1.35	0.618	23.4	1.23	0.552	4.9	1.2
A23	100	0.932	0.797	165	0.890	0.764	8.6	15
S75	100	1.06	0.640	42.0	1.06	0.640	1.3×10^5	2.0

$R = r(16^{1/3} + 28^{1/3})$, $r_{Coulomb} = 1.0$. Potential S75[1] is a fit to the data for $E_{16_O} \leq 81$ MeV only.

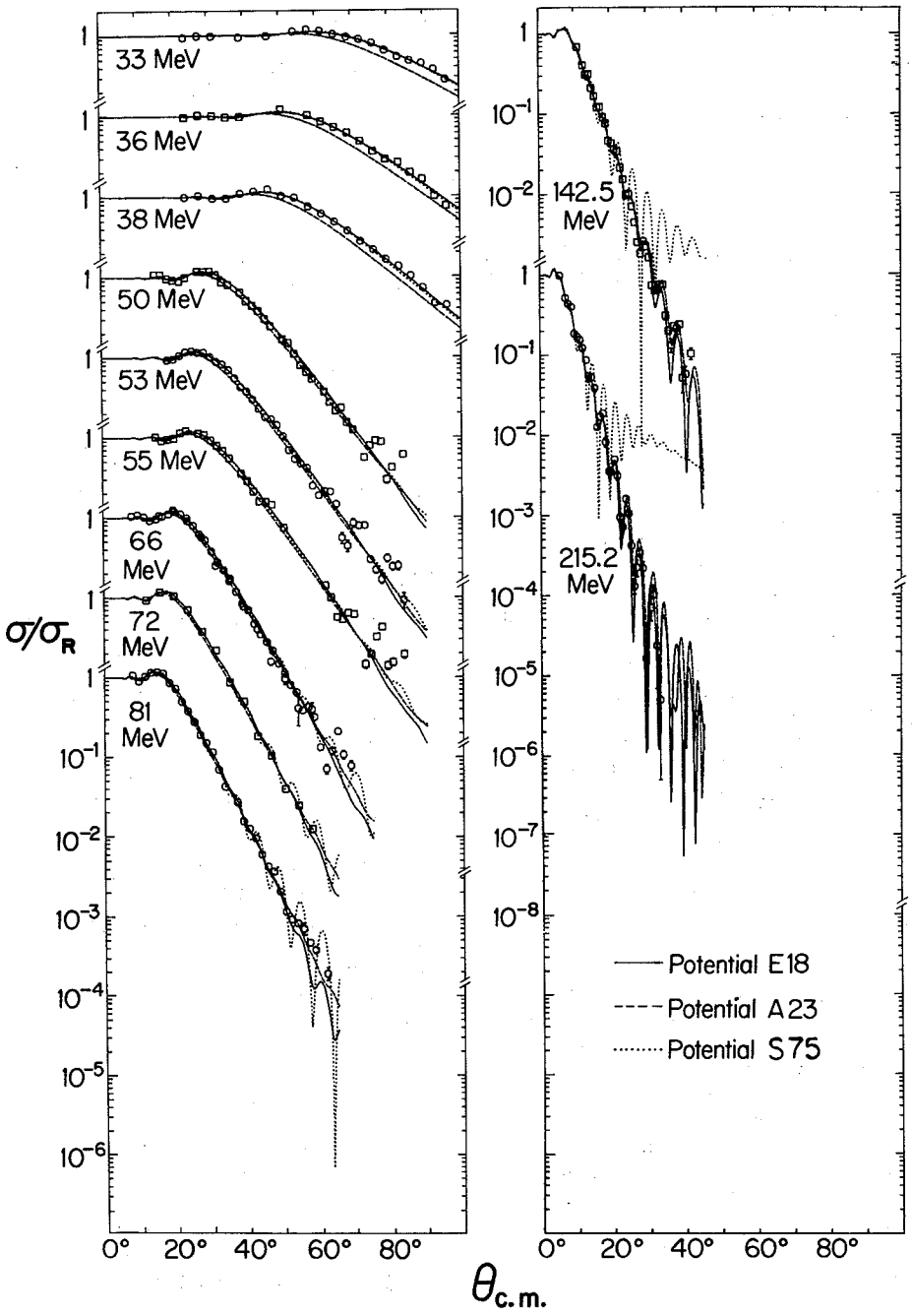

Fig. 1. Elastic $^{16}O + ^{28}Si$ scattering at the labeled incident energies. The lines are optical model calculations using the parameters sets indicated and listed in Table 1. (XBL 766-8272)

sensitivity indicate no contributions to the scattering from separation distances of less than 5.5 fm.[3] Thus the derived V = 10 MeV value only indicates the potential's behavior in the nuclear surface region in terms of a Woods-Saxon shape and does not preclude the existence of a soft repulsive core, for example. Moreover, the energy required to separate ^{44}Ti into $^{16}O + ^{28}Si$ is 11.48 MeV. Therefore, in the zero incident energy limit, the bound-state potential for this system would be considerably in excess of 10 MeV. Even with these qualifications, the derived V = 10 MeV value for ^{16}O ions represents a striking departure from the monotonic increase in real well depths found for light-ions, i.e., 50 MeV for nucleons, 80-100 MeV for deuterons, 110-130 MeV for alphas.

It is clear that more theoretical work on the potentials appropriate to heavy-ion interactions is indicated. More experimental data are needed on the elastic scattering at high and low energies of projectiles in the mass region $4 < A < 16$ so that optical potentials in this critical transition region can be determined.

Footnotes and References

*Department of Physics, University of Washington, Seattle, WA 98195.

†Department of Physics, University of Rochester, Rochester, NY 14627.

‡Department of Physics, University of Maryland, College Park, MD 20742.

1. J. G. Cramer et al., Nuclear Physics Laboratory Annual Report, University of Washington (1975), p.128.

2. G. R. Satchler, private communication.

3. J. G. Cramer, private communication.

$^{6}Li + ^{28}Si$ ELASTIC SCATTERING

J. G. Cramer,* R. M. DeVries,† D. A. Goldberg,‡
M. S. Zisman, and C. F. Maguire

The results of our study of the $^{16}O + ^{28}Si$ optical potential (see preceding paper) indicate that the ^{16}O potential is radically different from light ion potentials. Clearly a study of intermediate projectiles is of interest, concentrating on obtaining a large data set including both high and low energy data. For this reason we measured at the LBL 88-Inch Cyclotron 135.1 MeV ^{6}Li (the highest energy obtainable anywhere at this time) scattering from ^{28}Si as shown in Fig. 1. Data from Iowa[1] existed at 13 MeV and are also shown in Fig. 1. Subsequently we have measured 18 MeV and, preliminarily, 44 MeV (11 MeV on terminal) data at Rochester — see Fig. 1. The Rochester measurements were made with the Rochester Heavy-Ion Detector using a multi-slit aperture at the entrance to the Enge split-pole.

The analysis follows the same line as was used for the ^{16}O data even though the real potential is not expected to be as energy independent.[2] The value of V_0 was gridded on, while the other five Woods-Saxon parameters were free in a simultaneous search on the 135.1 MeV and 13 MeV data sets. Good fits could not be obtained for $V_0 \lesssim 25$ MeV while the fits for $V_0 \gtrsim 40$ MeV were all about equally good for both data sets — see Fig. 1 for $V_0 = 40$, 100, 150 MeV fits to the 135.1 MeV data. Therefore, at this time we have not succeeded in eliminating the discrete ambiguities for ^{6}Li optical potentials.

The parameters for the $V_0 = 100$ MeV potential are:

$V_0 = 100$, $r_0 = 1.30$, $a_0 = 0.784$, $W_{vol} = 36.7$

$r_I = 1.57$, $a_I = 0.883$, where $R = r \cdot 28^{1/3}$.

Most of the other potentials shared the following characteristics of this $V_0 = 100$ MeV potential:

a) W_0/V_0 much less than for ^{16}O and similar to that observed for ^{4}He;

b) $r_I > r_0$, $a_I > a_0$; this is opposite to what was found for ^{16}O. This behavior is a well-known feature of ^{6}Li optical parameters.

c) The fits to the intermediate energies (18 MeV and 44 MeV) are not acceptable, perhaps indicating that an energy dependence exists — again in contrast to the ^{16}O results.

We tentatively conclude, therefore, that ^{6}Li behaves more like a "light" than a "heavy" ion.

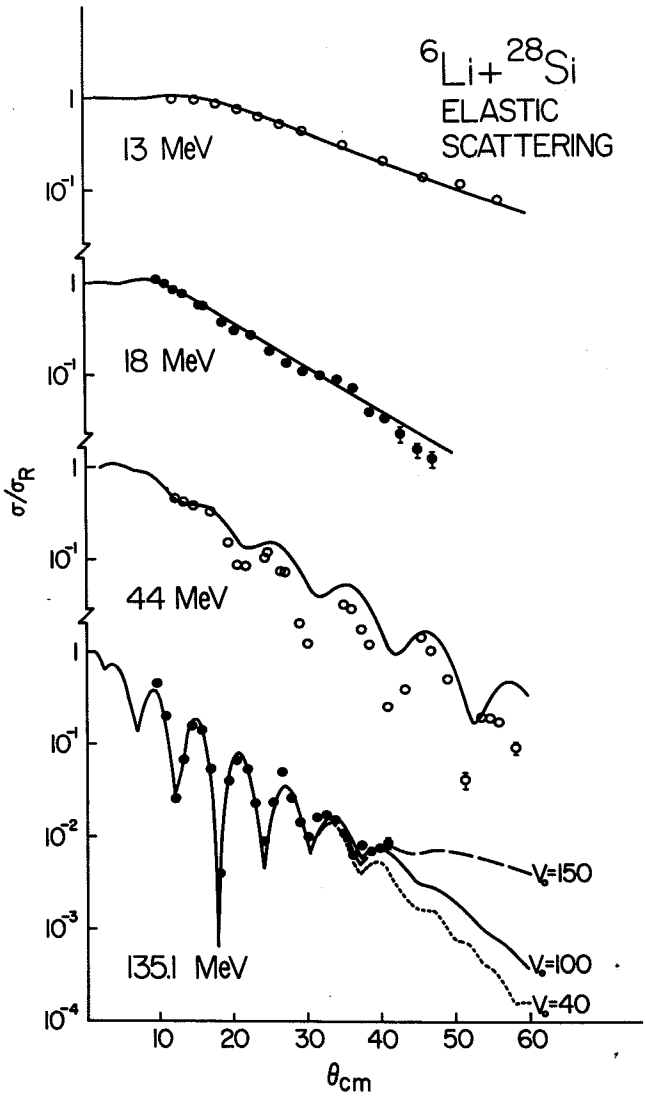

Fig. 1. Elastic scattering of $^{6}Li + ^{28}Si$ at the indicated laboratory energies. The curves are optical model fits (see text). (XBL 766-8295)

Finally, on the basis of the large angle differences in the predictions with the V_0 = 40, 100 and 150 MeV potentials, it appears possible to resolve the discrete ambiguities by taking more data at 135.1 MeV. We plan to do this along with other intermediate energy measurements.

Footnotes and References

*Physics Department, University of Washington, Seattle, WA 98195.

†Physics Department, University of Rochester, Rochester, NY 14627.

‡Physics Department, University of Maryland, College Park, Md 20742.

1. J. E. Poling, E. Norbeck, and R. R. Carlson, Phys. Rev. C 13, 648 (1976).

2. D. F. Jackson and R. C. Johnson, Phys. Lett. 49B, 249 (1974).

$^{40}Ca + {}^{40}Ca$ ELASTIC SCATTERING RESONANCES

C. F. Maguire,* D. L. Hendrie, U. Jahnke,†
J. Mahoney, and D. K. Scott

The gross structure observed in $^{16}O + {}^{16}O$ elastic scattering excitation functions,[1] but not observed in other systems,[2,3] can be explained by an ℓ-dependent term in the imaginary part of an optical potential.[4] This model also predicts that resonance effects, although much reduced, should appear in the elastic scattering of $^{40}Ca + {}^{40}Ca$. Such effects were looked for by Doubre et al.[5] at the Orsay Tandem from 110 to 150 MeV, and at 170 to 300 MeV with the Orsay cyclotron, ALICE. Although they saw no effect, some aspects of their work may have reduced their chances of observing the effect. In particular, the ℓ-dependent optical model predicts the largest effect near 160 MeV, just between the capabilities of their two machines.

We used the 88" Cyclotron to produce beams of 150- to 173-MeV ^{40}Ca, beams; up to 50 na on target were measured. The QSD spectrometer was used to detect and identify the outgoing ^{40}Ca. Since the detector length spanned only two charge states of the ^{40}Ca, only 40-45% of the scattered Ca could be used for the measurements. Because the distribution of charge states of the Ca leaving the target was energy dependent (and slightly target-dependent) tedious normalization runs were made to determine the distributions, in order to normalize the data and span the most prolific charge states (around Z = 16). Energy dependent corrections to Faraday cup and monitor counter readings were also required. Small amounts of ^{40}Ar in the beam were accounted for. Some inelastic events, especially to the region of the 2^+ at 3.90 and 3^- at 3.73 MeV were seen, but with too low a cross section in general to get meaningful data.

An elastic angular distribution was measured at 163 MeV, in order to extract an (ℓ-independent) optical potential (Fig. 1). No large sensitivity to optical potential parameters that fit the angular distributions was noted in the excitation work. Additional data points were taken between 26 and 56° (CM) with a solid-state detector, in close agreement with the spectrometer data and confirming the normalization corrections.

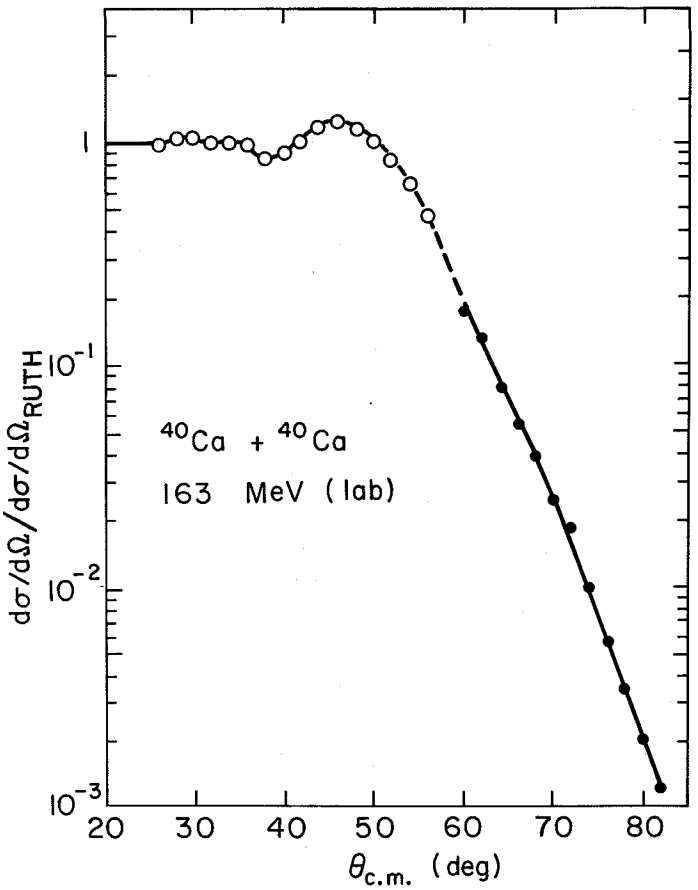

Fig. 1. Elastic scattering angular distribution at 163 MeV.

The excitation function data are seen in Fig. 2, along with the optical model predictions. The ℓ-independent prediction clearly misses the observed resonant effects by as much as a factor of two.

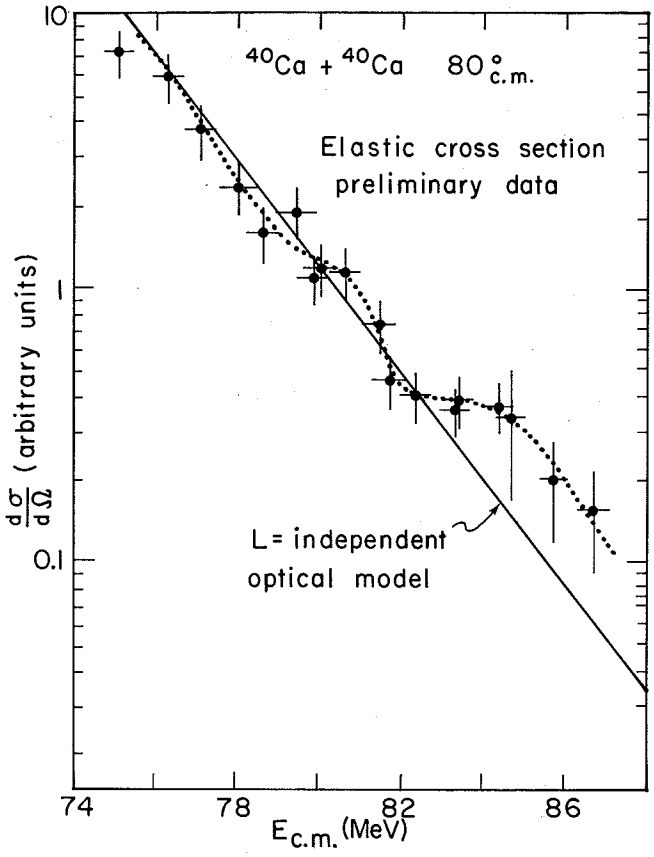

Fig. 2. Excitation function of $^{40}Ca + ^{40}Ca$, with ℓ-independent model predictions (solid line).

Because we have not made final adjustments to the data to convert the cross section into absolute values or made comprehensive checks of the ℓ-dependent model, our conclusion that weak resonances appear to be present in the data is tentative. Since the excitation functions were not measured at 90°, it is possible that the observed variation is due to sweeping over oscillatory structure in the differential cross sections as a function of energy.

The measured differential cross sections at 163 MeV however gave no evidence for oscillatory structure. Our preliminary ℓ-dependent optical model calculations predict effects too small to be measured by us at a CM angle of 70°, the largest angle measured using ALICE.

Footnotes and References

*Present address: Vanderbilt University, Nashville, Tenn.

†Present address: Hahn-Meitner Institut, Berlin.

1. R. H. Siemssen, J. V. Maher, A. Weidinger, and D. A. Bromley, Phys. Rev. Lett. 19, 369 (1967), and 20, 175 (1968); J. V. Maher, M. W. Sachs, R. H. Siemssen, A. Weidinger, and D. A. Bromley, Phys. Rev. 188, 1665 (1969).

2. R. H. Siemssen, in Proceedings of the Symposium on Heavy-Ion Scattering, Argonne National Laboratory Report No. ANL 7837, 1971 (unpublished), p. 145.

3. R. W. Shaw, R. Vandenbosch, and M. K. Mehta, Phys. Rev. Lett. 25, 457 (1970).

4. R. A. Chatwin, J. S. Eck, D. Robson, and A. Richter, Phys. Rev. C 1, 795 (1970).

5. H. Doubre, J. C. Roynette, J. C. Jacmart, N. Poffé, M. Riou, E. plagnol and P. de Saintignon, Phys. Rev. Lett. 35, 508 (1975).

ELASTIC SCATTERING OF ^{14}N ON ^{12}C AT 81 AND 100 MeV AND THE REACTION $^{12}C(^{14}N, ^{13}N)^{13}C^*$ (3.09 MeV)

C. Olmer, M. Buenerd, G. Delic, D. L. Hendrie, A. Menchaca-Rocha, and D. K. Scott

The observation[1] of an anomalous angular distribution in the single nucleon transfer reaction $^{12}C(^{14}N,^{13}N)^{13}C$ to the $2s_{1/2}$ state in ^{13}C at 3.09 MeV has provided the stimulus for similar work from several laboratories.[2-5,8] Essentially, the anomaly consists of distorted-wave Born approximation calculations predicting an angular distribution that is out of phase with the observed features of the differential cross section when employing optical model (OM) parameters that reproduce the appropriate elastic scattering angular distributions.

The aim of the present study was to investigate the $^{12}C(^{14}N, ^{13}N)^{13}C$ reaction after performing detailed OM analyses of the $^{14}N + ^{12}C$ elastic scattering. The motivation for this was that in the work of DeVries et al.[1] the elastic scattering data measured were too sparse. In the present work the elastic scattering measurements were performed using 100.3-MeV $^{14}N^{4+}$ and 80.7-MeV $^{14}N^{3+}$ beams produced at the 88-Inch Cyclotron. The reaction products scattered from the 1.07-mg/cm^2 ^{12}C target were detected in four 1.5-mm lithium-drifted silicon detectors placed 2° apart, each with an angular acceptance of 0.25°. Data were accumulated over the angular range 3° to 35° (representing approximately six orders of magnitude in the differential cross section), with an angular spacing of 0.5°.

The present experiment, because of the high density of data points as a function of angle

combined with the wider angular range, reveals features of the elastic ratio-to-Rutherford cross section which are not apparent in the earlier measurements[1,6] (see Figs. 1 and 2). At 100 and 81 MeV, the cross section has three distinct regions: (a) at forward angles it falls rapidly away from the Rutherford value by about an order of magnitude to the second minimum, (b) it then oscillates rapidly with a large amplitude (approximately through an order of magnitude), and (c) with increasing angle these oscillations are damped almost completely.

OM parameter searches were performed on the two sets of data with the search code SOPHIE[7] and Table 1 summarizes the results of the parameter searches so far. Parameter sets labelled 81A to D and 100A to D were obtained from searches on the data measured in the present experiment while sets 81E and 100E were obtained from searches on earlier data,[1,6] which were either too sparse or confined to a narrower range in angle. The OM predictions corresponding to the parameters of Table 1 are shown in Figs. 1 and 2 for the 100- and 81-MeV data, respectively. While data in the backward hemisphere could be expected to have an important effect on the OM parameters resulting from a search, it is clear from the present work that the OM does predict the qualitative features of the elastic scattering cross section throughout the measured angular range. Furthermore, fits of equivalent quality are obtained with either a

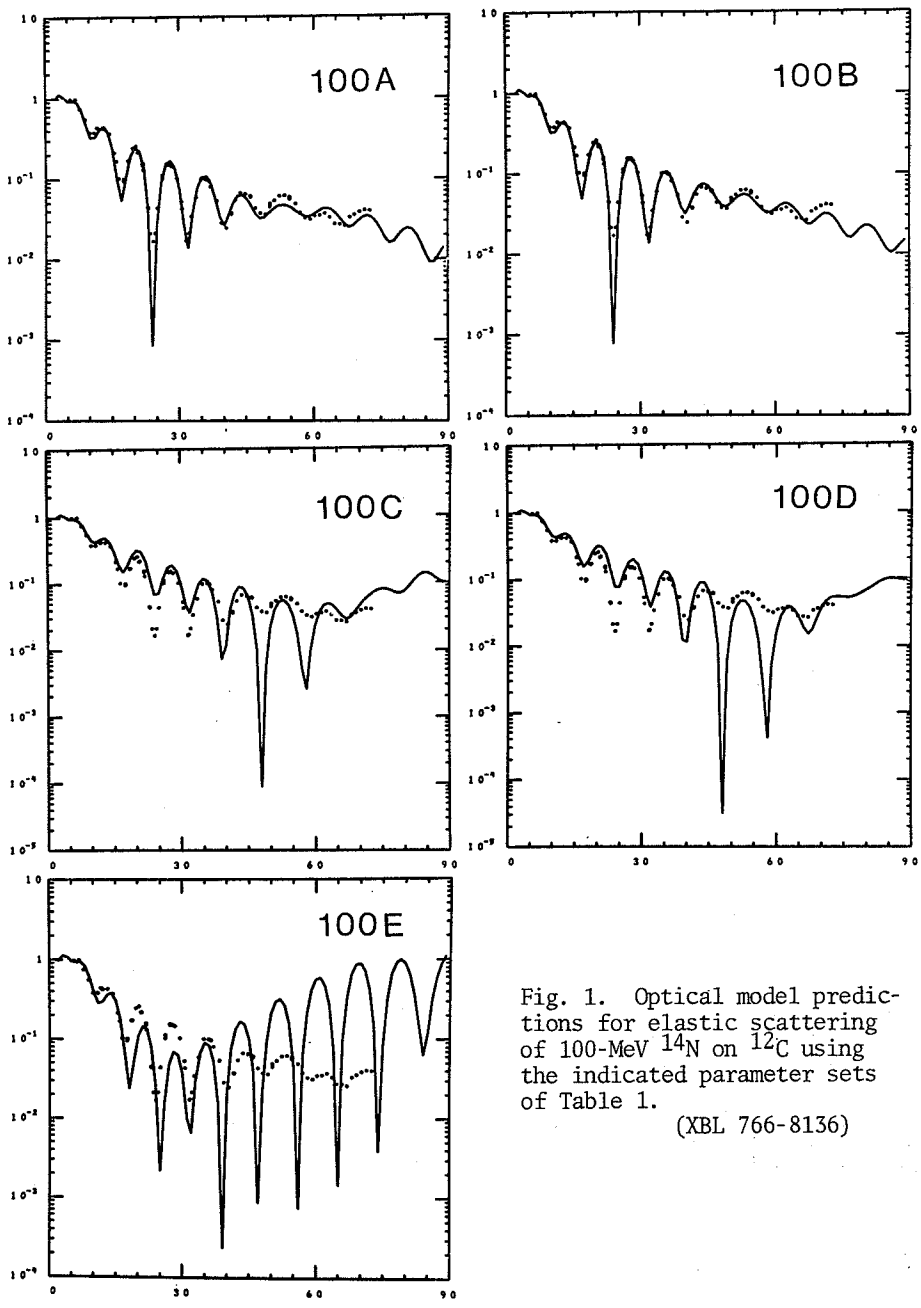

Fig. 1. Optical model predictions for elastic scattering of 100-MeV ^{14}N on ^{12}C using the indicated parameter sets of Table 1.

(XBL 766-8136)

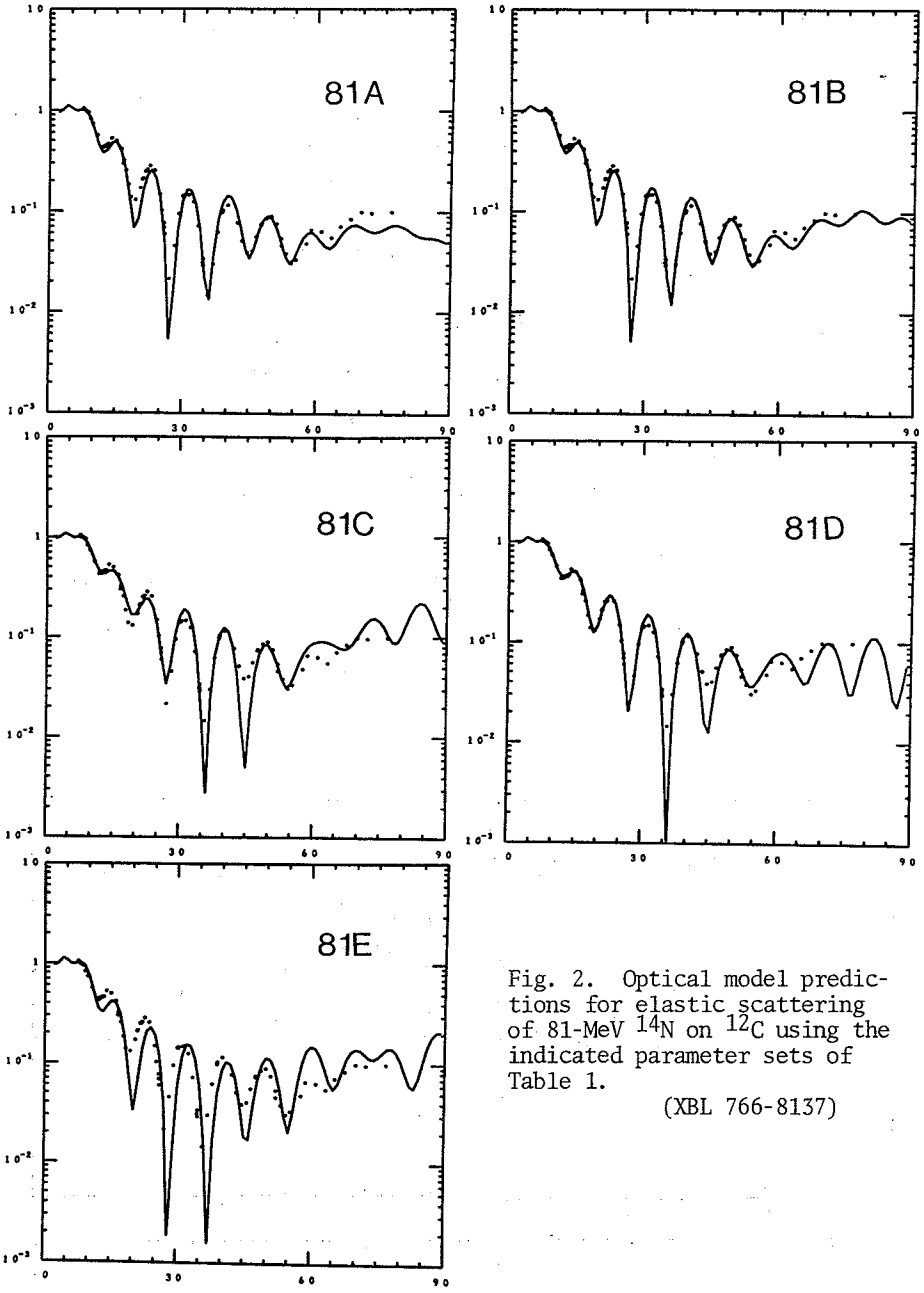

Fig. 2. Optical model predictions for elastic scattering of 81-MeV ^{14}N on ^{12}C using the indicated parameter sets of Table 1.

(XBL 766-8137)

volume or a surface type absorbing potential for example compare potentials 100A and 100B which have nearly identical real potentials.

The potentials listed in Table 1 were employed in DWBA calculations for the reaction $^{12}C(^{14}N, ^{13}N)^{13}C_{2s(1/2)}$. For the entrance channel, the 100-MeV potentials were used, while for the exit channel the 81-MeV ^{14}N + ^{12}C parameters were employed. The basis of the latter assumption is that the OM has a smooth mass number dependence and provides similar elastic scattering predictions for systems with similar values of η (Sommerfeld parameter) and k (asymptotic wave number). For the two systems ^{14}N + ^{12}C (at 81 MeV) and ^{13}N + ^{13}C in the exit channel of the reactions the respective values are 2.75 and 2.76 for η and 3.39 and 3.41 fm^{-1} for k. Some DWBA results are shown in Fig. 3. OM potentials of the type E produce cross sections in phase with the reaction data, but so far, potentials that fit the elastic data and predict the correct phase of the reaction data have not been found. However, a closer inspection of Fig. 3 shows that the DWBA cross section is very sensitive to the type of potentials employed. If OM potentials of type C, with imaginary diffuseness ~ 0.1 fm, are introduced then the DWBA cross section shows large changes in the angular region spanned by the available reaction data – even though all the potentials A to D come close to reproducing the elastic data well.

Table 1. Optical model parameters for $^{14}N + ^{12}C$ elastic scattering.

E^{lab} (MeV)	label	r_V (fm)	a_V (fm)	V (MeV)	r_W (fm)	a_W (fm)	W [a] (MeV)	r_{WV} (fm)	a_{WV} (fm)	W_V (MeV)
81	81A	1.020	0.5564	166.4	0.9216	0.3757	47.14			
	81B	1.041	0.5578	132.8				0.8571	0.6303	22.30
	81C	1.296	0.3144	93.52	0.9778	0.1089	126.4			
	81D	1.177	0.4562	79.80	1.002	0.1895	118.4			
	81E	1.069	0.5397	86.78	0.8967	0.1137	123.6			
100	100A	1.115	0.5304	100.5	1.088	0.3162	54.44			
	100B	1.096	0.5563	100.1				1.159	0.3306	62.75
	100C	1.270	0.3100	118.0	1.140	0.1050	200.0			
	100D	1.280	0.2920	116.0	1.140	0.1070	210.0			
	100E	1.065	0.5221	89.36	0.8901	0.1133	265.8			

a) Surface type imaginary potential W is as used in Ref. 7; Volume type imaginary potential is as usually defined.

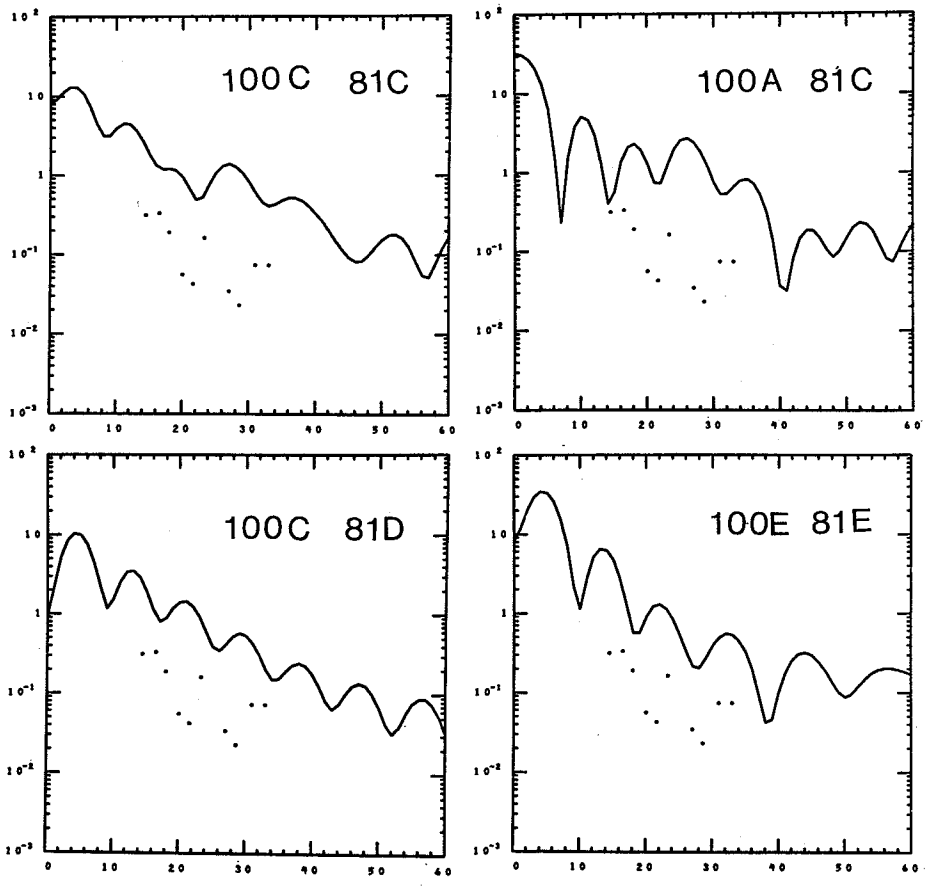

Fig. 3. Distorted-wave Born approximation calculations with KUNDRY for the reaction $^{12}C(^{14}N, ^{13}N)^{13}C_{2s(1/2)}$ using the parameters of Table 1. The cross sections are in mb/sr for unit spectroscopic factors; the data are those of Ref. 1. (XBL 766-8138)

Footnote and References

*Work in progress.

1. R. M. DeVries, M. S. Zisman, J. G. Cramer, K. L. Liu, F. D. Becchetti, B. G. Harvey, H. Homeyer, D. G. Kovar, J. Mahoney and W. von Oertzen, Phys. Rev. Lett. 32, 680 (1974).

2. K. G. Nair, H. Voit, M. Hamm, C. Towsley and K. Nagatani, Phys. Rev. 33, 1588 (1974).

3. K. G. Nair, H. Voit, C. W. Towsley, M. Hamm, J. D. Bronson and K. Nagatani, Phys. Rev. C12, 1575 (1975).

4. P. D. Bond, C. Chasman, J. D. Garrett, C. K. Gelbke, O. Hansen, M. J. LeVine, A. Z. Schwarzschild and C. E. Thorn, Phys. Rev. Lett. 36, 300 (1976).

5. T. Motobayashi, I. Kohno, K. Katori, M. Yoshie, T. Ohi and H. Kamitsubo, Phys. Rev. Lett. 36, 390 (1976).

6. W. von Oertzen, M. Liu, C. Caverzasio, J. C. Jacmart, F. Pougheon, M. Riou, J. C. Roynette and C. Stephan, Nucl. Phys. A143, 34 (1970).

7. G. Delic, Phys. Rev. Lett. 34, 1468 (1975).

8. K. I. Kubo, K. G. Nair, and K. Nagatani, Phys. Rev. Lett. 37, 222 (1976).

QUASI-ELASTIC COLLISIONS OF 315-MeV ^{16}O ON HEAVY ELEMENTS

M. Buenerd,* C. K. Gelbke, B. G. Harvey, D. L. Hendrie,
J. Mahoney, A. Menchaca-Rocha,† C. Olmer, and D. K. Scott

In the course of the last few years, particle transfer reactions between heavy ions at incident energies ⩾ 100 MeV have provided a large amount of data revealing the existence of two new reaction phenomena—the deep inelastic component (DIC) and the quasi-elastic (QEC) collisions. The kinetic energy distribution from these reactions is dominated by two components: 1) a high-energy peak (quasi-elastic), located well above the Coulomb barrier, which is observed only when a few particles are transferred and at forward angles (the study of this process reveals both statistical and direct reaction features): and 2) the deep inelastic peak at an energy close to the Coulomb barrier and interpreted as a fully relaxed process. These two features were interpreted as two aspects of the same phenomenon in the Wilczynski picture.[1] In the experiments reported here, beams of 315-MeV ^{16}O were used to bombard targets of ^{197}Au(2 mg/cm^2), ^{208}Pb(1.2 mg/cm^2) and ^{232}Th(10 mg/cm^2) in order to study the quasi-elastic processes around an incident energy of 10 MeV/A.

The experiments were carried out at the 88-inch cyclotron using the QSD spectrometer for high energy resolution and good particle identification but with limited energy range, and silicon ΔE-E counter telescopes providing broad energy range spectra. The thickness of the ΔE counter was chosen so as to permit both good Z identification and as broad an energy range as possible. The ΔE thickness ranged from 35μ to 100μ and permitted the identification of fragments between Z = 2 and Z = 9, but with some uncertainties in mass resolution for higher Z.

The kinetic energy distributions obtained with the silicon counter telescopes exhibit a strong quasi-elastic component (the fully relaxed region of the spectra could not be observed in the experiment on account of the ΔE counter thickness). Figure 1 shows a sample of energy spectra from the ^{16}O + ^{208}Pb reaction. For each spectrum, the optimum final kinetic energy corresponding to the centroid of the QEC peak has been extracted and the corresponding differential cross section. In most of the cases the shape of the peak can be

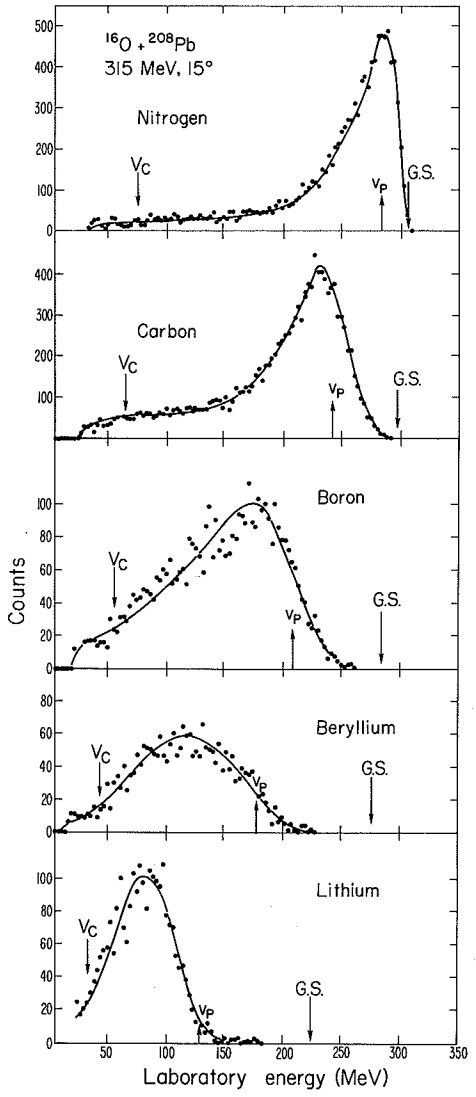

Fig. 1. Typical quasi-elastic energy spectra for the reaction ^{16}O + ^{208}Pb at 315 MeV. The arrows label points corresponding to: V_C, the exit Coulomb carrier; V_p, the beam velocity/G.S, the ground state transition. (XBL 768-3359)

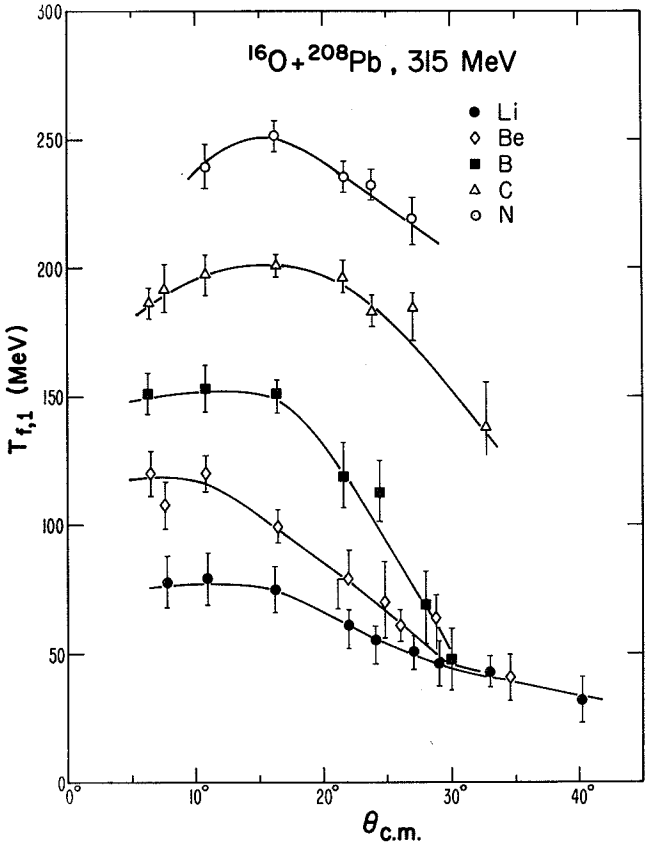

Fig. 2. Angular variation of the maximum in energy of the quasi-elastic peak for outgoing products in reactions induced by ^{16}O on ^{208}Pb, at 315 MeV. (XBL 769-4055)

reproduced with a Gaussian plus a low-energy exponential tail. As shown in Fig. 2, the optimum kinetic energy of the QEC peak exhibits a strong angular dependence. This effect is not observed at lower incident energy, although the results of Ref. 2 shows a slight tendency to vary the same way. The measured Q-values are roughly the same for the three targets used.

Preliminary angular distributions for the $^{16}O + ^{208}Pb$, reactions are plotted in Fig. 3; they fall off approximately exponentially with the angle as expected from a direct reaction process. The average slope decreases with the number of charge units transferred.

The data are also similar to the high energy fragmentation cross sections measured by Lindstrom et al.[3] for $^{16}O + ^{208}Pb$ at an energy of 33.6 GeV (2.1 GeV/nucleon). Figure 4 shows that the relative cross sections for the production of different isotopes are generally of the same magnitude in the two experiments, with a general trend towards larger cross sections for the production of more neutron deficient isotopes at the higher energy. Note, however, that the relative element yields are identical within the experimental errors. This is a most unexpected result, since similar experiments at energies only a few MeV/nucleon above the barrier give entirely different distributions of reaction products.[4] These results may indicate

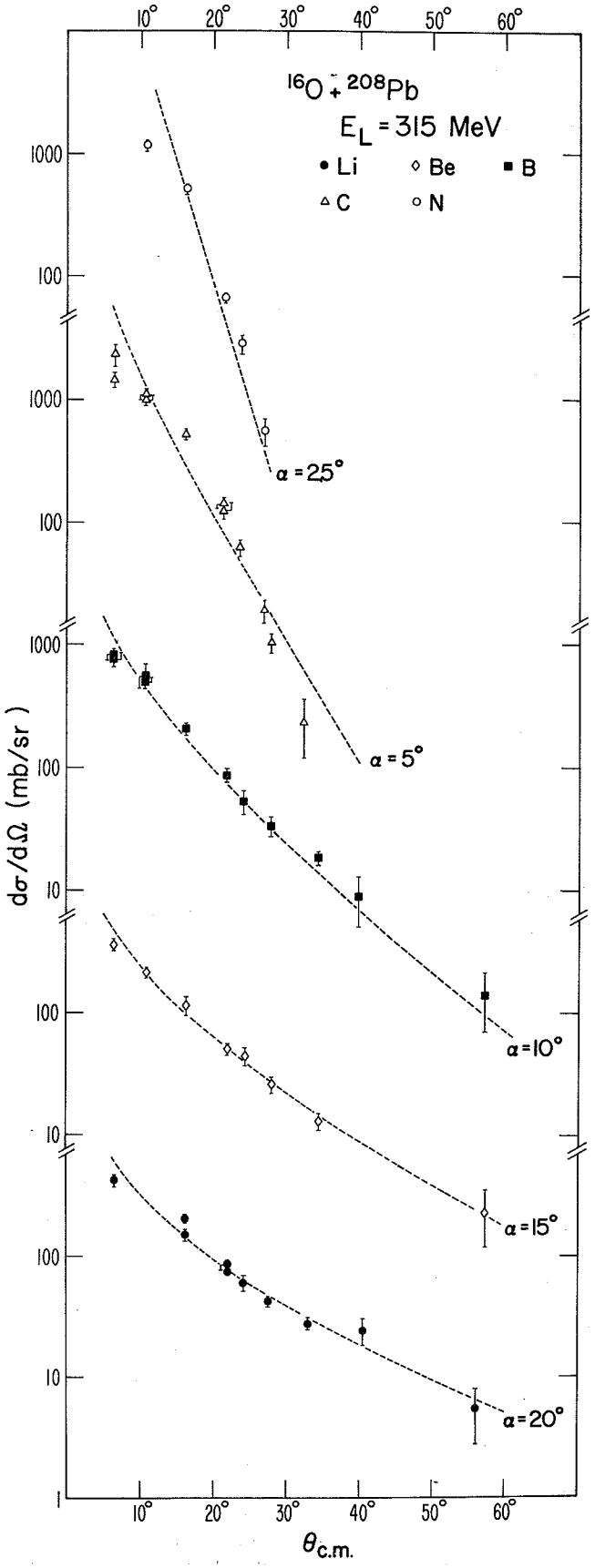

Fig. 3. Different cross sections of the quasi-elastic component in reactions with ^{16}O, ^{208}Pb at 315 MeV. The dotted curves are exponential decays with the indicated decay angles. (XBL 769-4054)

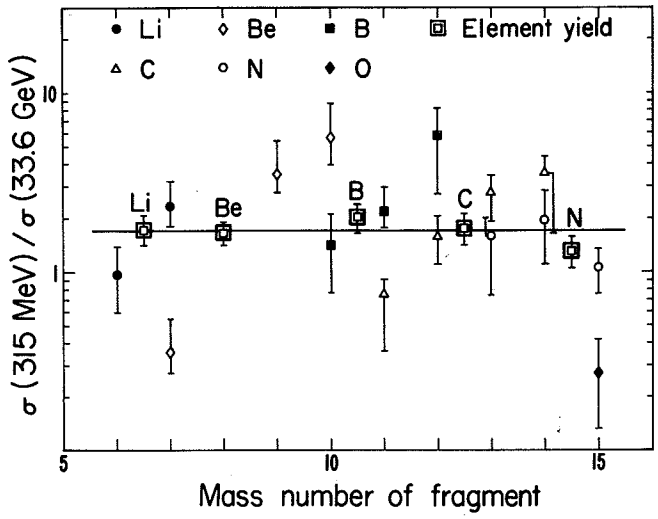

Fig. 4. Ratios of cross sections measured for the reactions ^{16}O + ^{208}Pb at 315 MeV and 33.6 GeV laboratory energies. (XBL 768-3340)

that the link between high and low energy phenomena can be made in the energy range of a few tens of MeV/nucleon where the ion velocities are comparable to the Fermi velocity.

Footnotes and References

*Permanent address: Institut des Sciences Nucléaires, Grenoble, France.

†Permanent address: Instituto de Fisica, U.N.A.M., Mexico.

1. J. Wilczynski, Phys. Lett. 47B, 484 (1973).

2. H. Kamitsubo, Proc. of Symposium on Macroscopic Features of Heavy-ion Collisions, Argonne, Illinois (1976) Vol. 1, p. 177.

3. P. J. Lindstrom et al., LBL-3650 (1975).

4. A. G. Artukh et al., Nucl. Phys. A160, 511 (1971).

SEARCH FOR SHOCK WAVES AT THRESHOLD ENERGY

D. L. Hendrie, M. Buenerd,* A. Menchaca-Rocha,†
C. Olmer, and D. K. Scott

At sufficiently high relative velocities, the central collision of two massive nuclei has been predicted to give rise to a new phenomenon. The high nuclear density at the point of contact was predicted to propagate through a massive nucleus in a fashion conceptualized as a nuclear compressional shock wave. Various models at relativistic energies have suggested differing possible manifestations of a shock process. Several investigations at relativistic energies have yielded conflicting, but probably negative results.[1] A calculation by Tsang[2] suggested that the conditions under which shock phenomena would occur still exist at energies accessible to the 88-Inch Cyclotron. The much higher beam intensities available there makes possible much more sensitive experimental tests for the effect.

Beams of 312-MeV ^{16}O (19.5 MeV/a) were directed onto an 8-mg/cm^2 ^{232}Th target; intensities of 50 nA (5×10^{10} particles/sec) were routinely available. Two independently moveable solid-state counter telescopes were used to detect and identify emitted fragments, both singly and in coincidence. Early results indicated that heavy fragment emission was quite small and gave rise to very few coincidences. Since our counters were inappropriate for singly charged ejectiles, and ^3He particles were always more than an order of magnitude reduced from ^4He, the bulk of our data and all of this report will be on emission of alpha particles.

Figure 1 shows a sample of single alpha particle spectra at several angles, in which (at least) two components can be discussed. At large angles, the spectra show a peak at the Coulomb barrier, and an exponentially decreasing tail. Under the simplest possible assumptions, this

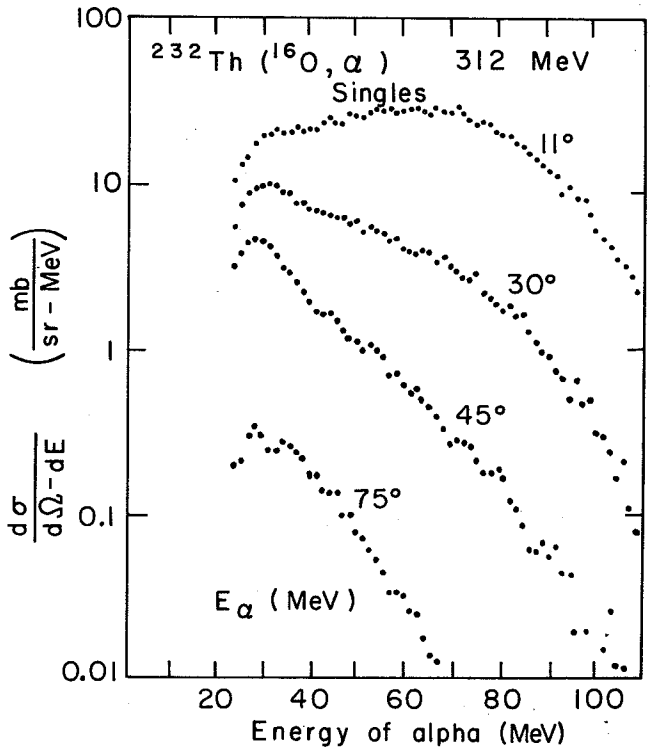

Fig. 1. Energy spectra of alpha particles detected in a counter telescope placed at angles from 11° to 75°. (XBL 766-8325)

could be attributed to compound nuclear decay, with a characteristic temperature of about 9 MeV. This is a much higher temperature than that expected by extrapolating from lower energy work. As yet, no additional effects such as multi-particle emission or effects of critical angular momenta in the absorption have been calculated. At forward angles, a direct component is seen, with a broad peak at 75 MeV. Very crude calculations indicate that this is consistent in cross section and energy and angular distributions with the projectile fragmentation seen by Heckman and coworkers at relativistic energies.[3]

Figures 2 and 3 show results of coincidences of two alphas on opposite sides of the incoming beam. In Fig. 2, both counters are moved symmetrically about the beam axis; in Fig. 3, one counter is held fixed, and the other moved. In these preliminary plots, the alpha spectra are summed over all energies, and the results were not corrected to obtain absolute cross sections. Chance coincidences were a minor contribution and are subtracted.

Interpretation of the coincidence data are consistent with the ideas from the singles data. No evidence for shock effects are seen. The cross sections with at least one of these counters at forward angles must be corrected if the fragmentation hypothesis is correct, for the fact that ^{16}O fragments into four alphas, only two of which are detected. Decomposing the coincident alpha spectra in several energy regions will significantly aid the interpretation. The high level of coincidences at large angles points out the need, not surprisingly, to take into account multi-alpha emission.

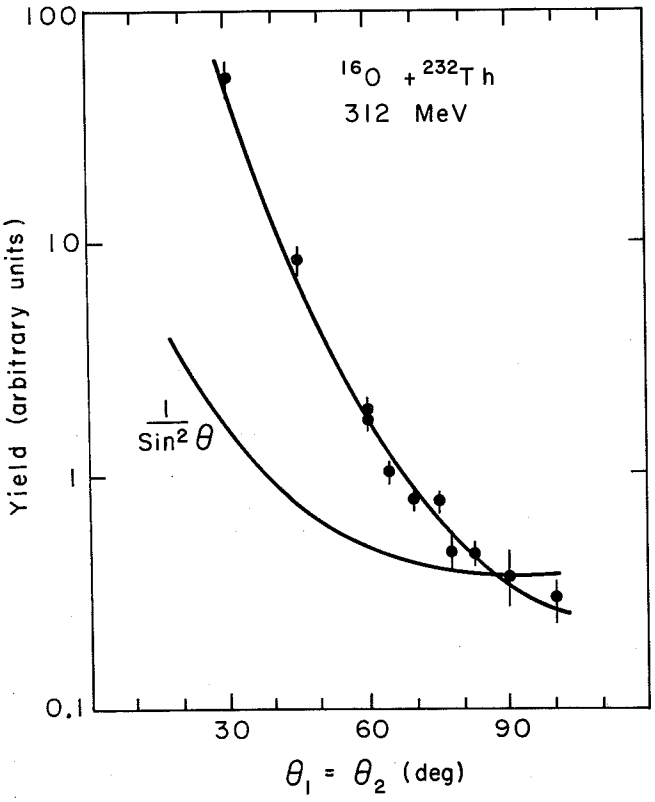

Fig. 2. Angular distribution of alpha particles detected in coincidence in two counter telescopes placed at symmetrical angles about the beam axis. An arbitrarily normalized ($1/\sin^2\theta$) curve is shown for comparison to the data. (XBL 766-8326)

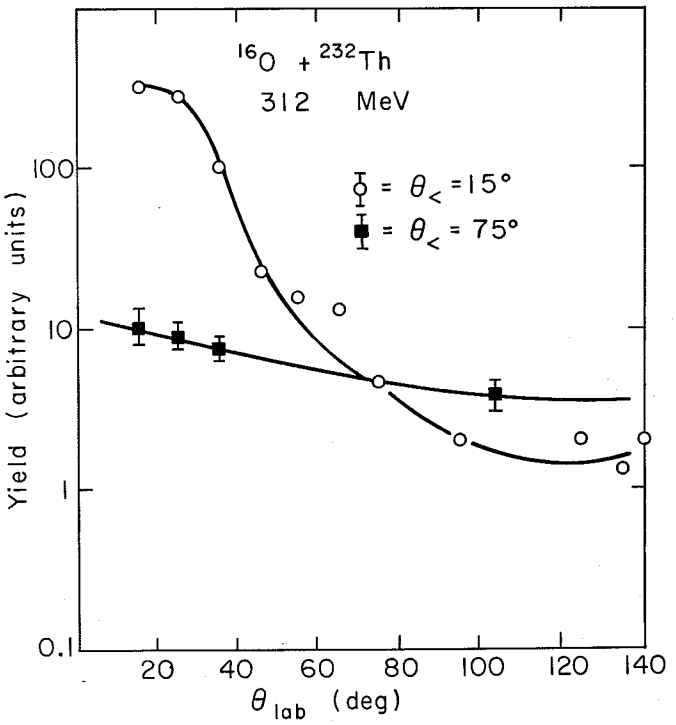

Fig. 3. Angular distribution of alpha particles detected in coincidence in two counter telescopes placed at asymmetrical angles about the beam axis. (XBL 766-8327)

Footnotes and References

*Present address: Institut des Sciences Nucléaires, Grenoble, France.

†Present address: Instituto de Fisica, U.N.A.M., Mexico.

1. A. M. Poskanzer et al., Phys. Rev. Lett. 35, 1701 (1975); H. G. Baumgardt et al., Z. Phys. A 273, 359 (1975).

2. C. F. Tsang, private communication.

3. D. E. Greiner et al., Phys. Rev. Lett. 35, 152 (1975).

2. Macroscopic

PRELIMINARY MEASUREMENT OF THE LIGHT CHARGED PARTICLES IN COINCIDENCE WITH HEAVY-ION RELAXATION PHENOMENA

G. J. Mathews, G. Wozniak, P. A. Russo,
R. C. Jared, and L. G. Moretto

Heavy-ion relaxation reactions are generally characterized by a complete dissipation of the incident kinetic energy, substantial mass transfer, and a nearly binary separation of the final fragments. Recent measurements of the angular correlation of the fragments,[1] and measurements of coincident gamma rays,[2] however, indicate that substantial quantities of emitted protons, neutrons, and alpha particles also characterize these interactions. We report here some results of a preliminary measurement of the feasibility of detecting, and the qualitative physics involved in, the light charged particles (LCP) in coincidence with such heavy-ion interactions.

The measurement has been attempted in the following way. A position-sensitive detector (PSD) is used to view the angular distribution of the LCP in coincidence with a ΔE-E telescope to identify a fragment Z. With the PSD fixed and the telescope varied in angle, one should expect different qualitative features to appear in the PSD depending upon the nature of the parture of the particle emission environment. In particular, one can envision three possible situations which might be observed:

(1) If the particles are emitted isotropically in the center of mass system of some quasi-spherical intermediate complex, one would expect no correlation between the final fragment angles and the LCP angular distribution.

(2) If the particles are emitted during the separation of two fragments, then (as in ternary fission) one would expect Coulomb focusing to result in an anticorrelation between the final fragment angles and the particle angular distribution.

(3) Particles which arise from the excited fragments after separation should be expected to exhibit some correlation between fragment angles and LCP distribution.

One can suppose that the energy spectra of the LCP from these possibilities may also exhibit qualitative differences.

So what one wishes to do then is to examine the PSD angular distribution in coincidence with a given fragment as the telescope angle changes. As the correlation angle for the partner Z passes through the PSD a change in the LCP angular distribution should indicate something of the nature of the environment from which the LCP were emitted.

The experiment, which has been performed to examine these phenomena, consisted of a thin Cu target bombarded by 252-MeV ^{20}Ne. An aluminum absorber was placed before the PSD with sufficient thickness to stop the elastically scattered ^{20}Ne, but thin enough to allow the LCP to enter the detector. A crude separation of the proton and heavier particle contribution was possible in the resulting PSD energy spectrum. Roughly equivalent

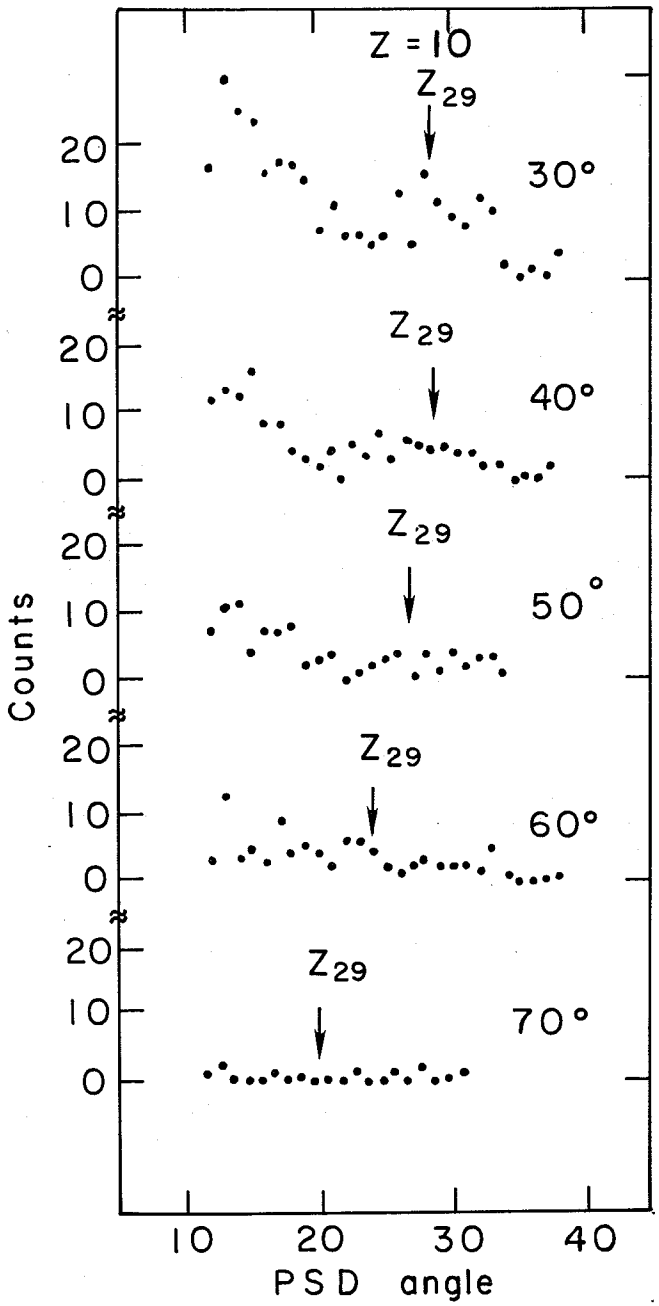

Fig. 1. PSD angular distributions for the LCP in coincidence with Z ~ 10 in the ΔE-E telescope. The predicted correlation angle of the heavy partner is indicated by the arrows.

(XBL 766-8301)

numbers of protons and heavier particles were observed. To enhance statistics, bands of several Z's in the telescope were summed to obtain coincident PSD angular distributions.

Events in the PSD as a function of telescope angle for Z's near 10 and 23 are shown in Figs. 1 and 2. The expected correlation angle of the heavy partner fragment is also shown on this figure. The qualitative features are some forward peaking at forward telescope angles which flattens at more backward telescope angles. Though it seems that there is, indeed, some change in the LCP angular distributions, it is not yet clear what these distributions indicate. To clarify the situation one needs to look at heavier Z's in the telescope, better statistics are needed at backward angles, and perhaps, the LCP kinetic energy spectra as well. Nevertheless, it seems that something other than the uninteresting evaporation from the separted fragments may appear in these angular distributions.

Future experiments are planned which shall employ a large solid angle position sensitive ΔE-E detector, currently being developed by our group. In this arrangement the LCP can be more clearly separated and identified. Also, the increase in solid angle will facilitate the obtainment of the much needed additional statistics at backward angles, and for higher Z's.

In conclusion, we have learned from this preliminary study of the feasibility of the detection of the light charged particles in coincidence with heavy-ion interactions. Most importantly, there is some indication that the ensuing angular distributions may contain interesting structure which could yield new insight into the details of the interaction mechanism.

References

1. P. A. Russo, B. Cauvin, G. Wozniak, M. Neuman, R. Schmitt, R. C. Jared, and L. G. Moretto, to be published.

2. K. Van Bibber, R. LeDoux, S. G. Steadman, F. Videback, G. Young and G. Flaum, in Symp. on Macroscopic Features of Heavy Ion Collisions, Argonne National Laboratory (1976).

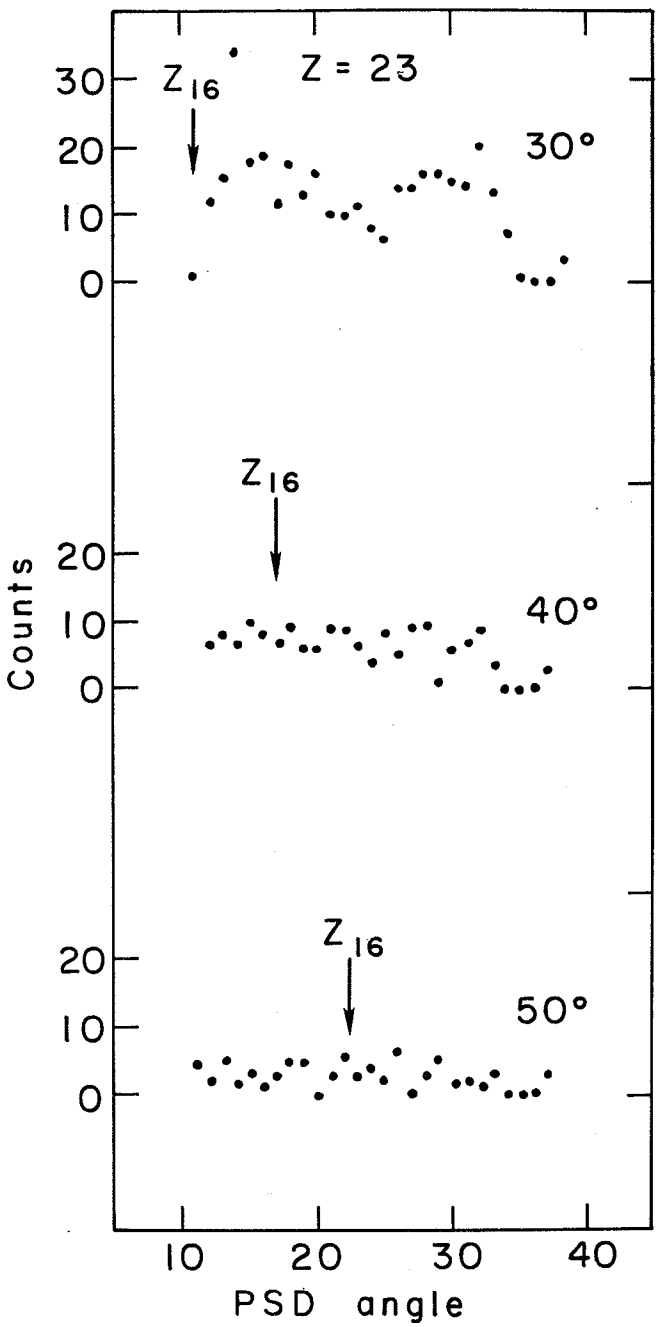

Fig. 2. PSD angular distributions for the LCP in coincidence with Z ~ 23 in the ΔE-E telescope. The predicted correlation angle of the partner fragment is indicated by the arrows. (XBL 766-8302)

FRAGMENT CORRELATION APPROACH TO THE STUDY OF PARTIAL RELAXATION IN HEAVY-ION COLLISIONS

M. Newman, B. Cauvin,* P. Russo,
R. Jared, and L. G. Moretto

In heavy-ion reactions a significant portion of the reaction cross-section appears in a component which has not fully equilibrated. That is, a compound nucleus does not form although the energy of the relative motion is essentially dissipated into the internal modes during the interaction. This is the "relaxed" component which has been ubiquitous in heavy-ion experiments.

In our 1st generation of heavy ion experiments we looked at uncorrelated events by means of an E-ΔE telescope. The singles data provided evidence for the formation of a short-lived intermediate complex with well-defined mass-asymmetry.[1] On this basis we began a second generation of heavy-ion studies in which two fragments produced in the decay of the intermediate complex are detected. A position-sensitive detector (PSD) is used in conjunction with an E-ΔE telescope.[2] In these experiments a number of special difficulties are encountered. In particular, correction for signal-nonlinearity and pulse-height defect has been made.[3] Because angular correlations are measured, one can make confirmation of a binary decay. More parameters concerning each event are measured in the coincidence experiment so that one can provide a more detailed description of the system. Energy dissipation and N/Z equilibration (perhaps at various stages of the interaction) can be studied more fully.

We here report on the coincidence study of the system $^{107,109}_{47}$Ag+252 MeV $^{20}_{10}$Ne at the 88-inch cyclotron. One telescope and one PSD were used. For practical reasons we identified the light fragment in the telescope and detected the heavy partner in the PSD. The telescope angle was fixed and the PSD was moved to various angular settings. The PSD was positioned in the reaction plane at 40°, 55° and 70° to the beam axis and the telescope always sat at 40° in the opposite hemisphere.

In a typical angular correlation (Fig. 1) we see that the heavy partner is found in a distribution of correlation angles, peaked about an average correlation angle. Another interesting feature is the broadness of the correlation.

Figure 2 shows the trends in the angular correlation parameters. We notice a nearly linear in-

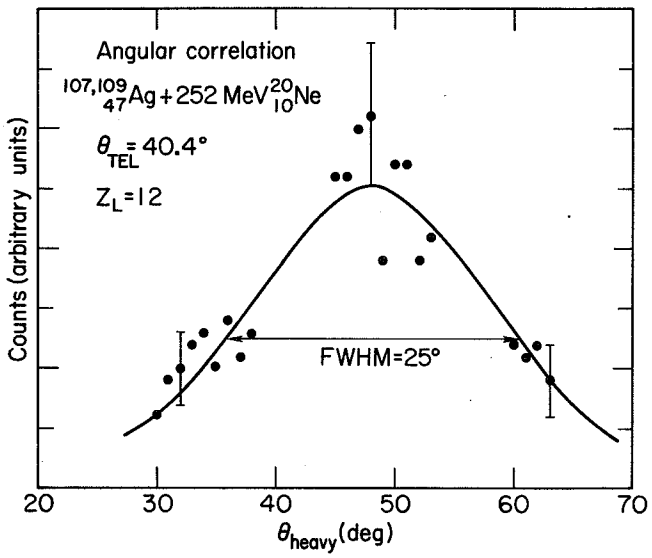

Fig. 1. Angular correlation for fragments in the PSD in coincidence with Z = 12 fragments observed in the telescope at 40°. Data points and typical errors are shown. The solid curve is a gaussian fit to the data. (XBL 764-2650)

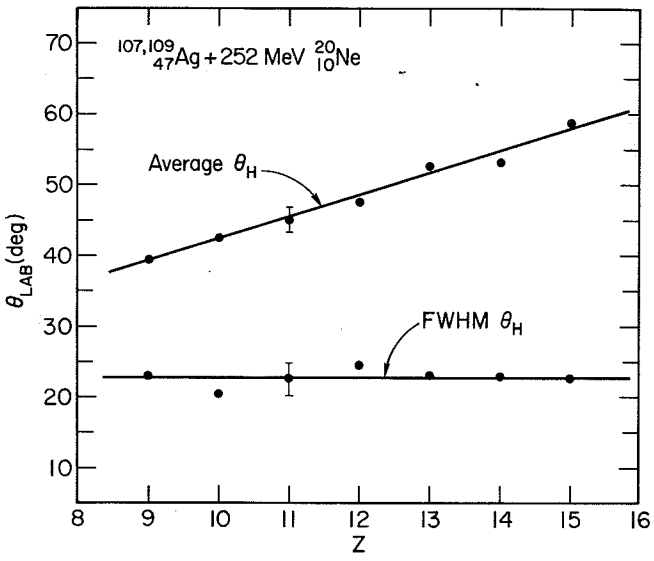

Fig. 2. Angular correlation parameters as a function of the Z in the telescope. Data points are hown along with lines to guide the eye. (XBL 764-2652)

crease in average correlation angle with Z. This same trend is predicted if one assumes an inelastic collision followed by the binary decay of two touching spherical fragments. The angular correlation widths are essentially constant with Z.

For two-body kinematics, conservation of linear momentum requires this relation:

$$E_L M_L = \frac{E_0 M_0 \sin^2(\theta_H)}{\sin^2(\theta_L+\theta_H)}$$

. In the present experiment E_0, M_0, and θ_L are fixed so that the correlation angle is a function of only the mass and energy of the light fragment. From other experiments[4,5] we know the variance in the energy and the mass of the light fragment and one can calculate the expected correlation width. However, only about 10% of the observed width can be accounted for in this manner, so it appears that one must ascribe the bulk of the observed width to particle evaporation from the two hot fragments. Since the present system is neutron rich and charged particles must overcome a Coulomb barrier, we expect neutron emission to to dominate (this assumption has been corroborated by an evaporation code).

In the center of mass (c.m.) energy distribution (Fig. 3) we observe that the c.m. kinetic energies for both singles and coincidence events (approximately Coulomb energies of two touching spheres) are the same. The same types of reactions are seen in both singles and coincidence.

In comparing the singles and coincidence yields (Fig. 4) we see that they are equal within error. This means that for every fragment entering the telescope, a second fragment can be detected in coincidence in the PSD in a well-defined distribution of correlation angles.

The sharing of the excitation energy of the intermediate complex between the two fragments may

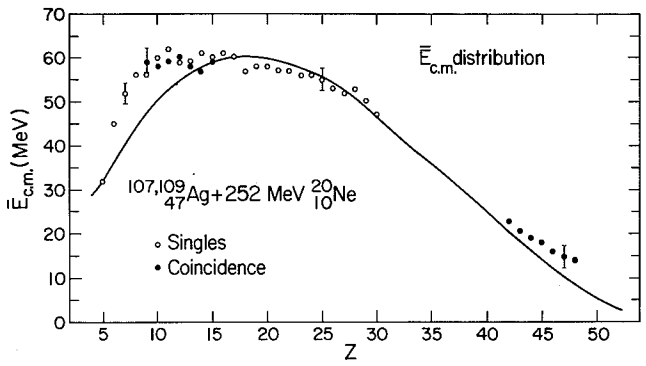

Fig. 3. Center of mass kinetic energies as a function of the fragment atomic number. Open circles show the singles data and the closed circles show the coincidence data. The solid line is the kinetic energy as a function of Z predicted for two touching spheres which are repulsed by their Coulomb field (not a fit). (XBL 764-2654)

be inferred from the number of secondary particles emitted by each fragment as it deexcites. The correlation between the fragment mass and atomic number is also of particular interest. In the coincidence experiment, since the energies and angles for both fragments are measured, we see essentially the complete kinematics of the reaction. In order to determine the fragment masses before secondary emission and the number of nucleons emitted by each fragment, we must solve a system of four equations ensuring energy, mass and linear momentum conservation in the reaction plane. These equations are nonlinear so that an iterative calculation is required in order to obtain a unique result for the desired quantities.[5]

In this manner we have determined the average number of neutrons emitted by a fragment of a given atomic number (Fig. 5). The number of neutrons shows a fairly smooth increase with the fragment Z. The linearity of the neutron yield is consistent with the assumption of equal temperatures. From this it appears that the intermediate complex is in thermal equilibrium at the time of decay.

The experimental fragment masses before secondary emission have also been determined (Fig. 6). Compare the experimental masses of the light fragment with two simple assumptions: 1) the neutron-to-proton ratio N/Z of the projectile ^{20}Ne since the Z of the light fragment is about the same as the Z of the projectile; and 2) the N/Z ratio of the hypothetical compound nucleus. We see that the experimental masses lie systematically along the N/Z line of the compound nucleus. This does not necessarily mean that a compound nucleus has been formed. The equilibrium N/Z ratio must be determined by minimization of the potential energy of the complex at fixed mass asymmetry. In this case the equilibrium N/Z is only nominally different than that for a compound nucleus. One can say that the N/Z ratio appears to be equilibrated throughout the intermediate system during the time of the reaction. Analogous results for the heavy fragment are shown in Fig. 6b and the same conclusion is drawn. We

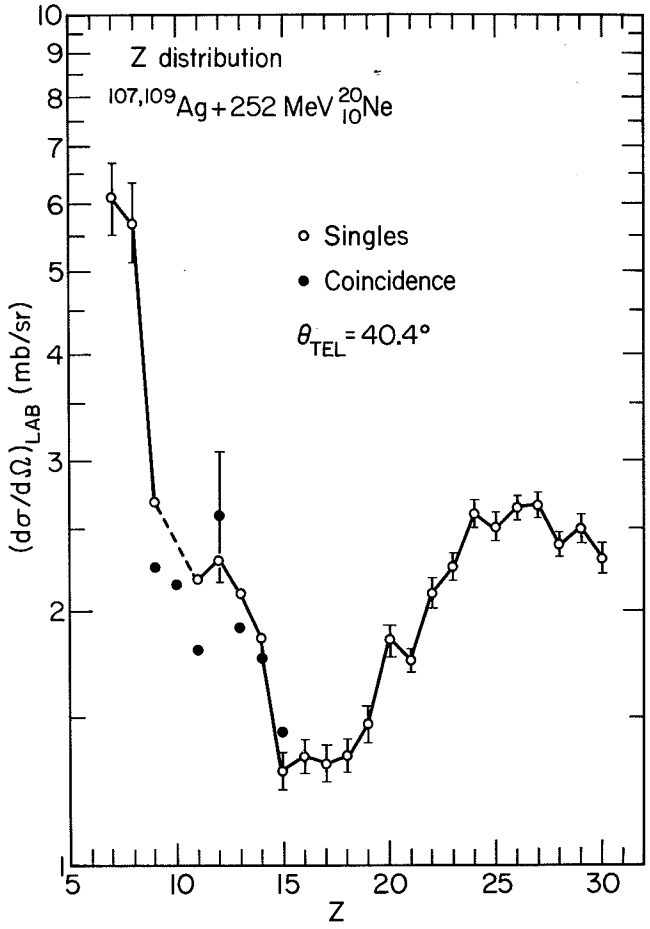

Fig. 4. Singles and coincidence cross-sections as a function of Z. Data points and typical error bars are shown. For Z = 10, the singles yield of the relaxed component could not be adequately measured. (XBL 764-2653)

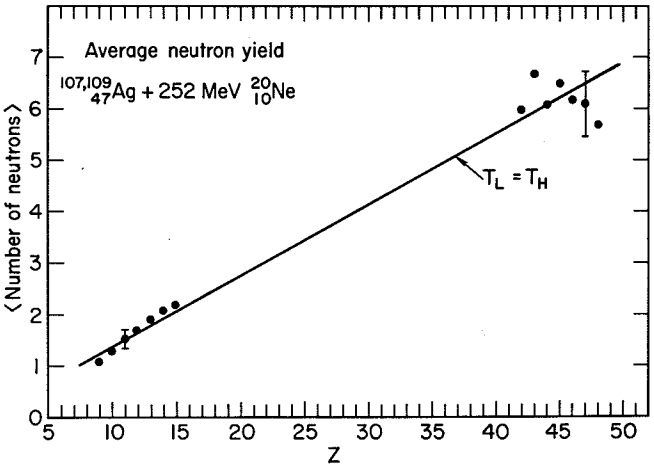

Fig. 5. Average number of neutrons emitted by a fragment of a given atomic number. Data points and typical errors are shown. The solid line shows the number of neutrons expected if the temperature of the light fragment and the temperature of the heavy fragment are equal. (XBL 764-2651)

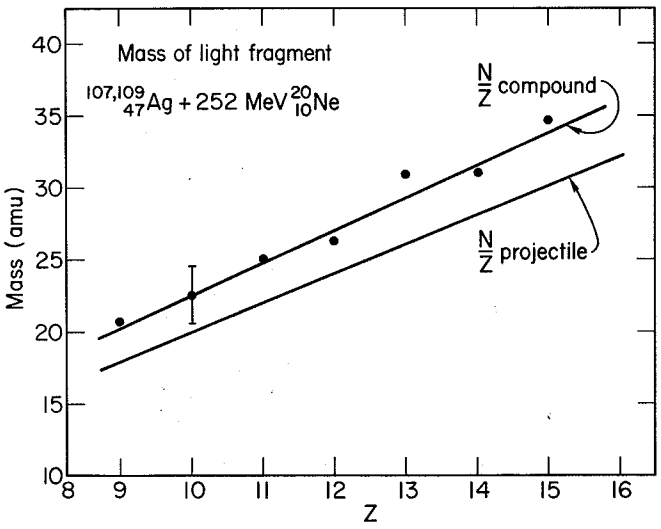

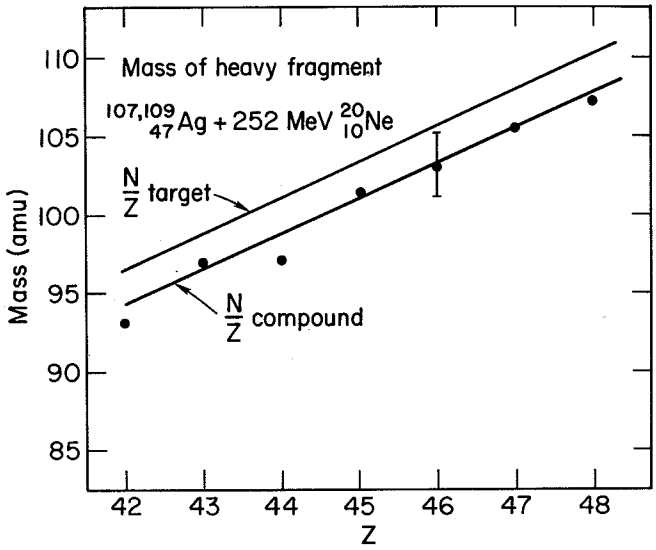

Fig. 6. (a) Mass of the light fragment before secondary emission as a function of the Z of the light fragment. Data points and a typical error are shown. The bottom line depicts the neutron-to-proton ratio, N/Z, of the projectile. The top line represents the N/Z ratio of the hypothetical compound nucleus. (b) Mass of the heavy fragment as a function of the Z of the heavy fragment. The top line shows the N/Z ratio of the hypothetical compound nucleus and the bottom line is the N/Z ratio for the target. (a) (XBL 764-2648) (b) (XBL 764-2649)

know that the system is not fully equilibrated along the mass-asymmetry degree of freedom, but it appears to have reached equilibrium in the N/Z coordinate.

In the near future we plan to use this same technique of correlated fragments to study partial relaxation with various projectile, target and beam energy combinations (especially krypton and xenon induced reactions). Azimuthal widths should not be sensitive to the intrinsic oscillations of the complex and might give a more sensitive measure of secondary emission from the fragments. Light particle emission from the intermediate complex would distort the kinematics in a complicated way and needs to be studied, as do secondary fission processes in heavier systems.

Footnote and References

*On leave from DPh-N/MF CEN, Saclay, France.

1. L. G. Moretto, R. P. Babinet, J. Galin and S. G. Thompson, Phys. Lett., 58B 31 (1975).

2. R. P. Babinet, Z. Frankel, P. Russo, R. Jared, L. G. Moretto and S. G. Thompson, Nucl. Chem. Annual Report 1974, LBL-4000, p. 108.

3. P. Russo, R. Jared, R. Babinet, and L. G. Moretto, "Energy Calibration of Solid State Counters for Heavy Ion Experiments", this report.

4. R. Babinet, L. G. Moretto, J. Galin, R. Jared, J. Moulton and S. G. Thompson, Nucl. Phys. A258 172 (1976).

5. B. Gatty, D. Guerreau, M. Lefort, J. Pouthas, X. Tarrago, J. Galin, B. Cauvin, J. Girard, and H. Nifenecker, Z. Physik A273 65 (1975).

6. B. Cauvin, R. Jared, P. Russo, P. Glässel, R. Schmitt, and L. G. Moretto, "Measurement of Pre and Post Evaporation Masses of Deep Inelastic Collisions Fragments of 340-MeV Ar + Ag," this report.

REACTION PRODUCTS FROM THE INTERACTION OF 170- AND 252-MeV ^{20}Ne ON Cu

G. J. Mathews, B. Cauvin,* R. Schmitt,
R. C. Jared, and L. G. Moretto

This study is a continuation of efforts to systematize the yields in heavy-ion reactions.[1] The particular interest in the ^{20}Ne + Cu system is that with the available charge resolution, products on both sides of a symmetric mass split can be clearly identified. A slight disadvantage of this system, however, is that kinematic compression prevents the detection of large Z's at large c.m. angles.

Thin targets (~400 μg/cm^2) of Cu have been bombarded with 170-MeV ^{20}Ne. The results of the bombardment with 252-MeV ^{20}Ne have been reported previously.[2] As in earlier experiments[3] the product Z's were identified with a ΔE-E gas ionization counter telescope. The data were stored serially on magnetic tape for later sorting and analysis.

The c.m. kinetic energy spectra for 170-MeV incident ^{20}Ne is shown in Fig. 1 for several product Z's. The features of the relaxed component at all angles, for all charges, and the quasi-elastic component near the grazing angle, Z's close to the projectile, are clearly visible. The cross sections for the relaxed component in these spectra were integrated and separated from the quasi-elastic peak by a Gaussian fitting procedure.

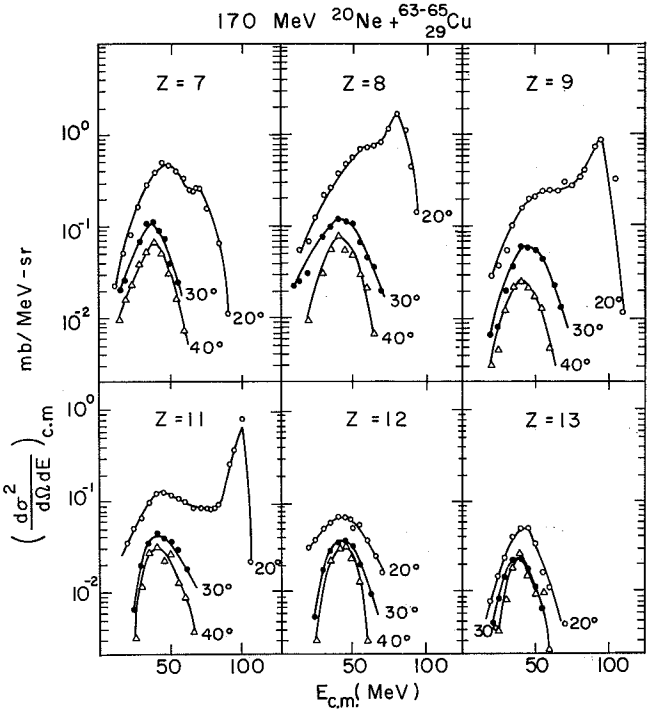

Fig. 1. Some c.m. kinetic energy spectra for products from 170-MeV incident ^{20}Ne on Cu. Quasi-elastic and relaxed components are visible.
(XBL 766-8303)

Laboratory cross sections for the relaxed component of the detected product Z's at different angles are shown in Figs. 2 and 3. As expected,[1] the general features of these figures are; (1) a decrease in cross section with decreasing energy, as fewer l-waves penetrate to contribute to the relaxed component; (2) a relatively flat charge distribution showing no substantial preference for a symmetric split, with considerably increased cross sections for products lighter than the projectile (these effects can be understood[1] in terms of the mass-asymmetry potential-energy surface at the point of injection), and (3) the odd-even effect.

Center of mass angular distributions are shown in Figs. 4 and 5. The results are again as

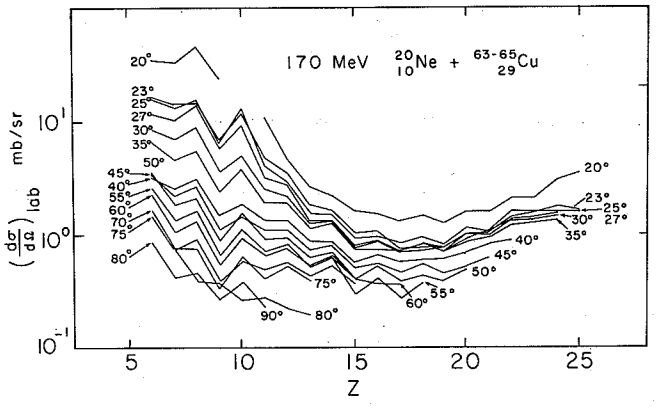

Fig. 2. Laboratory cross sections as a function of Z at various angles for the relaxed component in the reaction of 170-MeV ^{20}Ne + Cu.
(XBL 766-8304)

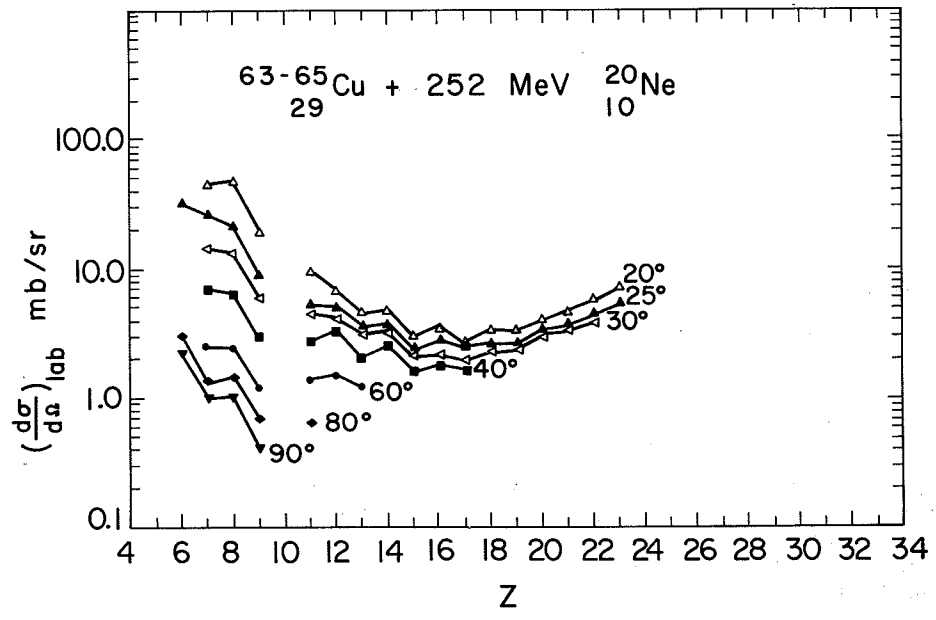

Fig. 3. Laboratory cross sections as a function of Z at various angles for the relaxed component in the reaction of 252-MeV ^{20}Ne. (XBL 752-2299)

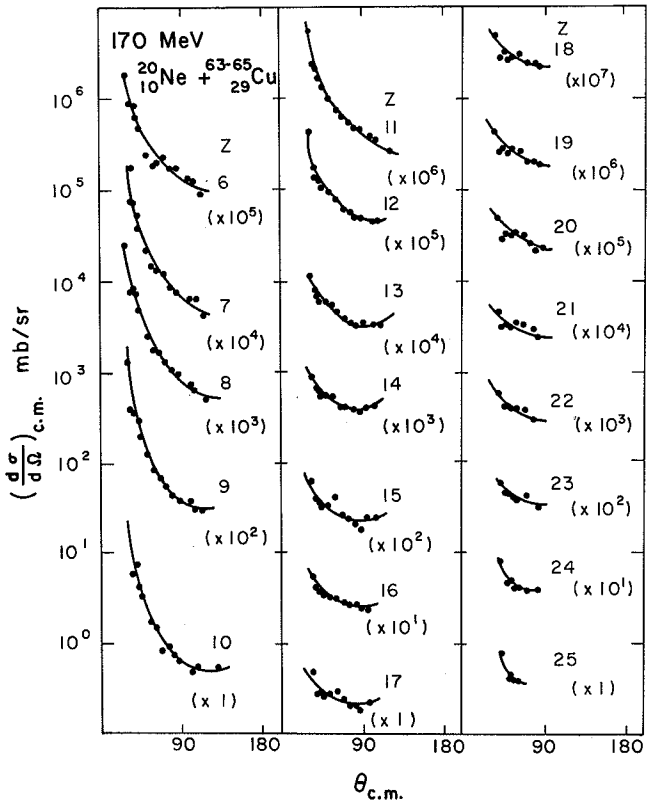

Fig. 4. Center of mass angular distributions for the ^{20}Ne + Cu reaction at 170 MeV laboratory energy. (XBL 766-8305)

expected. The angular distributions exhibit forward peaking for products near the projectile which gradually converts to a $1/\sin\theta$ distribution due to the longer times associated with greater mass transfer.

In conclusion, it seems that the qualitative features of the ^{20}Ne + Cu reaction are well understood. What is needed now are quantitative calculations to test the validity of current theories.

Footnote and References

*On leave from DPh-N/MF CEN, Saclay, France.

1. L. G. Moretto, and J. S. Sventek, Preprint, LBL-5006 (1976).

2. R. Jared, L. G. Moretto, R. Babinet, J. Galin, J. Hunter, R. Schmitt, J. Moutlon, and S. G. Thompson, Nuclear Chemistry Annual Report (1974), LBL-4000, p. 103.

3. R. Babinet, L. G. Moretto, J. Galin, J. Hunter, R. Schmitt, J. Moulton, and S. G. Thompson, Nucl. Phys. A258, 172 (1976).

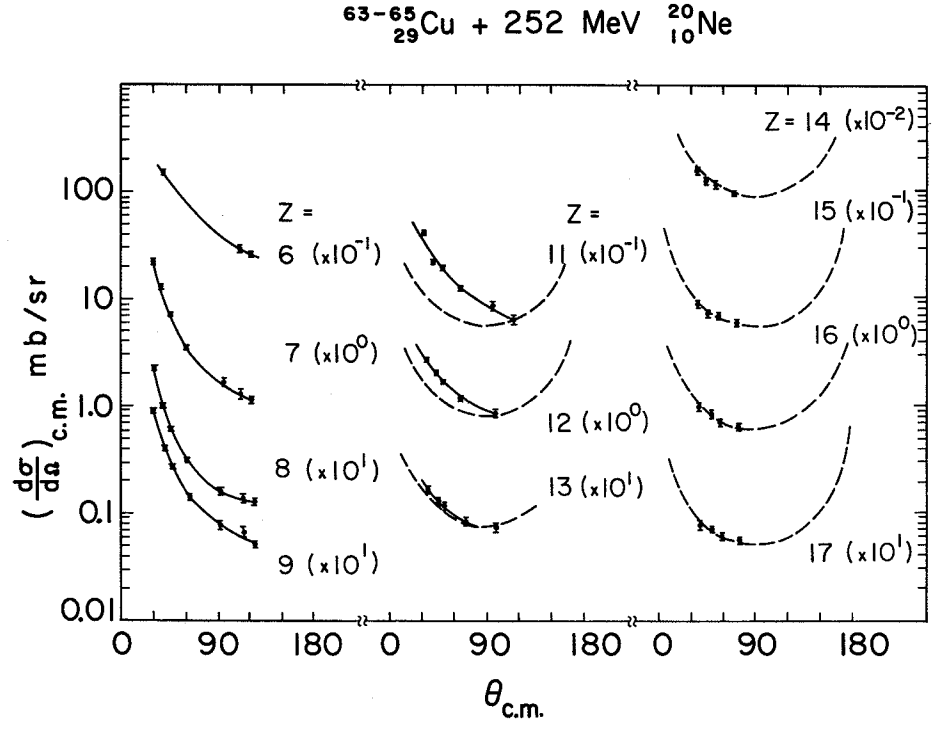

Fig. 5. Laboratory cross sections as a function of Z at various angles for the relaxed component in the reaction of 252-MeV ^{20}Ne. (XBL 752-2300)

DEEP INELASTIC REACTION OF 175-MeV Ne WITH Au

J. Moulton, G. Wozniak, B. Cauvin,* P. Russo,
R. Jared, and L. G. Moretto

The reaction of Ne with Au has been performed at the 88-inch cyclotron. The beam is focused on a thin metal target (300 to 800 μg/cm^2), and the Z and kinetic energy of the reaction products are measured in E-ΔE detectors. The ΔE counter is a gridded methane-gas ionization chamber developed by our group.[1] The E counter is a surface-barrier Si detector. With the low energy projectiles in this series of experiments, products up to about Z = 32 can be identified. (Much heavier products can be identified with more energetic projectiles.) The data pulses are amplified by a modular electronic system, converted to digital form in a 4096-channel ADC, and stored on magnetic tape by a PDP-5 computer. An elaborate sequence of data analysis programs have been developed, which sort events according to Z, and calculate lab and center-of-mass energies and cross sections. This data analysis is performed on our own PDP-9 computer.

The products of the Ne plus Au reaction have center-of-mass kinetic energies which are essentially equal to the Coulomb repulsion between the two separating fragments (see Fig. 1). The kinetic energy brought in by the projectile has relaxed into internal degrees of freedom. Actually, products observed around the grazing angle and lighter than Z = 11 have broadened or two-lobed kinetic energy spectra, arising from reactions in which the energy has not completely relaxed. Products produced far from the grazing angle or differing appreciably from the projectile mass have fully relaxed, single-peaked KE spectra at all angles. Products observed far from the grazing angle or, which are quite different from the projectile had to rotate and diffuse longer to reach the mass asymmetry at which they eventually split. Thus their kinetic energy spectra are relaxed and angle-independent.

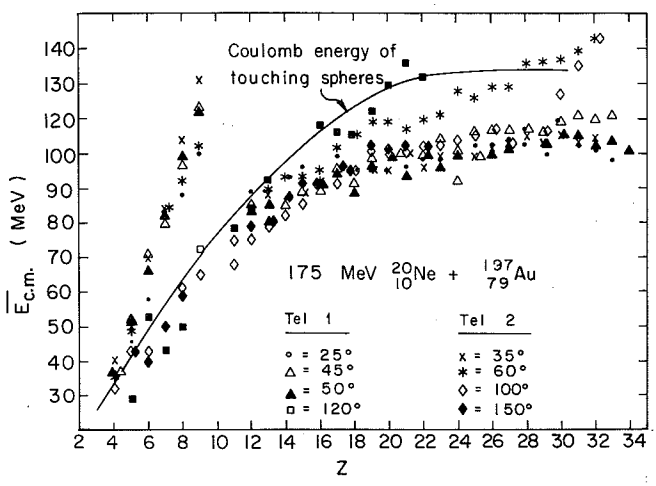

Fig. 1. Mean center-of-mass kinetic energy versus Z for various lab angles. The solid line is the Coulomb repulsion energy for two spheres calculated as $E = 1.44\ Z_1Z_2/1.4(A_1^{1/3} + A_2^{1/3})$.

(XBL 766-8200)

The lab cross sections in Fig. 2 present a striking picture. Considering those products and angles for which the kinetic energies are fully relaxed, we see a great rise in cross section from Z = 10 to Z = 32, covering three orders of magnitude. The cross section for energetically relaxed products rises by one factor of 10 from Z = 9 to Z = 4. The cross section for products lighter than Ne whose kinetic energies are significantly above the Coulomb energy is quite large, indicating a fast, non-equilibrium transfer process.

For a better understanding of the significance of these results, it is useful to compare them with those of two other reactions: 175-MeV Ne on Ag[2] and 288-MeV Ar on Au.[3] For both of these reactions the center-of-mass kinetic energies of the products generally agree with the Coulomb energy of the separating fragments, as was seen for Ne plus Au. This indicates that in all of the reactions the initial translational kinetic energy has relaxed into internal degrees of freedom. However, important differences are observed in the lab cross sections for the range of elements detected.

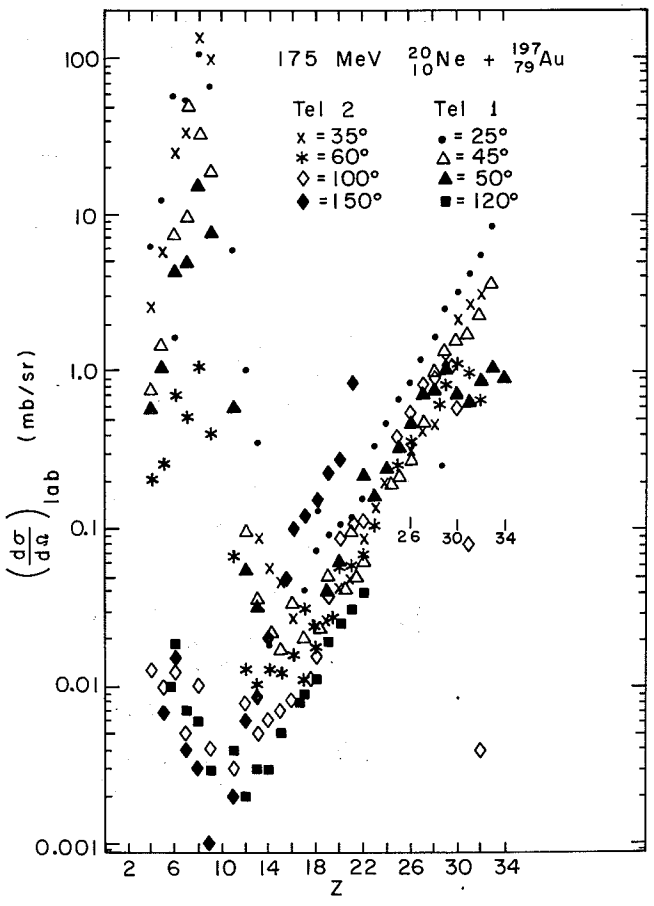

Fig. 2. Lab differential cross section versus Z for various lab angles.

(XBL 766-8201)

In the Ne-Ag system, the cross section rises abruptly for elements lighter than the projectile, and much more gently from Z = 11 to Z = 29. This is consistent with a picture of the reaction complex as two spheres stuck together and exchanging nucleons. The resulting Z distribution approaches what would be expected for a diffusion process controlled by a liquid drop mass asymmetry potential. The low mass of the projectile makes the starting asymmetry quite large, so the system finds itself trapped on a downslope leading to greater asymmetry. Thus the high yield for products lighter than Ne. With the large angular momenta of these reactions, (about 80ħ) a dip in the potential exists at symmetry, causing increased cross section around symmetric splitting for an equilibrated Z distribution. The rise in yield towards symmetry indicates that the system has moved significantly towards equilibration.

The reaction of Ar on Au is qualitatively similar. The Z distribution rises steadily with Z, which may arise from the very pronounced depression at symmetry in the mass asymmetry potential. There is little rise in cross section for low Z's. The initial projectile-target mass asymmetry probably lies on the inside of the hump which separates extreme asymmetry from symmetric splitting. This pulls the system "downhill" towards symmetry more strongly than in the reaction of Ne on Ag. Therefore one understands why one sees little rise in the cross section corresponding to the great drop in the potential for products lighter than about Z = 12. Also the center-of-mass angular distributions for all products up to Z = 24 are strongly forward peaked, with a minimum as far back as 120°. This angular asymmetry remains but diminishes through Z = 28°. Only for Z = 29 does the angular distribution follow $1/\sin\theta$. This forward peaking indicates rapid decay of the complex, in a time somewhat less than a rotatoinal period. The system quickly populates the Z's "downhill" from the initial projectile-target mass asymmetry, namely Z's from 18 up to symmetry. There is only a low probability that the system will get over the potential energy hump to populate Z's below 12 before breakup of the complex. However, it is possible that the cross section for Z's above Ar may arise in part from fission of a compound nucleus or of the target itself. This would also lead to an yield increasing with Z, and could supply the $1/\sin\theta$ component of the angular distribution of all Z's observed.

The difference between the Z distribution of the Ne-Ag and the Ne-Au systems is quite remarkable. In the former, the initial projectile-target mass asymmetry channeled much of the cross section to Z's below Ne, with lower, slowly rising cross section towards symmetry. In the latter case, most of the cross section is for elements above Ne, with much less rise in yield for light products.

One needs to examine the angular distributions from the Ne-Au reaction to determine the extent to which the strong population of heavy products is the result of a diffusive mechanism. Production of elements above the projectile by fission of a compound nucleus, of the target enriched by absorption of several nucleon from the projectile, or even of the target itself, would seem to be quite possible. However, the Ar-Au reaction demonstrated a significant non-fission component for products up to Z= 28. A major complicating factor in these reactions is that different angular momentum windows may be involved in these reactions. Work is continuing in this series of experiments, including analysis of a higher energy Ne-Au system (252 MeV).

Footnote and References

*On leave from DPh/MF CEN, Saclay, France

1. Malcolm Fowler et al., Nucl. Inst. Meth. 24:341 (1975).

2. Regis Babinet et al., Nucl. Phys. A258:172 (1976).

3. Luciano Moretto et al., Nucl. Phys. A259;173 (1976).

SYSTEMATICS OF THE ^{40}Ar + Cu REACTION

G. J. Mathews, B. Cauvin,* J. Moulton, R. Schmitt,
R. C. Jared, and L. G. Moretto

Preliminary results of the study of this reaction with 288- and 340-MeV incident ^{40}Ar were reported previously.[1] We report here an extension of the systematics of this system to 170 MeV. The present study includes more complete charge and angular distributions.

Reaction products from the interaction of incident ^{40}Ar on thin (~ 400 μg/cm^2) Cu targets were identified in a ΔE-E gas ionization counter telescope.

Kinetic energy spectra for some of the reaction products at 170 MeV are shown in Fig. 1. These exhibit the familiar strongly-damped component. The quasi-elastic contribution is also visible for products near the grazing angle and the projectile Z, although at these energies the quasi-elastic and relaxed components are difficult to distinguish.

Laboratory charge distributions at 170 MeV are shown in Fig. 2. These cross sections exhibit the expected features of an odd-even effect, a decrease in magnitude from the higher energy data, and a relatively flat charge distribution. The peaking of the cross sections near the projectile is due to the quasi-elastic component which was not separated out.

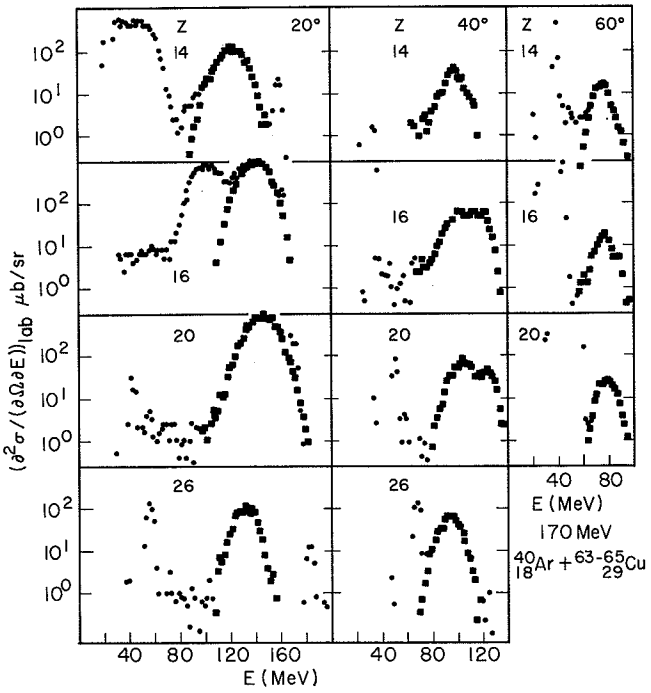

Fig. 1. Center-of-mass kinetic energy spectra for the ^{40}Ar + Cu reaction at 170 MeV. (XBL 7610-9377)

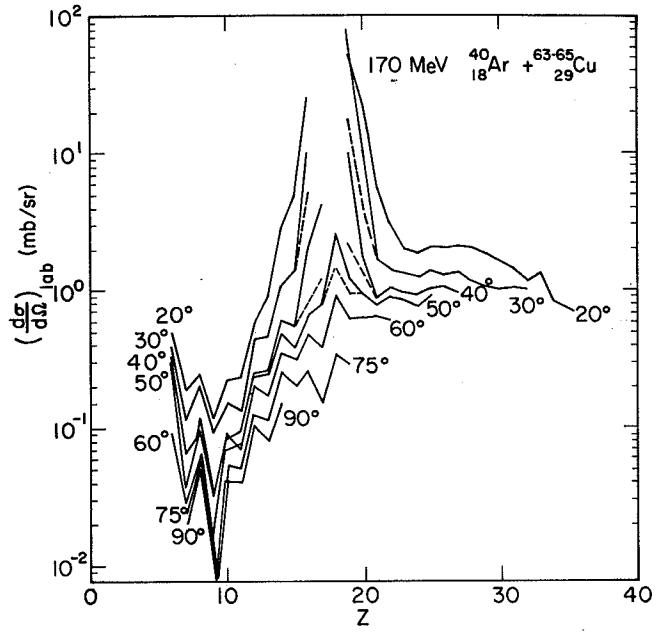

Fig. 2. Laboratory cross sections for products from the ^{40}Ar + Cu reaction at 170 MeV. (XBL 769-4064)

The center-of-mass angular distributions, not shown, exhibit the forward-peaking characteristic of the short interaction times involved in the formation of products near the projectile. The distributions approach $1/\sin\theta$ for products requiring more mass transfer.

In conclusion, it seems that the systematics of the ^{40}Ar + Cu reaction are consistent with current understanding of heavy-ion interactions.[2]

Footnote and References

*On leave from DPh-N/MF CEN, Saclay, France.

1. L. G. Moretto, R. C. Jared, R. Babinet, J. Galin, J. Hunter, and S. G. Thompson, Nuclear Chemistry Annual Report (1974), LBL-4000, p. 104.

2. L. G. Moretto, and J. S. Sventeck, Preprint, LBL-5006 (1976).

PRELIMINARY MEASUREMENT OF REACTION PRODUCTS FROM THE ^{40}Ar + Ag REACTION AT 170 MeV

G. J. Mathews, R. Schmitt, P. Glassel,* G. Wozniak,
R. C. Jared, and L. G. Moretto

This reaction is of interest because at such low energy above the Coulomb barrier a separation of the strongly damped product distribution into two components has been recently observed[1] for the similar system of ^{40}Ar + Au at 220 MeV. According to the results of Reference 1, the cross section for the relaxed products were observed to peak both near the projectile and near mass symmetry at angles close to the grazing angle. This was taken as an indication that two separate components contribute to the relaxed process. However, at these energies, the relaxed component is kinematically nearly indistinguishable from the quasi-elastic products, and hence may be responsible for the observed rise in cross section near the projectile.

Laboratory cross sections are shown in Fig. 1 The experimental technique to derive these data is described in detail elsewhere.[2] In Fig. 1 the cross section does appear to rise near the projectile and near symmetry, although the separation of the relaxed and quasi-elastic components is, indeed, not possible close to the projectile. To examine possible influence from the quasi-elastic contribution to the kinetic energy spectra, we plot in Fig. 2 the centroid of the c.m. energy spectrum for the relaxed plus quasi-elastic. In Fig. 3, the c.m. FWHM of the peaks are also plotted. The c.m. energy and FWHM tend to fall higher for products close to the projectile, consistent with an interpretation that the quasi-elastic products are largely responsible for the rise in cross section.

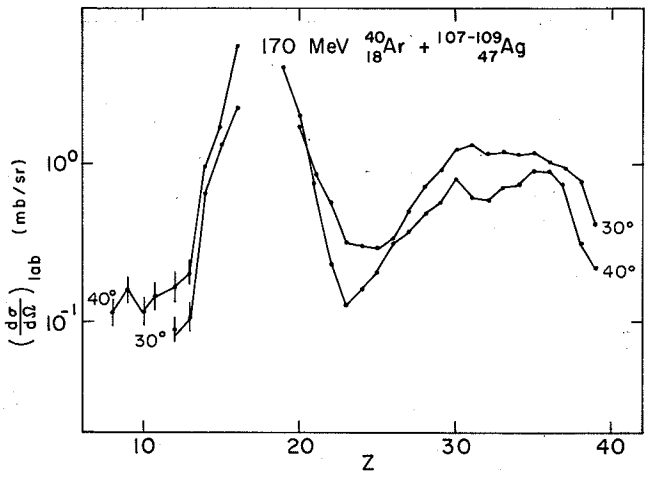

Fig. 1 Laboratory cross sections for ^{40}Ar + Ag at 170 MeV. (XBL 766-8306)

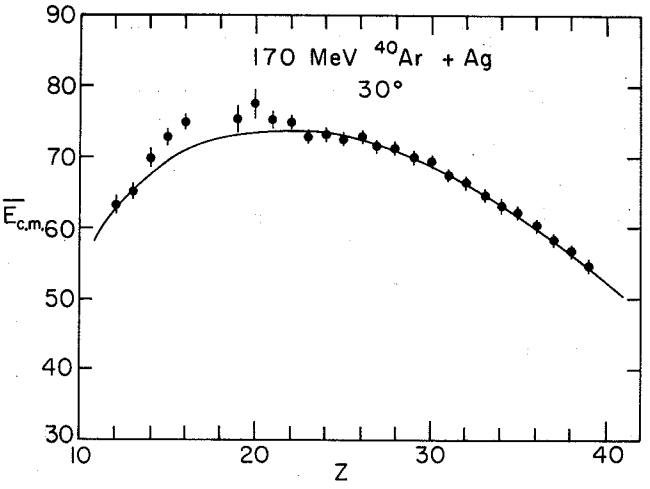

Fig. 2. The centroids of the c.m. relaxed quasi-elastic energy spectra at 30° lab. (XBL 766-8307)

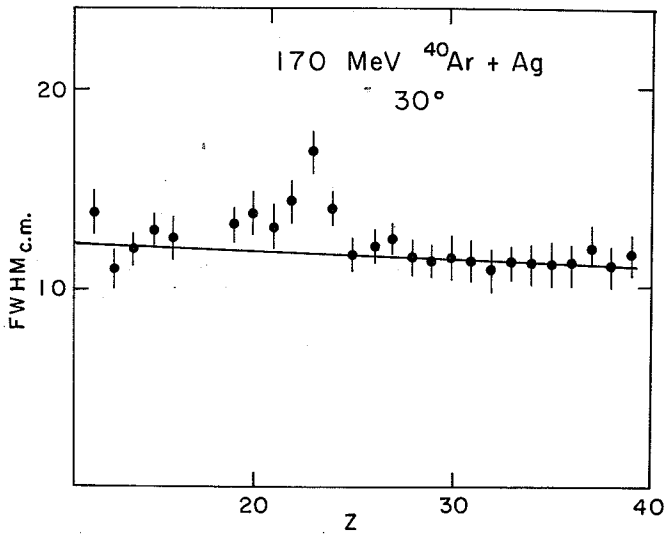

Fig. 3. FWHM's of the c.m. kinetic energy spectra at 30° lab. (XBL 766-8308)

Future experiments are planned to obtain a more complete angular distribution which should shed additional light on this problem.

Footnote and References

*NATO Fellow.

1. C. Ngo, Oui Chaoui, F. Plasil, J. Peter, B. Tamain, Berlanger, Hanappe, private communication.

2. J. Galin, L. G. Moretto, R. Babinet, R. Schmitt, R. Jared, and S. G. Thompson, Nucl. Phys. A255, 472 (1975).

MEASUREMENT OF PRE AND POST EVAPORATION MASSES OF DEEP INELASTIC COLLISIONS FRAGMENTS OF 340 MeV Ar + Ag

B. Cauvin,* R. Jared, P. Russo, P. Glassel,†
R. Schmitt, and L. G. Moretto

Several groups have attempted to determine the mass of the fragments in deep inelastic collisions (D.I.C) of heavy ions by means of various techniques. Some measurements of the fragment masses following particle evaporation have been performed in time of flight[1] and mass spectrometer[2] experiments. Also coincidence experiments which give the energies and angles of the correlated fragments permit the determination of the masses[3,4] before evaporation through the kinematics, provided the energies are corrected for neutron emission. This correction is generally performed by estimating the total number of neutrons from the energy balance and sharing them according to the masses of the fragments. This method is limited by the lack of knowledge of the fragment atomic numbers, which makes it difficult to estimate the total binding energies of the fragments.

The measurement of the Z of one of the fragments along with the energies and angle of both fragments provides the needed parameters to determine accurately these binding energies.

A coincidence experiment for the reaction 340 MeV Ar + Ag was performed at the SuperHILAC. In this experiment a ΔE-E telescope fixed at 40° measures the Z of one of the fragments. A position-sensitive detector (PSD) was placed successively at 30° and 50° (Fig. 1). The measured energies of both light and heavy fragments were corrected for pulse height defects.[5] A preliminary

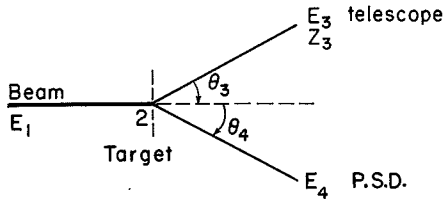

Fig. 1. Schematic diagram of the experimental set-up with the definitions of fragment numbers, energies and angles in the laboratory system. (XBL 766-8208)

analysis based upon the average values of the energy and angular distributions has been made. A more detailed event-by-event treatment of the data is in progress.

These data were first analyzed in the vicinity of Z = 32 for the light fragment. This corresponds to an almost symmetric splitting of the composite system. Near mass symmetry it is reasonable to assume that the ratio of the number of evaporated particles (ν^T) to the mass before evaporation (A^*) is the same for both fragments. With this assumption and the following equations we calculated conservation of linear momentum in the laboratory system [Eqs. (1) and (2)] conservation of mass [Eq. (3)] and charge [Eq. (4)], the masses of both fragments ($A^*_{3,4}$) prior to particle evaporation, and the total number of particles evaporated by each fragment ($\nu^T_{3,4}$). Superscript * denotes pre-evaporation. (See Fig. 1 for the definition of the parameters and subscripts)

$$\left.\begin{aligned} \frac{E_3}{1 - \frac{\nu_3^T}{A_3^*}}\, A_3^* &= E_1 A_1 \frac{\sin^2\theta_4}{\sin^2(\theta_3+\theta_4)} \\ \frac{E_4}{1 - \frac{\nu_4^T}{A_4^*}}\, A_4^* &= E_1 A_1 \frac{\sin^2\theta_3}{\sin^2(\theta_3+\theta_4)} \end{aligned}\right\} \text{conservation of linear momentum} \qquad (1), (2)$$

$$A_3^* + A_4^* = A_1 + A_2 \quad \text{conservation of mass} \qquad (3)$$

$$Z_3^* + Z_4^* = Z_1 + Z_2 \quad \text{conservation of charge} \qquad (4)$$

The results obtained with the assumption that no charged particle is evaporated by the fragments are shown in Fig. 2a. Since good agreement was obtained for the elastic scattering masses,[5] it appears that the systematic shift observed between the masses of the light and the heavy fragment is not due to experimental difficulties.[7] It is more likely the indication of charged particle evaporation from the light fragment. Since the fragments should be identical at symmetry the number of evaporated charges necessary to make the two lines agree at symmetry is given by the shift projected onto the Z axis. This number is 1.3 charge unit per fragment. In Fig. 2b the masses have been

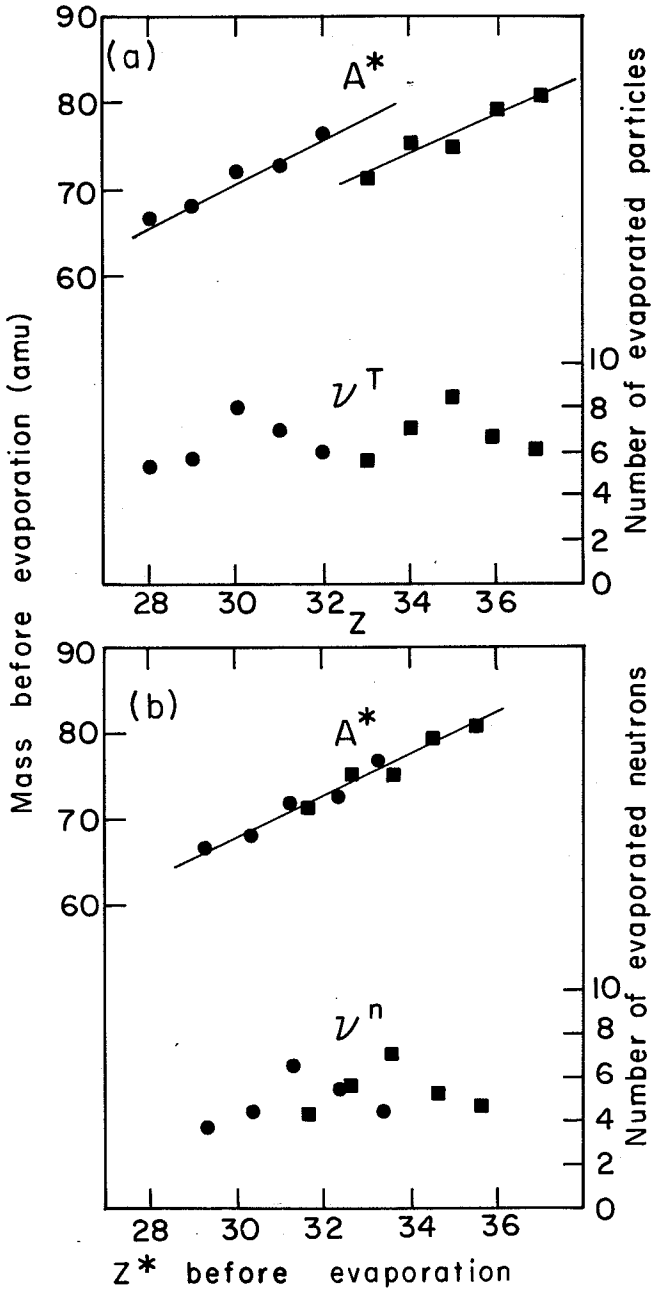

Fig. 2(a). Masses before evaporation and total number of evaporated particles for each fragment from the reaction of 340 MeV Ar + Ag, with the assumption that $(\nu_3^T/A_3^* = \nu_4^T/A_4^*)$. The solid circles refer to the light fragment and the solid squares to the heavy fragment; no charged particle evaporation is taken into account.

(b). 1.3 protons were evaporated from both fragments. (XBL 766-8209)

calculated with an average of 1.3 charge unit evaporated by the light fragment. The neutron numbers ν^n were obtained by subtracting from ν_T the experimental value of 1.3 charge unit. This implies that the evaporated charged particles are mainly protons.

In order to analyze the data away from symmetry, we can no longer assume that ν_T/A^* is the

same for both fragments. Instead we can use another equation [Eq. (5)] which expresses the conservation of energy in the laboratory system

$$E_1+B(A_1,Z_1)+B(A_2,Z_2) = E_3^*+E_4^* +B(A_3^*,Z_3^*) + B(A_4^*,Z_4^*) +E_\gamma^T+E_n^T+E_p^T. \quad (5)$$

E_γ^T, E_n^T and E_p^T are respectively the total energies associated with gamma, neutron, and proton emission. The total binding energies $B(A^*,Z^*)$ are taken the droplet mass table of Myers.[6]

Using this equation, along with Eqs. (1) to (4) where $\nu_{3,4}^T = \nu_{3,4}^n + \nu_{3,4}^p$ we developed a self-consistent procedure to obtain the masses and the number of evaporated neutrons for each fragment. This procedure assumes a binary process and that no particles are emitted by the composite system before the separation of the fragments [Eqs.(3) and (4)]. E_γ^T is the sum of the individual rotational energies of the fragments calculated from a simple model of two rigidly rotating spheres. Some competition with neutron emission is included by adding to these energies a fraction of the binding energy of the last neutron emitted in the average cascade. Since the excitation energies of the fragments are relatively high, it seems unlikely that strong shell effects would be present. The level desntiy parameter was simply taken to be $A^*/8$ in the determination of the average kinetic energies of the evaporated particles.

The above set of equations is highly nonlinear preventing a direct solution. An iterative procedure was developed to obtain the solution. Starting with a reasonable guess for A_4^*, A_3^* ν_4^n, ν^n:

(Step 1) The ratio $\frac{\nu_3^n}{\nu_4^n}$ is extracted from Eqs. (1) and (2);

(Step 2) ν_3^n and ν_4^n are obtained from Eq. (5);

(Step 3) With these values Eqs. (1) and (2) give the ratio $\frac{A_3^*}{A_4^*}$.

(Step 4) A_3^* and A_4^* are then calculated from the ratio $\frac{A_3^*}{A_4^*}$ and Eq. (3).

(Step 5) If the convergence is not obtained we start again at Step 1. Between Steps 1 and 2 the excitation energies, nuclear temperatures, and kinetic energies of neutrons and protons are calculated.

The number of evaporated protons is a free parameter in the program and is not part of the iteration. In the analysis of the reaction Ar + Ag, $|\nu^p|$ was estimated from the evaporation code of Dostrovsky et al.[7] and renormalized with the procedure explained later. In these evaporation calculations we used A/10 for the level density parameter and 1.5 fermi for the radius parameter. It was assumed that the total excitation energy is shared by the two fragments according to their mass. The initial masses A^* were calculated by minimizing the potential energy of two touching spheres[1] of given mass asymmetry with respect to the charge asymmetry degree of freedom. This evaporation code was developed by Dostrovsky et al.[6] for the analysis of compound nucleus reactions leading to masses and excitation energies similar to those of the D.I.C. fragments. No angular momentum is taken into account in this code. We do not expect this to affect the results substantially since in the D.I.C. one expects most of the initial angular momentum to go into relative motion. Table 1 summarizes the results of the calculations for the light fragments of the reaction. At symmetry these calculations predict an average number of evaporated changes ($\nu^p+2\nu^\alpha$) of 1.05. This number is close to the experimental value

Table 1.

Z^*	A^*	ν^n	ν^p	ν^α	$\nu^p+2\nu^\alpha$ (normalized)	Z^*	A^*	ν^n	ν^p	ν^α	$\nu^p+2\nu^\alpha$ (normalized)
10	22	0.98	~ 0	0.02	0.05	22	49	2.52	0.39	0.03	0.58
11	24	0.95	0.05	0.16	0.47	23	52	2.89	0.41	0.05	0.66
12	27	1.53	0.02	0.01	0.05	24	54	3.03	0.38	0.08	0.69
13	29	1.85	0.02	0.01	0.05	25	56	3.28	0.44	0.10	0.82
14	31	1.84	0.09	0.02	0.17	26	59	3.92	0.23	0.09	0.53
15	33	1.82	0.10	0.03	0.20	27	61	3.90	0.47	0.07	0.78
16	36	1.88	0.04	0.06	0.20	28	63	4.03	0.37	0.13	0.81
17	38	1.97	0.10	0.18	0.59	29	66	4.16	0.44	0.09	0.80
18	40	2.04	0.13	0.14	0.53	30	68	3.99	0.48	0.20	1.13
19	43	2.57	0.13	0.09	0.40	31	71	4.14	0.53	0.20	1.20
20	45	2.36	0.22	0.09	0.51	32	73	4.25	0.61	0.20	1.29
21	47	2.51	0.19	0.06	0.40	33	75	4.10	0.74	0.19	1.45

of 1.3. These calculated values were normalized to agree with the experimental number of 1.3 at symmetry.

Using the normalized values of Table 1 for $\nu^p_{3,4}$ in the full iterative calculation, we obtained the masses and neutron numbers of Fig. 3. Around

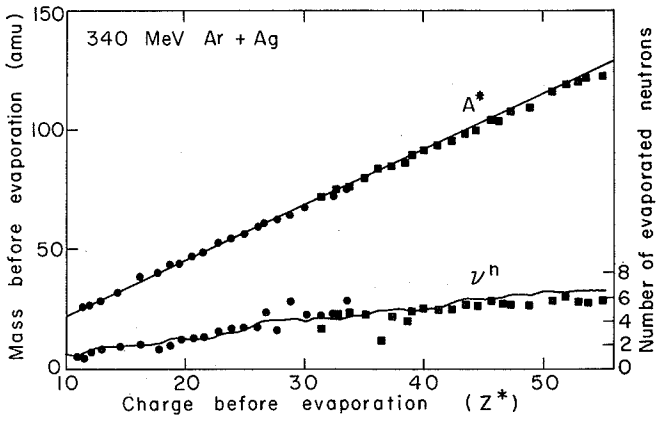

Fig. 3. Masses before evaporation and number of evaporated neutrons for each fragment calculated with the full iterative procedure. Symbols are the same as in Fig. 2. The upper solid line is the prediction of the charge equilibrium model described in the text. The lower solid line represents the number of neutrons ν^n obtained with the evaporation code of Ref. 6 assuming that the total excitation energy is shared by the fragments according to their mass. (XBL 766-8210)

symmetry the agreement with the simple analysis done before (Fig. 2b) is good. The upper solid line represents the masses calculated by assuming charge equilibration[1] between the two fragments. The good agreement obtained with this model confirms the conclusions of Gatty et al.[1] for the comparable system Ar + Ni, namely that charge equilibrium is indeed achieved in D.I.C. for the part of the angular distribution beyond the grazing angle. The lower solid line represents the calculated values of $|\nu^n|$ from Table 1 extended towards higher atomic numbers. The good agreement with the experimental values suggest that thermal equilibrium is achieved between the fragments as we postulated when establishing the input parameters of the evaporation calculations. Further analysis will allow us to "explore" the behavior of the system (masses and excitation energies) as it relaxes along the energy degree of freedom.

Footnotes and References

*On leave from DPh/MF CEN, Saclay, France.

†NATO Fellow.

1. B. Gatty, D. Guerreau, M. Lefort, X. Tarrago, J. Galin and B. Cauvin, J. Girard, H. Nifenecker, Nucl. Phys. A253, 511 (1975).

2. J. C. Jacmart, P. Colombani, H. Doubre, N. Frascaria, N. Poffé, M. Riou, J. C. Roynette and C. Stephan, Nucl. Phys. A242, 175 (1975).

3. F. Hannappe, M. Lefort, C. Ngo, J. Peter, and B. Tamain, Phys. Rev. Lett. 32, 738 (1974).

4. K. L. Wolf, J. P. Unik, J. R. Huizenga, J. Birkelund, H. Freiesleben and V. E. Viola, Phys. Rev. Lett. 33, 1105 (1974).

5. P. Russo, R. Jared, R. Babinet, and L. G. Moretto, Energy Calibrations of Solid State Counters for Heavy Ion Experiments, in this Annual Report.

6. W. D. Myers, LBL Report LBL-3428.

7. I. Dostrovsky, Z. Fraenkel, and G. Friedlander, Phys. Rev. 116, 683 (1959).

EVIDENCE OF INCOMPLETE RELAXATION IN THE REACTION $^{107,109}Ag = ^{40}Ar$ AT 288 AND 340 MeV BOMBARDING ENERGIES*

J. Galin,† L. G. Moretto,† R. Babinet,§
R. Jared, and S. G. Thompson

Light fragments emitted in the reaction $^{107,109}Ag + ^{40}Ar$ at 288 and 340 MeV have been studied. Using a ΔE-E telescope,[1] it was possible to identify particles with atomic numbers as high as Z = 30. Kinetic energy spectra for these fragments have been studied over a broad range of laboratory angles. Two distinct components are visible in these distributions: one is at nearly elastic energies, the "quasi-elastic" component; the other is near the expected Coulomb energy, the "relaxed" component. The quasi-elastic component is confined to a narrow angular region around the critical angle and is restricted to Z's close to that of the projectile. The relaxed component is present for all atomic numbers and at all angles.

In the center-of-mass system, the kinetic energy distributions are Gaussian in appearance. For fixed Z, the first and second moments are fairly constant over a wide angular range. The mean energies are close to that of two touching spherical fragments. The FWHM are approximately 25 MeV at the lower bombarding energy and about 30 MeV at the higher energy.

The laboratory yields of the relaxed component are given in Fig. 1. The cross section tends to in-

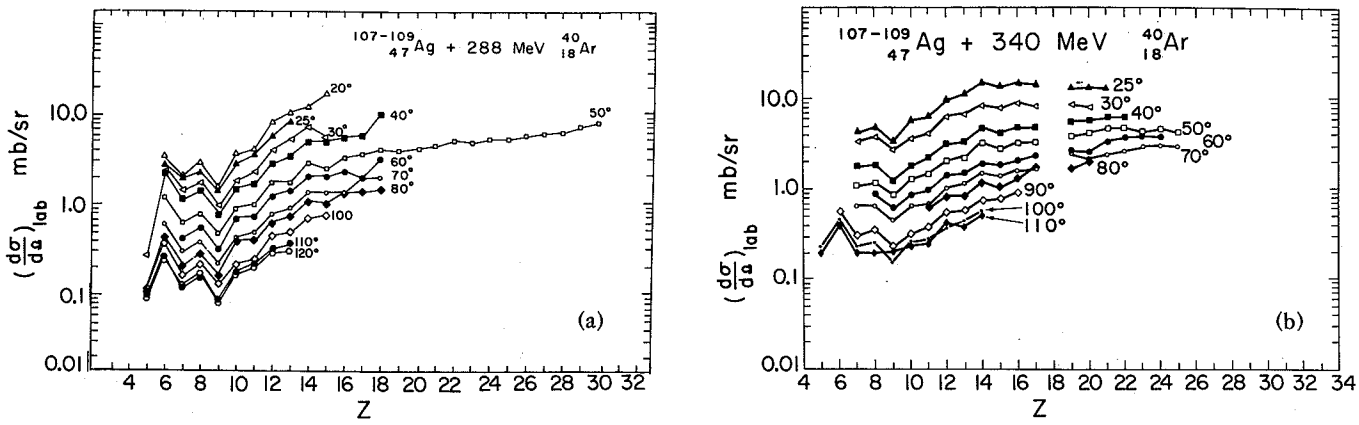

Fig. 1. Laboratory differential cross sections for various Z's and for various angles at both bombarding energies. (a) XBL 7411-8216-A, (b) XBL 752-2301

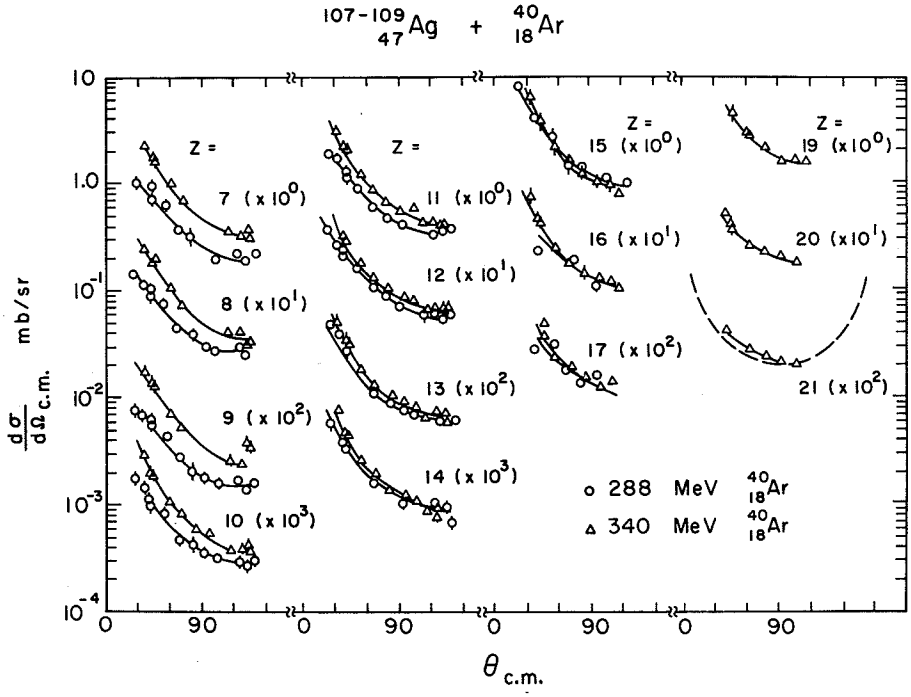

Fig. 2. Center-of-mass angular distributions for various charges at both bombarding energies. The dashed curve at Z = 21 corresponds to a $1/\sin\theta$ distribution. (XBL 752-2302)

crease with Z for Z > 9. The increase is somewhat more pronounced at the lower energy.

The center-of-mass angular distributions (Fig. 2) are all forward peaked in excess of $1/\sin\theta$, the distribution expected from the decay of a rapidly rotating compound nucleus. The forward peaking has been interpreted in terms of a short-lived intermediate complex consisting of two touching fragments.[2,3] The exchange of charge has been described as a diffusion process along the charge asymmetry coordinate of this complex. The predicted charge and angular distributions are in very good agreement with the experimental results.

Footnotes and References

*Condensed from LBL-4064 and Nucl. Phys. A255 472 (1975).

†Present address: Institut de Physique Nucléaire, Orsay, France.

‡Sloan Fellow 1974-1976.

§Present address: DPh/MF-CEN, Saclay, France.

1. M. M. Fowler, R. C. Jared, Nucl. Inst. Meth. 124, 341 (1975).

2. L. G. Moretto, R. P. Babinet, J. Galin and S. G. Thompson, Phys. Lett. 58B, 31 (1975).

3. L. G. Moretto and J. S. Sventek, Phys. Lett. 58B, 26 (1975).

POTENTIAL ENERGY EFFECTS AND DIFFUSION IN THE RELAXED COMPONENTS OF THE REACTION $^{197}Au + ^{40}Ar$ AT 288 AND 340 MeV BOMBARDING ENERGIES*

L. G. Moretto,† J. Galin,† R. Babinet,§ Z. Fraenkel,‖
R. Schmitt, R. Jared, and S. G. Thompson

The fragments produced in the reaction $^{197}Au + ^{40}Ar$ have been studied at 288 and 340 MeV bombarding energies. It was possible to resolve individual atomic numbers up to Z = 32 with a ΔE-E telescope.[1] Kinetic energy spectra and laboratory cross sections were obtained over a broad range of angles. The energy spectra of reaction products are similar to those obtained with N and Ne projectiles.[2,3] For Z's close to that of the projectile and for angles close to grazing, a high energy or "quasi-elastic" component is present. In addition, a "relaxed" component is visible at energies close to the expected Coulomb energy for two touching spherical fragments. The relaxed component is present for all Z's and presists through the angular range of the measurements. For angles near the grazing and Z < 18, the two components are not readily distinguishable, and the laboratory charge distributions (Fig. 1) peak near the projectile. For more backward angles the yields increase with Z above Z = 9.

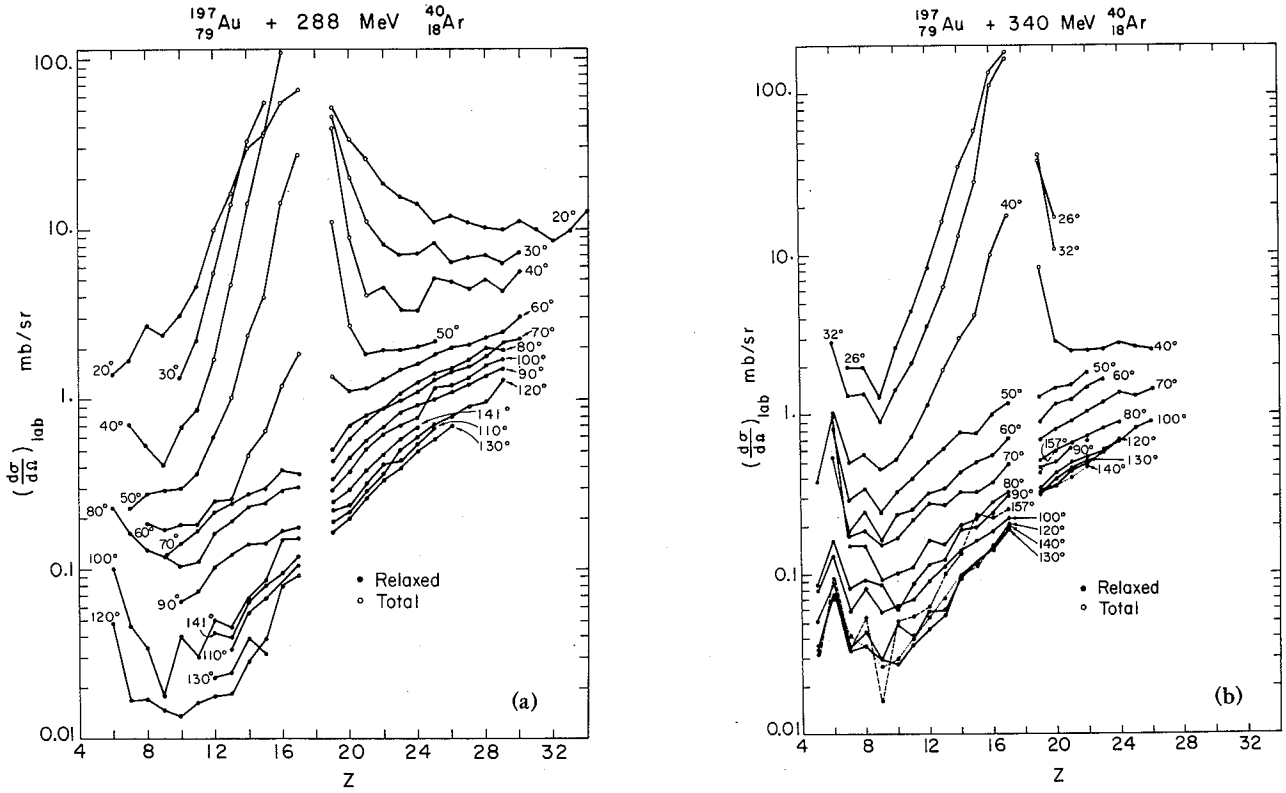

Fig. 1. Laboratory differential cross sections $(d\sigma/d\Omega\,|_{lab})$ as a function of atomic number for various lab angles. Filled points indicate that the cross sections were obtained by integrating a relaxed kinetic energy distribution. Open points indicate either the presence of quasi-elastic component or that the kinetic energy distribution was unusually borad. Notice how the peak around Z = 18 disappears at backward angles. a (XBL 752-2305), b (XBL 752-2306)

The center-of-mass angular distributions are depicted in Fig. 2. All the distributions are forward peaked in excess of 1/sinθ supporting the notion that the intermediate complex formed in the reaction is short-lived.[4,5] Such forward peaking has been observed in other heavy ion systems like Ag + N, Ne and Ar.[2,3,6] Unlike distributions obtained for these lighter systems, where the forward peaking yielded to 1/sinθ four or five atomic number units above the projectile, the forward peaking persists for atomic numbers as large as Z = 29, 11 atomic numbers above the pro-

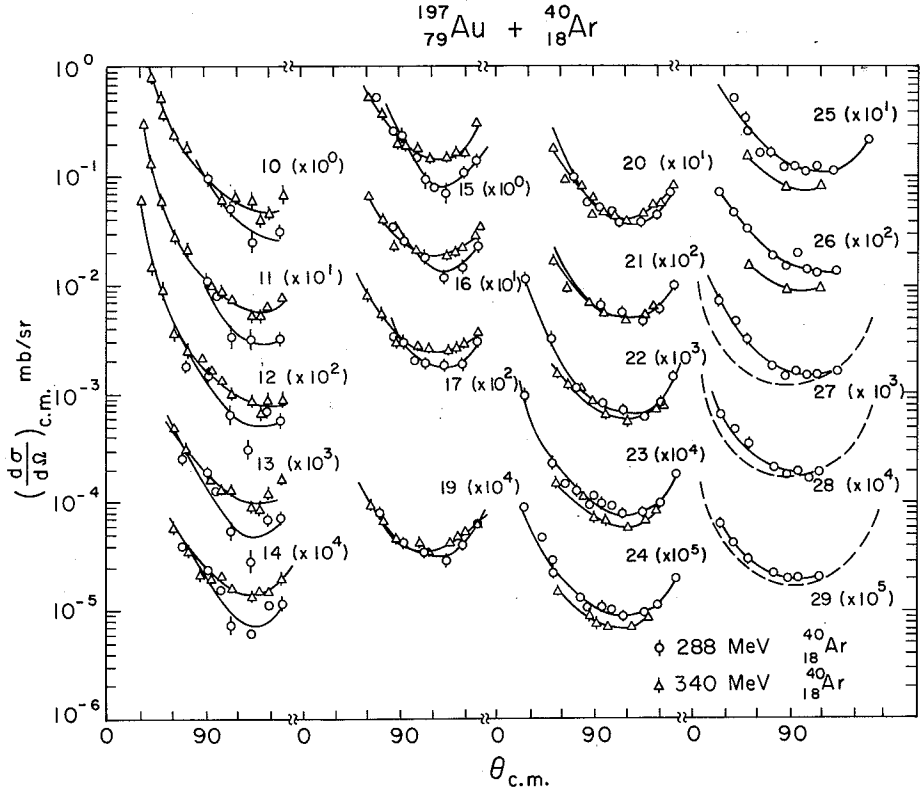

Fig. 2. Center-of-mass angular distributions for various atomic numbers. The quasi-elastic contributions have been subtracted when present as a distinct peak. The dashed curves plotted for Z = 27, 28 and 29 correspond to $1/\sin\theta$ distributions.
(XBL 752-2307A)

jectile. This "anomalous" behavior has been interpreted in terms of an enhanced diffusion towards symmetry, promoted by the potential energy which drives the intermediate complex consisting of two touching fragments toward more symmetric configurations.

Footnotes and References

*Condensed from LBL-4984 and Nucl. Phys., A259, 173 (1976).

†Sloan Fellow 1974-1976.

†Present address: Institut de Physique Nucleaire, Orsay, France.

§Present address: DPh/MF-CEN, Saclay, France.

||Present address: Weisman Institute, Israel.

1. M. M. Fowler and R. C. Jared, Nucl. Inst. Meth. 124, 341 (1975).

2. L. G. Moretto, S. K. Kataria, R. C. Jared, R. Schmitt and S. G. Thompson, Nucl. Phys. A255, 491 (1975).

3. R. Babinet, L. G. Moretto, J. Galin, R. Jared, J. Moulton and S. G. Thompson, Nucl. Phys. A258, 172 (1976).

4. L. G. Moretto, R. P. Babinet, J. Galin, and S. G. Thompson, Phys. Lett. 58B, 31 (1975).

5. L. G. Moretto and J. S. Sventek, Phys. Lett. 58B, 26 (1975).

6. J. Galin, L. G. Moretto, R. Babinet, R. Schmitt, R. Jared and S. G. Thompson, Nucl. Phys. A255, 472 (1975).

NUCLEAR RELAXATION PHENOMENA AND DIFFUSION IN THE REACTION ^{107,109}Ag + ^{84}Kr AT 7.2 MeV/NUCLEON

R. P. Schmitt, P. Russo, R, Babinet,*
R. Jared, and L. G. Morettoţ

Early reaction studies with heavy projectiles and large A targets like Bi + Kr have revealed the existence of what was considered a new mechanism, "quasi-fission."[1,2] The products of the quasi-fission process exhibit the following characteristics: fission-like kinetic energies, narrow mass distributions peaked near the projectile mass and side-peaked angular distributions. Since only very massive systems have been studied, it is worthwhile investigating the behavior of a system obtained with the same large projectiles but with a lighter target.

Fragments produced in the reaction Ag and a 7.2 MeV/nucleon Kr beam were detected with E-ΔE telescopes.[3] It was possible to resolve individual changes up to Z ≅ 50. The kinetic energy distributions of the products are very similar to those obtained with N, Ne and Ar.[4-7] Near the grazing angle quasi-elastic and relaxed components are present as two distinct peaks for Z's close to 36. Far forward of the critical angle, the two components overlap . At more backward angles only a relaxed fission-like component is visible. The centrods of the relaxed component are somewhat lower than the Coulomb energy of touching spheres (Fig. 1).

For backward angles the laboratory charge distributions (Fig. 2) appear to rise steadily towards symmetry, unlike those obtained with massive targets but similar to those obtained in Ar induced reactions. For angles inside the grazing angle, it is difficult to separate the relaxed and quasi-elastic components. As a result some peaking around the projectile is visible in the charge distribution for 24°.

The center-of-mass angular distributions are given in Fig. 3. The side peaking typical of heavier systems is conspicuously absent. Instead, the distributions are forward peaked in excess of $1/\sin\theta$ near the projectile, tending toward $1/\sin\theta$ as one moves away from Z = 36.

The patterns of the charge and angular distributions are not substantially different from those observed in Ar induced reactions and can be interpreted in terms of the diffusion model originally introduced to explain results observed with lighter projectiles.[8,9]

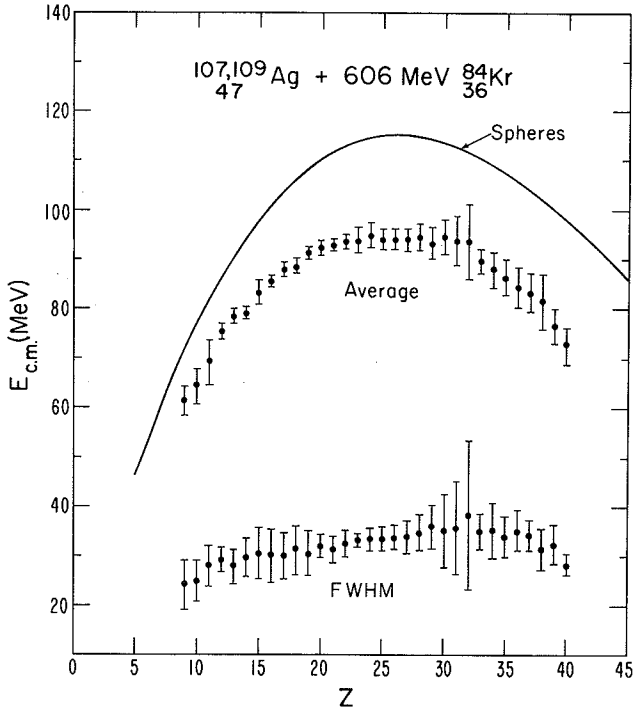

Fig. 1. Average mean center-of-mass kinetic energies and FWHM for the relaxed components. The averages have been made over the range 24-70° in the lab. Error bars are the standard deviations from the mean. (XBL 763-2479)

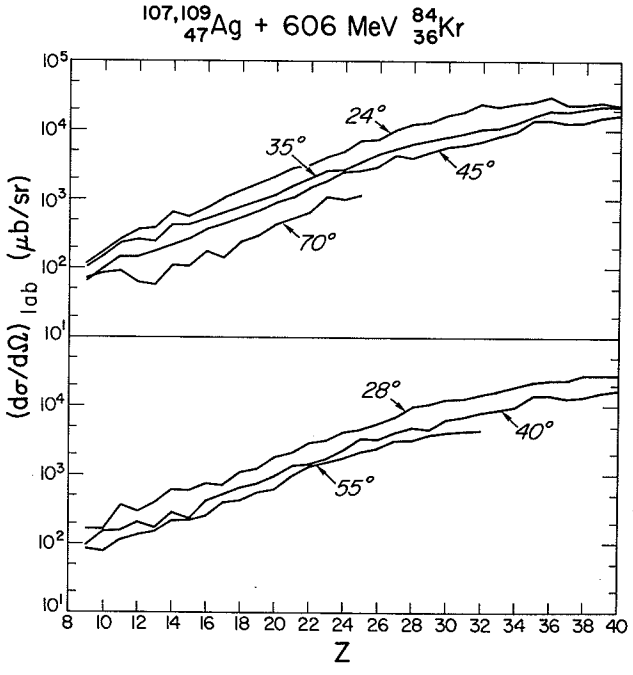

Fig. 2. Laboratory charge distributions at various lab angles. (XBL 763-2501)

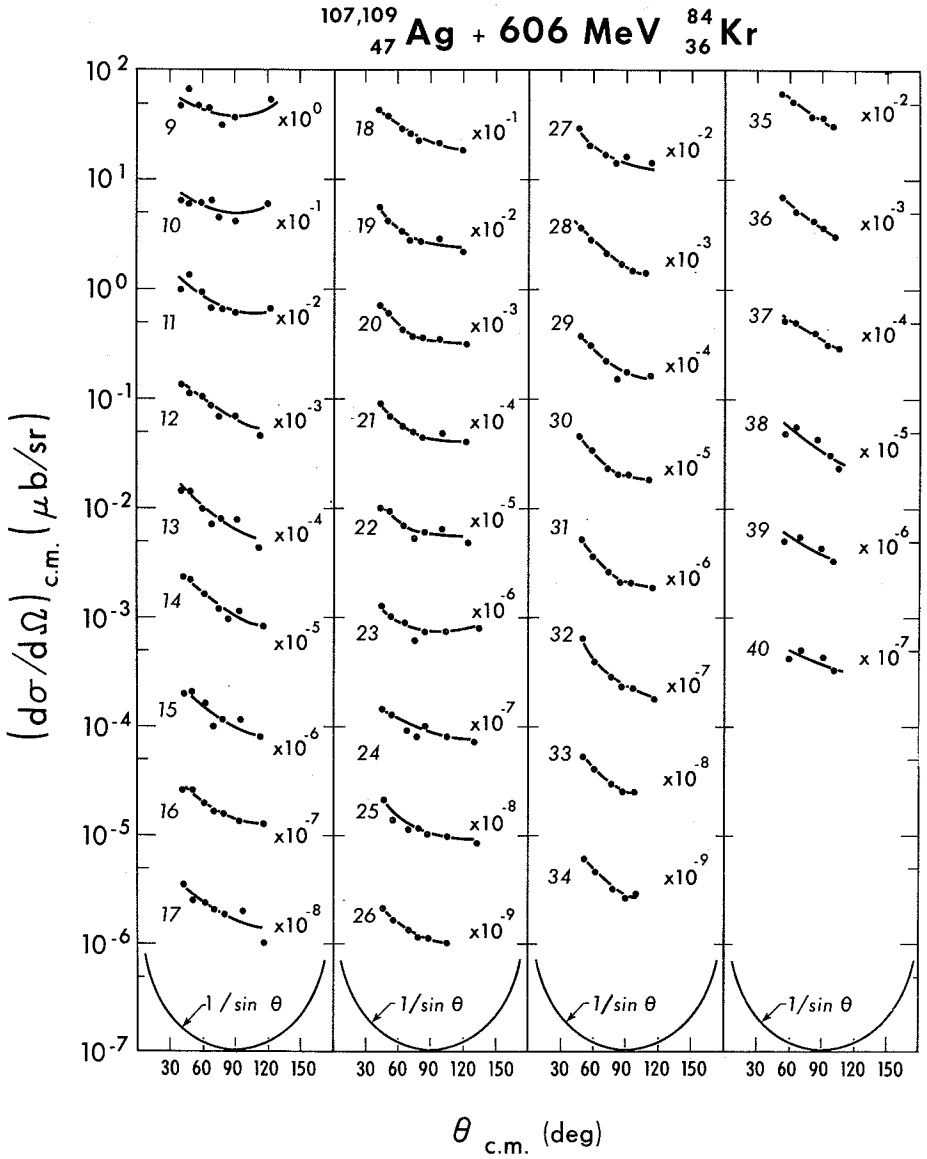

Fig. 3. Center-of-mass angular distributions for various atomic numbers. (XBL 763-2478)

Footnotes and References

*Present address: DPh/MF-CEN, Saclay, France

†Sloan Fellow 1974-1976.

1. F. Hanappe, M. Lefort, C. Ngo, J. Peter and B. Tamain, Phys. Rev. Lett. 32, 738 (1974).

2. K. L. Wolf, J. P. Unik, J. P. Huizenga, J. Birkelund, H. Freiesleben and V. E. Viola, Phys. Rev. Lett. 33, 1105 (1974).

3. M. M. Fowler and R. C. Jared Nucl. Inst. Method. 124, 341 (1975).

4. L. G. Moretto, S. K. Kataria, R. C. Jared, R. Schmitt and S. G. Thompson, Nucl. Phys. A255, 491 (1975).

5. R. Babinet, L. G. Moretto, J. Jalin, R. Jared, J. Moulton and S. G. Thompson, Nucl. Phys. A258, 172 (1976).

6. J. Galin, L. G. Moretto, R. Babinet, R. Schmitt, R. Jared and S. G. Thompson, Nucl. Phys. A255, 472 (1975).

7. L. G. Moretto, J. Galin, R. Babinet, Z. Fraenkel, R. Schmitt, R. Jared and S. E. Thompson, Nucl. Phys. A259, 173 (1976).

8. L. G. Moretto, R. P. Babinet, J. Galin and S. G. Thompson, Phys. Lett. 58B, 31 (1975).

9. L. G. Moretto and J. S. Sventek, Phys. Lett. 58B, 26 (1975).

10. L. G. Moretto, B. Canvin, P. Glässel, R. Jared, P. Russo, J. Sventek, and G. Wozniak, Phys. Rev. Lett. 36, 1069 (1976).

CHARGED FRAGMENTS PRODUCED IN THE INTERACTION OF ^{159}Tb AND ^{86}Kr AT 620 MeV BOMBARDING ENERGY

G. J. Wozniak, P. Glassel,* R. Schmitt, P. Russo,
B. Cauvin,† R. Jared, and L. G. Moretto

Early studies[1,2] of Kr induced reactions yielded results apparently very different from those observed in heavy systems involving lighter projectiles and prompted the claim that a new mechanism, "quasi-fission", was coming into play. In the system Kr + Bi the mass distributions were sharply peaked about the projectile and the angular distributions for the fission-like products were side peaked. Detailed systematics of several Kr induced reactions tend to discount the claim for a new mechanism (see this report). While peaked charge and angular distributions were observed with heavy targets like Au and Ta, the system Kr + Ag revealed characteristics reminiscent of ^{14}N, ^{20}Ne and ^{40}Ar induced reactions. In an attempt to locate the transition region between the ^{197}Au and ^{107,109}Ag targets we investigated the behavior of the Kr + ^{159}Tb system.

Fragments produced in the reaction ^{159}Tb + 620-MeV ^{86}Kr were identified with an E-ΔE telescope.[3] Utilizing this technique, it was possible to identify fragments with Z's up to a maximum of 50. The fragment kinetic energy distributions contained the two components common to such heavy ion systems: quasi-elastic and relaxed.

The distributions of atomic numbers(z) for the relaxed component for several lab angles are shown in Fig. 1. Comparing these Z distributions to those obtained in studies with ^{197}Au, ^{181}Ta and ^{107,109}Ag targets, one observes that the widths are intermediate to those of the Kr + ^{181}Ta and Kr + Ag systems. Preliminary theoretical calculations indicate that this behavior pattern is consistent with the assumption of a diffusive mechanism with respect to the charge asymmetry degree of freedom. Potential energy surfaces for the Kr systems are given in Fig. 2.

Angular distributions for this system (Fig. 3) are also intermediate to those obtained with light and heavy targets. The strong focusing effects observed with Ta and Au have become quite weak for Tb and are confined to Z's very near the projectile. For Z's further from the projectile the angular distributions are more strongly forwarded peaked than in the case of Ag + Kr. This implies that the ratio of the lifetime of the system to the rotational period is smaller than that of the Ag + Kr system. As a result, on the average the intermediate complex undergoes less rotation and yields more forward peaked distribution for

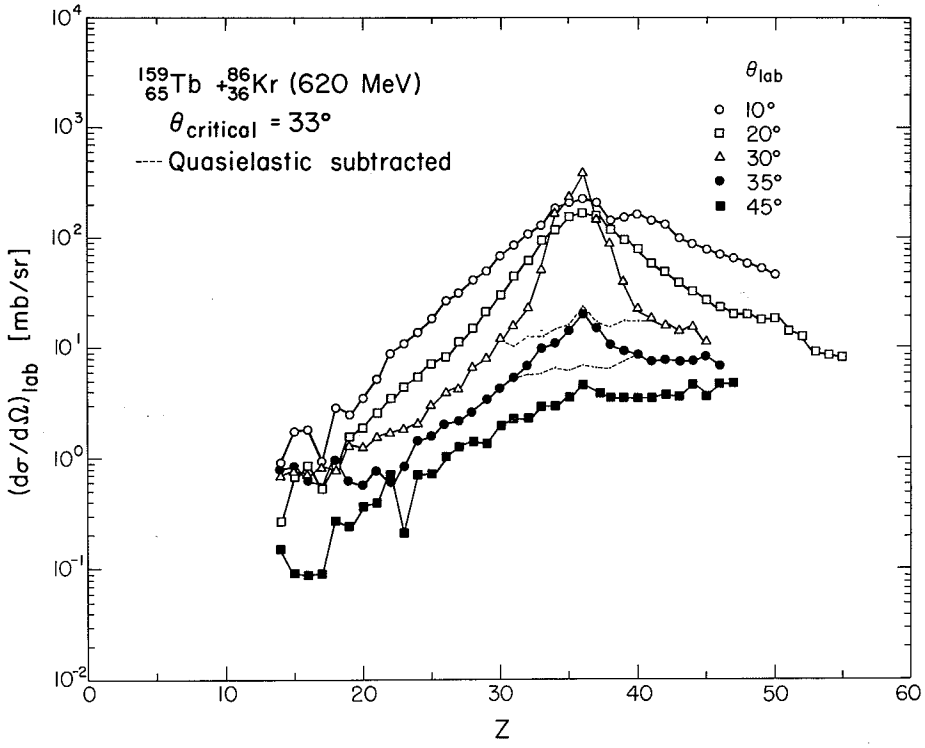

Fig. 1. Laboratory yields of the various fragments for several angles. Near the grazing the quasi-elastic and relaxed components are well separated in energy. The dashed curves for 30° and 35° represent only the relaxed contribution. Notice that in these cases the peaking around Z = 36 almost completely disappears. (XBL 766-2989)

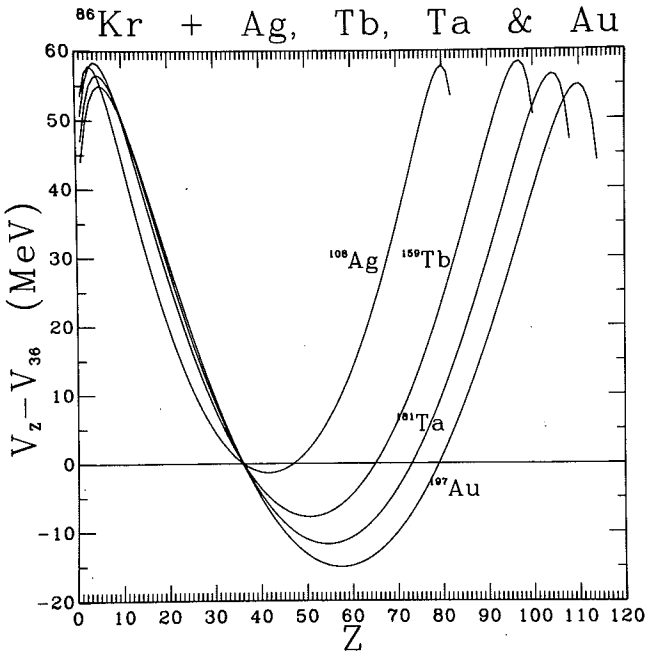

Fig. 2. Potential energy surfaces for an intermediate complex consisting of two touching spheres relative to the entrance channel for various Kr systems. (XBL 766-8174)

Kr + Tb. Since the small charge transfer involve even short times, the forward peaking yields to a slight side peaking for Z's near the projectile.

If one assumes that the intermediate complex consists for two touching spherical fragments rotating rigidly, the rotational period for the r.m.s. angular momentum tends to increase in going from Ag to Au targets. If the lifetime of the complex were constant and the complex is as described above, the gross features of the angular distributions would be reproduced. Long rotational periods would result in side-peaked distributions while shorter periods would give rise to forward-peaked distributions. However, there is no real evidence to support the notion that the lifetime of the complex is constant. In fact, the narrowed charge distributions obtained for the most massive systems seem to indicate that the lifetime of the complex is decreasing. Incomplete energy relaxation for the heavier systems supports this hypothesis. A detailed theoretical analysis of such a wide variety of systems should provide us with reliable estimates of the decay properties of the intermediate complex.

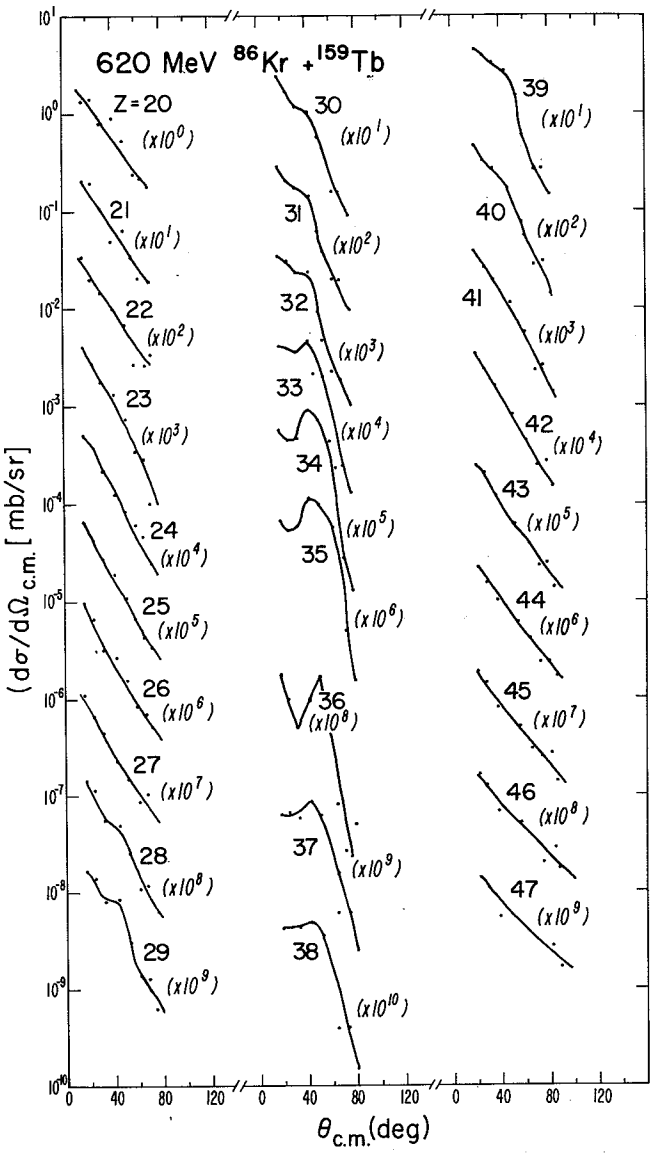

Fig. 3. Angular distributions for Tb + Kr for a variety of atomic numbers. (XBL 766-3008)

Footnotes and References

*NATO Fellow.

†On leave from DPhN/MF-CEN, Saclay, France

‡Sloan Fellow 1974-1976.

1. F. Hanappe, M. Lefort, G. Ngô, J. Peter and B. Tamain, Phys. Rev. Lett. 32 738 (1974).

2. K. L. Wolf, J. P. Unik, J. R. Huizenga, J. Birkelund, H. Freiesleben and V. E. Viola, Phys. Rev. Lett. 33, 1105 (1974).

3. M. M. Fowler and R. C. Jared, Nucl. Instr. Meth. 124, 341 (1975).

STUDY OF THE FRAGMENTS EMITTED IN THE INTERACTION BETWEEN ^{181}Ta AND ^{86}Kr AT 620 MeV BOMBARDING ENERGY

P. Glassel,* B. Cauvin,† G. Wozniak, P. Russo,
R. Schmitt, R. Jarred, and L. G. Moretto

The diffusion model proposed by Moretto and Sventek[1] has proved to be highly successful when applied to heavy ion reaction involving ^{14}N, ^{20}Ne and ^{40}Ar projectiles. Recent studies with Kr projectiles[2] (i.e. Au + Kr) seem to indicate that the model has a broader range of applicability. To further check the diffusion model the systematics of Kr induced reactions have been investigated over a broad range of targets.

The experimental technique employed is that of fragment Z-identification. Individual atomic numbers with Z as large as 50 have been identified by means of E-ΔE telescopes.[3] The resulting kinetic energy distributions showed the usual quasi-elastic transfer component at near-elastic energies and the relaxed component at near-Coulomb energies.

In Fig. 1 the mean c.m. kinetic energies of the relaxed components are plotted vs. Z. For comparison, the Coulomb repulsion of two touching spheres is given. In general, the trends and magnitudes agree, except near the projectile at the grazing angle where the relaxed and quasi-elastic contribution could not be separated. The widths of the kinetic energy distributions, which are also shown in Fig. 1, are rather constant, with the same exception as above.

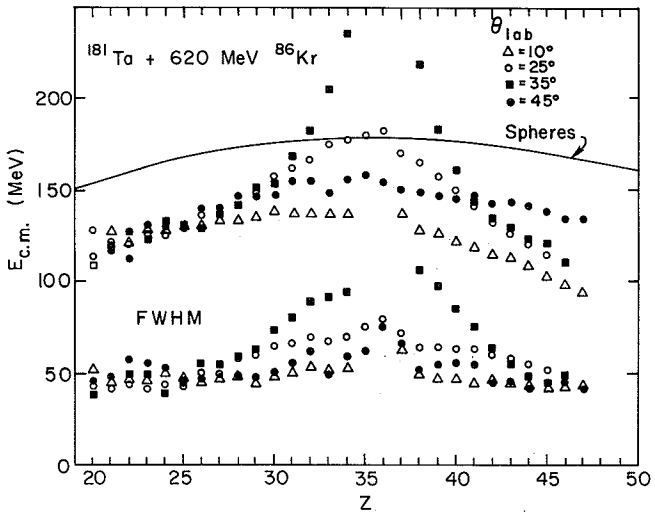

Fig. 1. Mean center-of-mass kinetic energies and FWHM for the relaxed component as a function of Z for various lab angles. (XBL 766-8215)

The Z-distributions in Fig. 2 are very similar to those obtained for Au + Kr. The yield tends to peak near the projectile Z and exhibits the same general behavior with angle as observed with Au (see Ref. 2 and this report).

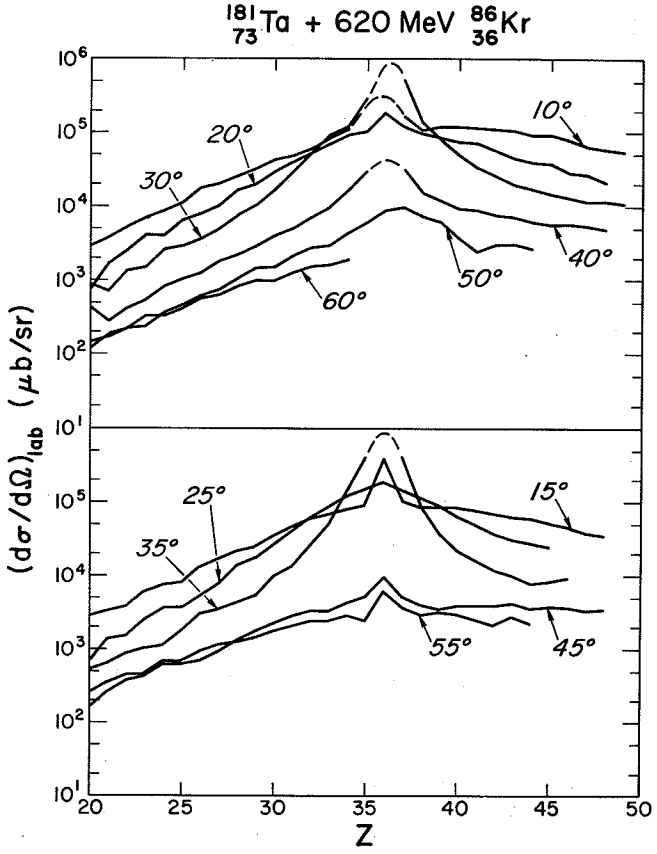

Fig. 2. Relaxed laboratory cross sections as a function of Z for several lab angles. For angles close to the grazing and Z's near the projectile, the decomposition of the relaxed and quasi-elastic components is somewhat uncertain as the dashed curves indicate. (XBL 763-2502)

Center of mass angular distributions for the relaxed components are given in Fig. 3. Like Au + Kr, the distributions show strong side peaking for atomic numbers in the vicinity of the projectile indicating that the intermediate complex formed in the reaction decays before it rotates much past the grazing angle. This side-peaking gradually decreases for atomic numbers farther removed from the projectile, since it takes more time for the diffusion process to reach these masses thus allowing the complex to rotate farther and eventually even cross 0°. The strong forward peaking persists for atomic numbers far away from the projectile, indicating that the lifetime of the intermediate complex is not sufficient for it to rotate more than about half a revolution.

While the system Ta + Kr is quite similar to that of Au + Kr there are significant differences: the charge distributions are not quite as

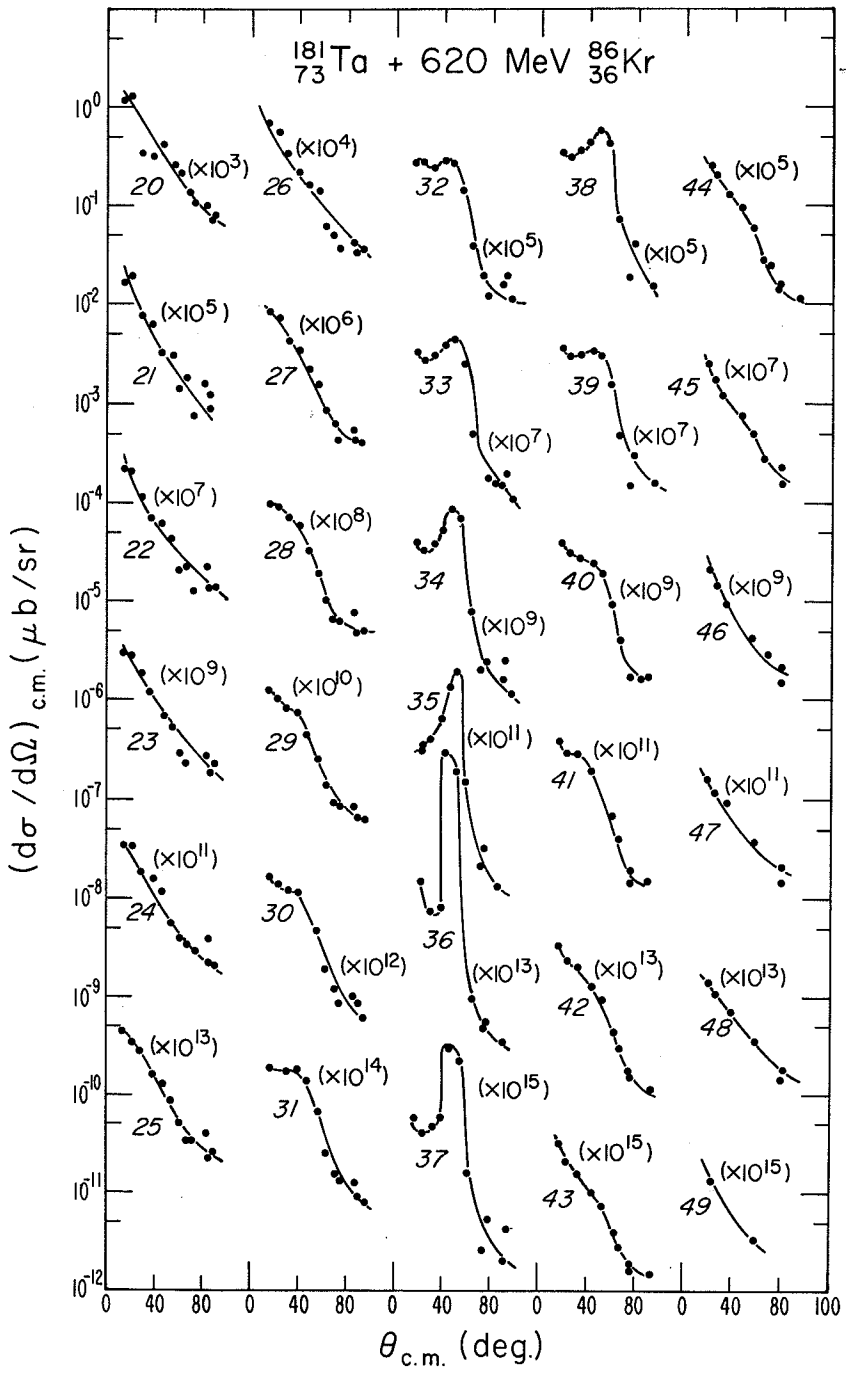

Fig. 3. Angular distributions for the relaxed component. The quasi-elastic and relaxed components are not well separated for Z = 36. (XBL 763-2499)

peaked in the case of Ta and the side-peaking in the angular distributions tends to die out more quickly with Z than it does with Au. Presumably, the differences are due to the difference in the Coulomb field (an 8% effect). Since the side-peaking seems so sensitive to the entrnace channel, it is hoped that one will be able to theoretically extract the details of the nuclear transport phenomena involved in heavy ion systems.

Footnotes and References

*NATO Fellow

†On leave from DPh/MF-CEN, Saclay, France.

‡Sloan Fellow 1974-1976.

1. L. G. Moretto and J. S. Sventek, Phys. Lett. 58B, 26 (1975).

2. L. G. Moretto, B. Cauvin, P. Glässel, R. Jared, P. Russo, J. Sventek, and G. Wozniak, Phys. Rev. Lett. 36, 1069 (1976).

3. M. M. Fowler and R. C. Jared, Nucl. Inst. Meth. 124 (1975) 341.

DIFFUSIVE PHENOMENA IN THE CHARGE AND ANGULAR DISTRIBUTIONS FOR THE REACTION ^{197}Au + 620 MeV ^{86}Kr*

L. G. Moretto,† B. Cauvin,† P. Glassel,§ R. Jared,
P. Russo, J. Sventek, and G. Wozniak

Charged fragments produced in the reaction ^{197}Au + 620 MeV ^{86}Kr have been studied by means of ΔE-E telescopes.[1] Individual atomic numbers have been resolved up to Z ≅ 50. The kinetic energy distributions of the fragments are similar to those obtained with lighter projectiles like N, Ne and Ar.[2,3,4,5] At near-elastic energies and atomic numbers near that of the projectile, there is a quasi-elastic component. This component is confined to a narrow angular range close to the critical angle. At lower energies there is a relaxed component which persists throughout the angular range of the measurements. The centroids of the relaxed peaks for the various fragments are close to the Coulomb repulsion energy expected for binary division (Fig. 1).

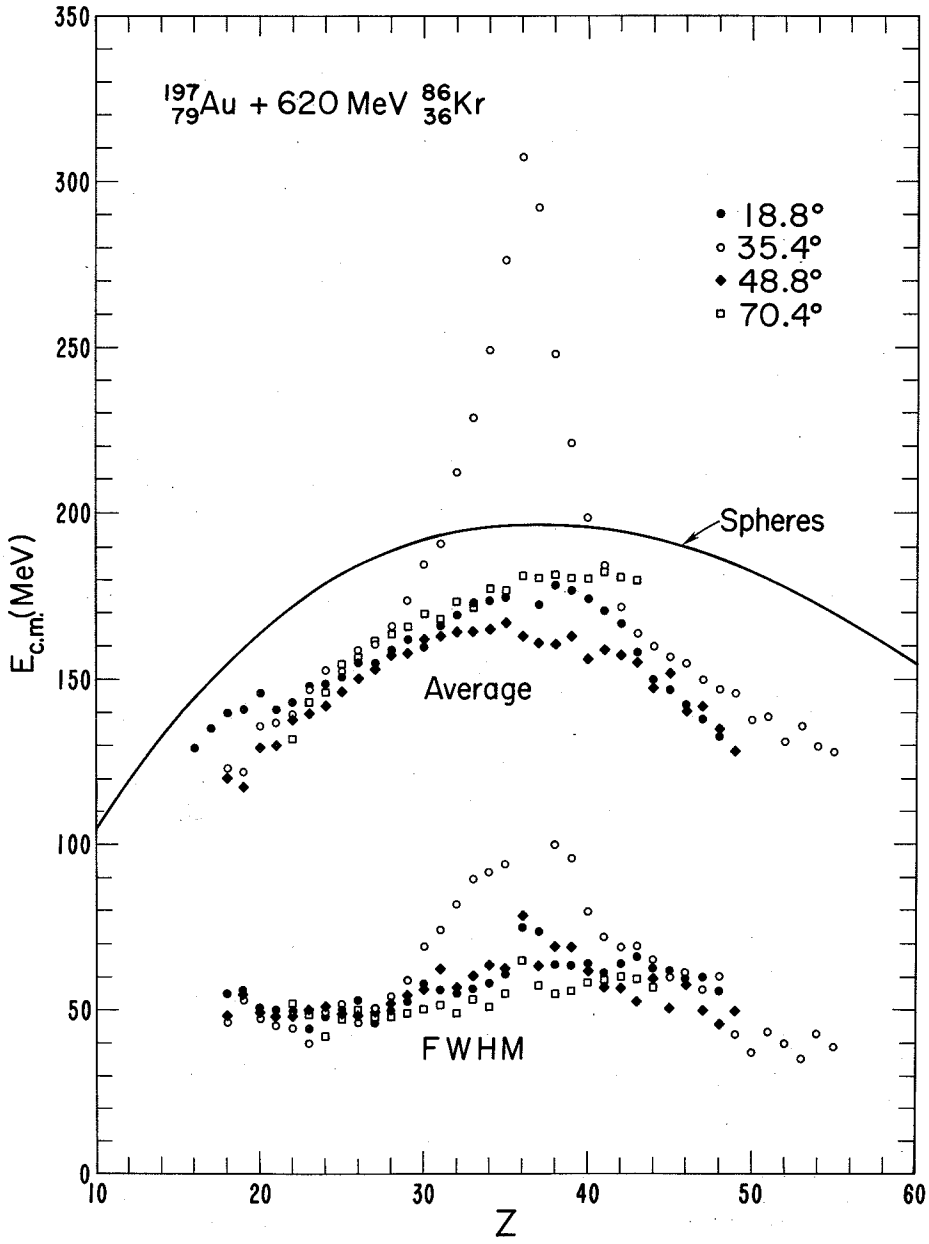

Fig. 1. Mean center-of-mass kinetic energies for the relaxed component. The solid curve is the expected Coulomb energy for touching spheres. (XBL 7512-9903)

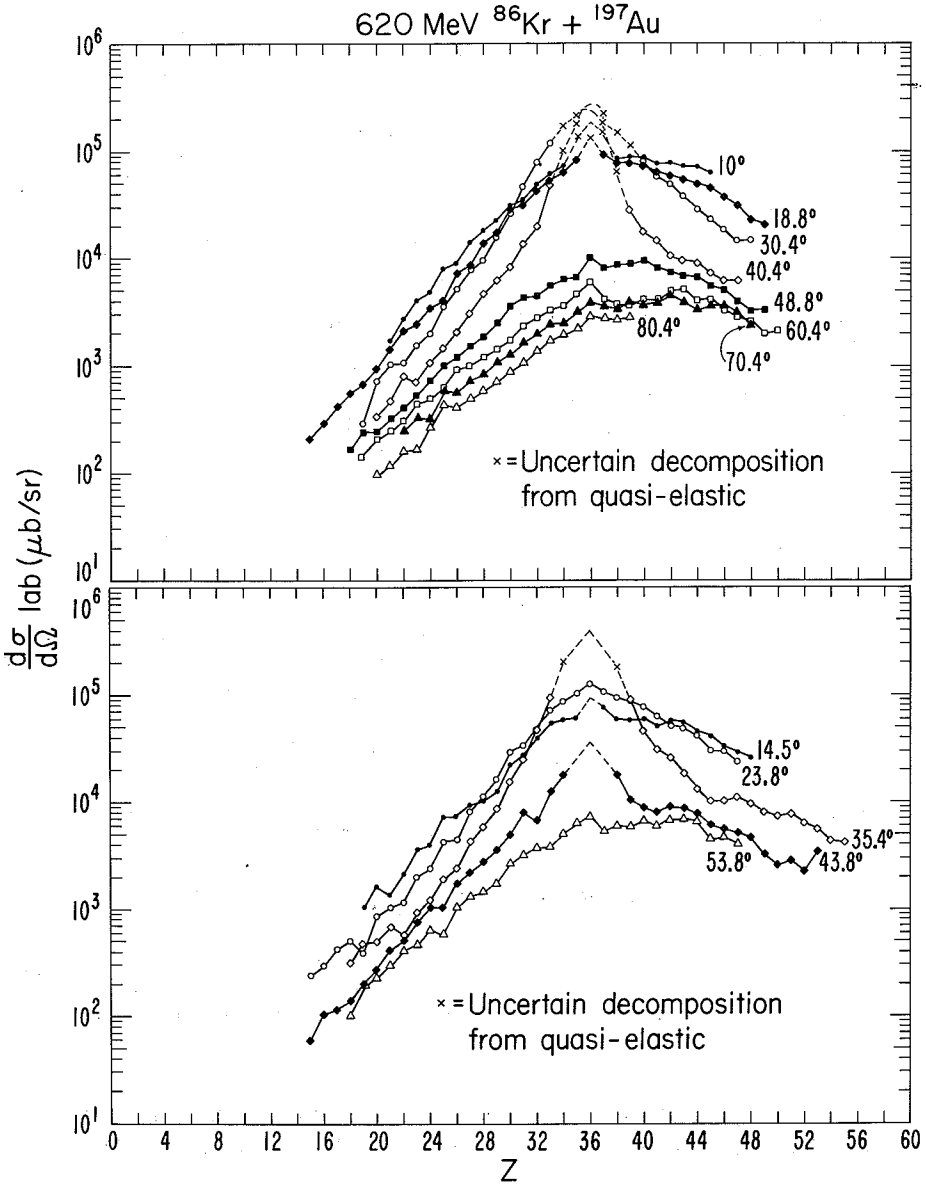

Fig. 2. Laboratory Z distributions for various lab angles.
(XBL 761-2088)

In apparent contrast to reactions induced by lighter projectiles, the charge distributions for the relaxed peak are strongly concentrated about the incident projectile (Fig. 2). Moreover, the shape of the charge distribution is strongly dependent on the angle of observation: for backward angles the distributions are broad; for very forward angles the distributions are somewhat narrower; finally, at intermediate angles the distributions are sharply peaked. The width of the charge distributions has been interpreted in terms of the age of the intermediate complex at the time of decay. Narrow or "young" distributions result from short decay times, before substantial charge transfer has occurred. Broad or "old" distributions are produced when long decay times permit large amounts of mass to be transferred.

The angular distributions are also quite different from those obtained with lighter projectiles (Fig. 3). For Z close to that of the projectile, the angular distributions are side peaked rather than forward peaked. This seems to indicate that the lifetime of the composite system is substantially shorter relative to its rotational period.[6,7] As one moves away from the projectile Z, the side peaking relaxes into forward peaking, thus corroborating the notion that longer times are involved in populating these Z's.

These experimental data have been interpreted in terms of the diffusion model developed from the study of reactions induced by lighter ions, i.e. N, Ne and Ar. The successful application of this model implies that so-called quasi-fission phenomena observed in other systems like $^{209}Bi + ^{84}Kr$ do not represent a new mechanism.[8,9] It seems likely that the diffusion model is capable of a unified explanation of charge and angular distributions observed in heavy-ion bombardments.

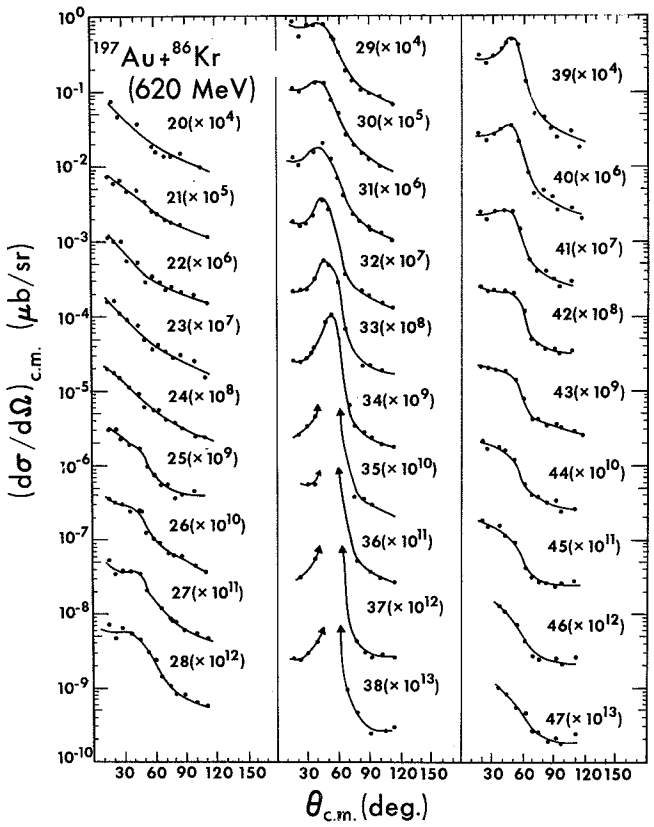

Fig. 3. Center-of-mass angular distributions for various atomic numbers. (XBL 7512-9891)

Footnotes and References

*Condensed from LBL-4362 and Phys. Rev. Lett. 36, 1069 (1976).

†Sloan Fellow 1974-1976.

‡On leave from DPhN/MF-CEN, Saclay, France.

§NATO Fellow.

1. M. M. Fowler and R.C. Jared, Nucl. Inst. Meth. 124, 341 (1975).

2. L. G. Moretto, S. K. Kataria, R. C. Jared, R. Schmitt, and S. G. Thompson, Nucl. Phys. A255, 491 (1975).

3. R. Babinet, L. G. Moretto, J. Galin, R. Jared, J. Moulton and S. G. Thompson, Nucl. Phys. A258, 172 (1976).

4. J. Galin, L. G. Moretto, R. Babinet, R. Schmitt, R. Jared and S. G. Thompson, Nucl. Phys. A255, 472 (1975).

5. L. G. Moretto, J. Galin, R. Babinet, Z. Fraenkel, R. Schmitt, R. Jared, and S. G. Thompson, Nucl. Phys. A259, 173 (1976).

6. L. G. Moretto, R. P. Babinet, J. Galin, and S. G. Thompson, Phys. Lett. 58B, 31 (1975).

7. L. G. Moretto and J. Sventek, Phys. Lett. 58B, 26 (1975).

8. F. Hanappe, M. Lefort, C. Ngo, J. Peter and B. Tamain, Phys. Rev. Lett. 32, 738 (1974).

9. K. L. Wolf, J. P. Unik, J. R. Huizenga, J. Birkelund, H. Freiesleben and V. E. Viola, Phys. Rev. Lett. 33, 1105 (1974).

EVIDENCE OF DEFORMATION AND INCOMPLETE RELAXATION IN A NEARLY-SYMMETRIC HEAVY SYSTEM: 979-MeV Xe + Tb

P. Russo, G. Wozniak, R. Schmitt, R. Jarred,
P. Glässel,* and L. G. Moretto

Relaxation processes in nuclei have been studied through experimental investigations of inelastic collisions between heavy targets and projectiles. The use of a gas ionization ΔE counter[1] with a solid state E detector enables the identification of elements up to and beyond the projectile Z and provides extensive information on the systematic features of these processes from singles measurements of the heavy ion products.[2] Such measurements have been performed with projectiles as heavy as Kr and have more recently been extended to include Xe projectiles.

The ability of the telescope to retain Z-resolution above atomic number 50 had not been tested prior to the Xe experiments. A very short exploratory run was performed with the Xe beam at lower energies to estimate the Z resolution in the region of atomic number 54. A further improvement in the process of Z-identification was obtained by means of a computerized method for the automatic statistical identification and subsequent fitting of the Z-lines in the E-ΔE map. These techniques were used exclusively in the analysis of the Xe data extending the Z-resolution to above 60. The detector performance and Z-identification process are described elsewhere in this report.[3]

A 979-MeV ^{136}Xe beam from the super-HILAC bombarded self-supporting natural terbium foils 0.6 to 0.7 mg/cm^2 thick. Pileup considerations limited the beam current to 5 to 10 nA at the most forward angles but approximately 50 nA were utilized at backward angles. Each of the two scattering chamber arms supported a mount which held two counter telescopes separated by 15° on one arm and 20° on the other. The arrangement was such that the telescope at the most backward angle was positioned

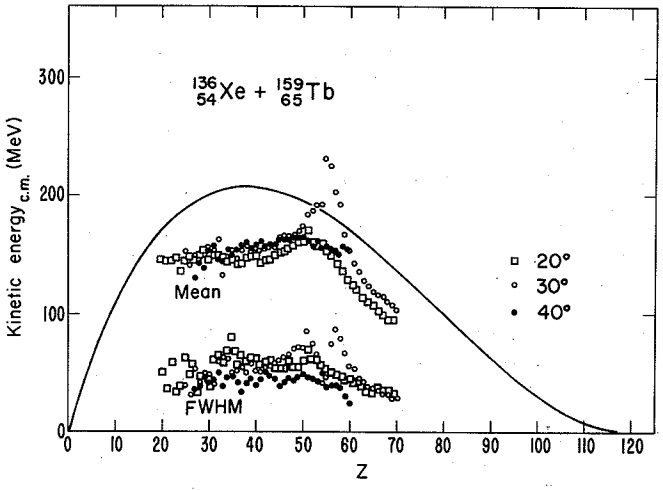

Fig. 1. Average c.m. kinetic energies and widths of the kinetic energy distributions for elements produced in the 979-MeV Xe+Tb experiment.
(XBL 766-2979)

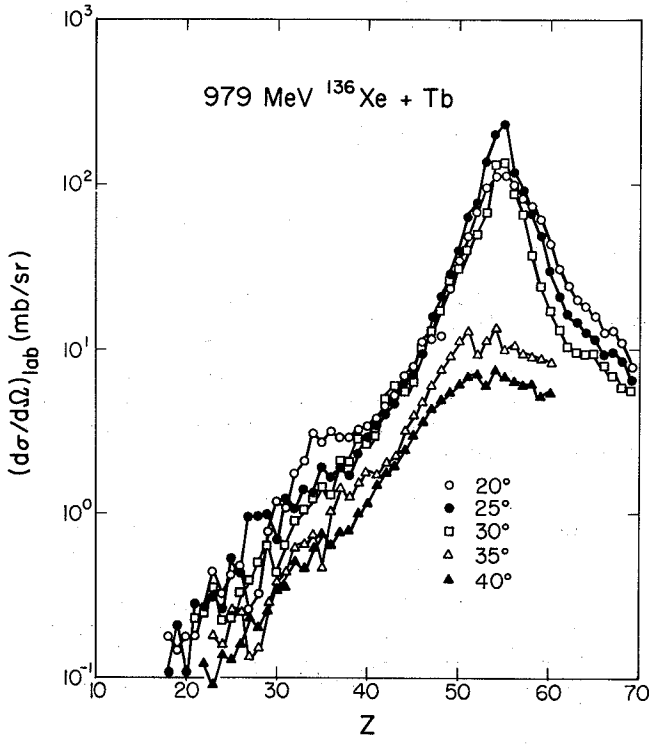

Fig. 2. Laboratory differential cross sections as a function of Z for five laboratory angles in the experiment 979-MeV Xe+Tb. The data includes quasi-elastic events which are inseparable from deep inelastic events near the grazing angle.
(XBL 766-2986)

closest to the target to minimize differences in count rates among the four counters. The gas counter entrance windows were 0.28 mg/cm^2 polycarbonate (Kimfol) foils at forward angles and 0.040 mg/cm^2 Formvar foils at more backward angles. Gas pressures in the forward and backward pair of counters were independently regulated.

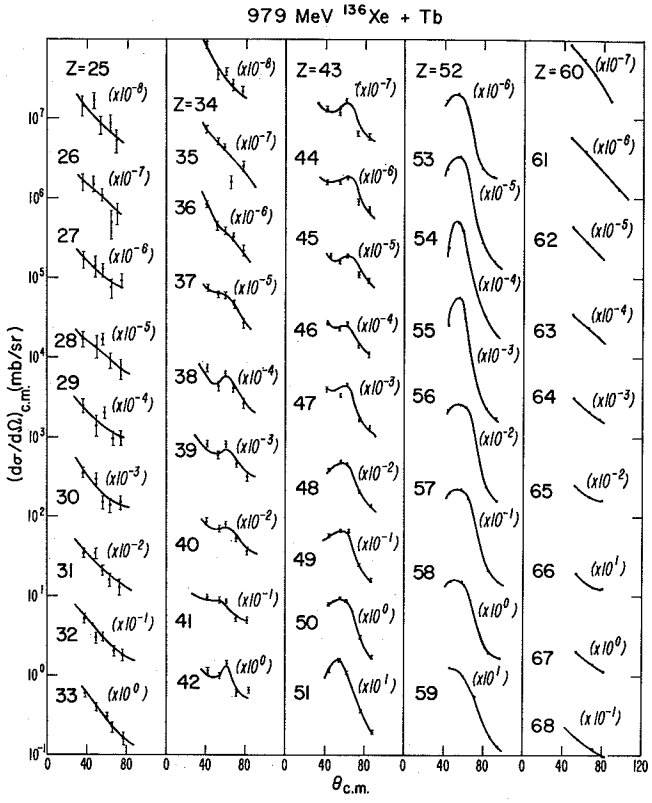

Fig. 3. Angular distributions in the center-of-mass for individual elements produced in the 979-MeV Xe+Tb experiment. (XBL 766-2975)

Periodically during the bombardment of terbium targets with Xe, a silver target with a thick nickel degrader foil was inserted to provide calibration points at Z = 28, 47 and 54. This calibration was most useful backward of the critical angle where the projectile Z line is weak. The data analysis techniques are described in detail elsewhere.[3]

The laboratory differential cross sections were determined for each element for the deep inelastic processes. The cross sections were transformed to the center of mass assuming charge-equilibrated fragment masses for the intermediate complex at fixed mass asymmetry. A relatively small correction (less than 10% of the laboratory energy) due to evaporation of neutrons from the fragments has been neglected in this transformation.

At the grazing angle and for Z's near the projectile, the widths of the kinetic energy distributions are broadened as the process of energy relaxation becomes less complete and the inelastic and transfer products become almost indistinguishable. These features are illustrated in Fig. 1 which is a graph of the average center-of-mass (c.m.) kinetic energies for each element and the widths of the kinetic energy distributions. Relative to Coulomb energies for touching sphere, the observed c.m. kinetic energies away from the grazing angle and the projectile are lower by approximately 25%. Some implications of this will be discussed below. Near the projectile the energies increase sharply and the widths broaden as energy equilibration diminishes.

Figure 2 shows the charge distributions obtained for measurements at five laboratory angles. The cross sections peak strongly at the projectile Z and are dominated by the 30° data which is closest to the grazing angle (31°) for this reaction. Far below the projectile Z, the cross section decreases with increasing laboratory angle.

Relative to Coulomb energies for spheres, the c.m. kinetic energies are significantly lower (25% compared to 15%) for the Xe+Tb data than for the Kr+AU data[2] with nearly the same composite A and Z. The higher temperature in the former case (the total c.m. kinetic energy is approximately 200 MeV for 979 MeV Xe+Tb and 150 MeV for 620 MeV Kr+Au) will cause more particle evaporation in the Xe+Tb experiment. The apparent c.m. kinetic energy is less than the true energy if particle evaporation is neglected in the transformation from laboratory to c.m., but this effect is small compared with the magnitude of the difference between the Xe+Tb and the Kr+Au results. It is likely that deformation is responsible for much of the reduction in kinetic energy for the Xe+Tb system, although reasons for larger fragment deformations for Xe+Tb are unclear. Thus for the two systems of comparable mass, a large difference in the moments of inertia might be expected. Therefore, while the Coulomb energy for the nearly symmetric Xe+Tb pair is larger than the Coulomb energy for the Kr+Au pair for spherical fragments, deformation may equalize the repulsive forces in the two systems and increase the rotational period of the higher average ℓ-wave system (Xe-Tb). The result is, perhaps, comparable breakup times and rotational periods for the two systems.

If fragment deformation is not larger in the Xe+Tb system than in Kr+Au, the experimental results might appear quite different due to large differences in the Coulomb energies (and, therefore, the complex lifetimes) and the average ℓ-value (and, therefore, the rotational period). However, the side peaking near the grazing angle in the angular distributions is about equally persistent into Z's above and below the projectile for both Xe+Tb (Fig. 3) and Kr+Au (Ref. 4 or 5). Even if mass transfer is more rapid for Kr+Au which might be expected this far from mass symmetry, the increased deformation for Xe-Tb may reduce the Coulomb energies and increase the rotational period enough that the same side peaking over a comparable range of masses is observed. The similarity in the widths of the charge distributions (Fig. 2 and Ref. 4) for both systems gives further support to this idea.

A more dramatic comparison between the two nearly-symmetric systems, Kr+Ag and Xe+Tb, illustrates large differences in the relative relaxation along the mass asymmetry coordinate. The angular distributions for 620-MeV Kr+Ag (Ref. 2 or 6) show no evidence of side peaking and are in fact forward peaked suggesting that the lifetimes are comparable to the rotational period. The more relaxed charge distributions for Kr+Ag (Ref.2 or 6) are extremely broad compared with Xe+Tb (Fig. 2) and are peaked not at the projectile but, perhaps, several Z's above the projectile which is closer to symmetry. In both systems, the potential energy governing the exchange of mass is fairly flat since the systems are close to symmetric and so the differences in the charge distributions must reflect the shorter lifetime for the higher Z Xe+Tb complex. The difference in the average lifetime of these two systems must be comparable to the time constant for mass equilibration to effect such a large difference in the character of the charge distributions.

An extension of the Xe+Tb data to more forward angles is presently being undertaken. This will better define the structure of the angular distribution and give improved estimates of the kinetic energies of the more completely relaxed process.

Footnote and References

*NATO Fellow.

1. M. Fowler and R. Jared, Nucl. Instr. and Method 124, 341 (1975).

2. L. G. Moretto and J. S. Sventek, LBL-5006, Lawrence Berkeley Laboratory (1976).

3. R. Jared, P. Glässel, R. Schmitt, P. Russo, and L. G. Moretto, Identification of Atom Numbers up to Z = 60 in Fragments from Heavy Ion Reactions, this Annual Report.

4. L. G. Moretto, B. Cauvin, P. Glässel, R. Jared, P. Russo, J. Sventek, and G. Wozniak, Phys. Rev. Lett., 36, 1069 (1976).

5. L. G. Moretto, G. Cauvin, P. Glässel, R. Jared, P. Russo, J. Sventek, and G. Wozniak, Diffusive Phenomena in the Charge and Angular Distributions for Reaction ^{197}Au + 620-MeV ^{86}Kr, this Annual Report.

6. R. P. Schmitt, P. Russo, R. Babinet, R. Jared, and L. G. Moretto, Nuclear Relaxation Phenomena and Diffusion in the Reaction ^{107,109}Ag + 84Kr at 7.2 MeV/Nucleon, this Annual Report.

BINARY BREAKUP (AND SECONDARY FISSION) OF A HEAVY DEFORMED SYSTEM: 979-MeV Xe + Au

P. Russo, R. Schmitt, G. Wozniak, B. Cauvin,*
P. Glassel,† R. Jared, and L. G. Moretto

Investigation of the binary deep inelastic process in heavy ion experiments performed by our group have recently been expanded to include xenon projectiles incident on medium to heavy targets. While Coulomb energies are larger for the higher Z systems, the experimental results appear to be modulated by significant fragment deformations.

The present experiments were performed with 979-MeV ^{136}Xe beams incident on 0.6 to 0.7 mg/cm^2 gold foil targets. The experimental details have been discussed elsewhere.[1]

The laboratory kinetic energy distributions for individual elements produced in the Xe+Au experiments are unique in that two well-resolved peaks in the kinetic energy spectra are apparent at forward angles up to 35°, particularly near Z = 40. Figure 1 shows the resolution and relative contributions of the two components observed in the 30° measurements. Above Z = 48, the lower energy peak has practically vanished. The energy of the lower energy component decreases at more forward laboratory angles so that at 20° nearly half of the kinetic energy distribution is below the experimental threshold. Further backward than 35° in the laboratory the energy difference between the two components decreases, and between 50 and 60° the two peaks merge and cross over.

The laboratory differential cross sections are plotted as a function of Z in Figs. 2 and 4. Figure 2 shows the charge distributions for the high-energy component of the kinetic energy spectrum shown in Fig. 1 for laboratory angles of 35° and forward (Fig. 2A) and for 35° and backward (Fig. 2B). The strong peak around the projectile and the dominance of the cross section near the grazing angle suggests that this component is associated with the binary inealstic process similar to that observed in the Xe+Tb data[1] as well as the Kr+Au and Kr+Ta data.[2] This (binary, inelastic) component in the Xe+Au data is characterized by side-peaked angular distributions and incomplete relaxation of the total kinetic energies near the projectile. The center-of-mass kinetic energies obtained for these events by a transformation which assumes a binary breakup of the complex resembles strongly the Xe+Tb center-of-mass kinetic energy distributions (Ref. 1, Fig. 3). The kinetic energies lie approximately 30% below the Coulomb energies for spherical fragments with energy relaxation diminishing steeply around the projectile and near the grazing angle.

Isolation of the deep inelastic component from the 60° data and all data below Z = 48 at 50° and below Z = 42 at 40° was not possible, and so so this data does not appear in the charge distributions. At 70 and 75° the binary inelastic energies extend below the experimental threshold.

The markedly low center-of-mass kinetic energies of the binary inelastic fragments suggest large fragment deformations. The charge distributions are equally broad if not broader than those observed

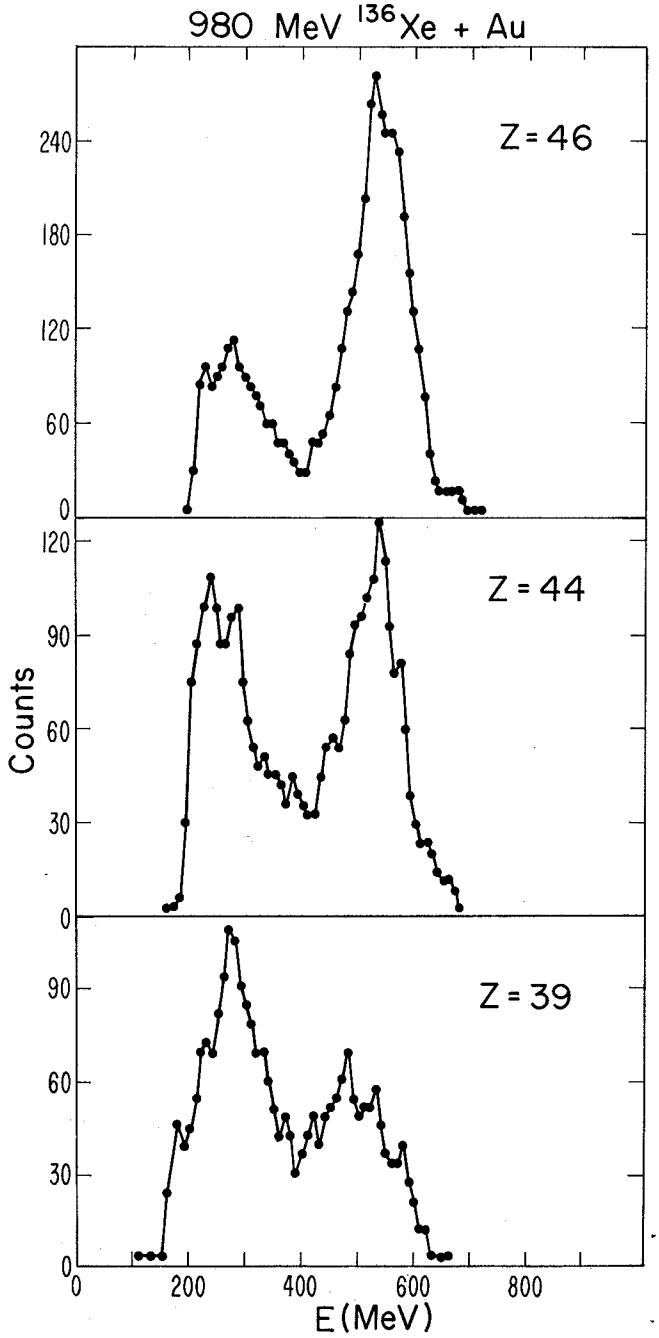

Fig. 1. Laboratory kinetic energy spectra obtained at 30° in the reaction 979-MeV Xe+Au. The resolution of two components is shown for three different elements. (XBL 766-2987)

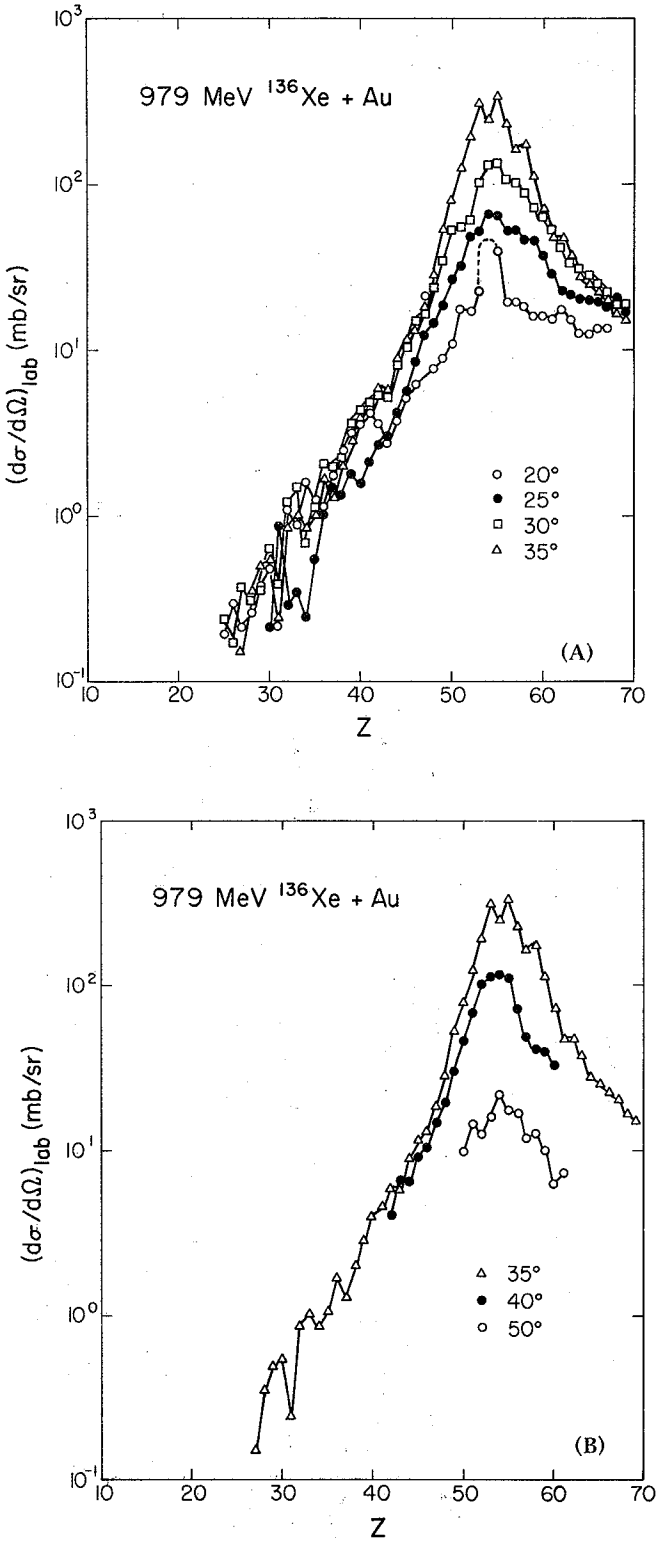

Fig. 2. Laboratory differential cross sections as a function of Z for the deep inelastic component from the experiment 979-MeV Xe+Au.
(A) Data forward of (including) 35°.
(XBL 766-2982)
(B) Data backward of (including) 35°.
(XBL 766-2980)

for the krypton experiments with gold targets. This observation was also made from the results of the xenon experiment with terbium targets.[1] Although Coulomb energies are largest for the Xe+Au system, increased deformation reduces the repulsive force so that break-up times may not be significantly reduced leaving the charge distribution widths unchanged. Furthermore the extended shapes increase the rotation time so that even the slower processes (involving large mass transfer) may be side-peaked. The center-of-mass angular distributions shown in Fig. 3 reflect this possibility. The persistence of the side peak for the entire range of elements is unique to this data and lends support to the previous argument that the average rotational period is increased, above that for the krypton experiments for example. A second feature of the angular distributions is the forward shift in the angle of the side peak for elements far-removed from the projectile. The persistence of the side peak due to an increased rotational period implies that the side peak is composed of events produced by a broader range of complex lifetimes. The angular distribution of events produced by a longer-lived complex will be shifted forward since the rotation has proceeded further, and it is the long-lived complex which gives rise to greater mass transfer. Thus the xenon-gold system may provide a means to study the time-evolution of the mass transfer process since the time constants for both mass transfer and rotation appear to be comparable in this case. Further measurements to include more forward and backward angles as well as intermediate angles are in progress.

Figure 4 shows the charge distributions for the resolved low energy component of the kinetic energy spectra shown in Fig. 1. These are peaked at approximately one-half the target Z suggesting that this component may originate from secondary fission of the target or perhaps ternary break-up of the complex. It is reasonable that the charge distributions for the products of fission of the gold-like fragment show peaks above Z = 40 since it may not be gold but in fact the more fissionable products of mass transfer away from the projectile which contribute to this phenomenon. The laboratory kinetic energies of this component, averaged for three Z's (36, 37 and 38) near the peak of the charge distribution are plotted in Fig. 5 as a function of laboratory angle. A parabolic curve peaked near 50° gives a reasonable approximation to the data points. This strong kinematic dependence of the kinetic energy on angle provides evidence that secondary fission of target-like products is the origin of the second component. The cross-section for the deep inelastic gold-like products of binary break-up peaks near 50° in the laboratory, consistent with a maximum in the kinetic energy distribution near 50° if secondary breakup is assumed. The cross section for these events, henceforth referred to as the fission component, increases slowly toward forward angles as is shown in Fig. 4. Forward of 30° in the laboratory, the cross section for the fission component cannot be determined due to the experimental low energy cutoff. However, a peak in the fission cross section more forward than the most probable

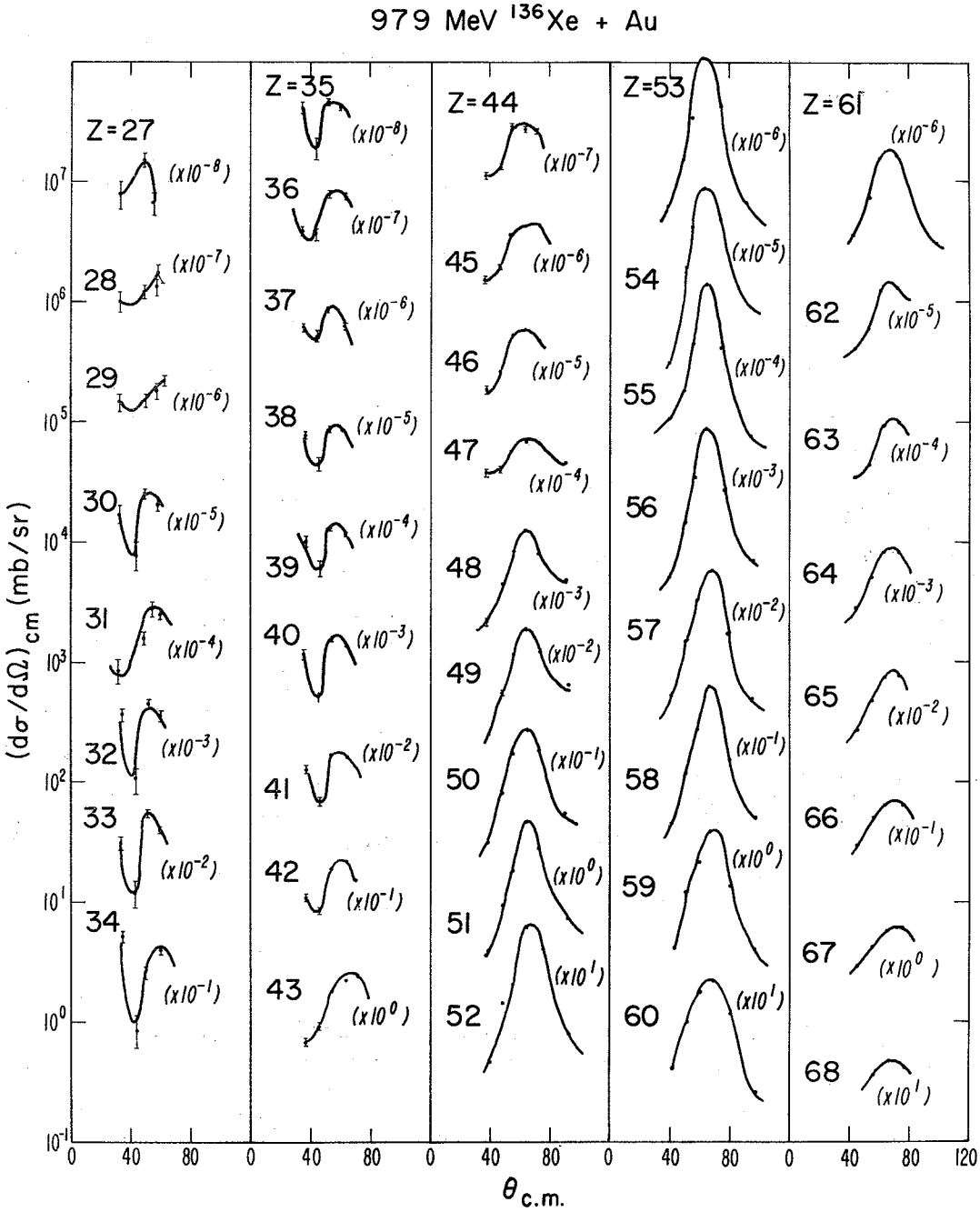

Fig. 3. Angular distributions of individual elements for the deep inelastic component in the experiment 979-MeV Xe+Au. (XBL 766-3007)

angle for the emission of target-like fragments is not surprising if the center-of-mass momenta of the fission fragments is a major fraction of that for the binary inelastic gold-like product as would be the case with the secondary break-up process.

The energy spectra for the fission component further forward than 30° will provide more definitive information concerning the origin of these events.

Footnotes and References

*On leave from DPh-N/MF CEN, Saclay, France.

†NATO Fellow.

1. P. Russo, G. Wozniak, R. Schmitt, R. Jared, P. Glässel, and L. G. Moretto, Evidence of Deformation and Incomplete Relaxation in a Nearly Symmetric Heavy System: 979-MeV Xe+Tb, this report.

2. L. G. Moretto, B. Cauvin, P. Glässel, R. Jared, P. Russo, J. Sventek and G. Wozniak, Diffusive Phenomena in the Charge and Angular Distributions for the Reaction ^{197}Au + 620-MeV ^{86}Kr, this Annual Report. P. Glässel, B. Cauvin, G. Wozniak, P. Russo, R. Schmitt, R. Jared, and L. G. Moretto, Study of Fragments Emitted in the Interaction between ^{181}Ta and ^{86}Kr at 620 MeV Bombarding Energy, this Annual Report.

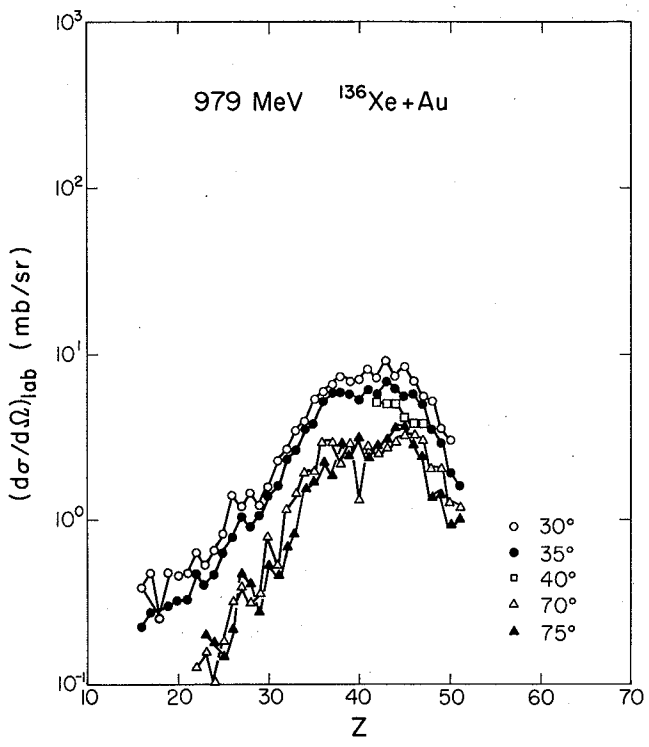

Fig. 4. Laboratory differential cross sections as a function of Z for the second (other than deep inelastic) component from the 979-MeV Xe+Au data. (XBL 766-2981)

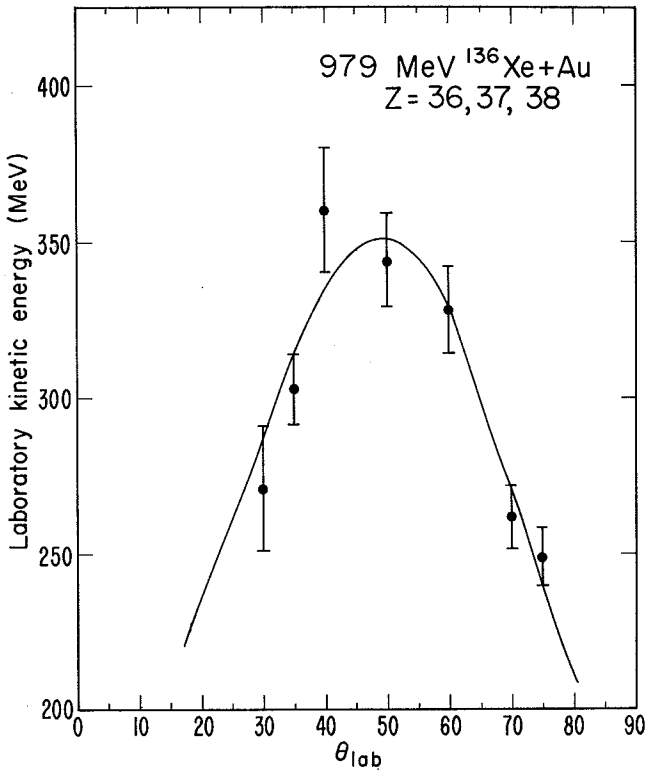

Fig. 5. Laboratory kinetic energies of the fission component as a function of laboratory angle from the 979-MeV Xe+Au experiment. (XBL 766-2977)

CHARGE- AND MASS-DISTRIBUTIONS IN THE REACTION OF ^{40}Ar IONS WITH ^{238}U*

J. V. Kratz,† J. O. Liljenzin,‡
A. E. Norris,§ and G. T. Seaborg

The reaction of 288-MeV ^{40}Ar ions with thick ^{238}U targets has been studied experimentally with radiochemical techniques. The formation cross sections of 130 radioactive nuclides were measured using their characteristic gamma-ray emission. The data have been used to delineate charge and mass distribution.

The independent and partial cumulative yields are plotted vs. mass number (after particle evaporation) in Fig. 1(a). The apparent scatter in the data in Fig. 1(a) occurs because independent yields, and even many of the cumulative yields, represent only a fraction of the total mass yields. Figure 1(b) is a contour map of the independent yields in a Z-A plane, indicating yield locations relative to the stability line. The structure revealed by the isopleths in Fig. 1(b) indicates that several yield distributions with different charge- and mass-dispersions, and hence different origins, are superimposed on each other. The overall distribution is dominated (1) by the high yields for transfer products near A = 40 and A = 238 ("rabbit ears," components E and F in Fig. 1[b]), and (2) by a broad fission product distribution centered around A ≈133. This distribution is not a single component, but consists of products from fusion-fission (component A), from fission of heavy products formed by transfer of a few nucleons and small amounts of excitation energy (component B), and from high energy fission of heavy products from deep inelastic processes (shaded area D). Furthermore, there are neutron-rich products ranging from low Z values up to Z ≈ 26 or even higher, that are attributed to deep inelastic transfer reactions (component C).

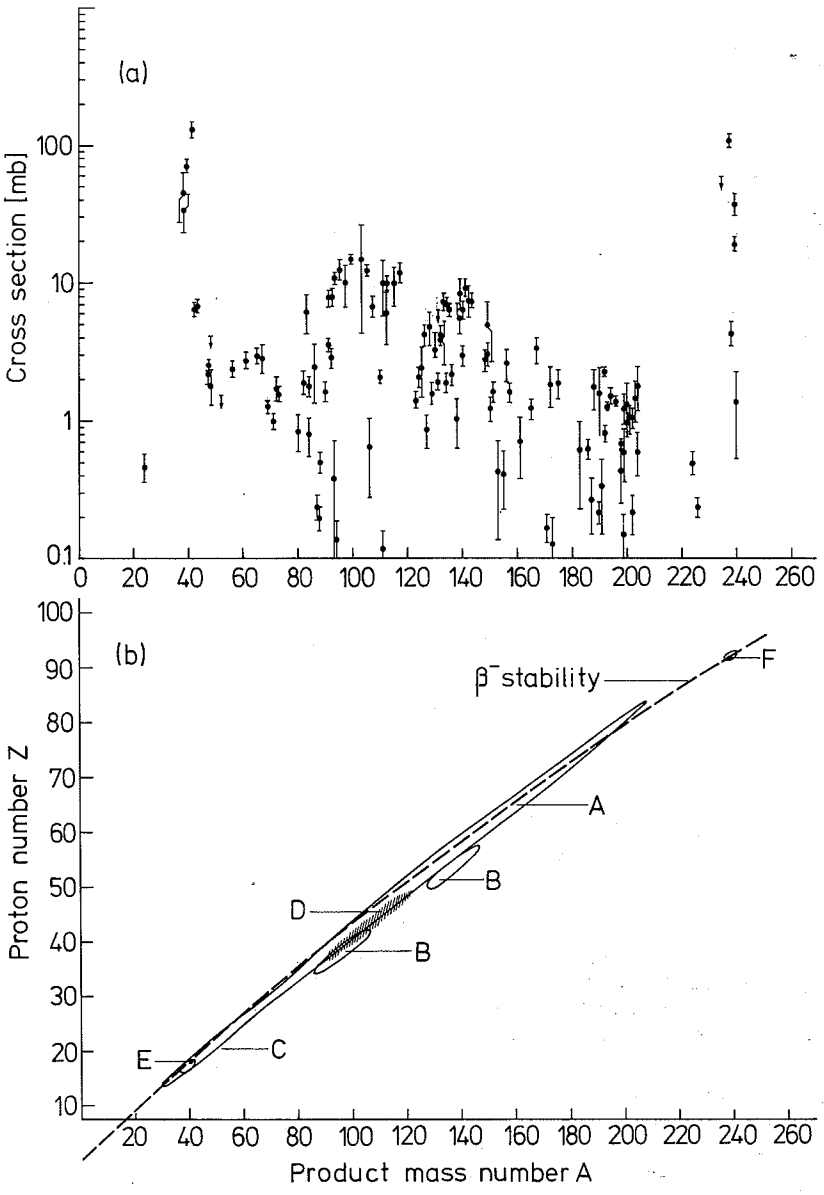

Fig. 1(a) Independent and cumulative formation cross sections of individual nuclides produced in the bombardment of a thick ^{238}U target with 288 MeV ^{40}Ar ions.

(b) Contour lines for equal independent formation cross sections in a Z,A plane. Isopleths of 1 mb are shown for components A, B and C. The isopleths for components E and F refer to 10 mb cross sections. (XBL 7511-8972)

For the deduction of the total mass yields from the yields of single isotopes, we used experimentally determined charge-dispersion curves for the mass chains. [In Fig. 1(b) a charge-dispersion curve would correspond to a cut through the indicated "yield mountains" at a fixed mass number.] Then the experimentally determined independent or cumulative yields were related to the total mass yield by correcting for the independent yields of unobserved members of the chain. To arrive at the total mass yield for a given mass, it was necessary to integrate the charge dispersion curve; i.e., sum up the independent yields of all isotopes with mass A.

Figure 2 shows the total integrated chain mass yields (upper and lower limits are indicated at those mass numbers for which experimental data were obtained) and their decomposition into individual components: (A) complete fusion-fission (620±150 mb), (B) transfer-induced fission (150±30 mb), (C) deep inelastic transfer (100±50 mb), (E) and (F) quasi-elastic transfer ("rabbit ears," 400±120 mb and approximately 200 mb, respectively).

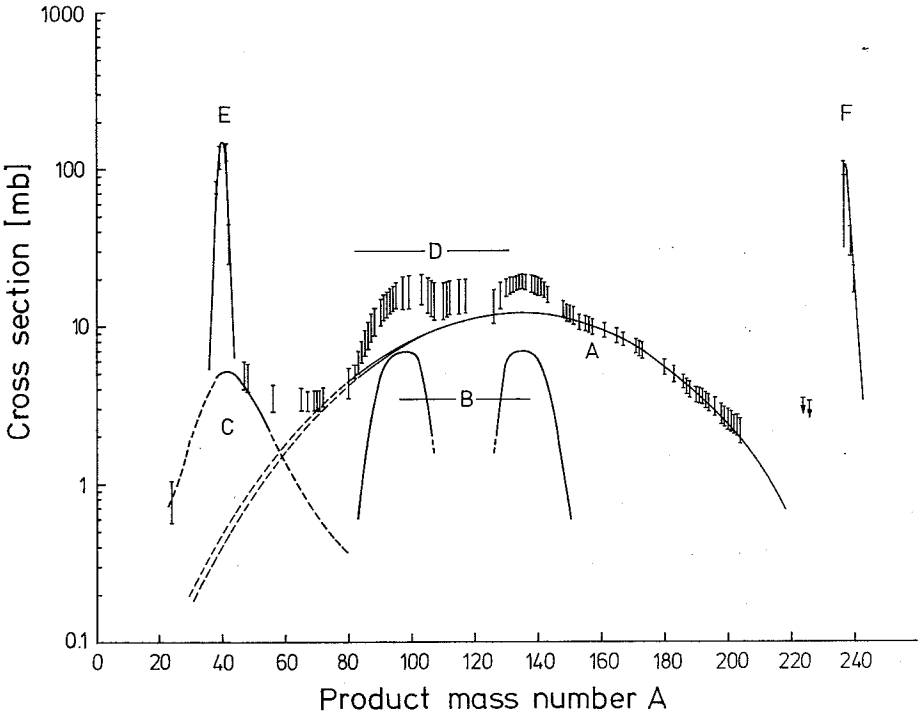

Fig. 2. Total integrated mass yields produced in the bombardment of a thick ^{238}U target with 288 MeV ^{40}Ar ions. Component A corresponds to 620 mb, B to 150 mb, C to 100 mb, D not determined, E to 400 mb and F to 220 mb. (XBL 7511-8975)

The existence of products from the sequential fission of heavy fragments formed in deep inelastic collisions (D) is also indicated; however, we are unable to deduce a complete mass distribution for this component.

The results obtained from this survey experiment can be summarized as follows:

1. In the energy interval investigated, fusion-fission accounts for about 55% of the total reaction cross section, while 35% quasi-elastic and 10% deep inelastic transfer are observed. The mass distributions of these components are shown in Fig. 2. The total reaction cross section amounts to about 1100 mb.

2. Evidence is presented for fission of heavy nuclei after transfer reactions. Quasi-elastic transfer leads to a double-humped fission product distribution signifying the transfer of relatively small amounts of excitation energy in grazing collisions. Fission after deep inelastic collisions seems to lead to a fission fragment mass distribution (incompletely determined) which is typical for higher excitation energies of the fissioning nucleus.

3. Proton pick-up reactions are observed leading to a build-up of products with $Z \approx 26$; i.e., the mass distribution for multi-nucleon transfer and fusion-fission overlap considerably.

4. It is shown that the mass to charge ratios for both multi-nucleon transfer- and fusion-fission fragments are equilibrated. No equilibration of this degree of freedom is attained for products formed by quasi-elastic transfer.

Footnotes

*Condensed from Phys. Rev. C 13, 2347 (1976).

†On leave from Institut für Kernchemie, Universität Mainz, Germany. Present address: Gesellschaft für Schwerionenforschung, GSI, Darmstadt, Germany.

‡ Department of Nuclear Chemistry, Chalmers University of Technology, Goteborg, Sweden.

§Los Alamos Scientific Laboratory, University of California, Los Alamos, New Mexico 87545.

MASS YIELD DISTRIBUTIONS IN THE REACTION OF ^{136}Xe IONS WITH ^{238}U*

R. J. Otto, M. M. Fowler,† D. Lee,
I. Binder, and G. T. Seaborg

Yields of 131 nuclides were measured radiochemically to delineate the mass distribution in the reaction of 1150-MeV ^{136}Xe with a thick ^{238}U target. Figure 1(a) shows the independent and partial cumulative yield cross sections for the nuclides identified by gamma ray analysis of six chemical fractions. Figure 1(b) depicts contours in the Z-A plane of constant independent yield and the most probable isobaric charge lines derived from the final charge distributions. Beginning with an approximate charge dispersion description an iterative fitting procedure was used to arrive at a final charge and mass distribution. Figure 1(c) shows the final integrated chain mass yield distributions. Six components were identified and associated with either the quasi-fission or the quasi-elastic transfer mechanism.

Component A is shown as an upper limit for the complete fusion-fission process. The quasi-elastic transfer mechanism can be assigned to components E and F. The asymmetric fission distribution, component B, is the result of low energy fission of the heavy elastic transfer product with mass numbers near that of ^{238}U. The mass distribution of the quasi-Xe (deep inelastic component) formed in the quasi-fission process is identified as component C. About 75% of the complementary quasi-U fragments undergo high energy binary fission resulting in the broad symmetric fission distribution shown as component D. Component G, colloquially labeled as the "gold finger" and not explained in the initial description of the Kr + U experiments,[1] can be attributed to the quasi-fission (deep inelastic) reaction mechanism. This interpretation of the components is supported by a mass balance of the composite mass distribution. Components H and I are the result of reactions with contaminants in the target.[2]

Further evidence that the "gold finger" represents quasi-U products that have survived de-excitation without undergoing fission can be found by comparing the Kr + Bi mass distribution[3] with the Xe + U results. The quasi-Bi yields show the same trend as component G except that a much smaller fraction of the quasi-Bi fragments undergo high-energy binary fission.

Table 1 gives the cross sections for the various components identified in the reaction of ^{40}Ar,[4] ^{84}Kr,[1] and ^{136}Xe with ^{238}U. Comparison of the fusion-fission cross section and the quasi-fission cross section (deep inelastic process) shows that for heavy ion reactions with uranium the transition from fusion-fission to quasi-fission occurs between argon and krypton upon increasing the mass of the projectiles from argon to krypton to xenon.

A second experiment was done using 1150 MeV ^{136}Xe with a thick ^{238}U target. Direct gamma-ray analysis of the bombarded target foil without

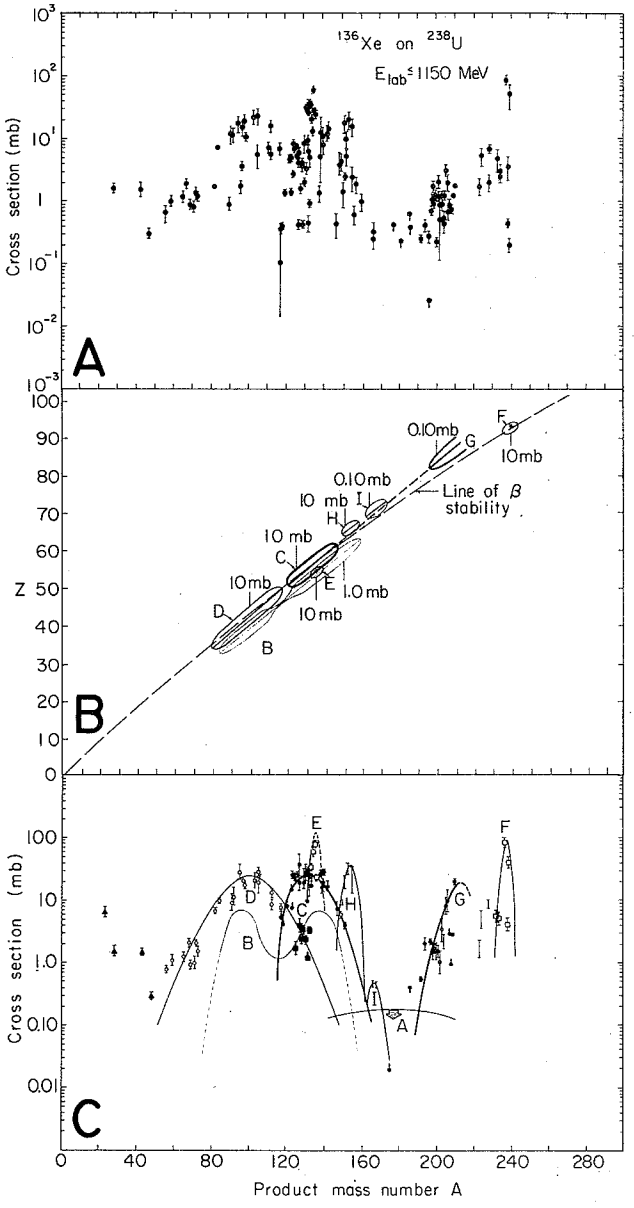

Fig. 1. Mass yield distribution for 1150 MeV ^{136}Xe + ^{238}U, determined by gamma-ray analysis of chemically separated fractions.

(a) Independent and cumulative yield formation cross sections.

(b) Contour lines for equal independent yields and lines of most probable charge for each component.

(c) Total integrated mass yields.

(XBL 758-3746B)

Table 1. Cross Section Comparison

Mechanism	Label Figure 1	Cross Section Xe + U	Kr + U	Ar + U
Fusion-fission	A/2	≤ 20 mb	55 ± 15 mb	620 ± 150 mb
Quasi-elastic transfer induced fission	B/2	∿ 185 mb	200 ± 40 mb	150 ± 30 mb
Quasi-fission (light product)	C	600 ± 125 mb	470 ± 70 mb	100 ± 50 mb
Quasi-ternary fission	D/2	400 ± 25 mb	420 ± 60 mb	?
Quasi-elastic transfer (light product)	E	600 mb	700 ± 120 mb	400 ± 120 mb
Quasi-elastic transfer (heavy product)	F	∿ 415 mb	∿ 420 mb	∿ 220 mb
Quasi-fission (heavy product)	G	∿ 140 mb	∿ 40 mb	small
Quasi-fission	σ_{Qf} = C = D/2+G	600 ± 125 mb	470 ± 70 mb	100 ± 50 mb
Quasi-elastic transfer	σ_{ET} = E = B/2+F	∿ 600 mb	700 ± 120 mb	400 ± 120 mb
Total Reaction	σ_R = A/2+C+E	1200 ± 200 mb	1265 ± 205 mb	1120 ± 200 mb

chemical separations gave the partial cumulative and independent yields shown in Fig. 2. Although the total integrated mass yield distribution must be determined from the cross sections shown in Fig. 2 in order to afford a complete analysis, these cross sections corresponding to independent and partial cumulative yields are consistent with the final mass distribution shown in Fig. 1(c).

Several conclusions can be drawn from these experiments. First, the probability is slight that part of the quasi-U fragments that were formed (and lost by undergoing fission) were in the superheavy element region. Second, it can be noted that component D has a full width at half maximum of 20 to 25 mass units. Component D is a composite of many Gaussian mass distributions of fission fragments from those products above astatine in the quasi-uranium mass distribution. However, the full width at half maximum of the quasi-Xe distribution (component C) appears to be only half as wide as component D. In such a situation the full width half maximum of component D is only slightly larger than the full width half maximum of any one of the individual curves making up the composite. Thus the width of component D is a direct measure of the excitation energy deposited in the quasi-uranium fragments. Third, the larger cross sections for producing the "gold finger" in the xenon reactions as compared with the krypton reaction is the result of the relative neutron richness of the ^{136}Xe projectile. This last conclusion follows if, as might be expected, the heavy quasi-fission fragments are more neutron excessive for the xenon reaction than for the krypton reaction and thus have greater stability against fission.

Footnotes and References

*Condensed from Phys. Rev. Lett. 36, 135 (1976).

†Present address: Los Alamos Scientific Laboratory, University of California, Los Alamos, New Mexico 87545.

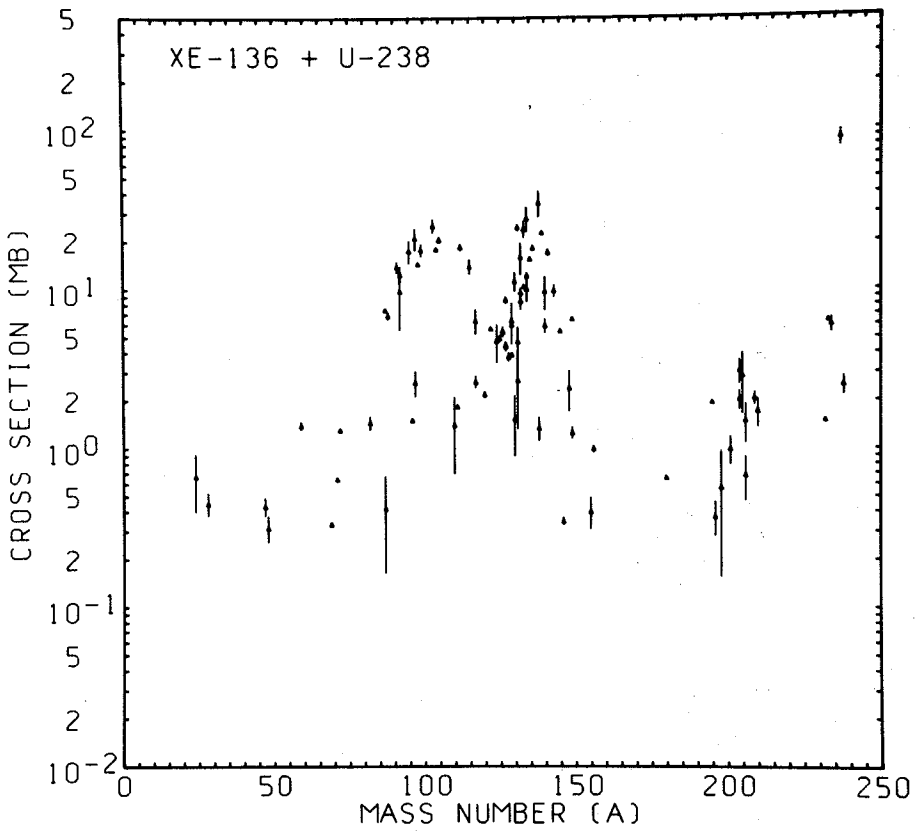

Fig. 2. Parial cumulative and independent yield cross sections for the reaction of 1150 MeV ^{136}Xe + ^{238}U, determined by direct gamma-ray analysis of the target without chemical separations.
(XBL 766-8093)

1. J. V. Kratz, A. E. Norris and G. T. Seaborg, Phys. Rev. Lett. 33, 502 (1974).

2. Al, Mg and Ar impurities in the target and target backing account for components H and I. The target was made by sputtering U onto an Al backing in an argon atmosphere. A thin Al deposit containing some Mg was used to cover the U to prevent oxidation.

3. I. Binder, M. M. Fowler, D. Lee, R. J. Otto and G. T. Seaborg, "Heavy-Ion Reactions with Heavy, Non-Fissioning Targets," in this Annual Report.

4. J. V. Kratz, J. O. Liljenzin, A. E. Norris and G. T. Seaborg, LBL-4339 and Phys. Rev. C/3, 2347 (1976), and "Charge- and Mass-Distributions in the Reaction of ^{40}Ar Ions with ^{238}U" in this Annual Report.

INVESTIGATION OF ^{211}At PRODUCED BY 230 MeV ^{40}Ar on ^{209}Bi

D. J. Morrissey, R. J. Otto, S. Yashita,
A. Ghiorso, and G. T. Seaborg

It has been known for some years that the cross section for the production of ^{211}At by the reaction ^{40}Ar on ^{209}Bi is on the order of millibarns.[1] ^{211}At is a readily measured reaction product because it decays by alpha particle emission and electron capture to ^{211}Po, also an alpha particle emitter,[2] thus giving one alpha particle per atom formed. The Orsay group has used this property along with similar properties of ^{149g}Tb, ^{150}Dy and ^{151}Dy to investigate the "quasifission" reaction mechanism.[1,3] Bimbot et al. performed a series of experiments, using a thin ^{209}Bi target, in which they measured the excitation function, and recoil range of the ^{211}At product. They found that the median range decreased as the bombarding energy increased, opposite to the trend expected for a compound nucleus evaporation reaction, and thus their conclusion was that the ^{211}At was produced in a characteristically non-compound nucleus reaction.[1] There are two reaction mechanisms that could explain or fit these experimental observations: they are the quasifission or multinucleon transfer mechanism, or a quasi-elastic transfer process. In our experiment we attempted to measure the recoil range and angular distribution of ^{211}At simultaneously and thereby could delineate these two mechanisms.

In a simple model of quasifission, one assumes complete damping of the energy in the entrance channel followed by separation of two fragments with the coulomb energy of two touching spheroids. Using this model, the angular and energy distribution of the products can be calculated by a two-step vector model shown in Fig. 1(b). These two vectors are the velocity of the center of mass and the velocity of the fission fragment in the center of the mass system. Also shown in Fig. 1(a) is the calculated distribution in an aluminum stopper of ^{211}At produced by 230 MeV ^{40}Ar on ^{209}Bi. In this reaction the velocity of the CMS is larger than the coulomb separation energy; therefore, all the ^{211}At nuclei have a forward velocity in the laboratory.

One can imagine that superimposed on the energy-angular distribution curve is a probability distribution. This is, of course, not shown. This distribution will be different for the two reaction mechanisms. Moretto et al. have measured the distribution for the complimentary light fragment in a similar reaction, 288-MeV ^{40}Ar on ^{197}Au.[4] They found that the $d\sigma/d\Omega$ curve for Z = 16 had a strong $1/\sin\theta$ component with some forward peaking

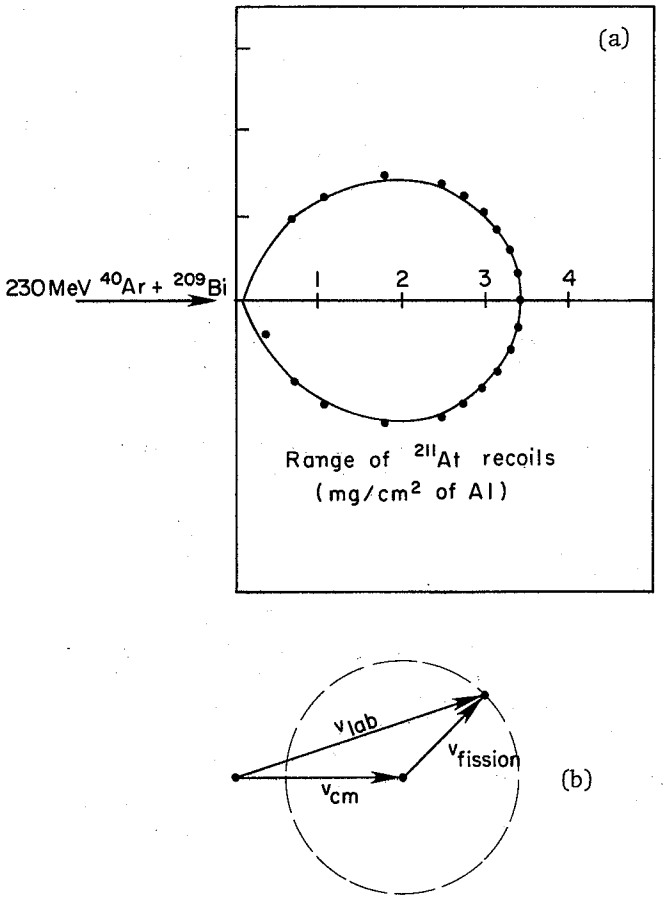

Fig. 1(a). The computer calculated range curve for recoiling ^{211}At produced by the simple vector model.
(b). Representation of simple vector model used to calculate curve in Fig. 1(a).
(XBL 766-2910)

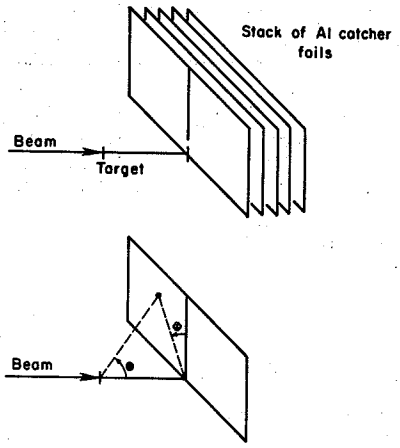

Fig. 2. Schematic representation of target and catcher foils with the orientation of laboratory angles θ and Φ. (XBL 766-2911)

in the center of mass system. Assuming the same type of angular distribution for $^{210}Ar + ^{209}Bi$, this would force our At (Z = 85) distribution to be $1/\sin\theta$ but be backward peaked in the center of mass system. When converted to a distribution in the laboratory, this would be seen as an almost constant probability along the curve (since $d\sigma/d\Omega$ = constant), with some rise in the probability of low laboratory energy ^{211}At recoils.

On the other hand, if the reaction mechanism is quasi-elastic transfer, the ^{211}At should be found at the classical grazing angle with little or none found elsewhere.

A one quarter inch diameter 0.116 mg/cm^2 Bi_2S_3 target, vacuum evaporated onto Be, was irradiated with 228 MeV ^{40}Ar ions from the SuperHILAC. This was the calculated energy in the center of the Bi_2S_3 target after passing through the Be target backing.[5]

The recoiling ^{211}At nuclei were caught by a stack of ~ 1 mg/cm^2 Al foils. These foils were located downstream and off axis from the target to allow a spatial separation of the recoils from the beam. This is shown schematically in Fig. 2. After the bombardment, each foil was divided in half to facilitate two counting methods. One half was placed in an ionization counter and the alpha half life followed. The other half was used to make a radioautograph.

Copies of the radioautographs of the second and third foils are shown in Figs. 3(a) and (b) respectively. These show concentric rings of alpha activity, with the ring on the third foil inside that on the second. These radioautographs were transformed into angular and energy distributions by projecting slide copies onto a ruled mask and counting the spots. In the case of foils 2 and 3, radioautographs of shorter exposure time were used because the intense bands were not resolvable.

The decay curve for foil 3 is shown in Fig. 4. This shows the half life of the alpha activity to be 7.7 hours, and allows us to attribute it exclusively to ^{211}At.

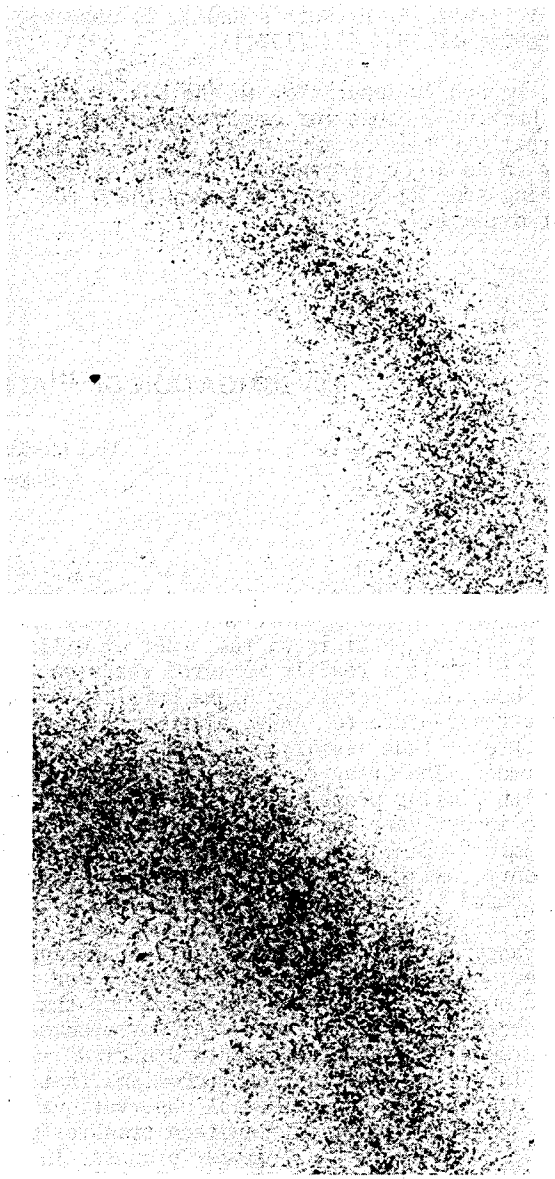

Fig. 3(a). Copy of a radioautograph of catcher foil 2 where dark spots result from alpha particle emission. (XBB 765-4462)

(b). Copy of a radioautograph of catcher foil 3 where dark spots result from alpha particle emission. (XBB 765-4461)

The results of the angular and energy distribution analysis can be seen in Fig. 5. Here the energy distribution is not explicit but can be discerned by remembering that these were stacked Al foils. Thus activity in the later foils had to pass through larger and larger amounts of Al and thus had to be higher energy recoils. The highest activity was found in the second foil in the angular range of 40-45° in the laboratory. This corresponds to a velocity vector that would be associated with an elastically recoiling ^{209}Bi nuclei. This lends

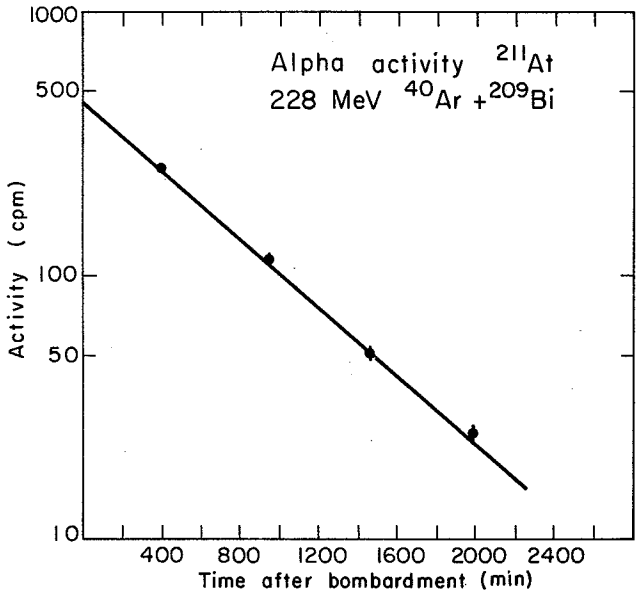

Fig. 4. Decay curve of catcher foil 3. (XBL 766-2912)

support to the idea that the majority of the ^{211}At is produced in an elastic type event. Foils 1 and 4 are shown here in an expanded scale. It is in these two foils that any $1/\sin\theta$ component would be prominent. Foil 4 seems to show an increase in count rate as one goes to smaller angles in the laboratory. This is what Bimbot et al. have seen for similar non-compound nucleus systems.[3]

Foil 1, on the other hand, shows a decrease in count rate with decrease in lab angle. The activity in Foil 4 has a distribution corresponding on the curve shown in Fig. 1(a); thus we would attribute it to a quasifission mechanism. If true, we would further expect a similar contribution all along the curve of Fig. 1. Foil 1 does not fulfill this expectation, in fact it seems to show the opposite to be true. However, this lack of low energy fragments at low laboratory angles may be due to the thickness of the target.

We feel that Fig. 5 shows the production of ^{211}At from 228 MeV ^{40}Ar on ^{209}Bi to follow a quasi-elastic transfer type mechanism with some lesser contribution from a quasifission mechanism. This small contribution is seen at low angles in Foil 4. We note that the activity is down 3 orders of magnitude from that in the quasi-elastic transfer region.

References

1. R. Bimbot, D. Gardes and M. F. Rivet, Phys. Rev. C4, 2180 (1971).

2. M. Lederer, J. Hollander and I. Perlman, Table of Isotopes, 6th ed. J. Wiley & Sons (1967).

3. R. Bimbot, D. Gardes, R. L. Hann, Y. De Moras, M. F. Rivet, Nucl. Phys. A228, 85 (1974).

4. L. G. Moretto, J. Galin, R. Babinet, Z. Fraenkel, R. Schmitt, R. Jared and S. G. Thompson, LBL-4084 (1975).

5. L. C. Northrop and R. F. Schilling, Nucl. Data A7, 233 (1970).

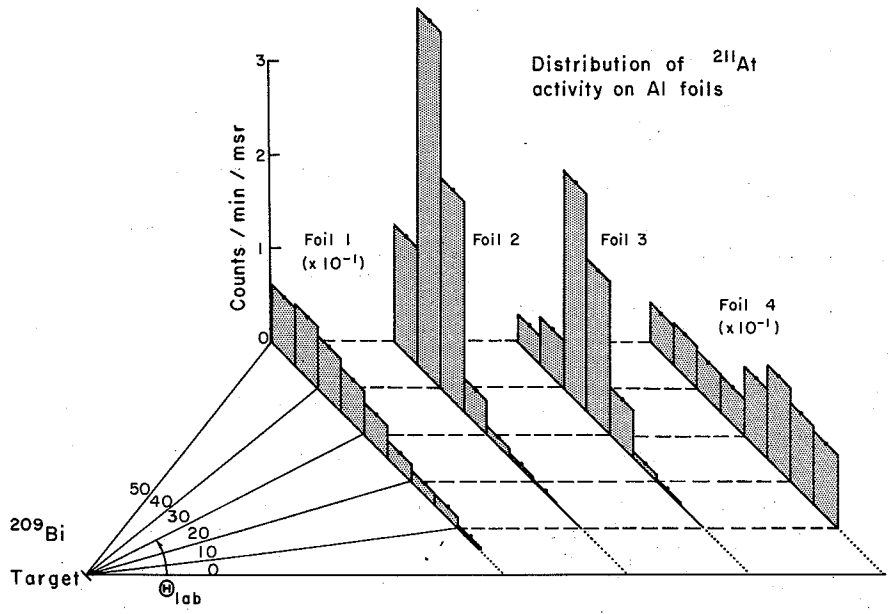

Fig. 5. Alpha activity distribution on catcher foils 1 through 4 (counts per minute per millisteradian vs θ_{lab}). Note that foils 1 and 4 are shown with an expanded scale. (XBL 766-2907)

HEAVY-ION REACTIONS WITH HEAVY, NON-FISSIONING TARGETS

I. Binder, M. M. Fowler,† D. Lee,
R. J. Otto, and G. T. Seaborg

As part of the program to study the reactions of heavy-ion projectiles (by radiochemical methods), targets of bismuth and gold have been bombarded with Kr and Ar beams available at the Berkeley SuperHILAC. The goal has been to investigate the yields of products in the neighborhood of the target nucleus without severe depletion of such products due to fission. Both low-energy asymmetric and high-energy symmetric fission are seen to occur when uranium is the target material; also seen among the uranium reaction products is the so-called "gold-finger."[1,2]

Thick Au and Bi foils have been bombarded with Kr and Ar ions. Some target foils were counted directly for gamma rays using large-volume Ge(Li) detectors and for X-rays using an intrinsic Ge detector. In this way uncertainties due to chemical yield losses are eliminated for all products so that absolute cross sections can be computed, and shorter-lived activities are accessible. Some of the foils were dissolved and chemically processed using methods similar to those developed for uranium targets.[3] This produced samples consisting of simple groups of elements. These samples were then examined for gamma-rays and alpha particles. In addition, some of these experiments included specific chemical procedures to isolate one particular element or one special group of elements (e.g., a lanthanide sample.)

The nuclides produced were identified using the knowledge of gamma-ray or alpha-particle energy, half life, relative intensities of gamma rays originating from one nuclide, and chemical characteristics of the element.

More than 130 nuclides were identified from the reaction 705 MeV $^{84}Kr + ^{209}Bi$. Charge dispersion curves were obtained for various regions of products, and this enabled integration of isobaric yields giving the total yield for each mass number. The integrated result can be seen in Fig. 1.

The total yield curve has been factored into components corresponding to yields from the various reaction mechanisms occurring. Seen are components[4] of quasi-elastic transfer (components E and F), deep-inelastic transfer or quasifission (components C and G) and high-energy symmetric fission, "quasi-ternary fission" (component D). The high energy symmetric fission takes place for nuclides in the neighborhood of and above the ^{209}Bi target. It is not possible to distinguish a fusion-fission component, but this outgoing reaction channel cannot be very large and an upper limit estimate is shown as component A. Table 1 contains the various cross sections for each of the identified components. The relative error for the cross sections in Table 1 is about 15%.

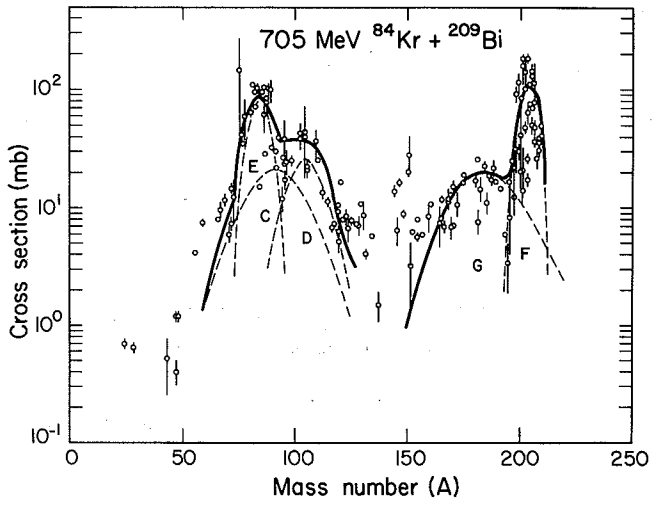

Fig. 1. Mass yield distribution[4] for the reaction 705 MeV $^{84}Kr + ^{209}Bi$. (XBL 766-8254)

Table 1. $^{84}Kr + ^{209}Bi$ yields.

Mechanism	Label (Figure 1)[4]	Cross Section
Fusion-Fission	A/2	$\leqslant$ 120 mb
Quasi-Fission (deep inelastic light product)	C	680 mb
Quasi-Fission (deep inelastic heavy product)	G	460 mb
Quasi-Elastic Transfer (light product)	E	880 mb
Quasi-Elastic Transfer (heavy product)	F	850 mb
Quasi-Ternary Fission	D/2	265 mb
Quasi-Fission	$\sigma_{QF} = C = D/2 + G$	~700 mb
Quasi-Elastic Transfer	$\sigma_{QET} = E = F$	~865 mb
Total Reaction	$\sigma_R = \sigma_{QF} = \sigma_{QET}$	~1600 mb

As first noted in the reaction $^{84}Kr + ^{197}Au$ and later confirmed in the case of $^{84}Kr + ^{209}Bi$,

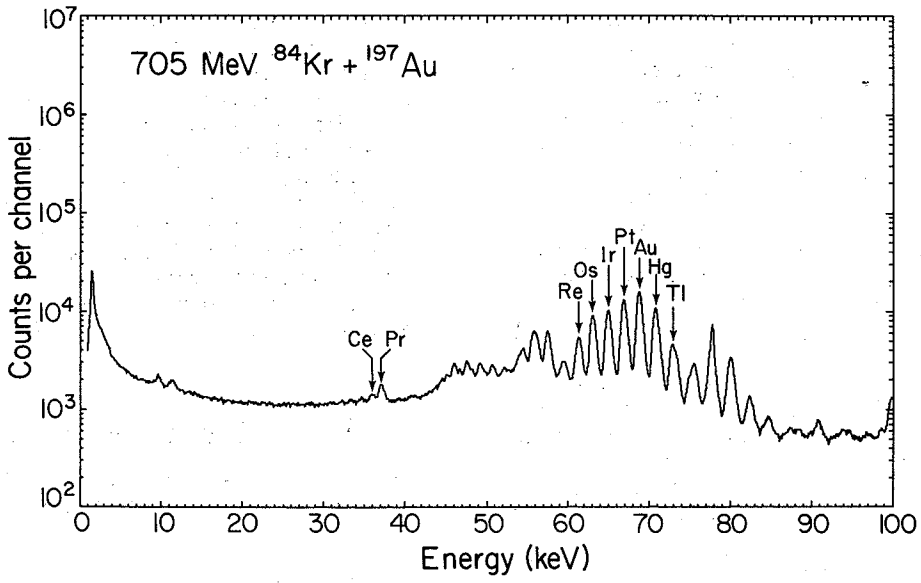

Fig. 2. X-ray spectrum of ^{197}Au target foil irradiated with 714 MeV ^{84}Kr. (XBL 766-8255)

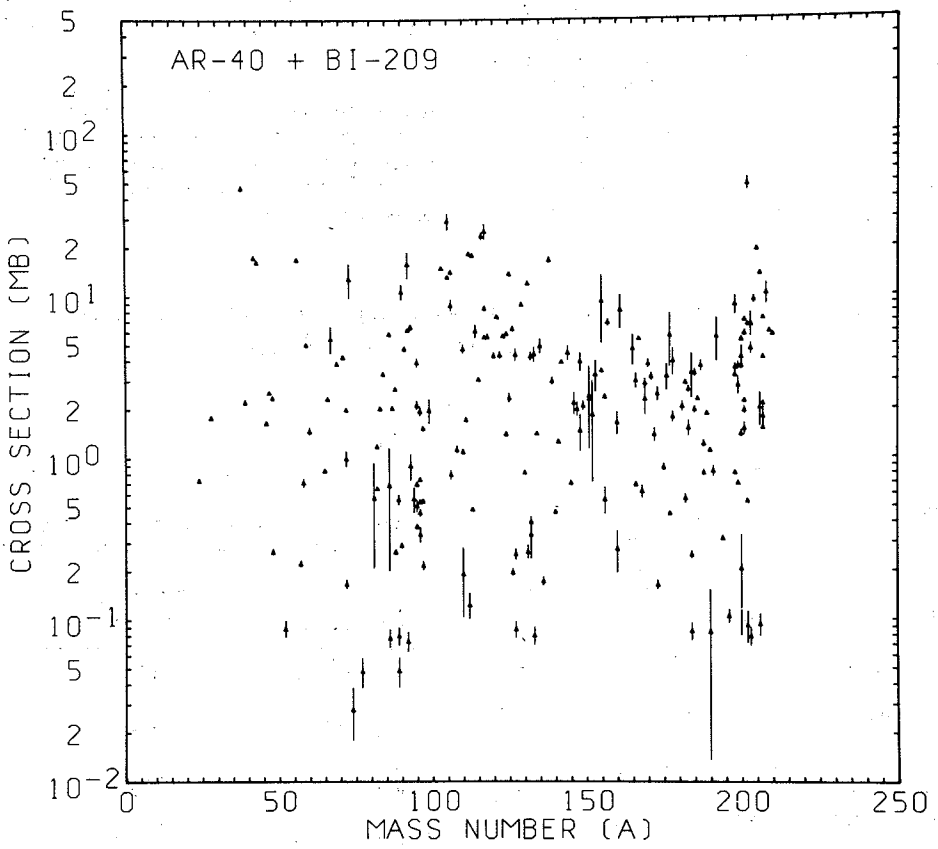

Fig. 3. Partial cumulative and independent yields from the reaction of 340 MeV ^{40}Ar + ^{209}Bi.
(XBL 766-8092)

products from the deep inelastic reactions extend forty to fifty mass units below the originating target nucleus. In addition, products in the region of lead are depleted due to high-energy, symmetric fission of the initial pre-evaporation products above bismuth. The fission barriers are significantly lower for these heavier products above the closed shells. These two factors -- yields up to fifty mass units below the target nucleus and fission above the lead shell closure -- are now believed to be responsible for the "goldfinger" products found in the reactions of heavy ions with uranium targets.

Figure 2 shows an x-ray spectrum taken of a gold foil that was bombarded with 714-MeV Kr ions. Yields are rapidly declining above the target nucleus, but extend down to lanthanum isotopes. This is consistent with the more quantitative mass distribution determined by gamma-ray analysis.

The balance of protons and neutrons in the incoming and outgoing channels in the krypton reactions shows that mass is preferentially transferred from the target nucleus to the Kr projectile in a deep-inelastic transfer reaction.

Results for the 340 MeV $^{40}Ar + ^{209}Bi$ reaction are given in Fig. 3, which shows the partial cumulative and independent yields of isotopes identified by gamma-ray analysis. These results represent the first part of a complete mass distribution analysis in which smooth chain yield cross sections will finally be obtained. The scatter in the cross sections shown results from the fact that each cross section represents a fraction of the chain yield. A broad symmetric fission mass distribution would account for the generally high yields around A≈110. A complete fusion-fission reaction mechanism must thus make up a large part of the total reaction cross section. There is also evidence for a deep inelastic quasi-bismuth component in the increasing yields between A≈180 and A≈200. These results are consistent with kinematic studies of the same target, projectile combinations, both in the overall mass distribution and in showing that the transition from complete fusion-fission to quasi-fission occurs when the mass of the projectile is increased from that of Ar to that of Kr.

Footnotes and References

†Present address: Los Alamos Scientific Laboratory, University of California, Los Alamos, New Mexico 87545.

1. J. V. Kratz, A. E. Norris and G. T. Seaborg, Phys. Rev. Lett. 33, 502 (1974).

2. R. J. Otto, M. M. Fowler, D. Lee and G. T. Seaborg, Phys. Rev. Lett. 36, 135 (1976).

3. J. V. Kratz, J. O. Liljenzin and G. T. Seaborg, Inorg. Nucl. Chem. Lett. 10, 951 (1974).

4. The letters used to identify the various components in the mass distribution are consistent with their usage in references 1 and 2. Letter B has been associated with quasi-elastic induced fission of the uranium target and is thus not required for Bi and Au targets.

POSSIBLE MECHANISMS FOR ^{256}Fm AND ^{256}Md PRODUCTION IN THE COMPOUND SYSTEM $^{264}104$

L. P. Somerville, D. J. Morrissey, R. J. Otto,
G. T. Seaborg, and A. Ghiorso

In heavy ion reactions designed to synthesize the heaviest elements (Z≥100), spontaneous fission from the 177 min ^{256}Fm is often observed. It may be produced either directly or as the daughter of 77-min ^{256}Md which decays by electron capture to ^{256}Fm which then undergoes spontaneous fission. The observed spontaneous fission activity in these reactions is often dominated by that of ^{256}Fm which has been found to have cross sections between 20 nb and 0.2 mb. It would be desirable to know the mechanism of how this nuclide is produced so that its yield could be estimated in future heavy element synthesis reactions. Also, a knowledge of how ^{256}Fm is produced in these reactions would give a better understanding of how nuclei with atomic numbers between those of the target and compound nucleus are made.

In this report, experimental data on the cross sections for production of ^{256}Fm from several heavy ion reactions listed in Table 1 are presented. These data are compared with kinematic studies of the reaction of $^{22}Ne + ^{232}Th$.[1]

Table 1. Nuclear reactions studied.

Reaction	Compound system	Range of energies studied (MeV)
$^{13}C + ^{249}Cf$	$^{262}104$	73.7
$^{15}N + ^{249}Bk$	$^{264}104$	77.9 - 100
$^{10}B + ^{253}Es$	$^{263}104$	67
$^{11}B + ^{253}Es$	$^{264}104$	55 - 115
$^{16}O + ^{248}Cm$	$^{264}104$	95.4
$^{12}C + ^{252}Cf$	$^{264}104$	55 - 115
$^{13}C + ^{252}Cf$	$^{265}104$	66 - 89
$^{18}O + ^{248}Cm$	$^{266}104$	98.7

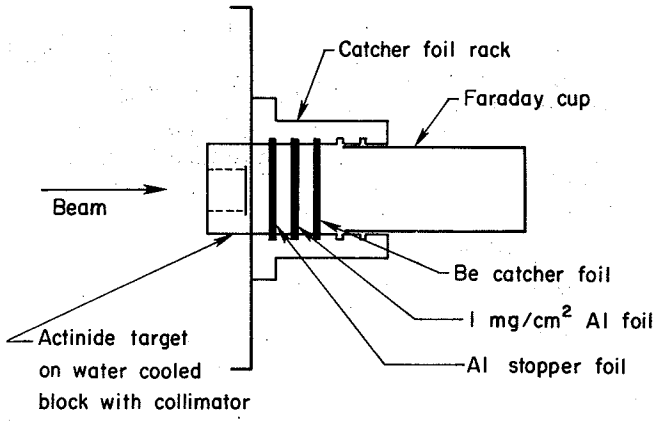

Fig. 1. Typical set-up for catcher foil experiments. The relative positions of the Al stopper foil (20-40 μg/cm^2) and Al catcher foil (1 mg/cm^2) are shown. A 1 mil Be foil was used in the $^{15}N + ^{249}Bk$ experiments. Greater than 95% of the ^{256}Fm activity was found in the Al catcher foil. (XBL 766-8579)

In a series of bombardments devoted to a search for $^{260}104$ the cross sections to produce ^{256}Fm were measured by Ghiorso and co-workers during the period 1963 to 1976. The experiments were conducted at the SuperHILAC and recently at the 88-inch cyclotron. The recoil nuclides from these bombardments were caught by a thin catcher foil in the path of the beam (Fig. 1). A 1 mg/cm^2 Al foil was used as a catcher foil in all experiments except for the reaction $^{12}C + ^{252}Cf$ in which a 0.83 mg/cm^2 Pd catcher was used. In most cases, a very thin 20-40 μg/cm^2 Al stopper foil was inserted between the target and the catcher foil to stop target atoms knocked out of the target. A comparison of the spontaneous fission activity (identified by half-life as ^{256}Fm) in the stopper and catcher foil indicated that greater than 95% of the heavy recoiling nuclei were caught in the 1 mg/cm^2 catcher foil. At the end of the bombardments the growth and decay of the spontaneous fission activity in both foils was followed in ionization chamber fission-alpha-beta counters.

Figure 2(a-d) shows plots of the spontaneous fission count rate versus time after the end of bombardment for the reactions $^{15}N + ^{249}Bk$, $^{10}B + ^{253}Es$, $^{11}B + ^{253}Es$, and $^{18}O + ^{248}Cm$. For the reactions $^{16}O + ^{248}Cm$ and $^{12}C + ^{252}Cf$, good decay curves are not available. However, spontaneous fission counting of the stopper foils from $^{16}O + ^{248}Cm$ bombardments suggest direct ^{256}Md production. The rates of direct formation of ^{256}Md and ^{256}Fm in those cases where decay curves were available were determined by a least square fit to the data using the standard growth and decay formulas.[2] Thus knowing the rates of formation, the beam intensities and target thicknesses, the cross sections to produce ^{256}Md and ^{256}Fm were calculated.

Excitation functions have been measured for reactions $^{15}N + ^{249}Bk$, $^{12}C + ^{252}Cf$, and $^{11}B + ^{253}Es$ (Fig. 3). However, an excitation function for ^{256}Fm production in the reaction $^{16}O + ^{248}Cm$ has not been measured; thus the cross section corresponding to 94.5 MeV could be 2-3 times lower than the peak cross section.

Figure 3(a-c) shows a trend toward decreasing width in excitation function as the atomic number of the target nucleus approaches that of Md and Fm. A 10 MeV decrease in the width of the excitation function is observed in moving from a ^{249}Bk target to an ^{253}Es target.

Figures 4(a) and 4(b) display the angular distributions of ^{256}Fm and ^{256}Md recoils for two of the reactions considered: $^{15}N + ^{249}Bk$ and $^{16}O + ^{248}Cm$. Considerable forward peaking is observed in each case. However, interpretation of these angular distributions is complicated by the fact that thick targets of ~0.5 mg/cm^2 ^{249}Bk and ~ 1 mg/cm^2 ^{248}Cm were used.

Figure 5 is a plot of the total cross section for making ^{256}Fm spontaneous fission activity (both by direct formation of ^{256}Fm and direct formation of ^{256}Md) versus the distance in units of Z from the target nucleus (Z_T) to Md (where Z_p = atomic number of the product). The error bar for the point corresponding to the reaction $^{16}O + ^{248}Cm$ is large enough to include the possibility that all of the observed spontaneous fission activity is due to the direct formation of ^{256}Fm. Figure 5 shows that the cross section falls off at the rate of roughly an order of magnitude for each additional unit of Z away from Md. The cross sections for these reactions used in Fig. 5, except $^{16}O + ^{248}Cm$, were those at the peaks of the respective excitation functions.

The importance of the target and projectile mass numbers, independent of $Z_p - Z_T$, can be seen in the ^{256}Fm cross sections for the reactions $^{13}C + ^{249}Cf$, $^{12}C + ^{252}Cf$, and $^{13}C + ^{252}Cf$. These cross section ratios are respectively 1×10^{-3}, 1, and 2.

In the system 174 MeV $^{22}Ne + ^{232}Th$, Artukh et al.[1] measured the yield of various projectile-like light fragments in the exit channel after a multinucleon transfer reaction had taken place. In order to correlate the $^{22}Ne + ^{232}Th$ results to the

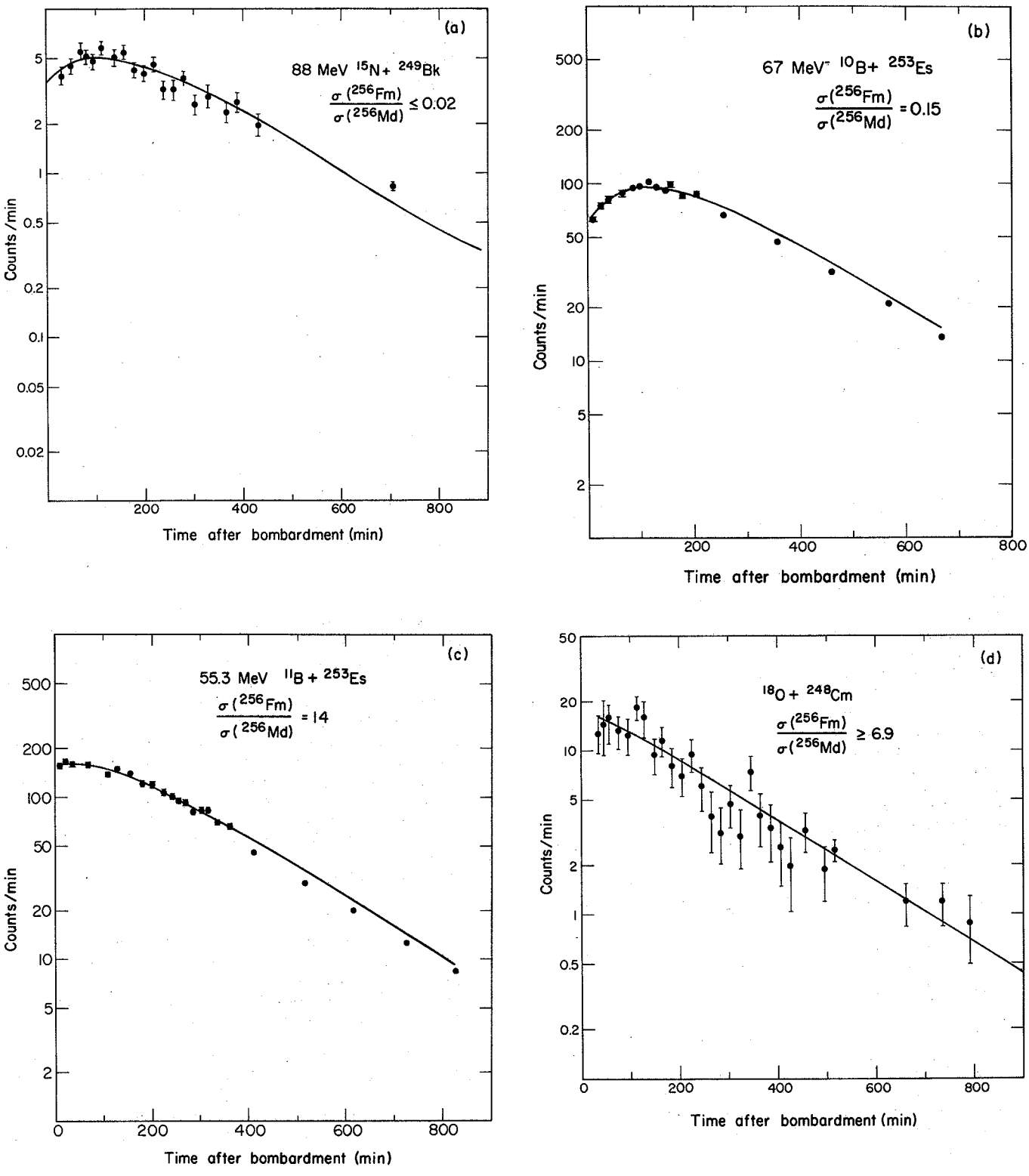

Fig. 2. Spontaneous fission decay curves for ^{256}Fm produced in the reactions (a) $^{15}N + ^{249}Bk$, (b) $^{10}B + ^{253}Es$, (c) $^{11}B + ^{253}Es$, and (d) $^{18}O + ^{248}Cm$.
(XBL 766-8580, -8226, -8227, -8228)

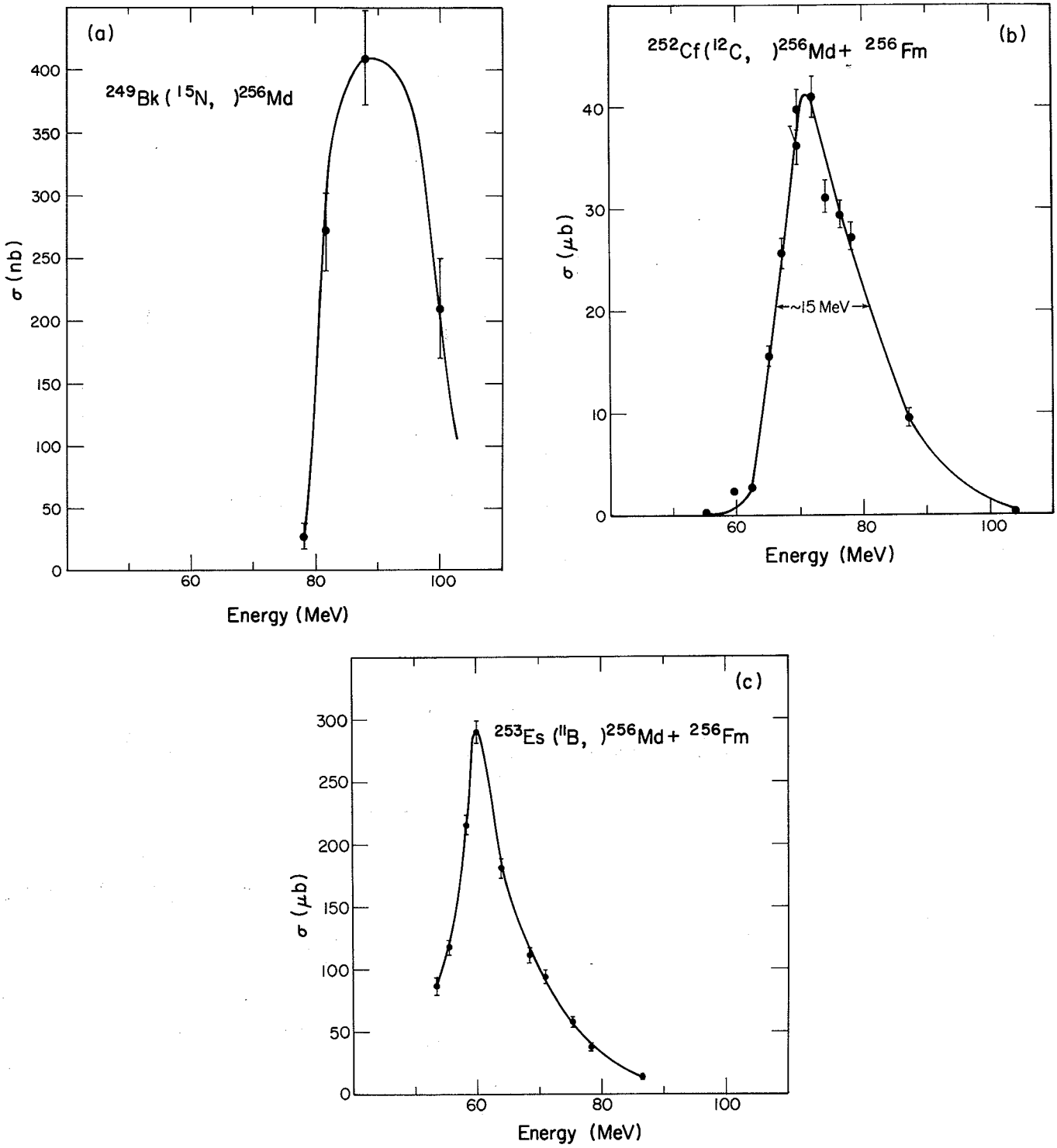

Fig. 3. Excitation functions for the reactions (a) $^{15}N + ^{249}Bk$, (b) $^{12}C + ^{252}Cf$, and (c) $^{11}B + ^{253}Es$. (XBL 766-8229, -8230, -8329)

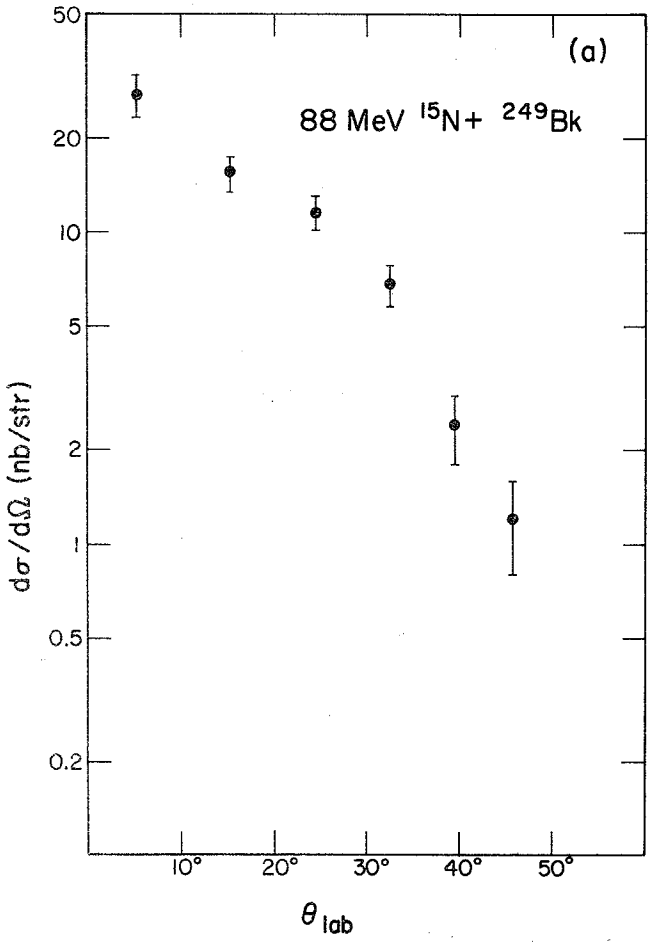

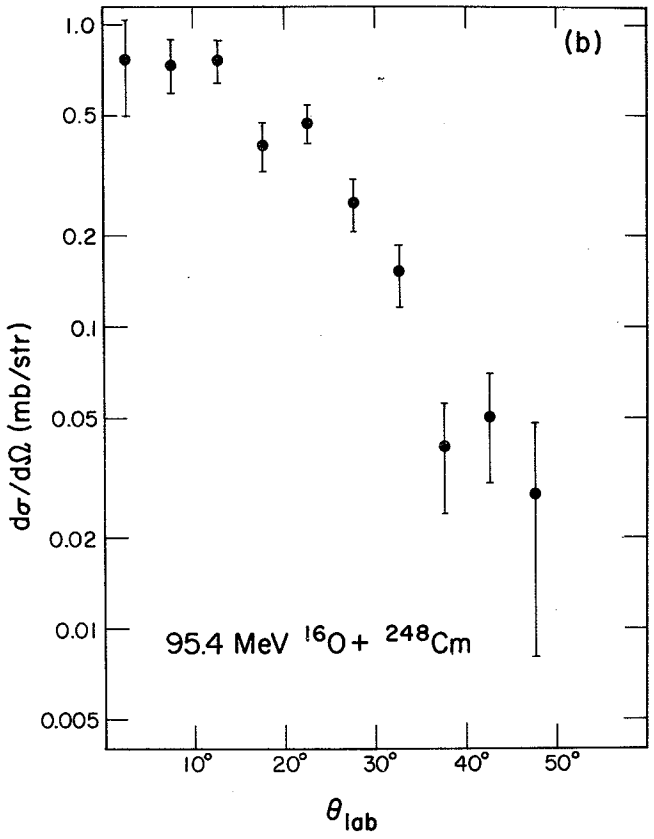

Fig. 4(a) Angular distribution of ^{256}Fm spontaneous fission activity from the reaction ^{15}N + ^{249}Bk.
Fig. 4(b) Angular distribution of ^{256}Fm spontaneous fission activity from the reaction ^{16}O + ^{248}Cm.
(XBL 766-8330, -8331)

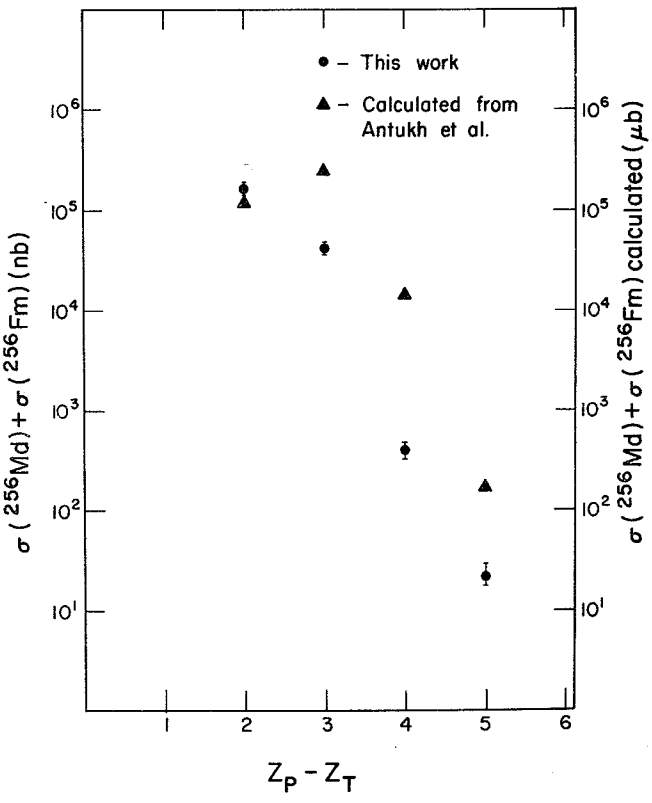

Fig. 5. Plot of production cross sections (represented by solid dots) to make ^{256}Md and ^{256}Fm in the compound system ^{264}104 vs $Z_p - Z_T$, where Z_p = product atomic number (Z_p = 100) and Z_T = target atomic number (left hand scale in nanobarns). The production cross sections (represented by triangle shaped points) for the light fragment vs $Z_p - Z_T$ for the reaction ^{22}Ne + ^{232}Th by Artukh et al. are also shown; for this reaction $Z_p - Z_T$ = number of protons lost by the projectile, presumably the number of protons picked by the target (right hand scale in μb/sr). (XBL 766-8332)

^{256}Fm yield data, we determined the number of protons and neutrons which had to be picked up by our target nuclei to produce ^{256}Md and/or ^{256}Fm. The cross section (or cross sections when both ^{256}Md and ^{256}Fm were formed directly) for the light fragment that corresponds to the same number of protons and neutrons lost by the light fragment projectile was identified in the data of the ^{22}Ne + ^{232}Th reaction. These cross sections (or the weighted average of two cross sections based on the relative production rates of ^{256}Md and ^{256}Fm) were then plotted versus $Z_P - Z_T$ in Fig. 5. The rate of decrease of the yield of these light ions with $Z_P - Z_T$ is similar to the rate of decrease of the yield for ^{256}Md and/or ^{256}Fm with $Z_P - Z_T$. This provides some evidence that the mechanism for producing the observed ^{256}Fm activity is the same as the mechanism Artukh et al. observed for the production of nuclides lighter than the projectile in the reaction ^{22}Ne + ^{232}Th, which they called multinucleon transfer or deep inelastic processes.

From the magnitude of the cross sections observed here, one can argue that the mechanism involved in the production of ^{256}Fm and ^{256}Md must be some type of transfer reaction. Cross sections for compound nucleus evaporation reactions in this reaction of heavy nuclei are typically much lower than for transfer reactions.

The large cross sections and the decreasing trend in the yield of the ^{256}Md and ^{256}Fm cross sections as $Z_P - Z_T$ increases, suggest that these products are produced in a transfer reaction mechanism. The many kinematic studies of the light fragments produced in similar heavy ion reactions have shown that there is a rapid transition from the quasi-elastic transfer mechanism to the multinucleon transfer mechanism for products a few Z units away from the target. Thus, we might expect that the final ^{256}Fm activity seen for all but the ^{11}B + ^{253}Es reaction is primarily from the multinucleon transfer reaction. Consistent with this is the fact that in Fig. 5, the ^{256}Fm/^{256}Md yields are about 1000 times less than the corresponding light fragment yields from the ^{22}Ne + ^{232}Th reaction, except for the ^{11}B + ^{253}Es yield, which is less than 100 times smaller than the corresponding ^{22}Ne + ^{232}Th light fragment yield. This is consistent with the fact that the fission competition following multinucleon transfer is very large because of the low fission barriers and high excitation energies of the heavy actinide fragments produced in these reactions.

Two factors could contribute to lower excitation energy and thus less fission competition in the ^{11}B + ^{253}Es reaction: first, the smaller Coulomb barrier with a lower Z projectile and, second, the role of quasi-elastic transfer as the most important transfer mechanism rather than deep inelastic scattering.

The increasing width in the excitation functions can be understood in terms of the number of nucleons transferred to the target. In these reactions to produce ^{256}Fm and ^{256}Md, the light projectiles such as ^{11}B and ^{12}C transfer only a few nucleons, while heavier particles such as ^{15}N transfer more nucleons. This is consistent with the observation that alpha particle induced reactions have narrow excitation functions while heavy ion induced reactions have broader excitation functions.

References

1. A. G. Artukh et al., Nuclear Phys. A211, 299-309 (1973).

2. Friedlander, Kennedy and Miller, Nuclear and Radiochemistry, John Wiley & Sons, New York, 2nd edition, pp. 78-79 (1964).

A RADIOCHEMICAL STUDY OF THE MASS YIELD DISTRIBUTION FROM THE REACTION OF 25.2-GeV ^{12}C IONS WITH NATURAL URANIUM

R. J. Otto, M. M. Fowler,* I. Binder,
D. Lee, and G. T. Seaborg

An analysis of the measured partial cumulative and independent yield cross sections from the reaction of 25.2-GeV ^{12}C with uranium has been made. The bombardment consisted of a four-hour irradiation of a stack of three 5-mil uranium metal foils at $\sim 6 \times 10^9$ particles/minute. The intersected beam area of the second foil was cut out, dissolved and a radiochemical group separation scheme carried out. Seven chemical fractions were obtained. Gamma-ray counting and analysis was done yielding cross sections for over 60 nuclides.

Due to the combined target thickness, a large fission product contribution may have resulted from secondary particles inducing intermediate energy fission of the uranium. The observed fission products were grouped into four regions and a two gaussian charge dispersion description was fitted to the data.

In Figs. 1(a) through 1(d), the final two gaussian charge dispersion arrived at is shown. Independent yield cross sections shown in Fig. 1(a-d) were calculated for all nuclides in this region using the charge dispersion description arrived at by an iterative fitting process and the growth and decay relationships for the observed nucldies. This method works well for regions where the cumulative yields represent 50% or less of the isobaric yield, as for the neutron-deficient nuclides. The procedure is less accurate for the neutron-excessive yields where greater than 90% of the chain yield is represented in the cross section of a single nuclide.

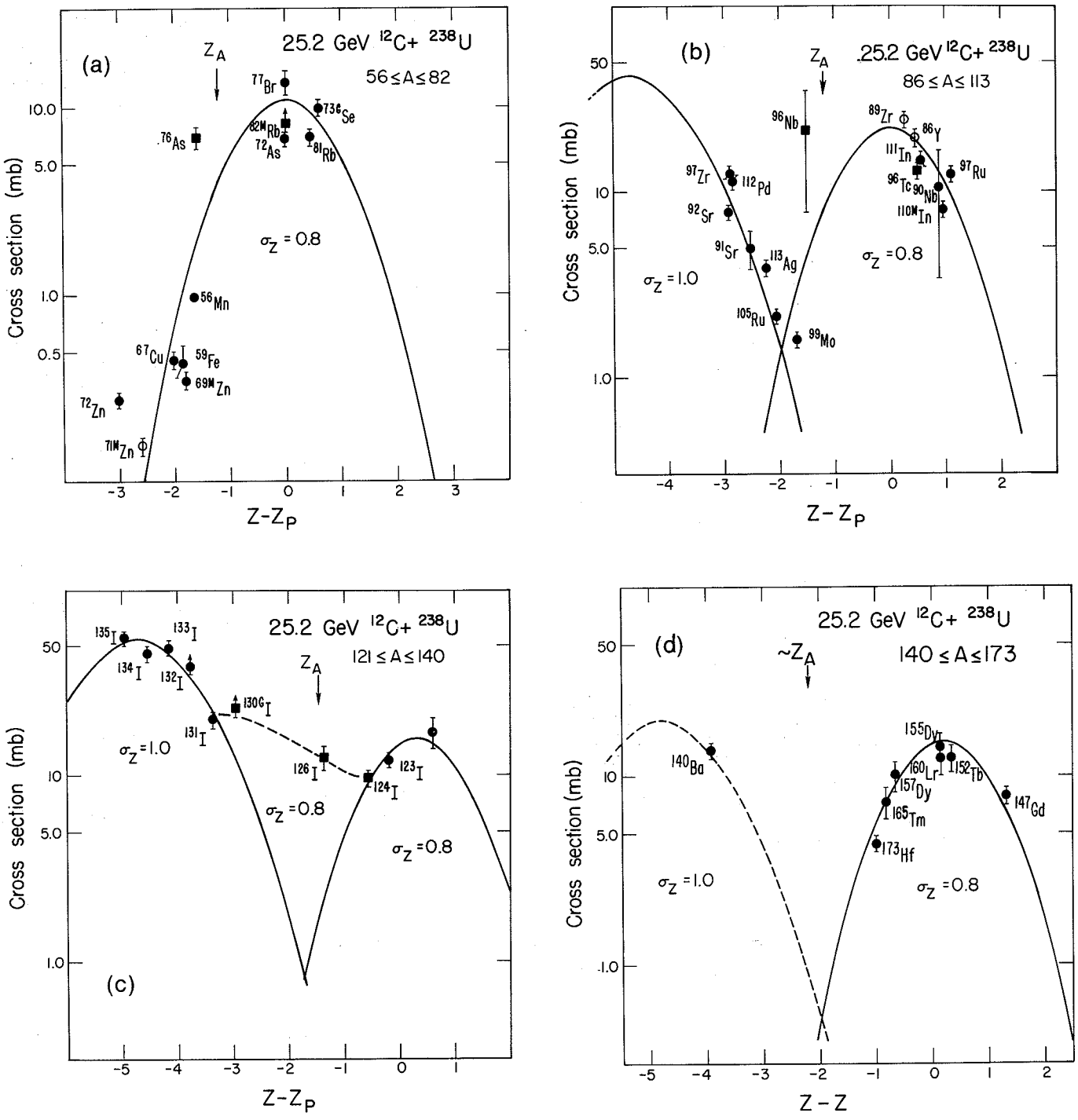

Fig. 1(a-d). Calculated and experimental independent yield cross sections in millibarns for the mass regions shown in the upper right plotted as a function Z - Zp. Where Zp is the most probable charge for the mass chain A, and Z is the charge of the experimentally observed nuclide. The cross sections shown as solid circles are independent yield cross sections calculated from the observed partial cumulative yield cross section. The cross sections shown as solid squares are experimentally measured independent yields. Z_A indicates the positions of the valley of beta stability in each of the mass regions. Neutron deficient nuclides lie to the right of Z_A in this figure. The symbol σ_z represents the gaussian width parameter defining the charge dispersion curves (see Ref. 2) (XBL 766-8248 to 766-8251)

Figure 1(c) shows the calculated independent yields for the iodine isotopes in the mass region A = 121 to A = 135. The two gaussian charge dispersion description in Fig. 1(c) is not consistent with GeV proton results in this region.[1] However, the cross sections for ^{130}I, ^{126}I and ^{124}I are experimentally determined independent yields. The dotted line indicates a neutron excessive component that would not be the result of low energy fission from secondary reactions. If the dotted line is included, the overall shape of the charge dispersion may be consistent with the GeV proton on uranium results. In the mass region A = 56 to A = 82, Fig. 1(a), a single neutron-deficient charge dispersion curve was obtained. A gaussian width parameter[2] of $\sigma_z \cong 0.8$ best fit the neutron-deficient yields for all four mass regions. The neutron-excessive yields were fitted to a value of $\sigma_z = 1.0$.

The final Z_P functions for the region of mass number 56 to 176 are shown in Fig. 2. The neutron-deficient yields were fitted using the modified UCD ruld whosn in Fig. 2 (upper left). The partial cumulative and independent yields for all nuclides except those identified as fission products from secondary induced fission of uranium are shown in Fig. 3. Yields for products near the mass of the target (^{232}Pa, ^{239}Np, ^{238}Np, ^{237}U) probably were formed in secondary reactions.

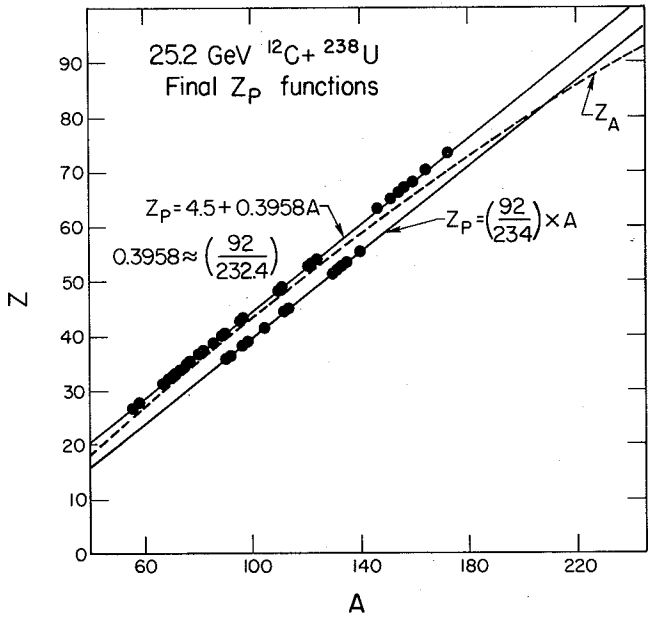

Fig. 2. Plot of Zp functions for the reaction of 25.2 GeV $^{12}C + ^{238}U$. Zp is the most probable charge for each mass chain A. The dotted line labeled Z_A corresponds to the charge at the center of the valley of beta stability. The solid circles are the experimentally determined Zp values. The two Zp functions correspond to the neutron-deficient charge distribution (left of curves) and the charge distribution for the neutron-excessive products (right of curves). (XBL 766-8252)

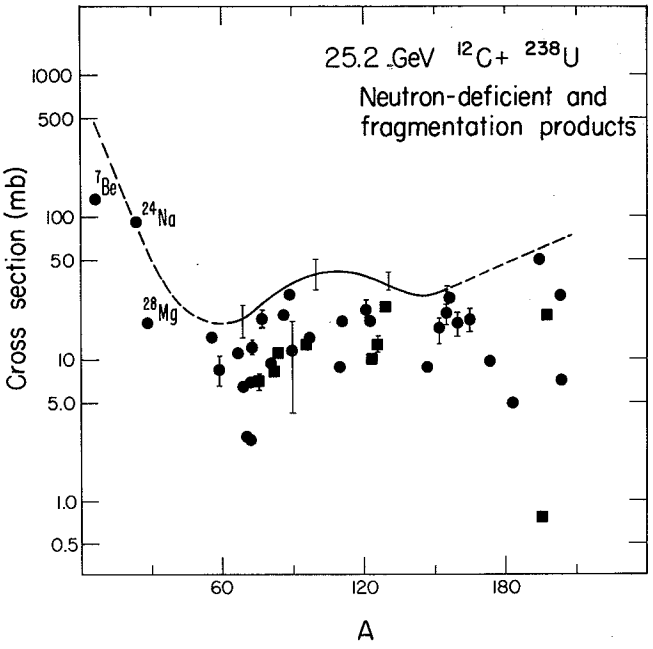

Fig. 3. The mass distribution for 25.2 GeV $^{12}C + ^{238}U$. The solid circles are the partial cumulative and independent yields of the neutron deficient and fragmentation products. Those nuclides identified as fission or evaporation products from the reaction of secondary particles with uranium are not shown. The solid line represents the integrated isobaric yield in the mass region of A = 60 to A = 150. (XBL 766-8253)

The solid line in this figure estimates the isobaric yields over the region A = 60 to A = 150 and was obtained by summing the four charge dispersion curves for the neutron-deficient yields. The total cross section under this curve is 2900 mb. Since a broad binary fission distribution is the dominant feature in this region, part of the 2900 mb should be divided by 2. Assuming a flat non-fission distribution of 10 mb between A = 60 and A = 150, a total cross section of approximately 2 barns would be divided evenly between binary fission and the nonfission mass distribution.

Nuclides were identified with mass above A = 180, but their cross sections did not conform to the Zp function that fit most of the data. The mass distribution is uncertain in this region and shown as a dotted line in Fig. 3.

Three product cross sections were measured in the fragmentation region: ^{7}Be, ^{24}Na, and ^{28}Mg. Although the measured beam intensity[3] is believed to be known only to within a factor of 2, the cross section for ^{24}Na production is much larger for the carbon on uranium reaction than for the GeV proton on uranium reaction.[4] At 2.1 GeV/nucleon, the ratio of cross sections is thirty [$\sigma_{(C+U)}/\sigma_{(P+U)} = 30$].

Footnotes and References

*Present address: Los Alamos Scientific Laboratory, University of California, Los Alamos, New Mexico 87545.

1. Yu-Wen Yu and N. T. Porile, Phys. Rev. C7, 1597 (1973).

2. The charge dispersion curves were assumed to have the following functional form:

$$P_{(z)} = \frac{P_A}{\sqrt{2\pi}\,\sigma_z} \exp\left(\frac{-(Z - Zp)^2}{2\sigma_z^2}\right)$$

where Zp is the most probable charge for the mass chain A and P_A is the integrated chain yield for the isobar with mass A, and σ_z is the Gaussian width parameter.

3. The beam was monitored using an ionization chamber. We would like to thank S. S. Markowitz and D. Murphy for their experimental determination of the average beam intensity.

4. A. M. Poskanzer, G. W. Butler, E. K. Hyde, Phys. Rev. C3, 882 (1971).

RECOIL RANGES OF HEAVY PRODUCTS IN THE QUASI-FISSION REACTION

R. J. Otto, M. M. Fowler,* I. Binder,
D. Lee, and G. T. Seaborg

The recoil range distributions for the elements hafnium to astatine produced from heavy ion reactions of krypton and xenon with gold, bismuth and uranium targets have been measured. These elements are part of the quasi-target mass distribution for the uranium reactions, the mass distribution colloquially referred to as the "goldfinger."[1,2] They also include the quasi-elastic transfer products in the reactions with gold and bismuth targets. The results of these studies have lent support to the identification of the "goldfinger" as the remnant mass distribution of the quasi-uranium products.

Kinematic analysis of the quasi-projectile projects in the quasi-fission or deep inelastic reaction of Kr with Au[3] and Bi[4,5] targets demonstrate several important characteristic features of the quasi-fission or the deep inelastic mechanism. First, the energies of the light and heavy fragments correspond to the Coulomb repulsion energy of two touching spheroids. Second, the angular distribution of the light fragments shows a definite sideways peaking. This sideways peaking effect disappears as the charge and mass of the light fragment becomes increasingly farther away from the original charge and mass of the projectile. Based on these observations, a two-step reaction model has been used to analyze and correlate the measured recoil range distribution of the heavy complementary elements with the light particle kinematic data on quasi-fission and quasi-elastic transfer reactions.

A stacked foil arrangement was used. The targets consisted of approximately 2 mg/cm^2 gold leaf, 3-4 mg/cm^2 bismuth metal on aluminum backing, and approximately 1 mg/cm^2 UF_4 on aluminum backing. These targets were placed directly onto and in front of a stack, typically ten or more, of 1.0 to 1.1 mg/cm^2 aluminum recoil catcher foils. Following irradiation with ^{86}Kr or ^{136}Xe ions at the SuperHILAC, the catcher foils were removed, separated and individually counted for x-rays. The decay of the observed x-ray peaks was followed in one of the more active foils.

Figure 1(a-c) shows typical x-ray spectra from experiments of ^{86}Kr with ^{197}Au, ^{209}Bi and ^{238}U targets. Each of the x-ray peaks in the spectra is a combination of the $K\alpha_1$ line of the element written above the peak in Fig. 1(a-c) and the $K\alpha_2$ line of the element of the next higher Z. Since the relative intensity of the $K\alpha_1$ and $K\alpha_2$ lines is 2 to 1, gamma-ray contributions in the x-ray peaks resulted in unacceptable intensity ratios and were easily recognized.

The recoil range distributions were determined from the x-ray data by determining the area under each x-ray peak and correcting for decay. The results of this analysis are plotted in Figs. 2 and 3. The most striking feature is the similarity of these differential recoil range distributions among the elements for a given bombarding energy and reaction. The similarity spans a much broader region of elements than would be expected for the span of elements contributing to a single recoil range distribution by growth and decay. Thus, these curves are somewhat independent of the growth and decay relationships and reflect the kinematic properties of the fragments produced and observed in these heavy ion reactions.

The majority (50-80%) of the activity of each of the reaction products for the krypton reactions was found in just two of the 1 mg/cm^2 recoil foils. In the ^{86}Kr + ^{197}Au reaction, the most probable range of the products increases as the bombarding energy decreases. We have been able to reproduce these experimentally measured recoil range distributions and this trend of increasing range with decreasing energy using the two-step quasi-fission model and the shift to larger angles of the peak in the angular distributions as the bombarding energy decreases, seen for the Kr + Bi[5] and Kr + Pb[4] reaction. Since the focused angular distribution of the quasi-krypton also results in a complementary focused angular distribution of the quasi-target product, the peak of the quasi-krypton must move to larger angles in the center of mass system as the bombarding energy decreases. Thus, the quasi-target products must move to smaller angles (closer to 0°) resulting in longer axial ranges exactly as observed.

The recoil range distributions from the Kr + U reaction shows the same general shape as the Kr + Au

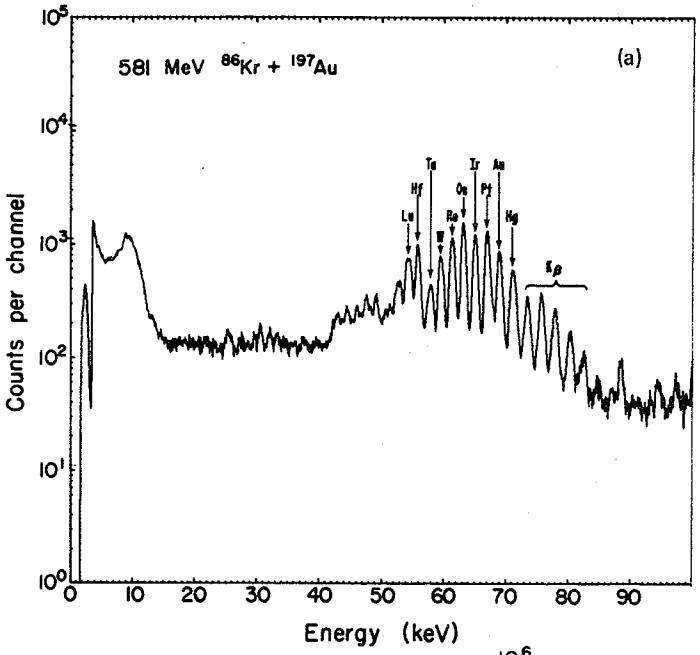

Fig. 1(a-c). X-ray spectra from the 1 mg/cm^2 Al recoil catcher foils for the reactions shown. Each peak is composed of the $K\alpha_1$ line from the element written above the peak and the $K\alpha_2$ line of of the element one Z higher.

(XBL 766-8283 / 766-8285)

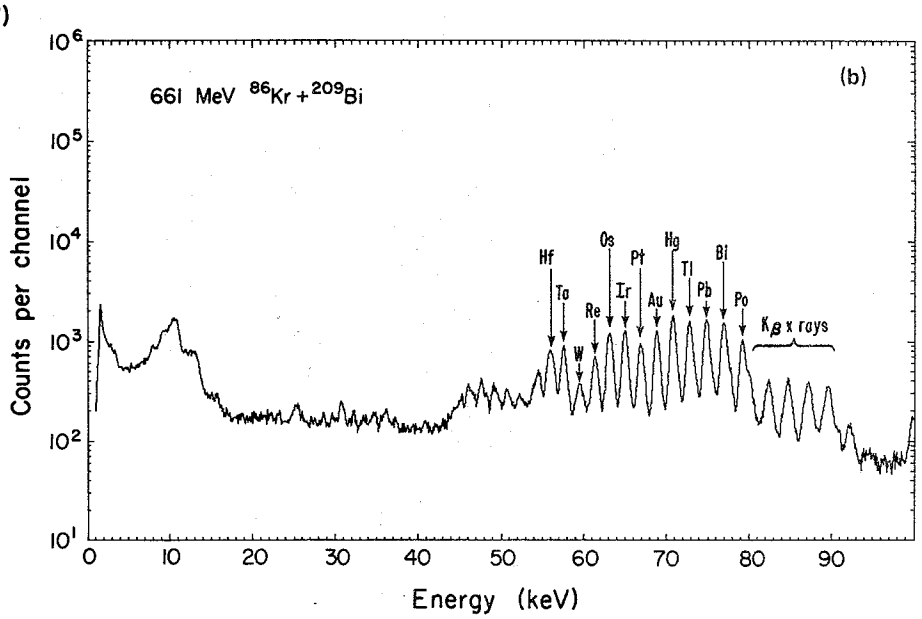

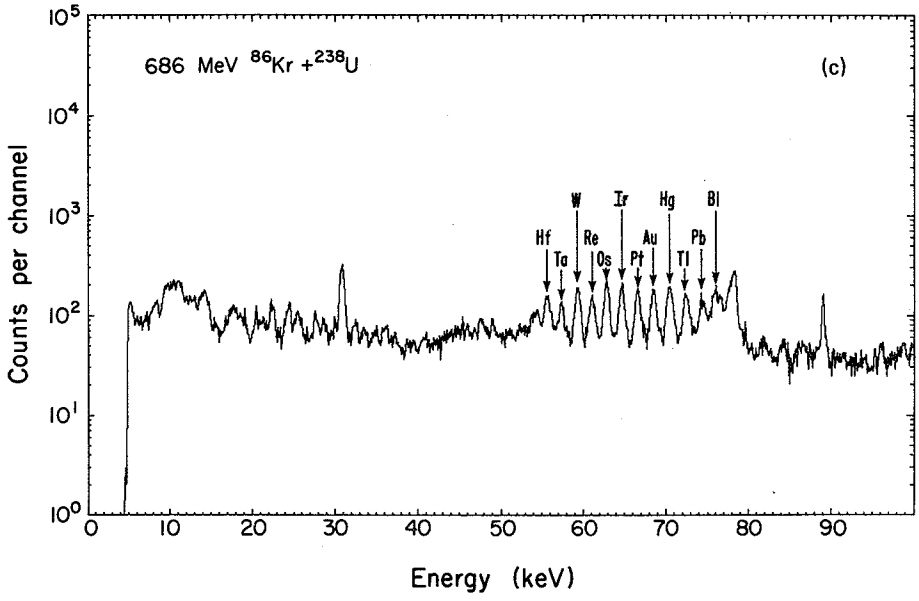

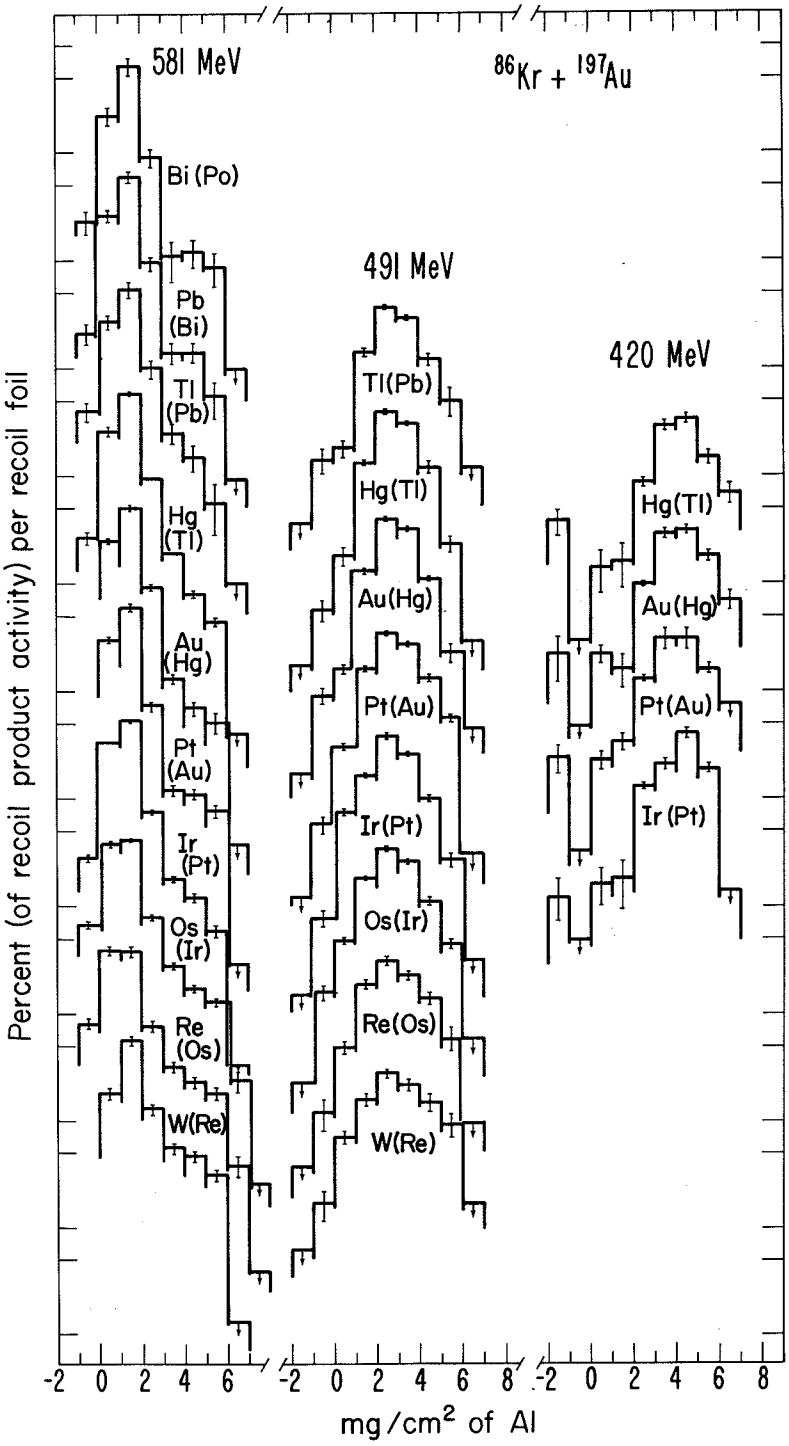

Fig. 2. Recoil range distributions from the analyzed x-ray spectra from the reaction of ^{86}Kr with ^{197}Au at 581 MeV, 491 MeV and 420 MeV. (XBL 766-8286)

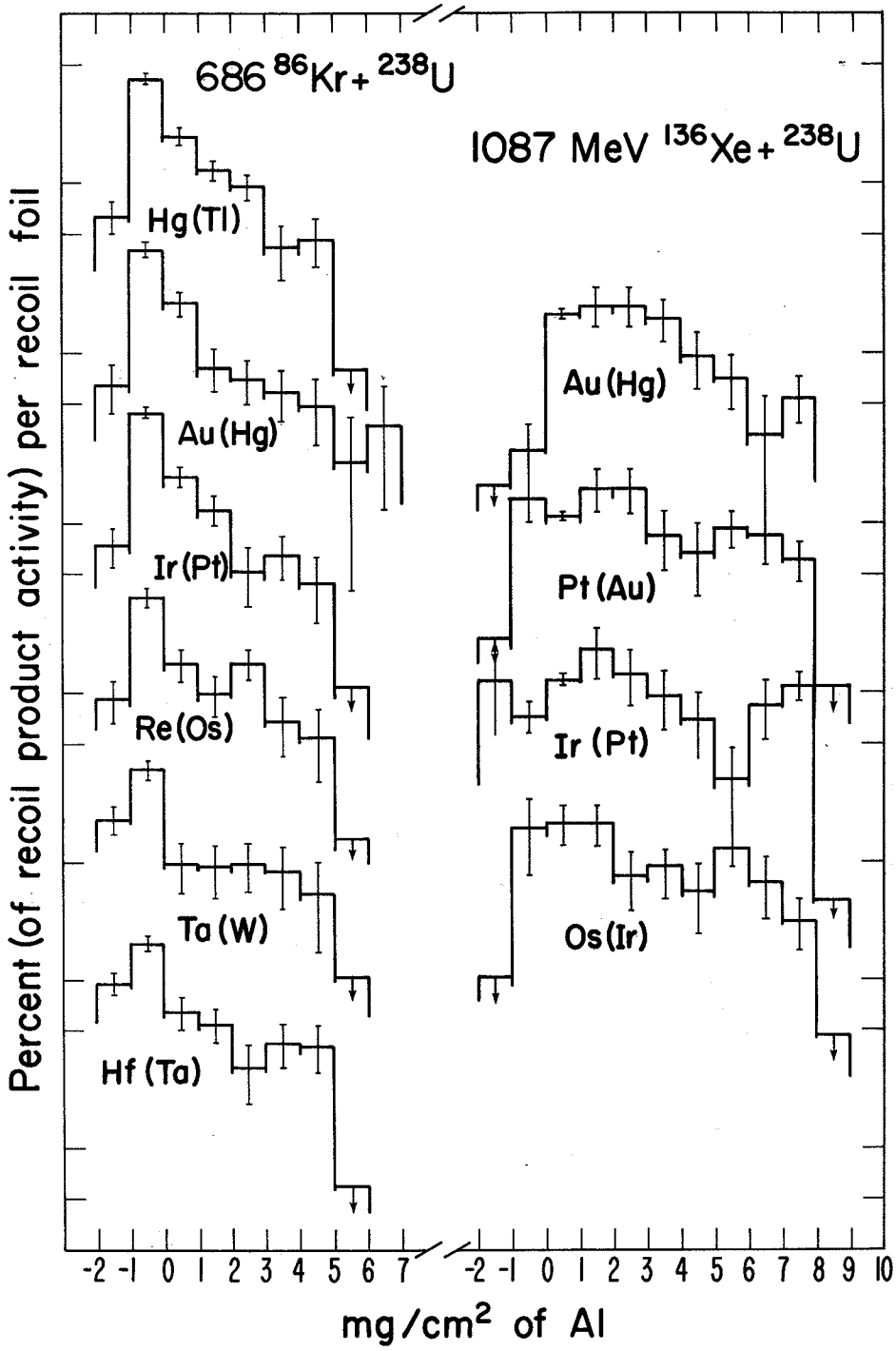

Fig. 3. Recoil range distributions from the analyzed x-ray spectra from the reactions 686-MeV ^{86}Kr with ^{238}U and 1087-MeV $^{136}Xe + ^{238}U$. (XBL 766-8287)

results. The quasi-uranium and therefore quasi-krypton reaction products must have the same sideways peaking in their angular distribution. Sideways-peaked angular distributions, used to calculate the recoil distributions, reproduced the observed recoil range distribution for the 686-MeV $^{86}Kr + ^{238}U$ reaction.

We found that our calculations predict differential recoil range distributions that are distinctly different for different angular distributions. A small $1/\sin\theta$ component in the angular distribution causes a significant fraction of the activity to have the maximum range corresponding to alignment of the center of mass and fission velocity vectors. No evidence for such a component can be seen in the 586-MeV $^{86}Kr + ^{197}Au$ reaction, although a difference in the long-range part of the recoil range distributions would have been seen with as little as 5% of the mechanism having a $1/\sin\theta$ component.

In the $^{86}Kr + ^{238}U$ and $^{136}Xe + ^{238}U$ reactions, there is some evidence for a fractional part of the mechanism to have a $1/\sin\theta$ component, but at least 80% of the Kr + U recoil distributions can be accounted for by using quasi-fission angular distributions similar to the Kr + Au[3] and Kr + Bi[4] angular distributions. The assumption of total damping in the entrance channel is not strictly adhered to in xenon heavy ion reactions[6] and this will affect the recoil range distribution for the Xe + U reaction. We would like to point out that a $1/\sin\theta$ angular distribution is a necessary but not sufficient condition of compound nucleus formation followed by fission, and it may only reflect nuclear orbiting of the quasi-projectile fragment.

As a test of our model to produce computer-simulated recoil range distributions, we have used the measured angular distributions of the complementary light fragment from a study of 620-MeV $^{86}Kr + ^{197}Au$[3] to predict the recoil range distributions of the complementary quasi-gold products for the reaction of 586 MeV $^{86}Kr + ^{197}Au$. The measured angular distributions and calculated recoil range distributions are shown in Fig. 4. The agreement between the experimental (Fig. 2) and the calculated (Fig. 4) range distributions is fairly good for the low ranges and exceptionally good for the longer range part of the distribution. It should also be pointed out that no normalizations of the percent activity in each foil has been made. One question that arises is why the range distributions for elements with the same Z as the target do not show strong evidence for quasi-elastic transfer. The answer, we believe, lies in the fact that we were looking at x-rays relatively soon after the end of the bombardment (typically 2-4 hours). Our greatest sensitivity by this method is for the shorter-lived neutron deficient nuclides that are primarily produced in the quasi-fission reaction.

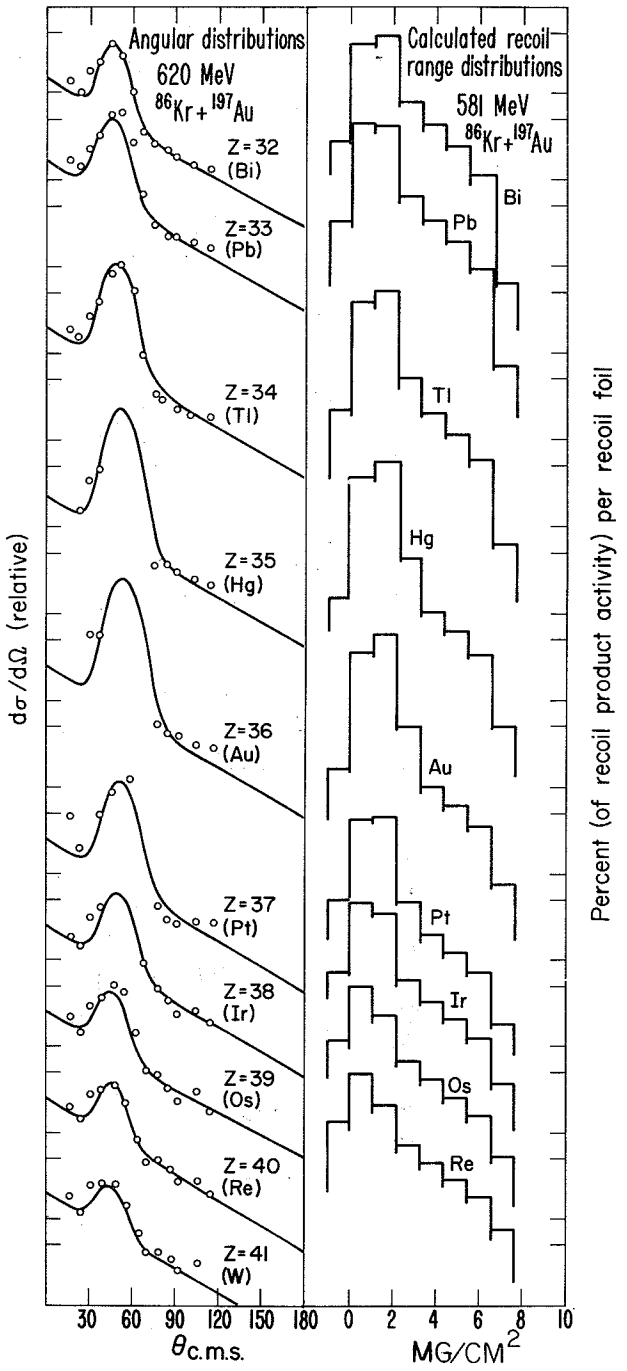

Fig. 4. Experimentally determined angular distributions for the quasi-krypton products from 620-MeV $^{86}Kr + ^{197}Au$ taken from Ref. 3, used to calculate the corresponding recoil range distributions for the complementary quasi-gold products for the reaction 581-MeV $^{86}Kr + ^{197}Au$. (XBL 766-8288)

Footnotes and References

*Present address: Los Alamos Scientific Laboratory, University of California, Los Alamos, New Mexico 87545.

1. R. J. Otto, M. M. Fowler, D. Lee and G. T. Seaborg, Phys. Rev. Lett. 36, 135 (1976).

2. J. V. Kratz, A. E. Norris and G. T. Seaborg, Phys. Rev. Lett. 33, 502 (1974).

3. L. G. Moretto, B. Garvin, P. Glässel, R. Jared, P. Russo, J. Sventek and G. Wozniak, Phys. Rev. Lett. 36, 1069 (1976); and LBL-4362.

4. R. Vandenbosch, M. P. Webb and T. D. Thomas, Phys. Rev. Lett. 36, 514 (1976).

5. K. L. Wolf, J. P. Unik, J. R. Huizenga, J. Birkelund, H. Freiesleben and V. E. Viola, Phys. Rev. Lett. 33, 1105 (1974).

6. I. Binder, M. M. Fowler, D. Lee, R. J. Otto and G. T. Seaborg, in this Annual Report

7. J. R. Birkelund, J. R. Huizenga, H. Freiesleben, K. L. Wolf, J. P. Unik and V. E. Viola, Phys. Rev. C13, 133 (1976).

C. RELATIVISTIC HEAVY IONS

1. Projectile Fragmentation

MOMENTUM DISTRIBUTIONS OF ISOTOPES PRODUCED BY FRAGMENTATION OF RELATIVISTIC ^{12}C AND ^{16}O PROJECTILES*

D. E. Greiner, P. J. Lindstrom, H. H. Heckman,
Bruce Cork, and F. S. Bieser †

Recently we have published measurements of the momentum distributions and production cross sections[1] of the high velocity fragments produced by beams of ^{12}C at 2.1 and 1.05 GeV/nucleon and ^{16}O at 2.1 GeV/nucleon on a variety of targets.

The momentum and cross-section measurements were performed using a single-focusing magnetic spectrometer with a half-angle acceptance of 12.5 mr about zero degrees.[2] Targets were Be, CH_2, C, Al, Cu, Ag and Pb. The charge and mass of the fragments were obtained by measuring their rigidity (Pc/Ze), energy loss in solid-state detectors, and time-of-flight. Particle trajectories were determined with multiple-wire proportional chambers. The longitudinal and projected transverse momenta, $P_{\parallel}$ and $P_{\perp}$, were obtained from the rigidity and direction of the particle at the focal plane of the spectrometer. The rigidity range was scanned in 0.1 GV steps from 0.8 to 10.2 GV for the 2.1 GeV/n ^{12}C and ^{16}O beams and 0.2 to 6.3 GV for the ^{12}C beam at 1.05 GeV/n. Because the velocities of the projectile fragments are near the beam velocity,[3] these rigidity ranges allowed us to observe all particles produced having a mass to charge ratio, A/Z, between 0.2 and 3.4.

For each isotope the longitudinal-momentum distribution, in the projectile rest frame, was fit to a Gaussian dependence on P. The fitted variables are amplitude, central momentum, $\langle P_{\parallel} \rangle$, and standard deviation $\sigma_{P_{\parallel}}$. Figure 1 illustrates the Gaussian fit and the variables $\langle P_{\parallel} \rangle$ and $\sigma_{P_{\parallel}}$ for the case of ^{10}Be produced by the fragmentation of 2.1 GeV/n ^{12}C on a Be target. The fits were restricted to the interval -400 MeV/c to +400 MeV/c which cover typically 1 to 2 decades in the magnitude of the differential cross section. The spectra of all the observed fragments exhibit properties similar to those shown in Fig. 1, namely, the momentum distributions have standard deviations of only 50-200 MeV/c, and the average momentum is slightly negative relative to the projectile.

We find that the Gaussian shape provides a good fit to the observed spectra for all isotopes regardless of beam, energy, or target except for the hydrogen isotopes. The ^2H and ^3H spectra are fit by a Gaussian curve in the region $-300 \leq P_{\parallel} \geq 400$ MeV/c, but exhibit an enhancement for $P_{\parallel} \leq -300$ MeV/c. The ^1H spectrum cannot be fit by a Gaussian

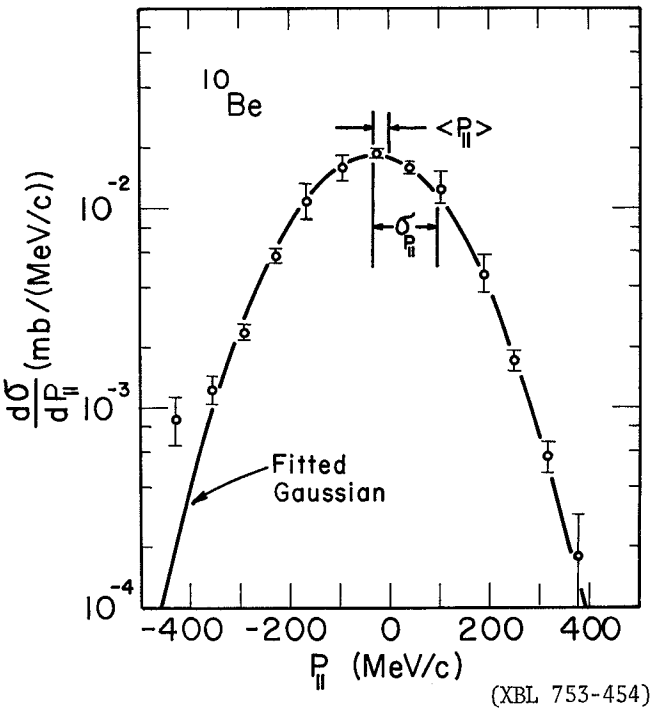

Fig. 1. The projectile-frame parallel-momentum distribution for ^{10}Be fragments from ^{12}C at 2.1 GeV/n on a Be target. The mean momentum $\langle P_{\parallel} \rangle = -30$ MeV/c and standard deviation $\sigma_{P_{\parallel}} = 129$ MeV/c are indicated.

shape in the central region $|P_{\parallel}| \leq 150$ MeV/c. In this region a fit to the ^1H spectrum is obtained with the exponential relation $d\sigma/dP \propto \exp(-|P_{\parallel}|/65)$. The result applies to the protons produced within our 12.5 mr acceptance cone and does not describe the spectra at larger production angles.

The $P_{\perp}$ distributions, projected onto the horizontal focal plane of the spectrometer, were measured for $A \geq 2$ fragments. We find $\sigma_{P_{\perp}} = \sigma_{P_{\parallel}}$ to an accuracy of 10%, consistent with the isotropic production of these fragments.

If these reactions are examples of limiting fragmentation, the large separation in rapidity, $y = \tanh^{-1}(P_{\parallel}/E)$, between the target and the fragmentation distribution requires the shape of the momentum distributions be independent of target

and beam energy.[4] For all reactions the target and energy dependence of the variables $\langle P_{\parallel} \rangle$ and $\sigma_{P_{\parallel}}$ were examined. Within the accuracy of this experiment we conclude there is no dependence on target mass above the 5% level for $\sigma_{P_{\parallel}}$ and above the 10% level for $\langle P_{\parallel} \rangle$. Because of this observed target independence we shall refer to the target-averaged values of σ_P and $\langle P_{\parallel} \rangle$ in the remainder of this paper. To determine if $\sigma_{P_{\parallel}}$ and $\langle P_{\parallel} \rangle$ are independent of energy we compare the measurements of these variables for the ^{12}C beam at 2.1 and 1.05 GeV/n. The weighted averages over all fragments of the quantities $\sigma_{P_{\parallel}}$ (2.1 GeV/n)/$\sigma_{P_{\parallel}}$ (1.05 GeV/n) and $\langle P_{\parallel} \rangle$ (2.1 GeV/n) - $\langle P_{\parallel} \rangle$ (1.05 GeV/n) are 1.02 ± 0.02 and -1.0 ± 2.0 MeV/c, respectively. This independence of beam energy and target leads to the conclusion that the ^{12}C reactions satisfy the limiting fragmentation hypothesis and the limiting energy region is reached before 1.05 GeV/n.

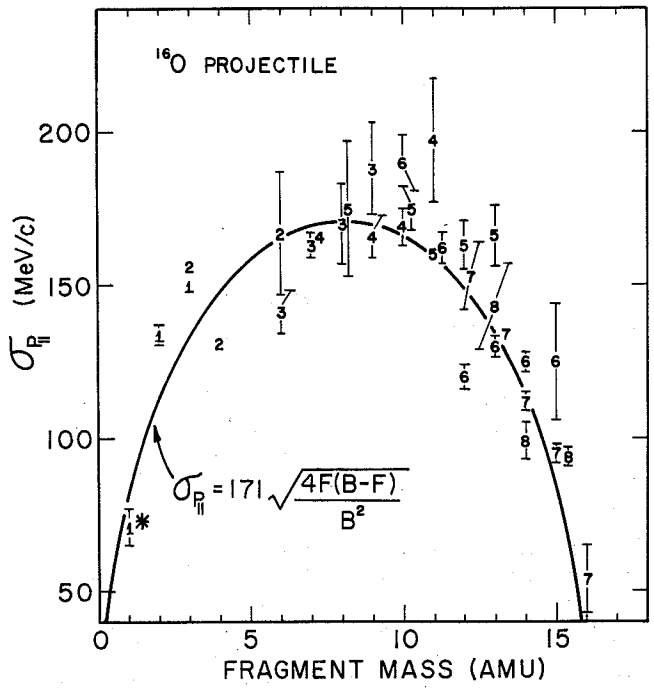

Fig. 2. Plotted are the target-averaged widths $\sigma_{P_{\parallel}}$ of the projectile-frame parallel-momentum distributions, in MeV/c, versus fragment mass in amu. The plotted symbol indicates the charge of the fragment. These data represent fragments of ^{16}O at 2.1 GeV/n. The asterisk denotes that the ^1H is a non-Gaussian momentum distribution and we have used the central region of this distribution to evaluate $\sigma_{P_{\parallel}}$. This result applies to the protons produced within our 12.5 mr acceptance cone and does not describe the spectra at larger production angles. The parabola represents the best fit to the data. (XBL 753-453)

In the limiting energy region the fragment distributions depend on the identity of the projectile and fragment.[4] In Fig. 2 we have plotted the values of $\sigma_{P_{\parallel}}$ for ^{16}O at 2.1 GeV/n versus the fragment mass in amu. The charge of each fragment is used as the plotting symbol. In an attempt to parameterize the mass dependence we have fit the data to the function $\sigma_{P_{\parallel}}(B,F) = 4\sigma_0^2 F(B-F)/B^2$ where B and F are the mass numbers of the beam and fragment nuclei respectively, and σ_0 is the fitted variable. The best-fit curve for ^{16}O is shown in Fig. 2. Although the parabola shape displays the general trend of the data, in no case does it provide a good fit to the observed values of $\sigma_{P_{\parallel}}$.[5] The poor fit is demonstrated by the fact that 50% of the data points are over two standard deviations from the curve. Particularly striking is the observation that the same complex variation of $\sigma_{P_{\parallel}}$ with fragment mass is exhibited by both the ^{12}C and ^{16}O fragments, indicating nuclear structure effects are important variables determining $\sigma_{P_{\parallel}}$.

The values of $\langle P_{\parallel} \rangle$ have an approximately linear dependence on $\sigma_{P_{\parallel}}$ ($\langle P_{\parallel} \rangle = -0.5\ \sigma_{P_{\parallel}} + 30.0$ MeV/c). The general shifts in the momentum distributions toward velocities less than the beam correspond to small energy transfers to the fragment, typically < 130 keV in the projectile frame. The obvious exceptions are reactions involving charge exchange, such as $^{12}C \rightarrow {}^{12}N$, and charge exchange plus loss of a nucleon, e.g., $^{16}O \rightarrow {}^{15}C$. The reactions involving charge exchange generally have larger negative values of $\langle P_{\parallel} \rangle \approx -100$ MeV/c. Calculation of the missing mass in these reactions gives values approximately 200 MeV/c after subtraction of the target mass. Thus the data are consistent with the assumption that the charge-exchange reactions proceed via pion production.

A parabolic dependence of $\sigma^2_{P_{\parallel}}$ on fragment mass of the form $\sigma^2_{P_{\parallel}} \propto F(B-F)$, Fig. 1, was first predicted by Wenzel,[6] later by Lepore and Riddell,[7] and indirectly by Feshbach and Huang[8] as extended by Goldhaber.[9] In general the parabolic shape arises when one assumes: i) the fragment momentum distributions are essentially those in the projectile nucleus, ii) that there are no correlations between the momenta of different nucleons, and iii) momentum is conserved. The validity and implications of these theories can be determined by comparison with the values of σ_0 measured by this experiment.

The work of Lepore and Riddell[7] is a quantum mechanical calculation that employs the sudden approximation with shell-model wavefunctions to predict $\sigma_0^2 = 1/8\ m_p B^{1/3}[45B^{1/3} - 25]$ (MeV/c).[2] This expression, where m_p is the proton mass, gives qualitative agreement with the measured values as shown in Table 1. Feshbach and Huang[8] assume sudden emission of virtual clusters and relate σ_0 to the Fermi momentum of the projectile, P_f and σ_0 is $\sigma_0^2 = 1/20\ P_f^2\ B^2/(B-1)$. The values of P_f determined by quasielastic electron scattering[10] give predicted values of σ_0 that are generally 25% higher than the measured values as shown in Table 1. An interesting point to note here is that through the predicted relationship between σ_0 and P_f, this experiment measures the projectile Fermi momentum via nuclear fragmentation (see Table 1). By assuming the projectile has come to thermal equilibrium at an excitation temperature T, Goldhaber[9] has shown that the parabolic shape is again predicted and relates σ_0 to T by the equation $kT = 4\sigma_0^2/m_n B$, where k is Boltzmann's constant and m_n is the nucleon mass. The measured values of σ_0 then reflect excitation energies which we have listed in Table 1 along with the average binding energies per nucleon as deter-

Table 1. Comparison with theory and experiment of parameters related to a $\sigma_{P_\parallel}$ mass dependence of the form $\sigma_{P_\parallel}^2 = 4\sigma_0^2 F(B-F)/B^2$. Derived quantities are Fermi momentum $P_f = 20\sigma_0^2(B-1)/B^2$ and average excitation energy $kT = 4\sigma_0^2/m_n B$.

Parameter	Origin	Projectile		
		^{16}O (2.1 GeV/n)	^{12}C (2.1 GeV/n)	^{12}C (1.05 GeV/n)
σ_0 (MeV/c)	This experiment	171±3	147±4	141±5
σ_0 (MeV/c)	Sudden approximation[7]	162	145	145
σ_0 (MeV/c)	Virtual clusters[8]	212	179	179
P_f (MeV/c)	This experiment	185±3	182±5	174±6
P_f (MeV/n)	Electron scattering[10]	230	221	221
kT (MeV/n)	This experiment	7.8±0.3	7.7±0.4	7.1±0.5
Average binding energy (MeV/n)	Mass measurements	8.0	7.7	7.7

mined by the projectile masses. Because our measured excitation energies are essentially the binding energy per nucleon of the projectiles, we infer that the fragmentation process which results in bound fragments involves very little energy transfer between the target and fragment.

The fragment momentum distributions in the projectile rest frame are, typically, Gaussian shaped, narrow, consistent with isotropy, depend on fragment and projectile, and have no significant correlation with target mass or beam energy. The nuclear temperature is inferred from the momentum distributions of the fragments and is approximately equal to the projectile nuclear binding energy, indicative of small energy transfer between target and fragment.

Footnotes and References

*Condensation of LBL-3651, Phys. Rev. Lett. 35 152 (1975).

†University of California Space Sciences Laboratory, Berkeley, California.

1. P. J. Lindstrom, D. E. Greiner, H. H. Heckman, Bruce Cork, and F. S. Bieser, LBL-3650 (submitted to Phys. Rev. Lett.).

2. D. E. Greiner, P. J. Lindstrom, F. S. Biesser and H. H. Heckman, Nucl. Inst. and Meth. 116, 21 (1974).

3. H. H. Heckman, D. E. Greiner, P. J Lindstrom, and F. S. Bieser, Phys. Rev. Lett. 28, 926 (1972).

4. W. R. Frazer, et al., Rev. Mod. Phys. 44, 284 (1972).

5. Preliminary results based on eight isotopes not including ^1H indicated $\sigma_{P_\parallel} \approx 140$ MeV/c, independent of mass (H. H. Heckman, 5th Intl. Conf. High-Energy Physics Nuclear Structure, Uppsala, Sweden, June 1973.) Based on all the data presented here, a constant value of $\sigma_{P_\parallel} = 137$ MeV/c gives a goodness-of-fit $\chi^2 = 600$ for the parabola with 32 degrees of freedom.

6. W. A. Wenzel, LBL Heavy Ion Seminar, 1973 (unpublished).

7. J. V. Lepore and R. J. Riddell, Jr., LBL-3086, 1974 (unpublished).

8. H. Feshbach and K. Huang, Phys. Lett. 47B, 300 (1973).

9. Alfred S. Goldhaber, Phys. Lett. 53B, 306 (1974); The fragmentation problem has also been studied by Fumiyo Uchiyama, LBL-3318, 1974 (unpublished).

10. E. J. Moniz, I. Sick, R. R. Whitney, J. R. Ficenec, R. D. Kephard, and W.P. Trower, Phys. Rev. Lett. 26, 445 (1971).

ISOTOPE PRODUCTION CROSS SECTIONS FROM THE FRAGMENTATION OF ^{16}O AND ^{12}C AT RELATIVISTIC ENERGIES*

P. J. Lindstrom, D. E. Greiner, H. H. Heckman,
Bruce Cork, and F. S. Bieser†

We have measured at the Bevatron the single-particle inclusive spectra of all isotope fragments of ^{16}O and ^{12}C at 2.10 GeV/n and of ^{12}C at 1.05 GeV/n. The targets were Be, CH_2, C, Al, Cu, Ag, and Pb. The hydrogen target data were obtained by CH_2-C subtraction. The measurements were limited to secondaries produced within a ±12.5 mr cone about 0° from the direction of the primary beam. Secondary momenta were limited to rigidities (pc/Ze) less than 9 GV. All secondaries with lifetimes greater than 10^{-8} seconds and production cross sections greater than 10 μb were observed. The spectrometer system[1] resolved charge, mass and momentum for all secondaries at any given spectrometer rigidity setting.

The observed longitudinal and transverse momentum spectra of the isotope fragments, when transformed to the projectile rest frame, have Gaussian distributions centered near 0-MeV/c, with standard deviations (S.D) ~ 60-200 MeV/c. The cross sections were obtained by integrating these momentum distributions.[2] Since the observed fragments were confined to a 12.5 mr cone, it was necessary to extrapolate the transverse momentum distributions to obtain the total partial cross section. Except for the $Z \leq 2$ fragments, the 12.5 mr region accounted for 70% - 100 % of the total cross sections. Both observed momentum systematics and measured angular distributions in nuclear emulsion give confidence in this extrapolation for $A \geq 2$ secondaries. The proton momentum distribution is non-Gaussian and no attempt was made to extrapolate this distribution to estimate total production cross section. The cross sections are corrected for beam and secondary fragmentation in the targets, vacuum windows, and scintillators, as well as for interactions in the Si(Li) detectors. The momentum distributions show the cross sections σ_{BT}^F, where beam B interacts with target T to produce fragment F, are measurements of fragments of the projectile and not fragments of the target. No nucleon-pickup isotopes were observed. Between 30% (Pb target) and 90% (H target) of all beam charge is accounted for by summing the σ_{BT}^F. The missing charge is principally in large momentum transfer protons.

The σ_{BT}^F, for a hydrogen target, can be compared with cross sections of proton-nucleus interactions at high energies. At proton energies ≥600 MeV, 42 measured cross sections for 15 different secondaries have been compiled.[3] We find agreement to within 3 S.D. for all except $p + {}^{16}O \rightarrow {}^{10}C + \cdots$ at T_p = 1 GeV and $p + {}^{16}O \rightarrow {}^{10}Be + \cdots$ at 600 MeV, where the disagreement is 3-4 S.D. Comparison of our results can also be made with the semi-empirical model by Silberberg and Tsao[4], which is based on the proton-nucleus data wet mentioned above. We find the experimental values σ_{BT}^F above 1 mb are greater than those given by the Silberberg and Tsao model by an average of 22%, with a S.D. of 37%.

We observe that the cross sections can be factored, $\sigma_B^F = \gamma_B^F \gamma_T$, where γ_B^F depends on the projectile and fragment and γ_T is the target factor (Fig. 1). Target factorization is expected both from high-energy phenomenology and from an impulse approximation model of nuclear fragmentation. The exceptions to strict factorization are: 1) γ_T for a hydrogen target has a weak dependence on the mass of fragment A_F, i.e., $\gamma_T(H) = 0.66 + 0.028\ A_F$ and 2) γ_T for single-nucleon stripping is enhanced for heavy targets. The cross sections for single-nucleon loss on the heavier targets include a component for Coulomb dissociation, via the giant dipole resonance, in the target's virtual photon field. The Coulomb dissociation part of the cross sections can be computed and subtracted from the measured σ_{BT}^F. The resultant cross sections are consistent with the target factors and fit the data with a confidence level of 0.6, and can be approxi-

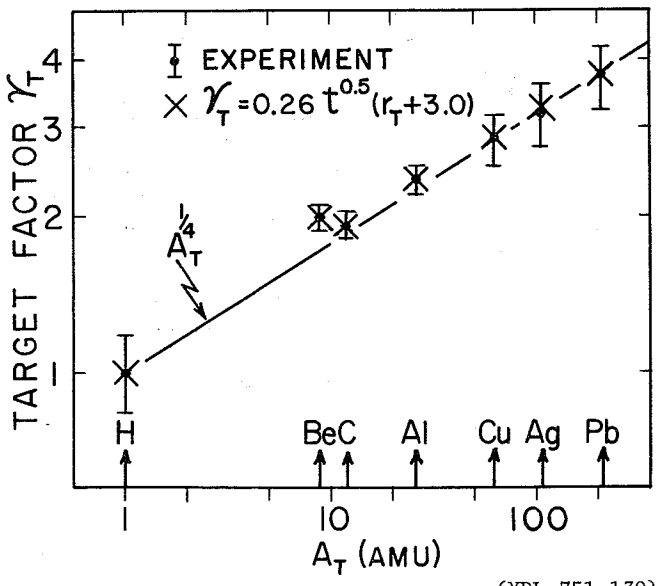

(XBL 751-130)

Fig. 1. The cross sections for B + T → + - can be expressed as $\sigma_{BT}^F = \gamma_B^F \gamma_T$, where γ_T is the target factor. Plotted are the mean target factors versus the target mass A_T (amu) for all cross sections measured in this experiment. The error bars represent the error-weighted standard deviations and reflect the distribution of errors in the individual cross sections σ_{BT}^F. The mean errors for γ_T are approximately the dot size. The computed values of γ_T using the empirical fit are given by the symbol X. Physical parameters in the empirical expression for γ_T are r_T, the half-density charge radius and t, the charge-skin thickness of the target nuclei. The line superimposed on the data points is an approximation for $\gamma_T = A_T^{1/4}$.

mately fitted by the expression $\gamma_T = A_T^{1/4}$ or $\gamma_T \propto (A_B^{1/3} - 1.6)$. Both formulations for γ_T indicate the cross sections we observed are produced by peripheral interactions with the target. Neither formulation for γ_T explains the observed structure, however, particularly the result $\gamma_T(\mathrm{Be}) \geq \gamma_T(\mathrm{C})$. An accurate fit to the target factor is obtained by the expression $\gamma_T = kt^n(r_T + b)$ where r_T is the measured half-density electric charge radius and t is the measured charge skin thickness of the target. The three fitted variables are: the exponent $n = 0.5$, $b = 3.0$ fm, and normalizing constant $k = 0.26$. This formula reproduces the structure in the mean target factor to an accuracy better than 2% and with a confidence level of 0.9. Since σ^F_{BT} factors and the momenta distributions are target indpendent,[1] the partial differential cross sections factor—a result expected by limiting fragmentation models. Whether γ_T contains beam-dependent terms, e.g., the sum of radii of the beam and target nuclei, as suggested above, cannot be determined with the present data.

The energy dependence of isotope production can be examined by: 1) comparing σ^F_{BT}, for the two ^{12}C-beam energies, and 2) comparing σ^F_{BT} with values from Ref. 3 measured at different energies. The carbon data for all fragments are energy independent between 1.05 and 2.10 GeV/n and have an error-weighted mean ratio $\sigma^F_{BT}(2.10)/\sigma^F_{BT}(1.05) = 1.01 \pm 0.01$. Energy independence of σ^F_{BT}, above some energy threshold, is another result expected from high-energy phenomenology. A comparison of σ^F_{BT} for the same fragments and targets but different beams, ^{16}O and ^{12}C, shows, in general, a weak beam dependence in the production cross sections of all fragments in common, as long as a charge-exchange reaction is not necessary. The ratio $\sigma^F_{BT}(^{16}\mathrm{O})/\sigma^F_{BT}(^{12}\mathrm{C}) = 0.4$-$1.35$, even though the individual cross sections vary over three orders of magnitude. It is noteworthy that more than 40% of the ratios are in the interval 1.0 ± 0.15.

Production cross sections for mirror nuclei should give insight into the mechanisms which produce the observed final state. If a neutron skin extends beyond the proton surface, a stripping process would result in $\sigma_N/\sigma_P \leq 1$. We observe that, to the contrary, $1.0 < \sigma_N/\sigma_P < 4.1$, with most values of the ratio being in the interval 1.1 to 1.7. That $\sigma_N/\sigma_P > 1$ is indicative of the effects of the binding energy of the final state fragment. For example, inspection of the mass excess vs σ^F_{BT} for isobars shows the fragment with the lower mass excess has the higher production cross section. This dominance of final state structure in σ^F_{BT} complicates the choice of any simple mechanism describing the interaction process.

The patterns observed in σ^F_{BT} and in the momentum distributions[1,2] indicate simplicity in the peripheral fragmentation process. Target factorization, energy independence, and small transverse momenta are observed features of σ^F_{BT} and directly relate to limiting fragmentation models. The inclusion of a charge skin-thickness term in the best fit for γ_T, along with small parallel momenta widths in the beam rest frame, imply the observed fragments are the result of peripheral interactions. Neutron rich enhancement of mirror-isotope cross sections, correlations in fragment binding energies, and a surprising degree of beam independence in σ^F_{BT} indicate a dominance of fragment nuclear structure in the production amplitudes.

Footnotes and References

*Condensed from LBL-3650.

†University of California, Space Sciences Laboratory, Berkeley, California.

1. D. E. Greiner, P. J. Lindstrom, F. S. Bieser, and H. H. Heckman, Nucl. Instrum. Meth. 116, 21 (1974).

2. D. E. Greiner, P. J. Lindstrom, H. H. Heckman, Bruce Cork, and F. S. Bieser, Phys. Rev. Lett. 35, 152 (1975).

3. R. Silberberg and C. H. Tsao, NRL Report No. 7593, (1973). Also, F. Yiou, G. Raisbeck, C. Perron, and P. Fontes, 13th International Cosmic Ray Conference, Denver, Colorado, August 17-30, Vol. I, Paper No. 251.

4. R. Silberberg and C. H. Tsao, Ap. J. Suppl. No. 220(I), 25, 315 (1973).

FRAGMENTATION OF ^{40}Ar AT 100 GeV/c

P. J. Lindstrom, D. E. Greiner, H. H. Heckman,
Bruce Cork, and F. S. Bieser*

Introduction. Relativistic nucleus-nucleus reaction cross sections are basic ingredients of many cosmic ray computations. Without experimental data these cross sections have been largely a matter of guesswork. Relativistic heavy ion beams in the Bevatron-Bevalac at Berkeley now make these measurements possible. We present reaction cross sections of ^{40}Ar at 1.8 GeV/n, along with ^{16}O and ^{12}C at 2.1 GeV/n, on a variety of targets, measured in a simple transmission detector system.

Experimental Procedures. The computer controlled detector system used to measure the cross sections consists of two detector modules containing four one-inch diameter lithium-drifted silicon detectors, 3 mm thick, in a telescope configuration (see inset Fig. 1). The leading detector module identified the charge of the incident beam by energy loss. The primary beam is confined to a one-fourth inch diameter spot in the center of the first module by an anticoincidence scintillator. Targets,

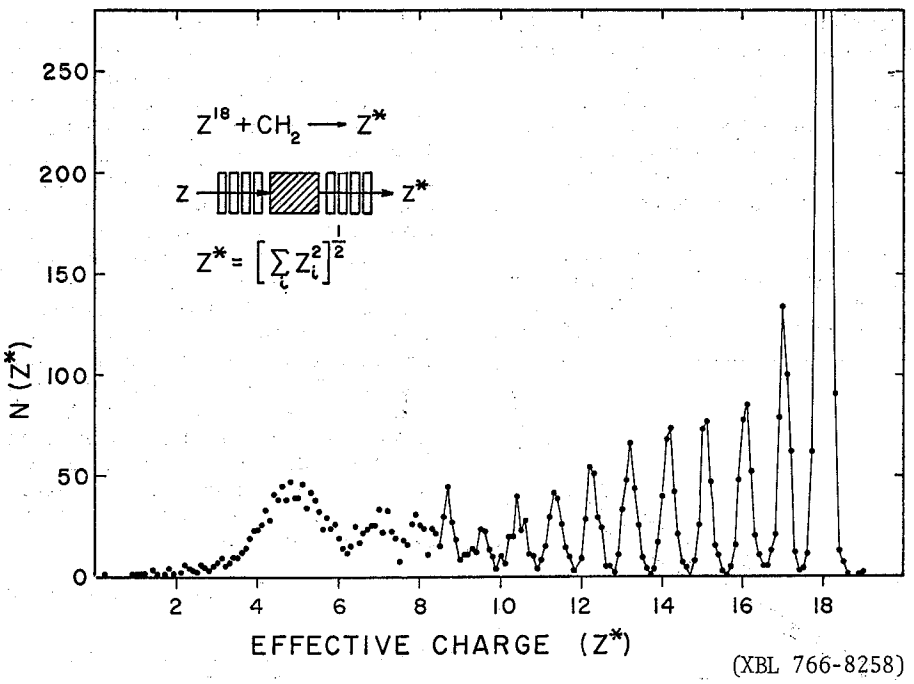

Fig. 1. Effective charge spectrum of fragments of ^{40}Ar at 1.8 GeV/c on a CH_2 target. The surviving primary beam is well resolved from the fragmentation products.

typically one-half of a mean free path thick, are placed between the detector modules. The second module of detectors serves to identify the interacting, as well as surviving, beam nuclei. The raw pulse heights of all eight detectors were preserved on tape for further analysis. The targets were CH_2, C, S, Cu, Ag, Pb, and U. In the analysis the events were ordered by their effective charge $Z^* = [(dE/dx)_{meas}/(dE/dx_p)]^{1/2}$ and by their $\chi^2 = \sum_{i=1}^{n} (Z^* - \bar{Z}^*)^2/\sigma_i^2$ in each detector module. Figure 1 is a typical spectrum of effective charge with $\chi^2 \leq 5.0$ for 1.8 GeV/n ^{40}Ar on a 6.981 g/cm^2 thick CH_2 target. The standard deviation of the Z =18 peak is $\sigma = \pm .11e$. The charge of the highest Z fragment is resolved down to Z = 10. Note that the effective charge peaks are shifted from unit charges, e.g., Z* (charge 10) $= [\Sigma Z_i^2]^{1/2} \approx [10^2 + 8]^{1/2} = 10.4$ implying the charge 10 fragments traveling at beam velocity. The cross section for $\Delta Z \geq 1$ of the primary beam is calculable from its survival. The partial production cross sections for element with $Z \geq 10$ can be calculated from their peaks.

Reaction Cross Sections. The results are presented in Table 1. The $\Delta Z \geq 1$ cross sections ^{12}C and ^{16}O at 2.1 GeV/n from an earlier run are also presented. By adding the isotope production cross section for $\Delta Z = 0$ to the $\Delta Z \geq 1$ cross section we obtain

Table 1. Reaction cross sections (barns).

	Beam						
	^{40}Ar		^{16}O		^{12}C		^{1}H
Target	$\Delta Z \geq 1$	$\Delta Z \geq 1$	$\Delta Z \geq 1$	$\Delta A \geq 1$	$\Delta Z \geq 1$	$\Delta A \geq 1$	Reaction[a]
H	.58±.04	.68±.05	.32±.02	.34±.02	.22±.02	.25±.02	
C	1.36±.03	1.52±.06	.94±.02	.98±.02	.75±.02	.81±.02	.23±.01
S	1.94±.07	2.13±.09	1.31±.05	1.37±.05	1.15±.05	1.22±.05	
Cu	2.62±.05	2.85±.08	1.82±.03	1.90±.03	1.62±.03	1.71±.03	.71±.02
Ag	3.20±.07	3.47±.11					
Pb	4.19±.13	4.51±.16	3.10±.07	3.24±.07	2.82±.06	2.97±	1.78±.05
U	4.61±.21	5.00±.24					

[a] 550 MeV protons from Ref. 3. Targets not in common are also plotted in Fig.2.

the reaction cross sections for $\Delta A \geq 1$. The isotope production cross section of Lindstrom et al.[1] for $\Delta A = 1$, two were used for correcting ^{12}C and ^{16}O. The computed isotope cross section for $\Delta Z = 0, \Delta A \geq 1$ by Silberberg and Tsao,[2] corrected by the $\Delta Z = 1$ production cross section of this ^{40}Ar data, were used to compute the $\Delta A \geq 1$ cross sections are in Table 1 along with σ_r for proton-nucleus from Renberg et al.[3]

An empirical expression for nucleus-nucleus reaction cross section, first proposed by Bradt and Peters, is $\sigma_{BT} = -\pi r_0^2 (A_B^{1/3} + A_T^{1/3} - b)^2$ where A_b and A_T are the mass numbers of the beam and target nuclei

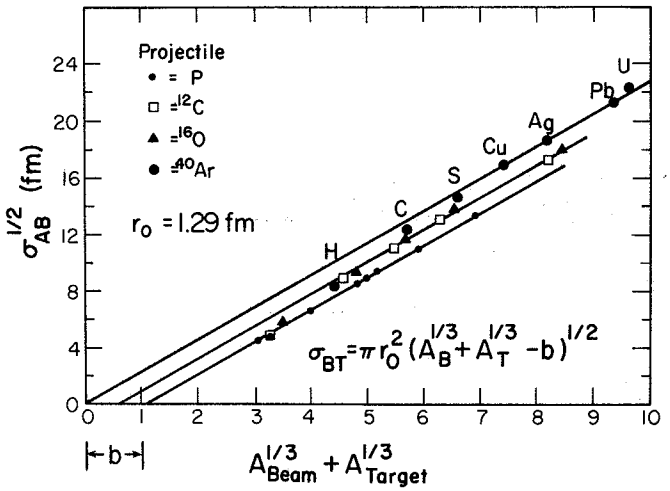

Fig. 2. Plotted are $\sigma_{AB}^{1/2}$ for 40 Ar, ^{16}O, ^{12}C, and ^{1}H on targets of mass A_T, where σ_{AB} = reaction cross section for nucleus A on nucleus B and $A_{T,B}$ = mass number of the respective nuclei. If $\sigma_{AB} = \pi r_0 (A_A^{1/3} + A_B^{1/3} - b)^2$ then all of the data should fall on a single straight line. (XBL 766-8259)

and b is an overlap parameter. Figure 2 is a plot of $\sigma_{BT}^{1/2}$ vs $(A_B^{1/3} + A_T^{1/3})$ of the reaction cross section in Table 1. The slope is $\pi^{1/2} r_0$ giving $r_0 = 1.29$, and the x intercept is b. The data can be roughly fitted by $b = 1 - 0.028\ A_{min}$ if the mininum mass number $A_{min} = \min(A_B, A_T) \leq 36$ and $b = 0$ if $A_{min} \geq 36$. This equation fits the experimental cross sections to within 10% in all but 3 cases; the worst excursion is 18%. Theoretical computations of the total reaction cross section σ_r by Barshay et al.[4] using the Glauber model support a variable overlap and indicate the minimum overlap is reached when $A_{min} \approx 40$. We find when $A_{min} = 40$, $b_{min} \approx 0$, consistent with black sphere geometrcial cross sections. The Glauber model production of total reaction cross sections fit the data with accuracy comparable to the variable overlap model. Both the Glauber model and the modified Bradt and Peters formula are well outside of experimental errors. There is room for further refinement in reaction cross section models.

Footnotes and References

*University of California Space Sciences Laboratory, Berkeley, California.

1. P. J. Lindstrom, D. E. Greiner, H. H. Heckman, B. Cork, and F. S. Bieser, 1975, LBL-3650 (to be published).

2. R. Silberberg and C. H. Tsao, Ap. J. Suppl. No. 220 (I), 25 315 (1973).

3. P. U. Renberg, D. G. Measday, M. Pepin, P. Schwaller, B. Favier, and C. Richard-Serre, Nucl. Phys. A183 81 (1972).

4. S. Barshay, C. B. Dover, and J. P. Vary, Phys. Rev., C11 860 (1974).

FRAGMENTATION OF ^{4}He, ^{12}C, ^{14}N, AND ^{16}O NUCLEI IN NUCLEAR EMULSION AT 2.1 GeV/NUCLEON*

H. H. Heckman, D. E. Greiner, P. J. Lindstrom, and H. Shwe†

We have undertaken a study of the interactions of 2.1-GeV/n ^{4}He, ^{12}C, ^{14}N, and ^{16}O nuclei in nuclear research emulsion, with emphasis on the interaction mean-free-paths and the properties of projectile fragmentation. The path-length data are satisfactorily interpreted in terms of a two parameter expression for the geometrical cross section. These parameters are r_0, defined by the expression for the nuclear radius, $r = r_0 A_i^{1/3}$, and b, the overlap parameter. The quantity b is equal to $\Delta r/r_0$, where Δr is the geometrical overlap between the colliding nuclei. About 13% of the interactions of C, N, and O beam particles with emulsion nuclei lead to "pure" projectile fragmentation, characterized by the fact that no target fragmentation, e.g., low energy, charged-particle evaporation, is detected in the interaction. We have selected these interactions for specific study of projectile fragmentation.

The emulsion stacks were fabricated from Ilford G.5 pellicles, 600 microns thick. The stacks were exposed to the heavy ion beams parallel to the emulsion planes. The scanning technique for each beam was to select an incident ion 1 to 2 mm from the entrance edge and scan along the track until the ion interacted or left the pellicle. The scanning and measurements were performed with three-coordinate digitized microscopes with one micron read-out accuracy. The interactions were classified as follows:

Type 1. Projectile fragmentation, no visible target fragmentation.

Type 2. Target and projectile fragmentation. Projectile may fragment, as in Type 1, or suffer catastropic destruction.

Type 3. Target fragmentation, no detectable change in charge of the incident ion, i.e., the inverse of Type 1.

Events of Type 1 were selected for the study of projectile fragmentation. They were intensively examined for all secondary particles, for which ionization and angle measurements were made [±0.16° (S.D.) in the horizontal plane and ± 0.39° in the vertical plane].

Table 1 summarizes the data interaction mean-free-path-length results of the experiment. The scanning efficiency was near 100% for events in which the difference betweeen the charges of the beam and principal fragment $\Delta Z = Z_B - Z_F \geq 2$. Fragmentation events for which $\Delta Z = 0$ or 1 tend to be missed, particularly when there is little or no evidence for excitation of the target nucleus. A re-scan of about one-third of the C,N, O-tract data contributed, out of 1059 events, 16 new events, all of which were Types 1 and 3, $\Delta Z = 0$, and 1 only.

The isotope production cross section of Lindstrom et al.[1] were used to correct for the scanning losses of $\Delta Z = 0$ and 1 events. The corrections to N_{obs} (to give N_{total}) were: ^{12}C, 16 ± 25; ^{16}O, 69 ± 21; and by interpolation of the C and O cross section ^{14}N, 31 ± 33. No corrections were made to the ^4He data. Given in Table 1 are the number of events $N_{\Delta Z \geq 1}$, for which the charges of the principal fragment differs from that of the incident ion by $\Delta Z \geq 1$. Table 1 concludes with the measured interaction-mean-free paths, λ_{total} and $\lambda_{\Delta Z \geq 1}$ in nuclear emulsion for ^4He, ^{12}C, ^{14}N, ^{16}O nuclei, E = 2.1 GeV/n.

An empirical expression for the total reaction cross section that is useful to interpret the data given in Table 1 is the geometrical formula first proposed by Bradt and Peters,[2]

$$\sigma_{BT} = \pi r_0^2 (A_B^{1/3} + A_T^{1/3} - b)^2. \qquad (1)$$

where A_B and A_T are the mass numbers of the beam and target nuclei, respectively, the constant b is the overlap parameter and r_0 is the constant of proportionality in the expression for the geometrical nuclear radius $r_i = r_0 A_i^{1/3}$. Because the parameters r_0 and b are coupled, we find that consistent fits to our mean-free-path data can be obtained for r_0 and b in the ranges $1.4 \leq r_0 \leq 1.7$ fm and $1.2 \leq b \leq 1.9$. The fragmentation cross sections ($\Delta Z \geq 1$) measured by Lindstrom, et al.,[3] for ^{12}C and ^{16}O, E = 2.1 GeV/n, gave the first evidence that the overlap b is not constant, but depends upon the mass, i.e., radius, of the beam nucleus. The theoretical results of Bowman, Swiatecki, and Tsang[4] and Barshay, Dover, and Vary[5] support this observation. Bowman et al., describe heavy ion collisions under the conditions of i) abrasion, the shearing off of nuclear volume of the projectile by the target and ii) ablation, further loss of material by the projectile due to evaporated particles. From this model one obtains and expression for the overlap parameter $b_{\Delta Z \geq 1}$ that is appropriate for the shearing-off of at least one unit of charge.[6] In their investigation on the factorization of total cross sections in nucleus-nucleus collisions, Barshay et al.[5] calculated the total reaction cross sections using Glauber theory and a geometrical nuclear model. The numerical results given in Tables 3 and 4 of Barshay et al.[5] can be ordered in terms of the Bradt-Peters relation, Fig. 1. We have determined, by least squares fitting, the overlap parameter b_{total} appropriate to these total reaction cross sections as a function of projectile mass A_B, i.e., the lighter of the two interacting nuclei.

Table 1. Interaction mean-free-path length data. Tabulated are: N_i, the number of observed interactions of type 1, $N_{obs} = \Sigma_i N_i$, $N_{total} = N_{obs}$ corrected for scanning losses of $\Delta Z = 0$ and 1 events, and $N_{\Delta Z \geq 1}$, the number of charge-changing ($\Delta Z \geq 1$ events. The interaction lengths evaluated from N_{total} and $N_{\Delta Z \geq 1}$ are λ_{total} and $\lambda_{\Delta Z \geq 1}$, respectively.

Beam	^4He	^{12}C	^{14}N	^{16}O
N_1	104	149	118	119
N_2	853	858	883	849
N_3	54	88	58	55
N_{obs}	1011	1095	1059	1023
N_{total}	1011	1111±39	1090±47	1092±38
$N_{\Delta Z \geq 1}$	957	1044±39	1031±45	1040±36
Pathlength(cm)	22080	15302	14895	14174
λ_{total} (cm)	21.8±0.5	13.8±0.5	13.7±0.6	13.0±0.5
$\lambda_{\Delta Z \geq 1}$ (cm)	23.1±0.8	14.7±0.6	14.5±0.6	13.6±0.5

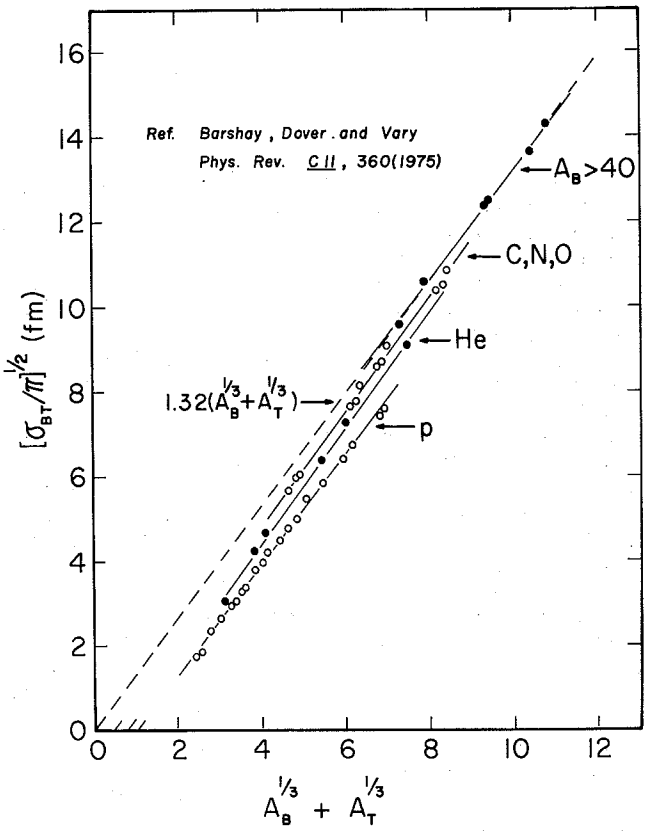

Fig. 1. Least squares fits to the total reaction cross sections computed by Barshay, Dover, and Vary (Ref. 5) ordered by $A_B \equiv A_{min}$, the mass of the lighter of the two interacting nuclei in terms of the Bradt-Peters relation, Eq. 1. The intercepts with the abscissa are the overlap parameters b for the specific cases where A_B is 1, 4, [12, 14, 16] and > 40. The values of b versus A_B are tabulated in Table 2. (XBL 758-1914)

Table 2. Overlap parameters b derived from theory and experiment used to calculate interaction path lengths $\lambda_{\Delta Z \geq 1}$ and λ_{total} for comparison with this experiment. The r_0 radii are from least squares fits to the numerical results given in Ref. 5.

Beam (A_B)	$b_{\Delta Z \geq 1}$ [a]	$b_{\Delta Z \geq 1}$ [c]	r_0 [d] (fm)	b_{total} [d]	b_{total} [c]
1	0.97-0.91	1.0(^{12}C),1.2(^{16}O)	1.31±0.02	1.04±0.07	1.0(^{12}C),1.2(^{16}O)
4	0.88-0.80		1.37±0.03	0.81±0.17	
12	0.81-0.71	0.66			0.47
12,14,16	0.80-0.70[b]		1.35±0.03	0.48±0.17	
16	0.79-0.69	0.50			0.30
≥40			1.29±0.02	-0.21±0.20	
			r_0(av.)= 1.32±0.02		

[a] Ref. 4. To indicate target dependence of Eq. 2, $b_{\Delta Z \geq 1}$ for H and Pb targets are given.
[b] Also equal to $b_{\Delta Z \geq 1}$ for A_B = 14.
[c] Ref. 3.
[d] Ref. 5 and Fig. 1.

To interrelate the results of this experiment with those of Lindstrom et al., Bowman et al. and Barshay et al., we take the following approach: 1) Select the appropriate value of the overlap parameters b, given in Table 2, for each beam particle and nuclear constituents in emulsion. 2) Compute $\lambda_{calc.} = (\Sigma_i n_i(T)\sigma_{BT})^{-1}$, where $n_i(T)$ is the number of nuclei T per milliliter in emulsion. 3) Determine the best estimate of r_0 by the minimization of $\chi^2 = (\Sigma_i \lambda - \lambda_{calc})^2/\sigma_i^2$.

The computed path lengths are compared with experiment in Table 3. We find that the mean-free-path lengths of ^{4}He, ^{12}C, ^{14}N and ^{16}O nuclei in

Table 3. Calculated interaction mean-free-path lengths (cm) using overlap parameters b derived from Refs. 3, 4, and 5 and values of r_0 that give minimum χ^2 fits to data of this experiment.

	b	r_0 (fm)	^{4}He	^{12}C	^{14}N	^{16}O
$\lambda_{\Delta Z \geq 1}$ (cm)	Eq. (2) Ref. 4)	1.24	22.3	15.2	14.3	13.6
	Table 4 (Ref. 3)	1.23		15.7	13.7	13.2
Experiment			23.1±0.8	14.7±0.6	14.5±0.6	13.6±0.5
λ_{total} (cm)	Table 3 (Ref. 5)	1.25	22.2	14.1	13.4	12.8
	Table 3 (Ref. 3)	1.23		14.7	13.4	12.4
Experiment			21.8±0.7	13.8±0.6	13.7±0.6	13.0±0.5

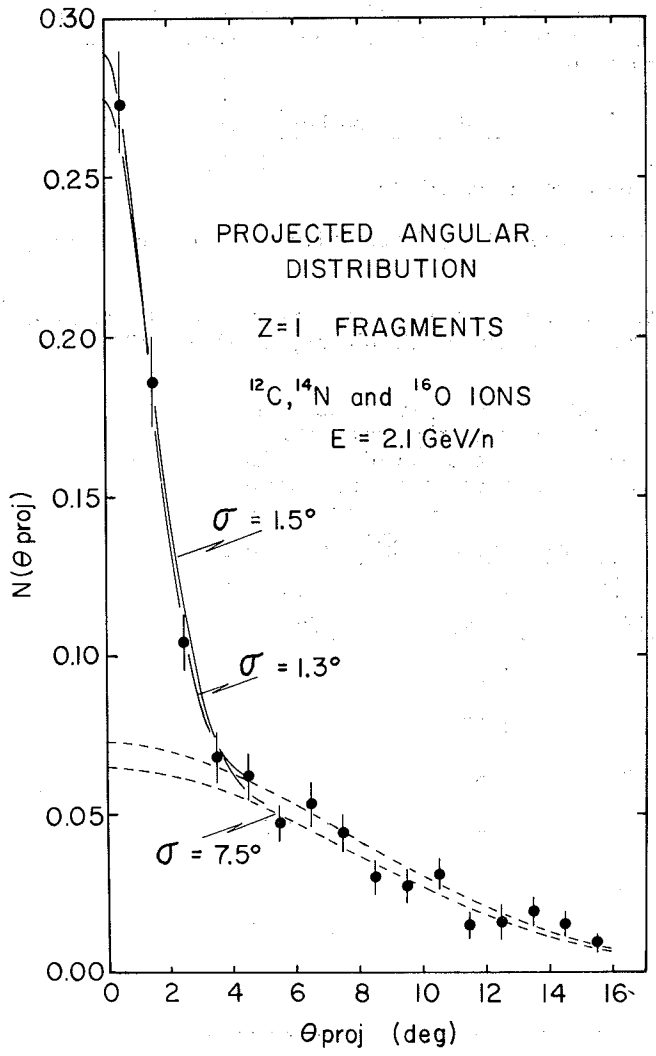

Fig. 2. The combined projected angular distribution for Z = 1 fragments, C, N, and O projectiles, $\theta_{proj} \leq 16°$. The shaded area is bounded by curves that are the sum of two Gaussian distributions, $\sigma = 1.3°$ and $1.5°$, and $7.5°$, normalized to unit areas. (XBL 758-1913)

emulsion are well accounted for by the Bradt-Peters expression, Eq. (1). The observations are best explained when $r_0 \approx 1.24$ fm and the overlap parameters b is a variable dependent on $A_B \equiv A_{min}$, the lighter of the projectile and target nuclei partaking in the collision, Fig. 1. However, the possibility that b may depend upon both the projectile and target nuclei cannot be rule out by the present experiment.

Approximately 10% of all the C, N, and O fragmentation is emulsion exhibit projectile fragmentation only, i.e., Type 1. Figures 2 and 3 present, respectively, the composite projected angular distribution for Z = 1 and Z = 2 secondaries from the fragmentation of ^{12}C, ^{14}N and ^{16}O nuclei at 2.1 GeV/n. The angular distribution data were combined because we observed no statistically significant difference between them. The projected angular distribution for Z = 1 particles, shows a peaked distribution at 0 deg, with about 99% of all secondaries restricted to the forward hemisphere. In Fig. 2 we show the structure of the Z = 1 distribution for $\theta_{proj} \leq 16$ deg. The projected angular distribution has a narrow central peak, superimposed upon, and distinct from, a broader distribution. The observed projected angular distribution for Z = 2 secondaries is given in Fig. 3. This distribution is dominated by a narrow forward peak, having a characteristic width $\lesssim 1.^0$

In Table 4 we tabulate the average momentum widths (S.D) for the CNO group measured by Greiner,

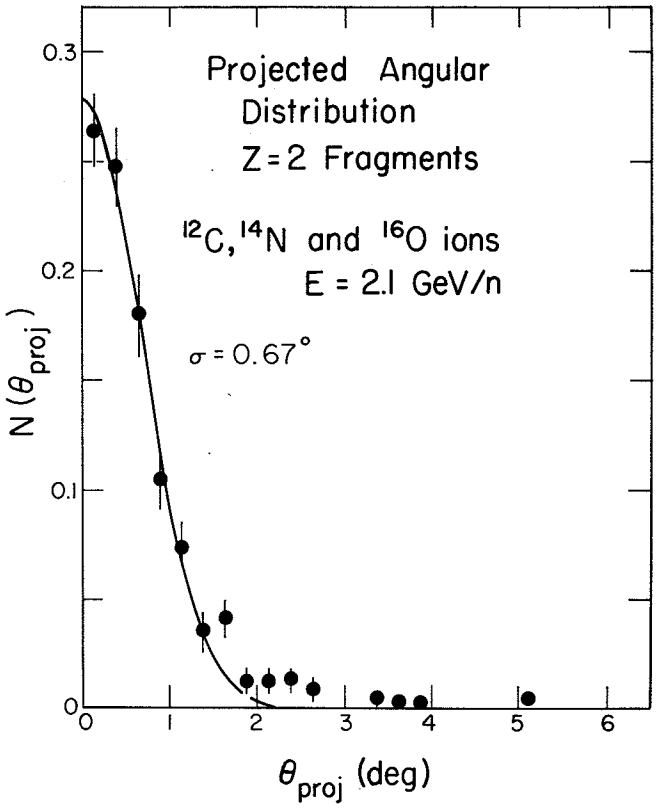

Fig. 3. Angular distribution, projected onto the emulsion plane, for He (Z = 2) fragments, from the fragmentation of ^{12}C, ^{14}N, and ^{16}O projectiles. All interactions of Type 1. Curve is a Gaussian distribution, $\sigma = 0.67°$, fitted to the data for $\sigma_{proj} \leq 1.5°$. (XBL 766-8257)

et al.[7] and given by the theoretical work of Lepore and Riddell,[8] and the corresponding angular widths $\sigma(\theta_{proj})$ for the Z=1 and 2 isotopes. The production-weighted values of $\sigma(\theta_{proj})$, denoted as $\sigma_{Z=1}$ and $\sigma_{Z=2}$ are the quantities to be compared with the experimental results.

Referring to Fig. 2, the narrow, forward peak of the Z=1 fragments can be fitted by a Gaussian distribution, with $\sigma_{Z=1} = 1.3\text{-}1.5°$, in good agreement with the results of Greiner, et al.[7] and the theory of Lepore and Riddell,[8] provided the large-angle background events can be described by a Gaussian distribution $\sigma \approx 7.5°$, whose amplitude is about 1/3 of the central peak. Figure 3 is the projected angular distributions for the Z=2 (He) isotopes from the fragmentation of C,N, and O nuclei in emulsion. Drawn through the distribution is a Gaussian curve whose σ(S.D.) = 0.67° is based on data restricted to $\theta_{proj} \leq 1.5°$. Correcting for measurement error, we obtain $\sigma_{Z=2} = 0.65°$.

The general agreement between the values of $\sigma_{Z=1}$ and $\sigma_{Z=2}$ from the data of Greiner, et al., (which pertain to longitudinal momentum distributions) and this experiment argues for the equality of the longitudinal and transverse momentum distributions inthe projectile frame for the respective Z=1 and Z=2 nuclei. Furthermore, within measurement errors, we also have verified that the transverse momentum distributions of the He nuclei projected onto orthogonal planes in the emulsion are equal. Thus, to about a 10% level, we have shown the momentum distribution of the He isotopes in the projectile frame of reference is consistent with isotropy.

Footnotes and References

*Condensed from LBL-3656.

†East Stroudsburg State College, East Stroudsburg, Pa.

1. P. J. Lindstrom, D. E. Greiner, H. H. Heckman, Bruce Cork, and F. S. Bieser, LBL-3650 (1975).

Table 4. Standard deviation widths of the momentum and projected angular distributions for the Z=1 and 2 secondary isotopes from the fragmentation of the CNO group at E=2.1 GeV/n. The production-weighted angular widths of Z=1 and Z=2, respectively. Experimental data based upon Type 1 events.

	Greiner, et al.[7]		Riddell and Lepore[8]		This experiment
Fragment (wt)	σ(p) (MeV/c)	$\sigma(\theta_{proj})$ (deg)	σ(p) (MeV/c)	$\sigma(\theta_{proj})$ (deg)	σ_{exp} (deg)
p (0.74)	69±6	1.38±0.11	79	1.58	
d (0.19)	134±4	1.34±0.04	107	1.07	
t (0.07)	144±6	0.96±0.04	126	0.84	
		$\sigma_{Z=1}$=1.35±0.11		1.45	1.3 -1.5
^{3}He(0.24)	150±6	1.00±0.04	126	0.84	
^{4}He(0.76)	130 ± 1	0.65±0.005	138	0.69	0.64±0.02
		=0.73±0.06		0.73	

2. H. C. Bradt and B. Peters, Phys. Rev. 77, 54 (1950).

3. P. J. Lindstrom, D. E. Greiner, and H. H. Heckman, Bull. Am. Phys. Soc. 17, 488 (1972). Also H. H. Heckman, Relativistic Heavy Ion Seminar, Internal LBL Report, 1973 (unpublished).

4. J. D. Bowman, W. J. Swiatecki, and C. F. Tsang, LBL-2908 (1973).

5. S. Barshay, C. B. Dover, and J. P. Vary, Phys. Rev. C 11, 360 (1975). Alsp private communication, J. P. Vary (1975).

6. W. J. Swiatecki and C. F. Tsang, private communication (1974).

7. D. E. Greiner, P. J. Lindstrom, H. H. Heckman, B. Cork, and F. S. Bieser, Phys. Rev. Lett. 35, 152 (1975).

8. J. V. Lepore and R. J. Riddell, Jr., LBL-3068, 1974 (unpublished).

COULOMB DISSOCIATION OF RELATIVISTIC ^{12}C AND ^{16}O NUCLEI

Harry H. Heckman and Peter J. Lindstrom

Experimental evidence for the dissociation of Bevatron/Bevalac beam nuclei in the nuclear Coulomb fields of target nuclei has come from experiments on the target dependence of the isotopic production cross sections for secondary nuclei produced by the fragmentation of ^{12}C and ^{16}O nuclei at energies E = 1.05 GeV/n (^{12}C) and 2.1 GeV/n (^{12}C and ^{16}O).[1] By use of photonuclear cross section data and the Weizsacker-Williams (WW) method of virtual quanta,[2,3] we are able to account for the measured cross sections and to determine the minimum impact parameters for Coulomb dissociation of heavy-ion projectiles.

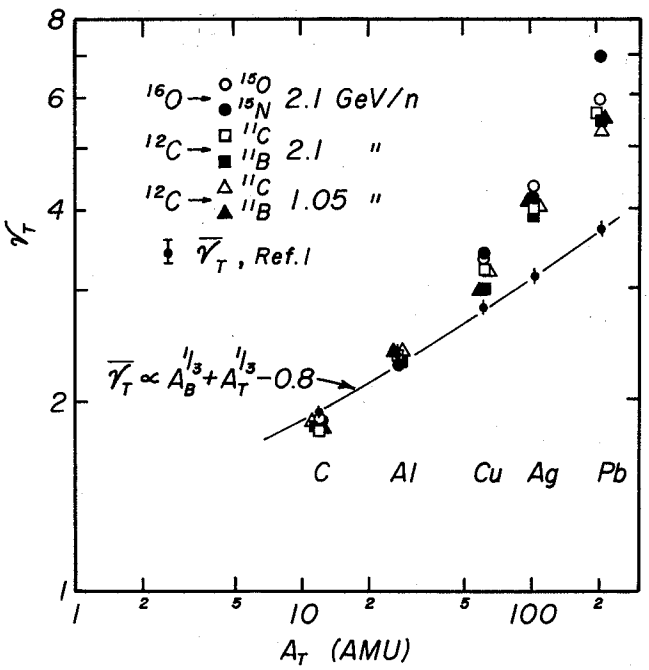

Fig. 1. Target factors γ_T plotted versus target mass A_T(AMU), from Lindstrom, et al.[1] Individual values of γ_T are shown for the single-nucleon-loss cross sections indicated. The curve $\bar{\gamma}_T \propto A_B^{1/3} + A_T^{1/3} - 0.8$ is drawn through the mean tarfet factors, shown with error bars, for all cross sections σ_{BT}^F, where $A_F \leq A_B - 2$. (XBL 763-882)

Essential to our analysis is that the cross sections σ_{BT}^F for the reaction B + T → F + ..., where B, T and F are the beam, target and fragment nuclei, are factorable. That is, $\sigma_{BT}^F = \gamma_B^F \bar{\gamma}_T$, where σ_B^F is dependent on B and F only and $\bar{\gamma}_T$ is the target factor. Plotted in Fig. 1 are the target factors $\gamma_T = \sigma_{BT}^F / \gamma_B^F$ versus target mass A_T(AMU).[1] For fragment nuclei with mass $A_F \leq A_B - 2$, i.e., at least two nucleons are removed from the beam projectile, all isotopic production cross sections, for a given target, are interrelated by a unique target factor, $\bar{\gamma}_T$. Striking deviation of γ_T from $\bar{\gamma}_T$, up to 30% in Pb, are observed for those fragmentation cross sections that involve the loss of one nucleon from the projectile. The differences between the observed values of γ_T and $\bar{\gamma}_T$ increase approximately as Z_T^2 of the target, indicative of the Coulomb effect.

We have applied the Weizsäcker-Williams method of virtual quanta to estimate the cross sections for Coulomb dissociation of relativistic nuclei.[2-4] To the extent that N(ω), the equivalent number of virtual photons per MeV, is the same for all electric and magnetic multipoles, the Weizsäcker-Williams cross section for the dissociation of a nucleus, at velocity β, by the Coulomb field of a target nucleus, atomic number Z, is given by

$$\sigma_{WW} = \int_{\omega_0} \sigma_\nu(\omega)\, N(\omega)\, d\omega \,, \qquad (1)$$

where $\sigma_\nu(\omega)$ is the measured photonuclear cross section at photon energy ω. The number density of virtual photons has the functional form $N(\omega) = (Z^2/\omega\beta^2)\, F(\beta, \omega b_{min}/\beta\gamma)$, where b_{min}, the minimum impact parameter, is the only adjustable parameter in σ_{WW}.

By equating σ_{WW}, Eq. (1), we have determined that the impact parameter b_{min} appropriate for each cross section. The minimum impact parameter is defined by the relation $b_{min} = r_{0.1}^B + r_{0.1}^T - d$, where the $r_{0.1}$'s are the 10% charge-density radii of the beam and target nuclei,[5] and d is the radial-overlap distance. The values of b_{min} obtained in this experiment are, to within the accuracy of the data, confined to a limited range

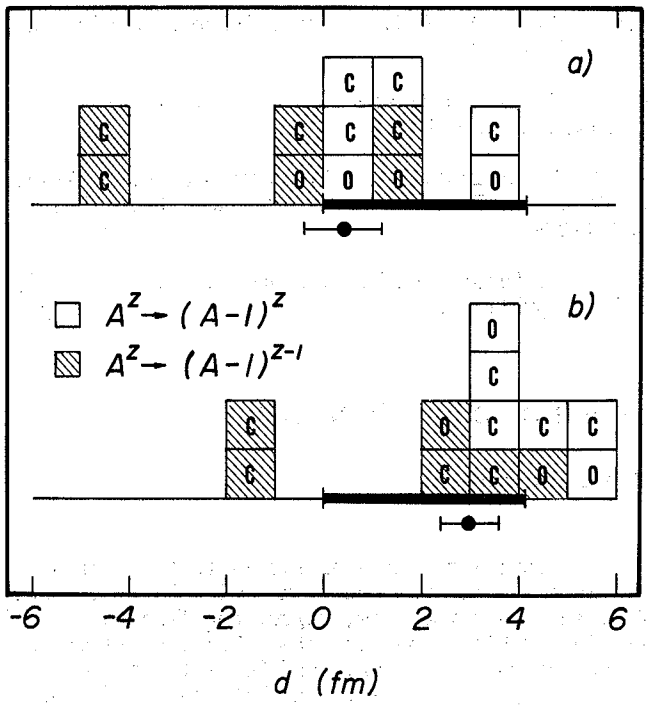

Fig. 2. Distributions of overlap distances $d(b_{min})$, and their means, derived from $\sigma_{WW}(exp)$ when fitted to the Weizsäcker-Williams cross sections σ_{WW}, as given by a) Jackson[2] and b) Jäckle and Pilkuhn.[3] The dark horizontal bar delineates the overlap region bounded by $0 \leq d \leq t_B + t_T$, the sum of the charge-skin thicknesses of the beam and target nuclei. (XBL 763-881)

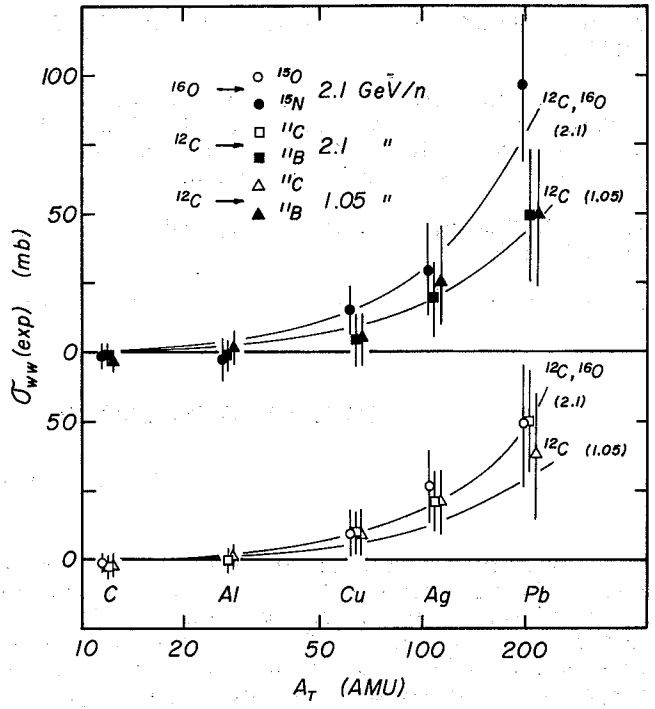

Fig. 3. Target dependence of the measured cross sections $\sigma_{WW}(exp)$ for the Coulomb dissociation reactions indicated. The curves are computed using the Jäckle and Pilkuhn form of σ_{WW} with $\bar{d} = 3.0$ fm. (XBL 763-883)

in d. Presented in Fig. 2 are histograms of the overlap-distances d that account for the experimental cross sections $\sigma_{WW}(exp)$ for ^{12}C and ^{16}O projectiles in Ag and Pb targets.

The standard deviations of the d-distributions are compatible with the statistical errors in σ_{WW} (exp). Principle systematic errors come from theory (N(ω)), the measure photonuclear cross sections $\sigma_\nu(\omega)$, and those inherent in the method used to extract $\sigma_{WW}(exp)$ from σ^F_{BT}. A 12% change in $\sigma_\nu(\omega)$, a typical error in the photonuclear cross section data, leads to a 1-fm change in $d(b_{min})$.

Figure 3 presents the cross-section data from this experiment, $\sigma_{WW}(exp) = \sigma^F_{BT} - \gamma^F_B \bar{\gamma}_T$, plotted as a function of target mass. Superimposed on the data are curves of the computed cross sections σ_{WW} (Jäckle and Pilkuhn) evaluated for a constant over overlap distance $\bar{d} = 3.0$ fm.

Following Lindstrom et al.,[1] we find that for $A_T \geq 12$, $\bar{\gamma}_T \propto (A_B^{1/3} + A_T^{1/3} - 0.8)$ (see Fig. 1), which when expressed in terms of $r_{0.1}$ becomes $\bar{\gamma}_T \propto (r^B_{0.1} + r^T_{0.1} - 2.0)$. Thus, we find that an effective overlap distance in $\bar{\gamma}_T$ of $d' = 2.0$ fm accounts for the nuclear (direct-interaction) part of the total fragmentation cross sections, a value that agrees well with the $\bar{d}$'s (0.4 and 3.0 fm, see Fig. 2) deduced from the impact parameters that account for the Coulomb dissociation cross sections.

The salient features of $\sigma_{WW}(exp)$, we conclude, are attributable to the fragmentation of projectile nuclei by the Coulomb field of the target nucleus. The value of b_{min} derived from $\sigma_{WW}(exp)$ limits the radial overlap, $\bar{d}$, of the colliding nuclei to distances comparable to their charge-skin thicknesses, t, a manifestation of the effects of nuclear absorption. The Coulomb and nuclear fragmentation processes are related by the result that $\bar{d} \approx d'$ which shows that the maximum overlap distance that accounts for Coulomb dissociation, in essence, tantamount to the nuclear overlap distance required to account for nuclear (direct-interaction) fragmentation.

Footnotes and References

*Condensed from LBL-4380.

1. P. J. Lindstrom, D. E. Greiner, H. H. Heckman, Bruce Cork, and F. S. Bieser, LBL-3650 (1975).

2. J. D. Jackson, Classical electrodynamics, 2nd ed., p 719, New York Wiley (1975).

3. R. Jäckle and Pilkuhn, Nuc. Phys. A247, 521 (1975).

4. X. Artru and G. B. Yodh, Phys. Letters 40B, 43 (1972).

5. R. Hofstadter and H. R. Collard, "Nuclear radii determined by electron scattering," in Numerical Data and Functional Relationship in Science and Technology, Vol. 2, H. Schopper, ed. (Springer Verlag, 1967, p.21.

PRODUCTION OF LIGHT NUCLEI IN NUCLEUS-NUCLEUS COLLISIONS AT 1.5 AND 2.1 GeV/NUCLEON

J. Papp,* J. Jaros,† L. Schroeder, J. Staples,
H. Steiner, A. Wagner,‡ and J. Wiss

The availability of heavy-ion beams at Berkeley with kinetic energies in the range of 1-2 GeV/nucleon has opened up new areas of experimental investigation. In this experiment, we measured the single-particle inclusive spectra of light nuclei (p,d,^{3}He,^{3}He, α) produce at 2.5° (lab) by beams of 1.05 and 2.1 GeV/n deuterons and alphas, and by 1.05 GeV/n carbon nuclei bombarding a variety of targets (Be,C,Cu,Pb). The detection system consisted of a magnetic spectrometer which measured p/z from 0.50 to 5.0 GeV/c, and plastic scintillation counters for measuring TOF and dE/dx.

There were several reasons for making these measurements:

1. To obtain information on the nuclear structure of the incident projectile by studying projectile fragmentation.

2. To test whether high energy physics concepts, such as scaling and limiting fragmentation can be applied to nuclear processes at these energies.

Data[1] for the production of light nuclei at 2.5° (lab) by 1.05 GeV/n incident deuteron, alpha, and carbon nuclei on a carbon target are shown in Fig. 1 (a,b,c). The Lorentz invariant cross section $E/k^2\ d^2\sigma/d\Omega dk$ is plotted against the momentum (k) of the detected fragment. From these data we can make the following observations concerning fragments lighter than the projectile:

1. The alpha particle is seen to fragment into protons, as well as significant numbers of deuterons, tritons, and ^{3}He.

2. For each projectile, the momentum spectra for individual fragments are strongly peaked, and extend over approximately 2 to 3 orders of magnitude in the cross

3. The value of the momentum at the peak of each of these fragmentation distributions is approximately equal to the momentum/nucleon in the incident projectile. This feature has been observed for heavier fragments from beams of carbon, nitrogen, and oxygen by Heckman and collaborators.[2]

4. Where overlapping data points exist, the ^{3}H and ^{3}He production cross sections agree reasonably well as expected for particles from the same isospin multiple.

For fragments more massive than the projectile (Fig. 1a) the spectra are observed to fall off as the momentum is increased. This is to be expected if these particles are either knocked out of the target, the result of pick-up processes, or arise from complicated final-state interactions.

Some insight into the production mechanism can be obtained by studying the dependence of the production cross section on the target mass. We have parametrized the production cross section in the form: $\sigma \propto A^n$, where A is the mass of the target. In Fig. 2 we have plotted the coefficient n versus the momentum of the produced particle for alpha particle collisions at 1.05 GeV/n. For momenta in the projectiles fragmentation region the cross section varies as $A^{1/3}$, suggestive of a peripheral interaction. At lower momentum the cross section exhibits a rapid growth. For the case of tritons the cross section starts to approach A^2. The following picture of the production of light nuclear particles at forward angles emerges. At high momenta, projectile fragmentation dominates all processes and is a surface phenomena varying as $\sim A^{1/3}$. As the momentum is decreased other processes start to contribute to the cross section. The exact nature of these processes is not known at present, but will be the subject of future investigations.

We are presently studying these data to see if limiting fragmentation for processes like $d + A \rightarrow p + X$ or $\alpha + A \rightarrow p + X$ holds at these energies.

Footnotes and References

*Watkins-Johnson Corp., Redwood City, California.

†Stanford Linear Accelerator Center, Stanford, California.

‡DESY - Heidelberg Group, Hamburg, Germany.

1. J. Papp, Single Particle Inclusive Spectra Resulting from the Collision of Relativistic Protons, Deuterons, Alpha Particles, and Carbon Ions with Nuclei, LBL-3633 (unpublished thesis).

2. H. H. Heckman, D. E. Greiner, P. J. Lindstrom, and F. S. Bieser, Phys. Rev. Letters, 28, 921 (1972); D. E. Greiner, P. J. Lindstrom, H. H. Heckman, B. Cork, and F. S. Bieser, Phys. Rev. Lett. 35, 152 (1975).

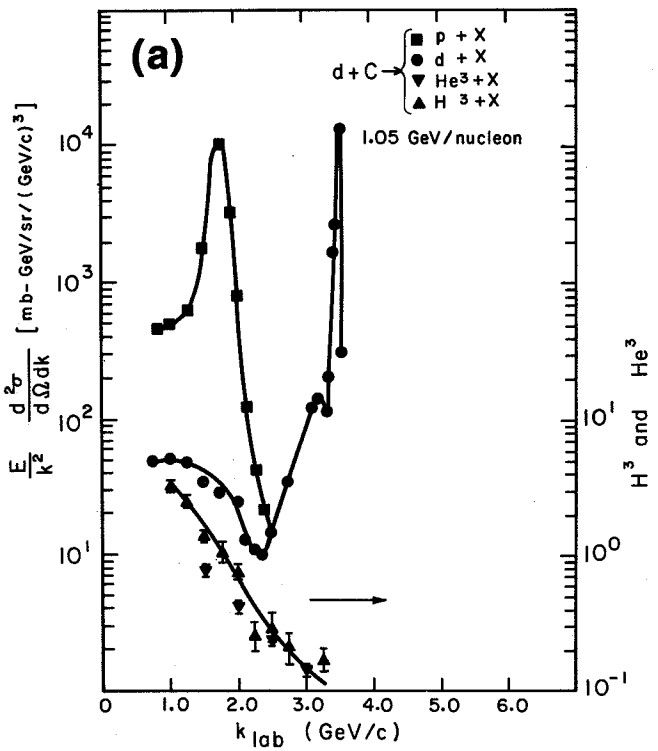

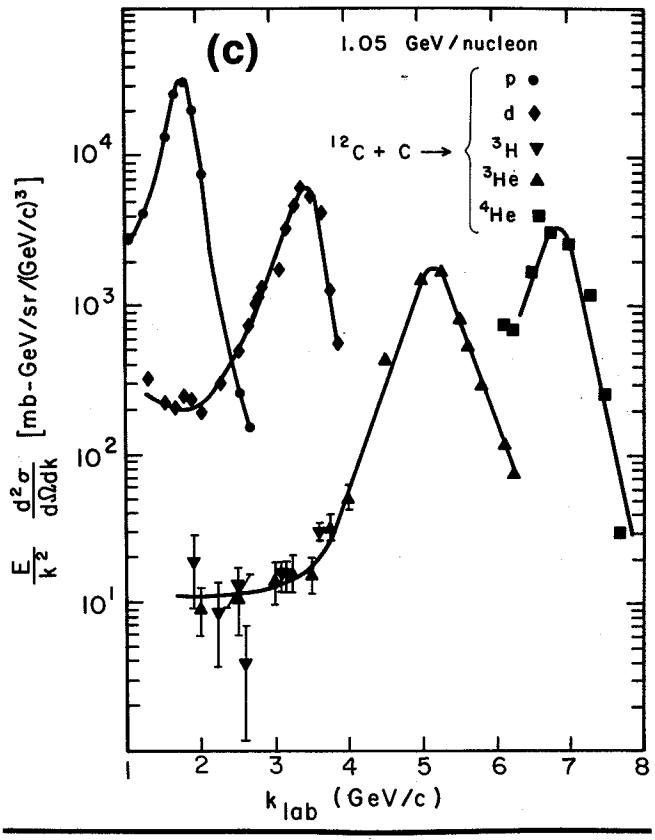

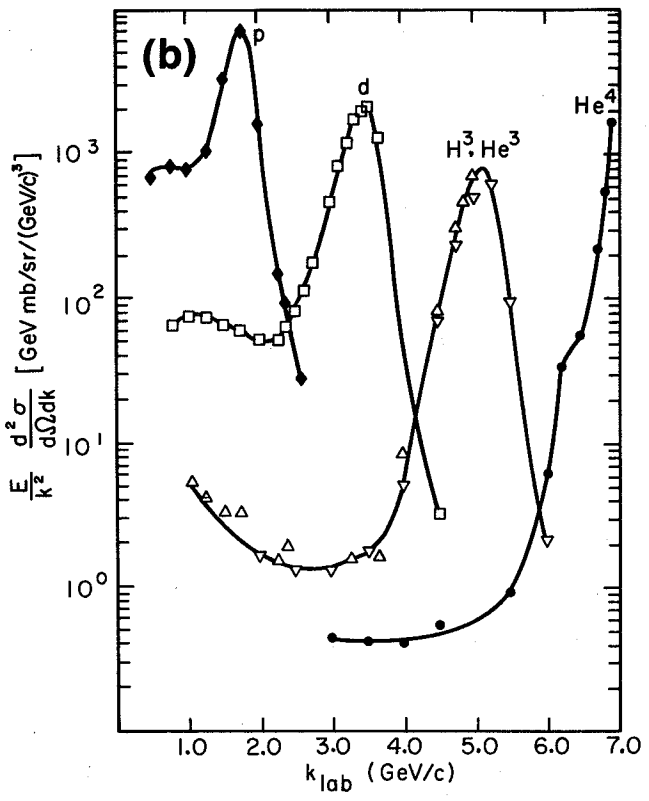

Fig. 1. Lorentz invariant cross section versus the momentum of the detected fragment for 1.05 GeV/nucleon (a) dC, (b) αC, (c) CC collisions. Fragments detected at 2.5°(lab). (XBL 748-3790, -3803, -3797)

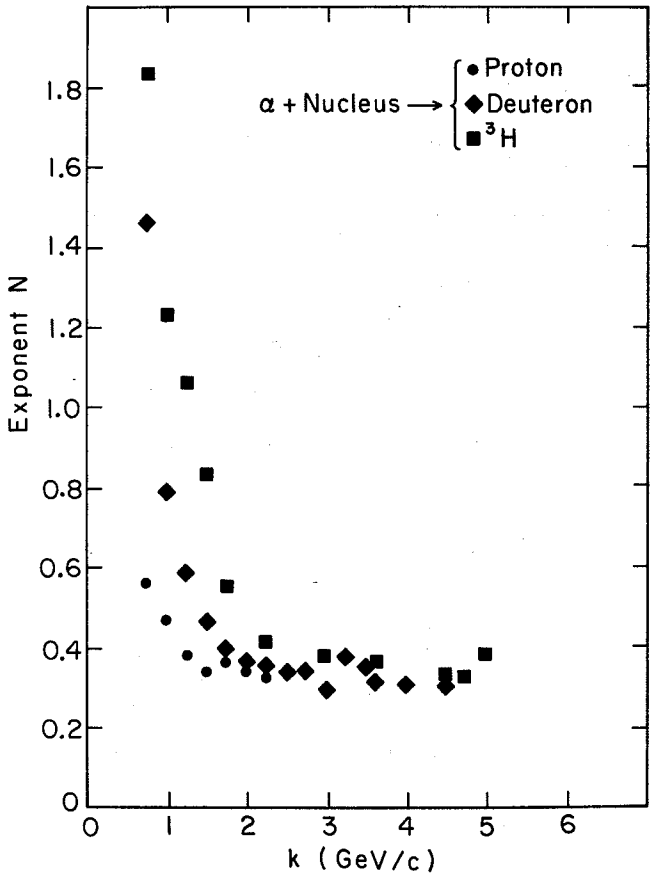

Fig. 2. Plot of the exponent N obtained from fitting the target dependence of various cross sections with an A^N type function. (XBL 7411-8320)

NUCLEUS-NUCLEUS TOTAL CROSS SECTIONS

John Jaros, Owen Chamberlain, Herbert Steiner, Albrecht Wagner,
Raymond Fuzesy, Lee Schroeder, Leonard Anderson, and Gilbert Shapiro

We performed an experiment at the Bevatron in which we measured the total cross section for reactions initiated by protons, deuterons, alphas, and carbon nuclei on targets of hydrogen, deuterium, helium, and carbon. Measurements of proton-nucleus cross sections in the GeV/nucleon energy range have already been well explained in terms of Glauber's multiple scattering theory.[1-3] Using parameters describing nucleon-nucleon scattering and the known nuclear sizes, Glauber theory has accurately predicted these total cross sections without invoking any special effects and, in fact, ignoring such genuine complications as nuclear correlations and Fermi momentum. The formalism of the theory has been extended to encompass nucleus-nucleus collisions[4] and has been used by several authors[5-9] to predict total and inelastic cross sections for various nucleus-nucleus reactions.

The theory is essentially geometrical and predicts that total cross sections are approximately proportional to the square of an interaction radius that goes like the sum of the radii of the colliding objects. If A_T and A_p are the atomic mass numbers of the target and projectile, $\sigma_{TOT} \sim (A_T^{1/3} + A_p^{1/3})^2$. Deviations from this simple behavior might indicate the presence of new processes in these collisions. In view of the unique conditions that occur in collisions of nuclei, we may hope for some surprises. A carbon-carbon collision at energies presently available can produce states of reasonably high energy density over a volume an order of magnitude greater than occurs in pp collisions. The Coulomb forces involved when large nuclei interact are no longer small compared to the nuclear forces. The interplay between the two should be important and interesting. The collision of two nuclei provides a new environment for nucleon-nucleon collisions. Does a proton which has interacted in one part of a nucleus behave as a "regular" proton in subsequent collisions?

An observation due to Gribov[10] also motivated this experiment. He noted that a naive application of Regge factorization to nucleus-nucleus reactions leads to a very different A dependence for σ_T than that expected from geometrical grounds. The argument is as follows: The optical theorem relates $\sigma_T(AB)$ to the imaginary part of the elastic scattering amplitude F. If we assume this amplitude is dominated by the Pomeron, factorization lets us write it as $F \sim g_{PA} g_{PB}$, where g_{PA} is the coupling of a Pomeron to nucleus A at $t = 0$, etc. for g_{PB}. Thus $\sigma_T(AB) \sim g_{PA} g_{PB}$; and similarly $\sigma_T(BB) \sim g_{PB}^2$ and $\sigma_T(AA) \sim g_{PA}^2$. Consequently, the "factorization relation" $\sigma_T(AA) = \sigma_T^2(AB)/\sigma_T(BB)$ obtains. If we use this to predict $\sigma_T(AA)$ from the input $\sigma_T(pA)$ and put $\sigma_T(pA) \sim A^{2/3}$ which roughly represents the data, we find $\sigma_T(AA) \sim A^{4/3}$. This differs radically from the behavior expected in a geometric picture where $\sigma_T(AA) \sim (A^{1/3} + A^{1/3})^2 \sim A^{2/3}$. Figure 1 shows the differences between geometrical and factorization relation predictions for $\sigma_T(AA)$ as a function of A.

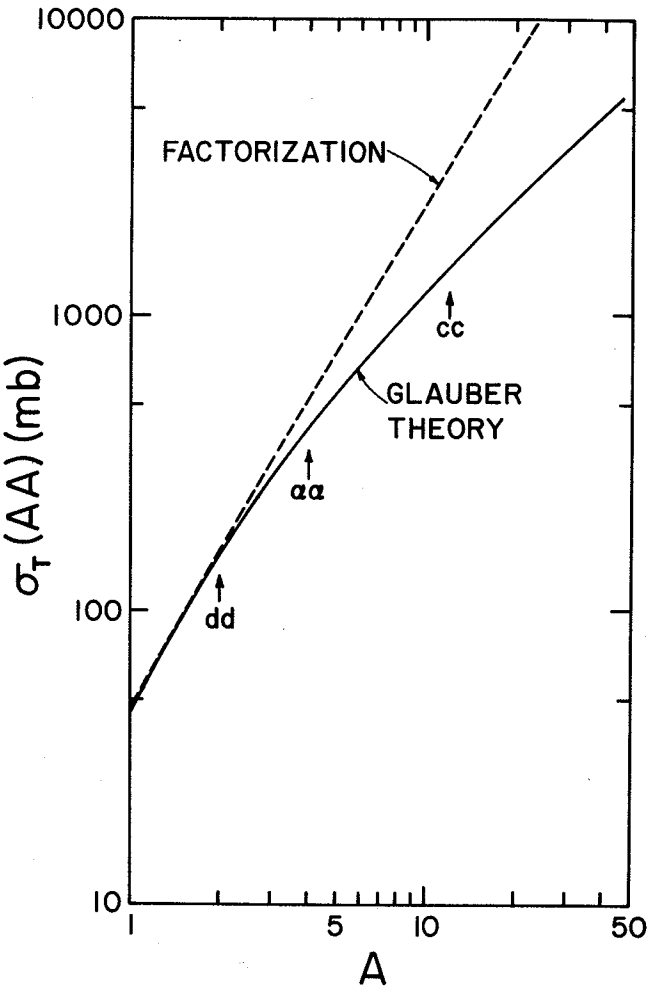

Fig. 1. Predictions for $\sigma_T(AA)$ vs A.
(XBL-7511-9047)

We measured total cross sections for protons, deuterons, alphas, and ^{12}C on hydrogen, deuterium, helium, and carbon targets at 1.55 and 2.89 GeV/c per nucleon using the "good geometry" transmission method. In addition, we measured the inelastic cross sections and elastic slope parameters for reactions initiated by deuterons, alphas, and ^{12}C. The factorization relation $\sigma_T(AA) = \sigma_T(AB)^2/\sigma_T(BB)$ is violated for some of these reactions. Our results generally agree with Glauber theory predictions except in their detailed energy behavior. We find $\sigma_T \approx 144(A_T^{1/3} + A_p^{1/3} - 1.48)^2$ and $\sigma_{IN} \approx 78(A_T^{1/3} + A_p^{1/3} - 1.25)^2$, where $A_T(A_p)$ is the atomic mass number of the target (projectile) and the cross sections are given in mb (see Figs. 2 and 3).

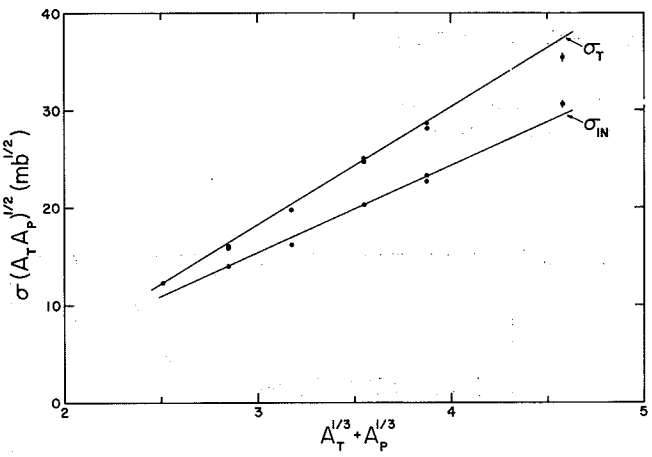

Fig. 2. $\sigma(A_P A_T)^{1/2}$ vs $(A_T^{1/3} + A_P^{1/3}$ at 0.87 GeV/ nucleon. (XBL 7511-9097)

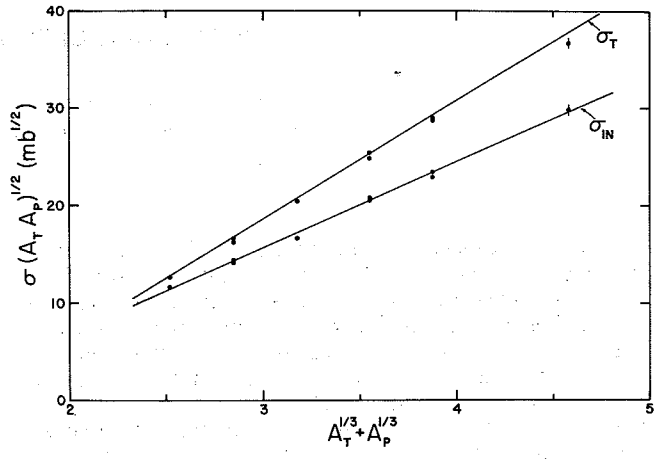

Fig. 3. $\sigma_T(A_P A_T)$ vs $(A_T^{1/3}+ A_P^{1/3})$ at 2.2 GeV/ nucleon. (XBL 7510-8499)

References

1. R. J. Glauber in Lectures in Theoretical Physics, Vol. 1 (Interscience, New York, 1959), p. 315.

2. R. J. Glauber in High Energy Physics and Nuclear Structure (North-Holland, Amsterdam, 1967), p. 311.

3. R. J. Glauber in High Energy Physics and Nuclear Structure (North-Holland, Amsterdam, 1969), p. 207.

4. W. Czyz and L. C. Maximon, Annals of Physics 52, 59 (1969).

5. A. Tekou, High Energy Elastic and Quasi-Elastic Deuteron-Nucleus Scattering, International Center for Theorectical Physics preprint No. IC/72/20 (unpublished).

6. V. Franco, Phys. Rev. Lett. 32, 911 (1974).

7. P. M. Fishbane and J. S. Trefil, Predictions for Nucleus-Nucleus Scattering at High Energies, University of Virginia preprent (unpublished).

8. W. L. Wang, Phys. Lett. B52, 142 (1974).

9. S. Barshay, C. B. Dover, and J. P. Vary, Phys. Lett. B51, 5 (1974); J. Vary, private communication.

10. V. N. Gribov, Sov. J. Nucl. Phys. 9, 369 (1969).

INCLUSIVE PION PRODUCTION IN COLLISIONS OF RELATIVISTIC PROTONS, DEUTERONS, ALPHAS, AND CARBON IONS WITH NUCLEI*

J. Papp,† J. Jaros,‡ L. Schroeder, J. Staples
H. Steiner, A. Wagner,§ and J. Wiss

We have measured single-particle inclusive spectra of π^+ and π^- mesons produced at 2.5° (lab) in the collision of 1.05–4.2-GeV protons, 1.05- and 2.10 GeV/nucleon deuterons and α particles, and 1.05 GeV/nucleon ^{12}C nuclei with various targets at an angle of 2.5° (lab). The negative-pion spectra show scaling behavior. The results are compared to a simple model in which individual nucleons in the projectile interact with the target to produce pions.

Our results on the yields of negative pions from collisions of 1.05-4.2-GeV (kinetic energy) protons with a carbon target are shown in Fig. 1(a). The Lorentz-invariant cross section $(E/k^2)d^2\sigma/d\Omega dk$, where E is the energy of the outgoing π^- and k is its momentum, is plotted against the scaling variable $x' = k_\parallel^*/(k_\parallel^*)_{max}$, where $k_\parallel^*$ is the longitudinal momentum of the pion in the overall center-of-mass system. The most striking feature of the data is that the spectra tend to lie on top of each other. Similar results are obtained for other targets. Higher-energy data[1,2] (12-, 19-, and 24-GeV protons on Be) also fall on the same curve. Scaling behavior, where the pion yield does not depend on the energy but only on a scaling variable x' (at fixed $k_\perp$), is familiar in high-energy nucleon-nucleon interactions. The remarkable feature of the present data is that scaling behavior persists, at least approximately, down to 1 GeV. It must be kept in mind that since this experiment was performed at a fixed lab angle of 2.5°, $k_\perp$ is not quite constant. This effect is most important near x' = 1 where it could change our results by as much as a factor of 2. However, since the scaling fit encompasses more than 6 decades, a variation of even a factor of 2 near the end points would not produce observable devia-

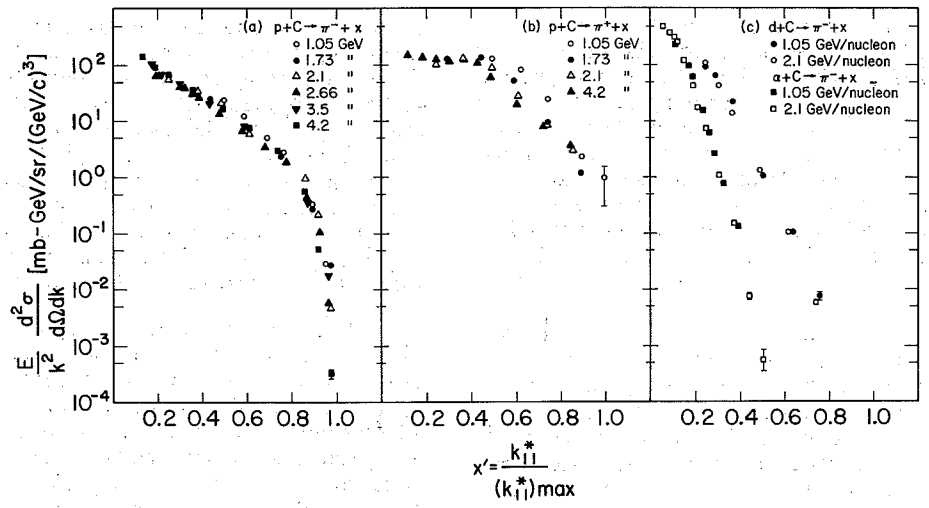

Fig. 1. Invariant cross section for pion production at 2.5° (lab) from a carbon versus the scaling variable $x' = k_{\parallel}^*/(k_{\parallel}^*)_{max}$: (a) Negative-pion production by 1.05-4.2-GeV protons, (b) positive-pion production by 1.05-4.2-GeV protons, (c) negative-pion production by 1.05- and 2.1-GeV/nucleon deuterons (circles) and α's (squares). (XBL-7411-8244)

tions from the trend of the data to scale. The π^+ production spectra are shown in Fig. 1(b). They do not scale nearly as well as those of negative pions, especially at low proton energies.

Invariant negative-pion production cross sections for 1.05- and 2.1-GeV/nucleon deuterons and α's incident on carbon are shown as a function of x' in Fig. 1(c). Again scaling is reasonably well satisfied. We see that the heavier the projectile the more rapid is the falloff as x' increases. This result indicates that nuclei, which are relatively loosely bound objects, tend not to transfer a large fraction of their kinetic energy to individual pions. In the case of deuterons, our x' distributions in the interval $0.5 \leq x' \leq 1$ fall much more steeply than those of Baldin et al.,[3] who measured π^- production at 0° by deuterons of about 8 GeV on Cu.

The pion production cross sections for 2.1-GeV/nucleon protons, deuterons, and α particles on carbon are compared in Fig. 2. Two features are evident: (1) The ratio of the cross sections for producing low-momentum negative pions (~1 GeV/c) by α's, deuterons, and protons is approximately 10:5:1. (2) The spectrum of observed pions extends to higher energies as the mass of the projectile is increased. The larger production cross sections in the case of deuterons and α's can be attributed to the presence of neutrons, which produce π^-'s more copiously than do protons, and to the increased energy of the system. Our measurements of π^- production by beams of 1.05-GeV/nucleon ^{12}C show that the ratio of π^- production by ^{12}C to π^- production by α particles is 3.0±0.3 at a momentum of 750 MeV/c for all targets.

In an attempt to determine the importance of mechanisms in which several nucleons in an energetic nuclear projectile act cooperatively to produce pions. we have compared our experimental results to calculations based on a model in which all pions are produced in individual nucleon-nucleus collisions.

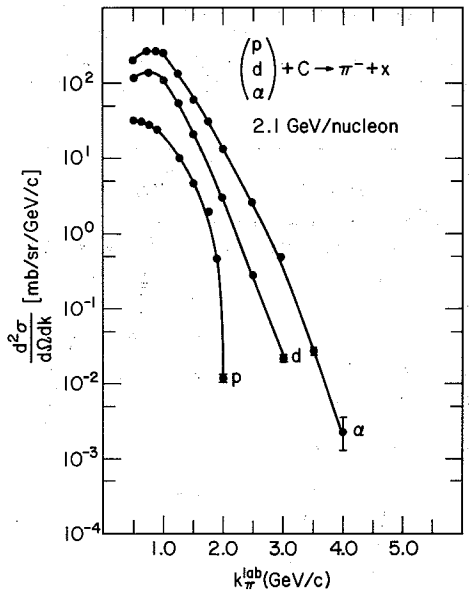

Fig. 2. Laboratory cross section $d^2\sigma/d\Omega dk$ for negative-pion production at 2.5° (lab) by 2.1-GeV/nucleon proton, deuteron, and α beams on carbon target versus the laboratory momentum of the pion. The solid lines are hand-drawn and are to serve as a guide to the eye only. Only statistical errors are shown. (XBL 748-3897)

We assume that

$$\sigma_{aA}^{\pi}(\vec{P}_a,\vec{k}_\pi) = \sum_N^a \int W_{aN}(\vec{P}_a,\vec{P}_N) \times \sigma_{NA}^{\pi}(\vec{P}_N,\vec{k}_\pi) d^3P_N,$$

where a refers to the projectile and A to the target nucleus. $W_{aN}(P_a,P_N)$ is the momentum distribution of the nucleon N inside the projectile as transformed to the lab system. By charge symmetry $\sigma_{pC}^{\pi^+}(\vec{P}_N,\vec{k}_\pi)=\sigma_{nC}^{\pi^-}(\vec{P}_N,\vec{k}_\pi)$. For $\sigma_{pC}^{\pi}(\vec{P}_N,\vec{k}_\pi)$ we have used our experimentally determined cross sections at 2.5° (lab) and corrected them for the transverse-momentum variation by assuming that at all momenta considered in these measurements such a variation can be fitted with an exponential of the form $\exp[-5|k_\pi|\sin(\theta_{\vec{k}_\pi}-\theta_{\vec{P}_N})]$

In the case of the deuteron $W_{dA}(\vec{P}_d,\vec{P}_N)$ was obtained from the Lorentz transformation of a normalized Hulthén wave function of the form $|\phi(q)|^2 \sim |q^2+\alpha^2)^{-1}-(q^2+\beta^2)^{-1}|^2$ with $\alpha = 45.7$ MeV and $\beta=5.2$ MeV (q is the nucleon momentum in the rest frame of the deuteron). The predictions are shown together with the data points in Fig. 3(a). The fits reproduce quite well the general behavior of the measured cross sections for fast pions as a function of pion momentum. There are no free parameters. These results disagree with the conclusions of Baldin et al.[3] who claim to be unable to fit their data with such a model.

The case of α's is complicated by the fact that the single-nucleon momentum distribution is not well known. From electromagnetic-form-factor experiments one can deduce a charge distribution but it is difficult to translate this to the momentum distribution of the individual nucleons $|\phi_\alpha(q)|^2$. As a first approximation to $\phi_\alpha(q)$ we Fourier transformed the square root of the nuclear-charge distribution.[4] As before $W_{\alpha N}(\vec{P}_\alpha,\vec{P}_N)$ was then obtained by transforming $|\phi_\alpha(q)|^2$ to the lab system. The results are shown in Fig. 3(b). Although the general trends of the data are reproduced by the model, quantitatively the agreement is not good. At this point we are unable to say whether this is due to a poor choice for $W_{\alpha N}(\vec{P}_\alpha,\vec{P}_N)$ or to a breakdown of the model. Further work is in progress for both deuterons and α's.

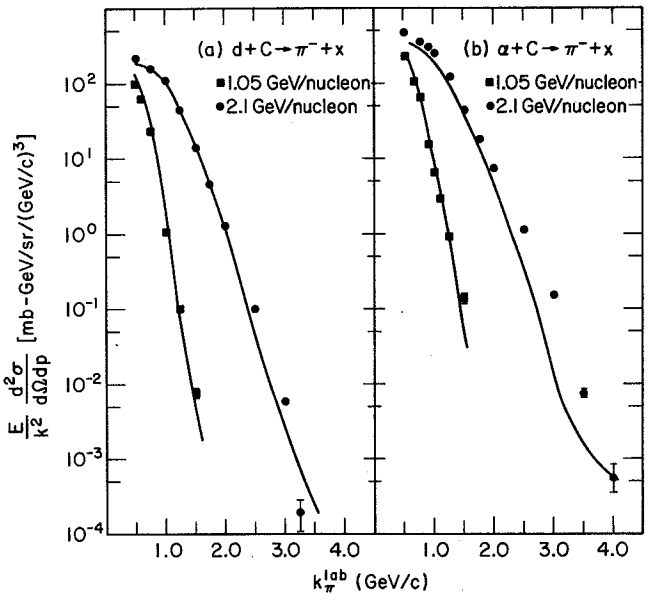

Fig. 3. Invariant cross section for negative-pion production at 2.5° (lab) by 1.05- and 2.1-GeV/nucleon (a) deuteron and (b) α beams versus the laboratory momentum of the pion. The solid lines in each case represent the predictions of the model as described in the text. (XBL 7411-8243)

Pion production from Be, Cu, and Pb is quite similar to that from carbon. The shape of the spectra is independent of the target material for $k_\pi > 1$ GeV/c. The magnitude of these cross sections is proportional to $A^{1/3}$, suggesting that fast pions are produced in peripheral collisions. For lower-momentum pions, the A dependence becomes more pronounced (e.g., $\sigma \propto A^{1/2}$ for $k_\pi = 500$ MeV/c), suggesting that slow pions are produced in more central collisions.

For isospin-zero nuclei like deuterons, α particles, and ^{12}C charge symmetry predicts that in the reactions $d + C \rightarrow \pi^\pm + X$ and $\alpha + C \rightarrow \pi^\pm + X$ the ratio of π^+ to π^- production should be unity. In every case our results are consistent with this prediction to within the experimental errors of about 10%.

Footnotes and References

*Based on Phys. Rev. Lett. 34, 601 (1975).

†Watkins-Johnson Corp., Redwood City, California.

‡Stanford Linear Accelerator Center, Stanford, California.

§Heidelberg - DESY Group, Heidelberg, Germany

1. G. J. Marmer and D. Lundquist, Phys. Rev. D3, 1089 (1971); G. J. Marmer, K. Reibel, D. M. Schwartz, A. Stevens, R. Winston, D. Wolfe, P. R. Phillips, E. C. Swallow, and T. A. Romanowski, Phys. Rev. 179, 1294 (1969).

2. D. Dekkers, J. A. Geibel, R. Mermond, G. Weber, T. R. Willitts, K. Winter, B. Jordan, M. Vivargent, N. M. King, and E. J. N. Wilson, Phys. Rev. 137, B962 (1965).

3. A. M. Baldin, S. B. Gerasimov, H. Guiordenescu, V. N. Zubarev, L. K. Ivanova, A. D. Kirillov, V. A. Kuznetsov, N. S. Moroz, V. B. Radomanov, V. N. Ramzhn, V. S. Stavinski, and M. I. Yatsuta, Yad. Fiz. 18, 79 (1973) [Sov. J. Nucl. Phys. 18, 41(1974)].

4. R. F. Frosch, J. S. McCarthy, R. E. Rand, and M. R. Yearin, Phys. Rev. 160, 874 (1967).

DIFFRACTIVE SCATTERING OF HEAVY IONS

A. R. Clark, W. R. Holley, D. Keefe, L. T. Kerth, R. E. Morgado,*
M. Richardson,† G. Schnurmacher, L. S. Schroeder, and A. R. Zingher

This experiment has measured $^{12}C+p \rightarrow X+P'$, $^{4}He+p \rightarrow X+p'$ and $p+p \rightarrow X+p'$ inelastic scattering. We used a Bevalac beam ^{12}C, ^{4}He, p at 4.2 GeV/c charge rigidity on a stationary liquid hydrogen target, observed the recoil proton p', and summed over X the unseen outgoing beam. We measured the double differential cross section $d^2\sigma/dtdM_X^2$ as a function of the momentum transfer ($\sqrt{-t}$ = 200-300 MeV/c) and the excitation energy ($E_X = M_X - M_{C,He,p}$ = 0-250 MeV). This is equivalent to missing mass squared $\Delta = M_X^2 - M_C^2$ = 0-6 GeV^2 and -t = .04 to .09 (GeV/c)^2. This probes both the nuclear structure and the dynamics of diffractive scattering. It tests whether ideas of asymptotic scattering, particularly Regge-Mueller pomeron phenomenology, are relevant to heavy baryon physics. These ideas of a collective baryon scattering contrast with individual nucleon models such as the Glauber model.

This region of relatively small momentum transfer t is expected to be dominated by diffractive scattering. It is relatively easy to measure a small momentum transfer to a stationary target. This is a major advantage over a proton beam on a carbon target; there a small change in a large momentum would require a high-resolution spectrometer. A small disadvantage is that we are somewhat sensitive to Coulomb scattering of the recoil proton. This region goes from elastic scattering, thru the nuclear excitations and beyond the pion threshold. At these large missing masses (or large excitation), should the cross section increase as the pion channel opens? The corresponding situation at F.N.A.L. is $p+p \rightarrow X+p$ with large excitation and small momentum transfer. Once the missing mass is large and many channels are open (e.g., X = p + many pions), then the double differential cross section approaches an asymptotic limit. Additional pion thresholds open up at the expense of previous channels. This can be understood via the Regge-Mueller pomeron phenomenology. Can relativistic nuclei be effectively described by the same ideas? This picture contrasts with the Glauber model of nucleus-proton collisions as a number of individual nucleon-proton collisions. The latter model predicts that the double differential cross section should rise when the pion channel opens up.

We have constructed a single arm spectrometer (Fig. 1) to look at the recoil protons. The spectrometer consists of three parts: a target, a quadrupole doublet, and scintillators. First is a liquid hydrogen target with a very thin aluminum wall. This minimizes Coulomb scattering to allow us to look at low recoil proton momenta, and thus low momentum transfer. The second part is a magnetic quadrupole doublet which rotates around the target. It is between the target and the detectors, and it focuses parallel to point in the horizontal plane, point to point in the vertical plane. This gives a large vertical acceptance with a precisely defined horizontal scattering angle. The third part is a sequence of eleven thin scintillators which measure

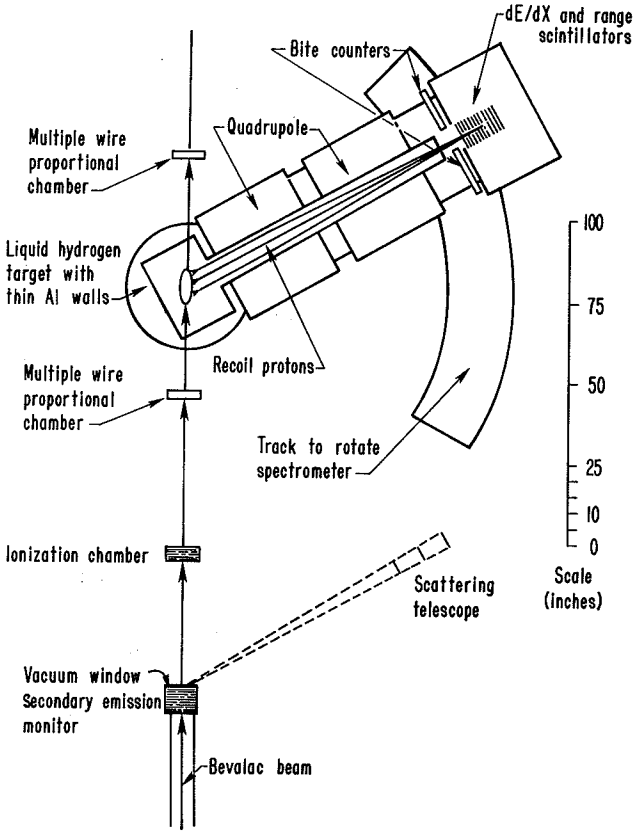

Fig. 1. A simplified plan view of the recoil proton spectrometer for this experiment.
(XBL 766-8333)

the proton kinetic energy from its range in the scintillators. In addition, detailed pulse height measurements in each scintillator show the characteristic Bragg peak from valid stopping protons. This separated them from the secondary pions, and from protons which interact in the scintillators or which go out the side. It is critical to avoid such contaminations at large excitation. There, valid protons are only a small fraction of the particles produced from the target.

A necessary part of this experiment was to calibrate absolutely the response of an ion chamber to these heavy ion beams. In conjunction with A. R. Smith and J. B. McCaslin we also measured the absolute cross section for $^{12}C + ^{12}C \rightarrow X + ^{11}C$. These calibrations should be useful for other experiments which use these techniques.

Our data are presently under analysis. A preliminary sample is shown in Fig. 2. There are several different dynamic regions. At the lowest excitation is a peak $^{12}Cp \rightarrow ^{12}Cp$. This preliminary sample cannot resolve $^{12}Cp \rightarrow ^{12}C(4.4\ MeV)\ p$ from truly elastic scattering; but with further analysis of more data we will try to resolve it. The next

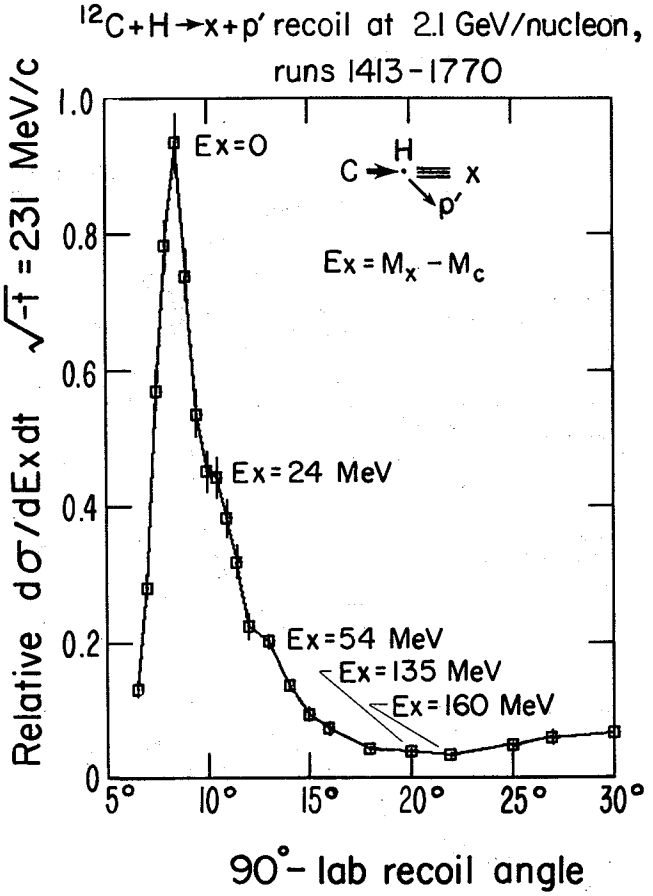

two shoulders may be due to the giant dipole resonance, or quasi αp scattering, and quasi pp scattering. Other data show these structures more clearly, and no conclusions should be drawn until the data analysis is complete. Beyond these peaks the cross section falls by an order of magnitude. This region puts new demands on Glauber calculations. Usually these calculations assume negligibly small energy transfer in the individual collisions, or else sum over all possible energy transfers. Here we measure a large excitation energy, so a better calculation is required. The relevant theory was discussed above. Again, no reliable conclusion can be drawn until the analysis is complete, and we are certain that there is no contamination. Our ultimate resolution should be a few MeV in excitation, above ±2% in momentum transfer $\sqrt{-t}$, and a few percent uncertainty in the cross section.

Footnotes

*Arizona Medical Center, Tuscon, Arizona.

†Physics Dept., Harvard University, Cambridge, Mass.

Fig. 2. Relative double differential cross section $d^2\sigma/dM_x^2\,dt$ at fixed momentum transfer $\sqrt{-t}$ = 231 MeV/c and variable laboratory proton recoil angle. The abscissa is 90 degrees minus the angle between the laboratory recoil proton direction and the beam direction. This angle determine the excitation energy, and some representative values are shown. These excitations include a 1 degree overall adjustment in the angular scale. The bars are nominal Poisson errors. (XBL 766-8334)

PROJECTILE FRAGMENTATION AND ASSOCIATED MULTIPLICITY DISTRIBUTIONS IN RELATIVISTIC HEAVY ION COLLISIONS

J. Carroll, V. Perez-Mendez, E. Whipple, M. Gazzaly,* J. Geaga,*
G. Igo,* J. McClelland,* M. Nsser,* A. Sagle,* and H. Spinka*

A large aperture, moveable magnetic spectrometer, instrumented with multi-wire proportional chambers and scintillation counters has been set up in Channel II at the Bevalac. The basic properties of the spectrometer (originally installed to study forward elastic scattering) are listed below.

$\Delta\Omega \approx$	0.8 msr	TOF	31 feet
theta:	range -1,14°	resolution	0.1°
		bite	±1°
P/Z :	range 0-7.5 GeV/c	resolution	0.5%
		bite	±20%

A layout of the spectrometer is shown in Fig. 1.

A preliminary parasitic run with 1.05 GeV/n ^{16}O incident on a ^{12}C target demonstrated that the spectrometer was suitable for measuring the fragmentation cross sections and was capable of identifying the light isotopes up to ^{4}He which dominate the flux of fragments scattered through more than a few degrees.

The spectrometer has since been augmented by an array of 30 lucite Cerenkov detectors surrounding the beam downstream from the target. These detectors are in the form of azimuthal segments covering all of the azimuthal coordinate which is not occupied by the spectrometer acceptance. The angular acceptance of the array can be adjusted to include the ranges 4-12° or 5-16° by varying the target-to-detector distance. The kinematics of the reaction ensure that this angular range will accept a large fraction of the fragments from the projectile which have received a momentum transfer greater than the typical nuclear Fermi momentum. The lucite detectors have a velocity threshold $\beta_{th} \approx 0.7$, and are thus completely insensitive to fragments evaporated from the target.

Using this array we can study the multiplicity distribution of projectile fragments (including the infrequent pions) in association with fragments of various masses, charges, momenta, and angles detected in the spectrometer. One can, of course, also

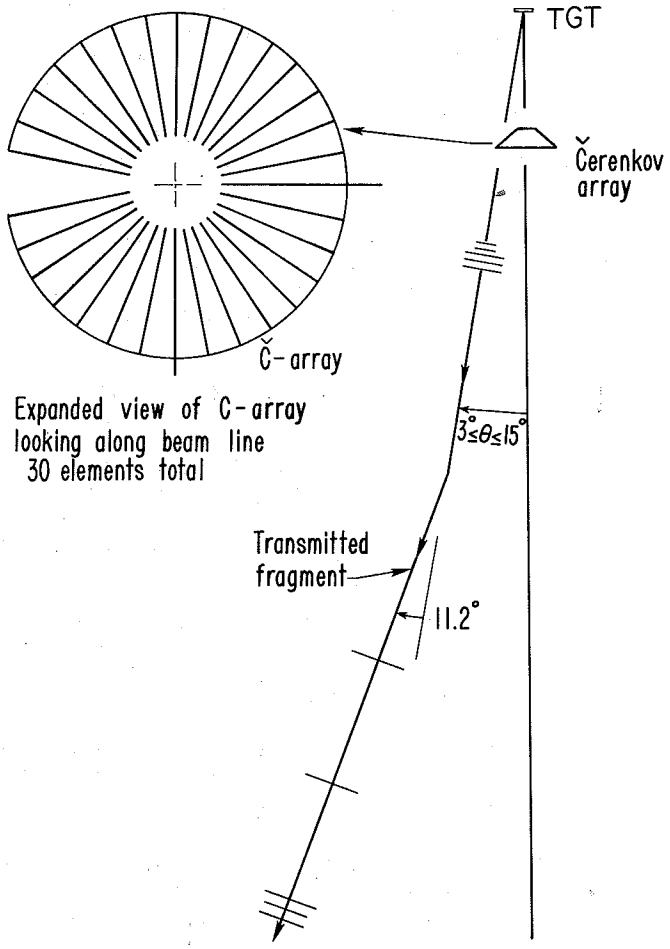

Fig. 1. Plan view of spectrometer for measuring multiplicities of projectile fragments associated with the transmitted fragment A_Z. (XBL 7611-4381)

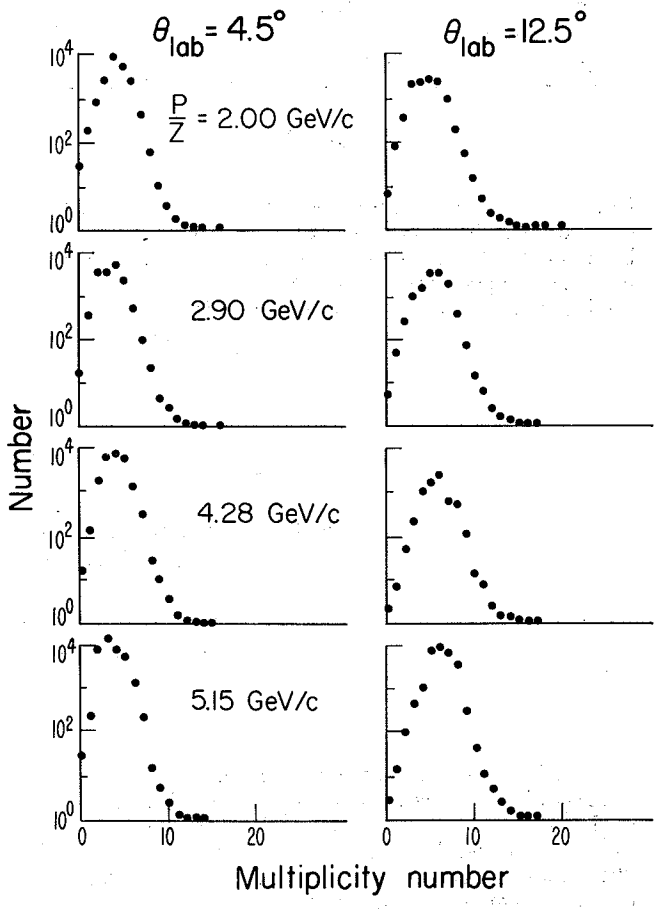

Fig. 2. Multiplicity distributions in the tag counters associated with fragments entering the spectrometer at 4.5° and 12.5° for the case of a 1.8 GeV/n ^{40}Ar beam on a ^{9}Be target.
(XBL 766-8581)

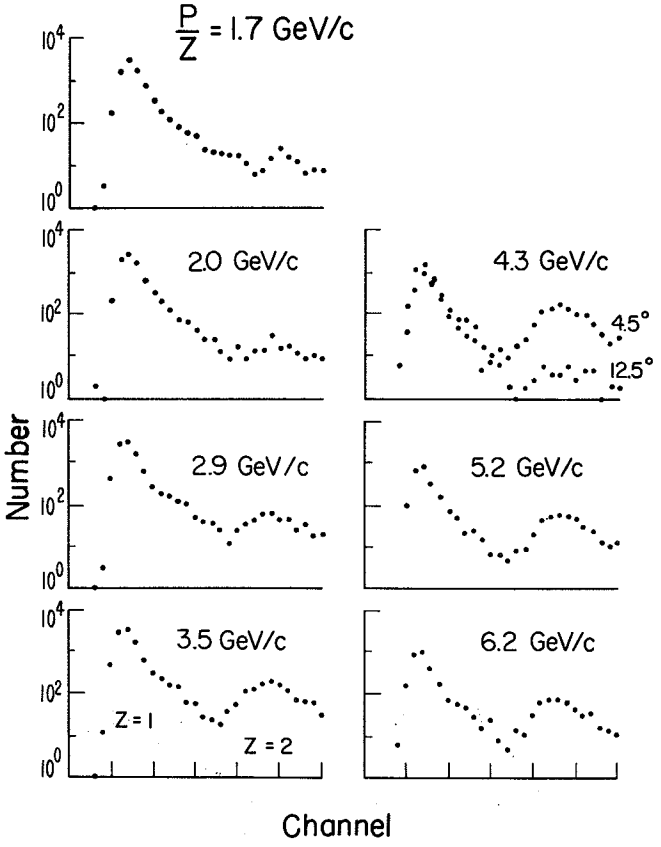

Fig. 3. Pulse height spectra from a scintillation counter in the spectrometer for a 1.8 GeV/n ^{40}Ar beam on a ^{9}Be targets. The two different peaks in any given spectrum indicate the relative amount of Z = 1 and Z = 2 particle fragmentation.
(XBL 7611-4485)

select for large multiplicity and study the effects on the distribution of particles in the spectrometer. Both spectrometer and Cerenkov array cover the range of angles at which one might expect to see shock waves, and one can use the spectrometer to see if larger multiplicities are associated with fragment momentum distributions that can be ascribed to an increased nuclear temperature.

Data have been taken for 2.1 GeV/nucleon ^{12}C and 1.8 GeV/nucleon ^{40}Ar beams on beryllium and copper targets. While even a preliminary analysis is not yet complete, certain observations can be made:

1. One can see a trend toward higher multiplicities associated with higher momentum transfers. This can be seen in Fig. 2 for the case of the 1.8 GeV/nucleon ^{40}Ar beam on the ^{9}Be target. The average multiplicity varies from ~4 to ~8 as the P/Z and angle are varied from 2.0 GeV/c at 4.5° to 5.15 GeV/c at 12.5°.

2. The production of charge 2 fragments relative to charge 1 fragments decreases with scattering angle and scattered momentum as shown in Fig. 3.

3. The widths of the fragmentation peaks in momentum are much broader than the Fermi momentum even at $\theta_{lab} = 4.5°$.

We are proceeding with the analysis and hope to soon have momentum, angular, and multiplicity distributions for the different types of fragments.

Footnote

*University of California, Los Angeles, California 90024.

2. Target Fragmentation

NUCLEAR GAMMA RAYS FOLLOWING INTERACTION WITH RELATIVISTIC CARBON PROJECTILES

T. Shibata,* H. Ejiri,* R. Anholt,† H. Bowman, J. G. Ioannou-Yannou, J. O. Rasmussen, E. Rauscher, S. Nagamiya,‡ and K. Nakai‡

Discrete nuclear gamma rays following interactions of relativistic ^{12}C projectiles with ^{12}C, ^{19}F, ^{38}Sr and ^{207}Pb were observed at $E(^{12}C)$ = 3 and 12.6 GeV. The lartest yields of the observed gamma rays were from low-lying excited states of target nuclei, and there were also identified lines from nuclei of mass number slightly less than that of the target nuclei.

The work reported here mainly involves bombardments by ^{12}C at 1.05 GeV/nucleon and 0.25 GeV/nucleon, and the targets studied were "teflon" (C_nF_{2n}), natural Sr (82.4% ^{88}Sr) and enriched ^{207}Pb (92.8%). The gamma-ray energy range studied was from 80 keV to 2.5 MeV.

The Bevatron provided relativistic carbon ^{12}C ion beams with energies 1.05 GeV/nucleon and 0.25 GeV/nucleon. (Earlier, 4.88 GeV/n protons and 0.4 GeV/n carbon ions were also used for survey runs.) The beam intensities were adjusted so as to get adequate peak counting rates of about 4,000 C/sec for gamma detectors and the proper live times (50-70%). They were about 0.25×10^7 carbon ions/burst for 0.25 GeV/nucleon. The accelerator was operated

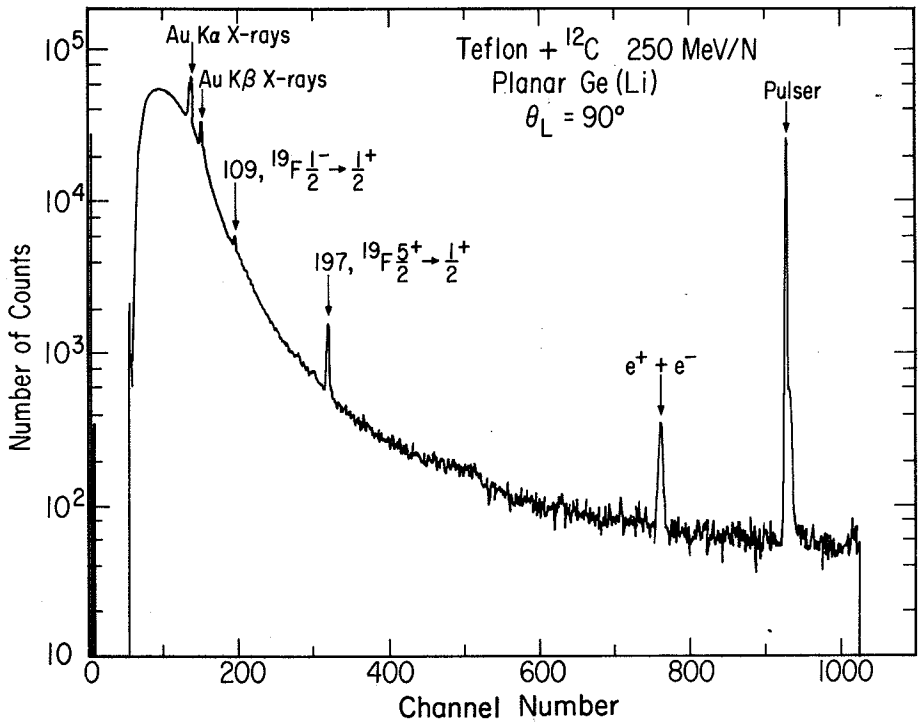

Fig. 1. Gamma-ray spectrum for the 3-GeV ^{12}C interaction with the teflon target measured by the planar Ge(Li) detector. (XBL 761-231)

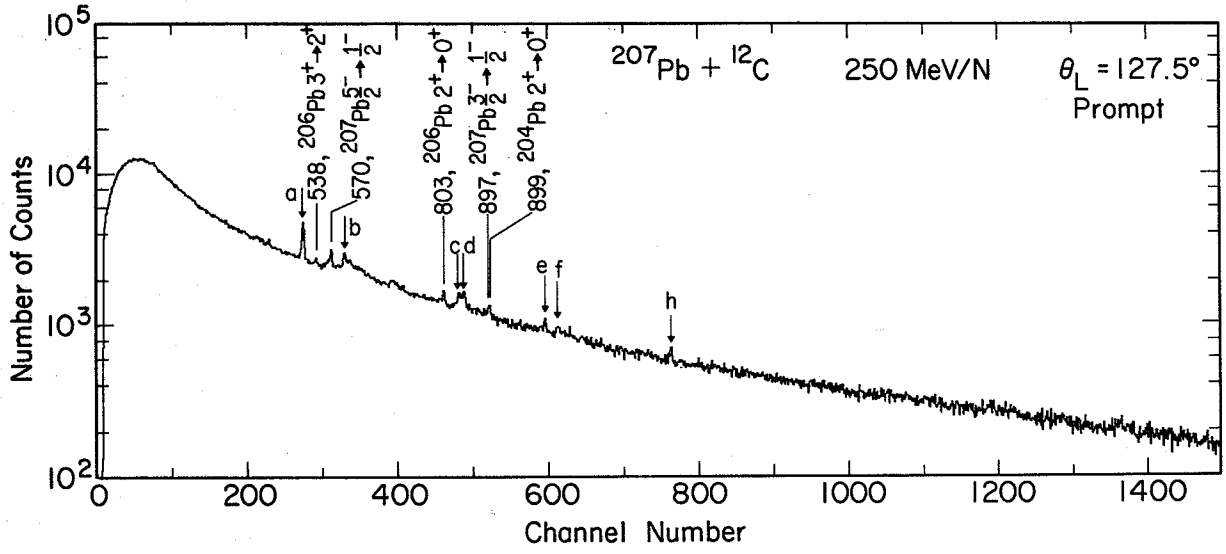

Fig. 2. Prompt gamma-ray spectrum for the 3 GeV ^{12}C + ^{207}Pb measured by the coaxial Ge(Li) detector. The common lines due to Ge of the detector, Al of the beam tube, ratioactivities, etc., are denoted as a) (511 keV $\beta^+\beta^-$), b) [596 keV $^{74}Ge(nn')$], c) (835 keV ^{54}Mn), d) (844 keV ^{27}Al), e) (1014 keV ^{27}Al), f) 1040 keV ^{70}Ge), h) (1277 keV ^{22}Na).
(XBL 761-227)

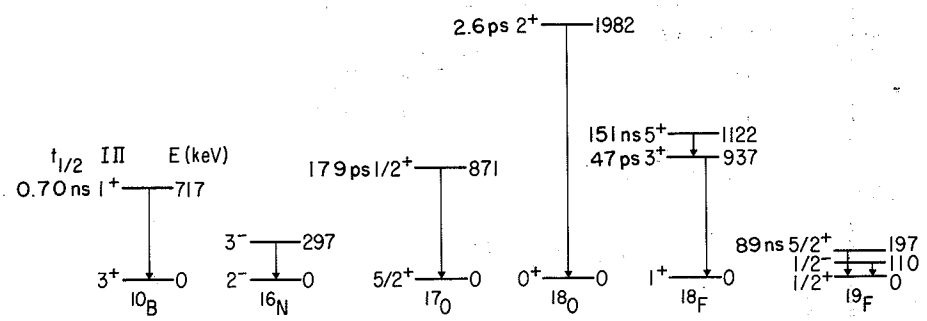

Fig. 3. Transition schemes for the prominent gamma rays observed with the teflon target. (XBL 761-235)

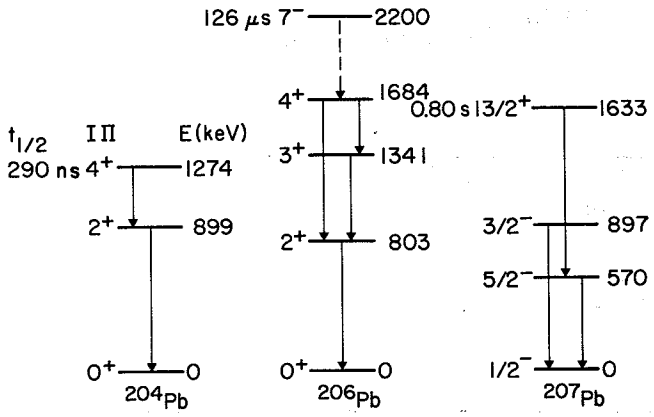

Fig. 4. Transition schemes for the prominent gamma rays observed with the ^{207}Pb target. (XBL 761-233)

in either of two modes, one with the rf power applied to the acceleration resonator and another without the rf power applied during the beam extraction from the accelerator. The former mode provides microscopic rf bunched beam pulses with intervals of 455 nsec for 1.05 GeV/n and 653 nsec for 0.25 GeV/n. Since the macroscopic beam bursts of about 1 sec duration come every 5 or 6 sec and each beam burst consists of a narrow ($\leq$20 nsec) microscopic beam pulse every ~500 nsec, the coincidence arrangement considerably reduced the gamma-ray background. The dead times were measured by comparing the number of pulser pulses recorded in the multichannel PHA and the number of those fed into the preamplifier. Here the pulser pulse fed into one preamplifier was triggered by the scaled-down gamma ray pulses from another detector, and vice versa.

Gamma rays from the teflon and strontium targets were measured at θ = 127.5° and θ = 90°. The gamma rays from the ^{207}Pb target were measured only at 127.5°

Many discrete gamma rays following relativistic ^{12}C-induced nuclear reactions on ^{12}C, ^{19}F, natural Sr (83% of ^{88}Sr) and ^{207}Pb were observed. Some of the observed gamma-ray spectra from the Ge(Li) detectors are shown in Figs. 1 and 2. The transition schemes for most of the observed gamma rays are given in Figs. 3 and 4. The observed gamma rays come from excited states of the target nuclei and nearby products derived by few-nucleon removal. The strong "continuum background" was established as largely target-originated, since it drops during target-out runs. The "continuum background" is considered to be mainly due to unresolved gamma rays and their Compton tails from numerous low-yield products of nonperipheral processes.

The cross sections for the prominent gamma lines were obtained from the observed yields at θ = 127.5°, where the angular distribution effect is negligible because $P_2(\cos\theta) \approx 0$. The measured relative intensities of the prominent gamma rays are given in Table 1. The absolute cross sections for the strongest gamma lines, the relative intensities of which are given as 100 in Table 1, are 39 ± 15 mb (24 ± 12 mb) for the ^{19}F $5^+/2 \rightarrow 1^+/2$ transition from the 3 GeV (12.6 GeV) ^{12}C + teflon, 100 ± 43 mb (74 ± 41 mb) for the ^{88}Sr $2^+ \rightarrow 0^+$ transition from the 3 GeV (12.6 GeV) ^{12}C + Sr, and 220 ± 130 mb (157 ± 100 mb) for the ^{207}Pb $5^-/2 \rightarrow 1^+/2$ transition from the 3 GeV (12.6 GeV) ^{12}C + ^{207}Pb.

The following observations can be made from the measured gamma ray yields:

1. Target nuclei (bound states) are strongly excited. Thus, gamma rays from the low-lying excited states are strong. The cross sections are of the order of 100 mb.

2. Gamma rays from the low-lying states (the second $5/2^+$ state in ^{19}F, the first 2^+ state in ^{88}Sr, the first $5/2^-$ state and the first $3/2^-$ state in ^{207}Pb) are always dominant. These low-lying states in ^{207}Pb are ^{88}Sr are partly (half or more) populated by gamma cascades from the higher excited states.

3. Delayed gamma rays from the $13/2^+$ state in ^{207}Pb are prominent for the ^{207}Pb target (spin 1/2). This indicates considerable excitation of high spin particle-hole states. Such excitation is quite unlikely in inelastic scattering of low-energy heavy ions.

4. Gamma rays following few-nucleon removal from the target nuclei are well observed with cross sections of 10 ~ 100 mb. Many bound states

Table 1. Relative intensities of γ rays following relativistic carbon-induced reactions.*

Target	E_γ(kV)	Transition	Reaction	I_γ(0.25 GeV/n)	I_γ(1 GeV/n)	Prompt or Delayed
^{12}C	717.4±0.7	^{10}B $1^+ \rightarrow 3^+$	-1n, -1p	92 ± 19	116 ± 23	Prompt
^{19}F	109.0	^{19}F $\frac{1}{2}^- \rightarrow \frac{1}{2}^+$	On, Op	24 ± 3		
	197.0±0.5	^{19}F $\frac{5}{2}^+ \rightarrow \frac{1}{2}^+$	On, Op	<u>100</u> ± 24	100 ± 31	Delayed $\tau_{1/2}$ = 89 ns
	1981.0±1.0	^{18}O $2^+ \rightarrow 0^+$	On, -1p	68 ± 16	83 ± 27	Prompt
	936.5±0.5	^{18}F $3^+ \rightarrow 1^+$	-1n, Op	38 ± 8	42 ± 23	Prompt only
	936.5±0.5	$^{18}F(5^+)$ $3^+ \rightarrow 1^+$	-1n, Op	16 ± 5	⩽38	Delayed $\tau_{1/2}(5^+)$ = 151 ns
	869.0±0.5	^{17}O $\frac{1}{2}^+ \rightarrow \frac{5}{2}^+$	-2n, -1p	30 ± 8	21 ± 12	Prompt
	297.2±0.5	^{16}N $3^- \rightarrow 2^-$	-1n, -2p	9 ± 2	---	Prompt
^{n}Sr (82.4% Sr)	1836.4±0.7	^{88}Sr $2^+ \rightarrow 0^+$	On, Op	<u>100</u> ± 28	100 ± 36	Prompt
	898.0±0.7	^{88}Sr $3^- \rightarrow 2^+$	On, Op	65 ± 18	33 ± 21	Prompt
	1049.4±0.5	^{86}Sr $2^+ \rightarrow 0^+$	-2n, Op	48 ± 12	55 ± 23	Prompt
	1153.0±0.5	^{86}Sr $4^+ \rightarrow 2^+$	-2n, Op	36 ± 18	64 ± 24	Prompt
	493.0±0.7	^{84}Sr $2^+ \rightarrow 0^+$	-4n, Op	36 ± 14	⩽27	Prompt
^{207}Pb	569.7±0.5	^{207}Pb $\frac{5}{2}^- \rightarrow \frac{1}{2}^-$	On, Op	<u>100</u> ± 18	100 ± 46	Prompt only
	569.9±0.5	^{207}Pb $\frac{13}{2} \rightarrow \frac{5}{2}^- \rightarrow \frac{1}{2}^-$	On, Op	84 ± 16		Delayed $\tau_{1/2}\left(\frac{13}{2}^+\right)$ = 0.85 s
	897.3±0.7	^{207}Pb $\frac{3}{2}^- \rightarrow \frac{1}{2}^-$	On, Op	43 ± 14	98 ± 52	Prompt
	1063.6±0.7	^{207}Pb $\frac{13}{2}^+ \rightarrow \frac{5}{2}^-$	On, Op	92 ± 28		Delayed $\tau_{1/2}\left(\frac{13}{2}^+\right)$ = 0.85 s
	803.2±0.5	^{206}Pb $2^+ \rightarrow 0^+$	-1n, Op	56 ± 13	91 ± 36	Prompt only
	803.2±0.5	$^{206}Pb(7^-)$ $2^+ \rightarrow 0^+$	-1n, Op	24 ± 8	⩽52	Delayed $\tau_{1/2}(7^-)$ = 126 μs
	537.5±0.5	^{206}Pb $3^+ \rightarrow 2^+$	-1n, Op	10 ± 3	⩽60	Prompt only
	881.0±0.7	$^{206}Pb(7^-)$ $4^+ \rightarrow 2^+$	-1n, Op	20 ± 8	⩽60	Delayed $\tau_{1/2}(7^-)$ = 126 μs
	899.2±0.7	^{204}Pb $2^+ \rightarrow 0^+$	-3n, Op	16 ± 15	⩽60	Prompt only
	899.2±0.7	$^{204}Pb(4^+)$ $2^+ \rightarrow 0^+$	-3n, Op	20 ± 8	⩽60	Delayed $\tau_{1/2}(4^+)$ = 0.29 μs
	374.7±0.7	$^{204}Pb(4^+)$ $4^+ \rightarrow 2^+$	-3n, Op	17 ± 11		Delayed $\tau_{1/2}(4^+)$ = 0.29 μs
	986.1±1.0	^{205}Pb $\frac{13}{2}^+$ $\frac{9}{2}^- \rightarrow \frac{5}{2}^-$	-2n, Op	19 ± 7		Delayed $\tau_{1/2}\left(\frac{13}{2}^+\right)$ = 5 μs

*Intensities are relative to the underlined <u>100</u>. Normalizations to absolute cross sections are given in the text.

are probably excited, and thus some particular gamma rays (mostly for the transition from the first excited state to the ground state) get the largest yield by feeding from the higher excited state.

5. The yield of gamma rays from residual nuclei signifies that protons as well as neutrons are likely to be removed from the light target nuclei (^{19}F and ^{12}C). On the other hand gamma rays from nuclei of the same Z but lower neutron number than the target are predominantly observed with the heavier targets nuclei (^{88}Sr and ^{207}Pb). The ^{86}Kr $2^+ \rightarrow 0^+$ gamma-ray cross section is less than one-quarter of that for ^{86}Sr for 0.25 GeV/n C^{12} on ^{88}Sr, and less than one-half for 1.05 GeV/n.

6. Little dependence of the gamma ray yield on the incident projectile energies is observed.

7. The total cross section for these peripheral processes amounts to an appreciable fraction (10 ~ 15%) of the geometrical cross section of $\pi(R_1 + R_2)^2$.

The measured relative intensities for the 4.8 GeV/c ^{12}C teflon target are 100±34, 44±21 and 29±9 for the ^{19}F $5^+/2 \rightarrow 1^+/2$, ^{18}O $2^+ \rightarrow 0^+$ and ^{19}F $1^-/2 \rightarrow 1^+/2$ transitions, respectively. The absolute value for the ^{19}F $5^+/2 \rightarrow 1^+/2$ is 41±15 mb. The values for the 4.88 GeV protons on the teflon target are 100±8, 47±10 and 32±3 for the ^{19}F $5^+/2 \rightarrow 1^+/2$, ^{18}O $2^+ \pm 0^+$ and ^{19}F $1^-/2 \rightarrow 1^-/2$ transitions, respectively. The absolute cross section for the ^{19}F $5^+/2 \rightarrow 1^+/2$ is 55±5 mb. It is interesting to note that both the relative and absolute cross sections for the 400 MeV/n ^{12}C and 4.88 GeV p^+ projectiles are not very much different from those for the 250 MeV/n and 1.05 GeV/n ^{12}C projectiles.

Earlier gamma-ray work with relativistic protons[1] and pions[2-4] on light target nuclei (A < 60) showed that alpha-removal products are prominent. It has been suggested that this observation may be explained by ordinary cascade-evaporation theory, for charged-particle evaporation is comparable to neutron evaporation for light elements and binding energy considerations force large yields on even-even products in the center of the valley of stability. There is no inconsistency in our observation of only small yields of alpha-removal products for strontium and lead targets, since at these higher atomic numbers neutron evaporation predominates over charged-particle evaporation. Our very recent, partially analyzed results from 250 MeV/n ^{12}C ions on sulfur and clacium targets show prominence of alpha-removal products, just as in the cited proton and pion work. In the case of our teflon targets, even if alpha-removal products are significant, we would not expect to observe any gamma rays, as their energies would be beyond our range of observation.

In Fig. 5 are plotted the $2^+ \rightarrow 0^+$ gamma-ray relative yields for various even-even products, as a function of neutrons removed from the target. Solid points are for 3 GeV and open circles, for 12.6 GeV ^{12}C irradiation. The points show an exponential fall-off of a factor of 1/e for about four neutrons removed. If each neutron removal requires 7-8 MeV, the exponential dependence implies a characteristic energy of about 30 MeV in the monotonic fall-off of probability of primary excitation energy.

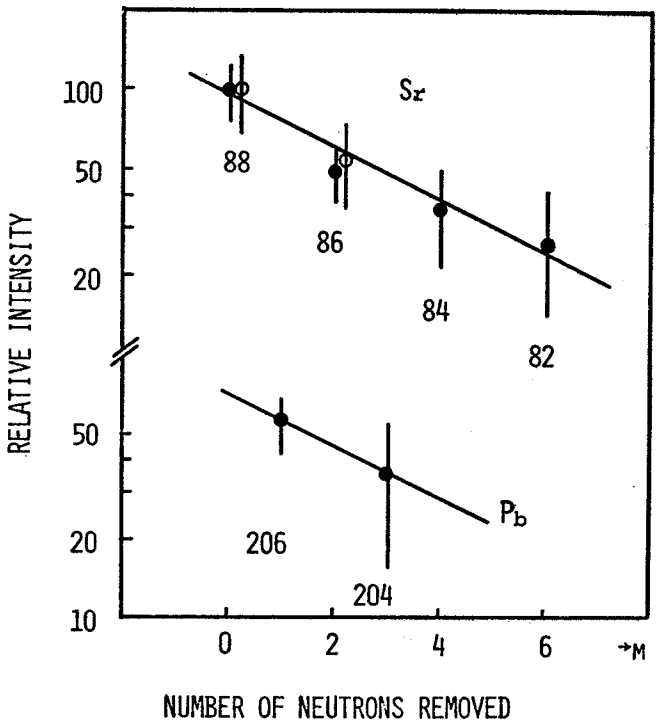

Fig. 5. Relative intensities of the $2^+ \rightarrow 0^+$ transitions in even Sr and Pb isotopes vs number (m) of neutrons removed. The closed and open circles are the values for the 3 GeV and 12.6 GeV ^{12}C, and mass numbers are also given. The solid lines represent the empirical expression $I(m) = \exp(-m/4.3)$. (XBL 766-8091)

Footnotes and References

*Department of Physics, Osaka University, Toyonaka, Osaka.

†Present Address: Department of Physics, Sanford University, Sanford, CA.

‡Department of Physics, University of Tokyo, Bunkyo-ku, Tokyo.

1. O. Artun, Y. Cassagnou, R. Legrain, N. Lisbonna, L. Roussel, J. P. Alard, A. Baldit, J. P. Castilhes, J. Furgeix, G. Roche, and J. C. Tamain, Phys. Rev. Lett. 35, 773 (1975).

2. H. E. Jackson, L. M. Schützmeister, T. P. Wangler, R. P. Reclwine, R. E. Segel, J. Town, and J. P. Schiffer, Phys. Rev. Lett. 31, 1353 (1973).

3. V. G. Lind, H. S. Plendl, H. O. Funsten, W. J. Kossler, B. J. Lieb, W. F. Landford, and A. J. Buffa, Phys. Rev. Lett. 32, 479 (1974).

4. H. E. Jackson et al., Phys. Rev. Lett. 35 641 (1975), ibid, 35, 1170 (1975).

FRAGMENTS FROM C, Al, Ag, AND U IRRADIATED BY HIGH ENERGY PROTONS

R. G. Sextro, G. D. Westfall, A. M. Poskanzer,
and A. M. Zebelman

Using a counter telescope consisting of a thin gas ionization ΔE counter and a 100 μm silicon E detector,[1] energy spectra and angular distributions of fragments produced by the irradiation of C, Al, Ag, and U with high energy protons have been measured. Previous measurements of fragments from these targets[2-4] were restricted by the lower energy cutoff of the ΔE detector which ranged from 1.5 MeV/nucleon for the lighter fragments to 2.5 MeV/nucleon for the heavier fragments. The present results extend down to 0.6 MeV/nucleon for all fragments observed.

The measurements consisted of three sets of experiments. The first used a 4.9 GeV proton beam to bombard C and Al targets where energy spectra were measured for all products at 20, 45, 90, 135, and 160°. The second set of experiments used 2.1 GeV protons on the same targets where measurements were made at 20, 90, and 160°. The third experiment used a 4.9 GeV proton beam to irradiate the Ag and U targets where energy spectra were observed at 90° for Ag and at 20, 90, and 160° for U.

Figure 1 shows the energy spectra of He through C fragments at 90° from 2.1 GeV protons on a C target. The dashed lines in this figure are drawn to guide the eye. Using projectile fragmentation data,[5] the observed energy spectra were extended to zero energy which allowed the integration of the energy spectra to obtain angular distributions and total production cross sections for each element observed.

The energy spectra of He through Na fragments observed at 90° from 4.9 GeV protons on Al are shown in Fig. 2. The solid lines indicate previous data taken with silicon detector telescopes while the dashed lines represent the gas telescope data. Despite the lower energy cutoff of the gas ΔE counter, the peak in the energy spectra of the higher-Z fragments from Al is not measured. Currently, an attempt is being made to calculate from available projectile fragmentation data this low energy part of the spectra in order to allow the integration of the energy spectra.

In Fig. 3 energy spectra for F through Ar fragments measured at 90° produced by 4.9 GeV protons incident on U are shown. Note that each successive element has been suppressed by a factor of two. The data points are shown for Ne and Ar to demonstrate the energy range of the gas telescope data. Beyond these points the solid line signifies data taken with silicon detector telescopes. The energy spectra were fitted using an evaporation model and parameters were derived which were similar to those found for the lower-Z fragments in previous works. The energy spectra were integrated to obtain angular distributions and total production cross sections for each element observed.

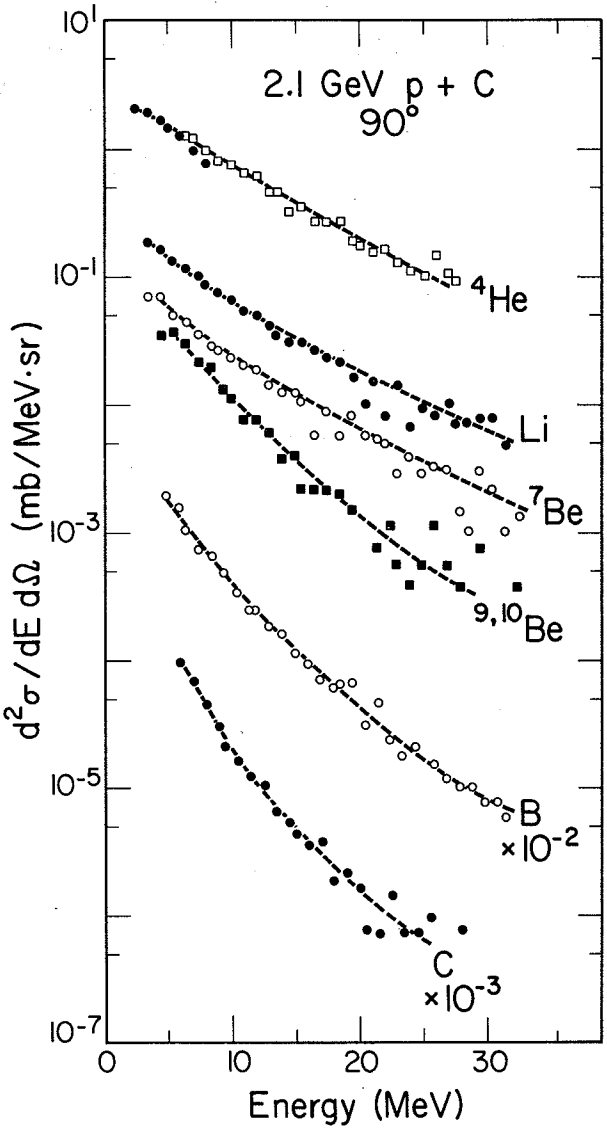

Fig. 1. Energy spectra at 90° for fragments from 2.1 GeV protons on C. The dashed lines represent the trend of the data. (XBL 758-7906A)

Figure 4 shows the energy spectra of F through Ar fragments produced by 4.9 GeV protons incident on a Ag target. A preliminary attempt was made to fit these spectra with a simple evaporation model. However, the parameters derived were not consistent with previous data on lower-Z fragments. This discrepancy may indicate the onset of some mechanism other than evaporation.

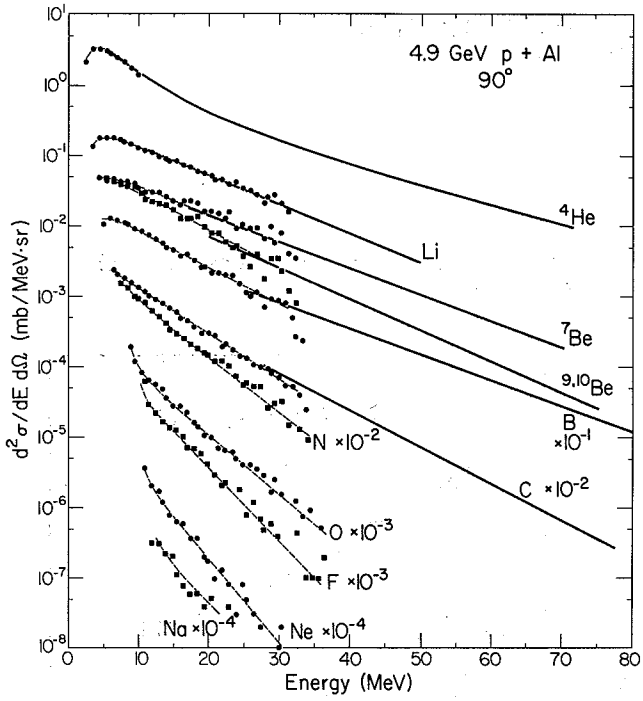

Fig. 2. Energy spectra at 90° for fragments produced by the irradiation of Al by 4.9 GeV protons. The dashed lines represent the trend of the gas telescope data and the solid lines signify the previous data taken with silicon detector telescopes. (XBL 758-7907A)

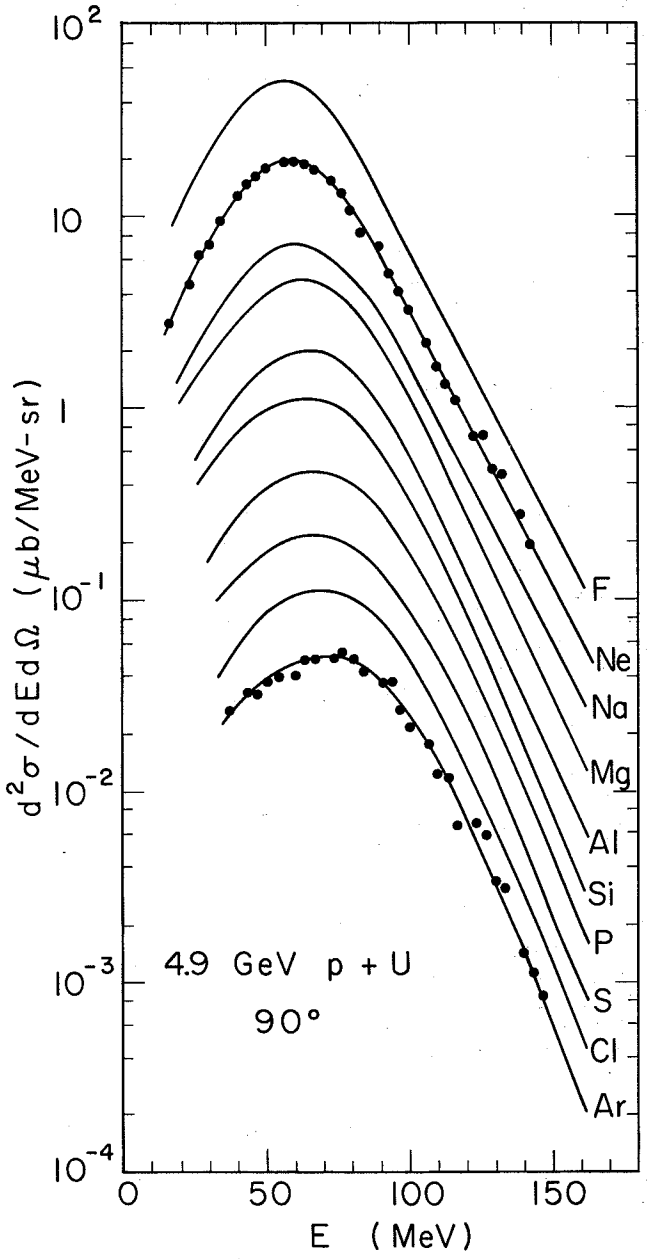

Fig. 3. Energy spectra at 90° for fragments from Z = 9 to 18 resulting from the irradiation of U by 4.9 GeV protons. Each successive element has been suppressed by a factor of two and the solid lines represent the trend of the data. (XBL 7511-8676)

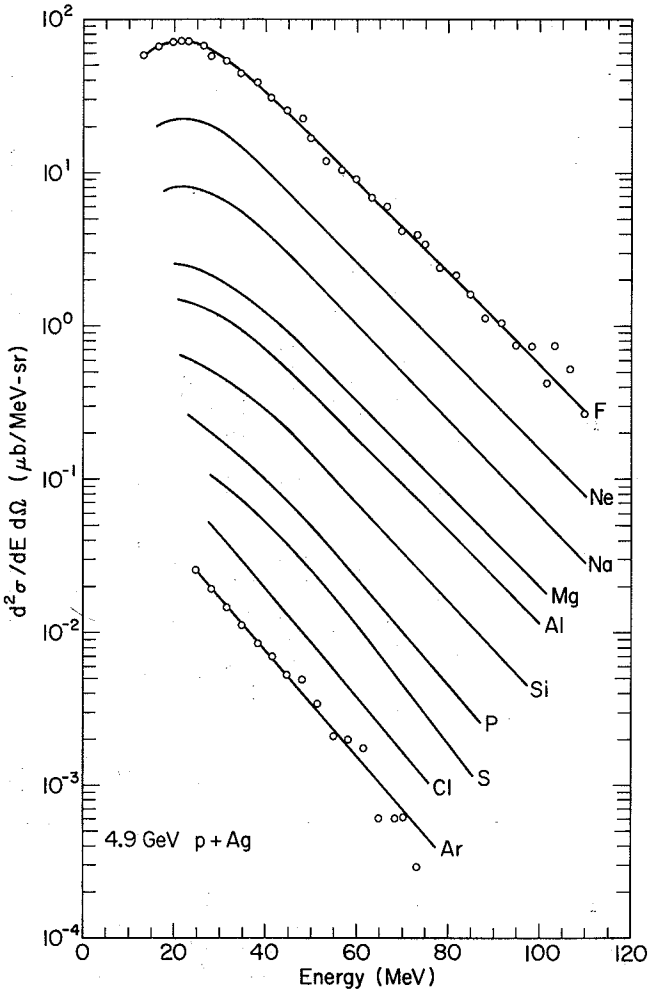

Fig. 4. Energy spectra for fragments at 90° from Z = 9 to 18 from Ag bombarded by 4.9 GeV protons. The solid lines represent the trend of the data and each successive element has been lowered by a factor of two. (XBL 764-2620)

References

1. R. G. Sextro, A. M. Zebelman, and A. M. Poskanzer, Nuclear Chemistry Division Annual Report, LBL-4000 (1974), p. 119.

2. A. M. Poskanzer, G. W. Butler, and E. K. Hyde, unpublished data (Al data).

3. E. K. Hyde, G. W. Butler, and A. M. Poskanzer, Phys. Rev. C 4, 1754 (1971); R. G. Korteling, C. R. Toren, and E. K. Hyde, Phys. Rev. C 7, 1611 (1973) (Ag data).

4. A. M. Poskanzer, G. W. Butler, and E. K. Hyde, Phys. Rev. C 3, 882 (1971) (U data).

5. P. Lindstrom, D. Greiner, H. Heckman, B. Cork, and F. Bieser, LBL-3650 (1975); D. Greiner, P. Lindstrom, H. Heckman, B. Cork, and F. Bieser, Phys. Rev. Lett. 35, 152 (1975).

COUNTER EXPERIMENTS IN THE THIN TARGET AREA AT LAMPF

G. W. Butler,* D. G. Perry,* A. M. Poskanzer,
J. B. Natowitz,† F. Plasil,‡ and L. P. Remsberg§

The energy spectra of boron through magnesium nuclides produced in the interaction of 800 MeV protons with a uranium target have been determined at 90° (lab) by dE/dx and time-of-flight techniques with a silicon detector telescope. The experiment was done in the LAMPF Thin Target Area at a proton beam intensity of 10 μA. Fragment flight times were determined over the 25 cm distance between the ΔE and E detectors and simultaneously over the 4.3 m distance from the target to the ΔE detector, utilizing the 201 MHz (5 nsec) Linac rf pulse as one of the timing signals. The nuclear charge (Z) of the fragments was determined from the dE/dx information and the mass (A) of the fragments was determined from both the time-of-flight and the energy signals via the equation $A = E \times T^2$. The time resolution over the 25 cm flight path was 0.25 nsec (FWHM) for carbon nuclides, corresponding to a mass resolution of 5.2%. The time resolution over the 4.3 m flight path was 0.9 nsec (FWHM), corresponding to a mass resolution of 1.1% for ^{13}C. This dramatic improvement in mass resolution is obtained using the information from the short flight path measurement to determine which rf pulse the fragment originated from, and then timing from the rf over the long flight path.

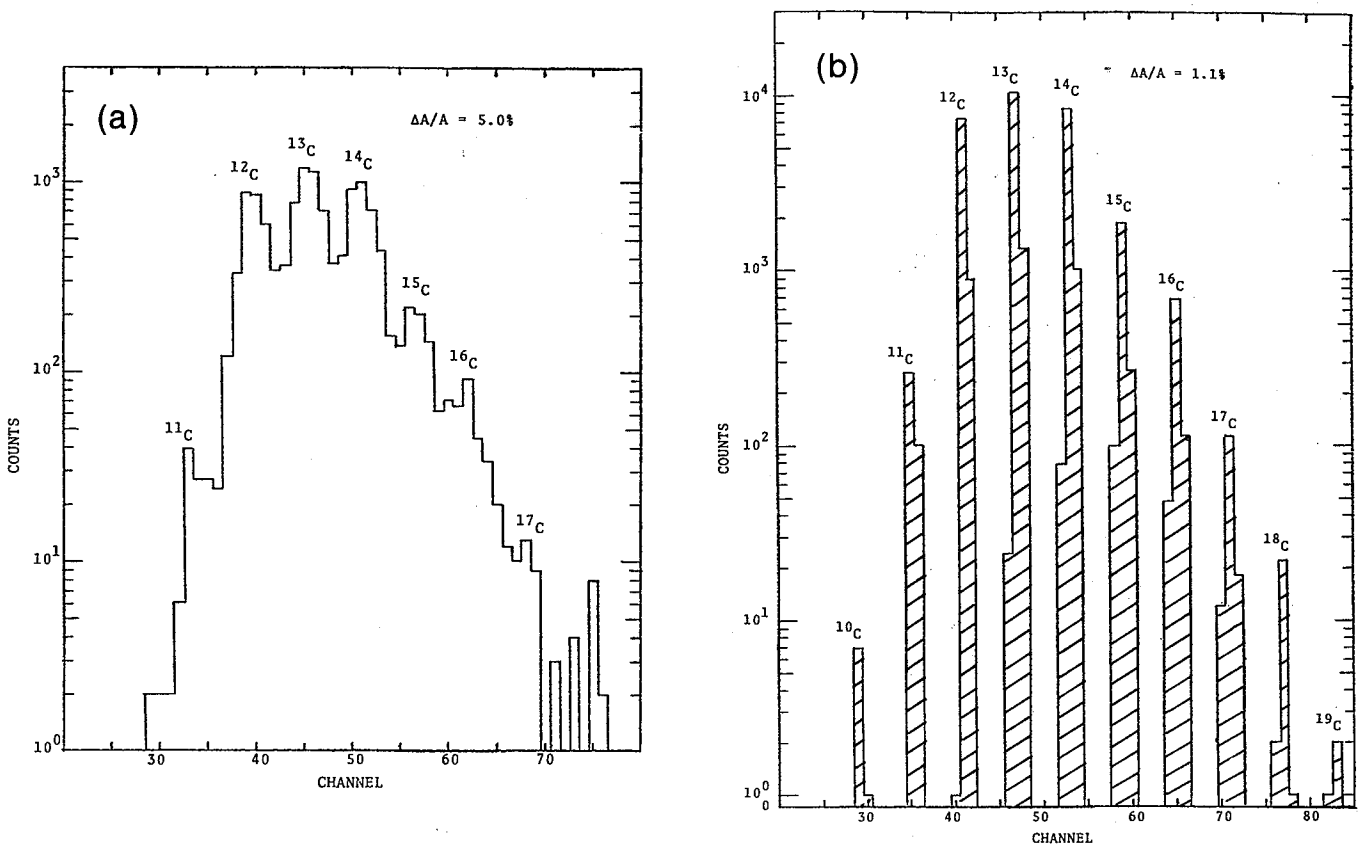

Fig. 1. Time-of-flight mass identification of carbon isotopes. (a) Obtained with a 25-cm flight path between the ΔE and E counters. (b) The same events bootstrapped to the 4.3-m flight path between the target (using the rf signal) and the ΔE counter. The four cycle semi-log scale shows the zero event level as well. (XBL 759-7993) (XBL 759-7995)

Footnotes

*Los Alamos Scientific Laboratory.

†Texas A&M University.

‡Oak Ridge National Laboratory.

§Brookhaven national Laboratory.

EVAPORATION-LIKE FRAGMENTS FROM URANIUM IRRADIATED BY 2.1 GeV/Nucleon ^{12}C AND ^{20}Ne IONS

A. M. Poskanzer, A. Sandoval, R. G. Sextro,
and H. H. Gutbrod

The study of low energy fragments from uranium irradiated by high energy protons[1] and alpha particles[2] has been extended to heavier projectiles at the Bevalac. The purpose of the experimental program is to study nuclear matter at high temperatures using the evaporation-like energy spectra of the light target fragments as a probe of highly excited nuclear matter.

The energy spectra for He through B fragments at 90° in the lab are shown in Fig. 1 for the ^{20}Ne irradiation. The shapes of the ^{4}He and ^{7}Li fragments are compared in Fig. 2 for all the projectiles used so far. It can be seen that the energy at the maximum, which is determined mainly by the Coulomb barrier, remains fixed. However, as the mass of the projectile increases, the spectra become considerably broader, the flattening on the high energy side being indicative of the high temperatures produced in the collision. (See Table 1). In Fig. 3 the strong increase in production cross section with mass of the projectile is shown for ^{4}He fragments. For the 2.1 GeV/nucleon ^{20}Ne ions the total ^{4}He production cross section is estimated to be ≈29 b, or an average of seven alpha particles emitted per

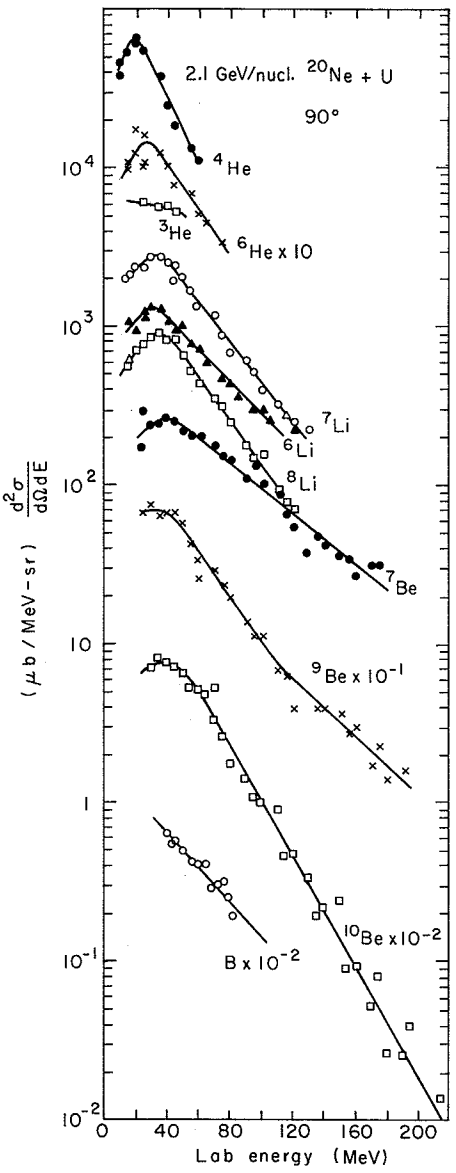

Fig. 1. Energy spectra at 90° in the lab for fragments from U irradiated with 2.1 GeV/nucleon ^{20}Ne ions. (XBL 758-3795)

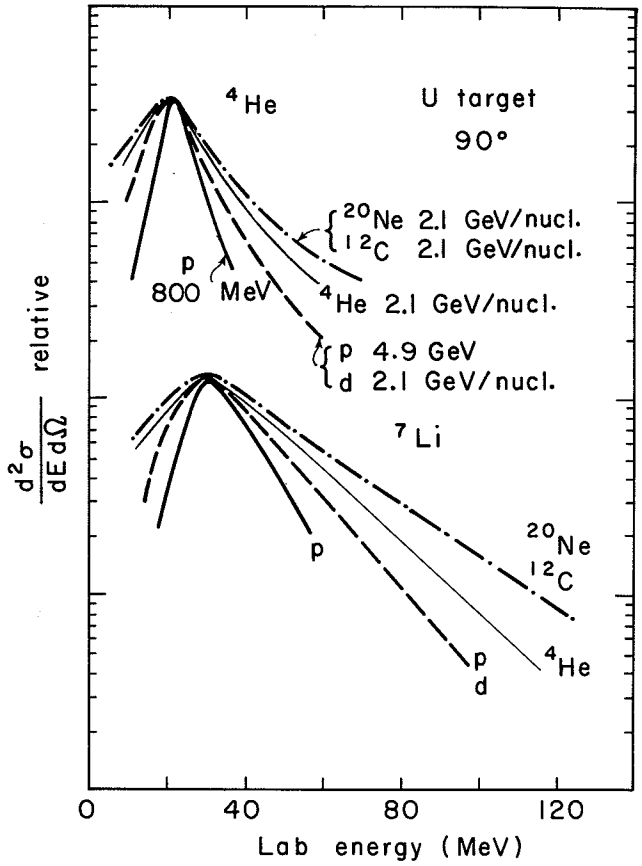

Fig. 2. Energy spectra of ^{4}He and ^{7}Li fragments from U irradiated with six different projectiles. The curves for each fragment are normalized at the same peak height in order to exhibit changes in shape. The curves for ^{7}Li are in the same order as for ^{4}He. (XBL 758-3796)

Table 1. Apparent temperatures and relative cross sections.

Projectile	Temperature (MeV)	Relative cross section		
	^{7}Li	^{4}He	^{7}Li	^{7}Be
5 GeV protons	10	1	1	1
2.1 GeV/nucleon alphas	12	3	4	5
2.1 GeV/nucleon ^{20}Ne	15	8	11	18

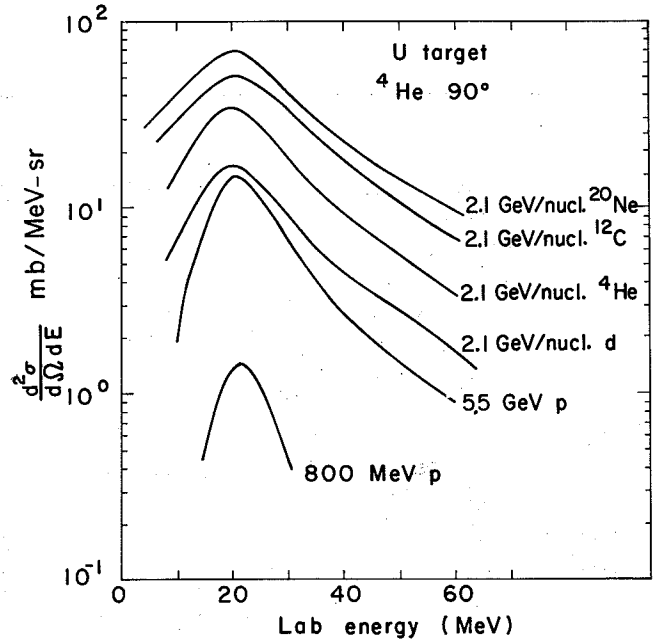

Fig. 3. Energy spectra of ^{4}He fragments from U (XBL 758-3793)

interaction. Lower-yield fragments, like ^{7}Be, which are known to be produced only at high excitation energies, show an even more dramatic increase in relative cross section, as shown in Table 1.

References

1. A. M. Poskanzer, G. W. Butler and E. K. Hyde, Phys. Rev. C 3, 882 (1971).

2. A. M. Zebelman, A. M. Poskanzer, J. D. Bowman, R. G. Sextro and V. E. Viola, Jr., Phys. Rev. C 11, 1280 (1975).

SEARCH FOR FRAGMENT EMISSION FROM NUCLEAR SHOCK WAVES*

A. M. Poskanzer, R. G. Sextro, A. M. Zebelman,
H. H. Gutbrod, A. Sandoval, and R. Stock †

For central collisions of nuclei at relativistic energies, recent theoretical investigations have focused on the question of how large amounts of energy and momentum are transferred from projectile to target nucleons, and on the early events in the evolution of hot, high-density regions as thermal equilibrium is approached. In particular, the formation of squirts of nuclear matter, or of nuclear shock waves carrying large transverse momentum and compressional energy, has been predicted. These would be formed in central collisions if the projectile velocity exceeds the nuclear sound velocity which is about 0.2 c. The models are in disagreement about the angles in the lab system at which emission should occur, some predicting a narrow peak at angles ranging from 25° to 45° depending systematically on the incident energy while others anticipate a broad range of forward angles for the fragments.

Baumgardt et al.[1] studied the prong angular distributions of star events produced in AgCl crystals irradiated with 0.87-GeV/nucleon ^{16}O ions. They report the observation of narrow peaking in $d\sigma/d\theta$, with angular widths of about 20° full width at half-maximum (FWHM). The prongs analyzed in that experiment are due to protons less than 28 MeV and He nuclei less than 200 MeV/nucleon, with no further discrimination with respect to energy and isotope.

We have, therefore, undertaken a study at the Bevalac of target-fragment energy spectra and angular distributions with a ΔE-E counter telescope that would identify He fragments with $15 \leq E \leq 150$ MeV/nucleon. The beams used were 2.7-GeV protons, 0.7- and 1.05-GeV/nucleon alpha particles, and 1.05-GeV/nucleon ^{16}O ions. Targets of natural silver and uranium, about 200 to 300 mg/cm^2 thick, were mounted in a scattering chamber equipped with a detector telescope consisting of a 1-mm-thick Si transmission counter as a ΔE detector, and a 5-cm-thick plastic scintillator (Pilot B) coupled to a 2.5-cm-diam phototube as an E detector. The telescope subtended a solid angle of 5 msr.

The energy calibration of the spectra was obtained for each kind of particle from the ΔE signals in the surface barrier detector by use of the known relation between energy loss in the ΔE counter and total kinetic energy. Due to the excellent resolution in ΔE and E, it was possible to identify the helium and lithium isotopes produced in the reaction. Spectra were taken in steps of 10° or sometimes in steps of 5°.

Spectra are shown in Fig. 1 for ^{3}He and ^{4}He emission at 20° in the lab system from a U target bombarded with several projectiles and energies. For energies above 50 MeV/nucleon, the cross

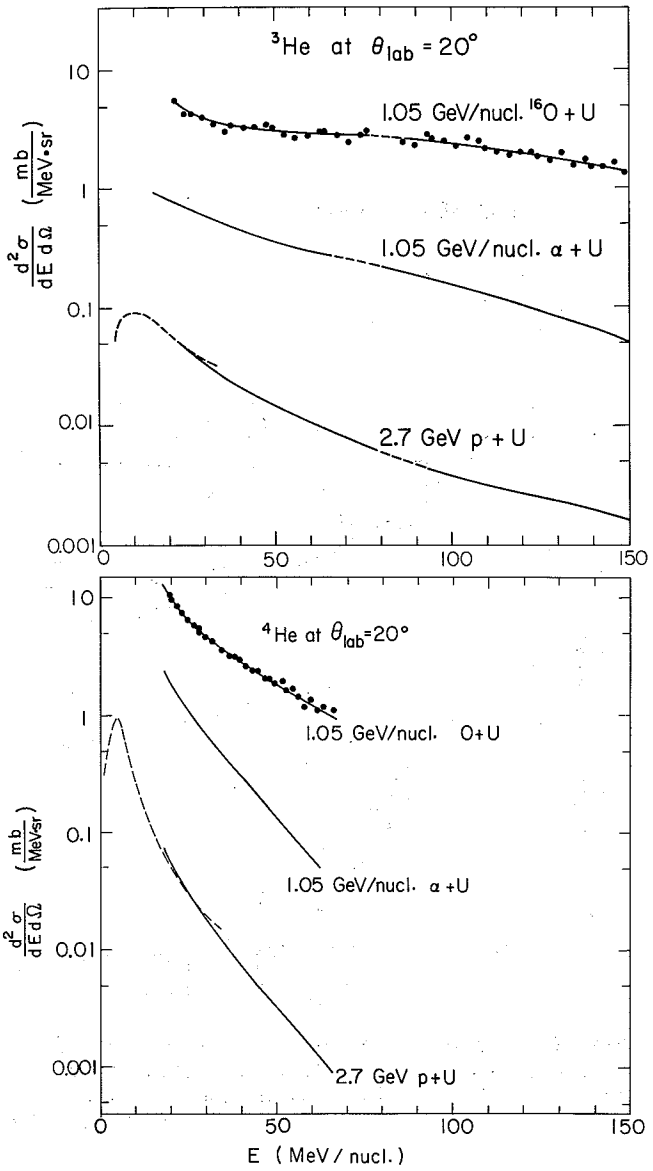

Fig. 1. Comparison of ^{3}He (upper part) and ^{4}He (lower part) spectra at 20° (lab) obtained upon bombardment of a uranium target with 2.7-GeV protons and with 1.05-GeV/nucleon α particles and ^{16}O ions. The data points are shown for the ^{16}O + U spectra. For p + U dashed curves are shown for the low-energy evaporation spectra obtained previously (Ref. 2). (XBL 759-3896)

sections increase by more than an order of magnitude as the projectile changes from p to ^{4}He, and from ^{4}He to ^{16}O. The ^{3}He spectrum from ^{16}O + U is remarkably flat, with cross sections above 1 mb/MeV-sr even at 150 MeV/nucleon.

For ^{3}He produced from ^{16}O + Ag, the angular distributions are shown in Fig. 2 for four successive bins of energy. The peak in dσ/dθ has a width of about 60° FWHM; its position shifts from 58° in the low-energy bin to about 30° above 100 MeV/nucleon where the angular distributions show little further change in shape. The same

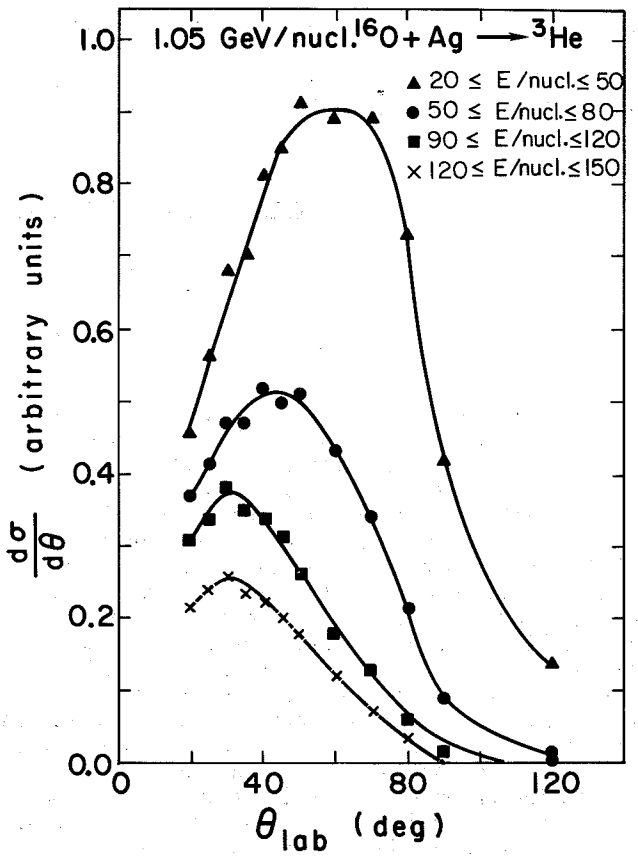

Fig. 2. Differential cross sections per unit angle, dσ/dθ, of ^{3}He fragments emitted in various energy domains between 20 and 150 MeV/nucleon from ^{16}O + Ag at 1.05-GeV/nucleon incident energy. (XBL 758-3792)

behavior is observed for all other combinations of target, projectile, and reaction product. No narrow peaking comparable with the 20° width observed by Baumgardt et al.[1] is found.

Even though our data are not selected for high multiplicity events we can compare our absolute cross section with those of Baumgardt et al.[1] Their reported peak (20° wide at 40° width dσ/dΩ = 0.7 b/sr) cannot be hidden under our smooth angular distributions for ^{16}O on Ag at 1.05 GeV/nucleon. We conclude that the events of Baumgardt et al.[1] are not due to high energy He nuclei.

Our data present evidence for the nonevaporative emission of ^{3}He and ^{4}He. Their cross sections scale roughly with A_p^2 (A_p being the projectile mass). At 1 GeV/nucleon, a possible explanation for the production of high energy ^{3}He and ^{4}He can be the final state interactions of cascade nucleons.

Footnotes and References

* Condensed from A. M. Poskanzer, et al., Phys. Rev. Lett. 35, 1701 (1975).

† University of Marburg.

1. Baumgardt et al., Z. Phys. A273, 359 (1975).

2. A. M. Poskanzer, A. Sandoval, R. G. Sextro, and A. M. Zebelman, unpublished data, 1975.

CENTRAL COLLISIONS OF RELATIVISTIC HEAVY IONS

H. H. Gutbrod, A. Sandoval, J. Gosset, W. G. Meyer,
A. M. Poskanzer, G. D. Westfall, and R. Stock*

A central collision of relativistic heavy ions with a target nucleus is characterized by a high multiplicity of emitted fragments. In nuclear track detectors[1] (AgCl and AgBr) star events with many prongs have been selected and analyzed in rough energy bins (white, grey, and black tracks) obtaining angular distributions. Since a full scanning with the determination of charge, mass, and energy of the prong is nearly impossible, conclusions drawn from this kind of data are very gross. To obtain more information regarding these central collisions we have improved our experimental setup[2] by installing 15 plastic scintillators (tag counters) connected to 2 in. diam photomultipliers around our scattering chamber. A special thin Al cover was built which served two purposes: (1) it increased the chamber volume by 80% so that large volume detector systems can be installed. (2) It serves as a thin (3/8 in.) absorber so that the tag counters do not measure the target-evaporation products. Furthermore, the tag counters did not subtend the angle from 0° to 15° in order to avoid any events due to break up of the projectile in a peripheral collision. The ΔE-E detector described in Ref. 2 was used as

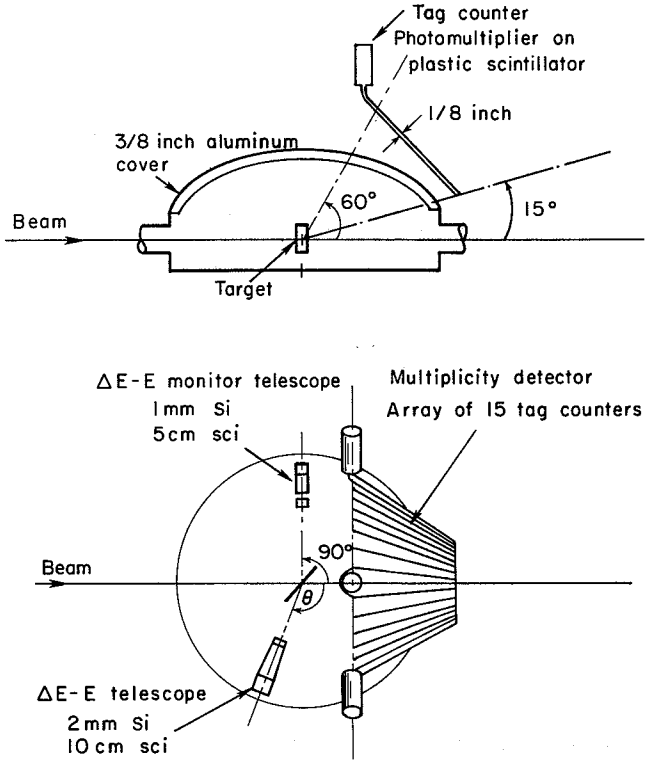

Fig. 1. 36-in. scattering chamber with telescopes and tag counters. (XBL 7512-9933)

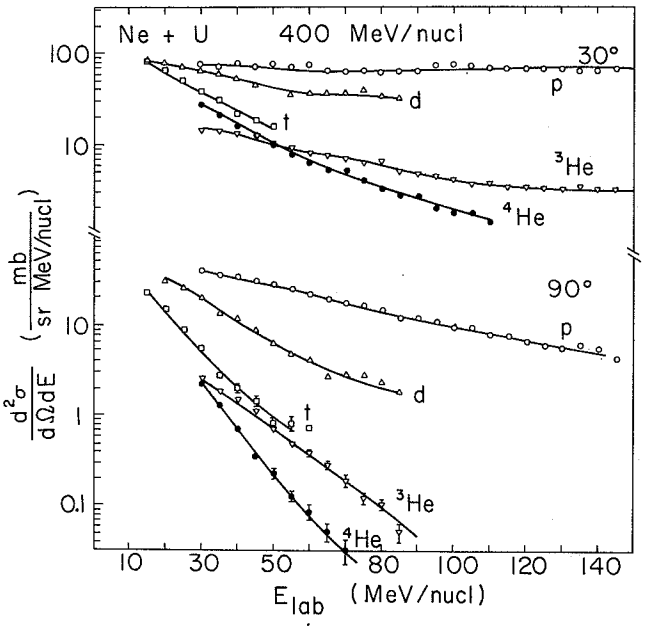

Fig. 2. Double-differential cross sections for hydrogen- and helium-isotopes resulting from the interaction of 400 MeV/nucleon ^{20}Ne with ^{238}U. (XBL 766-2954)

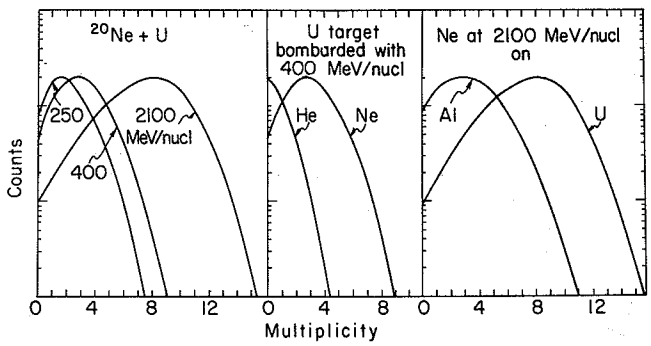

Fig. 3. Multiplicity distributions for the systems studied, as observed in the 15 tag counters. (XBL 766-2956)

Table 1. Average multiplicity of particles (outside the chamber dome) with E>45 MeV/nucleon for p, d, t, and E>20 MeV for pions associated to the reaction products detected in the telescope. Ω was determined from the angular distributions of protons with $45 \leq E_p \leq 300$ MeV.

$$1 + \frac{\bar{M}_{corr}}{\Omega}$$

	Particle Reaction	P	D	T	^{3}He	^{4}He
	MeV/Nucleon					
^{20}Ne + U	250	10.5	11	12	12	12
	400	16	17	18	18	19
	2100	~63	~68	~66	~77	~74
^{20}Ne + Al	2100	25	26	27	28	27
^{4}He + U	400	3.3	3.3	3.2	3.2	2.9

a monitor and a new silicon-scintillator telescope was built consisting of a 2 mm Si detector ΔE counter with an active area of 300 mm^2 followed by a 10 cm conically shaped plastic scintillator with a 2 in. phototube. A particle detected in this telescope opened a 30-nsec gate in the 16-fold discriminator and coincidence latch of the 15 tag counters. Therefore, a particle detected in the telescope was identified by A, Z, E, θ and the relative multiplicity of the star it belonged to, as well as by the information on which tag counters had fired. Thus, a rough spatial distribution of the multiplicity events could be detected.

Figure 1 shows the experimental layout. With this setup we studied ^{20}Ne induced reactions on U at 250, 400 and 2100 MeV/nucleon and on Al at 2100 MeV/nucleon, and ^{4}He induced reactions on U at 400 MeV/nucleon. Hydrogen and helium fragments could be measured up to an energy of 260 and 300 MeV/nucleon respectively, and isotopic separation was obtained in hydrogen up to 100 MeV/nucleon and in helium up to 130 MeV/nucleon. Figure 2 shows a comparison of some spectra. Figure 3 shows the difference in the multiplicity distribution for different target-projectile combinations at various energies. The single particle inclusive spectra of d, t, ^{3}He and ^{4}He could be related to the measured proton spectra using the Butler-Pearson formalism for final state interaction between cascade nucleons, as modified by Schwarzschild and Zupancic.[3] The final state interaction as a mechanism for the production of the complex fragments is furthermore suggested by the observation that the complex fragments are associated with a higher average multiplicity than that associated with protons (Table 1).

Footnotes and References

*University of Marburg.

1. Baumgardt et al., Z. Phys. A273, 359 (1975); H. Heckman et al., unpublished data, 1975; Otterlund et al., unpublished data, 1975.

2. A. M. Poskanzer, R. G. Sextro, A. M. Zebelman H. H. Gutbrod, A. Sandoval, and R. Stock, Phys. Rev. Lett. 35, 1701 (1975).

3. A. Schwarzschild and Č. Zupančič, Phys. Rev. 129, 854 (1963).

FINAL STATE INTERACTIONS IN RELATIVISTIC HEAVY-ION REACTIONS

P. J. Johansen, J. Gosset, H. H. Gutbrod, W. G. Meyer,
A. M. Poskanzer, A. Sandoval and G. D. Westfall

Experiments recently performed at the Bevalac by H. Gutbrod et al.[1] have been the study of this project. The projectiles were ^{20}Ne at 250 MeV/nucleon, 400 MeV/nucleon and 2.1 GeV/nucleon, and ^{4}He at 400 MeV/nucleon. The target was in all cases ^{238}U. From these experiments we have a series of double differential cross sections of the lighter fragments, p, d, t, ^{3}He and ^{4}He in an energy range from 15 MeV/nucleon to 100 MeV/nucleon.

To explain these spectra, a theory by S. T. Butler and C. A. Pearson[2] has been applied. The

theory was originally used to describe the deuteron production in 25-GeV p on ^{238}U reactions as a final state interaction. Here, the idea is to describe the spectra of the emitted composite particles, such as d, t, ^3He, ^4He, in the relativistic heavy ion reactions on the basis of the momentum distribution of the cascade nucleons. These nucleons can react with each other to form composite fragments with the surrounding nuclear matter acting as catalyst. In the phenomenological model this is described by assuming, that particles closer together in momentum space than a certain distance p_o will stick together and form heavier fragments.

A. Schwarzschild and Č. Zupančič[3,4] simplified the model of Butler and Pearson, and for the relativistic case we get:

$$\frac{d^2n}{p^2dpd\Omega}(N) = \frac{1}{N!}\frac{d^2n}{p^2dpd\Omega}\left(\frac{d^2n}{p^2dpd\Omega}\frac{4\pi}{3}\gamma p_o^3\right)^{N-1} . \quad (1)$$

N is the mass number of the fragment, p_o the radius in momentum space needed for the fragment to coalesce, $d^2n/p^2dpd\Omega$ is the number of shower particles per event per volume element in momentum space, $d^2n(N)/p^2dpd\Omega$ is the number of composite particles per event per volume element in momentum space, and γ is the Lorentz factor for a nucleon of momentum p.

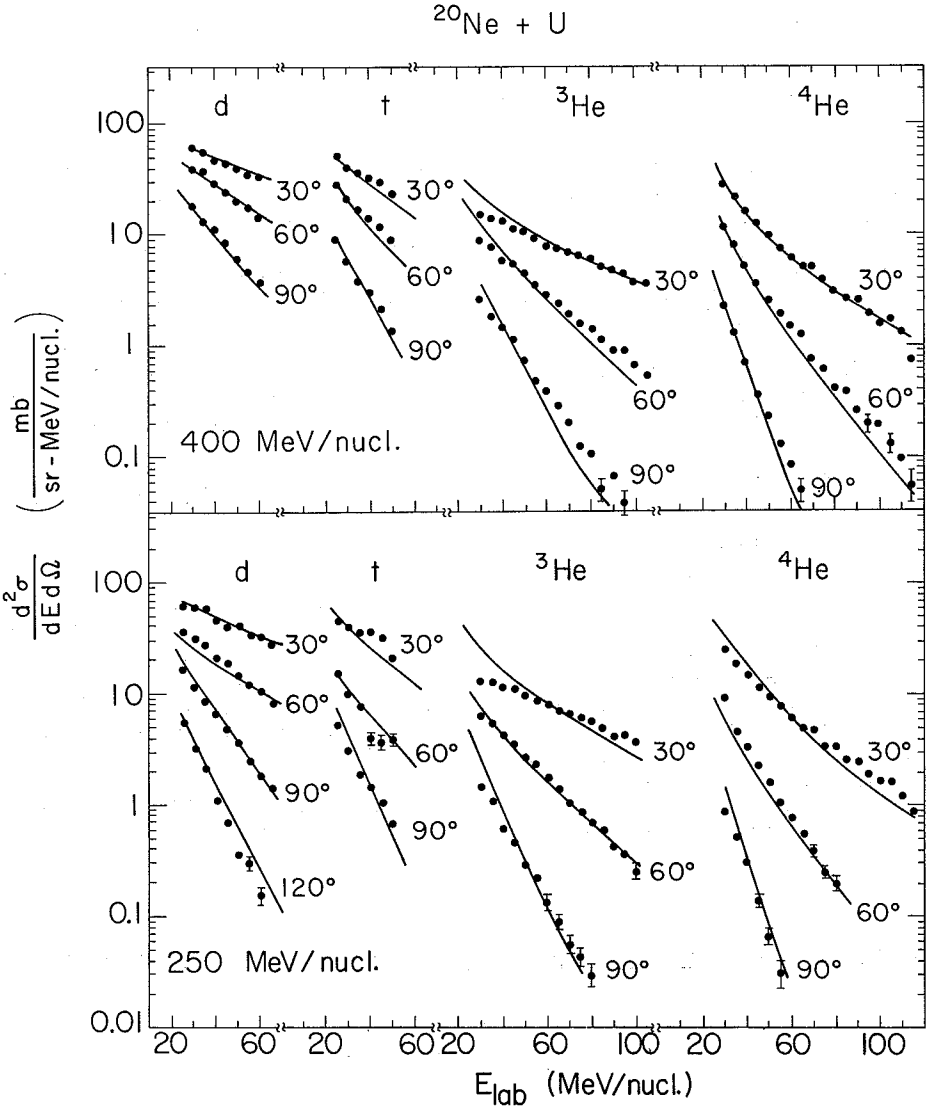

Fig. 1. Experimental and calculated double differential cross sections at various angles for 250 and 400 MeV/nucleon ^{20}Ne + U. (XBL 767-3109)

To test this theory, fits have been made for the different fragments. Input in this model is the experimentally determined distribution of protons. Since the total cross section for cascade particle production has not been measured, Eq. (1) has been rewritten in terms of the proton cross section. Neglecting the difference of σ_{pp} vs σ_{pn}, we get:

$$\frac{d^2\sigma(x,y)}{dEd\Omega} = \left(\frac{d^2\sigma(prot)}{dEd\Omega}\right)^{x+y} \frac{K(x,y)}{[m\sqrt{E(E+2m)}]^{x+y-1}} \qquad (2)$$

$$K(x,y) = \left(\frac{4\pi p_o^3}{3\sigma_o}\right)^{x+y-1} \frac{1}{x!y!} \left(\frac{N_p + N_t}{Z_p + Z_t}\right)^y .$$

Table 1. Radius p_o (MeV/c) of the momentum sphere for coalescence.

	$p_o(d)$ (MeV/c)	$p_o(t)$ (MeV/c)	$p_o(^3He)$ (MeV/c)	$p_o(^4He)$ (MeV/c)
^{20}Ne on ^{238}U 400 MeV/ nucleon	129	129	129	142

X being the number of protons and Y the number of neutrons in the composite particle.

So far we have been able to show, that the production of d, t, ^3He and ^4He in these reactions can be explained within a factor of 2 in the framework of A. Schwarzschild et al.[3,4] (Fig. 1).

The value of p_o (Table 1) is very sensitive to the value of σ_{geo} [see Eq. (2)]. Our estimate comes around 130 MeV/c as compared to 100 MeV/c of Ref. 2, and 400 MeV/c of Ref. 3.

In continuation of this project more work is in progress to examine the possibility of describing also the heavier fragments like the Li and Be isotopes by this mechanism, and to introduce a simple model to describe the energy and angular dependence of the shower particles.

References

1. H. Gutbrod, A. Sandoval, J. Gosset, W. G. Meyer, A. M. Poskanzer, G. D. Westfall and R. Stock, unpublished data, 1975.

2. S. T. Butler and C. A. Person, Phys. Lett. 1, 77 (1962).

3. A. Schwarzschild and Č. Zupančič, Phys. Rev. 129, 854 (1963).

4. Č. Zupančič, Phys. Lett. 4, 182 (1963).

D. MESONIC ATOMS AND ATOMIC PHYSICS

MESONIC ATOMS

Clyde Wiegand, Garry Godfrey and Gary Lum

Z-Dependence of Kaonic X-Ray Intensities

We completed a survey of the intensities of x rays emitted when negative kaons were stopped in 91 targets ranging from Z = 2 through Z = 92.[1] Some of the targets were pure isotopes and some were compounds. Included were x rays from kaonic atoms and Σ^- hyperonic atoms. Kaonic x-ray intensities for low principal quantum number, n, transitions varied from 0.1 to 0.5 x rays/K_{stop} and showed a remarkable dependence on Z (see Fig. 1). Peaks occurred near elements with closed electron shells. There is no satisfactory explanation of this Z dependence. A calculation of the kaons' cascade into the nuclei was made in an attempt to reproduce the measured intensities. Initial kaon distributions at n = 30 proportional to $(2\ell + 1)$ out to certain ℓ_{max} were used to begin the cascade. No kaons were assumed to be in angular momentum states higher than the assigned ℓ_{max}. Values of ℓ_{max} were changed with Z to fit the measured intensities. This scheme of arbitrarily truncated distributions reasonably reproduced the $\Delta n = -1$ transition but gave $\Delta n = -2$ intensities high by a factor of two. It was suggested that ℓ_{max} might be related to an impact parameter with a lever arm equal to one-half the distance between atoms, but this scheme was unsatisfactory.

Absence of Kaon Decay

There was a remote possibility that certain electronic configurations could result in metastable orbital states for kaons due to suppression of Auger emission. If the cascade got "hung up", kaons could decay with their natural meanlife of 1.24×10^{-8} sec. During some of the x-ray measurements we searched for muons from $K^- \rightarrow \mu^- + \nu$ and established an upper limit of 0.05 per K_{stop}.[2] Therefore, stopped kaons disappeared in nuclear reactions as had always been assumed.

Effect of Hydrides

We found that oxygen in a H_2O target and C in a target of CH (polyvinyltoluene) emitted markedly fewer kaonic x rays than oxygen or carbon alone, although it is known that only about 3% of the kaons interacted with free protons.[2] Several other hydrides have been tested to show that the presence of hydride bonds reduced the x-ray intensities. The mechanism that influences mesonic cascades in the presence of hydride bonds is probably related to the one that controls cascades in elements.

Loss of x-ray intensities from low n transitions is apparently caused by mesons being captured into predominantly low ℓ states where they react with nuclei at high n levels. Or, atomic capture starts with statistical distributions that shift toward low ℓ states due to Stark mixing or some other effect induced by electric fields of particular electronic configurations.

Observation of Dynamic E2 Mixing Via Kaonic X-Ray Intensities

A nuclear resonance effect was observed between a kaonic atom and a nuclear transition in ^{98}Mo.[3] Our intensity measurements gave $^{98}Mo(n=6\rightarrow5)/^{92}Mo(n=6\rightarrow5) = 0.16 \pm 0.16$ instead of the no-mixing value of 1. Dynamic E2 mixing caused kaons to be strongly absorbed from the ^{98}Mo atomic state n = 6, ℓ = 5, in agreement with theoretical predictions. The effect occurs when the energy of a nuclear excited state nearly equals a kaonic atom de-excitation energy. In ^{98}Mo mixing of the $|$kaon n = 6, ℓ = 5$\rangle|$nucleus 0^+ ground state$\rangle$ with the $|$kaon n = 4, ℓ = 3$\rangle|$nucleus 2^+ excited$\rangle$ is expected to cause kaons to be strongly absorbed from the new n = 6, ℓ = 5 eigenstate. In ^{98}Mo the first nuclear excited states lies at 787.4 keV and the kaonic atom transition n = 6→4 is 798.2 keV. As a control we compared ^{98}Mo with ^{92}Mo whose first nuclear excited state lies at 1540 keV. Figure 2 shows portions of the x-ray spectra where the intensities are equal for the undisturbed n = 7→6 transitions. The n = 6→5 line is present in ^{92}Mo and absent in ^{98}Mo. Studies of E2 mixing, which is due to the quadrupole moment of the excited nuclear state, could lead to information on states not directly accessible in kaonic atoms. In our case, the kaonic n = 4, ℓ = 3 state.

Anisotropy of X-Ray Angular Distributions

There is a possibility that the distribution of x rays emitted by mesonic atoms is not isotropic.[4] Anisotropy relative to the direction of the impinging beam could occur if the momenta of the mesons were sufficiently large at the instant of atomic capture. The axes of rotation of the mesonic atoms would be confined to a plane perpendicular to the beam direction. It was shown that theoretically the orientations should be preserved during Auger and dipole x-ray emission. Existence of an anisotropy would give valuable information on the mech-

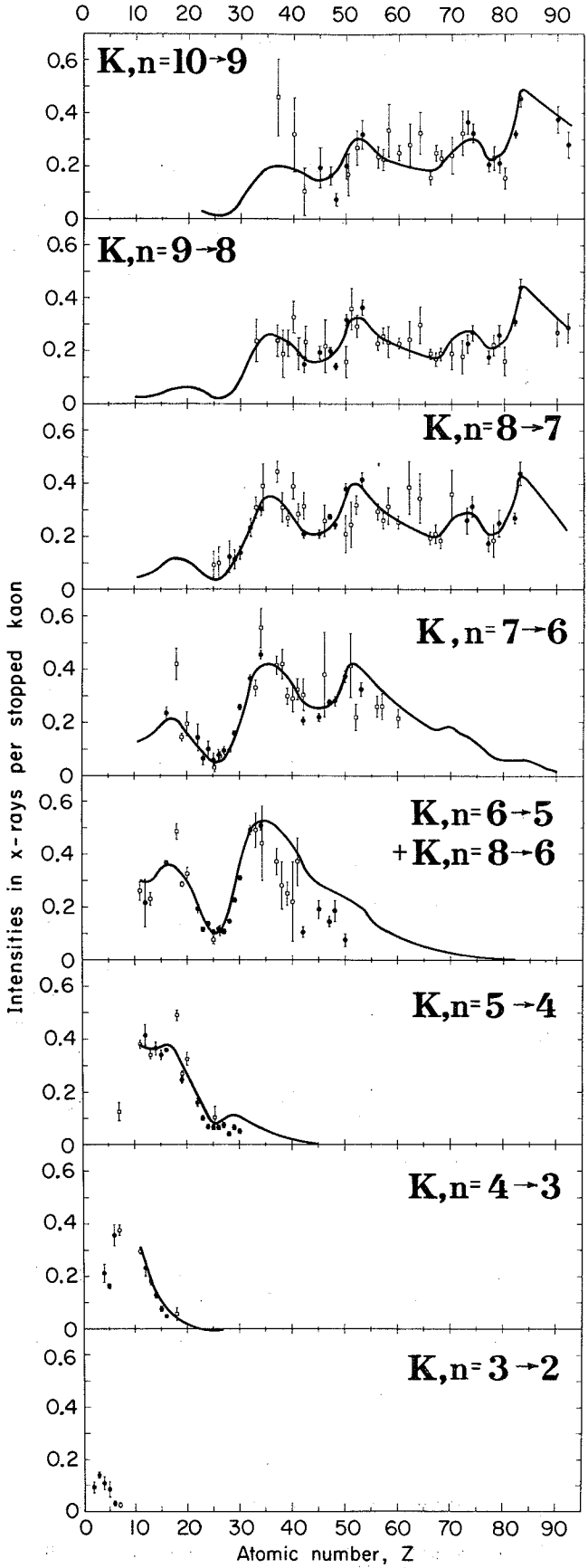

Fig. 1. Intensity versus Z of observed principal (n = -1) kaonic x-ray lines. Filled in and open points apply to experiments made at different times. The smooth curve shows intensities calculated by a cascade program. (XBL 752-2417)

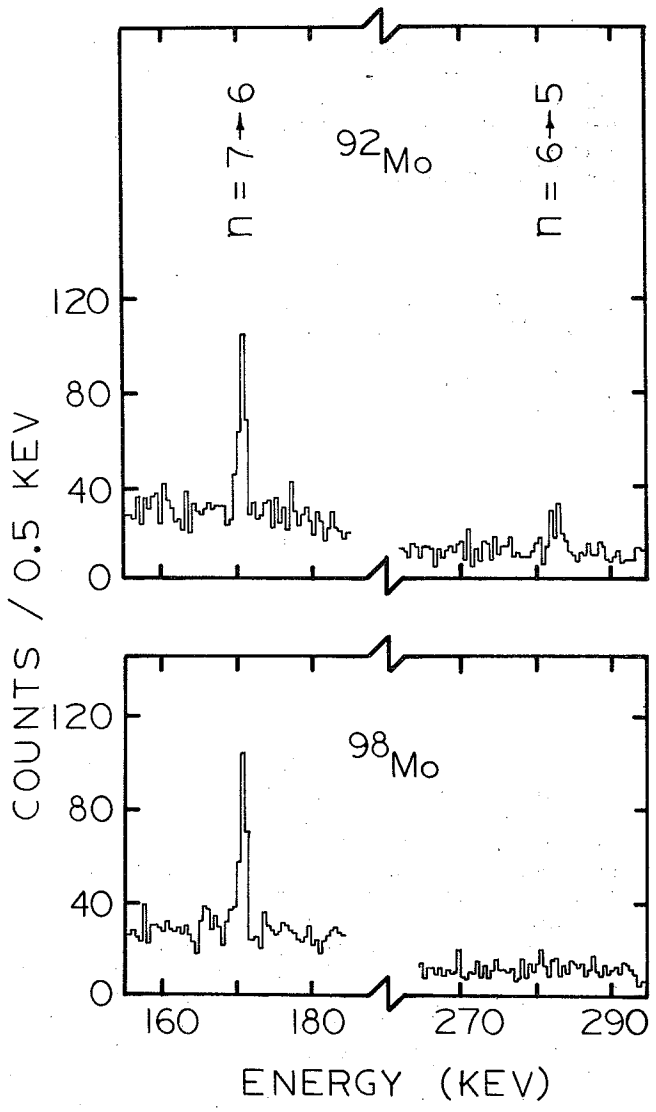

Fig. 2. Portions of the kaonic x-ray spectra of ^{92}Mo and ^{98}Mo showing the attenuation of the n = 6→5 line in ^{98}Mo due to dynamic E2 mixing of a nuclear and an atomic state. (XBL 7512-9940)

anism of formation of mesonic atoms. In a recent experiment we measured the distributions of x rays from pionic argon. Analysis of the results shows intensities in the beam direction and perpendicular to the beam direction to be equal within a few percent where the maximum effect could have been 50%.

References

1. Gary L. Godfrey, Lawrence Berkeley Laboratory Report LBL-3857, Ph.D. Thesis, May 1975.

2. G. L. Godfrey and C. E. Wiegand, Phys. Lett. 56B, 255 (1975).

3. G. L. Godfrey, G. K. Lum and C. E. Wiegand, Phys. Lett. 61B, 45 (1976).

4. G. Ya. Korenman, Sov. J. Nucl. Phys. 21, 398 (1975).

Additional Publications

Gary L. Godfrey, Strong Interactions, Zwieg's Rule, and Weaker Interactions, LBL-3697, February 1975.
R. Seki, C. Wiegand, Kaonic and Other Exotic Atoms, Annu. Rev. of Nucl. Sci. (Annual Reviews Inc., Palo Alto, California, 1975), Vol. 25, p. 241.

MULTIPLE SCATTERING AND ENERGY LOSS STRAGGLING OF HEAVY IONS

B. G. Harvey and J. Mahoney

The performance of instruments for the identification of heavy ions is often limited by multiple scattering and the energy loss straggling. For example, the resolution of angular measurement made by double position measurements in a spectrometer focal plane detector can be limited by heavy ion multiple scattering in the gas space between two position-counter planes. The determination of atomic number Z depends upon the measurement of energy loss dE/dx, and in a well-designed instrument the dE/dx resolution should be almost entirely fixed by the energy loss straggling. Instrument and experiment design, therefore, require the accurate calculation of heavy ion multiple scattering and energy loss straggling.

Multiple Scattering

The theory of multiple scattering[1,2] and the tables of Sigmund and Winterbon[2] are in good agreement with recent experimental work.[3,4] The Rochester measurements,[5] however, appear to give RMS multiple scattering angles that are too large by a factor of 2 or 3. We have compared multiple scattering angles $\theta_{1/2}$ (HWHM) extracted from the Sigmund and Winterbon tables with values calculated from the old formula.[6]

$$\theta_{1/2} = 0.585 \left[\frac{3.922 \times 10^{-8} t \, Z_1 (Z_1+1) Z_2^2}{A_1 E^2} \times \ln\left(\frac{211.9\, t}{Z_1^{2/3} + Z_2^{2/3}} \cdot \frac{Z_1 + 1}{A_1 Z_1} \right) \right]^{1/2} \text{rad}$$

where $\theta_{1/2}$ is the half width at half maximum, A_1 and Z_1 refer to the scattering medium, Z_2 to the heavy ion, t is the thickness of the scatterer in $\mu g/cm^2$, and E is the heavy ion energy in MeV. The empirical factor 0.585 brings the formula into agreement with Sigmund and Winterbon to within 10% over a very wide range of parameter values provided that t is greater than 20 $\mu g/cm^2$. Contrary to the findings of the Rochester group, agreement with experiment is obtained even down to 1 MeV/A when Z_2 is used rather than the effective charge of the heavy ion.

Energy Loss Straggling

In contrast, the theory of energy loss straggling still needs improvement. Moreover, experimental measurements in thin foils require a uniformity of thickness on a microscopic scale that is very difficult to obtain.[7] At low velocities, electron pick-up and loss contributes markedly to the energy loss straggling.

For the purpose of predicting the dE/dx straggling that will be obtained in a gas-filled proportional counter or ion chamber, we find that the simple equation

$$\delta E = K Z_2 \sqrt{t} \text{ keV FWHM}$$

is very useful. However, K is energy dependent. For ^{16}O in propane it varies from 1.13 (80 MeV) to 0.95 (300 MeV), the drop being perhaps due to the lesser importance of electron pick-up and loss at the higher ion velocity. In Ar-7%CH_4, the value of K is also about 1.

References

1. L. Meyer, Phys. Status Solidi 44B, 253 (1971).

2. P. Sigmund and K. B. Winterbon, Nucl. Instrum. Meth. 119, 541 (1974).

3. B. W. Hooton, J. M. Freeman and P. P. Kane, Nucl. Instrum. Meth. 124, 29 (1975).

4. G. Spahn and K. O. Groenveld, Nucl. Instrum. Meth. 123, 425 (1975).

5. C. K. Cline, T. E. Pierce, K. H. Purser and M. Blann, Phys. Rev. 180, 450 (1969).

6. E. J. Williams, Proc. Roy. Soc. 169, 531 (1939); Phys. Rev. 59, 292 (1940).

7. Preprint, VICKSI Group, Berlin.

MEASUREMENT OF ATOMIC CHARGE EXCHANGE CROSS SECTIONS FOR HIGH ENERGY HEAVY IONS

Fred Bieser,* Bruce Cork, Hank Crawford, Douglas Greiner,
Harry Heckman, Peter Lindstrom, Grant Raisbeck,† and Lance Wilson

The effective charge of an ion passing through matter is not a constant. The ion is continually picking up electrons from the medium, storing them in its vacant orbitals, and then losing them again in subsequent collisions. The rate at which this happens depends on the ion's nuclear charge Z_I, its velocity β_I, and the electron distribution in the medium, which is characterized by the nuclear charge of the medium Z_m. At low ion velocities, $\beta_I < Z_I\alpha$, the number of electrons localized on the ion, and hence its effective charge Z^*, is a rapidly varying function of β_I. At very high velocities, $\beta_I >> Z_I\alpha$, the ion spends most of its time fully stripped of electrons, occasionally attaching a single electron and losing it again before it has a chance to attach another. We are using the high velocity ($\beta \sim 0.65$ to 0.95), fully stripped ion beams of the Bevalac to investigate the rate at which single electron attachment and loss occurs for heavy ions ($6 \leq Z_I \leq 26$) as they pass through various solid and gaseous targets ($4 \leq Z_m \leq 79$). We present here some results for Ne ions incident at 250 MeV/nucleon and 2.1 GeV/nucleon on various thick solid targets.

The experiment was originally motivated by an astrophysical problem concerning the propagation of cosmic rays which can only decay by capturing a K-electron.[1] By measuring the relative abundance of these K-capture isotopes in the cosmic rays, as a function of energy, and measuring the single electron attachment and loss cross sections for them, we will have another way to probe the environment in which the cosmic rays travel.

The problem of the effective charge of ions passing through matter at low velocities [$\beta \leq .15$, (10 MeV/nucleon] has been investigated by many experimenters. Based on data for alpha particles and ions as heavy as ^{84}Kr at low β_I, a theoretical framework describing the attachment and loss process has evolved. This theory is most easily understood and applied to single electron systems; however, since even light ions like ^{40}Ar have more than one electron attached, on the average, at 10 MeV/nucleon, data to test the theories in their simple 1 e^- form has not been available before this experiment. By measuring the electron attachment and loss cross sections, σ_A and σ_L, as a function of β_I, Z_I, Z_m we will provide input for the cosmic ray propagation calculation and be able to test atomic-charge-exchange theories on simple systems at energies not previously investigated.

The experiment is performed in Bevalac Beam 33, using the spectrometer, by passing a beam of fully stripped ions, $Z^* = Z_I$, first through a target (gas or solid), then through a magnetic field and into a charge-measuring solid state detector telescope (four Si(Li) detectors in a row). The angle through which the ion is deflected by the magnetic field depends on the momentum and effective charge of the ion. By placing a detector telescope at the angle corresponding to $Z^* = Z_I - 1$ and a secondary emission monitor at the angle for $Z^* = Z_I$ we are able to count the number of ions emerging from the target with an electron attached $N(Z_I - 1)$, and the number which emerge fully stripped, $N(Z_I)$.

The ratio $N(Z-1)/N(Z)$ depends on the attachment and loss cross sections and on the target thickness, such that

$$N(Z-1)/N(Z) = \sigma_A/\sigma_L \, (1 - e^{-\sigma_L N_T X})$$

where N_T = number of target atoms/cm^3 and X = target thickness (cm). For thick targets, $X >> 1/N_T\sigma_L$, the ratio is independent of X and represents a dynamic equilibrium between attachment and loss processes. We can calculate σ_L assuming that electrons are lost in collisions with target electrons and nuclei in which the energy transfer exceeds the attached electrons binding energy, and that $\beta_I >> \beta_m$, the velocity of electrons in the medium. Thus, following Bohr,[2] we find per target atom,

$$\sigma_L = 4\pi a_o^2 \, \frac{Z_m^2 + Z_m}{Z_I^2} \left(\frac{\alpha}{\beta_I}\right)^2$$

where a_o = Bohr radius. For ^{20}Ne traversing ^{27}Al at $\beta_I \sim 0.95$, we expect to find that an equilibrium will be reached in targets thicker than 1 mg/cm^2. As we go to higher Z_m, however, $\beta_m \sim \alpha Z_m$ is no longer small with respect to β_I and our simple formula for σ_L is no longer valid. The loss cross section should decrease because low energy transfer collisions will become a larger fraction of the $e^- - e^-$ interactions. Thus, at $Z_m = 80$ we would expect the thickness in which equilibrium is reached to be greater than 300 μg/cm^2.

There are two distinct processes that can lead to electron attachment: nonradiative (dominating at low energies) and radiative. The nonradiative process is a three-body process involving the transfer of the electron from the target nucleus to the incident ion. Because little work exists on the relativistic problem, for comparison with experiment we have used the nonrelativistic calculation of

Brinkman and Kramers[3] for a hydrogenic medium. After making corrections for attachment into higher states, and the screening of the nuclear charge, we find the formula (per target atom) becomes,

$$\sigma_{n\text{-}rad} = 1.202\, r_K(\pi a_o^2\, 2^{18}/5)\, Z_I^5\, (Z_M - s_1)^5\, s^8 \times [s^2 + (Z_I + Z_M - s_1)^2]^{-5}\, [s^2 + (Z_I - Z_m + s_1)^2]^{-5}$$

where $s = \alpha^{-1}\sqrt{2(\gamma - 1)}$, a_o is the Bohr radius, r_K is the number of K shell electrons in the medium and s_1 is the K-shell screening constant (0 for hydrogen; 0.3 otherwise).

As the inverse to photoionization, the radiative attachment process is a two body process in which a "free" electron becomes bound to a nucleus and simultaneously emits a photon in order to conserve energy. In this context, the word free means that the orbital velocities of electrons in the medium are negligible when compared to the incident ion's velocity. We have used the principle of detailed balance, the relativistic photoionization formula of Pratt et al.[4] and corrected for attachments into higher states to obtain the following radiative attachment formula per atom

$$\sigma_{rad} = (1.202)\, 3/2\, Z_I^5\, Z_m \alpha^4\, \sigma_T \frac{T^2}{(T + M_u c^2)^2 - M_u^2 c^4} \times \left[\frac{M_u c^2}{T}\right]^5 (\beta\gamma)^3 \left[4/3 + \frac{\gamma(\gamma-2)}{\gamma+1} \times \left(1 - \frac{1}{2\beta\gamma^2}\, \ell n \left(\frac{1+\beta}{1-\beta}\right)\right)\right] f_{cor}(Z_I, \beta)$$

where σ_T is the Thompson cross section, M_u is an atomic mass unit, T is the kinetic energy per nucleon, and f_{cor} is the correction function of Ref. 3.

Note that for large γ, theory predicts $\sigma_{n\text{-}rad} \sim Z_m^5\, \gamma^{-6}$ and $\sigma_{rad} \sim Z_m\, \gamma^{-1}$ so that for each target there should exist an energy above which radiative attachment dominates. Thus, by varying the target materials and ion energies, we can test for a change in the relative importance of the two processes.

In June 1975 we made preliminary measurements of the thick target equilibrium ratio, $R_E = N(Z_I-1)/N(Z_I) = \sigma_A/\sigma_L$, for Ne^{+10} ions traversing targets of Be, Mylar, Al, Ni, and Ta. In Fig. 1 we show the equilibrium ratios for all targets relative to the equilibrium ratio for the Be target, $RE(Z_m)/RE(4)$, plotted against Z_m calculated according to the theoretical formulae presented above. In Fig. 2 we show the same ratios calculated for the cases of only nonradiative attachment process and only radiative attachment process at 250 MeV/nucleon. Our preliminary data show that we have clearly seen a contribution from the radiative attachment of electrons.

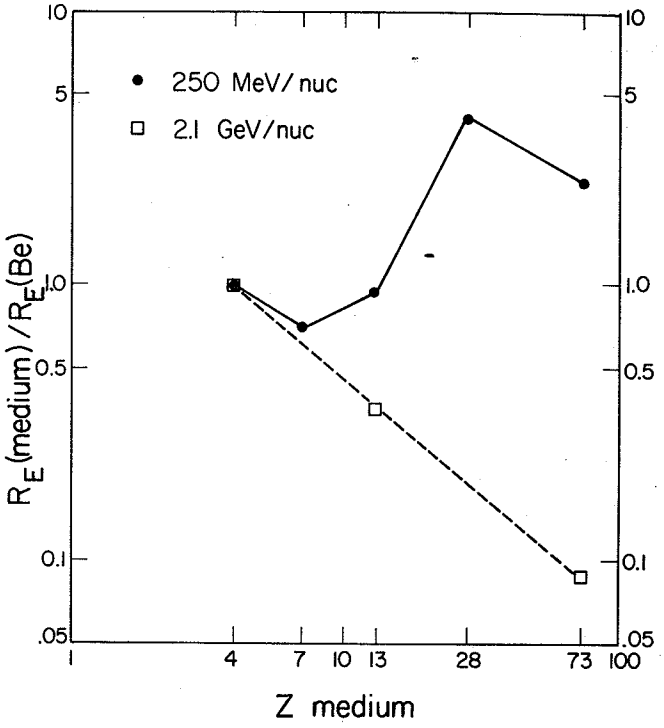

Fig. 1. Calculated equilibrium ratios $N(Z_I-1)/N(Z_I)$ relative to the ratio in Be target vs nuclear charge of target medium. (XBL 766-8269)

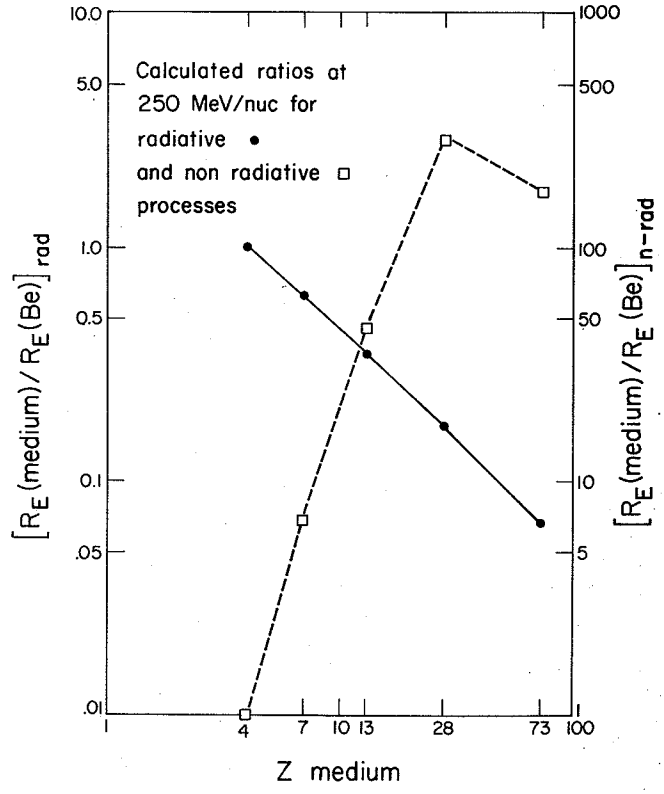

Fig. 2. Calculated equilibrium ratios relative to the ratio in Be assuming attachment occurs by either nonradiative process (right hand scale) or radiative process (left hand scale) only. (XBL 766-8270)

There are discrepancies between the theoretical calculations and the measured data. We are presently exploring a relativistically correct theoretical description based on the two processes mentioned earlier which we hope will more reasonably describe the measured data. We are continuing the experimental investigation in summer 1976 to measure both R_E and σ_A (and hence σ_L) for C and Ar beams at 250 MeV/nucleon and 2.1 GeV/nucleon as well as for Ne at 500 MeV/nucleon and 1 GeV/nucleon.

Footnotes and References

*University of California Space Sciences Laboratory, Berkeley, California.

†Laboratoire Rene Bernas, Orsay, France.

1. G. Raisbeck, C. Perron, J. Toussaint and F. Yiou, 13th Int. Cosmic ray conference, Denver (1973), Vol. 1, p.534.

2. N. Bohr, Kgl. Danske Videnskab. Selskab. Mat.-Fys. Medd. 18, 8 (1948).

3. H. C. Brinkman and H. A. Kramers, Proc. Acad. Sci. (Amsterdam) 33, 973 (1930).

4. R. H. Pratt, A. Ron and H. K. Tsang, Rev. Mod. Phys. 45, 273 (1973).

ATOMIC K-VACANCY PRODUCTION WITH 3 GeV CARBON IONS

R. Anholt,* J. Ioannou-Yannou, H. Bowman, E. Rauscher, S. Nagamiya, J. O. Rasmussen, T. Shibata,†‡ H. Ejiri †

K-vacancy production by relativistic heavy charged particles is a completely unexplored field. Measurements with relativistic protons[1,2] indicated that an additional term must be added to the cross section given by the Plane Wave Born[3] (PWBA) and Binary Encounter[4] (BEA) Approximations. These theories only account for the interaction between the static Coulomb fields of the projectile and electron. This contribution is called longitudinal excitation because the interaction exerts a force parallel to the momentum transfer. At relativistic energies, the current-current interaction between the two particles is also important and gives rise to transverse excitation.[5] For projectile energies greater than approximately 2 GeV/amu (v_1 constant $\approx$ c), the PWBA and BEA cross sections no longer change with projectile energy. The transverse contribution, however, causes the total cross section to rise as the $\ln \gamma^2 + C$ where $\gamma = [1 - \beta^2]^{-\frac{1}{2}}$, $\beta = v_1/c$, and C is a constant.

The experimental procedure was identical to the procedure described in Ref. 2.

The measured cross sections are compared with various theories in Fig. 1. The BEA and PWBA cross sections were obtained from universal curves given by Garcia et al.[3] and Basbas et al.[6] The reduced ion velocity was taken as $\beta c/v_K$ where $v_K = (2U_K/m)$ and U_K is the K binding energy.

Two relativistic modifications to these theories should be made. For large v_1/v_K, the PWBA and BEA cross sections approach (but never equal) the integrated Rutherford cross section (σ_R) for scattering an initially stationary electron with an energy transfer $\epsilon \geq U_K$. For relativistic heavy ions σ_K should approach the integrated McKinley-Feshbach cross section (σ_{MF}) for relativistic electrons on nuclei.

The second relativistic correction factor comes from the inclusion of the transverse term.[2]

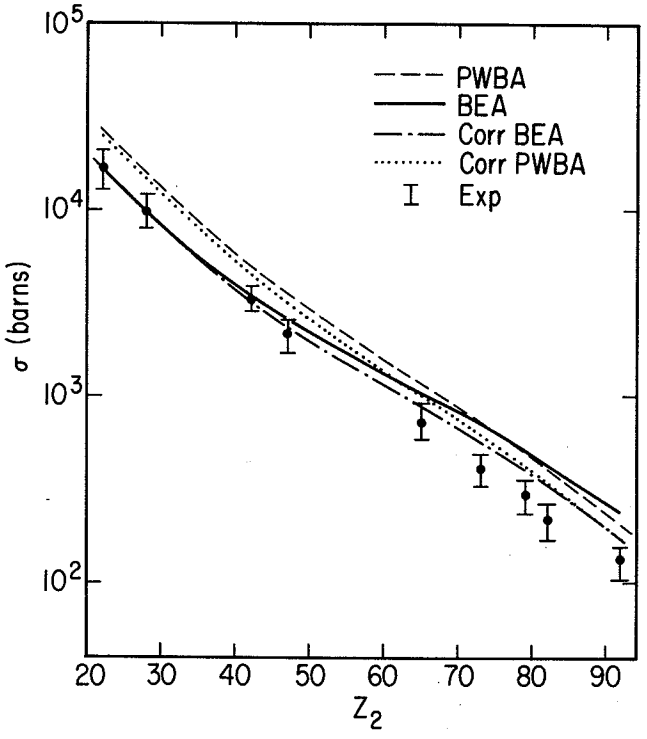

Fig. 1. K-vacancy production cross sections versus target atomic number. Comparison is made with the PWBA and BEA theories and relativistically corrected PWBA and BEA theories. (XBL 761-449)

We have evaluated this contribution using the PWBA dipole approximation which is only valid when $2\ v_1/v_K \gg 1$. In these cases $2\ v_1/v_K$ lies between 1.6 and 10.

The measured cross sections generally lie lower than the predictions of the PWBA, BEA, and

relativistically corrected theories. For lower atomic numbers, the BEA theory works best; for higher atomic number, all theories fail. The first relativistic correction becomes important at higher atomic numbers, lowering the cross sections, bringing them closer to experiment. The additive transverse contribution is not very important at these velocities.

We have considered whether the polarization,[7] binding,[6] and charge-exchange effects might account for the discrepancy between experiment and theory. For $2v_1/v_K > 1$, the polarization effect is expected to be more important than the binding correction and should give a positive contribution to the K-vacancy cross section. We evaluated the polarization contribution and found it adds only 2, 4, and 12%, respectively, for the Ni, Ag, and Pb targets. There are also negative contributions from the binding effect, so the net polarization plus binding correction is liable to be smaller than these factors. Charge-exchange contributions are expected to give a positive contribution to σ_K also.

Thus, while the measured cross sections clearly lie lower than the predictions of the first order PWBA and BEA theories, the polarization and charge exchange contributions to these cross sections appear to be negligible and, in any case, in the wrong direction to explain the discrepancy.

Footnotes and References

*Present address: Department of Physics, Stanford University.

†Laboratory of Nuclear Studies, Osaka University, Toyonaka, Osaka, Japan.

‡Supported by Mitsubishi Foundation.

1. O. N. Jarvis, C. Whitehead and M. Shah, Phys. Rev. A 5, 1198 (1972).

2. R. Anholt and the TOSABE Group, submitted to Phys. Rev. A (1976).

3. J. D. Garcia, R. J. Fortner and T. M. Kavanagh, Rev. Mod. Phys. 45, 111 (1973).

4. E. Merzbacher and H. Lewis, Hanbuch der Physik 34, 166 (Springer-Verlag, Berlin, 1958).

5. U. Fano, Annu. Rev. Nucl. Sci. 13, 1 (1963).

6. G. Basbas, W. Brandt and R. Laubert, Phys. Rev. A 7, 983 (1973).

7. G. Basbas, W. Brandt and R. Laubert, Phys. Lett. 34A, 277 (1971).

K VACANCY PRODUCTION BY 4.88 GeV PROTONS*

R. Anholt,† S. Nagamiya, H. Bowman, J. Ioannou-Yannou,
E. Rauscher, and J. O. Rasmussen

K-vacancy production cross sections were measured at the Berkeley Bevatron for 4.88 GeV proton bombardments of Ni, Zr, Mo, Ag, Tb, Ta, Pt, Au, Pb, and U. These cross sections were compared with the Binary Encounter[1] (BEA) and Plane Wave Born Approximations[2] (PWBA) and were found to lie higher than theory by a factor of 1.2 to 2.5.

The BEA and PWBA calculations account only for the interaction between the static Coulomb fields of the projectile and target electron. At relativistic energies, the interaction between the currents of the two particles is also important, since the projectile current has $\beta = v_1/c \approx 1$. The matrix element for this interaction is given by

$$\frac{Z_1 e^2}{2\pi^2} \int d\vec{k} \sum_s \frac{\langle \vec{p}' | \vec{\alpha}\cdot\hat{A}\exp(i\vec{k}\cdot\vec{r}) | p\rangle \langle n | \sum_j \vec{\alpha}_j \cdot \hat{A}\exp(i\vec{k}\cdot\vec{r}_j) | 0\rangle}{k^2 - (E_n/\hbar c)^2} \qquad (1)$$

where Z_1 is the projectile atomic number, $\vec{\alpha}$ and $\vec{\alpha}_j$ are Dirac matrices operating on projectile wavefunctions $|\vec{p}\rangle$ and $|\vec{p}'\rangle$ and electronic wavefunctions $|n\rangle$ and $|0\rangle$ respectively, and $E_n \equiv E_n - E_0$. We express $|\vec{p}\rangle$ and $|\vec{p}'\rangle$ as plane waves and following Fano[5], Eq. (1) is reduced and the cross section is obtained from

$$d\sigma_n = \frac{4\pi Z_1^2 e^4}{v_1^2} \int_{q_0}^{\infty} \frac{|\vec{\beta}_t \cdot \vec{G}_n(q)|^2 q dq}{(q^2 - E_n^2/c^2)^2} \qquad (2)$$

where $q_0 = E_n/v_1$, $\vec{\beta}_t = \vec{\beta} - (\vec{\beta}\cdot\vec{q})\hat{q}$, and $\vec{G}_n(q) = \sum_j \langle n | \vec{\alpha}_j \exp(i\vec{q}\cdot\vec{r}) | 0\rangle$. No interference between the longitudinal excitation amplitude (interaction between the static Coulomb fields) and the transverse amplitude (interaction between the currents) is present. It is seen that $G_n(q)$ is nothing more than the fully retarded dipole velocity matrix element for photoelectric absorption. Following Merzbacher,[2] we use nonrelativistic one electron continuum and 1s wavefunctions to calculate $\vec{G}_n(q)$. The cross section is integrated over continuum energies (excitation to bound states is neglected).

The cross section is unimportant at nonrelativistic projectile velocities. For relativistic projectiles, it rises as $\ell n\gamma^2$ with $\gamma = (1 - \beta^2)^{-1/2}$.

For reduced velocities $v_1/v_K = \beta c/v_K \gg 1$, it is given by making the dipole approximation ($\exp(i\vec{q}\cdot\vec{r}) = 1$): $\sigma_K = 1.06 \cdot 10^4 \, Z_1^2/Z_2^2(\ln(\gamma^2)-\beta^2)/\beta^2$ barns.

Figure 1 compares theory with experiment. The transverse term does not quite bring theory into agreement with experiment, but clearly helps. We should mention that the Bethe approximation[4] agrees better with experiment. The Bethe approximation includes the transverse contribution, but is based on the dipole approximation whose validity is not wholly justified for the case where v_1/v_K is only slightly larger than unity.

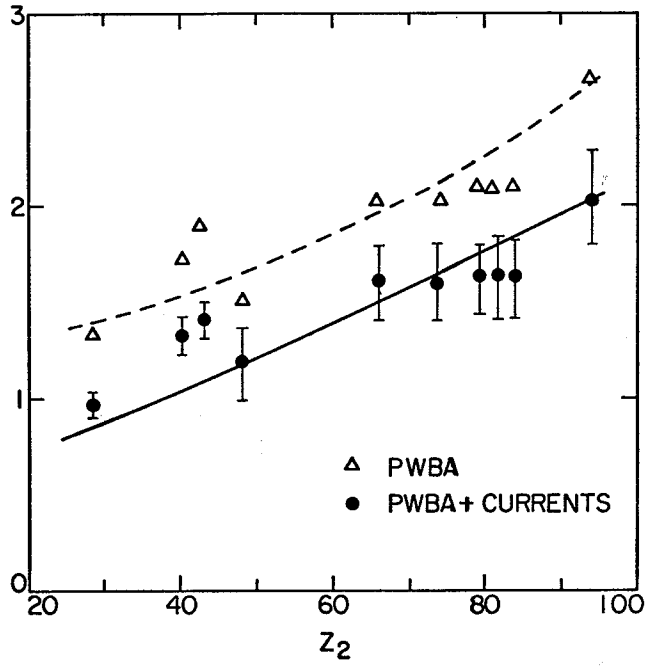

Fig. 1. Ratios of experimental to theoretically calculated cross sections. (XBL 766-8223)

Table 1.
K-vacancy cross sections from 4.88 GeV protons.

Z_2	σ (barns)
Ni	210 ± 25
Zr	102 ± 12
Mo	94 ± 12
Ag	58 ± 10
Tb	31 ± 7
Ta	22 ± 4
Pt	18 ± 4
Au	17 ± 3
Pb	15 ± 3
U	11 ± 3

Footnotes and References

*Abstract submitted to Fifth Int. Conference on Atomic Physics, Berkeley, California, July 1976.

†Present address: Department of Physics, Stanford University.

1. J. D. Garcia et al., Rev. Mod. Phys. 45, 111 (1973).

2. E. Merzbacher and H. Lewis, "Encyclopedia of Physics," 34, 166 (Springer-Verlag, Berlin, 1958).

3. U. Fano, Annu. Rev. Nucl. Sci. 13, 1 (1963).

4. M. Inokuti, Rev. Mod. Phys. 43, 277 (1971); private communication.

X-RAY CONTINUA OBSERVED WITH 326-470 MeV Xe IONS*

R. Anholt† and W. E. Meyerhof‡

The noncharacteristic continuum radiation observed between the X-ray transitions of the projectile and target atoms and the united atom is thought to come from transitions to the transiently formed 1sσ molecule orbital (MO) during the collision[1]. In this paper we report the observation of continua in Xe + Sn, Xe + Pr, and Xe + Bi bombardments with united atom charges 104, 118, and 137, respectively.

Figure 1 shows absolute thick target yields for these three systems. The experiments were done with intrinsic Ge X-ray and large volume intrinsic planar (Xe + Bi only) detectors at the Berkeley SuperHILAC. For the case of Xe + Sn, we show calculated yields due to Two Collision MO X rays[1] (TCMO), nucleus-nucleus bremsstrahlung[1] (NNB), secondary electron bremsstrahlung[2] (SEB), and primary bremsstrahlung or radiative ionization[3]

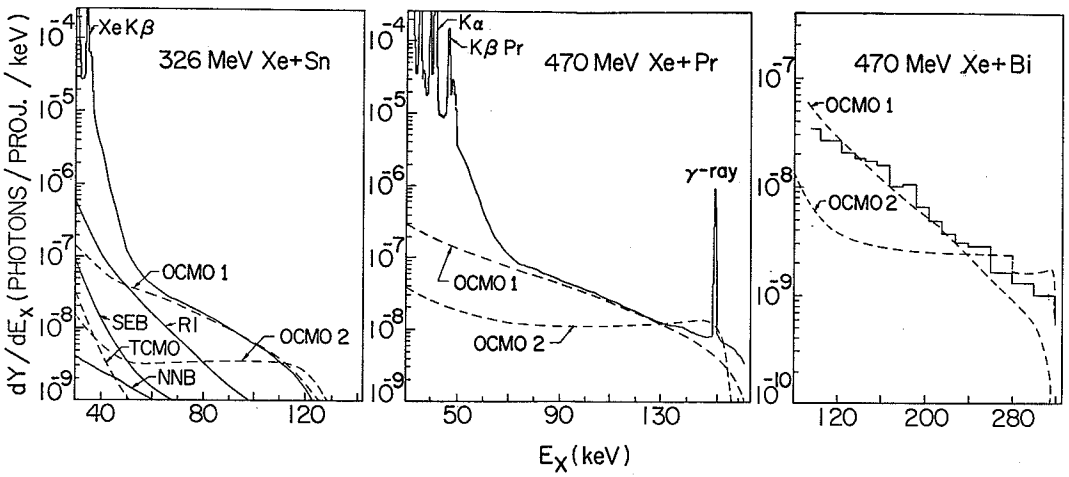

Fig. 1. Absolute thick target yields. Various calculated intensities are described in text.
(XBL 766-8220)

(RI). The sum of all of these contributions does not account for the experimental continuum yield, hence one has to invoke another process.

MO X rays may also be emitted in a one-collision process in which a 1sσ vacancy made early in a collision is radiatively filled later in the same collision. In Ref. 1 the probability for this process is written as the product of the probability for making a 1sσ vacancy P(b) times the probability for MO X-ray emission. Since P(b) is not well known it has been parametrized by the expression $P(b) \approx L[1 + e^{b/a}]^{-1}$. With this parametrization the 1sσ vacancy production cross section is given by $(\pi^3/6)\,La^2$. In Ref. 1 a was found to be approximately equal to the K radius a_K of the higher Z partner, whereas according to Ref. 4, it should be of the order of $2a_K(v_1/v_K)(U_K/U_{UA})$ where v_1 and v_K are the projectile and K electron velocities and U_K and U_{UA} are the K-shell binding energies of the heavier collision partner and of the united atom, respectively.

In the first calculation, we adjusted L and a to give the best fit to experiment (OCMO1) and again found $a \approx a_K$, but the computed value of $(\pi^3/6)\,La^2$ exceeded the experimental 1sσ cross section by factors of 5 to 20. In the second, we used a as suggested by Ref. 4 and the experimental 1sσ cross sections (OCMO2). While the shape is well represented by OCMO1, neither the shape nor intensity is well represented by OCMO2. Hence, the presently available prescription for the OCMO spectrum is not adequate to explain the observed continua.

Footnotes and References

*Abstract submitted to Fifth Int. Conference on Atomic Physics, Berkeley, California, July 1976.

†Present address: Department of Physics, Stanford University.

‡Department of Physics, Stanford University.

1. W. E. Meyerhof et al., Phys. Rev. Lett. 32, 1279 (1974).

2. F. Folkmann et al., Nucl. Instrum. Meth. 116, 487 (1974).

3. R. Anholt and T. K. Saylor, to be published in Physics Letters A.

4. W. Brandt, K. W. Jones and H. W. Kramer, Phys. Rev. Lett. 30, 351 (1973).

A NEW WAY OF PREDICTING 1sσ VACANCY PRODUCTION BY HEAVY IONS*

R. Anholt†

Basbas et al.[1] have previously shown that the cross section for the production by heavy ions of K vacancies in the 1s molecular orbital (MO) (or in the heavier collision partner) can be written as $\sigma_K = Z_1^2\sigma_0/\delta^9$. Here Z_1 and Z_2 are the projectile and target atomic charges and σ_0 can be either the theoretical or experimental K-vacancy production cross section by protons (or zero charged particles). We show that δ can be written as $1 + (U_{UA}/U_K - 1)g \times (1.3\,\xi_K)$ where U_{UA} and U_K are experimental binding energies of the combined $(Z_1 + Z_2)$ atom and the heavier atom respectively and g is a numerical function of the projectile velocity divided by the K electron velocity of the heavier partner, ξ_K =

$2v_1/v_K$. In the spirit of the approximations made in obtaining this result (see Eq. (A.10) of Ref. 1), it is also possible to write $\sigma_K = Z_1^2\sigma_0/\delta_0^{9g}$ where $\delta_0 = U_{UA}/U_K$. A plot of the log σ/Z_1^2 versus the log U_{UA} should give a straight line whose slope depends on just the reduce velocity v_1/v_K.

In Fig. 1 we show log-log plots of assorted data for 0.5 to 3 MeV/amu. p, α, Li, C, N, and O ions on Ni, Sb, and Rb.[2] In Fig. 2 we show values of $n \equiv 9g$ obtained from this data and other data. While the clustering of n values shown in Fig. 2 is not tight, n values can be taken from this figure and applied to many combinations of projectiles, targets and projectile energies to obtain σ_K. Only the proton cross section is required, which can be theoretically predicted or obtained from experiment. Generally predictions using this method are better than those obtained using "united atom" scaling laws[3] and better than the original binding correction method of Ref. 1. It is restricted to atoms with $20 \lesssim Z \lesssim 50$, however, where screening and

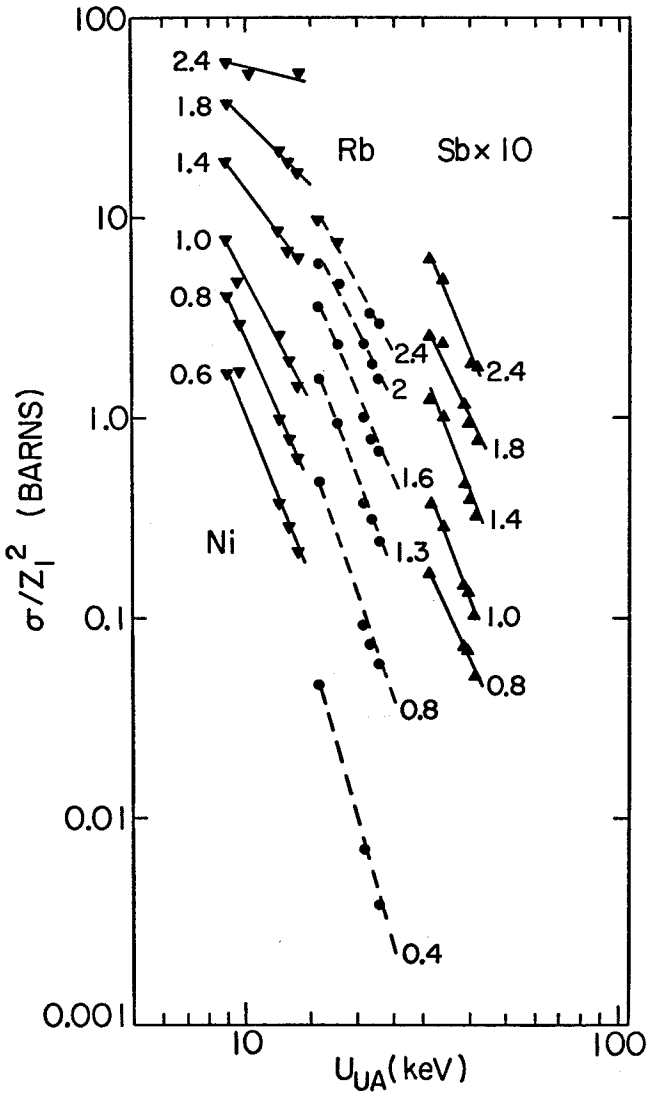

Fig. 1. σ/Z_1^2 vs U_{UA} for Ni, Rb and Sb K-vacancy production by p, Li, α, C, N, and O heavy ions. Numbers indicate projectile energy per nucleon. (XBL 766-8221)

relativistic effects are unimportant. The relation also works no matter if the projectile is the heavier partner or the target is. One simply interchanges the definition of Z_1 and Z_2 such that Z_1 is always the lower Z.

A fundamental interest in the n plot is that the binding-correction prediction of Basbas et al.[1] (shown by the dashed line in Fig. 2) does not

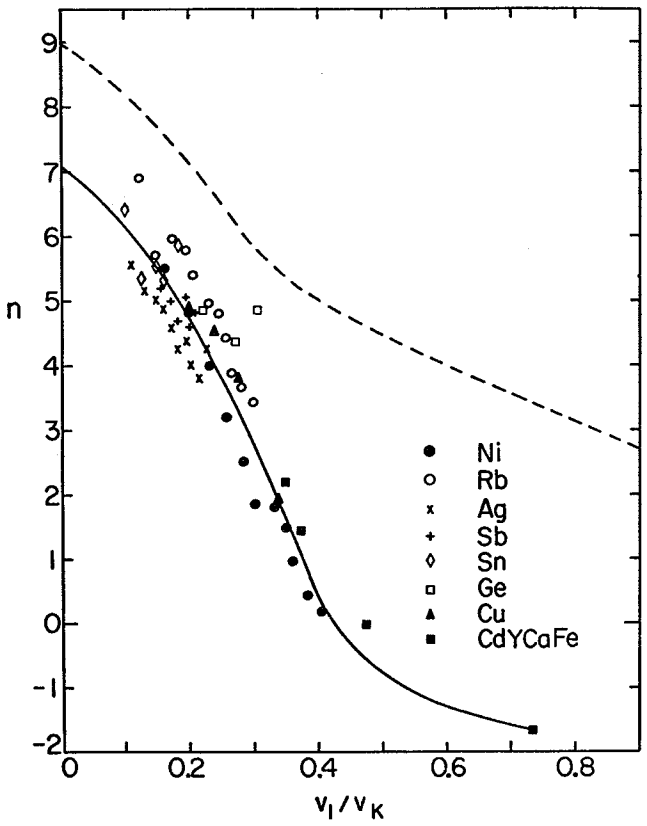

Fig. 2. n vs v_1/v_K for various targets. Solid line is an approximate vest fit. Dashed line is the prediction of Basbas et al.[1] (XBL 766-8222)

accurately predict the n values. This has been noted in the literature. Usually other corrections have been applied to specific pieces of heavy ion data. No ab initio theory of 1sσ vacancy production is currently available, however. Should such a theory become available, the n-plot will provide an excellent test of theory.

Footnotes and References

*Abstract submitted to Fifth Int. Conference on Atomic Physics, Berkeley, California, July 1976.

Present address: Department of Physics, Stanford University.

1. B. Basbas, W. Brandt and R. Laubert, Phys. Rev. A 7, 983 (1973).

2. Data taken from many sources, principally F. D. McDaniel, T. Gray and co-workers.

3. C. Foster et al., J. Phys. B 7, 2563 (1975).

II.

THEORY

A. NUCLEAR REACTIONS

1. Microscopic

ENHANCEMENT OF FORWARD-ANGLE CROSS SECTIONS IN HEAVY-ION REACTIONS BECAUSE OF PROJECTILE EXCITATION*

Norman K. Glendenning and Georg Wolschin†

A remarkable feature in the spectrum of out-oxygen nuclei from the reaction

$$^{122}Sn(^{16}O,\ ^{18}O)^{120}Sn, \qquad E = 104\ MeV$$

is that they are produced in the excited 2^+ state with a cross section which is about five times larger than the ground state cross section.[1] A typical spectrum taken at the Berkeley 88-inch cyclotron is shown in Fig. 1. Such a preference for excited states of the light outgoing nucleus has been observed for some other targets as well.

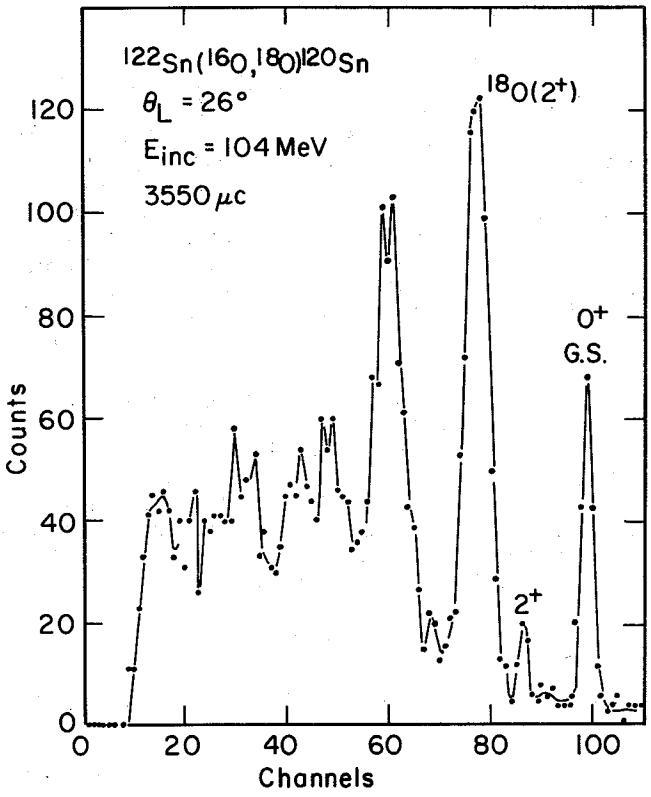

Fig. 1. Energy spectrum for the reaction indicated. Note large cross section for producing ^{18}O in its 2^+ state (with ^{120}Sn in its ground state.
(XBL 741-2191)

It is clear therefore that an accurate description of the reaction must include the coupling of the ground and excited states in oxygen.[2] The results of such a coupling can be seen in Fig. 2. Here we see a dramatic increase, by a factor of 10, in the ratio of forward to grazing-angle cross section for the ground state, when the effect of excitation of ^{18}O to its 2^+ state is included. Since the cross section to the $^{18}O(2^+)$ state is adjusted to agree with experiment, and the strength of the inelastic transition in the ^{18}O nucleus is prescribed by the measured β_2 of this nucleus, this result is quite firm. We note that the sign of the interference changes between grazing angle and forward angles.

The significance of this result must be viewed in connection with the interpretations of large for-

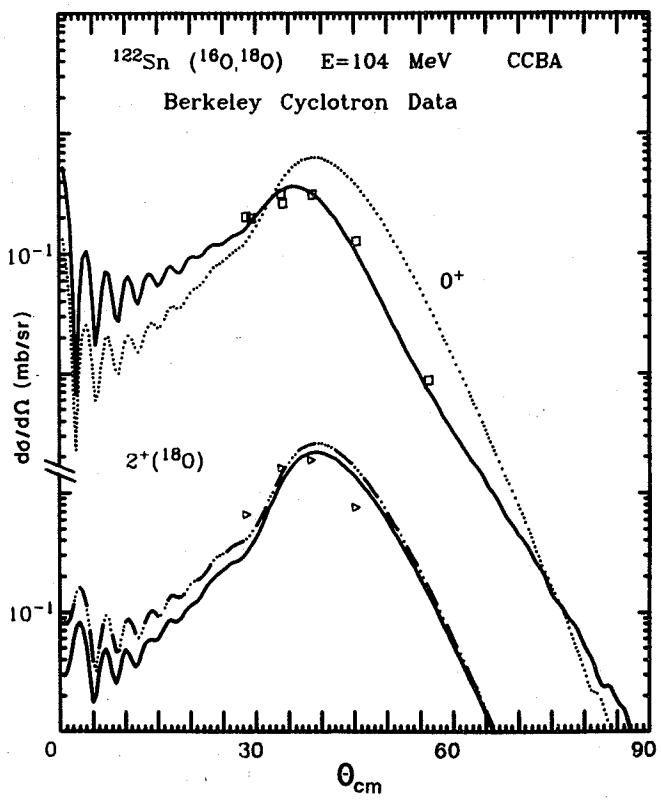

Fig. 2. Broken lines show direct cross sections for producing the ground state of ^{120}Sn with outgoing nucleus ^{18}O in its ground and excited state. Solid lines show effect of coupling these two levels. A common normalizing factor 2.7 is used for all curves.
(XBL 753-755)

ward-angle cross sections by the Brookhaven group. We recall that in the ^{A}Ni(^{18}O,^{16}O) reactions on a series of isotopes, the cross sections have normal grazing peaks for the heavier isotopes, while at the light end they have anomalously large forward cross sections.[3] In an early work they varied the parameters of a weakly absorbing potential to reproduce this trend.[3] Recently, they have treated only one of these cases using a surface transparent potential to obtain a large forward cross section.[4] It appears, however, that these potentials may actually be simulating the physical process of indirect feeding of the ground state through excited states of the light nucleus.

The indirect transitions have larger forward distributions compared to the direct. This can be understood as characteristic at energies for which the classical deflection function has a rainbow angle. First we recall a general principle.[5] The angular momentum region that dominates a given process is determined by the competition of several factors. Two competing factors are the absorption, which reduces the cross section for small angular momenta, and the preference for close collisions when particles are transferred. Naturally a two-step process requires a closer collision than a direct one. The balance of these two factors leads to a preference of two-step processes for orbits with angular momenta somewhat smaller than the rainbow or grazing angular momenta associated with the peak in the cross section of the direct process. Therefore, forward-angle scattering is enhanced for two-step processes compared to direct ones when the energy is such that the deflection function possesses the rainbow or grazing angle.

A different behavior is observed when the energy is lower and closer to the Coulomb barrier. In this case there is no rainbow angle, and the closer orbits preferred by the two-step process scatter to larger angles than the slightly more distant orbits preferred by the direct process. This is the case for the same reaction of Fig. 2 when the energy is just above the Coulomb barrier, as in Fig. 3. The forward-angle cross section at this energy is unaffected by the excitation of ^{18}O(2$^+$) but the back-angle cross section is reduced by the destructive interference between direct and indirect transitions. The improvement in the agreement is marked. The data are for the reaction inverse to the one for which we did the computation. They are equal by time reversal invariance. We only chose to do the calculation for the pickup reaction because this is the one for which the important intermediate state, ^{18}O(2$^+$), is a direct observable.

To summarize our results, we have found that transitions through excited states in the projectile involved in a transfer reaction can produce a large enhancement at forward angles in the ground state cross section, when the energy is sufficiently high above the barrier so that the grazing angle is truly a rainbow effect. Such an enhancement may occur when an excited state of one of the light nuclei is produced in the transfer reaction with larger cross section than its ground state, and the two are strongly coupled.

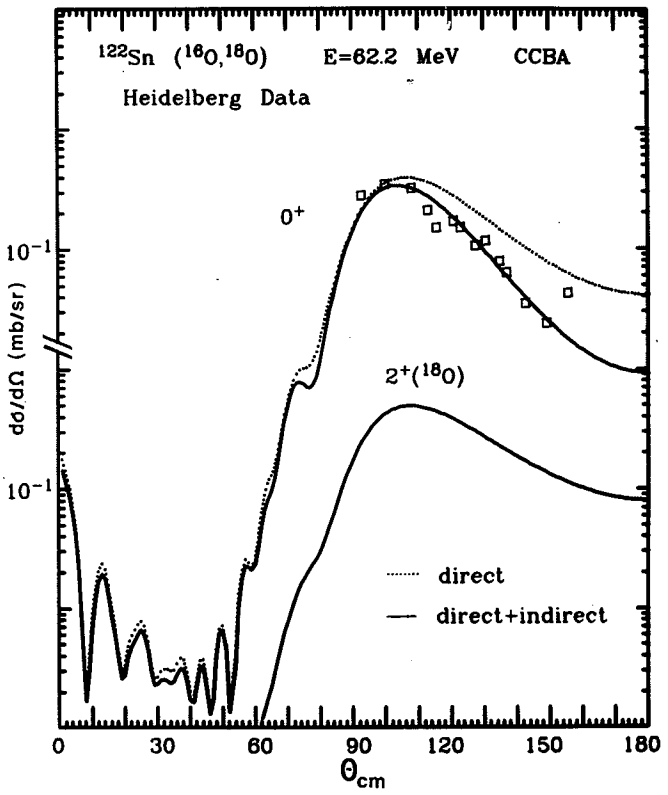

Fig. 3. Computed ground state cross section for pickup reaction is compared with data on the time reversed reaction (Ref. 6). The effect of indirect feeding of the ground state through the intermediate 2$^+$ state in ^{18}O is seen by comparing the dotted and solid curve. Cross section computed for the 2$^+$ state in ^{18}O is also shown, but no data are available. A common normalization factor 6.2 is used for all curves. The calculation is as described for Fig. 2. Optical parameters were derived from the ^{18}O + ^{120}Sn elastic scattering data at 60 MeV. (XBL 753-757)

Clearly it is of interest to perform the (^{16}O, ^{18}O) reactions on the nickely isotopes so as to measure the relative cross sections of ^{18}O(2$^+$) and ^{18}O(gs). If the ratio is large, then it is very likely that a substantial part of the forward-peaked cross sections in the ^{18}O,^{16}O) reactions measured by the Brookhaven group is due to the second order effect of the light-nucleus excitation.

Footnotes and References

*Condensed from LBL-3472, Phys. Rev. Lett. 34, 1642 (1976).

†Supported in part by the German National Fellowship Foundation.

1. D. K. Scott, private communication.

2. N. K. Glendenning and R. J. Ascuitto, Symposium on Heavy-Ion Transfer Reactions, Argonne, Ill. (1973) p. 513; Phys. Lett. 47B, 332 (1973).

3. E. H. Auerbach, A. J. Baltz, P. D. Bond, C. Chasman, J. D. Garrett, K. W. Jones, S. Kahana, M. J. LeVine, M. Schneider, A. Z. Schwarzschild, and C. E. Thorn, Phys. Rev. Lett. 30, 1078 (1973).

4. M. J. LeVine, A. J. Baltz, P. D. Bond, J. D. Garrett, S. Kahana, and C. E. Thorn, Phys. Rev. C 10, 1602 (1974).

5. N. K. Glendenning in International Conference on Reactions Between Complex Nuclei (Nashville, Tennessee) eds. R. L. Robinson et al. (North-Holland, 1974) Vol. II, p. 137.

6. H. G. Bohlen, A. Gobbi, K. D. Hildenbrand, and K. I. Kubo, Jahresbericht Max Planck Institut Heidelberg, 24 (1973).

PHYSICAL BASIS FOR ENHANCED FORWARD CROSS SECTIONS IN Ni (^{18}O, ^{16}O) REACTIONS*

Norman K. Glendenning and Georg Wolschin †

At moderate energies above the Coulomb barrier, quasi-elastic heavy ion reactions are expected to exhibit a "grazing" peak in the differential cross section.[1] Brookhaven experiments[2] produced the surprising result that several reactions of the type

$$^{60}\text{Ni}(^{18}\text{O}, ^{16}\text{O})\ ^{62}\text{Ni},\ E = 65\ \text{MeV} \qquad (1)$$

had a large cross section forward of the grazing angle. Although indirect transfer can produce such effects,[3] this was not at first suspected to be the explanation because the experiment did not reveal any likely candidates as intermediate states.

Recently the Brookhaven group proposed a surface transparent optical potential with the property that the edge of the absorptive part is very sharp and lies inside the real part.[4]

We now turn to what we consider to be the physical basis for the large forward cross section seen in the experiment. The clue was provided in a previous paper which took into account the fact that for the Sn(^{16}O,^{18}O) reactions, the ejectile, ^{18}O is produced in its excited 2^+ state more frequently than its ground state.[5] Its subsequent deexitation through an inelastic interaction with the residual nucleus has the effect on the ground state cross section of: 1) shifting the grazing peak forward by a few degrees and 2) producing a forward angle yield that is ten times larger than calculated from the direct process alone. The analogous process in the entrance channel of the reaction (1) above can explain the observed forward distribution when all relevant cross sections are determined to the extent possible by the available experiments.

In Fig. 1 our complete calculation is shown for the inverse reaction to (1) which includes the direct transition to the ground state of both final nuclei and the coherent indirect transition corresponding to particle transfer to the 2^+ state of ^{18}O followed by inelastic deexcitation to the ground state. We neglect the explicit calculation of recoil effects but employ the scaling factor $\alpha = 1.02$ which as far as the direct transition is concerned reproduce the angular distribution of the full recoil calculation. This point is not crucial, however, since with "normal" optical potentials the

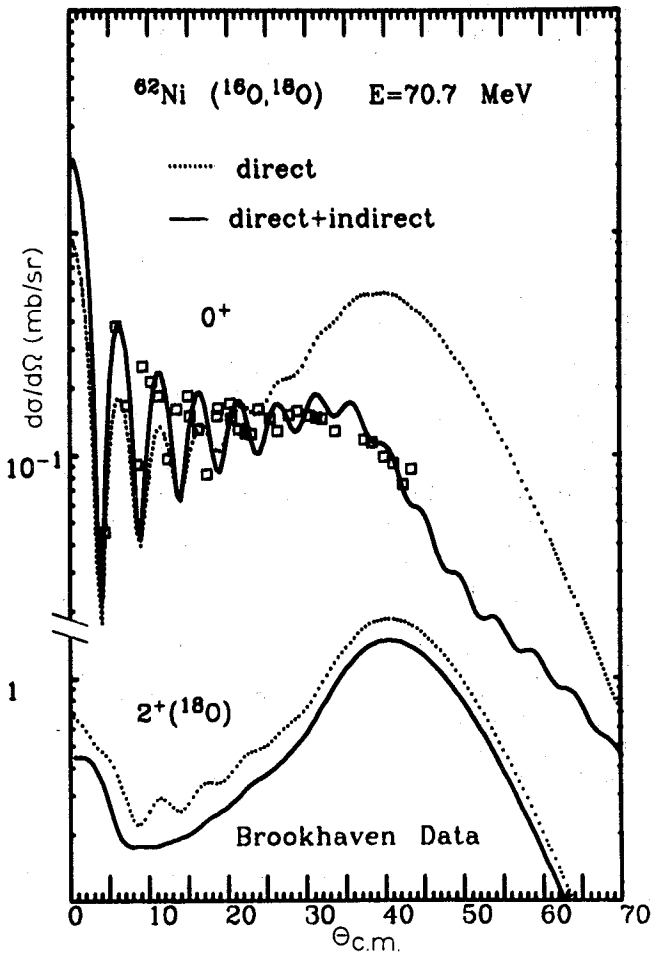

Fig. 1. The solid lines are cross sections based on a coupled calculation in which both states of oxygen, the 0^+ and 2^+ are fed both by direct transfer, and by indirect transfer through the other state. Dashed lines show cross sections computed for each state when only the direct transfer contribute (but the inelastic coupling is still included). All cross sections are normalized by the same factor. The ground state data[2] are for the time reversed reaction at the corresponding energy of E = 65 MeV (in the lab). (XBL 7510-8436)

sensitivity to α is quite small. Also shown in Fig. 1 is the cross section for direct transfer alone, which by comparison allows us to see the large effect of the indirect transition on the ground state cross section. In an earlier publication we gave a simple classical explanation of why the two-step process is forward biased compared to a single--step process.[5] In addition, it is broader because each scattering process introduces its own dispersion on the previous one. (Thus, a delta function angular distribution centered at θ_0 scatters to θ_0 for a single scattering, and all angles between θ and $2\theta_0$ for a double scattering. Both effects are apparent in the figure. The ratio at the nuclear surface of the two transfer form factors involving respectively the ground and excited state of ^{18}O is consistent with the data of the neighboring reaction as concerns the relative cross sections, although the forward peaking of the 2^+ cross section is not reproduced.[6] It is quite possible that its angular distribution would be modified by higher states just as transitions through it modify the ground state cross section. Since however, neither the experimental data for the 2^+ nor any higher state is available for the reaction inverse to (1), we leave this matter as it stands.

In conclusion, we have exhibited a physical process that is capable of accounting for the large forward cross section in the Brookhaven experiment $^{60}Ni(^{18}O,^{16}O)^{62}Ni$ at an energy where one would normally expect a grazing peak with sharply falling cross section on either side. This process consists of the inelastic excitation of the projectile ^{18}O followed by the transfer of two nucleons to form the ground states of ^{16}O and ^{62}Ni. The destructive interference of this process with the direct transfer causes a decrease of cross section in the region of the grazing angle where the two have comparable amplitudes. At angles forward of the grazing, the cross section is dominated by the second order process, since, as discussed above its distribution is ore forward biased and broader.

We note here two additional features that can be introduced by indirect transitions which may be observable in experiment. i) The destructive interference between the peaked direct amplitude and the broad indirect one can lead to a minimum somewhere in the grazing region or beyond followed by a second peak. Some indication of such a phenomenon exists in the $^{62}Ni(^{18}O,^{16}O)^{64}Ni$ data.[2] ii) In a series of isotopes the relative contribution of direct and indirect processes can change both because the structure of the nuclear wave functions change and because the Q of the reactions change. It is worth noting that the reaction under investigation is a badly Q-matched one. Based on a semiclassical argument[3] one can understand that indirect processes are not attenuated as strongly by Q-mismatch as direct ones. Thus the second order processes may be less important relative to the direct in other nickel isotopes where the Q-matching is better, unless the nuclear structure strongly favors the indirect. Assuming that it does not, then there ought to be an evolution in cross sections from one end to the other of the nickel isotopes from forward distributions at the large-Q end to more grazing peaked at the small-Q end. The data suggest this trend.[2]

Footnotes and References

*Condensed from LBL-4334, published in Phys. Rev. Lett. 36, 1532 (1976).

†Supported in part by the German National Fellowship Foundation.

1. N. K. Glendenning in Proc. of Int. Conf. on Reactions between Complex Nuclei, R. L. Ronbinson et al., eds. (North-Holland, Amsterdam 1974) vol. 2, p. 137 and Ref. Mod. Phys. 47, 659 (1975).

2. E. H. Auerbach et al., Phys. Rev. Lett. 30, 1078 (1973).

3. R. J. Acuitto and N. K. Glendenning, Phys. Lett. 45B, 85 (1973).

4. H. J. Levine, A. J. Baltz, R. D. Bond, J. D. Garrett, S. Kahana, and C. E. Thorn, Phys. Rev. C 10,1602 (1974; A. J. Baltz, P. D. Bond, J. D. Garrett, and S. Kahana, Phys. Rev. C 12, 136 (1975).

5. N. K. Glendenning and G. Wolschin, Phys. Rev. Lett. 34, 1642 (1975).

6. D. L. Hendrie, U. Jahnke, C. F. Maguire, J. Mahoney and D. K. Scott, private communication.

TWO-PARTICLE TRANSFER CONTRIBUTIONS TO ELASTIC AND INELASTIC HEAVY ION SCATTERING*

Norman K. Glendenning and Georg Wolschin†

The coherent appearance of scattering and particle transfer can occur in heavy ion reactions when the two colliding nuclei differ by only one or a few nucleons, leading to strong interferential oscillations in the angular distributions.

One aim of our analysis is to show that by including the indirect transfer processes in the $^{16}O + ^{18}O$ reaction at energies near the barrier, the slight discrepancy between elastic data and calculations[1,2] can be removed. Our second objective is to obtain a simultaneous fit of both elastic and inelastic data.

We consider the elastic scattering of projectile A from target nucleus B.

$$A + B \rightarrow A + B \qquad (1)$$

and the inelastic scattering to excited states of B

$$A + B \rightarrow A + B^*, \qquad (2)$$

where

$$B = A + X, \quad (3)$$

so that the core of B is identical to A, and the mass of X small compared to the mass of A. For simplicity, we assume A to have spin zero. Because of the identity of the cores, the transfer of particle(s) X leads into the same elastic and inelastic channels as the ordinary (direct) scattering, and therefore the two processes interfere.

The various processes that we include that lead to the elastic and inelastic channels are shown in Fig. 1. The method of calculation is the source term method.[3]

Coupled channel calculations for the $^{16}O+^{18}O$ elastic and $^{18}O(2^+)$ inelastic scattering without and with two-neutron transfer contributions are compared in Figs. 2-4 for the three energies $E_L(^{16}O)$

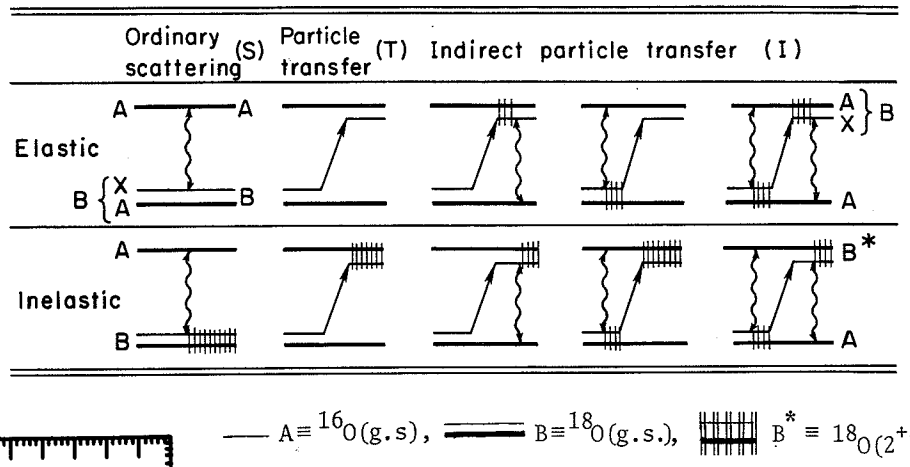

Fig. 1. Diagram representing the amplitudes considered in our calculation of elastic and inelastic $^{16}O + ^{18}O$ scattering. Wavy lines indicate scattering interaction (treated to all orders), straight lines with arrows two-neutron transfer (first order treatment). Symbols for the nuclear states are shown below the figure.

(XBL 7510-8562)

— $A \equiv ^{16}O(g.s)$, ═══ $B \equiv ^{18}O(g.s.)$, ▓▓▓ $B^* \equiv ^{18}O(2^+)$.

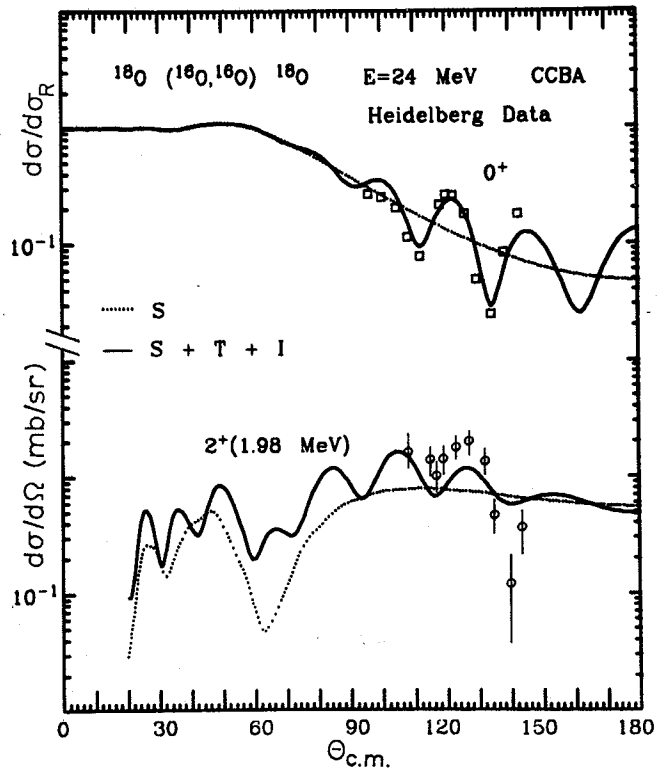

Fig. 2. Computed elastic and inelastic $^{16}O + ^{18}O$ cross sections for ordinary scattering (S) are compared with results where, in addition to the scattering, particle transfer (T) plus indirect particle transfer (I) are included. The data are from Refs. 7,8. Oscillations in both elastic and inelastic channel are identified as being due to the interference of scattering and transfer. Here and in all subsequent calculations, the transfer amplitudes are normalized by a common factor of 6.3. The center-of-mass energy is 12.71 MeV. Error bars on the inelastic data show statistical errors only. (XBL 7510-8440)

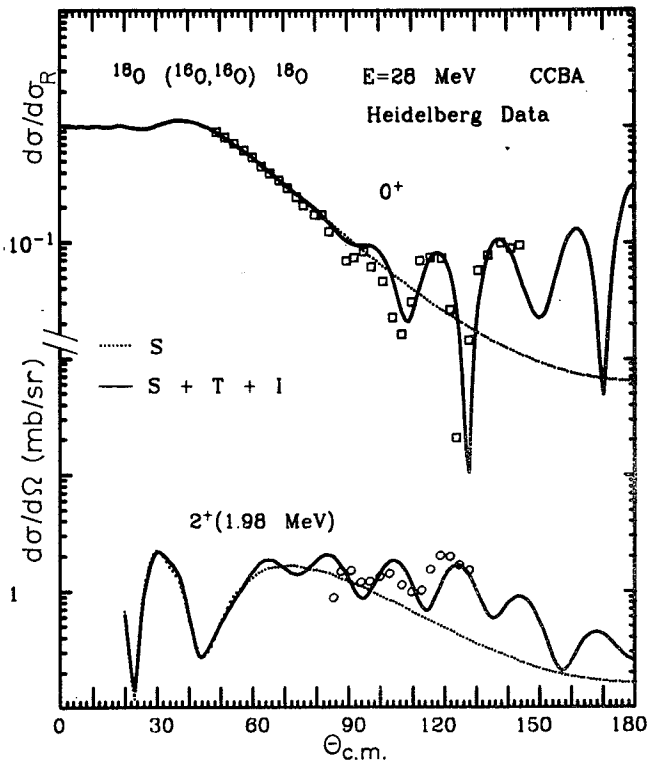

Fig. 3. As Fig. 2, but $E_L(^{16}O)$ = 28 MeV, corresponding to $E_{c.m.}$ = 19.06 MeV. Error bars not shown. (XBL 7510-8442)

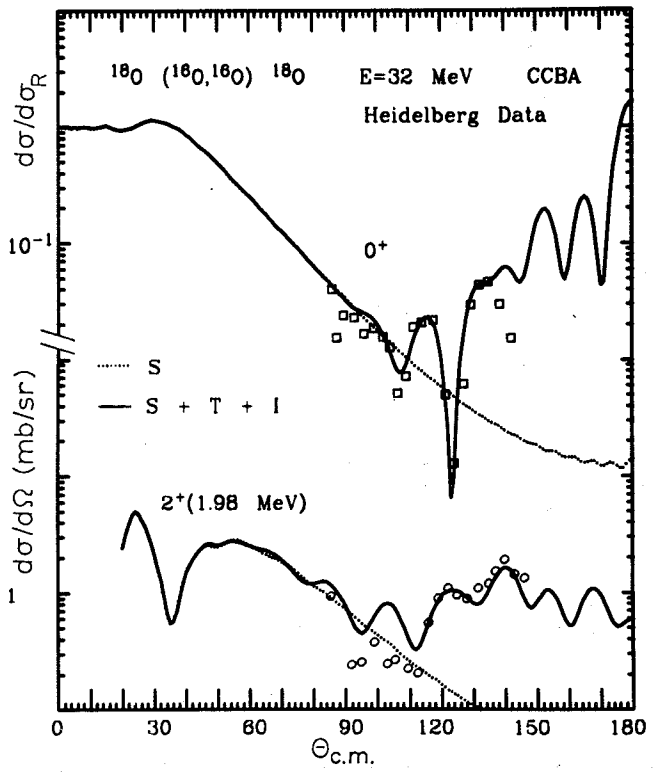

Fig. 4. As Fig. 2, but $E_L(^{16}O)$ = 32 MeV, corresponding to $E_{c.m.}$ = 19.06 MeV. Error bars not shown. (XBL 7510-8441)

= 24, 28, and 32 MeV where data are available. Whereas, the ordinary elastic and inelastic scattering cross sections show no oscillations at backward angles, the coherent addition of the transfer amplitudes reproduces the oscillatory and backward-rising structure of the data, although the agreement with the inelastic 24 MeV data is not good. Thus, the data for both elastic and inelastic channel find a consistent interpretation, if particle transfer is included.

In contrast, the DWBA calculations for the elastic channel reported in Refs. 1, 2 required different spectroscopic amplitudes for the transferred neutron cluster in order to account for the magnitude of the backward angle cross sections. The discrepancy is removed by means of the inclusion of indirect transfer mechanisms involving the $^{18}O(2^+)$ state.

Footnotes and References

*Condensed from LBL-4341, to be published in Nuclear Physics.

†Supported in part by the German National Fellowship Foundation.

1. C. K. Gelbke, R. Bock, P. Braun-Manzinger, D. Fick, K. D. Hildenbrand, R. Richter, and W. Weiss, Phys. Rev. Lett. 29, 1683 (1972).

2. C. K. Gelbke, R. Bock, and A. Richter, Phys. Rev., C 9, 852 (1974).

3. R. J. Ascuitto and N. K. Glendenning, Phys. Rev. 181, 1396 (1969).

TABLES OF NUCLEAR STRUCTURE AMPLITUDES FOR TWO-NUCLEON TRANSFER INVOLVING LIGHT PROJECTILES ($A \leq 4$)*

Norman K. Glendenning

Structure amplitudes for two-nucleon transfer reaction, denoted by

$$A(a,b)B, \quad b = a - 2, \quad B = A+2, \qquad (1)$$

are tabulated for light nuclei, $A_a \leq 4$ (denoted below by $a \leq 4$). Somewhat abbreviated tables were made available in unpublished report[1] dated August 1968. The depletion of the supply of these reports and the continued interest in two-nucleon transfer reactions are the occasion for the publication of the original tables, with the addition of some higher shell model configurations.

The structure tables facilitate the construction of the form factor for these reactions, which for a pure two-nucleon configuration $(n_1\ell_1 j_1)$ $(n_2\ell_2 j_2)$ is given by

$$f_{(j_1 j_2)_{LSJ}}(R) = \sum_N G_N u_{NL}(2\nu R^2). \qquad (2)$$

The structure amplitudes G_N are tabulated for the quantum numbers appearing as subscripts on $f(R)$. The function u_{NL} is an oscillator function, defined later. The size-parameter ν of the target nucleus is listed in the tables. For states more complicated than pure configurations, the form factor is merely an appropriate linear combination of the above.

In the distorted wave Born approximation (DWBA), the amplitude, when it is evaluated with a zero-range interaction, involves the following integrals over the form factors $f_{LSJ}(R)$

$$B^{M_L}_{LSL} = \frac{i^{-L}}{(2L+1)^{1/2}} \times \int \left[\psi_b^{(-)}\left(\frac{A}{A+2}R\right) f_{LSJ}(R) Y_L^{M_L}(R)\right]^* \psi_a^{(+)}(R)\, dR. \qquad (3)$$

Tables for the structure amplitudes from which f(R) can be constructed are given for the various possible shell model configurations appropriate to all regions of the periodic table. Since the allowed quantum numbers and size parameters depend on the particular reaction, they are tabulated for (^{3}He,p) (^{3}He,n), (t,p), and (α,d) reactions.

Footnote and References

*Condensed from Atomic Data and Nuclear Data Tables 16, 1-134 (1975).

1. N. K. Glendenning, "Tables of Structure Amplitudes for (p,t) Reactions," UCRL-18268; "Tables of Structure Amplitudes for (p, He^3) Reactions," UCRL-18269' "Tables of Structure Amplitudes for (α,d) Reactions," UCRL-18270, Berkeley, Calif. (1968).

POLARIZATION OF SINGLE-PARTICLE STATES INVOLVED IN HEAVY ION TRANSFER REACTIONS*

K. Pruess,† G. Delic, L. A. Charlton, and N. K. Glendenning

Direct reactions between heavy ions usually involve relatively little change in center-of-mass energy, angular momentum, charge or mass of any of the reacting nuclei:

$$\frac{\Delta E}{E}, \quad \frac{\Delta L}{L}, \quad \frac{\Delta Z}{Z}, \quad \frac{\Delta A}{A} << 1 .$$

The strong absorption of close collisions out of the direct reaction channels also implies that the collision is peripheral. Under all of these circumstances it follows that the optical potential which describes the elastic scattering also plays a dominant role for the direct reactions. Taking account also of the fact that the wave number is large, which implies that the density of angular momentum states per unit impact parameter is large, then classical conditions apply approximately.[1] In this circumstance the deflection function is a very useful vehicle for a discussion of the angular distribution of nucleon transfer reactions. One need only supplement it with several additional relevant facts to understand the angular distribution of a quantal calculation or experiment. One of these facts is that absorption out of the simple channels occurs if the reaction partners come too close. A second fact is that nucleons cannot be transferred if the reaction partners are too distant. These two effects which reduce respectively the contribution of low and high partial waves, imply the dominance of a band of grazing partial waves. Since most of these scatter within a small range of angles at or below the grazing angle, θ_g, a one-step transfer cross section will have a peak in the neighborhood of the classical grazing angle of the real part of the optical potential that describes the elastic scattering.

There are many examples in the literature where the angular distribution has a grazing peak shape located near the angle defined by the elastic optical potential. This situation is consistent with, but not a proof of the interpretation that the reaction is a one-step reaction and that the transfer occurs between normal states of the noninteracting nuclei. There are also a growing number of observations of angular distributions which do not have this form, but are biased toward the forward angle, even though the grazing angle is well removed from the forward direction. There are also many cases where, although the reaction has a peaked cross section, the peak is substantially shifted from the grazing angle. When the Q of the reaction is small, so that $\Delta E/E << 1$, the grazing angle can be read from the elastic cross section. When the Q is large, the grazing angle can be substantially different in the entrance and exit channels. A DWBA calculation will locate the position of the grazing peak that is expected in the sense described above. In either of these two situations, where the cross section is either forward biased, or has a grazing peak substantially shifted from the expected location, we have a clear signal that the reaction cannot be described as a dominantly one-step reaction between asymptotic states of the separated nuclei. It is interesting nonetheless that the DWBA can be forced to fit the anomalies rather consistently for a number of cross sections by the same change in optical model parameters.[2,3] However, once having made this observation, it does not make sense to continue to try to force these reactions into that framework by changing the optical model parameters so that they no longer describe the elastic scattering. This violates a sensible physical description and amounts to no more than a very elaborate (and costly) parametrization for which the parameters have no physical meaning or applicability beyond the isolated reaction.

When the angular distribution of a reaction is anomalous in either sense described above, we have the opportunity of learning something new about the reaction.

In earlier work our theoretical calculations predicted the first kind of anomaly.[4] A strongly biased forward cross section resulted from the interference of a one-step amplitude having a grazing peak, and a two-step amplitude, which was more forward biased. The destructive interference further resulted in a reduction of the grazing-angle cross section resulting in a forward-angle cross section with no evidence of a grazing peak. Experiments[5] from Brookhaven were reported at the same time which had this form of angular distribution and they have recently been interpreted successfully in the above way.[6]

This paper is devoted to a possible explanation of the second kind of anomaly where the angular distribution although having a grazing peak, is shifted substantially from the position expected from classical considerations, or in the case of

large Q, from the position expected on the basis of a DWBA calculation.

The physical process that we consider in this paper is the following. As two nuclei approach each other, the more weakly bound of the shell model states may be polarized by the field of the other nucleus. In the static case of two nuclei which are held stationary the polarization can be computed in the two-center shell model.[7] The result is that a nucleon which is originally in one nucleus may have an appreciable probability of being in the other when their surfaces are close. Whether during the time of a typical reaction, the shell model states undergo an adiabatic polarization depends on the ratio of transit time to nuclear period. This can be estimated as

$$\frac{\text{transit time}}{\text{nuclear period}} \sim \frac{E_{\text{Fermi}}}{E/A}^{1/2}$$

where $E_{\text{Fermi}} \sim 30$ MeV and the collision energy per projectile nucleon, E/A is of the order of 10 MeV. If this ratio were very large compared to unity then we would expect the adiabatic polarization to occur, whereas if it were very small, we would not. For the conditions cited it is $\sqrt{3}$ which is indecisive, but it appears worth investigating the magnitude and trends of the effect.

The trends that we expect are the following. 1) Since transfer can take place for larger impact parameters if polarization occurs, then the effect on the angular distribution will be a shift to smaller angles compared to normal DWBA. 2) the effect will increase for a sequence of states of decreasing binding in a nucleus. 3) the polarization effect will ultimately vanish at sufficiently high bombarding energy.

The cross section for the physical process described above can be computed approximately in the DWBA framework. We propose to compute a possibly upper limit on the effect in the following way. We will replace the asymptotic shell model states used in normal DWBA calculations by the polarized shell model states corresponding to the distance of closest approach of the grazing orbit. In some sense this is an upper limit on the magnitude of the effect, since the degree of polarization depends on the separation of the reacting nuclei. However, since the transfer is still expected to occur in a narrow annulus around the nucleus (with radius somewhat increased over that expected for the asymptotic states), the use of a fixed polarization distance may be a good first approximation of the effect.

In order to use existing DWBA computer programs it is most convenient to express the polarized wave function on a spherical harmonic oscillator basis. Thus a single-particle state which, asymptotically, is described by the quantum numbers $n\ell j\Omega$ (with Ω being the 3-projection of j on the axis joining the centers of the nuclei) at a finite separation will appear as

$$\phi_{n\ell j\Omega}(R_\beta, \underset{\sim}{r}_B) = \sum_{n'\ell'j'} A^{n\ell j\Omega}_{n'\ell'j'}(R_\beta)\, \phi_{n'\ell'j'\Omega}(\underset{\sim}{r}_B) \quad (1)$$

where R_β is the distance separating the mass centers in the system b+B and r_B is the displacement of the transferred nucleon from the mass center of B(=A+1). For two colliding spherical nuclei, the axis joining their centers is a symmetry axis. Choosing it to define the intrinsic 3-axis, the projection of j on it, which we call Ω, is conserved. For large separation, R_β, the polarized state goes over to the normal shell model state; i.e.,

$$A^{n\ell j\Omega}_{n'\ell'j'}(\infty) \to \delta_{nn'}\,\delta_{\ell\ell'}\,\delta_{jj'}\,. \quad (2)$$

In Fig. 1 we show a proton $f_{7/2}$ state in ^{48}Ca which is polarized by a nearby ^{16}O nucleus. We show the radial wave function along the line of centers of the two nuclei. One sees here clearly how the probability is distributed in part in the neighboring oxygen nucleus. A proton in the oxygen nucleus can more easily be transferred to such a polarized state than to the asymptotic state, also shown, which overlaps with oxygen only in its tail.

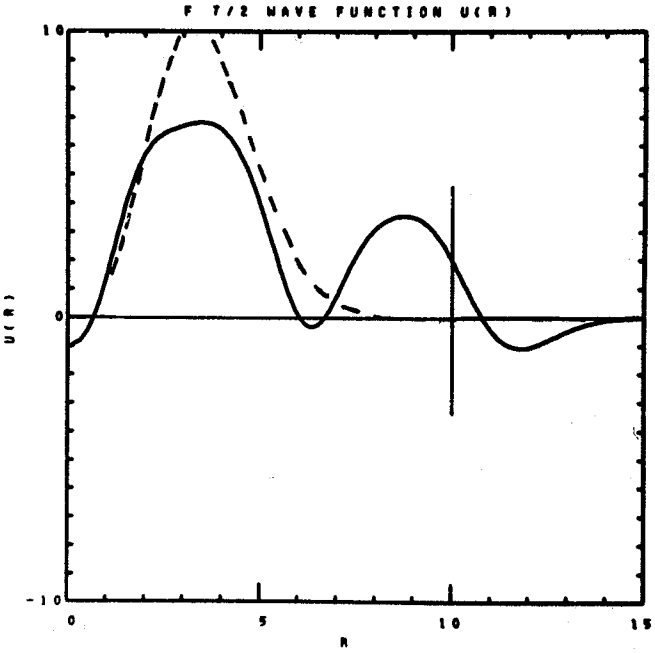

Fig. 1. The polarized wave function along the axis joining the centers of ^{48}Ca and ^{16}O is shown. For comparison the unpolarized wave function is shown. The center of ^{48}Ca is at the origin and the center of ^{16}O is at 10 Fm. (XBL 764-1027)

The wave function (1) is expressed on a basis which has the symmetry axis connecting the line of centers of the two nuclei as the Z-axis. We have to relate this correctly to the laboratory fixed axis, which we may take to be defined by $\underset{\sim}{k}_\alpha$ for the reaction

$$A(a,b)B, \quad a = b+1, \quad B = A+1.$$

The usual DWBA amplitude we take to be

$$T_{j_1 m_1 \to j_2 m_2} \sim \int \psi^{(-)*}(\underset{\sim}{k}_\beta, \underset{\sim}{R}_\beta)\, \phi^*_{n_2 \ell_2 j_2 m_2}(\underset{\sim}{r}_B) \times V(r_a)\, \phi_{n_1 \ell_1 j_1 m_1}(\underset{\sim}{r}_a) \psi^{(+)}(\underset{\sim}{k}_\alpha, \underset{\sim}{R}_\alpha)\, d\underset{\sim}{R}_\alpha d\underset{\sim}{R}_\beta \qquad (3)$$

where

$$r_a = R_{1a},\ R_\alpha = R_{aA},\ r_B = R_{1B},\ R_\beta = R_{Bb}. \qquad (4)$$

The connection between wave functions expressed in the intrinsic frame and the laboratory frame is

$$(\phi_{n\ell j\Omega})_{\text{int.}} = \sum_m D^{j*}_{m\Omega}(\omega)\, \phi_{n\ell\, jm} \qquad (5)$$

where D is the rotation function that rotates $\hat{k}_\alpha$ into the intrinsic axis (denote the Euler angles by ω). Since

$$\sum_\Omega D^j_{m\Omega}\, D^{j*}_{\mu\Omega} = \delta_{\mu m}$$

then

$$\sum_{\Omega\mu} D^j_{m\Omega}\, D^{j*}_{\mu\Omega}\, \phi_{j\mu} = \phi_{jm}.$$

Hence according to (5) we replace

$$\sum_\mu D^{j*}_{\mu\Omega}\, \phi_{j\mu} \text{ by } \phi_{j\Omega}(R,r).$$

Thus the amplitude for the transfer between polarized states is

$$T^P_{j_1 m_1 \to j_2 m_2} = \sum_{\Omega_1\Omega_2} \int \psi^{(-)*}(\underset{\sim}{R}_\beta)\, D^{j_2*}_{m_2\Omega_2}(\omega_\beta) \times \phi^*_{n_2 \ell_2 j_2 \Omega_2}(R_\beta, \underset{\sim}{r}_B) \times V(r_a)\, D^{j_1}_{m_1\Omega_1}(\omega_\alpha)\, \phi_{n_1\ell_1 j_1\Omega_1}(R_\alpha, \underset{\sim}{r}_\alpha) \times \psi^{(+)}(\underset{\sim}{R}_\alpha)\, d\underset{\sim}{R}_\alpha d\underset{\sim}{R}_\beta .$$

Introducing the expansion (1) for the polarized wave functions, but expressing the components through (5) in terms of the laboratory frame we have

$$T^P_{j_1 m_1 \to j_2 m_2} = \sum_{\Omega_1\Omega_2} \sum_{n'_1\ell'_1 j'_1 \mu_1} \sum_{n'_2\ell'_2 j'_2 \mu_2} \int A^{n_2\ell_2 j_2\Omega_2}_{n'_2\ell'_2 j'_2}(R_\beta)\, \psi^{(-)*}(\underset{\sim}{R}_\beta) \left(D^{j_2*}_{m_2\Omega_2}(\omega_\beta)\, D^{j'_2}_{\mu_2\Omega_2}(\omega_\beta)\right) \phi^*_{n'_2\ell'_2 j'_2\mu_2}(\underset{\sim}{r}_B)\, V(r_a) \left(D^{j_1}_{m_1\Omega_1}(\omega_\alpha)\, D^{j'_1*}_{\mu_1\Omega_1}(\omega_\alpha)\right) \phi_{n'_1\ell'_1 j'_1\mu_1}(\underset{\sim}{r}_a)\, A^{n_1\ell_1 j_1\Omega_1}_{n'_1\ell'_1 j'_1}(R_\alpha)\, \psi^{(+)}(\underset{\sim}{R}_\alpha)\, d\underset{\sim}{R}_\alpha\, d\underset{\sim}{R}_\beta .$$

If the polarization of the single-particle states produces the expected trends, and an effect of the magnitude commensurate with the anomalies observed in experiment, then we would contemplate more refined calculations. There are a hierarchy of improvements. The potential model for the two-center shell model is based on modified oscillator potentials. One could improve the model by using, say Woods-Saxon potentials. Beyond this a dynamical evolution of the polarization could be formulated.

Footnotes and References

*Condensed from LBL-5008.

†Fellow of Deutscher Akademischer Austauschdienst, Bonn, Germany.

1. N. K. Glendenning, Rev. Mod. Phys. 47, 659 (1975).

2. H. J. Körner, G. C. Morrison, L. R. Greenwood, and R. H. Siemssen, Phys. Rev. C 7, 107 (1973).

3. Y. Eisen, H. T. Fortune, W. Henning, D. G. Kovar, S. Vigdor, and B. Zeidman, Phys. Rev. C 13, 699 (1976).

4. N. K. Glendenning and R. J. Ascuitto, Argonne Symposium on Heavy-Ion Transfer Reactions, Vol. II,

513 (1973); Phys. Lett. 45B, 85 (1973); ibid. 47B, 332 (1973).

5. Auerbach, Baltz, Bond, Chasman, Garrett, Jones, Kahana, LeVine, Schnieder, Schwarzschild, and Thorn, Argonne Symposium on Heavy Ion Transfer Reactions, Vol. II, 419 (1973).

6. N. K. Glendenning and G. Wolschin, LBL-4334 (1975), to be published by Phys. Rev. Lett.

7. J. A. Maruhn and W. Greiner, Z. Phys. 251, 431 (1972).

POLARIZATION OF SINGLE PARTICLE STATES IN HEAVY ION INDUCED NUCLEAR REACTIONS WITHIN THE TWO CENTER SHELL MODEL: I. THE FORMALISM*

K. Pruess†

Two Center Shell Models (TCSM), using either pregiven or self-consistent potentials, have been applied to problems of nuclear fission and nucleus-nucleus collisions for quite some time.[1-10] They were used to calculate total energies of nuclear configurations as a function of macroscopic parameters. These energies were taken as potentials governing collective motions, such as the relative motion of two colliding nuclei.

Underlying these models is an adiabatic picture, with the single particle motion considered to be fast compared to the collective motion. If this is to be taken seriously, and consistently, then not only the single particle energies but also the wave functions should adjust to the collective motion.

We put forward the hypothesis that, in "slow" nucleus-nucleus collisions, rearrangement reactions will occur between polarized (two center) states rather than between asymptotic states of the free nuclei.[11]

Polarized states contain a mixture of different angular momenta. In order to use these states in reaction calculations a decomposition in terms of asymptotic states is required. We have developed a formalism to achieve this. Our method, although generally applicable, is formulated for the asymmetric two center shell model of Maruhn and Greiner.[6] The potential is a modified two center oscillator, with the potential between the centers expressed by a polynomial of fourth degree to avoid the unphysical cusp. The usual $\ell\cdot s$ and ℓ^2-forces are included. In the case of axial symmetry (collision of spherical nuclei) eigenstates may be written ($\Omega > 0$)

$$|E\Omega\rangle \equiv |Rn\ell j\Omega\rangle$$

$$= \sum_{n_z n_\rho} \left(a^{n\ell j\Omega\uparrow}_{n_z n_\rho}(R)\,|n_z n_\rho \Omega - \tfrac{1}{2}\rangle\,\chi_{1/2} + a^{n\ell j\Omega\downarrow}_{n_z n_\rho}\,|n_z n_\rho \Omega + \tfrac{1}{2}\rangle\,\chi_{-1/2}\right). \quad (1)$$

The only integrals of motion are the energy E and Ω, which is the projection of angular momentum on the z-axis (intrinsic symmetry axis). $n\ell j\Omega$ are the usual quantum numbers of the spherical oscillator shell model with $\ell\cdot s$ -force, which are asymptotic quantum numbers as the two center separation parameter $R \to \infty$. The $|n_z n_\rho m\rangle$ are eigenstates of the two center oscillator. χ_μ is a spin function. The coefficients a are obtained by numerically diagonalizing the Hamiltonian of the Maruhn/Greiner model on the basis of two center oscillator states. The 'asymptotic expansion' is written

$$|Rn\ell j\Omega\rangle = \sum_{n'\ell'j'} A^{n\ell j\Omega}_{n'\ell'j'}(R)\,|n'\ell'j'\Omega\rangle \xrightarrow[R\to\infty]{} |n\ell j\Omega\rangle \quad (2)$$

where $|n'\ell'j'\Omega\rangle$ are states of the oscillator shell model, referring to either of the colliding nuclei.

To bring Eq. (1) into the form Eq. (2) the states $|n_z n_\rho m\rangle\chi_\mu (m+\mu = \Omega)$ must be expanded in terms of states $|n'\ell'j'\Omega\rangle$. This is done in three steps. First, the z part of the two center oscillator states is expanded in terms of harmonic oscillator states

$$|n_z\rangle = \sum_{\hat{n}} h^{n_z}_{\hat{n}}\,|\hat{n}\rangle. \quad (3)$$

Calculation of the h involves integration over products of parabolic cylinder functions, which in part can only be done numerically. Then the states $|\hat{n}\, n_\rho m\rangle$, which are eigenstates of the spherically symmetric harmonic oscillator written in a cylindrical basis, are expanded in terms of eigenstates of ℓ^2

$$|\hat{n}\, n_\rho m\rangle = \sum_{\ell'} C^{\hat{n}}_{\ell'}(N',m)\,|n'\ell'm\rangle \quad (4a)$$

where

$$N' = \hat{n} + 2n_\rho + |m| = 2n' + \ell' \quad (4b)$$

is the phonon number. Calcuation of the c involves, for each N', m separately, diagonalization of the matrix of ℓ^2 on the basis of the $|\hat{n}\, n_\rho m\rangle$. Finally, the $|n'\ell'm\rangle\chi_\mu$ are expanded in terms of total angular momentum eigenstates

$$\langle\theta\phi|\ell'm\rangle\chi_\mu \equiv Y_{\ell'm}(\theta\phi)\chi_\mu = \sum_{j'\Omega} C^{m\mu\Omega}_{\ell' s j'}\,|\ell'j'\Omega\rangle. \quad (5)$$

With the explicit forms for the Clebsch-Gordon coefficients we obtain for the polarization amplitudes in Eq. (2) ($\Omega > 0$)

$$A^{n\ell j\Omega}_{n'\ell'j'_>}(R) = \sum_{n_z n_\rho} \left\{ \left(\frac{\ell'+\Omega+1/2}{2\ell'+1} \right)^{1/2} a^{n\ell j\Omega\uparrow}_{n_z n_\rho}(R)\, h^{n_z}_{N'-2n_\rho-\Omega+1/2}\, C^{N'-2n_\rho-\Omega+1/2}_{\ell'}(N',\Omega-1/2) \right.$$
$$\left. + \left(\frac{\ell'-\Omega+1/2}{2\ell'+1} \right)^{1/2} a^{n\ell j\Omega\downarrow}_{n_z n_\rho}(R)\, h^{n_z}_{N'-2n_\rho-\Omega-1/2}\, C^{N'-2n_\rho-\Omega-1/2}_{\ell'}(N',\Omega+1/2) \right\} \qquad (6a)$$

where $N' = 2n' + \ell'$; $j'_> = \ell' + 1/2$

$$A^{n\ell j\Omega}_{n'\ell'j'_<}(R) = \sum_{n_z n_\rho} \left\{ \left(\frac{\ell'+\Omega+1/2}{2\ell'+1} \right)^{1/2} a^{n\ell j\Omega\downarrow}_{n_z n_\rho}(R)\, h^{n_z}_{N'-2n_\rho-\Omega-1/2}\, C^{N'-2n_\rho-\Omega-1/2}_{\ell'}(N',\Omega+1/2) \right.$$
$$\left. - \left(\frac{\ell'-\Omega+1/2}{2\ell'+1} \right)^{1/2} a^{n\ell j\Omega\uparrow}_{n_z n_\rho}(R)\, h^{n_z}_{N'-2n_\rho-\Omega+1/2}\, C^{N'-2n_\rho-\Omega+1/2}_{\ell'}(N',\Omega-1/2) \right\} \qquad (6b)$$

where $N' = 2n' + \ell'$; $j'_< = \ell' - 1/2$.

As matrix elements of the TCSM-Hamiltonian are independent of the sign of Ω

$$A^{n\ell j-\Omega}_{n'\ell'j'} = A^{n\ell j\Omega}_{n'\ell'j'}. \qquad (7)$$

It is convenient to write down also a first-order perturbation expression for the A's.[12] Denoting with V_R the shell model potential of the polarizing nucleus at distance R we have, taking only momentum-independent parts of V_R into account

$$A^{n\ell j\Omega}_{n'\ell'j'}(R) \approx (E_{n\ell j} - E_{n'\ell'j'})^{-1} \sum_{m\mu} C^{m\mu\Omega}_{\ell's'j'}\, C^{m\mu\Omega}_{\ell sj}\, \langle n'\ell'm|V_R|n\ell m\rangle \qquad (8)$$

Footnotes and References

*Abridged version of LBL-5066, to be published in Nuclear Phys. A.

†Fellow of Deutscher Akademischer Austauschdienst, Bonn, Germany.

1. P. Holzer, U. Mosel, and W. Greiner, Nucl. Phys. A138, 241 (1969).

2. K. Pruess and W. Greiner, Phys. Lett. 33B, 197 (1970); K. Pruess, Thesis, Frankfurt/Main 1972 (unpublished).

3. U. Mosel, T. D. Thomas, and P. Riesenfeldt, Phys. Lett. 33B, 565 (1970).

4. D. Scharnweber, W. Greiner, and U. Mosel, Nucl. Phys. A164, 257 (1971).

5. M. Rayet and G. Reidemeister, J. Physique 32, 259 (1971).

6. J. A. Maruhn and W. Greiner, Z. Physik 251, 431 (1972); J. A. Maruhn, Diploma thesis, Frankfurt/Main 1971 (unpublished).

7. T. Morovic, Thesis, Frankfurt/Main 1973 (unpublished).

8. H. C. Pauli, Phys. Rep. 7C (1973) No. 1 (and references therein).

9. T. Tazawa, Progr. Theor. Phys. 51, 1764 (1974).

10. H. J. Specht, Rev. Mod. Phys. 46, 773 (1974) (and references therein).

11. K. Pruess, G. Delic, L. A. Charlton, and N. K. Glendenning, LBL-5008, presented at the Symp. on Macr. Features of Heavy Ion Collisions, Argonne, Ill., 1976, to be published.

12. A. S. Davydov, Quantum Mechanics, Pergamon Press, Oxford 1965.

POLARIZATION OF SINGLE PARTICLE STATES IN HEAVY ION INDUCED NUCLEAR REACTIONS WITHIN THE TWO CENTER SHELL MODEL: II. NUMERCIAL RESULTS*

K. Pruss†

We have programmed the calculation of polarization amplitudes, Eqs. (6) of preceding paper, on the CDC 7600 computer at LBL. Table 1 gives a summary of the steps and times involved. Careful checks of the numerical accuracy were made.

For collisions of spherical nuclei, our two center model has the following adjustable parameters

- R, the separation between the potential centers;
- ε, which measures the barrier height in units of the barrier for a two center oscillator at the same separation;
- ω_i $(i=1,2)$, the frequency parameters of the underlying two center oscillator;
- $\varkappa_i, \mu_i$ $(i=1,2)$, strength parameters of the $\underset{\sim}{\ell}\cdot\underset{\sim}{s}$ - and $\underset{\sim}{\ell}^2$ -forces, respectively.

Most of the calculations we have made so far are for the system $^{40}Ca + ^{16}O$. The parameters ω_i, $\varkappa_i$, μ_i were adjusted to the asymptotic values of the free nuclei ($\hbar\omega_1 = 10.90$ MeV,[1] $\hbar\omega_2 = 13.00$ MeV;[2] $\varkappa_{1,2} = 0.08$; $\mu_{1,2} = 0.0$).[3] Both rounded off ($\underline{r}$) and unmodified two center oscillator barriers ($\underline{c} \triangleq$ cusp) were used.

It turns out that the polarization amplitudes $A^{n\ell j\Omega}_{n'\ell'j'}$ vary slowly and smoothly with n' and ℓ' attaining a number of extrema in different $n'\ell'$ regions. A convenient way to present and discuss the data is in terms of contour maps (extending the A's to a continuous range of $n'\ell'$ through interpolation).

For each single particle state (asymptotic quantum numbers $n\ell j\Omega$), and each nucleus-nucleus distance R, there are two such maps: One for the $j'_> = \ell' + 1/2$ -states, and one for the $j'_< = \ell' - 1/2$ -states. Figure 1 shows polarization contour maps for the $1f_{7/2}$ $1/2^-$-proton-state in ^{40}Ca, polarized from ^{16}O at various distances near the grazing distance $R \approx 10$ fm. To obtain a general understanding of the polarization effect consider also Fig. 2, which shows contour maps of $|\psi|^2$ for the same state. It is seen that the single particle states are slightly distorted from their asymptotic appearance within the polarized nucleus, and, more important, have attained a whole new region of appreciable amplitude near the center of the polarizing nucleus. It is this latter part of the wave function which, when expanded on a ^{40}Ca basis some 10 fm away, requires expansion coefficients $A^{n\ell j\Omega}_{n'\ell'j'}$, varying slowly and smoothly with $n'\ell'$, as shown in Fig. 1.

The polarization effect has a characteristic dependence upon the relevant physical parameters—the nucleus-nucleus distance R, and the single particle quantum numbers E and Ω. Figures 1 and 2 show that, while the polarization admixtures become stronger for decreasing distance R, their general shape is nearly independent of R in the grazing region. As a natural measure of the overall strength of the polarization we introduce the total probability accounted for by the admixed states

$$P^{n\ell j\Omega}(R) = \sum_{n'\ell'j' \neq n\ell j} A^{n\ell j\Omega}_{n'\ell'j'}(R)^2 = 1 - A^{n\ell j\Omega\ 2}_{n\ell j}. \quad (1)$$

Table 1. Computation of a typical case: $^{40}Ca + ^{16}O$ at a grazing distance R = 10 fm.

	Calculation	Evaluated quantities	Remarks	Calculation time (sec)
(i)	two center oscillator basis states and diagonalization of TCSM Eq. (I.1)	$n_z(R)$ $a^{n\ell j\Omega}_{n_z n_\rho}(R)$	100 two center oscillator basis states ($E \leqslant 92.5$ MeV)	8
(ii)	expansion of z-part of two center oscillator states after harmonic oscillator states Eq. (I.3)	$h^{n_z}_{\hat{n}}$	13 two center oscillator states; 40 harmonic oscillator states Gaussian quadrature	60
(iii)	angular momentum eigenstates in a cylindrical basis Eq. (I.4)	$C^{\hat{n}}_{\ell'}(N',m)$	$N' = 0,\ldots,39$ $m = 0,\ldots,6$	10
(iv)	asymptotic expansion Eq. (I.6)	$A^{n\ell j\Omega}_{n'\ell'j'}(R)$	40 single particle states ($E \leqslant 58$ MeV) $2n' + \ell' \leqslant 39$	16

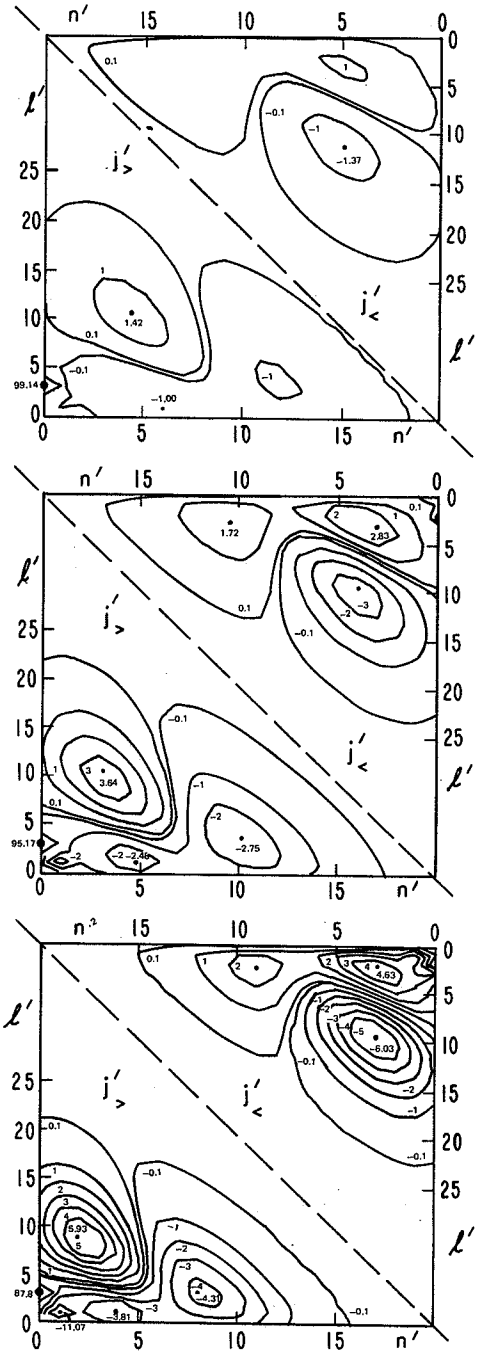

Fig. 1. Polarization amplitudes for the $1f_{7/2}\ 1/2$ proton state in ^{40}Ca, polarized from ^{16}O, as calculated from Eqs. (6) of preceding paper for a two center oscillator barrier (units along contours 10^{-2}). (XBL 766-2945)

Figure 3 shows that P increases by roughly an order of magnitude if R decreases by 1 fm. From the same figure it is also evident that the polarization decreases fast with increasing $|\Omega|$. This feature is of purely geometric origin, and can be understood from the first-order perturbation expression, Eq. (8) of the preceding paper. The state which is to be polarized has an angular dependence $Y_{\ell|\Omega|\pm 1/2}$. With increasing $|\Omega|$ it misses the polarizing potential on the z-axis (around $\theta = 0$) to an increasing extent.

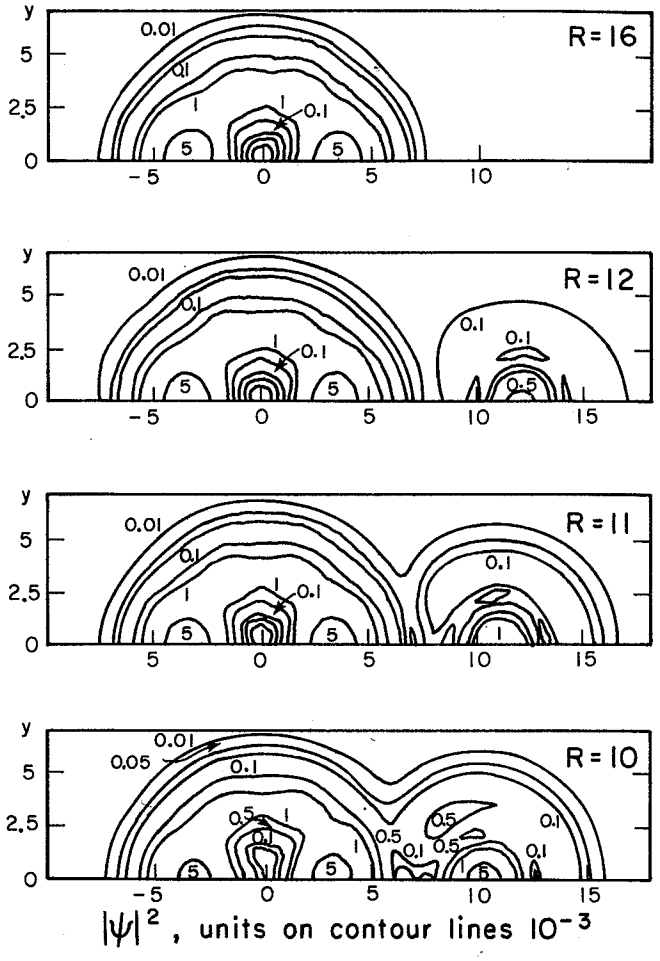

Fig. 2. Countour maps of $|\psi|^2$ for the same state as calculated from Eq. (1) of preceding paper for a two center oscillator barrier (R in fm). (XBL 766-2944)

From Eq. (8) of the preceding paper it is also clear that the polarization generally will increase with increasing excitation energy ($\hat{=}$ longer tail) of the polarized state. Figure 4 shows the polarization as calculated from Eq. (1) as a function of single particle energies at grazing distance R = 10 fm for a realistic barrier ($\epsilon = 0.8r$). It increases by roughly an order of magnitude in going to the next major shell. Superimposed on this general trend are resonance effects. When the energy difference between single particle states in the colliding nuclei is small, these states are mutually strongly polarized. A more careful analysis shows that the polarization effect essentially consists in admixing a few states of the polarizing nucleus which have neighboring energies. Efforts are under way to observe "resonance polarization" experimentally, and to clarify its connection to the familiar resonance exchange scattering.[4]

Investigations of the polarization effect for more realistic two center potentials (Woods-Saxon and constrained Hartree-Fock), and for other systems (especially $^{208}Pb + ^{12}C$) are in progress.

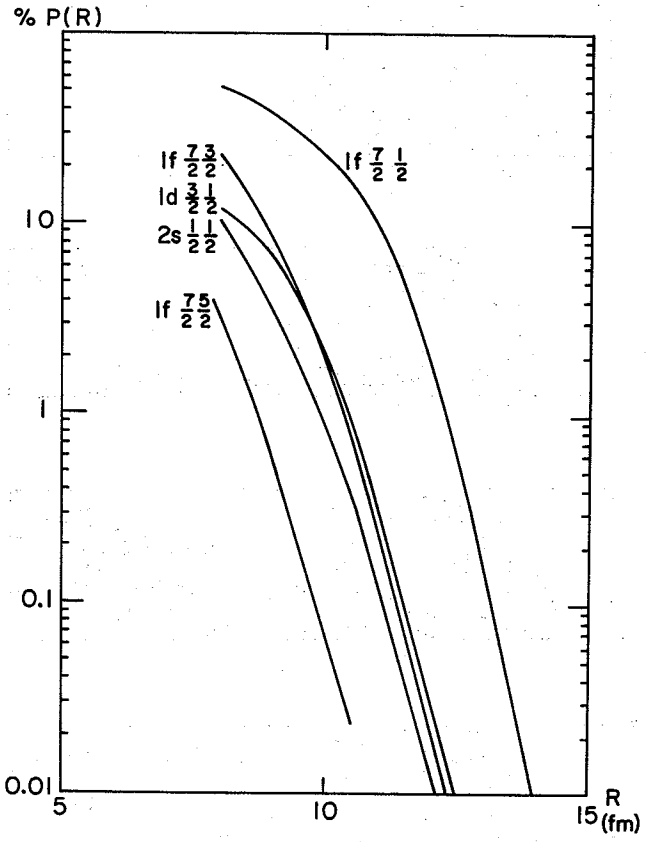

Fig. 3. Polarization for a number of ^{40}Ca proton states, due to ^{16}O, as calculated from Eq. (1) for a two center oscillator barrier. (XBL 766-2943)

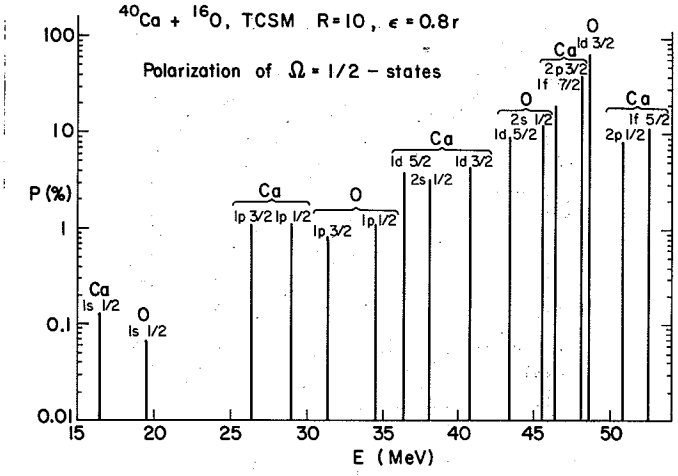

Fig. 4. Polarization as calculated from Eq. (1) for a realistic barrier (ε = 0.8, rounded). (XBL 766-2942)

Footnotes and References

*Abridged version of LBL-5066, to be published in Nuclear Phys. A.

†Fellow of Deutscher Akademischer Austauschdienst, Bonn, Germany.

1. T. W. Donnelly and G. E. Walker, Phys. Rev. Lett. 22, 1121 (1969).

2. R. W. Shaw et al., Proc. Phys. Soc. 86, 513 (1965).

3. C. Gustafsson, International Conference on the Properties of Nuclei Far from the Region of Beta-Stability, Leysin, Switzerland, 1970, CERN Report 70-30, p. 654; I. Ragnarsson, ibid., p. 847.

4. W. von Oertzen, Nucl. Phys. A148, 529 (1970); A. Gobbi, in Proceedings of the International Conference on Reactions Between Complex Nuclei Nashville, Tennessee (1974), Vol. 2, p. 211.

A NEW APPROACH TO ANTISYMMETRIZATION AND REARRANGEMENT IN NUCLEUS-NUCLEUS COLLISIONS*

K. Pruess† and P. Lichtner‡

We have investigated a new microscopic model for the description of nucleus-nucleus collisions.

Consider a system of A nucleons, divided into two fragment nuclei A_a, B_a. The usual microscopic description of their relative motion employs the vector

$$\underset{\sim}{r}_\alpha = \frac{1}{A_a}\sum_{i\varepsilon A_\alpha} \underset{\sim}{r}_i - \frac{1}{B_a}\sum_{i\varepsilon B_\alpha} \underset{\sim}{r}_i \qquad (1)$$

which connects their mass centers. The definition of $\underset{\sim}{r}_\alpha$ specifies what we call a "partition" $\alpha = (A_\alpha, B_\alpha)$, i.e., a certain arbitrary but fixed distribution of the A nucleons among the fragments. With $\underset{\sim}{r}_\alpha$ as given by Eq. (1) the kinetic energy separates exactly into a relative and an internal part, and the mass associated with the $\underset{\sim}{r}_\alpha$ motion is coordinate independent and equal to the reduced mass m_a.

Because of the identity of nucleons actual physical states are always "fragmentations" a = (A_a, B_a), i.e., only the nature of the fragments is specified. A description in terms of partitions as implied by Eq. (1) is unnecessarily detailed and leads to well known complications. $\underset{\sim}{r}_\alpha$ being defined differently for different partitions, antisymmetrization introduces nonlocal interactions.[1] The kinematical description of rearrangement reactions is difficult, because different relative motion coordinates are involved. The incorporation of polarization effects (channels which depend pa-

rametrically on the nucleus-nucleus distance) requires complicated expansions and lengthy computations (see foregoing papers).

To avoid these difficulties, we introduce symmetrical relative motion coordinates, i.e., coordinates which, being invariant with respect to nucleon permutations, directly apply to physical fragmentations.[2-5] They are defined on the basis of the quadrupole tensor $Q_{\gamma\delta}=\sum_{i=1}^{A} x_{i\gamma}\, x_{i\delta}$ of the A nucleon system. (Here $x_{i\gamma}=\underset{\sim}{r}_i\cdot\underset{\sim}{e}_\gamma(\gamma=x,y,z)$ are the nucleon coordinates referred to a c.m.-frame $\underset{\sim}{e}_x$, $\underset{\sim}{e}_y$, $\underset{\sim}{e}_z$).

The principal axis of $Q_{\gamma\delta}$ define an intrinsic coordinate frame $\underset{\sim}{e}_u$ (u = 1,2,3) and three Euler angles θ_s. They are clearly invariant with respect to nucleon permutations and can be used to describe the relative angular motion of two nuclei. A symmetrical relative distance coordinate may be defined in a number of ways, due to the fact that the concept of relative distance is unambiguous only in the asymptotic region of well separated nuclei. It is convenient to employ the rms radius $Q=\sum_{i,\gamma} x_{i\gamma}^2$ of all nucleons and to define

$$R_a = \sqrt{\frac{m}{m_a}Q}\,. \tag{2}$$

The complete kinematical transformation to a redundant set involving symmetrical relative motion coordinates $R_a\ \theta_s$ is defined as

$$x_{i\gamma} = \sum_{u=1}^{3} e_{\gamma u}(\theta_s)\, x_{iu} \tag{3a}$$

$$\zeta_u = \sum_{i=1}^{A} x_{iv}\, x_{iw} \tag{3b}$$

$$\zeta_4 = \sum_{i\gamma} x_{i\gamma}^2 - \frac{m_a}{m} R_a^2 \tag{3c}$$

(i = 1, ..., A; γ = x,y,z; s = 1,2,3; u = 1,2,3; u,v, w = 1,2,3 and cyclical permutations; $e_{\gamma u}=\underset{\sim}{e}_\gamma\cdot\underset{\sim}{e}_u$ is the rotation matrix).

In order to apply shell model ideas we want to keep the 3A intrinsic coordinates x_{iu} as independent coordinates, together with the four relative motion coordinates $\underset{\sim}{R}_a = (R_a\ \theta_s)$. This is achieved with the help of four spurious coordinates ζ_c (c = 1,2,3,4).[6-9] They have to be integrated out of matrix elements according to

$$\langle\Psi|A|\Phi\rangle = \int dx_{i\gamma}\, d\zeta_c\, \delta(\zeta_c)\, \Psi(x_{i\gamma}\zeta_c)\, A\Phi\,(x_{i\gamma}\zeta_c). \tag{4}$$

Practically, this can only be achieved in an approximate fashion. Calculations in the two center shell model indicate that matrix elements will typically be averaged over a region of $\Delta R_a \approx 0.5$ fm.

The 3A + 4 coordinates $(x_{iu} R_a \theta_s)$ offer the following advantages for a description of nucleus-nucleus scattering:

- antisymmetrization does not cause nonlocal interactions;
- relative distance coordinates for different two-body fragmentations are identical except for a trivial multiplicative factor

$$R_b = \sqrt{m_a/m_b}\ \ R_a \tag{5}$$

- the Euler angles contain the total angular momentum, so that no angular momentum coupling of internal and relative motion is necessary.

We have explicitly transformed the many-body Hamiltonian to the $(x_{iu}\ \underset{\sim}{R}_a)$ coordinates. With the usual volume element

$$d\tau = dx_{iu}\, d\underset{\sim}{R}_a\, R_a^2 \tag{6}$$

the radial part of the kinetic energy takes the form

$$T_{rad} = \frac{p_a^2}{2m_a} + T_{coupl} \tag{7a}$$

$$T_{coupl} = \frac{1}{4m_a}\sum_{iu}\left(x_{iu}p_{iu}x_{iu}\right)\left(\frac{1}{R_a}P_a + P_a\frac{1}{R_a}\right) \tag{7b}$$

where

$$P_a = -\frac{i\hbar}{R_a}\frac{\partial}{\partial R_a}R_a \tag{8a}$$

$$p_{iu} = -\,i\hbar\,\partial/\partial x_{iu}\,. \tag{8b}$$

P_a is the usual (Hermitean) radial momentum. The main result of this investigation is contained in Eqs. (7), stating that T_{rad} is by itself a Hermitean operator. It is, except for the coupling between radial and particle motion, identical in form to the radial part of the usual three-dimensional kinetic energy of a mass point. Angular and particle part of the kinetic energy turn out to be identical to the well known expressions of the unified model of nuclear rotations, and are not further discussed in this work.[6,9]

The coupling between radial and particle motion is of purely kinematical origin. It is the price paid for the simplifications introduced with symmetrical relative motion coordinates. Such coordinates, depending upon all nucleon indices in a symmetrical way, inevitably must contain a residual dependence upon the internal motion.

We have formulated coupled channel equations using the $(x_{iu}\underset{\sim}{R}_a)$ coordinates. Simplifying the Hamiltonian somewhat we obtain a free-motion solution in the form of an asymptotic series

$$\Psi_{an\ell m} = \frac{e^{\pm ik_aR_a}}{R_a}\sum_{\nu\lambda}\frac{K_\nu^{\lambda(\pm)}}{R_a^\lambda}\,\phi_{n+\nu\ell m} \tag{9}$$

$(\lambda = 0,\ldots,\infty;\ -n\leq\nu\leq\infty\ ;\ K_\nu^\lambda = 0 \text{ if } \lambda < |\nu|)$

$\phi_{n\ell m}$ is an oscillator state.

A recursion relation is derived for the coefficients $K_\nu^\lambda/R_a^\lambda$ of kinematical coupling. Numerical examples indicate that in the grazing region successive orders decrease fast. Further investigations of the coupling for $R_a \to 0$ are required before actual reaction calculations can be made.

The derivation of the two-center shell model from the coupled equations is also discussed.

Footnotes and References

*Abridged version of LBL-4381, in press in Nuclear Phys. A.

†Fellow of Deutscher Akademischer Austauschdienst, Bonn, Germany.

‡Institut fuer Kernphysik der Universitaet Mainz, Germany; Supported by Bundesministerium fuer Forschung und Technologie, Contract NV2002-L.

1. E. van der Spuy, Nucl. Phys. 11, 615 (1959).

2. K. Pruess, Thesis, Frankfurt, 1972 (unpublished).

3. K. Pruess, Proc. European Conf. on Nucl. Phys., Aix-en-Provence, 1972, Vol. II, p. 46; K. Pruess, GSI-Bericht 73-6, p. 62, Darmstadt 1973.

4. P. Lichtner, Thesis, Mainz, 1974 (unpublished).

5. W. Scheid, Habilitationsschrift, Frankfurt, 1970 (unpublished).

6. H. J. Lipkin, A. de Shalit, and I. Talmi, Nuovo Cim. II (1955) 773.

7. R. S. Nataf, Nucl. Phys. 2 (1956) 497.

8. F. Villars, Nucl. Phys. 3 (1957) 240.

9. F. Villars and G. Cooper, Ann. of Phys. (N.Y.) 56 (1970) 224.

FINITE RANGE EVALUATION OF (p-d, d-t) WITH MOMENTUM SPACE TECHNIQUES*

L. A. Charlton

Recently a great deal of work has been done to investigate the contribution of a sequential transfer mechanism in (p,t) reactions.[1-5] This is usually done by adding a simultaneous term, calculated using DWBA, and a sequential term using "second order" DWBA. Both terms are almost always evaluated using the zero-range approximation. This use of the zero-range approximation in the usual DWBA calculations (first order) does not allow the normalization of the cross section to be found with any confidence. Further, both the shape and the normalization of the sequential term (second order DWBA) can be uncertain when a zero range formalism is used. In the paper from which this report was condensed,[6] the contributions to (p,t) reactions from the simultaneous and the sequential mechanisms were considered using a full finite range evaluation of each term. This evaluation was performed by using momentum space techniques.[7]

The techniques used for the first order term had been previously reported.[8] The second order term required the calculation of two one-step matrix elements (p-d) and(d-t) and a Greens function to connect the two. The two one-step processes were evaluated as in Ref. 7. Since the Greens function is an inverse operator, an extension of the momentum space formalism was required. A method suggested, in a different context, by Lane and Robson[9] proved suitable. This method allows an inverse operator to be evaluated as follows. By definition an operator P satisfies

$$P\,P^{-1} = 1.$$

Forming a unit operator from a set of nonorthogonal discrete states and taking a matrix element gives

$$\sum_{n_2' n_2 = 1} \langle n_1' | P | n_2' \rangle N_{n_2' n_2} \langle n_2 | P^{-1} | n_1 \rangle = \langle n_1' | n_1 \rangle$$

where the $N_{n'n}$ orthogonalizes the discrete states. Writing the equation immediately above in matrix form gives

$$\underset{\sim}{P}\,\underset{\sim}{N}\,\underset{\sim}{\tilde{P}} = \underset{\sim}{0}$$

where $\tilde{P}$ contains the desired matrix element of P^{-1} and 0 contains the overlap of the discrete set. Solving the matrix equation gives

$$\underset{\sim}{\tilde{P}} = \underset{\sim}{N}^{-1}\,\underset{\sim}{P}^{-1}\,\underset{\sim}{N}^{-1}$$

where

$$\underset{\sim}{0} = \underset{\sim}{N}^{-1}$$

has been used. Reference 6 gives a more complete description of the above procedure.

This study of the simultaneous and sequential contributions to (p,t) reactions drew three conclusions: 1) finite range effects can be large 2) the shape of the calculated differential cross sections can be strongly dependent on the contribution from a sequential transfer mechanism and 3) the post-prior interchange usually used in the second order term is probably the best realistic approximation. These conclusions were based on consideration of $^{208}Pb(p,t)^{206}Pb_{g.s.}$ only. Work is now underway to establish systematics for the effect noted by looking at a variety of nuclei.

Footnotes and References

*Condensed from Ref. 6.

1. P. D. Kunz and E. Rost, Bull. Am. Phys. Soc. 17, 902 (1972).

2. N. B. de Takacsy, Nucl. Phys. A231, 243 (1974).

3. V. Managoli and D. Robson, Nucl. Phys. A252, 354 (1975).

4. H. Segawra, K. I. Kuho, and A. Arima, Phys. Rev. Lett. 35, 357 (1975).

5. N. Hashimoto and M. Kawai, Phys. Lett. 59B, 223 (1975).

6. L. A. Charlton, Phys. Rev. C14, 506 (1976).

7. L. A. Charlton, Phys. Rev. C 8, 146 (1973); L. A. Charlton, Phys. Rev. C 9,413 (1974).

8. L. A. Charlton, Phys. Rev. C 12, 351 (1975).

9. A. M. Lane and D. Robson, Phys. Rev. 185, 1403 (1969).

FINITE-RANGE EFFECTS IN MULTISTEP (p-d, d-n) REACTIONS*

P. D. Kunz,† and L. A. Charlton

Two step processes through reaction channels have been successful in explaining many phenomena. The most striking example has been the discrepancy in the population of high spin states in (^{3}He,t) reactions.[1] Further, the mechanism has successfully explained the L = 1 angular distributions seen in (^{3}He,t) reactions to anti-analogue states.[2] For (p,n) processes, however, a large renormalization of the direct charge exchange is needed in order to successfully fit shapes and magnitudes of angular distributions.[3] All the above calculations have used the zero-range approximation which, in part, is responsible for the renormalization problems in (p-d, d-n) reactions. This may be seen calculationally by referring to Fig. 1. The differential cross section for ^{58}Ni(p-d, d-n)^{58}Cu is shown. The use of the zero range approximation overpredicts the two-step contribution by a large factor.

Some understanding of the large finite-range effects can be gained by considering the first order finite-range correction to the zero-range calculation. This first order correction contains a term in which the deuteron Laplacian acts on the intermediate state Greens function. The properties of the Greens function may then be used to get

$$\frac{-\hbar^2}{2\mu_D} \nabla_D^2 \, G(R_D,R_D') = (E_D - V_D)\, G(R_D,R_D') - \delta(R_D - R_D').$$

The first term on the right hand side of the above equation is identical to the usual correction term found for (p-d) reactions. Since the zero range approximation works very well in these single step processes it would be expected to be small. The second term, however, gives the off-shell contributions which exist only in the (p-d, d-n) mechanism. This term will collapse the (p-d, d-n) term with an equivalent (p-n) term. Thus, when the single step contribution is large, finite range effects in the two step term can be large. A more complete explanation of the effect is contained in Ref. 4.

Work is now underway to establish systematics for finite range effects in (p-d, d-n) reactions. Other two-step reactions are also being examined with a full finite range evaluation of the two step amplitude.

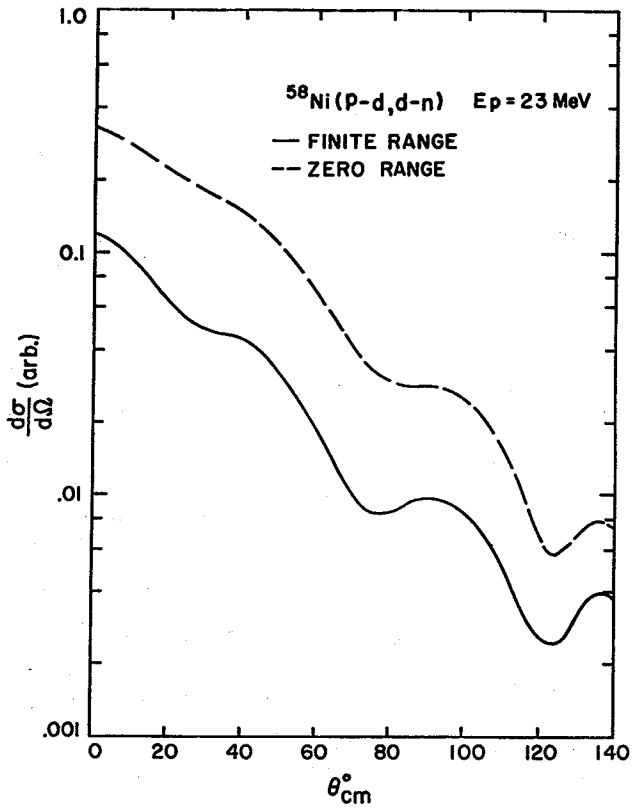

Fig. 1. The two-step differential cross sections with arbitrary overall normalization. The dashed curve shows the zero-range result and the solid curve shows the finite-range result for a model calculation for ^{58}Ni(p-d, d-n)^{58}Cu to the analogue state. The single-particle orbital involved was the $2P_{3/2}$ state. (XBL 766-8274)

Footnotes and References

*Condensed from Ref. 4.

†Dept. of Physics and Astrophsics, University of Colorado.

1. M. Toyama, Phys. Lett. 38B, 147 (1972); Nucl. Phys. A211, 254 (1973).

2. R. Schaefrer and G. F. Bertsch, Phys. Lett. 38B, 159 (1972); W. R. Coker, T. Udagawa and H. H. Wolter, Phys. Rev. Lett. 41B, 237 (1972).

3. L. D. Rickertsen and P. D. Kunz, Phys. Lett. 47B, 11 (1973).

4. P. D. Kunz and L. A. Charlton, Phys. Lett. 61B, 1 (1976).

CHEBYSHEV EXPANSIONS AND THE FINITE RANGE DISTORTED WAVE BORN APPROXIMATION FOR NUCLEAR TRANSFER REACTIONS*

George Delic

The epithet "exact" was introduced by Delic and Robson[1] to describe computation of the Distorted waves Born approximation in a formalism for nuclear reactions which allowed both non-S state stripping from the incident projectile in the transfer reaction A(a,b)B, and an interaction of finite range in the DWBA transition matrix amplitude. These computations, performed for d,p reactions, applied an approach suggested by Austern et al.[2] and did not introduce any further approximations of either a mathematical or numerical nature, other than that of truncating the area integrated in the two-dimensional radial integrals which need to be evaluated. The method requires the numerical evaluation of the Legendre series coefficients[3] g_K at each point of the two-dimensional grid of the double radial integral. The largest value of K is a few units larger than L_{max}, the value of the largest partial wave retained in the DW expansions describing the relative motions of a, A and b, B. Thus, the overall computation time of such calculations is dependent on the number of grid points used, as well as their distribution within the area to be integrated. There are basically three approaches to the problem of evaluating n-dimensional integrals numerical:[4-6] (1) application of a product rule, either of Newton-Cotes or Gauss type, (2) n-dimensional quadrature formulas based on construction of n-dimensional polynomials, (3) Monte Carlo, or number theoretical techniques. Monte Carlo techniques have been applied, with success, to nuclear reaction calculations by Bayman and Feng,[7] and a product Gauss rule appears to be the approach of Ref. 8. In the present study approach (2) is taken because the perfectly symmetric two-dimensional quadrature formulas of Rabinowitz and Richter[9] have fewer points than the product Gauss rules of equivalent degree and because such quadratures, based on polynomial interpolation,[10] will display rapid convergence with increasing degree (or decreasing area), i.e., with increasing number of grid points.

The algorithm programmed in KUNDRY consists of defining squares of side length S_c and packing the area to be integrated with these squares. Then squares of side length S_a and S_b are defined so that $S_a = 2S_b = 4S_c$, and the 48 and 28 point formulas of Ref. 9 are applied to the squares S_a^2 and S_b^2 respectively, and the 12 point formula of Tyler[10] to the square S_c^2. Product Gauss rules of equivalent degree would require 64, 36 and 16 points, respectively, thus the method used in the code KUNDRY leads to substantial gains in computational speed without loss in accuracy. A comparison with the code LOLA[8] showed KUNDRY to be typically four times faster in execution time, i.e., 62 versus 16 seconds.

The most important feature of the problem is determination of a criterion for truncation of the two-dimensional space in the radial coordinates r_{aA}, r_{bB} (the arguments of the DW radial wave functions) over which the double integral is performed. Assuming the bound state radial wave functions to be negligible when they have an asymptotic magnitude smaller than some number ϵ and defining the corresponding radii to be r^c_{xA} and r^c_{bx}, two estimates for the truncation radius in the first DW coordinate may be derived: $r^c_{aA} = r^c_{xA}/\{\alpha(1-\gamma)\}$, and $r^c_{aA} = r^c_{bx}/\{\alpha(1-\delta)\}$, where $\alpha = m_a m_B/\{m_x(m_A+m_a)\}$, $\gamma = m_b/m_a$, $\delta = m_A/m_B$, and m_i is the mass of particle i. For the range Δr_{bB} of the second variable r_{bB} about the value $r_{bB} = r_{aA}$, two estimates can also be made $\Delta r_{bB} = r^c_{xA}/(\alpha\ \gamma)$ and $\Delta r_{bB} = r^c_{bx}/\alpha$, i.e., $r_{bB} = r_{aA}$ with only positive values of r_{bB} allowed. The smaller of these two estimates is used in each case. Thus truncation errors arising from either the physical assumptions (truncation of the bound state wave functions) or the numerical assumptions (size of the area S_c^2) may be explicitly investigated by computation. Experience with the code has shown the need to take these truncation errors into serious consideration particularly for bound state wave functions which decay slowly or in reactions at high energies.

The time taken to compute the two-dimensional radial integral is measured in seconds or fractions thereof, whereas the time taken to evaluate the two-dimensional form factor $H^{L_a L_b \ell}_{\ell\ell' jj',t}(r_{aA}, r_{bB})$ which is in the integrand rapidly becomes orders of magnitude larger with increasing orbital angular momenta ℓ,ℓ' for x bound to A and b respectively. This is shown in Fig. 1 for a case with 1944 grid points[11] with $\ell' = 1$, $j' = 1/2$ and $\ell = 0$ to 13 and $L_{max} \sim 42$. Thus the dominant amount of computation time is spent in evaluating the expression

$$H^{L_aL_b\ell t}_{\ell\ell' jj'}(r_{aA},r_{bB}) = \sum_{\lambda=0}^{\ell}\sum_{\lambda'=0}^{\ell'}(-1)^{\lambda}\binom{2\ell}{2\lambda}^{1/2}\binom{2\ell'}{2\lambda'}^{1/2}(s_1r_{bB})^{\ell-\lambda}(t_1r_{aA})^{\lambda}(t_2r_{aA})^{\ell'-\lambda'}(s_2r_{bB})^{\lambda'} \tag{1}$$

$$\times \sum_{K}\hat{K}^2\, g_{K\ell\ell' jj'}(r_{aA},r_{bB})\, h^{L_aL_b\ell t}_{\lambda\lambda' K}$$

where

$$g_{K\ell\ell' jj'}(r_{aA},r_{bB}) = \int_{-1}^{+1}\frac{U_{n\ell j}(r_{xA})V_{bx}(r_{bx})\,U_{n'\ell' j'}(r_{bx})}{r^{\ell}_{xA}\,r^{\ell'}_{bx}}\,P_K(x)\,dx \tag{2}$$

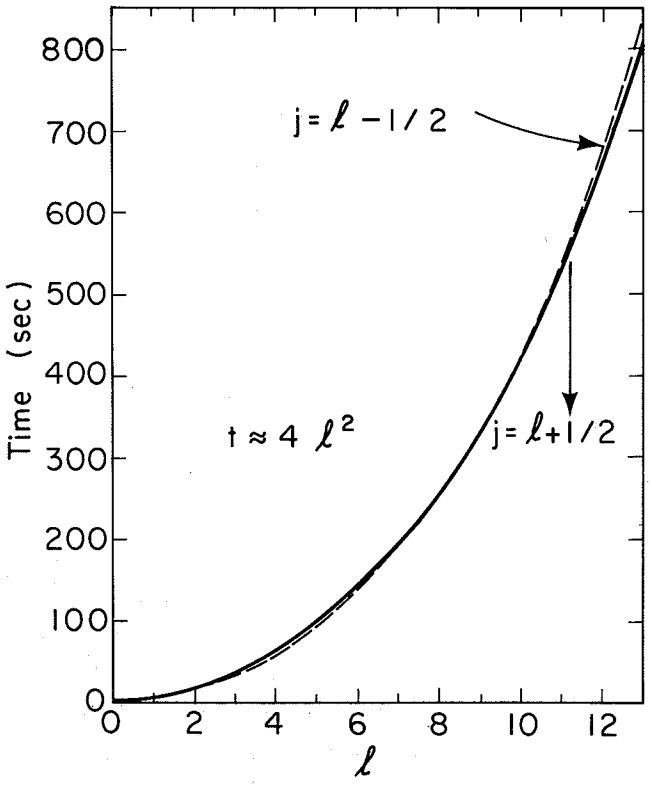

Fig. 1. Computation time (sec) for the form factor of Eq. (1) as a function of ℓ (see text). The shape of this curve is probably specific to the CDC 7600 and the remarkable properties of the CDC FTN4 compiler with OPT-2. For other machines and compilers the curve could be steeper. (XBL 766-8277)

and $h^{L_aL_b\ell t}_{\lambda\lambda' K}$ is a combination of angular momentum coupling coefficients.

The method proposed here is to expand the bound state wave functions in series of shifted Chebyshev polynomials

$$U_{n\ell j}(r_{xA}) = r^{\ell}_{xA}\sum_{m}^{M} a_m\, T^*_m(z) \tag{3}$$

$$V_{bx}(r_{bx})\,U_{n'\ell' j'}(r_{bx}) = r^{\ell'}_{bx}\sum_{m'}^{M'} a'_{m'}T^*_{m'}(y) \tag{4}$$

where $z = \left(\frac{r_{xA}}{r^c_{xA}}\right)^2$ and $y = \left(\frac{r_{bx}}{r^c_{bx}}\right)^2$.

Because z (or y) and x are linearly related at each grid point (r_{aA},r_{bB}) it is possible to make the equivalence

$$\sum_{j'=0}^{M} b_{j'}\,T_{j'}(x) = \sum_{m}^{M} a_m\,T^*_m(z) \tag{5}$$

$$\sum_{i'=0}^{M'} b'_{i'}\,T_{i'}(x) = \sum_{m'}^{M'} a'_{m'}\,T^*_{m'}(y) \tag{6}$$

and it is straightforward to derive explicit expressions for the coeffiecients $b_{j'}$ and $b'_{i'}$ without the need to evaluate intergrals. It follows that Eq. (2) reduces to

$$g_{K\ell\ell' jj'}(r_{aA},r_{bB}) = \sum_{j'=0}^{M}\sum_{i'=0}^{M'} b_{j'}\,b'_{i'}\,j^{K}_{j'i'} \tag{7}$$

where

$$J^K_{j'i'} = \int_{-1}^{+1} T_{j'}(x)\,T_{i'}(x)\,P_K(x)dx \tag{8}$$

is readily evaluated.

As in the Gaussian expansion method of Payne and Carlson,[12] the summations of Eq. (7) need to be evaluated at each grid point (r_{aA},r_{bB}). However, because $J^K_{j'i'}$, or Eq. (8) is the integral of a polynomial in x, an important consequence of the Chebyshev expansion technique is that the summation over K in Eq. (1) no longer needs to be performed separately for each grid point. In particular, for the

summation over K in Eq. (1) it is now possible to write

$$\sum_K \hat{K}^2 g_{K\ell\ell' jj'}(r_{aA}, r_{bB}) h^{L_a L_b \ell_t}_{\lambda\lambda' K} = \sum_{j'=0}^{M} \sum_{i'=0}^{M'} b_{j'} b'_{i'} S^{\lambda\lambda'}_{j'i'} \tag{9}$$

where

$$S^{\lambda\lambda'}_{j'i'} = \sum_K \hat{K}^2 h^{L_a L_b \ell_t}_{\lambda'\lambda K} J^K_{j'i'}. \tag{10}$$

This reduces the computational effort in calculating Eq. (1) as well as machine memory requirements, since the Legendre series coefficients need not be stored in the computer.

Footnote and References

*Work in progress.

1. G. Delic and B. A. Robson, Nucl. Phys. A156, 97 (1970).

2. N. Austern, R. M. Drisko, E. C. Halbert, and G. R. Satcher, Phys. Rev. 133, B3 (1964).

3. G. Delic, J. Comp. Phys. 14, 254 (1974).

4. A. H. Stroud, Approximate Calculation of Multiple Integrals, Prentice-Hall, Englewood Cliffs, 1971.

5. I. M. Sobol', Mnogomerniye Kvadraturniye Formuly i Funktsii Khaara (Multi-dimensional Quadrature Formulas and Haar Functions), Izdat. "Nauka," Moscow, 1969.

6. I. S. Haber, SIAM Rev. 12, 481 (1970).

7. B. F. Bayman and D. H. Feng, Nucl. Phys. A205, 513 (1973).

8. J. L. Perrenoud and R. M. De Vries, Phys. Lett. 36B, 18 (1971).

9. P. Rabinowitz and N. Richter, Math. Comput. 23, 765 (1969).

10. R. Franke, Math. Comput. 25, 803 (1971).

11. K. Pruess, G. Delic, L. A. Charlton, and N. K. Glendenning, LBL-5008 and LBL-5074.

12. G. L. Payne and R. R. Carlson, Phys. Rev. C 12, 1260 (1976).

OPTICAL MODEL ANALYSIS OF N + C AND C + C ELASTIC SCATTERING*

George Delic

The data[1-5] analyzed in the present work were as follows: (all energies are quoted in center-of-mass unless otherwise indicated) elastic scattering of ^{14}N by ^{12}C at 9.230, 9.922, 10.84, 11.54, and 12.60 MeV; ^{14}N by ^{13}C at 9.649 MeV; ^{14}N by ^{14}C at 10.00 and 12.50 MeV; ^{12}C by ^{13}C at 7.801 and 9.881 MeV; ^{13}C by ^{14}C at 7.778 and 9.852 MeV; and ^{12}C by ^{14}C at 8.078, 9.694 and 10.77 MeV. In Table 1 the data are arranged in increasing order of η (the Sommerfeld parameter), and asymptotic wave number k; $R=A_a^{1/3} + A_A^{1/3}$, Δ, σ_A (total absorption or reaction cross section) are also tabulated. Table 1 shows a selection of some of the optical model parameter sets which were found; those cases where the data did not cover a sufficiently broad range in angle were not searched upon. The definition of the optical model potential was the same as that of Ref. 6 with a surface type absorbing potential. For the searches all six optical model parameters were varied simultaneously. In the 500-odd searches performed in the present work the absolute normalization was not varied and a relative error of 5% was set on each data point. The comparison between experimental and theoretical ratio-to-Rutherford cross sections is shown in Fig. 1a and b for the parameters of Table 1. The potential found for the scattering of ^{12}C by ^{14}C at 9.694 MeV (18 MeV lab), which also gives a satisfactory description of the same system at 10.77 MeV (20 MeV lab) was used to show how the structure observed in the angular distributions evolved as a function of energy (cf. Fig. 1c). The optical model predicts that such structures change relatively rapidly for the extreme backward angles (> 120°) for energies above the Coulomb barrier. Another feature is that the optical model predictions (especially in the backward hemisphere) are sensitive to the choice of the Coulomb radius r_c. The Coulomb radius used throughout the searches was 1.45 fm, and the effects of changing this radius to 1.225 fm and 1.0 fm are shown in Fig. 1b by the solid and dotted curves, respectively, for $^{14}N + ^{12}C$ at 12.60 MeV, with the case corresponding to r_c = 1.45 fm shown in Fig. 1a.

Figure 1a and b together show 15 experimental angular distributions; a careful comparison of these data reveals why it is important to classify heavy-ion elastic-scattering data (and optical model potentials derived therefrom) according to the Sommerfeld parameter η, the asymptotic wave number k, and possibly some interaction radius, e.g., $R = A_a^{1/3} + A_A^{1/3}$, defined by the system under consideration. In the following discussion the notation: label_I vs label_{II}; $\delta\eta$, δk, δR, is used where the labels are those of Table 1, and $\delta\eta$ is η_I-η_{II} expressed as a percentage of η_I, etc. A variation of η alone produces a shift of the structures in the experimental angular distributions toward small angles (for a decrease in η) or toward large angles (for an increase in η)—compare C232 vs C243: -2.7, -0.8, -1.3, or C2N1 vs C3N1; -3.6, -0.7, -1.3. or C242 vs C341: -4.1, -0.3, 1.3, or C3N1 vs C342: 15.2,

Table 1. Optical model parameters for a(A,A)a.

A	a	label	Energy[a] (MeV)	r_v (fm)	a_v (fm)	V (MeV)	r_w (fm)	a_w (fm)	W (MeV)	σ_A (mb)	Δ^-	η	k (fm^{-1})	R[b]
^{12}C	^{14}C	C244	10.77 (20.00)	no search (parameter set C243 used)								4.391	1.825	4.700
^{12}C	^{13}C	C232	9.881(19.00)	1.019	0.7010	67.79	1.077	0.1002	50.82	773.0	28.38	4.505	1.717	4.641
^{12}C	^{14}C	C243	9.694(18.00)	0.9777	0.5256	88.26	1.027	0.1230	39.41	523.1	5.624	4.628	1.731	4.700
^{13}C	^{14}C	C342	9.852(19.00)	no search (parameter set C3N1 used)								4.690	1.782	4.761
^{14}N	^{12}C	C2N4	12.60 (27.30)	0.9703	0.6636	85.47	0.9661	0.09149	92.87	653.7	12.50	4.737	1.973	4.700
^{14}N	^{12}C	C2N3	11.54 (25.00)	1.034	0.5909	79.10	0.9940	0.07685	97.59	527.8	14.96	4.950	1.888	4.700
^{14}N	^{14}C	C4N2	12.50 (25.00)	1.053	0.5473	84.23	1.016	0.1027	67.82	675.6	21.35	4.950	2.046	4.820
^{12}C	^{13}C	C231	7.801(15.00)	1.065	0.6220	69.91	1.109	0.1221	28.94	442.7	13.97	5.070	1.526	4.641
^{12}C	^{14}C	C242	8.078(15.00)	1.001	0.6771	80.23	1.063	0.1393	40.50	547.0	3.196	5.070	1.580	4.700
^{14}N	^{12}C	C2N2	10.84 (23.50)	no search (parameter set C2N3 used)								5.105	1.831	4.700
^{13}C	^{14}C	C341	7.778(15.00)	0.9752	0.7456	80.10	0.8646	0.1255	33.08	523.9	30.73	5.278	1.584	4.761
^{14}N	^{12}C	C2N1	9.922(21.50)	0.9847	0.6206	83.55	0.9487	0.2038	33.29	449.6	15.87	5.337	1.751	4.700
^{14}N	^{13}C	C3N1	9.649(20.04)	0.9751	0.6866	87.17	1.012	0.1389	43.15	510.1	13.73	5.528	1.764	4.761
^{14}N	^{12}C	C2N0	9.230(20.00)	0.9865	0.6251	82.18	0.9477	0.2101	28.88	367.0	5.032	5.534	1.689	4.700
^{14}N	^{14}C	C4N1	10.00 (20.00)	no search (parameter set C4N2 used)								5.534	1.830	4.820

[a]Center-of-mass with lab energy in parentheses.
[b]$R = A_a^{1/3} + A_A^{1/3}$.

-1.0,0 or C243 vs C2N1: -15.3, -1.2,0, or C2N0 vs C232: 18.6, -1.7, 1.3. A variation of k alone produces a shift toward small angles (for an increase in k) or toward large angles (for a decrease in k)—compare C243 vs C342: -1.3, -2.9, -1.3, or C231 vs C242: 0, -3.5, -1.3, or C3N1 vs C2NO: -0.1, 4.3, 1.3, or C341 vs C2N1: -1.1, -10.5, 1.3, or C342 vs C2N4: -1.0, -10.7, 1.3, or C242 vs C2N2: -0.7, -15.9, 0. A variation in η alone produces either a compression or decompression of the structures in the experimental angular distribution, while a variation of k alone produces a difference in phase of the observed angular distributions, which changes as θ approaches 180°. The periodicity of this phase difference increases with increasing variation of k (cf. $\delta k \sim 10$) until (for $\delta k \sim 16$) the angular distributions are in phase throughout the measured angular range. An example where the variation of η and k act on the experimental angular distributions in an opposite sense to produce apparently little change in the positions of maxima and minima over the energy range 9.230 to 12.60 MeV is the data for ^{14}N scattered by ^{12}C where $\delta\eta = 14.4$ and $\delta k = 16.8$. That the optical model is successful in reproducing such effects, qualitatively, is demonstrated by the four cases of Table 1 for which no searches were performed and another parameter set was used, as well as the dotted curve for $^{14}N + ^{13}C$ at 9.649 MeV in which the optical model parameters were the same as those used for $^{14}N + ^{12}C$ at 9.922 MeV (cf. Fig. 1a).

The optical model has proved to be successful in its ability to reproduce the qualitative features of the fifteen experimental angular distributions shown in Fig. 1a and b. Therefore, such experimental angular distributions do not find a unique interpretation in terms of a model which requires the explicit inclusion of the elastic transfer channel. The potentials of Table 1 should not be interpreted too literally, however, as the experimental angular distributions analyzed are not of uniform quality; e.g., excepting $^{14}N + ^{12}C$ at 11.54 and 12.60 MeV, the points measured at forward angles are too sparse, or $^{14}N + ^{12}C$ at 10.84 MeV where there seem to be problems of absolute normalization of the data. A more thorough analysis should await more detailed measure-

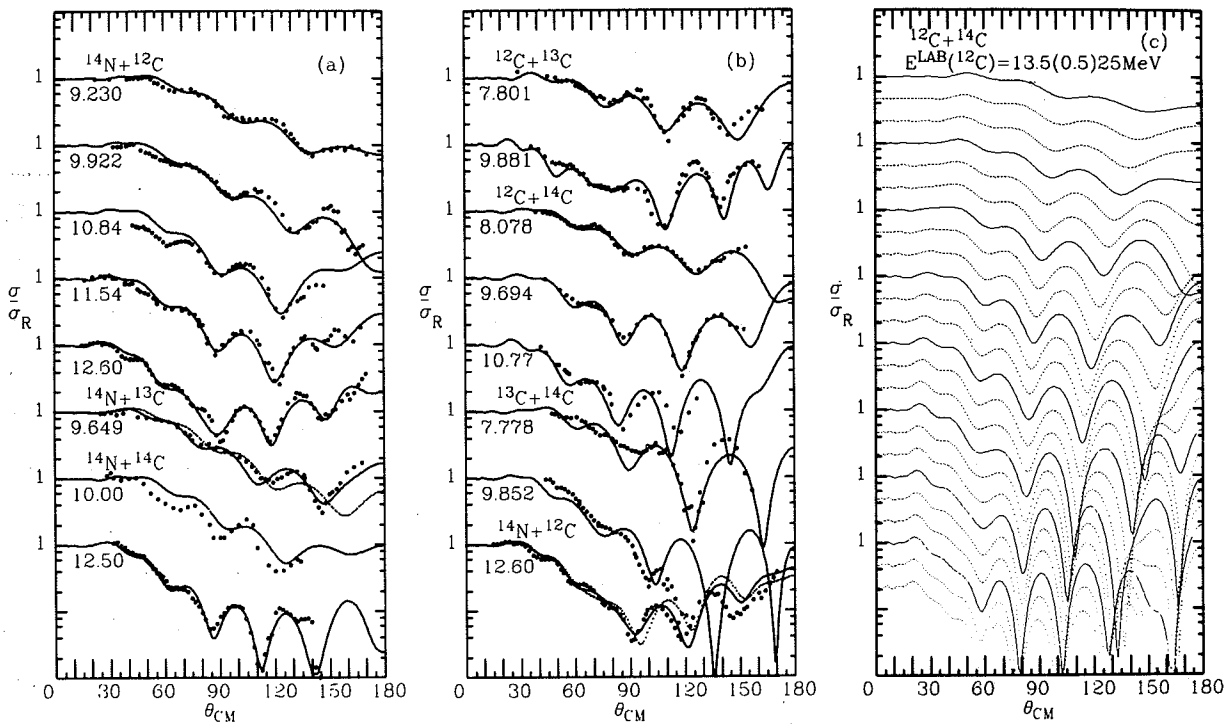

Fig. 1. Optical model predictions using the parameters of Table 1 for (a) N + C, (b) C + C and $^{14}N + ^{12}C$ at 12.60 MeV with r_C = 1.225 fm (solid curve) and 1.0 fm (dotted curve) and (c) $^{12}C + ^{14}C$ in the lab energy range 13.5 to 25 MeV in steps of 0.5 MeV, using C243 parameters, with some curves dotted for clarity. In (a) and (b) the c.m. energy (in MeV) is shown for each case-the data are from Refs. 1-4 (error bars are not shown) (XBL 754-870)

ments. An important qualitative result would seem clear, however: the heavy ion optical model potential for such systems has an imaginary part which produces sufficient reflected flux to allow for the possibility of interference with flux refracted by the real potential; this phenomenon provides a plausible interpretation for the structures observed in the experimental angular distributions in heavy ion elastic scattering for systems such as those discussed here.

Footnote and References

*Condensed from LBL-3492, published in Phys. Rev. Lett. 34, 1468 (1975).

1. W. von Oertzen, Proceedings of the symposium on Heavy-Ion Scattering, Argonne National Laboratory, March 1971, ANL-7837.

2. W. von Oertzen, G. Bohlen, B. Gebauer, E. E. Habib, and N. Marquardt, Phys. Lett. 34B, 51 (1971).

3. H. G. Bohlen and W. von Oertzen, Phys. Lett. 37B, 451 (1971).

4. H. G. Bohlen, M. Feil, A. Gamp, B. Kohlmeyer, N. Marquardt, and W. von Oertzen, Phys. Lett. 41B, 425 (1972).

5. W. von Oertzen and W. Nörenberg, Nucl. Phys. A207, 113 (1973).

6. G. Delic, Phys. Lett. 49B, 412 (1974).

COMPUTING THE FINITE RANGE DISTORTED WAVES BORN APPROXIMATION FOR $^{11}B(^{16}O, ^{15}N)^{12}C$*

George Delic

The FR DWBA code KUNDRY was applied to the study of the reaction $^{11}B(^{16}O,^{15}N)^{12}C$. This reaction is of particular interest in that it can be interpreted in terms of two reaction mechanisms: proton transfer at forward angles and direct alpha cluster transfer at backward angles. The final cross section for the reaction would thus be expected to include the effects of the coherent interference of the two reaction mechanisms. Previous studies[1,2] have analyzed some of the available data[3,4]

Table 1. Proton and alpha stripping for ^{16}O on ^{11}B.

E_{aA}[a] (MeV)	^{15}N[b] (MeV)	^{12}C[b] (MeV)	η_{aA}	k_{aA} (fm^{-1})	a+A OM[c]	η_{bB}	k_{bB_1} (fm^{-1})	b+B OM[c]	r_{xA}^c[d] (fm)	r_{bx}^c (fm)	r_{aA}^c (fm)	Δr_{bB} (fm)	ℓ_t[d]
32.5	6.324	g.s.	4.419	2.033	BO321	5.207	1.852	C3N1	10.4/10.1	10.0/9.5	17.2/16.1	1.42/4.28	0,1,2/0 or 2[c]
30.0			4.599	1.953	BO322	5.473	1.762	C2N4					
27.0			4.848	1.853	BO272	5.853	1.648	C3N1					
27.0	g.s.	4.44			BO271	5.296	1.821	C3N1	11.4/8.4	11.2/8.2	19.1/13.9	1.59/3.69	0,1/0,1,2,3,4
30.0	g.s.	g.s.	4.599	1.953	BO271	4.261	2.263	C2N4	10.4/8.4	11.2/9.5	19.2/15.2	1.57/4.28	1,2/2

[a] Lab energy.
[b] Excitation.
[c] See text.
[d] For proton and alpha, respectively.

in the FR DWBA but did not investigate the effects of coherent interference of the two reaction mechanisms. In a transfer reaction A(a,b)B the DWBA transition matrix amplitude at θ degrees (cm) is $T^1_{ab}(M_A,M_a,M_b,M_B,\theta)$, where M_i is the magnetic quantum number associated with the spin projection of particle i. In the FR DWBA this amplitude contains a summation over the allowed values of the transferred orbital angular momentum ℓ_t. For the transfer reaction A(a,B)b at π-θ degrees (cm), the DWBA amplitude is $T^1_{aB}(M_A,M_a,M_B,M_b,\pi-\theta)$; both FR DWBA amplitudes contain a product of two spectroscopic amplitudes,[5] specific to the transferred particle or cluster x in the initial and final bound state configuration. Furthermore, where more than one type of configuration or cluster is allowed, either (or both) of the DWBA transition matrix amplitudes is a sum over such clusters $T_{ab} = \sum T^i_{ab}$ and/or $T_{aB} = \sum T^k_{aB}$; an example of the latter is the alpha cluster bound to ^{11}B to form ^{15}N in the 6.3 MeV state, where both 3s and 2d clusters are allowed.[6] The cross section for the coherent interference of the two reaction mechanisms is the cross section formed from the amplitude $T(M_A,M_a,M_b,M_B,\theta) = T_{ab}(\theta) + T_{aB}(\pi-\theta)$.[7]

The transitions studied here were for the reactions induced by ^{16}O on ^{11}B for (i) the 6.324 MeV state to ground state, (ii) g.s. to 4.44 MeV state, and (iii) g.s. to g.s., respectively, in ^{15}N and ^{12}C. The first transition was studied at $E^{lab}(^{16}O)$ = 32.5, 30, and 27 MeV, the second at 27 MeV, and the third at 30 MeV bombarding energy. The proton bound state configurations were the same as those of Ref. 3, and the bound state alpha particle was assumed to have the p-shell cluster configurations of Kurath.[6] The bound state parameters for the proton were: radius $r_0 = 1.25$ fm, diffuseness of 0.65 fm, spin orbit strength 12 MeV · fm^2; for the alpha cluster the radius (r_0) and diffuseness parameters were the same as those for the proton. The radius of the Woods-Saxon potential, binding the transferred particle x, was taken as $r_0 A_i^{1/3}$, where A_i is the mass number of particle i to which x is bound. The depth of the binding potential was adjusted to give the correct separation energy for particle x. The truncation radii (cf. Table 1) corresponded to the bound state wave functions having a magnitude ~ 10^{-4}. The elastic scattering of ^{16}O on ^{11}B has been discussed in Ref. 8 and that of N on C in Ref. 9. The 32.5 and 27 MeV parameter sets of Ref. 8 are labeled here as BO321 and BO271. Two additional parameter sets yielding somewhat improved fits, especially for the 32.5 MeV data, were found with the optical model search code SOPHIE[9] 32.5 MeV (BO322), $r_V = 1.078$ fm, $a_V = 0.5660$ fm, V = 70.42 MeV, $r_W = 0.9810$ fm, $a_W = 0.1509$ fm, W = 77.86 MeV; 27 MeV (BO272), $r_V = 1.048$ fm, $a_V = 0.6264$ fm, V = 75.34 MeV, $r_W = 1.003$ fm, $a_W = 0.1269$ fm, W = 71.49 MeV, where the definition of the potential is the same as that of Ref. 8. In the optical model the elastic scattering A(a,a)A of any two systems for the same values of η (Sommerfeld parameter), k (asymptotic wave number) and $R(= A_a^{1/3} + A_A^{1/3})$ are the same. It therefore suffices to select potentials from Table 1 of Ref. 9 for the b-B channel in the reactions considered here. Since the effect of changes in η and k act on the elastic scattering angular distributions in an opposite sense,[9] where either parameter (η or k) in Table 1 of Ref. 9 is smaller (larger) than that required here, the other is chosen to be larger (smaller) by a similar percentage. The choice of OM parameters for the respective channels together with the values of η and k are given in Table 1, the corresponding fits to the transfer reaction data as calculated by KUNDRY are shown in Fig. 1. The unbroken curve corresponds to the coherent sum of the two reaction mechanisms; the dashed curves are proton transfer (at forward angles) and alpha cluster transfer (at backward angles). The bottom set of curves for the transition from the 6.3 MeV state in ^{15}N to the g.s. in ^{12}C at 27 MeV are calculated with the OM parameters of Ref. 3 for both channels: these parameters fitted the elastic $^{16}O+^{11}B$ data only at forward angles. All the calculated alpha cluster transfer cross sections contain the corresponding spectroscopic amplitudes of Ref. 6 together with the center-of-mass correction factors of Eq. (9) of Ref. 6: no other normalization factors are introduced. The proton transfer cross section is normalized to the data at forward angles; the factors by which the respective theoretical cross sections of Fig. 1 have been multiplied are (in order from the top): 1.367, 0.5252,

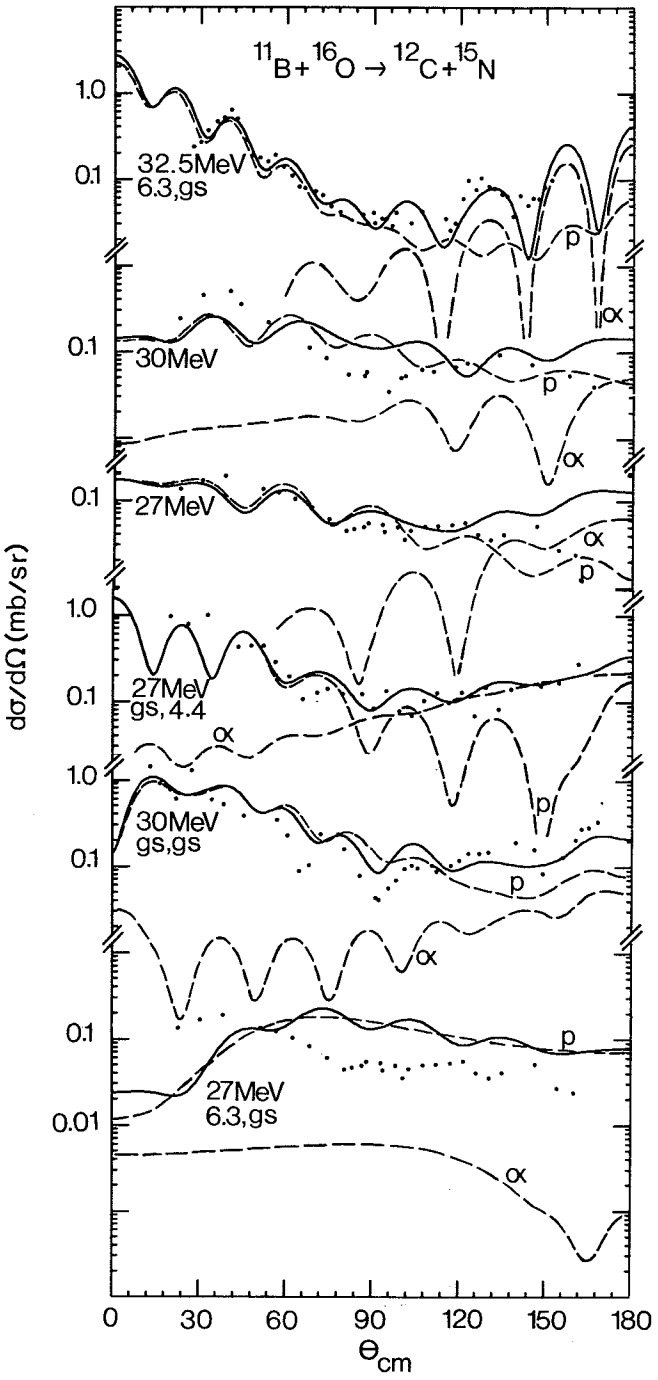

Fig. 1. Exact finite range DWBA calculations with KUNDRY for stripping of protons (at forward angles), and alpha clusters (at backward angles) are shown by the dashed curves denoted by p and α, respectively. The final cross section, formed from the coherent sum of the two reaction mechanisms, is shown by the unbroken curve. Laboratory energies of ^{16}O and excitation energies of ^{15}N and ^{12}C, respectively, are as shown. The bottom set of curves are for the parameters of Table 2 of Ref. 3. The data are those of Ref. 4; error bars are not shown.

(XBL 7511-9395)

0.3198, 0.2919, 1.147, 2.230. Given the spectroscopic amplitudes (Ref. 10) for $^{11}B+p = ^{12}C$(g.s.)and ^{12}C(4.4 MeV) respectively as -2.387 and -1.048, the present analysis yields for ^{15}N(g.s.)+p: -0.4821±7% and ^{15}N(6.3 MeV)+p: -0.3634±35%. These estimates ignore discrepancies between Ref. 3 and Ref. 4 in normalization of the data for the transitions to the excited states. It is seen from Fig. 1 that the OM parametrization of Ref. 3 provides an inadequate description of these reactions. Calculations for the other two transitions with these parameters (not shown) have forward peaked proton transfer cross sections but underestimate the cross section for alpha cluster transfer by two orders of magnitude: no such discrepancy occurs if OM parameters of the type discussed in Refs. 8 and 9 are used for the analysis of these transfer reactions.

Thus the present study shows that finite range DWBA calculations successfully predict the qualitative features of the cross sections for the reaction $^{11}B(^{16}O,^{15}N)^{12}C$, and that this success is due to the inclusion of coherent interferences between two reaction mechanisms, i.e., proton transfer at forward angles and alpha cluster at backward angles.

Footnote and References

*Condensed from LBL-4343, published in Phys. Rev. Lett. 36, 569 (1976).

1. T. Kammuri and H. Yoshida, Nucl. Phys. A129, 625 (1969).

2. R. Bock and H. Yoshida, Nucl. Phys. A189, 177 (1972).

3. U. C. Schlotthauer-Voos, H. G. Bohlen, W. von Oertzen, and R. Bock, Nucl. Phys. A180, 385 (1972).

4. U. C. Schlotthauer-Voos, R. Bock, H. G. Bohlen, H. H. Gutbrod, and W. von Oertzen, Nucl. Phys. A186, 225 (1972).

5. D. Kurath and I. S. Towner, Nucl. Phys. A222, 1 (1974).

6. D. Kurath, Phys. Rev. C 7,1390 (1973).

7. G. Delic, to be submitted for publication.

8. G. Delic, Phys. Lett. 49B, 412 (1974).

9. G. Delic, Phys. Rev. Lett. 34, 1468 (1975).

10. S. Cohen and D. Kurath, Nucl. Phys. A101, 1 (1967).

FINITE RANGE DISTORTED WAVES BORN APPROXIMATION CALCULATIONS FOR $^{13}C(^3He, ^6He)^{10}C$*

George Delic and Dieter Kurath†

Experiments reported by Kashy et al.,[1] measured angular distributions for the reaction $^{13}C(^3He, ^6He)^{10}C$ leading to the $J^\pi = 0^+$, ground state and the $J^\pi = 2^+$, 3.35 MeV state in ^{10}C for a 70.3 MeV ^3He beam. The experiments showed that both transitions, despite their low cross sections, were well resolved and displayed rather marked oscillatory structure indicative of a direct transfer reaction. The structures in the experimental differential cross sections for the two transitions were in phase at larger angles (25-43° cm) and were out of phase at smaller angles (7-25° cm). Furthermore, at the forward angles the observed strength to the 2^+ state in ^{10}C was as much as 40 times greater than that to the 0^+ state. In an attempt to describe these features of the data Kashy et al.[1] performed distorted waves Born approximation calculations and in their analysis, to simplify the computations, these authors assumed that the interaction occurring in the expression for the DWBA transition matrix amplitude was of zero range. The results of the analysis showed a strong disagreement with experiment, particularly for the relative strengths of the transitions to the 0^+ and 2^+ states, respectively, in ^{10}C.

Kashy et al.[1] concluded that nuclear structure considerations would not correct the discrepancy with experiment predicted by the zero-range DWBA analysis, and that the $^{13}C(^3He, ^6He)^{10}C$ reaction mechanism is probably not direct transfer. In the present study a full finite range DWBA analysis, which included recoil effects exactly, was performed and the results indicated that the reaction $^{13}C(^3He, ^6He)^{10}C$ can be interpreted as a direct cluster transfer to both final states in ^{10}C.

In the pick-up reaction B(b,a)A the 3 transferred neutrons are assumed to be bound as a cluster to the nucleus b with orbital angular momentum $\bar{L}$ and total angular momentum $\bar{J}$, and to the nucleus A with orbital angular momentum L and total angular momentum J. For the reaction $^{13}C(^3He, ^6He)^{10}C$ $\bar{J} = 1/2$ and I, the spin of the final nucleus ^{10}C, is 0 or 2. If j denotes the total angular momentum of the cluster, and Q and $\bar{Q}$ the number of oscillator quanta carried in the relative wave functions for the cluster bound to ^{10}C and ^3He, respectively, then the cross section for the pick-up reaction $^{13}C(^3He, ^6He)^{10}C$, in the absence of spin-orbit interactions in the optical model potentials, is given by

$$\frac{d\sigma}{d\Omega} = \frac{\mu_a \mu_b}{(2\pi\hbar)^2} \cdot \frac{k_a}{k_b} \cdot \frac{1}{4} \cdot \sum_{J\lambda\mu} \left| \sum_{QL\bar{Q}\bar{L}} B_{IJ\lambda}\, \beta_\mu^\lambda(\underline{k}_a, \underline{k}_b) \right|^2 \quad (1)$$

where the dependence of the cross section on the kinematics of the reaction is contained in the factor

$$K\, \beta_\mu^\lambda(\underline{k}_a, \underline{k}_b) = \sum_{M\bar{M}} (-1)^{\bar{L}-\bar{M}} < L\bar{L}\text{-}M\bar{M} | \lambda\text{-}\mu > \times \iint d\underline{r}_{aA} d\underline{r}_{bB} \chi_{bB}^{*(-)}(\underline{k}_b, \underline{r}_{bB}) \Phi_M^{QL*}(\underline{r}_{xA}) V_{bx} \Phi_{\bar{M}}^{\bar{Q}\bar{L}}(\underline{r}_{bx}) \chi_{aA}^{(+)}(\underline{k}_a, \underline{r}_{aA}) \quad (2)$$

and the dependence on the nuclear structure in the factor

$$B_{IJ\lambda} = K \sum_{jc} A_J^*\,(IjcQL) A_{1/2}\,(jc\bar{Q}\bar{L}) W(j\ \tfrac{1}{2}\ L\lambda;\bar{L}J) \quad (3)$$

The cross sections for the reaction can thus be expressed in terms of the $\beta_\mu^\lambda(QL,\bar{Q}\bar{L})$, the form factor integrals of Eq. (2), by inserting the numerical values of the $B_{IJ\lambda}$. For the I = 0 ground state of ^{10}C only J = 1/2 with $\lambda = L_p = 1$ contributes, whence

$$\sum_\mu \left| \sum_{QL\bar{Q}\bar{L}} B_{0\ \frac{1}{2}\ 1}\, \beta_\mu^1(QL,\bar{Q}\bar{L}) \right|^2 = 0.705 \sum_\mu \left| 0.264\beta_\mu^1(2D,1P) - 0.236\,\beta_\mu^1(2S,1P) + 0.358\beta_\mu^1(1P,0S) \right|^2. \quad (4)$$

For the 3.35 MeV, I = 2 state, there is a contribution with J = 3/2 and $\lambda = L_p = 1$ and also contributions for $\lambda = L_p = 2$ with J = 3/2 and J = 5/2. Thus the summation of Eq. (1) for this case becomes

$$\sum_{J\lambda\mu}\left|\sum_{QL\bar{Q}\bar{L}} B_{2J\lambda}\beta_\mu^\lambda(QL,\bar{Q}\bar{L})\right|^2 = (0.656+1.178)\sum_\mu\left|0.354\ \beta_\mu^2(2D,1P)\right|^2$$

$$0.295\sum_\mu\left|0.264\beta_\mu^1(2D,1P) - 0.236\,\beta_\mu^1(2S,1P) + 0.358\beta_\mu^1(1P,0S)\right|^2. \quad (5)$$

In a zero-range DWBA analysis only the $\beta_\mu^1(1P,0S)$ integral is nonvanishing[1] in Eqs. (4) and (5).

The optical model (OM) parameters determined for the ground state transition are given in Table 1, and the corresponding cross section is shown in Fig. 1. Also shown in Fig. 1 is the cross section calculated for the 2^+ transition with the same OM parameters. All finite range DWBA calculations reported in this study were performed with the code KUNDRY.[2]

In the parameter searches for the ^{6}He+^{10}C channel good fits to both transitions with the same OM parameters were not found. However, it is possible to fit the shape and magnitude of the 2^+ cross section with the OM parameters given in the last line of Table 1, as shown in Fig. 2. Also shown in Fig. 2 are the separate contributions for the two values of the transferred orbital angular momentum, λ. As can be seen from Fig. 2 the $\lambda = 2$ contribution, corresponding to the $\beta_\mu^2(2D,1P)$ term of Eq. (5), dominates the cross section. This feature of the finite range DWBA calculations is true for all our OM parameter variations. As is manifest in Eqs. (4) and (5) the shape of the ground state cross section is the same as that of the $\lambda = 1$ contribution to the 2^+ cross section. Furthermore, the magnitude of the latter should equal 0.418 times the ground state cross section (this ratio is calculated to be ~ 0.55 rather than 0.418 due to the difference in Q-values). These relationships can be used to find the weak $\lambda = 1$ contribution to the 2^+ cross section of Fig. 1 or to find the 0^+ cross section from Fig. 2.

Thus, while the difference in OM parameters between the last two lines of Table 1 is greater than would normally be expected on the basis of differences in energy of the outgoing ^{6}He in the two transitions, the analysis indicates that one could select a set of OM parameters in the range spanned by these limiting values. Such a choice would then give crude fits to cross section shapes for both transitions and still display the dominance of the 2^+ transition magnitude which is found at both limits of the OM parametrization.

Table 1. Optical model parameters for ^{13}C(^{3}He,^{6}He)^{10}C. The potential has the form $C - Vg(v) - iW_v g(wv)$, where $g(x) = \{1 + \exp[(r - r_x A^{1/3})/a_x]\}^{-1}$, C is the Coulomb potential for a uniformly charged sphere of radius $r_c A^{1/3}$ and A = 13 and 10, respectively, for the initial and final channels.

Nuclei	E^{cm} (MeV)	r_v (fm)	a_v (fm)	V (MeV)	r_{wv} (fm)	a_{wv} (fm)	W_v (MeV)	r_c (fm)
^{3}He+^{13}C	57.07	1.240	0.6650	125.0	1.240	0.6400	20.00	1.260
^{6}He+^{10}C(0^+)	41.82	1.650	0.9500	175.0	1.400	0.6400	35.00	1.260
(2^+)	38.47	1.460	0.7300	195.0	1.460	0.6400	50.00	1.260

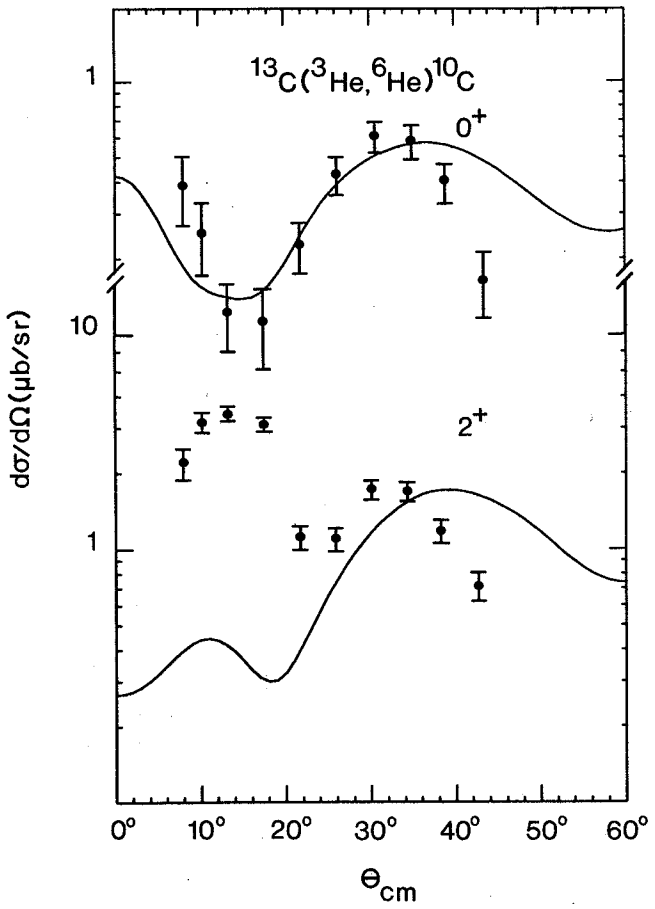

Fig. 1. Exact finite range DWBA calculations for the reaction $^{13}C(^3He,^6He)^{10}C$ for a 70.3 MeV ^3He beam. The upper curve is the transition to the 0^+ ground state in ^{10}C, and the lower curve the transition to the 2^+, 3.35 MeV state in ^{10}C for the same set of optical parameters in the ^6He + ^{10}C channel (the parameters are those given in the second line of Table 1). The data are those of Ref. 1. (XBL 761-339)

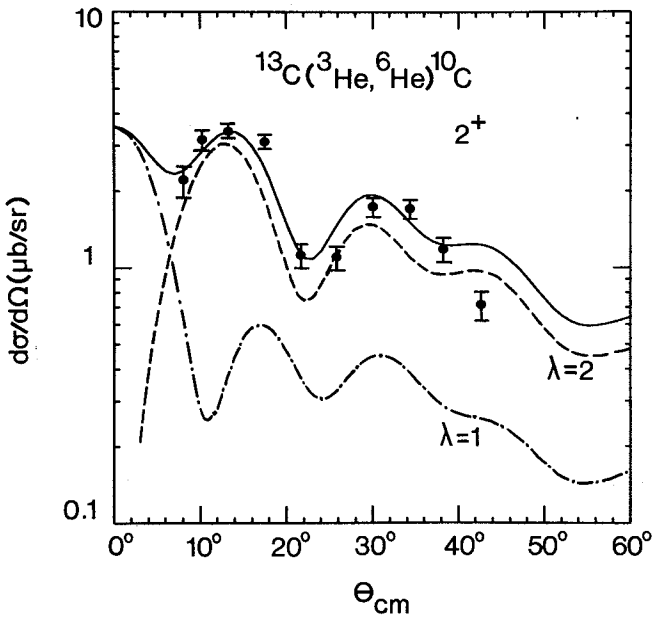

Fig. 2. Exact finite range DWBA calculations for the reaction $^{13}C(^3He,^6He)^{10}C$ leading to the 2^+, 3.35 MeV state in ^{10}C for a 70.3 MeV ^3He beam. The optical model parameters for the ^6He + ^{10}C channel are given in the third line of Table 1. The broken curve is the $\lambda = 2$ component of the cross section and the dashed and dotted curve is the $\lambda = 1$ component. The final cross section is the unbroken curve. The data are those of Ref. 1. (XBL 761-338)

Footnotes and References

*Condensed from LBL-4364, published in Phys. Rev. C14, 619 (1976).

†Physics Division, Argonne National Laboratory, Argonne, Ill.

1. E. Kashy, W. Benenson, I. D. Proctor, P. Hauge, and G. Bertsch, Phys. Rev. C7, 2251 (1973).

2. G. Delic, Phys. Rev. Lett. 36, 569 (1976).

2. Macroscopic

A THEORETICAL APPROACH TO THE PROBLEM OF PARTIAL EQUILIBRATION IN HEAVY ION REACTIONS*

L. G. Moretto† and J. S. Sventek

Many heavy ion reactions recently studied in our group[1-5] seem to indicate various stages of relaxation in the collective degrees of freedom excited in the process. In particular, a large fraction of the total cross section is associated with the production of fragments which, i) have fully relaxed kinetic energy spectra; ii) portray a mass (charge) distribution not wholly consistent with statistical equilibrium; iii) have angular distributions which are forward peaked, with the forward peaking largest for Z's near the projectile and decreasing for Z's farther removed from the projectile.

These general features appear to be consistent with the following qualitative picture: i) promptly after the initial collision, friction brings the two nucli into rigid contact with each other, while the initial kinetic energy is dissipated into the internal degrees of freedom; a rotating intermediate complex of well defined mass asymmetry is formed: ii) a diffusion process, comparable in rate to, or slower than, the rotation of the intermediate complex, leads to the exchange of particles between the two touching fragments, thus generating a time-dependent distribution in the asymmetry of the intermediate complex: iii) the complex decays with a time constant comparable to or shorter than the rotational period.

The central feature of the present model is the diffusion of the intermediate complex along the asymmetry degree of freedom. We use the Master Equation approach to describe the time-dependent population $\phi_Z(t)$ of systems whose asymmetry is characterized by the atomic number Z of one of the fragments:

$$\dot{\phi}_Z = \sum_{Z'} (\Lambda_{ZZ'} \phi_{Z'} - \Lambda_{Z'Z} \phi_Z) \qquad (1)$$

where $\dot{\phi}_Z$ represents the time derivative of ϕ_Z and $\Lambda_{ZZ'}, \Lambda_{Z'Z}$ are the macroscopic transition probabilities between the systems whose asymmetries are described by Z and Z'.

The macroscopic transition probabilities can be written in terms of the microscopic transition probabilities and of the level densities of the macroscopic states:

$$\Lambda_{ZZ'} = \lambda_{ZZ'} \rho_Z; \quad \Lambda_{Z'Z} = \lambda_{Z'Z} \lambda_{Z'};$$

$$\lambda_{ZZ'} = \lambda_{Z'Z}. \qquad (2)$$

The symmetry of the λ's stems from microscopic reversibility. The quantities ρ_Z represent the level densities of the intermediate complexes. These level densities can be written down in terms of the potential energy of the intermediate complex V_Z measured with respect to the rotating ground state,

$$\rho_Z = \rho(E-V_Z) \qquad (3)$$

where E is the energy of the system also measured with respect to the rotating ground state and $\rho(x)$ is the functional form for the level density.

Since $\Lambda_{ZZ'}$ must be the order of $\frac{V_F}{D}$ (where D is a typical linear size of the system and V_F is the Fermi velocity of the nucleons), the $\lambda_{ZZ'}$ decrease as the level densities increase. For lack of better knowledge, we assume:

$$\lambda_{ZZ'} = \frac{\lambda_0}{[\rho_Z \rho_{Z'}]^{1/2}} . \qquad (4)$$

The level densities can be expanded as follows:

$$\rho(E - V_Z) = \rho(E)\, e^{-V_Z/T} \qquad (5)$$

where

$$T^{-1} = \left.\frac{d \ln \rho(x)}{dx}\right|_{x=E-V_Z} \qquad (6)$$

and the master equation can be rewritten as:

$$\dot{\phi}_Z = \lambda_0 \sum_{Z'} e^{(V_Z+V_{Z'})/2T} \left[\phi_{Z'} e^{-V_Z/T} - \phi_Z e^{-V_{Z'}/T}\right] . \qquad (7)$$

This equation is certainly correct in the long time limit when $\dot{\phi}_Z = 0$. A sufficient condition which satisfies $\dot{\phi}_Z = 0$ is that each term of the sum is zero. This gives:

$$\frac{\phi_{Z'}}{\phi_Z} = \frac{\rho_{Z'}}{\rho_Z} = e^{-V_{Z'}/T} \Big/ e^{-V_Z/T} \qquad (8)$$

which expresses the equilibrium condition.

An important assumption in the present model is that the sum in Eq. (1) and Eq. (7) is extended only to $Z' = Z \pm 1$. In other words, we assume that there is no correlation among transferred particles. We also assume that, at least for the rather light systems which we have considered, the shape of the intermediate complex actually corresponds to a configuration of two touching spheres.

The angular momentum can in principal affect the shape of the intermediate complex and, consequently, the value of the potential energy. We write the potential energy as follows:

$$V(x_i) = V_{LD}(x_i) - V_{LD}\left(x_i^0\right) + \frac{\ell^2 \hbar^2}{2} \left[\frac{1}{\mathcal{J}(x_i)} - \frac{1}{\mathcal{J}\left(x_i^0\right)}\right] \qquad (9)$$

where the x_i is the set of coordinates chosen to describe the shape of the system; x_i^0 are the corresponding values for the ground state; V_{LD} is the liquid drop energy and $\mathcal{J}$ is the moment of inertia.

An example of the potential energies of the system Ag + Ar for various values of angular momentum is shown in Fig. 1(a)

The diffusion constant λ_0 should also depend on the shape of the intermediate complex. We have considered it to be proportional to the interaction area of the two touching spheres, which, in turn, is proportional to their reduced radius:

$$\lambda_0 = 2\pi \frac{R_1 R_2}{R_1 + R_2} \kappa \qquad (10)$$

where R_1 and R_2 are the radii of the two touching spheres.

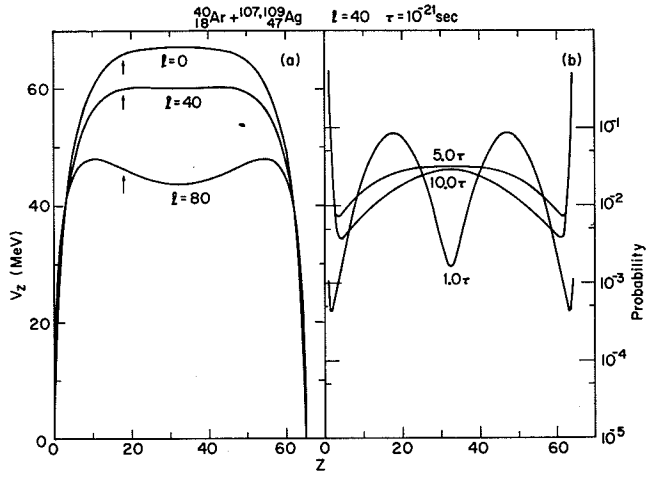

Fig. 1. (a) Potential energy of the intermediate complex as a function of Z for three ℓ-waves. (b) probabilities $\phi_Z(t)$ as a function of Z at three different times for the ℓ = 40 collision. For short times the distribution resembles a Gaussian as expected in a random walk problem. For longer times, the drift is more visible.
(XBL 753-2475)

A calculation of the populations ϕ_Z at various times after the beginning of diffusion is shown in Fig. 1(b). The calculation of the cross sections and angular distributions of the fragments requires that at least some essential part of the dynamics associated with the reaction be taken into account. We assume that, after collision, target and projectile slip one over the other by an angle θ_s proportional to the initial tangential velocity at the time of collision. As the slippage takes place, the kinetic energy is dissipated. After the slippage, the system rotates with a rigid moment of inertia. Furthermore, we assume that, after a given contact time t, the fragment is emitted at an angle θ with a new $Z = Z_{exit}$. This information allows one to calculate the set of impact parameters b which satisfy the above conditions. The final cross section is given by:

$$\frac{d\sigma_Z}{d\Omega} = \int_0^\infty \frac{dt}{\tau} e^{-t/\tau} \sum_b \phi_Z(b,t) \frac{bP(b)}{\left|\sin\theta \frac{d\theta}{db}\right|} \qquad (11)$$

where τ is the mean life of the intermediate complex and the sum contained in the integrand is carried over all the values of b which, after a time t, lead to the emission of a fragment of atomic number Z at a center-of-mass angle θ.

The quantity P(b) or P(ℓ) at a given bombarding energy is another quantity that cannot be determined on theoretical grounds as yet. It represents the probability $0 \leq P \leq 1$ that a given ℓ-wave will lead to a reaction of the kind described in this paper. It seems safe to assume that P(ℓ) will be substantially different from zero for rather large ℓ-waves, since the low ℓ-waves are certainly associated with the formation of the compound nucleus and thus responsible at least for the cross section of the evaporation residue. On the other hand, the highest ℓ-waves are associated with direct or quasi-elastic cross sections and, therefore, are not expected to be involved in the relaxed cross section studied here to any great extent. It is possible to construct a fairly satisfactory expression for P(ℓ) from experiment.

In the present paper we have tried to reproduce the experimental data obtained for the reaction Ag + 288 MeV Ar. The function P(ℓ) which we have used has a lower bound ℓ_{min} defined by the evaporation residue cross section of 670 mb[6] and an upper bound ℓ_{max} defined by the sum of the evaporation residue cross section and the relaxed cross section, which is ~1700 mb. Therefore, $P(\ell) = 1$ for $\ell_{min} \leq \ell \leq \ell_{max}$, and $P(\ell) = \phi$ otherwise. At the same time we have made the rather bold assumption that no sizable amount of fission is actually present in the cross section.

In Fig. 2 the calculated angular distributions of the fragments are plotted for atomic numbers of Z = 6 to Z = 32. The fragments with Z < 18 have a forward peaked angular distribution, the forward peaking being more enhanced for atomic numbers close to the projectile. The fragments with Z > 18 show angular distributions which quickly become asymmetric about 90° as the atomic number is farther removed from Z = 18. In fact, for atomic numbers close to symmetric division, the angular distribution becomes indistinguishable from $1/\sin\theta$. This result suggests that, even when particles are emitted with a $1/\sin\theta$ distribution, one should not draw the immediate conclusion that a compound nucleus has been formed.

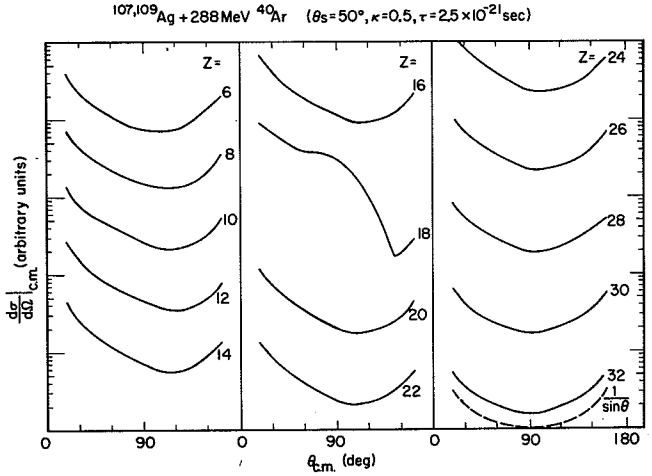

Fig. 2. Calculated center-of-mass angular distribution for various exit channels using the model described in the text. The main feature is the non-negligible forward peaking which decreases as the Z of the exit particle is further removed from the Z of projectile. The angular distributions approach $1/\sin\theta$ for exit channels far removed from the projectile.
(XBL 753-2472)

In Fig. 3 the comparison between experiment and theory is shown. It is important to notice that no normalization has been performed. The shapes of the angular distributions are reported with remarkable accuracy, while the absolute values are reporduced within better than 50%. No allowance for shell effects has been made in the evaluation of the ridge line potential, nor has the effect of secondary decay been accounted for.

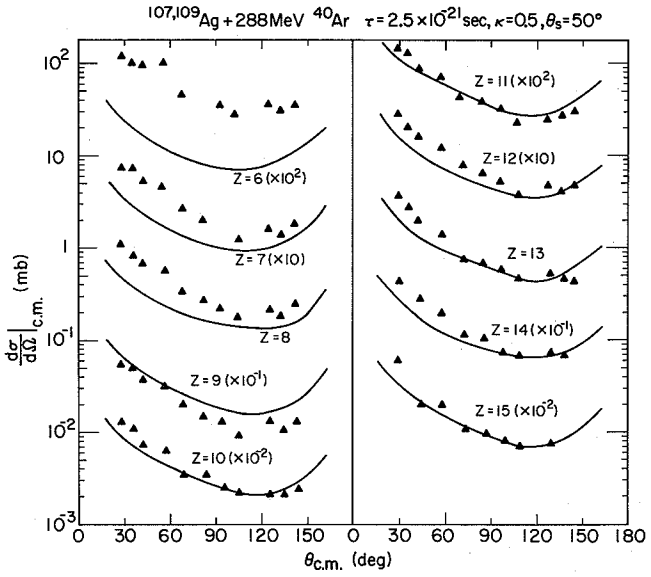

Fig. 3. Absolute comparison between the experimental and the theoretical angular distributions using the model described in the text. The values of the constants used are given in upper right hand corner of the figure. The constant has the dimensions $fm^{-1}10^{21}sec^{-1}$.

(XBL 753-2473)

A more extensive analysis of the available experimental data is in progress. An attempt is also being made to treat the thermalization of the kinetic energy and the particle diffusion occurring prior to the thermalization by means of a generalized theory.

Footnotes and References

*Condensed from LBL-3443.

†Sloan Fellow, 1974-1976.

1. L. B. Moretto, D. Heunemann, R. C. Jared, R. C. Gatti, and S. G. Thompson, Third Symposium on the Physics and Chemistry of Fission, August 1973, Rochester, NY, USA, IAEA-SM-174/75.

2. S. G. Thompson, L. G. Moretto, R. C. Jared, R. P. Babinet, J. Galin, M. M. Fowler, R. C. Gatti, and J. B. Hunter, Nobel Symposium on Superheavy Elements, June 1974, Ronneby Brun, Sweden, LBL-2940 (1974).

3. L. G. Moretto, S. S. Kataria, R. C. Jares, R. Schmitt, and S. G. Thompson, Nucl. Phys. A255, 491 (1975).

4. R. P. Babinet, L. G. Moretto, J. Galin, R. C. Jared, J. Moulton, and S. G. Thompson, Nucl. Phys. A258, 172 (1976).

5. J. Galin, L. G. Moretto, R. P. Babinet, S. Schmitt, R. Jared, and S. G. Thompson, Nucl. Phys. A255, 472 (1975).

6. H. H. Gutbrod, F. Plasil, H. C. Britt, B. H. Erkkila, R. H. Stokes, and M. Blann. Third Symposium on the Physics and Chemistry of Fission, August 1973, Rochester, NY, USA, IAEA-SM-174/59.

DIFFUSIVE PHENOMENA REFLECTED IN THE CHANGE AND ANGULAR DISTRIBUTIONS OF N, Ne, Ar, Kr INDUCED REACTIONS*

L. G. Moretto† and J. S. Sventek

A treatment which describes the time evolution of a probability distribution along a given coordinate is offered by the Master Equation. We have applied this equation to the problem of diffusion along the mass asymmetry coordinate.[1] Let $\phi(Z,t)$ be the probability distribution associated with a configuration of two touching fragments, one of which has atomic number Z (we assume equilibration in the neutron-to-proton ratio and we label the asymmetry by Z since this is the quantity we measure for each fragment). The Master Equation can then be written as:

$$\dot{\phi}(Z,t) = \sum_{Z'} \lambda_{ZZ'}(\phi_{Z'}\rho_Z - \phi_Z\rho_{Z'})$$

where $\lambda_{ZZ'} = \lambda_{Z'Z}$ is the microscopic transition probability, ρ_Z and $\rho_{Z'}$ are the level densities associated with the asymmetries Z and Z'.

Calculations of the probability distributions have been performed for some of the reactions studied experimentally.[2] An example is shown in Fig. 1.

The angular distributions, being so sensitive to short interaction times, give the first indication of the noncompound nucleus nature of the relaxed cross section. This was especially true for the reactions induced by Ar and lighter projectiles, or for that matter, for the reaction of Kr+Ag, where the charge distributions gave only an ambiguous answer regarding the degree of equilibration along the mass asymmetry coordinate.

In these reactions the center-of-mass angular distributions appear to be generally forward peaked, especially for fragments close in Z to the projectile.

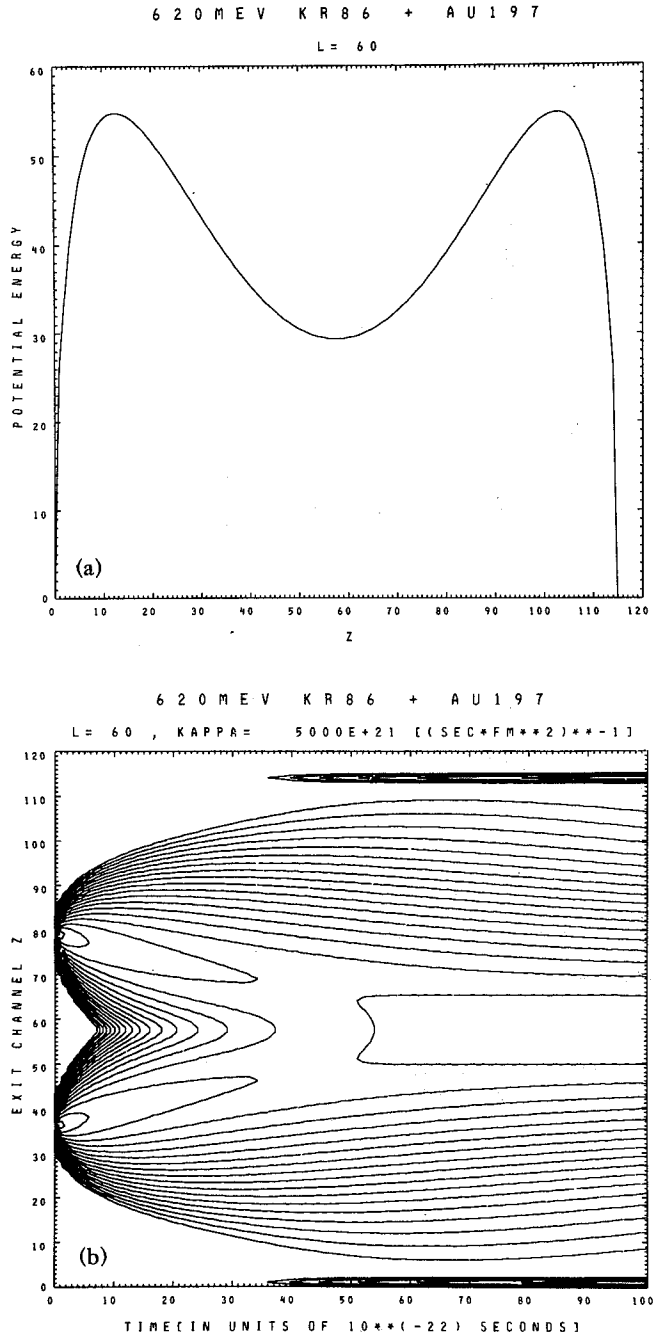

Fig. 1. a) Potential energy of the intermediate complex for the reaction Au+Kr (two touching spheres) as a function of the Z of one of the two fragments. b) Probability distributions along the mass asymmetry coordiante as a function of time. The calculation has been performed for $\ell = 60$.
(XBL 766-8335
and 766-8578)

This, by itself, is very significant in many respects. To begin with, there is some memory effect which couples entrance and exit channels. The intermediate complex can distinguish the forward from the backward direction in a way that a compound nucleus cannot, irrespective of its actual lifetime. The intermediate complex lifetime, of course, must be relatively short with respect to the mean rotational period; not too short though, otherwise the system could not rotate enough to cross the 0° line and would give rise to a side peak; not too long, otherwise the angular distribution would become symmetrized about 90°.

In *all* of these reactions, the forward peaking is stronger for fragments closer in Z to the projectile and decreases for fragments substantially removed from the projectile. This phenomenon finds its qualitative explanation in the increasing time lag, introduced by the diffusion process, in the population of configurations farther and farther removed in mass asymmetry from that associated with the target-projectile combination (injection asymmetry). In this way, fragments close in Z to the projectile are rapidly populated by the diffusion process and can rapidly decay, thus generating a substantially forward-peaked angular distribution. Fragments farther removed in Z from the projectile are populated on a longer time scale, so that their decay time is delayed. Such a delay allows the system to rotate for a longer time, which results in an increased tendency for the angular distribution to become more and more symmetric at about 90°.

When the reactions of Kr on heavy targets were first observed, the sharpness of the mass distributions associated with the side peaking of the gross angular distributions appeared to be so extraordinary that they were thought to be a completely new mechanism, which was named quasi-fission. Yet, this process resembles the deep inelastic processes described above in many respects. However, it seems that there is a continuous connection between the angular distributions observed in reactions induced by lighter projectiles (or by heavy projectiles on relatively light targets, like Ag + Kr), and the angular distributions observed in heavy projectile-heavy target reactions. The side peaking in the gross angular distribution of the products reflects a very short interaction time associated with a few Z's about the projectile. However, if one were to look at the angular distributions of individual Z's, one should observe a progressive change towards forward peaking as one moves away from the Z of the projectile. Examples of the cross sections and energies are given in Fig. 2. The angular distributions for individual atomic numbers, resolved up to $Z \approx 50$ are shown in Fig. 3. The effect we were looking for indeed appears with astounding clarity. Close to Z = 36 a very sharp side peak is observed (for the Z's closest to the projectile the separation of the quasi-elastic component appeared to be impossible so that some of the points close to the maximum of the peak are actually skipped). Such a side peak implies an interaction time so short that the intermediate complex does not have time enough to rotate past 0°. However, as one moves away in Z from the projectile, the progressively longer time delay imposed by diffusion allows the intermediate complex to reach closer to 0°, and eventually to reach past 0°. This results in a rapid filling in of the angles close to 0°, which slowly transforms the side peak first into a shoulder and later into a forward peak. In Au+Kr the side peak becomes a shoulder symmetrically about Z = 36, at $Z \approx 30$ and at $Z \approx 41$. The shoulder disappears around Z = 24 and $Z \approx 46$ where the angular distribu-

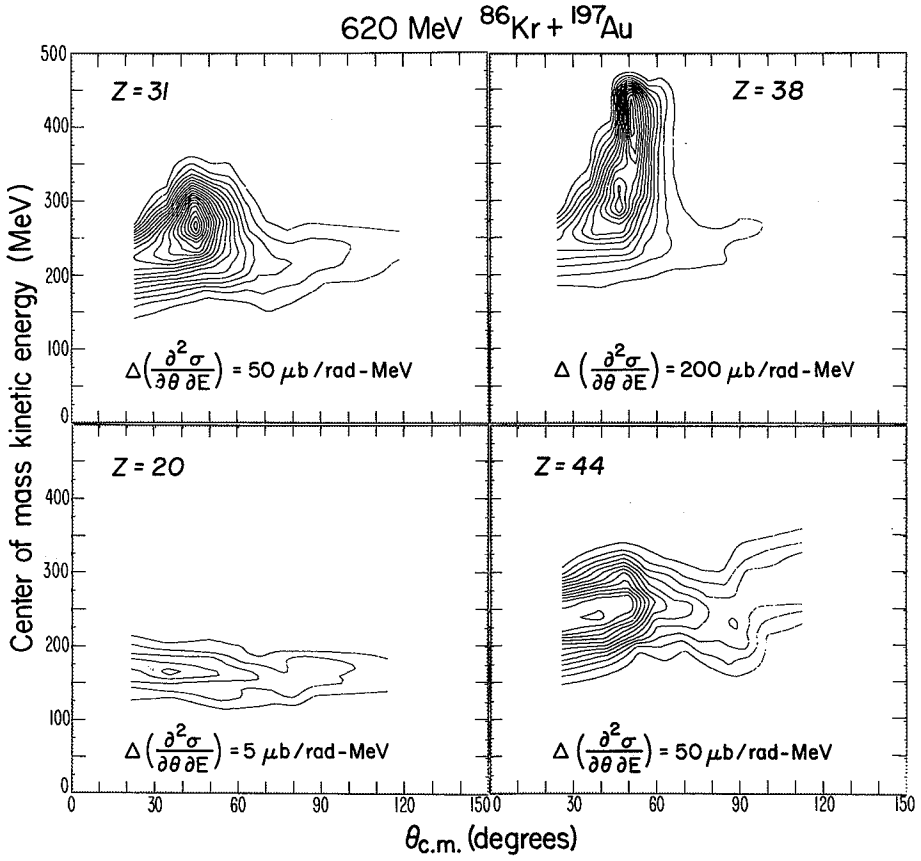

Fig. 2. Examples of contour plots of the center-of-mass cross section in the E, θ plane for various Z's in the reaction Au + ^{86}Kr. (XBL 761-2089)

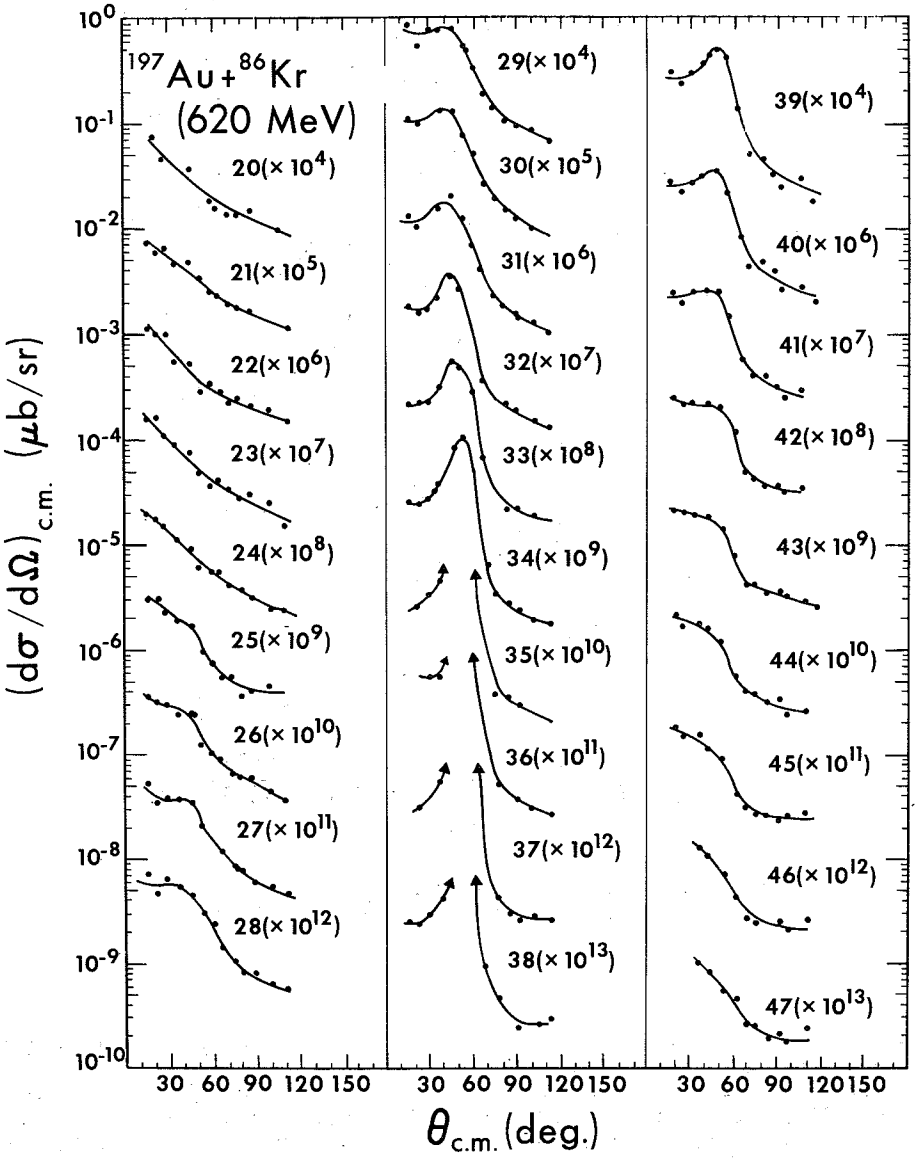

Fig. 3. Center-of-mass angular distributions for the reaction Au + ^{86}Kr. (XBL 7512-9891)

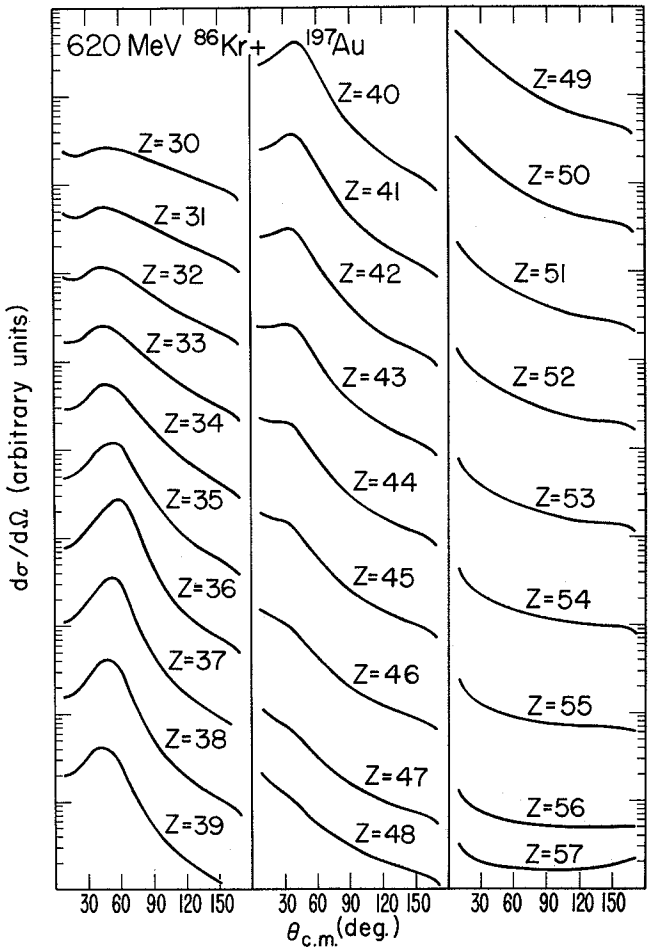

Fig. 4. Theoretical center-of-mass angular distributions for the reaction Au + ^{86}Kr at 620 MeV.
(XBL 763-2504)

tions become forward peaked. As expected, the side peak in the reaction of Kr+Ta, is less pronounced and disappears earlier. The forward peaking then extends to the extreme Z's, both high and low which were accessible in the present measurement. The theoretical calculation shown in Fig. 4 reproduces in detail the experimental effects. Thus in a single reaction, one observes the desired connection between the side-peaked and the forward-peaked angular distributions.

Footnotes and References

*Condensed from LBL-5006, Invited paper to the "Symposium on Macroscopic Features of Heavy Ion Collisions" ANL, Argonne, IL. April 1-3, 1976.

†Sloan Fellow 1974-1976.

1. L. G. Moretto and J. S. Sventeck, Phys. Lett. 58B, 26 (1975).

2. L. G. Moretto, R. P. Babinet, J. Galin, and S. G. Thompson, Phys. Lett. 58B, 31 (1975).

DIFFUSION MODEL PREDICTIONS FOR THE REACTION 620 MeV ^{86}Kr + ^{197}Au

J. S. Sventek and L. G. Moretto

In the Ref. 1, we have described the Diffusion Model that was postulated to explain the experimental features of the relaxed (deep-inelastic) cross section in the reaction 288 MeV ^{40}Ar + ^{107,109}Ag. Those experimental features are typical of most "light" target projectile systems that we have studied.

The purpose of this report is to extend the Diffusion Model to describe the experimental fea-

tures of the relaxed cross section in the reaction 620 MeV ^{86}Kr + ^{197}Au. This reaction is representative of "heavy" target projectile systems in that the relaxed component displays the following features[2]:

1) The angular distributions display Z-dependent side peaking. The side peak is largest for the projectile Z, diminishes to a shoulder for Z's removed on either side of the projectile, and eventually becomes a forward peak for Z's sufficiently far removed from the projectile.

2) The width of the Z-distribution at a given center-of-mass angle θ increases as θ is farther removed from the angle corresponding to the side peak in the projectile's angular distribution.

The fact that the angular distributions are side peaked as opposed to being forward peaked like the "light" systems[1] is due to the difference between the average rotational period for the complex τ_R and the average lifetime of the complex τ_C. The large mass of the "heavy" systems serves to make τ_R much larger than τ_C, which prevents partial orbiting, and results in side-peaked distributions.

As in Ref. 1, we have used the Master Equation to follow the time-dependent population $\phi_Z(t)$ of systems whose mass asymmetry is characterized by the atomic number Z of one of the fragments. We have assumed an equilibrated neutron to proton ratio, as shown to be true by Galin et al.[3] The potential energies used are those for two touching spherical fragments as in ref. 1. A plot of a typical potential energy curve vs. asymmetry can be seen in Fig. 1a.

The time dependence of the populations ϕ_Z is given by:

$$\dot{\phi}_Z = \sum_{Z' \neq Z} \lambda_{ZZ'} [\phi_{Z'}\rho_Z - \phi_Z\rho_{Z'}] \qquad (1)$$

where $\lambda_{ZZ'} = \lambda_{Z'Z}$ is the microscopic transition probability between systems specified by the asymmetries Z and Z', and ρ_Z is the level density of the system specified by Z. The level densities can be written in terms of the potential energy of the intermediate complex V_Z, discussed above, measured with respect to the rotating ground state, as $\rho_Z = \rho(E - V_Z)$. The $\lambda_{ZZ'}$ are the product of a diffusion constant κ and a normalized form factor.[1]

The system of equations in Eq. (1) can be solved by standard matrix techniques to give the time-dependent populations $\phi_Z(t)$ (normalized to 1). Fig. 1b is a map of contours of constant probability, calculated for the potential energy given in Fig. 1a, plotted as a function of mass asymmetry Z and the time t (in units of 10^{-22} seconds). Note that the drift and spread of the distribution can be easily discerned for short times, and the equilibration of the distribution can be seen for long times.

With the $\phi_Z(t)$'s, we can calculate the differential cross sections as

$$\frac{d\sigma_Z}{d\Omega}(\theta) = \int_0^\infty dt \left\{ \sum_b \frac{bP(b)}{\sin\theta \left|\frac{d\theta}{db}\right|} \phi_Z(b,t)\Pi(t;b) \right\} \qquad (2)$$

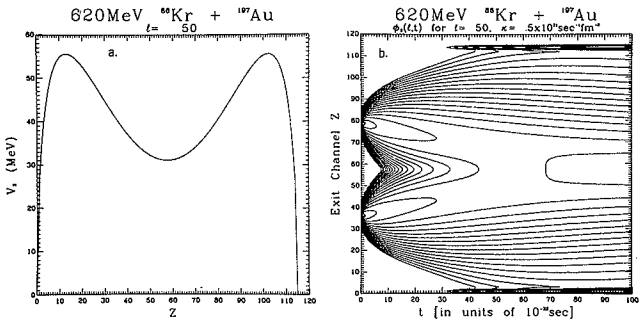

Fig. 1. (a) Potential energy of the intermediate complex as a function of Z for $\ell = 50$. (b) Probability distributions along the mass asymmetry coordinate as a function of time calculated for $\ell = 50$. (XBL 766-8131)

where P(b) is the probability that a collision at impact parameter b leads to a deep inelastic reaction. For this calculation, P(b) = 1 for all impact parameters $b \leq b_{lim}$, and P(b) = 0 for $b > b_{lim}$. The quantity b_{lim} is such that the cross section resulting from collisions at impact parameters in the range $b_{lim} \leq b \leq b_{max}$ (b_{max} corresponds to a grazing collision) is equal to the quasi-elastic cross section measured for Z's near the projectile Z at lab angles near the grazing angle. The sum in Eq. (2) is carried over all impact parameters b which result in particle Z being emitted at the angle θ after the complex has lived a time t. The quantity $\Pi(t;b)$ is the probability that the complex formed by a collision at impact parameter b will live a time t. In the previous work, we have assumed $\Pi(t;b) \exp(-t/\tau)/\tau$, independent of b with τ being the average lifetime of the intermediate complex. Moretto et al[2] have shown that the variation in the width of the Z distributions with angle can be explained by an average lifetime for the complex which decreases with increasing b. In the light of these results, these calculations have been performed with:

$$\Pi(t;b) = \frac{1}{N(b)} \exp\left[-\left(t - \tau(b) \right)^2 / \sigma^2(b) \right] \qquad (3)$$

where N(b) is a normalization factor and $\tau(b) = \tau(0)(1 - b/b_{max})$. Since the dispersion in any random walk process varies linearly with the elapsed time,[4] we have assumed that $\sigma^2(b) = \sigma^2(0)(1 - b/b_{max})$. The quantity $\tau(b)$ represents the average lifetime of the complex formed at impact parameter b, and $\sigma^2(b)$ represents the dispersion of the distribution of lifetimes about this average value. For these calculations, the values of $\sigma^2(0)$ and $\tau(0)$ are parameters but can in principle be determined from trajectory calculations.

The parameters used were: $\kappa = 0.25 \times 10^{21}$ sec^{-1}·fm^{-2}, $\tau(0) = 3.5 \times 10^{-21}$ sec, and $\sigma(0) = 1.0 \times 10^{-21}$ sec. The calculations have not been optimized with respect to the value of κ, and the value used was chosen because of the success of the previous work on light systems. The position and width of the side peak depends very strongly upon $\tau(0)$ and $\sigma^2(0)$, as one might expect. The position of the side peak in the experimental angular distribution determines $\tau(0)$ very uniquely,

and $\sigma^2(0)$ has the effect of making the side peak broader or narrower. The value of $\tau(0)$ should be compared with the rotational period of 8.6×10^{-21} seconds for the average ℓ-value of 185.

The angular distributions measured recently by our group[2] for 620 MeV $^{86}Kr + ^{197}Au$ are displayed in Fig. 2a. Figure 2b shows the angular distributions calculated for this system using the model described above. Note that the magnitude of the side peaking is greatest for Z = 36 and decreases on either side of the projectile. The gradual disappearance of the side peak for Z's above the projectile almost exactly parrots the experimental distributions. The distributions for Z's below the projectile follow a similar pattern, but the side peaking disappears too quickly (after too few Z's). This seems to be due to the assumption of two touching spheres for the shape of the intermediate complex.

Figure 3a shows the experimental Z-distributions for constant center-of-mass angles measured by our group. Note the increasing width of the distributions around Z = 36 as one moves both forward and backward in the center-of-mass with respect to 60°. Figure 3b is an analogous plot of the calculated values. The lack of shift of the most probable value in the experimental results is probably due to the difficulty of separating the relaxed component from the quasi-elastic component near the grazing angle.

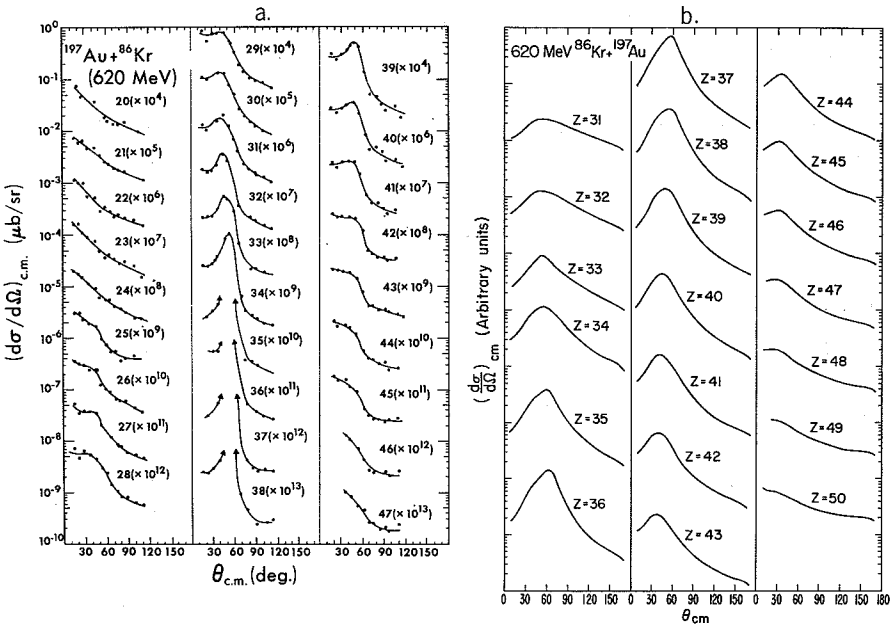

Fig. 2. (a) Experimental center-of-mass angular distributions for the reaction ^{197}Au + 620 MeV ^{86}Kr. (b) Theoretical center-of-mass angular distributions for the same reaction using model described in text. (XBL 766-2905A)

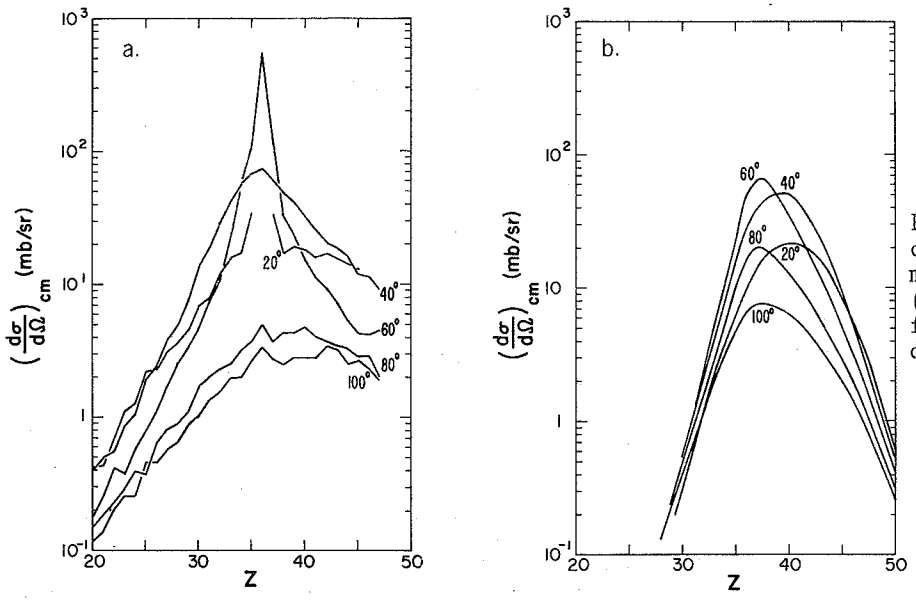

Fig. 3. (a) Experimental change of distributions for fixed center-of-mass angle for 620 MeV ^{86}Kr + ^{197}Au. (b) Theoretical charge distributions for the same reaction using model described in text. (XBL 766-2904A)

The absolute cross sections for Z's above the projectile are in agreement with a factor of 2, but the cross sections for Z's below the projectile are in error by much more. The large difference between the experimental and theoretical cross sections seen for Z's much below 36 can again be attributed to our assumption concerning the shape of the complex. Relaxation in the shape of the two touching fragments should allow the Z's below 36 to be populated on a much larger scale.

References

1. L. G. Moretto and J. S. Sventek, Phys. Lett. 58B, 26 (1975).

2. L. G. Moretto, B. Cauvin, P. Glassel, R. Jared, P. Russo, J. Sventek and G. Wozniak, Phys. Rev. Lett. 36, 1069 (1976).

3. B. Gatty, D. Guerreau, M. Lefort, X. Tarrago, J. Galin, B. Cauvin, J. Girard and H. Nifenecker, Nucl. Phys. A253, 511 (1975).

4. S. Chandrasekhar, Rev. Mod. Phys. 15, 1 (1943).

THE CLASSICAL-LIMIT S-MATRIX FOR COULOMB EXCITATION*

R. Donangelo, M. W. Guidry,
J. P. Boisson,† and J. O. Rasmussen

With the advent of very heavy nuclear projectiles there has grown a need for Coulomb excitation theory applicable in such systems. Exact quantum mechanical calculations of the Coulomb excitation process are quite impractical. However, the shortness of the de Broglie wavelength for heavy ions brings the problem more into the realm of classical mechanics. Semiclassical theories use this fact to find approximate solutions to the problem, such as in the Alder-Winther method[1] which is the foundation to the widely used Winther-deBoer code for Coulomb excitation.[2] Recently a quite different approach, the Uniform Semiclassical Approximation (USCA) was applied to this problem.[3]

We adapted and modified the formalism developed by Marcus[4,5] so as to study the Coulomb excitation process, and we show its relationship with the USCA as applied in Ref. 3.

We take as a target a deformed even-even nucleus in its ground state so that its initial spin is zero and its final spin quantum number I is an even integer. For simplicity we restrict ourselves to the case of a head-on collision.

Let H_o be the Hamiltonian of the system for distances large compared to the distance of closest approach, H_o includes then the kinetic energy and long-range Coulomb interaction terms. Let $|\phi_I\rangle$ be the eigenstate of H_o in the exit channel characterized by the spin quantum number I of the target. At short distances the Hamiltonian is $H = H_o + V$, where in V we include the remaining terms of the electromagnetic interaction. We designate by $|\psi^+\rangle$ the scattered part of the eigenstate of H corresponding to the initial conditions given before and evaluated long after the interaction has taken place.

From the usual definition of the S-matrix,

$$S_{I\leftarrow O} \equiv \langle\phi_I|\psi^+\rangle = \int\langle\phi_I|\underset{\sim}{q}\rangle\, d\underset{\sim}{q}\langle\underset{\sim}{q}|\psi^+\rangle \qquad (1)$$

where $\underset{\sim}{q}$ is a convenient representation and the integration is over all the $\underset{\sim}{q}$ space. Since we do not know the function $\psi^+(\underset{\sim}{q}) = \langle\underset{\sim}{q}|\psi^+\rangle$, we approximate it with the generalized WKB wave function

$$\bar{\psi}^+(\underset{\sim}{q}) = A(\underset{\sim}{q})\, \exp\{i\phi(\underset{\sim}{q})/\hbar\} \qquad (2)$$

where, as seen in Ref. 5, a conserves probability flux and the phase ϕ satisfies Hamilton-Jacobi equation.

We take the following coordinates to describe our system in the outgoing asymptotic region: χ, angle between the symmetry axis of the target and the line joining its center with the center of the projectile, and r, the distance between these centers. We denote by L the angular momentum of the target, by p_r the relative radial motion and by v the relative velocity. To obtain $\bar{\psi}^+(\underset{\sim}{q})$ trajectories are run with initial conditions: r large, $\chi = \chi_o$ (arbitrary), L = 0 and with a given projectile energy. From the values of the dynamical variables in the final asymptotic region we can determine A and ϕ, which are in our case

$$A = \sqrt{\frac{1}{2}\frac{\sin\chi_o}{\sin\chi}\frac{d\chi_o}{d\chi}\frac{v_o}{v}}\cdot\frac{1}{r} \qquad (3)$$

$$\phi = -\int(r(t)\, dp_r(t) + \chi(t)\, dL(t)) + rp_r + \chi L\ .$$

Here quantities with subscript zero represent initial values, and those without subscript, the values at the end of the trajectory. In the asymptotic region ϕ_I is given by:

$$\phi_I(\underset{\sim}{q}) \equiv \langle\underset{\sim}{q}|\phi_I\rangle = \qquad (4)$$

$$\frac{1}{2\pi}\sqrt{\frac{v_I}{v_o}\left(I+\frac{1}{2}\right)}\, P_I(\cos\chi)\, \frac{1}{r}\, e^{i\left[\frac{p_r r}{\hbar} - \eta\ln(2p_r r/\hbar)\right]}$$

where v_o and v_I are the asymptotic relative velocities for the values 0 and I respectively of the target spin quantum number, P_I is the usual Legendre polynomial and η is the Sommerfeld parameter for the exit channel.

Primarily because χ does not become constant in the asymptotic region it is not possible to define a good WKB wave function in this q = (χ,r) representation, so we transform it to a representation analogous to the one in Ref. 5, that is,

$$\bar{\chi} = \chi - \omega\tau \quad .$$

Here ω is the angular velocity of the target at the end of the interaction and τ is the time it would take the projectile to describe an elastic trajectory governed by the Hamiltonian H_o for an energy equal to that of the projectile in the outgoing asymptotic branch of its actual trajectory, measured from the point of closest approach on this trajectory.

In the same way as in Ref. 5 we can show that in this case the S-matrix is given by

$$S_{I\leftarrow O} = \int \phi_I^{*} \bar{\psi}^{+} \, 2\pi r^2 \sin\bar{\chi} d\bar{\chi} = \int \phi_I^{*} \bar{\psi}^{+} \, 2\pi r^2 \sin\bar{\chi} \frac{d\bar{\chi}}{d\chi_o} d\chi_o \tag{6}$$

or, more explicitly,

$$S_{I\leftarrow O} = \frac{\sqrt{2I+1}}{2} \int_0^{\pi} P_I(\cos\bar{\chi}) \sqrt{\sin\chi_o \sin\bar{\chi} \frac{d\bar{\chi}}{d\chi_o}} \, e^{i\phi'} d\chi_o \tag{7}$$

where

$$\phi' = -\frac{1}{\hbar}\int (r(t)\, dp_r(t) + \chi(t)\, dL(t)) + \frac{1}{\hbar}\bar{\chi}L + \eta \ln(2p_r r/\hbar) \quad . \tag{8}$$

We will examine Eq. (7) in more detail. Let us first consider the sudden impact limit for the case in which only the quadrupole moment of the target contributes to the excitation.

In this limit $\bar{\chi} = \chi_o$ and $\phi' = 2q\sin^2\chi_o$ where q is given by Eq. (5.11) of Ref. 1; therefore, Eq. (7) reduces to the expression found by Alder and Winther for this same case.[1] This result is interesting, considering the conceptually different approach we have taken.

If we now take the asymptotic expression for the Legendre polynomials

$$P_I(\cos\bar{\chi}) \approx 2\cos[(I+\tfrac{1}{2})\,\bar{\chi} - \tfrac{\pi}{4}]/\sqrt{\pi(2I+1)\sin\bar{\chi}}$$

and make use of the fact that the initial orientation angles χ_o and $\pi - \chi_o$ result in opposite final angular momenta, we find

$$S_{I\leftarrow O} \approx \frac{1}{\sqrt{\pi}} \int_o^{\pi} \sqrt{\sin\chi_o \frac{d\bar{\chi}}{d\chi_o}} \, e^{i[\phi' - (I+\frac{1}{2})\bar{\chi}]} \, d\chi_o \quad . \tag{7'}$$

The evaluation of this integral by the stationary phase approximation results in the USCA as applied on Ref. 3. The weighting factors introduced through geometrical arguments in that paper and also its use of the I + 1/2 spin quantization condition appear straightforwardly here from the asymptotic expression for the Legendre function.

We have applied Eq. (7) to several cases. In Fig. 1 we compare our calculations with those obtained by means of the Coupled-Channel quantum mechanical code AROSA.[6] The agreement is good, especially considering that in these cases the systems are not very classical. The method employed here should become more accurate for heavy-ion systems. No comparison with AROSA results is possible yet for very heavy ions, so that in Fig. 2 we have compared our results with the semiclassical Winther de Boer[2] code for a heavier projectile.

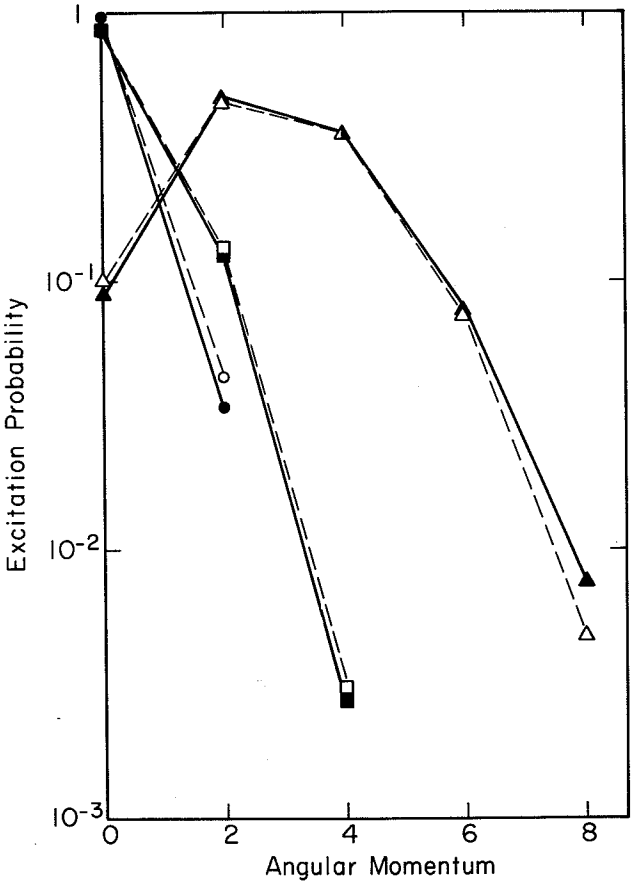

Fig. 1. Probabilities to Coulomb excite the rotational band of ^{168}Er for backscattering of 7 MeV deuterons, 14 MeV α-particles and 45 MeV ^{10}Be projectiles. The quantum mechanical results were obtained using the code AROSA, and are indicated by dark circles for ^{2}H, dark squares for ^{4}He and dark triangles for ^{10}Be, respectively, joined by solid lines. The results from Eq. (7) in the text are shown, respectively, by open circles, squares and triangles joined by dashed lines. The quadrupole moment of ^{168}Er is taken to be 7.67 barns, its energy levels are taken from the rotational model, and no nuclear forces were considered in any of the calculations.

(XBL 766-8124)

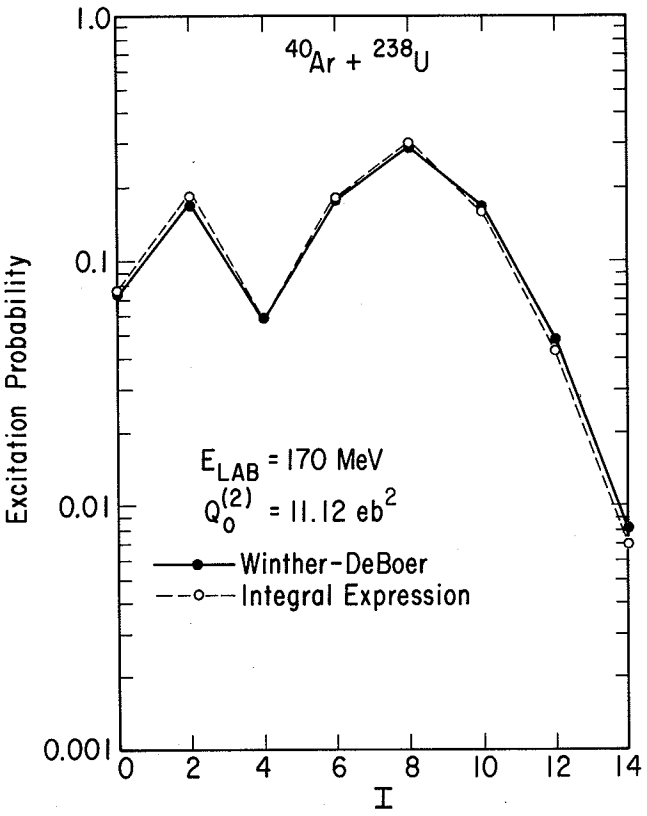

Fig. 2. Probabilities of Coulomb excite the rotational ground band in ^{238}U for backscattering of ^{40}Ar at 170 MeV. The results given by the Winther-deBoer code are shown by dark circles joined by full lines and the results from Eq. (7) in the text by open circles joined by dashed lines. The quadrupole moment of ^{238}U is taken to be 11.12 barns; the energy levels are taken from the rotational model, and no nuclear forces were considered in the calculations.

(XBL 7512-9896)

We should remark at this point that the validity of Eq. (7) is limited to those cases where the WKB wave function $\bar{\psi}^+$ is a good asymptotic approximation to the actual wave function ψ^+. This requires, in particular, that $\bar{\chi}$ be a monotonic function of χ_0; if not $\bar{\psi}^+$ will break down at the points where

$$\frac{d\bar{\chi}}{d\chi_0} = 0 \quad .$$

These difficulties can appear, and Kreek et al.[7] reported them in a related problem.

Equation (7) is applicable at energies around the Coulomb barrier if one includes the complex nuclear potential in the equations of motion, in the manner of Ref. 8.

The fact that the stationary phase approximation is not used makes Eq. (7) more straightforward to use than the USCA in cases where the stationary phase points are not easy to locate, or where there are more than two such points. Since this approximation is not used, there is even reason to think that our results could be more precise than those of the USCA, especially in cases where the exponent in the integrand of Eq. (7) varies slowly. For comparison purposes we give in Table 1 the results obtained by all the methods we have mentioned for a case where this exponent varies slowly. The USCA used there is the one based on Airy functions as considered in Ref. 3; for this case the Bessel uniform approximation given by Stine and Marcus[9] should be more appropriate. However, the results in Ref. 8 seem to indicate that an integral expression such as Eq. (7) is more accurate, even for these cases.

Table 1. Excitation probabilities of rotational levels in ^{168}Er for backscattering of 45 MeV ^{10}Be.

Spin	This Work (Eq. 7)	AROSA[6]	Winther-deBoer[2]	USCA[3]
0	0.1023	0.0890	0.1087	0.1167
2	0.4615	0.4754	0.4375	0.4928
4	0.3571	0.3522	0.3544	0.3336
6	0.0734	0.0775	0.0885	0.0531
8	0.00468	0.00756	0.0103	0.00395

Footnotes and References

*Condensed from LBL-4347, to be published in Phys. Lett. B.

†Permanent address: Institut des Sciences Nucleaires de Grenoble BP 257, 38044 Grenoble, France.

1. K. Alder and Aa. Winther, Mat. Fys. Medd. Dan. Vis. Selsk. 32(8) (1960).

2. Aa. Winther and J. DeBoer, in "Coulomb Excitation," K. Alder and Aa. Winther, eds. (Academic Press, NY, 1965), p. 303.

3. H. Massmann and J. O. Rasmussen, Nucl. Phys. A243, 155 (1975).

4. R. A. Marcus, Chem. Phys. Lett. 7, 525 (1970).

5. R. A. Marcus, J. Chem. Phys. 56, 3548 (1972).

6. F. Roesel, J. X. Saladin and K. Alder, Comp. Phys. Comm. 8, 35 (1974).

7. H. Kreek, R. L. Ellis and R. A. Marcus, J. Chem. Phys. 62, 313 (1975).

8. M. W. Guidry, H. Massmann, R. Donangelo, and J. O. Rasmussen, to be published in Nucl. Phys. A.

9. J. R. Stine and R. A. Marcus, J. Chem. Phys. 59, 5145 (1973).

THEORY OF COULOMB-NUCLEAR INTERFERENCE FOR HEAVY-ION EXCITATION OF ROTATIONAL STATES*

M. W. Guidry, H. Massman,†
R. Donangelo, and J. O. Rasmussen

The Uniform Semiclassical Approximation[1] (USCA) has been applied to the problem of Coulomb-nuclear interference for rotational states excited in heavy-ion interactions.[2] The classical model of the interference effect as a competition between electromagnetic and nuclear forces is illustrated in Fig. 1. By solving the (complex) classical equations of motion the quantum number function of Fig. 2 is obtained, which relates the final spin of the rotor $I(\beta_o)$ to an initial orientation angle β_o.

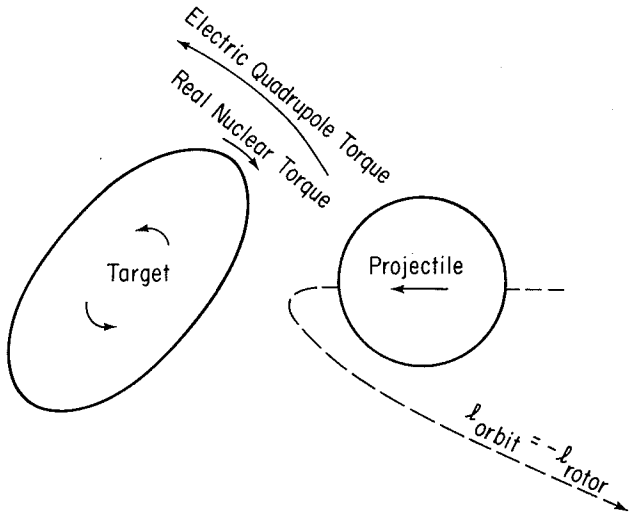

Fig. 1. The classical model for completition between the electromagnetic and nuclear forces.
(XBL 761-12A)

In this formalism, one finds that the excitation probability (the square of the S-matrix) is approximately given by

$$P_{I\leftarrow 0} \approx |\bar{p}_1| e^{-2\mathrm{Im}(\Phi_1)} + |\bar{p}_2| e^{-2\mathrm{Im}(\Phi_2)} + 2e^{1/2\mathrm{Im}(\Phi_1+\Phi_2)} \sqrt{|\bar{p}_1\bar{p}_2|}\sin(\mathrm{Re}(\Delta\Phi)+\alpha) \quad \text{"allowed transitions"} \tag{1a}$$

$$P_{I\leftarrow 0} \approx e^{-2\mathrm{Im}\Phi} |\bar{p}| \quad \text{"forbidden transitions"} \tag{1b}$$

where "allowed transitions" involved (approximately) those states below the maximum of the quantum-number function in Fig. 2, and "forbidden transitions" involve (approximately) those states above it. The classical probabilities $\bar{p}_j$ are defined by

$$\bar{p}_j = \frac{2\sin\bar{\beta}_j}{\left(\frac{\partial I(\bar{\beta}_j)}{\partial \beta_j}\right)} \qquad (\bar{\beta}_j \equiv (\beta_o)_j \;\; ; \;\; j = 1,2) \tag{2}$$

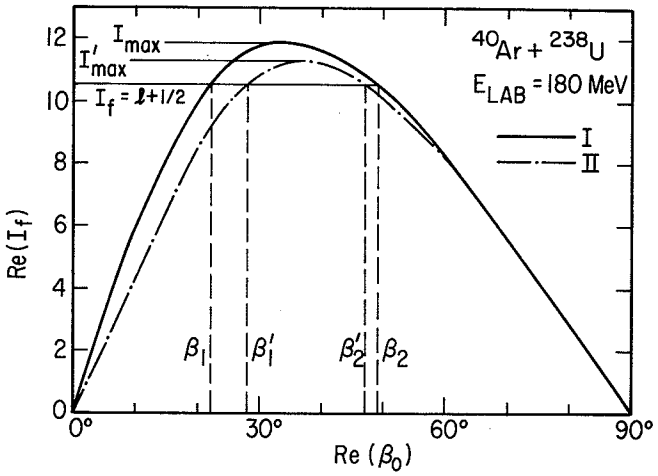

Fig. 2. The real part of the final spin vs the real part of the initial orientation angle- the quantum number function. For the complex trajectory case the function is complex. The effect of the real nuclear potential is to lower the final spin relative to the case of no nuclear potential. Graphical solutions for the 10+ state are indicated for the Coulomb excitation case (β_1 and β_2), and the Coulomb nuclear case (β'_1 and β'_2) when the imaginary potential can be ignored.
(XBL 761-20)

where the derivatives are determined from the function in Fig. 2 evaluated at the roots $\bar{\beta}_1$, $\bar{\beta}_2$, and the phase Φ_k is the classical action evaluated on the trajectory with an initial rotor orientation $\beta_o = (\beta_o)_k$. The quantity α is the phase of $-\bar{p}_1\bar{p}_2^*$ and is small for the cases considered here.[2] A uniform expression involving Airy functions was actually used for the calculations; but Eq. (2), which is an asymptotic form of the uniform expression, is useful in illustrating two important concepts: (1) the interference between the amplitudes arising from the different terms in the S-matrix, and (2) the exponential damping of the probability amplitudes by the imaginary part of the classical action Φ.

For the system $^{40}Ar + ^{238}U$ we have calculated excitation functions for excited states in the ground state band for the zero-impact parameter case. These are shown in Fig. 3 for pure Coulomb excitation (I), and for several representative complex nuclear potentials (II, III, IV) obtained from quasi-elastic heavy-ion scattering.[3,4] The deviation of the Coulomb nuclear probabilities from pure Coulomb excitation in these figures is easily expanded by the effect of the complex nuclear potential on the interference term of Eq. (1a) and the damping factor of Eq. (1b). The interference effects are significant and depend on the form of the nuclear potential.

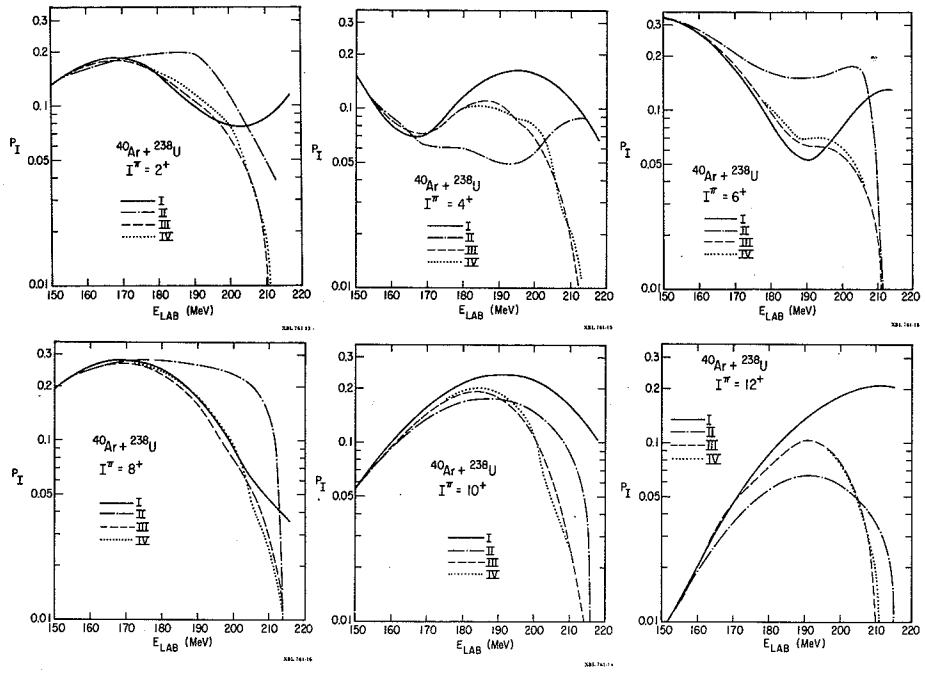

Fig. 3. Excitation functions for the 2^+ - 12^+ states in the reaction ^{40}Ar + ^{238}U. The calculation was restricted to the zero impact parameter.

(XBL761-19A)

Because the excitation probabilities are sensitive to Coulomb nuclear interference effects, we believe that heavy-ion rotational excitation patterns near Coulomb barrier energies could provide a detailed probe of the potential in the nuclear surface region. (The potential in the nuclear interior is probably inaccessible because of the strong absorption.) One may speculate that the potential for a deformed nucleus may exhibit irregular variations with polar angle β. For example, the imaginary potential may be largely due at barrier energies to loss of flux into neutron transfer channels, and hence be strongest in the zones of the lightly-bound Nilsson neutron orbitals. If the concept of a classical trajectory has any physical significance in these heavy-ion systems, excitation of different rotational states should probe different angular regions of the nuclear surface. Referring to Fig. 2, we would infer that the excitation probability for spin 8 in the case displayed there mainly probes the nuclear potential near $\beta_1' = 20°$, since the large-angle root β_2' feels less influence from the nuclear potential. Excitation of lower spins should be sensitive to regions closer to the nuclear tips. At sufficiently higher energies the low angle roots should be damped by the imaginary potential and the larger angle orientations, which now feel the nuclear force, should make the dominant contribution. Therefore, one would expect the probabilities in this case to be sensitive to the nuclear potential nearer the belly of the classical nucleus.

Footnotes and References

*Condensed from LBL-4357, to be published in Nucl. Phys. A.

†Present address: Hahn-Meitner Institut, Berlin. On leave from Faculad de Ciencias, Universidad de Chile, Santiago, Chile.

1. W. H. Miller, J. Chem. Phys. 53, 1946 (1970); ibid 53, 3578 (1970).

2. H. Massmann and J. O. Rasmussen, Nucl. Phys. A243, 155 (1975).

3. R. Vandenbosch, T. D. Thomas, and M. Webb, to be published.

4. J. R. Birkelund, et al, Phys. Rev. C 13, 133 (1976).

BARRIER PENETRATION THEORY IN MORE THAN ONE DIMENSION*

Peter Ring,† John O. Rasmussen, and Herbert Massman‡

We have reviewed quantum mechanical tunneling theory in more than one dimension.

Several systems from nuclear and molecular science were considered specifically, such as, alpha decay of spheroidal nuclei, spontaneous fission, and reactive collinear collisions of hydrogen atoms with hydrogen molecules. The range of validity of various approximations that reduce to one-dimensional path integrals or Fröman-Nosov matrices was examined, testing where possible against fully quantum mechanical coupled-channels solutions. The classical equations of motion methods using complex variables (uniform semi-classical approximation) were explored for nonseparable fission-like model systems. Effects of variable valley widths, curving valleys, and of variable inertial tensors were delineated.

In this brief report only one of the newer results is presented. More detail is contained in the paper from which this report has been condensed. The generalized WKB integrand for barrier penetration in spontaneous fission is

$$S=\hbar^{-1}\int_{\sigma_1}^{\sigma_2}\sqrt{2(E-W(\sigma))\sum_{ij}B_{ij}(q)\frac{dq_i}{d\sigma}\frac{dq_j}{d\sigma}}\,d\sigma$$

where σ is some arbitrary parameter along a trajectory and B_{ij} is the inertial tensor which may also depend on σ. During the tunneling process $W > E$, and the integrand is purely imaginary. The tunneling probability is given in the usual way by:

$$p = |\exp(iS)|^2 = e^{-2|S|}$$

In perhaps the most sophisticated fission barrier study of recent times Brack et al.[1] proceeded to find the trajectory which minimizes $|S|$. The trajectory so obtained usually did not follow the steepest descent of the potential and did not lead through the extremal points of the deformation energy. It should still be noted that the entrance (σ_1) and exit (σ_2) points should be determined in such a way that the action integral is also stationary against variation of these endpoints.

T. Ledergerber and H. C. Pauli[2] using the same method (as the one described in Ref. 1) have done calculations using three deformation parameters: an elongation coordinate, a constriction or necking-in coordinate, and a parameter describing the left-right asymmetry. The lifetimes obtained from these calculations are in order-of-magnitude agreement with the experimental data; they also show that mass-asymmetric fission is favored and that the most probable mass division (peak-to-peak ratio) agrees with the experimental data.

In this multidimensional approach,[1,2] however, they have still ignored the kinetic energy tied up in the motion orthogonal to the fission path (which may change along the path). It has been customary in shell-corrected liquid-drop model work (Strutinsky method) to ignore all zero-point vibrational energy corrections, since they would require assumptions about an inertial tensor. Thus, liquid drop model parameters are adjusted to fission barrier heights. With such a surface it is clearly incorrect simply to add zero-point energies. This point is closely related to the point made by Maruhn and Greiner;[3] for spontaneous fission from a spheroidal ground state the number of degrees of freedom for quadrupole vibrations is three, that is, the ground state would have (3/2) $\hbar\omega$ of zero-point energy. At the saddle the frequency of the beta-vibrational mode in the fission direction has become imaginary, leaving only two units of zero-point energy, those associated with the gamma-vibrational (axial-symmetry-breaking) mode. In order to include these zero-point energy corrections (without modifying the fission barrier heights) Maruhn and Greiner readjusted some of the liquid drop parameters of Myers and Swiatecki[4] to lower the ground state potential energy (and that of the final fragments) by the zero-point energy, which was obtained from the first 2^+ state experimentally observed.

Another way to consider this problem is in terms of tunneling and the Inverted Potential Energy Surface. Consider a system which moves toward a barrier and let time be the parameter in the equations of motion describing the system. If the time increments are kept real, the system will move toward the barrier and then reflect at the barrier and move back. If, however, one takes purely imaginary time increments when the system is at the turning point, the system will start tunneling. In other words, during the tunneling process, the system follows the classical equations of motion but with purely imaginary time increments.

If at the classical turning point of the fission degree of freedom all the other degrees of freedom are also at a turning point (or in other words, if the system when it reaches the barrier is at rest), then the tunneling process can be visualized by a very simple picture. If the system is at rest at the turning point and if one uses purely imaginary time increments thereafter (until the tunneling is completed), then all the coordinates will remain real, all quantities related to odd powers of the time (for example velocities, momenta, angular momenta, etc.) will be purely imaginary; quantities which depend on the square of momenta (for example, the kinetic energy, centrifugal force, etc.) will change sign. It is now easy to see that the system can equivalently be described by using only real time increments and changing

the sign of (V-E). That is, the tunneling trajectories can be obtained by finding how the system moves on the inverted potential surface.[5] For the fission example, the entrance point σ_1 will now be close to the top of a hill and the fission valley will be a mountain ridge starting somewhere close to the hill (see Fig. 1 for a simple illustration of this idea). If after the system reaches σ_2 the time increments are kept purely imaginary (or equivalently, using real time one keeps the inverted potential surface), the system will move toward σ_1 again. Finding the tunneling trajectory,then, is equivalent to finding the periodic orbit on the inverted potential surface. In the example shown in Fig. 1 there is only one point (in general, it is a certain interval) on the entrance and one point on the exit energy contour which are connected through classical equations of motion; therefore, when looking for the trajectory with the minimum action $|S|$ one also has to vary the endpoints σ_1 and σ_2 until the minimum is achieved.

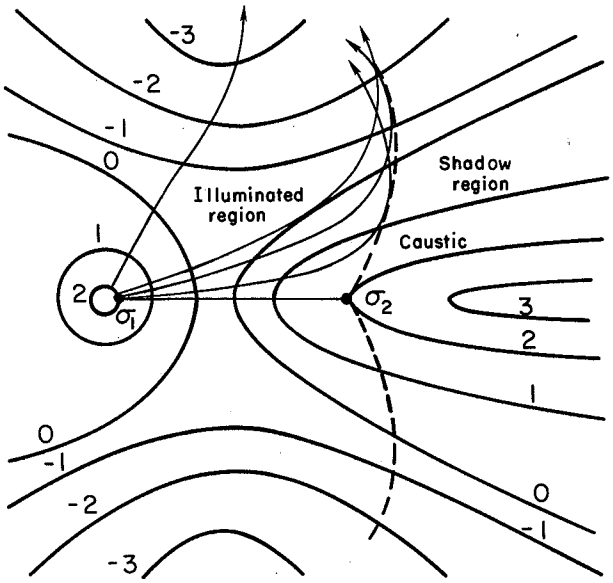

Fig. 1. Schematic representation of a contour map of a potential energy surface turned around to study the classical motion below the barrier. The entrance and exit points, σ and σ_2, lie on the same equipotential. The hill at the left side corresponds to the potential well in which the nucleus sits before fissioning and the mountain range at the right represents the fission valley.

(XBL 759-3877)

We have also studied a two-dimensional model of a fission-like barrier system. In order to investigate the full two-dimensional dynamics and to test various approximations it is of value to study a model system with the potential given by an analytical function. An example studied by Massmann et al.[6] takes a Hamiltonian with potential giving a Gaussian barrier in the x direction (x being the fission coordinate) and a harmonic potential in the y direction. The mass tensor was taken to be diagonal and constant; the width of the valley, however, was variable. The Hamiltonian considered was

$$H = \frac{p_x^2}{2m_x} + \frac{p_y^2}{2m_y} + V_o e^{-\left(\frac{x}{a}\right)^2} + \frac{1}{2} C\left(1 + \alpha e^{-\left(\frac{x}{a}\right)^2}\right) y^2 \quad .$$

A non-zero value of the "coupling constant" α allows the width of the valley to vary over the saddle, and by doing so couples the two degrees of freedom. The numerical values were chosen so as to correspond to a typical fission case: $m_x = 500\ \text{MeV}^{-1}$, $V_o = 7$ MeV, $m_y = 4.7\ \text{MeV}^{-1}$, $a = 0.185$, $C = 5.1$ MeV, $E_{tot} = 6.0$ MeV. This choice of C and m_y gives a frequency of about 1 MeV, typical of a gamma vibrational mode. The coordinates x and y are dimensionless and correspond for instance to the deformation parameters ε_2 and ε_4.

A fully two-dimensional quantum mechanical solution of this model is possible for not too strong coupling constant α. The method is analogous to the coupled channel calculations described for alpha-decay.

Figure 2 shows in its upper part the shape of the Gaussian barrier together with the adiabatic translational energies in the x direction for the three y-vibrational channels n = 0, n = 2, and n = 4. Let us remember that the problem we are solving is typical of sub-barrier fission, with ~4.5 MeV of excitation and ~1.5 MeV below the classical barrier threshold (the coupling is $\alpha = 0.1$). Higher n channels are obviously closed, and odd n channels are not coupled for parity reasons. The lower part of the diagram plots the square of the wave functions for an incident wave from the left in channel $\mu = 2$ (i.e., $|u_{2\nu}(x)|^2$). We note the standing wave in the channel $\mu = 2$ on the left side of the barrier, as most of the flux is elastically reflected. About 10^{-5} is inelastically reflected in channel $\mu = 4$ and 10^{-8} in channel $\mu = 0$. To the right of the barrier $\nu = 0$, 2 and 4 waves are transmitted at the 10^{-10}, 10^{-15}, and 10^{-24} probability levels, respectively. There is a vibrational "cooling" effect on the passage through the barrier, with $\nu = 0$ transmitted waves dominating regardless of vibrational state incident on the barrier. Only in the case of α very close to zero, a constant valley width, will the "cooling" feature not appear (see Fig. 3).

An obvious approximation to be tested by the coupled channel solution is that the y-direction wave function, particularly the Gaussian of the zero-point lowest state, adiabatically adjusts its width as the valley changes along the path. That is, in this so-called vibrationally adiabatic approximation (VA) one assumes that during the fission process the system always stays in the same oscillator state μ. Then one carries out a one-dimensional calculation, taking into

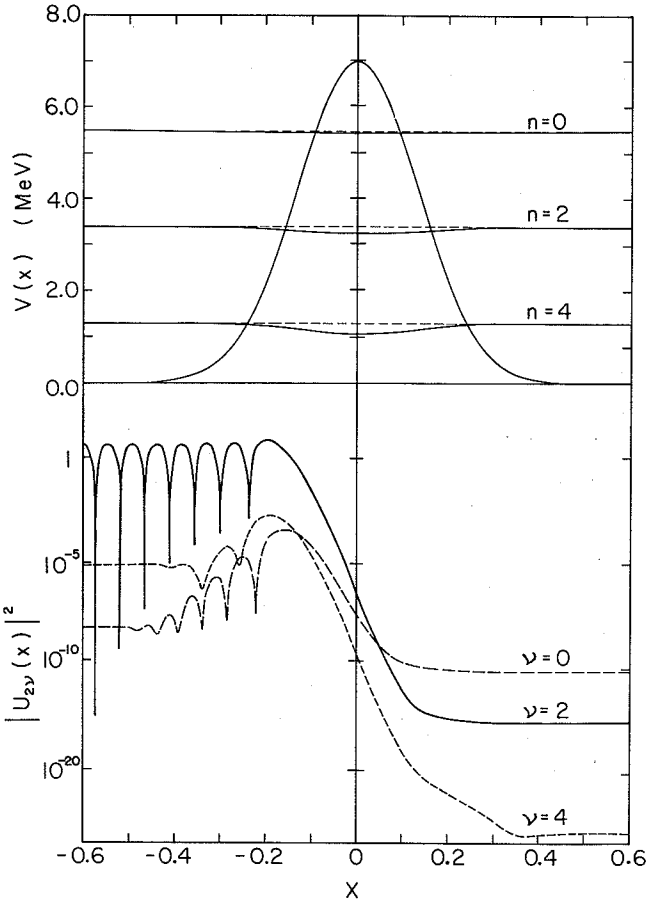

Fig. 2. Fission barrier and the square of the quantum mechanical channel function $U_{2\nu}(x)$ for an incoming wave or the channel $\mu = 2$.
(XBL 755-2883)

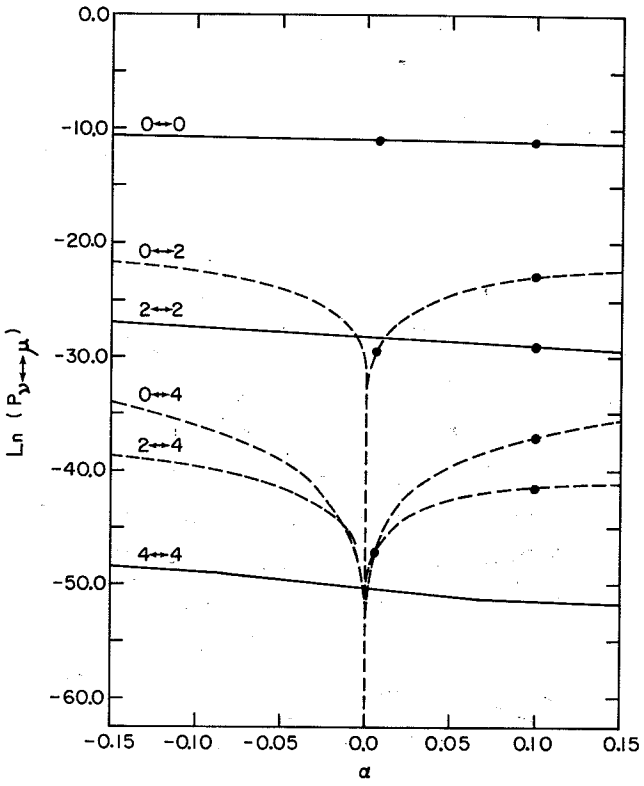

Fig. 3. Penetrabilities $P\mu\nu$ for different values of the coupling constant α. The lines correspond to the QM coupled channel calculations (solid line for the diagonal and broken lines for the off-diagonal penetrabilities) and the dots correspond to the USCA calculations.
(XBL 755-2884)

Table 1. Comparison between the QM and USCA transition probabilities.

	α = 0.1					α = 0.01		
	0↔0	0↔2	0↔4	2↔2	2↔4	0↔0	0↔2	0↔4
QM	1.40×10^{-5}	9.30×10^{-11}	1.03×10^{-16}	2.67×10^{-13}	9.86×10^{-19}	1.64×10^{-5}	1.22×10^{-12}	1.49×10^{-20}
USCA	1.44×10^{-5}	9.49×10^{-11}	0.97×10^{-16}	2.52×10^{-13}	9.15×10^{-19}	1.56×10^{-5}	1.30×10^{-12}	1.42×10^{-20}

account only the change of the oscillator energy. For this example the adiabatic approximation is good for penetration in the lowest state.

We also tested the validity of the USCA (uniform semiclassical approximation) on this model problem. The underlying idea of the USCA is that one uses the analytical continuation of the classical equations of motion to describe the dynamics of the system together with quantized boundary conditions and the quantum mechanical superposition principle in adding amplitudes for different trajectories. The foundations of the USCA and many applications to molecular scattering and reaction problems have been given by Miller and others (see Refs. 7 and 8). Here we will, therefore, only give the main results of the USCA as applied to our model.

Once the S-matrix is known the transition probabilities $P_{\nu\leftarrow\mu} = |S_{\nu\leftarrow\mu}|^2$ follow directly. There is very good agreement between these USCA calculations and the exact quantum mechanical coupled channel calculations, as can be seen from Fig. 3 and Table 1, even though the model here considered is highly nonclassical.

This very good agreement gives confidence that the semiclassical method may also be applied to more realistic cases with stronger coupling, where the numerical effort does not change very much and where a quantum mechanical calculation would be unfeasible. Since coordinate-dependent inertial parameters introduce no additional difficulty, the USCA could be a useful tool to investigate the full dynamics of the coupling between the fission coordinate and the other degrees of freedom such as hexadecapole deformations, mass asymmetries, and change in pairing correlation.

Recently attention has been focused on a barrier penetration method where one seeks a periodic orbit with time running in a purely imaginary direction. With imaginary time increments the kinetic energy terms of the classical equations of motion reverse sign and potential barriers invert into troughs. The approach is related to the more general semi-classical methods, except here the variables (except time) may remain real. Already this picture affords a useful way of thinking about multi-dimensional barrier penetration and the reciprocal behavior of positive and negative kinetic energy cases. One can appreciate that penetration paths cut inside the curving barriers by virtue of a negative centrifugal potential, while over-the-barrier trajectories are forced to the outside of the curving valley. Penetration paths of negative kinetic energy are pulled toward lower values of the penetration mass tensor component, while at positive kinetic energy the paths seek higher values of the mass tensor component. In a coupled channel situation there is a vibrational cooling effect for negative kinetic energies and a progressive exciting of vibrational modes for positive kinetic energies. We may reasonably surmise from the coupled-channel behavior that with inclusion of a friction term in the classical equations of motion we gain kinetic energy for tunneling paths, just as we lose kinetic energy to heat for increasingly rapid real velocities.

Footnotes and References

*Condensed from LBL-4028.

†Present address: Physik Department, Technische Universität München, West Germany.

‡Present address: Hahn Meitner Institut für Kernforschung, West Berlin.

1. M. Brack, J. Damgaard, A. Jensen, H. C. Pauli, V. M. Strutinsky and C. Y. Wong, Rev. Mod. Phys. 44, 320 (1972).

2. T. Ledergerber and H. C. Pauli, Nucl. Phys. A207, 1 (1973).

3. J. Maruhn and W. Greiner, Phys. Lett. 44B, 9 (1973).

4. W. D. Meyers and W. J. Swiatecki, Ark. Fiz. 36, 343 (1967).

5. W. H. Miller, J. Chem. Phys. 62, 1899 (1975).

6. H. Massmann, P. Ring, and J. O. Rasmussen, Phys. Lett. 57B, 417 (1975).

7. T. F. George and W. H. Miller, J. Chem. Phys. 57, 2458 (1972).

8. R. A. Marcus, J. Chem. Phys. 54, 3965 (1972).

3. Relativistic

NUCLEUS-NUCLEUS FRAGMENTATION PROBABILITIES ASSUMING EXACT ISOSPIN SYMMETRY

Y. Karant and R. Malfliet

In nucleus-nucleus collision in the 2 GeV/nucleon (lab frame kinetic energy) range, it has been suggested by experimental observations that the fragmentation cross sections for peripheral collisions factorize into a target factor and a projectile factor, each being independent.[1] Since the observed production cross sections for different isotopes show systematic behavior, it seemed of interest to see how much of an effect isospin symmetry might play in these regularities.

To do this, we assumed factorization and exact isospin symmetry. We then considered the possible isospace statistical breakups of isospin 0 nuclides on the assumption that all allowed paths in isospace are equally probable. Using a result of Yeivin and de Shalit,[2] we arrive at a formula for the relative probabilities of different states.

$$P_{II_3}(Z_F) = \sum_F P_{II_3}(F,Z_F) \ ,$$

where

$$P_{II_3}(F,Z_F) = \frac{1}{N} \sum_{I^F I^R}^{I^{F_{max}} I^{R_{max}}} |(I^F I_3^F I^R I_3^R | II_3)|^2 \frac{\gamma_F(I^F)\ _R(I^R)}{\gamma_A(I)},$$

$$\gamma_\alpha(I^\alpha) = \frac{(2I^\alpha + 1)\alpha!}{(\frac{\alpha}{2} - I^\alpha)!(\frac{\alpha}{2} + I^\alpha + 1)},$$

where α denotes F, R, or A, the nucleon number in the fragment, residue, or parent, respectively, and N is the sum of unnormalized probabilities.

To compare this with experiment, we note that experimentally only the charge and mass of the fragments are observed; that is, I_3 and A of the fragments are determined, but the actual I of the states is not observed. Hence, we may identify an experimental state by examining Z (which determines I_3) and A. For ^{16}O, this gives the relative probabilities in Table 1, with the experimental results beside them.

While noting that relative ratios in selected parts of the table are in fair agreement between experiment and this calculation, overall agreement is not good. For example, the experimental ratio between ^3H and ^3He or ^8Li and ^8B is not unity as exact symmetry would require. It is interesting to note that states such as ^{15}C and ^{16}N, which are forbidden by the theory, appear very weakly in the experimental results when compared with the allowed states near to them.

We attribute this disagreement to two causes. First, there is the usual effect from Coulomb symmetry breaking. However, this is minor compared to the second problem, which is that many of the states which are isospin allowed are not observed and are in fact unbound. Experimentally unobserved states were omitted as theoretical entries from Table 1, and the probabilities normalized to only the included states. Binding energy considerations were ignored in the calculation, and thus the calculated but unobserved states should really be intermediates, recoupled in isospace until only observed final states are fed. This was not done, since it is a dynamic symmetry breaking not predicted by exact isospace invariance.

Table 1.

A	Z	P_{theory}	P_{exp}
1	1	5.32(-2)	5.63(-2)
2	1	8.04(-2)	2.46(-1)
3	1	3.72(-2)	8.69(-2)
3	2	3.72(-2)	8.08(-2)
4	2	5.57(-2)	2.85(-1)
6	2	1.58(-2)	1.13(-3)
6	3	4.70(-2)	1.94(-2)
7	3	2.87(-2)	1.50(-2)
7	4	2.87(-2)	1.27(-2)
8	3	1.55(-2)	1.37(-3)
8	5	1.55(-2)	7.85(-4)
9	3	7.02(-3)	3.12(-4)
9	4	2.87(-2)	5.19(-3)
9	6	7.02(-3)	2.41(-4)
10	4	1.57(-2)	2.23(-3)
10	5	4.70(-2)	1.12(-2)
10	6	1.58(-2)	1.59(-3)
11	4	6.59(-3)	1.10(-4)
11	5	3.11(-2)	1.51(-2)
11	6	3.11(-2)	1.13(-2)
12	4	1.70(-3)	2.41(-5)
12	5	1.64(-2)	1.48(-3)
12	6	5.57(-2)	3.58(-2)
12	7	1.64(-2)	3.70(-4)
13	5	5.32(-3)	2.70(-4)
13	6	3.72(-2)	1.55(-2)
13	7	3.72(-2)	4.74(-3)
13	8	5.32(-3)	1.59(-4)
14	6	1.66(-2)	2.94(-3)
14	7	8.04(-2)	2.66(-2)
14	8	1.66(-2)	8.98(-4)
15	6	0	2.55(-5)
15	7	5.32(-2)	3.23(-2)
15	8	5.32(-2)	2.55(-2)
16	7	0	4.33(-5)

References

1. P. J. Lindstrom, D. E. Greiner, H. H. Heckman, B. Cork and F. S. Beiser, LBL-3650.

2. Y. Yeivin and A. de Shalit, Il Nuovo Cimento 1-6, 1147 (1955).

PERIPHERAL HIGH ENERGY COLLISIONS BETWEEN COMPLEX NUCLEI

R. Malfliet and Y. Karant

Recently, some attempts have been made to explain the observed cross sections for the production of specific isotopes in a peripheral heavy ion collision at relativistic energies[1] (2 GeV/nucleon). As proposed by Bowman, Swiatecki and Tsang[2] the process could be viewed as proceeding in two stages called abrasion (the scraping off of nuclear matter in the collision) and ablation (de-excitation of the remaining fragment). The abrasion part of the reaction has been reformulated by Hüfner et al.[3] starting from Glauber's multiple scattering theory. Using a sum rule they calculate the corresponding excitation energies which then dictate the ablation part through nucleon and light ion evaporation. Another model proposed by Lukyanov et al.[4] assumes a certain excitation energy distributed over the

whole fragment which then decays into different smaller fragments with probabilities governed by the Q-values.

Both descriptions depend very much on the amount of excitation energy released in the process and on the way in which it is distributed over the fragment. Therefore, a careful calculation of the abrasion stages seems to be of primary importance. However, both models neglect certain effects, and neither is easily changed to incorporate these neglected effects. On the other hand, because the abrasion-ablation model formally resembles the nuclear cascade-evaporation approach used in light ion reactions, one would be tempted to perform Monte Carlo type calculations. These are usually very tedious and, moreover, the underlying physics is not very transparent. In order to circumvent all these objections we have chosen a completely new approach which is equivalent to the Monte Carlo one, but handles the physics in a clear manner and contains the Hüfner model as a very special case.

Our starting point is the classical Boltzmann equation describing the evolution of the one particle distribution function $N(\vec{r},\vec{v},t)$ (position $\vec{r}$, velocity $\vec{v}$, time t):

$$\left\{\frac{\partial}{\partial t} + \vec{v}\cdot\vec{\nabla}_r + \frac{1}{m}\vec{F}\cdot\vec{\nabla}_v\right\} N(\vec{r},\vec{v},t) = \tag{1}$$

$$\iint d^3v_1 d^3v_1' d^3v' \left[N_1' N' W(\vec{v}_1'\vec{v}' \to \vec{v}_1\vec{v}) - N_1 N W(\vec{v}_1\vec{v} \to \vec{v}_1'\vec{v}')\right].$$

F is the external force (which we will neglect further on) and W denotes the transition probability for scattering of two particles. The right hand side of Eq. (1) indicates the gain and loss due to collisions into or out of the d^3v volume element. As a first application of the Boltzmann equation, we want to consider the case of proton scattering on a target nucleus. Thus the initial condition ($t \to -\infty$) for solving Eq. (1) is simply (in cylindrical coordinates for $\vec{r}$ and spherical ones for $\vec{v}$)

$$N(z,b,v,\Omega_v) = \delta(v - v_0)\delta(1 + \cos\theta_v)\delta(\phi_v)$$

$$[z \to -\infty]$$

where b is the impact parameter.

As it stands, Eq. (1) is a nonlinear partial integro differential equation which presents a non-trivial numerical problem. However, we can incorporate certain reasonable and physically plausible assumptions to reduce the complexity. These are: the so-called coherent approximation, which is to assume that the target nucleus remains in its ground state whenever an interaction has taken place; and there are no collisions between scattered particles (only between a scattered particle and one out of the target density distribution). These approximations should be reasonable in peripheral collisions where not too many scattering events take place. The Boltzmann equation now reduces to a transport equation:

$$\left\{\frac{\partial}{\partial t} + \vec{v}\cdot\vec{\nabla}_r\right\} N(\vec{r},\vec{v},t) = \int d^3v' \rho(\vec{r}) \tag{2}$$

$$\times \left[v' N(\vec{r},\vec{v},t)\sigma(\vec{v}' \to \vec{v}) - v N(\vec{r},\vec{v},t)\sigma(\vec{v} \to \vec{v}')\right]$$

where $\rho(\vec{r})$ represents the target mass distribution, σ denotes the cross section for nucleon-nucleon scattering, and $N(\vec{r},\vec{v},t)$ describes the density distribution of the scattered particles. By defining new coordinate, velocity, and time variables $\vec{r}_s$, $\vec{v}_s$, functions of a parameter s such that

$$\frac{d\vec{r}_s}{ds} = \vec{v}\,, \qquad \vec{r}_s(s=t) = \vec{r}(t)\,,$$

$$\frac{d\vec{v}_s}{ds} = 0\,, \qquad \vec{v}_s(s=t) = \vec{v}(t)\,.$$

we can transform the partial integro-differential Eq. (2) into an integral equation which is easier to handle, and which we are currently solving.

If one would solve Eq. (2) in a probalistic manner, it is completely equivalent to a Monte Carlo procedure. However, a direct (deterministic) solution of Eq. (2) has the advantage that special features like the Pauli exclusion principle, relativistic invariance, and production or absorption processes (for example, of pions) can be incorporated in a rather straightforward manner. Also, we believe that the more complex situation of two colliding heavy ions has a better chance for solution in this framework. Another advantage of this method is that once one knows $N(\vec{r},\vec{v},t)$, it is possible to calculate averages, such as the average number of particles, average velocity, and average temperature, giving one an important link with the vast knowledge developed in statistical mechanics. All the aforementioned aspects are currently under study and the results will be published elsewhere.

Finally, if one would set up an iteration scheme in orders of scattering and one also restricts the cross sections $\sigma(\vec{v}' \to \vec{v})$ to forward angle scattering only, Eq. (2) reduces to (in an obvious notation):

$$\frac{d}{ds} N^{(n)}(s) = \frac{1}{\lambda(s)} N^{(n-1)}(s) - \frac{1}{\lambda(s)} N^{(n)}(s)$$

$$N^{(0)}(s) = \exp\left[\frac{-s}{\lambda(s)}\right];$$

$$\frac{s}{\lambda(s)} = \int v\rho(\vec{r}_s)\,\sigma_{tot}(v_s)ds$$

which has the following general solution

$$N^{(n)}(s) = \left(\frac{s}{\lambda(s)}\right)^n \frac{1}{n!} N^{(0)}(s)\,.$$

This Poisson distribution is equivalent to a binomial distribution and the result is identical to the Hüfner model for abration.[3]

References

1. P. J. Lindstrom, D. E. Greiner, H. H. Heckman, B. Cork and F. S. Bieser, LBL-3650; D. E. Greiner, P. J. Lindstrom, H. H. Heckman, B. Cork and F. S. Bieser, Phys. Rev. Lett. 35, 152 (1975).

2. J. D. Bowman, W. J. Swiatecki, C. F. Tsang, LBL-2908.

3. J. Hüfner, K. Schäfer and B. Schürmann, Phys. Rev. C 12, 1888 (1975).

4. V. K. Lukyanov, A. I. Titov, Phys. Lett. 57B, 10 (1975).

RELATIVISTIC HEAVY ION PERIPHERAL REACTIONS

J. P. Boisson, T. Shibata, J. G. Ioannou-Yannou
and J. O. Rasmussen

Very recently peripheral reactions using relativistic heavy ions have been studied by observing particles[1-3] and γ rays.[4] The studies of projectile fragmentation have shown[1] that the linear momentum transferred from the target to the projectile is small (≲ 200 MeV/c). We have developed two models to try to explain isomeric ratios and cross sections for relativistic carbon beams on various targets.

In the first model (applicable to inelastic scattering) it is supposed that the target nucleus obeys a simple shell model of noninteracting particles in a potential well of Saxon-Woods type and that the grazing heavy-ion collision is reduced to an interaction between two peripheral nucleons. Furthermore, it is supposed that this interaction can be represented by the following time-dependent perturbing potential Gaussian in time and delta function in space at the edge of the nucleus:

$$V(t) = V_1(\vec{r} - \vec{R}_o)\, e^{-t^2/t_o^2} , \qquad (1)$$

where $t_o = r_o/v$, where r_o is the range of the interaction, v is the speed of the projectile, $\vec{R}_o = (R_o,\Omega_o)$ is the point where the interaction takes place, V_1 is the strength of the interaction which can depend upon the speed v of the projectile. As a consequence of this interaction the struck nucleon of the target is scattered from a bound orbit labeled a either to an unoccupied less bound orbit labeled b or to an unbound orbit labeled c.

In the target's shell structure it appears as a particle-hole in the first case and a hole in the second case. We have restricted ourselves to the first case for the calculation of isomeric ratios in the target-nucleus or to test the ISE (inelastic scattering followed by nucleon evaporation) mechanism for lighter-mass products. The transition probability leading to a final spin I is

$$p^I = \sum_{a,b} p^i_{a\to b} \qquad (2)$$

with

$$p^I_{a\to b} = \sum_{m_a,m_b} |\langle J_a M_a J_b M_b | I\ M_a+M_b\rangle|^2 \times P_{(aJ_aM_a)\to(bJ_bM_b)} \qquad (3)$$

where J_a and J_b are the spins of the bound states a and b. Furthermore it follows from the first order time-dependent perturbation theory that

$$P_{(aJ_aM_a)\to(bJ_bM_b)} = \left| \frac{1}{\hbar} \int_{-\infty}^{+\infty} dt\, e^{i(E_b-E_a)t/\hbar} \langle bJ_bM_b|V(t)|aJ_aM_a\rangle \right|^2 \qquad (4)$$

with

$$|\alpha J_\alpha M_\alpha\rangle = \frac{U_\alpha(r)}{r} \sum_{m_\alpha \mu_\alpha} \langle \ell_\alpha m_\alpha \tfrac{1}{2} \mu_\alpha | J_\alpha M_\alpha\rangle\, Y^{m_\alpha}_{\ell_\alpha}\, X^{\Sigma_\alpha}_{1/2} \qquad (5)$$

where $U_\alpha(r)$ is as follows

$$\left\{ \frac{d^2}{dr^2} + \frac{2m}{\hbar^2}(E_\alpha + V(r)) - \frac{\ell_\alpha(\ell_\alpha+1)}{r^2} \right\} U_\alpha(r) = 0 \qquad (6)$$

$$U_\alpha(0) = U_\alpha(\infty) = 0 \qquad (7)$$

In relations (6) and (7) α stands for a or b. The potential V(r) has been chosen according to Ref. 5. From relations (1) and (3-5) it can be shown that

$$p^I_{a\to b} = \frac{(2J_{a+1})(2J_{b+1})}{32\pi} \left[\langle J_a \tfrac{1}{2} J_b \tfrac{1}{2} |11\rangle \frac{V_1 t_o}{\hbar} \times \frac{U_a(R_o)\, U_b(R_o)}{R_o^2} \exp\left\{ -\left[\frac{(E_b-E_a)r_o}{2\hbar c} \right]^2 \right\} \right]^2 \qquad (8)$$

Using relation (8) we have calculated the probability P^I so that the total spin of the target nucleus,

just after the collision has taken place, is I. In these calculations R_o was chosen equal to the radius of the nucleus. The results obtained for ^{208}Pb and ^{88}Sr are indicated in Fig. 1. First we consider the experimental isomeric yield ratio $\sigma(13/2^+)/\sigma(5/2^-)$ in the ^{207}Pb target excited by inelastic scattering of relativistic ^{12}C ions. The in-beam gamma measurements of Shibata et al.[4] give a ratio of 0.84 ± 0.20. The 44 MeV proton ^{208}Pb (p,pn) measurements of Kawakami et al.[6] give 0.48 ± 0.16 and they concluded from various kinds of evidence that the reaction mechanism was predominantly clean knockout (CKO) and not inelastic scattering followed by evaporation (ISE). On Fig. 1b it is seen that the inelastic scattering (IS) gives a higher proportion of high spin states and thus explains the higher isomeric ratio for the inelastic scattering case. The result qualitatively supports the idea of random coupling of the particle and hole angular momentum vectors. Now we consider the $\sigma(7^-)/\sigma(2^+)$ isomeric yield ratio in ^{206}Pb. The 44 MeV proton

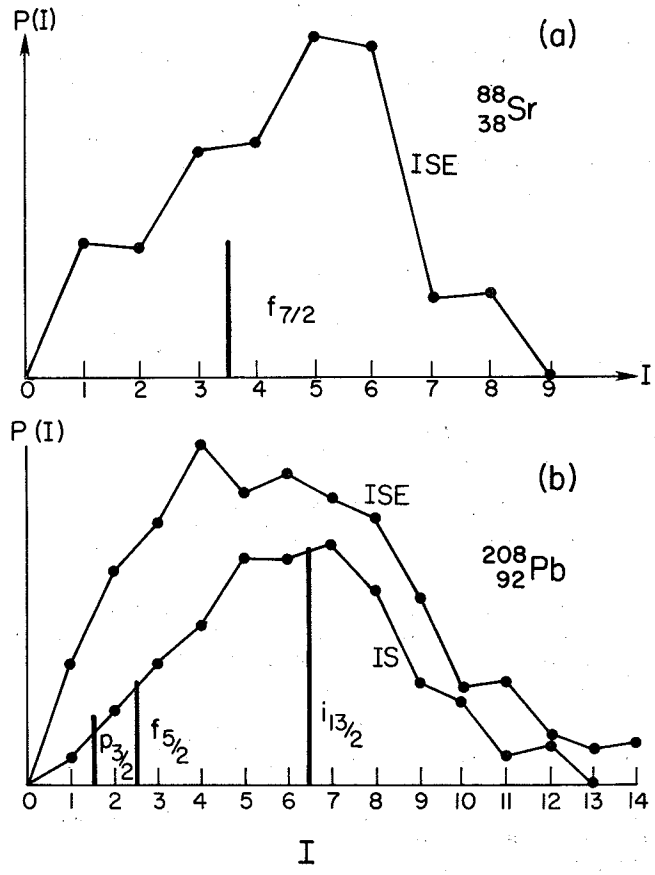

Fig. 1. Transition probability of a level of spin I. The curve of (a) corresponds to the transitions such as $S_{2n} = 20.7$ MeV $\leq E_b - E_a \leq S_{2n} = 36.7$ MeV. The lower curve (IS) of 1-b corresponds to the transitions such as $0 \leq E_b - E_a \leq S_n = 6.7$ MeV. The upper curve (ISE) of (b) corresponds to the transitions such as $S_n = 6.7$ MeV $\leq E_b - E_a \leq S_{2n} = 14.8$ MeV. The length of the vertical lines are proportional to the weighting factor $2I + 1$ of possible states for clean knock out process (CKO). The space between two different values of I is proportional to $A^{-1/3}$.

results of Kawakami et al[6], ^{208}Pb (p,p2n) gave 0.60 ± 0.2 for the ratio and they concluded that the dominant mechanism was knock-out of one neutron followed by evaporation. In the high energy heavy ion studies[4] on the ^{207}Pb target the isomer ratio in ^{206}Pb was 0.4 ± 0.2. Examination of Fig. 1b indicates that the CKO and ISE mechanism should give about the same isomeric ratios in the Pb region (this presumed insensitivity is similar to that observed by Yu, Caretto and Church[7] for ^{197}Au (p,pn) reactions). Within experimental error the low energy proton and high energy heavy-ion isomeric ratios are the same.

We consider now the $\sigma(9/2^+)/\sigma(1/2^-)$ isomeric yield ratio in ^{87}Y formed by ^{85}Rb (α,2n) at 13 to 29 MeV[8], ^{89}Y (p,p2n) at 25 to 80 MeV[9] and the ^{89}Y (^{12}C,X) ^{87}Y at 3 GeV. On the (α,2n) study at 22 MeV the angular momentum distribution in the ^{89}Y compound nucleus should be higher than for our ISE calculation plotted in Fig. 1a. The experimental isomeric ratio are ~ 6, indeed higher. In the low energy portion of the reaction the isomeric ratio levels off at ~ 2 between 50 and 85 MeV, and the 3 GeV ^{12}C results give a still lower ratio of 1.4 ± 0.3. Kawakami et al.[6] concluded that the (p,p2n) reaction on ^{208}Pb went by KOE (knock out followed by evaporation). For a ^{88}Sr target the only contributing neutron orbital for KOE is the f 7/2. Thus KOE should give lower isomeric ratio than either two-neutron knock out or ISE (inelastic scattering followed by two-neutrons evaporation). Thus the 3 GeV ^{12}C ratio suggests dominance of KOE.

The second model involves a classical kinetic theory calculation of the probability of one and only one nucleon-nucleon collision. We consider the target and projectile nuclei as consisting of nucleon-gas clouds, interpenetrating each other, and we assume a Gaussian mass density profile, in the nucleons rest frame, of the form:

$$\rho = \rho_o e^{-r^2/2a^2} \tag{9}$$

where in Eq. (9), ρ_o and a are related through the normalization condition

$$\int \rho d^3r = A \tag{10}$$

by

$$a = \frac{1}{\sqrt{2\pi}} \left(\frac{A}{\rho_o}\right)^{1/3} \tag{11}$$

with A being the atomic number of the nucleus. The values of ρ_o and a can be then calculated using the experimental value of the rms radius of the charge distribution of the nucleus and under the assumption of the same mass and charge distribution in the nucleus.[10] We then proceed to calculate the number of grazing nucleon collisions by employing classical kinetic theory arguments. We thus have that the number of collisions dR, in a volume element $d^3\vec{r}$, and between time t and t+dt, is given by:

$$dR = \sigma_o(\rho_T d^3\cdot\vec{r})(\rho_p v)dt \tag{12}$$

where in Eq. (12) T,p stand for target and projectile respectively, σ_o is the nucleon-nucleon collision cross section, and v is the velocity of the incoming projectile taken to be along the x-axis. Hence, we obtain an expression for the number of collisions $R(b_o)$ as a function of the impact parameter b_o, that is, the distance between the centers of the target and projectile density profiles. Thus,

$$R(b_o) = \sigma_o \frac{A^{4/3}}{2} \rho_o^{2/3} \exp\left[-b_o^2 \pi/2 \left(\frac{\rho_o}{A}\right)^{2/3}\right]. \quad (13)$$

We can therefore calculate the one nucleon collision cross section σ (one nucleon collision) either by equating it, as a first approximation to the area between two concentric circles with radii equal to the impact parameters corresponding to a number of collisions R = 0.5 and R = 1.5 respectively, or by assuming a Poisson distribution of the collision events and proceeding accordingly. In the former case, we have:

$$\sigma(\text{one nucleon collision}) = [[b_o(R=0.5)]^2 - [b_o(R=1.5)]^2] . \quad (14)$$

In the latter case, the probability P(m) of m collisions is given by:

$$p(m) = \frac{M^m e^{-M}}{m!} \quad (15)$$

with $M = R(b_o)$, so that the cross section is given by:

$$\sigma(\text{one nucleon collision}) = \int_{b_o=0}^{\infty} 2 b_o db_o p(m=1) = \frac{\pi}{C_2}[1 - e^{-C_1}] \quad (16)$$

where in Eq. (16)

$$C_1 = \sigma_o \frac{A^{4/3}}{2} \rho_o^{2/3}, \qquad C_2 = \frac{\pi}{2} \frac{\rho_o}{A}^{2/3}.$$

We apply the above results in the case of ^{12}C on ^{12}C, since this is a well experimentally studied process, so that we can compare results. From the literature[10,11] the pertinent values of σ_o and rms charge radius are:

$$\sigma_o \cong 16 \text{ mb (relativistic energies)}$$
$$[\langle r^2 \rangle]^{1/2} = 2.37 \times 10^{-13} \text{ cm for } ^{12}C . \quad (17)$$

Thus we have:
Using Eq. (14), we get: σ = 258 mb (18)
Using Eq. (16), we get: σ = 235 mb (19)

We compare Eqs. (18) and (19) with related experimental cross sections.[2,4] Table 1 gives for ^{12}C projectile on ^{12}C the cross section for one- and two-nucleon removal reaction. Clearly the experimental cross section for one- and two-removal product is lower than that given by Eqs. (18) or (19). It may be argued that inelastic scattering should be included in the total, and it may be around 24 mb, the cross section for the $5/2 \rightarrow 1/2$ (ground) transition in ^{19}F with 1.05 GeV/n ^{12}C on teflon. Probably the theoretical cross section needs to be reduced by a geometrical factor, so as to exclude collisions in which either nucleon enters the nucleus and causes a further reaction. These refinements are being considered.

Table 1. Cross sections by 1.05 GeV/N carbon bombardment on carbon.

Product	Cross Section (mb)[a]
^{11}C	44.7 ± 2.8
^{10}C	4.44 ± 0.24
^{11}B	48.6 ± 2.4
^{10}B	27.9 ± 2.2
^{10}Be	5.34 ± 0.29
sum	131

[a] Ref. 2.

References

1. D. E. Greiner, P. J. Lindstrom, H. H. Heckman, B. Cork and F. S. Bieser, Phys. Rev. Lett. 35, 152 (1975).

2. P. J. Lindstrom, D. E. Greiner, H. H. Heckman, B. Cork and F. S. Bieser, LBL-3650 (1975).

3. A. M. Zebelman, A. M. Poskanzer, J. D. Bowman, G. R. Sextro and V. E. Viola, Phys. Rev. C 11, 1280 (1975).

4. T. Shibata, H. Ejiri, R. E. Anholt, H. R. Bowman, J. G. Ioannou-Yannou, J. O. Rasmussen, E. A. Rauscher and S. Nagamiya, in this Annual Report (to be published in Nucl. Phys. A).

5. V. G. Soloviev, Theory of Complex Nuclei, translated by P. Vogel (Pergamon Press, New York, 1976).

6. H. Kawakami, M. Koike, K. Komura, M. Sakai, N. Yoshikawa, R. Donangelo and J. O. Rasmussen, Nucl. Phys. A262, 52 (1976).

7. Y. W. Yu, A. A. Caretto, Jr. and L. B. Church, Nucl. Phys. A152, 295 (1970).

8. R. Van den Bosch, L. Haskin and J. C. Norman, Phys. Rev. B137, 1134 (1965).

9. G. B. Saha, N. T. Porile and L. Yaffe, Phys. Rev. B144, 962 (1966).

10. R. Hofstader, Ann. Rev. Nucl. Sci. 7, 231 (1957).

11. N. Metropolis et al., Phys. Rev. 110, 185 (1958).

B. NUCLEAR STRUCTURE

1. Microscopic

EVIDENCE FOR TRIAXIAL SHAPES IN Pt NUCLEI*

J. Meyer-ter-Vehn†

From a theoretical standpoint, there are significant advantages in studying the motion of a high-j particle (e.g. $i_{13/2}$ or $h_{11/2}$) around a deformed core. First, these high j-orbitals have unique parity and hence the high-j system may be treated to a good approximation by considering only a single j-shell. Furthermore, positive (negative) parity states in odd nuclei in the mass region $150 < A < 200$ may be immediately associated with a predominant $\nu i_{13/2}$ ($\pi h_{11/2}$ or $\pi h_{9/2}$) component. Second, the large Coriolis force acting on the high-j particle tends to align its spin along the rotation vector, giving rise to characteristic decoupled level structures.[1] The degree to which the particle couples to or decouples from the intrinsic axes of the core strongly depends on the shape of the core, not only on its deformation β but also in a rather sensitive way on the γ-parameter which distinguishes between prolate ($\gamma = 0°$), oblate ($\gamma = 60°$), and various asymmetric, triaxial ($0 < \gamma < 60°$) shapes.[2,3] This leads to striking variations of the odd-A spectrum as a function of γ. As one of the characteristic features, second and third states of the same spin are considerably lowered in energy for triaxial shapes, parallel to the 2_2^+, 3_1^+, 4_2^+... states of the even core. This is important for odd-A Pt nuclei.

A number of these features have previously been noted[2,3] in the $h_{11/2}$ and $h_{9/2}$ proton structures of some odd-A Ir, Au, and Tl nuclei. It thus appears that the shape change from the axially symmetric deformed rare-earths to the spherical Pb nuclei proceeds through a triaxial region. The levels of the doubly even Pt nuclei which lie in this transitional region do indeed suggest triaxial shapes, with the 2_2^+ levels lying below the 4_1^+ levels.

In general, all the odd Pt nuclei we have studied have similar positive parity structures, a distinctive feature being the occurrence of decoupled $i_{13/2}$ bands with spacings very similar to those of the even-even neighbors. Many other positive parity levels are also observed, especially in ^{191}Pt, which we have also studied in the radioactive decay of ^{191}Au. In fact, the combined ^{191}Pt results provide the most complete set of data for an $i_{13/2}$ family and therefore a new, important test of the model of a high-j hole or particle coupled to a triaxial core. It should be noted that the Fermi surface lies well within the $i_{13/2}$ shell in Pt nuclei, a situation not hitherto encountered in tests of this model.

A partial level scheme for ^{191}Pt containing only the positive parity levels is shown on the left of Fig. 1. Levels in columns A, B, and C were observed in the (α,xn) experiments; the levels in column D plus the $13/2^+$ and $11/2^+$ levels of columns A and B were populated in the decay of ^{191}Au. The right side of Fig. 1 shows levels expected from coupling an $i_{13/2}$ hole to a triaxial core calculated

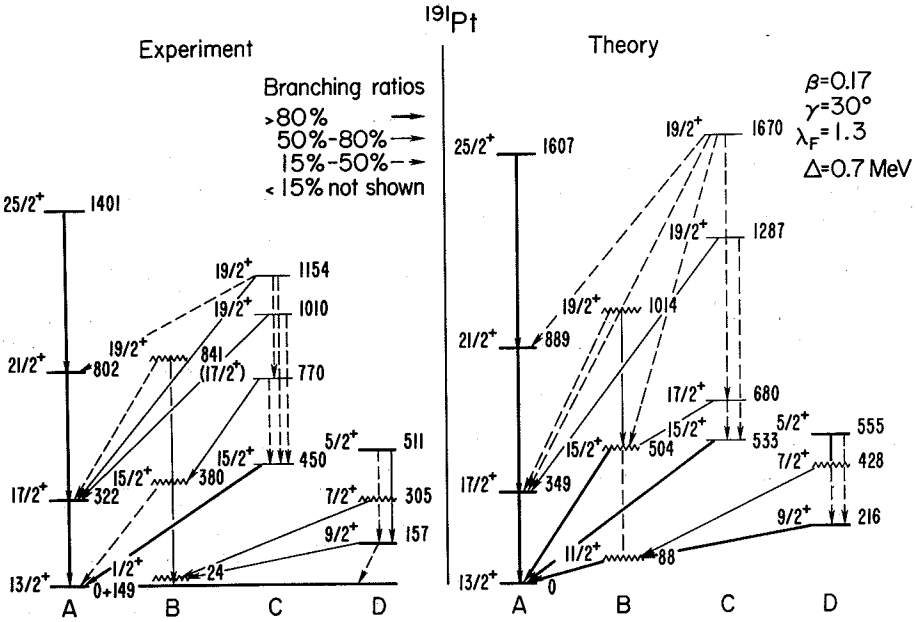

Fig. 1. Comparison of experimental and theoretical energies and branching ratios of positive parity levels in ^{191}Pt. Here zero energy is defined by the $13/2^+$ level (E_{exp} = 149.0 KeV). The $29/2^+$ and $(33/2^+)$ members of the decoupled band located at 2084 and 2791 keV are now shown. Parameters β, γ, λF and Δ, used in the calculation are defined in Ref. 3. Theoretical transition intensities were determined using calculated B(M1) and B(E2) values, but experimental energies. Members of the favored band are denoted by thick lines and those of the unfavored band by wavy lines. (XBL 761-2134)

as described in Ref. 3. The parameters β and γ were determined from the neighboring even cores. The Fermi level was located between the fifth and sixth members of the $i_{13/2}$ multiplet ($\nu = 5$ and $\nu = 5$ levels, in the notation of Ref. 3) by examining the single particle levels at $\gamma = 30°$ of Larsson.[5] The Coriolis matrix elements were attenuated by using the modified pairing factor, $(u_1u_2 + v_1v_2)$,[5] following the ad hoc prescription of Stephens and Simon.[6] This had the effect of reducing the matrix elements connecting states across the Fermi surface, a procedure previously found necessary for fitting $i_{13/2}$ bands in the rare-earth region.

The arrangement of levels in Fig. 1 has been guided by the main decay lines of the experimental spectrum and the calculated results. Although the wavefunctions of the particle-triaxial core model consist of a highly complicated mixture of different Nilsson bands and corresponding odd-A γ-bands, there are some approximate features which may give an intuitive picture. (1) Column A represents the decoupled yrast band corresponding to a maximum alignment of the $j = 13/2$ spin with the core angular momentum R: the 9/2 and 5/2 states in column D can be interpreted as anti-aligned states of the same band. (2) Similarly, column B and the anti-aligned 7/2 state of column D constitute a second (unfavored) decoupled band. It corresponds to incomplete alignment with a j projection of approximately 11/2 on R. In the $h_{11/2}$ and $h_{9/2}$ level families observed in neighboring Ir and Au nuclei, these unfavored levels appear much higher in energy. They are lowered in ^{191}Pt due to incomplete filling of the $j = 13/2$ shell by core particles and the resultant effect of the Pauli principle. This second decoupled band within the same j-shell family is found here for the first time. Similar bands have been observed in neighboring odd-A Pt isotopes and should also occur in Hg isotopes and in other mass regions. (3) The levels in column C reflect the additional rotational degrees of freedom due to triaxiality; levels with the same spin lie at much higher excitation (1.7 - 4.7 MeV) in calculations with axially symmetric shapes. There are additional levels in the theoretical spectrum below the 21/2 state which are not shown in Fig. 1: two 9/2 states at 367 and 624 keV, two 11/2 states at 574 and 747 keV, and three 13/2 states at 334, 730, and 875 keV. However, these are not expected to be populated with observable strengths in the experiments performed.

Figure 1 shows clearly that the calculated level energies and transition branching ratios reproduce very well the general trend of the data. The signs of the calculated E2/M1 mixing ratios also agree with experiment, where measurable. Considering that the parameters entering the calculation were obtained from "external" data and not otherwise adjusted to produce detailed fits here, the agreement between theory and experiment is excellent.

Footnotes and References

*Condensed from LBL-4349, submitted to Phys. Rev. Lett.

†Present address: SIN, CH 5234, Villigen, Switzerland.

1. F. S. Stephens, Rev. Mod. Phys. 47, 43 (1975).

2. J. Meyer-ter-Vehn, F. S. Stephens and R. M. Diamond, Phys. Rev. Lett. 32, 1383 (1974).

3. J. Meyer-ter-Vehn, Nucl. Phys. A249, 111 (1975); Ibid, 141 (1975).

4. M. Piiparinen, J. C. Cunnane, P. J. Daly, C. L. Dors, F. M. Bernthal and T. L. Khoo, Phys. Rev. Lett. 34, 1110 (1975).

5. S. E. Larsson, Physica Scripta 8, 17 (1973).

6. F. S. Stephens and R. S. Simon, Nucl. Phys. A183, 257 (1972).

SYMMETRY BETWEEN PARTICLE AND HOLE LEVELS SYSTEMS IN ^{189}Au*

J. L. Wood,† R. W. Fink,† and Meyer-ter-Vehn§

The $h_{11/2}$ and $h_{9/2}$ level systems in ^{189}Au have been studied both experimentally and theoretically. These negative parity families are now known in a number of odd-A Ir, Au, and Tl isotopes and are attributed to a hole in the $h_{11/2}$ shell and a particle in the $h_{9/2}$ shell, respectively. Going from ^{187}Ir to ^{195}Au, for example, the ordering of levels in these families indicates that the coupling to the core undergoes smooth changes as follows:

$h_{9/2}$ particle: decoupled → strongly coupled

$h_{11/2}$ hole: strongly coupled → decoupled

The different ordering of the levels has been explained in terms of the particle-rotor model.[1] More recently this model has been generalized for triaxially deformed cores.[2] The complementary behavior of the particle and the hole bands in ^{189}Au can be understood as a manifestation of the particle-hole symmetry underlying this model. The objective of this letter is to evaluate the available experimental data on the two level systems in ^{189}Au and to show that if scaled, they have almost identical energy spacings and therefore display this symmetry in a very striking way.

The excited states of ^{189}Au have been studied recently at UNISOR,[3,4] and at Orsay[5] by population through the β^+-decay of ^{189m}Hg(9m) and ^{189g}Hg(8m) and at Orsay[6] by in-beam spectroscopy using the reaction ^{181}Ta(^{12}C,4n)^{189}Au. The levels schemes based on the Orsay work differ from Fig. 1 in that, with reference to the Orsay schemes: the level at

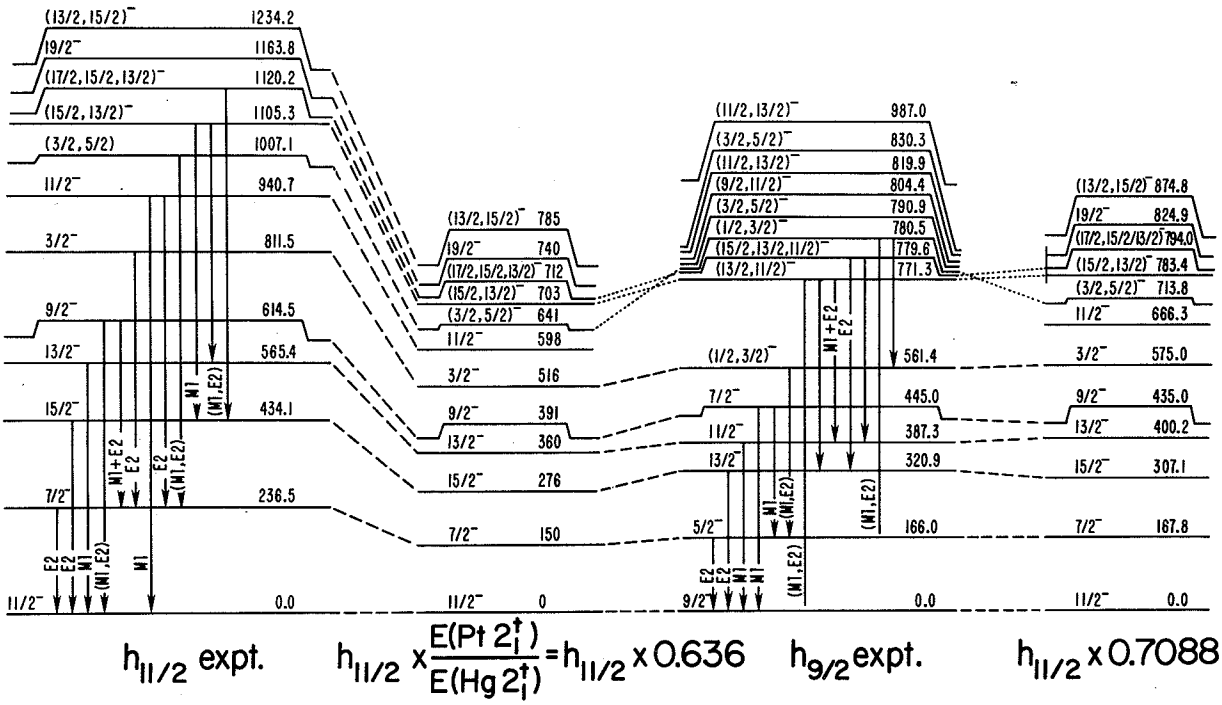

Fig. 1. The experimental $h_{11/2}$ and $h_{9/2}$ bands are based on the results of UNISOR experiments, together with the $10/2^-$ member assigned to the $h_{11/2}$ band in Ref. 6. Discrepancies between these data and those of Refs. 5 and 6 are discussed in the text. Multipolarities are included where known, and if ambiguous, are denoted (M1,E2) to mean an undetermined M1/E2 admixture, the ambiguity generally being due to the complexity of the spectra. Possible spin assignments rely mainly on multipolarities, population systematics from the decays of ^{189m}Hg$(13/2^+)$ and ^{189g}Hg$(3/2^-)$ and for the $h_{11/2}$ band, further support from the strong $h_{11/2}$ band energy systematics through $^{189\text{-}195}$Au.[3] The energy scale compression factors (0.636 and 0.7088) for the $h_{11/2}$ band are determined by the energy ratio of the 2_1^+ state in the effective cores (^{190}Hg for $h_{11/2}$, ^{188}Pt for $h_{9/2}$) and by an ad hoc ratio that gives the closest analogy for the two bands, respectively. In the region of the j+4 states, the particle-hole symmetry is less clear and transitions are only included for levels that have tentatively identified analogs: these levels are connected by dots instead of dashes. (XBL 761-2135)

1007.1 keV in the $h_{11/2}$ band is assigned $11/2^-$ (note that the energies of the levels within each band are specified relative to the band head); the $17/2^-$ member of the $h_{11/2}$ band is placed at 1472.6 keV; and no spin assignments are made to the levels at 1105.3, 1120.2, and 1234.2 keV. Further, in the $h_{9/2}$ band, the Orsay schemes do not contain the levels at 561.4, 780.5, 790.9, 830.3, and 987.0 keV; they have an assignment of $17/2^-$ to the 779.6 keV level; and they have no spin assignment for the level at 771.3 keV. Finally, in the $_{9/2}$ band, the 395.4 keV γ-line (the transition between the $1/2^-$ and $5/2^-$ levels in the UNISOR scheme) is reported in the Orsay work to be M1 multipolarity. Other discrepancies include insufficient evidence in the UNISOR work to support the level reported in the Orsay measurements at 990.6 keV in the $h_{9/2}$ band and minor ambiguities such as the assignment of γ-lines to more than one location. A detailed discussion of these differences is contained in the paper this report was condensed from.

The theoretical interpretation of these results is based on the model of a particle (or hole) coupled to a triaxially deformed core.[2] It has been shown that the model describes well the low-energy unique parity states of transitional odd-A nuclei in the A = 190 mass region.[2] The model spectrum $E_I(\beta,\gamma,\lambda_F)$ depends on the deformation β, the shape asymmetry γ, and the Fermi energy λ_F.

(The subscript I is the nuclear spin.) Particle and hole spectra are connected by the symmetry relation

$$E_I(\beta,\gamma,j\text{-particle}) = E_I(\beta,\gamma,j\text{-hole})$$

where λ_F is located well below the j-shell of the odd nucleon for the particle spectrum and well above the j-shell for the hole spectrum. This condition is essentially met in the Au isotopes with respect to the $h_{9/2}$ shell (λ_F below) and the $h_{11/2}$ shell (λ_F above). Taking into account that E_I is weakly dependent on j and depends on β strongly only through a scale factor $1/\beta^2$, but much less otherwise, we have approximately

$$\beta^2_{h_{9/2}} \cdot E_I(\gamma, h_{9/2}\text{ particle}) =$$

$$\beta^2_{h_{11/2}} \cdot E_{I+1}(60-\gamma, h_{11/2}\text{ hole}).$$

Based on this relation, the close resemblance of the proportionally scaled $h_{9/2}$ and $h_{11/2}$ systems in ^{189}Au (see Fig. 1) indicates that $\gamma_{h_{9/2}} = 60° - \gamma_{h_{11/2}}$. This includes the possibility of axially symmetric shapes, e.g., a prolate ($\gamma = 0°$) shape for the $h_{9/2}$ and an oblate ($\gamma = 60°$) shape for the $h_{11/2}$ system, and also permits an asymmetric shape with the same $\gamma_{h_{9/2}} = \gamma_{h_{11/2}} = 30°$ for both systems. The actual level spacings of the $h_{11/2}$ spectrum, which appear to be almost identical for $^{189\text{-}195}$Au,[2,3] indicates $\gamma_{h_{11/2}} = (37 \pm 2)°$. Consequently, we deduce $\gamma_{h_{9/2}} = (23 \pm 2)°$ for ^{189}Au. These values should be compared with $\gamma = (24 \pm 2)°$ derived from the ^{188}Pt spectrum and $\gamma = (38 \pm 2)°$ derived from the ^{190}Hg spectrum, specifically from the first and second 2^+ energies. Also, the ratio of the first 2^+ energies $E_2(^{188}\text{Pt})/E_2(^{190}\text{Hg}) = 0.64$ is close to the scaling ratio $E_I(h_{9/2})/E_{I+1}(h_{11/2}) = 0.7088$, which is found to give the best match in ^{189}Au (see Fig. 1).

From these results it is concluded that the $h_{9/2}$ and $h_{11/2}$ systems in ^{189}Au are based on different shapes (asymmetric prolate and asymmetric oblate) which are essentially those of the ^{188}Pt and ^{190}Hg cores, respectively. In the Orsay experiments[5] it was observed that the M1 transition between the $h_{9/2}$ and $h_{11/2}$ band heads is retarded by a factor 15000 relative to the Weisskopf single-particle estimate, and the relationship of these bands to the neighboring doubly-even cores was recognized. Interpreted within the frame of the triaxial particle-core model, the striking similarity in the level spacings of the two systems reflects a basic particle-hole symmetry and follows from the fact that the γ-values in ^{188}Pt and ^{190}Hg happen to lie symmetrically about $\gamma = 30°$. (It should be noted that the triaxial rotor spectrum of a doubly-even nucleus has reflection symmetry about $\gamma = 30°$ and thus, the odd-A spectrum must be used to determine whether the nuclear shape is prolate or oblate.) Comparing this model with the Alaga model, which also describes the $h_{11/2}$ spectra well in odd-A Au isotopes,[7] one notices that a corresponding symmetry relating the $h_{11/2}$ levels as 3-proton hole clusters coupled to phonons in closed-shell Pb and should treat (not done so far) the $h_{9/2}$ levels as 4-holes-1-particle clusters. The microscopic model of Hecht, based upon the pseudo SU_3 coupling scheme[8] appears to have the same limitation. The particle-hole symmetry arises under the assumption that the open-shell nuclei ^{188}Pt and ^{190}Hg are stable enough to be used as effective cores: this is done in the particle-core model by treating the core correlations in terms of triaxial shapes. The ^{189}Au spectrum provides strong evidence that such a treatment is justified and further, that the shapes of the even-A nuclei in this mass region – or at least their averaged parameters – are relatively stable, in contrast to general belief.

Footnotes and References

*Condensed from LBL-4350, submitted to Phys. Lett.

†Present address: Georgia Institute of Technology, Atlanta, Georgia.

‡Present address: SIN, CH 5234, Villigen, Switzerland.

1. F. S. Stephens, Revs. Mod. Phys. 47, 43 (1975).

2. J. Meyer-ter-Vehn, F. S. Stephens, and R. M. Diamond, Phys. Rev. Lett. 32, 1383 (1974); J. Meyer-ter-Vehn, Nucl. Phys. A249, 111 (1975); Ibid, 141 (1975).

3. E. F. Zganjar et al., Phys. Lett. 58B, 159 (1975).

4. J. L. Wood, E. F. Zganjar, and UNISOR coworkers, in preparation.

5. V. Berg, R. Foucher, and Å. Höglund, Nucl. Phys. A244, 462 (1975).

6. M. A. Deleplanque, C. Gerschel, N. Perrin, and V. Berg, Nucl. Phys. A249, 366 (1975).

7. V. Paar, Ch. Vieu, and J. S. Dionisio, preprint (1975).

8. K. T. Hecht, Phys. Lett. 58B, 253 (1975).

CROSSING OF ROTATIONAL BANDS IN THE CRANKING MODEL AND HIGH SPIN STATES

H. J. Mang*

The calculations which are reported here have been performed within the framework of the self-consistent cranking model.[1] Nevertheless the results can be interpreted as well as the consequence of the crossing of two bands, the ground state band, and the so called aligned band.[2]

The basic equations are constrained HFB equations which in a condensed notation can be written as

$$\delta\langle\Phi|H|\Phi\rangle = 0$$

$$\langle\Phi|Np|\Phi\rangle = Z\langle\Phi|Nn|\Phi\rangle = A - Z$$

$$\langle\Phi|Jx|\Phi\rangle = \sqrt{J(J+1) - \langle\Phi|J_z^2|\Phi\rangle}$$

where p refers to protons, n to neutrons and J is the total angular momentum. The quasi-particle operators $\beta\mu$ to which $|\Phi\rangle$ is the vacuum state are expanded in terms of particle operators C_k Bogolyubov Transformation. The transformation which solves Eq. (1) is determined by iteration. First a $|\Phi\rangle$ is constructed that fulfills the constraints. Then in each step of the iteration a Thouless-Transformation[3] is performed such that the energy decreases and the constraints remain unchanged. No Lagrangian multipliers are introduced. Fig. 1 shows the results obtained for ^{164}Er. A pairing plus quadrupole-quadrupole interaction was used and the configuration space was the same as in Ref. 1. In order to account for the effect of a core of 40 protons and 70 neutrons a moment of inertia of the core θ core = 6 MeV^{-1} was added. The characteristic features of the experimental data[4] are well reproduced. Up to angular momentum 14 the yrast states belong to the ground band and from 16 on to the aligned band.

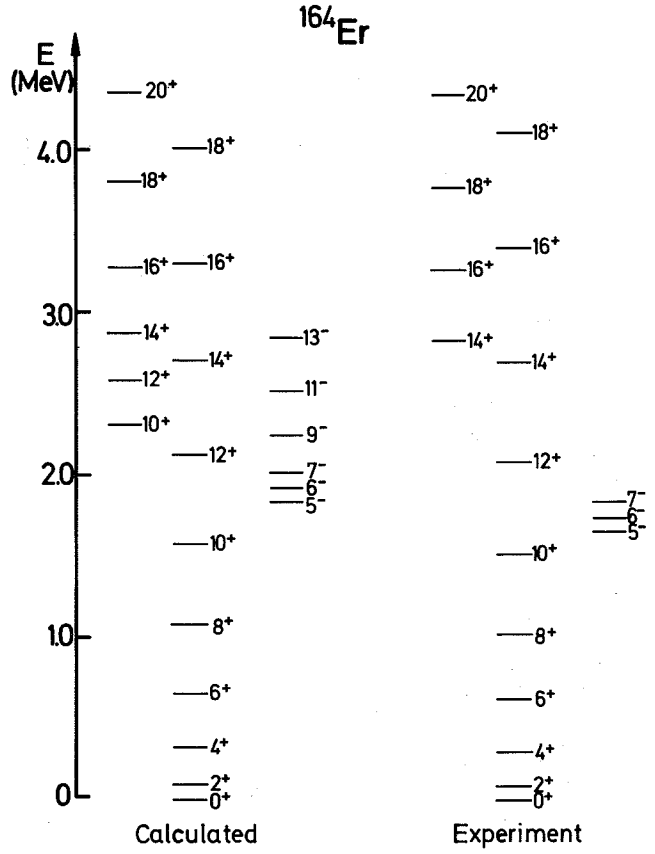

Fig. 1. (XBL 766-8280)

Footnotes and References

*Present address: Technische Universität München, D 8046 Garching, Germany.

1. H. J. Mang, Physics Reports Vol. 18, C No. 6 (1975).

2. F. S. Stephens, in Proc. Intern. Conf. on Nuclear Physics, Munich, Vol. 2 (1973), p. 367.

3. D. J. Thouless, The Quantum Mechanics of Many Body Systems (Academic Press, New York and London, 1961).

4. F. S. Stephens and R. Diamond, private communication.

SIMPLE DYNAMICAL MODELS INCLUDING PAIRING RESIDUAL INTERACTION*

J. Blocki† and H. Flocard‡

The microscopic description of the dynamics of a many nucleon system has been extensively investigated during recent years.[1] Significant progress has been achieved recently with the time dependent Hartree-Fock (TDHF) method that allows for a self-consistent description of the dynamics of the nucleus.[2-4] However, in this method, the residual interactions are neglected. This together with the symmetries imposed in the calculations, leads to the unpleasant feature that a system even moving infinitely slowly would not end up in its ground state. This will appear each time two single particle levels with different quantum numbers (and therefore no possibility of transition between them)

cross. Such a limitation of the TDHF method could for example decrease noticeably the calculated cross section of the compound nucleus formation in heavy ion collisions and it is likely to have a more serious effect for a slower collective motion like the one undergone by the nucleus during the fission process.

In order to avoid these difficulties one could either lift all the symmetries imposed on the system which leads to a large computational problem or introduce (in as simple as possible a way) a residual interaction that allowed for transitions between levels with different quantum numbers.

It is our aim to show that the second alternative can be achieved by using the pairing residual interaction. We have selected two models, which have been of great use in the static calculations including pairing: the constant gap Δ model and the constant pairing strength G model.

Starting from a variational principle we arrive at sets of coupled equations which contain the TDHF equations as a particular case plus simple equations governing the occupation probabilities of each single particle level.

By applying the equations to a simple two level model it is possible to show the connection with the Landau-Zener theory. Going to the many level problem one can show that each level undergoes a Landau-Zener type transition to a fictitious level symmetric with respect to the Fermi level and with a coupling strength determined by the magnitude of the gap. Formally the only difference between the two pairing models lies in the fact that the gap is calculated self-consistently from the pairing tensor solution when one is working with the constant G interaction.

From the solutions of the two level model it is also possible to extract the quantitative features of the transition induced by the two pairing models. Using the constant G interaction the transition between two unperturbed levels is weaker (it requires a slower motion) and also it is easier to populate the lower perturbed level contrary to the Landau-Zener type (and constant gap) coupling which gives equal probabilities of a jump from either perturbed level to the other one. Both pairing residual interaction models can be used in a phenomenological way to allow for the interaction between levels with different quantum numbers, however the constant gap formulation is much simpler. In this case the gap should be partly interpreted as a symmetry breaking matrix element of the field.

Footnotes and References

*Condensed from LBL-5016.

†Permanent address: Institute of Nuclear Research, 05-400 Swierk, Poland.

‡Permanent address: Division de Physique Theorique (laboratoire associé au CNRS) Institut de Physique Nucleaire BP no. 1, 91406 Orsay, France.

1. S. E. Koonin and J. R. Nix, Phys. Rev. C13, 209 (1976), and references quoted therein.

2. P. A. M. Bonche, S. E. Koonin and J. W. Negele, Phys. Rev. C13, 1226 (1976).

3. P. A. M. Bonche, S. E. Koonin, Proceedings from the Hirschegg Meeting (1976).

4. S. E. Koonin, Proceedings from the Hirschegg Meeting (1976).

TIME DEPENDENT HARTREE-FOCK CALCULATION OF NUCLEAR COLLECTIVE MOTIONS

J. Blocki* and H. Flocard†

The TDHF method[1] provides a way to explore in a both microscopic and self-consistent manner the dynamics of the nuclear motion. The method is microscopic because it uses as nuclear wavefunction a Slater determinant and therefore exhibits all the individual nuclear degrees of freedom. The Pauli principle is also properly taken into account. The method is self-consistent because one treats an N body problem and uses as a starting point a Hamiltonian with a two-body interaction. From this two-body interaction and the one-body density operator, associated with the Slater determinant, one constructs a one-body Hartree-Fock Hamiltonian. This Hamiltonian in turn governs the motion of each individual orbit by simple one-body time dependent Schrödinger equations. This method evidently relies on the validity of the nuclear shell model and assumes that the main effect of the nucleon-nucleon interactions is to generate a potential well which in turn determines the motion of the nucleons. The complicated N body problem is thus reduced to a set of coupled nonlinear equations whose solution appears feasible with the presently available computational facilities.

Because the individual nuclear degrees of freedom are explicitly taken into account in the TDHF equations, one can hope to describe both the coherent nuclear motion, also called collective modes, and the incoherent motions that are generally associated with the name of heat. The study of the correlations between these two types of nuclear motion, which introduces the notion of viscous damping of the collective modes, is also evidently within the range of the TDHF model.

We solve the TDHF equations by expanding the Hartree-Fock wavefunctions on a basis. The partial derivative equations are thus reduced to coupled differential equations of first order in time derivation. Presently our code uses an oscillator basis whose deformation can be adjusted to the

particular motion that is studied. Fourteen oscillator shells have been included in the basis which appears sufficient to study vibrations and the fission of any known nuclear system. A further improvement will be the introduction of a basis with a two center degree of freedom which will allow the study of heavy-ion reactions. The two-body interaction used is the Skyrme interaction and direct and exchange Coulomb potentials have been included. The numerical method used to calculate the time propagation is the usual Crank-Nicholson method. Particular attention has been devoted to the conservation of the total energy which is presently insured with a relative precision of 10^{-8}. Finally a TDHF + BCS code has been constructed. One is able to study the time evolution of a system having a Bogolyubov wavefunction. This enlargement of the TDHF method appears particularly useful for heavy systems where a simple Slater determinant is too restricted a wavefunction in view of the high density of individual levels near the Fermi surface.

Currently the main emphasis is on the study of the vibrational modes of the nuclei and the fission process. We are interested in the study of the viscous phenomena that could occur in such collective motions of the nuclei. A preliminary study of the light nuclei ($A \leqslant 80$) has shown no trace of viscosity in the monopole and quadrupole modes. Even when some trend appears indicating an exchange of energy between coherent and incoherent motions of the nucleons such an exchange is periodic (and therefore reversible) with a period of about 10^{-21} sec. This is probably not too surprising since the systems that we have studied up to now have too few degrees of freedom and a statistical irreversibility is unlikely to occur. We have some hope that in heavier nuclear systems the typical time necessary to have the energy associated to the incoherent motion of the nucleons converted in a collective motion will become much longer than the interesting nuclear times so that one could reasonably introduce the notion of irreversibility and viscosity. Of particular interest will be the study of possible viscous phenomena in the fission process where their existence still remains an open experimental and theoretical question.

Footnotes and References

*Permanent address: Institute of Nuclear Research, 05-400 Swierk, Poland.

†Permanent address: Division de Physique Theorique (laboratoire associé au CNRS), Institut de Physique Nucleaire Bp no. 1, 91406 Orsay, France.

1. P. A. M. Dirac, Proc. Camb. Phil. Soc. 26, 376 (1930).

ON THE SOLUTION OF CONSTRAINED HARTREE-FOCK-BOGOLYUBOV EQUATIONS*

H. J. Mang† B. Samadi,† and P. Ring†

The interest in solutions of the HFB equations stems mainly from the success of the theory in the calculation of energy surfaces[1] and properties of rotational states.[2] In the first case the expectation value of the quadrupole operator $\hat{Q}$, and if necessary of higher multipole operators, must be constrained whereas in the second case the expectation value of the angular momentum operator must be fixed at a given value. The conventional technique for solving such problems is to introduce a Lagrangian multiplier, i.e., to add a term $-\omega\hat{J}_x$ or $-\eta\hat{Q}$ to the Hamiltonian. Difficulties arise if the expectation value is not a single valued function of the Lagrangian multiplier. They can be overcome by using a quadratic constraint like $c(\hat{Q} - Q_0)^2$, which is added to the energy expression to be varied. In this paper a method is described which also circumvents such difficulties and has moreover the advantage that the energy is only calculated for a single given value of the expectation value of the constraining operator. For instance, in the case of rotational states one obtains solutions which exactly fulfil

$$\langle \hat{J}_x \rangle = J(J+1) - \langle J_z^2 \rangle \qquad (1)$$

and these are the only physically significant solutions. There is no need to do a calculation for several values of the Lagrangian multiplier and then interpolate between them.

For convenience the important equations of HFB theory are given. Details can be found in Ref. 2 and the literature cited there.

A Bogolyubov transformation is defined by

$$\alpha_\nu^+ = \sum_k A_{k\nu} C_k^+ + B_{k\nu} C_k \quad .$$

The coefficients $A_{k\nu}$ and $B_{k\nu}$ are only restricted by the requirement that the set of Fermi operators C_k^+, C_k are transformed into a new set of Fermi operators α_ν^+, α_ν. To each set of Fermi operators α_ν^+, α_ν belongs a uniquely defined vacuum state $|\Phi\rangle$ with the property

$$\alpha_\nu |\Phi\rangle = 0.$$

Given a Hamiltonian H one may now ask the question which vacuum state $|\Phi\rangle$ minimizes the expectation value $\langle\Phi|H|\Phi\rangle$. The equations of this variation principle are most conveniently formulated by transforming the Hamiltonian H into the quasiparticle representation

$$H = Ho + H_{11} + H_{20} + H_{22} + H_{31} + H_{40} \quad .$$

The equations to start with are

$$\frac{\partial}{\partial C_{\mu\nu}} \langle\Phi|H|\Phi\rangle = (H_{20})_{\mu\nu}$$

$$\frac{\partial}{\partial C_{\mu\nu}} \langle\Phi|\hat{J}|\Phi\rangle = (J_{20})_{\mu\nu}$$

$$\Delta E = \sum_{\mu\nu} C_{\mu\nu} (H_{20})_{\mu\nu} + O(C_{\mu\nu}^2)$$

$$\Delta J = \sum_{\mu\nu} C_{\mu\nu} (J_{20})_{\mu\nu} + O(C_{\mu\nu}^2) \quad .$$

From now only the terms linear in $C_{\mu\nu}$ will be taken into account. Clearly ΔE is negative and has its greatest absolute value if one sets

$$C_{\mu\nu} = -\eta (H_{20})_{\mu\nu} \qquad \eta > 0 \quad .$$

Then ΔJ is given by

$$\Delta J = -\eta \sum_{\mu\nu} (H_{20})_{\mu\nu} (J_{20})_{\mu\nu} \quad .$$

An expression like $\sum_{\mu\nu} (H_{20})_{\mu\nu}(J_{20})_{\mu\nu}$ can be interpreted as a scalar product of two vectors H_{20} and J_{20}. With this simplified notation ΔE and J_{20} take the form

$$\Delta E = -\eta \, (H_{20})^2$$

$$\Delta J = -\eta \, (H_{20} \cdot J_{20}) \quad .$$

Of course, ΔJ should vanish provided the expectation value $\langle\phi|\hat{J}|\phi\rangle$ equals J_o the desired value. If this is not the case on sets

$$C_{\mu\nu} = \frac{(J_o - \langle\hat{J}\rangle}{(J_{20})^2} J_{\mu\nu}$$

and repeats this procedure if necessary until $\langle\hat{J}\rangle$ equals J_o. From now on one decreases the energy without changing $\langle\hat{J}\rangle$ by setting

$$C_{\mu\nu} = -\eta \left[(H_{20})_{\mu\nu} - \frac{H_{20} \cdot J_{20}}{(J_{20})^2} (J_{20})_{\mu\nu} \right] .$$

The constraints used in applying HFB theory are

$$\langle\phi|\hat{N}_p|\phi\rangle = Z \qquad \text{(proton number)}$$

$$\langle\phi|\hat{N}_n|\phi\rangle = N = A - Z \qquad \text{(neutron number)}$$

$$\langle\phi|\hat{J}_x|\phi\rangle = J(JH) - \langle J_z^2\rangle \qquad \text{(angular momentum)}$$

$$\langle\phi|\phi_o\rangle = 0 \qquad \text{(for excited states } |\phi\rangle) \quad .$$

In the last case $|\phi_o\rangle$ is the wavefunction of the energetically lowest state with the same quantum numbers as $|\phi\rangle$. It should be noted at this point that the relation

$$\frac{\partial}{\partial C_{\mu\nu}} \langle\phi|\phi_o\rangle \Big|_{\{C_{\mu\nu}=0\}} = \langle\phi|\alpha_\mu\alpha_\nu|\phi_o\rangle = 0_{\mu\nu}$$

holds. The requirement on H_{20} is in this case

$$(0 \cdot H_{20}) = \bar{0}$$

in every step of the iterative solution of the constrained HFB equations. Calculations were performed for ^{164}Er and ^{168}Yb. The single particle configuration space was the same as used earlier.[2] The strength constants of the quadrupole-quadrupole force (Q) plus pairing force (G) were slightly changed compared to the earlier work in order to give somewhat more quantitative agreement with experimental data. Besides that, a moment of inertia of the core was introduced. The core consists of 40 protons and 70 neutrons in single particle states not taken into account explicitly. The magnitude of this moment of inertia was chosen as $\theta_{core} = 6$ MeV^{-1}. It should be mentioned that the use of θ_{core} requires the knowledge of the angular frequency ω which is obtained from the relation

$$\omega = \frac{\partial E}{\partial \langle J_x \rangle} = \frac{(H'_{20} \cdot J'_{20})}{(J'_{20})^2} \quad .$$

Here H'_{20} and J'_{20} are those parts of the vectors H_{20} and J_{20} that are orthogonal to $N_{P_{20}}$ and $N_{n_{20}}$.

Calculated and experimental results are shown in Fig. 1. The results on ^{168}Yb indicate that at

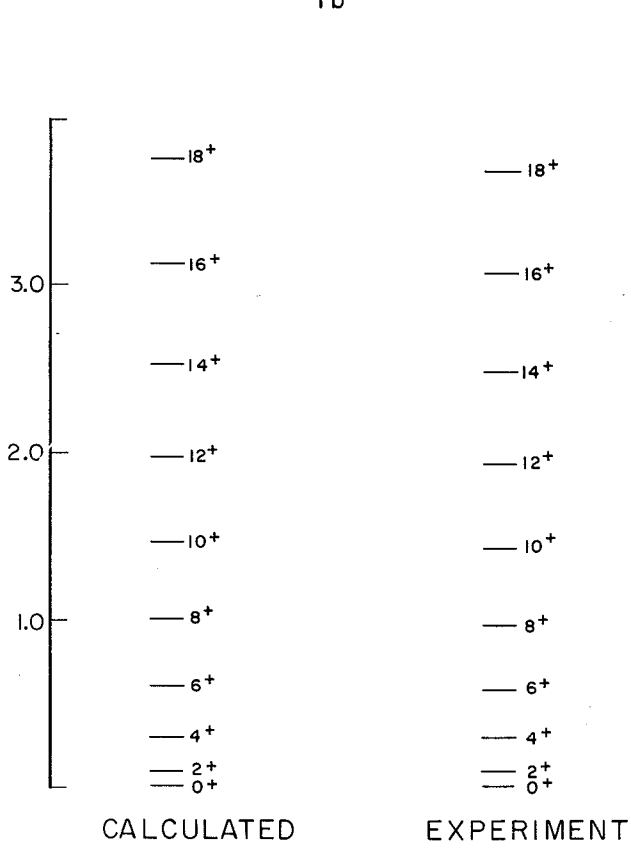

Fig. 1. Experimental and calculated energy levels of ^{168}Yb. (XBL 764-2776)

least within a limited range of mass numbers experimental data are reproduced by the same simple effective interaction. The results are encouraging enough to warrant the use of more sophisticated effective interactions in calculations of the type described here.

Footnotes and References

*Condensed from LBL-5015.

†Present address: Technische Universität München, D8046 Garching, Germany.

1. P. Quentin, H. Flocard and D. Vautherin in Proc. Intern. Conf. on Nucl. Phys., Munich, 1973, Vol. 1, p. 41.

2. H. J. Mang, Phys. Reports Vol. 18C, No. 6 (1975).

3. D. J. Thouless, The Quantum Mechanics of Many-Body Systems (Academic Press, New York and London, 1961).

TEST OF MANY-BODY METHODS ON AN EXACTLY SOLUBLE MODEL WITH BACKBENDING AND GAPLESS SUPERCONDUCTIVITY

S. Y. Chu, E. R. Marshalek,† P. Ring,‡
J. Krumlinde,§ and J. O. Rasmussen

The exactly soluble R(8) model of Krumlinde and Szymański has been used as a testing ground for three many-body methods applied to the yrast band: (i) the self-consistent cranking model (SCC), (ii) self-consistent cranking plus RPA, and (iii) variation after projection of particle number. All three methods agree very well with exact results outside of the critical region. The behavior in the critical region has been examined in detail.

The R(8) model consists of 2Ω identical fermions interacting via a pairing force, distributed among two 2Ω-fold degenerate single-particle levels separated by the energy 2ϵ and coupled to an external rotor with fixed moment of inertia a^{-1}. The Hamiltonian is

$$H = \left(\tfrac{1}{2}a\right)|\vec{I} - \vec{j}|^2 + H_{s.p.} + H_p \quad ,$$

where $\vec{I}$ is the total angular momentum of the system, and $\vec{j}$ is the particle angular momentum.

As discussed in Ref. 1, H is composed of generators of the group R(8). Exact eigenvalues and eigenfunctions can be found by diagonalizing a matrix in the Gelfand basis, so that the exact solution corresponds to a prototype shell-model calculation.

In the case of a self-contained many-fermion system with Hamiltonian H, the SCC model is usually derived by applying Hartree-Bogolyubov factorization to the operator $H - \omega j_x$. With the R(8) model, there is no need to subtract ωj_x since the rotor already cranks the system. Instead, we assume in the first approximation that the total angular momentum is aligned in the x-direction and has the classical c-number value I:

$$I_x \approx I, \qquad I_y \approx 0, \qquad I_z \approx 0 \ .$$

This form of the SCC model, which shall be specifically referred to as SCC1, is purely classical, and as such, valid mainly for high values of I. For low values of I, the rotational energy goes as I^2 rather than I(I+1). However, the addition of quantum fluctuations arising from the RPA, to be discussed later, gives the correct I(I+1) dependence. If RPA corrections are not included, the cranking energy may be improved for low I by some modifications.

We now consider the corrections to SCC1 described by the RPA. The boson-expansion technique provides a convenient way to introduce the additional correlations. Boson expansions to all orders for the group R(2n) have been given in Ref. 2. In the present problem, H must first be expressed in terms of the quasi-particles. Then, the quasi-particle pair operators are expanded in bosons to the RPA order.

In addition to the particles, the core must also be expanded in bosons, which physically corresponds to its wobbling motion about the steady rotation. A full description of the boson representation of a quantized rotor, with expressions valid to all orders, is given in Ref. 3. We follow here the lowest order treatment originally applied by Bohr and Mottelson to the asymmetric rotor,[4] which is applicable to the symmetric rotor as well. Upon adding the RPA correlations, one finds that the total Hamiltonian breaks up into two disjoint quadratic boson forms.

Since self-consistent cranking, or any Hartree-Bogolyubov approximation, in general violates symmetries of the exact Hamiltonian, one may hope to improve the situation by projecting out from such wavefunctions the components with the correct symmetry. The R(8) model is not suitable for testing angular momentum projection, since the particle angular momentum is not a constant of motion of the exact Hamiltonian. On the other hand, particle number is conserved by H, but not by H_ω, and we may therefore apply particle number projection, which has been used by several authors in the backbending region.[5] It is of interest to compare the projection method with the RPA, since both introduce correlations, and the RPA conserves particle number approximately (to order Ω^{-1}) through the pairing rotation term.

For optimum results, the variation is performed after projection (VAPN).

It can be shown that in the limit $\epsilon = 0$, VAPN reproduces the exact energies, as is the case for SCC1 + RPA.

Because of the size of the matrices to be diagonalized,[6] the maximum value of Ω for which exact solutions could be practicably obtained with our computing facilities was $\Omega = 4$. This means we were limited to not more than 8 particles.

The degree of backbending is controlled mainly by the ratio $\epsilon/(G\Omega)$: the smaller the ratio, the weaker the band mixing and the greater the tendency to bend back. We have followed the procedure of keeping G fixed and varying ϵ to control the degree of backbending. Exact solutions were obtained for Ω=3, G=0.1, a=0.02, and ϵ=0.05, 0.10, 0.15, and 0.20, and Ω=4, G=0.075, a=0.019736, and ϵ=0.05, 0.10, and 0.15, which covers the range from sharp backbending to no backbending and a smooth transition.

As shown in Ref. 1, the critical angular momentum I_c is given by

$$I_c = \Omega - \frac{1}{2} + \frac{1}{2}\,(G/a)(\Omega + 1) \quad .$$

The ratio G/a was fixed by the requirement that the phase transition occur between I = 12-14, in rough accord with experiment. The values of G were arbitrarily chosen to maintain about the same magnitude of ground state pair correlations as in Ref. 1.

The salient features emerging from the calculations are summarized in some representative figures.

It is seen from the figures that the yrast trajectories can have several regions of interest. The simplest picture is provided by the cranking model, in which the trajectories are composed of two segments, one with $\Delta \neq 0$, which may or may not have a backbending region (depending on the value of $\epsilon/G\Omega$)), along which Δ decreases and $\mathcal{I}$ increases continuously with increasing ω^2 until the intersection with the Δ=0 segment at some $\omega=\omega^*$, corresponding to a cusp. For $\omega^2 < \omega^{*2}$, the Δ=0 solution is unstable and is omitted. The situation becomes more complicated after adding the corrections due to the RPA, which tests the stability of the self-consistent cranking solutions.

The Δ=0 segment is always stable for $\omega^2 > \omega^{*2}$, but as $\omega \to \omega^*$, the doubly degenerate pairing vibration drops to zero frequency, signaling the onset of the transition from a pair-vibrational to a pair-rotational scheme. As ω^* is approached along the $\Delta \neq 0$ segment, one of the RPA frequencies approaches zero, in addition to the already present zero-frequency solution corresponding to the pair rotation. Also, as ω^* is approached along either segment, the derivative of the zero-point energy with respect to angular momentum, becomes infinite. Therefore, the RPA correction breaks down completely at the cusp, accounting for the hiatus in the RPA curves.

The $\Delta \neq 0$ segment can show instabilities since the RPA quadratic form is not necessarily positive. An unstable region occurs only along a portion of a backbending part, and only if the parameter a is sufficiently small compared to $G\Omega/\epsilon$. That is, the rotor must be sufficiently massive and the pairing correlations sufficiently strong. The unstable region is indicated by a dotted line in the figures. Figure 1, for example, shows quite clearly that as ϵ is increased for fixed a and $G\Omega$, the unstable region decreases in size. This instability in the backbending region is the result of competition between the particles, which favor increasing I with decreasing $|\omega|$ (the effect is proportional to $G\Omega/\epsilon$), and the rotor, which favors decreasing I with decreasing $|\omega|$ (the effect is proportional to a^{-1}). Figure 2, which is a plot of I vs $|\omega|$, shows that in the unstable region the rotor wins out, producing the peculiar "down bending." This is to be contrasted with Fig. 3, with another set of parameters, such that the yrast trajectories are stable everywhere. In this case, I increases with decreasing angular velocity in the backbending region. Fortunately, in realistic calculations an external rotor introduced to simulate a core would normally be small enough to avoid instability problems of this kind.

It has been seen that backbending per se does not necessarily imply instability (the criterion for which is the existence of an imaginary RPA frequency) as illustrated by Fig. 3. This is a counterexample to some claims made in previous work.[7]

Since, as was already noted, the VAPN and the SCC1 + RPA energies are both exact in the limit ϵ=0, it is clear that these two methods will be superior for very small ϵ (very sharp backbending), except that the second method breaks down in a small neighborhood of the cusp. Figure 4 is a plot of the yrast excitation energies vs I for this case of Ω=4, ϵ=0.1, while Fig. 5 is a similar plot for the case Ω=4, ϵ=0.15, in which the backbending disappears.

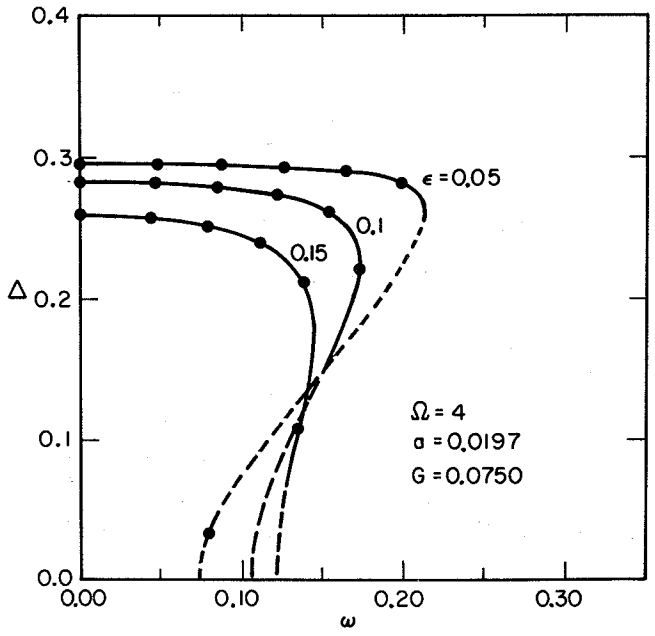

Fig. 1. The gap parameter Δ as a function of angular speed ω for SCC2. The discrete points correspond to integer values of angular momentum. The cranking model solutions are unstable along the dashed portions of the curves. (XBL 753-2501)

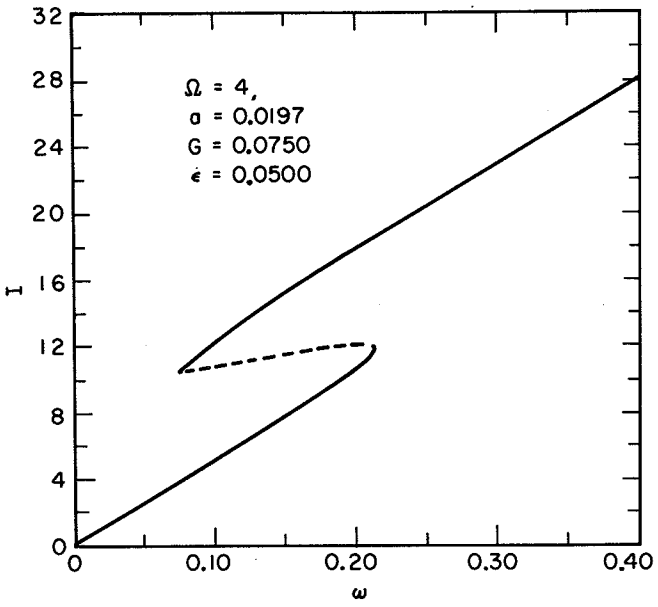

Fig. 2. The spin I as a function of angular speed ω for SCC2. The cranking model solution is unstable along the dashed part of the curve. (XBL 753-2502)

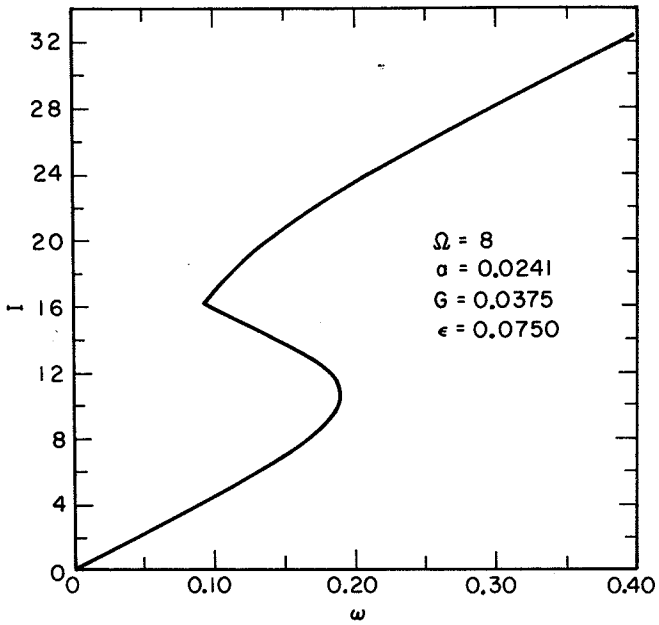

Fig. 3. The spin I as a function of angular speed ω for SCC2. The cranking model solution is stable everywhere. (XBL 753-2593)

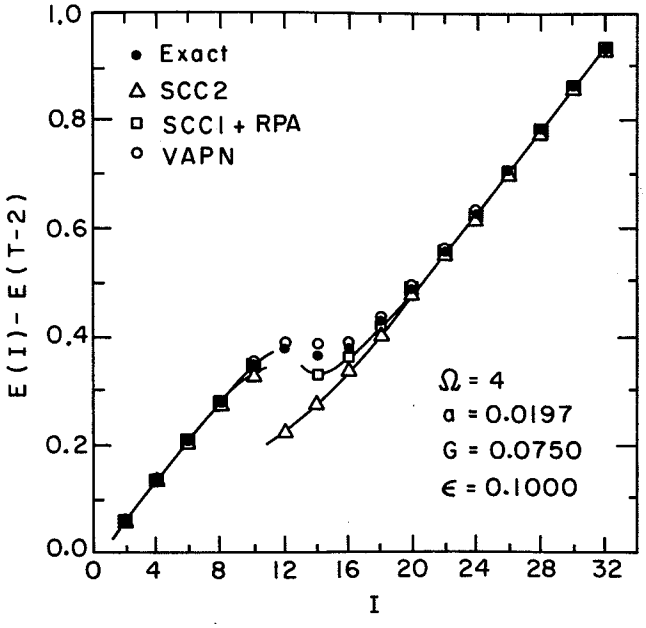

Fig. 4. Yrast excitation energies vs spin I. (XBL 753-2610)

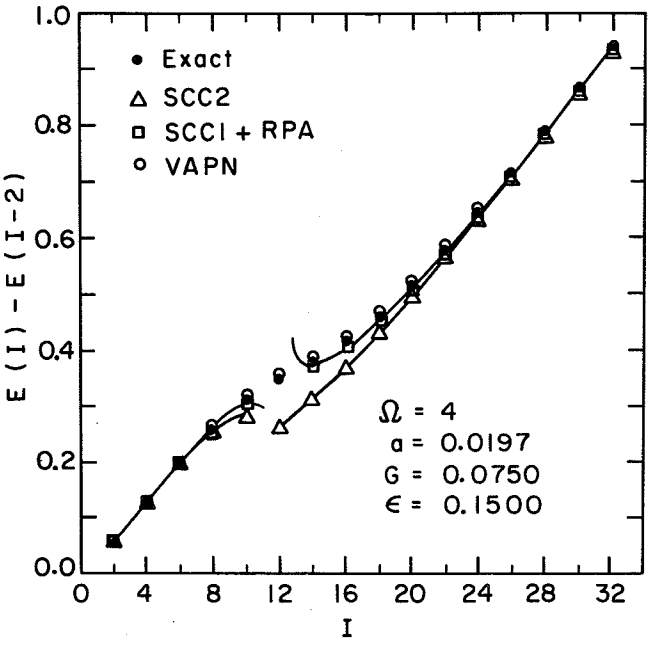

Fig. 5. Yrast excitation energies vs spin I. (XBL 753-2606)

It is seen that all three methods, SCC2, SCC1 + RPA, and VAPN are pleasingly accurate on the upper and lower branches outside of the transition region. The least embellished method, SCC2, is also least accurate, especially in the transition region, although it is asymptotically exact in the classical limit of large I, where all the methods eventually converge. The transition region, however, only encompasses three states or so. Clearly, SCC1 + RPA provides a nice improvement with only a bit more expenditure of time, except for the failure in the neighborhood of I=12, due partly to the pernicious influence of the cusp and partly to the large amplitude of the pair fluctuations. These effects, however, present no problem for the VAPN method, which is quite good all the way through. For large I, the absolute energies given by SCC1 + RPA are better than those given by VAPN.

As ϵ increases so that the backbending disappears, the VAPN method emerges as the best. SCC is also significantly less accurate with no backbending than with sharp backbending, which may be a general rule since this result is a consequence of the enlargement of the transition region in which the two bands are strongly mixed and zero-point oscillations become important.

Footnotes and References

*Condensed from LBL-4021, submitted to Phys. Rev.

†Permanent address: Dept. of Physics, University of Notre Dame, Notre Dame, Indiana 46556.

‡Permanent address: Technische Universität München, 8046 Garching, West Germany.

§Permanent address: Dept. of Mathematical Physics, Lund Institute of Technology, Lund, Sweden.

1. J. Krumlinde and Z. Szymański, Ann. Phys. (N.Y.) 79, 201 (1973).

2. E. R. Marshalek, Nucl. Phys. A224, 221 (1974).

3. E. R. Marshalek, Phys. Rev. C11, 1426 (1975).

4. B. Mottelson, "Rotational Motion in the Nucleus," in Proceedings Nuclear Structure Symposium of the Thousand Lakes, Joutsa, 1970 (Nordita publication, No. 417).

5. A. Faessler, F. Grümmer, L. Lin and J. Urbano, Phys. Lett. 48B, 87 (1974).

6. The matrix dimension = $(\Omega+5)!/(120\times\Omega!)$.

7. M. Sano, T. Takemasa and M. Wakai, Nucl. Phys. A190, 471 (1972).

ON THE SHELL EFFECT CONTRIBUTION TO THE MOMENT OF INERTIA AT VERY HIGH ANGULAR MOMENTUM

I. Ragnarsson,* D. P. Soroka, and F. S. Stephens

The yrast states of a nucleus are the states of lowest energy for each spin I. The internal degrees are not excited for these states, so they are especially easy to treat theoretically, and during the last few years some new approaches based on the shell correction method have been developed to describe them.[1,2] In addition, new experimental results have been obtained in this area.[3] Here we report some calculations on shell effects at very large angular momenta. These effects will be exemplified by nuclei in the Te region.

In the calculations presented here the macroscopic-microscopic method was used. The generalization of this method to high spin states is described in detail in Ref. 1, so here only the most important features of the method are given. The single-particle wavefunctions are extracted from a rotating modified oscillator (M.O.) potential corresponding to the Hamiltonian

$$H^{\omega} = \sum_i h_i^{\omega} = \sum_i (h^{\circ} - \hbar\omega j_x)_i \quad .$$

Here h° corresponds to the usual non-rotating M.O. Hamiltonian, while ωj_x can be regarded as the Hamiltonian form of the summed Coriolis and centrifugal terms. The wavefunctions χ_i^{ω} are obtained from the diagonalization of the one particle Hamiltonian

$$h_i^{\omega}\chi_i^{\omega} = e_i^{\omega}\chi_i^{\omega}$$

where e_i^{ω} can be regarded as energies in the system which is rotating with frequency ω. The "real energies" are calculated as expectation values

$$\langle e_i\rangle = \langle\chi_i^{\omega}|h^{\circ}|\chi_i\rangle = e_i^{\omega} + \hbar\omega m_i$$

where m_i is the expectation value of j_x. The order of the level occupation is determined from the order of the quantities e_i^{ω}, while the total energy is calculated as

$$E_{sp} = \sum\langle e_i\rangle = \sum e_i^{\omega} + \hbar\omega I \quad .$$

Here I is the total angular momentum, i.e., $I = \Sigma m_i$. All these sums are carried out over the occupied states $|i\rangle$.

By applying a generalized Strutinsky procedure, a smoothed energy $\tilde{E}$ can be calculated in a similar way as in the non-rotating case. The shell correction energy

$$E_{shell} = E_{sp} - \tilde{E}$$

is then calculated where all quantities are evaluated for the same I-value. Finally, the total energy is obtained as

$$E_{tot}(\epsilon,\gamma,I) = E_{macr}(\epsilon,\gamma,\epsilon_4 I) + E_{shell}(\epsilon,\gamma,I) \quad .$$

The macroscopic energy E_{macr} is composed of the surface energy, the Coulomb energy and the rotational energy corresponding to a rigid rotation. For the calculations reported here the macroscopic energy was minimized with respect to ϵ_4 while the shell correction energy was calculated for $\epsilon_4 = 0$.

The above formula for the shell correction energy was defined from a smearing over "the energies" $\langle e_i\rangle$ in the laboratory system. However, an alternative definition is[2]

$$E'_{shell}(\omega) = \sum e_i^{\omega}(\omega) - \sum e_i^{\omega}(\omega)$$

where all quantities are defined for the same ω-value and where the tilde denotes the smeared quantity. It is then possible to show that, except for a small correction term, $E_{shell}(\omega) = E_{shell}(I)$. Due to the equality above and due to the general features of the shell correction approach, in a plot of e_i vs ω, the regions of a low level density can be immediately identified as regions with a low value of E_{shell}. For the corresponding I-value there will then be a tendency to stabilize the nucleus to this shape.

In the calculations presented here pairing is completely neglected. For heavy and medium-heavy nuclei, the pairing correlations are expected to disappear for I ~ 20 - 30ħ, i.e., it is only for I-values larger than this limit that our calculations can be expected to be realistic. However, even for lower I values it is perfectly reasonable to define the shell correction energy. In Fig. 1 the proton energy levels e_i^{ω} at the prolate deformation $\epsilon = 0.3$ are plotted as a function of ω. In addition, some

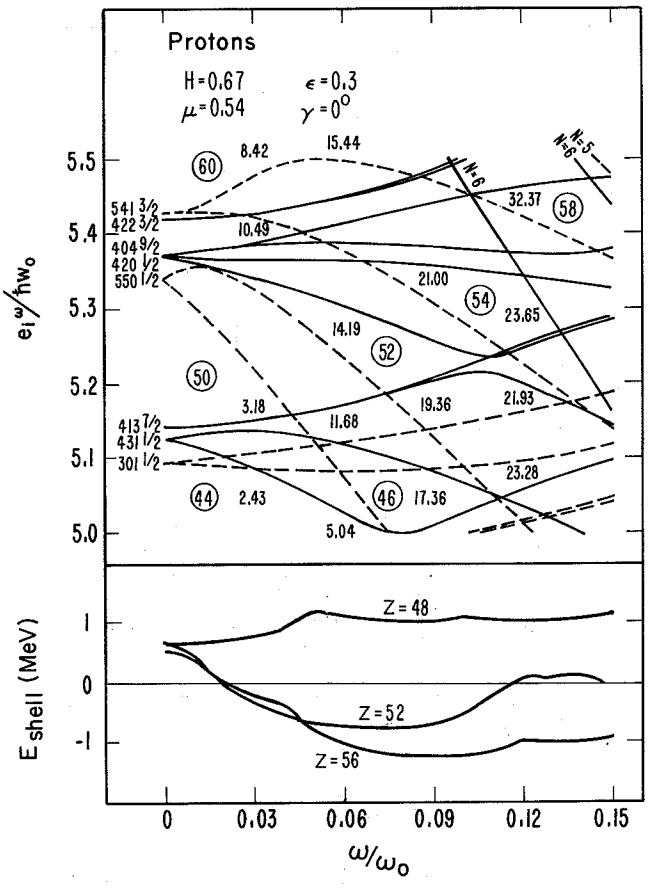

Fig. 1. In the upper part of the figure, the single-proton energies e_i^{ω} in the $Z \approx 50$ region are plotted as a function of the rotational frequency ω. Both the quantities are expressed in oscillator units, ω_o corresponding to the oscillator frequency. For different locations of the Fermi level energy, the proton number and the summed proton spin, $I_p = \sum_i m_i$, are given within circles and rectangles respectively. The total nuclear spin in addition has a neutron contribution. In the lower part of the figure shell correction energies corresponding to Z = 48, 52 and 56 are exhibited. (XBL 766-8216)

corresponding shell correction energies are exhibited. In this figure orbitals with a positive value of m_i will be down sloping while up sloping levels have negative m_i values; the larger is the slope, the larger is the absolute m_i-value. For low ω-values it is of particular interest to notice the influence on the shell correction energy on the alignment of the high j states. The phenomenon of alignment was first discussed in Ref. 5. In the single-particle diagram of Fig. 1 this alignment shows up in the fact that the two first orbitals of $h_{11/2}$, labelled by [550 1/2] for $\omega = 0$, become steeply down sloping, i.e., large m_i-values are obtained for quite small ω-values. For Z = 52, 54 and 56, they will open up a region of low level density and thus negative values of E_{shell} as seen in the bottom of the picture. This can then be expected to give rise to a more stable nuclear configuration.

Generally, the change in shell correction energy is mainly determined by the strongly sloping orbitals. Thus, in the very high spin region, the high j orbitals are expected to give the main effect. The reason is that these orbitals are most easy to align and in addition that they can carry the highest m_i-values. In Fig. 1 such orbitals, for $Z \approx 52$, begin to cut the Fermi surface at $\omega \approx 0.10$. Consequently, the level density becomes higher and E_{shell} increases. Generally, in Fig. 1, there is a direct correlation between the level density and the shell correction energies.

For the nucleus ^{118}Te the total energy was calculated on an (ϵ, γ) mesh and for different spins. For each spin I the minimum energy $E_{min}(I)$ was calculated. Then, the transition energies, for stretched E2 transitions along the yrast line, were calculated as $E_t(I) = E_{min}(I+2) - E_{min}(I)$. These transition energies in the region I = 20-70ħ are plotted in Fig. 2. Around I = 30ħ the lowest minimum changes its shape from prolate for $I \gtrsim 30\hbar$ to oblate for $I \leqslant 30\hbar$. However, for $I \leqslant 30\hbar$ there is also a prolate minimum with an energy close to that of the oblate minimum. In Fig. 2, for $I < 30\hbar$, the transition energies corresponding to prolate shapes are indicated as crosses. The change around I = 50ħ can be traced back to a general stretching of the nucleus. In this curve, due to the different approximations involved, each different point should certainly not be taken too seriously. However, the gross structure is expected to be significant. The gross structure can be characterized by the average density of transition energies per energy interval (essentially the slope in Fig. 2). This density corresponds to a directly observable feature in the experimental spectrum. In Fig. 2, the average density is almost twice as large around E_t = 1.7 MeV as it is just above E_t = 1 MeV. The aim of these calculations is to correlate the energies of Fig. 2 to the continuous γ-ray spectrum following a heavy ion reaction with ^{118}Te as the final product. However, this question remains to be investigated as does also the question of which orbitals are mainly involved in the changes of shapes and shell correction energies giving rise to the structure of Fig. 2.

Most of our computer codes were developed by the group of S. G. Nilsson and we want to thank

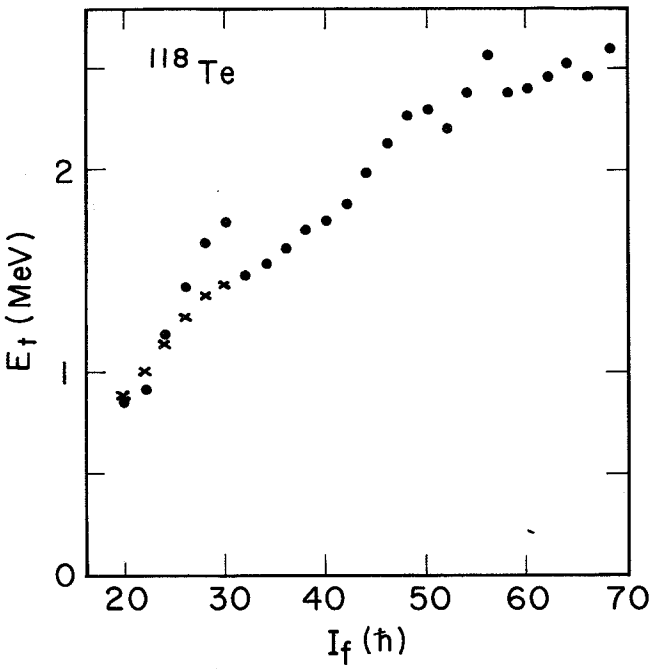

Fig. 2. The calculated stretched E2 transition energies E_t for ^{118}Te are shown as a function of the final spin I_f. For $I \approx 30\hbar$ the deepest minimum changes its shape from prolate to oblate. In the $I = 20 - 30\hbar$ region for the points the oblate (lowest) minima were used in calculating E_t while for the crosses the prolate minima were used.

(XBL 766-8217)

R. Bengtsson, S. E. Larsson, G. Leander, and S. Åberg for generous access to these codes.

Footnotes and References

*On leave from the Lund Institute of Technology, Lund, Sweden.

1. R. Bengtsson, S. E. Larsson, G. Leander, P. Moller, S. G. Nilsson, S. Åberg and Z. Szymański, Phys. Lett. 57B, 301 (1975); G. Andersson, S. E. Larsson, G. Leander, P. Moller, S. G. Nilsson, I. Ragnarsson, S. Åberg, R. Bengtsson, J. Dudek, B. Nerlo-Pomorska, K. Pomorski and Z. Szymański, submitted to Nucl. Phys.

2. K. Nergaard, V. V. Pashkevich and S. Frauerndorf, Nucl. Phys. A262, 61 (1976).

3. R. S. Simon, M. V. Banaschik, P. Colombani, D. P. Soroka, F. S. Stephens and R. M. Diamond, Phys. Rev. Lett. 36, 359 (1976), Refs. quoted therein.

4. V. M. Strutinsky, Nucl. Phys. A95, 420 (1966).

5. F. S. Stephens and R. S. Simon, Nucl. Phys. A183, 257 (1972).

SEMI-MICROSCOPIC ROTATIONAL BAND THEORY

D. Soroka, J. Rasmussen, and K. S. Tanabe*

We have carried out four-dimensional stretch model calculations of various properties of nuclear rotational bands—energies, quadrupole deformations (ϵ), proton and neutron gap parameters (ν_p and ν_n) and rotational g-factors. For each spin value the total energy minimum is found in a four-dimensional space of collective coordinates; these are the three degrees of freedom (ϵ, ν_p, and ν_n) and the tri-axiality parameter γ.

Our code is a generalization of the one-dimensional beta-stretch model of Diamond, Stephens and Swiatecki[1] and the two-dimensional stretch model of Ma and Rasmussen[2] (proton and neutron pairing). Except for one adjustable parameter normalizing the moment of inertia, the calculations are constrained by microscopic theoretical work both for potential energy surfaces and for inertial properties.

Our shape-potential surfaces are parametrized least-squares fits of shell-corrected energy surfaces calculated by the Lund-Warsaw groups.[3] Spring constants for pairing changes are taken from the number-projected BCS continuous model formula from Ref. 4. Spring constants for shape changes are determined by the curvature of the shell-corrected energy surfaces.

We used an exponential dependence of moment of inertia on pairing gap parameters, as determined by cranking model calculations of Ref. 2. Indeed, we constrained ourselves to the theoretically calculated exponential pairing coefficients γ_p and γ_n as given in Table 1 of Ref. 2.

The dependence of the three moments of inertia on asymmetry γ was taken in the form given by Bohr from the hydrodynamic model.

$$\mathcal{J}_x = \mathcal{J}(\epsilon)\, \sin^2\left(\gamma - \frac{2\pi\kappa}{3}\right) + \mathcal{J}_0 \quad ,$$

where $\kappa = 1,2$, or 3 for the principal axes of the ellipsoid. The small constant $\mathcal{J}_0$ is an effective moment of inertia for spherical nuclei, based on the energy of the giant quadrupole state. The coefficient $\mathcal{J}(\epsilon)$ is constrained to a rounded stair-step form suggested by cranking calculations and tied to the level density dependence on deformation as the integral of the Nilsson level density with respect to deformation.

In the overall normalization of $\mathcal{J}(\epsilon)$ we allow one adjustable parameter, the only one in the calculation; it is adjusted to fit one rotational transition ($4 \rightarrow 2$).

With the help of Dr. Eric Leber, we have explored the shape dependence of Δ_p and Δ_n, hence, Nilsson level densities ρ_p and ρ_n hear the Fermi surface. In this, ϵ, ϵ_4 and ϵ_6 were varied. However, for the calculations presented in this report we have held the values of ρ_p and ρ_N as constants independent of deformation, but they are fixed through the continuous expression (Eq. (79) of Ref. 5) to the experimental odd-even mass differences plotted in the comprehensive paper of Nilsson et al.[6]

Table 1 lists experimental and theoretical energies along with theoretical Δ_p, Δ_n, ϵ, and g_R values. In all cases calculated the equilibrium γ remained at zero (prolate). Evidently the neglect of zero-point vibration causes a lack of the "gamma band mixing" effect of the band energies. The general agreement of transition energies is unusually good for a one-parameter fit. The 2-0 transition energies are poor for N = 90 nuclei, but at this border of stable deformation it is felt that the 0^+ state energies may be anomalously low due to admixture with spherical states. The calculated amount of quadrupole stretching for N = 90 nuclei is less than experiment. Our preliminary calculations show that a falling Nilsson level density with increasing deformation would produce

Table 1. Rotational band properties.

Nucleus	Spin	Ground band transition energies (E_I-E_{I-2}) keV		Gap parameters (MeV)		Equilibrium deformation	Gyromagnetic coefficient
	I	$(E_I-E_{I-2})_{theor.}$	$(E_I-E_{I-2})_{exp.}$	$\Delta_p(I)$	$\Delta_n(I)$	$\epsilon_2(I)$	$g_R(I)$
$^{152}_{62}Sm$	0			1.10	1.15	0.2224	
	2	110.0	121.8	1.08	1.13	.2226	0.405
	4	244.6	244.7	1.05	1.08	.2230	.397
	6	355.8	340.7	1.01	1.01	.2234	.386
	8	440.5	418.1	0.97	0.93	.2240	.370
	10	500.8	483.5	0.93	0.84	.2245	.349
	12	540.7		0.90	0.74	.2249	.324
	14	564.3		0.88	0.63	.2253	.295
	16	575.0		0.87	0.53	.2257	.264
	18	576.3		0.88	0.43	.2260	.233
$^{154}_{64}Gd$	0			1.15	1.08	.2319	
	2	111.4	123.0	1.13	1.06	.2321	.412
	4	248.0	247.8	1.10	1.01	.2325	.403
	6	361.2	346.5	1.06	0.94	.2331	.389
	8	447.5	426.7	1.02	0.85	.2338	.370
	10	508.7	492.8	0.99	0.76	.2344	.347
	12	548.6	547.7	0.96	0.66	.2349	.319
	14	571.3	592.8	0.95	0.55	.2355	.288
	16	580.9	627.2	0.94	0.45	.2359	.256
	18	580.9	611.7	0.95	0.35	.2363	.226
$^{156}_{64}Gd$	0			1.05	1.00	.2513	
	2	88.4	88.9	1.04	0.98	.2513	.407
	4	199.2	199.2	1.01	0.94	.2515	.400
	6	295.4	296.5	0.98	0.89	.2517	.390
	8	373.5	380.7	0.95	0.82	.2519	.375
	10	433.5	451.3	0.91	0.74	.2522	.357
	12	477.1		0.89	0.65	.2524	.335
	14	506.7		0.87	0.56	.2527	.311
	16	524.7		0.85	0.47	.2529	.285
	18	533.5		0.85	0.38	.2531	.258
$^{158}_{64}Gd$	0			0.83	0.83	.2617	
	2	79.9	79.5	0.82	0.82	.2618	.404
	4	181.9	181.9	0.80	0.79	.2619	.403
	6	274.5	277.6	0.77	0.75	.2620	.400
	8	354.6	359.2	0.73	0.69	.2621	.396
	10	421.6		0.68	0.63	.2623	.391
	12	476.1		0.64	0.60	.2625	.385
	14	519.3		0.60	0.50	.2627	.378
	16	553.0		0.56	0.43	.2629	.369
	18	578.5		0.52	0.35	0.2630	0.358

an improvement in quadrupole stretching and retain good energy spacing, but we have not wished to involve more than one-parameter in the fitting to date.

The gyromagnetic ratio always monotonically decreases with spin. This is a consequence of the fact that the neutron pairing decreases more rapidly with spin than does proton pairing. In ^{154}Gd the calculations show onset of backbending at spin 18 in accord with experiment, but there is no pairing collapse. In fact, the proton gap parameter even increases slightly from spin 16 to spin 18.

Footnotes and References

*Present address: INS, University of Tokyo, Japan.

1. R. M. Diamond, F. S. Stephens and W. J. Swiatecki, Phys. Lett. 11, 315 (1964).

2. C. W. Ma and J. O. Rasmussen, Phys. Rev. 69, 1083 (1974).

3. S. E. Larsson, Physica Scripta 8, 17 (1973).

4. C. W. Ma and J. O. Rasmussen, Phys. Rev. C2, 798 (1970).

5. J. O. Rasmussen, "Models of Heavy Nuclei", in "Nuclear Spectroscopy and Reactions", Part D., J. Cerny ed., Academic Press, New York, 1975.

6. S. G. Nilsson, C. F. Tsang, A. Sobiczewski, Z. Szymansky, S. Wycech, Ch. Gustafson, I. L. Lamm, P. Moller and B. Nilsson, Nucl. Phys. A131, 1 (1969).

GENERALIZED PARTICLE CORE COUPLING

G. J. Mathews

Here, results are presented from a simple, general model capable of describing the excitations in vibrational, transitional, or deformed nuclei within a single spherical basis. The method has the advantages of a relatively small set of basis states and that the transformation of the single-particle states to a deformed basis is avoided.

Any model which addresses itself to so general a task as this must accommodate simultaneously the variation with deformation of the single-particle level spacings, and the pairing occupation probabilities. Approaches to this problem in the past have employed a many-body microscopic description such as the equations of motion method of Klein[1] or Goswami et al.[2] The disadvantage of these earlier formulations is that the microscopic basis becomes too cumbersome away from spherical nuclei.

The model discussed here is a generalization of the deShalit core excitation model[3] in that the nuclear core is described by a set of quadrupole matrix elements and diagonal even-even core energies. An equation of motion formalism permits simultaneous description of the states of the odd particle subject to pairing and shape correlations, the latter included as a "backwards" amplitude.

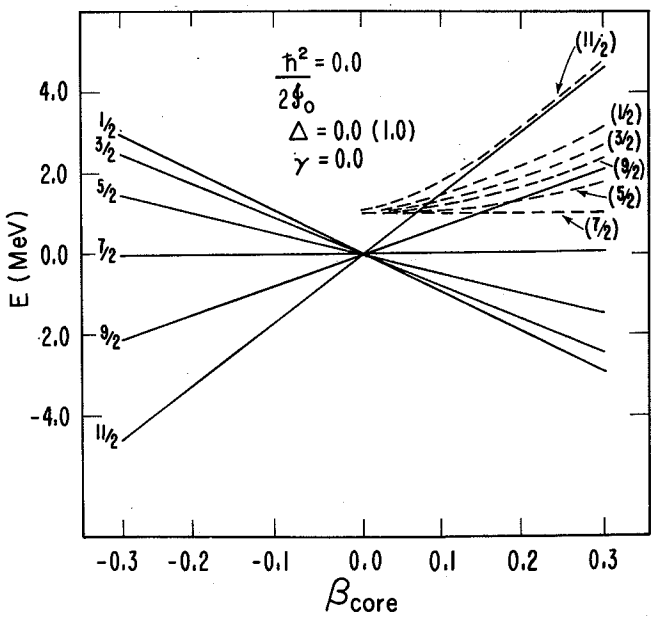

Fig. 1. Generalized particle core coupling for the $h_{11/2}$ shell with core energies = 0. The dashed lines include pairing with $\lambda = 0$, $\Delta = 1$ MeV. The results are indistinguishable from a single-j shell Nilsson calculation. (XBL 766-8298)

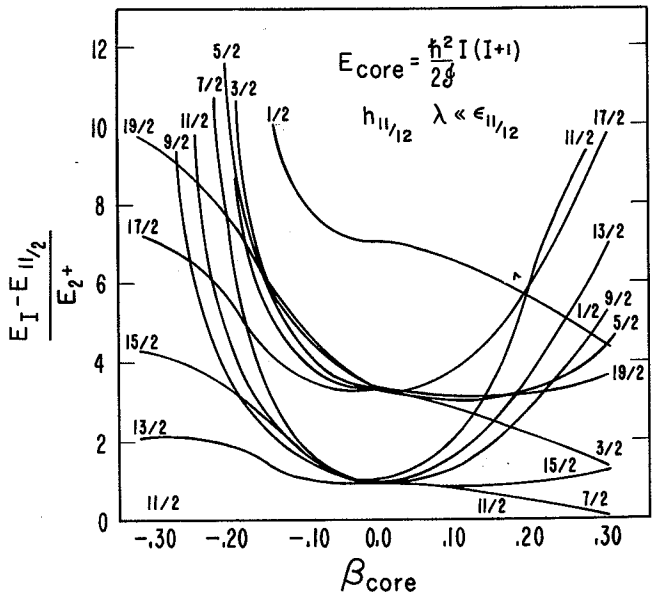

Fig. 2. Generalized particle core coupling for the $h_{11/2}$ level with $\lambda = -\infty$. Rotational core energies are assumed. The results are very similar to the coriolis coupling calculations of Ref. 4. (XBL 766-8299)

Some results for a single-j shell calculation are presented in Figs. 1 and 2. In Fig. 1, the macroscopic core energies are set equal to zero, and the pairing has been turned off. One should expect the theory to then describe the single-particle states as a function of deformation, analogous to a Nilsson calculation. In fact, Fig. 1 is indistinguishable from an exact Nilsson calculation of the $h_{11/2}$ shell. The same exact agreement is obtained when the pairing is turned back on for both models as can be seen by the dashed lines in Fig. 1.

In Fig. 2, the Fermi surface has been set well below the shell. The core energies are assumed to be rotational. In this case, one would expect results similar to the coriolis coupling calculations of F. Stephens.[4] Figure 2 is, indeed, nearly identical to Fig. 12 of Ref. 4. The familiar coriolis decoupled band behavior is visible for positive deformation. The strongly coupled limit is approached for negative deformation.

In conclusion, it seems that this simple model reproduces all of the familiar deformed model nuclear structure, though it employs a spherical basis. The extension of the model to compute triaxial core shapes,[5] electromagnetic moments, and transition probabilities is quite straightforward and currently underway.

References

1. A. Klein, Ann. Phys. 66, 390 (1971).

2. A. Goswami, O. Nalcioglu and A. I. Sherwood, Nucl. Phys. A153, 433 (1970).

3. A. deShalit, Phys. Rev. 122, 1530 (1961).

4. F. S. Stephens, Rev. Mod. Phys. 47, 43 (1975).

5. J. Meyer-ter-Vehn, Nucl. Phys. A249, 111 (1975).

THEORETICAL ESTIMATES OF MAGNETIC MOMENTS FOR EXCITED NUCLEI SHELL AND PAIRING EFFECTS

L. G. Moretto

The rotational constants, or moments of inertia, have been long recognized as valuable information regarding the flow of nuclear matter in nuclei. Spectroscopically detected rotational bands have produced evidence of moments of inertia smaller than expected from the charge quadrupole moment. Such a reduction has been elegantly explained in terms of the pairing interaction which makes the deformed nuclei superfluid. Variations in the moment of inertia with angular momentum have been observed quite recently and are particularly impressive in backbending nuclei. These variations seem to be the result of a decoupled pair and of the simultaneous disappearance of the pairing effects with angular momentum. It is not settled as yet which of the two connected causes is the dominant one.

Variations in the moment of inertia along the yrast line, now being observed experimentally, have also been considered theoretically, with various aims in mind. At lower angular momentum one is more interested in the collapsing of the pairing correlation; at larger angular momenta, the main interest is in gross changes in moments of inertia arising from radical changes in the nuclear shape (oblate to prolate). Calculations have been performed for excited spherical shell model nuclei. The semiclassical rotational quantities like the angular velocity and the moments of inertia have been used in describing the variation of pairing and its eventual collapse.

Very much like the moments of inertia, the nuclear magnetic moments reflect the internal flow of nuclear matter and therefore can yield information related to that provided by the moments of inertia. Yet, there are substantial differences. Protons, for example, contribute with their orbital motion and spin to the magnetic moment, while neutrons only contribute with their spin. Furthermore, the neutron intrinsic magnetic moment is small and negative while that of the proton is small and positive. These observations raise the hope that the simultaneous determination of both moments of inertia and magnetic moments may allow one to single out the contributions of each kind of particle to the overall generation of both the magnetic moment and the moment of inertia.

As a beginning, the most simple spherical case will be studied on the basis of the shell model and the BCS Hamiltonian. The expectation value of the BCS Hamiltonian, diagonal in quasi-particle space has the form

$$\langle H' \rangle = \langle H - \lambda N - \gamma M \rangle = \Sigma(\epsilon_k - \lambda - E_k) + \Sigma_{n_k}^{+}(E_k - \gamma m_k) + \Sigma_{n_k}^{-}(E_k + \gamma m_k) + \Delta^2/G \ .$$

In this expression N is the total particle number, λ is the corresponding Lagrange multiplier, M is the total angular momentum Z projection, and γ is the corresponding Lagrange multiplier which assumes the meaning of angular velocity

$$\gamma = \frac{\partial \langle H \rangle}{\partial M} \ .$$

We can thus generate the grand potential

$$\Omega = -\beta\Sigma(\epsilon_k - \lambda - E_k) + \Sigma \ln[1 + \exp\beta(E_k - \gamma m_k)] + \Sigma \ln[1 + \exp\beta(E + \gamma m_k)] - \beta\frac{\Delta}{G}$$

and from it the other thermodynamic functions

$$N = \Sigma\left[1 - \frac{\epsilon_k - \lambda}{2E_k}\left\{\tanh 1/2\ \beta(E_k - \gamma m_k) + \tanh 1/2\beta(E_k + \gamma m_k)\right\}\right]$$

$$M = \Sigma m_k\left[\frac{1}{1+\exp\beta(E_k - \gamma m_k)} - \frac{1}{1+\exp\beta(E_k + \gamma m_k)}\right]$$

$$E = \Sigma\epsilon_k\left[1 - \frac{\epsilon_k - \lambda}{2E_k}\left\{\tanh 1/2\ \beta(E_k - \gamma m_k) + \tanh 1/2\beta(E_k + \gamma m_k)\right\}\right] - \Delta^2/G \ .$$

The quantities Δ, β, λ, and j are related to each other by the gap equation

$$\frac{\partial\Omega}{\partial\Delta} = 0$$

or

$$\Sigma\ \frac{1}{2E_k}\left[\tanh 1/2\beta(E_k - \gamma m_k) + \tanh 1/2\beta(E_k + \gamma m_k)\right] = 2/G \ .$$

In the extreme single particle model, a nucleus is characterized by a magnetic moment which results from the vector sum of the magnetic moments of the individual nucleons. A simple approach to summing the contribution of individual nucleons is to sum the projections of each single particle magnetic moment on the Z axis, chosen so as to have the largest total angular momentum projection for the nucleus as a whole. The Z projection of the single particle magnetic moment can be written as follows

$$\mu_z = \mu\frac{m_j}{j} = \left(g_\ell\frac{\underset{\sim}{\ell}\cdot\underset{\sim}{j}}{j} + g_s - \frac{\underset{\sim}{s}\cdot\underset{\sim}{j}}{j}\right)\frac{m_j}{j}$$

where g_ℓ, g_s are the g factors associated with the orbital and spin single particle angular momentum ℓ and s; j is the total single particle angular momentum and m_j is its projection on the z axis. Since

$$\frac{\underset{\sim}{\ell}\cdot\underset{\sim}{j}}{j^2} = \frac{j(j+1) + \ell(\ell+1) - s(s+1)}{2j(j+1)}$$

and

$$\frac{\underset{\sim}{s}\cdot\underset{\sim}{j}}{j^2} = \frac{j(j+1)+s(s+1) - \ell(\ell+1)}{2j(j+1)} \ ,$$

we have for $j = \ell + 1/2$

$$\mu_z = \mu\frac{m_j}{j} = (1/2\ g_s + \ell\, g_\ell)\frac{m_j}{j}$$

and for $j = \ell - 1/2$

$$\mu_z = \mu\frac{m_j}{j} = \left(-1/2\ g_s\frac{2\ell-1}{2\ell+1} + g_\ell\frac{(\ell+1)(2\ell-1)}{2\ell+1}\right)\frac{m_j}{j}$$

or

$$\mu_z = \left[g_\ell \pm \frac{1}{2\ell+1}(g_s - g_\ell)\right] m_j \ .$$

The same result ought to be obtained if we project separately the orbital and spin components on the Z axis. Then

$$\mu_z = \sum_\ell (g_\ell m_\ell + g_s m_s) C_\ell^2$$

where C_ℓ is the relevant Clebsch Gordon coefficient. For $j = \ell + 1/2$ we have

$$\mu_z = \frac{j+m_j}{2j}\left[g_\ell(m_j - 1/2) + 1/2 g_s\right] + \frac{j-m_j}{2j}\left[g_\ell(m_j + 1/2) - 1/2 g_s\right]$$

$$= g_\ell m_j + \frac{m_j}{2j}(g_s - g_\ell)$$

$$= \left[g_\ell + \frac{1}{2\ell+1}(g_s - g_\ell)\right]m_j$$

as was obtained before. Similar calculations can be performed for $j = \ell - 1/2$.

Since $g_\ell = 1$, $g_s = 5.586$ for protons, and $g_\ell = 0$; $g_s = -3.826$ for neutron, the following expressions for μ_z are obtained.

For protons:

$$\mu_z^p = \left(1 - \frac{2.293}{j+1}\right)m_j^p \qquad \text{for } j = \ell - 1/2$$

$$\mu_z^p = \left(1 + \frac{2.293}{j}\right)m_j^p \qquad \text{for } j = \ell + 1/2$$

For neutrons:

$$\mu_z^n = \frac{1.913}{j+1}\ m_j^n \qquad \text{for } j = \ell - 1/2$$

$$\mu_z^n = \frac{1.913}{j}\ m_j^n \qquad \text{for } j = \ell + 1/2$$

The nuclear magnetic moment for a single neutron or proton component can now be written as follows:

$$M = \Sigma_{\mu_{z,k}}\frac{1}{1+\exp\beta(E_k - \gamma m_k)} - \frac{1}{1+\exp\beta(E_k + \gamma m_k)}$$

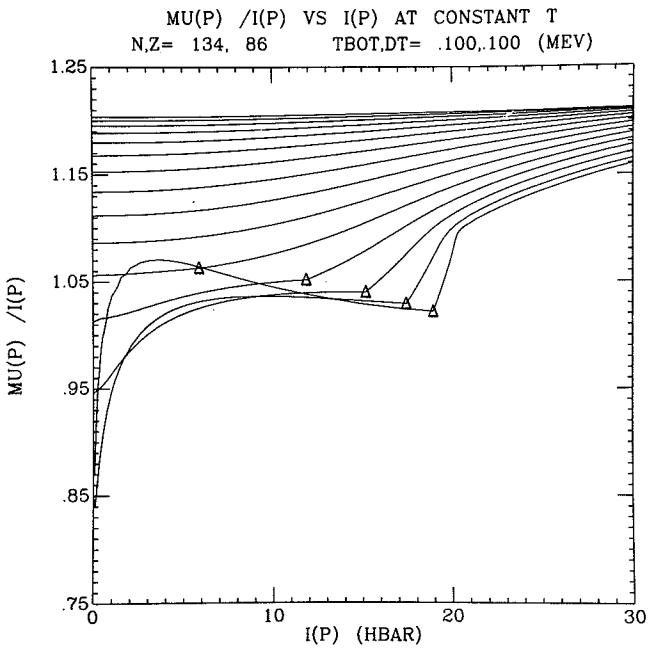

Fig. 1. Proton component g factor as a function of the proton component angular momentum for various temperatures. The triangles on the lower isotherms indicate the disappearance of the proton pairing correlation. The nucleus in study is ^{220}Rn. (XBL 7612-10861)

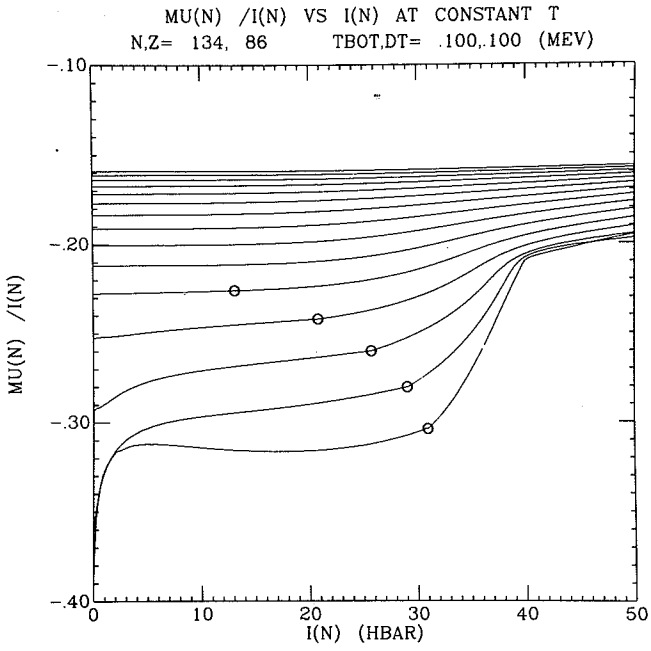

Fig. 2. Same as in Fig. 1 for the neutron component of the same nucleus. The open circles on the low isotherms indicate the disappearance of the neutron pairing correlation. (XBL 7612-10859)

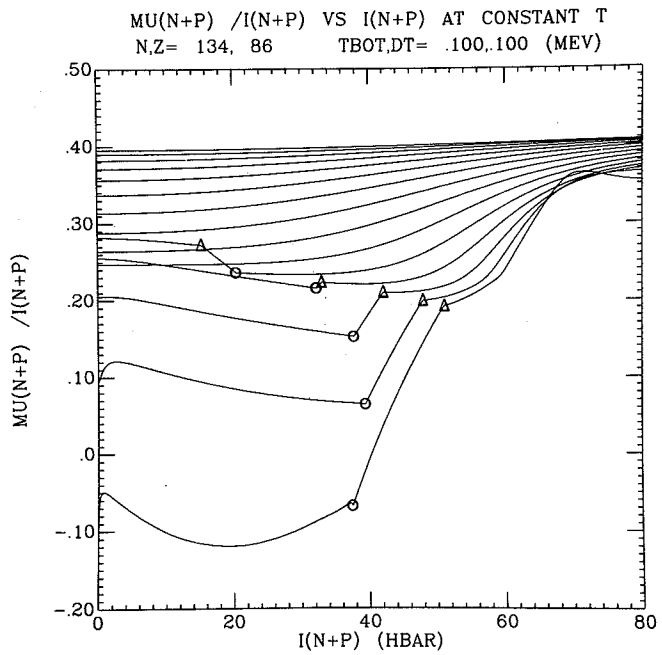

Fig. 3. Overall g factor as a function of total angular momentum for various temperatures in the nucleus ^{220}Rn. The triangles and open circles indicate the disappearance of proton and neutron pairing correlation respectively. (XBL 7612-10867)

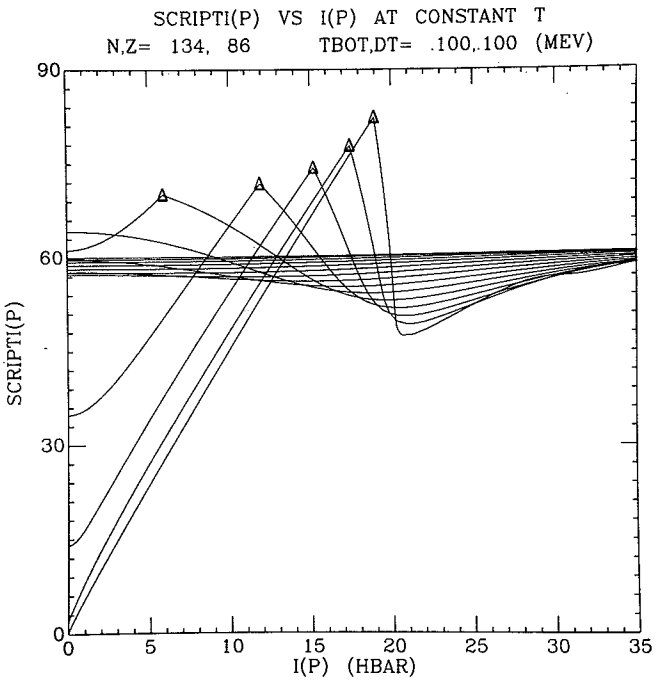

Fig. 4. Proton component of the moments of inertia as a function of the proton component angular momentum for various temperatures. Notice the effect of pairing in the lower isotherms. (XBL 7612-10856)

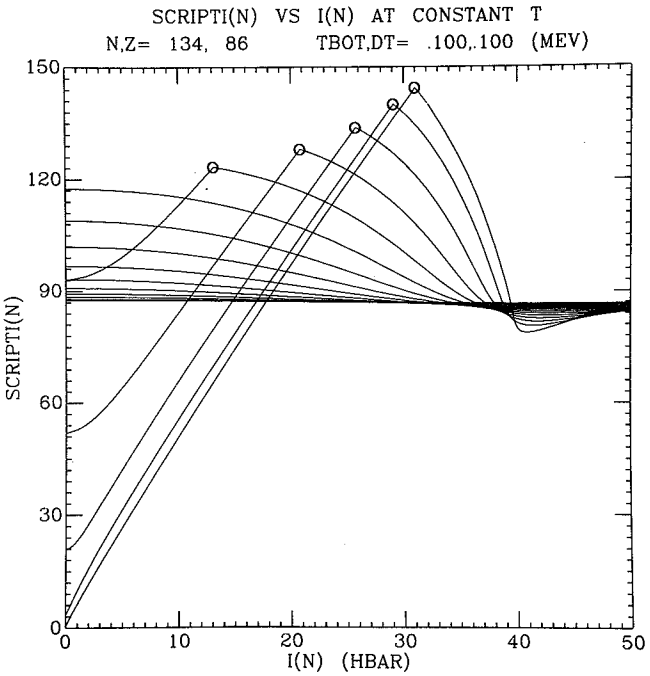

Fig. 5. Same as in Fig. 4 for the neutron component. (XBL 7612-10864)

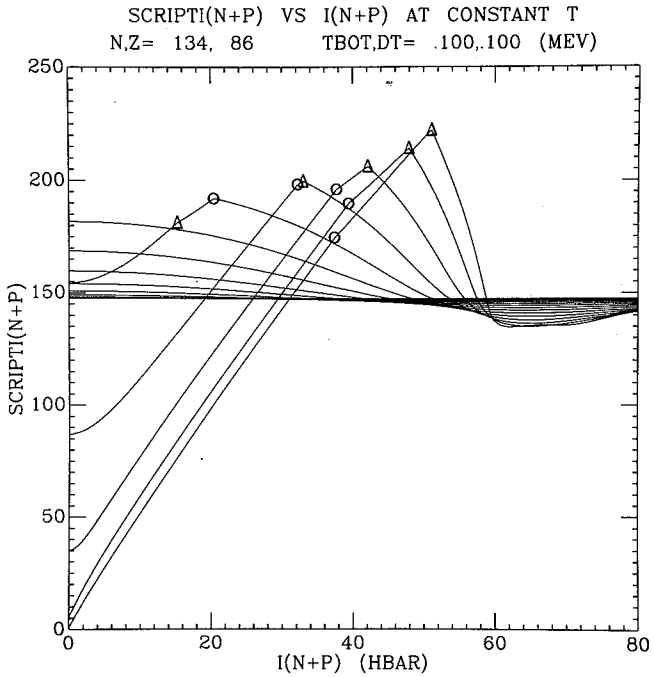

Fig. 6. Overall moments of inertia of ^{220}Rn as a function of total angular momentum for various temperatures. Notice the effect of neutron and proton pairing in the lower isotherms. (XBL 7612-10855)

Since the total energy is commonly specified rather than the individual energies of the proton and neutron components, the two components must share a common value for the Lagrange multiplier β (or in other words, the two systems have a common temperature $T = 1/\beta$). Similarly, as the total angular momentum rather than the individual contributions of the two components is specified, a common value for the Lagrange multiplier γ must be shared by the two components (or the two components share the same angular velocity).

Some examples of calculations of magnetic moments are shown in Figs. 1 - 3 for the nucleus ^{220}Rn. One can observe that the proton contribution is positive (Fig. 1) and that the neutron contribution is negative (Fig. 2). The lower isotherms are strongly affected by pairing at small angular momenta. At higher angular momenta the pairing effects vanish.

The total magnetic moment obtained by combining both components is shown in Fig. 3. It can be seen that at low temperatures the magnetic moment is negative, thus indicating the dominance of neutrons. At higher temperatures the magnetic moment is mainly controlled by the proton component. In Figs. 4 and 5 the neutron and proton contributions to the moment of inertia are shown and in Fig. 6 the total moment of inertia is shown. Notice that both components contribute substantially to the moment of inertia. Also notice how the pairing effects substantially reduce the moment of inertia.

NORMALIZED SHELL MODEL ALPHA DECAY THEORY APPLIED TO UNFAVORED DECAY*

T. Fliessbach,† H. J. Mang,‡ and J. O. Rasmussen

Antisymmetrization is usually taken into account in the shell model theory of alpha decay.[1] It enforces the requirements of the Pauli principle, preventing double occupation of states. However, antisymmetrization between two composite particles leads to non-normalized states. The proper normalization may be hidden in the function of relative motion between the alpha particle and the daughter nucleus. We are not able to calculation this function (including the normalization) exactly; instead we introduce a distorted wave approximation for the wavefunction of relative motion, and then it is vital to take the proper normalization explicitly into account.

This normalization results[2,3] in a considerable enhancement of the reduced width for alpha decay. Reduced width means here $\delta^2 = \hbar/(P \cdot \tau)$, with τ the mean life and P the barrier penetration factor.

Since the new theoretical absolute ground-to-ground state decay widths are strongly enhanced[2] over the previous version of the theory, we felt it important to check also on various cases of hindered alpha decay to see to what extent relative alpha transition rates would be affected by the normalization.

Tables 1 - 3 give the results for the relative and absolute alpha decay rates for ^{211}Po and ^{211}Bi.

The results for ^{212}Po are given in a different form: in Table 4 we listed the spectroscopic factors and the hindrance factors (reciprocal of S normalized to the ground state transition).

From examination of Table 1 it appears that the alpha branching ratios by the old and new theory are not much different. That is, the substantial enhancement of alpha decay rates by the new theory apply rather uniformly to the various state combinations of ^{211}Po and ^{211}Bi decay. This result is reassuring in that it suggests that extensive previous calculations in the literature with the old shell-model alpha decay theory are not all invalidated. Likewise, in Table 2 we see that the relative amplitudes for various ℓ values are not much altered, also there seems to be some systematic lowering of higher ℓ values by a few percent.

From Table 3 we see that the absolute decay widths are increased by two orders of magnitude in the new theory, giving good agreement with experiment. The ratio of widths for the two nuclei differs by a considerable amount for the old and new theories, with the result of the new theory in better agreement with experiment.

It is when we come to the spectroscopic factors for ^{212}Po in Table 4 that we find striking differences between the old and new theory. In particular the considerable hindrance factors predicted for the second 0^+ and second and third 2^+ states are lowered by an order of magnitude in the new theory.

As far as the absolute decay widths are concerned, the new theory can reproduce the ground state decay width (see also Ref. 2), the old theory falls short by two orders of magnitude. The ratio $\Gamma(18^+$, assumed to be the isomer at 2930 keV$)/\Gamma(0_1^+)$ comes out too large by a factor of 30 in the new theory and a factor of 150 in the old one.

Table 1. Alpha branching ratios for ^{211}Po and ^{211}Bi. The results of the old and new theory are displayed vs the experiment. The numbers in the upper line are from a channel radius dependent formula, the lower line is calculated with spectroscopic factors.

Parent nucleus	Daughter nucleus	Alpha branching ratios		
		Experiment	Old theory	New theory
^{211}Po	p1/2	99	98.0 98.0	96.8 97.8
	f5/2	0.5	1.6 1.6	2.7 1.7
	p3/2	0.5	0.4 0.4	0.5 0.5
^{211}Bi	s1/2	83	82 82	78 81
	d3/2	17	18 18	22 19

Table 2. Relative angular momentum mixing amplitudes. The numbers in the upper line are from a channel radius dependent formula, the lower line is calculated with spectroscopic factors.

Parent nucleus	State of daughter nucleus	Relative angular momentum mixing amplitudes		
		Experiment	Old theory	New theory
^{211}Po	f5/2	1 :-0.96:0.55	1 :-0.88:0.58 1 :-0.88:0.58	1 :-0.85:0.52 1 :-0.85:0.56
	p3/2	1 : -0.14	1 : -0.33 1 : -0.33	1 : -0.32 1 : -0.33
^{211}Bi	d3/2	1 : -0.27	1 : -0.33 1 : -0.33	1 : -0.32 1 : -0.33

Table 3. Alpha decay width in 10^{-22} MeV. The last line gives the ratio of the total decay width for ^{211}Po and ^{211}Bi.

Alpha emitter	Alpha decay width (10^{-22} MeV)		
	Experiment	Old theory	New theory
^{211}Po	8.8	9×10^{-2}	12
^{211}Bi	3.5×10^{-2}	5.4×10^{-4}	4.4×10^{-2}
Γ_{Po}/Γ_{Bi}	250	167	273

Footnotes and References

*Condensed from LBL-4335, Phys. Rev. C13, 1318 (1976).

†Present address: Technische Universität München, Physikdept., 8046 Garching, W. Germany.

‡Permanent address: Technische Universität München Physikdept., 8046 Garching, W. Germany.

1. H. J. Mang, Ann. Rev. Nucl. Sci. 14, 1 (1964).

2. T. Fliessbach, Z. Physik A272, 39 (1975).

3. T. Fliessbach and H. J. Mang, preprint (1975).

Table 4. Alpha decay theoretical properties from ground and excited states.

State of ^{212}Po	Spectroscopic factors S			Hindrance factors [S(0_1)/S(excited)]	
	Old theory (10^{-5})	New theory (10^{-2})	Ratio new to old (10^{2})	Old theory	New theory
0_1	6.0	2.6	4	1	1
0_2	0.71	3.1	44	8	0.8
0_3	0.17	0.16	9	35	16
2_1	1.6	0.56	3.5	4	5
2_2	0.09	0.40	44	66	7
2_3	0.17	0.47	3	35	6
2_4	0.08	0.04	5	71	68
2_5	1.6	0.29	2	4	9
4_1	0.79	0.20	2.5	8	13
10_1	2.8	0.76	3	2	3
16_1	0.79	0.39	5	8	7
18_1	6.0	0.50	1	1	5

APPLICATION OF THE COUPLED CHANNEL ALPHA DECAY THEORY TO ODD-MASS NUCLEI*

A. J. Soinski,† E. A. Rauscher,
J. O. Rasmussen, and D. G. Raich

The alpha decay of spheriodal nuclei in which coupling exists between the emitted alpha particle and the internal parent nuclear states, can be treated with a set of coupled equations. The primary noncentral coupling is the collectively enhanced rotational E2 transitions. We set up and numerically integrated a set of coupled second-order linear differential equations in the radial separation variable for the penetration through an anisotropic barrier.

Although other researchers have performed the numerical integration of coupled channel equations for the alpha decay of even-even spheriodal nuclei, only Chasman and Rasmussen[1] have considered alpha decay of odd-mass nuclei. In the latter case the conservation of angular momentum permits an alpha particle partial wave of a given orbital angular momentum, ℓ, to branch to more than one energy level of the daughter nucleus. Thus, for the favored alpha decay of ^{233}U Chasman and Rasmussen considered the decay of the s-wave to the 5/2 level and the branching of the d-wave to the 5/2, 7/2 and 9/2 levels of ^{229}Th. Channel coupling effects are most significant for the case of a relatively weak wave, such as the highly hindered g-wave, coupled to a strong wave such as the s-wave. Therefore, we have extended the work of Chasman and Rasmussen by considering the branching of the s-, d-, and g-waves in the favored alpha decays of both ^{253}Es and ^{255}Fm. Favored alpha decays are those in which the quantum numbers of the odd nucleon are the same for both the parent and daughter. Both ^{253}Es and ^{255}Fm are spin 7/2 nuclei and are ideal for applying an exact numerical treatment because alpha transitions to the favored bands of the daughters have been well studied.[2] And angular distribution data from low temperature nuclear alignment experiments are available.[3] If we include the $\ell = 0$, 2, and 4 partial waves, then nine coupled second-order differential equations must be solved for favored decays to the five lowest levels (7/2, 9/2, 11/2, 13/2, 15/2) of the daughter rotational band. Contribution from the $\ell = 6$ was found to be small, as it has a large hindrance factor.

The formalism for the alpha decay in the presence of a noncentral field is given by Perlman and Rasmussen.[4] A multipole expansion is made for the Coulombic potential energy outside the nuclear surface where the zero order term is the central Coulombic term. The E2 interaction contributes the only important coupling term for these nuclei. The coupled differential equations in the radial separation variable can be written

$$u''_{I_d,\ell} - \frac{2M}{\hbar^2}\left(\frac{2Ze^2}{r} + \frac{\hbar^2\ell(\ell+1)}{2Mr^2} - Q_{I_d}\right)u_{I_d,\ell}$$

$$= \sum_{I'_d,\ell'} K^2_{I_d\ell I'_d\ell'}\ u_{I'_d,\ell'}$$

where M is the reduced mass, Z is the charge of the daughter nucleus, Q_{I_d} is the effective Q value for the alpha particle (with electron screening and daughter recoil energy corrections), and the $K^{\ell}_{I_d \ell I_d' \ell'}$ are matrix element of the quadrupole coupling operator which is proportional to the product of the intrinsic nuclear quadrupole moment of the daughter times $P_2(\cos\theta)$ divided by r^3, and r is the radial separation variable.

Explicit expressions for the quadrupole coupling matrix element were given for alpha decay by Perlman and Rasmussen[4] and for optical model scattering applications by Tamura.[6] The general method of solution of coupled equations is given by E. A. Rauscher et al.[7] Solutions of the coupled differential equations approach the Coulomb functions asymptotically at large radius.

We construct a set of nine second-order coupled differential equations which is transformed into a set of eighteen first-order coupled differential equations having eighteen linearly independent solutions or, equivalently, nine complex solutions. Because the physically meaningful solutions are exponentially decreasing going outward through the barrier, it was not possible to obtain stable solutions by outward numerical integration. Instead we used Coulomb functions as starting conditions at a radius sufficiently large (150 fm) such that the coupling forces were small and integrated inward to 10 fm. The solutions of interest then increased in the direction of integration and thus were stable. In general the phase of an oscillating coupled-channel solution in the far region will differ from the phase of the corresponding Coulomb function. This phase difference will be referred to as the quadrupole phase shift, ϕ_{I_d}. Although phase shifts do not affect intensity data, they do affect angular distribution data through the interference terms between different alpha waves going to the same final state I_d.

The experimental intensities are sensitive only to the relative partial wave intensities whereas the alpha particle angular distributions are sensitive to both the relative partial wave intensities and phases. The angular distribution data yield directly a maximum of two numbers to compare with theory whereas the intensity data yield four. For odd-mass nuclei there are insufficient relative intensity data to provide the required boundary conditions. For the problem considered here, eight boundary conditions are required. For the five levels of the daughter there are only four relative intensities, and there exist no direct experimental measurements of the mix and the relative phases of the partial waves. The low temperature angular distribution data provide two experimental numbers (the coefficients of the $P_2(\cos\theta)$ and $P_4(\cos\theta)$ terms in the angular distribution), but they do not determine uniquely relative partial wave amplitudes and phases.[8] Because there are insufficient experimental data to completely fix the boundary conditions, we used nuclear model constraints. The remaining two boundary conditions were left as free parameters and are denoted by α_2, the ratio of total d- and s-wave amplitude at R_0 the nuclear surface and α_4, the ratio of total g- to s-wave amplitude at R_0.

The numerical integration of the coupled differential equations permits us to test two assumptions of the strong coupling model as usually applied.[8] The first is that near the nuclear surface only $m_\ell = 0$ alpha partial waves occur. Subject to this $m_\ell = 0$ constraint, we wish to determine if the coupled channel treatment can reproduce both the experimental relative intensities to the five lowest rotational levels (with spins 7/2, 9/2, 11/2, 13/2 and 15/2) of the daughter and the angular distribution data.

The coupled channel treatment can also improve the usual approximate handling of anisotropic barrier penetrability by setting the relative intensity of a given wave to a given level equal to (the square of a Clebsch-Gordan coefficient) times (a calculated spherical barrier penetrability factor for the alpha group). (This approximation is exact only in the limit of infinite moment of inertia or vanishing nuclear quadrupole moment.)

The most general way to present the results of the numerical integration is in the form of the complex matrix $\underset{\sim}{U}^{-1}$ (the inverse of a complex 9×9 matrix $\underset{\sim}{U}$). The matrix elements of U are the amplitudes of the linearly independent solutions on or near the nuclear surface. These matrices reduce to unit matrices for vanishing nuclear quadrupole moment. Operation with either complex matrix on any boundary conditions on a sphere near the nuclear surface will yield partial wave amplitudes and quadrupole phase shifts at large distances. If boundary conditions are fixed on the spheroidal nuclear surface, then a Fröman matrix can be used to transform them to boundary conditions on a sphere at 10 fm. The real and imaginary components of our matrix are given in Table 1 for ^{253}Es. In Ref. 9, we presented the percentage intensities for favored rotational band alpha decay for the two odd mass nuclei discussed here.

It is still not clear why it is insufficient to have only K = 0 components of alpha waves to fit the experimental alpha population pattern to the ground basis. This question was discussed in more detail in Ref. 8.

Table 1. Inverse of ^{253}Es surface amplitude matrix.

I_f^{π}, ℓ'	7/2, 0	7/2, 2	7/2, 4	9/2, 2	9/2, 4	11/2, 2	11/2, 4	13/2, 4	15/2, 4
	Real Components								
7/2, 0	2.8389E-13	-4.6847E-14	1.9146E-15	4.3804E-14	-3.7024E-15	-2.1475E-14	4.2709E-15	-3.2217E-15	1.4631E-15
7/2, 2	-4.3547E-14	2.0829E-13	-2.3962E-14	1.9060E-14	2.5946E-14	1.1510E-14	-1.0063E-14	-6.9621E-16	-8.9831E-16
7/2, 4	1.4277E-15	-2.0215E-14	1.3146E-13	-8.5929E-15	1.4367E-14	-1.7849E-15	5.4143E-15	9.1879E-16	1.8802E-16
9/2, 2	3.3704E-14	1.5873E-14	-8.4537E-15	1.8553E-13	-4.3859E-15	2.2326E-14	2.0732E-14	-1.5144E-14	-1.9630E-15
9/2, 4	-2.2258E-15	1.8075E-14	1.1941E-14	-3.7263E-15	1.0910E-13	-2.7208E-15	1.2417E-14	4.2887E-15	5.2145E-16
11/2, 2	-1.2974E-14	7.4187E-15	-1.3697E-15	1.7650E-14	-2.5409E-15	1.3910E-13	1.0486E-15	1.0774E-14	-1.6848E-14
11/2, 4	1.9536E-15	-5.5072E-15	3.5009E-15	1.3687E-14	9.8292E-15	8.4889E-16	8.2428E-14	8.0484E-15	2.1089E-15
13/2, 4	-1.0550E-15	-2.6002E-16	4.0641E-16	-7.3796E-15	2.5092E-15	6.7963E-15	6.0775E-15	5.7544E-14	3.9566E-15
15/2, 4	3.1896E-16	-2.0937E-16	5.1909E-17	-5.8781E-16	1.9458E-16	-7.2664E-15	1.1137E-15	2.8357E-15	3.7143E-14
	Imaginary Components								
7/2, 0	-3.0880E-15	7.1623E-15	-6.0093E-16	-5.2612E-15	1.0389E-15	1.8321E-15	-1.0344E-15	6.4430E-16	-2.2668E-16
7/2, 2	9.0650E-15	4.8316E-16	2.8864E-15	-1.8774E-15	-2.1759E-15	-1.9257E-15	3.0429E-16	9.5706E-17	2.0476E-16
7/2, 4	-7.6426E-16	5.0520E-15	-7.1092E-16	2.1082E-15	-1.7815E-15	6.1921E-16	-8.0746E-16	-2.7953E-16	-7.2756E-17
9/2, 2	-8.4270E-15	-2.7345E-15	1.6148E-15	-3.0496E-15	3.5162E-16	-2.8575E-15	-1.8721E-15	7.3266E-16	4.0018E-16
9/2, 4	1.3129E-15	-5.2155E-15	-2.3553E-15	7.6912E-16	-1.4927E-15	4.3253E-16	-1.5535E-15	-5.6217E-16	-1.3488E-16
11/2, 2	3.9184E-15	-2.4771E-15	5.2540E-16	-3.8694E-15	3.2717E-16	-1.4089E-15	-3.7746E-16	-6.6735E-16	8.5652E-16
11/2, 4	-1.2899E-15	1.7539E-15	-1.0952E-15	-4.2999E-15	-2.1287E-15	-4.3671E-16	-1.0788E-15	-8.2390E-16	-1.8860E-16
13/2, 4	7.8883E-16	1.4832E-16	-2.5308E-16	2.7423E-15	-8.2254E-16	-2.0551E-15	-1.2873E-15	-4.2879E-16	-2.6281E-16
15/2, 4	-2.7308E-16	1.8442E-16	-4.7919E-17	-4.3275E-16	-1.2334E-16	2.9673E-15	-3.5411E-16	-5.5705E-16	-3.7901E-17

Footnotes and References

*Condensed from LBL-5075.

†Presently at LFE Environmental Analysis Laboratory, Richmond, California.

1. R. R. Chasman and J. O. Rasmussen, Phys. Rev. 115, 1257 (1959).

2. I. Ahmad, F. T. Porter, M. S. Freedman, R. F. Barnes, R. K. Sjoblom, Phys. Rev. C2, 390 (1971).

3. A. J. Soinski, R. B. Frankel, W. O. Navarro and D. A. Shirley, Phys. Rev. C2, 2379 (1970).

4. I. Perlman and J. O. Rasmussen, Handbuch der Physik, ed. S. Flügge, 42, 169 (1957).

5. J. O. Rasmussen, Alpha-Beta and Gamma-Ray Spectroscopy, K. Siegbahn, ed. (North-Holland Pub. Co., The Netherlands, 1965), Vol. 1, p.701.

6. T. Tamura, Rev. Mod. Phys. 37, 679 (1965).

7. E. A. Rauscher, J. O. Rasmussen and K. Harada, Nucl. Phys. A94, 33 (1967).

8. A. J. Soinski, LBL-3411, September 1974 (Thesis, unpublished).

9. A. J. Soinski, D. G. Raich, J. O. Rasmussen and E. A. Rauscher, Nuclear Chemistry Annual Report, LBL-2366 (1973).

2. Macroscopic

MODIFIED THOMAS-FERMI APPROXIMATION FOR MOMENTUM-DEPENDENT INTERACTIONS*

J. Randrup†

A modification of the standard Thomas-Fermi approximation has been suggested for the treatment of interactions having a quadratic momentum dependence.[1] While of general theoretical nature this subject has particular interest to nuclear physics, where numerical studies are carried out with phenomenological momentum-dependent interactions.

Suppose, in a many-particle system, a two-body interaction is present which depends quadratically on the relative momentum $\vec{p}_{12}$. Let the spatial dependence be given by the function $g(\vec{r}_{12})$, where $\vec{r}_{12}$ is the particle separation. For the following discussion the momentum-independent part of the interaction can be disregarded. Such interaction may then have the form $1/2(p^2g + gp^2)$, or $\vec{p}g\vec{p}$, or a linear combination of these two forms. This group constitutes the class of interactions to which the suggested modification applies.

The standard Thomas-Fermi treatment is briefly recalled. Suppose that the local Fermi momentum $p_F(\vec{r})$ is a known function of position. At each point the particles are assumed to be distributed uniformly within the available momentum sphere. This implies that the local density $\rho(\vec{r})$ is given by

$$\rho(\vec{r}) = \frac{t}{h^3}\int^{p_F(\vec{r})} d^3\vec{p} = \frac{4\pi}{3}\, t\, \frac{p_F(\vec{r})^3}{h^3}$$

where t denotes the degeneracy in each single-particle orbit. The (only) kinetic density is given by

$$\tau(\vec{r}) = \frac{t}{h^3}\int^{p_F(\vec{r})} p^2 d^3\vec{p} = \frac{3}{5}\, p_F(\vec{r})^2\, \rho(\vec{r})$$

Any two-body interaction of the form $\vec{p}^2 g(\vec{r})$ gives rise to the same effective static potential $V = p^2\mathcal{R}(r) + \mathcal{G}(r)$ irrespective of the particular algebraic form of the interaction. Here the functions $\mathcal{R}$ and $\mathcal{G}$ are obtained by folding ρ and τ by the spatial function g. Furthermore, the associated interaction energy density is given by $v = 1/2(\tau\mathcal{R} + \rho\mathcal{G})$.

Thus, in the standard Thomas-Fermi treatment, no distinction is made between the different interactions mentioned above. However, at least in the nuclear case, different algebraic forms may lead to significantly different results for the self-consistent many-particle solution. Therefore, it is desirable to have available, within the simple Thomas-Fermi framework, a tool for the general analysis of such models.

The modification suggested may be formulated as follows. Any of the momentum-dependent interactions considered can be rewritten in the general form

$$W_{12}(\eta) = 1/2\{\vec{p}_{12}, 1/2\{\vec{p}_{12} g_{12}\}\} - \eta\, 1/2[\vec{p}_{12}, 1/2[\vec{p}_{12}, g_{12}]]$$

where $g_{12} = g(\vec{r}_{12})$. The square brackets denote the commutator and the curly brackets the anti-commutator. The parameter η is a real number characterizing a given particular interaction. For example, the first of the two forms mentioned above corresponds to $\eta = -1$ and the second one corresponds to $\eta = 1$.

The double-anticommutator algebraic form has been exhibited because this particular form tends to average out the undulations in the density distributions due to the quantum phase correlations in the single-particle wave functions. The presumption is now made that the Thomas-Fermi approximation, which completely neglects phase correlations, is most accurate for the quantities represented in terms of the double-anticommutator form. The modification suggested thus amounts to adding to the standard Thomas-Fermi formulas the contribution arising from the remaining η-dependent term.

Consequently, the effective single-particle potential V takes on the form $V_\eta = V_0 + \eta\delta V$, where V_0 is the effective potential given by the standard Thomas-Fermi approximation. The modification potential (which is momentum independent) is given by

$$\delta V(\vec{r}) = \hbar^2 \Delta\mathcal{R}(\vec{r})$$

where the function $\mathcal{R}$ is obtained from the density distribution ρ by folding with the spatial part of the interaction, g.

Correspondingly, the interaction-energy density v takes on the form $v_\eta = v_0 + \eta\delta v$, where v_0 is the standard Thomas-Fermi result and the modification term is given by

$$\delta v = 1/2\, \hbar^2\, 1/4(\rho\Delta\mathcal{R} + 2\vec{\nabla}\rho \cdot \vec{\nabla}\mathcal{R} + \Delta\rho\mathcal{R})$$

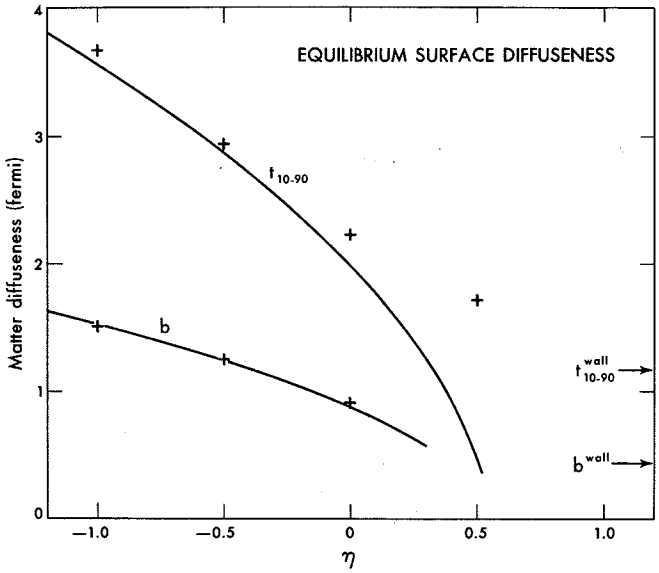

Fig. 1. Surface diffuseness. As a function of the parameter η is plotted the surface diffuseness for the self-consistent solution obtained with the modified Thomas-Fermi approximation. The quantities displayed are the 10-90% diffuseness, $t_{10\text{-}90}$, and the second surface moment b. The crosses indicate results obtained in the Hartree approximation. (XBL 759-3871)

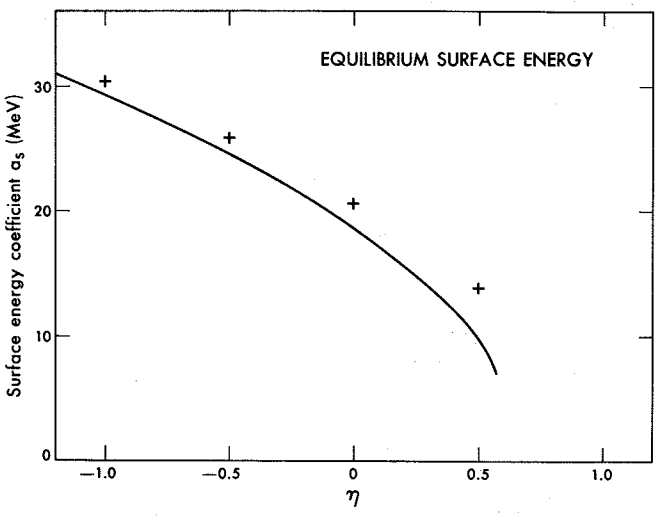

Fig. 2. Surface energy. As a function of the parameter η is plotted the surface energy coefficient a_s for the self-consistent solution obtained with the modified Thomas-Fermi approximation. The crosses indicate results obtained in the Hartree approximation.
(XBL 759-3870)

It is noted that in regions of constant ρ and ℜ there is no modification.

As an illustration, the case of the nuclear surface is considered. For this, a Seyler-Blanchard[1] type model is used,

$$W_{12}^{SB} = -Cg\left(\frac{r_{12}}{a}\right)\left(1 - \frac{p_{12}^2}{b^2}\right)$$

where g(r) = exp(-r)/r. Following Myers and Swiatecki[2] the three parameters entering are taken as a = 0.62567 fm, b = 372.48 MeV/c, and C = 328.61 MeV. Numerical calculations have been carried out for the family of interactions corresponding to the above form.

The self-consistent solution was calculated by use of modified Thomas-Fermi approximation, as a function of the parameter η. Figures 1 and 2 display the results for the surface diffuseness and the surface energy. Furthermore, "exact" values were obtained by use of the Hartree approximation, which maintains the independence of the particles while treating the quantum mechanics in an exact manner.

It is seen that the general η dependence of the results, as given by the Hartree values, is well reproduced in the modified Thomas-Fermi approximation. The systematic underestimation by the Thomas-Fermi approximation can be mainly accounted for by the lack of a density tail and the neglect of phase correlations near the surface.

When judging the value of the modification is should be borne in mind that without the modification all the different Hartree results would be approximated by the Thomas-Fermi results obtained for η = 0.

The suggested modified Thomas-Fermi approximation is currently being employed in a study of the nuclear surface.[3]

Footnotes and References

*Condensed from LBL-4308.

†On leave from the University of Aarhus, Aarhus, Denmark.

1. R. G. Seyler and C. H. Blanchard, Phys. Rev. 124, 227 (1961); 131, 355 (1963).

2. W. D. Myers and W. J. Swiatecki, Ann. Phys. 55, 395 (1969).

3. J. Randrup, Nucl. Phys. A259 (1976) 253.

THE NUCLEAR SURFACE STUDIED WITH A MOMENTUM-DEPENDENT INTERACTION IN THE THOMAS-FERMI AND HARTREE APPROXIMATIONS*

J. Randrup †

Further studies of the nuclear surface have been carried out with momentum-dependent effective interactions which in the classical limit reduce to the form

$$V_{12} = -Cg\left(\frac{r_{12}}{a}\right)\left(1 - \frac{p_{12}^2}{b^2}\right) \quad . \tag{1}$$

Here the separation between the two interacting particles is denoted by $\vec{r}_{12} = \vec{r}_1 - \vec{r}_2$ and their relative momentum by $\vec{p}_{12} = \vec{p}_1 - \vec{p}_2$ (it is assumed that all particles have the same mass m). The spatial dependence, assumed to possess spherical symmetry, is contained in the function g. (The Seyler-Blanchard[1] model corresponds to the special case of g being a Yukawa function.)

For the development of the quantum-mechanical model the interaction-energy operator corresponding to the classical interaction (1) must be specified. According to the standard rules of quantization, this is accomplished by replacing the momentum variable $\vec{p}$ in the classical interaction by the differential operator $-i\hbar\vec{\nabla}$, paying due respect to the requirement that the emerging operator be Hermitean. As is readily seen, there is no unique way of "quantizing" the classical product $p^2g(r)$. Rather, there exists a whole family of quantum-mechanical operators which all have the same classical limit. This family of operators may be parametrized by one real parameter since all of the possible algebraic constructions may be reduced to the form

$$p^2g(\vec{r}) \to 1/2\{\vec{p},1/2\{\vec{p},g(r)\}\} - \eta\, 1/2[\vec{p},1/2[\vec{p},g(\vec{r})]] \quad . \tag{2}$$

Here, the sharp brackets denote the commutator, $[a,b] = ab - ba$, and the curly brackets the anticommutator, $\{a,b\} = ab + ba$.

This unified formulation makes it possible to discuss in parallel the whole family of different quantum interactions. In passing it should be noted that $\eta = -1$ leads to $1/2(p^2g + gp^2)$ and $\eta = +1$ leads to pgp.

The two-particle interaction-energy density w is given by

$$w_\eta(\vec{r}',\vec{r}'') = -Cg(r/a)\ \rho(\vec{r}')\Big(\rho(\vec{r}'') + 2\vec{\pi}(\vec{r}')\cdot\vec{\pi}(\vec{r}'') - \rho(\vec{r}')\,\gamma(\vec{r}'') - \gamma(\vec{r}')\,\rho(\vec{r}'') - \eta\frac{\hbar^2}{b^2}\frac{1}{4}\Delta(\rho(\vec{r}')\,\rho(\vec{r}''))\Big) \tag{3}$$

where the Laplace operator Δ acts with respect to $\vec{r}$. The one-particle density distributions entering are the matter density ρ, the momentum density $\vec{\pi}$, and the kinetic density γ (which is not the standard kinetic-energy density but is defined in terms of the double-anticommutator construction).

The corresponding effective Hamiltonian may be written on the form

$$H_\eta^{\text{eff}} = 1/2\left\{\vec{p},1/2\left\{\vec{p},\frac{1}{2B}\right\}\right\} + U_\eta \quad , \tag{4}$$

i.e., in terms of a variable mass B and a static potential U_η. The effective mass B is given by the relation

$$\frac{1}{2B(\vec{r})} = \frac{1}{2m}\left(1 + \frac{C}{b^2/2m}\,\mathcal{R}(\vec{r})\right) \quad . \tag{5}$$

The renormalization of the particle mass arises from the quadratic momentum dependence of the interaction. The effective mass B does not depend on η, i.e., on which actual algebraic quantization form is chosen. The effective potential U is given by

$$U(\vec{r}) = -C\left(\mathcal{R}(\vec{r}) - \mathcal{G}(r) - \eta\frac{\hbar^2}{b^2}\Delta\mathcal{R}(\vec{r})\right) \quad . \tag{6}$$

(In the above expressions the functions $\mathcal{R}$ and $\mathcal{G}$ are obtained from the densities ρ and γ by folding with the spatial interaction g.) It should be pointed out that while the choice of another algebraic form of the kinetic term in the effective Hamiltonian would not affect the effective mass B as given above, it would lead to an modification of the effective potential U. A simple feature of the effective Hamiltonian is that it does not depend on which particle is considered; the functions B and U are common to all the particles.

The η-dependent term introduces an explicit sensitivity to density inhomogenities. For negative values of η such inhomogeneities will raise the energy and the term will have the effect of smearing out the inhomogenities. For positive values of η, however, the energy will be lowered by inhomogenities and the η-dependent term will tend to enhance them. This may prevent the existence of a self-consistent solution.

Studies were carried out for the case where the spatial dependence of the two-body interaction is a Yukawa function, $g(r) = \exp(-r)/r$. This corresponds to the type of interaction introduced by Seyler and Blanchard.[1] For the three model

parameters entering are chosen the values determined by Myers and Swiatecki[2] in their study of average nuclear properties. It should be added that the substance of the conclusions is not expected to depend either on the specific choice of a Yukawa spatial dependence or on the actual parameter values, as long as they are reasonable.

The properties of the nuclear surface have been studied by considering a semi-infinite system. It is easy to understand the general behavior of the self-consistent solution, considered as a function of the parameter η:

For a semi-infinite system the essential degree of freedom is associated with the surface diffuseness. As a function of the diffuseness, the part of the energy arising from the η-independent part of the interaction has a minimum at a certain diffuseness, the equilibrium diffuseness in the case of vanishing η. For the nonvanishing values of η, there is an additional energy contribution, proportional to η for a given system. The term multiplying η is negative; it tends to zero for very diffuse systems and to minus infinity for systems with very sharp surfaces. Hence, for negative η values, the additional term gives rise to an increase of the surface energy. Furthermore, it follows that the diffuseness equilibrium value is shifted towards larger values. It is worthwhile noticing that an equilibrium always exists for negative η. In the opposite case, $\eta > 0$, there is a negative contribution from the η-dependent term. For sufficiently small η values, the addition of the above-mentioned diverging function to the original function pertaining to $\eta = 0$ will still result in a function having a local minimum (as well as maximum). The value at the minimum as well as the corresponding diffuseness will be decreased relative to the case of $\eta = 0$. However, as is evident in this simple picture, for positive η values above a certain critical value the minimum disappears and no self-consistent solution exists.

These simple qualitative considerations are borne out by actual calculations, as is illustrated in Fig. 1, which is a plot of the surface energy vs the surface diffuseness. The circles indicate the locations of the equilibrium solutions obtained with the modified Thomas-Fermi approximation described in the previous contribution to this report. The figure also displays the two curves referred to in the preceding qualitative discussion, namely the η-independent part of the surface energy, a_s^o, and the contribution δa_s from the term multiplying η. The first curve is to a very good approximation identical to what would result from a simple scaling (stretching or compression) from the equilibrium solution corresponding to $\eta = 0$; this fact underscores the close relation between the surface diffuseness and the freedom associated with the η parameter. In this figure is also shown parts of the surface-energy curves for a few nonvanishing η values. Finally it should be added that the results for η values larger than 0.5 are less accurate and are indicated by dashed lines.

The self-consistent solution has also been

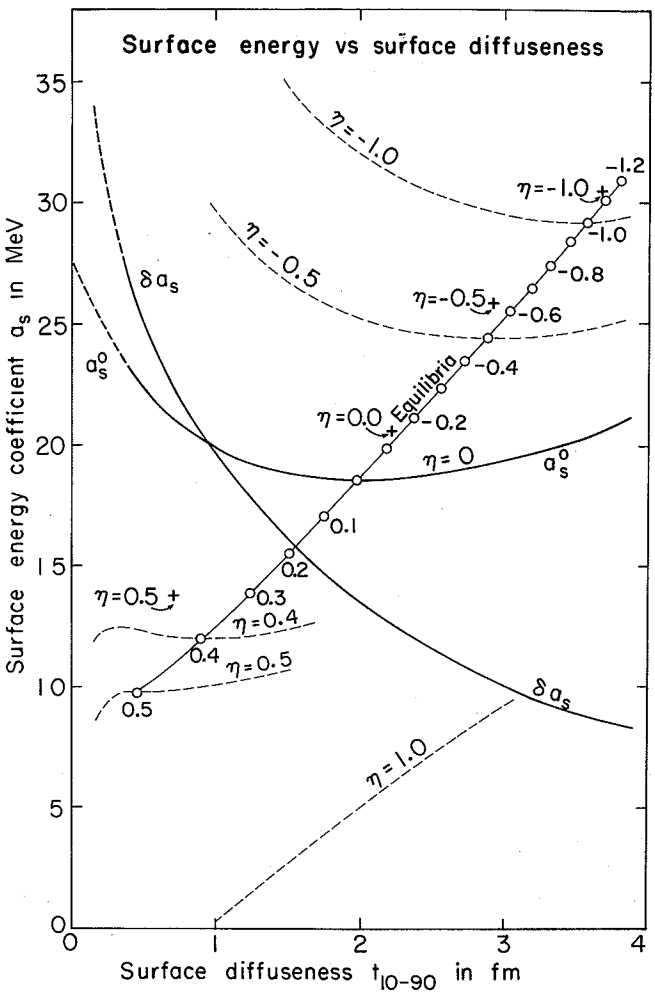

Fig. 1. Surface energy vs surface diffuseness. The curve labeled "equilibria" joins the locations of the Thomas-Fermi equilibrium solutions obtained for a series of values of the parameter η. The abscissa is the 10-90% matter diffuseness t_{10-90} and the ordinate is the surface energy coefficient a_s. The curve labeled "a_s^o" is the contribution to the surface energy originating from the η-independent part of the Hamiltonian; it is to a very good approximation identical to what would result from simply stretching or compressing the equilibrium solution corresponding to $\eta = 0$. The curve labeled "δa_s" is the contribution to the surface energy due to the η-dependent term (with the η divided away). The total surface energy $a_s = a_s^o + \eta \delta a_s$ is plotted as a function of the diffuseness for some values of η (dashed curves). The crosses indicate the self-consistent Hartree solutions calculated for four selected values of η.
(XBL 759-3876)

calculated in the Hartree approximation, for η = -1.0, -0.5, 0.0, and 0.5. Figure 2 displays the resulting matter density distributions; the corresponding Thomas-Fermi densities are indicated by dashed lines. The extracted values for the surface diffuseness and the surface energy are indicated in Fig. 1 by crosses.

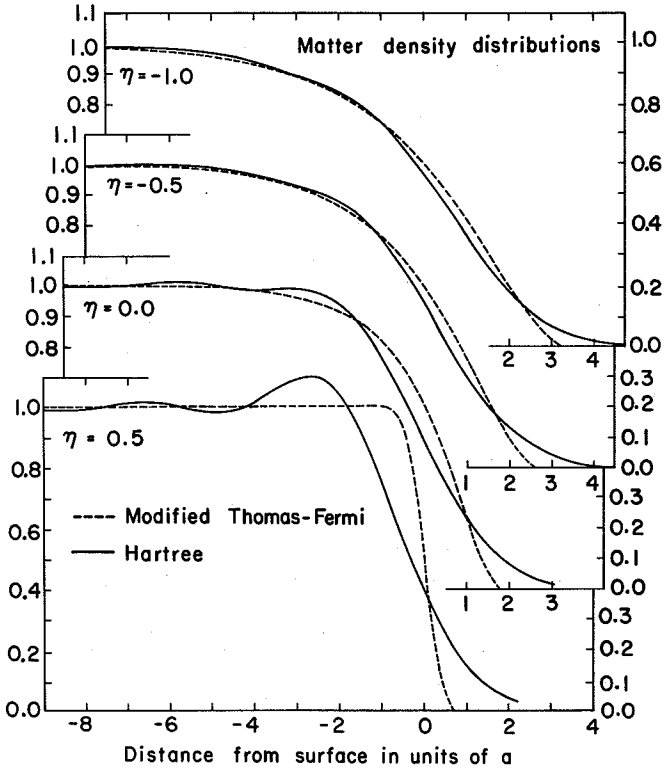

Fig. 2. Matter density distribution (in units of the bulk value) for four selected values of the parameter η. The dashed curves are the results obtained with the modified Thomas-Fermi approximation while the Hartree results are shown by the full curves.

(XBL 759-3874)

The general trend given by the modified Thomas-Fermi analysis is well reproduced on the whole by the Hartree calculation. In particular, the results indicate that no Hartree solution exists for η values appreciably above 0.5. The 10-90% surface diffusenesses obtained in the Hartree calculations are somewhat larger than the corresponding Thomas-Fermi values. This is mainly due to the density tail extending into the classically forbidden region outside the surface. This effect becomes particularly noticeable for positive η values when the Thomas-Fermi diffuseness approaches zero. For large negative values of η, where the system becomes more and more diffuse, the geometric properties of the surface profile will scale with the diffuseness. Hence, the absolute discrepancy between the Thomas-Fermi value and the Hartree value for t_{10-90} will increase while the ratio will tend to a constant value. For η = 0 the relative underestimation is 10.4% and for η = -1 it is 3.2%.

For the surface energy there is also general agreement as to the dependence on η. The modified Thomas-Fermi approximation underestimates the surface energy, and increasingly so with increasing η. For η = -1 the discrepancy amounts to 3.6% and for η = 0 to 9.7%.

Table 1. Results for the surface diffuseness t_{10-90} and the surface energy a_s, for various values of the parameter η. The upper results are obtained in the modified Thomas-Fermi approximation while the lower results are obtained in the Hartree approximation.

η	-1.0	-0.5	0.0	0.5
t_{10-90}(fm)	3.58	2.88	1.99	0.53
	3.70	2.95	2.22	1.71
a_s(MeV)	29.25	24.48	18.56	9.77
	30.34	25.85	20.55	13.75

A summary of the results for the surface diffuseness t_{10-90} and the surface energy a_s is presented in Table 1. Generally, the results obtained with the modified Thomas-Fermi approximation agree relatively well (typically to within 10%) with the Hartree results. The surface diffuseness as well as the surface energy are somewhat underestimated by the Thomas-Fermi treatment. For the surface diffuseness, this is mainly a consequence of the absence of a density tail. The underestimation of the surface energy can (for the main part) be traced to the neglect of the phase correlations in the surface region.

In conclusion the following can be stated. In the nuclear case, the particular algebraic form of the momentum dependence of the two-body interaction has a large bearing on the surface properties of the corresponding self-consistent many-particle solution; this is underscored by the fact that for certain (not extreme) forms no solution exists. With a simple modification, the Thomas-Fermi approximation can be used for the treatment of many-particle systems with (quadratically) momentum-dependent interactions. This extends appreciably the applicability of the Thomas-Fermi approximation for the study of nuclear properties.

Footnotes and References

*Condensed from LBL-4302, Nucl. Phys. A257 (1976) 253.

†On leave from Aarhus University, Aarhus, Denmark.

1. R. G. Seyler and C. H. Blanchard, Phys. Rev. 124, 227 (1961); 131, 355 (1963).

2. W. D. Myers and W. J. Swiatecki, Ann. Phys. 55, 395 (1969).

THE NUCLEAR INTERACTION POTENTIAL IN A FOLDED-YUKAWA MODEL WITH DIFFUSE DENSITIES*

J. Randrup †

The study of the interaction between two nuclei has become of increasing interest in recent years. Several models have been suggested for the calculation of the nuclear interaction potential. For example, Krappe and Nix[1] have proposed a model in which the interaction energy is calculated as the Yukawa interaction between two nuclear distributions with sharply defined surfaces and uniform interior. The Yukawa interaction is supposed to contain the combined effect of two diffuse matter distributions interacting via some short range interaction. This procedure leads to a simple analytic potential.

A different approach is represented by the Proximity Formula,[2] which expresses the force between two gently curved leptodermous surfaces as a product of a geometrical factor proportional to the mean radius of curvature of the gap between the surfaces and a universal function equal to the interaction energy per unit area between two parallel surfaces. This latter approach approach is very general and has the advantage of being simple to use, once the problem involving the parallel surfaces has been solved.

In this work an analytical model has been studied which enables one to gain insight into the accuracy of some of the various approaches, including the two mentioned above. In the model studied, each of the two interacting objects has a diffuse surface which is generated by folding a Yukawa function into a generating sharp-surface distribution. The interaction energy is subsequently obtained on the basis of a two-body Yukawa interaction.

This model can be considered a generalization of the Krappe-Nix[1] model. Hence it permits a test of the idea that the interaction can be represented as a single effective Yukawa interaction acting between sharp-surface distributions. Moreover, the model is sufficiently realistic to present a good test case for the Proximity Formula.[2] So far, such tests have only been carried out for the extreme cases of zero-diffuseness distributions (the Krappe-Nix model) or a zero-range interaction between diffuse surfaces.[2]

The interaction energy V between two matter distributions ρ_1 and ρ_2 is given by

$$V = -C \iint \rho_1(r_1)\, Y_{a_0}(r_{12})\, \rho_2(\vec{r}_2)\, d^3\vec{r}_1 d^3\vec{r}_2$$

where the notation

$$Y_a(r) \equiv \frac{1}{4\pi a^3} \frac{e^{-r/a}}{r/a}$$

has been introduced. The strength of the interaction is governed by the constant C which is positive for an attractive interaction. The matter density distribution ρ_i (i = 1,2) is obtained by folding a Yukawa function of some range a_i into a generating sharp distribution $\hat{\rho}_i$,

$$\rho_i(\vec{r}_1) = \int Y_{a_i}(r_{12})\, \hat{\rho}_i(\vec{r}_2)\, d^3\vec{r}_2 \quad .$$

The starting point for the analytical treatment of this model is the observation that the interaction energy may be calculated as the interaction between the two sharp generating densities arising from a composite two-body interaction $-C\mathscr{Y}$. This composite interaction is given as the folding product of the three entering Yukawa interactions,

$$\mathscr{Y} = Y_{a_0} * Y_{a_1} * Y_{a_2}$$

(the symbol * denotes the folding).

It should be stressed at this point that the above observation implies that the formulated generalized folded-Yukawa model is conceptually similar to the standard folded-Yukawa model due to Krappe and Nix[1] in that it calculates the energy by folding some kernel into generating sharp densities. The generalized model thus applies to all cases covered by the Krappe-Nix model. In particular, the modified surface-energy prescription suggested by Krappe and Nix[1] can be generalized by employing the composite kernel $\mathscr{Y}$ rather than a single Yukawa function.

The final formula for the interaction potential may be written in the form

$$V(d) = -C \sum_{i=0}^{2} \left(1 - \frac{a_j^2}{a_i^2}\right)^{-1} \left(1 - \frac{a_k^2}{a_i^2}\right)^{-1} \Gamma_{a_i}(R_1)\, \Gamma_{a_i}(R_2)\, Y_{a_i}(d) \quad .$$

This formula is valid in the case where the two generating spheres are positioned outside each other (which is the case of interest in the present study); otherwise more complicated expressions will result (they may be obtained by the same method). Furthermore,

$$\Gamma_a(R) \equiv 4\pi a^3 \left(\frac{R}{a} \cosh \frac{R}{a} - \sinh \frac{R}{a}\right)$$

is a geometrical factor depending on the size of the sphere. It has the limiting forms, $\Gamma \sim \frac{4\pi}{3} R^3$ for $R \ll a$ and $\Gamma \sim 2\pi a^2 (R - a) \exp(R/a)$ for $R \gg a$.

The above formula applies to the case of different Yukawa ranges, $a_0 \neq a_1 \neq a_2 \neq a_0$. The various degenerate cases can be obtained by taking the appropriate limit. This leads to relatively complicated expressions. However, for most numerical purposes it is satisfactory to use the above formula with a small arbitrary splitting of the degenerate ranges; this has been done in the present study. It should be noted that if one of the Yukawa ranges tends to zero the corresponding term simply drops out.

The general formulation given above covers a number of special cases of interest, in particular the case of zero density diffuseness and the case of zero interaction range. These two particular models may be discussed relative to a more realistic reference case having diffuse densities and a finite interaction range.

The reference case, which shall henceforth be noted as the standard model, is characterized by the following parameter values:

$$\gamma = 1 \text{ MeV/fm}^2$$

$$a_o = 1 \text{ fm}$$

$$a_1 = a_2 = 1/\sqrt{2} \text{ fm} \quad .$$

Here γ is the nominal surface energy coefficient defined as minus half the interaction energy per unit area for two parallel semiinfinite system at contact. It is more convenient to specify γ than the interaction strength C. With the above values for γ and the ranges a_0, a_1, and a_2, the value of the interaction strength follows as

$$C = 1/\left(1 - \frac{7}{16}\sqrt{2}\right) \text{ MeV} \quad .$$

The value of 1 MeV/fm^2 chosen for the nominal surface energy is realistic.[2] Furthermore, it is noted that the surface diffuseness implied by the values chosen for a_1 and a_2 is given by b = 1 fm which is also a realistic value.[3] As an illustration, Fig. 1 shows a comparison of the above standard model and the zero-diffuseness (Krappe-Nix) models (the quantity b is the second surface moment), with the following set of parameter values:

$$\gamma = 1 \text{ MeV/fm}^2$$

$$a_0 = \sqrt{2} \text{ fm}$$

$$a_1 = a_2 = 0 \quad .$$

It should be noted that the value of the range parameter a_0 is close to the value of 1.4 fm employed by Krappe and Nix.[1] It is seen that while agreeing on the whole quite well when close to contact (which is a consequence of the demand that the nominal surface energies be the same) the zero-diffuseness model gives rise to a longer tail. This is because the long-range behavior is governed by the largest of the

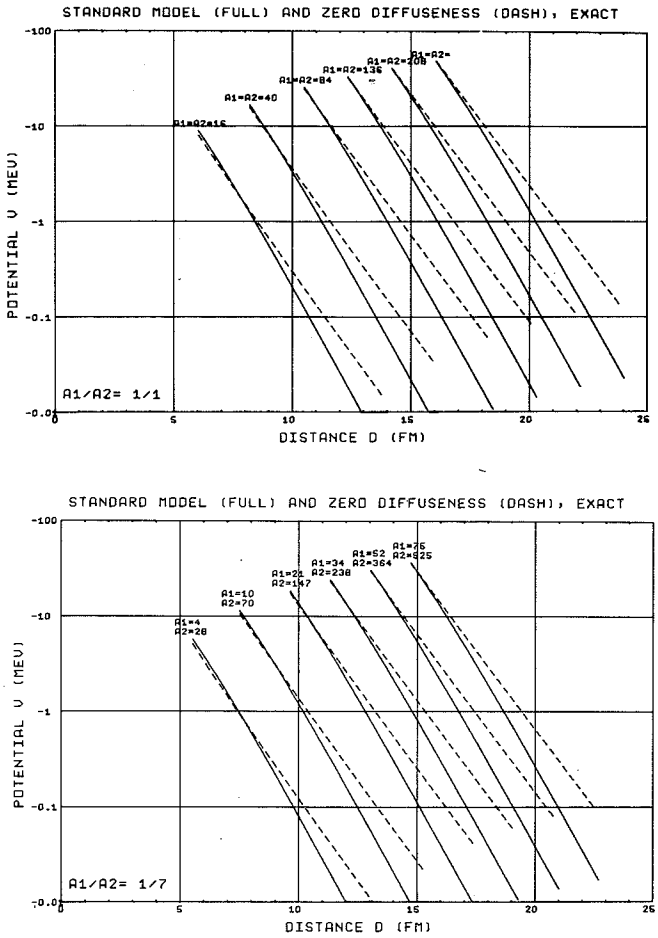

Fig. 1. The potential obtained by the standard model (full lines) and the zero-diffuseness (dashed lines), (b) for two different values of the mass ratio. (XBL 759-8226) (XBL 759-8238)

three Yukawa ranges entering in each model.

The Proximity Formula[2] reads

$$V_p(s) = 2\pi\bar{R}\int_s^\infty e(s')\,ds' = 2\pi R\bar{e}(s) \quad .$$

Here s is the separation between the effective surfaces which are located at the radii C_1 and C_2. The geometrical factor $\bar{R}$ is given in terms of the effective radii by the relation $\bar{R}^{-1} = C_1^{-1} + C_2^{-1}$. Furthermore, the function e(s) is the interaction energy per unit area between two parallel semi-infinite surfaces with a separation equal to s.

In the generalized folded-Yukawa model, the expression for the integrated function $\varepsilon(s)$ is

$$\varepsilon(s) = -C\sum_{i=0}^{2} a_i^3\left(1 - \frac{a_j^2}{a_i^2}\right)^{-1}\left(1 - \frac{a_k^2}{a_i^2}\right)^{-1}\frac{1}{2a_i}e^{-s/a_i} \quad .$$

As in the preceding, the proper limit must be taken if some of the Yukawa ranges a_i are equal.

The geometrical factor $\bar{R}$ entering in the Proximity Formula is given in terms of the effective radius C_i which is taken as the average of the density profile location and the potential profile location,[2]

$$C_i = R_i - \frac{a_0^2 + 2a_i^2}{R_i} \quad .$$

The separation s between the effective surfaces is given by $s = d - C_1 + C_2$ where d is the distance between the two centers.

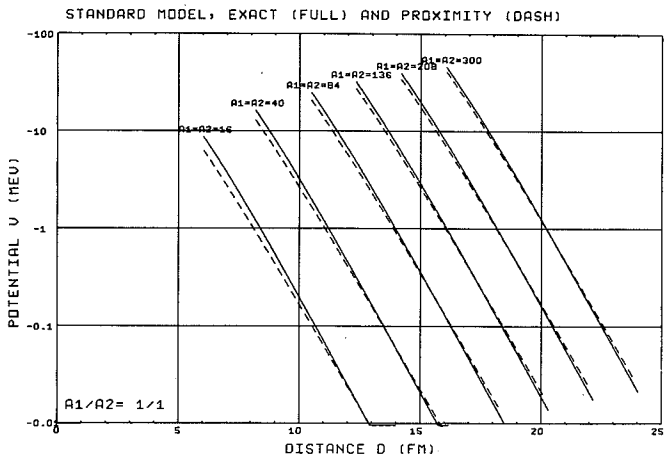

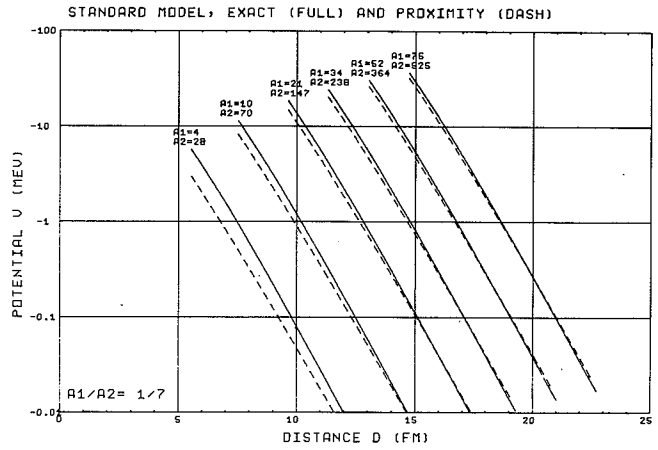

Fig. 2. Standard model. The exact interaction potential is given by the full curves while the proximity expression is indicated by the dashed curves. Results for two different mass ratios are displayed. (XBL 759-8221) (XBL 759-8233)

The Proximity Formula has been compared numerically with various exact models. As an example, Fig. 2 shows a comparison made for the standard model. On the whole the reproduction of the exact results is good, except for systems containing very light nuclei. It should be stressed that the absolute as well as the relative agreement is good, over the wide range of nuclear combinations considered and over distances where the potential changes by more than a factor of a hundred. This result provides support for the applicability of the Proximity Formula[2] to the study of heavy-ion interactions.

The folded-Yukawa model[1] has been generalized to the case where the two interacting objects have a diffuse surface, generated by folding a Yukawa function into a sharp generating distribution. While only slightly more complicated to treat than the usual folded-Yukawa model, the generalized model is conceptually more appealing. Furthermore, it includes the folded-Yukawa model as well as the δ-interaction model as special cases. This facilitates the analytical study of effects associated with the density diffuseness and the interaction range.

Moreover, the generalized folded-Yukawa model provides a realistic case for testing approximative representations of the interaction potential. In this study the Proximity Formula[2] was investigated; its quanitative validity was generally supported.

Finally, it should be recalled that the possible applicability of the generalized folded-Yukawa model extends beyond the nuclear interaction potential. For example, the modified-surface-energy prescription suggested by Krappe and Nix[1] can be easily generalized along the same lines.

Footnotes and References

*Condensed from LBL-4317.

†On leave from the University of Aarhus, Aarhus, Denmark.

1. H. J. Krappe and J. R. Nix, Proc. Third IAEA Symposium on the Physics and Chemistry of Fission, Rochester, NY, IAEA-SM-174/12 (1973) 159.

2. J. Blocki, J. Randrup, W. J. Swiatecki and C. F. Tsang, LBL-5014, to be published.

3. W. D. Myers, Nucl. Phys. A204, 465 (1973).

MACROSCOPIC ASPECTS OF NUCLEUS-NUCLEUS INTERACTIONS*

J. Blocki,† J. Randrup, ‡ W. L. Swiatecki, C. F. Tsang§

The following qualitative classification of nucleus-nucleus interactions has been found to be useful in sorting out the great variety of experimental data (see Fig. 1). Nuclei that do not Touch undergo Distant Collisions, where only electromagnetic interactions, modified by the tail of the

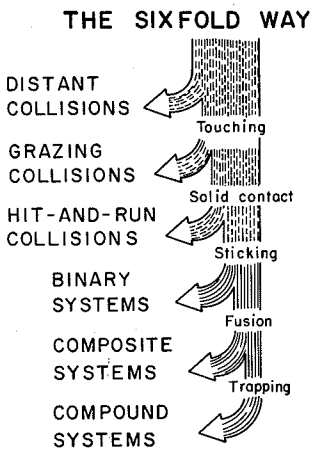

Fig. 1. An attempt to classify collisions between two nuclei into six main categories. (XBL 759-4071)

nuclear potential, come into play. (Touching could be defined approximately as touching of the Fermi levels of the two systems.) Nuclei that touch but do not make Solid Contact undergo Grazing Collisions. (Solid Contact might be defined approximately as beginning when the half-density contour acquires the topology of a single object.) Nuclei that make solid contact but do not Stick make Hit-and-Run Collisions. (Sticking might be defined approximately in terms of the sharing of linear momentum.) Nuclei that stick but do not Fuse form a Binary System. (Fusion might be defined in terms of the loss of identity of the pieces, associated with a filling-in of the neck.) Nuclei that fuse but are not Trapped form a Composite System. The remainder are trapped in a potential energy hollow, and form a Compound System.

The first problem in describing the above processes, whether quantally or classically, is to map the potential energy as a function of the shape of the system.

With certain qualifications it is possible to prove the following theorem about the functional form of the potential energy V(shape) of a thin-skinned system of volume $\mathcal{V}$ whose shape is specified by an (effective sharp) surface Σ.

$$V(\text{shape}) = V_{\text{Bulk}} + V_{\text{Surface Layer}} \qquad (1)$$

where

$$V_{\text{Bulk}} = c_1 \mathcal{V} \quad ,$$

and

$$V_{\text{Surface Layer}} = c_2 \mathcal{S} + c_3 \mathcal{K} + c_4 \mathcal{G} + c_4' \mathcal{Q}$$

+ corrections that tend to zero as $\mathcal{V}$ grows + Proximity Energy V_p .

Here $c_1 \ldots c_4'$ are, for a fixed $\mathcal{V}$, constants independent of shape. The shape dependence is given by the Proximity Energy V_p and by the following functionals of shape: $\mathcal{S}$ = area of surface Σ, $\mathcal{K}$ = integral over Σ of κ ($\equiv R_1^{-1} + R_2^{-1}$), $\mathcal{G}$ = integral over Σ of $(R_1 R_2)^{-1}$, $\mathcal{Q}$ = integral over Σ of κ^2. Here R_1, R_2 are the principal radii of curvature at a point on Σ. For a nucleus the terms in c_i are of order $A(A^{-1/3})^{i-1}$. The last term in Eq. (2) is less familiar and is the subject of the next subsection.[1]

The expansion in $A^{-1/3}$ given above is an asymptotic[2] expansion and fails if there are violent contortions in Σ, for example, such that elements such that elements of the surface face each other across a gap or crevice whose width is of the order of the surface thickness. If this width D is only a slowly varying function of position the additional energy may be approximated by

$$V_p \approx \iint e(D)\,dx\,dy \quad . \qquad (3)$$

Here e(D) is the interaction energy per unit area between two flat parallel surfaces at separation D and the integral is over the gap or crevice, assumed to lie approximately in the x-y plane.

For the family of gap or crevice functions D(x,y) defined implicitly by

$$\sum_{n=0}^{N} c_n d^n = \alpha x^2 + \frac{1}{\alpha} y^2 \qquad (\equiv r^2) \quad ,$$

where α is an area-preserving transverse stretching parameter, Eq. (3) leads to the simple result (independent of α)

$$V_p = \pi \sum_{1}^{N} n\, c_n\, I_{n-1} \quad ,$$

where

$$I_n = \int_{s \text{ or } 0}^{\infty} D^n\, e(d)\,dD \quad ,$$

are moments of the universal interaction function e(d). The lower limit s or 0, distinguishes between gaps (in which case D has a least value s and, for negative s, the two objects overlap) and crevices (in which case D is zero at a finite value of r, given by $\sqrt{c_0}$, and there is no density doubling.) The case N = 2, for which the relation between D and the "stretched" cylindrical radius vector r is a conic section, gives

$$V_p = \pi\, c_1 I_0 + 2\pi\, c_2 I_1 \qquad (4)$$

where, for gaps, I_0, I_1 are two "universal" functions and, for crevices, two "universal" constants, characteristic of the material of which the surfaces are made. Gaps or crevices corresponding to the following shapes are covered by Eq. (4). (For crevices the overlapping portions are erased.) (i) For two juxtaposed coaxial paraboloids with radii of curvature at tips C_1, C_2 and tip distance s (which may be negative): $c_1 = 2\bar{R}$, $c_2 = 0$, where $R = C_1 C_2/(C_1 + C_2) \equiv \bar{C}$. (ii) For two equal coaxial spheroids with semi-axes C, B (C along the line of

centers) and tip distance s: $c_1 = B^2(C + s/2)/C^2$, $c_2 = -B^2/4C^2$. For spheres C = B. (iii) As above but with one spheroid infinitely large (i.e., a plane): $c_1 = 2B^2(C + s)/C^2$, $c_2 = -B^2/C^2$. (iv) For two equal juxtaposed hyperboloids with axes C, B, (C along the line of centers) and tip distance s: $c_1 = B^2(C - s/2)/C^2$, $c_2 = B^2/4C^2$. (v) As above, with one hyperboloid degenerating into a plane: $c_1 = 2B^2(C - s)/C^2$, $c_2 = B^2/C^2$. (vi) Single hyperboloid of one or two sheets: $c_1 = 0$, $c_2 = B^2/4C^2$. (vii) Coaxial juxtaposed circular cones with semi-opening angles α_1, α_2 and tip distance s: $c_2 = (\cot\alpha_1 + \cot\alpha_2)^{-2}$, $c_1 = -2sc_2$. (viii) In addition, for the case of a gap between two coaxial elliptic paraboloids with tip distance s, with radii of curvature A_1 and B_1 in the principal planes of curvature through the tip of paraboloid 1, and A_2, B_2 for paraboloid 2, and azimuthal angle ϕ between the principal planes of curvature of 1 and 2: $c_1 = 2\bar{R}$, $c_2 = 0$, where

$$\frac{1}{\bar{R}^2} = \frac{1}{A_1B_1} + \frac{1}{A_2B_2} + \left(\frac{1}{A_1B_2} + \frac{1}{B_1B_2}\right)\sin^2\phi + \left(\frac{1}{A_1B_2} + \frac{1}{A_2B_1}\right)\cos^2\phi \quad .$$

By taking the negative derivative of V_p with respect to s in case (i) (which is a lowest order approximation to the general case of arbitrary gently curved surfaces with least separation s) we arrive at the following Proximity Force Theorem: "The force between two gently curved surfaces as a function of the separation degree of freedom is equal to the interaction potential per unit area between two flat surfaces, times 2π into the geometric mean of the principal radii of curvature of the gap width function." Thus

$$F(s) \equiv -\frac{\partial V_p}{\partial s} = 2\pi\,\bar{R}\,e(s) \quad . \qquad (5)$$

The (universal) function e(s) vanishes for s beyond the range of the surface width, has a minimum of about minus twice the surface energy coefficient γ when the surfaces are in solid contact at $s \approx 0$ (and the two bodies have combined to make approximately uniform bulk matter), and then rises linearly to infinity as the bodies pile up, with s going to negative values. It follows that the maximum attraction between two gently curved bodies is $F_{max} \approx 4\pi\bar{R}\gamma$.

Introducing a unit of length b proportional to the width (diffuseness) of the surface, the proximity potential may be written in terms of a dimensionless universal function $\Phi(\zeta)$:

$$V_p = 4\pi\gamma\,\bar{R}b \cdot \Phi(\zeta) \quad , \qquad (6)$$

where

$$\Phi(\zeta) = (2\gamma b)^{-1}\int_s^\infty e(s)ds, \qquad \zeta = s/b \ .$$

Using W. D. Myers' version of the Seyler-Blanchard nuclear Thomas-Fermi method[3] we have calculated the universal nuclear function Φ, to which an excellent analytic approximation is (see Fig. 2):

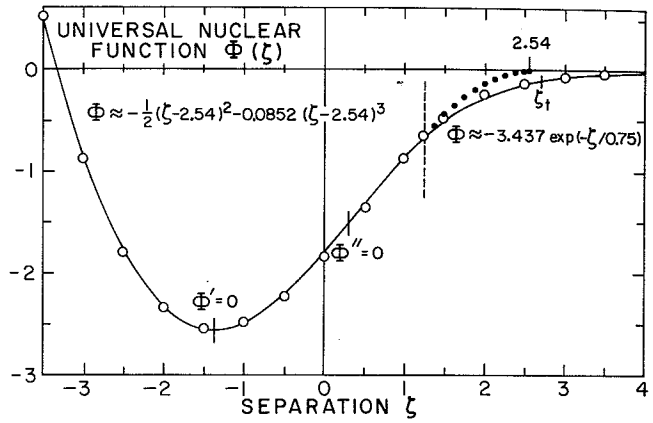

Fig. 2. The universal nuclear function $\Phi(\zeta)$. The circles give the cubic and exponential approximations joined smoothly at the dashed line. The dots are the continuation of the cubic to where it touches the ζ axis at 2.54. The Fermi levels touch at $\zeta_t = 2.71$. (XBL 769-4073)

$$\Phi(\zeta < 1.2511) = -\frac{1}{2}(\zeta - 2.54)^2 - n(\zeta - 2.54)^3, \qquad (7)$$

with $n = 0.0852 \approx 1/12$.

$$\Phi(\zeta > 1.2511) = -3.437\exp(-\zeta/0.75) \ . \qquad (7a)$$

The following values of the parameters entering V_p would be reasonable for a nuclear system with total neutron, proton, and mass numbers N, Z, A:

Surface energy,[4]

$$\gamma = 0.9517\left[1 - 1.7826\left(\frac{N-Z}{A}\right)^2\right] \approx 1 - 2\left(\frac{N-Z}{A}\right)^2 \text{ MeV/fm}^2,$$

Surface Width,[5] $b \approx 1$ fm,

Nuclear Central[5,6] Radius $C = R - b^2/R$,

where R = Effective Sharp Radius
$= 1.28A^{1/3} - 0.76 + 0.8A^{-1/3}$ fm.

The accuracy of the Leptodermous Theorem has been tested against the exactly soluble Krappe-Nix model of interacting nuclei[7] and against computer-generated models based on the "energy-density formalism."[8] Very recently a comparison of the Proximity Potential was made with 57 experimental interaction depths deduced from elastic scattering data. These comparisons suggest that the Leptodermous Theorem, including the Proximity Potential, should be useful down to quite small systems, with mass numbers of about 15 or even lower.

Using the Proximity Potential for the nuclear interaction and freezing all degrees of freedom

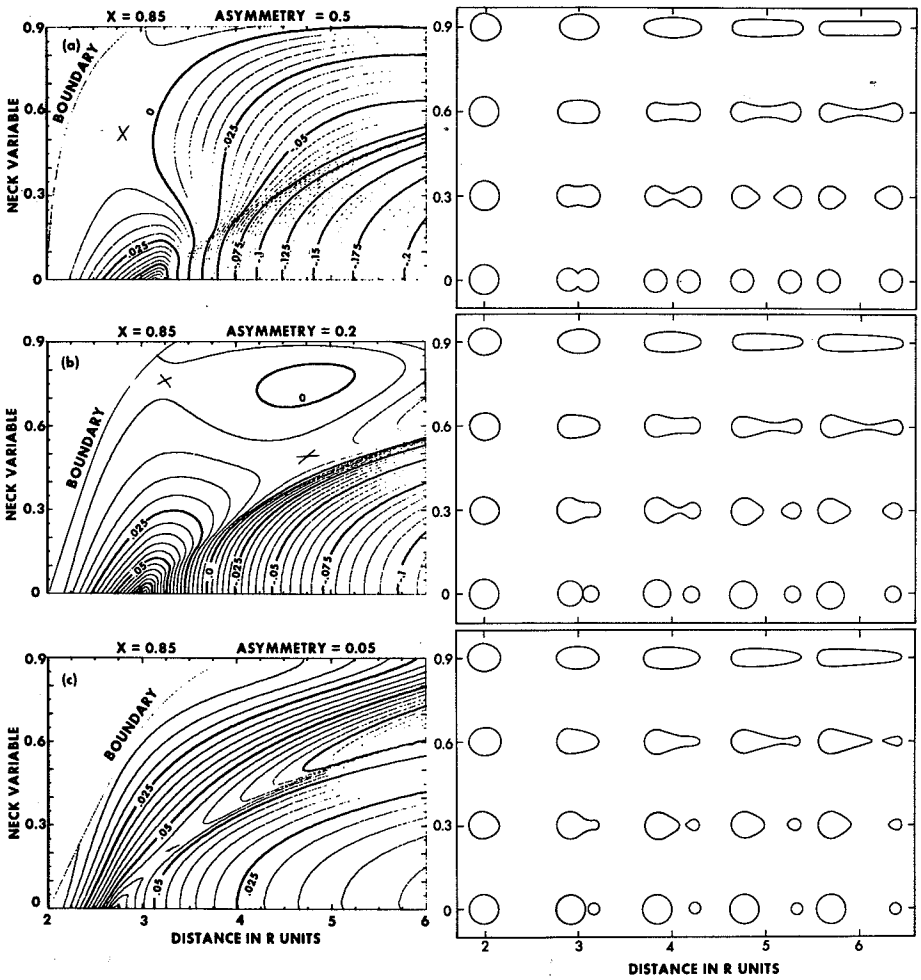

Fig. 3. Potential energy maps corresponding to families of shapes shown on the right. (The maps stop at the line marked "Boundary".) The deformation energy is in units of the surface energy of the standard sphere. (XBL 759-8199)

except the separation between the nuclei, an approximate but wholly analytic description of nucleus-nucleus scattering may be derived. One consequence of this is the isolation of a scaling parameter X, proportional to $Z_T Z_P / A_T^{1/3} A_P^{1/3} (A_T^{1/3} + A_P^{1/3})$, where T, P refer to target and projectile. For two systems with the same value of X (e.g., $^{180}Hg + ^{40}Ar$ and $^{84}Kr + ^{84}Kr$) the plots of properly scaled cross sections against properly scaled bombarding energies would be identical if the frozen idealization were valid. This is analogous to macroscopic fission theory, where properly scaled fission barriers, fragment energies, etc., should be primarily universal functions of a scaling parameter x, proportional to Z^2/A. The ordering of experimental scattering data according to X might serve a similar purpose as the ordering of fission data according to x: the assessment of the validity of the underlying idealizations and the isolation of the expected deviations.

The expected deviations from the frozen idealization are associated with unfreezing: (a) Other shape degrees of freedom, (b) Fragment-orientation degrees of freedom,[9] (c) Internal degrees of freedom (this leads to dissipation). In connection with (a) we have prepared an extensive atlas of nuclear potential maps (primarily sums of Coulomb and surface energies). This parametrization is two spheres joined by a conic; each map is for a fixed mass asymmetry of the spheres and displays the deformation energy as function of elongation and neck degrees of freedom. Figure 3a shows such a family of shapes and the associated energy for a mass ratio 1:1, Fig. 3b for 1:4, and Fig. 3c for 1:19. The fissility parameter x for the whole system is 0.85 in each case ($Z \approx 102$). Colliding nuclei would come in from the right, touch at the top of the ridge, and either be trapped near the sphere (left lower corner) or re-separate, making use – as in fission – of the neck degree of freedom. The atlas covers x's from 0 to 1.5 and mass ratios 1:1 to 1:49.

Footnotes and References

*Condensed from LBL-4296.

†Permanent address: Institute for Nuclear Research, 05-400 Swierk, Poland.

‡Permanent address: Institute of Physics, University of Aarhus, Aarhus, Denmark.

§Energy and Environmental Division.

1. J. Randrup, W. J. Swiatecki and C. F. Tsang, LBL-3603 (December 1974); and J. Blocki, J. Randrup, W. J. Swiatecki and C. F. Tsang, LBL-5014, to be published.

2. H. Krappe, private communication.

3. W. D. Myers and W. J. Swiatecki, Annals of Phys. 55, 395 (1969).

4. W. D. Myers and W. J. Swiatecki, Arkiv f. Fysik 36, 343 (1967).

5. W. D. Myers, Nuclear Physics A204, 465 (1973).

6. G. Süssmann, LBL-1615 (May 1973).

7. H. J. Krappe and J. R. Nix, Proc. Third IAEA Symp. on Physics and Chemistry of Fission, Rochester, 1973, Vol. 1, p. 159, IAEA, Vienna 1974.

8. C. Ngo et al., "Properties of Heavy Ion Interaction Potentials Calculated in the Energy Density Formalism", Preprint IPNO/TH 75-13 (April 1975), submitted to Nucl. Phys.

9. For example, J. P. Bondorff, M. I. Sobel and D. Sperber, Phys. Report 15C, 83 (1974); C. F. Tsang, Physica Scripta 10A, 90 (1974).

PROXIMITY FORCES*

J. Blocki, † J. Randrup, § W. J. Swiatecki, and C. F. Tsang

For certain physical systems such as homogeneous solids, fluids or the heavier atomic nuclei, made up of elements interacting by short-range forces and possessing a surface region which is thin compared to the size of the object under consideration (leptodermous systems), the potential energy of the system may be decomposed into a bulk term and a surface-layer term. The surface-layer term is associated with the surface region and is, therefore, approximately proportional to the area of the surface bounding the object. For a simply connected system the above decomposition is accurate if the principal radii of curvature of the surface are everywhere much larger than the thickness of the surface region. Moreover, when this condition is satisfied, corrections to the leading area-proportional term in the surface-layer energy (such as the curvature correction) may be derived by expansions in powers of the ratio of the thickness of the surface to the size of the system, thus making the expression for the potential energy even more accurate. Such a series expansion has been useful in discussing the average binding energies (masses) of atomic nuclei, and one might have thought that, apart from effects associated with the discreteness of nucleons (shell effects) there was no more to the problem of average nuclear energies than the calculation of the above series expansions to a sufficiently high order. This is not the case. Thus, when the surface of the system becomes contorted into features whose characteristic dimensions are of the order of the thickness of the surface region itself, the above series expansions become useless. This failing is by no means of merely academic interest: it may be serious for a system with a thin neck, on the verge of dividing into two fragments (as in nuclear fission), or in the case of two sub-systems about to come into contact (as in collisions between heavy nuclei). In the latter case in particular, when the system is not simply connected, a calculation of the surface layer energies of the two pieces, no matter how accurately they are corrected for the curvatures of the two surfaces, can never give rise to the (strong) attraction that in practice appears when the two surfaces approach to within a distance comparable with the surface thickness.

Various attempts to remedy these failings have been made in the past. They range from microscopic computer calculations on individual pairs of nuclei[1-3] through various folding prescriptions where a potential well is folded into a density distribution,[4-6] to direct estimates of certain aspects of the nucleus-nucleus force in terms of the experimentally known surface-energy coefficient.[7,8]

In line with the latter development we have found it possible to derive simple expressions for the additional potential energy (or forces) associated with certain of the more important types of violently contorted surfaces, which should enable one to complement in a useful way the usual series expansions of the nuclear energy. We shall call these additional forces "Proximity Forces" because they arise from the proximity of elements of the contorted surface, the contortion being such that different pieces of the surface actually face each other across a (small) gap or crevice. In particular we have re-derived and extended a theorem that makes it possible to relate (approximately) the interaction between two finite nuclei to the interaction between two flat parallel slabs of semi-infinite nuclear matter — a problem that is simpler, and can be solved (in a suitable approximation) once and for all.

Footnotes and References

*Condensed from LBL-5014.

†Permanent address: Institute for Nuclear Research,

05-400 Swierk, Poland.

‡Permanent address: Institute of Physics, University of Aarhus, Aarhus, Denmark.

1. W. Greiner, Proceedings of Heavy-Ion Summer Study at Oak Ridge National Laboratory, June 12-July 1, 1972, p.1.

2. K. A. Brueckner, J. R. Buchler, S. Jorna and R. J. Lombard, Phys. Rev. 171, 1188 (1968).

3. For example, C. Ngô et al., Nucl. Phys. A240, 353 (1975); J. Galin et al., Phys. Rev. C9, 1018 (1974).

4. H. J. Krappe and J. R. Nix, Proceedings of the Third IAEA Symposium on Physics and Chemistry of Fission, Rochester, New York, August 1973, p.159.

5. D. M. Brink and N. Rowley, Nucl. Phys. A219, 79 (1974).

6. R. A. Broglia and A. Winther, Phys. Reports 4, 153 (1972).

7. J. Wilczynski, Nucl. Phys. A216, 386 (1973).

8. R. Bass, Phys. Lett. 47B, 139 (1973).

HEAVY-ION POTENTIAL DERIVED FROM A VELOCITY-DEPENDENT NUCLEONIC INTERACTION*

J. Randrup†

Recently,[1] a simple expression for the nuclear interaction potential has been derived on the basis of the proximity formula. In that treatment the matter distributions of the two interacting nuclear systems were superimposed without readjustments while the nucleonic momenta were redistributed in order to comply with the exclusion principle. However, when the two nuclei are in relative motion the importance of the exclusion principle is decreased and eventually for velocities higher than and twice the Fermi velocity (which corresponds to a kinetic energy of around 100 MeV per nucleon), it ceases to be in effect. In concert with this gradual disappearance of the effects of the exclusion principle, the velocity dependence of the basic two-nucleon interaction is expected to become of increased significance in the ion-ion potential.

In order to obtain a simple tool which may yield rough but not too unrealistic estimates of the expected dynamical implications of such velocity dependence, the following approach has been taken. At first the exclusion principle is neglected all together (as stated above, this is strictly valid only for sufficiently high velocities) and the ion-ion interaction is derived on the basis of an effective nucleon-nucleon interaction. It should be pointed out that the assumption of no dynamical readjustment of the colliding density distributions is not decisive for the present approach to be applicable. The essential point is the assumption that the two nuclei preserve their identity such that, at any stage, the situation may be described as an interaction between two distinct systems. The exclusion principle may be taken approximately into account subsequently by an appropriate interpolation between this noadjustment limit and the full-adjustment limit treated in Ref. 1.

The effective nucleon-nucleon interaction employed is of the following form

$$V_{12} = -C\, g\left(\frac{r_{12}}{a}\right)\left(1 - \frac{p_{12}^2}{b^2}\right) .$$

This type of momentum-dependent interaction was first introduced by Seyler and Blanchard[2] and has proved very useful for the discussion of gross nuclear properties, see for example Ref. 3. The parameter a governs the spatial range of the interaction while the parameter b is that "critical" momentum at which the interaction changes from attractive to repulsive. The strength constant C is here assumed to be the same for all nucleon pairs, as is justified for systems with identical neutron and proton distribution; the extension to asymmetric systems is straightforward. An approximate amount of the nuclear asymmetry may be taken by scaling the emerging potentials in proportion to the surface energy of the actual system under study.

The interaction energy U_V of the two nuclei can be written as

$$U_V = U + \frac{1}{2} W V^2$$

where the velocity-independent functions U and W are given by

$$U = -C \iint \Big(\rho_a(\vec{r}') \rho_b(\vec{r}'') + 2\vec{\pi}_a(\vec{r}') \cdot \vec{\pi}_b(\vec{r}'') - \rho_a(\vec{r}') \gamma_b(\vec{r}'') - \gamma_a(\vec{r}') \rho_b(\vec{r}'') \Big) g\left(\frac{r}{a}\right) d^3\vec{r}'\, d^3\vec{r}''$$

and

$$W = m \frac{C}{b^2/2m} \iint \rho_a(\vec{r}') \rho_b(\vec{r}'')\, g\left(\frac{r}{a}\right) d^3\vec{r}'\, d^3\vec{r}''$$

It follows that the total energy of the two-ion system may be written in the form

$$E = E_{c.m.} + \frac{1}{2} B V^2 + U$$

where $E_{c.m.}$ is the energy of the overall center-of-mass motion. Thus the relative motion is described in terms of a static potential U (in which the Coulomb contribution should be included) and an effective mass $B = \mu + W$ where μ is the usual reduced mass, $1/\mu = 1/M_a + 1/M_b$.

As stated earlier, the potential U derived above applies to large relative velocities only. In the intermediate region a partial readjustment of the nucleonic momenta must take place because of the exclusion principle. This adds an implicit velocity dependence of the interaction to the explicit velocity dependence represented by the variable effective mass B. The question concerning the proper form of the interpolation between the two extremes is currently being pursued in a separate study.

The general formulas may be transformed into a practical tool for simple analyses by use of the proximity formula.[1] This formula expresses a short-range overlap integral between curved surfaces as a geometrical factor containing the actual geometry (such as size and deformation) times a "universal" function evaluated (once and for all) for a semi-infinite configuration. For a detailed discussion see Ref. 1. The application of the proximity formula leads to the following simple expressions,

$$U \approx 2\pi \bar{R}\, \tilde{u}(s)$$

$$W \approx 2\pi R\, \tilde{w}(s)$$

Here the geometrical factor $\bar{R} = C_a C_b/(C_a + C_b)$ measures the radius of curvature of the gap between the surfaces. As discussed in Ref. 1, the effective surface locations C are given approximately by $C \approx R - b^2/R$ where the nuclear radius $R \approx 1.15\ A^{1/3}$ fm and the surface diffuseness $b \approx 1$ fm. The variable s denotes the effective surface separation, $s = R - C_a - C_b$.

A numerical calculation of the "universal" functions $\tilde{u}$ and $\tilde{w}$ has been carried out. The parameter values are those determined in Ref. 3: a = 0.62567 fm, b = 372.48 MeV/c and C = 328.61 MeV. The results are displayed in Figs. 1 and 2. Two parallel sets of calculations have been performed, one based on the Thomas-Fermi approximation and one based on the Hartree approximation (see Ref. 4 for the formulation of the model in the Hartree approximation). The overall shift towards larger separation for the Hartree results is a consequence of the extended density tails, which are not present in the Thomas-Fermi treatment. As discussed in Ref. 1, the associated uncertainty is greatly reduced by scaling the separation according to the surface diffuseness. Included in Fig. 2 is the potential obtained in Ref. 1 based on a total momentum readjustment, $\tilde{v}_p$.

A simple approximate representation of the elastic ion-ion interaction has been suggested. The interaction contains an explicit velocity dependence in the form of a variable reduced mass; this is due to the velocity dependence of the basic nucleonic interaction. In addition an implicit

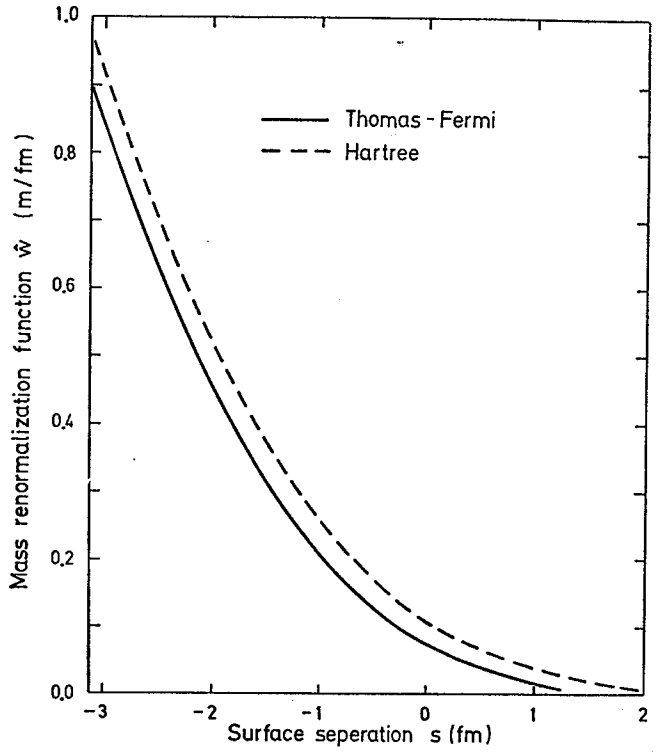

Fig. 1. The "universal" mass-renormalization function $\tilde{w}$ as calculated on the basis of the velocity-dependent effective interaction in the Thomas-Fermi (full curve) and Hartree (dashed curve) approximations. (XBL 766-8275)

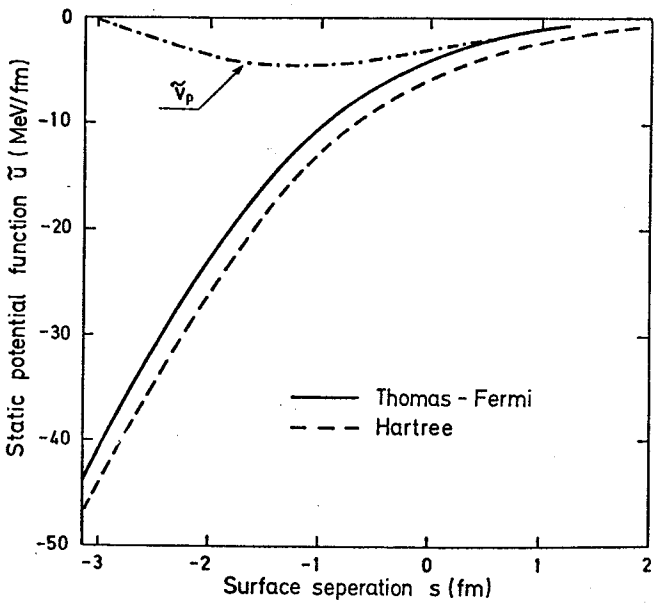

Fig. 2. The "universal" static-potential function $\tilde{u}$. Similar to Fig. 1. The proximity function $\tilde{u}_p$ derived in Ref. 1 is indicated by the dot-dashed curve. (XBL 766-8276)

velocity dependence appears because of the exclusion principle. A major simplification is accomplished by employing the proximity formula for the evaluation of the overlap integrals. The corresponding "universal" mass and potential functions have been calculated numerically. The very simple form of the final formulas makes the model a practical tool for discussing the gross features associated with nuclear collisions. A study of heavy-ion dynamics based on this model is currently underway.

Footnotes and References

*Condensed from LBL-4376.

†On leave from University of Aarhus, Aarhus, Denmark. Present address: The Niels Bohr Institute, Copenhagen, Denmark.

1. J. Blocki, J. Randrup, W. J. Swiatecki and C. F. Tsang, "Proximity Forces", LBL-5014, to be published.

2. R. G. Seyler and C. H. Blanchard, Phys. Rev. 124, 227 (1961).

3. W. D. Myers and W. J. Swiatecki, Ann. Phys. 55, 395 (1969).

4. J. Randrup, LBL-4302, Nucl. Phys. A, 257 (1976) 253.

CONVOLUTION AS A GEOMETRICAL ANSATZ*

William D. Myers

In a detailed study of the geometrical properties of nuclei[1] it was pointed out that a number of problems arise when one attempts to generate optical model potential wells by folding a short range interaction into the density distribution. However, there are a number of applications where simple folding is an extremely useful approach. One of these applications concerns a modified definition of the liquid-drop model surface energy[2] that is free of spurious sensitivity to high-multipole wiggles in the shape of the drop. Another application whose significance is just beginning to be realized is the use of convolution as a geometrical ansatz for creating diffuse surface distributions. In virtually all of the literature of nuclear physics, diffuse surface distributions (of density or potential) are represented by Fermi functions. This choice has a number of awkward features which are easily overcome by creating the diffuse distribution from one with a sharp surface by convolution.

One of the more obvious advantages of using the convolution method for generating the surface diffuseness concerns the question of normalization. When a Fermi function is used to represent a nuclear density distribution its volume integral must be chosen to contain the correct number of nucleons. This isn't a simple task even for spherical nuclei. The integral must be done numerically and the half-radius c chosen by successive approximations. For a deformed nucleus this becomes a two or three-dimensional numerical integration and iteration procedure. (Or one can use analytic approximations of various kinds if it isn't important to have the number of particles exactly right.) By contrast, the normalization problem completely disappears when the diffuse density distribution is generated by folding. The volume of a distribution generated by folding two other distributions together is the product of their separate volumes. If the convolution function is normalized to unit volume, then the diffuse surface function has the same volume as the sharp distribution it is derived from and no calculation whatever is required.

Another advantage of using convolution to generate diffuse surfaces is that the diffuseness normal to the surface is nearly the same at any point on the surface. This is true as long as the local curvature of the surface is not too great. When Fermi functions are used, the diffuseness normal to the surface is proportional to the cosine of the angle between the radius vector and a normal at that point. This kind of angular dependence of the surface diffuseness can generate spurious multipole moments that have no basis in reality.

Perhaps the most useful feature of diffuse distributions created by convolution is that their multipole moments are identical to the moments of the sharp-surfaced generating functions they are based on.[3] This means that only sharp distributions need be employed in the discussion of any physical phenomena that is concerned with multipole moments. Because of the identity of the moments, such a discussion applies equally well to diffuse distributions created by convolution. This is certainly not the case when Fermi functions are used to create the diffuseness.

Papers have been written and tables of numerically calculated conversion factors have been compiled,[4] for relating the multipole moments of a Fermi function to those of the generating shape. The need for such conversions is not a general feature of diffuse distributions, but simply an artifact created by the poor choice of method for creating the diffuseness.

Another important application of the convolution method is in the calculation of moments of inertia. A number of nuclear phenomena depend upon the moments of inertia of nuclei whose deformations are sometimes simple (nuclear ground states) and sometimes complex (fission barriers, for example, or colliding heavy-ions.) Questions often arise as to the effect of diffuseness on these phenomena which, up until now, have usually been discussed only in terms of sharp-surfaced density distributions. Of course, if Fermi functions are used to

create the diffuseness, numerical integrations would be required to calculate the conversion factors for every case of interest.

If convolution is used to create the diffuseness, then the moments of inertia of the diffuse and sharp distributions are related by the simple expression,[3]

$$I_2 = I_1 + 2Mb_c^2 \quad .$$

In this expression I_2 is the moment of inertia of the diffuse distribution about an arbitrary axis and I_1 is the corresponding moment of inertia for the sharp-surfaced function it is derived from. The quantity M is the total mass of the object and b_c is the "width" of the convolution function,[1] where $b_c^2 = 1/3\langle r^2\rangle_c$.

Actually generating the density distribution itself (or the diffuse surface potential well) by folding may be complicated, depending on the generating shape. But, since one is usually interested in the properties of the distribution such as radial moments, multipole moments, moments of inertia, etc., it is often unnecessary to generate the distribution. If the diffuseness is thought of in terms of convolution as a geometrical ansatz, then only sharp distributions need actually be employed in the calculations.

Footnotes and References

*Condensed from Ref. 3.

1. W. D. Myers, Nucl. Phys. A204, 465 (1973).

2. H. J. Krappe and J. R. Nix, Proceedings of the Third Symposium on the Physics and Chemistry of Fission, Rochester (August 1973).

3. W. D. Myers, Nukleonika 21, 3 (1976).

4. L. W. Owen and G. R. Satchler, Nucl. Phys. 51. 155 (1964).

THE NUCLEAR SURFACE DIFFUSENESS*

W. D. Myers and H. von Grotte †

The nuclear radius constant r_0 is a fundamental constant of nuclear physics which is defined in terms of the equilibrium density of infinite nuclear matter by the expression $\rho_0 = (4/3\ \pi r_0^3)^{-1}$. The "effective sharp radius" (the terminology and notation of Ref. 1 is used) of a nucleus is not simply $r_0A^{1/3}$, but is smaller for light nuclei which are squeezed by surface tension, and larger for heavy nuclei where dilation (due to Coulomb and neutron excess effects) begins to dominate. In addition the neutron excess in heavier nuclei is expected to produce a neutron skin of thickness $t = R_n - R_z$, where R_n and R_z are the effective sharp radii of the neutron and proton density distributions respectively.[2] A model that includes these features can be used to infer the fundamental quantity r_0 from the experimental measurements of the radii of actual nuclei.

In a similar way the diffuseness of semi-infinite nuclear matter b_0 can be inferred from experimental measurements of the diffuseness of actual nuclei by using a model that describes the deviations to be expected because of the Coulomb repulsion.

Both the surface energy and Coulomb energy of a nucleus depend on the surface diffuseness. Consequently, variations in diffuseness effect the total energy through the two terms in the expression,

$$E_{\text{diffuseness}} = E_s^0\left[1 + \frac{1}{2}(\phi_1\eta_n^2 - 2\phi_2\eta_n\eta_z + \phi_1\eta_z^2) + \ldots.\right] + E_c^0\left[1 - \gamma_2\beta_z^2 + \gamma_3\beta_z^3 + \gamma_4\beta_z^4 + \ldots.\right] \quad . \qquad (1)$$

In this expression $E_s^0 = a_2/A^{2/3}$, the quantity a_2 being the equilibrium surface energy coefficient of semi-infinite nuclear matter. The second term in the brackets describes the increase in surface energy associated with deviations of the neutron and proton diffusenesses from their semi-infinite nuclear matter values. The quantities η_n and η_z are defined by the expression

$$\eta_{\substack{n\\z}} = (b_{\substack{n\\z}} - b_0)/b_0 \quad , \qquad (2)$$

where b_n and b_z are the diffusenesses of the neutron and proton density distributions and b_0 (the fundamental quantity whose value we seek) is their value in the absence of outside influences. A Thomas-Fermi calculation (similar to the ones described in Ref. 3) was performed,[4] which yielded the following estimate for the coefficients appearing in Eq. (1):

$$\phi_1 = 0.45 \quad , \qquad \phi_2 = 0.23 \quad . \qquad (3)$$

The second term in Eq. (1) represents the Coulomb energy and its dependence on the diffuseness of the proton distribution. The coefficient $E_c^0 = c_1Z^2/A^{1/3}$, where c_1 is the Droplet Model Coulomb energy coefficient. The expansion parameter β_z is defined by the expression,

$$\beta_z = b_z/R_z \quad , \qquad (4)$$

where R_z and b_z are "the equivalent sharp radius" and "surface width", respectively, of the proton

density distribution. For a Fermi function density distribution the coefficients have the values,[5]

$$\gamma_2 = 5/2$$
$$\gamma_3 = 3.02168 \qquad (5)$$
$$\gamma_4 = 1 \quad .$$

For the Droplet Model coefficients a_2 and c_1 we will use the values of a_2 and r_0 from the latest droplet model fit to nuclear masses, fission barriers and radii,[6] which are

$$a_2 = 20.69 \text{ MeV} \quad ,$$

and

$$r_0 = 1.18 \text{ fm} \quad , \qquad (6)$$

hence

$$c_1 = \frac{3}{5}\frac{e^2}{r_0} = 0.7322 \text{ MeV} \quad .$$

For purposes of illustrating the consequences of Eq. (1) it is sufficient to set $R_z = R = r_0 A^{1/3}$ in Eq. (4), to retain only the terms in γ_2 and γ_3 in the Coulomb energy, and to expand the Coulomb energy to second order in η_z. The resulting energy expression is

$$E = E_s^0 \phi_1 \left[\text{constant} + \frac{1}{2}\eta_n^2 - 2\epsilon\eta_n\eta_z + \eta_z^2 - C(1-\delta)\eta_z - C(1-2\delta)\eta_z^2 + \ldots \right] , \qquad (7)$$

where

$$\epsilon = \phi_2/\phi_1 \quad ,$$

$$\delta = \frac{3}{2}(\gamma_3/\gamma_2)(b_0/r_0)A^{-1/3} \quad ,$$

$$C = (5c_1/a_2\phi_1)(b_0/r_0)^2 Z^2 A^{-5/3} \quad . \qquad (8)$$

Minimization with respect to η_n and η_z results in the following expressions for the equilibrium values:

$$\eta_z = C(1-\delta)/[(1-\epsilon^2) - C(1-2\delta)],$$

$$\eta_n = \epsilon\eta_z \quad . \qquad (9)$$

In order to estimate the value of b_0 we have calculated the values of b_z for nuclei along beta-stability [using Green's approximation[7] that $N - Z = 0.4\, A^2/(200 + A)$] assuming various values of b_0. These predictions are compared with the experimental results[8] in Fig. 1a, from which we estimate that

$$b_0 = 0.82 \pm 0.05 \text{ fm} \qquad (10)$$

In the lowerpart of Fig. 1 the predicted diffusenesses (b_n for neutrons and b_z for protons) are plotted against the mass number A for nuclei along beta-stability. At the bottom of the figure the neutron skin thickness predicted by the Droplet Model is plotted.[6] If it were not for the neutron skin the diffuseness of the total matter distribution b (neutrons plus protons) would simply be the weighted mean of b_n and b_z that is shown by the dashed line. The actual value of b_ρ is always larger since the separation between the neutron and proton surfaces contributes to the apparent diffuseness. The relationship between b_ρ, b_n, b_z and the skin thickness t is

$$b_\rho^2 = \left(\frac{N}{A}\right) b_n^2 + \left(\frac{Z}{A}\right) b_z^2 + \left(\frac{N \cdot Z}{A^2}\right) t^2 \quad . \qquad (11)$$

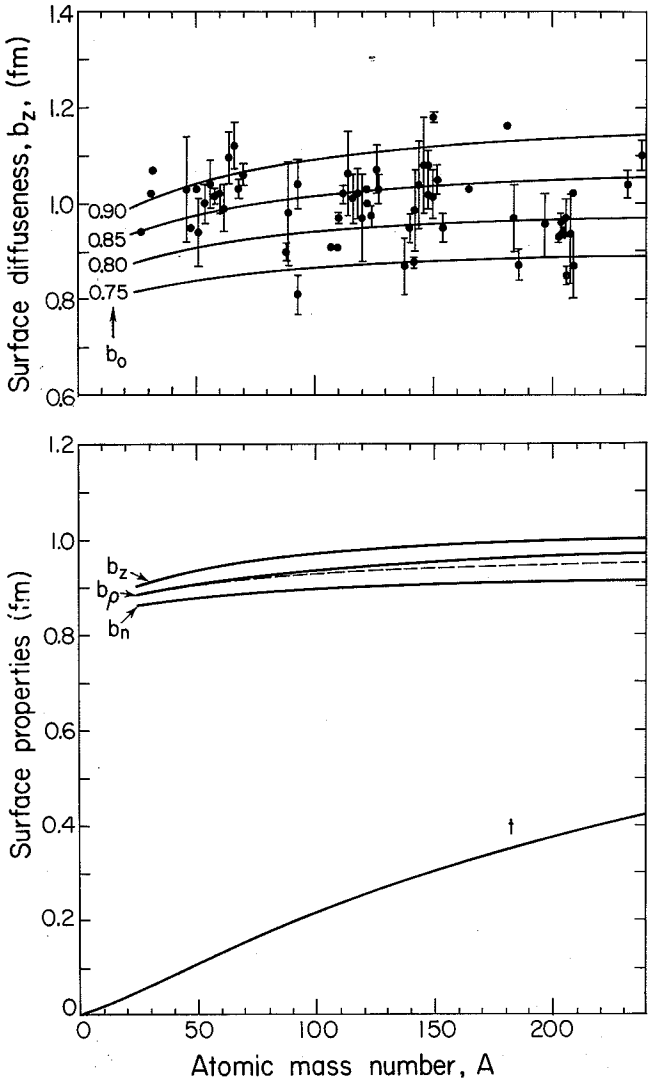

Fig. 1. In the upper part of the figure calculated and experimental values of the diffuseness of the proton distribution b_z are plotted against the atomic mass number A. The different curves correspon to different values of the fundamental constant b_0. In the lower part of the figure the calculated values of the neutron skin thickness t and the diffusenesses b_n, b_z, and b_ρ are given for nuclei along beta-stability. (XBL 7510-8557A)

Recognition of the nuclear diffuseness degree of freedom also has important implications in the

field of collective nuclear excitations. In principle, both T = 0 and T = 1 nuclear diffuseness vibrations are possible and these may be of monopole, quadrupole, or higher multipole order. The excitation energies are probably quite high because the restoring force is large and the inertial parameters are small. In addition these vibrations are probably strongly mixed with the corresponding bulk vibrations because of the inertial coupling between them.

Footnotes and References

*Condensed from Physics Letters 61B, 125 (1976).

†Institut für Kernphysik, Darmstadt, Germany.

1. W. D. Myers, Nucl. Phys. A204, 465 (1973).

2. W. D. Myers, Phys. Lett. 30B, 451 (1969).

3. W. D. Myers and W. J. Swiatecki, Ann. Phys. (N.Y.) 55, 395 (1969).

4. H. von Groote, Proceedings of the First International Workshop on "Gross Properties of Nuclei and Nuclear Excitations", Hirschegg (Jan. 1973).

5. B. C. Carlson, Iowa Stat J. of Sci. 35, 319, (1961), and more recently, J. Jänecke, Nucl. Phys. A181, 49 (1972).

6. W. D. Myers, LBL-3428 (November 1974).

7. A. E. S. Green, Nuclear Physics (McGraw-Hill, New York, 1955).

8. H. R. Collard, L. R. B. Elton and R. Hofstadter, in "Nuclear Radii", Vol. 2, Group I; Landolt-Bornstein, Numerical Data and Functional Relationships in Science and Technology (Springer-Verlag, Berlin, 1967); C. W. deJager, H. deVries and C. deVries, Atomic Data and Nucl. Data Tables 14, 479 (1974); and R. Engfer, et al., ibid., p.509.

THE DROPLET MODEL OF THE GIANT DIPOLE RESONANCE*

William D. Myers

Since the early work of Goldhaber and Teller[1] (GT) and the related work of Steinwedel and Jensen[2] (SJ) most of the progress in our understanding of the nuclear Giant Dipole Resonance (GDR) has been concerned with the microscopic basis of the phenomena. There have also been attempts to include compressibility effects or surface diffuseness effects but there seems to have been no recognition of the fact that the macroscopic nature of the GDR is probably best described as a superposition of the two modes (GT and SJ) discussed earlier.

In addition to considering the coupling of these two modes (both inertial and potential) we chose to calculate the restoring forces from the Droplet Model.[3] This choice puts both the GT And SJ calculations on a sounder footing since the Droplet Model has the important feature that it includes the neutron skin thickness as a degree of freedom.

The actual calculations were performed with the vector $\bar{\alpha}$ whose two components α_1 and α_2 represent the relative magnitudes of the GT and SJ modes respectively.

The GT mode is simply a rigid displacement of the protons with respect to the neutrons by an amount $d = \alpha_1 R$. Actually, since the center-of-mass remains fixed the relative proton and neutron displacements are

$$d_z = \frac{N}{A} d \qquad \text{and} \qquad d_n = -\frac{Z}{A} d \quad (1)$$

The SJ mode corresponds to a vibration of

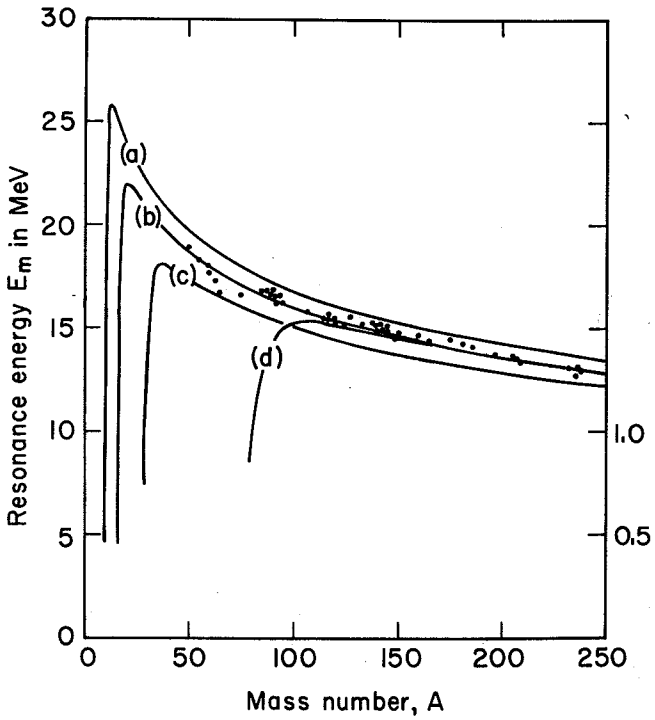

Fig. 1. The energy of the GDR in MeV is plotted against the mass number A, for nuclei throughout the Periodic Table. The curve labeled (b) corresponds to the set of Droplet Model coefficients given in the text. The experimental points are from Ref. 4. (XBL 766-8278)

protons against the neutrons, with the total density held constant, corresponding to the lowest acoustic mode in a spherical cavity. For this mode the proton and neutron density variations are given by

$$\delta\rho_z = \frac{N}{A}\rho_z\delta\eta \quad \text{and} \quad \delta\rho_n = -\frac{Z}{A}\rho_n\delta\eta, \tag{2}$$

where

$$\delta\eta = \alpha_2 C j_1(kr)\cos\theta \ . \tag{3}$$

The constant $C = 2a/j_0(a)$ is chosen so that equal displacements in α_1 and α_2 produce equal dipole moments. The quantity $a = kR = 2.081576$ is determined by the boundary conditions and j_1 and j_0 are spherical Bessel functions.

In terms of these degrees of freedom the inertia matrix B is

$$B = \begin{pmatrix} 1 & 1 \\ 1 & \frac{a^2 - 2}{2} \end{pmatrix} \cdot mr_0^2 \left(\frac{NZ}{A^2}\right) A^{5/3} \tag{4}$$

and the components of the potential matrix are

$$C_{11} = \frac{2}{3} HA^{4/3} \ ,$$

$$C_{12} = C_{21} = \frac{4}{3} PA\left(\frac{NZ}{A^2}\right) a^2 \ , \tag{5}$$

$$C_{22} = JA\left(\frac{NZ}{A^2}\right)^2 4a^2(a^2 - 2) - \frac{8}{3} GA^{2/3}\left(\frac{NZ}{A^2}\right)^2 a^4 \ .$$

The quantities r_0, H, P, J and G are Droplet Model coefficients.

The eigenvalue equation, $\mathrm{Det}|\omega^2 B - C| = 0$, can be solved and the corresponding energies compared with the experimental values for the GDR. Figure 1 shows the results (which have been scaled using an effective mass $m^* = 0.7\ m$) for nuclei throughout the Periodic Table. The different curves correspond to different sets of values for H, P and G. These coefficients are not uniquely determined by the Droplet Model fit to masses because they only appear in the mass equation in the combination represented by the symbol Q, where

$$Q = \frac{H}{\left(1 - \frac{2}{3}\frac{P}{J}\right)} \quad \text{and} \quad \frac{G}{P} = \frac{3}{2}\frac{J}{Q} \ . \tag{6}$$

For the curve labeled (b) the values used were

$$r_0 = 1.18 \text{ fm} \qquad H = 12 \text{ MeV}$$
$$J = 36.8 \text{ MeV} \quad \text{and} \quad P = 16.235 \text{ MeV} \tag{7}$$
$$Q = 17 \text{ MeV} \qquad G = 52.717 \text{ MeV} \ .$$

The A dependence of the GDR energy is well reproduced (which is not possible with the GT or SJ modes alone).

Footnotes and References

*In collaboration with L. J. El-Jaick and T. Kodama of Centro Brasileiro de Pesquisas Fisicas, Rio de Janerio, Brazil.

1. M. Goldhaber and E. Teller, Phys. Rev. 74, 1046 (1948).

2. H. Steinwedel and J. H. D. Jensen, Z. Naturf. 5a, 413 (1950).

3. W. D. Myers, LBL-3428 (November 1974).

4. B. L. Berman and S. C. Fultz, Rev. Mod. Phys. 47, 713 (1975).

PROXIMITY FISSION

J. S. Sventeck, L. G. Moretto, and W. J. Swiatecki

Recently, we have investigated the theoretical possibility for a new process, which we have termed Proximity Fission (PF). This process should occur as follows (see Fig. 1 for the relevant shapes at each step of the process):

1) A target nucleus, with a reasonably large spontaneous fission barrier, is struck by a projectile which has just enough energy to overcome the Coulomb barrier.

2) While the short range nuclear force maintains the contact between target and projectile, the target deforms and, if the atomic number of the projectile is large enough, fissions along the incident direction.

3) The projectile is re-emitted in the backward direction.

The experimental earmark for such a process would be the coincidence of fission fragments from a "target-like" nucleus in the forward direction with a "projectile-like" nucleus in the backward direction. This process should be distinguishable from Coulomb Fission (CF) since the most probable direction of emission of CF fragments is perpendicular to the incident direction,[1] while the most probable direction of emission of PF fragments is

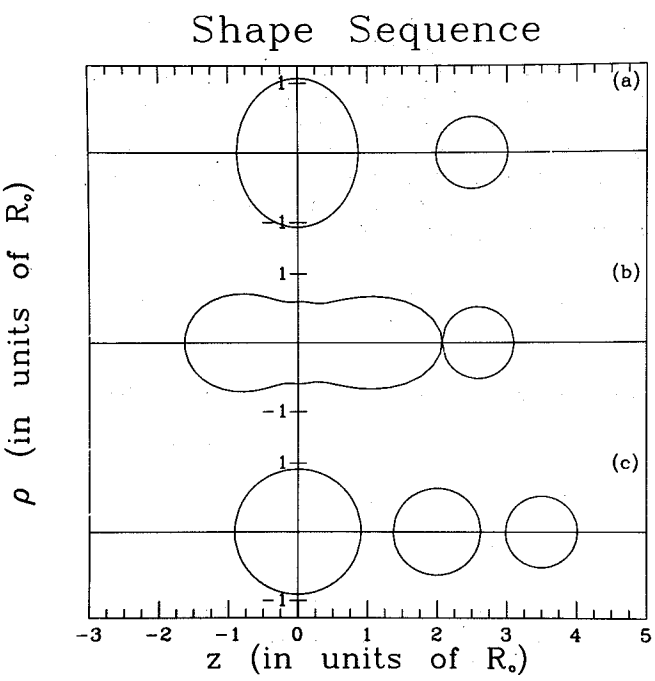

Fig. 1. a) Shape prior to and just as the collision takes place. b) Deformed shape of target while in the proximity of the projectile. c) Projectile re-emitted in the backward direction. (XBL 766-8289)

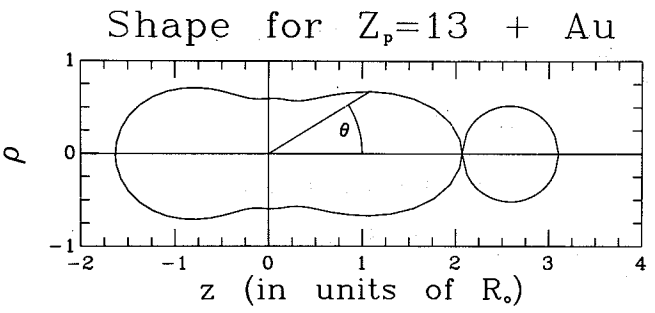

Fig. 2. A typical shape encountered in the calculation. The angle θ is measured counter clockwise from the positive z-axis. (XBL 766-8292)

in the incident direction.

The potential energy calculations were performed by expanding the radius of the target in Legendre polynomials, i.e.,

$$R_t(\theta) = u\,[1 + \sum_i \alpha_i P_i(\cos\theta)]$$

where the α_i's are expansion parameters and u allows volume normalization. The projectile, which throughout the process is assumed to remain spherical with radius R_p, is placed at a distance $R_t(0) + R_p$ (see Fig. 2). The liquid drop potential energy (surface + Coulomb) is then calculated for the shape described by the parameters $\{\alpha_i\}$, and

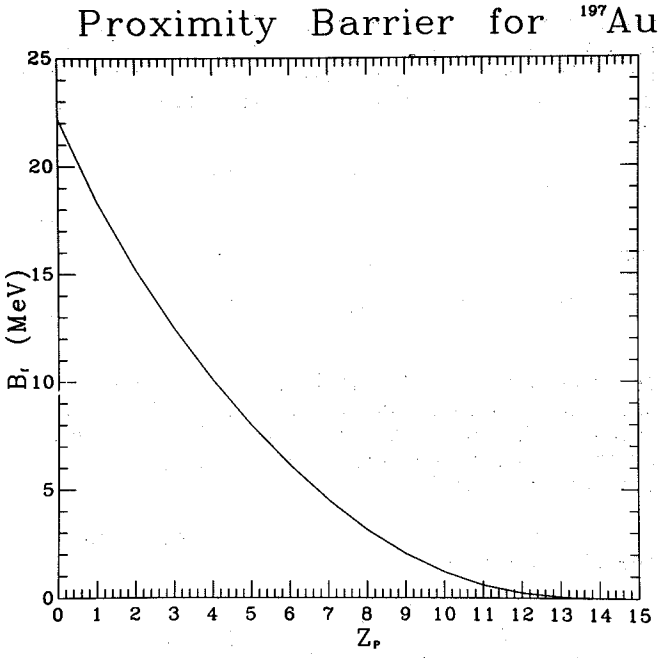

Fig. 3. Proximity barrier (in MeV) as a function of Z_p for x = 0.67 (a gold target nucleus). (XBL 766-8293)

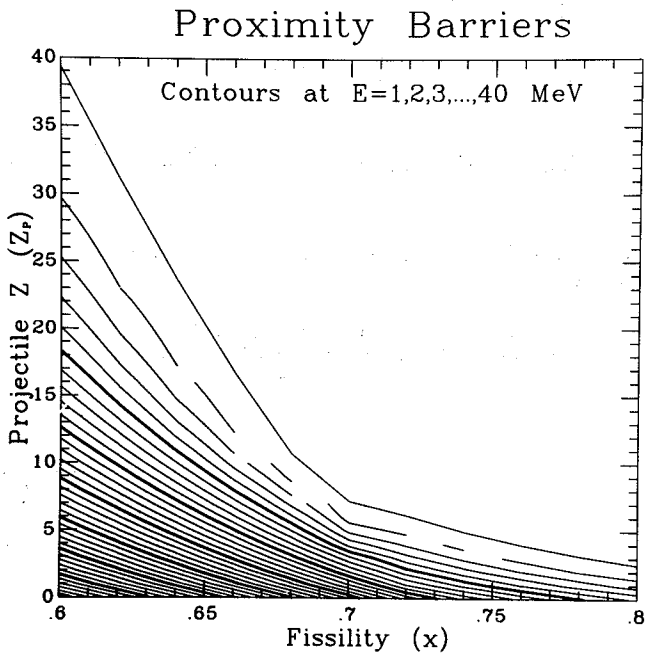

Fig. 4. Contours of constant proximity barrier (in MeV) as a function of Z_p and x. The solid line at which the contours end is the line $Z_{cr}(x)$. (XBL 766-8294)

the resulting potential energy surface is searched for the perturbed ground state and saddle point. The proximity fission barrier is then the difference in energy between the perturbed ground state and saddle point.

Prior to considering the problem dynamically, we have here studied the static problem, i.e., the

potential energy only. Unfortunately, the stationary points in an unlimited parametrization are the trivial solutions corresponding to the regular ground state and saddle point shapes of the target connected to the projectile by an infinitely long, infinitesimal thread of zero volume and surface area. It is conceivable that dynamical considerations may prevent such instabilities from developing. On this basis, we have proceeded to evaluate the ground state and saddle point shapes and energies in the restricted parametrization of P_2, P_3, P_4 and P_5 deformations.

In general, the fission barrier of the target is reduced as the atomic number Z_p of the projectile is increased from 0. (It is assumed that $A_p = 2Z_p$, and $R_p = 1.2249\ A_p^{1/3}$.) This behavior for a target in the gold region of the Periodic Chart is displayed in Fig. 3. For a critical atomic number Z_{cr}, the perturbed ground and saddle shapes coalesce, with the result that the fission barrier of the target vanishes. There is also no barrier for projectiles with $Z_p > Z_{cr}$. This behavior is analogous to that displayed by the spontaneous fission barrier for rotating, charged liquid drops.[2] As the rotational parameter y increases from the value 0, the barrier for spontaneous fission decreases, and ultimately disappears for $y \geq y_{cr}$, where y_{cr} represents the maximum amount of angular momentum that the liquid drop can tolerate.

Like y_{cr}, the value of Z_{cr} is a function of the fissility parameter x of the target. A contour map of the barrier for proximity fission of the target (in MeV) as a function of the fissility parameter of the target and the atomic number of the projectile can be seen in Fig. 4. The solid line at which the contours end is the line $Z_{cr}(x)$. As one would expect, Z_{cr} is a monotonically decreasing function of x, and vanishes for $x = 1$, since the liquid drop is unstable to spontaneous fission (or proximity fission with $Z_p = 0$) at $x = 1$.

The situation of most interest to us occurs for target nuclei in the gold region ($0.65 \leq x \leq 0.70$). Since the spontaneous fission barriers in this region are in the neighborhood of 20 MeV, true fission probabilities remain negligible until several tens of MeV of excitation energy are deposited in the target. The expected yield of fission products for interactions near the Coulomb barrier is essentially zero. On the other hand, as can be seen in Fig. 4, the proximity fission barrier for targets in this region vanishes for projectiles with $Z_p > 13$. Therefore, projectiles with $Z_p > 13$ could induce fission at energies just slightly above the Coulomb barrier.

More precisely, we would expect to see a dramatic increase in fission products as the energy of the projectile (with $Z_p > 13$) is varied from energies below to energies above the Coulomb barrier. For very high energies, the fission products could be attributed to an highly excited gold nucleus fissioning after the projectile has been re-emitted, but the yield near the barrier, where no products can be expected from the fission of an excited gold nucleus, would be due solely to the proximity of the perturbing charge. We are presently preparing experiments to try to detect such products.

References

1. E. Guth and L. Wilets, Phys. Rev. Lett. 16, 30 (1966).

2. S. Cohen, F. Plasil and W. J. Swiatecki, Annals of Phys. 82, 557 (1974).

C. DAMPING, FISSION, GENERAL RELATIVITY

SCHRÖDINGER EQUATION FOR SCATTERING WITH ENERGY LOSS*

R. Lipperheide†

An attempt has been made to establish a model Schrödinger equation for the description of heavy ion scattering with energy loss. This equation is linear and can be related to the quantal coupled channels approach. A possible parametrization of the model Hamiltonian is considered. Energy nonconservation in the Schrodinger picture can be connected with an explicit time dependence of the scattering potential between two heavy ions:

$$(-i\partial/\partial t - \nabla^2/2m + V + V^L(t))\,\phi(\underset{\sim}{r}, t) = 0. \qquad (1)$$

To describe energy loss in the relative motion owing to internal excitation, the energy-losing potential V^L must contain only positive frequencies,

$$V^L(t) = \int_{0^+}^{\infty} \tilde{V}^L(\omega) e^{i\omega t}\, d\omega. \qquad (2)$$

Transforming Eq. (1) to the energy dependent form

$$(E + \frac{\nabla^2}{2m} - V)\tilde{\phi}(\underset{\sim}{r},E) = \int_{E^+}^{\infty} \tilde{V}^L(E'-E)\,\tilde{\phi}(\underset{\sim}{r},E')\,dE', \qquad (3)$$

we see indeed that the term $\tilde{V}^L(\omega)$, $\omega > 0$, appears in a source term via which current from wavefunction components $\tilde{\phi}(\underset{\sim}{r},E')$ with energy E' is fed into components $\tilde{\phi}(\underset{\sim}{r},E)$ with the lower energy $E = E' - \omega$, thus describing energy loss.

The initial condition for the solution of Eq. (1) is that it starts out as a free normalized wave packet with mean momentum $\underset{\sim}{k}_0$. The corresponding boundary condition for Eq. (3) is[1] that the solution $\tilde{\phi}(\underset{\sim}{r},E)$ must consist of an incident free wave at energy E_0

$$\phi^0_{\underset{\sim}{k}_0}(\underset{\sim}{r},E) = [\Delta(E-E_0)]^{1/2}\, e^{i\underset{\sim}{k}\cdot\underset{\sim}{r}} \qquad (4)$$

plus terms at all energies which asymptotically are purely outgoing. Here $\Delta(x)$ is a narrow distribution about $x = 0$, normalized to unity. Equation (3) automatically restricts the solution to energies $E \lesssim E_0$, as is most easily seen by a perturbation theory argument. Asymptotically we have

$$\phi(\underset{\sim}{r},E) \to [\Delta(E-E)]^{1/2}\, e^{i\underset{\sim}{k}_0\cdot\underset{\sim}{r}} + F(\Omega,E)\,\frac{e^{ikr}}{r}, \qquad (5)$$

where the scattering amplitude $F(\Omega,E)$ determines the differential cross section per unit energy for final energies $E \leqslant E_0$:

$$\frac{d^2\sigma}{d\Omega dE} = \frac{k}{k_0}\,|F(\Omega,E)|^2. \qquad (6)$$

The requirement that during scattering the wave may lose energy but not probability current, implies

$$\int_0^{E_0} dE(\langle \tilde{\phi}(E),\ \mathrm{Im}\ V\,\tilde{\phi}(E)\rangle + \mathrm{Im}\,\langle \tilde{\phi}(E), \int_{E^+}^{E_0} dE'\tilde{V}^L(E'-E)\tilde{\phi}(E')\rangle) = 0. \qquad (7)$$

The second term in Eq. (7) receives contributions only from those components in the bra $\langle\phi(E)$ which have energy $E < E_0$, and contain only outgoing waves; thus

$$\int_0^{E_0} dE\,\langle \tilde{\phi}(E),\ \mathrm{Im}\ V\,\tilde{\phi}(E)\rangle = -\int_0^{E_0} dE(\int_0^{E_0} dE''\langle\tilde{\phi}(E''),\ \tilde{V}^{L^+}(E''-E)\ \mathrm{Im}\ G_+^+(E)\int_{E^+}^{E_0} dE'\tilde{V}^L(E'-E)\tilde{\phi}(E')\rangle), \qquad (8)$$

where $G_+(E) = (E + i\eta - T - V)^{-1}$. Since the r.h.s. of Eq. (8) is negative, we see that the introduction of the energy losing potential $\tilde{V}^L(\underset{\sim}{r},\omega)$ requires the presence of absorption in the energy conserving potential, $\mathrm{Im}\ V < 0$. This has a natural interpretation (cf. Eq. (3)): the wave component $\phi(E)$ at energy E receives current influx via the source term from components $\phi(E')$ at higher channel energies $E' > E$; but since in turn this wave component $\phi(E)$ appears again in the source term for components $\phi(\bar{E})$ with $\bar{E} < E$, feeding current into the latter, this current loss for $\phi(E)$ must be accounted for by an absorptive part in the energy conserving potential V. Condition (7) reads in the time dependent description

$$\int_{-\infty}^{\infty} dt\,\langle\phi(t),\ (\mathrm{Im}\ V + \mathrm{Im}\ V^L(t))\phi(t)\rangle = 0, \qquad (9)$$

which implies, using Eq. (1), the conservation of

probability:

$$\langle \phi(t),\ \phi(t) \rangle_{t=-\infty}^{t=\infty} = 0.$$

The condition of probability conservation thus gives rise to a relation between the energy losing potential V^L and the absorptive part of the energy conserving "optical" potential. This relation is rather indirect, however, as it involves the wavefunctions and an integral over channel energies or equivalently, time. An analogous relation between the imaginary part of the optical potential and the friction force appears in the perturbation theory of nuclear friction.[2]

It is interesting to note that Eq. (3) is closely analogous to the usual system of coupled elastic and inelastic channels,

$$(E_0 - \varepsilon_\mu - T - V_{\mu\mu})\ \psi_\mu = \sum_{\substack{\nu=0 \\ (\nu\neq\mu)}} V_{\mu\nu}\ \psi_\nu, \qquad (10)$$

where the ψ_μ are the channel wavefunctions and ε_μ is the internal excitation energy of the fragments. Ordering the channel labels according to increasing excitation energy ε_μ (with degeneracies taken care of appropriately), we can eliminate, in the equation for a given channel μ, the coupling to all channels with lower channel energy $E_\nu = E_0 - \varepsilon_\nu$, $E_\nu < E_\mu$, i.e., higher excitation energy $\varepsilon_\nu > \varepsilon_\mu$ and obtain

$$(E_\mu - T - V_\mu(E_\mu))\ \psi_\mu = \sum_{\underline{\nu}(<\mu)} V_{\mu\underline{\nu}}(E_\mu)\psi_{\underline{\nu}}, \qquad (11)$$

with

$$V_\mu(E) = V_{\mu\mu} + \sum_{\substack{\bar{\nu},\bar{\nu}' \\ (>\mu)}} V_{\mu\bar{\nu}} \left(\frac{1}{E^+ - E + \varepsilon_\mu - H}\right)_{\bar{\nu}\bar{\nu}'} V_{\bar{\nu}'\nu}. \qquad (12)$$

$$V_{\mu\underline{\nu}}(E) = V_{\mu\underline{\nu}} + \sum_{\substack{\bar{\nu},\bar{\nu}' \\ (>\mu)}} V_{\mu\bar{\nu}} \left(\frac{1}{E^+ - E + \varepsilon_\mu - H}\right)_{\bar{\nu}\bar{\nu}'} V_{\bar{\nu}'\underline{\nu}}. \qquad (13)$$

In Eq. (11) the channels are coupled via a triangular coupling matrix. The elastic channel $\mu = 0$ is uncoupled, and is described by the optical-model equation

$$(E_0 - T - V_0(E_0))\ \psi_0 = 0 \qquad (14)$$

where the optical potential V_0 is given by Eq. (12) with $\mu = 0$ (Geshbach's generalized optical potential,[3] but would in practice be constructed phenomenologically. The first inelastic channel is explicitly coupled only to the elastic channel, but loses current to the second, third, etc. channels via the imaginary part of V_1. So it goes down to the last open channel with $E_\mu = 0$. The optical potential $V_\mu(E)$ in channel μ [Eq. (12)] at energy $E_\mu = E$ is quite similar in structure to the optical potential in the elastic channel, $V_0(E)$. In the coupling terms $V_{\mu\nu}$ we neglect the sum on the r.h.s. of Eq. (13) since, in contrast to the analogous sum in Eq. (12), it consists of terms with indefinite sign. Thus we write $V_{\mu\underline{\nu}}(E) \approx V_{\mu\underline{\nu}}$ in Eq. (11).

In typical inelastic heavy ion scattering situations the number of channels to be included in the system is very large. Going over to a continuous distribution of channel energies we may write

$$(E_0 - \varepsilon + T - V_0(E_0 - \varepsilon))\phi_\varepsilon = \int_0^{\varepsilon_-} V^L(\varepsilon,\varepsilon')\ \phi_{\varepsilon'}\ d\varepsilon', \qquad (15)$$

where the "channel density wavefunction"

$$\phi_\varepsilon = \sqrt{\bar{\rho}\ (\varepsilon)}\ \bar{\psi}_\mu(\underset{\sim}{r}) \qquad (16)$$

is the average[4] of the usual channel wavefunction in the interval $\varepsilon - d\varepsilon < \varepsilon_\mu < \varepsilon + d\varepsilon$ multiplied by the square root of the average number of channels per unit excitation energy. The integral kernel on the l.h.s. of Eq. (15) is

$$V^L(\varepsilon,\varepsilon') = \sqrt{\bar{\rho}(\varepsilon)}\ \bar{V}(\underset{\sim}{r};\varepsilon,\varepsilon')\sqrt{\bar{\rho}\ (\varepsilon')},\ \varepsilon > \varepsilon', \qquad (17)$$

$$= 0, \quad \varepsilon < \varepsilon',$$

where $\bar{V}(\underset{\sim}{r};\varepsilon,\varepsilon)$ is some average matrix element of the internuclear interaction taken between internal states with excitation energies ε and ε'. If one simply sets $V^L(\varepsilon,\varepsilon') = \bar{V}^L(\varepsilon - \varepsilon')$, then with $E_0 - \varepsilon = E$, $E_0 - \varepsilon' = E'$,

$$(E + T + V_0(E))\phi_\varepsilon = \int_{E^+}^{E_0} \tilde{V}^L(E' - E)\phi_{\varepsilon'}\, dE'. \qquad (18)$$

Identifying $\phi_\varepsilon(r)$ with $\tilde{\phi}(r,E)$, we find that Eq. (18) is the same as Eq. (3) [the integral in Eq. (3) is effectively cut off at $E' = E_0$, owing to condition (4)]. The square of the outgoing part of the channel density wavefunction (16) yields the scattering cross section per unit excitation energy, as in Eqs. (5) and (6). The energy conserving optical potential $V_0(E) \approx V_\mu(E)$ is complex and time reveral noninvariant because in rearranging the original time reversal invariant system to obtain Eq. (11), the boundary condition of outgoing waves in all channels with lower channel energy has been incorporated in $V_\mu(E)$. The current conservation relation (7) follows from the hermiticity of the original coupled channels problem (10). We see that in physical content, the "smoothed-out" coupled channels problem (18) is closely analogous to a linear (as opposed to Ref. 5) Schrödinger equation with a time dependent potential.

Footnotes and References

*Condensed from LBL-4333, submitted to Phys. Rev. Lett.

†On leave from the Hahn-Meitner-Institut für Kernforschung Berlin, Bereich Kern- und Strahlenphysik, and Freie Universität Berlin, Fachbereich Physik, Berlin-West, Germany.

1. A. Messiah, Quantum Mechanics, North-Holland Publ. Co., Amsterdam (1964), ch. X, Sec. 5.

2. H. H. E. Gross, Nucl. Phys. A240, 472 (1975).

3. H. Feshbach, Ann. Phys. (N.Y.(5, 357 (1958)

4. A. K. Kerman and S. E. Koonin, Physica Scripta 10A, 118 (1974).

5. K. K. Kan and J. J. Griffin, Phys. Lett. 50B, 241 (1974). K. Albrecht, Phys. Lett. 56B, 127 (1975).

ONE BODY VISCOSITY; COMPARISON BETWEEN QUANTUM MECHANICAL AND CLASSICAL DESCRIPTIONS

J. Blocki,* Y. Boneh,† and J. Randrup‡

Recent calculations have shown that a one-body type of viscosity can play an extremely important role in the dynamics of collective processes.[1] In this situation it seemed reasonable to make some fundamental studies in order to obtain a better understanding of the physical picture of the phenomenon we are dealing with. We decided to study the simple case of quadrupole vibrations and calculate how much internal excitation is produced by the motion. In the quantum mechanical calculations we solve the time dependent single-particle Schrödinger equation using a Woods-Saxon potential adapted to the deformed shapes. The excitation energy is calculated simply as a difference between the actual time dependent energy at a given deformation and the ground state energy at this point.

In the classical calculations we assumed the model of independent particles colliding with boundaries changing in time (surface of the nucleus). In each collision the change of the velocity (or energy) of the particle can be calculated. Assuming the initial distribution of the velocities of the particles to be that of a Fermi gas and the initial density to be uniform within the boundaries, we calculated the energy gained by the particles during the motion of the boundaries using a Monte Carlo numerical technique. On the other hand, on the assumption that the initial distribution does not change too much during the motion of the boundaries, we arrived at a simple analytic formula for the dissipation energy (see J. Błocki, J. Randrup, M. Robel, and W. J. Swiatecki, One-Body Dissipation and a New Dynamics,in this Annual Report). The formula, apart from a constant factor depending on density and the average velocity of the particles, consists of an integral over the surface of the square of the normal surface velocity. Once the time evolution of the surface is known the dissipation energy can be easily calculated with this expression. It seems worthwhile to establish on the one hand the correspondence between the quantum mechanical and classical picture and on the other the applicability of the analytic expression. We have done calculations of the quadrupole vibrations for six different values of the frequency, starting from the frequency, estimated for the Liquid Drop Model and then increasing the frequency by doubling.

The comparison shows that the analytic formula cannot reproduce the Monte Carlo and quantum mechanical results at low frequencies, because of their reversibility. At high frequencies the agreement between all three cases is much better; however, in the quantum mechanical calculations the dissipated energy is lower because of shell effects. We have also compared the Monte Carlo results with the analytic expression for low frequency vibrations of higher multipolarity. It was found that beginning from multipolarity equal to six both curves are almost indistinguishable. The result indicates that the simple analytic formula can be applied in such processes like fission, where shapes of the nuclei are that of the higher multipolarity.

Footnotes and Reference

*Permanent address: Institute of Nuclear Research, 05-400 Swierk, Poland.

†Present address: Nuclear Research Center, Negev, Beer-Sheva, P.O.B. 9001, Israel.

‡Present address: Niels Bohr Institute, DK-2100, Copenhagen, Denmark.

1. W. J. Swiatecki, in Proceedings of the International School Seminar on Reactions of Heavy Ions with Nuclei and Synthesis of New Elements, Dubna, USSR (Oct. 1975).

ONE-BODY DISSIPATION AND A NEW DYNAMICS*

J. Blocki,† J. Randrup,‡ M. Robel, and W. J. Swiatecki

Ordinary viscosity in liquids is the result of two-body molecular forces which degrade nonuniform collective flows into heat. A different, one-body mechanism for exchanging energy between collective and internal degrees of freedom is the collision of particles with a moving container wall. This energy

exchange between wall and particles, calculated to lowest order in the ratio of particle to wall velocities, is responsible for the Ideal Gas Law $pV = RT$. By going to the next order in the ratio of velocities we arrive at the following "wall formula" for the rate of energy flow $\dot{E}$ into a gas (with mass density ρ) composed of independent particles with average speed v, and contained in a vessel of fixed volume, whose walls deform with slow normal velocities $\dot{n}$ with respect to the bulk of the gas

$$\dot{E} = \rho v \oint \dot{n}^2 \, d\sigma.$$

[For a degenerate Fermi gas $v = (3/4)$ (Fermi velocity.)]

To illustrate the order of magnitude of the dissipation predicted by the above formula we added such a damping to the equations of motion of an idealized nuclear droplet vibrating irrotationally around the spherical shape in its nth multipole mode. One may define a factor of overdamping μ, which gives the number of times the dissipation term exceeds the value for which critical damping would occur for the given mode. The formula for μ is

$$\mu = \frac{3\sqrt{3}\,(9\pi)^{1/3}}{16} \sqrt{\frac{\hbar^2/mr_0^2}{4\pi r_0^2 \gamma}} \left\{\frac{n-1}{n}\left(n+2-\frac{20x}{2n+1}\right)\right\}^{-1/2} A^{1/6},$$

where m is the nucleon mass, γ the surface energy coefficient and r_0 the nuclear radius constant. The following table illustrates the degree of overdamping for three idealized nuclei and four harmonics (Lysekil[1] nuclear parameters were used):

	n=2	n=4	n=8	n=16
$^{20}_{10}Ne$	1.50	0.97	0.69	0.50
$^{120}_{50}Sn$	2.62	1.44	0.97	0.69
$^{238}_{92}U$	4.73	1.79	1.14	0.79

The damping appears to be large (as with ordinary viscosity when applied to small systems[2]), but note that contrary to conventionally damped drops the damping is largest for long-wavelength modes (and large systems). A high nuclear viscosity is indeed implied by deep inelastic scattering, which suggests that nuclei often behave like two pieces of tar that get stuck but do not flow together. However, high two-body viscosity is inadmissible in fission[3] where it would predict stretched out scission shapes leading to much too low fission-fragment kinetic energies. The stretching out is due to the stronger damping of short-wavelength modes (like necking) compared to a general elongation. Since with one-body damping the situation is just the reverse, it is quite possible that in a fission process dominated by one-body damping the scission shape would be moderately compact and would reproduce the observed fragment energies.

To test this possibility Nix & Sierk have made dynamical saddle-to-scission calculations with the one-body dissipation replacing ordinary (two-body) viscosity in the equations of motion. The resulting calculated fission-fragment kinetic energies for elements throughout the periodic table are compared with experiment in Fig. 1. The solid curve shows that the calculation (which has no adjustable parameters) is not in drastic disagreement with experiment, even though the descent from saddle-to-scission is overdamped (creepy). In contrast, an overdamped system with ordinary viscosity would correspond to the dashed curve, giving energies as much as a factor of 2 too low. The reason for the difference is as anticipated, namely the greater compactness of the scission shapes in the case of the calculation with the one-body dissipation.

In order to test whether the one-body dissipation can indeed account for deep inelastic scattering as well as fission-fragment energies, we have begun a dynamical study of nucleus-nucleus collisions in the presence of such dissipation. The relevant dissipation formula for the geometry of two nuclei beginning their interaction by way of a neck or window of area $\Delta\sigma$ is the following "window formula"

$$\vec{F} = -\frac{1}{4} \rho v [\vec{U} + (\vec{U}\cdot\hat{n})\hat{n}] \, \Delta\sigma.$$

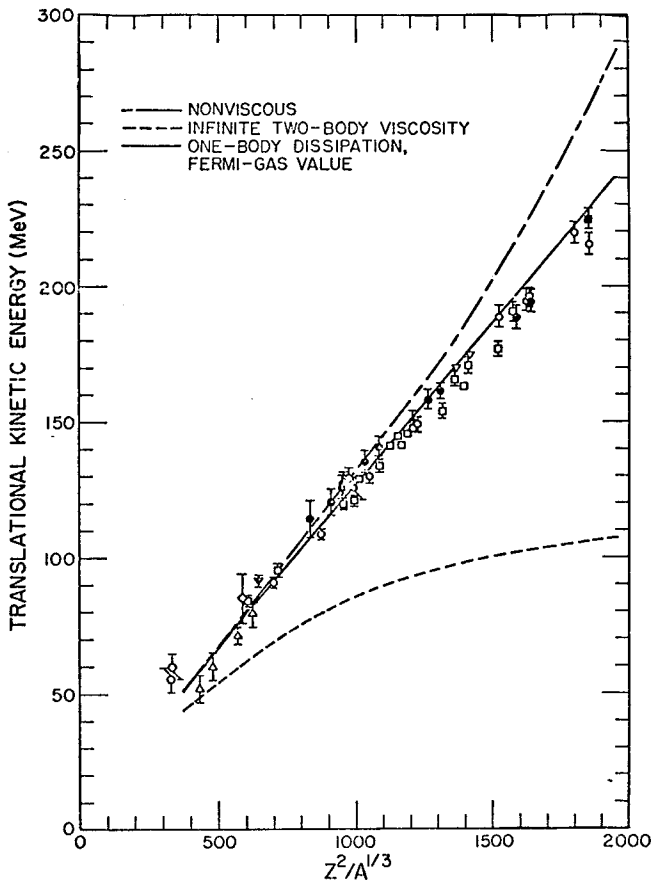

Fig. 1. Kinetic energies of fission fragments calculated without dissipation (dot-dash curve), with a large two-body viscosity (dashed curve) and with one-body dissipation (solid curve).

(XBL 766-8224)

Here $\vec{F}$ is the dissipative force resisting the relative motion of the two nuclei, whose relative (vector) velocity is $\vec{U}$. The symbol $\hat{n}$ stands for a unit vector normal to the window $\Delta\sigma$. If the two nuclei are in grazing motion $\vec{U}$ is at right angles to $\hat{n}$, the term $(\vec{U}\cdot\hat{n})\hat{n}$ is zero, and the result reduces to the window formula of Ref. 2.

The order of magnitude of the frictional force predicted by the window formula appears to be sufficient to account for the damping of the kinetic energy in deep inelastic scattering. The remaining crucial question is whether one will find at the same time that the mass transfer between the nuclei remains small, as required by experiment.

In addition to confronting the "one-body dissipation dynamics" with experiment we are testing the analytic "wall formula" against

a) Microscopic computer calculations of classical particles bouncing inside a deforming container,

b) The corresponding quantized problem (work with Y. Boneh, et al., A Microscopic Method for Calculating the Intrinsic Excitation Occurring in Nuclear Fission in this Annual Report),

c) Self-consistent time dependent Hartree-Fock calculations (see J. Błocki and H. Flocard, Time Dependent Hartree-Fock Calculation of the Nuclear Collective Motions, in this Annual Report).

The indications so far are that: (i) quantization does not invalidate the wall formula in any catastrophic way (as one might have feared) and (ii) that the symmetries of the nuclear potential well may crucially affect the dissipation, both in the quantal and classical calculations. (Koonin and Randrup have recently derived a quantal wall formula which reduces exactly to our expression in the appropriate limit).

The emerging picture of the "New Dynamics" for macroscopic nuclear processes seems to be analogous to the Two-Part approach to nuclear statics:

NEW DYNAMICS =

SMOOTH BACKGROUND + EFFECTS OF SYMMETRIES.

The "Smooth Background" is a type of dynamics governed by the balance of conservative and dissipative forces, the latter given approximately by the wall formula. Inertial effects, apart from translations and rigid-body type rotations, are often dominated by the dissipation and may be disregarded in a first approximation. In that case the intrinsic shape of the macroscopic nuclear system changes according to a normal surface displacement δq (at each point on the surface) whose time evolution is given by the following simple first-order differential equation (free of adjustable or unknown parameters):

$$\delta q = - \frac{1}{\rho v} (\phi - \bar{\phi})\, \delta t.$$

Here ϕ is the surface potential due to conservative and centrifugal forces and $\bar{\phi}$ is its surface average.

In cases when the topology of the system is about to change (as in the last stages of fission, or in the initial stages of a nucleus-nucleus collision) the wall formula for dissipation gives place to the window formula. (The transition from one to the other remains to be worked out.) This is analogous to the need for a special Proximity Formula for the static nuclear potential energy, associated with changes in the topology of the system.

The second aspect of the New Dynamics, the "Effects of Symmetries," is analogous to major shell effects in nuclear statics, which have been shown in the past few years to be associated with symmetries in the nuclear potential well.

The working out of the New Dynamics and its confrontation with relevant macroscopic nuclear experiments is our current objective.

Footnotes and References

*In collaboration with J.R. Nix and A. J. Sierk, LASL.

†Permanent address: Institute for Nuclear Research, 05-400 Swierk, Poland.

‡Permanent address: Niels Bohr Institute, DK-2100, Copenhagen, Denmark.

1. W. D. Myers and W. J. Swiatecki, Ark. Fys. 36, 343 (1967).

2. W. J. Swiatecki, J. Phys. Suppl., No. 8-9, 33, 45 (1972).

3. J. R. Nix and A. J. Sierk, Physica Scripta 10A, 94 (1974).

A MICROSCOPIC METHOD FOR CALCULATING THE INTRINSIC EXCITATION OCCURRING IN NUCLEAR FISSION*

Y. Boneh,† J. P. Blocki,‡ and W. D. Myers

One of the often observed features of atomic nuclei is the damping of large scale collective motion into intrinsic excitation.[1] (An excellent list of references related to the work described here is contained in Ref. 2.) The fact, that dipole and quadrupole vibrations are heavily damped while rotations seem to be unaffected, indicates that the damping is associated with changes in shape of the nuclear density distribution. The evaporation of neutrons from the separating fragments in nuclear fission is another indication that collective motion has been converted to internal excitation. The origin of this energy has usually been associated with vibrations of the separating nuclei as a consequence of their deformation at scission. This view is now being questioned because microscopic calculations[2,3] (like those described here) have shown that considerable internal excitation is to be expected at an earlier stage in the fission process during the descent from saddle to scission.

While the familiar phenomena just mentioned give clear indications of the importance of nuclear damping none of them is quite so dramatic as that seen in the collisions of very heavy ions (Refs. 12-42 of our Ref. 2). The so-called "deep inelastic" processes seen in reactions such as Kr on Bi are characterized by almost total damping of the relative motion of the colliding nuclei. The separating fragments seem to have started from rest and have only the energy gained from Coulomb repulsion.

Efforts to understand the damping of nuclear collective motion in terms of a classical hydrodynamic viscosity have not been very successful. Calculations have shown that the measured asymptotic kinetic energy release in fission[4] is only compatible with a relatively small viscosity coefficient while the "deep inelastic" processes in heavy-ion reactions seem to require a large value. The idea of a hydrodynamic viscosity is also questionable on fundamental grounds. Such a damping mechanism requires that the constituent particles have a rather short mean-free-path which seems to be incompatible with the fact that many nuclear phenomena are consistent with a completely independent particle model.

One way to determine the importance of the "single-particle" damping of collective motion into intrinsic states is simply to calculate the excitation produced in a system of independent particles when the shape of the potential well is changed as a function of time. In this paper, which is a continuation of Ref. 5, we want to describe a particularly simple approach and some preliminary applications that have been made to the fission of ^{236}U.

We have solved the time dependent Schrödinger equation in two sequences of potential wells whose shapes correspond to those determined by following the classical hydrodynamical evolution of the nucleus in the course of its descent from saddle to scission[4] (see Fig. 1).

The Schrödinger equation was solved in a fixed basis corresponding to a shape intermediate between the saddle and scission shapes using the method of Ref. 6. The time dependent equations were solved numerically with an improved version of the predictor-corrector method.[7] Only neutron levels were considered in this preliminary work and we we did not include either spin-orbit coupling or residual interactions.

The results obtained in the damped hydrodynamic calculations[4] for the fission of ^{236}U indicate that of the 60 MeV that becomes available in the course of the motion (1 MeV of kinetic energy in the fission direction and 59 MeV from the saddle-to-scission change in potential energy) approximately 21.3 MeV is dissipated as a consequence of the viscosity assumed. Another 38.7 MeV appears as collective kinetic energy. The time development of these

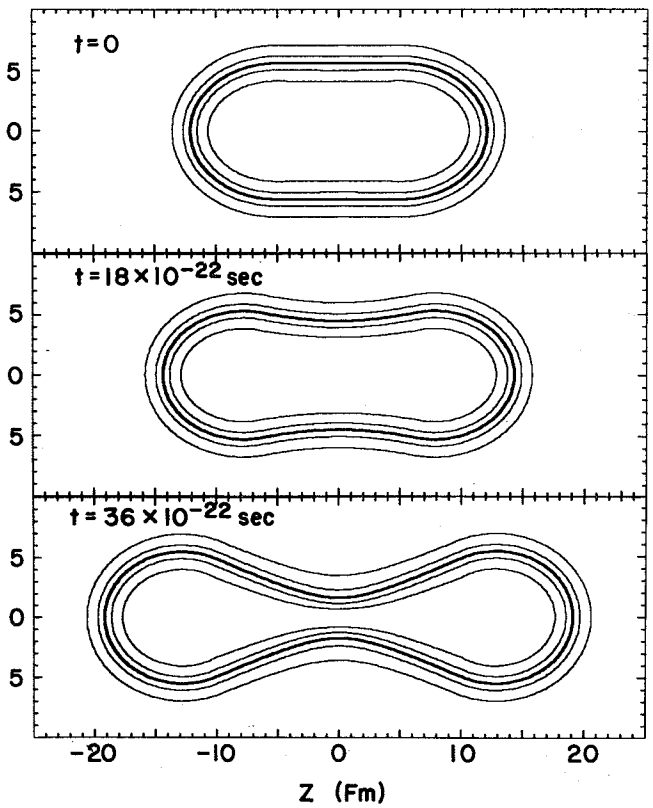

Fig. 1. The 10, 30, 50, 70 and 90% contours are shown for three shapes in the saddle-to-scission sequence used in the calculations described here. (XBL 763-2374)

quantities is shown in Fig. 2. The dashed line indicates how the collective kinetic energy increases during the 38.5×10^{-22} sec period necessary to move to scission. The solid line is obtained by adding the dissipated energy. (Both of these curves are scaled down by a factor of 144/236 so they can more easily be compared with the microscopic calculation which was done for the neutrons alone.)

For comparison with the collective kinetic energy found in the classical hydrodynamic calculation we calculated the microscopic quantity E_{coll},[8] where

$$E_{coll}(t) = \int \frac{1}{2} \rho \bar{v}^2 \, d\bar{r} \, . \qquad (1)$$

The local flow velocity is calculated from the expression $\bar{v} = \bar{j}/\rho$. Where ρ and $\bar{j}$ are, respectively, the quantum mechanical density and current.

The values we calculated for E_{coll} all lie above the curve of hydrodynamic values in Fig. 2. This result might have been anticipated since the hydrodynamic calculations assume almost irrotational flow which yields the lowest possible kinetic energy. The microscopic calculations are presumedly more turbulent.

The comparison of the dissipation energy in the two cases is not so straightforward. Because of the axial symmetry of the system the magnetic quantum number m of a given level must remain the same in the course of the motion. The same is true for the parity π_z in the case of reflection symmetric shapes. Consequently, even if the motion of the potential is extremely slow (adiabatic) the system may end up in an excited state since there is no way for a particle to change to an empty level that moves down through the Fermi surface if its quantum numbers m and π_z are different from the levels being crossed. In our calculations a substantial part of the apparent excitation energy is of this type. This part of the energy E_s (where the subscript s indicates that it has its origin in symmetry effects) is simply the difference between the ground state of the system E_0 (filling the lowest levels) and the "adiabatic" energy E_a (where the quantum numbers appropriate to the system are conserved).

$$E_s = E_a - E_0 \qquad (2)$$

$$E_0 = \sum_{i=1}^{N} E_i(\beta), \quad \text{lowest N levels,} \qquad (3)$$

$$E_a = \sum_{i=1}^{N} E_i(\beta), \quad \text{lowest N levels having the appropriate quantum numbers.} \qquad (4)$$

In this expressions β is a one-dimensional deformation parameter measuring the distance along the dynamical path.

The total excitation energy E_t is defined as the difference between the total energy E^* of the system described by the time dependent Schrödinger equation and the ground state at the same value of β, where

$$E_t = E^* - E_0, \qquad E^* = \sum_{i=1}^{N} E_i[\beta(t)], \qquad (5)$$

and the $E_i[\beta(t)]$ are the time dependent energy expectation values. Of course, E_t contains E_s (the apparent excitation arising purely from symmetry), as well as E_{coll}.

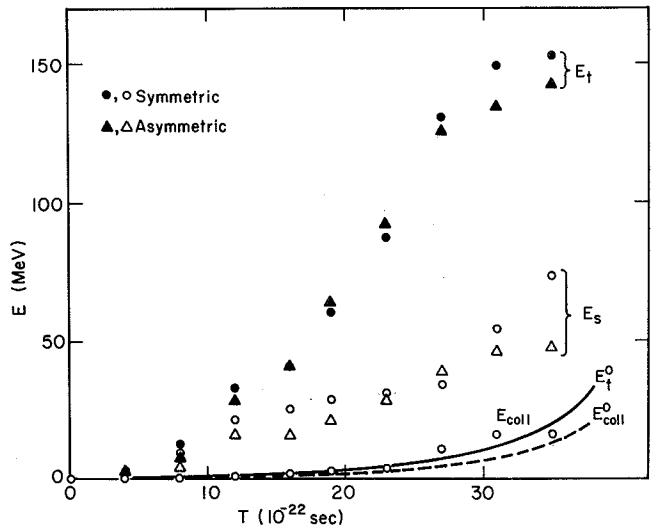

Fig. 2. The results of our microscopic calculations for the intrinsic excitation of the neutrons in ^{236}U for a hydrodynamically[4] determined sequence of shapes from saddle to scission. The dashed line is the corresponding hydrodynamic collective kinetic energy (irrotational flow assumed) and the solid line is obtained by adding the internal energy arising from the viscous damping of the motion. The circles represent the results of our calculation of E_{coll} the collective kinetic energy, E_t the total excitation and E_s, which is that part of the total excitation connected with the symmetry of the potential. The triangles represent these same quantities in the case when reflection asymmetry is introduced. (XBL 763-5237)

In Fig. 2 both the total excitation energy E_t and that part arising from symmetry E_s are plotted against time for the two cases we have considered. One is the purely symmetric case and the other is a similar case where an asymmetry was gradually introduced along the trajectory so that the mass ratio was 1.4 to 1 at scission. The reason for comparing these two calculations was to determine whether the microscopic dynamics would give preference to asymmetric scission shapes as has often been speculated.

The results of this work serve to draw attention to the importance of single particle damping for large scale collective motion. They show that the energy dissipation profile is quite different than that associated with a hydrodynamic (or "two-body") viscosity. They also show (as has been frequently speculated) that asymmetric fission is preferred over symmetric fission on the basis of microscopic dynamical considerations. Another interesting result is that the microscopic collective kinetic energy is greater than that for irrotational flow indicating that some turbulence is generated by the

collective motion. Consequently, we are inclined to question the applicability of the hydrodynamical saddle-to-scission trajectories. Both the dissipation and internal flow may well prefer a different sequence of shapes.

Footnotes and References

*Condensed from LBL-4374.

†Present address: Nuclear Research Center-Negev, Beer-Sheva P.O.B. 9001, Israel; partially supported by an IAEA fellowship.

‡Present address: Institute of Nuclear Research, 02-400 Swierke, Poland; partially supported by a Fulbright-Hays senior fellowship.

1. R. Wieczorek, R. W. Hasse and G. Sussmann, in "Proceedings of the Third International Atomic Energy Agency Symposium on Physics and Chemistry of Fission", Rochester, N.Y., 1975 (International Atomic Energy Agency, Vienna, 1974).

2. S. E. Koonin and J. R. Nix, Phys. Rev. C13, 209 (1976).

3. G. Schutte and L. Wilets, in "Proceedings of the Third International Atomic Energy Agency Symposium on Physics and Chemistry of Fission", Rochester, N. Y. 1973 (International Atomic Energy Agency, Vienna, 1974).

4. K. T. R. Davies, A. Sierk, and J. R. Nix, Los Alamos Scientific Laboratory Report LA-UR-76-362 (Feb. 1976).

5. Y. Boneh and Z. Fraenkel, Phys. Rev. C 10, 893 (1974).

6. H. C. Pauli, Phys. Rep. 7C, 35 (1973).

7. R. W. Hamming, J. Assoc. Comp. Mach. 6, 37 (1959).

8. According to a suggestion of S. E. Koonin.

MICROSCOPIC AND MACROSCOPIC CALCULATIONS OF ONE-BODY DAMPING IN FISSION*

Y. Boneh,† J. P. Blocki,‡ and W. D. Myers

As a part of a continuing study of the damping of large-scale collective motion into intrinsic excitation, we have solved the time-dependent Schrödinger equation for a sequence of shapes corresponding to the fission of ^{236}U. These calculations, which are described in detail in Ref. 1, were motivated by the fact that classical hydrodynamical calculations of the fission process seem to be incompatible with the strong damping observed in heavy-ion collisions. We wanted to compare the actual flow of energy into single-particle states with that calculated using a classical viscosity.

The microscopic calculations that have been performed so far are not self-consistent, and two major defects remain even when the viscosity has been varied in the hydrodynamical calculations until the total energy absorbed is the same as that found in a microscopic calculation for the same sequence of shapes:[2] (1) The calculations no longer agree with experiment, and (2) the energy absorption profiles differ along the trajectory. These calculations served to dramatize the fact that the concept of hydrodynamic viscosity poorly represents the damping mechanism that creates the internal excitation in the single-particle calculations.

In order to obtain results from the hydrodynamical calculations that would be more nearly comparable to the microscopic calculations it was necessary to find a classical damping mechanism analogous to that seen in the microscopic calculations. Such a mechanism is obtained[3] from classical kinetic theory by carrying the system energy expressions, for volume conserving systems, to second order in the appropriate expansion parameter (the ratio of the wall velocity to the average velocity of the particles). We have used this method to calculate the damping to be expected from such a mechanism and have compared it with our earlier microscopic calculations, which are described elsewhere in this report.

Some difficulty is encountered in interpreting the microscopic calculations because the special symmetries of the sequence of potentials that are employed led to apparent excitation even in the case of adiabatic motion. In Fig. 1 we have plotted the total microscopic excitation energy (along the saddle-to-scission trajectory) minus the microscopic collective kinetic energy as the quantity E_d^{max}. When the contribution to the total energy from symmetry effects is removed the points labeled E_d^{min} are obtained. In both cases we have we also considered another sequence of shapes derived from the symmetric ones by introducing a mass asymmetry that increases linearly from the saddle to a value of 1.4 at scission.

For comparison we have plotted the calculated value of the energy dissipation from the hydrodynamical calculations on which the sequence of shapes is based.[4] For comparison with the microscopically determined energy flow into intrinsic states we also calculated the dissipation to be expected on the basis of the classical one-body damping expression mentioned earlier.[3] The rate of energy absorption is given, in this theory, by the surface integral

$$\dot{E} = \rho_m \bar{v} \oint \dot{n}^2 \, d\sigma, \qquad (1)$$

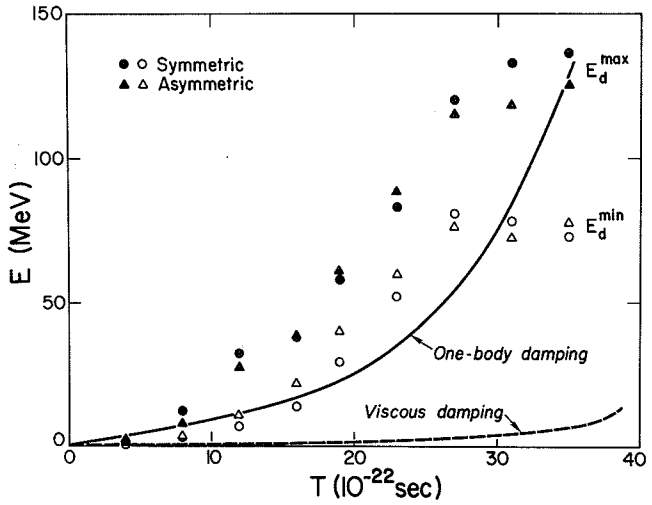

Fig. 1. The largest and smallest amounts of internal excitation consistent with our microscopic calculations are plotted as E_d^{max} and E_d^{min} for the two cases considered (symmetric and asymmetric). For comparison the one-body damping from Eq. (1) is shown as a solid line and the viscous damping (from the calculation used to generate the shapes)[2] is shown as a dashed line. (XBL 764-2731)

where ρ_m is the mass density, $\bar{v}$ the average velocity of the particles (3/4 v_F in the Fermi gas model), and $\hat{n}$ is the normal velocity of the nuclear surface. Note that unlike ordinary viscous damping, this expression contains no adjustable parameters.

The results of this work serve to draw attention to the importance of single particle damping for large-scale collective motion. They show that the energy dissipation profile is quite different than that associated with a hydrodynamic (or "two-body") viscosity.

They also show that the results for one-body dissipation treated quantum mechanically and classically are very close and it seems that this type of dissipation is more neary comparable to that which takes place in nuclei where an independent particle description certainly applies.

Classical hydrodynamical calculations performed recently with this new type of damping give rise to a distinctly different sequence of shapes than those used here.[5] An important step in the continuation of this work would be to perform the microscopic calculations in potential wells following the new shape sequence obtained with the use of one-body damping to see if the damping along the path to scission is more nearly like that of the classical prediction.

Footnotes and References

*Condensed from LBL-4397.

†Present address: Nuclear research Center-Negev, Beer-Sheva P.O.B. 9001, Israel.

‡Permanent address: Institute of Nuclear Research, 05-400 Swierk, Poland.

1. Y. Boneh, J. P. Błocki, and W. D. Myers, Lawrence Berkeley Laboratory Report, LBL-4374 (Feb. 1976).

2. S. E. Koonin and J. R. Nix, Phys. Rev. C 13, 209 (1976).

3. W. J. Swiatecki, in "Proceedings of the Intern. School Seminar on Reactions of Heavy Ions with Nuclei and Synthesis of New Elements", Dubna, USSR (Oct. 1975).

4. K. T. R. Davies, A. J. Sierk, and J. R. Nix, Los Alamons Scientific Laboratory Report LLA-UR-76-361 (Feb. 1976).

5. J. R. Nix and A. J. Sierk, private communication.

FURTHER STUDIES ON SPONTANEOUS-FISSION HALF-LIVES FOR EVEN NUCLEI WITH $Z \geq 20$*

J. Randrup,† S. E. Larsson,‡ P. Moller,‡ S. G. Nilsson,‡
K. Pomorski,§ and A. Sobiczewski**

Since an earlier semi-empirical study of the spontaneous-fission process for transthorium elements, improved theoretical deformation-energy surfaces have been obtained,[1] based on the Modified-Oscillator single-particle model and the macroscopic Droplet Model.[2] In those calculations the effect of axial asymmetric distortions as well as reflection asymmetric distortions is included in a more accurate way.

On the basis of new calculational material, we have considered the even-even elements beyond thorium, for the purpose of increasing the accuracy of the theoretical calculations of the spontaneous fission half-lives.

The fission process is treated as a penetration through a one-dimensional potential barrier, calculated along an effective path in the multi-dimensional deformation space. The penetrability is calculated in the WKB approximation. Thus one needs the action integral K along the fission path,

$$K = \frac{2}{\hbar}\int_{r_1}^{r_2} \sqrt{2B(r)(V(r) - E_{vib})}\,dr \ . \qquad (1)$$

The path is described by the fission coordinate r. V(r) is the deformation energy of the shape described by r, and B(r) is the effective inertial mass function corresponding to a motion along the fission path. Moreover, E_{vib} denotes the fission mode zero point energy in the initial state; it is taken to 0.5 MeV. The integral limits r_1 and r_2 are the entrance and exit point, respectively. From the integrated action K the half-life $T_{1/2}$ is given by the relation

$$T_{1/2} = 10^{-28.04}\ (1 + e^{K})\ \text{years}. \qquad (2)$$

The fission barrier potential V(r) is calculated theoretically. In the present study V(r) is based on recent calculations presented in Ref. 1.

At present the theoretical calculations of the effective fission inertial-mass function B(r) are less accurate than the calculations of the potential V(r). Therefore we introduce one overall mass-renormalization parameter which is subsequently determined by fitting to the known halflives. In this paper two trial forms of B(r) are studied. One is based on macroscopic (hydrodynamical) irrotational-flow calculations and is similar to what was previously studied. In addition to this, we have calculated microscopic inertial-mass parameters in the cranking approximation and used these for the determination for the effective fission inertia.

According to the semi-emperical method, the fission barrier potential is generated from the stationary points on the deformation-energy surface (i.e., the minima and saddle points) together with one (or more) additional point(s) in the exit region beyond the last saddle point.

We have included the effect of axially asymmetric nuclear shapes as described by the γ deformation coordinate. A detailed study of the γ deformation in the actinide region is performed in Ref. 3 and a similar study for the super-heavy region in Ref. 4. Here we put the emphasis on the most recent results employing a three-dimensional variation in the $(\varepsilon\varepsilon_{\mu}\gamma)$-space.

In the nuclear region considered here, reflection asymmetric shapes play an important role for large nuclear distortions. For our present study we have employed the reflection-asymmetry corrections to the second saddle given in Ref. 5. They were obtained by calculating a two-dimensional map using a a combined symmetrical coordinate ε_{24} and a combined asymmetrical coordinate ε_{35}.

We have also studied the effect of P_6 deformation at the ground state minimum. The P_6 deformation energies used are those given in Ref. 1. Most of the nuclei considered have some P_6 deformation in the ground state and it turns out that the inclusion of the correction improves the overall fit to experiment by a factor of around five. For this reason we have included this effect in the fission barriers.

The explicit form of the macroscopic inertial mass function is

$$B_r^{macro}(r) = 1 + k\frac{17}{15}\exp\left(\frac{c}{\lambda}\left(\frac{3}{4} - r\right)\right). \qquad (3)$$

Here r is measured in units of the nuclear radius $R = r_o A^{1/3}$ and B_r^{macro} is measured in units of μ, the reduced mass of the final two-fragment system (which we assume to be symmetrical). Moreover, λ is a numerical constant equal to 1/2.452 determined from a fit to the exact curve[6] for B_r^{irrot}

In addition to the renormalization parameter k we have introduced a second parameter c governing the slope of the mass function. For k = c = 1 the irrotational-flow inertial-mass function is approximately reproduced.

As an alternative, we have calculated the spontaneous fission half-lives on the basis of inertial-mass parameters calculated in the cranking approximation.

One adjustable parameter is introduced in this case in the form of the overall renormalization factor ρ. One should bear in mind that because of the approximate treatment of the inertial matrix one cannot expect ρ to come out exactly equal to unity, even if the basic inertial-mass parameters were correct. On the other hand, since the adopted treatment is expected to include the main part of the inertia, the factor ρ should not be too different from unity. Recalling the empirical finding that the microscopically calculated mass parameters in the rotational case tend to come out somewhat too large, it appears satisfactory that the best fit is obtained for $\rho = 0.80$.

With the fission barrier potentials established as described, we have, using the different sets of trial inertial-mass functions, calculated the spontaneous=fission half-lives for the known even-even nuclei ranging from ^{232}U to ^{258}No. Minimization of the average logarithmic deviation Δ of the calculated half-lives from the experimental ones determines, for each set of intertial functions, the adjustable parameter(s) entering in the trial functions.

For the hydrodynamic type inertial-mass function with c = 1 the best reproduction of experimental half-lives is obtained for k = 11.5. This value is larger than the previously[7] employed value of 10.0. This change is mainly due to the inclusion of the ε_4 dependence of the r coordinate. The average logarithmic deviation is $\Delta = 1.7$, which corresponds to a factor of around 50.

The half-lives obtained with this type of effective mass function are shown in Fig. 1 together with the experimental data.

The isomeric fission tests a more limited part of deformation space as it only explores the second barrier region and this serves to favor one solution.

In Fig. 1 we have included some calculated (with k = 11.5 and c = 1.0) and experimental isomeric half-lives. For the calculated isomeric half-lives there is a pronounced erroneous trend in going from U through Pu to Cm. For the two measured U isomers (^{236,228}U) the calculated values are around five orders of magnitude too long. This may indicate that the second barriers of these isotopes are too large. One should notice that for ^{234}U the calculated value is of the same order as the two experimental numbers for ^{236,238}U. For Pu the overall agreement is fairly good but the isotopic variation is in error. This may reflect the sensitivity to the more detailed structure of the second barrier, which we treat here in a rather crude manner. Finally, the calculated values for ^{242,244}Cm come out around seven orders of magnitude too short as compared with experiment. The similar calculations with k = 6.5 and c = 0.5 yield isomeric half-lives which are one to two orders of magnitude longer (this change can be estimated). Although the present results for the isomeric half-lives are far from satisfactory, the results do seem to point in favor of the irrotational-type slope, i.e., a value of the slope parameter c not far from unity.

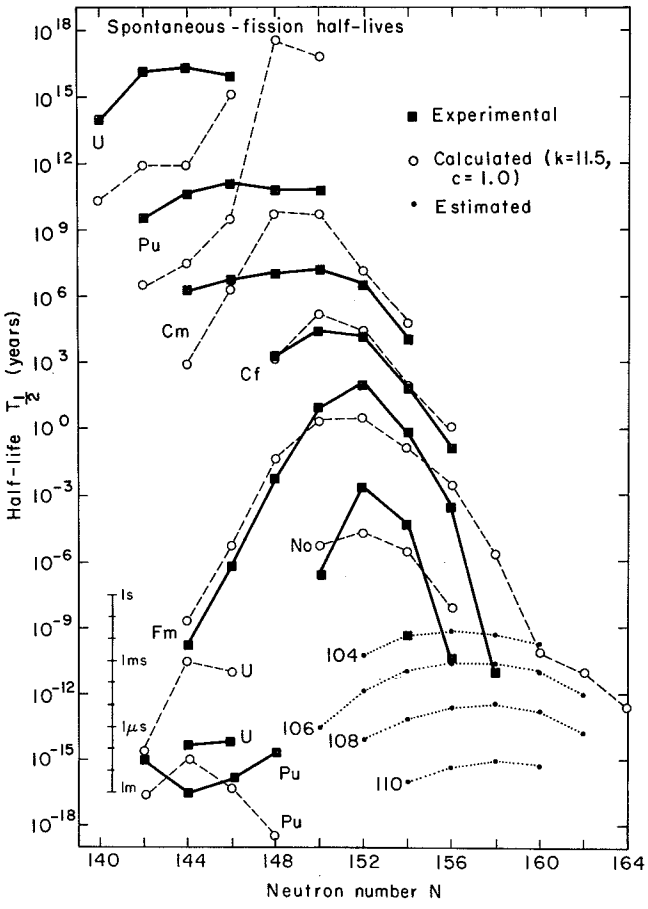

Fig. 1. Spontaneous-fission half-lives calculated with the macroscopic inertial-mass functions having k = 11.5 and c = 1.0 (open circles joined by dashed lines). The experimental values are indicated by full squares joined by full lines. In the lower-left corner are included some isomeric half-lives. Also included in the figure are the half-lives calculated with the estimated approximate barriers for the transuranium elements (dots joined by dotted lines). (XBL 756-3150)

Similarly, for the microscopic inertial-mass functions the renormalization factor ρ is determined by fit to experiment. The optimum fit obtains for ρ = 0.80, corresponds to Δ = 1.3, which is a factor of around twenty. One should thus note that the microscopic calculations with one overall normalization factor leads to a fit which is equally good as that obtained with two parameters in the case of a macroscopic type inertial function. Figure 2 shows the corresponding results for the spontaneous-fission half-lives. Also in this figure we have included isomeric half-lives.

We have made preliminary estimates of the spontaneous-fission and alpha decay half-lives for the elements with Z between 104 and 110. For this purpose we have estimated the fission barrier potentials by calculating the deformation energy in five deformation points fixed a priori.

Beyond nobelium the theoretical fission barriers have only one peak. Consequently, the calculated fission half-lives are relatively short (at most milliseconds) and, moreover, exhibit a smooth variation with neutron number. It follows from our

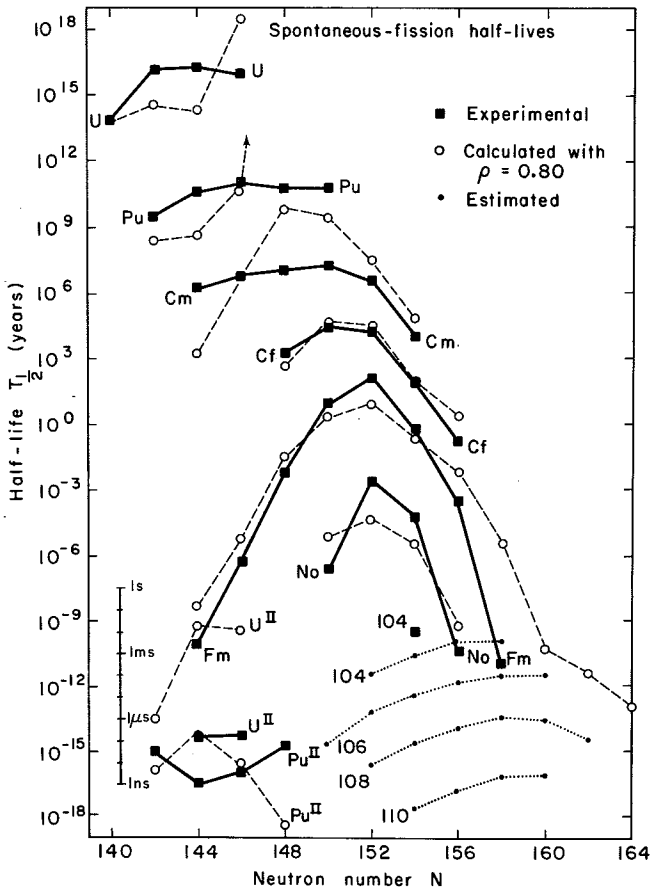

Fig. 2. Spontaneous-fission half-lives calculated with the microscopic inertial-mass functions having ρ = 0.80. Similar to Fig. 1. (XBL 756-3149)

remarks above that the existence of a shell at N = 152 could drastically change this behavior in the neighborhood of that neutron number. A possible experimental measurement of the spontaneous-fission half-life of the isotope ^{256}104 would add a valuable piece of information concerning this crucial point.

Taken at their face value, the present calculations indicate that the isotopes of the element 106 generally have spontaneous-fission half-lives which are shorter by a factor of around 30 than the 104 isotopes with the same neutron number. This suggests that even 106 isotopes may exist with a spontaneous-fission half-life not much shorter than that of ^{258}Fm. Because of the uncertainty arising from the N = 152 problem it is not possible to predict with confidence which neutron number will give the largest stability.

The calculated half-lives for the element 108 show the same trend as thos for 106 but are generally a factor of around 10^2 shorter. The half-lives of the 110 isotopes are further reduced by a factor of 10^3, approximately.

It appears that more accurate theoretical predictions for this particular region of nuclei cannot be made until more accurate deformation energy surfaces have been established.

In our previous calculations[7] of the spontaneous-fission half-lives for the superheavy elements the ε_4 dependence of the r coordinate was not included. A consistent inclusion will lead to longer half-life predictions for nuclei with less extended barriers. We have therefore reexamined the superheavy region, with the present more complete treatment.

On the whole, the resulting effect is small, particularly so for the most stable nuclei near the center of the superheavy island. For nuclei with half-lives of around one year the increase in the stability only amounts to less than a half order of magnitude. The general conclusions of our previous study in the superheavy region[7] are thus not significantly altered by the present investigation.

Footnotes and References

*Condensed from LBL-4036.

†On leave from the University of Aarhus, Aarhus, Denmark.

‡Department of Mathematical Physics, Lund Institute of Technology, Lund, Sweden.

§Institute of Physics, Maria Sklodowka-Curie University, Lublin, Poland.

**Institute for Nuclear Research, Hoza 69, PL-00681 Warszawa, Poland.

1. S. E. Larsson, P. Möller, S. G. Nilsson, I. Ragnarsson, J. Randrup, C. F. Tsang, Nucl. Data, to be submitted.

2. W. D. Myers and W. J. Swiatecki, Ann. Phys. 84, 186 (1974).

3. S. E. Larsson and G. Leander, Proceedings of Third IAEA Symposium on Physics and Chemistry of Fission, IAEA, Rochester, N. Y. (1973), p. 177.

4. S. E. Larsson, P. Möller, and S. G. Nilsson, Physica Scripta 10A, 53 (1974).

5. P. Möller, Nucl. Phys. A192, 529 (1972).

6. E. O. Fiset and J. R. Nix, Nucl. Phys. A193, 647 (1972).

7. J. Randrup, S. E. Larsson, P. Möller, A. Sobiczewski, and A. Kukasiak, Physica Scripta 10A, 60 (1974).

INTERSTELLAR DEUTERIUM ABUNDANCE AND THE CLOSED VERSUS OPEN UNIVERSE

Elizabeth A. Rauscher

With the advent of Einstein's general relativity theory in 1915[1] the distribution of matter and energy became describable in terms of the geometric structure of space. The spatial distribution of matter-energy in a localized region of space determines the local curvature of space in that region. In 1919 with the occurrence of a complete solar eclipse in Chili, Einstein's theory appeared to be tested.[2] Light from distant stars is bent in the gravitational space of the sun or to say this another way, the space next to the sun is curved due to the mass of the sun, and light from distant stars follows the shortest pathlength which is a geodesic of the curved space.[3,4]

Within the context of this curved space description, one can ask what is the nature of the curvature of space of the entire universe. If the curvature due to the universe matter energy content is everywhere and always positive (and enough matter is present), then the universe will be finite and closed. From Einstein's field equations, (which describe the dynamical evolution of the universe and the manner in which matter and energy curve space) we can define three possible universe models.[5] We can define these three models in terms of the solutions of Einstein's field equations where we have the curvature constant, k, derived from the curvature in the field equations.[6] Then, we have three possible values

of the curvature of k = 0, ±1 which corresponds respectively to Euclidian (flat space), closed, or open universe models.

Before proceeding further, we should mention several assumptions. They are that the universe is isotropic and homogeneous (called the cosmological principle) in which stars and galaxies are just small perturbations. The isotropy hypothesis appears to be observationally valid.[5,7]

Two other observations are of particular interest. The first is that made by E. P. Hubble in the early 1920's that the universe was dynamic and expanding.[8] In 1915 it was thought that the universe was fixed and static so that, although Einstein's field equations describing the manner in which the matter-energy content determined the curvature of space, he added the "cosmoligical constant" to give static solutions to his equations.[7] (Later, Einstein was to have said that his was the biggest mistake of his life!)

Another significant prediction and observation was the hypothesis of the "big bang" cosmology theories of A.G.E. Lemaitré and G. Gamow[9,10] in observation of the 3° K black body radiation[11] in the 1960's. The big bang model assumes that all the matter in the universe originated from a highly condensed, singular state and that it exploded and is expanding at the rate Hubble predicted.[8]

The Hubble recession is determined from the red shifting of the spectra observed from stars. Independently, a distance scale can be set.[12] The Hubble's constant is then defined as $H = (\dot{R}/R)$ or the velocity of recession over the distance away from us. The inverse of H or $t_o < 1/H$ sets an upper limit on the age of the universe. From the solutions to Einstein's field equations we can derive the relationship of the critical density for a just closed universe and the Hubble's constant,[5] or $\rho_c = 3H^2/8\pi G$, where G is the gravitational constant.

Since the field equations do not specify k, the curvature, how can it be determined? One observation may be a critical and sensitive test and that is the amount of interstellar deuterium.[13,14] In the early stages of the evolution of the universe, the temperature was very large; initially (according to some models), the big bang temperature was $T \sim 10^{32}$ °K. The onset of nucleo synthesis occurs around $T \sim 10^9$ °K (called the T_9 era) in which the temperature is cool enough for nucleons to stick together. Since stellar processes appear to destroy deuterium, it is then assumed that all the present deuterium abundance was created in the T_9 era.[5] (Stellar creation occurs around the T_4 (or $T \sim 10^4$ °K era.) There are approximately 144 reactions which determine the deuterium abundance but there are six primary ones that we need to consider.[13] We can relate the decay constant of these six reactions to the nuclear species concentration and express these in terms of the baryon number density and the temperature in T_9 units.[13]

Deuterium is created by the reaction n+p→D+γ. Most nuclear processes "burn" or destroy deuterium. (See Ref. 5 and Table 1 for the five other reactions.) Also in Ref. 5 is given some observed values of neutral interstellar deuterium ratio to neutral hydrogen is about $D/H \sim 10^{-5}$. Analysis of the six equations gives an 8th power law of the mass

Table 1. Six basic reactions for the abundance of deuterium.

	Reaction	Q
(1)	$n + p \rightarrow D + \gamma$	+2.22 MeV
(2)	$D + D \rightarrow {}^3H + p$	+4.03 MeV
(3)	$D + D \rightarrow {}^3He + n$	+3.25 MeV
(4)	${}^3H + D \rightarrow {}^4He + n$	+17.60 MeV
(5)	${}^3He + n \rightarrow {}^3H + p$	+0.76 MeV
(6)	${}^3He + D \rightarrow {}^4He + p$	+18.35 MeV

Note that $D \equiv {}^2H$, and $t \equiv {}^3H$, and $p \equiv H$. Equation creates D and all others burn D to ${}^4He$ essentially. In Eq. (2), D's → ${}^3H+p$ later burned to ${}^4He+n$ in Eq. (4), p's and n's produced are burned in Eq. (1). In Eq. (1) the only tie to radiation as γ's is created.

fraction of deuterium near the critical density, or $D/H \propto \rho_b{}^8$ near $\rho_b \approx \rho_c$. Recalling that the critical density for a just closed universe depends on the Hubble's constant squared, we then have a range of possible values. The recessional red shift is quite well determined but the distance scale is not so well known. Although previous values of H and hence ρ_c, compared to the observed D/H ratio implied an open cosmology, recent observations and determinations of H imply that a closed cosmology (k = +1) is also possible. See Fig. 1.[5,6] For H ≈ 50 km/sec·Mpc,

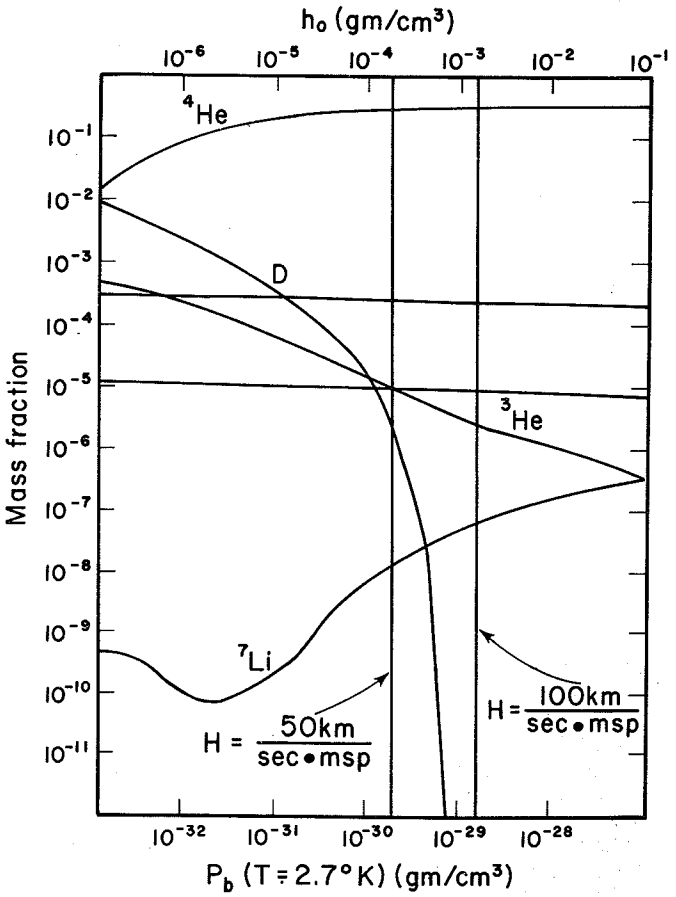

Fig. 1. Ratio of deuterium to hydrogen abundance vs nuclear density. (XBL 766-8225)

$\rho_c \approx 4\times10^{-30}$ gm/cm^3 which is consistent with the D/H ratio.[16] (A parsec is 3.26 light years, where one light year is 5.8 trillion miles and Mpc stands for mega parsec.)

The theoretical determination of the curvature constant is given in Ref. 17 in which an additional constraint on Eistein's field equation is given in terms of geometrical constaint which are expressed in terms of universal constants. The value of the curvature constant is found to be positive, giving closed cosmological solutions.

References

1. A. Einstein, Annalen der Physik. 49, 169 (1916).

2. C. W. Misner, K. S. Thorne, and J. A. Wheeler, Gravitation, (W. H. Freedman, 1973).

3. W. Pauli, The Theory of Relativity, (Pergamon Press, N. Y., 1958).

4. A. Einstein, The Meaning of Relativity, (Princeton University Press, New Jersey, 1955).

5. E. A. Rauscher, LBL-4353, December, 1975.

6. E. R. Harrison, Ann. Phys. 35, 437 (1965).

7. E. A. Rauscher, UCRL-71435, October 1968 and Bull. Am. Phys. Soc. 13, 1643 (1968).

8. E. P. Hubble, Proc. Nat. Acad. Sci. 15, 169 (1929).

9. A. G. E. Lemaitré, The Primeval Atom, (Van Nostrand Press, N.Y., 1950).

10. G. Gamow, Nature 162, 680 (1948).

11. R. H. Dicke, P. T. E. Peebles, R. G. Roll, and D. T. Wilkenson, Astrophys. J. 142, 414 (1965).

12. Edited by Hong-Yee Chiu and Amador Muriel, Stellar Evolution, MIT Press, Cambridge, Mass., 1972).

13. R. V. Wagoner, W. A. Fowler, and F. Hoyle, Astrophys. J. 148, 3 (1967).

14. R. V. Wagoner, Astrophys. J. 179, 343 (1973).

15. P. J. E. Peebles, Astrophys. J. 146, 542 (1966).

16. R. P. Kirshner and J. Kwan, Astrophys. J. 193, 27 (1974).

17. E. A. Rauscher, Nuovo Cimento Lett. 5, 925 (1972).

III.

APPARATUS

A. ACCELERATOR OPERATIONS AND DEVELOPMENT

88-INCH CYCLOTRON OPERATION, DEVELOPMENT AND STUDIES

J. Bowen, D. J. Clark, P. E. Frazier, L. Glasgow, R. A. Gough,
D. L. Hendrie, W. R. Holley, A. Jain,* and D. Morris

During 1975 and the first half of 1976, the cyclotron was scheduled for 20 eight-hour shifts per week for experiments in nuclear science, isotope production, and beam development. Distribution of beam time for 1975 is shown in Table 1, while an updated particle distribution history is shown in Fig. 1. Table 2 lists external beam intensities of ions which have been accelerated through May 1976 along with the energy range available with each ion. New beams in 1975-76 include $^{6}Li^{3+}$, $^{11}B^{4+}$, $^{12}C^{5+}$, $^{16}O^{6,7+}$, $^{19}F^{5+}$, $^{20}Ne^{7+}$, $^{28}Si^{5,6,7+}$, $^{40}Ca^{6,7+}$, and $^{40}Ar^{10+}$. New special-isotope beams of $^{15}N^{4+}$ and $^{22}Ne^{5+}$ have also been developed.

Table 1. 88-inch cyclotron operation time distribution 1975.

	(%)
Tune-up	7
Beam optics	4
Experiments	52
Beam development	6
Operating time (5663 hours)	69%
Planned maintenance	24
Unplanned maintenance	7
Total maintenance (2545 hours)	31%
Total work time (8208 hours)	100%

A new PIG source design with larger clearances and a smaller bore diameter has greatly increased the availability and reliability of high charge state beams. The 172 MeV $^{40}Ca^{7+}$ beam for example, had never been obtained with earlier source designs. The recently developed $^{16}O^{7+}$ beam at ~ 27 MeV/nucleon, believed to be the first verified O^{7+} beam extracted from a PIG source, is now in use by experimental groups.

Another ion source design, similar to the above but with provision for filament heating of the cathodes, has been fabricated and is undergoing testing. This new feature is intended to provide a simple means of controlling the source output.

A new bending magnet was designed, fabricated, and installed in an experimental beam line. This magnet is used to steer the beam into one of the three different experimental caves. It replaced an older magnet and has greatly improved the beam optical characteristics. A regulated 1000A dc power supply has been built for the new magnet. High current "hockey-puck" diodes and Darlington power transistors are used to simplify its circuit design and construction.

A flammable-gas venting system has been installed in some of the experimental caves to safely provide for experiments that require these gases.

A continuing strong effort is being made to improve day to day operating reliability. Minor changes are being made in components as weaknesses occur. There are indications that we are making progress towards increased reliability. A considerable amount of available manpower goes into this aspect of cyclotron improvement.

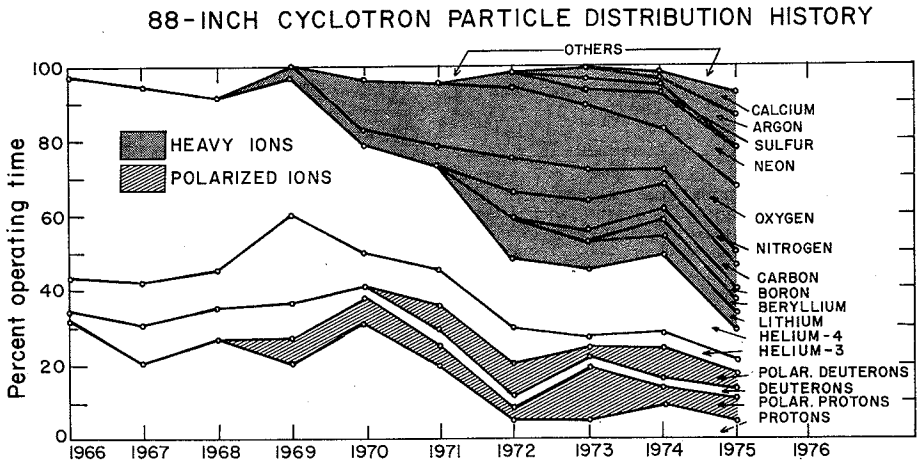

Fig. 1. 88-inch cyclotron particle distribution history. (XBL 7512-9594A)

Table 2. 88-inch cyclotron beams, to May 1976.

Ion	Energy[a] (MeV)	External beam (eμA[b])	Ion	Energy[a] (MeV)	External beam (eμA[b])
p	0.2-55	100-20	$^{20}Ne^{4+}$	63-112	10
p(polarized)	6-55	0.40	$^{20}Ne^{5+}$	112-175	5
d	0.5-65	100-20	$^{20}Ne^{6+}$	175-252	1
	-	-	$^{20}Ne^{7+}$	252-343	0.014
d(polarized)	10-65	0.40	$^{22}Ne^{5+}$	100-159	5
$^{3}He^{2+}$	1-140	100-10	-	-	-
$^{4}He^{2+}$	3-130	100-10	$^{24}Mg^{4+}$	50-93	2
$^{6}Li^{1+}$	2-23	10	$^{24}Mg^{5+}$	93-146	0.2
$^{6}Li^{2+}$	23-93	5	$^{25}Mg^{4+}$	50-90	2
$^{6}Li^{3+}$	93-195	1	$^{26}Mg^{4+}$	48-86	2
$^{7}Li^{2+}$	20-80	5	-	-	-
			$^{28}Si^{5+}$	80-125	1
$^{9}Be^{2+}$	15-62	5	$^{28}Si^{6+}$	125-180	0.2
$^{9}Be^{3+}$	62-140	2	$^{28}Si^{7+}$	180-245	0.08
			$^{32}S^{6+}$	100-158	2
$^{10}B^{2+}$	14-56	10	$^{32}S^{7+}$	158-214	0.2
$^{10}B^{3+}$	56-126	10	$^{40}Ar^{2+}$	35-14	0.4[c]
$^{11}B^{2+}$	12-51	10	$^{40}Ar^{6+}$	3.5-126	4
$^{11}B^{3+}$	51-115	10	$^{40}Ar^{7+}$	126-172	2
$^{11}B^{4+}$	115-204	0.3	$^{40}Ar^{8+}$	172-224	0.5
$^{12}C^{3+}$	45-105	20	$^{40}Ar^{10+}$	280-350	10^3 part/sec
$^{12}C^{4+}$	105-187	5	-	-	-
$^{12}C^{5+}$	187-292	0.05	$^{40}Ca^{6+}$	85-126	1
			$^{40}Ca^{7+}$	126-172	0.2
$^{14}N^{2+}$	10-40	20	-	-	-
$^{14}N^{3+}$	40-90	15	$^{56}Fe^{10+}$	180-250	1 part/sec
$^{14}N^{4+}$	90-160	15	$^{84}Kr^{2+}$	5-19	.001
$^{14}N^{5+}$	160-250	2	$^{84}Kr^{12+}$	200-240	1 part/sec
$^{14}N^{6+}$	250-360	10^3 part/sec	-	-	-
$^{15}N^{4+}$	130-233	15	-	-	-
$^{16}O^{3+}$	35-79	20	-	-	-
$^{16}O^{4+}$	79-140	20	-	-	-
$^{16}O^{5+}$	140-219	2	-	-	-
$^{16}O^{6+}$	219-315	2	-	-	-
$^{16}O^{7+}$	315-429	~ 50 epA[a]	-	-	-
$^{18}O^{4+}$	70-124	10	-	-	-
$^{19}F^{4+}$	66-118	10	-	-	-
$^{19}F^{5+}$	118-184	2	-	-	-

[a] Energy range for heavy ions indicates nominal maximum energy for the particular charge state down to the energy which can be reached from the next lower charge state. Beams can also be run with lower charge than shown at energies below 1 MeV/Nucleon.

[b] Electrical microamperes except as noted.

[c] 9th harmonic.

[d] 15th harmonic.

A new servo control has been desgined and built and will soon be installed to replace the existing rf trimmer control unit. A 16-channel digital readout unit has been built and installed. Four of these channels are used to display center region parameters. More of these channels will be used to monitor vital parameters in the center region and plans are being made to interface this unit to the TI 960A computer. A new program for the TI 960A is now being written and it will be ready shortly.

The use of additional dee-to-ground capacity to extend the lower limit of the rf frequency toward 4 MHz has been shown to be feasible. A disconnect switch is being designed so the additional capacitance can be added or removed without having to let the cyclotron tank to atmospheric pressure.

A project was undertaken to develop the cyclotron for ninth harmonic acceleration. The object of this development was to enable heavy masses (~300 amu) to be accelerated in the cyclotron. This would make possible certain experiments like searching for the existence of minute traces of the so-called "superheavy elements" in nature with a high resolution and sensitivity. Extracted beams have been observed up to 15th harmonic. Some center region modifications were necessary to correct problems associated with orbit centering and the long source to puller transit time. On 9th harmonic, 370 nA of $^{40}Ar^{2+}$ were seen as external beam and ~1nA of $^{84}Kr^{2+}$ was observed on 15th harmonic. The basic capability has been developed for acceleration of mass 300^{8+} ions in the cyclotron with substantial intensities.

A project was undertaken to study systematics in the control settings of the 88-inch cyclotron. The motivation was to predict the control settings of a new beam with sufficient accuracy to avoid time consuming beam development and calculations. About 60 parameters need adjustment (e.g., main coil current, frequency, 17 trim coil currents, center region and deflector parameters, valley coils, etc.) for the acceleration of a beam of specified energy/nucleon and charge to mass (e/m) ratio. Expressions have been derived describing the phase history of a particle $(e/m)_b$ accelerated in a magnetic field tuned for another particle $(e/m)_a \neq (e/m)_b$. By placing constraints on the allowed phase excursions, limiting values of $(e/m)_b$ have been obtained as a function of $(e/m)_a$. Similar calculations are in progress to determine by how much the energy/nucleon can be changed without modifying the basic cyclotron solution. It appears that about 200 model beams will adequately span the entire energy/nucleon and e/m spectrum of the cyclotron on such a two-dimensional grid. Other new beams could then be accelerated by interpolating or "stretching" the control settings of the nearest model beam. A compilation of the 60 control settings for each of these 200 chosen model beams (about $60 \times 200 = 12{,}000$ significant numbers) has therefore been undertaken. Wherever possible, control settings of model beams were taken from previously run beams. For model beams which had not been run, trim coil parameters were calculated using the computer code CYDE designed for this purpose. Other parameters were obtained by scaling laws. This vast compilation is now nearing completion and shall be helpful in accelerating beams of new energy/nucleon or e/m.

A project has been started to redesign the ion optics of the axial injection system for the future addition of an external heavy ion source. In this

design the acceptance of the axial injection line is matched with a 200 mm•mrad emittance from a PIG heavy ion source to permit efficient transfer of heavy ions from the source to the machine center. The matching is done with the aid of an electrostatic quadrupole triplet and a 90° bending magnet with edge focusing. The optimization of the ion optics was done with the computer code BELIN (a version of TRANSPORT) and a very satisfactory solution of the beam transport element parameters was found. Experimental tests of the performance of this and other optics designs are being planned on a test bench.

Footnote

*On leave from the Bhabha Atomic Research Center, India.

150 MeV PROTON MEDICAL CYCLOTRON DESIGN STUDY*

R. J. Burleigh, D. J. Clark, and W. S. Flood

A brief design study has been done for a 150 MeV proton sector cyclotron. The object was to minimize cost but maintain good reliability and easy maintenance. The use of the proton beam would be therapy, radiography, and isotope production.

Protons have the advantage over x-rays and neutrons of having a fixed range and a high rate of energy loss near the end of the range. This makes possible the radiation of small internal tumors with low dosage to the surface tissue. Heavier ions and π^- mesons also have fixed ranges and advantage over protons of a low OER (oxygen enhancement ratio) which reduces damage to normal tissue, but they require considerably larger accelerators to produce beams with enough range to penetrate the human body. So we present this preliminary design study in the hope that there is an area of therapy which can utilize the high definition of protons at a cost which is much less than for heavier ions or π^- mesons.

For a 150 MeV proton cyclotron for the modest current of 0.1 μA external beam we have a choice between a sector-focused and a synchro-cyclotron. Some may like the synchro-cyclotron for its simplicity of magnetic field design and loose tolerance on dee voltage regulation. We prefer the sector-focused design because there is no rotating capacitor and high currents of 100 μA are easily available for optional isotope production. The magnetic field design is similar to many such cyclotrons and the magnetic field, frequency and dee voltage stabilization are routine engineering design jobs now.

A new design option has arisen in the past several years: normal conducting vs superconducting main coil. Although the superconducting design has a pole diameter about 40% that of the normal design, the higher cost of the superconducting technology makes the overall costs about the same, for this size. At larger K values the superconducing design becomes cheaper than the normal one. Because some development still is necessary for the superconducting design such as deflection, and because a medical environment requires high reliability and proven design, we decided on a normal coil magnet.

Another design choice is that of the dee configuration. The dee or dees can extend over both hill and valleys, as in most of the sector cyclotrons. Or two dees can lie in two opposite valleys of a 4-sector magnet as in the UCLA design. In the first case (dee-over-hill) the magnet gap is determined by the dee-ground clearance over the hills. In the second case (dee-in-valley) it is determined by the dee-ground clearance in the valleys, and the magnet gap can be considerably smaller. In comparison of these two options it was found that if other factors are left constant (such as average field, current density, dee-ground clearance, etc.) the dee-in-valley design requires only 60% of the copper, 60% of the magnet power, and 80% of the steel, compared to the dee-over-hill design.[1] So the dee-in-valley design was chosen for this study.

The parameters chosen are shown in Table 1.

Table 1. Specifications.

Proton Energy	150	MeV
Beam Current (External)	0.10	μA
Beam Current (Internal,max.)	100.0	μA
Average Field	2.0	T
Hill Field	2.4	T
Valley Field	1.6	T
Field in Return Path	1.7	T
Hill Gap	5	cm
Valley Gap	12	cm
Orbit Radius at Output Energy	91	cm
Pole Diameter	198	cm
Weight of Steel	1.44×10^5	kg
Weight of Copper in Main Coils	2.6×10^3	kg
Main Coil Power	120	kw
Trim Coil Power	20	kw
No. of Dees	2	
Dee-to-Ground Clearance	2.5	cm
Design Dee Voltage	60	kv
RF Power	70	kw
RF Frequency	30	MHz

The high field level of 2.0 T average is based on similar values used at UCLA. For a fixed energy design such as this the steel can be run into saturation in the gap region, but 1.7 T is used in the return yoke to conserve coil power. These values were not optimized. The small average gap allows

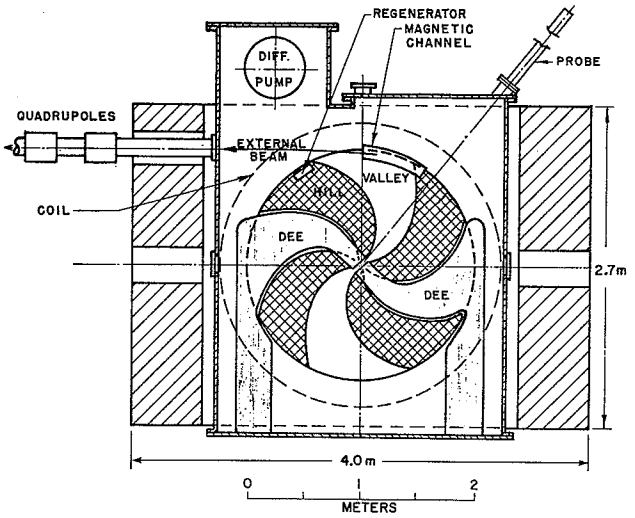

Fig. 1. Plan view of magnet and rf system at median plane. (XBL 757-3580)

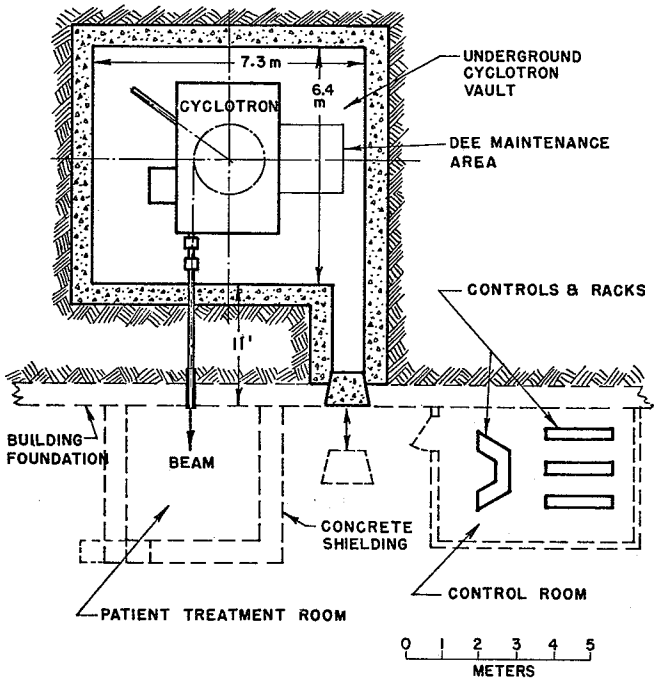

Fig. 2. Plan view of vault, control room, and one treatment room. (XBL 757-3576)

the outer orbit to come close to the pole edge for easier extraction, and also requires only a small main coil power. The dee voltage of 60 kV across a 2.5 cm gap is consistent with previous cyclotron experience.

The layout of the magnet and dees is shown in Fig. 1. The side return legs of the magnet are quite close to the dee tank and are wider than the pole diameter to reduce cost at the expense of accessibility. The larger size makes the 1/4 wave dee stems end at the tank wall, giving a unit structure which can be rolled away from the magnet for maintenance. The ion source is inserted axially through the pole and is not shown in this figure. Alternatively it could come in radially on the deflector side, if space above the roof were not available. One probe for beam measurements is shown. This could be specially cooled for isotope production. Modern computer programs are so accurate that a centered orbit geometry can be designed in advance, so other probes should not be necessary. Extraction is shown using a regenerator.

Dee support structure is simplified and rf power minimized by using separate grounded dee stems. The total rf power to dees, stems and liners is 70 kW at 60 kV dee voltage, 30 MHz. This requirement is well within ratings of a single forced-air cooled power tube (4CX35000).

No detailed beam dynamics calculations have been done on this design. The inner section out to 50 MeV is very similar to the UCLA cyclotron as far as center region, magnetic field level and flutter, and dee system are concerned. The spiral angle necessary to obtain vertical focusing out to 150 MeV was calculated using the approximate formula: $\nu_z^2 = 1 - \gamma^2 + F(1+2\tan^2\alpha)$, where ν_z^2 is the square of the vertical frequency, $\gamma = m/m_0$, F is the magnetic field flutter and α is the spiral angle (angle between hill edge and a radial line).

The layout of the cyclotron in a vault is shown in Fig. 2. This is a minimum cost configuration, using earth shielding around concrete walls. Space is provided in the vault to remove the rf system for maintenance. One or more patient treatment rooms can be provided in the building. It is assumed that space for the vault is available at ground level next to the building where treatments take place. This makes installation inexpensive. Also any serious repair on the cyclotron which requires taking apart the magnet can be done easily by removing the roof blocks with a commercial crane.

Footnote and Reference

*Condensed from LBL-4085.

1. R. Burleigh, LBL Engineering Note M4582, Feb. 1973.

HEAVY-ION BOOSTER CYCLOTRON DESIGN STUDIES AT BERKELEY*

R. J. Burleigh, D. J. Clark, and L. R. Glasgow

Design studies on four booster cyclotrons for heavy ions are described. Comparisons are made of normal vs superconducting main coils, and K = 400 and 800 sizes. Performance and cost estimates are given.

The present heavy ion accelerators at LBL are the SuperHILAC, the Bevatron and the 88-inch cyclotron. In Fig. 1 the solid lines show the performance of these existing accelerators when developed to their full potential. The regions inaccessible to our present machines are the energy region above the 88-inch cyclotron and the SuperHILAC but below the Bevalac, and the heavier mass region at Bevalac energies. We explore some of the options for using single pole cyclotrons as boosters (post accelerators) for the SuperHILAC and the 88-inch cyclotron. The cyclotron has the desirable characteristic of 100% macroscopic duty factor. Since this cyclotron study was done it was decided that the highest priority for a proposal at LBL for heavy ion beam expansion is in the extension of the Bevalac to heavier ions and lower energies ("Improved Bevalac," Fig. 1) and increasing the SuperHILAC intensity for heavier masses.

There are several types of sector-focused cyclotron designs which can be used. These are illustrated schematically in Fig. 2. The four cases show relative sizes of cyclotrons with either a single pole or separate sectors, and with either normal conducting or superconducting coils. These cases all have the same K or maximum bending strength. The pole diameter is about twice as large for the separate sector as for the corresponding single pole design, because of the smaller average field around the orbit. The pole diameter is about 3 times as large for the normal conducting as for the corresponding superconducting machine, since the field is 3 times lower. The peak field for the normal conducting cases is 1.7 T. The field in the return yoke is 1.7 T for all cases. The beam injection and extraction would be easier in the separate sector Cases 1 and 3, but they are more expensive than Cases 2 and 4. Injection would be by a stripping foil to get the beam across the magnetic field in Cases 2 and 4.

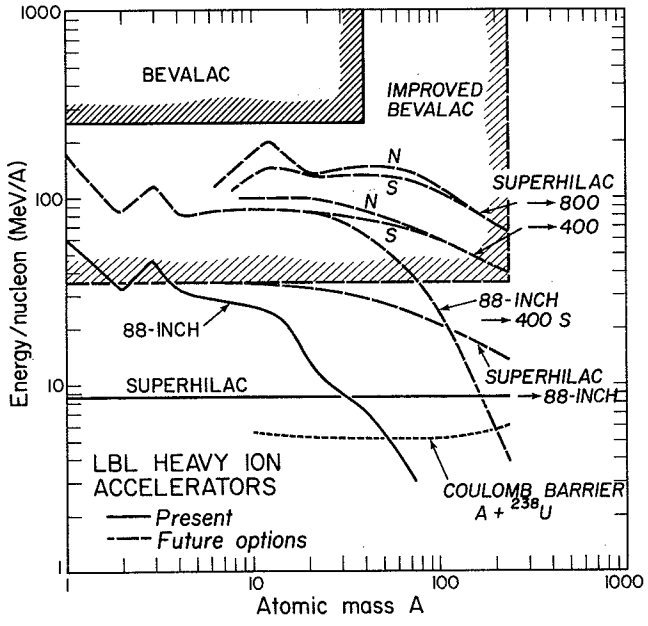

Fig. 1. Performance predictions for present and possible future LBL heavy-ion accelerators. (XBL 757-3584)

For this study Cases 2 and 4 were chosen because of their lower cost compared to Cases 1 and 3. Case 4 is interesting because of its small size and resultant low cost. The extraction is a special challenge because of the 5.0 T field level in the pole. The sizes chosen are K = 400 and K = 800 for each case, where K is the energy constant in the

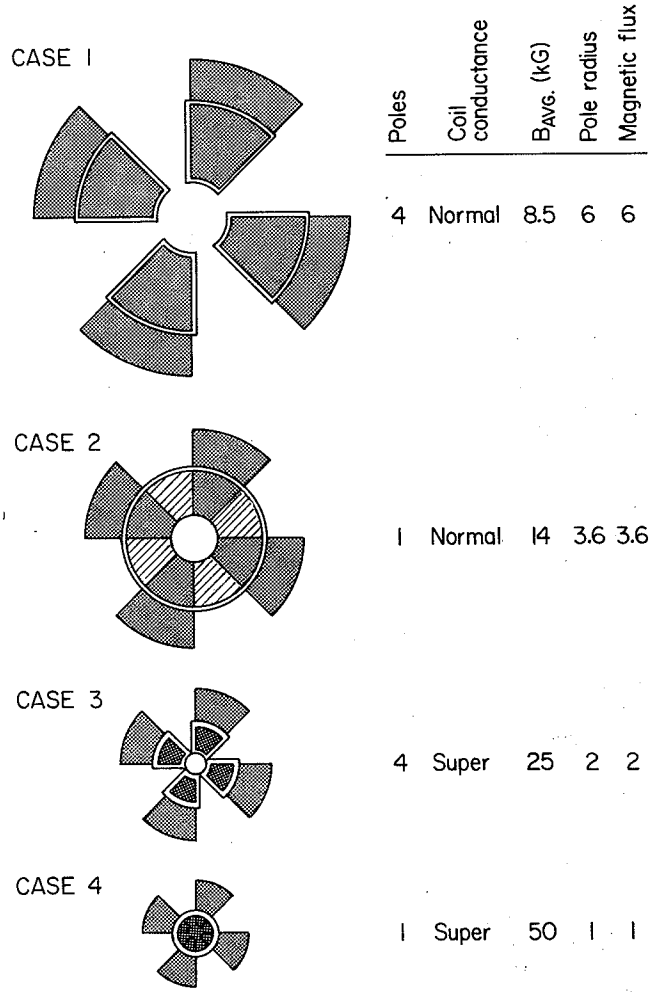

Fig. 2. Four cyclotron structures with the same K value or bending strength. (XBL 757-3586)

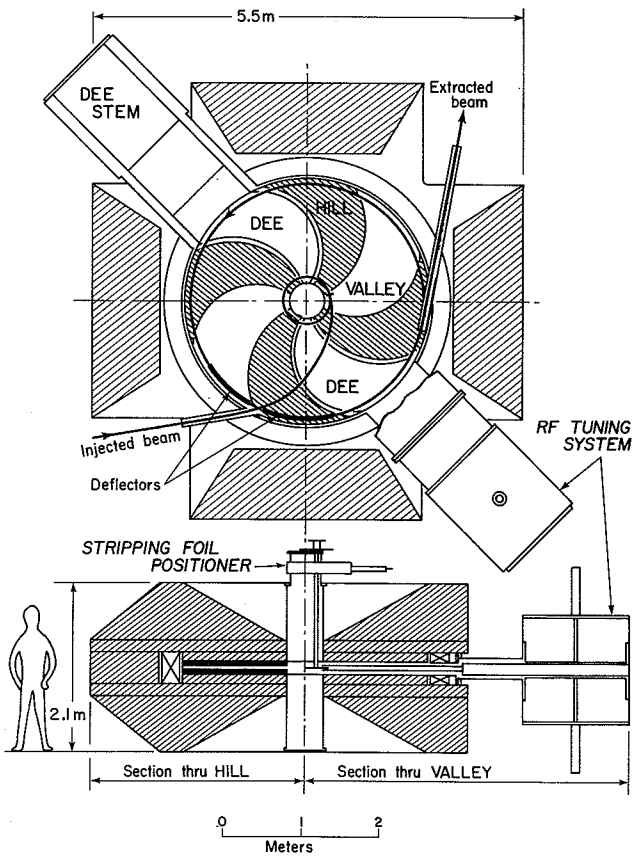

400 N CYCLOTRON

Fig. 3. The 400 N booster cyclotron. (XBL 757-3590)

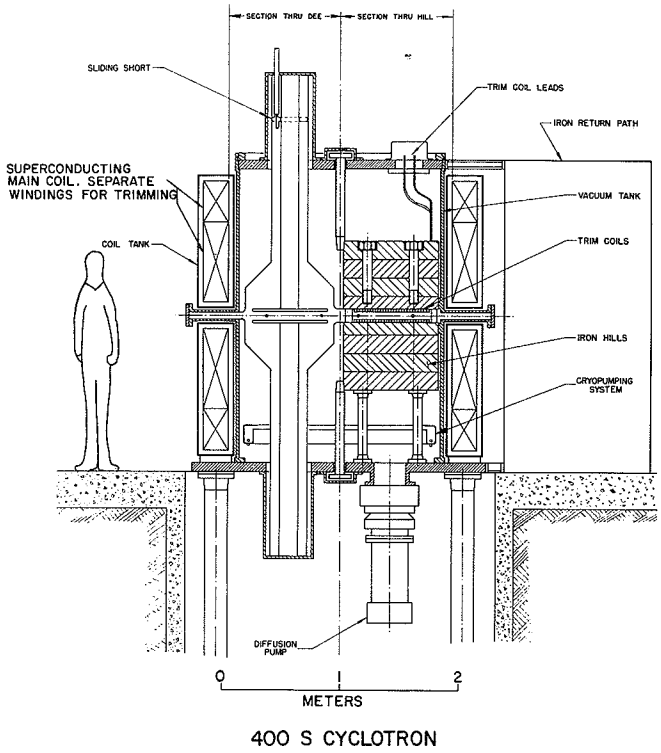

400 S CYCLOTRON

Fig. 4. Elevation view of the 400 S cyclotron. (XBL 757-3589)

equation $E = KQ^2/A$ where E is maximum energy, Q and A are particle charge and mass in proton units. In the following sections the letters S and N follow the K to denote superconducting or normal conducting main coils.

A schematic design for a 400 N booster cyclotron is shown in Fig. 3. Four magnet return legs are used to reduce the amount of steel. A high average field of 2.0 T is used to minimize the size and cost.

The rf system has 2 dees in the valleys to minimize magnetic gap. The hill gap is 5 cm—large enough to withdraw the dee system without raising the upper magnet yoke. Harmonics are 2-4 which give high energy gain/turn with 45 degree wide dees. The energy range is then covered with an rf frequency range of 2 to 1.

The coils are tape wound with slots for the dees and injection and extraction channels. This construction gives good magnetic field out to large radius, and fast fall-off for easier extraction. A lifting system for the upper yoke would be used for installation and maintenance of the deflection system.

A schematic elevation view of a 400 S cyclotron is shown in Fig. 4. The superconducting coil provides 5.0 T average field in the bore. It has a geometry similar to that of large bubble chamber coils. Argonne National Laboratory, U.S.A. has built a "15 foot" bubble chamber coil[1] with an inside diameter of 14 feet (4.3 m), a central field of 3.0 T and a maximum field at the coil of 5.0 T. The coil in the 400 S cyclotron is 1.9 m inside diameter and has a maximum field at the coil of 5.0 T with some iron just inside the coil for shielding. Thus it is well within current engineering practice. Each coil is shown split into an upper and lower section for trimming the radial field profile.

Flutter in the magnet is provided by saturated steel sectors supported inside the superconducting coil bore. The field in the saturated steel is 2.0 T higher than in the space between sectors. But in a practical geometry the hill-valley difference on the median plane is typically 1.0 T. Calculations of the flutter from several gap configurations were made using the program TRIM.

The dees are supported by dee stems coming in axially in two of the valleys. This is a natural configuration since the valleys are empty and there is little space for the dee stems between the main coils, which need to be close together for a good magnetic profile.

The vacuum system is a cryopump, which is supplied with cold helium gas by a small fraction of the refrigeration used for the main coil. A small diffusion pump or turbo-pump can be used to pump hydrogen and helium.

The estimated performance of each option with injection from either the SuperHILAC or the 88-inch cyclotron is shown in Fig. 1. Since the SuperHILAC

produces higher energies for ions with A > 30, it makes a better injector than the 88-inch. The gain in going from a K of 400 to 800 is not great. The superconducting and normal conducting versions have similar performance. An interesting option is injecting the 88-inch with the SuperHILAC. The machines are assumed not to be limited by extraction.

Table 1. Cost summary. U.S. k$ 12/74

	400 S	400 N	800 S	800 N
Total minimum cost	4,900	10,300	7,800	18,000

Cost estimates for the 4 designs studied are shown in Table 1. They include engineering and construction of the cyclotron, but not shielding, beam transport or building. The costs are based on standard LBL construction account rates. The lowest cost option is the 400 S, and its performance is very good in Fig. 1.

Footnote and Reference

*Condensed from LBL-4086.

1. J. Purcell et al., ANL/HEP 7215, February 1973.

A FAST-CLOSING VACUUM FOR THE 88-INCH CYCLOTRON

R. A. Gough, R. Lam, D. Morris, and C. Martinez

A fast-closing vacuum valve was recently developed to protect the 88-inch cyclotron against contamination during bombardments of highly radioactive targets. Such a "slammer" valve is particularly necessary during bombardments of transuranic targets mounted on the vacuum foil window of a gas jet system.[1] Should the foil break due to mechanical or thermal stresses, the radioactivity could be carried into the acceleration chamber of the cyclotron by a sonic expansion of gas into the cyclotron vacuum. The development of this valve and associated trigger circuity is an outgrowth of earlier work at this laboratory.[2] Commercial explosives in the form of squibs were chosen as a power source for the valve. Among the advantages of using an electro-explosive device are its very high degree of reliability, the reproducibility, uniformity, and magnitude of the force it creates, and its compatibility with fast electronic firing mechanisms.

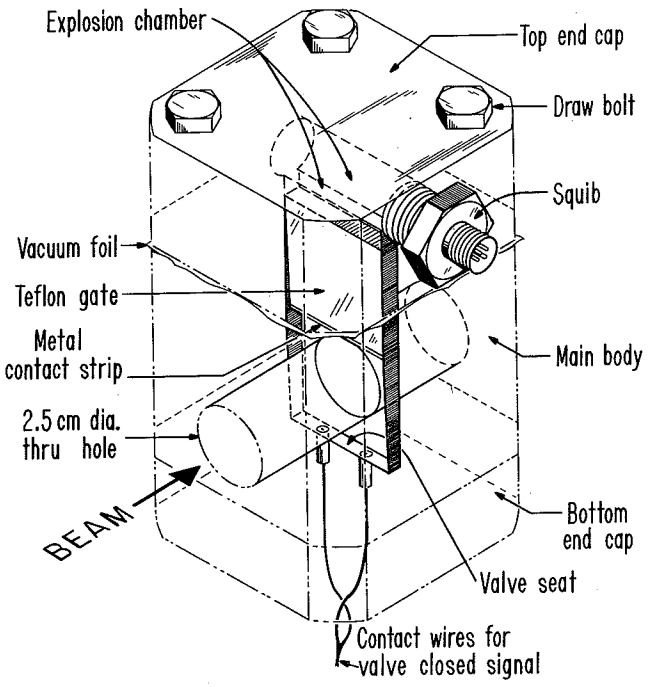

Fig. 1. An isometric view of the slammer valve. (XBL 766-2960)

The valve is pictured in Fig. 1. It has a very light replaceable teflon gate and a case hardened steel body which, unlike mechanical prototypes tested, and has shown no signs of distortion even after many firings. A 2.5 cm diameter hole is provided for passage of the beam. Only 2 msec are required to move the teflon gate from fully open to the fully-closed, vacuum-sealed position. 550 mg of Bullseye pistol powder, chosen for its fast-burning qualities, was found to be an adequate and reliable charge for the squib. A metal contact strip on the bottom surface of the teflon gate provides an electrical indication when the valve is fully closed. To reload the valve after each firing it is necessary to remove and replace the squib, the teflon gate and a vacuum foil, all of which takes about 10 min.

Some experimentation was necessary to determine the optimum compression of the teflon by the groove in which it travels. A 3° standard Morse taper was cut on both the teflon gate and the groove. When the valve is fired and the gate moves across the hole toward the valve seat, the leading edge of the teflon makes a vacuum seal ~5mm before reaching the end of its travel. During the last 5 mm of travel the wedging action serves to decelerate the gate. About 5% compression on the teflon is sufficient for a good seal. One gate having ~10% compression failed to close fully with the same 550 mg charge. Too little compression could result in a poor vacuum seal or in the gate bouncing from the valve seat and settling in a partially open position.

There are two independent channels from which the trigger signal can be derived (see Fig. 2). Each channel can accommodate up to 8 inputs from some appropirate sensor such as an ion gauge or vacuum analyzer. At present, two ion gauges (one for each channel) are used to monitor the beam line pressure near the entrance to the target chamber. A Granville-

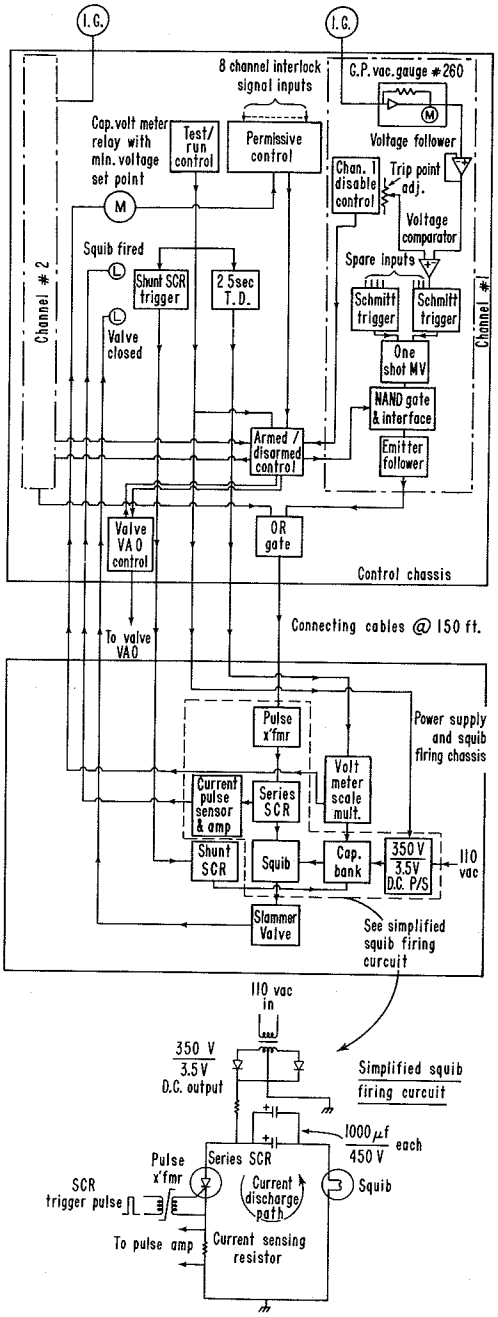

Fig. 2. An electrical schematic of the triggering and firing circuitry. (XBL 766-2959)

Phillips (G.P.) power supply (series 260) is used because its output is compatible with the TTL (transistor transistor logic) input requirements. However, a voltage follower has been added to the output of the electrometer amplifier for better isolation and impedance matching. The output of the voltage follower, which has the same voltage level as the meter reading on the G.P. unit, is compared with an adustable voltage derived from a 10-turn helipot whose output voltage is such that the dial reading of the helipot is the same as the meter reading of the G.P. power supply. This correspondence simplifies the setting of the trip-point of each channel. The comparator output is fed into a Schmitt trigger and a one shot multivibrator to produce a fast rising trigger pulse with a minimum width of 5 msec. The trigger pulse is then fed into a NAND gate, used for arming or disarming each channel, followed by an OR circuit which permits either channel to independently trigger the gate of the SCR. The response time of the trigger circuit to a sudden pressure rise is ~1 ms and is completely dominated by the response time of the ion gauge.

The squib is fired by a simple capacitive discharge from a 2000 μF/450 V capacitor bank in series with an SCR which acts an an electronic switch. The capacitor bank is charged to (and maintained at) 350 V by a high voltage dc power supply while the SCR is biased off. When the trigger pulse turns on the SCR as described above, the energy stored by the capacitor (~ 100 joules) is discharged through the fuses of the squib, and the heat thus generated ignites the gunpowder. A current pulse of 140 A peak (exponentially decaying to 50A in 4 msec) causes the gunpowder to be completely burned in less than 0.1 msec.

The electrical continuity of the firing circuit and of the squib can be readily verified by lowering the capacitor voltage to 3.5 V and discharging the capacitor into the squib. The current pulse through the squib is then sufficiently reduced that it will not cause the squib to fire. A return signal from the current sampling resistor (see Fig. 2) serves to confirm the circuit continuity. If the trigger signal is initiated from an ion gauge, the entire trigger and firing chain can be simultaneously tested. This can be done by turning on the "degas" switch on the G.P. power supplies thereby checking each channel independently.

A control unit for the slammer valve system has been built and installed in the cyclotron control room but, in order to minimize the attenuation of the current pulse, the capacitor bank is located near the squib. The valve itself is located where the beam is well focused in a beam line leading to the high level cave area (see Fig. 3) some 9 m upstream of the target chamber. Both air driven vacuum valves-designated in Fig. 3 as VA0 and V_{Exit} would normally close automatically if the beam line pressure exceeds 50 μ but have a relatively slow closing time ~1 sec. When the slammer system fires, both these valves will also close for added protection in case the slammer fails to completely seal. An interlock feature prevents opening valve VA0 until the slammer is armed and similarly prevents disarming the slammer until the valve VA0 is closed again. The system cannot be armed if the firing capacitors lose voltage or if either ion gauge filament is not drawing current. Located on the control unit are a series of diagnostic lights which indicate if the SCR gate has been opened, if the squib has fired, and if the gate is fully closed. They also indicate which channel(s) caused the valve to be fired.

A simple simulator has been built to substitute for the electrical interaction with valve VA0 and V_{Exit}. It is also possible to substitute a simple fuse for the squib. This simulation has proven very useful for debugging and operator training. In this way, for example, the trigger circuit was desensitized to random electrical noise, a problem

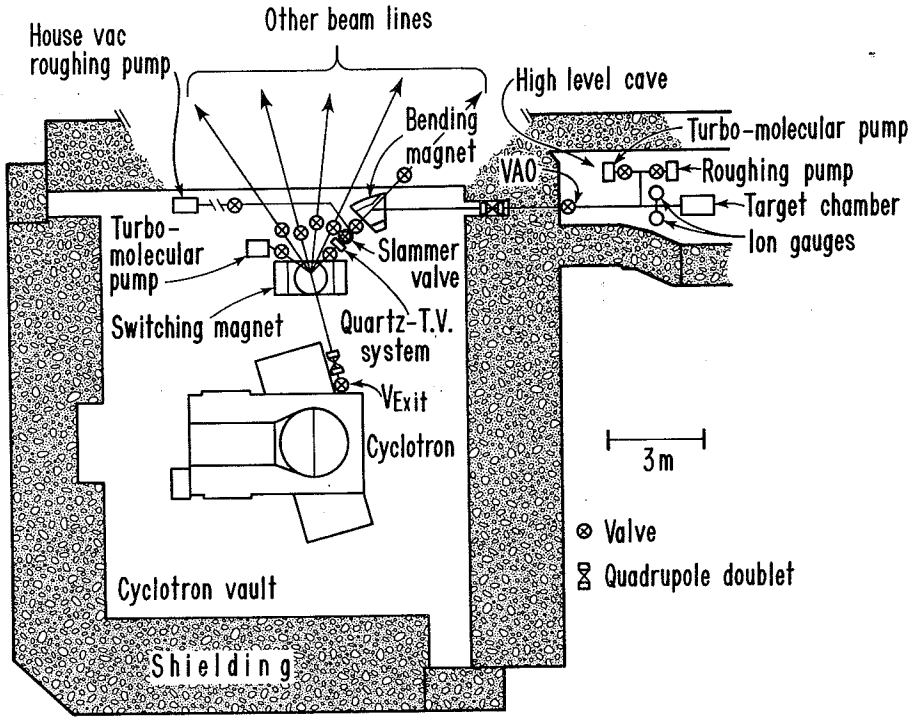

Fig. 3. A schematic layout of the slammer valve beam line.
(XBL 766-2958)

which caused several misfirings in the early stages of development. The slammer has now been successfully operated for ~2 months on the simulator and longer than 100 hours of real time operation without incident.

Reference

1. A. Ghiorso et al., Phys. Rev. Lett. 33, 1490 (1974).

2. R. Aune et al., Second International Conference on Accelerator Dosimetry and Experience, Stanford, California, 886 (Nov. 5-7 (1969).

HEAVY ION SOURCE DEVELOPMENT

David J. Clark

The objective of this project is to improve the performance of the ion sources used on the LBL heavy ion accelerators: the SuperHILAC, the Bevatron, and the 88-inch cyclotron. The common goals required by all the accelerators are to produce beams of new ions, or beams of higher intensity and better quality, and sources with longer lifetime and better reliability. The achievement of these goals opens up new fields of research in nuclear science and medicine, and makes more of the scheduled time available for research.

In 1975 the small groups working at each accelerator on ion source development were consolidated into one central group. This has greatly improved communication between groups. The moving of the scattered test stand work into a central building is now in progress. All accelerators use the same type of source: the Penning Ion Gauge or "PIG" source, which has proven over the years to produce the highest intensities of high charge state heavy ions. The configurations vary for the different accelerators, but the sharing of experience and useful techniques is proving of great value.

Development work is done both at test stands and at the accelerators. It is important to have some people working on the same source at both the test stand and the accelerator so that improvements developed at the test stand can be applied quickly at the accelerator, and problems arising at the accelerator can be solved on the test stand to save valuable accelerator time. For this reason a strong effort is being made to duplicate the accelerator conditions as closely as possible at the test stand.

The SuperHILAC compact Adam ion source (2.5 MV) for the heaviest ions was developed for produc-

tion of new solid material beams of iron, calcium and gold. A special source insert for calcium (Ca^{3+}) will make possible the recovery of most of the calcium when running beams of the very expensive isotope ^{48}Ca.[1] The output of gold ions Au^{10+} and Au^{11+} on the test stand was increased by a factor of 3 by splitting the sputter electrode into 2 rings. Calcium and iron were accelerated through the SuperHILAC to full energy. Studies are underway to improve the Adam source by lengthening the arc chamber.

The SuperHILAC Eve source (750 kV) produces ions up to argon for the SuperHILAC and Bevalac. Studies were done on using a duoplasmatron for high currents of Ne^{3+}.[2] They demonstrated a serious space charge blow-up when analyzing beams of 20 mA at low energy. Plans are underway to study acceleration of the beam to 750 kV in a spare injector before analyzing, and to use the promising new geometry of Darmstadt in the source.

The PIG source used at the Bevatron has improved transmission resulting from improved vacuum pumping and gas pulsing. Beam intensities of carbon and oxygen have doubled.

The hot cathode PIG source used by the 88-inch cyclotron was developed both on a test stand[3] and on the cyclotron. The emphasis is on new higher charge states, since the cyclotron energy is proportional to charge squared. New beams accelerated include Ar^{9+}, Ar^{10+}, and Ne^{7+}. Careful emittance measurements have been made on the test stand source showing emittance to be nearly independent of charge state, but dependent on arc density.[4] A new type of cathode mounting is working well on the test stand and will be tried soon on the cyclotron.

The automatic emittance measuring system became fully operational on the test stand, and is being used to study dependence of source emittance on various operating parameters. It is important that the emittance area of any source be small enough to be accepted by the accelerator.

The second International Conference on Heavy Ion Sources was held in Gatlinburg, Tennessee, October 27-30, 1975. This provided an excellent opportunity to discuss recent developments with delegates from most of the heavy ion source groups in the world.

Under construction this year are two new test stand facilities in the central ion source building. One is an exact duplicate of the Adam accelerator source system. This will make possible the testing and debugging of sources for the accelerator off-line, saving valuable accelerator time. Also improvements in structure and power supplies can be tested before installation at the accelerator. The other new facility is a 180 degree PIG source test magnet with a new pulsed arc supply. Here all the LBL PIG sources can be tested, compared, and developed. Also prototype sources incorporating all the best features of the existing sources will be tested. These will be used at the existing accelerators and in the proposed 3rd injector for the SuperHILAC. Also in the design stage is an improved Adam source which will have large cathode-cathode spacing, fil-

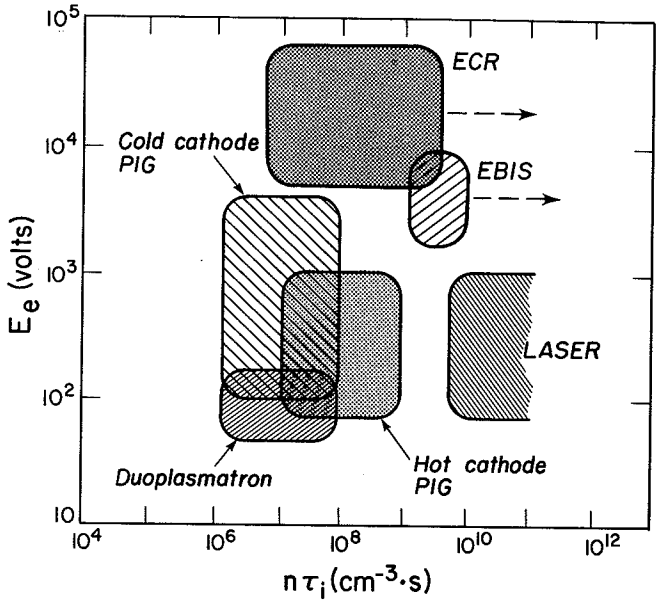

Fig. 1. Plasma parameters of positive ion sources. E_e is electron temperature, n is electron density. τ_i is ion confinement time. (XBL 7512-9583)

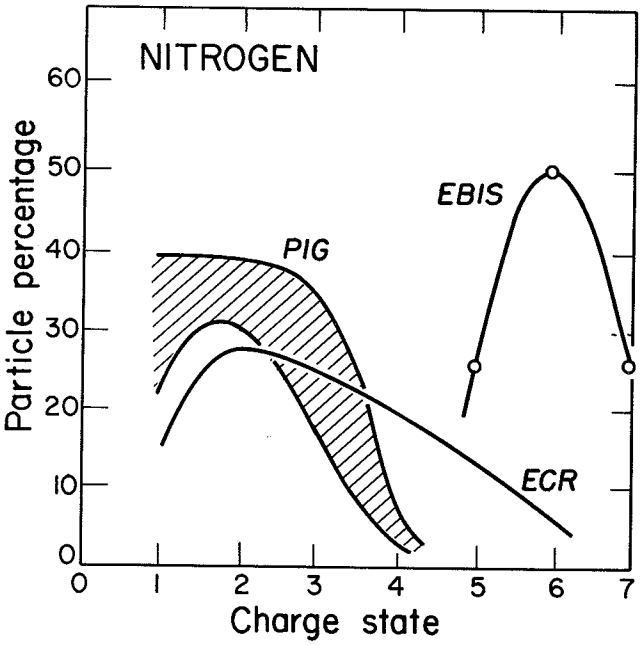

Fig. 2. Charge state distributions of three types of positive ion sources (XBL 7512-9582)

ament heating of one cathode, and a mirror magnetic field. Evaluation is being completed on new concepts in heavy ion sources so that a choice can be made on which type of advanced source development to implement. Comparisons of some advanced sources are given in Figs. 1 and 2 (Ref. 5).

The heavy-ion source group has members from the accelerators, who are listed as authors in the reports below. Another member is D. Spence.

References

1. Basil Gavin, Anode Sputtering Characteristics of the Berkeley 2.5 MV Source, Proc. Int. Conf. on Heavy Ion Sources, Gatlinburg, Tennessee, October 27-30, 1975, IEEE Trans. Nucl. Sci. NS-23, 2 (1976).

2. R. M. Richter and E. Zajec, Heavy Ion Source Development at the Bevatron, Proc. Int. Conf. on Heavy Ion Sources, Gatlinburg, Tennessee, October 27-30, 1975, IEEE Trans. Nucl. Sci. NS-23, 2 (1976).

3. L. Bex, D. J. Clark, C. E. Ellsworth, W. S. Flood, R. A. Gough, W. R. Holley, J. R. Meriwether, and D. Morris, High Charge State Heavy Ion Production from a PIG Source, Proceedings of the Particle Accelerator Conference, Washington, D.C., March 12-14, 1975, IEEE Trans. Nucl. Sci. NS-22, 3 (1975).

4. L. Bex, D. J. Clark, C. E. Ellsworth, R. A. Estrella, R. A. Gough, and W. R. Holley, Emittance Measurements of High Charge State Argon Beams from a PIG Source, Proc. Int. Conf. on Heavy Ion Sources, Gatlinburg, Tennessee, October 27-30, 1975, IEEE Trans. Nucl. Sci. NS-23, 2 (1976).

5. D. J. Clark, Conference Summary, Proc. Int. Conf. on Heavy Ion Sources, Gatlinburg, Tennessee, October 27-30, 1975, IEEE Trans. Nucl. Sci. NS-23, 2 (1976).

SUPERHILAC - 1975

The year was an eventful one for the SuperHILAC. An extensive effort to increase the reliability and voltage holding capabilities of Adam, the 2.5 MV injector, was completed in December 1974, and Adam was used to deliver krypton beams successfully in January. Also in January, the first ModComp computers were delivered, the first (visible) indication at the SuperHILAC of the computer control hardware destined to play such a prominent part in machine operation in the coming months.

A new "puffer" valve system was installed on the Adam ion source early in February, with the object of more easily attaining the very low gas flow rates needed for running heavy ions. This was very successful. In February modifications were begun to make the SuperHILAC ready for computer control and timeshare operation. Computer interface hardware was installed for control and monitoring of rf gradient and phase in the eight accelerating tanks and for the pulsed magnets. The control room changes needed were so extensive that a decision was made not to attempt a complete conversion at this time, but to modify the existing control room, primarily an enlargement, so as to permit two control stations to be manned, while postponing the major rebuilding until later.

The machine was turned on, primarily for test purposes, for three weeks in April. Two beams were accelerated together for the first time. After this, the shutdown work was completed, and late in May the accelerator was ready for delivering beam to experimenters. The remaining six months of the year the accelerator ran for experiments. From the start, it was clear that the time-sharing operation was much more difficult than any previous operations of the SuperHILAC. The operators had to keep abreast of many more parameters than before, and tuning was much sharper, with less room for error. For these reasons beam intensity was frequently low for some beams in the first week of operation; however, by September it had been demonstrated conclusively that beams of krypton and neon, both of adequate intensity, could be time-shared together.

Operations for 1975 are summarized in Figs. 1-4. The number of actual research hours devoted to the ion species studied (Fig. 1) shows a general

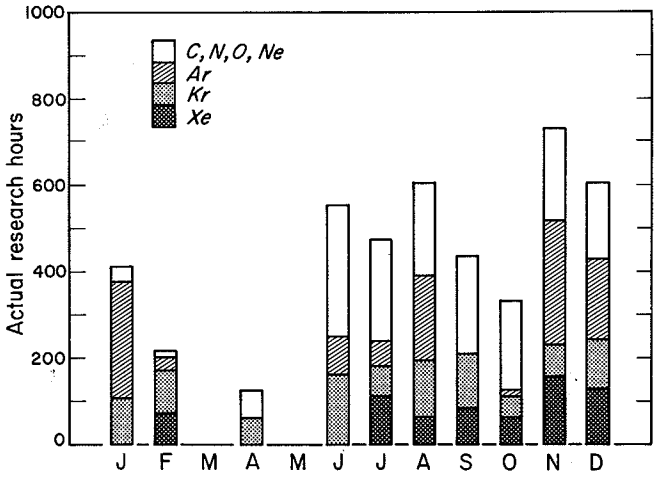

Fig. 1. Ions used for research at the SuperHILAC in 1975. (XBL 761-2091)

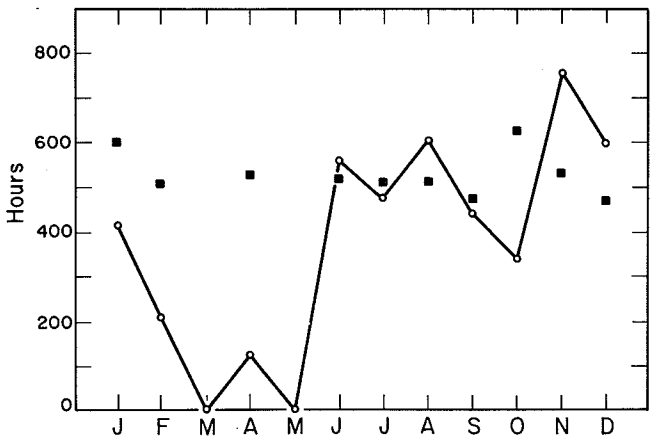

Fig. 2. Monthly accounting of research hours in 1975. Open circles are total actual research hours; closed squares are total scheduled crew time. March, part of April, and May were shutdown months. (XBL 761-2092)

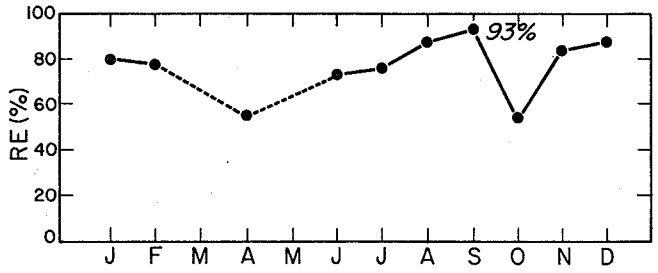

Fig. 3. The research efficiency (RE) of the SuperHILAC in 1975, expressed as the ratio of actual research hours to scheduled research hours. (XBL-761-2093)

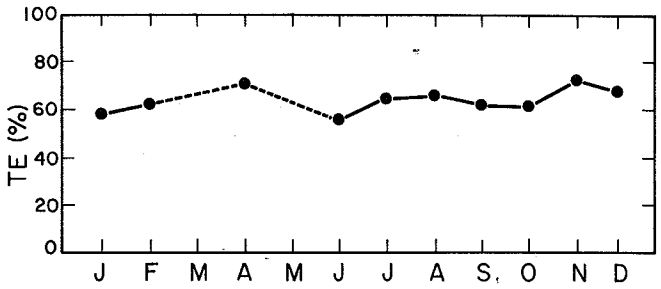

Fig. 4. The proportion of research hours in 1975 in which the beam was actually on target—known as the Target Efficiency (TE). (XBL 761-2094)

increase during the year. In Fig. 2 both actual research hours and scheduled crew time are presented for comparison. The crew time includes all of the time that the machine is available for use and includes scheduled maintenance.

The month of January thus represents "best" operation before the introduction of timeshare. Beam was delivered to experimenters for 70% of the available machine time, which is good "innage" time for a research machine such as the SuperHILAC, considering the necessity for source changes and the setups required for new ion species, etc. In contrast, in June, the first month with full time-share operation, the number of research hours exceeded the available machine time. This is simply a result of the multiplicity of beams available with timeshare, permitting two experiments to be done simultaenously.

The ratio of actual research hours to scheduled research hours (Fig. 3) is here called research efficiency. If there were no breakdowns, unscheduled maintenance, or source changes, this ratio would be 100%. Most months it ranged between 70 and 90%, with two unusually poor months below 60%.

Some of the research hours are spent in setup including such processes as getting equipment ready, switching monitoring from one beam line to another, and tuning. Thus the proportion of research hours in which the beam is on target, called here the target efficiency, is of interest as a useful indication of accelerator performance. It can be seen in Fig. 4 thatmonth by month, during the year, this target efficiency remained relatively constant within the range of 60-70%.

SuperHILAC Operations Summary for December

Scehduled time	Hours	Percent of crew time
Research hours, 686		
Machine studies, 26		
Machine operation for research	385	78.6
Machine studies and tuning	66	13.5
Maintenance	39	7.9
Total scheduled crew time	490	100%
Actual time		
Setup	54.75	11.2
Tune-up	132.5	27.0
Target time	417.25	85.2
Total actual research	604.50	123.4%
Parasitic time, 64.50		
Machine tune	27.25	5.6
Machine studies	7.50	1.5
Maintenance	190.25	38.8
Total support time	225.00	45.9%

B. NUCLEAR INSTRUMENTATION

A LARGE SOLID ANGLE ^{8}Be IDENTIFIER*

G. J. Wozniak, N. A. Jelly,† D. P. Stahel, and Joseph Cerny

A counter-telescope system with a large effective solid angle (~1 msr) for detecting ^{8}Be events and incorporating kinematic compensation[1] is described below. A position-sensitive E detector is used to measure both the energy and the direction of the ^{8}Be events. Thus the detection efficiency and the energy resolution can be optimized concurrently with minimal restrictions on the ^{8}Be acceptance angle.

The distribution of the breakup α particles is sharply peaked at the surface of the breakup cone (apex angle ~6°); thus, in order to detect a substantial fraction of the ^{8}Be events, a detector should subtend an angle larger than the opening angle of the cone. For a large angular acceptance (10°), a considerable variation in the detection angle (θ_{lab}) of the ^{8}Be events is possible. On light targets ($A \leq 16$), a typical value of $dE/d\theta$ near 25° (lab) for the (α, ^{8}Be) reaction at $E_\alpha = 65$ MeV is around 500 keV/deg. By measuring the direction of a ^{8}Be event and kinematically correcting its energy, the energy resolution can be greatly improved.

A particle striking a position-sensitive detector generates both an energy signal E, and a signal XE proportional to the product of its energy E and its distance of impact X from one side of the detector (see Fig. 1). For high energy ^{8}Be events, the breakup Q-value is small compared to the ^{8}Be energy, and so the two α particles have, to a good approximation, equal energies. Since both α particles arrive within a fraction of a nanosecond of one another, the individual E and XE signals are automatically summed in the detector and the resultant E signal gives the energy of the ^{8}Be event. The position signal X obtained by dividing out the energy dependence is given by:

$$X = (X_1E/2 + X_2E/2)/(E/2 + E/2) = (X_1 + X_2)/2.$$

In addition to having equal energies, the two α particles are detected at approximately equal distances from the axis of the ^{8}Be breakup cone, which corresponds to the direction of the original ^{8}Be event as shown in Fig. 1. This average position X establishes the direction of the ^{8}Be event and can be used to kinematically correct the ^{8}Be event's energy.

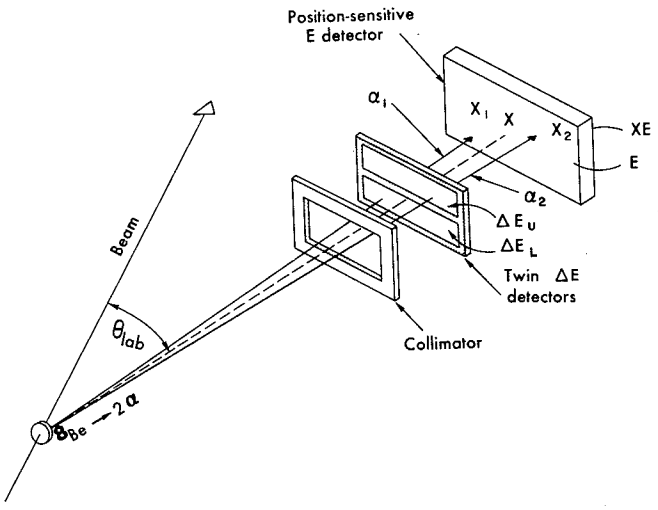

Fig. 1. A. schematic diagram of the ^{8}Be identifier showing the twin transmission detectors, the PSD, the trajectories of the breakup α-particles (solid lines), and the measured direction X of the ^{8}Be event. (XBL 7511-8675)

While good efficiency and energy resolution can be obtained with a PSD alone, numerous particle-stable nuclei would also be detected and obscure ^{8}Be events except when they happened to be more energetic. To select only ^{8}Be events, a twin transmission detector is placed in front of the PSD as shown in Fig. 1. This detector consists of a single silicon wafer with two ΔE counters diffused side by side. Because the two breakup α particles have approximately the same velocity, their time-of-flight difference (ΔTOF) to the upper and lower ΔE detectors is approximately zero. The full width at the base of the peak in Fig. 2a (2 ΔTOF = 0.85 ns) illustrates the similiar flight times of the two α particles and the central dip is the effect of collimation on their velocity distribution. By performing a subnanosecond coincidence between the upper and lower halves of the twin ΔE detectors, ^{8}Be events can be selectively observed and the intra-beam-burst chance background reduced by a factor of ten. Some further reduction in background and additional selection of ^{8}Be events is obtained by performing particle identification with the summed ΔE and E signals as shown in Fig. 2b (^{8}Be identifies as if it were a ^{7}Li event).[2]

Since commercially available PSD's give position information along their longest dimension, the largest effective solid angle and kinematic compensation are obtained by orienting the twin transmission detector as shown in Fig. 1. In this configuration ^{8}Be events can be detected over an angular spread of several degrees with an almost constant detection efficiency. Characteristics of this particular geometry (V) and the other geometries (I-IV) previously employed are given in Fig. 3 and Table 1.

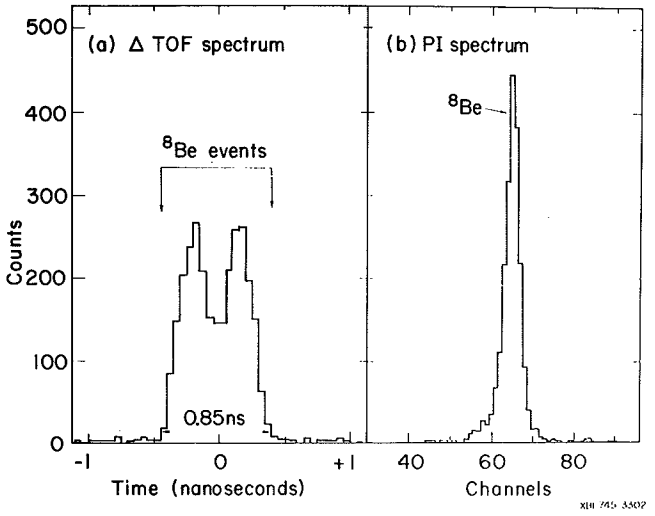

Fig. 2. (a) Differential time of flight ΔTOF, (b) particle identification PI spectra obtained with the ^{8}Be identifier. (XBL 745-3302)

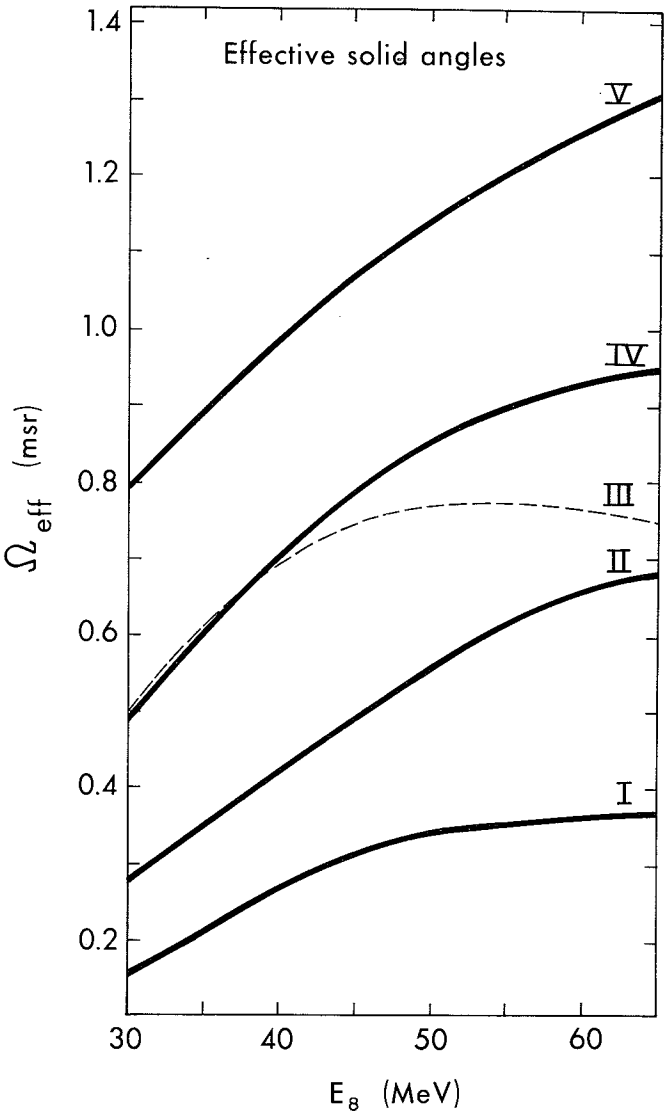

Fig. 3. The effective solid angles Ω_{eff} (I→V) which were used to study solid targets (solid lines) and gas targets (dashed line). See Table 1 for a description of the geometries of these identifiers. (XBL 7511-8673)

Table 1. ^{8}Be Identifier geometries.

Experiment	Target to PSD distance (cm)	Collimator[a]	Diameter[a] (cm)	Width[a] (cm)	Height[a] (cm)	Post or[b] gap-width (cm)	Position[c] gate-width (cm)	Acceptance angle (^{8}Be) (deg)
I	8.00	circular	0.83	-	-	0.28 (V)	0.12	0.9
II	13.00	rectangular	-	1.12	1.25	0.30 (V)	0.25	1.1
III	7.45	gas[d]	-	0.78	0.81	0.24 (V)	0.26	2.0
IV	13.35	rectangular	-	1.51	0.98	0.19 (V)	0.53	2.3
V	13.05	rectangular	-	2.00	0.99	0.09 (H)	1.07	4.7

[a] Projected dimensions of the collimator on the PSD.

[b] Projected dimension on the PSD of the divided collimator post-width or the gap-width of the undepleted region between the twin transmission detectors. The letters V or H indicate whether the gap was vertical (V) or horizontal (H).

[c] If more than one position gate was set, only the summed width is given.

[d] The distances from the target to the gas collimator (L_1) and from this collimator to the second one (L_2) were 3.60 cm and 3.85 cm, respectively. Only the dimensions of the second collimator are listed above. The dimensions of the width, height, and post of the front gas collimator were 0.38 cm, 0.38 cm, and 0.12 cm, respectively.

Shown in Fig. 3 are the effective solid angles Ω_{eff} for these geometries as a function of the ^{8}Be energy; Table 1 gives the geometric parameters employed. The effective solid angle decreases at lower energies due to the increasing size of the breakup cone ($\Omega_{eff} = \varepsilon\Omega_{acc}$ where Ω_{acc} is the acceptance solid angle and ε is the detection efficiency). By employing a 1 X 2 cm PSD, >1 msr effective solid angles (geometry V) have been obtained for detecting ^{8}Be nuclei. Furthermore, high selectivity for ^{8}Be events and kinematic compensation have been incorporated into this detection system which has been successfully used to study the (α,^{8}Be) reaction on 1p and 2s-1d shell targets.

Footnotes and References

*Condensed from LBL-4368, Phys. Rev. C14, 815 (1976).

†Present address: Nuclear Physics Laboratory, University of Oxford, England.

1. G. J. Wozniak, N. A. Jelley, and Joseph Cerny, Nucl. Instrum. Meth. 120, 29 (1974).

2. G. J. Wozniak, N. A. Jelley, and Joseph Cerny, Phys. Rev. Lett. 31, 607 (1973).

COMPLETION OF A RECOIL ATOM MASS ANALYZER (RAMA)

D. M. Moltz, R. A. Gough, M. S. Zisman,
D. J. Vieira, and J. Cerny

Decay studies of neutron-deficient nuclei become increasingly difficult the further one explores from the line of β-stability. Competing reactions create a formidable background interfering with the study of nuclei with low production cross sections and making conventional experimental techniques inadequate. To overcome this obstacle we have coupled the helium jet recoil transport method[1,2] with mass spectrometry techniques. We can now report the completion of a Recoil Atom Mass Analyzer (RAMA) with this on-line mass separation capability.

Figure 1 is an overall schematic of the RAMA system. The operation of the system through the Wien filter has been previously described.[3] In an effort to increase the ion source efficiency, the auxiliary support gas inlet was changed to a point nearer the arc. The total extracted beam remained approximately constant, but a factor of five less arc support gas was needed. Attempts to detect the β-delayed α-emitter ^{20}Na were made difficult by a large sea of electrons and neutrals downstream of the Wien filter. With the addition of the electrostatic quadrupole and dipole magnet, these electrons should no longer be a problem.

Physically the remainder of the system is in place and aligned. At present off-line beam calibrations are beginning (using ions from the RAMA ion source) in order to map out the focal plane of this QSDS system (quadrupole, sextupole, dipole, and sextupole). The two sextupoles are needed to rotate the focal plane perpendicular to the beam axis as well as to reduce second-order aberrations, thereby improving the mass resolution to an expected 1:180 at 50% transmission from the ion source. The focal plane has a mass range of approximately ± 10% from the central mass. To separate the various isotopes

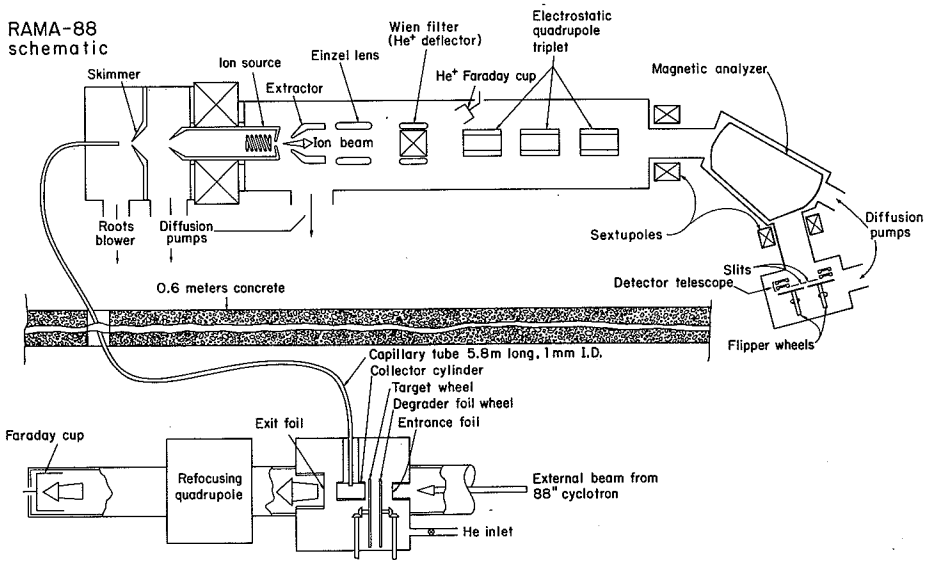

Fig. 1. (XBL 758-3797A)

in the mass region of interest, a pair of symmetrically opening slit systems have been built. The opening width and the position of the slits can be adjusted to within a few mils. Behind each slit is positioned a collector foil attached to a 180° flipper wheel driven by a rotary solenoid. Rotational bounce is greatly damped by means of a magnetic clutch-brake. The flipper wheels remove the activity from the slit area to the side of the detector box for counting, thereby providing a large physical separation of the collected sample. Provisions have been made for solid-state detector telescopes, a plastic scintillation telescope, and gamma-ray detectors for studying the decays of the exotic nuclides under investigation.

References

1. R. G. Sextro, R. A. Gough, and J. Cerny, Phys. Rev. C 8, 258 (1973).

2. Nuclear Chemistry Division Annual Report for 1972, LBL-1666, p. 361.

3. Nuclear Chemistry Division Annual Report for 1973, LBL-2366, p. 443.

A PROPORTIONAL COUNTER TIME-ZERO SYSTEM

G. KeKelis, G. Gabor, D. K. Scott, and C. K. Gelbke

A new system has been developed to perform time-of-flight measurements in the 88-inch cyclotron magnetic spectrometer. With the present time-zero system, which consists of an NE111 foil coupled to two photomultipliers with a lucite light cone, it is not possible to measure cross sections at angles smaller than 10°. This is because taking data at such small angles requires that the beam be stopped in a Faraday cup which is located inside the scattering chamber. Since a photomultiplier time-zero system is sensitive to the gamma radiation and large neutron fluxes produced at the Faraday cup, there is considerable "in" and "between" beam-burst background.

The new time-zero system is a parallel plate proportional counter (see Fig. 1). It consists of three electrodes which are located symmetrically between two gas containment windows. The electrodes are each separated by 1 cm and the central plane, which is used as the anode, is completely shielded from all ground surfaces except for the ground plane electrodes. A propane gas fill is used at 10 Torr with approximately +1000 volts on the anode. Electrodes and gas containment windows are made of aluminized mylar, and the active area is 15 cm^2.

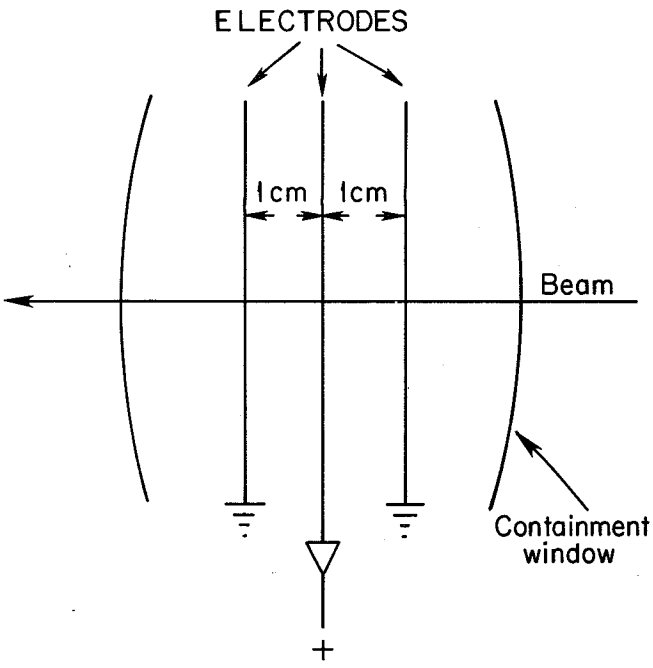

Fig. 1. Schematic of the parallel plate, gas proportional counter. (XBL 766-8312)

The signal resulting from the passage of a charged particle consists of primary ionization which is enhanced about 100 times by electron multiplication. Signal rise times are limited by the electron collection and are typically ~10 nsec. Associated positive ion collection times are 5 to 8 μsec and are the limiting factor when counting at high rates. The fast output of a fast-slow preamp is used for the timing signal.

Using the above detector at the entrance of the magnetic spectrometer time resolution between the gas counter and a large plastic scintillator has been limited to about 2 nsec, although resolution of better than 300 psec has been reported between a very thin gas counter of this type and a solid state counter.[1]

Currently, the above detector is being used to measure (^{4}He,^{8}He) reactions at angles between 4° and 10°. The detector has proven to be relatively insensitive to gamma rays and neutrons, making it ideal for the present application. Detection efficiency is 100% for charged particles which lose at least 5 keV (100 MeV ^{4}He) when counting at less than 1×10^5 Hz. In (^{4}He,^{6}He) experiments efficiencies of at least 70% have been attained at a count rate of 1×10^6 Hz. The ultimate goal of this development program is to produce a time-zero detector which may also be used for heavy-ion measurements.

Reference

1. H. Stelzer, submitted to Nucl. Instrum. Meth., January 1976.

RESPONSE OF PILOT U SCINTILLATOR TO HEAVY IONS*

M. Buenerd, D. L. Hendrie, U. Jahnke,† J. Mahoney,
A. Menchaca-Rocha,‡ C. Olmer, and D. K. Scott

The measurement of the time-of-flight (TOF) and of the specific energy loss (dE/dx) of particles detected and localized in the focal plane of a magnetic spectrometer, permits an identification of Z and A for fully ionized particles (Z and A are the atomic number and the mass of the ion). Unfortunately, this method leaves an ambiguity in the identification arising from different charge states q of particles of given Z, because both TOF and dE/dx depend on A/q. The response of a scintillator stopping the detected particles in the focal plane of a magnetic spectrometer depends on the energy E, the charge Z and the mass A of the ion through a function L(E,Z,A). Since $E \alpha q^2/A$, the parameter $L(q^2/A, Z, A)$ can remove the A/q ambiguity if the dependence of L on E and Z are sufficiently distinct. For that purpose the response of a pilot U scintillator has been measured for various ions at several incident energies.

The experiments were carried out at the 88-inch cyclotron and the measurements were performed with the detection system and the QSD spectrometer; the geometry of the detector is shown in Fig. 1.

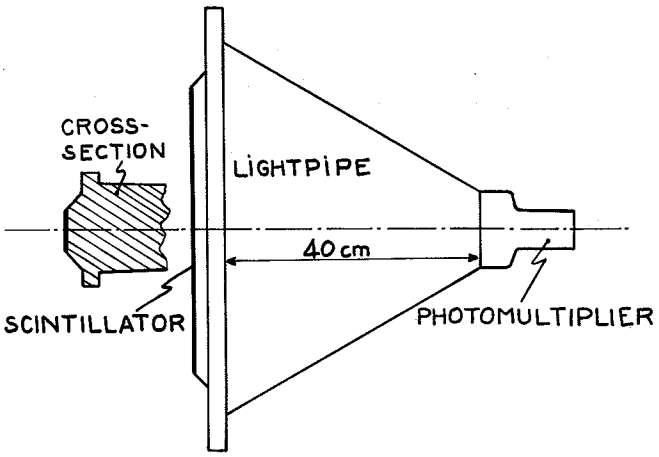

The scintillator was placed at the focal plane and a 5 mm wide slit was placed in front of it. The measurements were made with particles elastically scattered from a thin gold target. For each incident beam, a set of different particle energies was obtained by degrading the energy of the scattered particles with aluminum absorbers placed in the scattering chamber before the entrance aperture of the spectrometer. For each particle energy in the focal plane, the spectrometer was tuned so as to center the elastic peak on the slit in front of the scintillator, ensuring a constant positioning of the particles in the focal plane. The energies were determined from the field setting of the magnetic spectrometer. The light output was collected with a XP1040 photomultiplier through a lucite light pipe (Fig. 1). The signal proportional to light output was taken from the ninth dynode of the photomultiplier, and fed to an ORTEC type 113 scintillator preamplifier.

The data were analyzed in such a way as to provide experimentalists with a means of deducing with reasonable accuracy the Z of a particle from the knowledge of the scintillation response and energy. To that end, we used a convenient parametrization to reproduce the data.

The set of data points obtained from the measurements are shown in Fig. 2. For simplicity, the

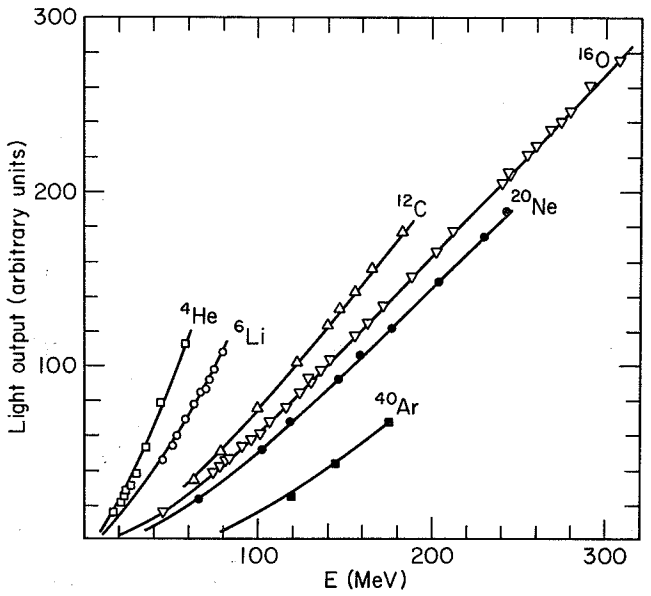

Fig. 2. Experimental results obtained in this work. The error bars are less than the size of the data points. The curves are obtained from a parametrization of the light output L as a function of energy using Eq. 1 in the text. (XBL 762-2313)

data were fitted with a simple analytical parametrization suggested from the shape of the experimental curve. Good results were obtained with the trial function (see Fig. 2):

$$L(E) = \gamma E + \beta(e^{-\alpha E} - 1) \qquad (1)$$

where γ is the slope of the light output in the region linear with energy. The values of γ for the different particles are plotted as a function of Z^{-1} in Fig. 3a; they are well reproduced by the first order equation:

$$\gamma = 0.58 + 3.87\ Z^{-1}. \qquad (2)$$

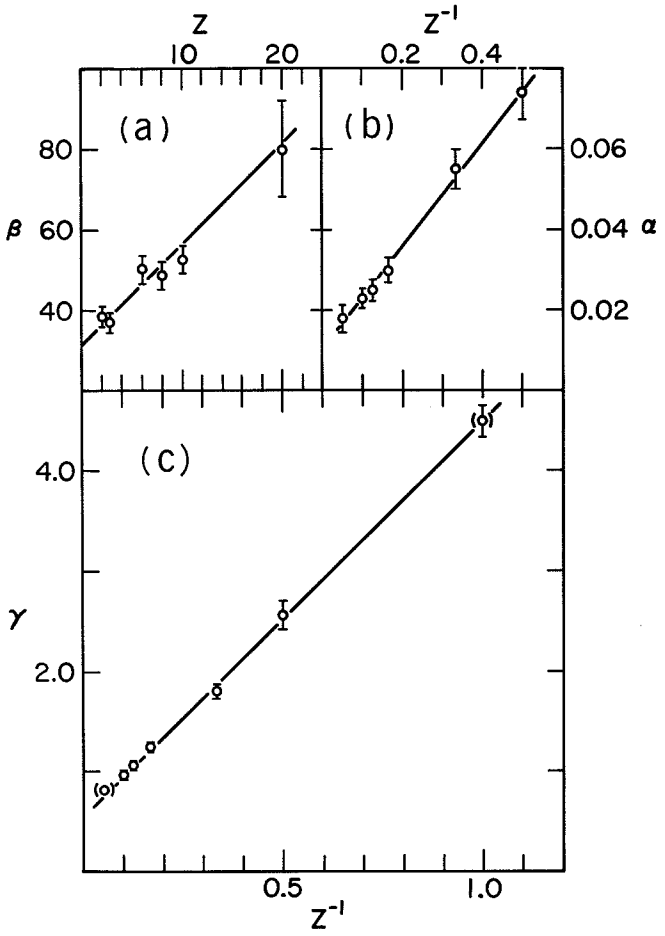

Fig. 3. The values of the parameters γ, β, α from Eq. 1. For each particle, β is plotted as a function of Z, and α and γ as a function of Z^{-1}. The equations of the straight lines are given in the text (Eqs. 2, 3, 4). (XBL 762-2311)

The value of γ for Z=1 was extracted from the proton data of Becchetti et al.[1] The values of L(E) for the two experiments were normalized with the data for α-particles. Although the measurements of Becchetti[1] are for NE102 scintillator, the properties of NE102 and Pilot U scintillators are close enough to justify the assumption of similar responses.

The values of the parameter β were deduced from extrapolation of the asymptote (γE-β) to the E axis, and the values of α from the data points in the curved region of the response. The Z dependence of the β and α parameters is shown in Figs. 3b and 3c. Their empirical values are:

$$\beta = 32 + 2.6\ Z \quad (3)$$

$$\alpha = 0.01 + 0.13\ Z^{-1}. \quad (4)$$

Note that L(E) in Eq. (1) is always positive for $\gamma > \alpha\beta$. In practice γ was obtained slightly smaller than αβ for the cases studied here, and thus relation 4 is not valid for E lower than the root E_0 of Eq. (1). The value of E_0 is lower than 10 MeV from ^{4}He to ^{16}O; it is about 20 MeV for ^{20}Ne and about 60 MeV for ^{40}Ar. As shown by Fig. 2 this description is not expected to be accurate for energies below those of our experiments, especially for ^{40}Ar ions lower than 100 MeV. For this latter projectile, a more complicated parametrization is probably called for.

Collecting all the previous results, one can predict the response of a Pilot U scintillator to an ion (between ^{4}He and ^{40}Ar) of given Z by using the relation:

$$NL(E) = \left(0.58 + \frac{3.87}{Z}\right) E + (32.+2.6Z)\left[e^{-\left(0.01+\frac{0.13}{Z}\right)E} - 1\right] \quad (5)$$

where N is a normalization coefficient, accounting for the effects of the photomultiplier, of the light-pipe attenuation and of the experimental geometry.

Footnotes and Reference

*Condensed from LBL-4872.

†Hahn-Meitner Institute, Berlin, Germany.

‡Instituto de Fisica, Mexico 20 DF, Mexico

1. F. S. Becchetti, private communication.

SPECTROMETER FOCAL PLANE DETECTOR SYSTEM

B. G. Harvey, J. Mahoney, and R. F. Burton

Identification of heavy ions in a magnetic spectrometer requires the measurement of several parameters. The focal plane detector that has been in use on the spectrometer at the 88-inch cyclotron for several years[1] measures, for each particle, position (i.e., $B\rho$), time-of-flight (TOF), energy loss dE/dx, and the residual energy (with rather poor resolution).

Resolution in TOF is limited to about 1-2% by the dispersion in flight paths caused by the finite radial angle of acceptance into the spectrometer. We have therefore built a new detector that measures the position of a particle in two Borkowski-Kopp resistive wire proportional counters[2] placed 11 cm apart, thus determining the angle at which the particle arrives at the focal surface and the angle of emission from the target. TOF can thereby be adjusted for flight path variation. Hopefully it will now be possible to increase the spectrometer solid angle by a factor of two or more while retaining TOF resolution at close to the zero-solid-angle value of 0.5%.

The angular resolution of the double position measurement depends upon the intrinsic resolution of the two position-sensitive counters and upon the multiple scattering in the gas-filled space between them. As a compromise between these two effects, a separation of 11 cm was chosen, although the multiple scattering must still be minimized by the use of a low-Z counter gas such as propane.

The space between the two position counters is used as an ion chamber with a cylindrical rod as anode, shielded by a tungsten wire mesh "grid" as shown in Fig. 1. Electron collection times for particle tracks at the top or bottom of the ion chamber differ by about 2 μs, thus permitting the vertical position of a track to be determined by measurement of the time difference between signals from the stopping plastic scintillator and the ion chamber signals.

Resolution in the dE/dx measurement appears to be limited almost entirely by energy loss straggling, although calculations of this quantity for comparison with experimentally measured resolutions are not very reliable. For 104 MeV ^{16}O, the measured (calculated) FWHM is 2.5% (2.3%) with 200 Torr of propane. For 315 MeV ^{16}O, the experimental resolution is 5.4% FWHM.

The whole detector is constructed in a modular fashion so that configurations most suitable for a specific experiment can be assembled. For example, a second dE/dx ion chamber or a stopping ion chamber can be inserted between the second position counter and the plastic scintillator.

Residual energy resolution in the scintillator is a strong function of particle energy, varying from 20% (104 MeV ^{16}O) to 6% (315 MeV ^{16}O), where the energies are those of the particle at the entrance window of the whole system. Due to energy loss straggling in windows, the position counters and the dE/dx ion chamber, a stopping ion chamber would be expected to give a resolution of at best about 2.5%.

References

1. B. G. Harvey, et al., Nucl. Instrum. Meth. 104, 21 (1974); B. G. Harvey, H. Homeyer, and J. Mahoney, Nucl. Instrum. Meth. 118, 311 (1974).

2. C. J. Borkowski and M. K. Kopp, IEEE Trans. Nucl. Sci. NS-17, 340 (1970).

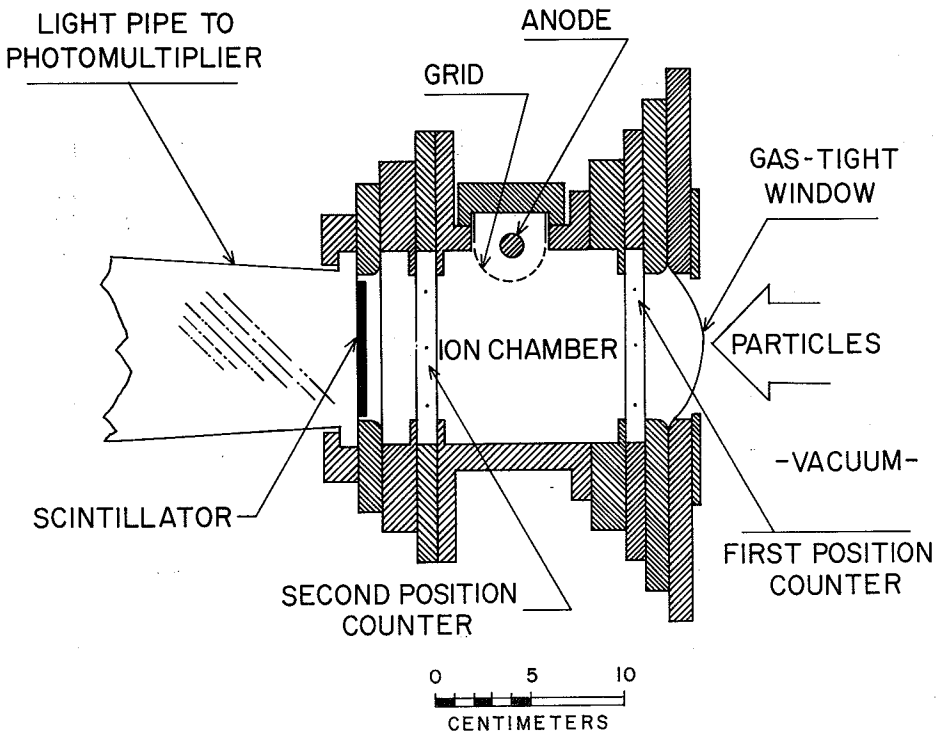

Fig. 1. Spectrometer focal plane detector system. Gas is usually 200 Torr propane. (XBL 766-8219)

IDENTIFICATION OF ATOM NUMBERS UP TO Z = 60 IN FRAGMENTS FROM HEAVY-ION REACTIONS

R. Jared, P. Glassel, R. Schmitt,
P. Russo, and L. G. Moretto

The study of heavy ion reactions has stimulated the development of hardware and software tools for the identification of the products. A telescope composed of a gas ionization ΔE counter and a solid state E counter which has been developed in our group allows us to identify the fragment atomic numbers (Z) over more than half of the periodic table. Unfortunately, the commonly used particle identification algorithms to not work reliably if used over a large range of atomic numbers (Z = 4 to 60). In response to this need for a better algorithm, a data reduction system has been devised which uses the experimental ΔE-E two dimensional maps to determine the location of the individual Z ridges.

This system has been used to reduce data obtained from reactions involving many[2-4] different beam-target-combinations at the 88" cyclotron and at the SuperHILAC. Typically the data are taken in a scattering chamber with two to four counter telescopes. The signals from the counters are subject to normal amplification and coincidence requirements. The experimental data in digitizwd forms are stored on magnetic tape in an event by event form.

The data so collected are then assembled into ΔE - E arrays (E = 100, ΔE = 960 channels) on a PDP-9 computer. A simple array is shown in Fig. 1. This map shows that ridges associated with individual atomic numbers cross the array with well-behaved slopes. The average slope is used to compress several adjacent columns into a few new compressed columns with improved statistics. Figure 2 is a column obtained from the ΔE, E map of reaction 600 MeV Xe + Cu. The peaks in the histogram due to individual Z's are nearly equidistant.

In principle, the peaks in the reduced columns could be fitted to find the centroid of each Z, but this approach is ineffective at very high Z's because of statistical difficulties and poor resolution. In order to exploit the periodicity of the spectrum a convolution integral of the compressed column with a three peaked mask [M(Z)] is employed—

$$C(Z) = \int_0^\infty \phi(Z')\, M(Z-Z')dZ',$$

$$M(Z) = \sum_{i=0}^{2} [r(Z-i-1) - 2r(Z-i-0.5) + r(Z-i)],$$

r(Z) is a unit ramp, and $\phi(Z)$ is the data to determine the ridge points; this method requires little computer time. Three pieces of information are used in the program: the average slope, the average Z spacing in ΔE and the number of columns to be compressed. The convolution sum is evaluated for compressed columns and a triangular peak mask with a base width of one average Z spacing. The significant peaks in the convolution sum are used to define a new Z spacing. This is then used to improve the Z spacing as a function of ΔE and E. Three adjacent triangular wave shapes with a base width of one Z unit for each peak are then convoluted with each compressed column, and normalized to one (Fig. 3). The peaks in each convolution sum are then stored along with the statistical significance of each peak. The standard deviation is shown for several peaks in Fig. 3. The figure also shows the valley-to-peak ratio and the FWHM. These were calculated from the convolution integral of several unit area Gaussians one Z unit apart with a triple triangle wave form. The two curves are for the envelope of the maximum and minimum of the convolution sum. It should be noted that these two curves apply to the compressed column. The Z resolution is affected by the slope used. The slope was optimized for large atomic numbers where the resolution is more critical. The maxima of the convolution sum generate an array of ridge points associated with the various Z's. A fourth order polynomial is fitted to these points by means of an interactive program.

These ridge equations, for each Z, the energy calibration equations, the dead layers, the constants necessary to determine absolute cross sections and the Z of one of the ridges are then used to produce energy spectra for each atomic number. These spectra are also interactively decomposed on the PDP-9 computer into the various components of the energy spectrum. The center-of-mass spectra are also used to produce Wilczynski-type contour plats on the CDC 7600 computer.

References

1. M. M. Fowler, R. C. Jared, Nucl. Instrum. Meth. 124 341 (1975).

2. P. Rosso, et al., Binary Breakup (and Secondary Fission) of a Heavy Deformed System: 979 MeV Xe + Au, in this Annual Report.

3. R. P. Schnitt, et al., Nuclear Relaxation Phenomena and Diffusion in the Reaction ^{107,109}Ag + ^{84}Kr at 7.2 MeV/nucleon, in this Annual Report.

4. P. Gläßel et al., Study of Fragments Emitted in the Interaction Between ^{181}Ta and ^{86}Kr at 620 MeV Bombarding Energy, in this Annual Report.

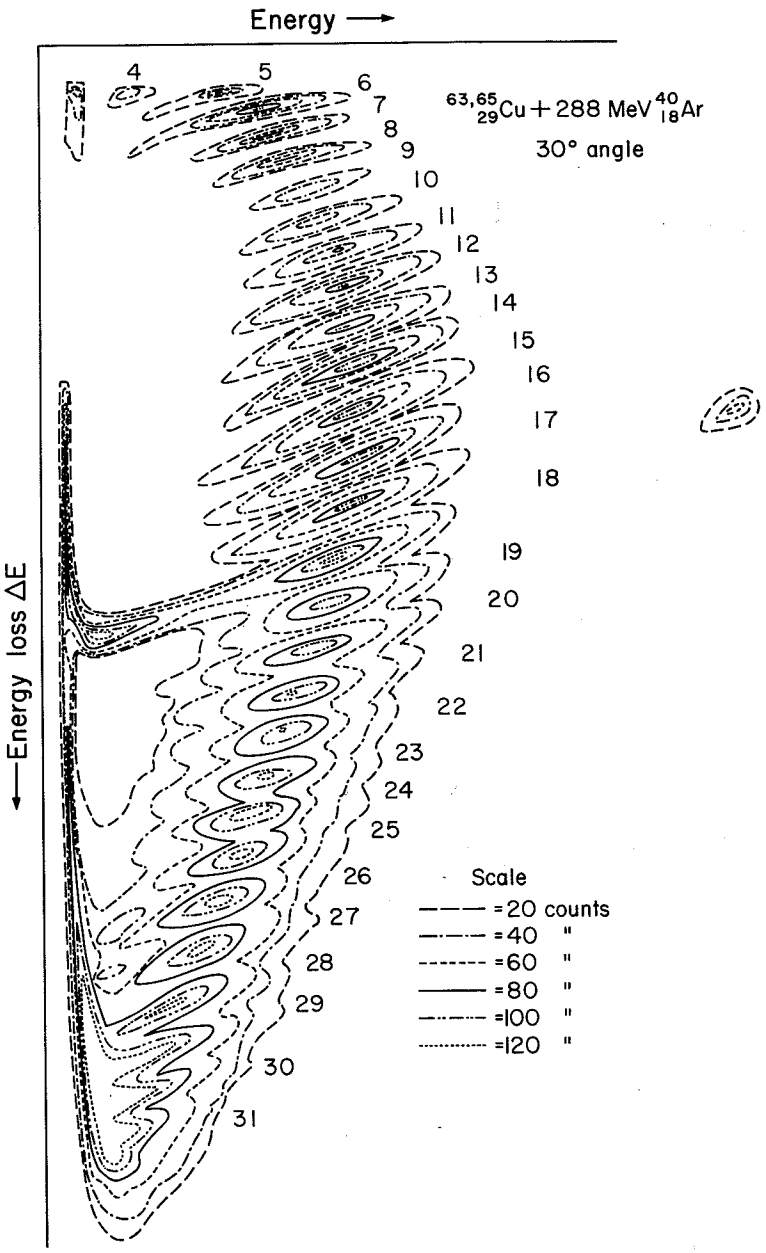

Fig. 1. Map of the energy deposited in the gas counter vs that observed at the energy detector.
(XBL 7411-8233)

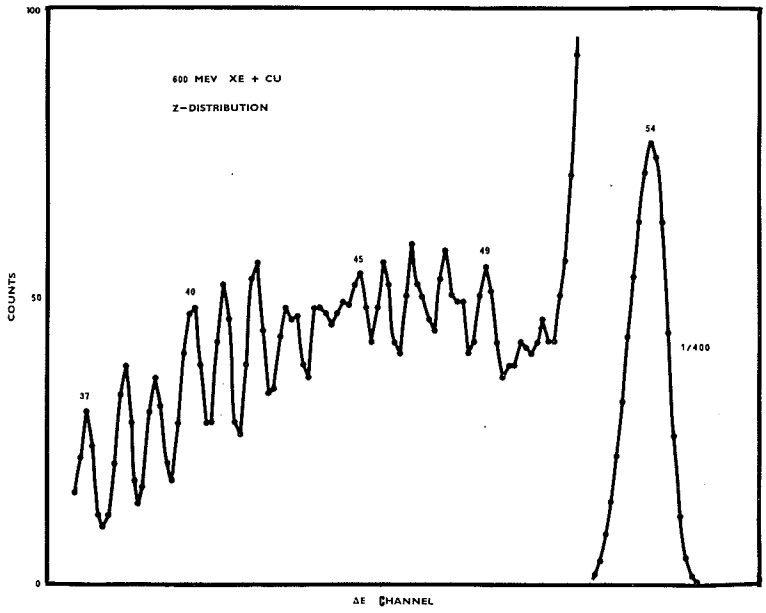

Fig. 2. Spectrum of ΔE counts obtained by adding adjacent columns of a ΔE-E map with an average slope. (XBL 766-8281)

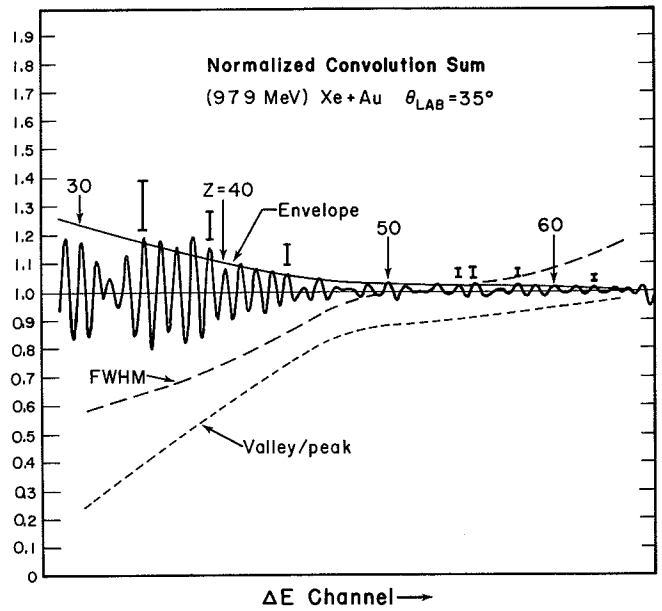

Fig. 3. Composite diagram showing the result of the convolution sum. The calculated full width at half maximum (dashed line) and calculated valley-to-peak ratio (dotted lines) for several adjacent equal area Gaussians are shown for the envelope of the convolution sum. (XBL 766-8282)

ENERGY CALIBRATIONS OF SOLID STATE COUNTERS FOR HEAVY ION EXPERIMENTS

P. Russo, R. Jared, R. Babinet, and L. G. Moretto

A new class of heavy ion experiments investigates processes in which the break-up of the intermediate system occurs in a time scale which is some fraction of the total time required for the equilibration of all degrees of freedom. Accurate measurements of the laboratory energies and angles of the two correlated heavy fragments originating from the binary break-up of the heavy complex are necessary to determine such quantities as the masses of the two fragments at the time of breakup and the number and type of particles emitted by the fragments. Details such as these reflect the properties of the partially relaxed complex on its way to equilibrium, and so it is compelling to perform such measurements as a probe for understanding relaxation phenomena in nuclear matter.

Critical to the success of heavy-ion coincidence measurements in predicting the masses of the heavy fragments at the time of breakup is an accu-

rate determination of the energies and angles in the laboratory and of the z for at least one of the fragments. Heavy-ion measurements are complicated by unusually high ionization densities and a broad range in the z of the product. The use of a telescope which consists of a gas ionization (ΔE) detector with a solid state silicon surface barrier (E) counter allows for resolutions in Z up to Z = 60.[1] A small thin window on the telescope permits accurate determination of the angle of the detected fragments. Measured in coincidence with the telescope events are fragments which are stopped in a hight-resistivity silicon position sensitive detector which defines the position of the detected fragment of measured energy to within 1 mm. It remains to obtain a precise calibration of the analog response of the solid state counters to the ionization produced by the stopping heavy fragments.

The pulse height defect (PHD) denotes the apparent energy defect of a charged particle detected by a solid state counter. While the effect is very small for low z ions, detected in silicon, the pulse height of the signal produced by a heavy ion of the same kinetic energy will be less than that for the light ion due primarily to the effects of recombination which occurs increasingly with ionization density and is enhanced in high-resistivity silicon.

The PHD in the PSD and the telescope E counter has been determined from measurements of elastically scattered argon in coincidence with recoil gold, silver and copper target nuclei. A beam of 163 MeV argon from the 88-inch cyclotron was incident on thin (200 to 350 μg/cm^2) self-supporting foils of natural gold, silver, and copper. The incident projectile energy is below the Coulomb barrier for gold and very near the Coulomb barrier for silver eliminating the possibility of contamination of the elastic peak with transfer products. The observed energies of detected elastics and recoils were corrected for energy defects due to dead layers and target and window thicknesses using the range-energy calculated elastic and recoil energies, differences being attributed to the PHD. The PHD for gold, silver and copper ions in the high-resistivity silicon of the PSD is plotted in Fig. 1 as a function of the energy of the ion as it enters the silicon. The dimensionless energy units (LSS units) defined[3] by Lindhard, Scharff and Schiott have been formulated in order to express in terms of a single function of ion energy the pulse height defect of any ion in the same medium. The PHD is approximately linear with the stopping power so that the relationship between energy in MeV and LSS units is a function of the z and A of the ion in the stopping medium. This relationship for an ion stopping in silicon is:

$$\frac{E_{LSS}}{E_{MeV}} = 6.525\times10^4 \frac{(z^{2/3} + 5.808)^{-1/2}}{z(A + 28.09)} .$$

A single, empirically-determined[4] function of the form:

$$PHD = \frac{6E}{E+B_1} + \frac{B_2}{1 + 500\ E^{-1.4}}$$

where PHD and E, the ion energy, are in LSS units can then be fitted to all of the PHD data obtained with a given detector. Figure 2 is a plot of the PHD data from Fig. 1 converted to LSS units. A fit to the data with the empirically-determined function gives values of 25 for B_2 and 15 for B_1. A similar technique applied to the silicon surface bar-

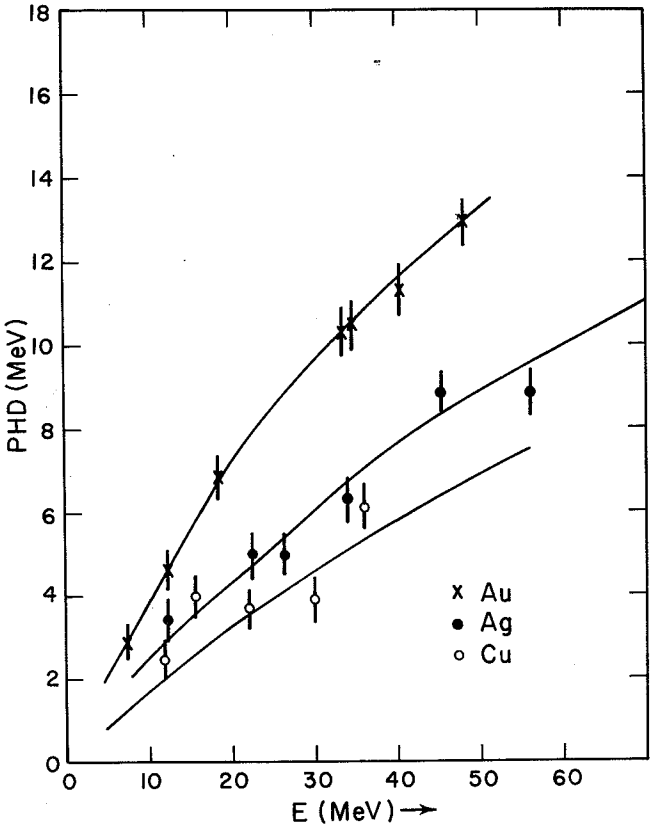

Fig. 1. Experimentally determined pulse-height defects for gold, silver, and copper ions of various energies detected by a high-resistivity (25000 ohm/cm position sensitive silicon counter. (XBL 766-8211)

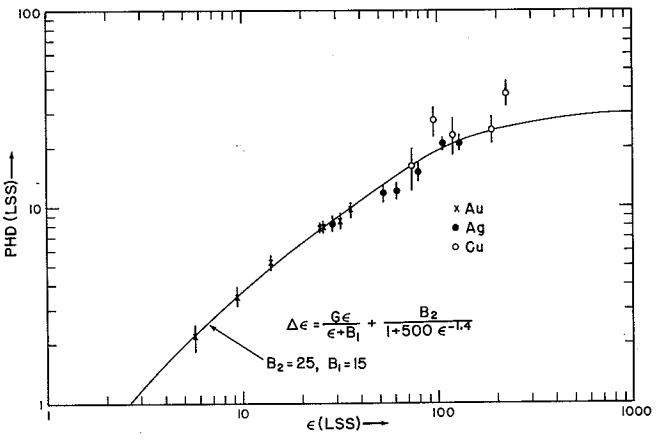

Fig. 2. The pulse height defects of gold, silver, and copper ions converted to LSS units and plotted as a function of ion energy in LSS units. The solid line is a fit to the data allowing the coefficients B_1 and B_2 to vary. (XBL 766-8212)

rier detector gives values of 18 for B_2 and 8 for B_1, in the agreement with previously determined[4] parameters for detectors of this type. The resistivities of the PSD and the surface barrier detectors are approximately 25,000 ohm cm and 4000 ohm cm respectively.

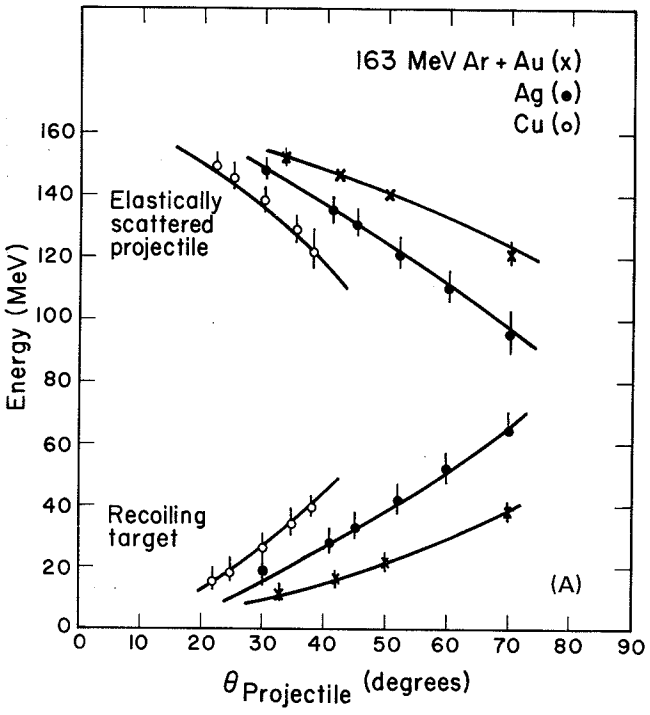

Fig. 3. Results of elastic-recoil coincidence measurements for 163 MeV argon incident in copper, silver, and gold targets. (A) Experimental laboratory energies of the elastically scattered projectile and the recoil target plotted vs angle for the elastic projectile. The solid lines are the calculated results for elastic scattering. (B) Experimental laboratory angles for target recoils plotted vs angle for the elastic projectile.

(XBL 766-8213)
(XBL 766-8214)

cases, the PSD was the recoil detector. The agreement with elastic scattering (solid lines) is good except when the recoil energy drops below about 15 MeV. At such low energies, the net energy correction approaches the recoil energy for the heaviest ions. Table 1 gives the values of the recoil energies and the summed c.m. angles for the coincident fragments. Again, deviations from 180° occur when the recoil energy falls below 15 MeV.

The coincidence data obtained in the experiment with a silver target and 340 MeV argon projectiles requires a precision of 2% in the energy calibration of the PSD in order that a determination of the masses of the two fragments be accurate to within one mass unit. The accuracy of the measurement is within this limit since the fragment energies are approximately 50 MeV in the laboratory frame.

A critical test of the accuracy of the energy corrections for heavy ions is the ability to reproduce elastic-recoil coincidence kinematics. The results of correlated elastic-recoil measurements made with 163 MeV Argon incident on gold, silver and copper targets are shown in Figs. 3A and 3B. In all

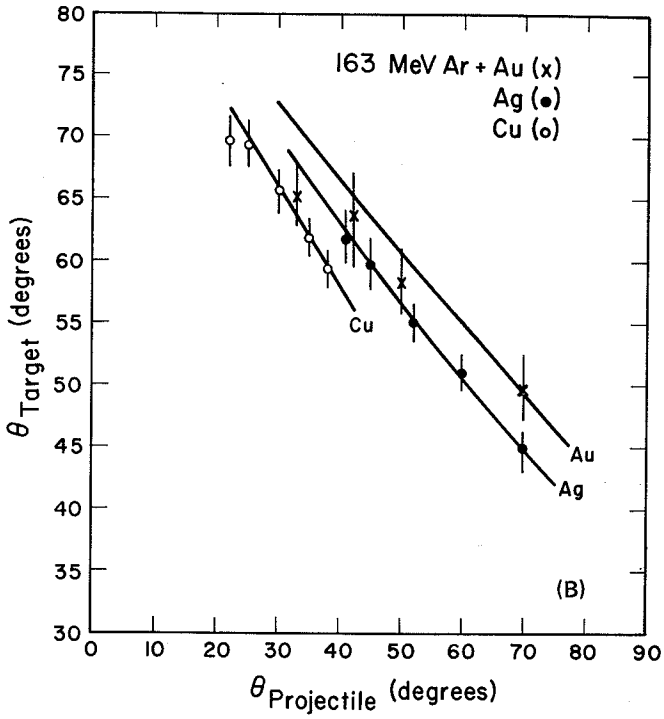

Table 1.

Z_{Proj}	Z_{Tgt}	θ^{Scatt}_{Proj}	E^{*}_{Recoil} (MeV)	Observed $(\theta_1+\theta_2)$cm
18	29	38°	39.1	179.2°
		35°	33.9	179.3°
		30°	25.6	179.7°
		25°	18.2	179.2°
		22°	14.3	142.3°
18	47	70°	64.7	180.6°
		60°	51.7	180.2°
		52°	41.2	180.0°
		45°	32.3	179.3°
		41°	27.5	178.8°
18	79	70°	38.6	179.9°
		50°	22.1	179.5°
		42°	16.2	179.3°
		33°	10.4	175.8°

*Computed from elastic scattering.

References

1. R. Jared, et al., Identification of Atom Numbers Up to Z = 60 in Fragments from Heavy-Ion Reactions, in the Annual Report.

2. L. C. Northcliffe and R. F. Schilling, Nuclear Data Tables 7, 322 (1970).

3. J. Lindhard, M. Scharff, and H. E. Schiott, Mat. Fys. Medd. Dan. Vid. Selsk. 33, 14 (1963).

4. S. B. Kaufman, E. P. Steinberg, B. D. Wilkins, J. Unik, and A. J. Gorski, Nucl. Instrum. Meth. 115, 47 (1974).

WILCZYNSKI PLOTS: AN EFFECTIVE WAY TO DISPLAY SINGLES DATA

J. S. Sventek and L. G. Moretto

In order to provide a more powerful means of displaying the large amount of Z-resolved singles data taken by our group for various reaction systems, we have developed a set of interactive computer programs which allow us to draw Wilczynski plots[1] (maps of contours of constant double differential cross section $\partial^2\sigma/(\partial\theta_{c.m.}\partial E^{tot}_{c.m.})$ plotted with respect to $\theta_{c.m.}$ and $E^{tot}_{c.m.}$ for each Z resolved in these reactions. A quick perusal of Figs. 1-4 will indicate to the reader the amount of information which can be conveyed in such a plot.

The initial results of our data reduction are kinetic energy spectra for each Z in the lab system, $\partial^2\sigma/(\partial\Omega_{lab}\partial E^1_{lab})$. By making an assumption about the mass of the fragment and assuming a binary breakup of the complex, these spectra can be converted to the center-of-mass system giving $\partial^2\sigma/(\partial\Omega_{c.m.}\partial E^1_{c.m.})$. Conservation of linear momentum gives $E^{tot}_{c.m.} = E^1_{c.m.}\frac{m_T}{m_T-m_1}$, where $E^1_{c.m.}$ is the center-of-mass kinetic energy of the detected fragment, m_1 is its mass, and m_T is the total mass. Since the reaction is binary, there is no azimuthal dependence

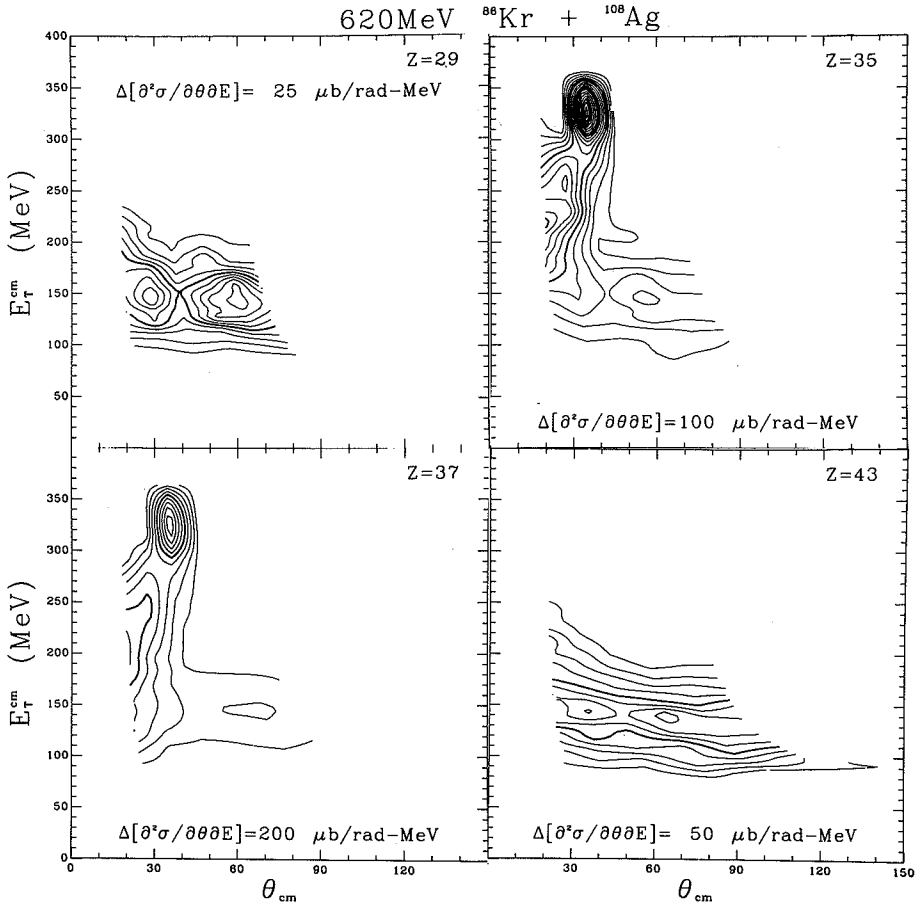

Fig. 1. Wilczynski plots for four representative Z's for the reaction 620 MeV ^{86}Kr + 107.109Ag.

(XBL 766-8167)

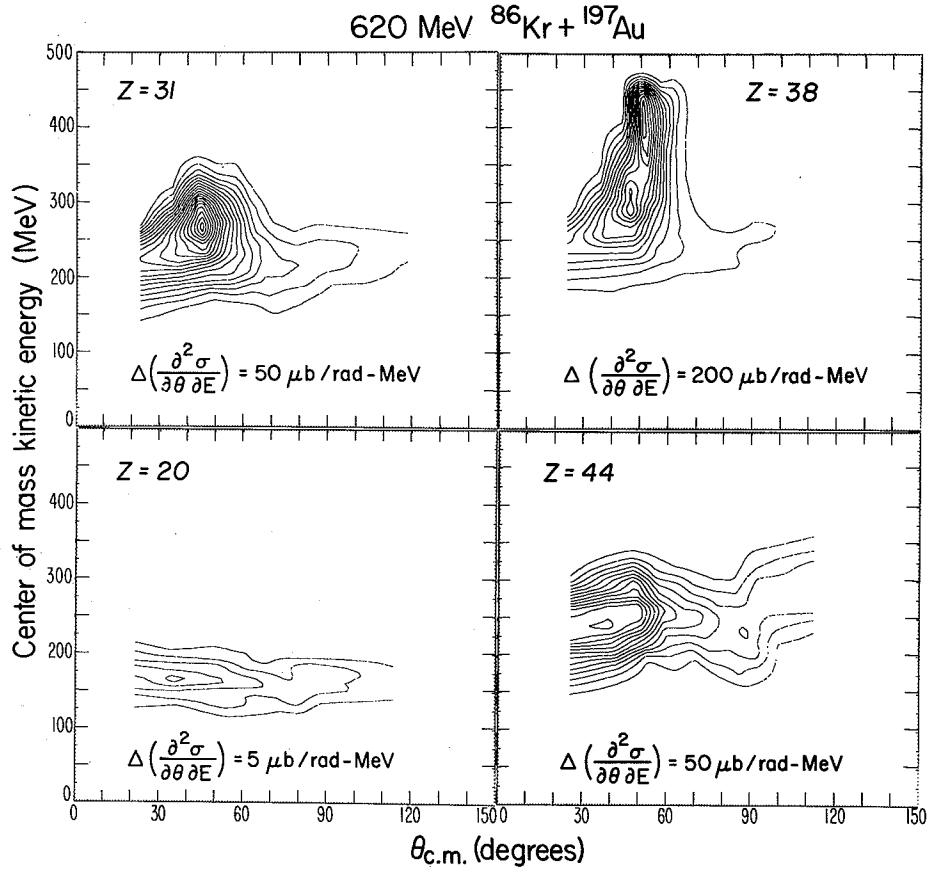

Fig. 2. Same as Fig. 2 for the reaction 620 MeV ^{86}Kr + ^{197}Au. (XBL 766-2089)

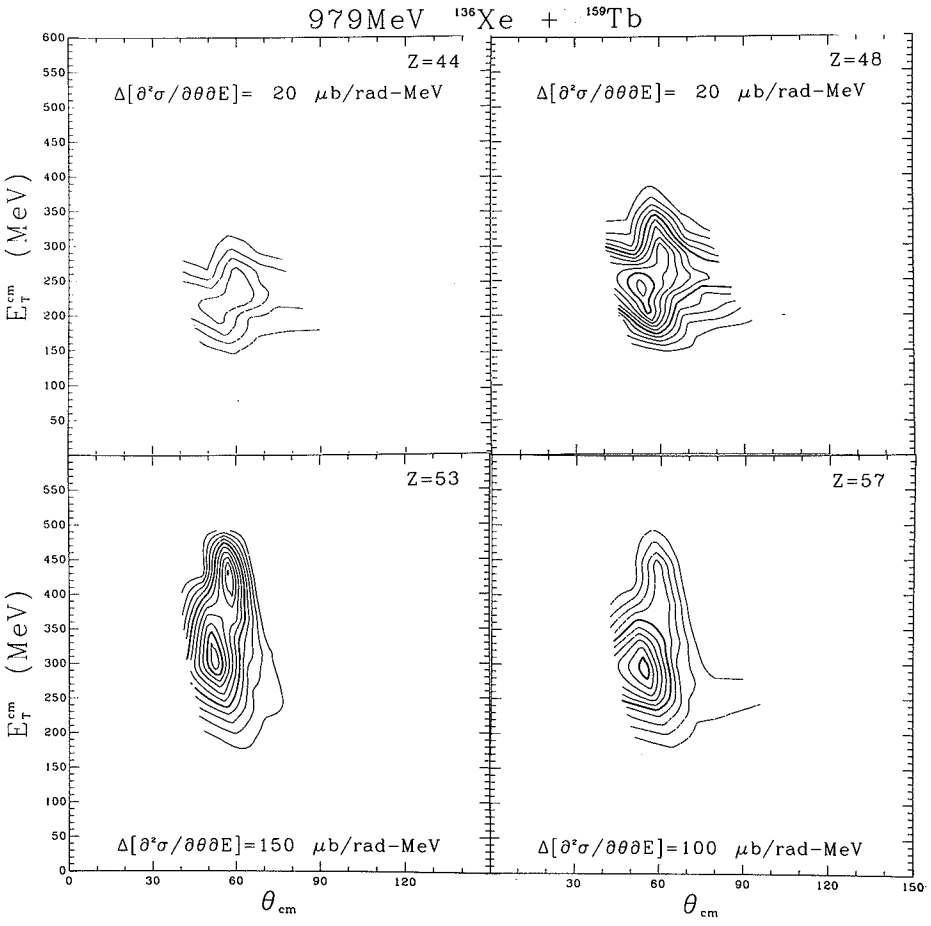

Fig. 3. Same as Fig. 1 for the reaction 979 MeV ^{136}Xe + ^{159}Tb. (XBL 766-8153)

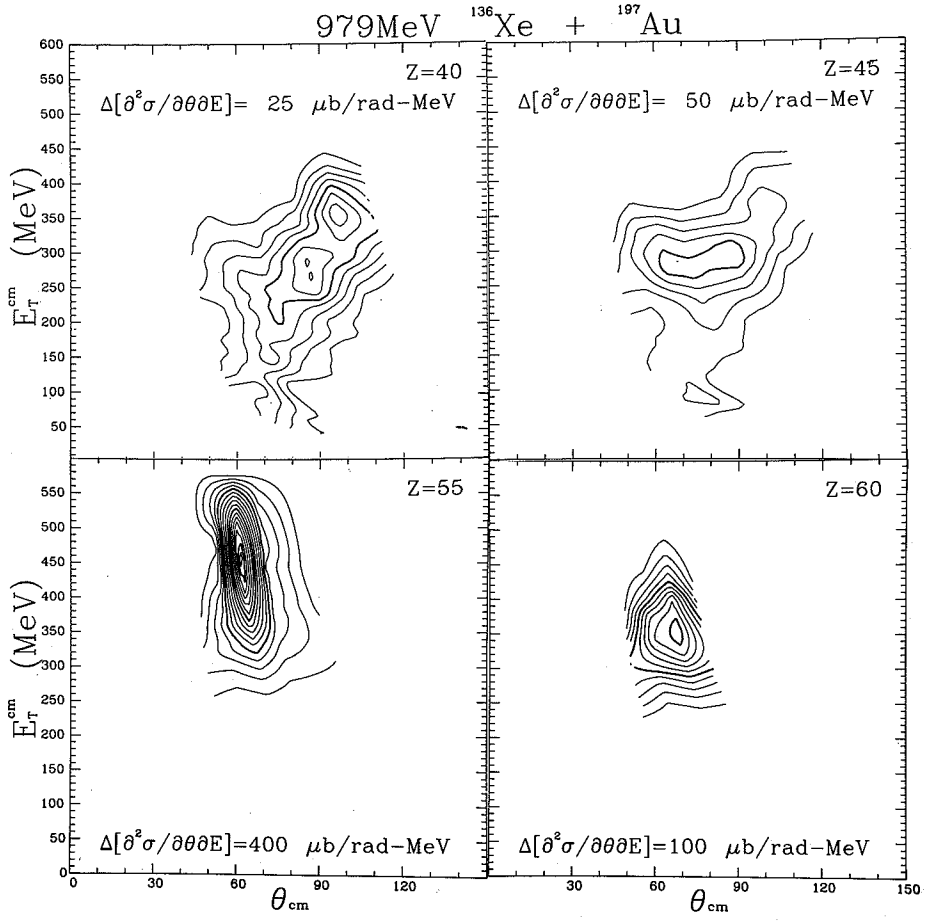

Fig. 4. Same as Fig. 1 for the reaction 979 MeV ^{136}Xe + ^{197}Au. (XBL 766-8152)

of the cross section, so $d\Omega_{c.m.} = 2\pi \sin\theta_{c.m.} d\theta_{c.m.}$. The transformation of the cross section to $\partial^2\sigma/(\partial\theta_{c.m.}\partial E^{tot}_{c.m.})$ is now trivial.

We assume that the neutron to proton ratios of the two fragments are equilibrated, as has been shown to be true experimentally by Galin et al.[2] This means that for a given division of the total mass, the atomic number Z of one of the fragments takes the value which minimizes the liquid drop potential energy for the shapes involved. For very large target-projectile systems (such as Kr + Au), such an assumption differs negligibly from assuming the N/Z ratio to be the same as that for the hypothetical compound nucleus. The masses have not been corrected for neutron evaporation, but, even though such a correction will only cause small shifts in the features of the maps, such corrections are being considered.

Automation was employed to draw the maps since hand-drawing all the maps would have been very similar to requiring a medieval monk to transcribe 20 copies of the bible. (Consider the fact that in reaction systems measured recently, we have had to draw 30 to 40 maps for each system.) The computer also has the advantage of total lack of bias. Hand-drawn maps suffer from a subconscious smoothing algorithm which is extremely nonlinear and device (person) dependent. The method is extremely sensitive to calibration problems; it is this inability to subjectively compromise that has helped us to discover problems which would not have manifested themselves otherwise.

Figures 1-4 display sets of 4 maps from 4 different reaction systems. As you can see, an enormous amount of information can be had at a glance. The real power of this method of display, though, is the ability to quickly scan from one Z to the next through a whole sequence of Z's from a single reaction. The Z-dependence of certain topographical features of the maps then become overwhelmingly obvious, such as the gradual appearance and then disappearance of the quasi-elastic component as one scans from Z's far below to Z's far above the projectile.

The computational method can be easily modified to display any experimental quantity which depends upon two variables. Of course, the plotting subroutines are site-dependent, but one only needs a local subroutine which draws straight lines between two points. We are presently planning to compile a

paper which consists solely of these contour diagrams for all the singles data we have collected over the past few years.

References

1. J. Wilczynski, Phys. Lett. 47B, 484 (1973).

2. B. Gatty, D. Guerreau, M. Lefort, X. Tarrago, J. Galin, B. Cauvin, J. Girard and H. Nifenecker, Nucl. Phys. A253, 511 (1975).

A HIGH INTENSITY HEAVY-ION RECOIL TARGET SYSTEM

Joachim M. Nitschke

At present the power density of beam windows and recoil targets at heavy ion accelerators is limited to approximately 10 to 20 W/cm^2. In typical experiments to produce transfermium elements this corresponds to a production yield of about 10 atoms/hr per nanobarn. Since the cross section for the production of new elements including superheavy elements might well be in the picobarn range, a target system was developed which increases the present capabilities substantially.

The operation principle of the new target system can best be understood by referring to Fig. 1. The conventional single target which also acted as a window to separate the recoil stopping gas from the machine vacuum is replaced by a double window. A similar arrangement is used for the exit of the beam. A high velocity gas stream passes between each of the two foils and removes the heat generated by the beam in the entrance and exit windows, the gas itself, the target backing, and the target. It is important to realize that the differential pressure across the target can be made zero if the cooling gas has the same pressure as the stopping gas. This greatly reduces mechanical stress on delicate targets. Even a slight "leak" in the target is of no consequence if the cooling and stopping gas are of the same species (in general He).

For vacuum spectrometers, etc., a single "dual window" can, of course, be used. A detailed account of the experimental and theoretical investigations

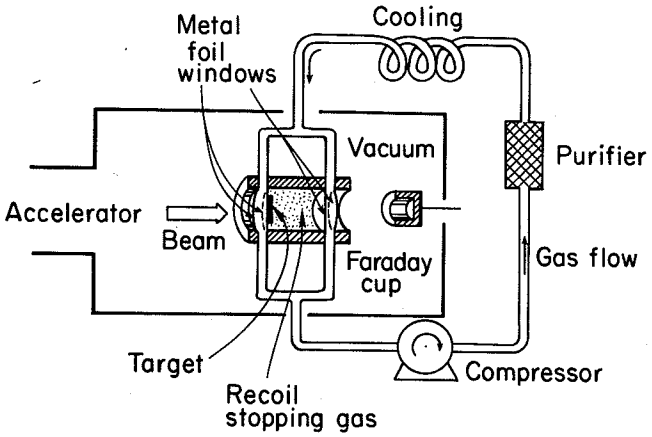

Fig. 1. The operating principle of the gas-cooled target system. (XBL 764-2617)

of this target system is given in Ref. 1. A theoretical expression for the film transfer coefficient α is obtained:

$$\alpha = \text{const.} \frac{\lambda}{\ell} (\text{Re})^{0.8} \cdot (\text{Pr})^{0.3}.$$

Here λ is the thermal conductivity of the gas, ℓ a characteristic length, Re the Reynolds number and Pr the Prandl number. From this expression it is calculated that hydrogen and helium are the best candidates for a cooling gas.

The experimental investigations are carried out with an electron gun and an infrared TV system which is used to determine the temperature distribution of the windows. The temperature of the cooling gas can be lowered to 77° K. A gas circulator system is capable of delivering up to 34 cfm of gas at this temperature and one atmosphere pressure.

The goal of the measurements was to find the optimum cooling conditions by varying the following parameters:

- the window material
- the nature of the cooling gas
- the gas flow
- the gas temperature.

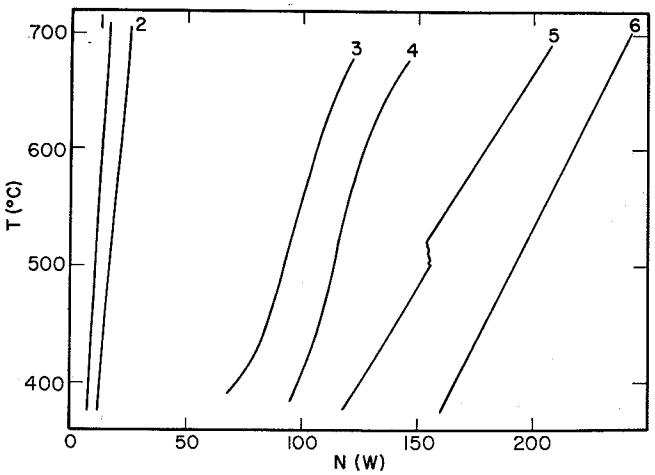

Fig. 2. Window temperature T as a function of beam power N for different cooling conditions. (1) vac on both sides, (2) 1 atm, 290° C, stagnant He on one side; vac on the other side, (3) 12.5 scfm He flow at 290° K, (4) 25 scfm He flow at 77° K, (5) 10.1 scfm H_2 flow at 290° K, (6) 18.2 scfm H_2 flow at 77° K. (XBL 766-8232)

Figure 2 shows an example of the results obtained. With hydrogen as a cooling gas more than one order of magnitude improvement of the beam power capability is achieved.

Reference

1. J. M. Nitschke, LBL-4387 (to be published in Nucl. Instrum. Meth.).

A HEAVY-ION SPECTROMETER FOR THE SUPERHILAC

Joachim M. Nitschke

For the investigation of heavy-ion nuclear reaction mechanisms and the identification of reaction products, a magnetic spectrometer can be of great benefit.

The proposed spectrometer for the SuperHILAC would have the following principal features:

(1) Physical separation between the primary beam and the recoil products if these differ in one or more of the following parameters: velocity (v), energy to charge (E/q), or mass to charge ratio (m/q). The suppression of unwanted particles will depend on the extent to which they differ from the desired particles in these three quantities.

(2) Mass determination up to the superheavy element region with unit mass resolution.

(3) Physical separation of masses according to their m/q values for further study of decay modes.

(4) Z-identification. The Z-resolution will depend on the detials of the reaction and the construction of the spectrometer. In favorable cases unit Z-resolution up to Z = 100 can be expected.

(5) The full angular range from 0° to approximately 160° can be studied.

(6) All particles which can be accelerated by the SuperHILAC can be analyzed.

Limitations imposed by target thickness and uniformly, scattering and straggling, beam quality and beam intensity, high Coulomb barriers, kinematic broadening, etc. make it advisable to consider—as the first spectrometer for the SuperHILAC—an instrument with moderate energy resolution but great flexibility as a kinematic tool.

The basic concept is therefore a velocity filter coupled with a magnetic spectrometer (Fig. 1). The whole instrument is dispersionless in energy and constitutes a recoil mass spectrometer. Moderate energy information will however be obtained from the focal-plane detector and/or time-of-flight measurements.

The following is a brief description of the principle of the spectrometer. The electrostatic deflection in the velocity filter can be expressed as

$$F\rho = \frac{mv^2}{q} ,$$

and the magnetic deflection as

$$B\rho = \frac{mv}{q} .$$

F is the electric field, all other letters have the usual meaning.

The principal components of the spectrometer consist of one electrostatic followed by two magnetic deflectors.

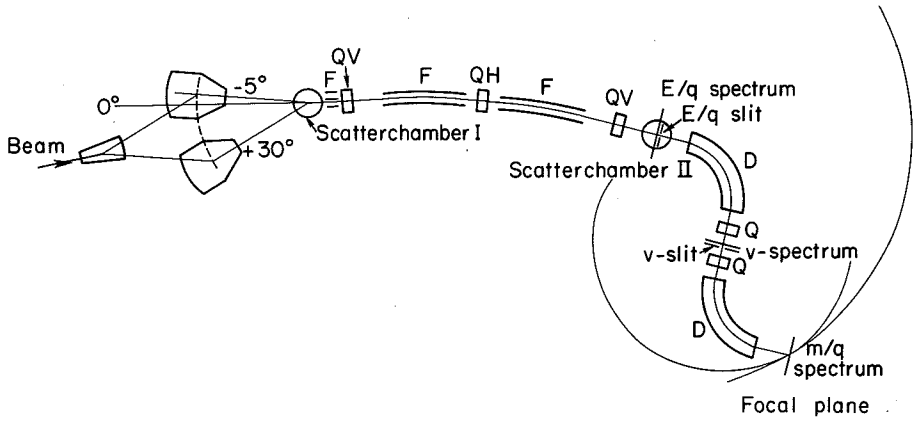

Fig. 1. Heavy ion spectrometer. (XBL 762-2199)

A variation in the electric rigidity can be expressed to first order as:

$$\frac{\Delta(F\rho)}{F} = K_{el}\left(\frac{\Delta m}{m} + \frac{2\Delta v}{v}\right).$$

K is the dispersion constant. This is followed by a magnetic field. Its variation in rigidity is expressed as:

$$\frac{\Delta(B\rho)}{B} = K_{mag}\left(\frac{\Delta m}{m} + \frac{\Delta V}{v}\right).$$

If the magnetic is opposite and equal to the electric dispersion $K_{el} = -K_{mag}$ one obtains a pure velocity spectrum (the $\Delta m/m$ - terms cancels). The second magnetic dipole is identical to the first one and compensates the remaining velocity dispersion so that a pure mass spectrum results. Schematically this can be written as:

$$\frac{\Delta(F\rho)}{F} - \frac{\Delta(B\rho)_1}{B_1} - \frac{\Delta(B\rho)_2}{B_2} = -\frac{\Delta m}{m}.$$

All mass lines in the focal plane will however be split into "multiplets" according to their ionic charge. In some cases these lines will overlap. To remove this charge ambiguity a time-of-flight system forms an integral part of the spectrometer. Start detectors can be located behind the E/q-slit and/or the velocity slit. The focal-plane detector acts as a stop-detector. In addition the focal-plane detector allows a coarse energy measurement. This coarse energy measurement ($\tilde{E}$) and the velocity measurement from TOF result in a coarse mass determination ($\tilde{m}$) which allows to resolve the m/q ambiguities. Schematically:

$$\tilde{E} + v\ (TOF) \Rightarrow \tilde{m}$$
$$\tilde{m} + m/q \Rightarrow m.$$

The "exact" energy of the particle can then be obtained from

$$m + v\ (TOF) \Rightarrow E.$$

Two modes of operation of the spectrometer are anticipated. For compound nucleus reactions and other reactions near zero degrees a beam inflection system will be used which scans a moderate angle of -5° to +30°. For studies at angles larger than 30° the first part of the spectrometer (the electrostatic deflector) will be bypassed and the second part used as an "ordinary" magnetic analyzing system. The angle over which this magnetic part of the spectrometer can turn will be as large as practical: - 10° to approximately + 160°. The idea here is that for large angles the beam separation afforded by the electrostatic deflector is not necessary because the intensity of the scattered beam falls sharply with increasing angle.

A VERSATILE SPUTTERING SYSTEM

S. W. Eckroad, R. E. Leber, and A. Ghiorso

Well-controlled material removal and deposition have been achieved with a sputtering system constructed from components readily available in the laboratory environment.

Fabrication of uniform films (here, targets for nuclear reaction studies) from high-melting-point or refractory substances is often difficult to realize with standard evaporators, in that the requisite high temperatures may damage the physical and/or chemical integrity of substrate and deposit. Additionally, the need to provide (accelerated) ions of specific and well-resolved energies frequently dictates the availability of uniform degrader foils of varying thickness. A sputtering system recently developed at this Laboratory has a breadth of application inclusive of these purposes.

The sputtering-electrode assembly (Fig. 1) is housed in a bell jar (the inverted base of a vacuum desiccator) evacuated by a (21 cfm) mechanical rotary pump with a liquid-nitrogen cold trap. As shown in the block circuit diagram (Fig. 2), a 3 kV/40 mA regulated power supply is used in this system in conjunction with meters to monitor voltage and arc current and a strip-chart recorder, which provides the history of the discharge.

Interchangeable parts in the cathode allow for considerable latitude in application. Selective conductive shielding within the discharge dark zone will enable differential sputtering of the cathodic material and may provide a degree of collimation to enhance the line-of-flight (vs diffusion) component of deposition. With the discharge thus restricted, a defined portion of the cathode foil is preferentially removed.

Sputtering progress is monitored in situ by measuring with a surface-barrier silicon detector the energy loss of alpha particles of known incident energy. Information on cathode and/or deposit thickness may thereby be conveniently obtained without having to remove the material for weighing (with the concomitant risk of breaking the foils).

Argon—the preferred sputtering gas—is metered into the bell jar through double needle valves at a rate sufficient to maintain an ambient pressure of 20 to 200 mTorr. At these pressures and a discharge potential of from 0.5 to 3.0 kV, the cathode fall (dark zone) attains a maximum length of approximately one inch and the arc current varies between 1 and 40 mA. Industrial-grade argon is of sufficient purity in most cases. Although at the higher pressures, contaminants in the gas show a propensity to react with—generally oxidize—the more reactive sputtered materials. Such chemistry (in-flight or surface-catalyzed) is a potential means by which to obtain oxide or halide films from elemental cathodes.

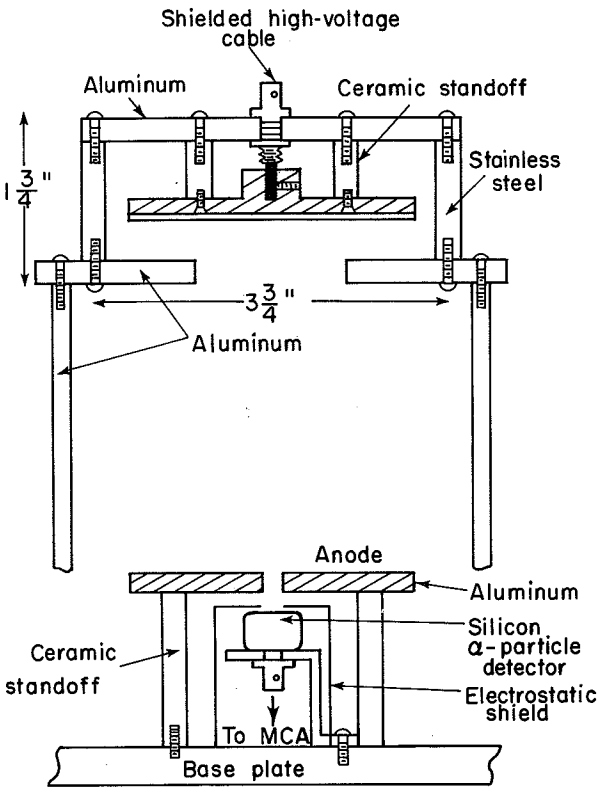

Fig. 1. Full-scale mechanical drawing of the sputtering-electrode assembly. (XBL 766-3009)

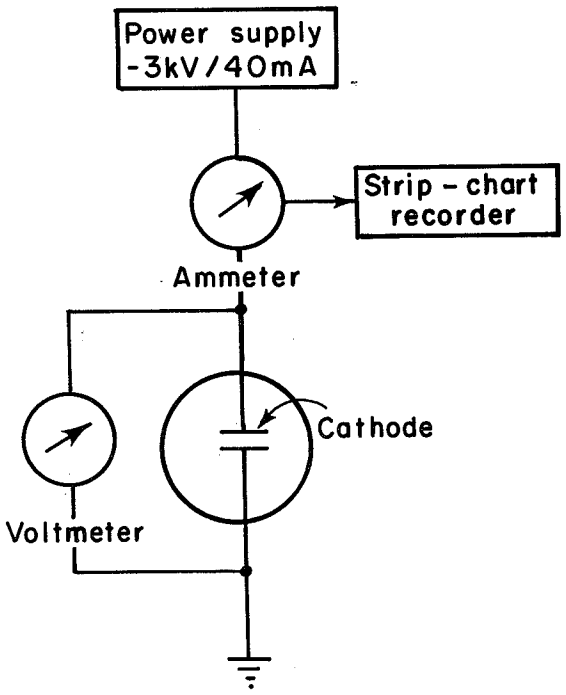

Fig. 2. Block diagram of sputtering circuit. (XBL 766-3010)

Crystal structure has been observed to be an important factor in producing quality films through sputtering. Insofar as the sputtered material will tend to conform in lattice structure to the substrate (epitaxial growth), it is advantageous from the mechanical stability standpoint to choose a substrate whose unit cell shape and size closely resemble those of the crystalline deposit. Limitations to the quality of films made by thinning commercial foils are the uniformity and crystal-lattice integrity of the original foil. Initial surface discontinuities and unequal sputtering susceptibilities due to lattice defects for example, from stress hardening will be manifested in the induction of pinholes. (This situation may be improved to some extent by annealing the foils prior to sputtering.)

Built from low-cost, off-the-shelf components, this sputtering system has been valuable in making thin films of gold, molybdenum, and platinum, and in thinning foils of aluminum, molybdenum, and beryllium. In the future, consideration will be extented to new cathode-substrate systems with work continuing on present combinations and the functional dependence of operating parameters: pressure, temperature, voltage, and current will be established.

A TIMING DETECTOR UTILIZING ISOCHRONOUS TRANSPORT OF SECONDARY ELECTRONS

A. M. Zebelman, W. G. Meyer, K. Halbach, A. M. Poskanzer,
R. G. Sextro, G. Gabor, and D. A. Landis

A timing detector has been developed for use in reaction product mass identification, utilizing the time-of-flight technique. The detector, as schematically pictured in Fig. 1, has as its novel feature an isochronous electron transport system.

Secondary electrons produced when particles pass through a thin foil (approximately 10 $\mu g/cm^2$ of carbon) are accelerated to approximately 2 kV by 0.0005 inch stainless steel wires arranged in the form of a harp of 99% transmission. The accelerated electrons are then transported 180° in a uniform field of a permanent magnet, through a 90° collimator and a suppression grid. The electron detector is comprised of two micro-channel plates which are operated in a tandum configuration. The channel plates act as an electron multiplier and the electrons are collected on a 50 ohm anode, from which a fast timing signal is obtained.

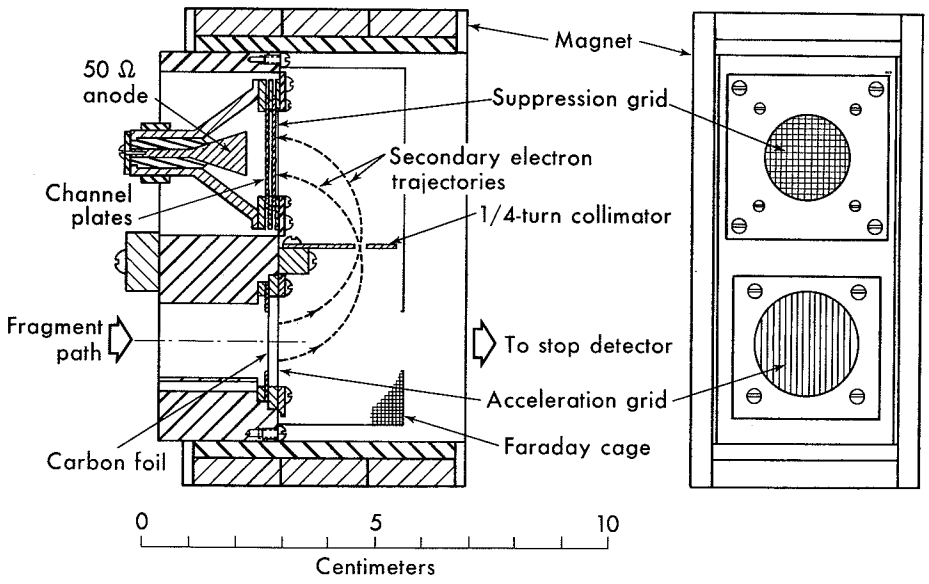

Fig. 1. Schematic view of timing detector. (XBL 757-3468)

The basic concept for this timing device arose from a desire to use a thin foil which was oriented perpendicular to the fragment flight path and to remove and shield the channel plates from the beam and reaction products. The concept of a 180° magnetic transport was chosen because it is isochronous, independent of changes in the lateral position of the origin of the electrons and their energy. However, the transport time is sensitive to the angle of emission of the electrons in the plane perpendicular to the magnetic field. The divergence in this angle is small because of the 2 kV acceleration and because the harp structure produces a uniform accelerating potential in this plane. The affect of this angular divergence on the electron transport time is minimized further by the quarter-turn collimator. The suppression grid serves to eliminate background originating from interactions at the surface of the channel plate.

Tine-of-flight measurements have been made between this timing detector and a 120 μm Si detector with 100 MeV ^{16}O ions (from the 88-inch cyclotron) and 8.78 MeV alpha particles; the results are tabulated in Table 1. Figure 2 shows a time spectrum obtained with 100 MeV ^{16}O ions.

Table 1. Time resolution and detection efficiency

	FWHM(picosec.) Particles	Pulser	% Efficiency
100 MeV ^{16}O	90	31	95
8.7 MeV ^{4}He	156	96	56

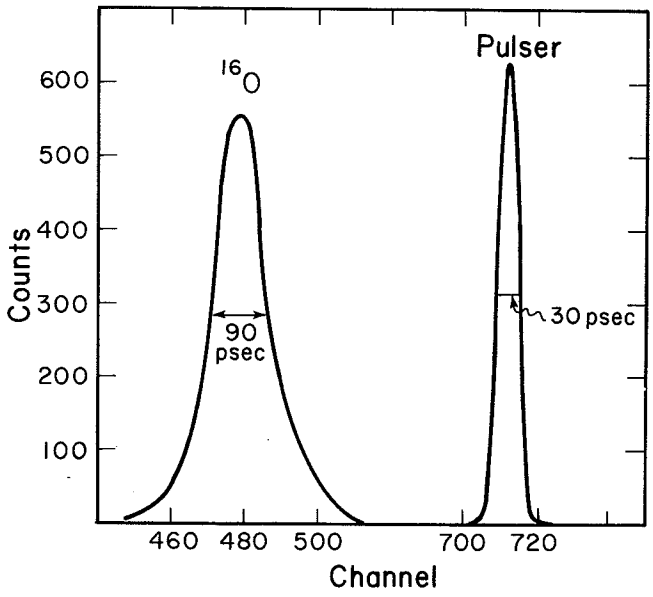

Fig. 2. Time spectra for the reaction ^{197}Au (^{16}O, ^{16}O). (XBL 766-8256)

The authors wish to express their greatful appreciation to D. J. Vieira, F. S. Goulding, C. E. Hartsock, M. Maier, G. D. Westfall, W. S. Cooper, and M. Zisman for their help in different phases of this work.

AN EASY-TO-BUILD WIRE CHAMBER WITH GOOD POSITION AND PULSE-HEIGHT RESOLUTION

J. C. Lugol* and F. S. Bieser †

A simply constructed multiwire drift chamber has been developed. The left-right ambiguity inherent in all multiwire chambers is solved using two staggered planes per axis (Fig. 1). The cathode planes (double-sided aluminized mylar) and field wires (75 micron Be-Cu) are held at negative high voltage while the anodes (20 micron tungsten) are dc coupled to amplifiers at ground potential.

Using P-10 gas (90% Argon, 10% methane), the correlation between drift time and position can be approximated by a single straight line with < ± 0.5 mm error (Fig. 2). The spatial resolution is approximately $\sigma = 0.1$ mm. The pulse-height resolution for 6 keV gammas from ^{55}Fe is < 20% (Fig. 3).

Footnotes

*On leave from Centre D'Etude Nucleaires de Saclay, 91 Gif-sur-Yvette, Paris, France.

†University of California Space Sciences Laboratory, Berkeley, California.

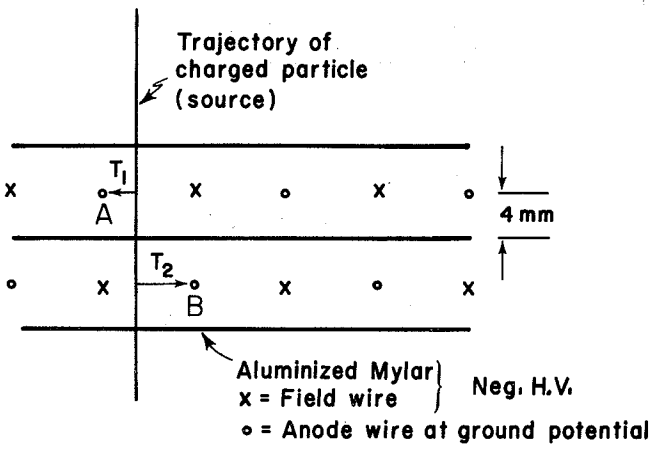

Fig. 1. Construction of a 1-axis pair of multiwire planes. Drift times to anode wires A and B are T_1 and T_2. (XBL 766-8260)

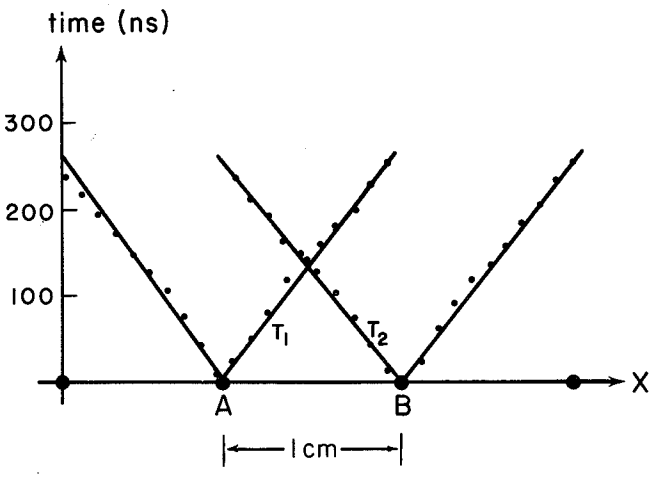

Fig. 2. Drift times T_1 and T_2 as a function of source location (x) to anode wires A and B. (XBL 766-8261)

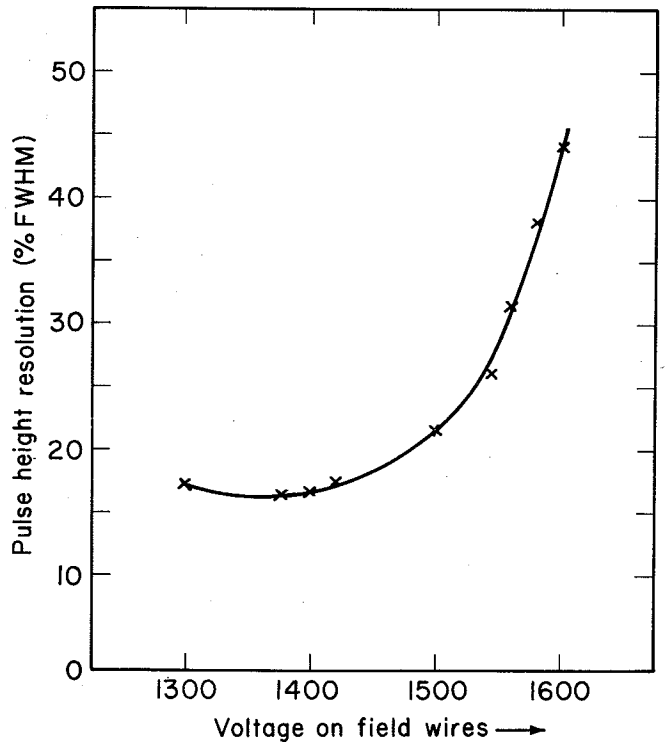

Fig. 3. Pulse-height resolution of 6 keV gammas from ^{55}Fe as a function of high voltage. (XBL 766-8262)

DRIFT CHAMBERS FOR HEAVY-ION COSMIC RAY EXPERIMENT

Fred Bieser* and Douglas Greiner

An array of six single wire proportional drift chambers has been developed for use in the UCSSL/LBL High Energy Cosmic Ray Experiment on the NASA ISEE-C SATELLITE. Three X-Y pairs of chambers are used to measure the angle of incidence of energetic heavy-ion cosmic rays entering a "telescope" of ten lithium-drifted silicon detectors. Single-wire drift chambers were chosen over multiwire systems for several reasons: 1) the readout system for many wires requires many amplifiers (too much power) or a large delay line (too heavy). 2) fewer wires reduces the probability of failure due to wire breakage. 3) a single-wire system lends itself to a simple solution to the problem of resolution degradation caused by delta rays.

Saudinos, et al., have constructed single wire drift chambers up to 50 cm × 50 cm with resolutions (FWHM) of 0.6 mm at 11 cm drift length and 1.6 mm at 50 cm.[1] The task at hand was to squeeze six of these chambers (each being ~1 inch thick) into three inches, orient them into orthogonal pairs without distorting the electric fields in the drift region, and learn how to deal with the copious delta-ray signals.

The chamber thickness was reduced to 6 mm by scaling down the width and spacing of the parallel field-shaping metalized strips, and increasing the sensitivity of the amplifier-discriminator. Unless the electric field is very precisely formed the drifting electron cloud will diffuse and never reach the collecting anode. "Cross-talk" between the electric fields of adjacent chambers can be eliminated by staggering the metalization on the two sides of the kapton (Fig. 1). This results in a pattern that gives 100% electrostatic shielding while allowing the substantial field gradient (500 v/cm) along the drift axis. This gradient is established by a thick-film resistor network connected to both sides of the kapton by pressure contact.

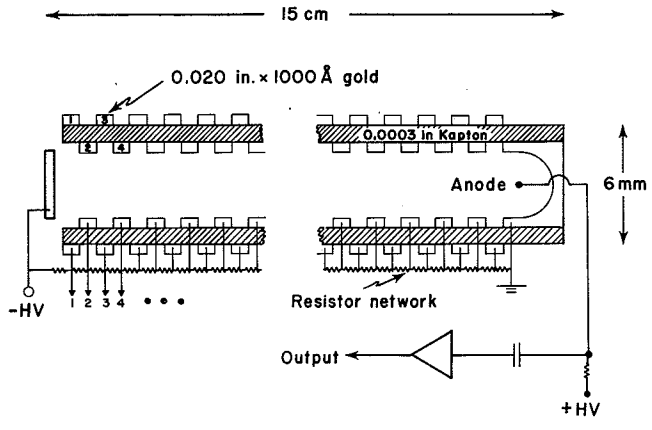

Fig. 1. Schematic structure of single-wire drift chamber showing a cross-section view of the kapton metalization scheme for the elimination of cross talk between adjacent chambers. (XBL 766-8263)

While the chamber and electronics must be sensitive to all particles (Z =1 to 26), relativistic heavy ions produce hundreds of delta rays in the windows and gas which often make larger signals than the lighter cosmic rays.[2] If a large delta-ray signal occurs on the anode side of the central core ionization, the observed drift time and hence the deduced position will be incorrect. A log-compressed integrating constant-fraction discriminator has been developed which can pick-off the core ionization of any particle (Z =1 to 26) regardless of attendant delta rays (Fig. 2.)

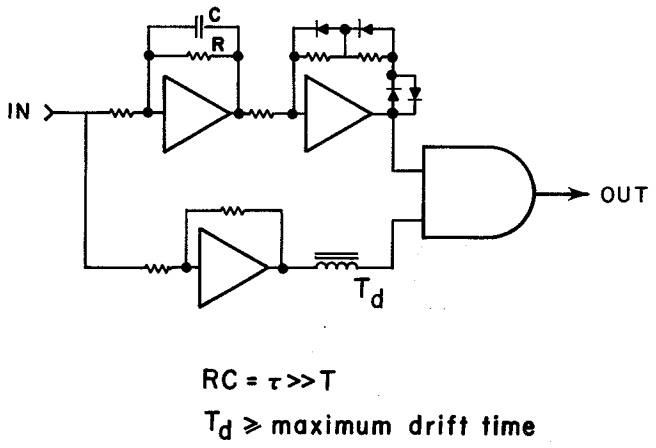

Fig. 1. Schematic diagram of discriminator. (XBL 766-8264)

Footnote and References

*University of California Space Sciences Laboratory, Berkeley, California.

1. J. Saudinos, et al., Nucl. Instrum. Meth. 111, 77 (1973).

2. E. Beleal, A Monte Carlo Calculation of δ-ray Effects on Drift Chamber Resolution, in this Annual Report.

AN INTELLIGENT MULTICHANNEL PDM TRANSMITTER

A. Ross Harrower,* Chuck McParland,* and R. C. Zink*

An INTEL 8080 Microprocessor PDM (Pulse Delay Modulation) Controller with 8 addressable line drivers was developed to control up to 8 magnets for the Bevalac Experiment 162H. The controller can operate in conjunction with its companion module, an eight-channel PDM Receiver, in either an automated feedback loop controlled by a PDP 11-45 or in OFF-LINE mode independent of the computer.

The block diagram is shown in Fig. 1. The module contains 2k bytes of PROM (Progammable Read Only Memory) and 2.5k bytes of RAM, of which 2k bytes are used as a WCS (Writable Control Store)during the initial debug stages. These 2k bytes are made to appear in the PROM address space during debugging. After the software has been debugged and the PROM programmed, this 2k of RAM is freed and can be used as satellite memory and processor to the PDP-11 via CAMAC.[1]

The ODT (Octal Debugger) and Binary Loader programs from the Livermore MCS-8 system were installed in the lowest 512 words of PROM. For ease of software development, an external teletype interface is provided. When a teletype is connected, the 8080 microprocessor is able to sense its presence and thus power up in the ODT mode. When no teletype is connected, the microprocessor automatically goes into the magnet controller program. CAMAC initialization (Z) and module powerup are treated by the 8080 microprocessor as separate starting procedures so that processor restarts are possible without destroying volatile RAM.

The controller has various control modes depending on the restrictions imposed on the various magnets: a) slewing control, b) instantaneous control, and c) battery control. Each of the eight magnets can simultaneously be slewing to either higher or lower currents at one of two slewing rates. Battery changes required in any of these operations are handled automatically. A visual display of magnet values (manually selectable) is available on the front panel. Interrupts for the 8080 Microprocessor are provided to allow for CAMAC communication in the ON-LINE mode or for communication through the Front Panel INCREMENT-DECREMENT lever in the OFF-LINE mode.

Footnote and Reference

* University of California Space Sciences Laboratory, Berkeley, California.

1. CAMAC, A modular instrumentation system for Data Handling, USAEC Document #TID-25875, 1972.

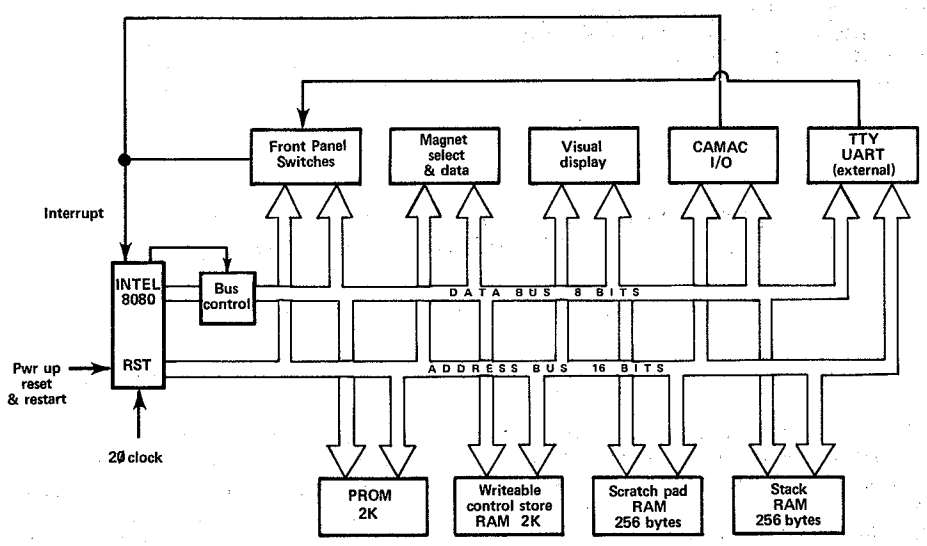

Fig. 1. Block diagram of an INTEL Microprocessor PDM Transmitter. (XBL 766-8266)

HIGH INTENSITY FLUX MEASUREMENTS USING CURRENT TO FREQUENCY CONVERTERS

A. Ross Harrower*

A twelve channel current-to-frequency converter module (double width NIM) has been designed and built to facilitate high-intensity beam flux measurements. By integrating the current output from a photomultiplier tube viewing a plastic scintillator, fluxes up to 10^{10} pps or more can be measured and digitized with high accuracy using inexpensive scalers.

A simplified schematic diagram of the circuit is shown in Fig. 1. By removing the anode bleeder resistor from the base, all the PMT output current flows into the charge summing node of OA-1. The extremely low input bias current (~10 pA) of the CA3130 eliminates all critical components except one feedback resistor (R_f). R_f determines the amount of charge $Q = \frac{V_{Ref}}{R_f} \Delta t$ fed back to the summing node per output pulse. The output is thus a pulse rate sufficient to maintain a charge balance of zero at the summing node.

The integral linearity over any 5 decades of count-rate is < 0.2% from 2 nA input (1 Hz output) to 200 μA input (max. output from RCA 8575; 100 kHz output). The 100 kHz clock frequency allows time-incremental flux measurements with 1% resolution in 1 millisecond windows. Note that while the converter has a limited dynamic range, any particle flux can be measured by simply adjusting the PMT gain, the scintillator-to-PMT light transmission, or the feedback resistor R_f.

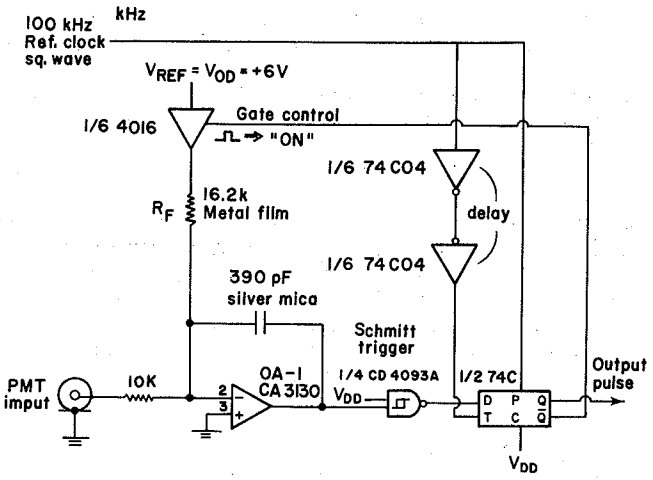

Fig. 1. Simplified logic schematic for current-to-frequency converter. (XBL 766-8265)

Footnote

* University of California Space Sciences Laboratory, Berkeley, California.

A MONTE CARLO CALCULATION OF δ-RAY EFFECTS ON DRIFT CHAMBER RESOLUTION

Ernestine Beleal, Douglas E. Greiner, and Fred Bieser*

A significant problem associated with any sensitive particle position measuring instrument is the distortion introduced in the signal of the particle of interest by δ-ray production along the particle's trajectory through the instrument. In the worst case, the additional signal introduced by δ-rays can mask the true signal enough to make subsequent analysis impossible. The character of such distortion is directly related to the design of the instrument. Therefore, detailed knowledge of the signal and inherent distortions in it is necessary both for developing optimum instrument design and planning analysis procedures.

The handling of this problem becomes especially critical for the experimenter considering instruments to be used with high-Z beams such as those produced at the Bevalac. Since the number of δ-rays produced varies approximately as the square of the charge of the incident particle, the resolution of the signal given by a heavy ion becomes increasingly difficult as the charge increases. In the case of a multiwire chamber, a large number of δ-rays accompanying the primary ion can cause so many wires to fire that an intolerable area of uncertainty will surround the true coordinate location. By contrast, a drift chanber may give better results for high-Z beams because the signal of the primary is generally large enough to override the accumulated contribution of its accompanying background. In order to develop a design which will minimize distortion and improve resolution, it becomes necessary to study, not only the ramifications of different instrumental configurations, but also the influence of varying charges and energies on the instrument.

Our first motivation for developing a computer simulation of δ-ray production came as the result of designing drift chambers for use in a space flight experiment. In this experimental situation an instrument was needed which could supply signal information, clean enough to distinguish between particles sampling the whole range of cosmic radiation (from protons to very high-Z). Using Monte Carlo techniques to simulate δ-ray production by particles traversing the drift chamber system, we were able to study the signal generated by ions of various charge and energy incident on the detector at either specific or random angles. We were also able to simulate changes in design of the instrument with respect to materials, scale, and configuration. Having generated those signals typical of the expected final experimental situation, we were then able to work backwards and analyze our simulated data with knowledge of what the answer should be, thus supplying a powerful tool for evaluating the design and developing future analysis programs.

This computer program, initially intended to create a model for the specific study of δ-ray effects on drift chamber resolution has now evolved as a more general tool. It will be possible to simulate other detection instruments and other experimental situations by the introduction of relatively minor changes in the general program such as a subroutine which establishes the experimental configuration and variable parameters containing the pertinent specifications. Figure 1 shows a block diagram detailing organization of the program.

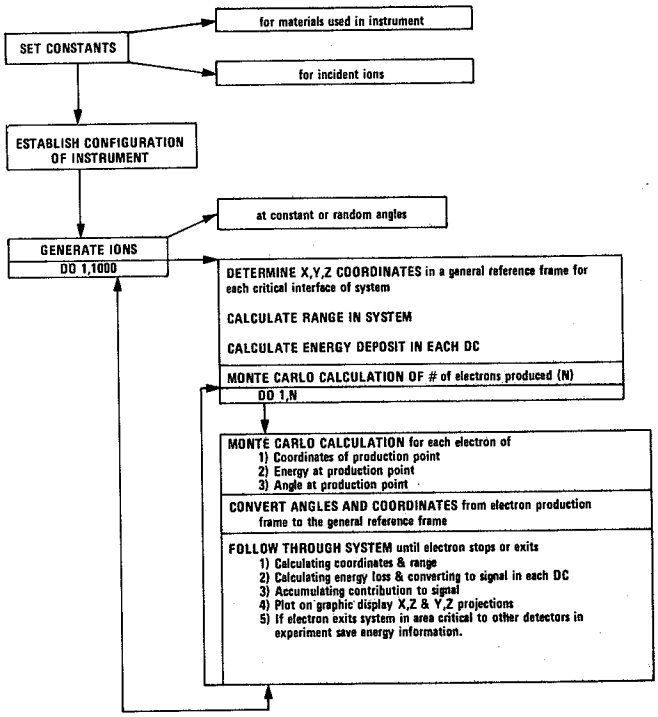

Fig. 1. Skeletal framework of program showing establishment of instrument configuration, generation of ions, production, and trace through system of δ-rays. (XBL 766-8267)

The graphic display of a particle and its accompanying δ-rays in both x-z and y-z coordinate systems was found helpful in debugging the program and in giving a visual understanding of the physical situation. Figure 2 shows a plot in x-z projection of a typical heavy ion and the δ-rays it produced in traversing the drift chamber. Each δ-ray was plotted from its origin to that point where it either stopped or exited the configuration.

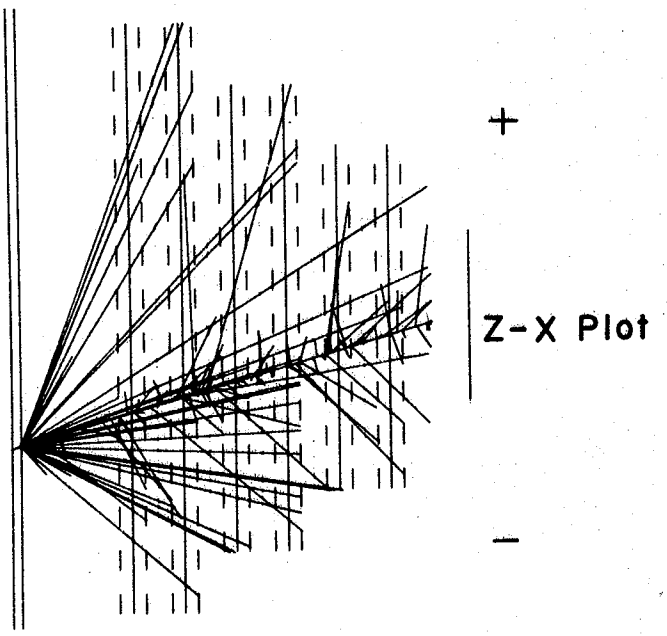

Fig. 2. Computer produced plot in an X-Z coordinate frame, of an $^{56}Fe_{26}$ ion at 455 MeV and the electrons produced along its path through the drift-chamber system. (XBL 766-8268)

Footnote

*University of California Space Sciences Laboratory, Berkeley, California.

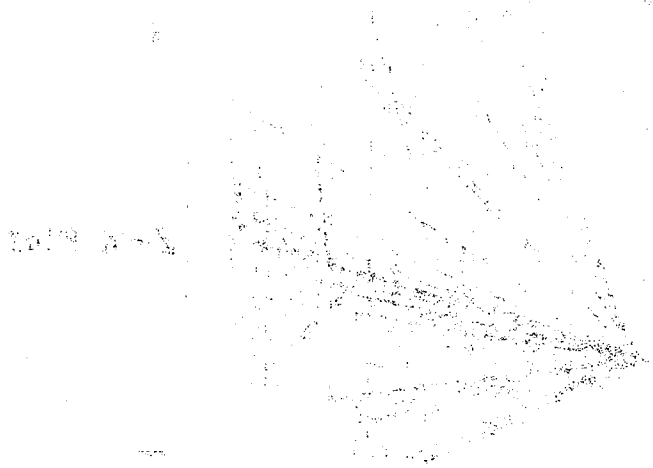

IV.

THESIS ABSTRACTS

K VACANCY PRODUCTION IN MEDIUM-Z HEAVY ION COLLISIONS

R. Anholt

(LBL-4312)

During slow encounters between projectile and target atoms, the electronic atomic wavefunctions of the two collision partners distort and form Molecular Orbitals (MOs). This thesis considers K vacancy formation in slow heavy-ion collisions which occur when electrons are excited out of the 2pσ and 1sσ MOs.

Experimental work using 200 MeV Kr ions is described. Thick target yields of projectile and target K x rays coming from 2pσ and 1sσ excitation are identified.

Our main interest is the excitation of electrons from the 1sσ MO. This cannot be observed in symmetric or near symmetric collisions since Demkov coupling between the projectile and target K shells at large internuclear distances cause vacancies, which are created in the 2pσ orbital, to be transferred into the 1sσ orbital giving an apparent 1sσ yield many orders of magnitude larger than for direct excitation. In collisions involving Kr ions, 1sσ vacancy production is only observed in very asymmetric collisions: as Kr K x rays in encounters with target atoms between H and Ar, and as target K x rays in encounters with atoms between Ce and U.

Theoretical approximate calculations of 1sσ ionization cross sections are described. The calculations indicate that when the experimental proton $+Z_2$ cross section (σ_p) is known (where Z_2 is the target atomic number), the $Z_1 + Z_2$ cross section can be calculated from the relation:

$$\sigma(v_1) = \sigma_p(v_1) Z_1^2 \left[\frac{U_K(Z = Z_2 + 1)}{U_K(Z = Z_1 + Z_2)}\right]^n$$

where Z_1 ($< Z_2$) is the projectile atomic number, U_K is the K binding energy, and n is a constant depending on the reduced projectile velocity v_1/v_K (v_K is the velocity of the K-shell electron). This formula may also be used where $Z_2 < Z_1$ by interchanging Z_1 and Z_2 everywhere.

Data from experiments where the target K vacancy cross section is measured as a function of the projectile charge (at the same velocity) are discussed. The above relationship fits the data but n is not as large as theory indicates. Finally we compare our Kr data and other heavy ion data with this relation.

APPLICATION OF GENERALIZED CLASSICAL TRAJECTORIES IN NUCLEAR PHYSICS

Herbert Massman Leser

(LBL-4316)

A new semi-classical method, the so-called uniform semiclassical approximation, is described briefly and then applied to two nuclear physics problems. The basic features of this method are that the dynamics of the problem is treated completely classically (that is, one solves classical equations of motion), but the quantum mechanical superposition principle is retained by evaluating a phase along the classical

trajectory and adding probability amplitudes for indistinguishable processes rather than probabilities themselves.

The first problem considered is the backscattering from a deformed nucleus and the excitation of rotational states in the target at energies up to the Coulomb barrier. The multiple Coulomb excitation calculations are in quantitative agreement with a very different method (the de Boer-Winther code). A nuclear optical potential is also considered and the nuclear-Coulomb interference for heavy ions is studied.

The second problem considered is the tunneling through a two-dimensional barrier. This problem (which is supposed to simulate the penetration through a two-dimensional fission barrier) is investigated by a fully quantum-mechanical coupled-channel calculation and by the uniform semiclassical approximation. A quantitative agreement is found.

THE EFFECT OF FREE-PARTICLE COLLISIONS IN HIGH ENERGY PROTON AND PION-INDUCED NUCLEAR REACTIONS

Norman P. Jacob, Jr.

(LBL-4067)

The effect of free-particle collisions in simple "knockout" reactions of the form (a,aN) and in more complex nuclear reactions of the form (a,X) was investigated in a two part study by using protons and pions as the incident projectiles. In the first part of this study, cross sections for the $^{48}Ti(p,2p)\,^{47}Sc$ and the $^{74}Ge(p,2p)^{73}Ga$ reactions were measured from 0.3 to 4.6 GeV incident proton energy. The results indicate a rise in (p,2p) cross section for each reaction of about (25±3)% between the energies 0.3 and 1.0 GeV and are correlated to a large increase in the total free-particle pp scattering cross sections over the same energy region. The experimental results are compared to previous (p,2p) excitation functions in the GeV energy region and to (p,2p) cross section calculations up to 1 GeV incident proton energy based on a Monte Carlo intranuclear cascade-evaporation model. This model yields cross sections that are generally a factor of 2 greater than the experimental values.

In the second part of this thesis, cross section measurements for $\pi^{\pm},\pi N)$ and other more complex pion-induced spallation reactions were measured for the light target nuclei ^{14}N, ^{16}O, and ^{19}F from 45 to 550 incident pion energy. These measurements indicate clearly a broad peak in the excitation functions for both $(\pi, \pi N$ and (π,X) reactions near 180 MeV incident pion energy. This corresponds to the large resonances observed in the free-particle $\pi^{+}p$ and $\pi^{-}p$ cross sections at the same energy. Striking differences in $(\pi,\pi N)$ cross section magnitudes are observed among the light nuclei targets. The experimental cross section ratio $R_{\pi^-/\pi^+} = \sigma(\pi^-,\pi^-n)/\sigma(\pi^+,\pi N)$ at 180 MeV is 1.7±0.2 for all three targets. The experimental results are compared to previous pion and analogous proton-induced reactions, to Monte Carlo intranuclear cascade-evaporation calculations, and to a semi-classical nucleon charge exchange model in an effort to understand the mechanism of pion reactions, particularly of the $(\pi,\pi N)$ reaction.

MASS MEASUREMENTS OF HIGHLY NEUTRON-EXCESS NUCLEI IN THE LIGHT ELEMENTS

Kenneth Hugh Wilcox

(LBL-4029)

The $^{26}Mg(^{7}Li,^{8}B)^{25}Ne$ reaction at 78.9 MeV was used to measure the mass-excess of ^{25}Ne(-2.18±0.10 MeV) and several low-lying excited states. Mass-excesses for ^{43}Ar (-31.98±0.07 MeV), ^{45}Ar (-29.727±0.06 MeV), and ^{46}Ar (-29.732±0.07 MeV) were determined from the $^{48}Ca(\alpha,^{9,7}Be)^{43,45}Ar$ reactions at 77.7 MeV and the $^{47}Ca(^{6}Li,^{8}B)^{46}Ar$ reaction at 80.1 MeV. Several excited states of ^{43}Ar and ^{45}Ar were observed. These and the excited states of ^{25}Ne are compared with theoretical predictions. Ground state differential cross sections are given for all reactions, ranging from 0.1 to 1 μb/sr at forward angles. Upper limits of about 1 to 25 nb/sr were determined for the ground state cross sections of the reactions $^{48}Ca(\alpha,^{8,10,11}B)^{44,42,41}Cl$ and $^{48}Ca(\alpha,^{10\text{-}13}C)^{42\text{-}39}S$ at 110 MeV.

Recoil coincidence techniques were used to measure the mass-excess of the particle-unbound nucleus ^{10}Li(33.83±0.25 MeV) by the $^{9}Be(^{9}Be,^{8}B)^{10}Li$ reaction at 121 MeV; the ground state cross section was 30 nb/sr. The $^{14}C(^{9}Be,^{8}B)^{15}B$ reaction at 120 MeV was also investigated using coincidence techniques. Contamination problems only permitted determining a ground state cross section upper limit of 50 ng.sr.

A simple mass relation is derived, similar in approach to the Garvey-Kelson method but taking more explicit account of shell effects. Comparison is made with the Garvey-Kelson relation, and predictions of masses and of the stability of neutron-excess light nuclei are given for both methods. The modified mass relation is shown to often better account for highly neutron-excess nuclei, including the values reported here for ^{25}Ne and $^{43,45,46}Ar$.

V.

PUBLICATIONS

PAPERS PUBLISHED AND LBL REPORTS ISSUED
1974

ANHOLT, R., S. Nagamiya, J. O. Rasmussen, H. Bowman, J. G. Ioannou-Yannou, and E. Rauscher
K Vacancy Production by 4.88 GeV Protons
LBL-4307 Rev., April 1976

ANHOLT, R.
K Vacancy Production in Medium-Z Heavy Ion Collisions
LBL-4312, December 1975
Ph.D. Thesis

ANHOLT, R., J. Ioannou-Yannou, H. Bowman, E. Rauscher, S. Nagamiya, J. O. Rasmussen, T. Shibata, and H. Ejiri
Atomic K Vacancy Production with 3 GeV Carbon Ions
LBL-4359, January 1976

ANHOLT, R. and T. K. Saylor
Radiative Ionization in Slow Ion-Atom Collisions
LBL-4360, January 1976
Phys. Letters A263, 500 (1976)

ANHOLT, Robert (See Meyerhof, W. E., LBL-4078)

ANHOLT, R. (See Meyerhof, W. E., LBL-4019)

ANHOLT, R. and T. K. Saylor
Anomalous X-Ray Continua in Heavy Ion Collisions
LBL-4066, July 1975
Phys. Rev. Letters

ANHOLT, R.
On the Separated Atom Lorentzian Contribution to the Molecular Orbital X-Ray Yield
LBL-4301, August 1975
Journal of Physics B

ANHOLT, R. and the TOSABE group
K Vacancy Production by 4.88 GeV Protons
LBL-4307, September 1975
Phys. Rev. A

ARTZY, Michal, F. Asaro, and I. Perlman
Alašiya of the Amarna Letters
LBL-2375, June 1974
J. of Near Eastern Studies 35, 171 (1976)

ARTZY, Michal, I. Perlman, and F. Asaro
Wheel-Made Pottery of the M.C. III and L.C. I in Cyprus Identified by Neutron Activation Analysis
LBL-2975, August 1975
Report of the Department of Antiquities of Cyprus

ARTZY, Michal
An Archeologist Looks at X-Ray Fluorescence va. Neutron Activation Analysis
LBL-5017, April 1976
Applications of Science to Medieval Ceramics, Lawrence Berkeley Laboratory, Berkeley, CA
March 18-22, 1975

ARTZY, Michal
Alasia I
LBL-5024, May 1976

ASARO, F. (See Artzy, Michal, LBL-2975)

ASHERY, D. (See Wilcox, K. H., LBL-4089)

ASHERY, D., M. S. Zisman, G. W. Goth, G. J. Wozniak, R. B. Weisenmiller, and Joseph Cerny
Study of T=2 States in ^{12}C and ^{12}B
LBL-4315, November 1975
Phys. Rev. C 13, 1345 (1976)

AZJENBERG-SELOVE, F. (See Maguire, C. F., LBL-4338)

BABINET, R. (See Nifenecker, H. C., LBL-1950)

BABINET, R. P. (See Thompson, S. G., LBL-2940)

BABINET, R. P. (See Moretto, L. G., LBL-3444)

BABINET, R. (See Galin, J., LBL-4064)

BABINET, R., L. G. Moretto, J. Galin, R. Jared, J. Moulton, and S. G. Thompson
Diffusion Processes in the Relaxed Cross Section for the Reaction $^{107,109}Ag + {}^{20}Ne$
LBL-4080, August 1975
Nucl. Phys. A258, 172 (1976)

BABINET, R. (See Moretto, L. G., LBL-4084)

BANASCHIK, M. V., R. S. Simon, P. Colombani, D. P. Soroka, F. S. Stephens, and R. M. Diamond
Transitions Between High-Spin Nuclear States
LBL-3456, January 1975
Phys. Rev. Letters 34, 892 (1975)

BANASCHIK, M. V. (See Bertschat, H., LBL-4039)

BANASCHIK, M. V. (See Simon, R. S., LBL-4313)

BECK, F.
Angular Focussing in HEAVILY Damped Heavy Ion Collisions
LBL-4300, August 1975
Phys. Letters B

BERTSCHAT, H. (See Ward, D., LBL-3446)

BERTSCHAT, H. (See Butler, P. A., LBL-3483)

BEX, L., D. J. Clark, C. E. Ellsworth, W. S. Flood, R. A. Gough, W. R. Holley, J. R. Meriwether, and D. Morris
High Charge State Heavy Ion Production from a PIG Source
LBL-3433, 1975
Presented at the 1975 Particle Accelerator Conf. and published in the Proceedings, page 1702

BEX, L., D. J. Clark, C. E. Ellswoth, R. M. Estrella, R. A. Gough, and W. R. Holley
Emittance Measurements of High Charge State Argon Beams from a PIG Source
LBL-4075, October 1975
International Conference on Heavy Ion Sources, Gatlinburg, TN, October 27-39, 1975

BIRCHALL, J., H. E. Conzett, F. N. Rad, S. Chintalapudi, and R. M. Larimer
The Depolarization Parameter in $\vec{p}$ - ^{10}B Elastic Scattering and the Spin-Spin Interaction
LBL-4054, June 1975
4th International Symposium on Polarization Phenomena in Nuclear Reactions, Zürich, Switzerland, August 24-29, 1975

BŁOCKI, J. (See Boneh, Y., LBL-4374)

BŁOCKI, J. P. (See Boneh, Y., LBL-4397)

BŁOCKI, J., J. Randrup, W. J. Swiatecki, and C. F. Tsang
Proximity Forces
LBL-5014, April 1976

BŁOCKI, J. and H. Flocard
Simple Dynamical Models Including Pairing Residual Interaction
LBL-5016, April 1976

BOISSON, J. P. (See Donangelo, R., LBL-4347 Rev.)

BONEH, Y., J. P. Błocki, and W. D. Myers
A Microscopic Method for Calculating the Intrinsic Excitation Occurring in Nuclear Fission
LBL-4374, February 1976

BONEH, Y., J. P Błocki, and W. D. Myers
Microscopic and Macroscopic Calculations of One-Body Damping in Fission
LBL-4397, April 1976

BOND, P. D. (See Meyerhof, W. E., LBL-4079)

BOWMAN, J. D. (See Zebelman, A. M., LBL-3427)

BOWMAN, H. (See Anholt, R., LBL-4307 Rev.)

BOWMAN, H. (See Anholt, R., LBL-4359)

BUCHER, J. J. and R. M. Diamond
Backbending and Other Deviations from Ideality in Extraction Systems
LBL-3453, January 1975
J. Chem. Phys. 79, 2259 (1975)

BUENERD, M., D. L. Hendrie, U. Jahnke, J. Mahoney, A. Menchaca-Rocha, C. Olmer, and D. K. Scott
Response of Pilot U Scintillator to Heavy Ions
LBL-4372, January 1976
Nucl. Instr. and Meth.

BURLEIGH, R. J., D. J. Clark, and W. S. Flood
150 MeV Proton Medical Cyclotron Design Study
LBL-4085, August 1975
7th International Conference on Cyclotrons and Their Applications, Zürich, Switzerland, August 19-22, 1975

BUTLER, P. A. (See Ward, D., LBL-3446)

BUTLER, P. A., J. Meyer-ter-Vehn, D. Ward, H. Bertschat, P. Colombani, R. M. Diamond, and S. S. Stephens
Triaxial Shapes in Light La Nuclei
LBL-3483, March 1975
Phys. Letters 56B, 453 (1975)

BUTLER, P. A. (See Guidry, M. W., LBL-4038)

BUTLER, P. A. (See Ward, D., LBL-4375)

BUTLER, P. A. (See Colombani, P., LBL-5027)

BUTLER, P. A. (See Lee, I. Y., LBL-5031)

CAUVIN, B. (See Moretto, L. G., LBL-4362)

CAVELL, Ronald G.
Core Photoelectron Spectroscopy of Some Acetylenic Molecules
LBL-2941, March 1974
J. Electron Spectroscopy and Related Phenomena 6, 281 (1975).

CAVELL, Ronald G.
Core Photoelectron Spectroscopy of Some Volatile Phosphorus Halides
LBL-4095, May 1975
Inorg. Chem. 14, 2830 (1975)

CERNY, Joseph (See Jelley, N. A., LBL-3414)

CERNY, Joseph (See Wilcox, K. H., LBL-4089)

CERNY, Joseph (See Weisenmiller, R. B., LBL-4304)

CERNY, Joseph (See Ashery, D., LBL-4315)

CERNY, Joseph (See Vieira, D. J., LBL-4321)

CERNY, Joseph (See Wozniak, G. J., LBL-4368)

CERNY, Joseph
Studies of Exotic Nuclei
LBL-5054, May 1976
3rd International Conference on Nuclei Far from Stability, Cargese, Corsica, Italy, May 19-23, 1976

CHARLTON, L. A. (See Kunz, P. D., LBL-4345)

CHARLTON, L. A.
Finite Range Evaluation of (p-d, d-t) with Momentum Space Techniques
LBL-4356, January 1976
Phys. Rev. C

CHARLTON, L. A. (See Pruess, K., LBL-5008)

CHARLTON, L. A. (See Glendenning, N. K., LBL-5009)

CHASE, L. F., Jr. (See Meyerhof, W. E., LBL-4078)

CHINTALAPUDI, S. (See Birchall, J., LBL-4054)

CHU, S. Y., E. R. Marshalek, P. Ring, J. Krumlinde, and J. O. Rasmussen
Test of Many-Body Methods on an Exactly Soluble Model with Backbending and Gaples Superconductivity
LBL-4021, May 1975
Phys. Rev. C 12, 1017 (1975)

CLARK, D. J. (See Bex, L., LBL-3433)

CLARK, D. J. (See Bex, L., LBL-4075)

CLARK, D. J. (See Burleigh, R. J., LBL-4085)

CLARK, D. J. (See Burleigh, R. J., LBL-4086)

CLARK, D. J. (See Burleigh, R. J., LBL-4086)

CLARK, David J.
Conference Summary
LBL-4348, October 1975
International Conference on Heavy Ion Sources, Gatlingburg, TN, October 27-30, 1975

CLINE, D. (See Colombani, P., LBL-5027)

CLINE, D. (See Lee, I. Y., LBL-5031)

COLOMBANI, P. (See Ward, D., LBL-3446)

COLOMBANI, P. (See Banaschik, M. V., LBL-3456)

COLOMBANI, P. (See Butler, P. A., LBL-3483)

COLOMBANI, P. (See Guidry, M. W., LBL-4038)

COLOMBANI, P. (See Simon, R. S. LBL-4313)

COLOMBANI, P. (See Ward, D., LBL-4375)

COLOMBANI, P., P. A. Butler, I. Y. Lee, D. Cline, R. M. Diamond, F. S. Stephens, and D. Ward
Subcoulomb Fission Induced by Xe and Kr Ions
LBL-5027, May 1976

COLOMBANI, P. (See Lee, I. Y., LBL-5031)

CONZETT, H. E. (See Seiler, F. LBL-3496)

CONZETT, H. E. (See Rad. F. N. LBL-4040)

CONZETT, H. E. (See Roy, R. LBL-4041)

CONZETT, H. E., W. Dahme, Ch. Leemann, J. A. Macdonald, and J. P. Meulders
The Vector Analyzing Power in $\vec{d}$-^{4}He Elastic Scattering Between 15 and 45 MeV
LBL-4042, June 1975
4th International Symposium on Polarization Phenomena in Nuclear Reactions, Zürich, Switzerland, August 25-29, 1975

CONZETT, H. E. (See Seiler, F., LBL-4043)

CONZETT, H. E., F. Seiler, F. N. Rad, R. Roy, and R. M. Larimer
Measurement of the Vector Analyzing Power Near the Value $A_y \simeq 1.0$ in $\vec{d}$-^{4}He Elastic Scattering
LBL-4044, June 1975
4th International Symposium on Polarization Phenomena in Nuclear Reactions, Zürich, Switzerland, August 25-29, 1975

CONZETT, H. E. (See Seiler, F., LBL-4045)

CONZETT, H. E. (See Seiler, F., LBL-4047)

CONZETT, H. E. (See Seiler, F., LBL-4048)

CONZETT, H. E., W. Dahme, R. M. Larimer, Ch. Leemann, and J. S. C. McKee
The Vector Analyzing Power in Elastic Deuteron-Deuteron Scattering Between 20 and 40 MeV
LBL-4049, June 1975
4th International Symposium on Polarization Phenomena in Nuclear Reactions, Zürich, Switzerland, August 25-29, 1975

CONZETT, H. E., J. S. C. McKee, R. M. Larimer, and Ch. Leemann
The Vector Analyzing Power in the $^2H(\vec{d},p)^3H$ Reaction at 30 MeV
LBL-4050, June 1975
4th International Symposium on Polarization Phenomena in Nuclear Reactions, Zürich, Switzerland, August 25-29, 1975

CONZETT, H. E., R. M. Larimer, F. N. Rad, R. Roy, and F. Seiler
The Vector Analyzing Power in the $^2H(\vec{d},p)^3H$ Reaction Between 15 and 25 MeV
LBL-4051, June 1975
4th International Symposium on Polarization Phenomena in Nuclear Reactions, Zürich, Switzerland, August 24-29, 1975

CONZETT, H. E. (See Roy, R., LBL-4052)

CONZETT, H. E. (See Roy R., LBL-4053)

CONZETT, H. E. (See Birchall, J., LBL-4054)

CONZETT, H. E.
Polarization Symmetries in Direct Reactions: $^3He(t,d)^4He$ and $^2H(\vec{d},p)^3H$
LBL-4087, August 1975
4th International Symposium on Polarization Phenomena in Nuclear Reactions, Zürich, Switzerland, August 25-29 (1975)

CONZETT, H. E. (See Rad, R. N., LBL-4091)

CONZETT, H. E.
Polarization Phenomena in Few Body Systems
LBL-4351, December 1975
VII International Conference on Few-Body Problems in Nuclear and Particle Physics, Delhi, India, December 29, 1975 - January 3, 1976

DAHME, W. (See Conzett, H. E., LBL-4042)

DAHME, W. (See Conzett, H. E., LBL-4049)

de BOER, J. (See Grosse, E., LBL-4037)

DELIC, George
Optical Model Analyses of N+C and C+C Elastic Scattering
LBL-3492, March 1975
Phys. Rev. Letters 34, 1469 (1975)

DELIC, George
Computing the Finite Range Distorted-Wave Approximation for $^{11}B(^{16}O,^{15}N)^{12}C$
LBL-4343, November 1975
Phys. Rev. Letters 36, 569 (1976)

DELIC, George and Dieter Kurath
Finite Range Distorted Waves Born Approximation Calculations for $^{13}C(^3He,^6He)^{10}C$
LBL-4364, January 1976
Phys. Rev. C

DELIC, G. (See Pruess, K., LBL-5008)

DELIC, G. (See Glendenning, N. K., LBL-5009)

DER MATEOSIAN, E. (See Rezanka, I., LBL-2965)

DIAMOND, R. M. (See Newton, J. O., LBL-2333)

DIAMOND, R. M. (See Ward, D., LBL-3446)

DIAMOND, R. M. (See Bucher, J. J., LBL-3453)

DIAMOND, R. M. (See Banaschik, M. V., LBL-3456)

DIAMOND, R. M. (See Butler, P. A., LBL-3483)

DIAMOND, R. M. (See Grosse, E., LBL-4037)

DIAMOND, R. M. (See Guidry, M. W., LBL-4038)

DIAMOND, R. M. (See Ward, D., LBL-4375)

DIAMOND, R. M. (See Colombani, P. LBL-5027)

DIAMOND, R. M. (See Lee, I. Y., LBL-5031)

DIAMOND, R. M.
Continuum Gamma Rays Following (HI,xnγ) Reactions
LBL-4081, August 1975
Eighth Summer School on Nuclear Physics, Mikotajki, Poland, August 24-September 6, 1975

DIAMOND, R. M. (See Simon, R. S. LBL-4313)

DONANGELO, R. (See Kawakami, H., LBL-4303)

DONANGELO, R., M. W. Guidry, J. P. Boisson, and J. O. Rasmussen
The Classical-Limit S-Matrix for Coulomb Excitation
LBL-4347 Rev., June 1976

DONANGELO, R. (See Guidry, M. W., LBL-4357)

EGGERS, R. C., W. S. Ribbe, and J. O. Rasmussen
Argon Ion Reaction Studies on Tantalum and Gold Near Coulomb Barrier Energies
LBL-4097, August 1975
Nuclear Physics 56A, 455 (1976)

EICHLER, R. (See Guidry, M. W., LBL-4038)

EICHLER, E. (See Lee, I. Y., LBL-5031)

EJIRI, H. (See Anholt, R., LBL-4359)

ELLSWORTH, C. E. (See Bex, L., LBL-3433)

ELLSWORTH, C. E. (See Bex, L., LBL-4075)

ESTRELLA, R. M. (See Bex, L., LBL-4075)

FINK, R. W. (See Wood, J. L., LBL-4350)

FLIESSBACH, T. and P. Manakos
Alpha-Spectroscopic Factors for Light Nuclei
LBL-4094, August 1975
Nucl. Phys. A

FLIESSBACH, T., H. J. Mang, and J. O. Rasmussen
Normalized Shell Model Alpha Decay Theory Applied to Unfavored Decay
LBL-4335, October 1975
Phys. Rev. C 13, 1318 (1976)

FLOCARD, H. (See Błocki, J., LBL-5016)

FLOOD, W. S. (See Burleigh, R. J., LBL-4085)

FOWLER, M. M. (See Thompson, S. G., LBL-2940)

FOWLER, Malcolm M. and Richard G. Jared
A Gas Ionization Counter for P article Identification
LBL-3435, October 1974
Nucl. Instr. Methods 124, 341 (1975)

FOWLER, M. M. (See Otto, R. J., LBL-4322)

FRAENKEL, Z. (See Moretto, L. G., LBL-4084)

GALIN, J. (See Thompson, S. G., LBL-2940)

GALIN, J. (See Moretto, L. G., LBL-3444)

GALIN, J., L. G. Moretto, R. Babinet, R. Schmitt, R. Jared, and S. G. Thompson
Evidence of Incomplete Relaxation in the Reaction Ag+^{40}Ar at 288 and 340 MeV Bombarding Energies
LBL-4064, July 1975
Nucl. Phys. A255, 472 (1975)

GALIN, J. (See Babinet, R., LBL-4080)

GALIN, J. (See Moretto, L. G., LBL-4084)

GATTI, R. C. (See Thompson, S. G., LBL-2940)

GAVIN, Basil
Anode Sputtering Characteristics of the Berkeley 2.5 MV Source
LBL-4291, October 1975
IEEE Conference on Plasma Science, Gatlinburg, TN., October 27-30, 1975

GHIORSO, Albert
The Berkeley New Element Program
LBL-4346, September 1975
International Summer School Seminar on Reactions of Heavy Ions with Nuclei and Synthesis of New Elements, Dubna, Moscow, USSR, September 3-October 4, 1975

GLASGOW, L. R. (See Burleigh, R. J., LBL-4086)

GLÄSSEL, P. (See Moretto, L. G., LBL-4362)

GLENDENNING, N. K.
Classical and Quantum Mechanical Descriptions of Heavy-Ion Interactions
LBL-2905, June 1974
Invited paper for the International Conference on Reactions Between Complex Nuclei, Nashville, Tennessee, June 10-14, 1974

GLENDENNING, N. K.
Interplay of Classical and Quantal Description of Heavy-Ion Interactions
LBL-2905 Rev., June 1974
Rev. Mod. Phys. 47, 659 (1975)

GLENDENNING, N. K. (See Scott, D. K., LBL-3415)

GLENDENNING, Norman K. and Georg Wolschin
Enhancement of Forward-Angle Cross Sections in Heavy-Ion Reactions Because of Projectile Excitation
LBL-3472, 1975
Phys. Rev. Letts. 34, 1642 (1975)

GLENDENNING, Norman K.
Tables of Nuclear Sturcture Amplitudes for Two-Nucleon Transfer Involvinb Light Nuclides ($a \leq 4$)
LBL-3490, March 1975
Nuclear Data Tables 16, 1 (1975)

GLENDENNING, Norman K. and Georg Wolschin
Physical Basis for Enhanced Forward Cross Sections in Heavy Ion Reactions
LBL-4334, October 1975
Phys. Rev. Letters 36, 1532 (1976)

GLENDENNING, Norman K. and Georg Wolschin
Two-Particle Transfer Contributions to Elastic and Inelastic Heavy Ion Scattering
LBL-4341, November 1975
Nucl. Phys. A

GLENDENNING, Norman K. and Georg Wolschin
Physical Basis for Large Forward Cross Sections in $^{60}Ni(^{18}O,^{16}O)$ Reaction
LBL-5007, March 1976
Symposium of Macroscopic Features of Heavy Ion Collisions, Argonne, IL, April 1-3, 1976

GLENDENNING, N. K. (See Pruess, K., LBL-5008)

GLENDENNING, N. K., L. A. Charlton, G. Delic, and M. A. Nagarajan
A New Recoil Effect in Nucleon Transfer Reactions between Heavy Ions
LBL-5009, March 1976
Symposium on Macroscopic Features of Heavy Ion Collisions, Argonne, IL., April 1-3, 1976

GOTH, G. W. (See Ashery, D., LBL-4315)

GOUGH, R. A. (See Bex, L., LBL-3433)

GOUGH, R. A. (See Bex, L., LBL-4075)

GOUGH, R. A. (See Vieira, D. J., LBL-4321)

GOULDING, F. S. and B. G. Harvey
Identification of Nuclear Particles
LBL-2952, February 1974
Ann. Rev. of Nucl. Sci. 25, 167 (1975)

GROSSE, E., J. de Boer, R. M. Diamond, F. S. Stephens, and P. Tjøm
Coulomb Excitation of High-Spin States in ^{238}U
LBL-4037, June 1975
Phys. Rev. Letters 35, 565 (1975)

GUIDRY, M. W., P. A. Butler, P. Colombani, I. Y. Lee, D. Ward, R. M. Diamond, F. S. Stephens, E. Eichler, N. R. Johnson, and R. Sturm
Reduced Transition Probabilities for High Spin States in ^{232}Th
LBL-4038, January 1976
Nucl. Phys. A

GUIDRY, M. W. (See Donangelo, R., LBL-4347 Rev.)

GUIDRY, M. W., H. Massmann, R. Donangelo, and J. O. Rasmussen
Theory of Coulomb-Nuclear Interference for Heavy-Ion Excitation of Rotational States
LBL-4357, January 1976

GUIDRY, M. W. (See Lee, I. Y., LBL-5031)

GUTBROD, H. H. (See Poskanzer, A. M., LBL-4309 Rev.)

HALBACH, Klaus
A Simple Class of Beam Transport Systems with Optically Axisymmetric Transfer Properties
LBL-5026, May 1976

HALBACH, K. and F. R. Holsinger
Superfish--A Computer Program for Evaluation of Rf Cavities with Cylindrical Symmetry
LBL-5040, June 1976

HARVEY, B. G. (See Goulding, B. G., LBL-2952)

HARVEY, B. G. (See Scott, D. K., LBL-3415)

HARVEY, B. G.
Recent Multinucleon Transfer Experiments with Heavy Ions at Berkeley
LBL-34 87, 1975
Presented at Second International Conf. on Clustering Phenomena in Nuclei, College Park, MD, April 21-25 1975

HARVEY, Bernard G.
Radioactivity
LBL-5030, May 1976
Encyclopedia of Physics

HECKMAN, Harry H. and Peter J. Lindstrom
Coulomb Dissociation of Relativistic ^{12}C and ^{16}O Nuclei
LBL-4380, March 1976
Phys. Rev. Letters

HENDRIE, D. L. (See Yagi, K., LBL-2982)

HENDRIE, D. L. (See Scott, D. K., LBL-3415)

HENDRIE, D. L. (See Scott, D. K., LBL-3445)

HENDRIE, D. L. (See Scott, D. K., LBL-4059)

HENDRIE, D. L. (See Sherman, Joseph D., LBL-4306)

HENDRIE, D. L. (See Maguire, C. F., LBL-4338)

HENDRIE, D. L. (See Buenerd, M., LBL-4372)

HENDRIE, D. L. (See Yagi, K., LBL-4382)

HENDRIE, D. L. (See Stock R., LBL-5041)

HOLLEY, W. R. (See Bex, L., LBL-3433)

HOLLEY, W. R. (See Bex, L., LBL-4075)

HOLSINGER, R. F. (See Halbach, K., LBL-5040)

HUNTER, J. B. (See Thompson, S. G., LBL-2940)

IOANNOU-YANNOU, J. G. (See Anholt, R., LBL-4307 Rev.)

IOANNOU_YANNOU, J. (See Anholt, R. LBL-4359)

JAHNKE, U. (See Scott, D. K., LBL-3415)

JAHNKE, U. (See Scott, D. K., LBL-3445)

JAHNKE, U. (See Buenerd, M. LBL-4372)

JAHNKE, U. (See Yagi, K., LBL-4382)

JAHNKE, U. (See Stock, R., LBL-5041)

JAHN, R., G. J. Wozniak, D. P. Stahel, and Joseph Cerny
The $(\alpha,{}^{2}He)$ Reaction as a Spectroscopic Tool for Investigating High Spin States
LBL-5038, June 1976

JARDINE, L. J. and Shihab-Eldin, A.
Alpha Decay of ^{210}At to Levels in ^{206}Bi
LBL-2943, October 1974
Nucl. Phys. A224, 34 (1975)

JARDINE, L. J. and A. A. Shihab-Eldin
The Electron-Capture Decay of ^{206}Po
LBL-3447, January 1975
Phys. Rev. C 13, 348 (1976)

JARDINE, K. J. (See Shihab-Eldin, LBL-3409)

JARED, R. C. (See Thompson, S. G., LBL-2940)

JARED, Richard G. (See Conway, John LBL-3435)

JARED, R. C. (See Moretto, L. G., LBL-4063)

JARED, R. (See Galin, J., LBL-4064)

JARED, R. (See Babinet, R., LBL-4080)

JARED, R. (See Moretto, L. G., LBL-4084)

JARED, R. (See Moretto, L. G., LBL-4362)

JELLEY, N. A., Cerny, Joseph, Stahel, D. P. and Wilcox, K. H.
Predictions of the Masses of Very Neutron-Excess Light Nuclei
LBL-3414, November 1974
Phys. Rev. C11, 2049 (1975)

JELLEY, N. A. (See Wilcox, K. H., LBL-4089)

JELLEY, N. A. (See Weisenmiller, R. B. LBL-4303)

JELLEY, N. A. (See Wozniak, G. J., LBL-4368)

JOHNSON, N. R. (See Lee, I. Y., LBL-5031)

JOHNSON, N. R. (See Gukdry, M. W., LBL-4038)

KATARIA, S. S. (See Moretto, L. G., LBL-4063)

KAWAKAMI, H., M. Koike, K. Komura, M. Sakai, N. Yoshikawa, R. Donangelo, and J. O. Rasmussen
Cross Section and Reaction Mechanisms of (p,pxn) Reactions on ^{208}Pb in the 24-52 MeV Range
LBL-4303, August 1975
Nuclear Physics A

KOMURA, K. (See Kawakami, H. LBL-4303)

KOIKE, M. (See Kawakami, H., LBL-4303)

KOLBE, W. (See Church, D. A., LBL-3464)

KRATZ, J. V., J. O. Liljenzin, A. E. Norris, and G. T. Seaborg
Charge- and Mass-Distributions in the Reaction of ^{40}Ar Ions with ^{238}U
LBL-4339, November 1975
Phys. Rev. C 13, 2347 (1976)

KRAUS, L. (See Yagi, K., LBL-2982)

KRAUS, L. (See Scott, D. K., LBL-3415)

KRAUS, L. (See Scott, D. K., LBL-3445)

KRAUS, L. (See Scott, D. K., LBL-4059)

KRUMLINDE, J. (See Chu, S. Y., LBL-4021)

KUNZ, P. D. and L. A. Charlton
Finite-Range Effects in Multi-Step (p-d, d-n) Reactions
LBL-4345, December 1975
Phys. Letters

KURATH, Dieter (See Delic, George LBL-4364)

LADENBAUER-BELLIS, I. M. (See Rezanka, I., LBL-2965)

LARIMER, R. M. (See Conzett, H. E., LBL-4044)

LARIMER, R. M. (See Conzett, H. E., LBL-4049)

LARIMER, R. M. (See Conzett, H. E., LBL-4050)

LARIMER, R. M. (See Conzett, H. E., LBL-4051)

LARMIER, R. M. (See Roy, R., LBL-4052)

LARIMER, R. M. (See Roy, R., LBL-4053)

LARIMER, R. M. (See Birchall, J., LBL-4054)

LARSSON, S. E. (See Randrup, J., LBL-4036)

LAZARUS, S. M. (See Meyerhof, W. E., LBL-4078)

LEE, D. (See Otto, R. J., LBL-4322)

LEE, I. Y. (See Guidry, M. W., LBL-4038)

LEE, I. Y. (See Ward, D., LBL-4375)

LEE, I. Y. (See Colombani, P., LBL-5027)

LEE, I. Y., D. Cline, R. S. Simon, P. A. Butler, P. Colombani, M. W. Guidry, F. S. Stephens, R. M. Diamond, N. R. Johnson, and E. Eichler
Coulomb Excitation into the Backbend Region of ^{164}Er
LBL-5031, May 1976

LEEMANN, Ch. (See Conzett, H. E., LBL-4042)

LEEMANN, Ch. (See Conzett, H. E., LBL-4049)

LEEMANN, Ch. (See Conzett, H. E., LBL-4050)

LESER, Herbert Massman
Application of Generalized Classical Trajectories in Nuclear Physics
LBL-4316, September 1975
Ph.D. Thesis

LICHTNER, P. (See Pruess, K., LBL-4381)

LILJENZIN, J. O. (See Kratz, J. V., LBL-4339)

LINDSTROM, Peter J. (See Heckman, Harry H. LBL-4380)

LIPPERHEIDE, R.
Schrödinger Equation for Scattering with Energy Loss
LBL-4333, October 1975
Phys. Rev. Letters

LIPPERHEIDE, R.
Quantal Description of Inelastic Heavy-Ion Scattering
LBL-4336, October 1975
Nuclear Physics A260, 292 (1976)

LITTLE, A. (See Meyerhof, W. E., LBL-4078)

LOW, K. S. (See Yagi, K., LBL-2982)

McKEE, J. S. C. (See Conzett, H. E. LBL-4049)

McKEE, J. S. C. (See Conzett, H. E., LBL-4050)

MACDONALD, J. A. (See Conzett, H. E., LBL-4042)

MAGUIRE, C. F. (See Yagi, K., LBL-2982)

MAGUIRE, C. F. (See Scott, D. K., LBL-3415)

MAGUIRE, C. F. (See Scott, D. K., LBL-3445)

MAGUIRE, C. F. (See Scott, D. K., LBL-4059)

MAGUIRE, C. F., D. L. Hendrie, D. K. Scott, J. Mahoney, and F. Ajzenberg-Selove
Energy Levels of ^{12}N
LBL-4338, October 1975
Phys. Rev. C 13, 933 (1976)

MAGUIRE, C. F. (See Yagi, K., LBL-4382)

MAGUIRE, C. F. (See Stock, R., LBL-5041)

MAHONEY, J. (See Yagi, K., LBL-2982)

MAHONEY, J. (See Scott, D. K., LBL-3415)

MAHONEY, J. (See Scott, D. K., LBL-3445)

MAHONEY, J. (See Scott, D. K., LBL-4059)

MAHONEY, J. (See Maguire, C. F., LBL-4338)

MAHONEY, J. (See Buenerd, M., LBL-4372)

MAHONEY, J. (See Yagi, K., LBL-4382)

MAHONEY, J. (See Stock R., LBL-5041)

MANAKOS, P. (See Fliessbach, T., LBL-4094)

MANG, H. J. (See Fliessbach, T., LBL-4335)

MARSHALEK, E. R., (See Chu, S. Y., LBL-4021)

MASSMANN, Herbert and Rasmussen, John O.
Uniform Semiclassical Orbital Calculations of Heavy Ion Coulomb Excitation
LBL-3440, November 8, 1974
Nucl. Phys. A243, 155 (1975)

MASSMANN, H., P. Ring, and J. O. Rasmussen
Quantum Mechanical and Semiclassical Description of a T wo-Dimensional Fission Model
LBL-4023, May 1975
Phys. Letters 57B, 417 (1975)

MASSMANN, Herbert (See Ring, Peter LBL-4028)

MASSMANN, H. (See Guidry, M. W., LBL-4357)

MENCHACA-ROCHA, A. (See Buenerd, M., LBL-4372)

MERIWETHER, J. R. (See Bex, L., LBL-3433)

MEULDERS, J. P. (See Conzett, H. E., LBL-4042)

MEYERHOF, W. E., T. K. Saylor, S. M. Lazarus, A. Little, B. B. Triplett, L. F. Chase, Jr., and Robert Anholt
Molecular-Orbital K X-Ray Formation in Heavy-Ion Collisions
LBL-4078
Phys. Rev. Letters 32, 1279 (1974)

MEYERHOF, W. E., R. Anholt, T. K. Saylor, and P. D. Bond
K X-Ray Yield from 100 MeV Pb + Pb Collisions
LBL-4079
Phys. Rec. A 11, 1083 (1975)

MEYER-TER-VEHN, J.
Rotational Band-Structures in Transitional Odd-A Nuclei
LBL-3416, September 19, 1974
Phys. Rev. Letters 55B, 273 (1975)

MEYER-TER-VEHN, J.
Collective Model Description of Transitional Odd-A Nuclei I. The Triaxial-Rotor-Plus-Particle Model
LBL-3458, 1975
Nucl. Phys. A249, 111 (1975)

MEYER-TER-VEHN, J.
Collective Model Description of Transitional Odd-A Nuclei II. Comparison with Unique Parity States of Nuclei in the A = 135 and A = 190 Mass Region
LBL-3459, 1975
Nucl. Phys. A249, 141 (1975)

MEYER-TER-VEHN, J. (See Butler, P. A., LBL-3483)

MEYER-TER-VEHN, J. (See Wood, J. L., LBL-4350)

MOLLER, P. (See Randrup, J., LBL-4036)

MORETTO, L. G. (See Thompson, S. G., LBL-2940)

MORETTO, L. G. and J. S. Sventek
A Theoretical Approach to the Problem of Partial Equilibration in Heavy Ion Reactions
LBL-3443, November 1974
Phys. Letters 58B, 26 (1975)

MORETTO, L. G., R. P. Babinet, J. Galin, and S. G. Thompson
Experimental Evidence of a Diffusion Process Associated with the Mass Asymmetry Degree of Freedom in Heavy Ion Reactions
LBL-3444, November 1974
Phys. Letters 58B, 31 (1975)

MORETTO, L. G.
Statistical Emission of Large Fragments: A General Theoretical Approach
LBL-3454, January 1975
Nucl. Phys. A247, 211 (1975)

MORETTO, L. G.
Antipairing Effects in the Collective Nuclear Motion and Their Relevance to the Saddle to Scission Descent in Fission
LBL-3499, 1975
Phys. Letts. 57B, 317 (1975)

MORETTO, L. G., S. S. Kataria, R. C. Jared, R. Schmitt, and S. G. Thompson
Intermediate-Mass Fragments Emitted in the Reaction Ag+^{14}N at 100, 160, 250 MeV Bombarding Energy
LBL-4063, July 1075
Nucl. Phys. A255, 491 (1975)

MORETTO, L. G. (See Galin, J., LBL-4064)

MORETTO, L. G. (See Babinet, R., LBL-4080)

MORETTO, L. G. (See Nardi, E., LBL-4083)

MORETTO, L. G., J. Galin, R. Babinet, Z. Fraenkel, R. Schmitt, R. Jared, and S. G. Thompson
Potential Energy Effects and Diffusion in the Relaxed Components of the Reaction ^{197}Au+^{40}Ar at 288 and 340 MeV Bombarding Energies
LBL-4084, September 1975
Nuclear Physics A259, 173 (1976)

MORETTO, L. G., B. Cauvin, P. Glässel, R. Jared, P. Russo, J. Sventek, and G. Wozniak
Diffusive Phenomena in the Charge and Angular Distributions for the Reaction ^{197}Au+620-MeV ^{86}Kr
LBL-4362, January 1976
Phys. Rev. Letters 36, 1069 (1976)

MORETTO, L. G. and J. S. Sventek
Diffusive Phenomena Reflected in the Charge and Angular Distributions of N, Ne, Ar, Kr Induced Reactions
LBL-5006, March 1976
Symposium on Macroscopic Features of Heavy Ion Collision,ANL, Argonne, Il., April 1-3, 1976

MORETTO, L. G. (See Sventek, J., LBL-5012)

MORRIS, D. (See Bex, L., LBL-3433)

MOULTON, J. (See Babinet, R., LBL-4080)

MYERS, W. D. and H. von Groote
The Nuclear Surface Diffuseness
LBL-4327, October 1975
Phys. Letters 61B, 125 (1976)

MYERS, William D.
The Droplet Model Atomic Mass Predictions
LBL-4332, October 1975
Atomic Data and Nuclear Data Tables

MYERS, Willam D.
Lectures on Geometrical Properties of Nuclei
LBL-4342, November 1975
Eighth Summer School on Nuclear Physics, Mikolajki, Poland, August 24-September 6, 1975

MYERS, W. D. (See Boneh, Y., LBL-4374)

MYERS, W. D. (See Boneh, Y., LBL-4397)

NAGAMIYA, S. (See Anholt, R., LBL-4307 Rev.)

NAGAMIYA, S. (See Anholt, R., LBL-4359)

NAGARAJAN, M. A. (See Glendenning, N. K., LBL-5009)

NARDI, E., L. G. Moretto,and S. G. Thompson
Statistical Decay of Gamma Rays in (n_{th},γ) Reactions
LBL-4083, April 1974
Nuclear Physics A237, 419 (1975)

NEWTON, J. O., F. S. Stephens, and R. M. Diamond
Rotational Bands in the Light Odd-Mass Thallium Nuclei
LBL-2333, January 1974
Nucl. Phys. A236, 225 (1974)

NIFENECKER, H., C. Signarbieux, R. Babinet, and J. Poitou
Neutron and Gamma Emission in Fission
LBL-1950, July 1973
(Third Symposium on the Physics and Chemistry of Fission, Rochester, New York, August 13-17, 1973), Vol. II, 117, (1974)

NILSSON, S. G. (See Randrup, J., LBL-4036)

NITSCHKE, Joachim M.
A High Intensity Heavy-Ion Recoil-Target System
LBL-4387, May 1976

NITSCHKE, Joachim M.
Heavy Ion Spectrometer at the SuperHILAC
LBL-5044, May 1976

NORRIS, A. E. (See Kratz, J. V., LBL-4339)

OLMER, C. (See Buenerd, M. LBL-4372)

OTTO, R. J., M. M. Fowler, D. Lee, and G. T. Seaborg
Mass Yield Distributions in the Reaction of ^{136}Xe Ions with ^{238}U
LBL-4322, October 1975
Phys. Rev. Letters 36, 135 (1976)

PERLMAN, I. (See Artzy, Michal, LBL-2975)

POITOU, J. (See Nifenecker, H. C., LBL-1950)

POMORSKI, K. (See Randrup, J., LBL-4036)

POSKANZER, A. M. (See Zebelman, A. M., LBL-3427)

POSKANZER, A. M., R. G. Sextro, A. M. Zebelman, H. H. Gutbrod, A. Sandoval, and R. Stock
Search for Fragment Emission from Nuclear Shock Waves
LBL-4309 Rev., October 1975
Phys. Rev. Letters 35, 1703 (1975)

PRUESS, K. and P. Lichtner
A New Approach to Antisymmetrization and Rearrangement in Nucleus-Nucleus-Collisions
LBL-4381, March 1976
Nucl. Phys.

PRUESS, K., G. Delic, L. A. Charlton, and N. K. Glendenning
Polarization of Single-Particle States Involved in Heavy Ion Transfer Reactions
LBL-5008, March 1976
Symposium on Macroscopic Features of Heavy Ion Collisions, Argonne, IL., April 1-3, 1976

RAD, F. N. (See Seiler, F., LBL-3496)

RAD, F. N., H. E. Conzett, R. Roy, and F. Seiler
Measurement of the Proton Analyzing Power in the p-d Breakup Reaction
LBL-4040, June 1975
4th International Symposium on Polarization Phenomena in Nuclear Reactions, Zürich, Switzerland, August 25-29, 1975

RAD, F. N. (See Roy, R. LBL-4041)

RAD, F. N. (See Seiler, F., LBL-4043)

RAD, F. N. (See Conzett, H. E. LBL-4044)

RAD, F. N. (See Seiler, F., LBL-4045)

RAD, F. N. (See Seiler, F. LBL-4047)

RAD, F. N. (See Seiler, F. LBL-4048)

RAD, F. N. (See Conzett, H. E., LBL-4051)

RAD, F. N. (See Roy, R., LBL-4052)

RAD, F. N. (See Roy, R., LBL-4053)

RAD, F. N. (See Birchall, J., LBL-4054)

RAD, F. N., H. E. Conzett, R. Roy, and F. Seiler
Polarization Effects in the Final-State Interaction Region of the p-d Breakup Reaction
LBL-4091, August 1975
Phys. Rev. Letters 35, 1134 (1975)

ROY, R. (See Conzett, H. E., LBL-4051)

ROY, R., H. E. Conzett, F. N. Rad, F. Seiler, and R. M. Larimer
Cross-Sections and Vector Analyzing Powers in $\vec{d}$-^{3}He Elastic Scattering Between 15 and 40 MeV
LBL-4052, June 1975
4th International Symposium on Polarization Phenomena in Nuclear Reactions, Zürich, Switzerland, August 24-29, 1975

ROY, R., F. Seiler, H. E. Conzett, F. N. Rad, and R. M. Larimer
Cross-Section and Vector Analyzing Powers in the ^{3}He($\vec{d}$,p)^{4}He Reaction Between 15 and 40 MeV
LBL-4053, June 1975
4th International Symposium on Polarization Phenomena in Nuclear Reactions, Zurich, Switzerland, August 25-29, 1975

ROY, R. (See Rad, F. N., LBL-4091)

RUSSO, P. (See Moretto, L. G., LBL-4362)

SAKAI, M. (See Kawakami, H., LBL-4303)

SANDOVAL, A. (See Poskanzer, A. M., LBL-4309 Rev.)

SAYLOR, T. K. (See Anholt, R., LBL-4066)

SAYLOR, T. K. (See Meyerhof, W. E., LBL-4078)

SAYLOR, T. K. (See Meyerhof, W. E., LBL-4079)

SAYLOR, T. K. (See Anholt, R., LBL-4360)

SCHMITT, R. (See Moretto, L. G., LBL-4063)

SCHMITT, R. (See Moretto, L. G., LBL-4084)

SCHMITT, R. (See Galin, J., LBL-4064)

SCHNEIDER, W. F. W. (See Stock, R., LBL-5041)

SCOTT, D. K. (See Yagi, K., LBL-2982)

SCOTT, D. K., B. G. Harvey, D. L. Hendrie, U. Jahnke, L. Kraus, C. F. Maguire, J. Mahoney, Y. Terrien, K. Yagi, and N. K. Glendenning
The Interference Between Direct and Indirect Modes in Two-Nucleon Transfer Reactions with Heavy-Ions
LBL-3415, January 1975
Phys. Rev. Letters 34, 895 (1975)

SCOTT, D. K., D. L. Hendrie, U. Jahnke, L. Kraus, C. F. Maguire, J. Mahoney, Y. Terrien, and K. Yagi
The Energy Variation of Multinucleon Transfer Reactions with Heavy-Ions
LBL-3445, July 1075
Phys. Rev. Letters

SCOTT, David K.
New Aspects of High Energy Heavy-Ion Transfer Reactions
LBL-3495, March 1973
(Presented at the International Conference on Cluster Structure of Nuclei and Transfer Reactions Induced by Heavy Ions, Tokyo, Japan, March 17-22, 1975)

SCOTT, D. K., D. L. Hendrie, L. Kraus, C. F. Maguire, J. Mahoney, Y. Terrien, and K. Yagi
Semiclassical and Quantum Mechanical Comparison of One and Two Nucleon Transfer
LBL-4059, May 1975
Phys. Rev. Letters 36, 226 (1976)

SCOTT, D. K. (See Maguire, C. F., LBL-4338)

SCOTT, D. K. (See Buenerd, M., LBL-4372)

SCOTT, D. K. (See Yagi, K., LBL-4382)

SCOTT, D. K. (See Stock R., LBL-5041)

SEABORG, Glenn T.
The Search for New Elements: The Projects of Today in a Larger Perspective
LBL-3423
Physica Scripta 10A, 5 (1974)

SEABORG, G. T. (See Otto, R. J., LBL-4322)

SEABORG, G. T. (See Kratz, J. V., LBL-4339)

SEILER, F., F. N. Rad and H. E. Conzett
Extreme Values $A_y = \pm 1$ of the Analyzing Power for Spin-1 Polarization
LBL-3496, September 1975
Phys. Rev. Letters

SEILER, F. (See Rad, F. N., LBL-4040)

SEILER, F. (See Roy, R., LBL-4041)

SEILER, F., F. N. Rad, and H. E. Conzett
Extreme Values of the Analyzing Power for Spin-1 Polarization
LBL-4043, June 1975
4th International Symposium on Polarization Phenomena in Nuclear Reactions, Zürich, Switzerland, August 25-29, 1975

SEILER, F. (See Conzett, H. E., LBL-4044)

SEILER, F., H. E. Conzett, F. N. Rad, and R. Roy
Points of Maximum Polarization Efficiency in $^{4}He(\vec{d},d)^{4}He$
LBL-4045, June 1975
4th International Symposium on Polarization Phenomena in Nuclear Reactions, Zürich, Switzerland, August 25-29, 1975

SEILER, F.
Maximum Tensor Analyzing Power $A_{yy} = 1$ in the $^{3}He(\vec{d},p)^{4}He$ Reaction
LBL-4046, June 1975
4th International Symposium on Polarization Phenomena in Nuclear Reactions, Zürich, Switzerland, August 25-29, 1975
Phys. Letters 61B, 144 (1976)

SEILER, F., R. Roy, H. E. Conzett, and F. N. Rad
Points of Maximum Analyzing Power in the $^{3}He(\vec{d},p)^{4}He$ Reaction
LBL-4047, June 1975
4th International Symposium on Polarization Phenomena in Nuclear Reactions, Zürich, Switzerland, August 25-29, 1975

SEILER, F., F. N. Rad, H. E. Conzett, and R. Roy
Extreme Values of the Analyzing Power in the $^{6}Li(\vec{d},\alpha)^{4}He$ Reaction
LBL-4048, June 1975
4th International Symposium on Polarization Phenomena in Nuclear Reactions, Zürich, Switzerland, August 25-29, 1975

SEILER, F. (See Conzett, H. E., LBL-4051)

SEILER, F. (See Roy, R., LBL-4052)

SEILER, F. (See Roy, R., LBL-4053)

SEILER, F. (See Rad, F. N., LBL-4091)

SEILER, F.
Analysis of Reactions Induced by Polarized Particles
LBL-4096, August 1975
4th International Symposium on Polarization Phenomena in Nuclear Reactions, Zürich, Switzerland, August 25-29, 1975

SEXTRO, R. G. (See Zebelman, A. M., LBL-3427)

SEXTRO, R. G. (See Poskanzer, A. M., LBL-4309 Rev.)

SHERMAN, Joseph D., D. L. Hendrie, and M. S. Zisman
Spectroscopy of the $(\alpha,2\alpha)$ Reaction at E_{α} = 90 MeV
LBL-4306, September 1975
Phys. Rev. C 13, 20 (1976)

SHERMAN, D. F. (See Vieira, D. J., LBL-4321)

SHIBATA, T. (See Anholt, R., LBL-4359)

SHIHAB-ELDIN, A. (See Jardine, L. J., LBL-2943)

SHIHAB-ELDIN, A. A., L. J. Jardine, and J. O. Rasmussen
Extension of Relative Alpha Decay Rate Theory to Spherical Odd-Odd Nuclei (^{210}At)
LBL-3409, September 1974
Nucl. Phys. A244, 435 (1975)

SHIHAB-ELDIN, A. A. (See Jardine, L. J., LBL-3447)

SIGNARBIEUX, C. (See Nifenecker, H. C., LBL-1950)

SIMON, R. S. (See Banaschik, M. V., LBL-3456)

SIMON, R. S., M. V. Banaschik, P. Colombani, D. P. Soroka, F. S. Stephens, and R. M. Diamond
Moments-of-Inertia in ^{162}Yb at Very High Spins
LBL-4313, September 1975
Phys, Rev. Letters 36, 359 (1976)

SIMON, R. S. (See Ward, D., LBL-4375)

SIMON, R. S. (See Lee, I. Y., LBL-5031)

SOBICZEWSKI, A. (See Randrup, J. LBL-4036)

SOROKA, D. P. (See Banaschik, M. V., LBL-3456)

SOROKA, D. P. (See Simon, R. S., LBL-4313)

STAHEL, D. P. (See Jelley, N. A., LBL-3414)

STAHEL, D. P. (See Wozniak, G. J., LBL-4368)

STEPHENS, F. S. (See Newton, J. O., LBL-2333)

STEPHENS, F. S.
Coriolis Effects and Rotation Alignment in Nuclei
LBL-2352, January 1974
Rev. Mod. Phys. 47, 43 (1975)

STEPHENS, F. S. (See Ward, D., LBL-3446)

STEPHENS, F. S. (See Banaschik, M. V., LBL-3456)

STEPHENS, F. S. (See Butler, P. A., LBL-3483)

STEPHENS, F. S. (See Grosse, E., LBL-4037)

STEPHENS, F. S. (See Guidry, M. W., LBL-4038)

STEPHENS, F. S.
Experimental Status of High-Spin States
LBL-4311, September 1975
Conference on Highly Excited States of Nuclei, Jülich, Germany, September 22-27, 1975

STEPHENS, F. S. (See Simon, F. S., LBL-4313)

STEPHENS, F. S. (See Ward, D., LBL-4375)

STEPHENS, F. S. (See Colombani, P., LBL-5027)

STEPHANS, F. S. (See Lee, I. Y., LBL-5031)

STEPHENS, F. S.
Nuclei at High Angular Momenta
LBL-5034, June 1976

STOCK, R. (See Poskanzer, A. M., LBL-4309 Rev.)

STOCK, R., U. Jahnke, D. L. Hendrie, J. Mahoney, C. F. Maguire, W. F. W. Schneider, D. K. Scott, and G. Wolschin
On the Contribution of Alpha Cluster Exchanges to Elastic and Inelastic $^{16}O+^{20}Ne$ Scattering
LBL-5041, June 1976

STURM, R. (See Guidry, M. W., LBL-4038)

SVENTEK, J. S. (See Moretto, L. G., LBL-3443)

SVENTEK, J. (See Moretto, L. G., LBL-4362)

SVENTEK, J. S. (See Moretto, L. G., LBL-5006)

SVENTEK, J. S. and L. G. Moretto
Diffusion Model Predict-on for Heavier Systems: The Reaction ^{197}Au + 620 MeV ^{86}Kr
LBL-5012, April 1976

SWIATECKI, W. J. (See Błocki, J., LBL-5014)

TAMURA, T. (See Yagi, K., LBL-2982)

TERRIEN, Y. (See Yagi, K., LBL-2982)

TERRIEN, Y., (See Scott, D. K., LBL-3415)

TERRIEN, Y. (See Scott, D. K., LBL-3445)

TERRIEN, Y. (See Scott, D. K., LBL-4059)

THOMPSON, S. G., L. G. Moretto, R. C. Jared, R. P. Babinet, J. Galin, M. M. Fowler, R. C. Gatti, and J. B. Hunter
Macroscopic Aspects of Heavy Ion Reactions
LBL-2940, June, 1974
(Presented at the Nobel Symposium on Superheavy Elements, Ronneby Brunn, Sweden, June 11-15)
Physica Scripta 10A, 36 (1974)

THOMPSON, S. G. (See Moretto, L. G., LBL-3444)

THOMPSON, S. G. (See Moretto, L. G., LBL-4063)

THOMPSON, S. G. (See Galin, J., LBL-4064)

THOMPSON, S. G. (See Babinet, R., LBL-4080)

THOMPSON, S. G. (See Nardi, E., LBL-4083)

THOMPSON, S. G. (See Moretto, L. G., LBL-4084)

TJØM, P. (See Grosse, E., LBL-4037)

TRIPLETT, B. B. (See Meyerhof, W. E., LBL-4078)

TSANG, C. F. (See Błocki, J., LBL-5014)

UDAGAWA, T. (See Yagi, K., LBL-2982)

von GROOTE, H. (See Meyers, W. D., LBL-4327)

VIEIRA, D. J., D. F. Sherman, M. S. Zisman, R. A. Gough, and Joseph Cerny
Extension of the T_Z = -3.2 Beta-Delayed Proton Precursor Series to ^{57}Zn
LBL-4321, November 1975
Phys. Letters 60B, 261 (1976)

VIOLA, V. E., Jr. (See Zebelman, A. M., LBL-3427)

WARD, D., H. Bertschat, P. A. Butler, P. Colombani, R. M. Diamond, and F. S. Stephens
High-Spin States in $^{127,129}La$; A Test of Backbending in the Even Ba and Ce Nuclei
LBL-3446, December 1974
Phys. Rev. 56B, 139 (1975)

WARD, D. (See Butler, P. A., LBL-3483)

VI.

AUTHOR INDEX

AUTHOR INDEX

☆GPO 790-232-1977